Development of THz Coherent Sources Using Quantum Cascade Lasers

S. Shiba[1,2], **N. Sekine**[2], **Y. Irimajiri**[2], **I. Hosako**[2], **T. Koyama**[2,3], **H. Maezawa**[3], **and S. Yamamoto**[1]

[1]Department of Physics, Faculty of Science, The University of Tokyo, Japan
[2]National Institute of Information and Communications Technology, Japan
[3]Solar-Terrestrial Environment Laboratory, Nagoya University, Japan

Abstract— We are developing quantum cascade lasers (QCLs) and superconductive hot-electron bolometer (HEB) mixers for a THz heterodyne receiver system. We have successfully fabricated QCLs which can be operated in a continuous oscillation mode at the frequency around 3.1 THz. The QCLs are made of a GaAs/$Al_{0.15}Ga_{0.85}As$ material system using a resonant LO phonon scattering depopulation scheme, and are processed in a metal-metal waveguide with the size of 40 μm wide and 1.5 mm long by using gold-gold thermo compression wafer bonding technique and a dry-etching method. We have also succeeded in operating the quasi-optical HEB mixer at 3.1 THz by using the fabricated QCL as a local oscillator source. We report the current status of our developments, demonstrating possibilities of THz-QCLs for heterodyne sensing applications in various research fields.

1. INTRODUCTION

Quantum cascade laser (QCL) is a promising THz radiation source as a local oscillator for heterodyne receivers because of their high output power and high frequency purity. Furthermore, QCLs have potential for various applications such as security, foods inspection, medical, non-destructive inspection, imaging, and spectroscopic observation of astronomy and atmosphere [1] in the THz region (0.1–10 THz).

In the frequency range from millimeter wave up to ∼2 THz, combination of a solid state oscillator and frequency multiplier chains can be used as a local oscillator for heterodyne receivers. However, this method can no longer provide enough power for the HEB operation above that frequency. The THzQCL is promising solutions for this problem, because it has good spectral purity ($\triangle f/f \sim 10^{-7} \sim 10^{8}$) and enough output power (order of mW) to drive the HEB mixer. For this purpose, the THz QCL has to be operated in the continuous wave mode under the relatively high-temperature operation by liquid nitrogen or Peltier cooling. With these in mind, we are developing the THzQCLs for heterodyne receivers at NICT. So far we have succeeded in fabricating the THzQCL that can be operated in the continuous wave (CW) mode at 3 THz, measuring its oscillation spectrum, and evaluating a performance of the HEB mixer receiver combined with the THzQCL.

2. FABRICATION OF QCL

In this study, we employ the waveguide structure of metal-metal type for THzQCL, which has a low threshold (low consumption power). The output power is expected to be an order of 10 mW, which is lower than the SISP (semi-insulation surface plasmon) type. However, the required power for the HEB mixer is an order of 100 nW [2]. Even if the beam splitter coupling efficiency is 10% or less, necessary power is about 10 μW. Hence, the output power from the above type THzQCLs should practically be enough for driving the HEB mixer, even if we consider various losses due to imperfect optical alignments.

The design of the QC structure is referred to the GaAs/$Al_{0.15}Ga_{0.85}As$ resonant LO phonon scattering scheme, which achieved the CW operation up to 117 K at 3.0 THz [3, 4]. The thickness of each layers are **4.9**/7.9/**2.5**/6.6/**4.1**/15.6/**3.3**/9 (nm) (bold fonts represent $Al_{0.15}Ga_{0.85}As$). The THz-QCLs are fabricated in Photonic Device Lab. of NICT. First, we grow 178 periods of the QC structure about 10 μm thick on a semi insulating GaAs substrate by MBE, and confirm that the error is less than 1% from the design by X ray diffraction For metal-metal waveguide structure, we deposit a 350 nm thick gold film on this epi-wafer and the n-GaAs substrate, and bond them by using the gold-gold thermo compression wafer bonding method. After removing the substrate of the epi-wafer side, we fabricate a Fabry-Perot resonator whose size is 40 μm in width and 1.5 mm in length by using a dry etching process. Finally we wrap the n-GaAs substrate down to about 180 μm thickness to improve thermal conduction. Figure 1 shows a picture of the device, where the side surface is etched almost vertically.

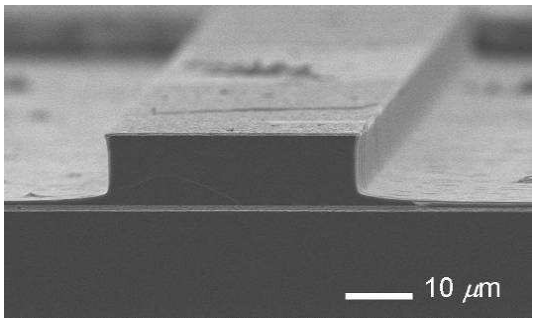

Figure 1: SEM view of the device cross section.

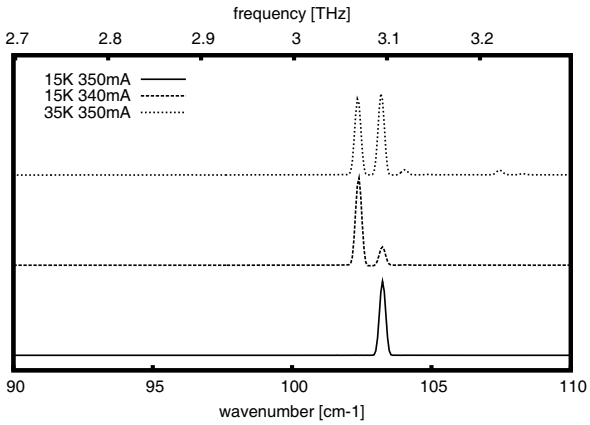

Figure 2: Spectrum of the THz-QCL measured at different operation conditions.

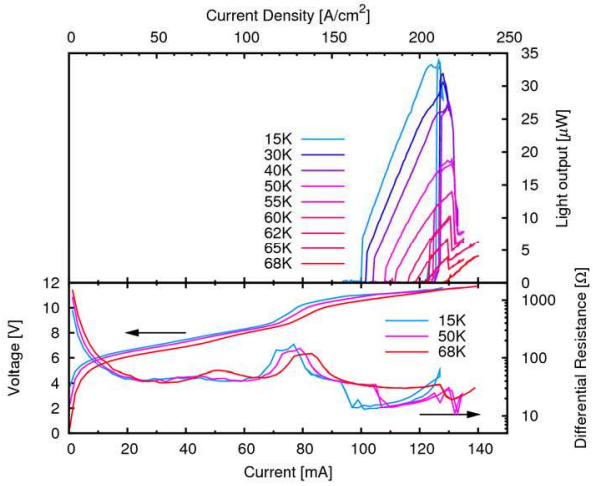

Figure 3: IVL characteristics and temperature performance of THz-QCL.

3. CHARACTERIZATION OF QCLS

The fabricated QCL is then fixed on a chip carrier using Au-Sn eutectic alloy, and is wirebonded with $\phi 18\,\mu$m gold wires. The device is cooled in a flowtype liquid helium dewar, where the temperature is controlled by a heater. The output from the QCL is detected by a liquid-helium-cooled Ge bolometer or a Pyro electric detector. The QCL is operated by a CW driver. The output power is modulated by an optical chopper and is lock-in detected. Prior to the measurements, the optical alignment is tuned as much as possible with the aid of the He-Ne laser optics in cooled conditions Figure 3 shows the I-V, I-L, and differential resistance characteristics of the QCL measured under various heat-sink temperatures. This device has achieved the maximum output power of about 30 μW. Both the threshold current density and output power are relatively low in comparison with the results given in the earlier studies [3, 4], which may come from insufficient optimization of doping density in our case. It should be noted that the laser oscillation threshold seems fairly higher than differential resistance jump (147 A/cm^2). Hence there is a possibility that a low-level output power which is undetectable with the present detection system may come out even below the oscillation threshold down to the differential resistance jump position. The consuming power of this device is about 1 W, and the heat sink temperature during the CW operation is about 15 K. The I-L curve exhibits hysteresis; it differs between increasing and decreasing bias current. The maximum operating temperature is 74 K, and the characteristic temperature T_0 is 14 K.

We measure the QCL spectrum using the Fourier transform spectrometer. Figure 2 shows examples of the obtained spectra. The oscillating frequencies for the main modes are 3.07 THz and 3.09 THz, which are close to the designed frequency. The oscillating frequency can be changed by varying the operating temperature or the bias current. Although the frequency resolution of FTIR is about 3 GHz, we can actually see the change by determining the center frequency

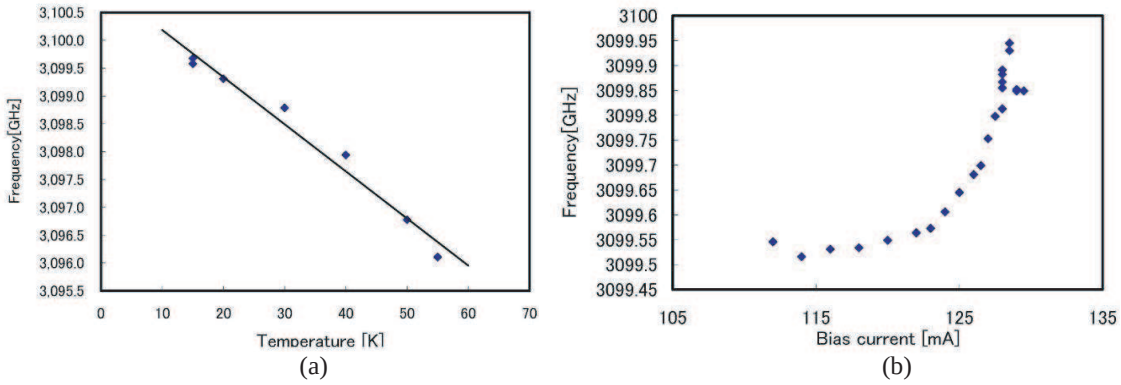

Figure 4: Oscillation frequency of the same Fabry-Perot mode as a function of the (a) operation temperature and (b) bias current.

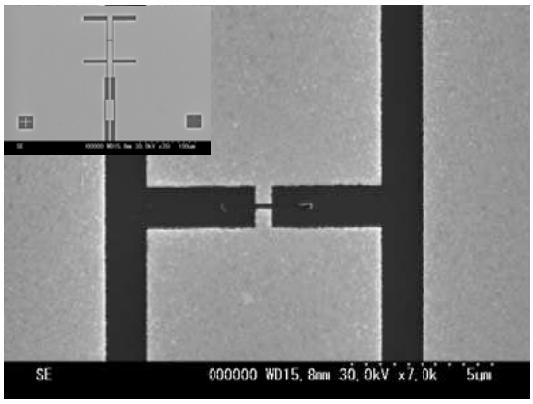

Figure 5: Quasi optical HEB mixer structure.

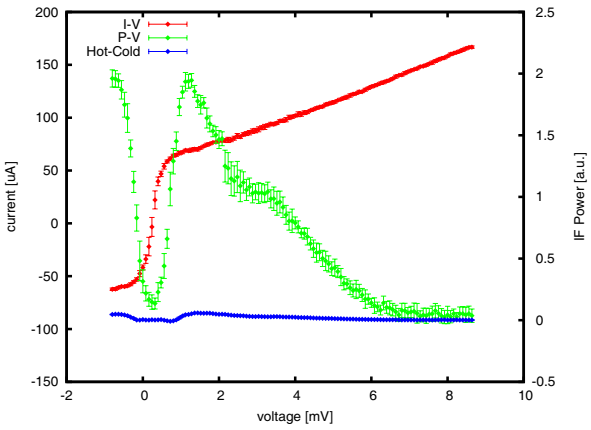

Figure 6: HEB mixer IV characteristics.

of the spectrum carefully through the Gaussian fit (Figure 4). Tuning sensitivities by the bias current and the operation temperature are roughly estimated to be 30 MHz/mA and 90 MHz/K, respectively, although the dependences on the bias current and the operation temperature are not linear. This frequency variation is caused by change of refractive index or cavity length by temperature difference [5, 6]. We also see the mode hopping during the temperature and bias tuning.

4. COMBINATION WITH HEB MIXER

The output power of the THz-QCL is fed into the HEB mixer, where the HEB mixer is mounted on the different dewar cooled by liquid helium. The operating temperature of THz-QCL is around 25 K in the CW mode. Each dewar has a window of high density polyethylene with 1 mm thickness and an infrared filter of Zitex G104. The transmission of these films is estimated to be about 90% on the basis of the FTIR measurement. To focus the QCL beam, an AR coated hyper hemispherical Si lens made of high resistivity silicon (10 kΩ/cm) is attached [7].

The HEB mixer employed utilizes the superconducting NbTiN film with thickness of about 10 nm deposited on the Si substrate. The size of the micro bridge structure is 2 µm in width and 0.3 µm in length. For the coupling with the THz radiation, a quasioptical twin-slot antenna pattern is used. Figure 5 shows a picture of the HEB device fabricated in The University of Tokyo [8]. We use a wire grid as a beam splitter to couple the QCL output to the HEB mixer, where the coupling efficiency is controlled by its tilt angle. Figure 6 shows the I-V characteristics of HEB mixer and the IF output power. The maximum Y-factor of about 0.15 dB is obtained, which corresponds to the receiver noise temperature of $\sim$ 6000 K (DSB). This value is not so good in comparison with the other reports [9–11], because the HEB mixer and the antenna pattern are not designed for the QCL frequency (3 THz) but for the 2.5 THz band. Furthermore we need to optimize the optics between the QCL and the HEB mixer. We expect better performance when these are optimized

reasonably.

5. CONCLUSIONS

We have successfully established the fabrication process of the THz-QCL, which can be operated at 3.1 THz in the continuous wave mode, and have used it as a local oscillator of our THz heterodyne receiver system using the HEB mixer. The receiver noise temperature of about 6000 K is obtained with this system.

ACKNOWLEDGMENT

The authors thank T. Yamakura for providing the quasi-optical HEB mixer elements.

REFERENCES

1. Irimajiri, Y., T. Manabe, S. Ochiai, H. Masuko, T. Yamagami, Y. Saito, N. Izutsu, T. Kawasaki, M. Namiki, and I. Murata, "BSMILES — A balloon-borne superconducting submillimeter-wave limb-emission sounder for stratospheric measurements," *Geosci. Remote Sensing Lett.*, Vol. 3, No. 1, 88–92, 2006.
2. Jiang, L., S. Shiba, T. Shiino, K. Shimbo, N. Sakai, T. Yamakura, Y. Irimajiri, P. G. Ananthasubramanian, H. Maezawa, and S. Yamamoto, "Development of 1.5 THz waveguide NbTiN superconducting hot electron bolometer mixers," *Supercond. Sci. Technol.*, Vol. 23, 045025, 2010.
3. Kumar, S., B. S. Williams, S. Kohen, Q. Hu, and J. L. Reno, "Continuous-wave operation of terahertz quantum-cascade lasers above liquid-nitrogen temperature," *Appl. Phys. Lett.*, Vol. 84, No. 14, 2494–2496, 2004.
4. Williams, B. S., S. Kumar, Q. Hu, and J. L. Reno, "Operation of terahertz quantum-cascade lasers at 164K in pulsed mode and at 117 K in continuous-wave mode," *Opt. Express*, Vol. 13, No. 9, 3331–3339, May 2005.
5. Betz, A. L., R. T. Boreiko, B. S. Williams, S. Kumar, Q. Hu, and J. L. Reno, "Frequency and phase-lock control of a 3 THz quantum cascade laser," *Opt. Lett.*, Vol. 30, No. 14, 1837–1839, 2005.
6. Rabanus, D., U. U. Graf, M. Philipp, O. Ricken, J. Stutzki, B. Vowinkel, M. C. Wiecner, C. Walther, M. Fischer, and J. Faist, "Phase locking of a 1.5 Terahertz quantum cascade laser and use as a local oscillator in a heterodyne HEB receiver," *Opt. Express*, Vol. 17, No. 3, 1159–1168, 2009.
7. Lee, A. W. M., Q. Qin, S. Kumar, B. S. Williams, Q. Hi, and J. L. Reno, "High-power and high-temperature THz quantum-cascade lasers based on lens-coupled metal-metal waveguides," *Opt. Lett.*, Vol. 32, No. 19, 2840–2842, 2007.
8. Yamakura, T., "Development of THz band quasi-optical hot-electron bolometer mixer employing superconducting NbTiN microbridge," dissertation, University of Tsukuba, 2010.
9. Gao, J. R., J. N. Hovenier, Z. Q. Yang, J. J. A. Baselmans, A. Baryshev, M. Hajenius, T. M. Klapwijk, A. J. L. Adam, T. O. Klaassen, B. S. Williams, S. Kumar, Q. Hu, and J. L. Reno, "Terahertz heterodyne receiver based on a quantum cascade laser and superconducting bolometer," *Appl. Phys. Lett.*, Vol. 86, 244104, 2005.
10. Khosropanah, P., W. Zhang, J. N. Hovenier, J. R. Gao, T. M. Klapwijk, M. I. Amanti, G. Scalari, and J. Faist, "3.4 THz heterodyne receiver using a hot electron bolometer and a distributed feedback quantum cascade laser," *J. of Appl. Phys.*, Vol. 104, 113106, 2008.
11. Gao, J. R., M. Hajenius, Z. Q. Yang, J. J. Baselmans, P. Khosropanah, R. Barends, and T. M. Klapwijk, "Terahertz superconducting hot electron bolometr heterodyne receivers," *IEEE Trans. on Appl. Superconductivity*, Vol. 17, No. 2, 2007.

Modeling by FDTD of Some Optical Properties of Photonic Crystals Based on a Nanocomposite of Silver in TiO_2

A. Labbani and A. Benghalia
Laboratoire Hyperfréquences et Semi-conducteurs, Faculté des Sciences de l'ingénieur
Université Mentouri Constantine, Route d'Ain El Bey Constantine 25000, Algérie

Abstract— Using a finite-difference time domain method (FDTD), we investigate photonic band gaps in one-dimensional photonic crystal (PC's) based on nanocomposite of silver and dielectric. To describe the optical properties of silver nanoparticles in TiO_2 matrix of various volume fractions f, we use Maxwell-Garnett theory. In this approach the metallic nano-objets are considered as spherical and very small compared to the wavelength of the incident light. The position and the width of photonic band gaps (PBGs) sensitively depend on the dielectric permittivity of the nanocomposite material and the nanoparticle concentration. Considered effects give new possibilities for manufacturing photonic crystals.

1. INTRODUCTION

Photonic crystals (PC's) have attracted an important attention due to potential applications of photonic band gap(PBG) [1]. From works of Yablonovitch [2] and John [3], on such structures, often called photonic crystals, becomes one of the most popular branches of investigations in optics. Photonic crystal represented by natural or artificial structures with periodic modulation of the dielectric permittivity. One of the characteristic properties of PCs is the localization and the controllable inhibition of spontaneous emission of light. It is found, that periodic structures can have an absolute photonic band gap (PBG): a frequency region where light propagation in the crystal is totally prohibited, regardless of the polarization or propagation direction. This ability is the basis of a large number of possible applications of photonic crystals, such as waveguides, in laser physics, and optical communication [4].

In this paper, we present the optical response of Titanium dioxide (TiO_2) doped with Ag nanoparticles. Titanium dioxide have attracted much attention in the past as their chemical stability, high refractive index allow their use as components in optoelectronic devices, sensors, and photocatalysts [5]. We have calculated the photonic band gaps in one-dimensional (1D) photonic crystals based on TiO_2 doped with Ag nanoparticles by the FDTD method [6]. We have investigated the position, width of PBG as a function of the permittivity of the nanocomposite material and the volume fraction f.

2. DETERMINATION OF DIELECTRIC PERMITTIVITY OF COMPOSITE MATERIAL

It is possible to get an organised 1D structure of Ag nanoparticles embedded in a TiO_2 by using a phase mask or an interferogram. It has already been done with Ag particles in gelatin [7].

The schematic result of the structuring is given on Figure 1. The dielectric permittivity of Ag nanoparticles is obtained from a modified Drude model has the following form [8]:

$$\varepsilon_n(w) = \varepsilon_a - \frac{(\varepsilon_b - \varepsilon_a)\, w_p^2}{w\,(w + i\gamma)} \tag{1}$$

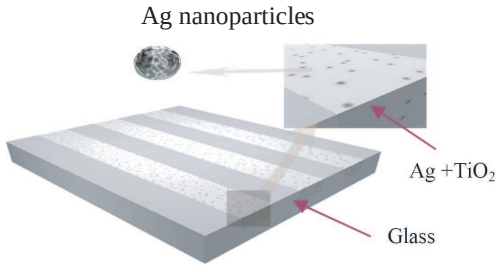

Figure 1: Structure TiO_2 matrix doped with Ag nanoparticles.

where: $\varepsilon_a = 5.45$, $\varepsilon_b = 6.18$, w_p is a plasma frequency ($w_p = 1.72 \times 10^{16}$ rad/s), γ is a relaxation constant and it can be written as:

$$\gamma = \frac{v_F}{l} + \frac{v_F}{r} \tag{2}$$

where $v_F = 1.38 \times 10^6$ m/s (Fermi velocity), $l = 52$ nm (electron mean free path at room temperature), and $r = d/2$ with d being the Ag particle diameter. To define the effective dielectric permittivity, $\tilde{\varepsilon}$, of such a composite system, we use the Maxwell-Garnett theory [9] is expressed approximately by [10]:

$$\tilde{\varepsilon}(w) = \varepsilon_m \frac{\varepsilon_n(1+2f) + 2\varepsilon_m(1-f)}{\varepsilon_n(1-f) + \varepsilon_m(2+f)} \tag{3}$$

where ε_m is the dielectric permittivity of the host matrix and f is the volume fraction occupied by Ag nanoparticles. Substituting Eq. (1) in Eq. (2), we can deduce the real and imaginary parts of $\tilde{\varepsilon}$ by the expression:

$$\tilde{\varepsilon}(w) = \varepsilon'(w) + i\varepsilon''(w) \tag{4}$$

Nanoparticles are distributed randomly but homogenously in transparent matrix. Let us consider that silver nanoparticles are spherical form and have a size of 10 nm in diameter. The Equation (3) is only valid if the particles size and the distances between them are much smaller than the wavelength of the interacting light.

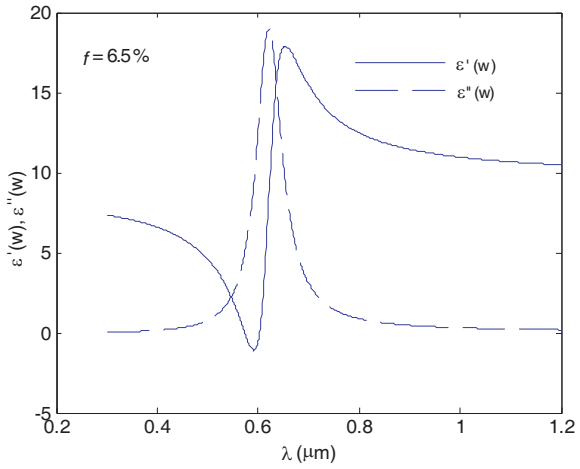

Figure 2: Real and imaginary parts of composite dielectric permittivity of Ag nanoparticles embedded in TiO_2 matrix for $f = 6.5\%$ and $\varepsilon_m = 8.12$.

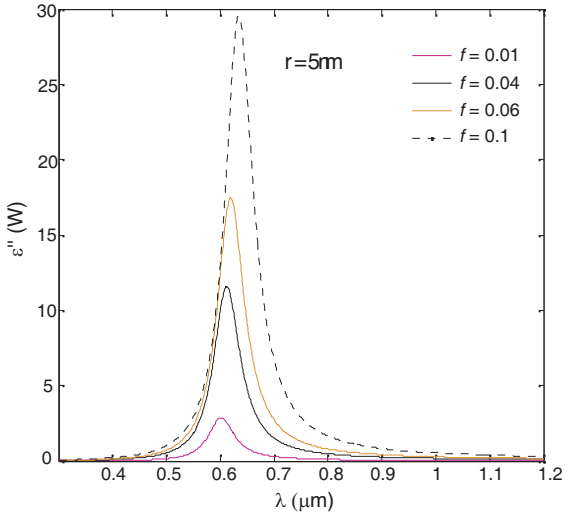

Figure 3: Modification of the imaginary part of the dielectric permittivity of TiO_2 containing Ag nanoparticles calculated according to the Maxwell-Garnett theory.

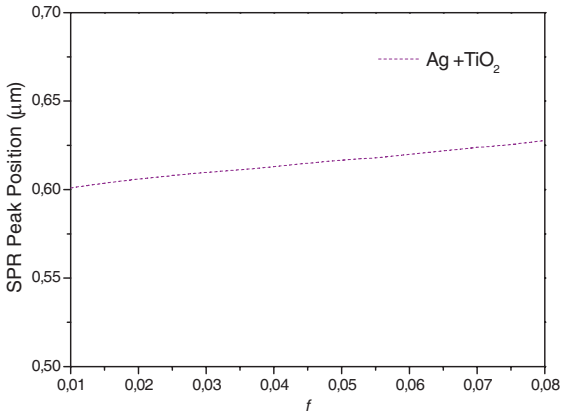

Figure 4: The peak wavelength of the surface Plasmon band as a function of filling factor for fixed particles radius ($r = 5$ nm).

Figure 2 shows the real and imaginary parts of the dielectric permittivity $\tilde{\varepsilon}$ of the composite material $\mathrm{Ag} + \mathrm{TiO_2}$ as a function of wavelength for parameters $f = 6.5\%$ and $\varepsilon_m = 8.12$. As has been shown in Figure 2 that curves have resonances with the prominent plasmon polariton absorption at $\lambda = 0.62\,\mu\mathrm{m}$.

The absorption spectra shown in Figure 3 demonstrate that the collective dipolar interaction between Ag particles embedded in $\mathrm{TiO_2}$ matrix causes an important broadening and red-shift which varies from $0.601\,\mu\mathrm{m}$ to $0.63\,\mu\mathrm{m}$ of the absorption band with increasing volume fraction f of Ag inclusions in $\mathrm{TiO_2}$ matrix from 1% to 10%.

As can be seen from Figure 4 the peak position of the surface Plasmon resonance (SPR) of the Ag aggregates in the surrounding medium depends considerably on the silver fill factor.

3. 1D PBG SIMULATIONS

3.1. Modulation Effects Due to the Dielectric Permittivity of the Nanocomposite Material

In order to investigate the influence of the permittivity of the nanocomposite material on the photonic band gap (PBG) we have calculated the photonic band structures in one-dimensional photonic crystal for two types of Bragg mirrors $\mathrm{Ag} + \mathrm{glass}/\mathrm{glass}$ and $\mathrm{Ag} + \mathrm{TiO_2}/\mathrm{glass}$ at normal incidence, for $f = 6.5\%$. Ideally the thickness of the glass, $\mathrm{Ag} + \mathrm{glass}$ and $\mathrm{Ag} + \mathrm{TiO_2}$ layers are $0.11\,\mu\mathrm{m}$, $0.1\,\mu\mathrm{m}$ and $0.036\,\mu\mathrm{m}$ respectively, corresponding to $\lambda/4n$, where n is the optical index of each of the materials and $\lambda = 0.656\,\mu\mathrm{m}$. The optical indices of $\mathrm{Ag} + \mathrm{glass}$ and $\mathrm{Ag} + \mathrm{TiO_2}$ are $\tilde{n} = 1.658 + i0.009$ and $\tilde{n} = 4.349 + i1.015$ correspondingly. The numerical tools used for our simulations are based on the finite difference time-domain method (FDTD) [6]. The result comes from the fact that for our simulation we took a purely real refractive index neglecting the imaginary part and, thus, absorption. This was made for the sake of simplicity. We present in Figures 5(a)

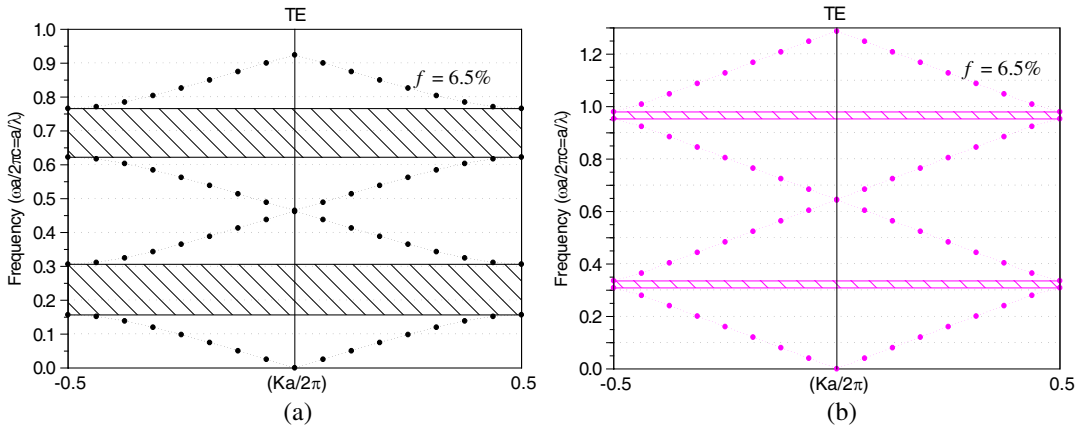

Figure 5: Photonic band structure of the Bragg mirror. (a) $(\mathrm{Ag} + \mathrm{TiO_2})/\mathrm{glass}$ and (b) $(\mathrm{Ag} + \mathrm{glass})/\mathrm{glass}$ for $f = 6.5\%$.

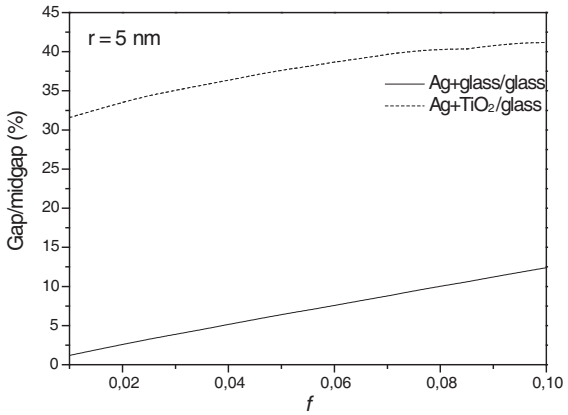

Figure 6: Gap width to midgap frequency ratio of the Bragg mirrors (Ag+glass)/glass $(\mathrm{Ag} + \mathrm{TiO_2})/\mathrm{glass}$ on the glass substrate as a function of the filling factor f. The radius of the nanoparticles $r = 5\,\mathrm{nm}$.

and (b) the photonic band structures of the mirrors (Ag + glass)/glass and (Ag + TiO_2)/glass. We can see from Figure 5(a) that there are two PBGs in the frequency range 0.1596–0.3107 ($wa/2\pi c$) for the first gap (G_1); 0.62–0.78 ($wa/2\pi c$) for the 2nd gap (G_2). Results are presented in terms of frequencies $wa/2\pi c = a/\lambda$ where a is the lattice constant, c the speed of light in a vacuum and λ the vacuum wavelength. Figure 5(b), shows that there are also two photonics bands in the region 0.3086–0.3356 ($wa/2\pi c$) for G_1 gap and 0.9529–0.9795 ($wa/2\pi c$) for the G_2 gap. G_1 and G_2 are situated in the visible and UV region respectively. Comparing Figure 5(a) with Figure 5(b), we can find that, the width of the PBGs of (Ag + glass)/glass is reduced due to the refractive index contrast and the position of the PBGs is shifted. Hence we have the conclusion that the PBGs sensitively depend on the dielectric permittivity of the nanocomposite material.

3.2. Modulation Effects Due to the Filling Factor

To illustrate the effect of the metal inclusions in the host matrix on PBG, we have calculated the gap width to midgap frequency ratio ($\Delta w/wm$ with wm the middle frequency of the PBG) of the first PBG for (Ag + glass)/glass and (Ag + TiO_2)/glass as a function of the filling factor f, the result is shown in Figure 6. For example, for (Ag + TiO_2)/glass the width (Δw) for the G_1 gap is (0.136) $wa/2\pi c$ for $f = 3.5\%$. Similarly, (Δw) is (0.163) $wa/2\pi c$ for $f = 10\%$.

Figure 6 shows that the PBG appears when the volume fraction of the silver component exceeds a certain critical value, and increases quickly when f enhances. These results clearly indicate that the width (Δw) increases when the concentration of the Ag particles in the dielectric matrix increased. By doping a dielectric matrix with Ag aggregates we can tune the widths of gaps. This new optical properties can be used to manufacturing optical components.

4. CONCLUSIONS

In conclusion, we have study the possibilities to modify and tune the optical properties of dielectric matrix doped with silver nanoparticles. We have investigated photonic band gap for 1D photonic band structures using FDTD simulation. Our results show that the position and the width of photonic band gaps (PBGs) sensitively depend on the dielectric permittivity of the nanocomposite material and the volume fraction of the silver particles. Considered effects give new possibilities to fabricate different useful optical devices.

REFERENCES

1. Joannopoulos, J. D., S. G. Johnson, J. N. Winn, and R. D. Meade, *Photonic Crystals: Molding the Flow of Light*, Princeton University Press, Princeton, 2008.
2. Yablonovitch, E., "Inhibited spontaneous emission in solid-state physics and electronics," *Phys. Rev. Lett.*, Vol. 58, 2059–2061, 1987.
3. John, S., "Strong localization of photons in certain disordered dielectric superlattices," *Phys. Rev. Lett.*, Vol. 58, 2486–2488, 1987.
4. Sakoda, K., *Optical Properties of Photonic Crystals*, Springer, Germany, 2001.
5. Chrysicopoulou, P., D. Davazoglou, C. Trapalis, and G. Kordas, "Optical properties of very thin (< 100 nm) sol-gel TiO_2 films," *Thin Solid Films*, Vol. 323, 188–193, 1998.
6. Taflov, A. and S. C. Hagness, *Computational Electrodynamics: The Finite-Difference Time-Domain Method*, Artech House Publishers, Boston, 2000.
7. Kok, M. H., et al., "Photonic band gap effect and structural color from silver nanoparticle gelatin emulsion," *Phys. Rev E*, Vol. 72, 047601, 2005.
8. Xiao, J. J., J. P. Huang, and K. W. Yu, "Optical response of strongly coupled metal nanoparticles in dimmer arrays," *Phys. Rev. B*, Vol. 71, 045404, 2005.
9. Maxwell-Garnett, J. C., *Phil. Trans. R. Soc. A*, Vol. 203, 1904.
10. Abdolvand, A., A. Podlipensky, G. Seifert, and H. Graener, "Electric field-assisted formation of Percolated silver nanolayers inside glass," *Opt. Express*, Vol. 13, 1266–1274, 2005.

Materials Adsorption Characterization by Random Coherent Electromagnetic Waves

C. I. Cabello[1], G. Bertolini[1], M. J. González[2], I. L. Botto[2], R. Arizaga[3], and M. Trivi[3]

[1]Centro de Investigación y Desarrollo en Ciencias Aplicadas Dr. J. Ronco
(CINDECA-CONICET La Plata-UNLP), Calle 47 No. 257, (1900) La Plata, Argentina
[2]Centro de Investigaciones en Química Inorgánica
(CEQUINOR-CONICET La Plata-UNLP), Calle 47 y 115, (1900) La Plata, Argentina
[3]Centro de Investigaciones Ópticas (CIC-CONICET La Plata) and UID Optimo
Dpto. Ciencias Básicas, Facultad de Ingeniería, Universidad Nacional de La Plata
Casilla de Correo 3, (1897) Gonnet, La Plata, Argentina

Abstract— Speckle is a random interference pattern of electromagnetic waves provided by a rough surface illuminated by a laser coherent light. In this paper we use a dynamic speckle technique to characterize the hydro-adsorption of alumina-silicates mineral materials with different chemical composition, surface area and pore volume. This study has a potential interest for catalytic and environmental processes.

1. INTRODUCTION

When a coherent beam coming from a laser illuminates a rough object, a typical granular interference pattern named speckle is observed [1]. Besides, a laser light scattered from diffuse objects produces a similar pattern.

If this surface does not remain rigid, but it presents some type of local movement, then the intensity pattern evolves in time. This phenomenon, well known as dynamic speckle, is characteristic of biological samples [2]. This behavior can also be observed in non-biological industrial processes, including the drying of paint, corrosion and heat exchange.

This activity takes place when the sample changes its properties due to movement of the scattering centers, changes in the optical path due to variations of refractive index, configuration changes or combination of these situations [3].

The study of the temporary evolution of the speckle patterns may provide an interesting tool to characterize the parameters involved in these processes.

The present work addresses the implementation of dynamic laser speckle technique to the hydro-adsorption analysis of two types of clay minerals with 1 : 1 and 2 : 1 structural distribution of the Si, Al-O layer: kaolinite, and bentonite-type. This last because of hydrophilicity properties can be functionalized. The adsorption capacity can be improved by chemical modification with surfactants and TEOS to give porous clays heterostructured (PCH) phases. Samples present different structural and chemical composition, surface area, pore volume and hydration capability. Experimental results show the temporal evolution of the materials speckle patterns during the process of water adsorption. Studies with commercial silica (SiO_2) with different textural properties show the correlation of the speckle activity with the hydro-adsorption process [4].

The isomorphous Al-Si replacement in the covalent structure and the variable proportion of large cations is different, so the surface behavior is affected and therefore the availability of the surface groups to interact with water by H-bonding. From these distinctive properties, it is possible to correlate the dynamic speckle stabilization time of each species with the Si/Al ratio.

This analysis can be considered as a potential new method to study different porous and small size particles of interest such as absorbents or catalysts supports.

2. MATERIALS AND METHODS

2.1. Materials

Natural materials, from different Argentine deposits, were selected among alumina-silicates species according to the X Ray Diffraction technique (XRD) and ICP chemical analysis for major and trace elements. Kaolinite is used pure whereas montmorillonite (bentonite-type) was employed pure and chemically modified by intercalating species into the layers and improving the surface capacity

to give a PCH. All materials show comparatively different Si/Al ratios and the textural properties (by the BET method) increase according to the kaolinite, bentonite and modified bentonite sequence [5, 6].

The organo-bentonite was prepared adding surfactants as ammonium hexadeciltrimetil-bromide (HDTMA-Br) to obtain the cationic form (B+) and a mix of dodecilamine (DDA) and tetraetoxiortosilicate (TEOS) in a B+/DDA/TEOS specific ratio to increase the relatively low natural surface area, obtaining a porous structure after heating at 550°C, as it was reported [7].

2.2. Dynamic Speckle Technique

Dynamic speckle patterns were obtained by illuminating the samples with a He-Ne laser of 10 mW and the images were recording with a CCD camera connected to a PC with an image digitizer. See Fig. 1.

To show the temporal evolution of speckle was used the Oulamara et al. method [8]. For each state of the adsorption process, 320 successive images of dynamic speckle are recorded, capturing 25 frames per second and select a column of them. These columns are building a pseudo-image of 320×240 so-called Temporary History Speckle Patterns (THSP). The activity of the sample changes of intensity (gray levels) in the horizontal direction. The THSP shows more or less elongated shapes when the phenomenon under study has low or high activity as shown in Fig. 2. In our case, speckle high activity corresponds to the initial hydro-adsorption process. When this process is complete, the speckle activity is minimal. To establish a quantitative estimate of THSP, we use the moment of inertia of the co-occurrence matrix method [8, 9].

3. EXPERIMENTS

In the experiments, 30 mg of each material was soaked with 10 µl of distilled water. The experience was monitored every second and the outcome was followed for 6 minutes. Ambient temperature: 19°C, Humidity: 60%.

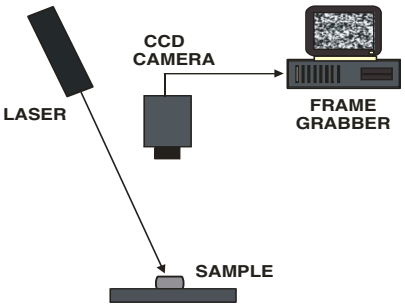

Figure 1: Experimental set-up for dynamic speckle technique.

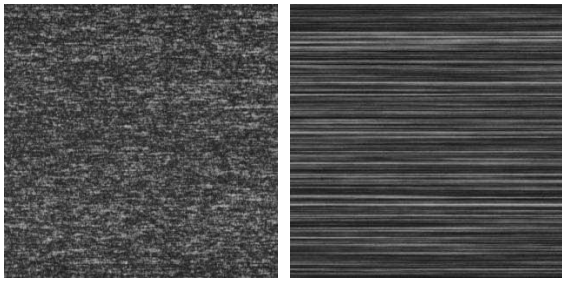

Figure 2: THSP matrix. (a) High activity, (b) low activity.

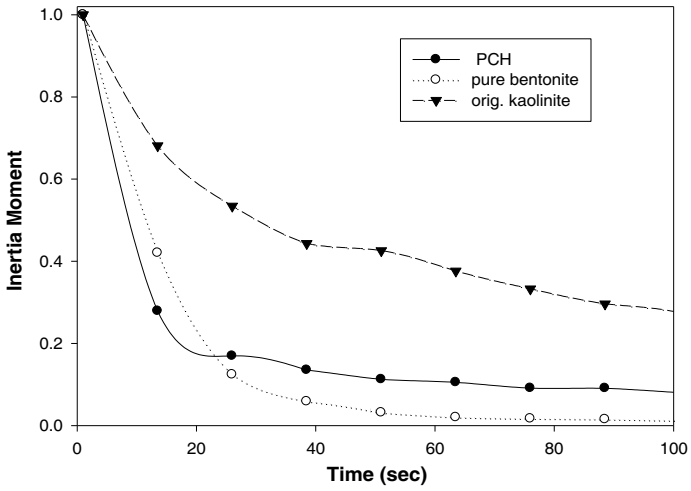

Figure 3: Normalized inertia moment for three different samples.

Stabilization time speckle was observed during adsorption of water using the Inertia Moment method. The initial activity was normalized for all samples. Fig. 3 shows the behavior of the three selected samples with different Si/Al ratio: kaolinite (2.25), bentonite (3.64) and PCH (8.91). It can be observed that the PCH has the shortest stabilization time, about 20 sec., while the bentonite without chemical modification has about 50 sec. The kaolinite is not stabilized after 100 sec. The result obtained for the material of larger Si/Al rate, showing the shortest time to stabilize the speckle activity, indicate a rapid hydro-adsorption. The chemical modification improves the surface area and consequently the number of active sites (more basic oxygen atoms) which are available to interact with water-molecules by a Lewis process. The behavior of the other materials, showing lower stabilization time speckle (longer hydro-adsorption period) is in agreement with the original structure, particularly the different distance between the covalent layers which reveal for the bentonite a higher exposed surface to react with the water molecules. So, there was an opposite behavior with decreasing the Si/Al ratio. This effect can be correlated to the hydrophilicity of siliceous materials [4].

4. CONCLUSIONS

The dynamic speckle technique was used in the study of natural and chemically modified silicoaluminates hydrophilicity, presenting different availability of surface active sites to interact with water by H-bonding.

Experimental measurements showed the temporal evolution of speckle diagrams, making possible the correlation among the time THSP stabilization of each species and their Si/Al ratio.

The speckle method provides an effective comparison among different species and can be considered an alternative method for the study of materials of interest as adsorbents or catalyst supports.

ACKNOWLEDGMENT

This work was supported by CONICET, CIC, ANPCyT and Universidad Nacional de La Plata, Argentina.

REFERENCES

1. Goodman, J. W., *Speckle Phenomena in Optics: Theory and Applications*, Ben Roberts & Company, Colorado, USA, 2006.
2. Aizu, Y. and T. Asakura, "Biospeckle," *Trends in Optics*, A. Consortini, Ed., Chap. 2, Academic Press, 1996.
3. Trivi, M., "Dynamic speckle: origin and features," *Dynamic Laser Speckle and Applications*, H. Rabal, R. Braga, Eds., Chap. 2, CRS Press, Taylor and Francis Publisher, Boca Ratón, FL, USA, 2009.
4. Rouquerol, F., J. Rouquerol, and K. Sing, *Adsorption by Powders and Porous Solids*, Elsevier, 1999.
5. Gil, A., L. M. Gandia, and M. A. Vicente, *Catal. Rev. Sci. Eng.*, Vol. 42, 145–212, 2000 (references cited therein).
6. Gregg, S. J. W. and K. S. Sing, *Adsorption, Surface Area and Porosity*, Academic Press, London, 1982.
7. Benjelloum, M., P. Cool, P. Van Der Voort, and E. F. Vansant, *Phys. Chem.*, Vol. 4, 2818, 2002 (references cited therein).
8. Oulamara, A., G. Tribillon, and J. Duvernoy, "Biological activity measurements on botanical specimen surfaces using a temporal decorrelation effect of laser speckle," *Journal of Modern Optics*, Vol. 36, 165, 1989.
9. Arizaga, R., M. Trivi, and H. Rabal, "Speckle time evolution characterization by the co-occurrence matrix analysis," *Optics & Laser Technology*, Vol. 31, 163–169, 1999.

A Proposal for a Low-cost TO-can 25-Gb/s Laser Diode Package

Tien-Tsorng Shih[1], **Pei-Hao Tseng**[2], **Yung-Yu Lai**[1], **Yaw-Dong Wu**[1], **and Wood-Hi Cheng**[2]

[1]Electronic Engineering Department, National Kaohsiung University of Applied Sciences
Kaohsiung, Taiwan
[2]Department of Photonics, National Sun Yat-sen University, Kaohsiung, Taiwan

Abstract— A novel high bandwidth laser diode package is proposed and characterized theoretically. A three dimensional full wave electromagnetic field simulation and a time domain simulator are used to investigate S-parameters and eye-diagrams, respectively. The new designed TO-can header exhibits an over 40-GHz inherent 3-dB bandwidth. Different wire bond configurations have been studied under a 50-Ω terminal resistance and get an optimal 3-dB bandwidth of 36-GHz. In considering a practical situation, the 50-Ω terminal resistance has been separated into a 5-Ω laser diode and a matching resistor of 45-Ω. When the matching resistor decreases to 20-Ω and 0-Ω, the 3-dB bandwidth deteriorates to 35-GHz and 12-GHz, respectively. The clear 25-Gb/s eye-diagrams are simulated and the calculated rise time and fall time are around 14-ps for the cases of the matching resistor of 45-Ω and 20-Ω.

1. INTRODUCTION

A low cost 25-Gb/s laser diode package is very important for next generation optical fiber communication networks. More and more fiber systems construct on the basis of 20∼25-Gb/s transmission channel, such as 21GBaud fiber channel (20GFC) and 100-Gb/s Ethernet (100GbE) [1–3]. The 25-Gb/s laser diode package is usually a box type format which is more expensive compared with a TO-can type format [4–6]. However, due to the limited space and the difficulty of impedance matching, TO-can package is applied nowadays under 10-Gb/s [6–8]. Therefore, a low cost TO-can package is proposed for the application of 25-Gb/s networks. A simulation method composed by a three dimensional full wave electromagnetic field simulation and a time-domain simulator is developed to investigate the electrical package performance of the 25-Gb/s TO-can laser diode package. The frequency-domain S-parameter characteristics and time-domain eye-diagrams are obtained through the simulation. The electrical characteristics of the new designed TO-can header, the influence of different wire bond configurations, and the effect of matching resistor are discussed and designed to an optimum condition.

2. NEW DESIGNED TO-CAN HEADER

Usually, a TO-56 header is used to package a laser diode. However, the transmission bandwidth is limited due to discontinuities of impedance. Therefore, a new designed TO-can header is proposed to achieve the purpose of 25-Gb/s transmission through the impedance optimization. In the mean time, the TO-can header has to take account of the realization and the limitation on assembly. The structure of the TO-Can header is illustrated in Fig. 1(a). The diameter and thickness of the base are 5.6-mm and 2-mm, respectively. The feed-lead is straight and the diameter is 0.25-mm. The feed-through hole is filled with a low dielectric constant material. The stem acts as an electrical ground and extends to the edge as wide as possible. The calculated reflection loss (S_{11}) and insertion loss (S_{21}) of the new TO-Can header with an impedance terminal of 50-Ω is shown in Figs. 1(b) and (c), respectively. The reflection loss (S_{11}) remains below −10-dB at frequencies lower than 22-GHz and the insertion loss (S_{21}) diagram shows a 3-dB bandwidth over 40-GHz. For comparison, the characteristics of the conventional TO-56 header are shown in figures. The inherent electrical performance of the new designed TO-can header is improved from the conventional TO-56 header significantly.

3. WIRE BOND CONFIGURATIONS

The proposed component and wire bond configuration is shown in Fig. 2. A LD chip is bonded on the top of a submount. The surface of the submount is assumed to be a conductor and connect with the LD cathode perfectly. To adjust the terminal resistance, a matching resistor is placed between the feed lead and LD chip. The wire bond is divided into three portions (A), (B), and (C) which represent the connection between the feed-lead and the matching resistor, the matching resistor and the LD chip, and the submount (LD chip cathode) and the stem, respectively. To investigate

the degradation of the electrical performance by wire bond configurations, the matching resistor is assumed to be a perfect conductor and the LD chip is assumed to be 50-Ω, as shown in Fig. 2(a). The relationship between the 3-dB bandwidth and different number of bond wire is summarized in Table 1. The optimum 3-dB bandwidth is 35.83-GHz at a configuration of 4 bond wires between the feed-lead and the matching resistor (wire-bond (A)), 3 bond wires between the matching resistor and the LD chip (wire-bond (B)), and 6 bond wires between submound and the stem (wire-bond (C)).

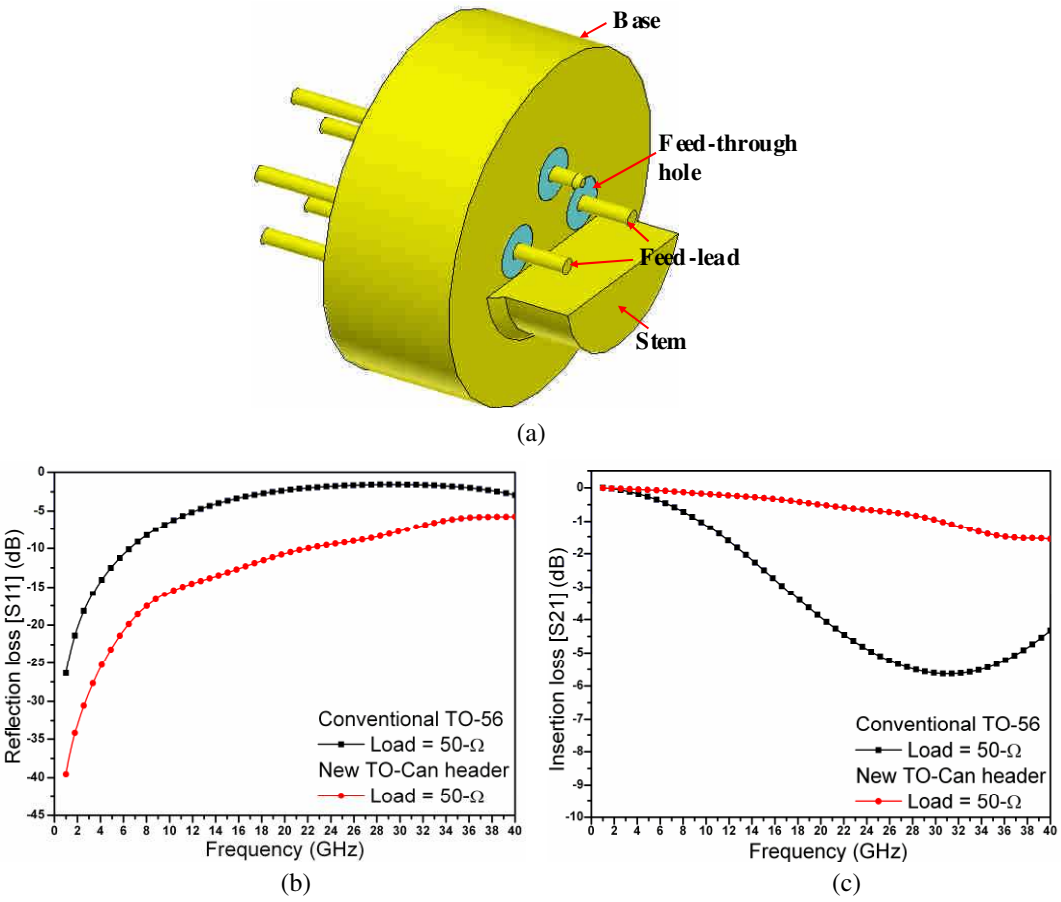

Figure 1: Inherent electrical characteristics of the new designed TO-can header, (a) structure, (b) calculated reflection loss diagram, (c) calculated insertion loss diagram.

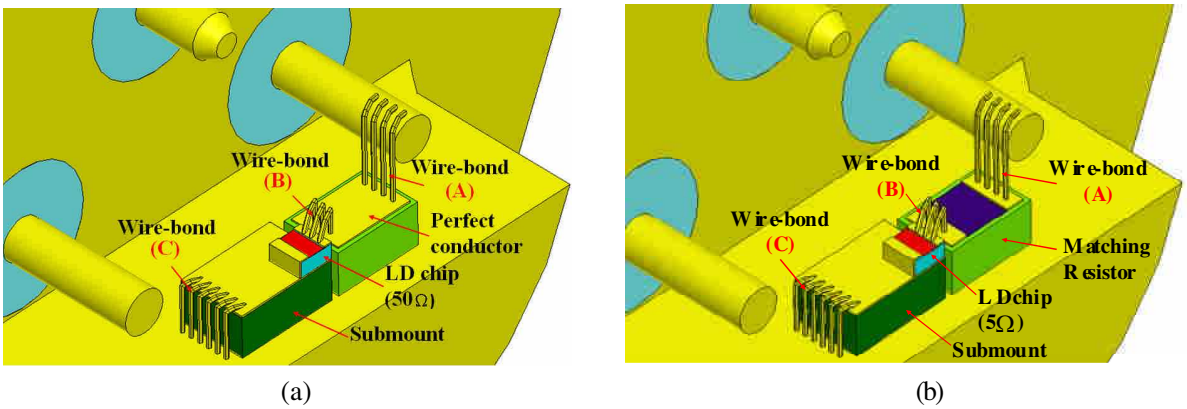

Figure 2: Component and wire bond configurations, (a) 50-Ω terminal resistance, (b) practical package.

4. EFFECTS OF MATCHING RESISTOR

A laser diode is usually operated in the linear region of the I-V curve. Owing to the fact that a LD chip of intrinsic resistance is between 5 to 8-Ω [9], the resistance of the LD chip is assumed to be 5-Ω in the package, as shown in Fig. 2(b). Under the optimum wire bond configuration, various matching resistor of 0-Ω, 20-Ω, and 45-Ω are assumed. The calculated insertion loss (S_{21}) characteristics are shown in Fig. 3. This TO-can laser diode package provides a 3-dB bandwidth of 12-GHz, 35-GHz, and 36-GHz for a matching resistor of 0-Ω, 20-Ω, and 45-Ω, respectively. By applying a time-domain simulator, the 25-Gb/s eye-diagrams of the package with different matching resistors are simulated and shown in Fig. 4. Due to a big impedance discontinuity, the package with a zero matching resistor exhibits a blurred eye-diagram. The eye-diagram of a package with a matching resistor of 45-Ω is slightly better in compare with the package of a matching resistor of 20-Ω. The rise time and fall time are 13.9 and 13.86-ps for the package with a 45-Ωgatching resistor and 14.6 and 14.62-ps for the package with a 20-Ωgatching resistor, respectively.

Table 1: The relationship between the 3-dB bandwidth and different number of bond wire.

A \ B	C	1	2	3	4	5	6
1	1	28.16	31.99	33.06	33.58	33.88	34.03
1	2	28.26	31.40	33.29	33.86	34.19	34.33
1	3	28.24	31.58	33.35	33.86	34.27	34.46
2	1	27.75	32.57	34.01	34.50	34.87	35.07
2	2	27.81	32.67	34.15	34.79	35.13	35.42
2	3	27.85	31.60	34.23	34.79	35.26	35.50
3	1	27.36	32.53	34.19	34.73	35.03	35.34
3	2	27.66	32.77	34.29	34.95	35.40	35.59
3	3	27.60	32.80	34.40	35.09	35.48	35.71
4	1	26.99	32.47	33.96	34.77	35.13	35.37
4	2	27.33	32.75	34.31	35.07	35.46	35.69
4	3	27.38	32.82	34.42	35.18	35.53	35.83

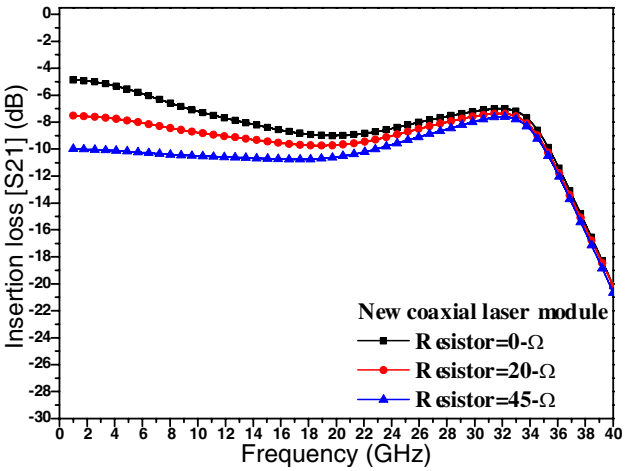

Figure 3: The calculated insertion loss (S_{21}) diagram of the TO-can laser diode package with different matching resistors.

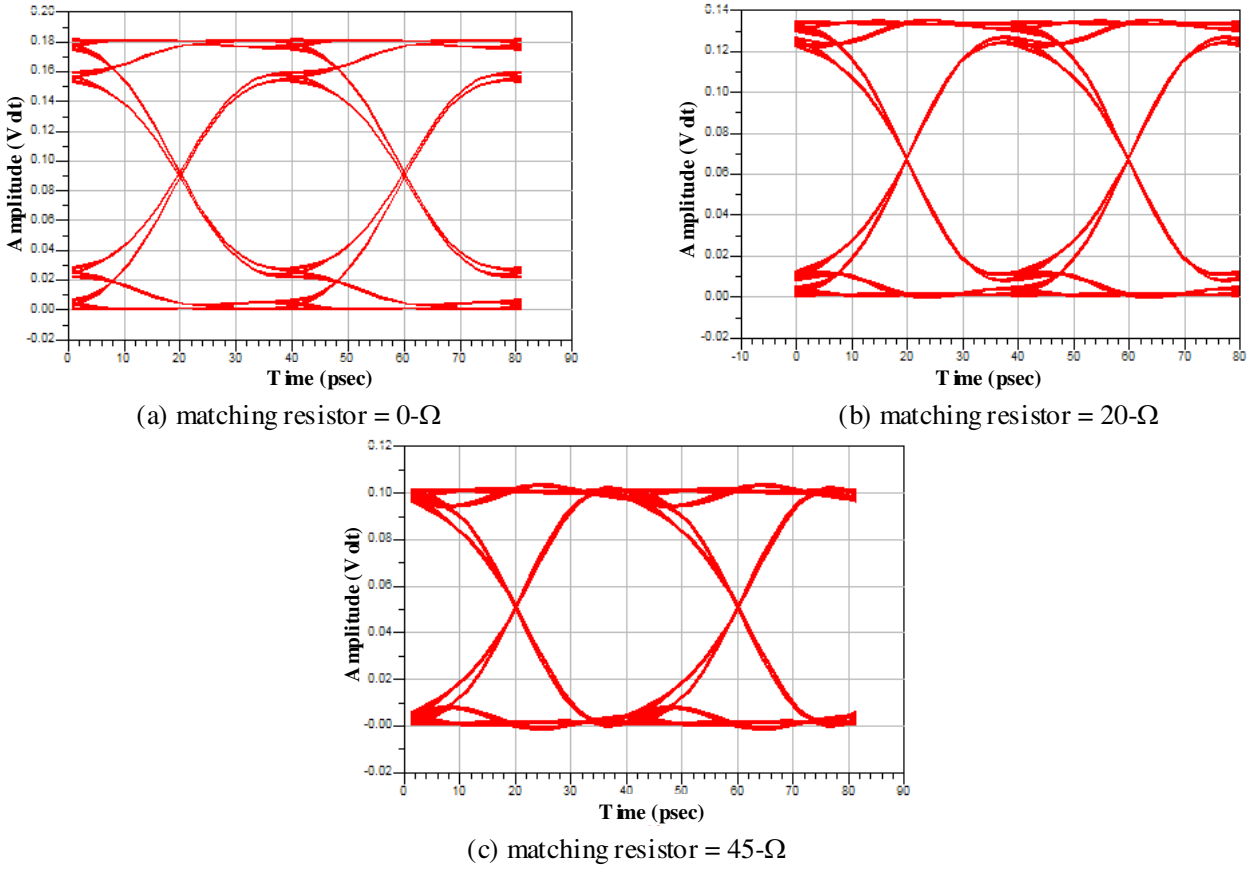

Figure 4: The simulated 25Gb/s eye-diagrams with matching resistors of (a) 0-Ω, (b) 20-Ω, and (c) 45-Ω.

5. CONCLUSIONS

A new-designed TO-can header is proposed, the inherent 3-dB bandwidth is calculated to be above 40-GHz. After taking account of the bond wires, the 3-dB bandwidth is degraded to 28∼36-GHz for different numbers of bond wire. Without a proper matching resistor, the 3-dB bandwidth is deteriorated to only 12-GHz. With a matching resistor of 20-Ω and 45-Ω, the 3-dB bandwidth restore to 35 and 36-GHz, respectively. The time-domain simulation shows a clear 25-Gb/s eye-diagram with a rise time and a fall time of 13.9-ps and 13.86-ps, respectively, for a package of a matching resistor of 45-Ω. In general, a low-cost 25-Gb/s TO-can laser diode package has been proposed and demonstrated by simulations. The electrical performance of different wire bond configurations and matching resistors have been studied comprehensively and can be referred in the future application.

ACKNOWLEDGMENT

Authors would like to thank Professor Tzyy-Sheng Horng of National Sun Yat-sen University for technical support. This work was supported by the NSC under the Contract NSC-99-2221-E-151-045 and the MOE Program of the Aim for the Top University Plan.

REFERENCES

1. Fibre Channel Industry Association (FCIA), [Online] Available: http://www.fibrechannel.-org/.
2. Roese, J., R. P. Braun, M. Tomizawa, and O. Ishida, "Optical transport network evolving with 100 gigabit ethernet," *IEEE Communications Magazine*, Vol. 48, No. 3, S28–S34, Mar. 2010
3. Anderson, J. and M. Traverso, "Optical transceivers for 100 gigabit ethernet and its transport," *IEEE Communications Magazine*, Vol. 48, No. 3, S35–S40, Mar. 2010
4. Lee, J., S. Nam, S. H. Lee, and J. Jeong, "A complete small-signal equivalent circuit model of cooled butterfly-type 2.5 Gbps DFB laser modules and its application to improve high frequency characteristics," *IEEE Trans. Adv. Packag.*, Vol. 25, No. 4, 543–548, Nov. 2002.

5. Baek, J. M., H. S. Seo, B. O. Jeon, H. Y. Kang, D. Y. Rhee, S. K. Yang, M. K. Park, J. W. Burm, and D. H. Jang, "High sensitive 10-Gb/s APD optical receivers in low-cost TO-can-type packages," *IEEE Photon. Technol. Lett.*, Vol. 17, No. 1, Jan. 2005.
6. Shih, T.-T., M.-C. Lin, and W.-H. Cheng, "High-performance low-cost 10-Gb/s coaxial DFB laser module packaging by conventional TO-can materials and processes," *IEEE J. Select. Top. Quant. Electron.*, Vol. 12, No. 5, 1009–1015, Sep./Oct. 2006.
7. Chen, C., N. H. Zhu, S. Jian Zhang, and Y. Liu, "Characterization of parasitics in TO-packaged high-speed laser modules," *IEEE Trans. Adv. Packag.*, Vol. 30, No. 1, 97–103, Feb. 2007.
8. Kim, D., J. Shim, Y.-C. Keh, and M. Park, "Design and fabrication of a transmitter optical subassembly (TOSA) in 10-Gb/s small-form-factor pluggable (XFP) transceiver," *IEEE J. Select. Top. Quant. Electron.*, Vol. 12, No. 4, 776–782, July/Aug. 2006.
9. Nakahara, K., T. Tsuchiya, T. Kitatani, K. Shinoda, T. Taniguchi, T. Kikawa, M. Aoki, and M. Mukaikubo, "40-Gb/s direct modulation with high extinction ratio operation of 1.3-μm InGaAlAs multiquantum well ridge waveguide distributed feedback lasers," *IEEE Photon. Technol., Lett.*, Vol. 19, No. 19, 1436–1438, Oct. 2007.

1D Inversion of Multi-component and Multi-frequency Low-induction Number EM Device (PROMIS) for Near-surface Exploration

C. Schamper and F. Rejiba
UMR 7619 Sisyphe, University of Paris 6, France

Abstract— Most of the low-induction number ElectroMagnetic sensors measure only the vertical magnetic field component for a vertical magnetic dipole source. We propose here to present the results of a sensitivity analysis of a slingram device, named PROMIS (Iris Instruments), which allows the measurement of ten frequencies ranging from 110 Hz to 56 kHz and the three components of the magnetic field. The main objective is to analyze how the radial component H_r, which varies during a profiling acquisition above a horizontally-layered ground, could improve the inversion process of the usual H_z, by essentially decreasing the number of equivalences as well as improving the convergence. First results coming from separated sensitivity analysis of H_r and H_z have shown that H_r is more sensitive to the variation of the thickness of a near-surface conductive layer. Analysis of the RMS error in the parameters' space (resistivity and thickness of the conductive layer) indicates less dispersion associated to equivalences for H_r rather than for H_z. The inversion process involving both H_r and H_z components have been performed using several methods (gradient and Monte Carlo types) including a Marquardt-Levenberg-like approach. The sensitivity analysis shows a "narrow banana" distribution of equivalences for the parameters' pair thickness/resistivity of the conductive layer, which leads to convergence problems that cannot be solved easily by the lone use of a damping factor. In order to improve significantly the convergence rate, we have implemented a two step inversion process that includes an intermediary random search step, associated to the Marquardt-Levenberg technique. This helps to circumvent the issue of equivalences in the "narrow banana" zone. Synthetic tests demonstrate clearly that, at least for thicknesses larger than few meters, the joint inversion of H_r and H_z measured with the PROMIS improves the estimation of the physical parameters.

1. INTRODUCTION

Low-induction number electromagnetic (EM) or slingram devices have been widely used for environmental and archaeological purposes (e.g., [1, 2, 7–11]). Due to the short offset between the source and the receiver compared with the wavelength of the emitted sinusoïdal signal (often below 100 kHz), these EM devices are suited for detecting conductive targets. The most widespread devices are made of magnetic transmitter and receiver coils, often configured in the Horizontal Co-Planar (HCP) design where the planes of both coils are horizontal and held at the same height. Single-offset and single-frequency devices, like EM-31 of Geonics (offset of 3.66 m and frequency of 9.8 kHz), are designed for making maps of apparent resistivity in order to delineate conductive structures. In order to get an information in depth, it is necessary to vary offset (EM-34 of Geonics) or frequency, or both of them.

The PROMIS device, developed by IRIS instruments, offers the possibility to tune the offset and the frequency in order to perform soundings. One single offset (20 m) was considered here, and all frequencies recorded by the device (10 frequencies ranging from 110 Hz to 56 kHz) were studied. The particularity of the PROMIS, among the available slingram devices, is that it records the three components of the magnetic field in the same time, i.e., H_r, in the axis of the source-receiver line, H_ϕ, perpendicular to the source-receiver line, and H_z, the vertical component. The emitting coil of the PROMIS has to be configured before the beginning of the measurements. In the present case, the source-receiver setup includes $H_z - H_z$ and $H_z - H_r$ configurations.

To our knowledge, little work has been made for exploiting more than one component with slingram devices in the frequency domain, even less by inverting all components at once. Multi-component magnetic receivers have been developed for well logging, in order to determine the anisotropy in resistivity (e.g., [3, 12]). Presently, the main issues are the possibility to invert both H_r and H_z to interpret near-surface geophysical data in an 1D assumption, and then to delete some equivalent models which are well-known in geophysics inversion.

A sensitivity study of both components associated to a near-surface conductive layer is firstly undertaken. Then, we present the inversion algorithm implemented in order to check the inter-

pretation performance by using both components rather than H_z only. Then, inversion results of synthetic data show how the definition of the conductive layer is improved.

2. SENSITIVITY TO A NEAR-SURFACE CONDUCTIVE LAYER

A common issue in near-surface exploration is to determine the thickness of a conductive overburden (with clay) above a resistive formation like limestone. Then, a simple three-layers model is considered, with a first resistive layer ($\rho_1 = 70\,\Omega{\cdot}\mathrm{m}$, $h = 1\,\mathrm{m}$) which corresponds to the soil, a conductive layer ($\rho_2 \approx 20\,\Omega{\cdot}\mathrm{m}$, $e \approx 4\,\mathrm{m}$) and a semi-infinite resistive layer with a resistivity fixed at $\rho_3 = 120\,\Omega{\cdot}\mathrm{m}$. The sensitivities of H_r and H_z to the resistivity, and to the thickness of the conductive layer are defined as:

$$S_{H_{r,z}|\rho_2} = \sqrt{\int_f \left|\frac{\partial H_{r,z}(\rho_1,\rho_2,\rho_3,h,e,f)}{\partial \rho_2}\right|^2 df} \quad S_{H_{r,z}|e} = \sqrt{\int_f \left|\frac{\partial H_{r,z}(\rho_1,\rho_2,\rho_3,h,e,f)}{\partial e}\right|^2 df} \qquad (1)$$

where f is the frequency (Hz).

Since data are recorded in the frequency domain, magnetic components are split into two parts, the in-phase (Ip) and the out-of-phase (Op, or quadrature) parts. The sensitivities of PROMIS to ρ_2 and e are displayed in Fig. 1. The two components can be compared, since they are normalized by the primary field which corresponds to the electromagnetic field diffusing from the transmitter to the receiver in the air. As can be seen, the sensitivity of the H_r component is larger than the sensitivity of the lone H_z for almost all models, and for both in-phase and out-of-phase parts. Despite this observation, it doesn't mean that H_r can help to determine the parameters of the ground finer than if the H_z component is considered only; however, this result encourages to test

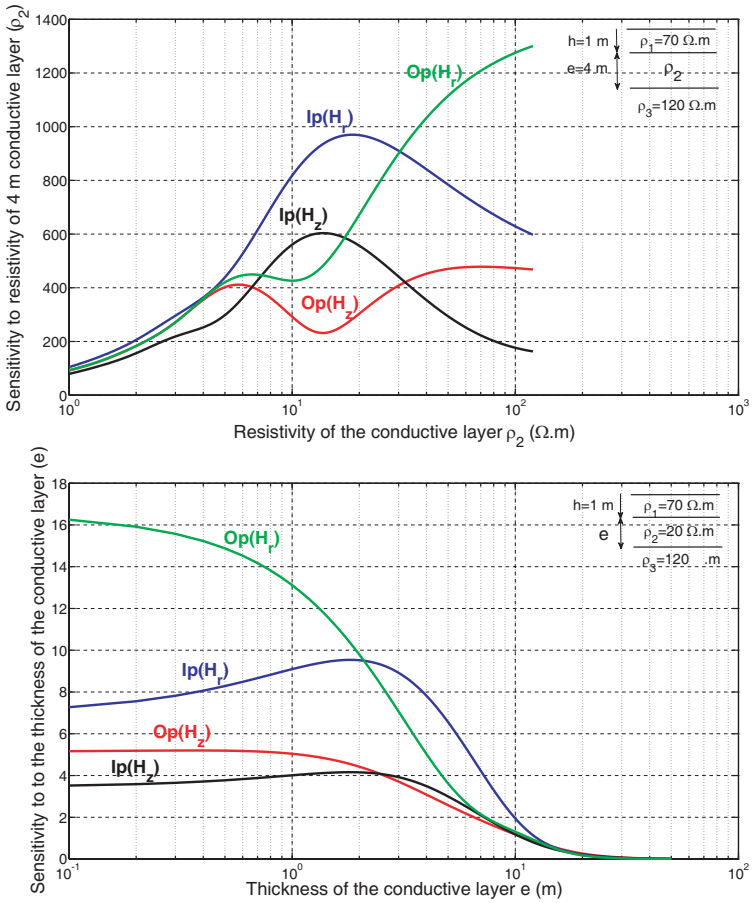

Figure 1: Sensitivity of H_r and H_z components recorded by PROMIS at 10 frequencies (110 Hz–56 kHz). Up: sensitivity to the resistivity ρ_2 of the conductive layer (see $S_{H_{r,z}|\rho_2}$ in Equation (1)). Down: sensitivity to the thickness e of the conductive layer (see $S_{H_{r,z}|e}$ in Equation (1)). In-phase (Ip) and out-of-phase (Op) are separated.

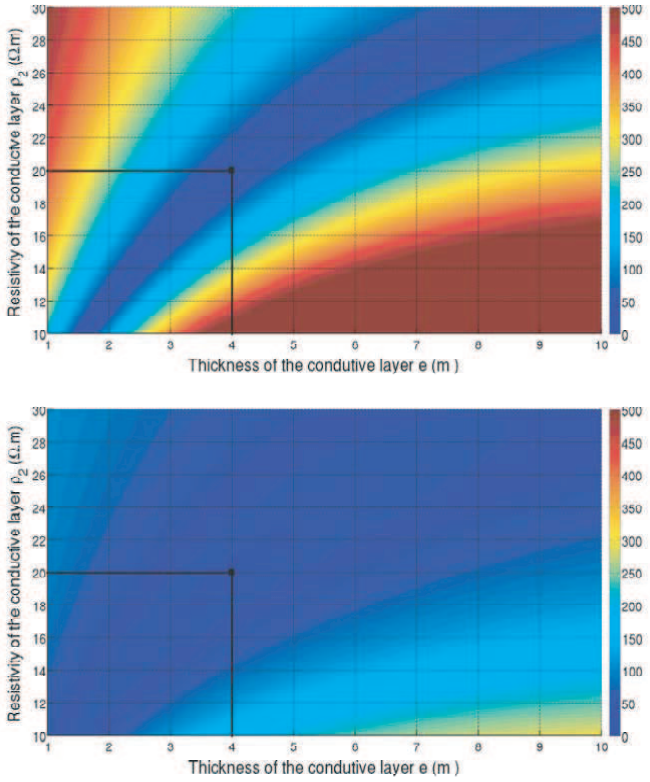

Figure 2: RMS error normalized by the minimum for the H_r component (up), and for the H_z component (down). All parameters of the tabular ground are fixed, except the thickness and the resistivitity of the conductive layer. The true model has a conductive layer with a thickness of 4 m and a resistivity of 20 Ω·m.

the inversion by combining both H_r and H_z components. Normalized RMS error around the model cited above can be plotted by varying both the thickness and the resistivity of the conductive layer (Fig. 2). An elongated "banana" corresponds to an equivalence area where the RMS error is very small, for both H_r and H_z. However, H_r shows a sharper low-RMS zone, which indicates that the convergence toward a likely solution should be easier than with the H_z component. This additional observation confirms the interest of performing inversion of both components.

3. INVERSION SCHEME: MARQUARDT-LEVENBERG WITH RANDOM SEARCH

Marquardt-Levenberg algorithm, associated to a damping factor, is a well-known technique in the inversion theory, and particularly when it is applied to geophysical data (e.g., [5, 6]). At each iteration, the vector of model parameters $\underline{m}^n$ is updated to better fit the field data. This updating process can be summarized as below:

$$[t][\underline{\underline{J}}^{nT}\underline{\underline{J}}^{n} + \lambda^n \underline{\underline{I}}]\Delta\underline{m}^n = -\underline{\underline{J}}^{nT}\underline{r}^{n-1} \tag{2}$$

where:

$\underline{\underline{J}}^n$ is the Jacobian or sensitivity matrix at iteration n,

λ is the damping factor,

$\underline{\underline{I}}$ is the identity matrix,

$\Delta\underline{m}^n$ is the updating vector of the model parameters at the n^{th} iteration,

and $\underline{r}^{n-1}$ is the residual vector, i.e., the difference between the forward model and the data.

The damping factor λ has the purpose to decrease the instability of the solving of the linear system due to a bad matrix conditioning. The way to make λ evolving at each iteration is an object of constant research (e.g., [4]).

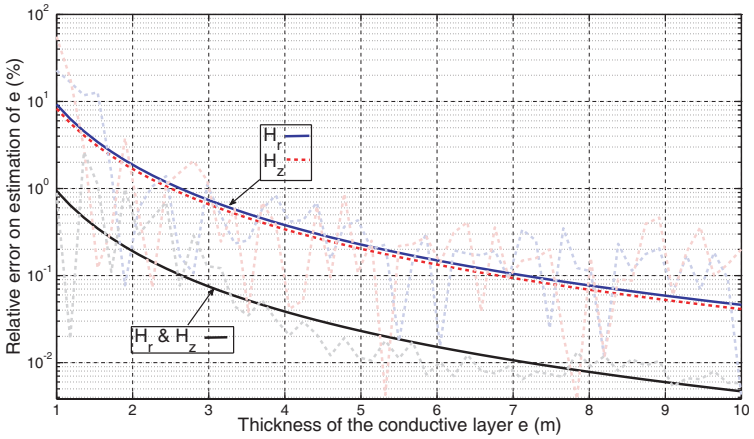

Figure 3: Relative error on the estimation of the thickness of the conductive layer e in function of the thickness e. The inversion was perfomed with the mixed Marquardt-Levenberg/random-search algorithm.

One of the major drawback of this gradient method is to be stuck in a local minimum while almost-random algorithms, like Monte-Carlo, are well-suited to determine if there are several local minima. However, the computation cost of a random search grows up quickly as soon as the number of parameters increases. To take advantage of both the gradient method and random search, we combined them to develop an own mixed inversion approach. The Fig. 3 is obtained by applying the current inversion algorithm to synthetic data. Several data are generated for a thickness ranging from 1 m to 10 m. Since no random noise was added to the synthetic signals, the RMS error is very low, but shows that the inversion of both H_r and H_z components allows to decrease the RMS error by a decade factor compared with the inversion performed with the H_z component only.

4. CONCLUSION

An hybrid inversion algorithm, combining the gradient method of Marquardt-Levenberg and a random search, was developed and showed good matches for inversion of synthetic data that could be measured by an EM slingram device, like the PROMIS. In addition, the inversion results demonstrate that the consideration of both H_r and H_z components leads to a decrease of the RMS error by a decade factor in comparison to the use of the H_z component only. Future developments consist in the application of the algorithm to field data.

REFERENCES

1. Everett, M. E. and M. A. Meju, "Near-surface controlled-source electromagnetic induction," *Hydrogeophysics*, 157–183, 2005.
2. Greenhouse, J. P. and D. D. Slaine, "The use of reconnaissance electromagnetic methods to map contaminant migration," *Ground Water Monitoring & Remediation*, Vol. 3, No. 2, 47–59, 1983.
3. Kriegshäuser, B., O. Fanini, S. Forgang, G. Itskovich, M. Rabinovich, L. Tabarovsky, L. Yu, M. Epov, P. Gupta, and J. van der Horst, "A new multi-component induction logging tool to resolve anisotropic formations," *41st Annual Symposium, Society of Professional Well-Log Analysts*, paper 2000 D, 2000.
4. Madsen, K., H. Bruun, and O. Tingleff, "Methods for non-linear least squares problems," *IMM*, 2004.
5. Marquardt, D. W., "An algorithm for least-squares estimation of nonlinear parameters," *Journal of the Society for Industrial and Applied Mathematics*, Vol. 11, No. 2, 431–441, June 1963.
6. Marquardt, D. W., "Generalized inverses, ridge regression, biased linear estimation and nonlinear estimation," *Journal of the Society for Industrial and Applied Mathematics*, Vol. 12, No. 3, 591–612, August 1970.
7. Martinelli, H. P. and A. M. Osella, "Small-loop electromagnetic induction for environmental studies at industrial plants," *Journal of Geophysics and Engineering*, Vol. 7, No. 1, 91–104, 2010.

8. Monier-Williams, M. E., J. P. Greenhouse, J. M. Mendes, and N. Ellert, "Terrain conductivity mapping with topographic corrections at three waste disposal sites in Brazil," *Geotechnical and Environmental Geophysics*, Vol. 2, 41–55, 1990.
9. Pellerin, L. and P. E. Wannamaker, "Multi-dimensional electromagnetic modeling and inversion with application to near-surface earth investigations," *Computers and Electronics in Agriculture*, Vol. 46, No. 1–3, 71–102, 2005.
10. Sambuelli, L., S. Leggieri, C. Calzoni, and C. Porporato, "Study of riverine deposits using electromagnetic methods at a low induction number," *Geophysics*, Vol. 72, No. 5, B113–B120, 2007.
11. Sheets, K. R., J. P. Taylor, and J. M. H. Hendrickx, "Rapid salinity mapping by electromagnetic induction for determining riparian restoration potential," *Restoration Ecology*, Vol. 2, No. 4, 242–246, 1994.
12. Tompkins, M. J., D. L. Alumbaugh, D. T. Stanley, and X. Lu, "Numerical analysis of near-borehole and anisotropeic layer effects on the response of multicomponent induction logging tools," *Geophysics*, Vol. 69, No. 1, 140–151, 2004.

3D Laser Imaging

Gerard Berginc and Michel Jouffroy
THALES, 2 avenue Gay Lussac, Elancourt Cedex 78995, France

Abstract— This paper addresses $3D$ laser imaging. $3D$ active imaging or $3D$ laser imaging has been greatly improved with the development of highly sensitive, high pixel density cameras. In this paper, we develop a $3D$ laser imaging method using tomographic algorithm. We obtain the three-dimensional reconstruction by a cone-beam algorithm [1], which is a convolution back-projection algorithm deduced from the Radon transform. This algorithm uses a set of two-dimensional projections which contain the data collected by the pixels of a focal plane area. These data are related to the intensity backscattered by the scene illuminated by a laser pulse. The scattered intensity contains the information for the $3D$ reconstruction. This process allows the reconstruction of a $3D$ scene from a series of images parameterized by an angle of axial rotation. In this paper, we study the robustness of this algorithm. To analyze the $3D$ reconstruction algorithm, we give experimental proof of the theory. We develop a $3D$ imaging experiment based upon a two-dimensional imaging device with high pixel density in the visible band.

1. INTRODUCTION

In this paper, we present $3D$ laser imaging experimental data. There is a considerable interest in the development of new optical imaging systems that are able to give three-dimensional images. Potential applications range across the field of defense and security for the recognition of targets, the medical field for the detection of subcutaneous and cutaneous tumors or the field of micro-electronics for the observation of hardware components during their manufacture. Identifying targets or objects concealed by foliage or camouflage is a critical requirement for operations in public safety, law enforcement and defense. The most promising techniques for these tasks are $3D$ laser imaging techniques. Active imaging systems use a near-infrared or visible laser and a suitable detector. We propose a tomographic method to enable a super-resolution $3D$ reconstruction from several intensity images of hidden objects. The laser illuminates the scene and the reflected radiation is collected by a detector to give a two-dimensional image. We obtain a three-dimensional image through a tomographic algorithm taking into account $2D$ images with different angles of view.

2. THREE-DIMENSIONAL REFLECTIVE TOMOGRAPHIC RECONSTRUCTION

An optronic system creates a $3D$ image of an object present in a complex optronic scene. This image must for example make it possible to pick out camouflaged targets behind camouflage netting, under trees, etc. This operational condition constitutes the major problem. Our technique is based upon a $3D$ tomographic reconstruction [2, 3]. In this field of $3D$ imaging, it is necessary to obtain a set of measured data of the considered object to be reconstructed dependent on a variable parameter (angle of view). This data set makes it possible to reconstruct the volume by applying inverse reconstruction techniques. From a mathematical point of view, the technique breaks down into two steps: direct measurement, optionally processed using a model of the physical phenomena which are measured or in our case measured data, and then reconstruction by inversion on the basis of these direct measures. The first problem consists in providing in a reasonable time a set of direct data that can be utilized for the inversion process. This problem naturally covers all the technological difficulties (high rate illumination laser, short pulse, detector block, pointing. . .). The second problem relates to the inversion procedure used and its mathematical implementation. For the inversion method, we use a cone-beam algorithm, which is a convolution back-projection algorithm deduced from the Radon transform.

In classical tomography, a thin beam (X-ray, laser . . .) propagates through the studied volume and reaches the detector which collects the data given by the transmitted electromagnetic waves. The obtained projection represents the attenuation by the penetrated volume along a straight line of the ray. As shown in Fig. 1, the projection data P_θ obtained for a given angle of observation θ is the line integral of the $2D$-object $f(x, y)$ in the (t, s) axis.

The line integral $P_\theta(t)$ is defined as follows [1]:

$$P_\theta(t) = \int_{(\theta,t)line} f(x, y)\, ds \tag{1}$$

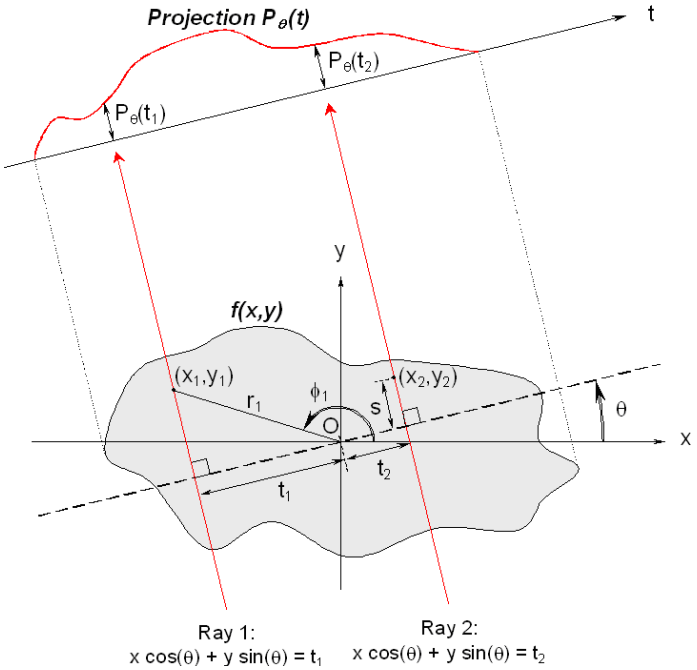

Figure 1: Representation of a line integral for a $2D$-object $f(x,y)$ for the θ observation angle.

which can be expressed using a delta function to give the Radon transform of the function f:

$$P_\theta(t) = \int_{-\infty}^{+\infty}\int_{-\infty}^{+\infty} f(x,y)\,\delta(x\cos(\theta) + y\sin(\theta) - t)\,dxdy \tag{2}$$

As the object has a finite size, we can define the t_m value for which $P_\theta(t) = 0$ with $|t| > t_m$ in all projections. Using the Fourier Slice Theorem, we can express the object function $f(x,y)$ as a function of the parallel projections $P_\theta(t)$ and the impulse response $h(t,\theta)$ of a filter with which the projection must be processed:

$$f(x,y) = \int_0^{\pi}\int_{-t_m}^{+t_m} P_\theta(t)\,h(x\cos(\theta) + y\sin(\theta) - t)\,dtd\theta \tag{3}$$

The formulas of this algorithm appear as weighted sums of conical integral projections.

In Fig. 2(b), we give a reconstructed image corresponding to the scenario of the Fig. 2(a). We consider a scenario with a vehicle which is not occluded by some elements of the optronic scene. We simulate the backscattered intensity, the physics based model includes the different electromagnetic interaction mechanisms. The surface of hard objects is considered as randomly rough surfaces and we compute the laser signature (i.e., laser cross-section) of the object. To estimate the laser interaction with the randomly rough surfaces, we use the second-order Small Slope Approximation method. All the scattering coefficients (coherent and incoherent components of the electromagnetic field) are functions of the azimuth angles, and the cross-polarized terms do not vanish. And we define the Mueller matrix, which gives all the combinations of the polarization states of the scattered electromagnetic waves. The randomly rough surfaces of the complex object are characterized by electromagnetic parameters (permittivity...) and roughness parameters (standard deviations of rough surface height and autocorrelation functions). For the simulated vehicle, we use a pulse laser with a wavelength of 1.54 µm. We consider that the windows of the vehicle (windscreen, side and rear windows) are made of glass (BK7 type) and the surfaces of the vehicle are considered as metallic. The Fig. 2(c) gives the reconstruction obtained from a real laser image sequence at 543 nm and we consider the same type of vehicle.

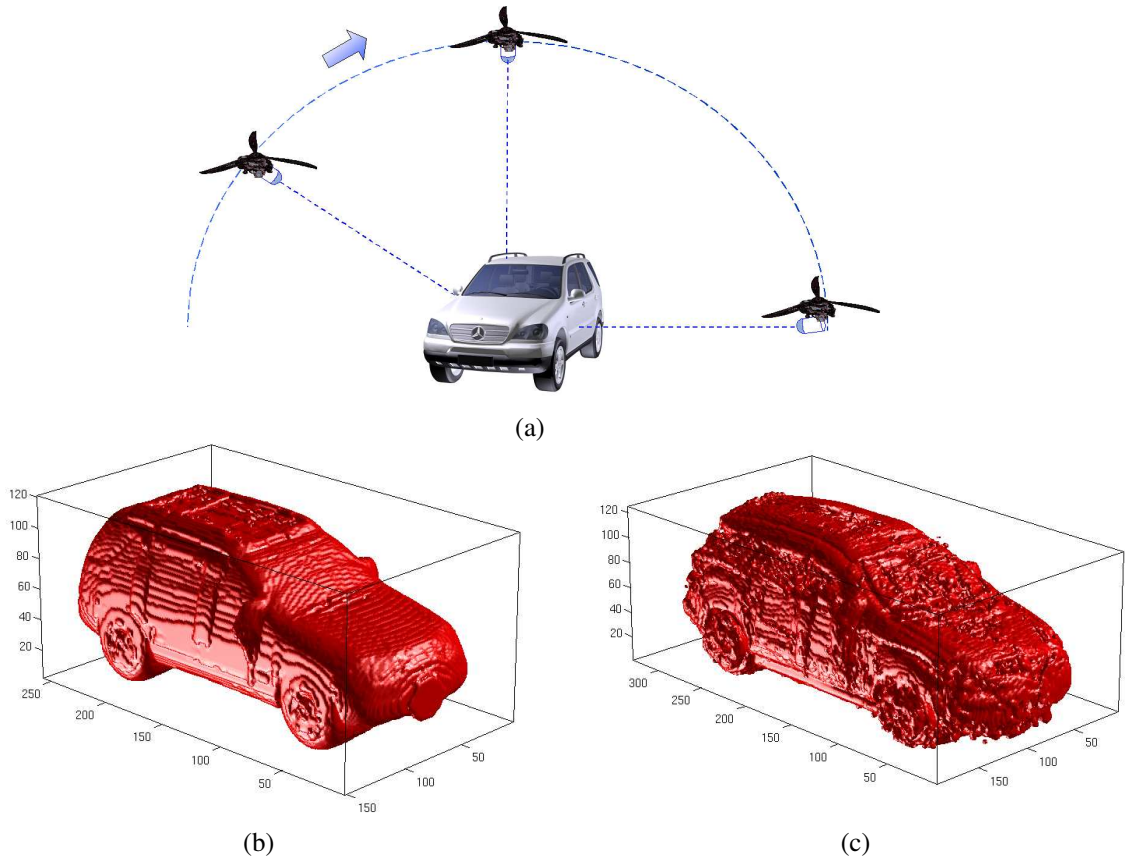

Figure 2: Simulated (b) and experimental (c) reconstructions of the considered scenario (a).

3. RECONSTRUCTION FROM EXPERIMENTAL LASER IMAGES OF VEHICLES: AIR-TO-GROUND CASE

In this section, we give a reconstruction example from experimental active images of a concealed target. The Fig. 3(a) gives laser images of the scene coded in false colors. The wavelength of the laser is 543 nm. The laser imaging device is used in mono-static or quasi mono-static configuration (the angle of emission is equal to the angle of reception), this configuration is interesting because the illuminated scene has a minimum of shadow zones. Moreover, the optic used is dimensioned for the sensor and the wavelength chosen, here again with the aim of improving the contrast of the scene. The whole scene is illuminated by the laser pulse. We consider an air-to-ground scenario. The process comprises the following successive steps:

- Acquisition of a sequence of laser images of the scene with a chosen reference.
- Reconstruction of the object in three dimensions by a tomography function utilizing the two-dimensional images representing the intensity levels of the electromagnetic backscattered intensity, the image can be re-dimensioned with respect to a reference image.
- Extraction of the zone of the three-dimensional reconstruction comprising the object to be identified.
- Reconstruction of the surface of the object in three dimensions.

The Fig. 3(b) shows the reconstruction of the vehicle hidden by a dense foliage. The occultation rate of the target is about 50% depending on the observation angle.

Detailed $3D$ structural information is obtained from the measured data. The vehicle data consist of a cloud of structured points (volumic pixel or voxel). We can then identify the object within a database of CAD models. This $3D$ representation can perform geometrical surface matching between a library of $3D$ surface models and the reconstructed object.

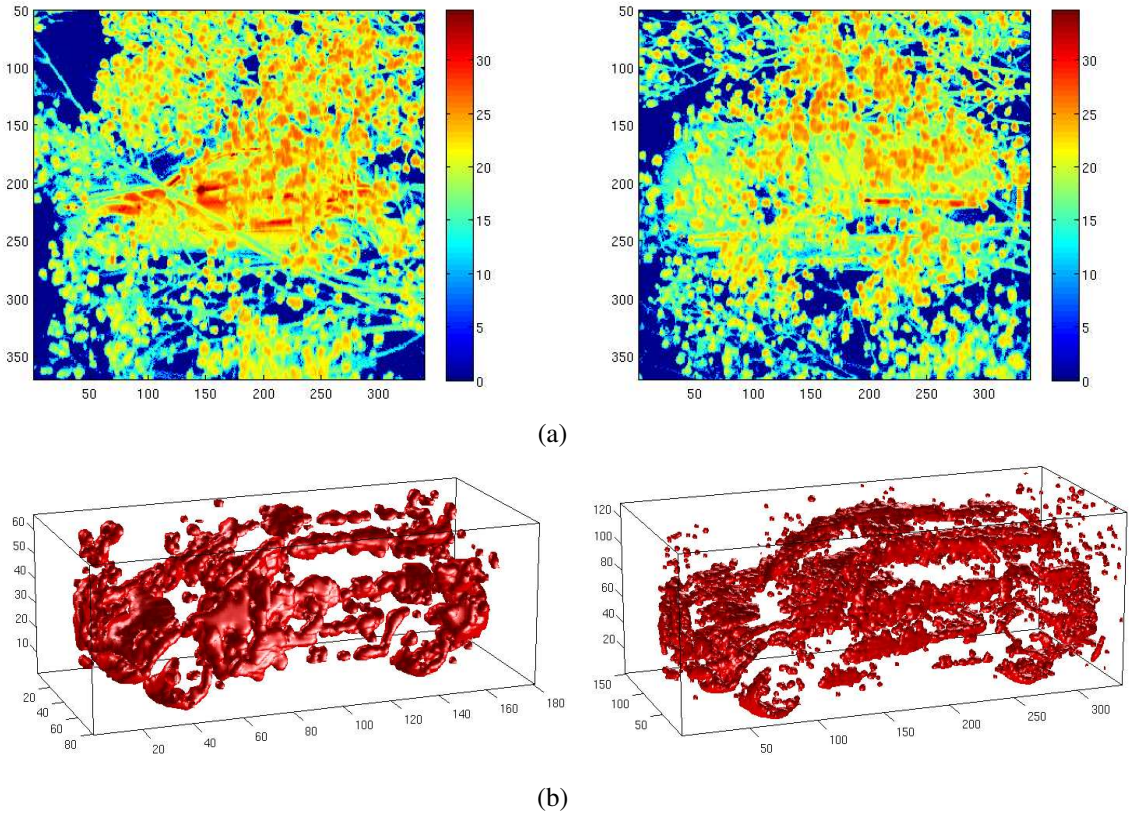

Figure 3: Laser images (a) and reconstructions (b) of the air-to-ground scenario.

The reconstruction is given for two resolutions: 180 (left picture) and 360 (right picture) voxels. For the lower resolution, the $3D$ surface is smoother than for the higher that appears a bit noisy. High resolution brings a lot of details that enhance the identification probability.

4. RECONSTRUCTION FROM EXPERIMENTAL LASER IMAGES OF VEHICLES: GROUND-TO-GROUND CASE

To test the practicability of our method, we carry out an outdoor experiment to construct a $3D$ laser image. We consider a ground-to-ground case (Fig. 4(a)). We give results of $2D$ laser imaging (for example Fig. 4(b)). The vehicle is positioned behind trees and foliage. The occultation rate of the sequence fluctuates between about 30% and 50% depending on the observation angle. We take laser images over 180^o. We consider a visible band for the laser.

It can be observed that a ground-to-ground scenario gives only lateral images of the vehicle: we have a unique possible scenario with this configuration contrary to an air-to-ground scenario where the exploration planes remain infinite. That is why we have so few information about the structure of the vehicle roof.

The reconstruction is given Fig. 4(c) for two resolutions: 230 (left picture) and 460 (right picture) voxels. As shown earlier in the air-to-ground scenario the $3D$ surface is smoother for lower resolutions. Although the reconstructed surface is noisier for the high resolution, fine details corresponding to the edges of the vehicle remain. Moreover, the noisy voxel clouds corresponding to the plane surfaces of the vehicle are correctly located on the reconstruction. They can be seen as a proof of the location of a plane object surface with a high probability and participate to the global identification of the camouflaged target. In the reconstruction process highly detailed structures appear first (strong intensity) then plane structures. The intensity threshold allowing to keep a given voxel or not is manually tuning to extract a structure from the noise. When the target is concealed like in this case, the density of a voxel cloud can bring a further information for the identification of the object.

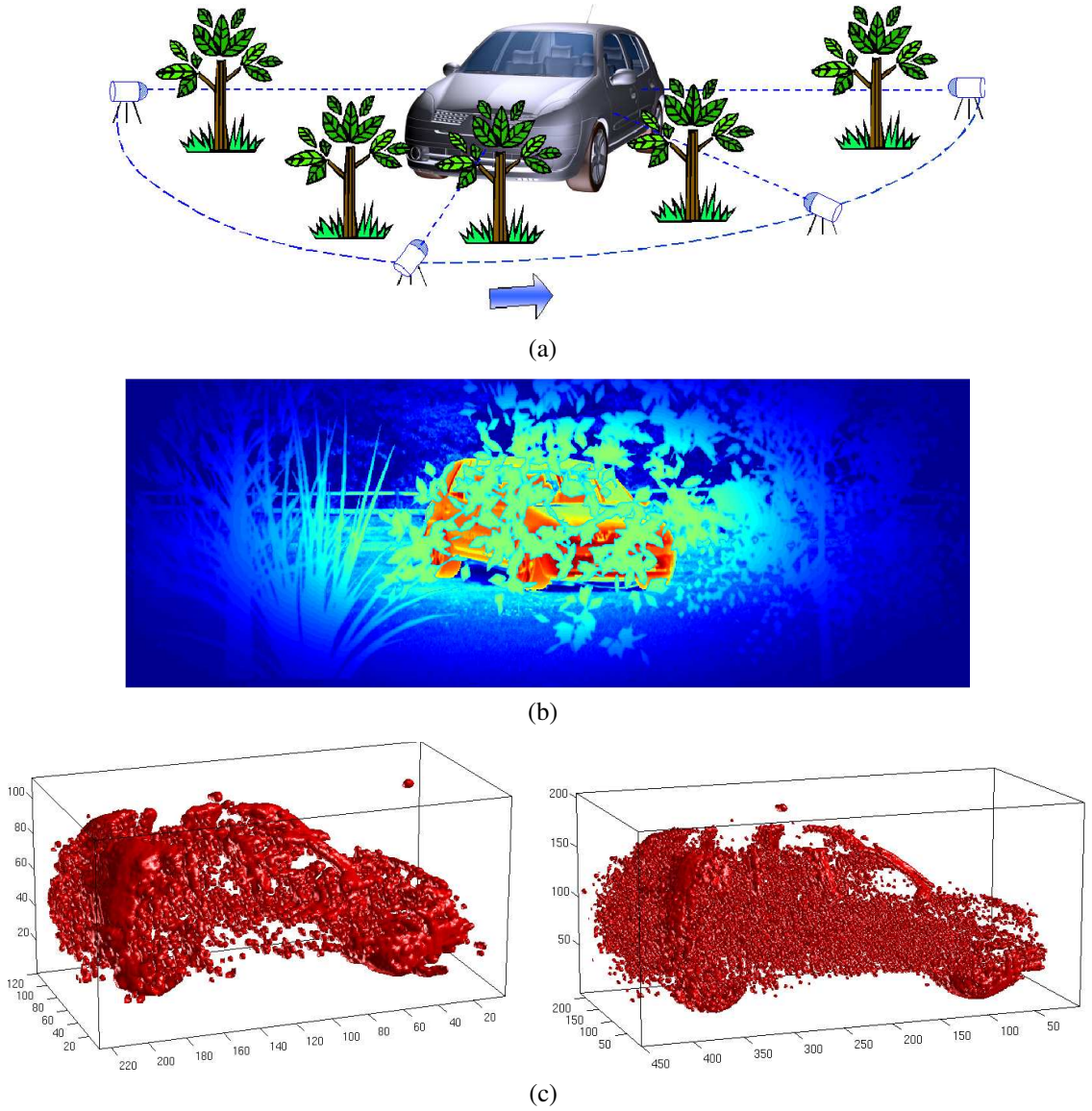

Figure 4: Scenario (a), laser image (b) and reconstructions (c) for the ground-to-ground scenario.

5. CONCLUSION

We present a $3D$ laser imaging using $2D$ laser images and a reconstruction algorithm. The reconstructions with the simulated data [3] and the measured data demonstrate both the ability to obtain detailed $3D$ images of objects under dense foliage. With these reconstruction procedures, we can separate objects from foliage and reconstruct a three-dimensional image of the considered object. With measured data, we have demonstrated that a tomographic reconstruction algorithm can provide $3D$ images of camouflaged vehicles.

REFERENCES

1. Feldkamp, L. A., L. C. Davis, and J. W. Kress, "Practical cone-beam algorithm," *J. Opt. Soc. Am.*, Vol. A6, 612–619, 1984.
2. Berginc, G. and M. Jouffroy, "Simulation of $3D$ laser systems," *Proceedings of the 2009 IEEE International Geoscience & Remote Sensing Symposium*, 440–444, Cape Town, South Africa, July 12–17, 2009.
3. Berginc, G. and M. Jouffroy, "Simulation of $3D$ laser imaging," *PIERS Online*, Vol. 6, No. 5, 415–419, 2010.

Amplified Stimulated Terahertz Emission from Optically Pumped Graphene

T. Otsuji[1,4], **S. A. Boubanga Tombet**[1,4], **S. Chan**[2], **T. Watanabe**[1], **A. Satou**[1,4], **and V. Ryzhii**[3,4]

[1]Research Institute of Electrical Communication, Tohoku University, Japan
[2]Nano-Japan Program, University of Pennsylvania, USA
[3]Computational Nano-Electronics Laboratory, University of Aizu, Japan
[4]JST-CREST, Japan

Abstract— The gapless and linear energy spectra of electrons and holes in graphene lead to nontrivial features such as negative dynamic conductivity in the terahertz spectral range. This paper reviews the recent advances in theoretical and experimental study on terahertz light amplification by stimulated emission of radiation in optically pumped graphene.

1. INTRODUCTION

Graphene, a monolayer sheet of carbon atomic honeycomb lattice crystal, has attracted attention owing to the massless Dirac Fermions of electrons/holes [1, 2]. The gapless and linear energy spectra of electrons/holes lead to nontrivial features such as negative dynamic conductivity in the terahertz (THz) spectral range under optical pumping [3], which may lead to the development of a new type of THz lasers [4]. In this paper, we'll review the theory and experimental results of THz amplified stimulated emission from optically pumped graphene.

2. THEORITICAL MODEL

When graphene is pumped with the infrared (IR) photon having an energy $\hbar\Omega$, electrons/holes are photogenerated via interband transitions. When the photogenerated electrons and holes are heated in case of room temperature environment and/or strong pumping, collective excitations due to the carrier-carrier (CC) scattering, e.g., intraband plasmons should have a dominant play to perform an ultrafast carrier redistribution along the energy as shown in Fig. 1 [5, 6]. Then optical phonons (OPs) are emitted by carriers on the high-energy tail of the electron and hole distributions. This energy relaxation process accumulates the nonequilibrium carriers around the Dirac points as shown in Fig. 1. Due to a fast intraband relaxation (ps or less) and relatively slow interband recombination ($\gg 1$ ps) of photoelectrons/holes, one can obtain the population inversion under a sufficiently high pumping intensity. Due to the gapless symmetrical band structure of graphene, photon emissions over a wide THz frequency range are expected if the pumping IR photon energy is properly chosen.

We consider an intrinsic graphene under the optical pulse excitation in the case where the CC scattering is dominant and carriers always take quasi-equilibrium. We take into account both the

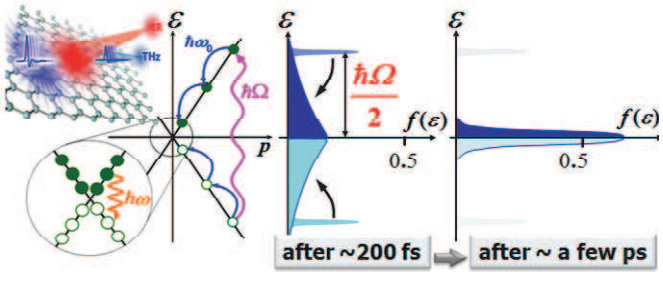

Figure 1: Carrier relaxation/recombination dynamics in optically pumped graphene.

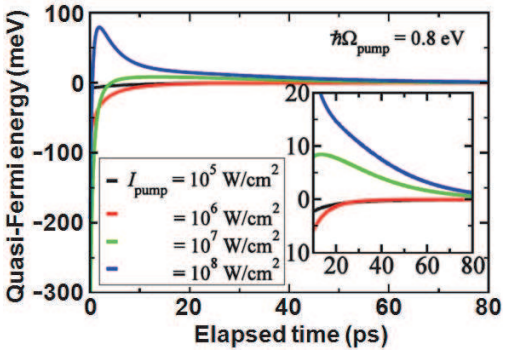

Figure 2: Temporal evolution of the quasi-Fermi energy after impulsive pumping.

intra and interband OPs [7, 8]. The carrier distribution (equivalent electron and hole distributions) is governed by the following equations for the total energy and concentration of carriers:

$$\frac{d\Sigma}{dt} = \frac{1}{\pi^2}\sum_{i=\Gamma,K}\int d\mathbf{k}\left[(1-f_{h\omega_i-v_w\hbar k})(1-f_{v_w\hbar k})/\tau^{(+)}_{iO,inter} - f_{v_w\hbar k}f_{h\omega_i-v_w\hbar k}/\tau^{(-)}_{iO,inter}\right],$$

$$\frac{dE}{dt} = \frac{1}{\pi^2}\sum_{i=\Gamma,K}\int d\mathbf{k}v_w\hbar k\left[(1-f_{h\omega_i-v_w\hbar k})(1-f_{v_w\hbar k})/\tau^{(+)}_{iO,inter} - f_{v_w\hbar k}f_{h\omega_i-v_w\hbar k}/\tau^{(-)}_{iO,inter}\right]$$
$$+\frac{1}{\pi^2}\sum_{i=\Gamma,K}\int d\mathbf{k}h\omega_i\left[f_{v_w\hbar k}(1-f_{v_w\hbar k}+h\omega_i)/\tau^{(+)}_{iO,intra} - f_{v_w\hbar k}(1-f_{v_w\hbar k}-h\omega_i)/\tau^{(-)}_{iO,intra}\right]$$

where Σ and E are the carrier concentration and energy density, f_ε is the quasi-Fermi distribution, $\tau^{(\pm)}_{iO,inter}$ and $\tau^{(\pm)}_{iO,intra}$ are the inverses of the scattering rates for inter and intraband OPs ($i = \Gamma$ for OPs near the Γ point with $\omega_\Gamma = 196\,\mathrm{meV}$, $i = K$ for OPs near the zone boundary with $\omega_\Gamma = 161\,\mathrm{meV}$, $+$ for absorption, and $-$ for emission). Time-dependent quasi-Fermi energy ε_F and the carrier temperature T_c are determined by these equations. Fig. 2 shows the typical results for fs pulsed laser pumping with photon energy 0.8 eV [9]. It is clearly seen that ε_F rapidly increases with cooling the carrier and it becomes positive when the pumping intensity exceeds a certain threshold level. This result proves the occurrence of the population inversion. After that, the recombination process follows more slowly ($\sim 10\,\mathrm{ps}$).

3. EXPERIMENTAL RESULTS AND DISCUSSION

We observed the carrier relaxation and recombination dynamics in optically pumped graphene using THz time-domain spectroscopy based on an optical pump/THz-and-optical-probe technique [10]. An exfoliated monolayer-graphene/SiO_2/Si sample is placed on the stage and a 0.12-mm-thick (100)-oriented CdTe crystal is placed on the sample, acting as a THz probe pulse emitter as well as an electrooptic sensor. A single 80-fs, 1550-nm fiber laser beam having 4-mW average power and 20-MHz repetition is split into two: one for optical pumping and generating the THz probe beam in the CdTe crystal, and one for optical probing. The pumping laser, which is linearly polarized, is simultaneously focused at normal incidence from the back surface on the graphene sample to induce population inversion and the CdTe to induce optical rectification and emission of THz pulse (the primary pulse marked with "①" in Fig. 3). This THz beam reflecting back in part at the CdTe top surface stimulates the THz emission in graphene, which is electrooptically detected as a THz photon echo signal (the secondary pulse marked with "②" in Fig. 3).

Figure 4 shows a typical temporal response under the maximal pumping intensity. The black/red curve is the response when the pumping beam is focused onto the sample with/without graphene. The second pulse, the THz photon echo signal, obtained with graphene is more intense compared with that obtained without graphene. This indicates the graphene act as an amplifying medium.

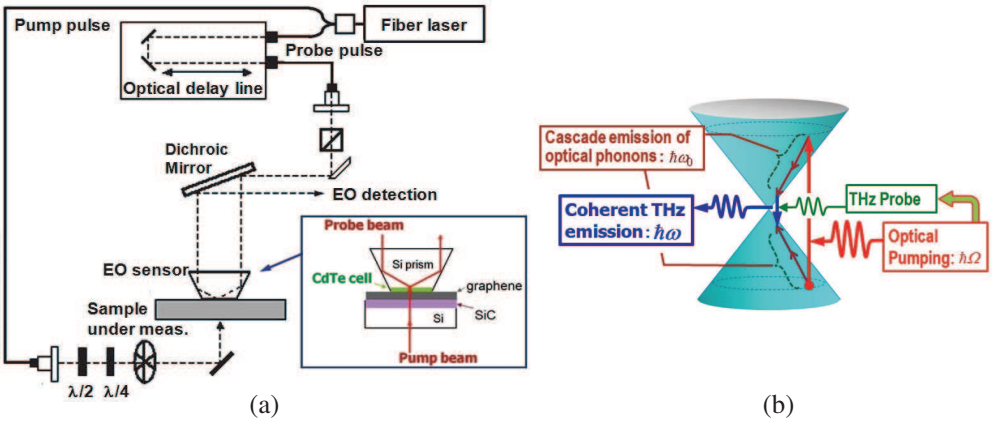

Figure 3: (a) Experimental setup and (b) the scheme of coherent emission from graphene by an optical-pump/THz-probe technique. Time-resolved electric field intensity is electroopticaly sampled by the probe beam throughout the CdTe sensor crystal in total reflection geometry. The CdTe also works as a THz probe beam source.

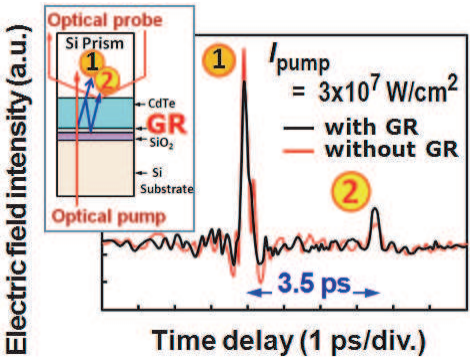

Figure 4: Measured temporal profile. The secondary pulse is the THz photon echo transmitted and reflected through graphene.

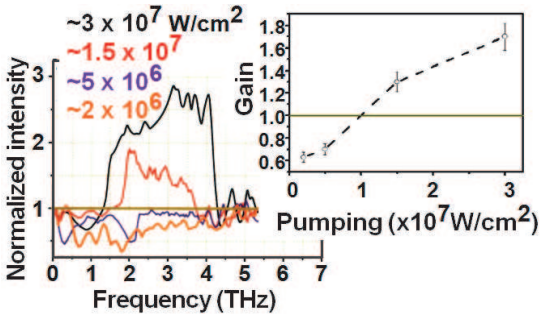

Figure 5: Normalized Fourier spectra and gain profile.

Fig. 5 shows the emission spectra from graphene after normalization to the one without graphene. The inset in Fig. 5 shows the measured gain as a function of the pumping power. A threshold like behavior can be seen testifying the occurrence of the negative conductivity and the THz light amplification by stimulated emission of radiation.

4. CONCLUSIONS

We have successfully observed coherent amplified stimulated THz emissions arising from the carrier relaxation/recombination dynamics of an exfoliated graphene. The results provide evidence of the occurrence of negative dynamic conductivity, which can potentially be applied to a new type of THz lasers.

ACKNOWLEDGMENT

This work is financially supported in part by JST-CREST, Japan, and JSPS-BR(S), Japan.

REFERENCES

1. Novoselov, K. S., A. K. Geim, S. V. Morozov, D. Jiang, Y. Zhang, S. V. Dubonos, I. V. Grigorieva, and A. A. Firsov, "Electric field effect in atomically thin carbon films," *Science*, Vol. 306, 666–669, 2004.
2. Geim, K. and K. S. Novoselov, "The rise of graphene," *Nat. Mat.*, Vol. 6, 183–191, 2007.
3. Ryzhii, V., M. Ryzhii, and T. Otsuji, "Negative dynamic conductivity of graphene with optical pumping," *J. Appl. Phys.*, Vol. 101, No. 7, 083114-1–4, 2007.
4. Ryzhii, V., M. Ryzhii, A. Satou, T. Otsuji, A. A. Dubinov, and V. Y. Aleshkin, "Feasibility of terahertz lasing in optically pumped epitaxial multiple graphene layer structures," *J. Appl. Phys.*, Vol. 106, No. 8, 084507-1–6, 2009.
5. George, P. A., J. Strait, J. Dawlaty, S. Shivaraman, M. Chandrashekhar, F. Rana, and M. G. Spencer, "Ultrafast optical-pump terahertz-probe spectroscopy of the carrier relaxation and recombination dynamics in epitaxial graphene," *Nano Lett.*, Vol. 8, 4248–4251, 2008.
6. Breusing, M., C. Ropers, and T. Elsaesser, "Ultrafast carrier dynamics in graphite," *Phys. Rev. Lett.*, Vol. 102, 086809–086813, 2009.
7. Suzuura, H. and T. Ando, "Zone-boundary phonon in graphene and nanotube," *J. Phys. Soc. Jpn.*, Vol. 77, 044703, 2008.
8. Rana, F., P. A. George, J. H. Strait, J. Dawlaty, S. Shivaraman, M. Chandrashekhar, and M. G. Spencer, "Carrier recombination and generation rates for intravalley and intervalley phonon scattering in graphene," *Phys. Rev. B*, Vol. 79, 115447, 2009.
9. Satou, A., T. Otsuji, and V. Ryzhii, "Study of hot carriers in optically pumped graphene," *Ext. Abstract Int. Conf. Solide State Devices and Materials*, 882–883, JSAP, Tokyo, Japan, Sep. 2010.
10. Karasawa, H., T. Komori, T. Watanabe, A. Satou, H. Fukidome, M. Suemitsu, V. Ryzhii, and T. Otsuji, "Observation of amplified stimulated terahertz emission from optically pumped heteroepitaxial graphene-on-silicon materials," *J. Infrared Milli. Terhz. Waves*, online, 2010, doi:10.1007/s10762-010- 9677-1.

Recent R&D Trends in Broadband Optical Access System Technologies towards the Second-generation FTTH Era in Japan

Naoto Yoshimoto
NTT Access Network Service Systems Laboratories, Japan

Abstract— This paper provides an overview of recent technical trends in passive optical network (PON) systems, which have been widely deployed throughout the world. Based on the migration from the current system towards the next-generation system, and the convergence of several technologies, this work introduces several possible ways to develop the optical access network over the next decade, which has been called "the second-generation FTTH era", from the telecom operator's viewpoint.

1. INTRODUCTION

In the last decade, the ultimate broadband infrastructure, namely Fiber To The Home (FTTH), has been deployed throughout large parts of the world, especially Japan, East Asia, and North America, by using passive optical network (PON) technologies, i.e., B-PON, G-PON and 1G-EPON, to provide attractive broadband services such as the delivery of video content and IP-TV. Operators have been steadily deploying optical cables and compact state-of-the-art transmission equipment, and so the replacement of equipment and system migration have not proved very complicated. Today, the number of FTTH subscribers in Japan has exceeded 10 million and 90% of the population have FTTH coverage as shown in Figure 1. Therefore, we must carefully consider a way to upgrade the deployed systems and introduce new technologies to maintain sustainable revenue in an extremely competitive environment. The first priority is to reduce capital expenditure (CAPEX) and operational expenditure (OPEX). Based on the customers' demand for bandwidth, next-generation PON systems such as 10G-EPON will be a most attractive candidate. If H.264 codec high definition video is provided on the current 1G-EPON system, only 2 or 3 channels can be supported per dwelling. To overcome this lack of bandwidth, 10G-EPON with a large bandwidth will be needed in the near future. Along with the progress of high-speed Ethernet technology towards 40GE/100GE, high-speed PON technology has also been vigorously investigated, and 10G-class PON, both the ITU-T series of G. 987 (XG-PON) [1] and IEEE 802.3av (10G-EPON) [2], has already been standardized. The next challenge is to decide how such a new PON system will be deployed to meet the demand for increased bandwidth. Moreover, we must reduce the power consumption of the PON system to meet the social requirement to reduce carbon dioxide, because the power consumption of ONUs on users' premises accounts for approximately half that of the entire network [3]. These requirements indicate that telecom operators and service providers are facing a new management environment, namely "the second-generation FTTH era", in terms of sustaining the optical broadband service business and investing in new broadband access network technologies to provide new sources of revenue. This is because additional investment to increase bandwidth will enable telecom operators to provide new attractive services in the near future, and social responsibility must be honored as regards environmental issues. A recent topic of considerable interest has been the launch of actual broadband wireless services such as LTE and WiMAX. As shown in Figure 1, the bandwidth of these services will increase approximately tenfold in the next five years at a similar pace to FTTH. This means there will be an increasing need for an optical backhaul network with a large bandwidth for broadband mobile services. This fact also means that technical convergence and a complementary relationship between optical systems and wireless systems in metro/access networks will be indispensable in this decade. Taking the deployment penetration and technical trends of broadband services into consideration, the author describes two possible approaches to realizing future optical access networks. One approach involves upgrading the bandwidth of current TDM-PON, i.e., G-PON and 1G-EPON, in addition to reach extension using optical amplifiers. The other approach employs wavelength demultiplexing (WDM) to obtain flexibility as regards such factors as increasing the splitting number for CAPEX/OPEX reduction, meeting the bandwidth requirement, and power saving.

2. UPGRADE TDM-PON

From the telecom operator's point of view, effective ways of introducing the next-generation PON system while minimizing CAPEX include both increasing the number of users accommodated by

one system, and realizing a wide area of coverage. Figure 2 shows an example 10G-EPON system configuration with an increased splitting number and an extended reach. The particular merit of upgrading the bandwidth of the existing PON system currently focuses on cost reduction per subscriber by increasing the splitting number of PON systems, as well by providing larger broadband services. Moreover, the number of OLTs at the central office can be reduced due to the increased splitting number. This results in reduced power consumption by the central office.

As a way of extending reach [4–6], the PON Extender, which uses a burst-mode optical amplifier compactly integrated with up/downstream components, and an auto-level control circuit with high-speed operation, have been demonstrated as shown in Figure 2. This approach can achieve optical burst mode operation with a wide dynamic range and a large loss budget of over 40 dB, which is equivalent to a transmission distance of 60 km [7]. To further reduce equipment size and cost, and to accommodate a variety of wavelength allocations, semiconductor burst-mode optical amplifiers have been investigated [8].

With respect to CAPEX reduction, we should also consider how to ensure that the current subscribers migrate smoothly from the existing system to a new broadband system. Operators will address, for example, the problem of realizing a configuration where 1G/10G-EPON co-exist on the same optical distribution network. First, 1G-OLT will be upgraded to 1G/10G dual-rate OLT, which will be able to connect to both 10G/10G symmetric ONUs and 1G/10G asymmetric ONUs as well as 1G-ONUs. 10G-ONUs will be steadily deployed according to the demand for broadband services. Therefore, operators can consider various migration scenarios from the existing 1G-EPON, when 10G-EPON is flexibly deployed according to customer demand. To realize this 1G/10G co-existing configuration, the 1G/10G dual-rate dynamic bandwidth allocation (DBA) technique and the 1G/10G dual-rate burst-mode transceiver are key technologies for handling 1G- and 10G-data simultaneously. A practical demonstration of dual-rate receivers has recently been reported [9, 10].

3. WDM ACCESS TECHNOLOGIES

However, if the required bandwidth is larger than 10G, the required electric circuits will be more expensive and consume more energy. The WDM access approach is a promising way of avoiding

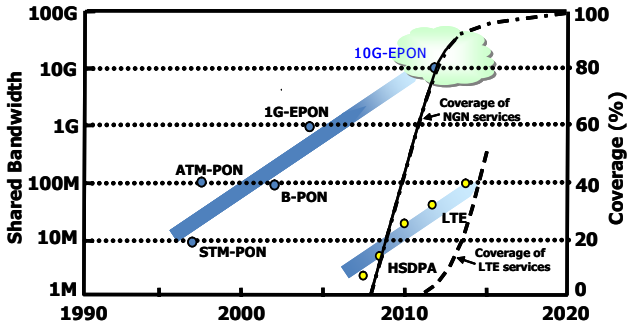

Figure 1: Bandwidth and coverage trends in FTTH and mobile services in Japan.

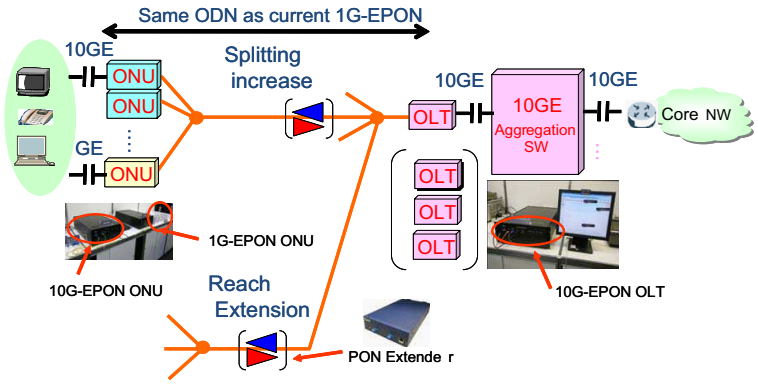

Figure 2: Possible PON system configuration of 10G-EPON and its reach extension/splitting increase.

these problems. Legacy WDM-PON is basically defined as a PON system on which each ONU is assigned a different wavelength. This approach can simplify the logical relationship between an ONU and an OLT by considering it equal to a Point-to-Point connection, and assign sufficient bandwidth per customer. Meanwhile, many wavelength resources will be needed, more effective use of wavelength resources will make sense in the future and will be achieved for example by using the dynamic wavelength assignment technique and wavelength selectable components. Figure 3 shows an example of a PON system employing WDM. It has a large splitting WDM/TDM hybrid PON configuration using a passive wavelength router such as a cyclic arrayed waveguide grating, in which time and wavelength are shared for advanced bandwidth resource allocation among a larger number of customers than that with the current commercialized TDM-PON [11]. This makes it possible to allocate the bandwidth more flexibly and widely and so meet bandwidth demand instantly. It can therefore implement a load-balanced function and a redundant configuration in a wide-area access network to better handle traffic congestion [12]. Moreover, power saving is possible by setting unused wavelength channels in the "sleep mode". This mode depowers all electric circuits and optical components of the sleep channels, which can lead to an effective reduction in power consumption. In addition, the passive wavelength router provides a port distribution function, which is part of the role of the aggregation switch. Therefore, the power consumption of the aggregation switch can be reduced using such a passive router. These techniques will contribute to the global effort to emphasize green network technologies.

Finally, such an advanced PON system of the future should be positively utilized for other network services such as the backhaul of 4G mobile services, broadband ubiquitous and cloud services [13]. Figure 4 shows an example of a future wired and wireless convergence network using WDM technologies. In this case, optimized wavelength resources will be flexibly prepared in the extended network to take account of the customer's demand for bandwidth for attractive new services and optical cable deployment scenarios for constructing next-generation mobile base stations. As the utilization efficiency of the optical cable infrastructure increases, we can expect a great reduction in the CAPEX of the telecom operators.

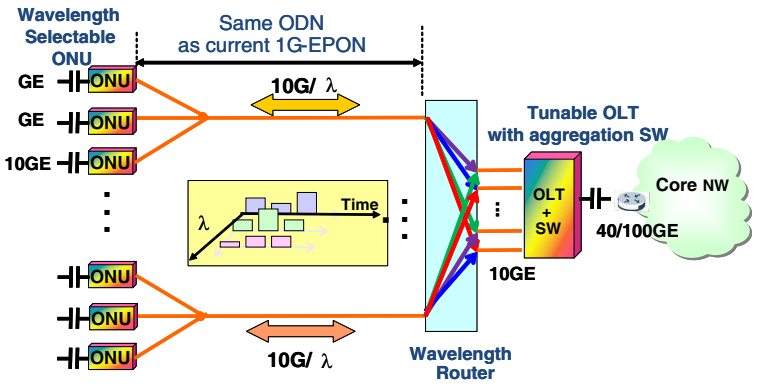

Figure 3: Large splitting WDM/TDM-PON approach using wavelength router.

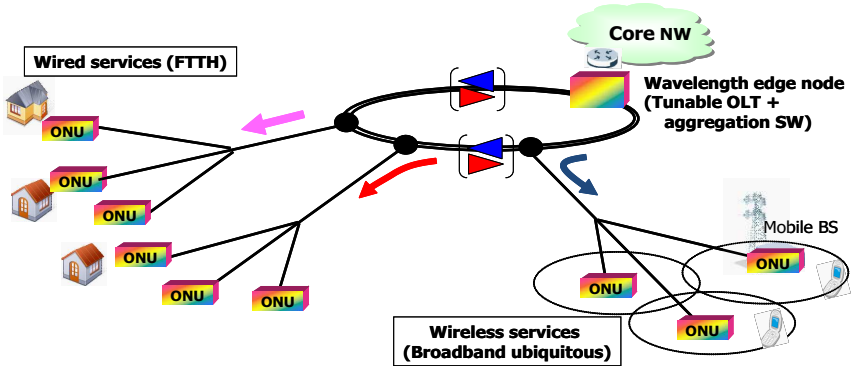

Figure 4: Example of future wired and wireless convergence network.

4. CONCLUSION

Having achieved the goal of widely deploying FTTH services as the first priority, we are now facing a new period, namely the second generation FTTH era, in which various requirements should be considered with respect to reducing both CAPEX/OPEX and CO_2 emissions, as well as continuously increasing the customer's bandwidth. To deal with these issues, 10G-class TDM-PON with an increased bandwidth, an increased splitting number or extended reach, and a PON system employing WDM technology with smart wavelength resource handling are promising candidates for future access networks. In the near future, as the demand for bandwidth increases for mobile services according to the popularity of smart phones, a larger capacity optical access system with bandwidth flexibility will be needed as a mobile backhaul network.

REFERENCES

1. ITU-T Recommendation G.987 series, "10-Gigabit-capable passive optical network (XG-PON) systems".
2. IEEE Std 802.3av-2009, "Physical layer specifications and management parameters for 10Gb/s passive optical networks," 2009.
3. Kubo, R., J.-I. Kani, H. Ujikawa, T. Sakamoto, Y. Fujimoto, N. Yoshimoto, and H. Hadama, "Study and demonstration of sleep and adaptive link rate control mechanisms for energy efficient 10G-EPON," *J. Opt. Commun. Netw.*, Vol. 2, No. 9, 716–729, 2010.
4. Suzuki, K., Y. Fukada, D. Nesset, and R. Davey, "Amplified gigabit PON systems," *J. Opt. Netw.*, Vol. 6, No. 5, 422–433, 2007.
5. Davey, R. P., D. B. Grossman, M. Rasztovits-Wiech, D. B. Payne, D. Nesset, A. E. Kelly, A. Rafel, S. Appathurai, and S.-H. Yang, "Long-reach passive optical networks," *J. Lightwave Technol.*, Vol. 27, No. 3, 273–291, 2009.
6. Saliou, F., P. Chanclou, F. Laurent, N. Genay, J. A. Lazaro, F. Bonada, and J. Prat, "Reach extension strategies for passive optical networks," *J. Opt. Comm. Netw.*, Vol. 1, No. 4, C51–C60, 2009.
7. Fujiwara, M., K.-I. Suzuki, K. Hara, T. Imai, K. Taguchi, H. Ishii, N. Yoshimoto, and H. Hadama, "Burst-mode compound optical amplifier with automatic level control circuit that offers enhanced setting flexibility in a 10G-class PON," *in Proceedings of ECOC 2010*, PDP 3-2, Torino, Italy, September 2010.
8. Nesset, D. and P. Wright, "Raman extender GPON using 1240 nm semiconductor quantum-dot lasers," *Proceedings of OFC 2010*, OThW6, San Diego, CA, March 2010.
9. Hara, K., S. Kimura, H. Nakamura, N. Yoshimoto, and K. Kumozaki, "Burst-mode bit-rate discrimination circuit for 1.25/10.3-Gbit/s dual-rate PON systems," *Proceedings of OFC/NFOEC 2009*, OWH2, San Diego, CA, March 2009.
10. Nakagawa, J., M. Noda, N. Suzuki, S. Yoshima, K. Nakura, and M. Nogami, "First demonstration of 10G-EPON and GE-PON co-existing system employing dual-rate burst-mode 3R transceiver," *Proceedings of OFC/NFOEC 2010*, PDP-D10, San Diego, CA, March 2010.
11. Kani, J., "Challenges for next generation optical access networks — An operator's view," *Proceedings of ECOC 2010*, WS5, Torino, Italy, September 2010.
12. Nakamura, H., N. Yoshimoto, K. Hara, S. Kimura, and H. Hadama, "A highly scalable and reliable network architecture for wide-area optical access using lamda-tunable stacked-PONs," *Proceedings of ACP 2010*, PD3, Shanghai, China, December 2010.
13. Tsukamoto, K., T. Nishiumi, T. Yamagami, T. Higashino, S. Komaki, R. Kubo, T. Taniguchi, J. Kani, N. Yoshimoto, H. Kimura, and K. Iwatsuki, "Convergence of WDM access and ubiquitous antenna architecture for broadband wireless services," *PIERS Online*, Vol. 6, No. 4, 385–389, 2010.

A New Configuration of Broadband Wireless Access in Heterogeneous Ubiquitous Antenna and Its Experimental Investigation

T. Higashino[1], **K. Miyamoto**[1], **K. Tsukamoto**[1], **S. Komaki**[1], **T. Tashiro**[2], **K. Hara**[2], **J. Kani**[2], **N. Yoshimoto**[2], **and K. Iwatsuki**[3]

[1]Graduate School of Engineering, Osaka University, Japan
[2]NTT Access Network Service Systems Laboratories, Japan
[3]NTT Service Integration Laboratories, Japan

Abstract— Recently, multi-antenna technology is used in almost new wireless radio communication technology such as MIMO (multiple–input multiple-output) towards high throughput and high reliable communication [1–3]. The heterogeneous wireless networking is required to achieve high data rate and wide area coverage. The Radio on Fiber (RoF) is one of the candidates to construct "Wireless Cloud" infrastructure with low cost [4, 5]. This paper proposes a new configuration of broadband access network for heterogeneous radio which is based on distributed antenna system (DAS) [10–12] over the wavelength division multiplexing-passive optical network (WDM-PON) [6, 7]. A fundamental experiment is conducted for the performance evaluation in physical layer.

1. INTRODUCTION

In the next generation wireless access network, various kind of high-throughput internet services are provided at any time and any place. It is requested that throughput is equivalent of the optical fiber internet access service up to Gigabit per second [6–9]. In addition to the radio regulation (RR) strictly limits the transmitting power and bandwidth of RF signal. The higher radio frequencies will be assigned to new wireless services because of the lack of bandwidth at present. The higher radio frequency band such as microwave-band, millimeter wave band, and terahertz band is promising resource of the high-throughput wireless local/personal area network. Then, not only a lot of radio base stations, but also broadband entrance network to backbone IP networks are required. As for the recent wireless radio technology, multi-antenna technology is used in almost new wireless radio communication such as MIMO (multiple-input multiple-output) towards high throughput and high reliable communication [1–3]. The heterogeneous wireless networking is required to achieve high data rate and wide area coverage. The Radio on Fiber (RoF) is one of the candidates to construct "Wireless Cloud" infrastructure with low cost, because the RoF technology can realize different kind of air interface. Figure 1 shows the MIMO system over the ubiquitous antenna. The ubiquitous antenna system is a kind of distributed antenna system (DAS) using RoF network [10–15]. This network is constructed one centralized control station (CCS) and plural remote antenna elements connected with CCS via fiber-radio link. A remote antenna element have only a function of media conversion that is radio-to-optical (R/O) and optical-to-radio (O/R) conversion. The other functions of radio transceiver, modulation, demodulation, diversity, and handover are processed in the CCS. Especially in MIMO, multiplexing and decomposition process of plural spatial streams is processed at the CCS. At the remote antenna, multiple RF services are fed and make radio coverage of heterogeneous wireless services. In this configuration, antenna elemental distance can be expanded so that MIMO spatial filtering process overcome correlated fading channel [1, 14]. To fully utilize an optical wavelength resource, a lot of remote station needed to be accommodated [16, 17]. Then, multiplexing method for not only remote antennas, but also RF services is required.

This paper proposes a new architecture to multiplexing method for RoF link based on direct optical switching time division multiplexing (TDM) the over wavelength division multiplexing (WDM)-passive optical network (PON). In the system, bit-streams are spatially multiplexed in MIMO system, plural MIMO spatial streams on RoF link are multiplexed in time domain, RF services are also multiplex in time domain, optical signals are multiplexing in wavelength domain, and optical up/down streams are duplex in wavelength domain. The bandpass sampling technique [19] is used in the TDM. The IEEE802.11n WiFi 2 by 2 MIMO signals at 2.4 GHz and 5 GHz is experimentally transmitted [18] in the proposed link with RF fading channel.

2. CONFIGURATION

Figure 2 shows the configuration of wireless MIMO distribution system on Radio on Fiber with WDM-PON. A control station (CS) is located at the interface between backbone Internet and the access network. In the CS, plural MIMO transceivers are equipped, and the number of transceivers is the same of the femto-cell. Lots of the base stations (BSs) are connected to the CS, and different wavelengths are assigned to the BSs. Multiplexing and de-multiplexing is performed by using arrayed waveguide grating (AWG). In the BS, optical circulator and fiber grating are used to decompose optical upstream and downstream. This configuration achieves the transparency of transmission fiber through its lack of optical filters, and thus has scalability of upgrading wavelength channels easily in the future. Remote antenna elements are equipped in the BSs. In Figure 2, the femto-cell is build by multiple antenna elements.

3. EXPERIMENT

3.1. Setup

Figure 3 shows an experimental setup to transmit MIMO downstream spatial stream in RoF-DAS over WDM-PON with optical TDM and the signal transition diagram at each component [13]. The 2×2 MIMO signal transmission is assumed in a cell as shown in Figure 2. Two wavelengths were used to realize 2 by 2 MIMO signal transmission; two 802.11n RF signals in the 2.4 and 5 GHz bands were multiplexed in each wavelength with optical TDM and transmitted to the BS.

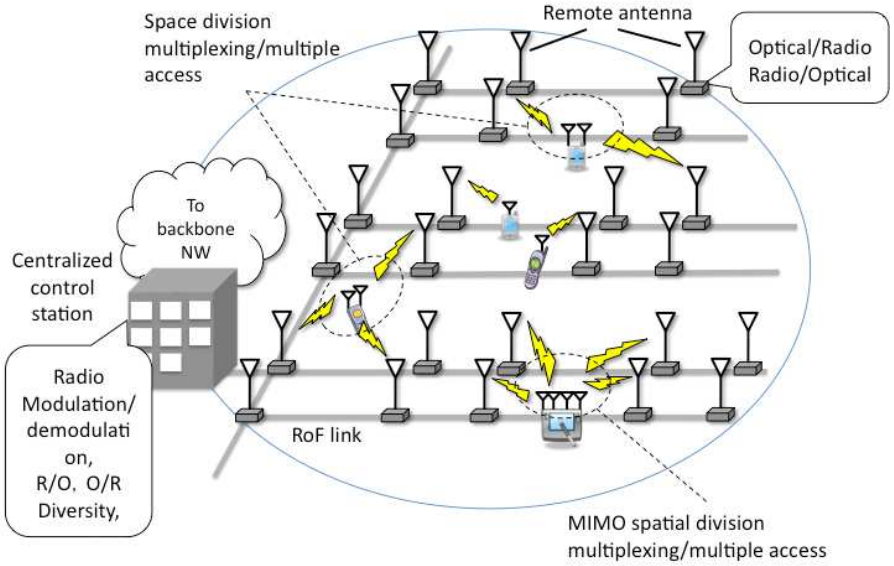

Figure 1: MIMO system over the ubiquitous antenna.

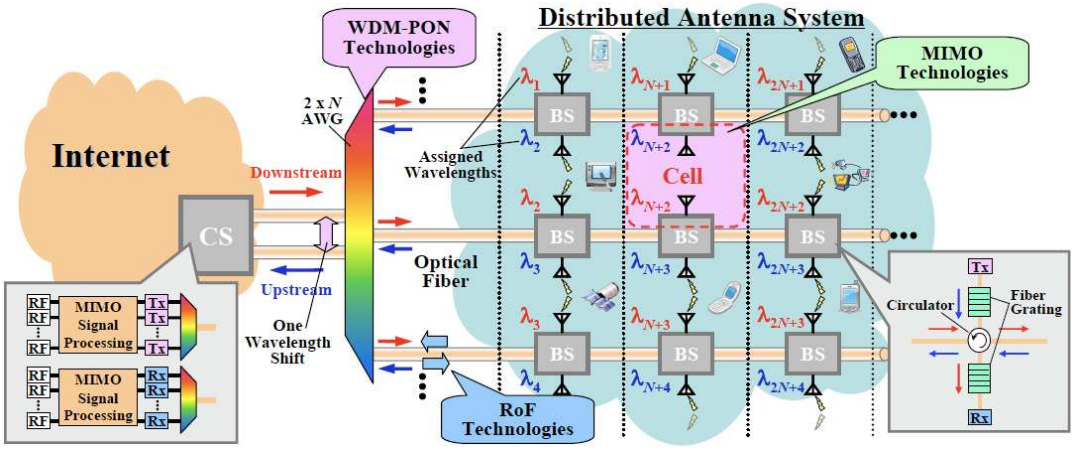

Figure 2: Wireless MIMO system on RoF DAS over WDM-PON.

The two continuous lightwaves emitted from DFB-LDs were wavelength-multiplexed in Figure 3(a), and modulated with a lithium niobate Mach-Zehnder modulator (LN-MZM) driven with a return to zero (RZ) pulse of 100 ps pulse width at a 1 GHz repetition rate from a pulse pattern generator (PPG) in Figure 3(b). Two wavelength signals were amplified with an erbium doped fiber amplifier (EDFA) and demultiplexed with an AWG of 25 GHz wavelength spacing. Each wavelength was divided with a 3 dB coupler and modulated with each LN-MZM driven by 802.11n RF signals with 40 MHz bandwidth whose center frequencies were 2.422 GHz (ch 3) and 5.230 GHz (ch 46) from the vector signal generator (VSG) in Figure 3(c). At the output of each LN-MZM, we obtained the bandpass-sampled RF signals [19] of the 2.4 and 5 GHz bands. The modulation and coding scheme (MCS) index of 802.11n RF signals was 15 [14], i.e., 64-quadrature amplitude modulation (QAM) orthogonal frequency division multiplexing (OFDM) signals. The optical delay line and 3 dB couplers is employed to optically multiplex the bandpass-sampled RF signals and dummy RF signals of an adjacent cell. The optically multiplexed RF signals were wavelength-multiplexed again and transmitted through the optical feeder fiber as a downstream signal.

The transmitted signals from the CS were distributed to each BS with the AWG, and the wavelength assigned at the BS was dropped by the 3-port circulator. The downstream signal dropped at the BS was converted by the photo diode transimpedance amplifier (PD-TIA), and demultiplexed with a high-speed electrical switch (SW) in Figure 3(f). The SW was driven by a control signal with a 300 ps pulse width at 1 GHz repetition rate from the PPG. The demultiplexed RF signals were converted to original RF signals with the band pass filter (BPF), which were transmitted as wireless signals from remote antennas at BS in Figure 3(g).

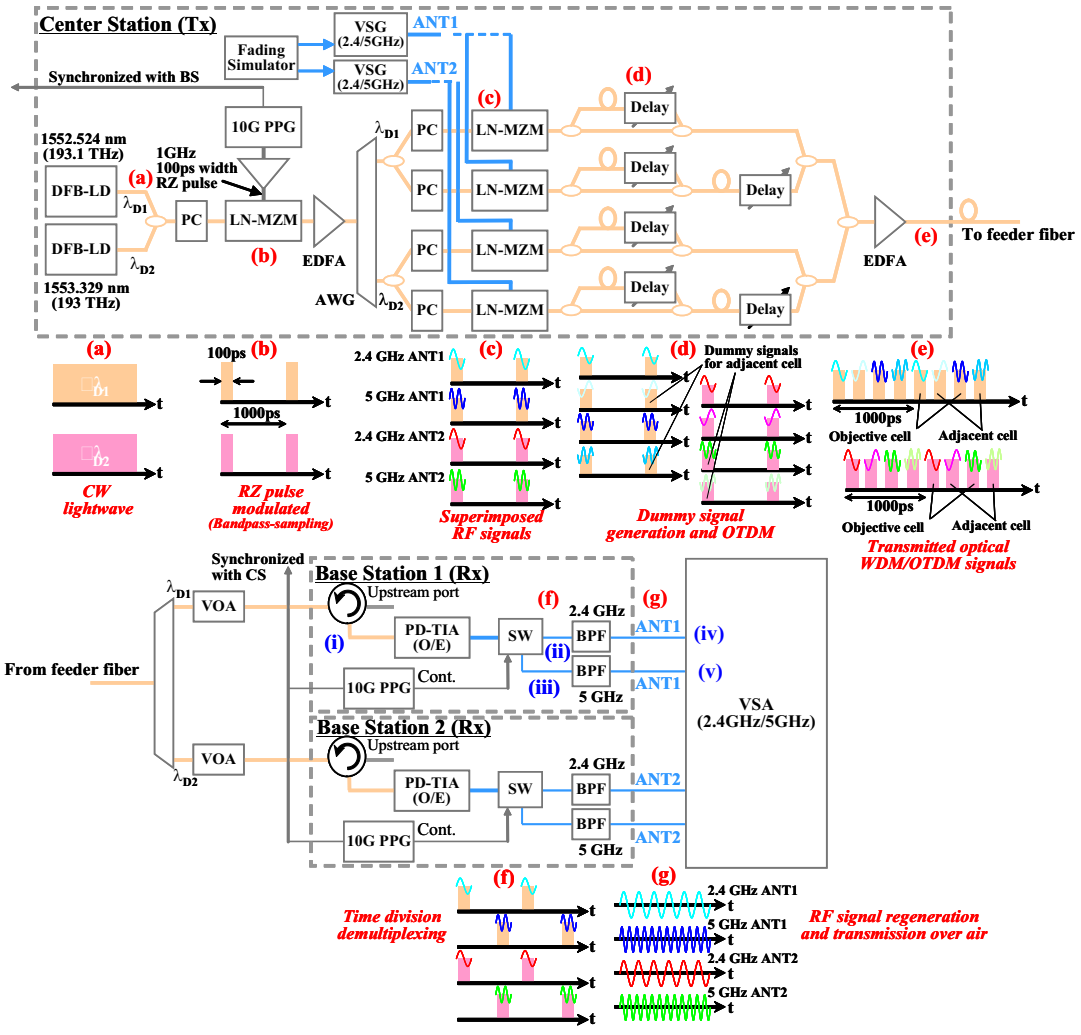

Figure 3: Experimental setup for 2 by 2 MIMO RF down stream transmission with 2.4 GHz and 5 GHz using direct optical switching (DOS)-TDM.

3.2. Results

In order to investigate the link nonlinearity, the 2-tone test of RF band is conducted. Figure 4 shows the results of 2-tone test. RF carrier power is proportional to the input power, but the IMD is increased by a factor of 3. This nonlinearity is caused by an external modulation of voltage-optical transmissivity in MZM as shown in Figure 3(c). High carrier-to-noise-plus-distortion power ratio (CNDR) is obtained of 55 dB at the input power of 2 dBm/RF tone. In this measurement, it is found that noise power is increased according to the input RF power. Observed noise power includes receiver thermal noise, PD shot noise, relative intensity noise of the optical source, amplified spontaneous emission (ASE) of EDFA, but dominant factor is considered to the beat noise between optical carrier with the same wavelength that is generated at the square-low detection of PD. Not enough extinction ratio (shown in Figure 3(b)) made unexpected mixing between one time slot and an adjacent time slots in time domain. The noise power is proportional to the RF power modulated onto the optical intensity that is optical modulation index.

Figure 5 shows that the results of MIMO de-multiplexing of 2 spatial streams in IEEE 802.11n 2 by 2 MIMO signals over frequency selective fading channel. Good error vector magnitude (EVM) performances are obtained of −22.7 dB and −21.9 dB, respectively. Figures (c) and (d) shows that

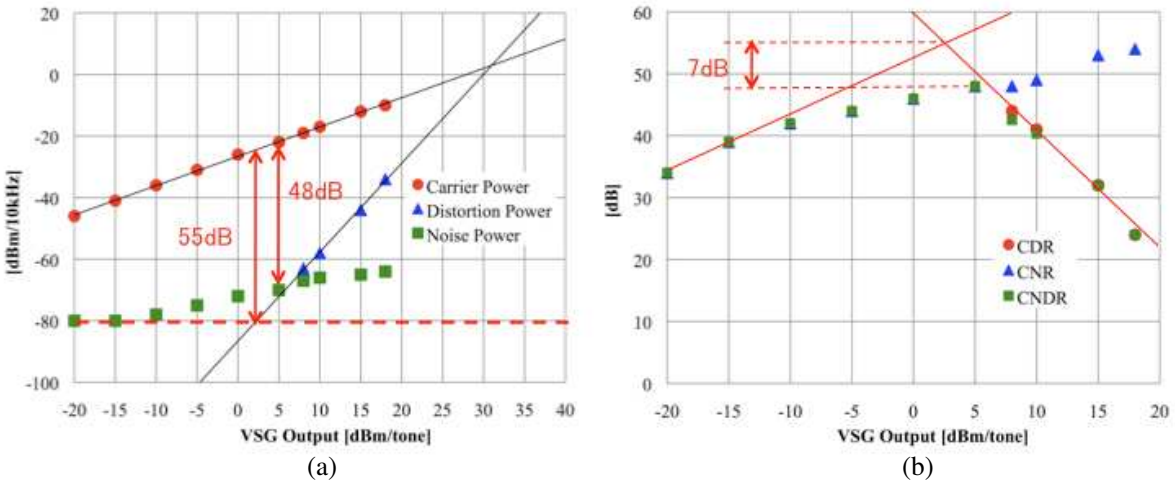

Figure 4: 2-tone test measurement. (a) RF carrier power [dBm/tone], output noise power [dBm/10 kHz], and (b) IMD3 (3-rd order intermodulation distortion [dBm/IMD tone]).

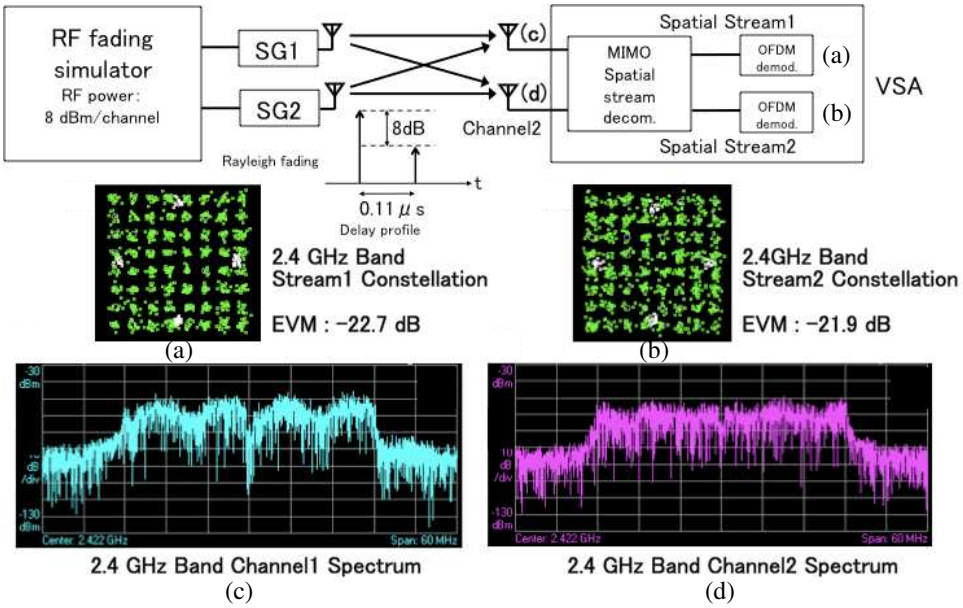

Figure 5: MIMO receiving test (a) and (b) constellation, (c) and (d) spectrum of received signal.

regeneration process is performed at the BPF without fatal degradation.

4. CONCLUSIONS

This paper shows a new architecture of heterogeneous wireless access network. This provides heterogeneous MIMO RF services over WDM-PON, and it accommodates a lot of femto-cell. The DOS TDM technique is used to multiplex multiple RF service fed to each remote antenna. The 2-tone test and fundamental transmission tests are conducted to investigate link budget and nonlinearity. Experimental results asserted good performance for RoF link without fatal degradation of MIMO receiving.

REFERENCES

1. Van Zelst A. and J. Hammerschmidt, "A single coefficient spatial correlation model for multiple-input multiple-output MIMO radio channel," *Proc. of URSI-GA*, Vol. 1, August 2002.
2. Biglieri, E., R. Calderbank, A. Constantinides, A. Goldsmith, A. Paulraj, and H. V. Poor, *MIMO Wireless Communications*, Cambridge University Press, New York, 2007.
3. Karachontzitis, S. and D. Toumpakaris, "Efficient and low-cost complexity user selection for the multiuser MISO downlink," *Proc. of PIMRC 2009*, Vol. 1, No. 1, 1–5, September 2009.
4. Tsukamoto, K., et al., "Convergence of WDM access and ubiquitous antenna architecture for broadband wireless services," *PIERS Online*, Vol. 6, No. 4, 385–389, April 2010.
5. Nirmalathas, A., P. A. Gamage, C. Lim, D. Novak, R. Waterhouse, and Y. Yang, "Digitized RF transmission over fibers," *IEEE Microwave Magazine*, 75–81, June 2009.
6. Prince, K., et al., "Converged wireline and wireless access over a 78-km deployed fiber long-reach WDM PON," *IEEE PTL*, Vol. 21, No. 17, 1274–1276, 2009.
7. Shaw, W.-T., et al., "An ultra-scalable broadband architecture for municipal hybrid wireless access using optical grid network," *OFC/NFOEC 2009*, OThP2, March 2009.
8. Iwatsuki, K., et al., "Access and metro networks based on WDM technologies," *IEEE JLT*, Vol. 22, No. 11, 2623–2630, 2004.
9. Iwatsuki, K., "Application and technical issues of WDM-PON," *SPIE*, OptEast, 7620-11, 2010.
10. Kobyakov, A., D. Thelen, A. Chamarti, M. Sauer, and J. Winters, "MIMO radio signals over fiber in picocells for increased WLAN coverage," *Proc. of OFC/NFOEC 2008*, 2008.
11. Monteiro, S. P., N. J. Gomes, A. Gameiro, and T. Kawanishi, "Next-generation distributed and heterogeneous architectures: The FUTON project," *Proc. of APMP 2009*, Vol. 1, No. 1, 1–4, April 2009.
12. Liu, C. and A. Seeds, "Transmission of MIMO radio signals over fibre using a novel phase quadrature double sideband frequency translation technique," *Technical Digest of International Topical Meeting on MWP 2008/APMP 2008*, Vol. 1, No. 1, 23–27, October 2008.
13. Yonezawa, K., S. Okamura, K. Tsukamoto, and S. Komaki, "Pre-weighting space division mutiplexing reception based on RoF ubiquitaous antenna system," *Technical Digest of International Topical Meeting on MWP 2002*, P3–10, 249–252, November 2002.
14. Yamakami, T., T. Higashino, K. Tsukamoto, and S. Komaki, "An experimental investigation of applying MIMO to RoF ubiquitous antenna system," *Technical Digest of International Topical Meeting on MWP 2008/APMP 2008*, Vol. 1, No. 1, 201–204, October 2008.
15. Okamura, S., et al., "Impact of successive interference canceller on the performance of ubiquitous antenna-based SDMA system," *Electronics and Communications in Japan*, Part 3 (Fundamental Electronic Science), Vol. 1, No. 3, 10–24, December 2004.
16. Jia, Z., J. Yu, et al., "Key enabling technologies for optical-wireless networks: Optical millimeter-wave generation, wavelength reuse, and architecture," *IEEE JLT*, Vol. 25, No. 11, 3452–3471, 2007.
17. IEEE Std. 802.11n-2009.
18. Kohlenberg, A., "Exact interpolation of band-limited functions," *AIP J. of Applied Physics*, Vol. 24, No. 12, 1432–1436, December 1953.
19. Kani, J., "Trends in next generation optical access networks and a proposed hybrid optical/wireless wide-area access network," *PIERS Online*, Vol. 4, No. 1, 101–105, 2008.

Radio Agents Technologies for Wireless-as-a-service Network

Katsutoshi Tsukamoto, **Takeshi Higashino**, **and Shozo Komaki**
Division of Electrical, Electronic and Information Engineering, Graduate School of Engineering
Osaka University, Japan

Abstract— Mobile users will be able to utilize a large variety of application services from cloud network, and also one of various types of wireless service should be provided from cloud according to users' preference or their location. The latter is able to be realized by use of Wireless service over IP technology, and its concept is called "Wireless as a Service (WIaaS)", or "Wireless Cloud".

Radio Agents technologies in the WIaaS networks have been proposed to achieve a good balance between users demands in charge, QoE, or so on, operators' demands in penetrations, investments, or so on, and regulation demands for radio regulations and frequency efficiency. Radio agents will decide the assignment of frequency or network resources, or the selection of service content to user on the basis of these utility functions. This paper will classify radio agents in terms of time and objective scale, and propose user utility function, that is derived by AHP (analytic hierarchy process) method and also agent system operating based on the utility function.

1. INTRODUCTION

Ubiquitous network should offer users the environment to access any communication service at any time, any place, and any situations. The demand of users for various multimedia services will be increasing more and more; therefore full IP connectivity will be required to accommodate the variety of contents. However, such diversification appears not only in application services but also in air interfaces of wireless access methods. The heterogeneous wireless networks also strongly depend on users' different demands for applications, quality, latency, and moreover users' situations such as indoor, outdoor, and fast/slow mobility. Therefore, the platform for heterogeneous wireless network becomes a key issue to realize ubiquitous networks.

Current and next generation wireless access such as 3.9G, 4G, and WiMAX, will provide full internet services with IP networks as a core network. In addition, the flexible and effective use of radio frequency spectrum will accelerate the convergence of fixed optical broadband access and heterogeneous wireless access via femtocell architecture. Mobile users will be able to utilize a large variety of application services from cloud network, and also one of various types of wireless service will be provided from cloud according to users' preference or their location. The latter is able to be realized by use of Wireless service over IP technology, and its concept is called "Wireless as a Service (WIaaS)", or "Wireless Cloud".

Radio Agents technologies [1] in the WIaaS networks have been proposed to achieve a good balance between users demands in charge, QoE (Quality of Experience), or so on, operators' demands in penetrations, investments, or so on, and regulation demands for radio regulations and frequency efficiency. Radio agents, that are middleware implemented at several locations like mobile terminals, AP, and proxy/application servers on the application layer of the network, will tend to realize user centric wireless services.

To realize future user centric wireless service networks, software definable radio network (SDRN) has been proposed [2], that can be configured with the combination of RoF (Radio on Fiber) entrance networks, software definable radio gateway, wireless service over IP, and radio agents. This paper will classify radio agents in terms of time and objective scale, and propose user utility function derived by AHP (analytic hierarchy process) method and agent system operating based on the utility function.

2. SOFTWARE DEFINABLE RADIO NETWORKS FOR WIRELESS CLOUD

Figure 1 illustrates the concept of Software Definable Radio Network (SDRN) and its configuration [2]. The SDRN is composed with Radio on Free Space (RoFSx) networks, universal RBS and software definable control server (SDRCS) in IP network for various types of wireless services, and SDRGW (Software Definable Radio Gateway), which provides a seamless connectivity between local RoF networks and IP network. *User Centric Radio Space Control Agents*: The SDRN can realize an easy spectrum delivery to users, but its operation should be performed not only to enhance

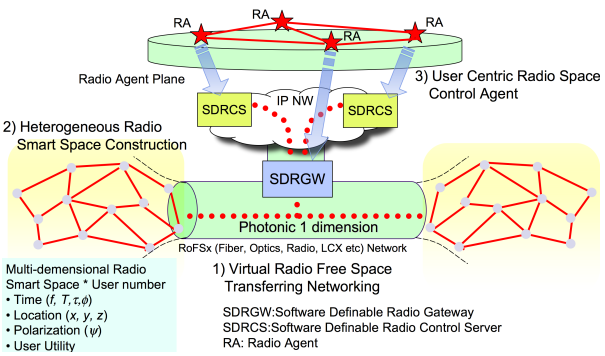

Figure 1: Concepts of software definable radio networks.

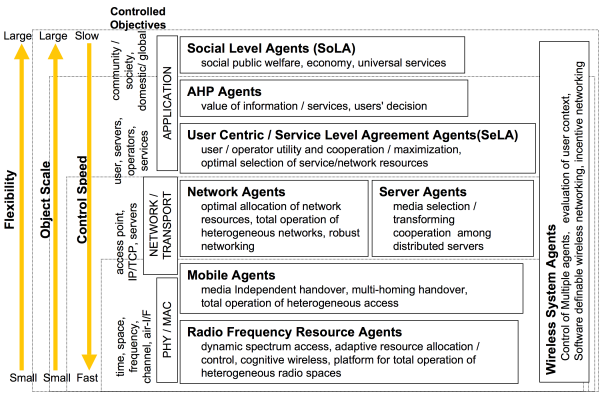

Figure 2: Radio agents.

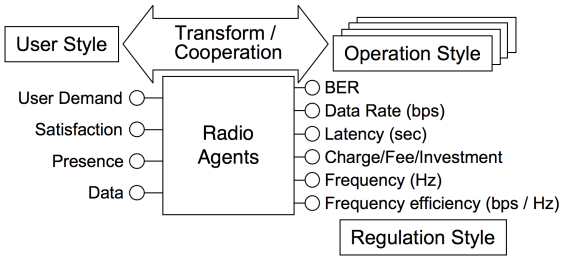

Figure 3: The concept of SeLA agent.

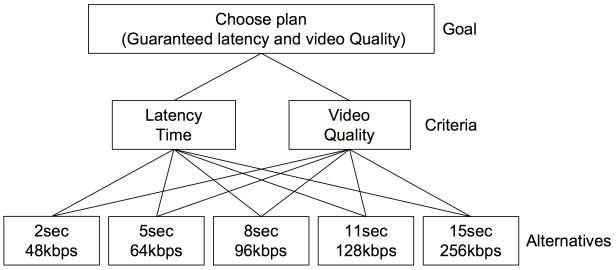

Figure 4: AHP hierarchy.

frequency efficiency but also to satisfy users' and operators' demands. Even if accessing the same wireless services, user utilities depend on their mobility and situations. In order to realize such seamless session handover or service handover in heterogeneous wireless, we need Radio Agents on Layer 7, which controls layer 1–3 according to users' and operators' demands, and radio regulations.

3. RADIO AGENTS

In order to flexibly and effectively use different radio frequency or network resources, and to increase users' satisfactions (user utility), radio agents technologies are required on radio access networks. Radio agents help users', operators', regulations', and social demands act in harmony with their requiring QoS (Quality of Service) and also QoE, and those are distributed middleware in diverse locations of the network, like access points, gateway, or servers. Their equipped layers or locations depend on their controlling objects or methods. There are various types radio agents [1]. Figure 2 shows a classification of various types pf radio agents. Radio agents control radio frequency resource, network resources, service contents, QoS to satisfy users' and operators' demands. Their controlling speed and the scale of controlled objects have a large variety. Objects controlled by radio agents are allocations of radio frequency resource or network resource, radio modulation formats, QoS, service contents, service fee, and so on. Some of these controlled objects are located on a physical layers, and others are upper layer. For example, radio resource allocation is controlled at a physical layers, and a vertical handover among heterogeneous wireless access is executed on network or upper layer [3]. These cross control over cross layers have to be on a overall network including internet, core, entrance, and access networks, and its provision requires some radio agents which are located on application layer, and control lower layers with mutual harmonized operation.

For example, a frequency resource agent select and allocate an air-interface for a user to receive a QoE guaranteed service according to the user's utility and also operators utilities (less resource consumption, less investment). To provide the user centric wireless service, user centric service level agent estimates users satisfaction (user utility) and instruct radio frequency agents to effectively use the radio spectrum according user's utility function and operators utility, and radio regulations. The concept of SeLA (service level agreement) agent is illustrated in Figure 3.

Table 1: Averaged priority for alternatives; latency time.

Latency; t (sec)	$\overline{X_G(g)}$
2	2.96
5	1.14
8	0.59
11	0.32
15	0.19

Table 2: Averaged priority for alternatives; video quality.

Video Rate; R (kbps)	$\overline{X_L(t)}$
48	0.26
64	0.27
96	0.84
128	1.30
256	1.98

4. SELA (SERVICE LEVEL AGREEMENT) AGENT

4.1. Estimation of User Utility Function by Using AHP

Even if wireless services are provides with the same QoS, different users have naturally different satisfactions for the services. The QoE is also influenced by user's preference, situation, or paid fee. It is difficult to measure the individual QoE or the satisfaction for service in numerical values. There are some statistical analysis methods to measure users' satisfaction, MOS (Mean Opinion Score) experiments [4], AHP (analytic hierarchy process) [5], logistic regression and so on. We applied AHP in users decisions to choose one from service plans with various QoS, and from the results, estimated user's utility function when they receive wireless services.

Assuming a mobile video streaming service, we executed questionnaires for some subjects, and performed the paired comparison of answers obtained from 139 subjects. The number of effective answers based on AHP consistency index was 86. Figure 4 shows AHP hierarchy used in questionnaire assuming mobile video streaming service. There are 5 Alternatives for choosing QoS of video streaming which are some combinations of the latency time till video beginning (storing time in memory plus processing time) and the quality of video (bit rates) at mobile terminal. Two criteria were Latency time till video beginning and quality of video.

Through the paired comparison and AHP analysis, we can obtain some estimated utility functions for wireless video streaming service. The individual utility function for ith subject, U_i and the averaged utility function over all subjects, $\overline{U}$ are given by

$$U_i(R;g) = w_{Li}a_i e^{-b_i\frac{gsr}{R}} + w_{Gi}X_{Gi}(g) \quad (1)$$

$$\overline{U(R;g)} = \overline{w_L}ae^{-b\frac{gsr}{R}} + \overline{w_G}\overline{X_G(g)} \quad (2)$$

where w_{Li} and $\overline{w_L}$ are the individual priority and its mean value over all subjects for one criterion, the latency time, respectively. w_{Gi} and $\overline{w_G}$ are the individual priority and its mean value over all subjects for another criterion, video quality, respectively. $\overline{w_L}$ and $\overline{w_G}$ were 0.465 and 0.534 from AHP analysis for obtained answers, respectively. It is found from the results that the subjects have almost same priority for two criteria, latency time and video quality.

$X_{Gi}(g)$ and $\overline{X_G(g)}$ are the individual priority of ith subject and its mean value over all subjects for the alternative of video quality, g, respectively. The individual priority, $X_{Li}(t)$, for the alternative of latency time, t, and its mean value. $\overline{X_L(t)}$, can be approximated by an exponential function as shown in Eqs. (1) and (2), where s [sec], r[%], and R [kbps] are the length of video, the data stored ratio in memory, and the allocated throughput for each user, respectively. Tables 1 and 2 show the averaged priority for alternatives of latency time and video quality, $\overline{X_L(t)}$ and $\overline{X_G(g)}$. In the questionnaire, aspiration level of each user was also researched, and its mean value was 6 sec and 96kbps for the latency time and video quality, respectively. These aspiration levels are observed as the threshold value for latency time and video quality which yield the averaged priority of 1. Figure 5 shows measured and averaged priority for latency time criterion, $\overline{X_L(t)}$ and the approximated line which is given by the former term in Eq. (2) with a of 3.67 and b of 0.211. From Eqs. (1) and (2), We had estimated user's individual satisfaction and also that of relatively small mass for QoS in wireless video streaming service.

4.2. User Centric Video Quality Control Agent as a SeLA (Service Level Agreement) Agent

By the use of the utility function derived in 4.1., the radio agent on network can choose for user a video quality (bit rate) to achieve his satisfaction for the service according to the allocated radio bandwidth resource. When the agent choose an adequate video content to provide a user his

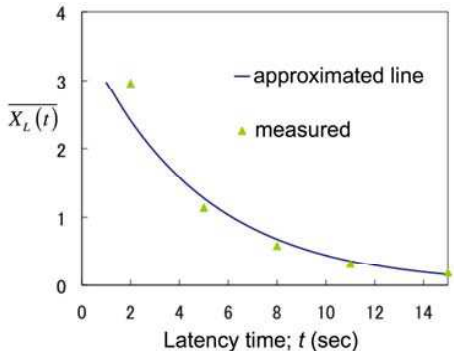

Figure 5: Averaged priority for latency time criterion.

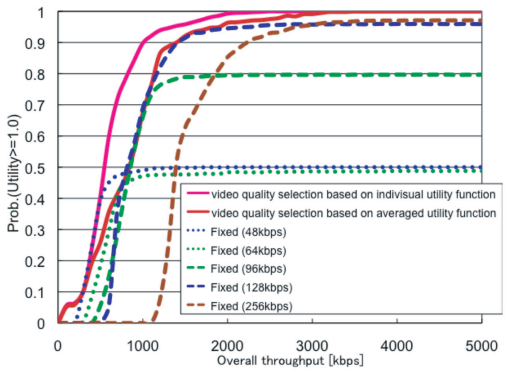

Figure 6: Satisfaction probability vs overall throughput.

Table 3: Specification of simulation.

Interval of user's service request	Exponential distribution (average value; 20 sec)
Number of users	86
Length of video; s (sec)	30
Video data stored ratio in memory at terminial r [%]	5
Alternatives for video quality (kbps)	48, 64, 96, 128, 256

aspiration level and to avoid excess consumption of frequency resource, consequently an effective radio frequency utilization can be expected.

The proposed agent choose a video quality according to current throughput and user's utility, $U_i(R; g)$. The operation of the Agent is as following;:

1) User request a video streaming service by using Mobile terminal.
2) Agent estimates a current achieved throughput per user, $\hat{R}$.
3) Agent decide a video quality $g_{\max}$ to maximize $U_i(\hat{R}; g)$ and request the video correspondent to the $g_{\max}$.
4) The server deliver the video to the user.

When agent uses the averaged utility function $\overline{U(R; g)}$ instead of $U_i(R; g)$, all users are delivered a video with the same quality to maximize $\overline{U(R; g)}$.

Computer simulation was performed with the specifications summarized in Table 3 to evaluate the achieved user satisfaction. Figure 6 shows the simulation results of the satisfaction probability that user's utility is more than his aspiration level as function of the overall throughput in application layer provided for all users. The figure also shows the case that the agent chooses a video quality according averaged utility function and also that the vide is delivered with some fixed rates. It is seen from the figure that for the conventional service with a fixed video quality, the satisfaction probability is saturated to a certain value decided by the fixed video rate. In the proposed system, on the other hand, the satisfaction probability is improved, and we can have the maximum probability for individual selection of video quality based on $U_i(\hat{R}; g)$. Even the agent system choosing a quality based on the averaged utility function can improve the satisfaction probability, but it depends on the provided throughput.

5. CONCLUSIONS

This paper classified radio agents in terms of time and objective scale, and proposed user utility function derived by AHP method and agent system operating based on the utility function.

ACKNOWLEDGMENT

The authors thank members of wireless network Lab. for their fruitful discussion. This work is supported by KDDI Foundation.

REFERENCES

1. Komaki, S., K. Tsukamoto, et al., *Wireless Agents Technologies*, Maruzen, Tokyo, July 2008 (in Japanese).
2. Komaki, S., "Microwave technologies for software radio networks," *Proceedings of APMC 2003*, Vol. 3, No. FC7-1, 1780–1785, November 2003.
3. Morioka, Y., T. Higashino, K. Tsukamoto, and S. Komaki, "Proposal of SIP based AP selection agent system in wireless LAN," *Proc. of the 18th Annual IEEE International Symposium on Personal, Indoor Radio Communications (PIMRC'07)*, Vol. 1, No. 1, 1–6, September 2007.
4. Shutto, N., Y. Handa, Y. Minoda, T. Higashino, K. Tsukamoto, and S. Komaki, "Measurements of a utility function for video download service and its application to service management," *Proc. of WCNC 2007*, Vol. 1, No. 1, 2894–2898, March 2007.
5. Saaty, T. L., *The Analytic Hierarchy Process*, McGraw-Hill, 1980.

Next Generation Free Space Optics System for Ubiquitous Communications

Pham Tien Dat[1], **Chedlia Ben Naila**[1], **Peng Liu**[1], **Kazuhiko Wakamori**[1], **Mitsuji Matsumoto**[1], **and Katsutoshi Tsukamoto**[2]

[1]GITS/GITI, Waseda University, Tokyo, Japan
[2]Graduate School of Engineering, Osaka University, Osaka, Japan

Abstract— Free Space Optics (FSO) is being realized as an alternative means to compensate and/or replace the traditional optical communications in many applications where the fiber cable is not available. The next generation FSO systems in which the propagated signal after transmission over freespace is directly coupled into a single mode fiber have attracted much interest recently. However, the system performance is highly affected by the atmospheric environment, especially the atmospheric turbulence due to the random change in the air temperature and pressure. In this paper, we present the propagation characteristics of a newly developed Radio on FSO (RoFSO) system based on next generation FSO technology capable of transparent transmission of multiple wireless signals under effects of atmosphere turbulence. The system performance enhancement using atmospheric turbulence mitigation techniques will also be outlined.

1. INTRODUCTION

Light-wave communications has been become an attractive means for broadband wireless access networks. Recently, there is much attention in Free Space Optics (FSO) systems to provide broadband communications due to its remarkable advantages including flexibility, easy-to-install, and license-free. FSO systems can be categorized in 2 broad groups, i.e., conventional FSO based systems, and next generation FSO based systems. Conventional FSO systems operates at 800 nm wavelength band, and needs to use O/E and E/O conversions before emitting/coupling optical signals from/into an optical fiber. They have been used for signal transmission, but due to power and bandwidth limitation of optical devices in this wavelength band, it is not possible to operate above 2.5 Gbps [1].

Next generation FSO technology has been developed in order to overcome the limitation of the conventional FSO systems. Unlike conventional FSO systems, in the next generation FSO systems the necessity of converting the signal from electrical to optical and vice versa before transmitting or receiving through free space is eliminated. In this configuration the signal is emitted directly to freespace from the fiber termination point and at the receiving end focused directly into the fiber core. Therefore, a protocol and data rate transparent FSO link is achieved. The seamless interconnection of standard single mode fiber (SMF) and FSO links, whereby an optical signal is coupled from one media to another without any optical-electrical conversions, creates an opportunity for cost savings and other remarkable advantages. However, atmosphere has many deleterious effects on the system performance especially atmospheric turbulence which makes the received signal fluctuate randomly. The system thus needs specially designed terminals and tracking scheme.

Recently, based on a previously developed next generation FSO system [2], we developed and demonstrated successfully an advanced Radio on FSO (RoFSO) system capable of transferring multiple wireless signals using WDM FSO channel [3]. In this paper, we present the propagation characteristics of this new system and compare to that of a conventional FSO system co-located in the experiment field. The newly derived characteristics will be helpful in the system evaluation and its further optimization. We also outline some methods to improve the system performance using different kinds of diversity.

2. CONVENTIONAL FSO AND ROFSO SYSTEMS CHARACTERISTICS

2.1. Experimental Set up

The experimental set up for characterizing optical and wireless signal transmission of the RoFSO systems is illustrated in Fig. 1. Two RoFSO antennas are installed on the rooftops of two buildings at Waseda University campus in Tokyo. The transmission distance is about 1 km. Co-located on the rooftops is a conventional FSO system. A weather measurement device for recording temperature, rain rate and visibility data is also available. In this paper we focus on the optical propagation

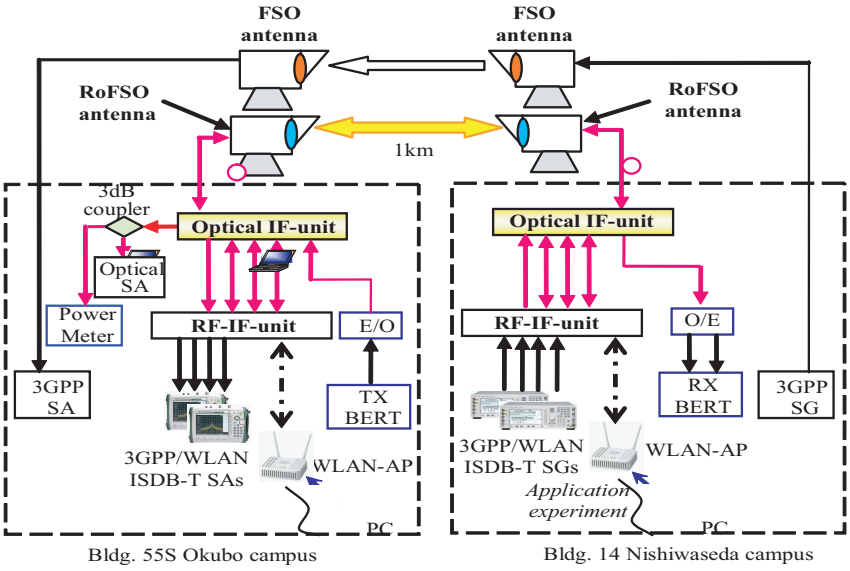

Figure 1: Experimental setup diagram.

Table 1: Conventional FSO and RoFSO systems specifications.

Parameters	Conventional FSO	RoFSO
Communication wavelength	785 nm	1550 nm band
Antenna aperture	80 mm	80 mm
Beam divergence	±0.75 mrad	±47.3 μrad
Tracking method	Auto tracking	Rough, Fine tracking

characteristics of the system under effects of atmospheric turbulence and coupling fading, and compare to that of a conventional FSO system. Details of the experimental set up for wireless signals transmission over the RoFSO system can be referred to [3]. The specifications of these two systems are shown in Table 1.

2.2. Conventional FSO and RoFSO Systems Characteristics

In a conventional FSO system, the signal is emitted from transmitting antenna in a very large beam divergence, and at the receiver the beam is detected by a photodetector which has a size of about 500 μm, therefore there is almost no coupling loss between free-space and detector. On the contrary, in a next generation FSO system, the tracking scheme plays an important role in focusing the received signal into a SMF. An example of received optical power in the RoFSO system (when the tracking is ON and OFF) and in the conventional FSO system measured at 15 : 30 pm, 21 January 2009 is shown in Fig. 2(a). Fig. 2(b) shows the power spectrum characteristics. The data is recorded within 3 seconds with a sampling rate of 10 kHz. It can be observed that the tracking capability of the Fine Pointing Mirror manages to control and steer most of the received light into the SMF. The power fluctuations observed when the tracking is switched to OFF are remarkably suppressed and improvement in the fiber received power is realized. However, compared to that of the conventional system, the fluctuations of received power in the RoFSO system is larger. This can be explained that even though the tracking scheme can significantly enhance the received signal level, it cannot suppress completely the random change in the position of the coming signal due to the effect of angle of arrival. This can be observed more clearly by the power spectrum property in Fig. 2(b).

In a system characterized by the random change in the received level like FSO communications, using statistical models like probability density function (PDF) is the good methods to represent the system property. There are many research works conducted so far both in theory and experiment to find out the appropriate models for FSO systems. Among these models, log-normal, Gamma-Gamma and Gamma are widely used and have been demonstrated to present approximately the behavior of a FSO beam under effects of atmospheric turbulence [4]. However, these models were

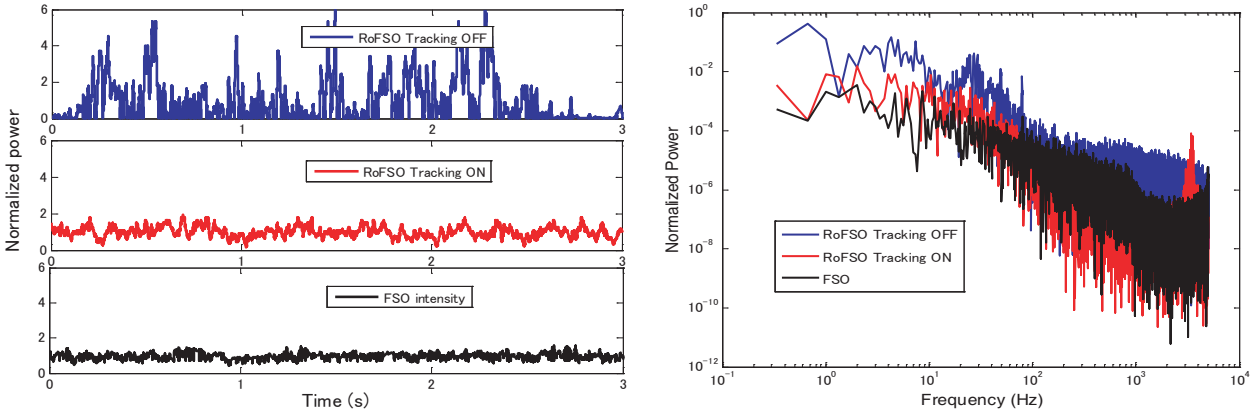

Figure 2: (a)Time series received power in SMF and (b) power spectrum characteristics.

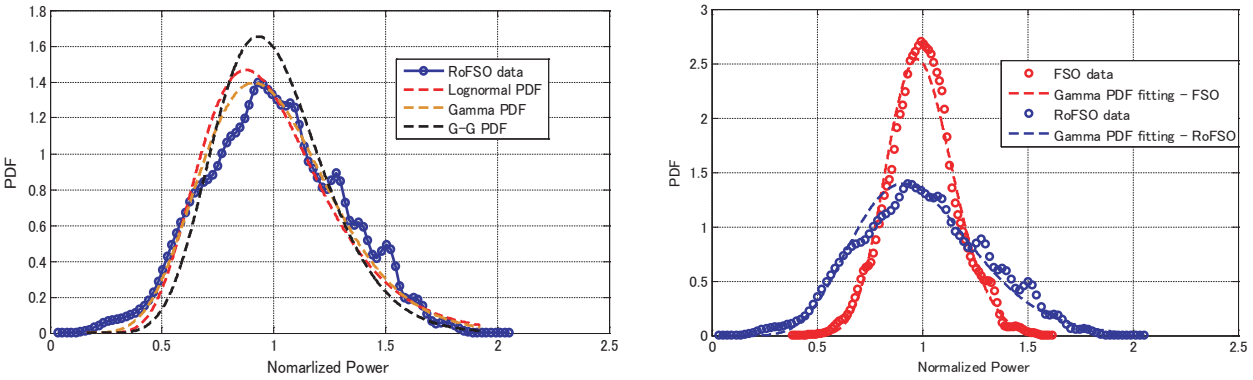

Figure 3: (a) PDF of received power in the RoFSO and (b) comparison to the FSO system.

developed for conventional FSO systems taking only the impact of turbulence on the transmission path into account. For next generation FSO systems, besides this effect, the systems are impacted by an additional coupling fading. Unfortunately, there is no research work so far considering the combined effects for these systems. An example of received power distribution in the RoFSO system is shown in Fig. 3(a). The fitting curves using lognormal, Gamma and Gamma-Gamma PDF are also shown. It is seen that unlike conventional FSO systems, Gamma function (Eq. (1)) presents the closest property to the RoFSO system. Fig. 3(b) shows a comparison of received power distributions in the conventional FSO and RoFSO systems. We can see that Gamma PDF can relatively characterize both systems behavior, however, the variance of these distributions is different. The parameter determining the variance of a Gamma PDF is power scintillation index, as shown in Eq. (2) [5]

$$p_X(x) = \frac{x^{\alpha-1}e^{-x/\beta}}{\beta^{\alpha}\Gamma(\alpha)} \tag{1}$$

where $\Gamma(\alpha)$ is gamma function, and the parameters α and β are related to measured values by

$$\beta = \sigma_P^2$$
$$\alpha = \frac{1}{\sigma_P^2}$$

where σ_P^2 is power scintillation index and in the conventional FSO systems, it relates to scintillation at the receiver plane by [4],

$$\sigma_{P\text{-}FSO}^2 = \exp\left\{\frac{0.49\sigma_R^2}{(1+0.65d^2+1.11\sigma_R^{12/5})^{7/6}} + \frac{0.51\sigma_R^2(1+0.69\sigma_R^{12/5})^{-5/6}}{(1+0.9d^2+0.62d^2\sigma_R^{12/5})^{7/6}}\right\} - 1 \tag{2}$$

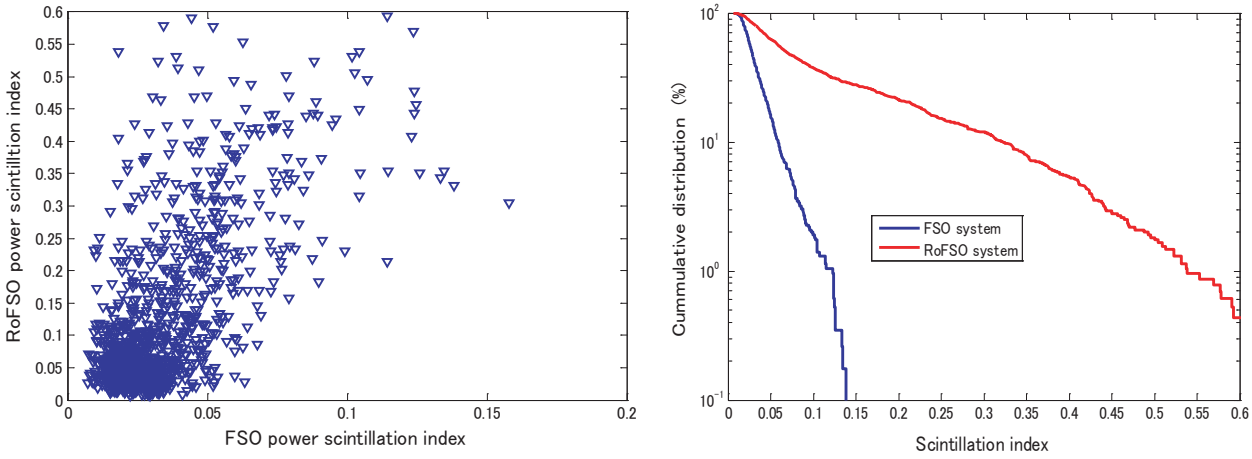

Figure 4: Relation between scintillation index of FSO and RoFSO systems (a) and their CDF (b).

where $\sigma_R^2 = 1.23k^{7/6}L^{11/6}C_n^2$ is Rytov variance parameter and $d = \sqrt{kD^2/4L}$ is the ratio of the aperture radius to the Fresnel zone size, D is receiver aperture diameter.

In next generation FSO systems, the power scintillation index not only reflects scintillation but also depicts the coupling fading at the terminal. A relation of power scintillation index of the FSO and RoFSO systems for the data measured in 5 clear days is shown in Fig. 4(a). The statistics for the data using cumulative distribution function (CDF) is also shown in Fig. 4(b). It is observed that due to the added coupling fading, scintillation index in the RoFSO system varies in a larger range compared to that in the FSO system. Under moderate to strong turbulence conditions, power scintillation index of the RoFSO system can be derived as

$$\sigma_{P\text{-}RoFSO}^2 = \sigma_{P\text{-}FSO}^2 + \theta \tag{3}$$

where θ is an additional factor presenting coupling fading. From our experimental data, we can estimate the value for this factor of about 0.4 for the condition from which more than 99% of power scintillation index is less than (Fig. 4(b)).

It is important to note that even though the newly developed system based on next generation FSO technology is affected by a larger fading compared to the conventional one, it can manage to provide a stable connection for heterogeneous wireless signals over 1 km transmission, especially in the absence of severe weather conditions like strong turbulence and heavy rain [3]. The derived characteristics shown in this part will be helpful for the system modeling, theoretical evaluation and its further optimization as well as enhancement. Next session will describe some possible techniques that can be employed to further improve the system performance using the model derived in this part.

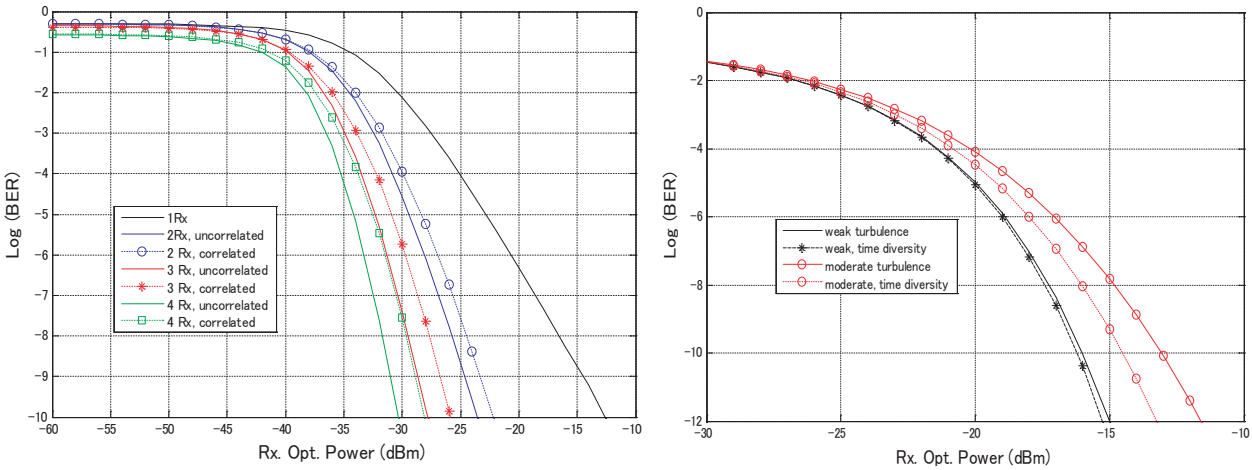

Figure 5: RoFSO system enhancement using (a) reception diversity, (b) time diversity.

3. SYSTEM PERFORMANCE ENHANCEMENT

To improve the performance and increase the availability, FSO as well as next generation FSO systems can employ other atmospheric turbulence mitigation techniques such as forward error coding (FEC), high power and bandwidth efficiency modulations, transmitting signal at different times (time diversity) or using multiple transmitters and/or receivers (space diversity). In this part we give some examples of system performance enhancement using receiver diversity and time diversity. In the former method, the optical signal is transmitted by one transmitter antenna but at receiving site, multiple receivers are used to collect the data. The output signal is the combination of different received signals using one of the processing methods like equal gain combining (EGC), maximum ratio combining (MRC) or select best combining (SBC). In next generation FSO systems, thank to the use of direct coupling at the receiver, the received signals can be combined optically, the combined signal then is transferred through a pre-amplifier before detected by a photodetector. Multiple receivers in this case are sets of receiving aperture and coupling scheme to couple received signal into fiber core. As depicted in the previous session, the power fluctuations in the fiber core of each signal can be modeled by the modified Gamma PDF with power scintillation index is derived from the strength of scintillation and coupling fading factor. An example of system performance using receiver diversity is shown in Fig. 5(a). In this example we take the parameters of the RoFSO system into calculation with the gain value of pre-amplifier is 20 dB. We consider the impact of scintillation and coupling fading at the receiver by using the modified Gamma PDF function as presented in Session 2. We assume that the optical power from different apertures and couplers can be combined equally using for example optical coupler. The distribution of the combined optical power after optical coupler is not a single model any more but a series of Gamma function [6]. We also take different noise sources including thermal noise, shot noise and especially pre-amplifier produced noises into consideration. It is clear that the system performance is improved significantly when multiple receivers are employed. The performance also depends on the distance between receivers, when the distance is large there is no correlation between the receivers fading so the performance is better. If the distance is small, the fading between receivers correlates resulting in performance reduction.

In time diversity solution, a signal is transmitted many times using one pair of transmitter and receiver, and at the receiving site different signals transmitted at different times are synchronized and combined. There are many methods to implement time diversity in FSO communications regarding the way to differentiate different signals. We proposed a new time diversity for FSO systems using OCDMA code [7]. The optical signal at the transmitting site is divided into many branches, each branch is coded by a OCDMA code and delayed by a time period. The signals then are combined before transmitting over FSO channel, and at the receiving site are inversely synchronized, decoded and combined again. An example of system performance using this solution in which the signal is transmitted two times is shown in Fig. 5(b). The method demonstrates a good improvement for the system especially when atmospheric turbulence increases.

4. CONCLUSION

We have presented a study and characterization on the performance of a next generation FSO system under effects of atmospheric turbulence and coupling fading. We verified that the system is affected by an additional fading due to direct coupling between free-space and SMF, and a distribution model is derived to describe the system behavior using Gamma function and newly derived power scintillation index. Even though the system is affected by a larger fading, it has been demonstrated previously that it can maintain a stable connection for various wireless signal transmission, especially in the absence of severe weather conditions. The information derived in this paper will be helpful in the system modeling, theoretical evaluation and further optimization. The system performance improvement using receiver diversity and time diversity is also presented. It is shown that a significant enhancement in system performance can be obtained by using one of these solutions, especially when the atmospheric turbulence is strong.

ACKNOWLEDGMENT

This work is supported in part by a Grant-in-aid of High-tech Research Center Project by the Ministry of Education, Culture, Sports, Science and Technology, Japan.

REFERENCES

1. Kedar, D. and S. Arnon, "Urban optical wireless communication networks: The main challenges and possible solutions," *IEEE Commun. Mag.*, Vol. 42, No. 5, s2–s7, May 2004.
2. Kazaura, K., et al., "Performance evaluation of next generation free-space optical communication system," *IEICE Transactions on Electronics*, Vol. E90-C, 381–388, 2007.
3. Dat, P. T., A. Bekkali, K. Kazaura, K. Wakamori, and M. Matsumoto, "A universal platform for ubiquitous wireless communications using radio over FSO system," *IEEE/OSA Journal of Lightwave Technology*, Vol. 28, No. 16, 2258–2267, 2010.
4. Andrews, L. and R. Phillips, *Laser Beam Propagation Through Random Media*, 2nd Edition, SPIE Press, 2005.
5. Epple, B., "Simplified channel model for simulation of free-space optical communications," *IEEE/OSA Journal of Opt. Commun. Netw.*, Vol. 2, No. 5, 293–304, 2010.
6. Alouini, M. S., A. Abli, and M. Kaveh, "Sum of Gamma variates and performance of wireless communication systems over nakagami-fading channels," *IEEE Transaction of Vehicular Technology*, Vol. 50, No. 6, 2001.
7. Liu, P., P. T. Dat, K. Wakamori, and M. Matsumoto, "A new scheme on time-diversity atmospheric ocdma system over atmospheric turbulence channels," *Proceeding of 2010 IEEE Workshop on Optical Wireless Communications*, in conjunction with *IEEE GLOBECOM 2010*, Miami, USA, December 2010.

Checking of Combustion Chamber of Rocket Using ECT with AMR Sensor

D. F. He[1], **M. Shiwa**[1], **J. Takatsubo**[2], **and S. Moriya**[3]

[1]National Institute for Materials Science, 1-2-1 Sengen, Tsukuba 305-0047, Japan
[2]Advanced Industrial Science and Technology, 1-2-1 Namiki, Tsukuba 305-8564, Japan
[3]Japan Aerospace Exploration Agency, 2-1-1 Sengen, Tsukuba 305-8505, Japan

Abstract— Eddy current testing (ECT) system with high sensitive AMR sensor was developed. To reduce the influence of experimental noise and the influence of lift off variance, a differential AMR sensor was used in this system, which was composed of two AMR sensors in parallel and their outputs were subtracted. The sensing direction of the AMR sensor was along Z direction and the distance between two sensors was about 3 mm. The AMR sensor was mounted with an X-Y stage for the scanning. In our experiments, a specimen of cooper plate with grooves and slits was used to simulate the cooling grooves of the combustion chamber of liquid rocket and the defect in it. Three defects, with the width of 0.2 mm, the length of 4 mm and the depth of 0.2 mm, 0.5 mm and 0.8 mm respectively, were made in the bottom of the grooves. With a ϕ4.5 mm and 30 turn circular excitation coil to produce the excitation field, the frequency of about 2 kHz, and the current amplitude of about 50 mA, ECT experiments were done and the defects could be successfully detected.

1. INTRODUCTION

For the liquid rocket using liquid oxygen and liquid hydrogen as the propellants, the combustion chamber is made of Cu-Cr-Zr copper alloy. Inside of the combustion chamber is the ultra high temperature gas of about 3000 K. Cooling grooves are made in the wall of the cooper alloy and liquid hydrogen flows in them for the cooling. Due to the big thermal gradient, small cracks are easily generated in the wall of the combustion chamber. For the recycling and safety checking, nondestructive testing of the combustion chamber is necessary. The aim of this research is to detect the defect in the copper alloy wall of combustion chamber using high sensitive eddy-current testing (ECT) method.

As the preliminary test, we once checked the specimen of an aluminum plate [1], which was used to simulate the combustion chamber and the defect in it. The small artificial defects could be successfully detected using the ECT method with anisotropic magneto resistance AMR sensor, and the best signal-to-noise ratio was obtained at about 8 kHz. However, the combustion chamber of liquid rocket is made of copper alloy, which has different conductivity compared to the aluminum plate; and the combustion chamber also has the curve surface, which may cause the variance of lift off during scanning.

In this report, we will illustrate the experiments and the results of the checking of a copper alloy plate, which is used to simulate the combustion chamber. To reduce the noises caused by the variance of the lift off, Differential way by subtracting the output of two AMR sensors was also used.

2. EXPERIMENTAL SETUP

Figure 1 shows the block diagram of the experimental setup of ECT with AMR sensor. The coil was used to produce the AC magnetic field, then, eddy current was induced in the sample and the distribution of the eddy current is influenced by the defect. The magnetic field produced by the eddy current was measured by the AMR sensor. Through the lock-in amplifier, the amplitude signal and the phase signal could be obtained; then was sent to a computer for data acquisition and data procession. In our experiment only the amplitude signal was used. The AMR sensor was fixed with the X-Y stage for the scanning. The position resolution of the X-Y stage was about 50 µm. The scanning steps were 1 mm along the direction perpendicular to the grooves and 2 mm along the direction parallel to the grooves. The measuring time for each point was 0.5 second. The AMR sensor of HMC1001 was used [2]. With the low noise driving circuit, the magnetic field resolution of the AMR sensor was about 15 pT/$\sqrt{\text{Hz}}$ above 1 kHz [3].

For the ECT method, if the specimen has a curve surface, big variance of the lift off may happen during scanning and the variance of the lift off produces big noises. To reduce it, a differential way

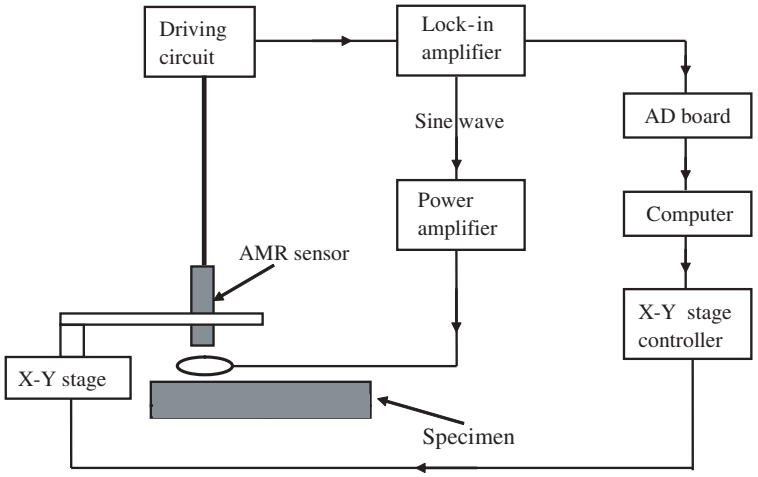

Figure 1: The setup of eddy-current NDE system using AMR sensor.

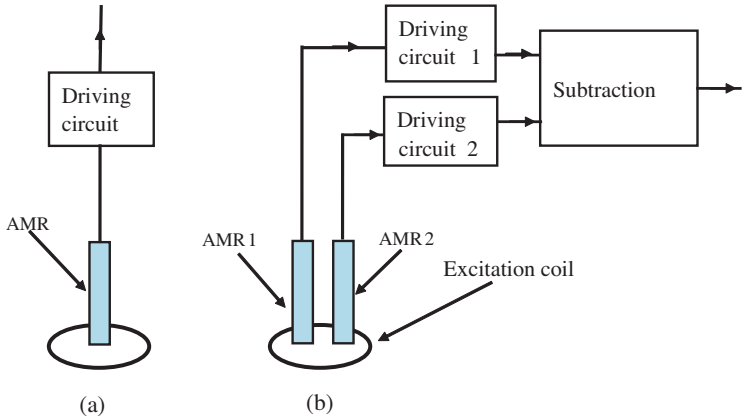

Figure 2: (a) ECT with one AMR sensor and a circular coil. (b) ECT with two AMR sensors and a circular coil.

by subtracting the outputs of two AMR sensors was used. Fig. 2(a) shows the ECT with one AMR sensor and a circular excitation coil, and Fig. 2(b) shows the ECT with two AMR sensors and a circular excitation coil. The distance between the two AMR sensors was about 3 mm. The coil was 30 turns and the diameter of about 4.5 mm. For the ECT with one AMR sensor, the position of the coil was adjusted to make the AMR output biggest. For the ECT with two AMR sensors, the position of the coil was adjusted to make the subtraction output smallest.

To simulate the combustion chamber of liquid rocket, the specimen made of copper alloy plate was used. Fig. 3 shows it. The thickness of the plate was 4 mm. Grooves with the width of 1 mm and the depth of 3 mm were made on one side of the copper plate. Three slit defects were made in the bottom of some grooves with the length of 4 mm, the width of 0.2 mm and the depth of 0.2 mm, 0.5 mm, and 0.8 mm respectively. The surface of the copper was not flat; small bending existed in some part of the copper plate, which caused the variance of the lift off. The variance of the lift off was in the range of about 1 mm.

The conductivity of the copper alloy is about 5.8×10^6 S/m. In our experiments, the excitation frequency was 2 kHz. From the formula $\delta = 1/\sqrt{\pi f \mu \sigma}$, where, δ is the penetration depth, f is the excitation frequency, μ is the permeability of the material and σ is the conductivity, the penetration depth is about 1.5 mm for copper alloy at 2 kHz.

3. EXPERIMENTAL RESULTS

We first did the ECT experiment with one AMR sensor. Fig. 4(a) shows the results with different excitation frequencies. The Y direction was perpendicular to the direction of the grooves. Due to the variance of the lift off, the line of one scanning was not flat. The best signal was obtained at the excitation frequency of about 2 kHz.

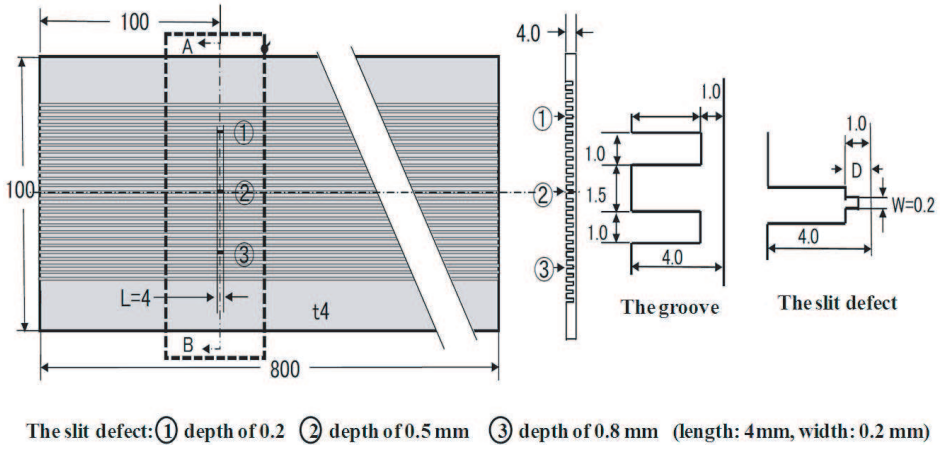

Figure 3: The specimen of copper plate with grooves and slit defect to simulate the combustion chamber of liquid rocket.

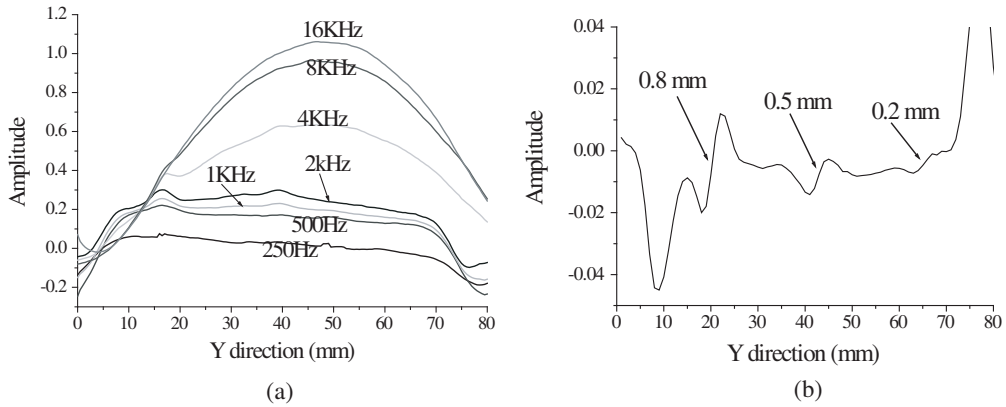

Figure 4: (a) Signal of ECT with one AMR sensor for different frequencies. (b) Signal of ECT with two AMR sensors.

Figure 4(b) shows the ECT signals when using subtraction method of two AMR sensors. The line was flatter than that with one AMR sensor, and the smallest defect with the depth of 0.2 mm could also be observed.

4. SUMMARY

Differential method with two AMR sensors was effective to reduce the influence of the variance of lift off. The small defect in copper alloy plate could be detected using ECT method.

ACKNOWLEDGMENT

We thank the useful advice from Dr. H. Yamawaki, I. Uetake, and helps from Prof. H. Itozaki and Dr. M. Tachiki.

REFERENCES

1. He, D. F., M. Shiwa, H. Yamawaki, M. Tachiki, H. Itozaki, S. Moria, T. Masuoka, and I. Uetake, "Basic examination for the defect detection of combustion chambers using ECT with an AMR sensor," *Journal of JSNDI*, Vol. 59, No. 10, 510–514, 2010.
2. Data sheet of HMC1001, Honeywell, http://www.ssec.honeywell.com/magnetic/products.html.
3. He, D. F., M. Tachiki, and H. Itozaki, "Highly sensitive anisotropic magnetoresistance magnetometer for Eddy-current nondestructive evaluation," *Rev. Sci. Instru.,* Vol. 80, 036102, 2009.

Estimation of Reinforcing Bars by Using Real GA with Discrete Chromosomes

Toshiyuki Tanaka, **Takahiro Matsuoka**, **Takashi Takenaka**, **and Toshifumi Moriyama**
Nagasaki University, Japan

Abstract— This paper discusses estimation of reinforcing bars by using Real-coded GA with discrete chromosomes. A chromosome consists of some genes which are position, depth, and radius of reinforcing bars. As the calculation of fitness is used FDTD method, each gene is divided according to the sell size of FDTD. Then the crossing-over and the mutation are calculated by the same method to the real number gene, the obtained gene is discretized again. Numerous chromosomes of real number arise during evolution, but many of them are same discrete chromosome. So the discretized chromosome is numbered and the chromosome and the value of the fitness are memorized. Because the fitness to the same discrete chromosome is not necessary to calculate, the computing time for exploration can be greatly shortened. Also the validity of the estimated result is discussed using the average, the standard deviation and the deviation.

1. INTRODUCTION

As for concrete structures, it is expected the long durability. It is necessary to make a close investigation of the condition of concrete structures with respect to cracks, cavities, and corrosion of reinforcing bars in order to prevent dangerous accidents such as drop of a mass of concrete [1]. Important factors of the strength investigation of the concrete structure are position and size of the reinforcing bars. The existence of reinforcing bars in the concrete structure can be confirmed by conventional concrete radars easily. However, the exact position and the radius of the reinforcing bar in concrete structure cannot be presumed with conventional concrete radars. We use Real-corded GA (RGA) to estimate the exact position and the radius of the reinforcing bar in concrete structure. There are many researches about the exploration by using GA [2–10]. In RGA, the chromosome for a reinforcing bar is composed of three genes. These genes are radius, location and depth of the reinforcing bar. The fitness is defined by the norm which is the summation of the absolute value of the difference between the observation field and the estimate field. The estimate field is calculated by using FDTD method. We succeed in estimation of the position and the radius of reinforcing bars by using RGA. But, an enormous computing time is necessary for RGA.

The gene updated by RGA is a real number. On the other hand, it is necessary for the investigation field to be divided at the cell size of the FDTD method. Therefore, even if the gene of the real number is defined, the discrete gene rounded by the size of the sell will actually be used when FDTD is executed. Therefore, the calculated electromagnetic field with the chromosome with only a difference that is smaller than the size of the cell will have the same value. In this paper, we propose RGA with discrete chromosome divided at the sell size of the FDTD method. The crossing-over and the mutation are calculated by the same computational method as gene of the real number, and obtained gene is discretized. Numerous chromosomes of real number arise during evolution, but many of them are same discrete chromosome. So the discretized chromosome is numbered and the chromosome and the value of the fitness are memorized. Because the fitness to the same discrete chromosome is not calculated, the computing time until the investigation is completed can be greatly shortened.

The effectiveness of the presented method has been confirmed using calculated data.

2. DISCRETIZATION OF CHROMOSOM

The Building Standards Law in Japan has determined the covering protection in the every structure. Minimum covering protection is 30 mm. Standards of the diameter of the reinforcing bars are 6 mm, 9 mm, 10 mm, 13 mm, 19 mm, ... In this reason, the exploration accuracy is decided at 1 mm. Therefore, the mesh size of FDTD method for calculating the estimation field is also made to be $\Delta d = 1$ mm. A chromosome is constructed by genes which composed position, depth and radius of reinforcing bars in exploration of reinforcing bars by using R-GA. In Figure 1, flowcharts for usual real-coded GA (UR-GA) and discrete real-coded GA (DR-GA) are shown. The new chromosome which is got by the technique (selection, crossing-over, mutation) of UR-GA is a real number. In most case the new chromosome is different to old chromosomes. The FDTD method is the

discrete calculation technique, therefore the new chromosome has to be discretized to perform the FDTD method. If the new chromosome has only the small difference compared with the cell size of the FDTD method, the discretized new chromosome is the same as old chromosomes. Then it is impossible to obtain exploration accuracy which is more detailed than the sell size of the FDTD method. For that reason, genes are discretized like Eq. (1).

$$\bar{x} = \mathrm{int}(x/\Delta d), \quad \bar{y} = \mathrm{int}(y/\Delta d), \quad \bar{r} = \mathrm{int}(r/\Delta d), \tag{1}$$

where, x, y, and r are position, depth, and radius of reinforcing bar respectively. Over-line denotes discretized value. If the chromosome obtained by the nth generation change is new one, FDTD method is executed, the fitness is calculated and the chromosome and the value of fitness are stored. If the chromosome is old one, FDTD method isn't executed. A great shortening at the computing time can be achieved by avoiding the recalculation of the fitness.

Figure 2 shows the arrangement of a transmitter and receivers over one reinforcing bar. The search area is as follows: $-2.5\,\mathrm{cm} \le x \le 2.5\,\mathrm{cm}$, $4.5\,\mathrm{cm} \le y \le 2.5\,\mathrm{cm}$, $0.5\,\mathrm{cm} \le r \le 1.5\,\mathrm{cm}$. As sell size of FDTD is 1 mm, the number of different discretized genes to x, y, and r is $N_x = 50$, $N_y = 50$, and $N_r = 10$ respectively. Therefore, the total number of different chromosomes is $N_x N_y N_r = 25000$. Figure 3 shows the computation time by using UR-GA and DR-GA. The number of trials is ten. The average computation time of UR-GA is 10.5 hours and the average computation time of DR-GA is 2.2 hours. The computation time by using DR-GA was compared with that of UR-GA at about 0.21 times. The average number of chromosomes calculated for one search was 388 in UR-GA, and 116 in DR-GA. To obtain one estimated result, GA of ten times is calculated. We call this one trial. Therefore, the computing time of GA of one time is about 1/10 at the time of one trial.

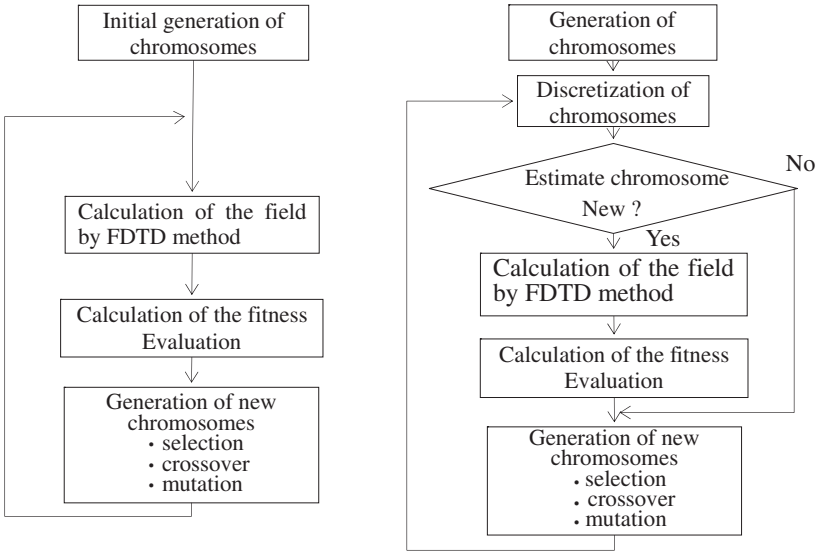

(a) UR-GA (b) DR-GA

Figure 1: Flowchart of real-coded GA.

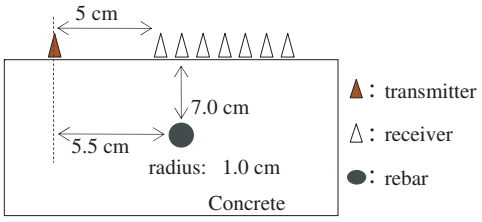

Figure 2: Arrangement of a transmitter and receivers.

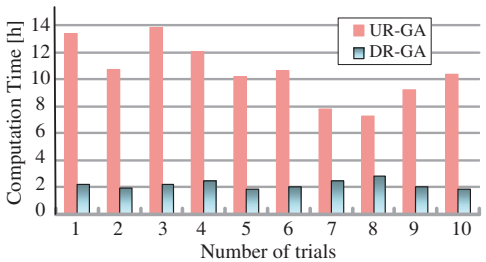

Figure 3: Computation time.

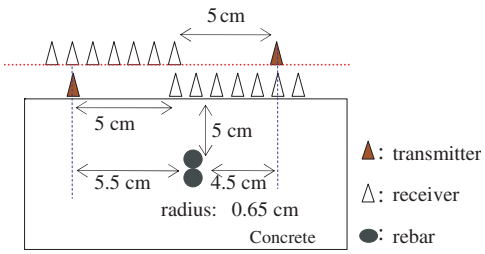

Figure 4: Arrangement of a transmitter and receivers.

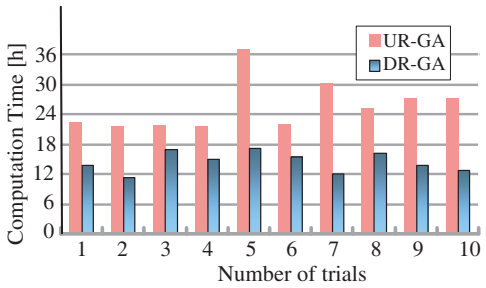

Figure 5: Computation time.

Table 1: The frequency distribution of the relation of between error of radius and error of depth.

		error of radius [mm]					
		$0 \sim 1$	$1 \sim 2$	$2 \sim 3$	$3 \sim 4$	$4 \sim 5$	sum
error of depth [mm]	0	546	1	0	0	0	547
	1	92	102	1	0	0	195
	2	0	35	78	0	0	113
	3	0	0	35	40	1	76
	4	0	0	0	14	30	44
	$5 \sim$	1	0	0	0	24	25
	sum	639	138	114	54	55	1000

Figure 4 shows the arrangement of a transmitter and receivers over two vertical closely-attached reinforcing bars. The search area is the same as the case of the exploration of one reinforcing bar. The total number of different chromosomes is 6.25×10^8 as a chromosome is composed by six genes of two reinforcing bars. Figure 5 shows the computation time by using UR-GA and DR-GA. The average computation time of UR-GA is 25.6 hours and the average computation time of DR-GA is 14.4 hours. The computation time by using DR-GA was compared with that of UR-GA at about 0.56 times. The reason why the shortening rate of the computation time is lower than the case of one reinforcing bar exploration is that the probability whose chromosome generated by the generation change is a new chromosome is high because the number of different discretized chromosomes is squares at one reinforcing bar exploration.

3. EVALUATION OF ESTIMATED RESULT

The inverse problems have a lot of local minima for the ill-posedness and nonlinearity of these problems. Therefore, the method of evaluating the estimated result becomes important in exploration by using GA. Until now, N-times calculation of GA were performed for one trial, and the chromosome that gave the largest fitness was assumed to be the result. As the noise is included in measured data, the chromosome that gives the maximum fitness is not necessarily a true solution. Then, the method to decide a final estimation value from N-chromosomes is discussed.

Table 1 shows the frequency distribution of the relation between error of the estimated radius and error of the estimated depth in the case of Figure 2. When the difference between each estimated depth and average depth is large, it is found that the difference between each estimated radius and average radius is also large. It can be judged that the estimated result in which the error is large is local minimum. Local minimum is distinguished by criterion Eq. (2).

$$|r(n) - r_{Ave}| < \alpha \quad n = 1, 2, \ldots, N \tag{2}$$

N-times GA calculations are carried out to one exploration. The criterion which the result of exploration is local minimum is provided in consideration of the standard deviation of N-estimated radiuses.

$$\sigma_r = \sqrt{\frac{1}{N}\sum_{n=1}^{N}(r(n) - r_{Ave})} \tag{3}$$

Table 2: The frequency distribution of the deviation for the estimated radiuses.

deviation	$r < 9$	$9 \leqq r \leqq 11$	$11 < r$
$25 \sim 30$	30	0	0
$30 \sim 35$	59	0	0
$35 \sim 40$	41	5	0
$40 \sim 45$	48	35	0
$45 \sim 50$	26	164	0
$50 \sim 55$	2	319	38
$55 \sim 60$	0	102	34
$65 \sim 70$	0	1	30
$70 \sim 75$	0	2	23
$75 \sim 80$	0	0	5

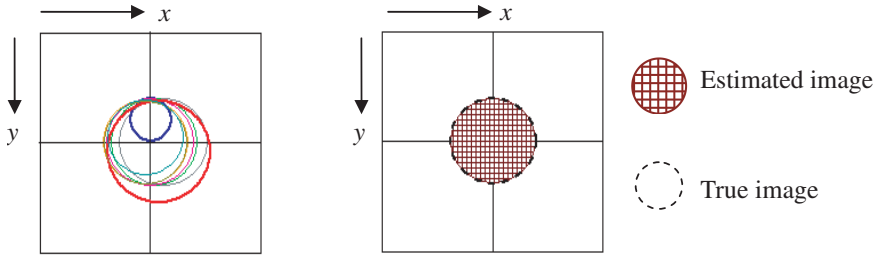

(a) Ten estimated images (b) Final result after evaluation

Figure 6: Estimated result.

It is judged that the reliability of the final estimated result is high because N-estimated results converge when the value of standard deviation is small. On the other hand, when the value of standard deviation is large, it is highly possible that the final estimated result is local minimum. The deviation (4) is introduced.

$$T_r = 50 + \frac{10(r(n) - r_{Ave})}{\sigma_r} \tag{4}$$

Table 2 shows the frequency distribution of the deviation for the estimated radiuses to 1000 trials. The true value of radius is 10 mm. The deviation of N-estimated radiuses is almost included from 45 to 55, when the error margin with a true value is ± 1 mm. Therefore, the following judgment standards is used.

$$\begin{aligned} &1. \quad 0.0 \leq \sigma_r < 0.7 \;\Rightarrow\; 35 \leq T_r \leq 65 \\ &2. \quad 0.7 \leq \sigma_r \leq 2.2 \;\Rightarrow\; 40 \leq T_r \leq 60 \\ &3. \quad 2.2 < \sigma_r \;\Rightarrow\; \text{Recalculation} \end{aligned} \tag{5}$$

If the standard deviation of the estimated radiuses is greater than 2.2, it is judged that exploration is failure and the recalculation is carried out. It is guaranteed that the error of the estimated radius is within 1 mm on the judgment standards 1 and 2. The final estimated result of the radius is the average of the genes of the radius which satisfies the range of the deviation defined by Eq. (5). The estimated result for a reinforcing bar is shown in Figure 6. The number of GA calculations is 10. Figure 6(a) shows each estimated images for ten-GA calculations and Figure 6(b) shows the final result after evaluation. The standard deviation of the estimated radiuses is 1.66.

4. CONCLUSIONS

The estimation of reinforcing bars by using Real-coded GA with discrete chromosomes was proposed. The computing time was able to be shortened greatly by avoiding the recalculation of the

fitness to the same discretization chromosome. In addition, the final evaluation of the estimated result obtained by Real-coded GA was discussed by using the average, the standard deviation, and the deviation. The validity of the proposed algorithm for measured data will be in future work.

ACKNOWLEDGMENT

This work was supported by Grant-in-Aid for Scientific Research (C: 20560455).

REFERENCES

1. He, X.-Q., Z.-Q. Zhu, Q.-Y. Liu, and G.-Y. Lu, "Review of GPR rebar detection," *PIERS Proceedings*, 804–813, Beijing, China, Mar. 23–27, 2009.
2. Benedetti, M., M. Donelli, and A. Massa, "Multicrack detection in two-dimensional structures by means of GA-based strategies," *IEEE Trans. Antennas Propagat.*, Vol. 55, 205–215, Jan. 2007.
3. Huang, C. H., H. C. Lu, C. C. Chiu, T. A. Wysocki, and B. J. Wysocki, "Image reconstruction of buried multiple conductors by genetic algorithms," *International Journal of Imaging Systems and Technology*, Vol. 18, 276–281, Oct. 2008.
4. Meng, Z. Q., T. Takenaka, and T. Tanaka, "Image reconstruction of two-dimensional impenetrable objects using genetic algorithm," *Journal of Electromagnetic Waves and Applications*, Vol. 13, No. 1, 95–118, 1999.
5. Takenaka, T., Z. Q. Meng, T. Tanaka, and W. C. Chew, "Local shape function combined with genetic algorithm applied to inverse scattering for strips," *Microwave Opt. Technol. Lett.*, Vol. 16, No. 6, 337–341, 1997.
6. Zhou, Y., J. Li, and H. Ling, "Shape inversion of metallic cavities using hybrid genetic algorithm combined with tabu list," *Electron. Lett.*, Vol. 39, No. 3, 280–281, 2003.
7. Li, F., X. Chen, and K. Huang, "Microwave imaging a buried object by the GA and using the S_{11} parameter," *Progress In Electromagnetics Research*, Vol. 85, 289–302, 2008.
8. Caorsi, S., A. Massa, and M. Pastorino, "A computational technique based on a real-coded genetic algorithm for microwave imaging purposes," *IEEE Trans. Geosci. Remote Sensing*, Vol. 38, 1697–1708, Jul. 2000.
9. Udo, K., T. Tanaka, T. Takenaka, and T. Moriyama, "The improvement of the radar for the exploration of buried objects in the concrete," *IEICE Technical Report*, No. 442, 111–116, 2008, SANE2007-121.
10. Matsuoka, T., T. Tanaka, T. Takenaka, and T. Moriyama, "Accuracy enhancement of the exploration for vertical buried objects in concrete structure by using Real-GA," *IEICE Technical Report*, 37–42, 2009, SANE2009-71.
11. Rocca, P., M. Benedetti, M. Donelli, D. Franceschini, and A. Massa, "Evolutionary optimization as applied to inverse problems," *Inverse Problems*, Vol. 25, No. 123003, 1–41, Dec. 2009.
12. Benedetti, M., M. Donelli, D. Lesselier, and A. Massa, "An innovative microwave imaging technique for non destructive evaluation: Applications to civil structures monitoring and biological bodies inspection," *IEEE Trans. Instrumentation and Measurement*, Vol. 55, No. 6, 1878–1884, Dec. 2006.
13. Benedetti, M., M. Donelli, A. Martini, A. Massa, and A. Rosani, "A two-step inverse scattering procedure for the qualitative imaging of homogeneous cracks in known host media — Preliminary results," *IEEE Antennas and Wireless Propagation Letters*, Vol. 6, 592–595, 2007.
14. Benedetti, M., M. Donelli, G. Franceschini, M. Pastorino, and A. Massa, "Effective exploitation of the A-priori information through a microwave imaging procedure based on the SMW for NDE/NDT applications," *IEEE Trans. Geosci. Remote Sensing*, Vol. 43, No. 11, 2584–2592, Nov. 2005.

A Comparison of Focusing Algorithms for Ground Based SAR System

C. Ozdemir, E. Yiğit, and Ş. Demirci
Department of Electrical-Electronics Engineering, Mersin University, Mersin, Turkey

Abstract— In this work two common and reliable Synthetic Aperture Radar (SAR) focusing algorithms; namely Range Doppler Algorithm (RDA) and Chirp Scaling Algorithm (CSA) are revisited and checked against each other in terms of their focusing and processing abilities. In the classical Range Doppler (RD) algorithm an interpolation step is needed to migrate the dispersed signal energy through the accurate range cells. Generally, this step requires important processing time, and leads to loss of image quality. The CSA avoids any interpolation step and performs range cell migration correction procedure. In order to examine the focusing performances of the algorithms, a simulation data is utilized as the example and the resultant focused images are presented accordingly.

1. INTRODUCTION

Synthetic aperture radar (SAR) is an important remote sensing technique for ground monitoring and many other scientific applications. A SAR system generates the radar image from airborne or satellite platform by transmitting phase encoded pulses and recording the reflected echoes from the Earth's surface. Since collected data from the radar is raw; i.e., not focused, concentration techniques must be applied in range and cross-range dimensions to generate a focused image. There are several techniques and algorithms for focusing the SAR data: The range-Doppler algorithm (RDA) [l] has been the base for more than a decade. RDA can be executed in different ways [2–5]. They all have similar steps and the implementation of secondary range compression (SRC) [2] is the main difference among them.

Usually, the scattered energy from the scene is collected in two-dimensional (2D) spatial-time domain. This SAR data is usually transformed to other domains (2D frequency domain or range-doppler domain) for further processing. The reflections from the targets which are at the same range but different azimuth cells are situated on the same azimuth frequency. So, to separate these targets from each other, RDA uses Range Cell Migration Correction (RCMC) routine which is the most important step of the RDA. RCMC is performed in both range and azimuth frequency domain. RCMC is a kind of time domain interpolation which compensates the effect of range cell migration. Although RDA is the most preferred algorithm in most SAR operations thanks to its high precision; phase perturbations, aliasing effects and complication of the processing due to extra interpolation process are the main disadvantages.

New algorithms [6, 7] have been developed to avoid interpolation while mitigating the range cell migration. Chirp Scaling Algorithm (CSA); for example, allows high precision SAR processing without applying any interpolation scheme in the SAR processing chain [8]. CS algorithm starts with scaling of chirp signal by multiplying it with a specific phase term (as given in Eq. (6)) to equalize the range migration of all target trajectories. As it will be presented in section 3, there are only multiplications and Fourier transforms (FT) in the algorithm and no interpolation is needed for the complete matched filtering, SRC and bulk RCMC. Therefore, CSA is inherently phase preserving and its focusing quality is neither restricted by wide swath nor by high squint angle.

The organization of the paper is as follows: In section 2 and 3, the formulations of RDA and CSA are revisited. In section 4, algorithms are applied and compared on SAR images. The simulated SAR data is generated with a MATLAB® code. In the last section, issues regarding the effectiveness and limitations of both methods are also discussed and concluding remarks are given.

2. RANGE DOPPLER ALGORITHM

There are three main steps in implementing RDA: range compression, range cell migration and azimuth compression. Processing steps are illustarted in Fig. 1(a) and all detailed formulas can be found in [9]. We begin by considering the low squint case for presenting the basic RDA, so the SRC is not required in this derivation. For a center frequency f_0 and chirp FM rate of K_r, the

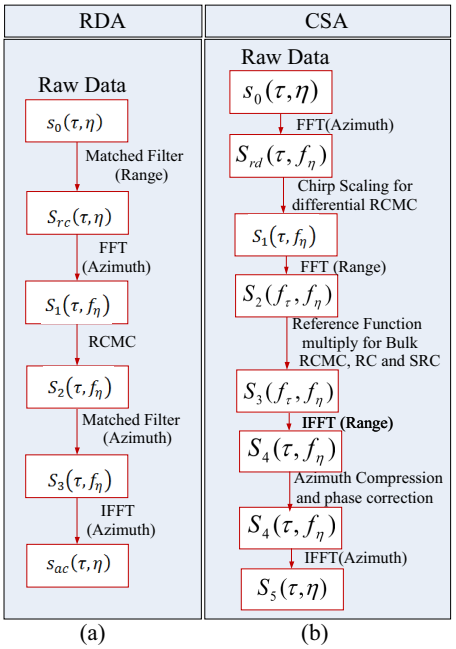

Figure 1: Flow chart of the (a) RDA, (b) CSA.

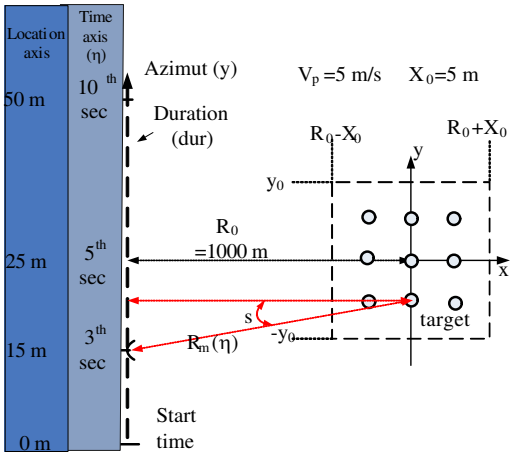

Figure 2: Geometry of the simulated SAR data.

demodulated radar signal $s_0(\tau, \eta)$ received from a point target can be modeled as

$$s_0(\tau,\eta) = A_0 \cdot w_r\left[\tau - \frac{2R(\eta)}{c}\right] w_a(\eta-\eta_c)\exp\{-j4\pi f_0 R(\eta)/c\} \cdot \exp\{jK_r(\tau - 2R(\eta)/c)^2\} \quad (1)$$

where A_0 is an arbitrary complex constant, τ is a range time, η is azimuth time and η_c is a beam center offset time. The range and azimuth envelopes are expressed by $w_r(\tau)$ and $w_a(\eta)$. The instantaneous slant range $R(\eta)$ is given by

$$R(\eta) = \sqrt{R_o^2 + V_r^2\eta^2} \quad (2)$$

where R_0 is the slant range of the zero Doppler of the cross range axis. The output of the range matched filter is the range compressed signal that is interpolated via RCMC and given by

$$S_2(\tau,\ f_\eta) = A_0 p_r\left[\tau - \frac{2R_0}{c}\right] W_a(f_\eta - f_{\eta c}) \cdot \exp\left\{-j\frac{4\pi f_0 R_0}{c}\right\} \cdot \exp\left\{j\pi\frac{f_\eta^2}{K_a}\right\} \quad (3)$$

$S_2(\tau,\ f_\eta)$ is the Fourier transformed signal via azimuth FFT and RCMC is performed, but without azimuth matched filtering. The matched filter $H_{az}(f_\eta)$ is the complex conjugate of the last exponential term in $S_2(\tau,\ f_\eta)$ as

$$H_{az}(f_\eta) = \exp\left\{-j\pi\frac{f_\eta^2}{K_a}\right\} \quad (4)$$

After azimuth matched filtering and IFFT operation, then compression is completed as

$$S_{ac}(\tau,\ \eta) = A_0 P_r\left[\tau - \frac{2R_0}{c}\right] p_a(\eta) \cdot \exp\left\{-j\frac{4\pi f_0 R_0}{c}\right\} \cdot \exp\{j2\pi f_{\eta c}\eta\} \quad (5)$$

where p_a is the amplitude of the azimuth impulse which is similar to p_r.

3. CHIRP SCALING ALGORITHM

There are a lot of similarities between CSA and RDA. Chirp Scaling factor which affects the FM rate can be taken as the main difference of CSA. All processing steps are listed in Fig. 1(b) and

formulas are given in [9]. The scaling function is given by

$$S_{sc}(\tau',\, f_\eta) = \exp\left\{ j\pi K_m \left[\frac{D\left(f_\eta, V_{r_{ref}}\right)}{D(f_\eta, V_{r_{ref}})} - 1 \right] (\tau')^2 \right\} \tag{6}$$

where

$$\tau' = \tau - \frac{2R_{ref}}{cD(f_\eta, V_{r_{ref}})} \tag{7}$$

CSA starts with azimuth FFT of the demodulated radar signal s_0. The FM rate is gathered from the result of the azimuth FFT as

$$K_m = \frac{K_r}{1 - K_r \frac{cR_0 f_\eta^2}{2V_r^2 {f_0}^2 D^3(f_\eta, V_r)}} \tag{8}$$

where $D(f_\eta, V_r)$ is the migration parameter expressed as

$$D(f_\eta, V_r) = \sqrt{1 - \frac{c^2 {f_\eta}^2}{4V_r^2 {f_0}^2}} \tag{9}$$

After the azimuth FFT of the Eq.(1), the RD domain signal is multiplied by the scaling function given in Eq.(6). Therefore, we get the scaled signal as

$$s_1(\tau,\, f_\eta) = s_{sc}(\tau',\, f_\eta) s_{rd}(\tau,\, f_\eta) \tag{10}$$

Then a range FT is performed. When a range matched filtering and bulk RCMC is applied to the Fourier transformed data, the range-compensated signal in the RD domain is obtained. After this, a range IFFT is performed:

$$\begin{aligned} s_4(\tau,\, f_\eta) \;=\; & A_2 p_r \left(\tau - \frac{2R_0}{cD(f_{\eta ref},\, V_{\tau ref})} \right) W_a(f_\eta - f_{\eta c}) \cdot \exp\left\{ -j \frac{4\pi f_0 R_0 D(f_\eta,\, V_\tau)}{c} \right\} \\ & \cdot \exp\left\{ -j \frac{4\pi K_m}{c^2} \left[1 - \frac{D(f_\eta,\, V_{\tau ref})}{D(f_{\eta ref},\, V_{\tau ref})} \right] \cdot \left[\frac{R_0}{D(f_\eta,\, V_\tau)} - \frac{R_{ref}}{D(f_\eta,\, V_\tau)} \right]^2 \right\} \end{aligned} \tag{11}$$

where A_2 is complex constant. In this equation, the complex conjugate of the first exponential term is the azimuth matched filter and the complex conjugate of the second exponential term is the residual phase correction multiplier. After the azimuth compression and residual phase correction, the final data is transformed back to the azimuth time domain as the compressed signal as

$$s_5(\tau,\, \eta) = A_4 p_r \left(\tau - \frac{2R_0}{cD(f_{\eta ref},\, V_{\tau ref})} \right) p_a(\eta - \eta_c) \exp\left\{ j\theta(\tau,\, \eta) \right\} \tag{12}$$

where $p_a(\eta)$ is the IFFT of $W_a(f_\eta)$, and $\theta(\tau,\, \eta)$ is the target phase.

4. SIMULATION RESULTS

To illustrate the effectiveness of the preferred algorithms, a hypotetical target composed of nine point scatterers for the ground based low squint angle case have been simulated: the experimental geometry of the simulation is depicted in Fig. 2. The point targets are centered at the $x = 1000$ and $y = 25\,\mathrm{m}$ relatively. The back-scattered electric field is collected along the synthetic aperture in y direction ranging from $y = 0\,\mathrm{m}$ to $y = 50\,\mathrm{m}$ for a total of 1000 discrete spatial points. The choice of pulse repetition frequency (PRF), bandwidth (B_0) and range distance to center of the target area (R_0) affected the maximum range, range resolution and azimuth resolution which are given in Table 1 and determined via the following parameters:

$$R_{\max} = \frac{c}{2}\left(\frac{1}{PRF} - T_p \right) \quad \Delta_R = \frac{c}{2 \cdot B_0} \quad \Delta_A = \frac{\lambda \cdot R_0}{v_p \cdot dur} \tag{13}$$

Table 1: Parameters for strip-map mode.

Parameters	
Pulse Repetition Frequency (Hz)	$PRF = 100$
Time of Flight (sec)	$dur = 10$
Velocity of platform (m/s)	$v_p = 5$
Carrier frequency (Hz)	$f_0 = 4.5e^9$
Antenna length actual (m)	$L_a = 1$
Chirp Pulse Duration (sec)	$T_p = 2.5e^{-7}$
Baseband bandwidth (Hz)	$B_0 = 500e^6$
Unambiguous range (m)	$R_{\max} = 1500e^3$
Range resolution (m)	$\Delta_R = 0.3$
Azimuth resolution (m)	$\Delta_A = 1.33$

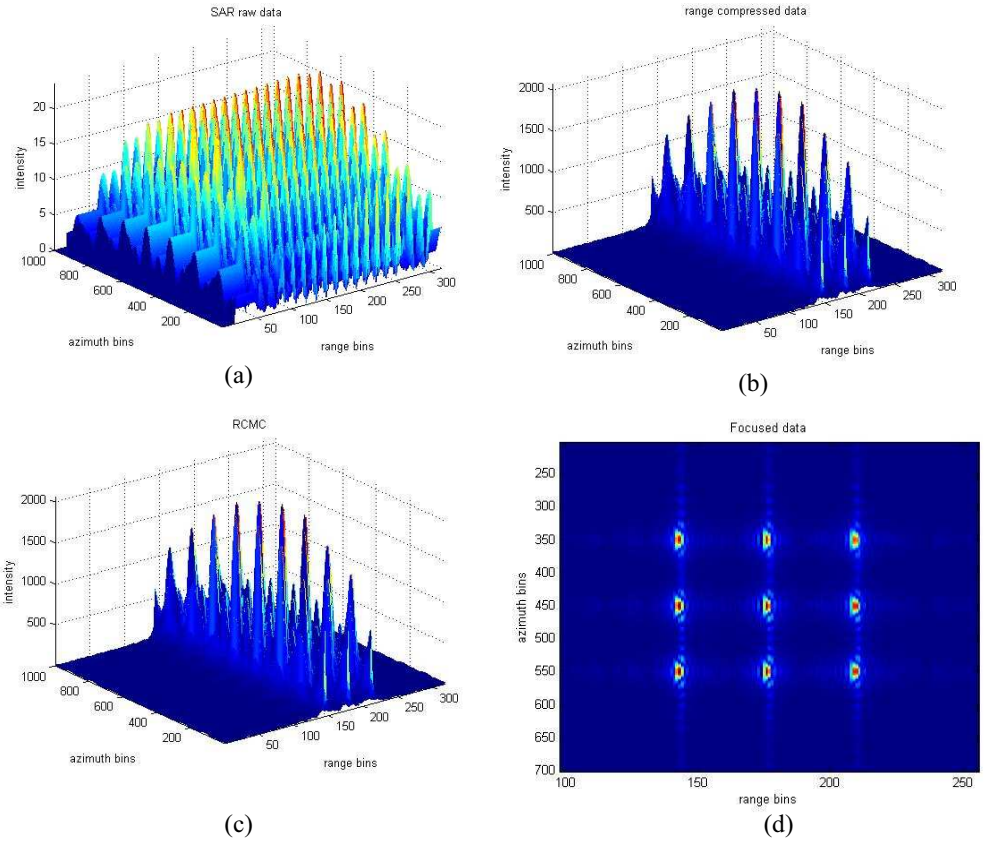

Figure 3: RDA results: (a) SAR raw data of simulated targets, (b) range compressed signal, (c) RCM corraleted signal, (d) focused SAR data with RDA.

Note that the parameters of the simulation are chosen for ground based SAR applications. For these parameters, the SAR simulation of the point targets is performed, and reflections from the point targets are gathered in the raw data as it shown in Fig. 3(a). The range matched filtered image, RCM correlated image and azimuth IFFT of RCMC are shown in Figs. 3(b), (c) and (d), respectively. The results for the CSA is also shown in Figs. 4(b), (c) and (d) for the same raw data. As seen from Figs. 3(d) and 4(d), the resultant images are successfully focused and estimates exact locations of the scattering points. When the results of the algorithms are compared based on their appearance, CSA performs a little bit better than the RDA based on image resolution. Therefore; CSA's performance looks better in terms of focusing quality and sidelobe levels of the point-spread-function. If the computation time values of the algorithms are compared, the CSA is also a little bit better than RDA. The simulations were performed with standard PC that has

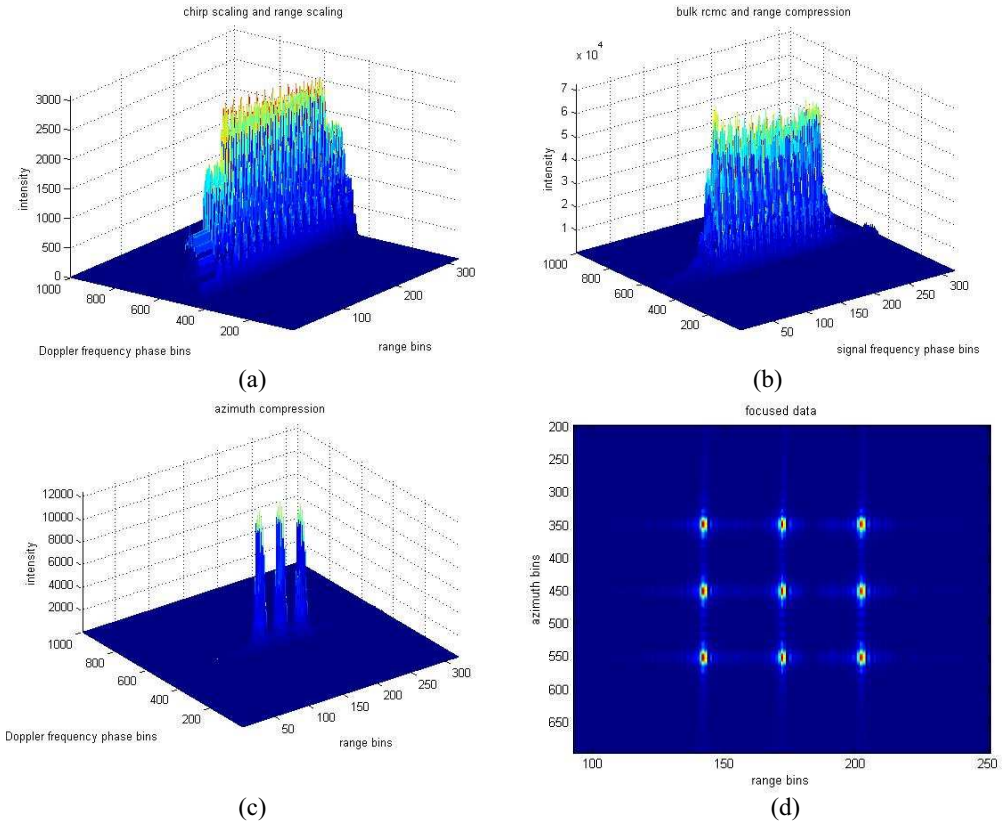

Figure 4: CSA results: (a) Chirp scaled signal. (b) RCMC and range compressed signal. (c) azimuth compressed signal. (d) focused SAR data with CSA.

AMD Athlon II X2 2.90 GHz processor and 2 GB RAM. The elapsed time of simulation of CSA is 0.511197 seconds and RDA is 0.631322 seconds. This difference is due to the fact that only FFTs and multiplications are used in the CSA. In the absence of significant Doppler variation, the CSA requires almost 5% less arithmetic than the RDA, a saving mainly due to the removal of the eight point RCMC interpolator [8].

5. CONCLUSIONS

In this work, two common algorithms are revisited and compared against each other based on the image quality and processing abilitites. The formulations of the algorithms are basically given. The algorithms are tested with the simulated data whose parameters are chosen for ground based (slower, shorter and low squint angle) SAR systems. Almost perfect focused images are achieved after applying these algorithms to the simulated SAR data. The simulation results shows that, the accuracy and image quality of CSA is better and even more sensitive than RDA. CSA shows better performance for a relatively wide range of parameters, including low squinted angle operation. CSA also outrun RDA in terms of processing the SAR data and getting the final image.

REFERENCES

1. Bennett, J. R. and I. G. Cumming, "A digital processor for the production of Seasat synthetic aperture radar imagery," *Proc. SURGE Workshop*, Frascati, ESA-SP-154, 1979.
2. Jin, M. Y. and C. Wu, "A SAR correlation algorithm which accommodates large range migration," *IEEE Trans. Geosci. Remote Sensing*, Vol. GE-22, 592–597, 1984.
3. Wong, F. H. and I. G. Cumming, "Error sensitivities of a secondary range compression algorithm for processing squinted satellite SAR data," *Proc. IGARSS '89*, 2584–2587, Vancouver, 1989.
4. Chang, C. Y., M. Jin, and J. C. Curlander, "Squint mode SAR processing algorithms," *Proc. IGARSS '89*, 1702–1706, Vancouver, 1989.
5. Smith, A. M., "A new approach to range-Doppler SAR processing," *Int. J. Remote Sensing*, Vol. 12, 235–251, 1991.

6. Cumming, I., F. Wong, and K. Raney, "A SAR processing algorithm with no interpolation," *Proc. IGARSS '92*, 376–379, Houston, 1992.
7. Runge, H. and R. Bamler, "A novel high precision SAR focussing algorithm based on chirp scaling," *Proc. IGARSS '92*, 372–375, Houston, 1992.
8. Raney, R. K., H. Runge, R. Bamler, I. G. Cumming, and F. H. Wong, "Precision SAR processing using chirp scaling." *IEEE Trans. Geosci. Remote Sensing*, Vol. 32, No. 4, 786–799, July 1994.
9. Cumming, I. G. and F. H. Wong, *Digital Processing of Synthetic Aperture Radar Data*, Artech House Remote Sensing Library, 2005.

Imaging of Wide-angle Near-field Inverse Synthetic Aperture Radar Data Using Back-projection Algorithm

Şevket Demirci[1], **Deniz Üstün**[2], **and Caner Özdemir**[1]

[1]Department of Electrical-Electronics Engineering, Mersin University, Mersin, Turkey
[2]Department of Electronic and Computer Education, Mersin University, Mersin, Turkey

Abstract— In this paper, the focused image formation problem of inverse synthetic aperture radar (ISAR) data collections that use wide angular apertures are considered. A two-dimensional near-field back-projection algorithm is presented which compensates the range migration effects resulted from wide-angle data collection set-up. The algorithm is applied to a hypothetical target model and validated through the produced wide-angle near-field ISAR image. Resolution measures for wide-angle data collection scheme and imaging are also evaluated by comparing the impulse response functions.

1. INTRODUCTION

Inverse synthetic aperture radar (ISAR) systems generally use narrow angular integration widths that may typically extent to only a few degrees while collecting the reflectivity data from the target. This is mainly due to the fact that using narrow look-angle apertures provide major simplifications in signal processing and image formation. The plane-wave illumination assumption can be made under most narrow-angle situations and therefore direct Fourier transformation procedure can be efficiently employed in forming the final ISAR images. Besides these benefits, noting that the cross-range resolution is inversely proportional to the look-angle width, high resolution ISAR images of targets which have large cross-range extents cannot be possible with the narrow angle data. Therefore, collecting the backscattered data over a wide angular width will improve the cross-range resolution [1]. Furthermore, wide-angle data collections can also provide high range resolutions even with relatively narrow waveform bandwidth [2]. On the other hand, wide-angle systems significantly face with the problem of unfocused images. Plane-wave illumination assumption is no longer valid in the wide-angle set-up and hence the imaging algorithm must take wavefront curvature effects into account. One possible solution is the sub-aperture approach which assumes planar wavefronts in smaller sub-apertures of the wide-angle data [3]. This procedure exhibits resolution degradations because of not using the whole angle aperture at the same integration time.

In this work, an imaging procedure based on back-projection algorithm [4, 5] with near-field corrections is developed in aiming to obtain a focused image out of the wide-angle data. The outline of the paper is as follows: Section 2 provides a brief formulation of the near-field back-projection algorithm. In Section 3, the resolution metrics for wide-angle data collection and imaging processes are provided. Section 4 demonstrates the validation results of the proposed algorithm using the simulation data of a hypothetical target. Conclusions and suggestions for future work are given in the last section.

2. IMAGE FORMATION BASED ON BACK-PROJECTION PROCEDURE

Data collection geometry for a two-dimensional (2-D) monostatic ISAR measurement set-up is shown in Fig. 1. The target is represented by a reflectivity function $g(x, y)$ and is assumed to be in the near-field of the antenna positioned along the $\vec{u}$-direction.

At each observation angle θ, radar measures the range profile $d_\theta(r)$ as observed from its instantaneous location and is given by;

$$d_\theta(r) = \int_{-\infty}^{\infty}\int_{-\infty}^{\infty} g(x, y)\delta(r_u - r)dxdy \tag{1}$$

where r_u stands for the near-field range from a viewpoint defined by $\vec{u}$ to any location (x, y). ISAR systems generally acquire Fourier Transform (FT) data of this range profile which is given by;

$$D_\theta(K_r) = \int_{-\infty}^{\infty} d_\theta(r)\exp(-jk_r r)dr \tag{2}$$

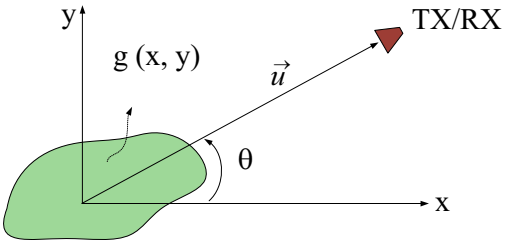

Figure 1: Data collection geometry for a 2-D monostatic ISAR.

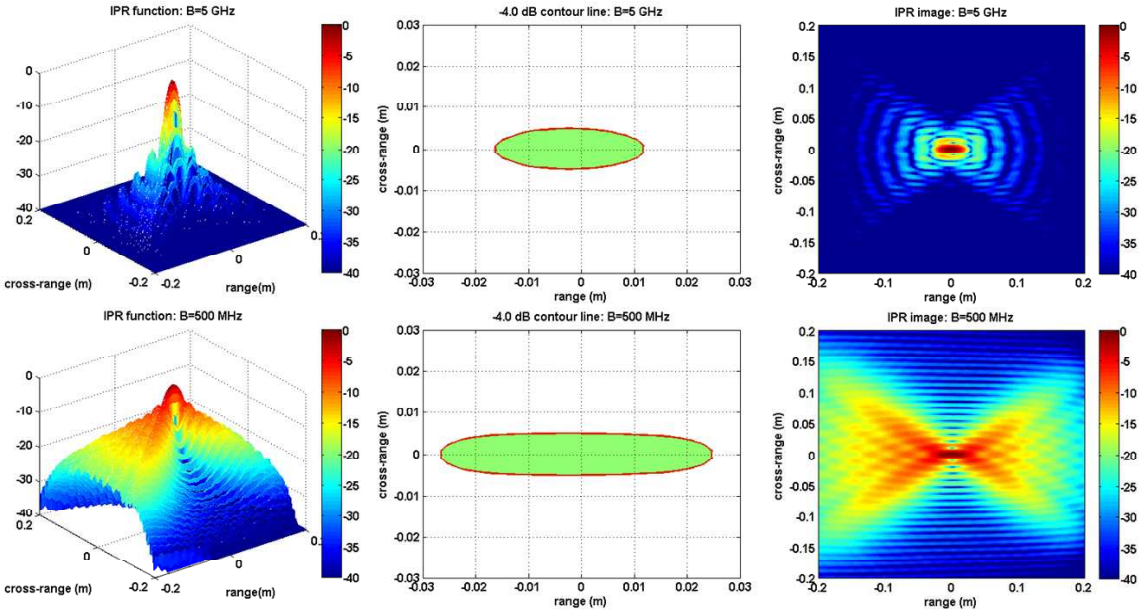

Figure 2: IPR plots for wide-angle ($\Delta\theta = 90°$) data processing. Left: IPR functions for wideband (top) and narrowband (bottom). Middle: corresponding -4 dB contour lines. Right: resulted IPR images.

where k_r is the wavenumber defined as $k_r = 4\pi f/c$. From the projection-slice theorem [6], $D_\theta(K_r)$ can be linked to the target's FT $G(k_x, k_y)$ by $D_\theta(K_r) = G_\theta(K_r)$. Hence, a sampled representation of $G(k_x, k_y)$ can be obtained from the projections $d_\theta(r)$ measured at various observation angles. The back-projection algorithm uses this fact when utilizing the FT relationship between $g(x, y)$ and $G(k_x, k_y)$. Then, the resulted equation for an estimate of $g(x, y)$ is found as;

$$g(x, y) = \int_{-\pi}^{\pi} \left[\int_0^{\infty} D_{\theta_u}(k_r) \exp(jk_r r_u) k_r dk_r \right] d\theta_u \tag{3}$$

where the bracketed term in Eq. (3) is the 2-D filtered back-projection at the angle θ_u. Denoting this by $q_{\theta_u}(r_u)$, it can be simply calculated by weighting the FT of the range profile using a high-frequency filter k_r, and then by taking the inverse transform. The consequential projections for different azimuth angles are then added to reconstruct an image of $g(x, y)$. In the implementation of the algorithm, a one-dimensional (1-D) interpolation procedure is required in image domain when the value of $q_{\theta_u}(r_u)$ is obtained for each pixel. At this back-projection step, if the true vector magnitudes of the near-field ranges r_u are taken, then the algorithm compensates the wavefront curvature effects. Therefore, the back-projection algorithm can be conveniently applied to near-field ISAR scenarios.

3. IMPULSE RESPONSE FUNCTION OF THE PROCESSING

Impulse Response (IPR) functions can be used to evaluate the resolution performance of the wide-angle ISAR data collection and image reconstruction procedure. For this purpose, the back-projection imaging process was applied to the return of a single point scatterer from a wide-angle ($\Delta\theta = 90°$) aperture. Two different data collection situations; one for a wideband (e.g., $B = 5$ GHz)

Table 1: Theoretical and true resolutions for wide-angle ISAR (x; range and y; cross-range).

Aperture	Bandwidth	Theoretical Resolution		True Resolution	
$\Delta\theta$, deg.	B, GHz	$dx = c/(2B)$, cm	$dy = c/(2f_c\Delta\theta)$, cm	dx, cm	dy, cm
90°	5	3	0.95	2.82	0.94
90°	0.5	30	0.95	5.01	1.09

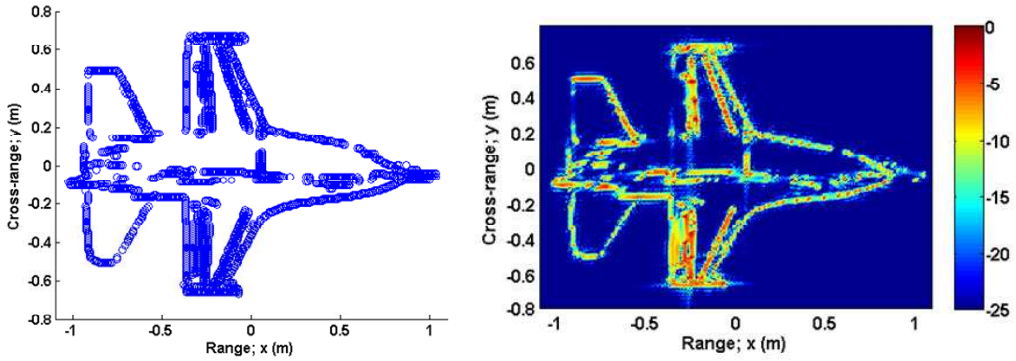

(a) (b)

Figure 3: Hypothetical target consists of perfect point scatterers. (b) focused image of the wide-angle ISAR data.

and one for a narrowband (e.g., $B = 500\,\text{MHz}$) which both have a center frequency of $f_c = 10\,\text{GHz}$ were considered. The resulted IPR plots are shown in the relevant figures of Fig. 2. From the IPR functions of the left images, it is observed that the reduction in the bandwidth leads to significantly higher sidelobes which are also evident in the right IPR images. The $-4\,\text{dB}$ resolutions calculated from the contour lines are shown in the middle column images. These true $-4\,\text{dB}$ resolutions and also the theoretical resolutions calculated via the conventional range and cross-range resolution formulas are given in Table 1. It is seen from the table that while the theoretical resolutions are nearly in good agreement with the true resolutions in the wideband, the theoretical range resolution value significantly deviates from the true value in the narrowband. This shows that range and cross-range resolutions are not independent for a wide-angle case and classical narrow angle resolution formulas cannot be readily applied. Most importantly, it should be noted that the reduction in the bandwidth by a factor of 10 causes to a reduction only by a factor of 1.7 in the range resolution for this particular example. Hence, it is still possible to achieve good range resolutions in the wide-angle imaging when narrowband waveforms are used. Despite this utility of wide-angle set-up, its cross-range improvement can be easily assessed by comparing the resolution values for the wide-angle and narrow angle cases. For a bandwidth of 5 GHz, the cross-range resolutions for the wide and the narrow angle cases are found as 0.94 cm and 8.15 cm respectively. Hence, the improved cross-range resolution in the wide-angle case clearly illustrates the benefit of this wide-angle set-up.

4. SIMULATION RESULT

A wide-angle near-field ISAR imaging experiment was simulated to combine the benefits of wide angular apertures and near-field scanning. Although, isotropic point scattering assumption cannot be often appropriate and realistic for the wide angular apertures, we adopted this assumption in the simulation for the validation purposes of the imaging algorithm. For this goal, a hypothetical target consists of perfect point scatterers of equal magnitudes was constructed as shown in Fig. 3(a). In the monostatic configuration, antenna was located at 10 m distance from the target center which results a near-field illumination according to the far-field requirement formula ($r \geq 2W^2/\lambda$) since the target has the range and cross-range extents of 2.07 m and 1.35 m, respectively. Data was collected for an angular span of 90° at 361 points and a frequency span of 6 GHz to 12 GHz for 201 stepped frequencies. The focused image is shown in Fig. 3(b) which clearly demonstrates the effectiveness and the success of the algorithm.

5. CONCLUSIONS

In this paper, we have demonstrated a 2-D imaging algorithm based on back-projection that has the capability of forming the ISAR images under wide-angle and near-field situations. The algorithm was tested and validated on the simulation data. Since a significant aspect of wide angular aperture is its high resolution capability, the wide-angle resolution metrics were derived for an isotropic point scattering case. However, the limited persistence of targets (i.e., 10 to 20 degrees) in real measurements may restrict this high resolution property. Hence, this angle-dependent amplitude scattering will constitute the subject of our future research.

REFERENCES

1. Wehner, D. R., *High Resolution Radar*, Artech House, Norwood, Mass, USA, 1997.
2. Luminati, J. E., "Wide-angle multistatic synthetic aperture radar: Focused image formation and aliasing artifact mitigation," Ph.D. Thesis, Air Force Institute of Technology, Wright-Patterson Air Force Base, Ohio, USA, 2005.
3. Ozdemir, C., O. Kirik, and B. Yilmaz, "Sub-aperture method for the wide-bandwidth wide-angle inverse synthetic aperture radar imaging," *Int. Conf. Electric. and Electron. Engin. — ELECO'2009*, 288–292, Bursa, Turkey, December 2009.
4. Munson, D. C., J. D. O'Brien, and W. K. Jenkins, "A tomographic formulation of spotlight-mode synthetic aperture radar," *Proc. IEEE*, Vol. 71, No. 8, 917–925, 1983.
5. Knaell, K. and G. P. Cardillo, "Radar tomography for the generation of three-dimensional images," *Proc. Inst. Electr. Eng. — Radar, Sonar, Navig.*, Vol. 142, No. 2, 54–60, 1995.
6. Mersereau, R. and A. Oppenheim, "Digital reconstruction of multidimensional signals from their projections," *Proc. IEEE*, Vol. 62, No. 10, 1319–1338, 1974.

Novel Symmetrical EH-horn Antennas Based on EBG Technology

I. Khromova, **I. Ederra**, **and R. Gonzalo**
Public University of Navarra, Spain

Abstract— In this paper, the design of a novel F band pyramidal horn antenna based on Electromagnetic Band Gap structures (EBGs) is presented. Along with a symmetrical and directive radiation pattern the reported antenna possesses a wide operation frequency band. Being based on an EBG technology, the antenna is implemented as a complex hollow defect in a three-dimensional periodic dielectric structure and does not require metallic components. The latter makes it especially valuable for sub-millimetre and THz frequency range.

1. INTRODUCTION

The scientific and technological interest towards electromagnetic band gap (EBG) structures has been growing rapidly since their discovery. The essence of any EBG structure, a periodical dielectric structure with certain geometry and dimension, is that it is a resonance structure. Due to this fundamental property different interesting well-known effects, such as band gaps, controllable dispersion, defect-based waveguiding, field localization or resonant transmission are observed [1, 2].

In recent years EBGs have been widely exploited for the purpose of shaping and improving the radiation characteristics of antennas of different types. In particular, EBG resonator cavities and defects [1–3] have been used to create antennas with large directivities and high efficiencies. Finally, following the analogy with classical metallic horn antennas, introducing a horn-shaped hollow defect can make the EBG-based system work as a horn antenna [4, 5].

However, EBG-based horn antennas in their present form despite offering a wide spectrum of applications still have several fundamental gaps and drawbacks. Up to now only sectoral horns embedded in one layer of rods in a woodpile structure have been designed. The reason for this is the lack of understanding of electromagnetic processes inside such structures. The other principal drawback of the woodpile horn antennas is the absence of mirror symmetry in the stacking direction of a woodpile structure, which results in non-symmetrical radiation patterns of the antennas.

This paper presents the design of a novel symmetrical pyramidal horn antenna based on EBG structures. The main concept of the design lies in turning the EBG structure at the antenna flare angle and thus forming the EBG "walls" of the horn. The main difficulty in creating an pyramidal antenna or even a sectoral antenna embedded in various adjacent layers of a woodpile structure, lies in the fundamental difference between the processes of mode formation in metallic and EBG waveguides and horns. Unlike the analogous situation in metallic horns, forming a horn antenna by cutting out a pyramidal shaped defect results in creating abrupt transition between effective EBG waveguides (the local waveguides in each cross-section of the horn antenna). Using the proposed concept of rotating the woodpile structure and thus shifting the EBG lattice nodes provides the real adiabatic transition between en EBG waveguide and the free space.

2. PYRAMIDAL EBG HORN ANTENNA

This paper presents a novel pyramidal woodpile-based horn antenna possessing a symmetrical radiation pattern and competitive parameters. Such antennas can substitute metallic horns in certain circumstances, which is especially valuable for millimeter and THz devices. In this paper the design of a woodpile horn antenna operating at frequencies around 110 GHz is presented.

In order to provide an adiabatic transition between an EBG waveguide and the free-space, one has to turn the whole EBG structure at an angle equal to horn antenna flare angle and to create a slow and gradual aperture. If the lattice nodes are not displaced along the way from the antenna throat to the antenna aperture, the abrupt changes in the horn cross-sections make the initial electromagnetic mode break up into higher-order modes.

Figure 1 presents the geometrical structure of the proposed EBG horn antenna. It is fed by an EBG hollow waveguide [6] consists of four slabs of woodpile structure oriented at a certaing angle with respect to the direction of propagation. Between these slabs a hollow horn-shaped space is created. Due to the fact that the whole lattice of the periodic structure is shifted along the direction of propagation, the propagating wave faces the same conditions at the boundary of the horn. This fact allows one to achieve proper reflection and adiabatic transition between the EBG waveguide and the free space.

3. ANTENNA PERFORMANCE

According to numerical simulations the presented pyramidal woodpile horn antenna shows a good performance in terms of operating frequency bandwidth, input reflection coefficient, directivity and radiation efficiency. Fig. 2 presents the reflection coefficient spectrum together with the directivity distribution within the operating frequency band.

The operating bandwidth of the present EBG horn antenna is estimated as 10.75%: in the region from 100.4 GHz to 111.8 GHz the input reflection coefficient is above −10 dB, and the peak directivity value does not drop to more than 3 dB less than the maximum value within the operating bandwidth.

Figure 3 presents a typical radiation pattern of the proposed EBG horn antenna configuration. It can be noticed that the pattern is symmetrical in both E- and H-planes, this property could not be achieved in the previously reported configurations of the woodpile-based horn antennas.

Thus, the presented woodpile horn antenna posessess a symmetrical radiation pattern in both E- and H-planes. Being directive and having almost equal beamwidth in both planes, this antenna shows nice performance and can be considered as a promising novel device for many applications requiring EBG technology solutions.

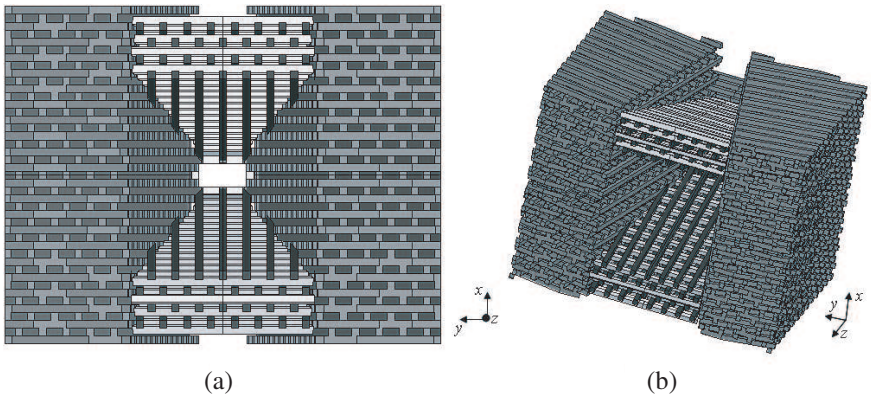

(a) (b)

Figure 1: Woodpile based symmetrical EH-horn antenna ((a) front view, (b) 3D view). The flare angles in the E- and H-planes were both set as $\alpha_E = \alpha_H = 12.5°$.

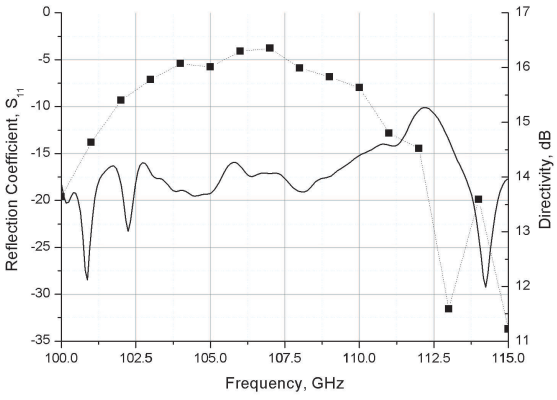

Figure 2: Input reflection coefficient (black solid curve) and peak directivity value (dashed curve with black squares) of the symmetrical woodpile pyramidal horn antenna.

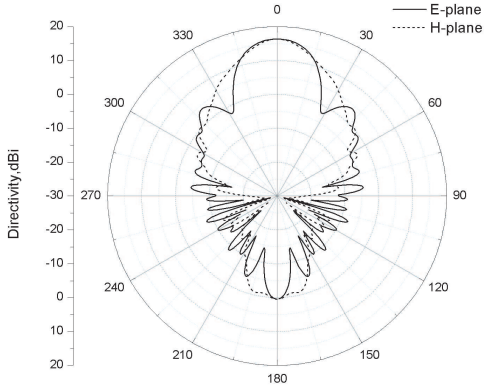

Figure 3: Radiation pattern of the symmetrical woodpile pyramidal horn antenna at 107 GHz.

4. CONCLUSIONS

This paper presents a novel pyramidal EBG horn antenna design. The concept, on which the antenna is based, lies in combining slabs of woodpile turned at different angles in order to form a hollow horn antenna within the EBG "walls". Previously reported woodpile based horn antennas

were restricted to be sectoral since the embedding medium did not allow to create apertures in both E- and H-planes by bending the woodpile bars. Moreover, the woodpile based horn antennas used to have a non-symmetrical radiation pattern due to the absence of mirror symmetry in the stacking direction of the embedding periodic structure. The approach presented in this paper allows one to create apertures in both E- and H-planes and also to introduce symmetries which the embedding woodpile medium does not possess. Thus, it became possible to design the pyramidal woodpile-based horn antenna with a symmetrical radiation pattern and competitive parameters. The presented woodpile-based horn antenna is made of silicon and operates in the F band. According to numerical simulation results it exhibits a 10.2% bandwidth. Such EBG-based components can be used when designing integrate EBG-based devices and can serve as alternatives of metallic horns in certain situations. This is especially actual for sub-millimetre and THz applications.

ACKNOWLEDGMENT

This work is supported by the Spanish Ministry of Science and Innovation Project Nos. TEC2009-11995 and CSD2008-00066.

REFERENCES

1. Meade, R. D., K. D. Brommer, A. M. Rappe, and J. D. Joannopoulos, "Photonic bound states in periodic dielectric materials," *Phys. Rev. B*, Vol. 44, No. 24, 13772–13774, 1991.
2. Noda, S., A. Chutinan, and M. Imada, "Trapping and emission of photons by a single defect in a photonic band gap structure," *Nature*, Vol. 407, No. 6804, 608–610, 2000.
3. Khromova, I., R. Gonzalo, I. Ederra, and P. de Maagt, "Resonance frequency behavior of 3D EBG cavities," *J. Appl. Phys.*, Vol. 106, 014901–01498, 2009.
4. Weily, A. R., K. P. Esselle, and B. C. Sanders, "Layer-by-layer photonic crystal horn antenna," *Phys. Rev. E.*, Vol. 70, 037602-4, 2004.
5. Khromova, I., I. Ederra, J. Teniente, R. Gonzalo, and K. P. Esselle, "Evanescently-fed electromagnetic band gap horn antennas and arrays," submitted to *IEEE Transactions on Antennas and Propagation*, 2010.
6. Ederra, I., I. Khromova, R. Gonzalo, N. Delhote, D. Baillargeat, A. Murk, B. E. J. Alderman, and P. de Maagt, "Electromagnetic band gap waveguide for the millimeter range," *IEEE Transactions on Microwave Theory and Techniques*, Vol. 58, No. 7, 1734–1741, 2010.

Developments Low Cost Probe Compensated Cylindrical Near Field Measurement for Antenna Radiation Wave

E. T. Rahardjo, F. Y. Zulkifli, M. D. Firmansah, and C. Apriono
Antenna propagation and Microwave Research Group (AMRG), Department of Electrical Engineering
Universitas Indonesia, Kampus Baru UI Depok, Depok 16424, Indonesia

Abstract— In this paper, a low cost near field measurement technique has been developed. The measurement design uses a probe mounted on the vertical frame of the scanner to pick up the cylindrical surface of the test antenna near field. The Fast Fourier Transform (FFT) method is utilized to transform near field to far field data. Firstly the developed scanner and near field to far field transformation program are compared to the commercial software based on finite element method (HFSS). The comparison of the developed near field measurement technique with the finite element method (HFSS) program is discussed using dipole antenna as a probe antenna to measure microstrip array antenna as test antenna. Both compensated and uncompensated probe are described.

1. INTRODUCTION

Antenna measurement is needed to ensure that the design of an antenna is in accordance with the expected performance. Far field antenna measurement, however, require a large real estate and high cost. In the far field method, when the antenna has a large size, a problem occurs concerning the large distance needed to measure the radiation pattern of the antenna. As for the limited space availability, the measurement of the antenna then can only be done with near field method.

There are three near field methods known which are: the planar, cylindrical and spherical surfaces [1–3]. The design of the near field method with cylindrical surface is proposed as well as it probe compensation technique. In this paper, the measurement design is developed to transform near field data to far field data. It uses the Fast Fourier Transform (FFT) method for the computation process. This FFT method is more efficient for the computer process compared to other method. The developed near field to far field transformation program is compared to the commercial software based on finite element method (HFSS). The comparison of the developed transformation program with the finite element method (HFSS) program is discussed using dipole antenna as a probe antenna to measure microstrip array antenna as test antenna.

2. THE CYLINDRICAL NEAR FIELD MEASUREMENT SYSTEM

The cylindrical nearfield measurement system is shown in Fig. 1. The design of this system can be divided into 3 parts; they are the scanner with the scanning area, measuring equipment and management system [4].

The scanner has a probe antenna mounted on vertical frame that moves at certain points of the cylindrical surface. The scanning area is designed to cover the cylindrical surface in the near field region of the antenna under test (AUT). Furthermore, the probe also can be rotated to get the variable component in the vertical and horizontal polarization. This design will be very appropriate to be placed in an anechoic chamber with limited dimension.

The scanner has a pair of stepper motor which is controlled by a computer to determine the probe position on the cylindrical surface scanning area. It is also needed to change the polarization of the probe. The probe was designed to move vertically up to 2 meters, and the rotator is designed to rotate in the range -180° to 180°. The distance of the sampling point must be correctly calculated because it concerns with the accuracy in the evaluation of the Fourier integral. The Fourier integral requires grid spacing $\Delta\phi$ and Δz on the measurement surface to be less than or equal to π/ka and $\lambda/2$, respectively [7], where k is the wave number and a is rotator radius.

Figure 2 shows a sample of scanning grid for the distribution of the measurement locations on the surface of the cylindrical scanning area [1].

The measurement equipment is the Vector Network Analyzer (VNA), provided in the anechoic chamber, Electrical Engineering Department, Faculty of Engineering, Universitas Indonesia. At the same time, a computer as management and communication system is used to control the movement of the stepper motor. This is to obtain data from the VNA and the data transferred from the VNA to the computer. This computer will then calculate near field to far field transformation.

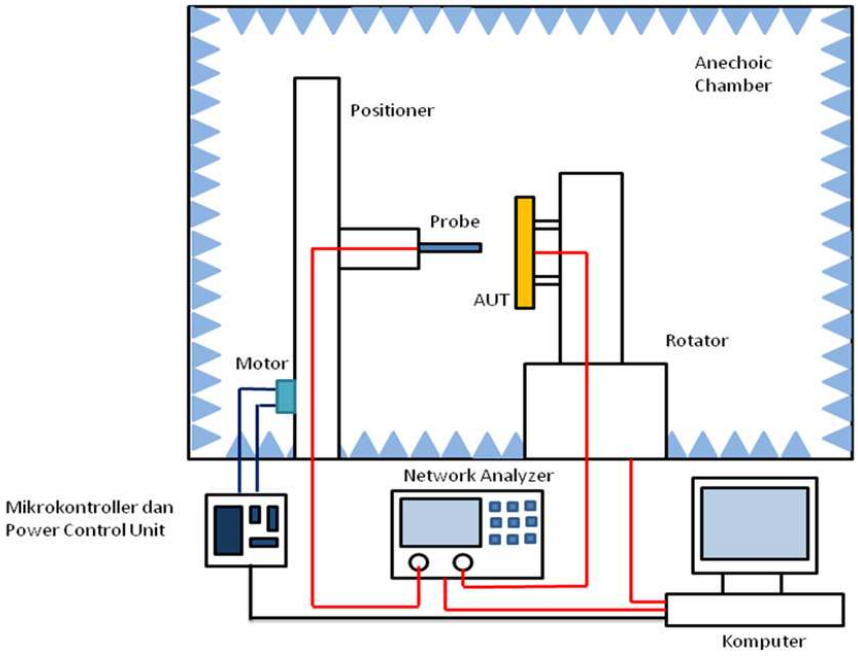

Figure 1: Near field measurement system set up.

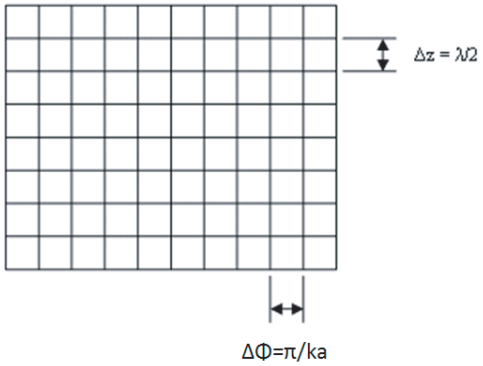

Figure 2: A sample scanning grid.

From the measurement data pattern of each measurement point, it will appear as the data is on a line with few points. Furthermore, the measured data will be obtained only in the form of $(m \times n, 1)$ matrix data, with m and n respectively are the amount of sampling points in each vertical and horizontal line. The dimensional measurement data will be arranged to the matrix of $(m \times n)$, and there has to be a procedure to convert the early data measured. The design of the system can be developed into the cylindrical measurement system by adding the rotating feature on the AUT [4]. After the design of cylindrical near field measurement is completed as implemented in Fig. 1, the process of cylindrical near field measurement can be carried out. The processes are generally divided into two parts, consists of data acquisition and data transformation. At the first stage, the process takes place on the hardware system. The main objective is to obtain data from the near field antenna under test that consists of several phases which are [5]:

1. The computer will determine the measurement position on the measurement area.
2. The probe moves into the position which was determined.
3. The measurement is done in that position and than save the measurement result.
4. Repeat step 1 until all position measured for both polarizations: horizontal and vertical.

Data transformation is used to process the near field measured data which is obtained from the previous process. The near field data is used for transformation into far field data to see the antenna

performance. These processes can be divided into two steps, they are the transformations of near field measurements to far field data and plot the results of the transformation [5].

3. RESULTS AND DISCUSSION

The measurement system, which is used, consists of a probe antenna as the transmitter and an antenna under test (AUT) as the receiver antenna. The probe antenna is a dipole antenna. In the process of near field data, it is assumed as a dipole antenna detector. While the AUT is a 2-dimensional array antenna with the dimension of 12 cm length, 4 cm width and 0.32 cm thickness. The probe antenna and the AUT are shown in Fig. 3. With this dimension, the near field range of the antennas can be calculated.

The distance between the AUT and probe antenna is set to 0.30 m. For the cylindrical surface method, if the distance between AUT and scanning area is defined for 0.30 meter, the measurement system designed can reach vertical variation for the probe in the range of -1 m to 1 m and variation of φ in the range of $-180°$ to $180°$.

Simulation results of the transformation method compared to HFSS far field simulation is displayed in Fig. 4(a) in which shows the far field radiation pattern at θ plane. The comparison exhibits very good agreement in the bore sight direction.

Moreover Fig. 4(b) shows the far field radiation pattern for far field measurement, probe compensation and no probe compensation near field measurement. The results show similarity bore sight pattern but show some discrepancies in the side lobe.

(a) (b)

Figure 3: (a) A microstrip array antenna as test antenna, (b) a dipole antenna as a probe antenna.

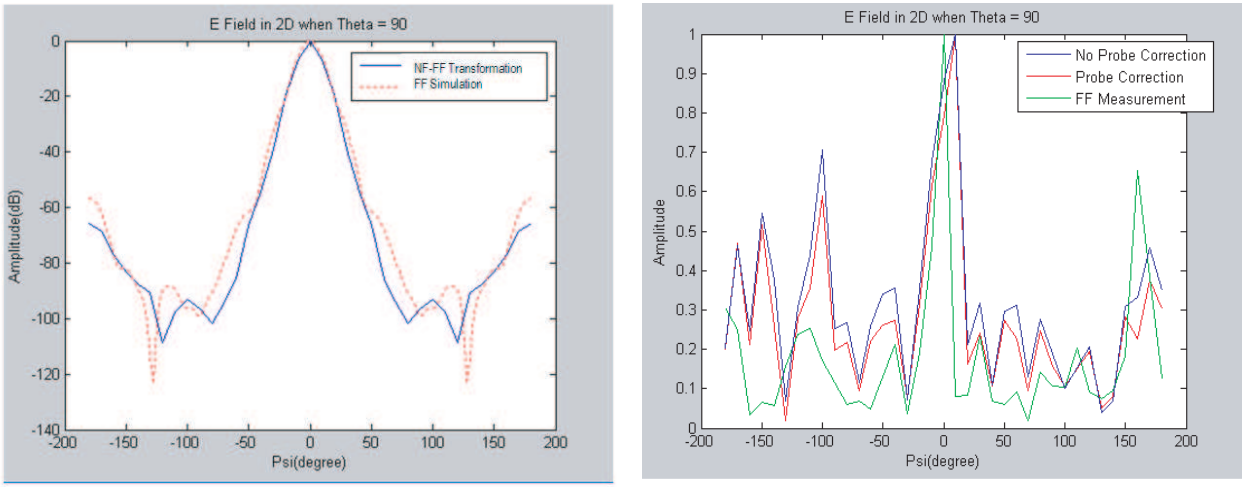

(a) (b)

Figure 4: (a) A comparison of far field radiation pattern at θ plane, (b) a comparison of far field radiation pattern and probe compensation and no probe compensation near field measurement.

4. CONCLUSIONS

The simulation of near field measurements show that the far field radiation pattern can be produced using the near field measurement data generated by HFSS in which use a dipole as probe antenna. The results have been compared and agree with the simulated far field radiation pattern. Therefore this transformation program can be used to predict the far field radiation pattern. Furthermore the proposed cylindrical near field system also confirms well between measurement and simulation results.

ACKNOWLEDGMENT

This work is partly supported by Universitas Indonesia under National Research Strategic Grant contract No. 407C/DRPM-UI/A/N1.4/2009 and RUUI Grant contract No. 2585/H2.R12/PPM.00.01 Sumber Pendanaan/2010.

REFERENCES

1. Yaghjian, A. D., "An overview of near-field antenna measurements," *IEEE Trans. Antennas Propagat.*, Vol. 34, No. 1, 30–45, 1986.
2. Joy, E. B., W. M. Leach, and G. P. Rodrigue, "Applications of probe-compensated near-field measurements," *IEEE Trans. Antennas Propagat.*, Vol. 26, No. 3, 379–389, 1978.
3. Paris, D. T., W. M. Leach, and E. B. Joy, "Basic theory of probe-compensated near-field measurements," *IEEE Trans. Antennas Propagat.*, Vol. 26, No. 3, 373–379, 1978.
4. Yan, B., S. A. Saoudy, and B. P. Sinha, "A low cost planar near-field/far-field antenna measurement system," *C-CORE*, Memorial University of Newfoundland, IEEE, 1997.
5. Slater, D. and G. Hindman, "A low cost portable near-field," Near-field System Incorporated, October 9–13, 1989.
6. Narasimhan, M. S. and M. Karthikeyan, "Evaluation of fourier transform integrals using FFT with improved accuracy and its applications," *IEEE Trans. Antennas Propagat.*, Vol. 32, No. 4, 404–408, 1984.
7. Tkadlec, I. R., *Near-field Antenna Measurements*, Dept. of Radio Electronics FEEC BUT.

A Circularly Polarized Microstrip Antenna Array with a Binomial Power Distribution

N. R. Rishani, A. Ramadan, M. Al-Husseini, K. Y. Kabalan, and A. El-Hajj
ECE Department, American University of Beirut, Beirut 1107 2020, Lebanon

Abstract— The design of a four-element circularly polarized microstrip antenna array, which is based on Binomial power distribution, is presented in this paper. For a (1-3-3-1) power distribution, the elements' coefficients are (1-1.73-1.73-1). This is the distribution of a four-element Bessel, or better called a Taylor one-parameter, array with a sidelobe level of −20 dB. The proposed printed-type array is based on a 1.6 mm-thick FR4-epoxy substrate with dimensions 200 mm × 120 mm, has a microstrip-line-formed Binomial power distribution-based feeding network using equal/unequal Wilkinson power dividers, and features four identical circularly polarized patch antenna elements. Each array element incorporates two opposite 0.65 mm-wide 90° sectoral slots to achieve circular polarization at 3 GHz. The proposed antenna array is designed and simulated using Ansoft HFSS. The computed axial ratio and peak gain of the antenna, at 3 GHz, are 2.42 dB and 5.75 dB, respectively. A prototype of the antenna is fabricated and measured. A credible analogy between measured and simulated results is attained. Compared to the Uniform-based array, the Bessel-based one's radiation pattern reveals lower side-lobes and a wider half power beam-width (HPBW) over the operating frequency band.

1. INTRODUCTION

Microstrip antennas have received increasing attention in satellite and communications applications because of their low profile, small size, light weight, low cost and ease of fabrication [1]. Their simple feed methods, especially microstrip-line and coplanar waveguide (CPW) feeds, make them compatible with wireless communication integrated circuitry. However, their narrow bandwidth and low directivity raise the need for antenna array design in order to get higher directivity and other capabilities such as beam steering or pattern adjustment. Feeding networks play a crucial role in antenna array design. In addition to guiding the current that excites the elements, its design dictates which radiation pattern the array will have. Generally speaking, a well-designed feeding network results in less reflections and low radiation over the desired frequency band. Several feeding network structures have been recently reported. A self-matching wideband feed network for microstrip arrays was presented in [2]. In [3], it was demonstrated that feed structures, which are Wilkinson power divider-based, had better return loss characteristics than a structure incorporating T-sections.

In this paper, a 3 GHz four-element circularly polarized Taylor one-parameter array is presented. The array's feed network employs equal/unequal Wilkinson power dividers to obtain a (1-3-3-1) power distribution among the elements. For comparison purposes, a uniform array of the same elements, whose feeding network is based on equal Wilkinson power dividers, is included in this paper. The computed radiation patterns, at 3 GHz, show that the proposed Taylor-one parameter array has lower side-lobe level (SLL) and wider half power beam-width (HPBW) than the uniform one.

2. DESIGN GUIDELINES

The geometrical structure of the proposed printed array antenna is depicted in Figure 1(a). The substrate, which is 1.6 mm in thickness, is based on the low-cost FR4-epoxy material with a dielectric constant $\varepsilon_r = 4.4$. The other dimensions of the substrate are 200 mm for the width and 120 mm for the height. The spacing between the elements' edges is $0.5\lambda_o$, where λ_o is the effective wavelength at 3 GHz. The design guidelines of the proposed design are presented herein.

1) The array is made up of four circularly polarized identical antenna elements, as the one shown in Figure 2. The element features a matching section, which connects the 50 Ω feed line to the circular patch. To achieve circular polarization, two opposite 0.65 mm-wide 90° sectoral slots are incorporated in the patch. The simulated return loss and axial ratio of the employed element are depicted in Figure 3.

2) As illustrated in Figure 4(a), equal/unequal Wilkinson power dividers (WPDs) are used to build up the array's feed network. An equal WPD is used to feed two identical unequal WPDs in

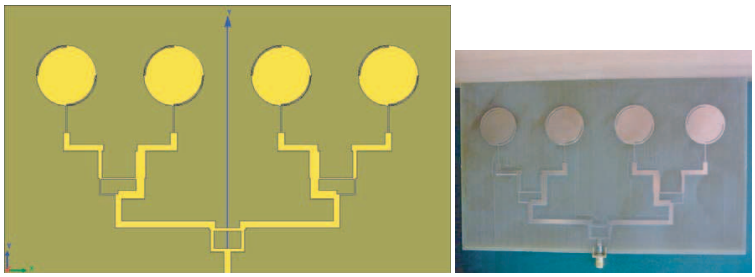

(a) (b)

Figure 1: (a) Geometry of the proposed Taylor-one parameter array, and (b) a photo of the fabricated prototype.

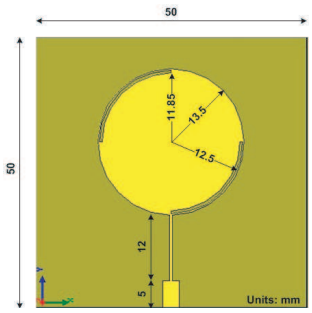

Figure 2: Geometry of the antenna element.

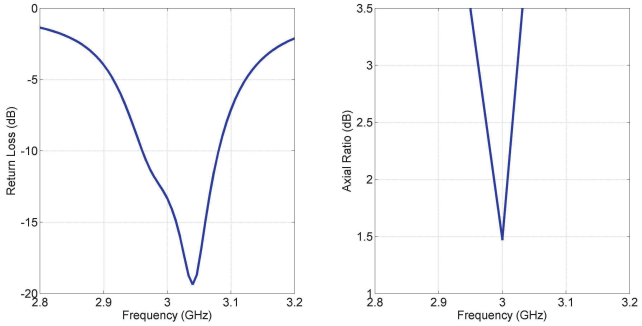

Figure 3: Simulated return loss and axial ratio of the antenna element.

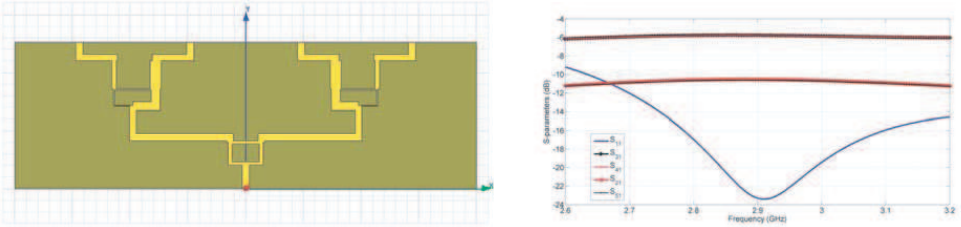

(a) (b)

Figure 4: (a) Geometry of the feeding network, and (b) its computed S-parameters.

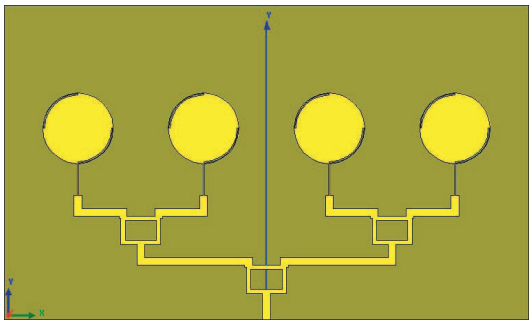

Figure 5: Geometry of the uniform array.

order to get a (1-3-3-1) Binomial power distribution at the output ports. The dimensions of the feed network are computed using [4] at 3 GHz. The S-parameters of the feeding network are shown in Figure 4(b). It's worth mentioning that a 1 : 3 power ratio is attained per each output port pair, leading to a (1-3-3-1) overall Binomial power distribution.

3) The combined outcomes of the preceding two steps build up the proposed array. However, a 3 GHz uniform array, as depicted in Figure 5, is designed and included in this paper to show that a

Taylor-one parameter-based feeding network can be implemented in microstrip-line form to control both the side-lobe level and half power beam-width of the array.

3. RESULTS AND DISCUSSION

The proposed antenna array was designed and simulated using Ansoft HFSS, which is based on the Finite-Element Method (FEM). A prototype of the antenna, shown in Figure 1(b), was fabricated and measured. A good agreement between simulated and measured return loss plots is witnessed, as illustrated in Figure 6. The axial ratio of the antenna, computed over the 2.6–3.2 GHz frequency range, is given in Figure 7 . An axial ratio of 2.42 dB is attained at 3 GHz. The peak gain of the antenna at 3 GHz is 5.75 dB. Figure 8 depicts the normalized gain patterns, in the X-Z plane, of both array configurations. Compared to the Uniform array, the Taylor-one parameter array reveals lower side-lobe level and wider half power beam-width over the frequency of operation.

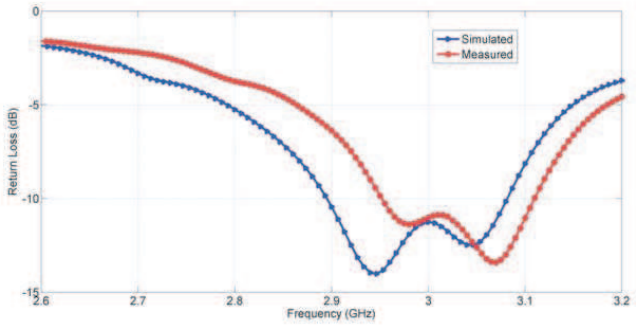

Figure 6: Return loss of the proposed array.

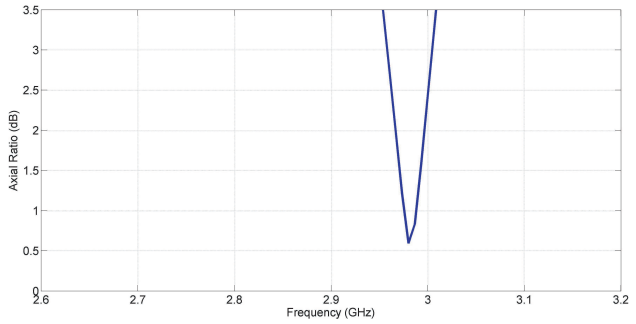

Figure 7: Axial ratio of the proposed array.

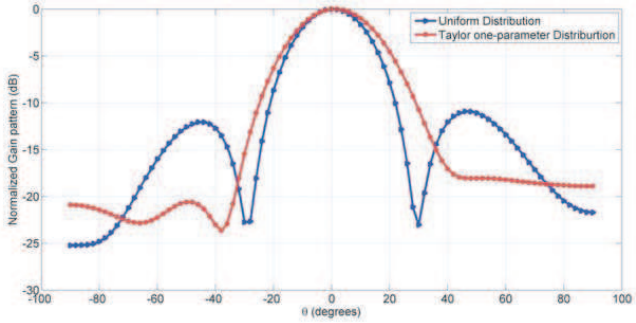

Figure 8: Normalized gain patterns of the uniform and Taylor one-parameter arrays in the X-Z plane.

4. CONCLUSION

A low-profile and easy-to-fabricate circularly polarized Taylor one-parameter array was presented in this paper. The antenna is based on a 1.6-mm-thick, 20 cm × 12 cm FR4-epoxy substrate, and incorporates circularly polarized elements. An equal/unequal Wilkinson power divider-based feeding network achieves a 1-3-3-1 binomial power distribution among the array elements. A prototype of the proposed antenna was fabricated and measured over the 2.6–3.2 GHz frequency range. A credible analogy between measured and simulated results was obtained. The proposed array has a 5.75 dB peak gain and a 2.42 dB axial ratio figures at 3 GHz. The normalized gain patterns, in the X-Z plane, were computed for both uniform and Taylor-one parameter arrays. Compared to the uniform configuration, the latter revealed lower side-lobe level and wider half power beam-width at the frequency of interest.

REFERENCES

1. Balanis, C. A., *Antenna Theory, Analysis and Design*, John Wiley & Sons, New Jersey, 2005.
2. Legay, H. and L. Shafai, "A self-matching wideband feed network for microstrip arrays," *IEEE Transactions on Antennas and Propagation*, Vol. 45, No. 4, 715–722, 1997.
3. Tarmizi, A. M., M. T. Mohd Nor, A. R. Tharek, and R. Abdolee, "Reconfigurable microstrip patch antenna array with beam shaping," *Proceedings of The Second European Conference on Antennas and Propagation*, 1–5, Edinburgh, UK, November 2007.
4. Pozar, D. M., *Microwave Engineering*, John Wiley & Sons, 2005.

Performance Characteristics of a Dual-sense Helical-beam Antenna

S. A. Adekola[1, 2], **A. Ike Mowete**[1], **and A. A. Ayorinde**[1]

[1]Department of Electrical and Electronics Engineering, Faculty of Engineering
University of Lagos, Lagos, Nigeria
[2]Department of Electrical and Electronics Engineering, Niger Delta University
Wilberforce Island, Yenegoa, Nigeria

Abstract— Several years ago, Coleman and Wright [1], experimentally demonstrated the feasibility of exciting a dual-sense circularly polarized field, using a single-element helical antenna. The results obtained and described by [1] suggest that good on-axis axial ratios then become available, and that the off-axis axial ratios may be rated 'reasonable'. It was discovered [1], in particular, that the off-axis axial ratio for the added port of the antenna's feed arrangement was significantly worse on account of an imbalance in the feed as well as currents excited along the axially located outer coaxial conductor.

This paper, using a moment-method analytical approach earlier developed for elliptical cylindrical thin-wire helical antenna [2], investigates the possibility of improving off-axis ratios for the dual-sense helical antenna through an informed location of the added port and choice of amplitude and relative phase of feed point excitation voltage. Computational results obtained suggest that both choice of location and magnitude and relative phase of feed point excitation voltage can lead to significant improvements in both on-axis and off-axis axial ratios for the dual-sense helical antenna. In addition to offering possibilities for compensating for the imbalance in the feed and effects of currents excited in the outer coaxial conductor alluded to in [1], the proposals described in this paper indicate such other antenna parameters as polarization sense of radiated field, of interest to optimum energy transfer can be controlled through the use of the dual-feed arrangement of the type proposed in [1].

1. INTRODUCTION

For the axial-mode helical antenna situated above a ground plane and fed from the end closest to the ground plane, the radiated field is circularly polarized [5]. Several other methods of feeding the helical beam antenna, have been developed since its introduction by Kraus in 1947, and most of these feed arrangements involve feeding the antenna at one point only; at either ends, or at its geometrical center [3, 4]. A few years ago, Coleman and Wright [1], suggested that when the axial-mode helical antenna is fed from the end remotely located from the ground plane, the radiated field should have a circular polarization of sense opposite to that of the conventionally fed axial-mode antenna. And based on that observation [1] experimentally explored the feasibility of designing a dual (polarization) sense or orthogonal mode helical antenna through the incorporation of an additional port. They modified an existing helicone antenna to experimentally demonstrate the possibility, in practice, of such an antenna, and obtained measurement data that indicated that the so-modified antenna's performance is promising. The experiment results described in [1], however suggested that off-axis axial ratio's performance was poor for the orthogonal mode antenna; and although the authors suggested that this performance index could be improved by correcting an imbalance in feed and excitation currents, they did not qualify or quantify the nature of this predicted improvement. It is, in that connection, the main objective of this paper, to investigate how feed location and excitation specification for the added port of the orthogonal-mode helical antenna, affects off-axis and on-axis axial ratio. Computational results obtained from a modification of a compact theory earlier proposed [2], reveals that of-axis axial ratio performance can indeed be improved through an informed choice of feed location and specification of excitation voltage, in magnitude and relative phase.

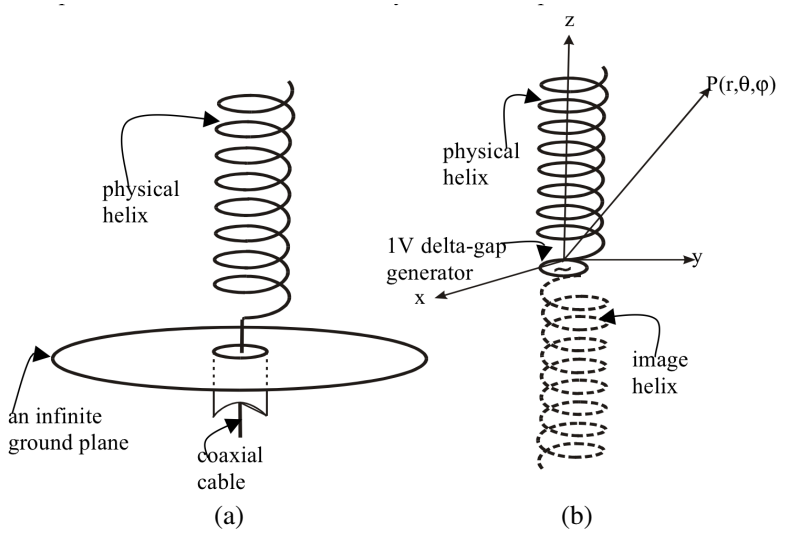

Figure 1: Physical model. (a) Axial-mode helix mounted on a large ground plane. (b) Image theory model.

2. THEORY

For the physical antenna model displayed in Figure 1, it has been shown elsewhere [2], that the radiation fields may be described by the integral expressions given as

$$E_\theta(\theta,0^\circ) = \frac{-j\omega\mu_o a e^{-jk_o r}}{4\pi r}\int_0^{2\pi N} I^p(\phi')[-\cos\theta\sin\phi' - \sin\theta\tan\alpha]e^{jk_o a\zeta\sin\theta}d\phi' + \frac{-j\omega\mu_o a e^{-jk_o r}}{4\pi r}\int_0^{-2\pi N} I^k(\phi')\,[-\cos\theta\sin\phi' - \sin\theta\tan\alpha]e^{jk_o a\zeta\sin\theta}d\phi', \quad (1a)$$

and

$$E_\phi(\theta,0^\circ) = \frac{-j\omega\mu_o a e^{-jk_o r}}{4\pi r}\left\{\int_0^{2\pi N} I^p\left(\phi'\right)\cos\left(\phi'\right)e^{jk_o a\sin\theta(\cos(\phi')+(\tan\alpha\cot\theta)\phi')}d\phi' + \int_0^{-2\pi N} I^k\left(\phi'\right)\left(-\cos\left(\phi'\right)\,e^{jk_o a\sin\theta(\cos(\phi')-(\tan\alpha\cot\theta)\phi')}d\phi'\right)\right\}, \quad (1b)$$

provided that $\zeta = \cos\varphi' + (\tan\alpha\cot\theta)\varphi'$, and that the symbols ($a$, α, N) stand for the helix radius, pitch angle and number of helix turns, respectively, with all other symbols assuming their conventional meanings.

On-axis components of the radiated field are specified by the choice of $\vartheta = 0$ in (1a) and (1b), whilst non-zero values of θ in the same expressions give the off-axis radiated field components. As explained in [2], numerical values for the radiated fields are readily obtained through a method-of-moments solution, and with the availability of numerical values, axial ratio of the radiated fields (E_θ, E_φ) both on- and off-axis, can be computed. When, for the general case, it may not be assumed that E_θ and E_φ are in time-phase quadrature, axial ratio (AR) is given by the following expression [7]:

$$AR(dB) = 10\log_{10}\left[\frac{|E_\theta|^2 + |E_\phi|^2 + \left[|E_\theta|^4 + |E_\phi|^4 + 2|E_\theta|^2|E_\phi|^2\cos(2\delta)\right]^{1/2}}{|E_\theta|^2 + |E_\phi|^2 - \left[|E_\theta|^4 + |E_\phi|^4 + 2|E_\theta|^2|E_\phi|^2\cos(2\delta)\right]^{1/2}}\right], \quad (1c)$$

in which δ denotes the time-phase difference between the field components.

3. RESULTS AND DISCUSSIONS

As earlier remarked, the dual-sense helical antenna is obtained by adding a second feed point to the conventional helix, already excited at the end close to the ground plane. Our interest in this presentation is to explore the influence of choice of added the port's location and excitation (magnitude and relative phase) on both the on-axis as well as the off-axis axial ratio performance. And to that end, three port locations and three excitation models (delta-gap feed voltages) of the added port were considered as follows:

Added port locations

(i) open end of the helix;
(ii) geometrical centre of the helix;
(ii) beginning of the seventh turn of the helix;

Excitation arrangement

(i) in-phase, same magnitude;
(ii) in-phase half magnitude;
(iii) $-90°$ out-of-phase, half magnitude;

with a delta-gap model of gap voltage 1 V utilized for the feed at end close to the ground plane.

Figure 2(a) displays the AR profiles of the dual-sense helix when the added port is located at the open end of the helix, and for the different feed models listed in the foregoing.

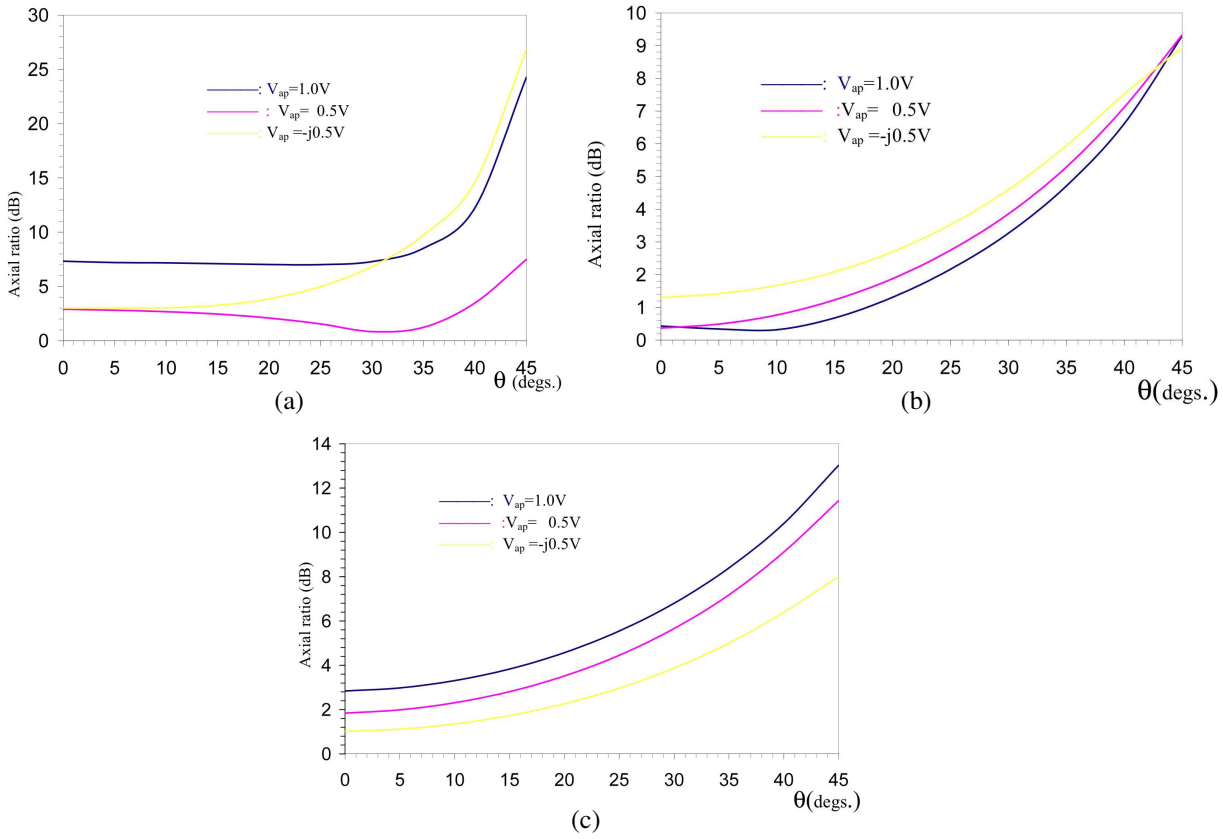

Figure 2: (a) Variations of the axial ratio as a function of the elevation angle (θ) when the added port is at the open end with feed arrangement modeled by the gap voltages $V_{ap} = 1.0\,\text{V}$, $0.5\,\text{V}$ and $-j0.5\,\text{V}$. (b) Variations of the axial ratio as a function of the elevation angle (θ) when the added port is at the geometrical center with feed arrangement modeled by the gap voltages $V_{ap} = 1.0\,\text{V}$, $0.5\,\text{V}$ and $-j0.5\,\text{V}$. (c) Variations of the axial ratio as a function of the elevation angle (θ) when the added port is at the beginning of the 7th turn with feed arrangement modeled by the gap voltages $V_{ap} = 1.0\,\text{V}$, $0.5\,\text{V}$ and $-j0.5\,\text{V}$.

On the basis of the '3 dB condition', the dual-sense helices with added port voltages of 1 V and $-j0.5$ V have unsatisfactory values of axial ratio. However, when a feed voltage of 0.5 V is employed, the performance is much better.

Computational results generated for the case when the added port is at the geometrical centre of the helix are displayed in Figure 2(b). And it is Interesting to observe that for all the three feed models specified, the dual-sense helical antenna appears to have satisfactory on-axis AR as well as off-axis AR over a reasonable range of the elevation angle θ ($0^\circ \leq \theta \leq 25^\circ$).

The variations of the axial ratio when the added port is located at the beginning of the seventh turn of the helix are graphically illustrated in Figure 2(c). Again, if the design goal is the 3 dB axial ratio, the dual-sense helix with added port voltage of $-j0.5$ V appears to be the most promising in comparison with the dual-sense helix of added port voltages of 1.0 V and 0.5 V. We may therefore conclude that off-axis axial ratio performance can be controlled through an informed choice of excitation location and/or relative magnitude and phase, for the added port of the orthogonal-mode helix.

4. CONLUSIONS

We have in this presentation, investigated a proposal earlier suggested by Coleman and Wright that the performance of a dual sense (orthogonal mode) helical antenna, assessed in terms of the on- and off-axis axial ratios, can be improved through the correction of an inherent imbalance in the feeding arrangement. Computational results obtained from a method of moments' implementation of a model developed for the antenna indicate that choice of feed location and relative magnitude and phase of excitation for the added port has significant influence on the values of axial ratio.

REFERENCES

1. Coleman, H. P. and B. D. Wright, "An orthogonal mode (dual-sense) helical antenna," *IEEE Transactions on Antennas and Propagation*, Vol. 32, No. 4, 414–415, April 1984.
2. Adekola, S. A., A. I. Mowete, and A. A. Ayorinde, "Compact theory of the broadband elliptical helical antenna," *European Journal of Scientific Research*, Vol. 31, No. 3, 446–490, 2009.
3. Nakano, H., Y. Samada, and J. Yamauchi, "Axial mode helical antennas," *IEEE Trans. Ant. & Prop.*, Vol. 34, No. 9, 1143–1148, 1986.
4. Kraus, J. D., *Antennas*, 2nd Edition, 1–85, 265–339, 388–408, McGraw-Hill, Inc., USA, 1988.
5. Kraus, J. D., "Helical beam antenna," *Electronics*, Vol. 20, 109–111, April 1947.

Analytical Prediction of Feed Efficiency in Offset Gregorian Reflector Antennas with Non Planar Log-periodic Type Feeds

D. I. L. de Villiers
University of Stellenbosch, South Africa

Abstract— Non-planar log-periodic antennas are finding increasing application in wide band reflector antenna systems due to their excellent wide band performance in terms of input impedance and pattern stability. However, the frequency dependent phase center position will cause defocussing and therefore a loss in aperture efficiency when they are used in a wide band reflector antenna system. A popular reflector system in high performance systems, such as radio telescopes, is the offset Gregorian reflector antenna due to the high levels of efficiency that can be obtained by eliminating feed or subreflector blockage from the system. Unfortunately, subreflector edge diffraction effects still cause a loss in efficiency, and these should be included to obtain accurate performance predictions. This paper presents a technique to get an initial estimate of the performance of an offset Gregorian reflector antenna fed by a non planar log-periodic antenna by using closed form expressions and simple one dimensional integration of analytical functions. An analytical function is used to approximate the radiation pattern of the feed antenna, and this approximated pattern is used to calculate the efficiency of the reflector antenna system. The frequency dependent phase center position of the feed antenna as well as subreflector edge diffraction is included in the calculations. The results compare favorably with physical optics simulations of the structure, and some simple design guidelines are derived.

1. INTRODUCTION

The offset Gregorian dish configuration is an attractive option for modern multiple-dish radio telescopes because of the clear aperture it provides and the corresponding decrease in blockage losses. Such a configuration is already employed in the Allen Telescope Array (ATA) [1], and is strongly considered for the Square Kilometer Array (SKA) [2] and one of its precursors the Karoo Array Telescope (meerKAT) [3]. These telescopes are all required to operate over large bandwidths, typically in excess of several octaves, and therefore require feeds with stable wide band performance. A possible feed for such applications is a non-planar log-periodic (NPLP) feed, such as the one used in the ATA [1, 4]. Several variations of this type of feed have been reported for use in large reflectors, including a pyramidal arrangement of log-periodic dipole arrays [5] and the log-periodic zigzag antenna [6, 7].

A major drawback of NPLP antennas is the frequency dependent phase center position. This causes defocussing of the feed and a corresponding loss in gain performance, the extent of which is well known for symmetrical paraboloidal reflectors [8]. A similar effect will be present in offset Gregorian antennas, and some calculations of defocussing loss of such a system is reported in [9]. This loss must be taken into account when designing a reflector system for optimum performance.

In this paper, a technique is presented to predict the performance of an offset Gregorian reflector fed by a NPLP antenna using closed form expressions and simple one dimensional integration of analytical functions. By approximating the radiation pattern of the feed by an appropriate analytical function, and using the equivalent paraboloid of the offset Gregorian reflector [10], an approximation of the gain of the reflector system can be found from the equivalent aperture fields which includes defocussing and subreflector diffraction losses. This method closely follows and expands on the method in [11], which describes a similar technique for calculation of symmetrical paraboloidal reflector gain. Some simple design rules are derived from the results which can aid the antenna designer in finding a first order design solution for offset Gregorian reflector fed by NPLP antennas.

2. FEED MODEL

It is customary to approximate the radiation pattern of reflector antenna feeds by a $\cos^n(\theta)$ family of functions, since these functions provide closed form solutions to the efficiency integrals which arise from the analysis of a paraboloidal reflector [12]. It is shown in [11] that the radiation pattern of a NPLP antenna is approximated very well by such a pattern, with the power n being related to the spreading angle of the antenna. A wider spreading angle will provide a wider beam with

corresponding lower n. Also, an antenna with a wider spreading angle will be shorter than the same antenna with a narrow spreading angle, and will therefore have less variation in the phase centre position. A sketch of a typical zigzag NPLP antenna is shown in Figs. 1(a) and 1(b), where an axially symmetric pattern is obtained if $\gamma \approx 2\alpha$. Fig. 1(c) shows a graph of the predicted n value in the feed function

$$G_f(\theta) = \begin{cases} 2(n+1)\cos^n\theta & 0 <= \theta <= \pi/2 \\ 0 & \pi/2 < \theta <= \pi \end{cases}, \tag{1}$$

which best fits the radiation pattern of an antenna with a specific spreading angle α.

3. EFFICIENCY CALCULATIONS

To find the approximate gain of an offset Gregorian antenna fed by a source with a theoretical radiation pattern given by (1), the total efficiency of the reflector and feed system must be calculated. This total efficiency, for a paraboloidal reflector, can be subdivided into several sub-efficiencies as described in [12, 13]. In the case of an idealized, perfectly rotationally symmetric, linearly polarized, and axially displaced feed, the only efficiencies that must be considered are the illumination efficiency η_t, the spillover efficiency η_s, and the phase efficiency η_ϕ. Since an offset Gregorian reflector system can be described by an equivalent paraboloid [10], the efficiency of the offset Gregorian system can be calculated in a similar manner to that of a paraboloidal reflector. To include the effects of diffraction from the edge of the subreflector, a diffraction efficiency factor η_d will be included in the total efficiency.

3.1. Equivalent Paraboloid Efficiencies

A typical offset Gregorian configuration, with definitions of the variables used to describe it is shown in Fig. 2. To minimize cross polarization most offset Gregorian reflectors will be designed to satisfy the Mizugutch condition [14]

$$\tan a = \frac{|e^2-1|\sin\beta}{(1+e^2)\cos\beta - 2e}, \tag{2}$$

with e the eccentricity of the ellipsoid. When (2) is enforced on the geometry it turns out that the angle a is also the axis of the equivalent paraboloid, which can be made axially symmetric in order to minimize spillover losses by ensuring [10]

$$\tan\frac{\beta}{2} = \left(\frac{e-1}{e+1}\right)^2 \tan\left(\frac{\beta-\theta_0}{2}\right). \tag{3}$$

The illumination efficiency and the spillover efficiency in a paraboloidal reflector system is often combined to give what is termed the aperture efficiency as $\eta_{ap} = \eta_t\eta_s$. For a feed pattern described by (1), this aperture efficiency is given by [12]

$$\eta_{ap} = \cot^2\left(\frac{\theta_e}{2}\right)\left|\int_0^{\theta_e}\sqrt{G_f(\theta)}\tan\left(\frac{\theta}{2}\right)d\theta\right|^2, \tag{4}$$

with θ_e the subtended half angle of the equivalent paraboloid when (2) and (3) are satisfied. The integral in (4) has closed form solutions for all n.

If the antenna shown in Fig. 1 is assumed to radiate from the region where the elements are approximately a half wavelength long, as with standard log-periodic antennas, and it is placed such that the phase center displacement is equal at the high and low end of the operating frequency band, it can be shown that the phase efficiency is given by [11]

$$\eta_\phi = \frac{\left|\int_0^{\theta_e}\sqrt{G_f(\theta)}e^{-j\Phi(\theta,f)}\tan\left(\frac{\theta}{2}\right)d\theta\right|^2}{\left[\int_0^{\theta_e}\left|\sqrt{G_f(\theta)}e^{-j\Phi(\theta,f)}\right|\tan\left(\frac{\theta}{2}\right)d\theta\right]^2}, \tag{5}$$

with

$$\Phi(\theta,f) = \frac{2\pi}{\lambda}\rho(\theta)\left(\sqrt{1+\frac{\delta(f)}{\rho(\theta)}\left[\frac{\delta(f)}{\rho(\theta)}+2\cos\theta\right]}-1\right), \tag{6}$$

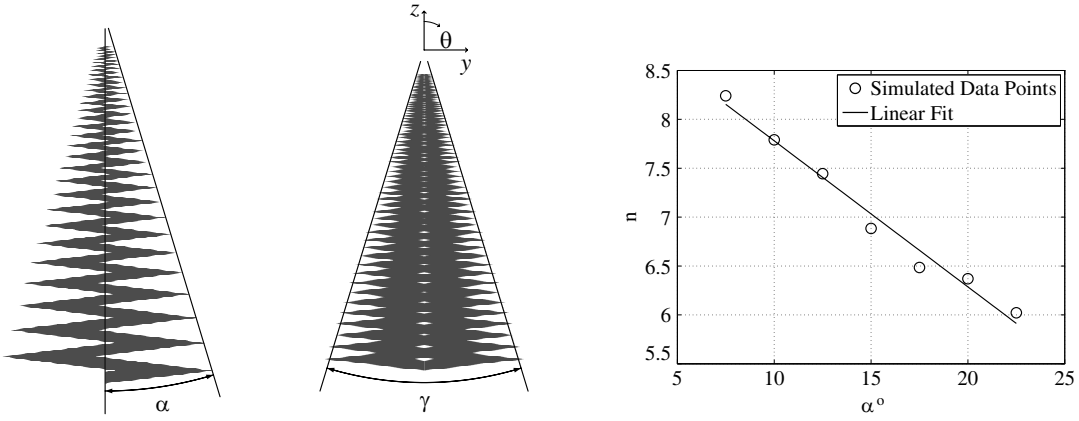

(a) (b) (c)

Figure 1: Geometry and radiation characteristics of a pyramidal zigzag antenna showing (a) one arm and the spreading angle of the antenna, (b) the full pyramidal configuration placed with the projected apex at the origin of the coordinate system, and (c) the simulated and approximated $n - \alpha$ relationship of the antenna. (From [11]).

and

$$\rho(\theta) = \left(\frac{2F}{1+\cos\theta}\right)\left(\frac{|e^2-1|}{(e^2+1)-2e\cos\beta}\right). \tag{7}$$

The displacement factor, $\delta(f)$, is calculated as

$$\delta(f) = \frac{\cos\alpha}{\tan\alpha}\frac{c}{4f}\left(1-\frac{2f}{f_l+f_h}\right), \tag{8}$$

where c is the speed of light, and f_l and f_h respectively correspond to the lowest and highest frequency of operation. The integral in the numerator of (5) proceeds rapidly and accurately by the trapezoidal approximation.

3.2. Subreflector Diffraction Efficiency

Diffraction from the subreflector edge has a detrimental effect on the gain of the reflector system. This effect has been studied by many workers and an elegant description in terms of a subreflector diffraction efficiency η_d has been suggested in [15, 16], where it is shown that the diffraction efficiency of a symmetrical multi-reflector system can be predicted by a single wavelength dependent parameter, namely, the lateral extent of the transition region $\Delta\rho$. The results found for the symmetrical case are also valid in the symmetry plane of the offset antenna, and for a system such as the one in Fig. 2, $\Delta\rho$ can be calculated in the symmetry plane as

$$\Delta\rho = \sqrt{\frac{\lambda(\rho_m+\rho_s)}{\pi}\left|1-\frac{\rho_m+\rho_s}{\rho_s}\right|}. \tag{9}$$

If the subreflector reflection boundary lies on the main reflector edge, and a feed model of the form in (1) is used, the diffraction efficiency of the system can be approximated as (from Eq. (34) in [16])

$$\eta_d \approx \left|1+\frac{\sqrt{2(n+1)\cos^n\theta_e}\sin\theta_e(j-1)\Delta\rho_0}{\sqrt{2\pi\eta_{ap}}D}\right|^2, \tag{10}$$

with $\Delta\rho_0$ taken as $\Delta\rho$ when evaluated at θ_0 to provide an average value between the extremes at θ_L and θ_U.

4. RESULTS

Some results found for a system with $D = 250\lambda_0$, $D_m = 225\lambda_0$, $D_s = 75\lambda_0$ and $d_c = 0$, with λ_0 the midband wavelength, are shown in Fig. 3.

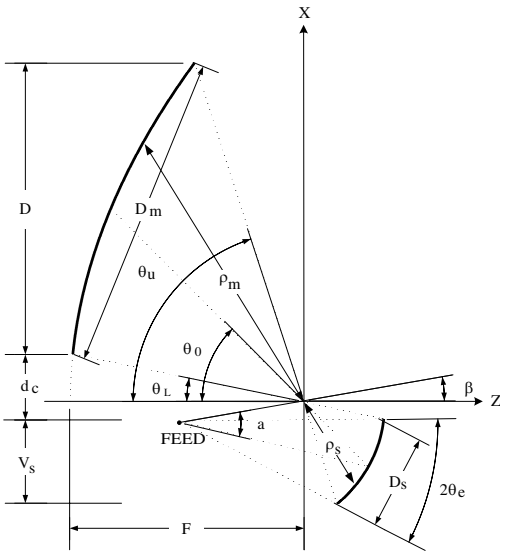

Figure 2: Offset Gregorian geometry.

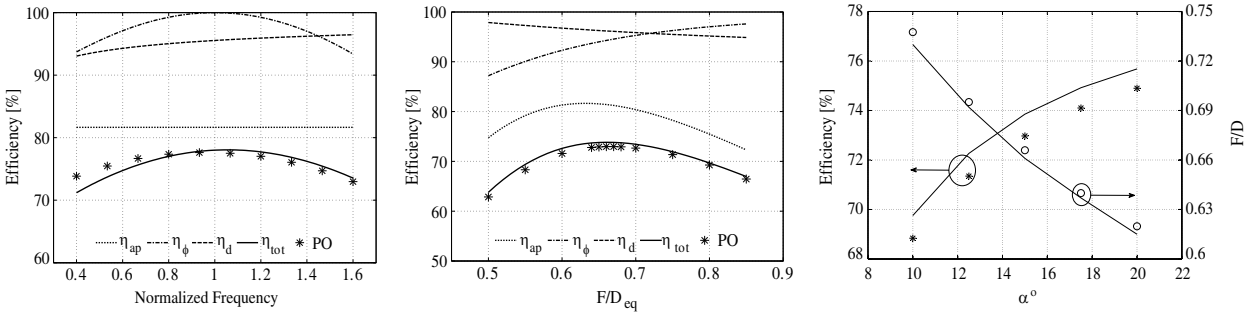

Figure 3: Calculated results showing the effect of various parameters on the different efficiencies. The markers show some physical optics simulated results, and the lines the analytically predicted results. (a) The equivalent paraboloid $F/D = 0.66$, and $\alpha = 15°$ which corresponds to $n \approx 7.0$. (b) The feed angle is $\alpha = 15°$, with the normalized frequency 1.6. (c) The maximum obtainable efficiency, as well as the equivalent F/D-ratio where it is achieved is shown at a normalized frequency of 1.6.

Figure 3(a) shows the frequency dependence of the efficiencies for a 1 : 4 bandwidth. Good agreement between the physical optics (PO) and predicted results is seen at the higher frequencies, with some deviation noticed at the lower end of the band due to secondary effects such as the effect of defocussing on aperture efficiency being ignored in the predictions.

The familiar result that a maximum efficiency for a certain feed taper is only achieved at a single equivalent F/D-ratio is confirmed in Fig. 3(b). Here the equivalent F/D which provides the maximum efficiency is seen to be higher than that expected for the equivalent focus-fed paraboloid (which is just the η_{ap} result) due to the effects of defocussing and diffraction. This provides a useful design guideline which requires a higher equivalent F/D ratio to be used for defocussed offset Gregorians than would have been used for the equivalent focussed paraboloid to obtain maximum efficiency (A similar result is also found in [11] for defocussed paraboloids). Since the F/D dependence of the efficiency is rather flat around the maximum, this increased F/D-ratio, to achieve a high band-edge efficiency, should not affect the midband (focussed) efficiency much. PO results show good agreement with the predictions.

A calculation of the maximum obtainable band-edge efficiency, and the equivalent F/D-ratio where it is achieved, is shown in Fig. 3(c) for several feed antenna spreading angles at a normalized frequency of 1.6. Good agreement is again seen between the PO and predicted results, where the upward trend of the maximum efficiency with increasing α is of special significance. A final design guideline can be deduced from this result which states that: Maximum band-edge efficiency can be obtained by using the feed with the widest spreading angle available, which still performs adequately in terms of secondary effects such as cross-polarization, impedance match, side lobe levels, etc. A similar result is reported in [11] for symmetrical paraboloidal reflectors, where shorter antennas

also provide better band-edge efficiency even though they must be placed closer to the reflector (smaller F/D) than their longer (smaller α) counterparts to still illuminate the dish optimally.

5. CONCLUSION

A simple method, including defocussing and diffraction effects, has been presented to predict the efficiency of offset Gregorian reflector antenna systems. The predictions agree very well with PO simulations of the structure, and are much faster to compute since they only require analytical function evaluations and a one dimensional numerical integral in the solution. Parameter sweeps were performed to provide some design guidelines for offset Gregorian antenna systems fed by a wideband feed with a frequency dependent phase center.

ACKNOWLEDGMENT

This work was supported financially in part by the South African SKA project and EMSS Antennas in Stellenbosch, South Africa.

REFERENCES

1. Welch, J., et al., "The Allen telescope array: The first widefield, panchromatic, snapshot radio camera for radio astronomy and SETI," *Proceedings of the IEEE*, Vol. 97, No. 8, 1438–1447, Aug. 2009.
2. Dewdney, P. E., P. J. Hall, R. T. Schilizzi, and T. J. L. W. Lazio, "The square kilometer array," *Proceedings of the IEEE*, Vol. 97, No. 8, 1482–1496, Aug. 2009.
3. Jonas, J. L., "MeerKAT — The South African array with composite dishes and wide-band single pixel feeds," *Proceedings of the IEEE*, Vol. 97, No. 8, 1522–1530, Aug. 2009.
4. Engargiola, G., "Non-planar log-periodic antenna feed for integration with a cryogenic microwave amplifier," *IEEE Antennas and Propagation Soc. Int. Symp.*, 2002.
5. Dubrovka, F. F., M. M. Lytvyn, S. M. Lytvyn, S. Y. Marttynyuk, Y. V. Ryabkin, and O. O. Vtorov, "Ultrawideband log-periodic dipole arrays for the frequency range 0.7–12 GHz," *Fifth International Conference on Antenna Theory and Techniques*, 110–115, Kyiv, Ukraine, May 2005.
6. Balanis, C. A., *Modern Antenna Handbook*, Ch. 18, 906, Wiley, 2008.
7. Lippincott, W. L., "Design of a broadband zig-zag pyramidal log-periodic antenna," *Antennas and Propagation Soc. Int. Symp.*, 2009.
8. Ingerson, P. G. and W. V. T. Rusch, "Radiation from a paraboloid with an axially defocused feed," *IEEE Trans. Antennas Propag.*, Vol. 21, No. 1, 104–106, 1973.
9. Ericsson, D., P. S. Kildal, and S. Weinreb, "Study of efficiencies and phase centers of broadband log-periodic feeds for large offset dual-reflector antennas using formulas for bodies of revolution (BOR_1 extraction)," *Antennas and Propagation Soc. Int. Symp.*, Vol. 1, 241–244, 2003.
10. Rusch, W. V. T., Y. Rahmat-Samii, and R. A. Shore, "Derivation and application of the equivalent paraboloid for classical offset cassegrain and gregorian antennas," *IEEE Trans. Antennas Propag.*, Vol. 38, No. 8, 1141–1149, Aug. 1990.
11. De Villiers, D. I. L., "Analytical prediction of the feed efficiency in symmetrical paraboloidal reflector antennas with non planar log-periodic type feeds," submitted for publication.
12. Balanis, C. A., *Antenna Theory: Analysis and Design*, 3rd Edition, Ch. 15, 893–915, Wiley, 2005.
13. Collin, R. E., "Aperture effeciency of paraboloidal reflectors," *IEEE Trans. Antennas Propagat.*, Vol. 32, No. 9, 997–1000, Sep. 1984.
14. Mizugutch, Y., M. Akagawa, and H. Yokoi, "Offset dual reflector antennas," *IEEE Antennas Propag. Soc. Symp. Dig.*, 2–5, Amherst, MA, Oct. 1976.
15. Kildal, P.-S. and K. J. Stamnes, "Asymptotic transition region theory for edge diffraction, Part I: Tracing transition regions via reflectors," *IEEE Trans. Antennas Propag.*, Vol. 38, No. 9, 1350–1358, Sep. 1990.
16. "Asymptotic transition region theory for edge diffraction, Part II: Calculation of diffraction losses in multireflector antennas," *IEEE Trans. Antennas Propag.*, Vol. 38, No. 9, 1359–1365, Sep. 1990.

Study of Microstrip Patch Resonator Printed on Anisotropic Substrate Characterized by Permittivity and Permeability Tensors

S. Benkouda and T. Fortaki
Electronics Department, University of Batna, Algeria

Abstract— In this paper Galerkin's method in the vector Fourier transform domain is used for computing the resonant frequencies of rectangular microstrip patch resonators printed on anisotropic substrates. The anisotropic substrates are characterized by both permittivity and permeability tensors. Using a matrix representation of the anisotropic layer, the dyadic green's function of the problem is efficiently determined in the vector Fourier transform domain. The effects of the permittivity and permeability variations on the operating frequency are investigated. Both variations in the permittivity as well as in the permeability perpendicular to the optical axis of the dielectric and along this axis are considered.

1. INTRODUCTION

Some dielectric substances exhibit anisotropy due to their natural crystal structures or as the result of their production processes [1]. Isotropic substances may also exhibit anisotropy at high frequencies. In the design of microwave integrated circuit components and microstrip patch antennas, anisotropic substances have been increasingly popular. Especially the effects of uniaxial type anisotropy have been investigated [1–6] due to availability of this type of substances such as Sapphire, Magnesium fluoride and Epsilam-10. In the previous studies the uniaxially anistropic substrates considered are nonmagnetic. In this paper, we extend the theoretical analysis presented in [3] to investigate microstrip patch resonators printed on anisotropic substrates, which are characterized by both permittivity and permeability tensors. The paper is organized as follows. In Section 2, using a matrix representation of the dielectric anisotropic layer, a new approach to derive the dyadic Green's function of the problem is proposed. Although a single-layer microstrip antenna is considered in this paper, we show that it is quite straightforward to extend the analysis presented to structures involving stratified substrates, which are characterized by both permittivity and permeability tensors. In Section 3, the validity of the solution is tested by comparing the computed results with previously published data. The effects of the permittivity and permeability variations on the operating frequency are also investigated in Section 3. Both variations in the permittivity as well as in the permeability perpendicular to the optical axis of the dielectric and along this axis are considered. Finally, concluding remarks are summarized in Section 4.

2. THEORY

The geometry under consideration is illustrated in Fig. 1. A rectangular microstrip patch with dimension (a, b) along the two axes (x, y), respectively, is printed on a grounded dielectric slab of thickness d. The metallic patch is assumed to be perfect electric conductor of neglecting thickness. The ambient medium is air with constitutive parameters ε_0 and μ_0. The anisotropic substrate layer

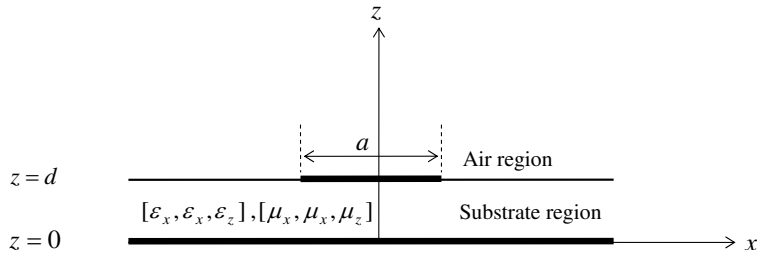

Figure 1: Geometrical structure of a rectangular microstrip patch printed on a uniaxial anisotropic substrate characterized by permittivity and permeability tensors.

is characterized by a permittivity and permeability tensors of the form

$$\bar{\varepsilon} = \varepsilon_0 \begin{bmatrix} \varepsilon_x & 0 & 0 \\ 0 & \varepsilon_x & 0 \\ 0 & 0 & \varepsilon_z \end{bmatrix} \tag{1}$$

$$\bar{\mu} = \varepsilon_0 \begin{bmatrix} \mu_x & 0 & 0 \\ 0 & \mu_x & 0 \\ 0 & 0 & \mu_z \end{bmatrix} \tag{2}$$

The transverse fields inside the uniaxial anisotropic region ($0 < z < d$) can be obtained via the inverse vector Fourier transforms as

$$\mathbf{E}(\mathbf{r}_s, z) = \begin{bmatrix} E_x(\mathbf{r}_s, z) \\ E_y(\mathbf{r}_s, z) \end{bmatrix} = \frac{1}{4\pi^2} \int_{-\infty}^{+\infty} \int_{-\infty}^{+\infty} \bar{\mathbf{F}}(\mathbf{k}_s, \mathbf{r}_s) \cdot \mathbf{e}(\mathbf{k}_s, z) dk_x dk_y \tag{3}$$

$$\mathbf{H}(\mathbf{r}_s, z) = \begin{bmatrix} H_y(\mathbf{r}_s, z) \\ -H_x(\mathbf{r}_s, z) \end{bmatrix} = \frac{1}{4\pi^2} \int_{-\infty}^{+\infty} \int_{-\infty}^{+\infty} \bar{\mathbf{F}}(\mathbf{k}_s, \mathbf{r}_s) \cdot \mathbf{h}(\mathbf{k}_s, z) dk_x dk_y \tag{4}$$

where

$$\bar{\mathbf{F}}(\mathbf{k}_s,\ \mathbf{r}_s) = \frac{1}{k_s} \begin{bmatrix} k_x & k_y \\ k_y & -k_x \end{bmatrix} e^{\mathrm{i}\mathbf{k}_s \cdot \mathbf{r}_s},\ \mathbf{r}_s = \hat{\mathbf{x}}x + \hat{\mathbf{y}}y,\ \mathbf{k}_s = \hat{\mathbf{x}}k_x + \hat{\mathbf{y}}k_y, k_s = |\mathbf{k}_s| \tag{5}$$

$$\mathbf{e}(\mathbf{k}_s, z) = e^{-\mathrm{i}\bar{\mathbf{k}}_z z} \cdot \mathbf{A}(\mathbf{k}_s) + e^{\mathrm{i}\bar{\mathbf{k}}_z z} \cdot \mathbf{B}(\mathbf{k}_s) \tag{6}$$

$$\mathbf{h}(\mathbf{k}_s, z) = \bar{\mathbf{g}}(\mathbf{k}_s) \cdot \left[e^{-\mathrm{i}\bar{\mathbf{k}}_z z} \cdot \mathbf{A}(\mathbf{k}_s) - e^{\mathrm{i}\bar{\mathbf{k}}_z z} \cdot \mathbf{B}(\mathbf{k}_s) \right] \tag{7}$$

In (6) and (7) $\mathbf{A}$ and $\mathbf{B}$ are two-component unknown vectors and

$$\bar{\mathbf{k}}_z = \mathrm{diag}\left[k_z^e, k_z^h\right],\ \bar{\mathbf{g}}(\mathbf{k}_s) = \mathrm{diag}\left[\frac{\omega\varepsilon_0\varepsilon_x}{k_z^e}, \frac{k_z^h}{\omega\mu_0\mu_x}\right] \tag{8}$$

k_z^e and k_z^h are, respectively, propagation constants for TM and TE waves in the uniaxial substrate. They are given by

$$k_z^e = \sqrt{\frac{\varepsilon_x}{\varepsilon_z}} \left(\mu_x\varepsilon_z k_0^2 - k_s^2\right)^{\frac{1}{2}},\ k_z^h = \sqrt{\frac{\mu_x}{\mu_z}} \left(\mu_z\varepsilon_x k_0^2 - k_s^2\right)^{\frac{1}{2}},\ k_0^2 = \omega^2\varepsilon_0\mu_0 \tag{9}$$

Writing (4) and (5) in the plane $z = 0$ and $z = d$, and by eliminating the unknowns $\mathbf{A}$ and $\mathbf{B}$, we obtain the matrix form

$$\begin{bmatrix} \mathbf{e}(\mathbf{k}_s, d^-) \\ \mathbf{h}(\mathbf{k}_s, d^-) \end{bmatrix} = \bar{\mathbf{T}} \cdot \begin{bmatrix} \mathbf{e}(\mathbf{k}_s, 0^+) \\ \mathbf{h}(\mathbf{k}_s, 0^+) \end{bmatrix} \tag{10}$$

with

$$\bar{\mathbf{T}} = \begin{bmatrix} \bar{\mathbf{T}}^{11} & \bar{\mathbf{T}}^{12} \\ \bar{\mathbf{T}}^{21} & \bar{\mathbf{T}}^{22} \end{bmatrix} = \begin{bmatrix} \cos\bar{\theta} & -i\bar{\mathbf{g}}^{-1} \cdot \sin\bar{\theta} \\ -i\bar{\mathbf{g}} \cdot \sin\bar{\theta} & \cos\bar{\theta} \end{bmatrix},\ \bar{\theta} = \bar{\mathbf{k}}_z d \tag{11}$$

which combines $\mathbf{e}$ and $\mathbf{h}$ on both sides of the uniaxial anisotropic region as input and output quantities. Now that we have the matrix representation of the anisotropic substrate characterized by both permittivity and permeability tensors, it is easily to derive the dyadic Green's function of the problem in a manner very similar to that shown in [3].

3. COMPUTATION RESULTS

We have studied the effect of varying ε_x and ε_z on the resonant frequency for the case of a substrate with ($\mu_x \neq \mu_z$). The conclusions obtained are very similar to that obtained for a non-magnetic substrate [2]. Now we investigate the effect of varying μ_x and μ_z on the operating frequency. The resonant frequency of a rectangular microstrip patch antenna with dimensions $a = 1.9\,\mathrm{cm}$, $b = 2.29\,\mathrm{cm}$, substrate thickness $d = 0.159\,\mathrm{cm}$ and $(\varepsilon_x,\ \varepsilon_z) = (1, 1)$, for different pairs of relative

Table 1: Dependence of resonant frequency on relative permittivities (μ_x, μ_z).

Uniaxial anisotropy type	Relative permeability μ_x	Relative permeability μ_z	Anisotropic ratio $AR = \mu_x/\mu_z$	Resonant frequencies fr (GHz)	Fractional change $\frac{\Delta f_r}{f_r}$ (%)
Isotropic	2.4	2.4	1	4.020	0
Negative	4.8	2.4	2	2.979	25.90
Negative	2.4	1.2	2	4.032	0.31
Positive	1.2	2.4	0.5	5.436	35.22
Positive	2.4	4.8	0.5	4.013	0.17

permeabilities (μ_x, μ_z) is depicted in Table 1. The change in the resonant frequency relative to the isotropic case ($\mu_x = \mu_z = 2.4$) is calculated using the following expression:

$$\frac{\Delta f_r}{f_r} = \left| 1 - \frac{f_{ra}}{f_{ri}} \right| \tag{12}$$

where f_{ri} and f_{ra} are, respectively, the resonant frequencies of the antenna for the isotropic and uniaxial anisotropic cases. We observe also that, for negative uniaxial anisotropy with $AR = 2$, the resonant frequency f_{ri} can shift to a lower value of 2.979 GHz or higher frequency of 4.032 GHz. A similar remark can be made for the positive uniaxial anisotropy case with $AR = 0.5$; the corresponding values of lower and higher frequencies are, respectively, 4.013 GHz and 5.436 GHz. Consequently, the AR parameter alone is not sufficient to enhance a decision about whether there is an increase or decrease in resonant frequency to be made. Note, also that, as μ_x is decreased (increased) from 2.4 to 1.2 (4.8), the resonant frequency increases (decreases) from 4.020 GHz to 5.436 GHz (2.797 GHz) for a large fractional change of 35.22% (25.90%); when μ_z is changed, however, low values of fractional change are obtained, the maximum change being less than 1%. We conclude that, for a uniaxial anisotropic substrate, the operating frequency is strongly dependent on the permeability variations perpendicular to the optical axis.

4. CONCLUSIONS

Galerkin's method in the vector Fourier transform domain has been used for computing the resonant frequencies of a rectangular microstrip patch printed on a uniaxial substrate characterized by both permittivity and permeability tensors. Computations show that to predict frequency variations with anisotropic substrate permittivity, it is necessary to consider both the variations of μ_x and μ_z, and not only the ratio μ_x/μ_z. The investigations shows also that the permeability μ_x perpendicular to the optical axis is the most important factor in determining the resonant frequency when (μ_x, μ_z) vary.

REFERENCES

1. Gurel, C. S. and E. Yazgan, "Characteristics of a circular patch microstrip antenna on a uniaxially anisotropic substrate," *IEEE Trans. Antennas Propagat.*, Vol. 52, No. 10, 2532–2537, 2004.
2. Bouttout, F., F. Benabdelaziz, A. Benghalia, D. Khedrouche, and T. Fortaki, "Uniaxially anisotropic substrate effects on resonance of rectangular microstrip patch antenna," *Electron. Lett.*, Vol. 35, No. 4, 255–256, 1999.
3. Fortaki, T. and A. Benghalia, "Rigorous full-wave analysis of rectangular microstrip patches over ground planes with rectangular apertures in multilayered substrates that contain isotropic and uniaxial anisotropic materials," *Microwave Opt. Technol. Let.*, Vol. 41, No. 6, 496–500, 2004.
4. Fortaki, T., L. Djouane, F. Chebara, and A. Benghalia, "On the dual-frequency behavior of stacked microstrip patches," *IEEE Antennas Wireless Propagat. Lett.*, Vol. 7, 310–313, 2008.
5. Boufrioua, A. and A. Benghalia, "Radiation and resonant frequency of a resistive patch and uniaxial anisotropic substrate with entire domain and roof top functions," *Engineering Analysis with Boundary Elements*, Vol. 32, No. 7, 591–596, 2008.
6. Barkat, O. and A. Benghalia, "Radiation and resonant frequency of a resistive patch and uniaxial anisotropic substrate with entire domain and roof top functions," *Progress In Electromagnetics Research B*, Vol. 22, 103–119, 2010.

Design of Flat Gain UWB Tapered Slot Antenna for on-body Concealed Weapons Detections

Ali Atiah and N. Bowring
Electrical Engineering Department, Manchester Metropolitan University, UK

Abstract— The detection of human body worn concealed weapons based on the late time resonance (LTR) method is a considerable challenge. Successful LTR extraction to identify the target signature and its correct interpretation requires UWB antenna, which can cover the frequency of the fundamental (lowest) complex natural resonance (CNR) of the target(s) under detection. A flat gain UWB tapered slot antenna with operating bandwidth of 0.25–3 GHz to cover the lowest CNR frequencies was designed and fabricated. Antenna tests made in an anechoic chamber provide complete back scattering and signal radiation data. The results showed that the fabricated antenna has relative flat gain from about 0.3 GHz to just over 3 GHz with distortion less narrow pulse transmission.

1. INTRODUCTION

Standoff detection of on-body concealed weapons is a considerable challenge. Achieving a UWB antenna that is capable of having non-resonant (flat) gain across all frequencies in the desired band is a key role for the successful detection of on-body concealed objects, such as guns and knives. In fact, to achieve an impulse response of on-body concealed weapon(s), the weapon(s) need to be illuminated in the far field region by a very narrow pulse, equivalent to a UWB frequency sweep. As the pulse propagates through the concealed objects, omni-directional reflections and scattering occur at the interfaces [1]. Of particular interest are the aspect independent resonances and their associated dampening which can be measured by a receiving UWB antenna, the amplitude and phase of such backscatter is aspect dependent relative to the linear polarisation. For an effective detection system with high resolution and dynamic range, the transmitting/receiving UWB antenna should be flat gain (non-zeros resonant) as much as possible, have distortion less pulse transmission, reception and be directive with high-radiation efficiency. Tapered slot antennas (TSA) have been widely used in different radar applications, especially the Vivaldi antenna that was first brought out by Gibson in 1979 [2]. These have been recently widely investigated and developed by many researchers and institutions [3–6]. Several excellent TSAs with improved antenna parameters involving dual exponentially tapered slot antenna [7], dual elliptically tapered antipodal slot antenna [8], antipodal exponentially tapered slot antenna [9], dual V-type linear taper slot antenna [10] have been developed and optimized for issuing ultra-wideband (UWB) applications and millimetre-wave detection systems. Practically, in the frequency range 0.25–3 GHz, none of the improved TSAs has non-resonant flat gain around 10 dBi that is required for successful standoff concealed weapon detection based on late time responses, by covering all of the basic frequencies of common interested objects. Two specific Vivaldi antennas were studied and investigated in [11]. Regrettably, antenna gain characteristics are not available. The ridged horn antenna [12] shows high antenna gain with ultra-wide bandwidth, but it does not meet the non-resonant demands needed to cover the fundamental CNR of the target(s) under detection. Instead, TSA arrays [13] usually achieve 10-dBi or higher antenna gain covering the frequency of interest. However, compared with the single tapered slot antenna element, an antenna array is more difficult not only because of its larger size due to the extra feeding networks but also it is harder to design and fabricate. Most of the compact UWB antennas presented in the literature exhibit omni-directional radiation patterns with comparatively low gain and an impulse response with observable distortion [14]. These types of UWB antennas are convenient for short-range indoor and outdoor communication applications. However, for radar systems, used for the detection of weapons concealed under clothing, upon the human body or within carried bags at standoff distance, a flat gain directional antenna and VSWR around unity is advantageous. This criterion is required to enable effective deconvolution of the antenna response from the received scattered signal, which is essential to enable successful extraction of CNR modes. Nevertheless, having a less than desirable antenna response, may lead a detection system to have unauthentic resonances as any antenna resonance could mask concealed on-body objects. The bandwidth must be sufficiently wide to cover all of the basic frequencies of the most common firearms. In this paper, a compact UWB antenna exponentially tapered slot with a bandwidth of the operating frequency 0.25 to 3 GHz is developed. This operating bandwidth chosen

to cover the fundamental CNR modes of most firearms and to give a fine enough time resolution to resolve these CNR, and to minimize clutter from the human subjects and other objects in the surveillance area.

2. ANTENNA DESIGN

For the 0.25–3 GHz with flat gain operation bandwidth a tapered slot antenna TSA was developed and optimized as successfully used for radar applications. The presented TSA antenna will be used in concealed on-body weapon detection. The detection system includes identical TSA antennas, one used to transmit a sharp UWB pulse while the other receives the back scattering signal. The proposed antenna is fabricated on FR4 epoxy substrate with 0.5-oz copper and dielectric constant 2.33. A top view of designed antenna illustrated in Figure 1.

The design objective is to obtain a UWB antenna with non-zeros resonant frequency as any antenna resonant can mask the very important aspect independent late time response of objects concealed on the human body. The exponential taper profile is determined by the opining rate and two points $p_1(x_1, y_1)$ and $p_2(x_2, y_2)$.

$$y = c_1 e^{Rx} + c_2 \tag{1}$$

where,

$$c_1 = \frac{y_2 - y_1}{e^{Rx_2} - e^{Rx_1}} \tag{2}$$

$$c_2 = \frac{y_1 e^{Rx_2} - y_2 e^{Rx_1}}{e^{Rx_2} - e^{Rx_1}} \tag{3}$$

c_1, c_2 are constants and R the opening rate of the exponential taper. Note that (y_1, x_1) and (y_2, x_2) are the coordinates of the origin and end of flare curve, respectively and the taper length $L = x_2 - x_1$. An exponentially tapered slotline rather than an elliptically antipodal tapering structure was exploited to make the antenna simulation and optimization easier. The width W of the proposed antenna controls the lowest operation frequency, which is set at $0 : 47\lambda$, where λ is the free space wavelength at 0.25 GHz. The length could affect the front-to-back ratio of the radiation patterns at the lowest frequency band, which is set at around $0 : 4, \lambda$. The antenna is excited with a Gaussian monocycle pulse in the time domain and is optimized and simulated using the electromagnetic FTD solver *CST microwave studio* transient solver mode, which helped to reveal the most critical antenna areas to reduce cavity resonance and to ameliorate their related transmitted and received amplitudes. The excited monocycle pulse has maximum amplitude at a frequency 0.75 GHz, which carefully selected to excite basic CNR for most common firearms [15].

3. SIMULATION AND DISCUSSIONS

An optimum antenna design is achieved by the adjustment of the following parameters: flare angle, cavity radius and throat width to reduce the antenna ringing as much as possible. The ultra wideband antenna designed according to the mentioned procedure and it is manufactured using FR4 epoxy ($\varepsilon_r = 2.33$, $h = 0.125$ cm) as substrate. The taper rate was 0.18 cm and radial stub angle $(\theta) = 105°$. The radiating microstrip is on the bottom layer of the substrate whereas the

Figure 1: A view of the top of the designed antenna.

ground plane is printed on the top. The validity of the proposed design methodology is verified using CST simulator which is based on finite element technology. The antenna is located in the x-y plane, the E-plane of the antenna is in the x-z plane ($\varphi = 0°$) and H-plane is in the y-z plane ($\varphi = 90°$). Antenna measurements have been made in an anechoic chamber. The simulated and measured 10 dB return loss bandwidth extends from 0.25 GHz to 4 GHz covering the required UWB of 0.25 to 3 GHz. As shown in Figure 2, the simulated results closely resemble the measured result confirming the design procedure of the antenna.

Both the measured and simulated figures show that the antenna gain of the designed antenna achieves the requirements of flatness and VSWR outlined earlier, as illustrated in Figure 3.

The far-field radiation patterns of the antenna were again calculated by using CST microwave studio. These far field results are presented in Figure 5 for the frequencies 0.7 GHz and 1.5 GHz. The antenna achieves directive properties with an average front-to back ratio which is greater than 10 dB across the whole band, making it convenient for standoff detection applications. The time domain performance of the presented antenna was measured also. Two identical co-polarized antennas were set facing each other across a distance of 50 cm; the measured results are illustrated in Figure 6. The figure shows that the time pulse of the antenna is 0.7 nanoseconds. The results show that the optimized antenna provides a distortion less narrow pulse that makes it an excellent radiator for the application of a detection system with high resolution.

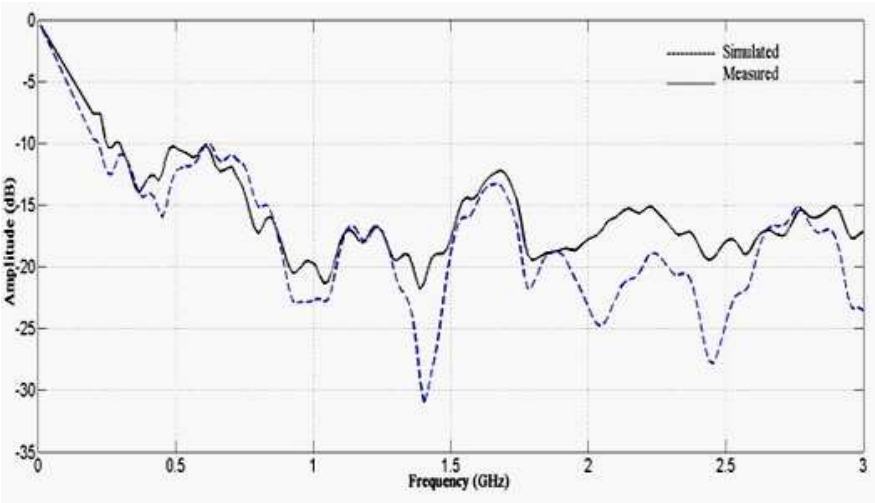

Figure 2: Measured and simulated S_{11} return loss.

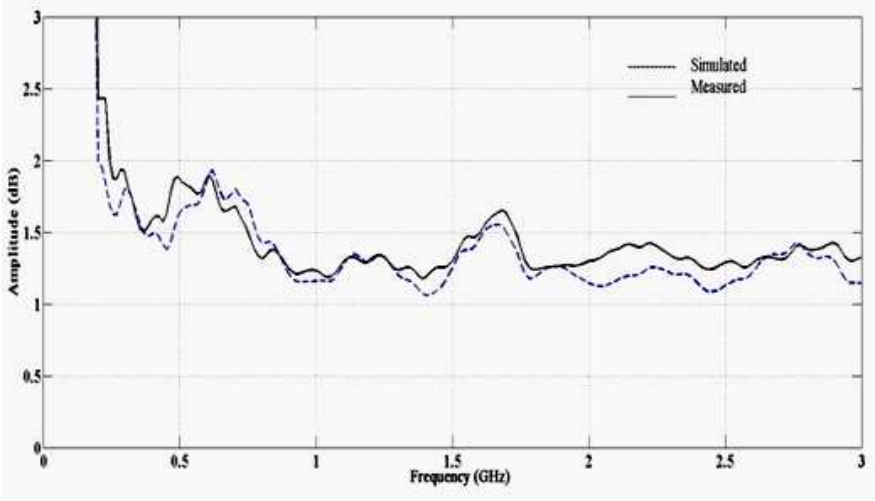

Figure 3: Measured and simulated VSWR.

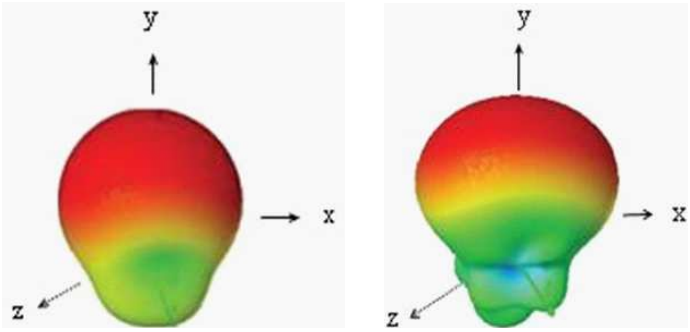

(a) (b)

Figure 4: Simulated three-dimensional far field radiation pattern (a) 0.7 GHz and (b) 1.5 GHz.

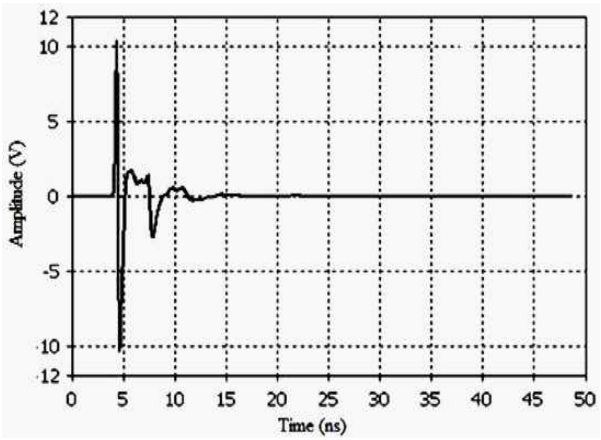

Figure 5: Measured impulse response.

4. CONCLUSIONS

The design of ultra-wideband tapered slot antenna for use in concealed weapon detection has been given. Detection of concealed on-body weapons is limited by antenna response as any antenna ringing could mask very important aspect independent scattering related to the concealed object signature. An approach is described based on relatively flat gain antenna across the operating bandwidth. Simulated and measured antenna characteristics illustrate that the developed antenna has relative flat gain cross-proposed band from 0.25 GHz to more than 3 GHz. The time domain of the antenna has been studied as well. It has been illustrated that the presented antenna could send and receive very narrow pulses in a distortion less manner to meet the requirements of successful concealed weapon detection based on the late time response scattered from the illuminated objects.

REFERENCES

1. Harmer, S., A. David, N. Bowring, and N. Rezgui, "Detection of handguns by their complex natural resonant frequencies," *IET Microwave, Antennas & Propagation*, Vol. 4, No. 9, 1182–1190 Sep. 2010.
2. Gibson, P. J., "The Vivaldi aerial," *Proc. 9th European Microwave Conference*, 101–105, 1979.
3. Gazit, E., "Improved design of the Vivaldi antenna," *IEE Proceedings: Microwaves, Antennas and Propagation*, Vol. 135, No. 2, 89–92, 1988.
4. Yngvesson, K. S., D. H. Schabubert, L. Kolberg, and J. Johansson, "End fire tapered slot antenna on dielectric substrates," *IEEE Transactions on Antennas and Propagation*, Vol. 33, No. 12, 13921400, 1985.
5. Kim, S. G. and K. Chang, "Ultra wideband exponentially-tapered antipodal vivaldi antennas," *IEEE Antennas and Propagation Society, AP-S International Symposium (Digest)*, Vol. 3, 2273–2276, 2004.
6. Janaswamy, R. and D. H. Schaubert, "Analysis of the tapered slot antenna," *IEEE Transactions on Antennas and Propagation*, Vol. 35, No. 9, 1058–1065, 1987.

7. Ponchak, G. E., J. L. Jordan, and C. T. Chevalier, "Characteristics of double exponentially tapered slot antenna (DETSA) conformed in the longitudinal direction around a cylinder," *IEEE Antennas and Wireless Propagation Letters*, Vol. 6, 60–63, 2007.
8. Langley, J. D. S., P. S. Hall, and P. Newham, "Balanced antipodal Vivaldi antenna for wide bandwidth phased arrays," *IEE Proceedings Microwaves Antennas and Propagation*, Vol. 143, No. 2, 97–102, 1996.
9. Qing, X. M., Z. N. Chen, and M. Y. W. Chia, "Parametric study of ultra-wideband dual elliptically tapered antipodal slot antenna," *International Journal of Antennas and Propagation*, 2008.
10. Cheng, Y. J., W. Hong, and K. Wu, "Design of a mono pulse antenna using a dual V-type linearly tapered slot antenna (DVLTSA)," *IEEE Transactions on Antennas and Propagation*, Vol. 56, No. 9, 2903–2909, 2008.
11. Mehdipour, A., K. M-Aghdam, and R. Faraji-Dana, "Completed dispersion analysis of Vivaldi antenna for ultra wideband applications," *Progress In Electromagnetics Research*, Vol. 77, 85–96, 2007.
12. Abbas-Azimi, M., F. Arazm, J. Rashed-Mohassel, and R. Faraji Dana, "Design and optimization of a new 1–18 GHz double ridged guide horn antenna," *Journal of Electromagnetic Waves and Applications*, Vol. 21, No. 4, 501–516, 2007.
13. Yang, Y., Y. Wang, and A. E. Fathy, "Design of compact Vivaldi antenna arrays for UWB see through wall applications," *Progress In Electromagnetic Research*, Vol. 82, 401–418, 2008.
14. Chen, F. C. and W. C. Chew, "Time-domain ultra-wideband imaging radar experiment for verifying super-resolution in nonlinear inverse scattering," *Journal of Electromagnetic Waves and Applications*, Vol. 17, No. 9, 1243–1260, 2003.
15. Andrews, D., N. Bowring, N. Rezgui, M. Southgate, E. Guest, S. Harmer, and A. Atiah, "A multifaceted active swept millimetre-wave approach to the detection of concealed weapons," *SPIE Security and Defense Conference*, Cardiff, UK, Sep. 2008.

Surface Wave Enhancement Using HF Metamaterials

L. Petrillo[1], **F. Jangal**[1], **M. Darces**[2], **J.-L. Montmagnon**[2], **and M. Hélier**[2]

[1]The French Aerospace Lab, ONERA, France
[2]L2E, UPMC Univ. Paris 06, France

Abstract— HF Surface Wave Radar (HFSWR) seems to be the most relevant and lowest cost solution for the surveillance of the Exclusive Economical Zone [1]. The HFSWR is a land based system that can watch over large maritime areas and detect low-altitude aircrafts and surface vessels beyond the electromagnetic horizon [2]. However, one of its major problems lies in the emitting antennas: since HF wavelength extends between 10 m and 100 m (most often in the order of 30 m), antenna dimensions can become a restraint for radar deployment. For this reason, equivalent quarter-dipole antennas are usually employed. This simple solution lacks in directivity and therefore causes energy dispersion towards the sky. As a consequence, ionospheric clutter corrupts radar data. We aim to solve those problem (i.e., energy wasting and clutter corruption) right from the conception. We are of the opinion that the design of a radiator dedicated to surface wave excitation cannot be achieved if the electromagnetic problem is ill-posed. In a recent paper [3] we have introduced the modal decomposition method [4] to study the influence of the Zenneck wave on the field excited by any vertical source placed at the sea surface. It has been found that the Zenneck wave contribution is masked by an infinite spectrum of bulk waves that are not confined at the sea surface. The excitation of the bulk waves does not permit to concentrate the radiated power at the interface between sea and air and therefore it lowers HFSWR performances. An interesting solution could come from the domain of negative parameters materials: an interface between air and a material having a negative permittivity can support a complex mode that may be not masked by the bulk waves. In this paper, with a similar approach of [5], we propose two different structures capable of sustaining a guided complex wave and of concentrating the radiated power at lower elevation angles.

1. INTRODUCTION

As ONERA has installed a HF Surface Wave Radar at the Biscay Bay in south of France, we are currently investigating a proper designed Surface Wave launcher to increase radar's performances. One of the problems arisen from the studies that have been made [6] is the presence of clutter in the back scattered signal received by the system: this unwanted signal corrupts radar images and makes targets identification hard. The clutter is originated from sky waves emitted by radar antennas that interact with the ionosphere. Even if signal processing to digitally eliminate clutter has been investigated [6], sky wave excitation still represents a major problem: in fact, for HFSWRs, the energy radiated towards the sky is lost. Emitting antennas used for ONERA radar are biconic antennas that, even if they have the interesting properties of being wide band, lack in directivity when radiating close to the ground at HF frequencies (3 to 30 MHz). This is a common problem for vertical wire antennas and no classical solution is able to concentrate the radiated energy close to the ground without extending antenna's dimensions and complicating radar system practical installation. To reach our goal, we focused on Kistovich modal decomposition of the field at the surface [4]: this approach allows to study the "free" modes, which form a continuous spectrum of bulk waves propagating in air and the complex mode which is bound to the interface. The first part of this paper reminds of the behavior of field contributions on the sea surface. The second one presents results obtained on surface with negative dielectric permittivity. In the last part of this paper two different structures capable of sustaining the complex mode are simulated and provide an enhancement of surface waves.

2. FIELD ON SEA

In a coordinate cartesian system, we consider two semi-infinite homogeneous half-spaces separated by an interface parallel to xy plane at $z = 0$. The upper half-space is supposed to be free-space and the lower one, sea water. At HF frequencies sea water is considered to be conductive, since the imaginary part of the complex dielectric constant is bigger than the real part. We have decomposed the magnetic field excited by a y-homogeneous current distribution $\vec{J} = J_0\delta(x)\delta(z)\vec{z}$ using Kistovich method [3]. Looking at Fig. 1, we see that the complex mode is masked by the infinite spectrum of bulk waves.

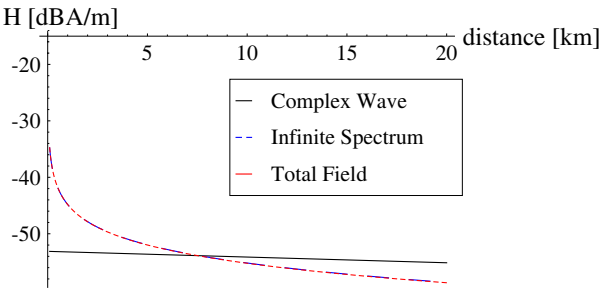

Figure 1: Decomposition of the magnetic field on sea water ($\varepsilon_r = 81$, $\sigma = 5\,\mathrm{S/m}$) at a frequency of 10 MHz.

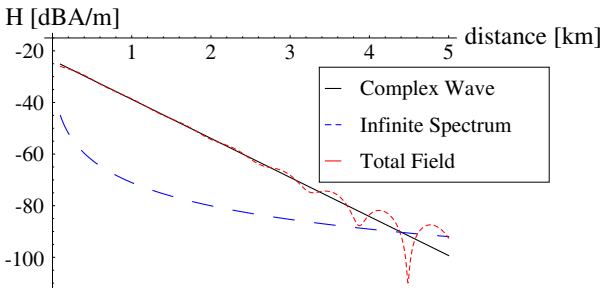

Figure 2: Decomposed magnetic field on negative dielectric material at a frequency of 10 MHz.

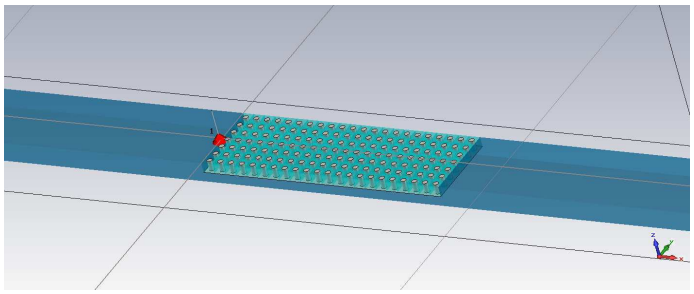

Figure 3: King structure (on monopole's right). Rods are immersed in a grounded, 1.5λ long perfect dielectric having $\varepsilon_r = 3$. The slab where the structure in immersed is taken to be sea water in order to compare structure effect on the electromagnetic field.

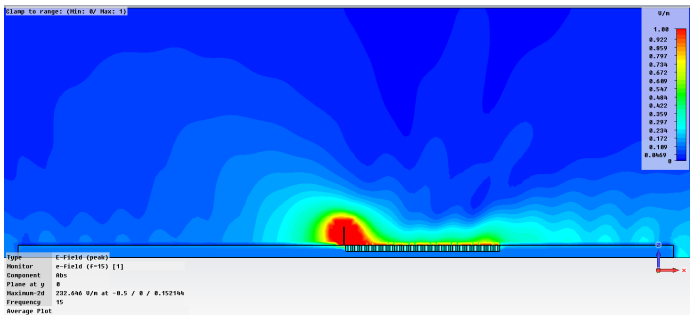

Figure 4: King structure test at 15 MHz.

3. FIELD ON NEGATIVE DIELECTRIC SURFACE

Changing the nature of the lower half-space can give rise to a relevant behavior with respect to previous section's results. Choosing a homogeneous medium having small conductivity, $\sigma < 0.001\,\mathrm{S/m}$, and negative relative dielectric permittivity, we have decomposed the field excited by the same current distribution $\vec{J} = J_0\delta(x)\delta(z)\vec{z}$. In Fig. 2 it can be seen that the magnetic field at the air/metamaterial interface is nearly given only by the complex wave contribution several wavelength far from the source. With the choice of a negative electrical permittivity material the complex wave is successfully excited. Therefore, the electromagnetic field radiated by a Hertz dipole is concentrated at the surface, since the magnitude of complex mode decreases fast in the direction normal to the surface.

4. STRUCTURES AND RESULTS

We have tested two structures that reproduce the surface impedance of a negative dielectric material. The first solution has firstly been proposed by King [7]. It consists basically of vertical cylindrically-shaped rods made of perfect electric conductor, immersed in a grounded dielectric. King made the measurements as described in [7] in order to evaluate the surface impedance of the structure considered as homogeneous for different values of the electric permittivity of the medium

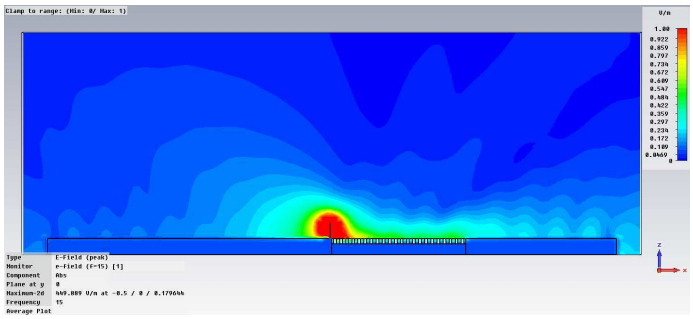

Figure 5: Modified King structure tested at 15 MHz. Bars have same height and width than King structure's rods. The structure is filled with a perfect dielectric material having $\varepsilon_r = 3$, it is grounded and it is 1.5λ long. As previously, the structure is immersed in sea water.

and height of the rods. We have used his results to simulate a monopole radiating above the structure in Fig. 3, which presents the surface impedance of a homogeneous medium having negative electrical permittivity. In Fig. 4, we see that the electric field is fed by King structure from the energy that would have been radiated if the structure was not present.

King structure has been modified substituting horizontal parallelepiped-shaped bars for the cylindrical rods. In Fig. 5, a monopole is radiating above the bars structure: it is seen that the second structure is equivalent to the first one. The choice of the structure is therefore not unique.

5. CONCLUSION

In this paper, we have applied decomposition analysis to identify a negative dielectric material presenting a surface impedance able to sustain a complex wave. This result has been used to adapt King structure dimensions to our scope and therefore to concentrate the energy radiated by a monopole in HF band at the surface of the sea. Moreover, it has been shown that the choice of the structure is not unique and the two examples we have chosen only represent a starting point for further optimized geometries.

REFERENCES

1. Menelle, M., G. Auffray, and F. Jangal, "Full digital high frequency surface wave radar: French trials in the biscay bay," *2008 International Conference on Radar*, 224–229, 2008.
2. Sevgi, L., A. Ponsford, and H. C. Chan, "An integrated maritime surveillance system based on high-frequency surface-wave radars. 1. Theoretical background and numerical simulations," *IEEE Antennas and Propagation Magazine*, Vol. 43, No. 4, 28–43, 2001.
3. Petrillo, L., F. Jangal, M. Darces, J.-L. Montmagnon, and M. Helier, "Towards a better excitation of the surface wave," *Progress In Electromagnetics Research M*, Vol. 13, 17–28, 2010.
4. Kistovich, Y. V., "Possibility of observing Zenneck surface wave in radiation from a source with a small vertical aperture," *Sov. Phys. Tech. Phys.*, Vol. 34, No. 4, 391–394, 1989.
5. Jangal, F., L. Petrillo, and F. Darces, "Towards HF metamaterials," *Antenna and Propagation Conference, 2009, LAPC 2009*, 629–632, Loughborough, 2009.
6. Jangal, F., S. Saillant, and M. Helier, "Ionospheric clutter mitigation using one-dimensional or two-dimensional wavelet processing," *Radar, Sonar and Navigation, IET*, Vol. 3, No. 2, 112–121, 2009.
7. King, R., D. Thiel, and K. Park, "The synthesis of surface reactance using an artificial dielectric," *IEEE Transactions on Antennas and Propagation*, Vol. 31, No. 3, 471–476, 1983.

Consequences of Localization of Non-linear Effects in Magnetic Dots

Jean-Claude Serge Levy
Laboratoire Matériaux et Phénomènes Quantiques, Université Paris 7 Denis Diderot, UMR 7162 CNRS
75201 Paris Cedex 13, France

Abstract— In the recent years, polar vortices were observed in magnetic dots, in perfect agreement with theoretical and numerical investigations based on the competition between local exchange and long-ranged dipole-dipole interactions. Quite recently some authors observed a frequency doubling of spin waves in such nanostructures as well as other non-linear properties. These highly non-linear effects occur precisely at domain walls. Such a localization of non-linear effects is explained here from a Taylor expansion of dipolar interactions which results in an effective local non-linear interaction. And non linear terms occur only at the places where static magnetization is not uniform. Thus the present step proposes to observe the occurrence of non-linear effects in magnetic dots where vortices are formed. This brings new geometrical constraints for induced high frequency magnons. Applications of non-linear effects to ferroelectric materials and to other vortex structures are suggested.

1. INTRODUCTION

Since the discovery of polar magnetic vortices in magnetic dots [1, 2], many projects of magnetic memories using such magnetic dots have been proposed. Reasons for that development are both the low size of such magnetic dots with vortices leading to high density structures and the recent occurrence of suitable low sized magnetic detectors [3] issued from giant magnetoresistance technology which can be used to detect these structures. In such magnetic dots, large variations of spin orientation occur within a quite restricted region and this property is expected to induce strong non-linear properties in the dipole-dipole interaction [4–6]. So another interesting property of magnetic dots could be the occurrence of such strong non-linear properties perfectly localized, while other sample parts do not exhibit any non-linear property. For the study of this non linear behaviour we will introduce here a local writing of the dipole-dipole Hamiltonian. This local writing, based upon a Taylor treatment of dipole-dipole Hamiltonian is derived. The local writing reveals to be highly non-linear in well defined places. And this strong localization can be helpful for filtering convenient non-linear properties.

2. AN EFFECTIVE LOCAL DIPOLE-DIPOLE HAMILTONIAN

The dipole-dipole interaction Hamiltonian reads:

$$H_{dip} = \sum_{i,j\neq i} \frac{\vec{S}_i * \vec{S}_j}{r_{ij}^3} - 3 \sum_{i,j\neq i} \frac{\left(\vec{S}_i * \vec{r}_{ij}\right)\left(\vec{S}_j * \vec{r}_{ij}\right)}{r_{ij}^5} \tag{1}$$

The Taylor's expansion of spin field within a 2D lattice writes:

$$\vec{S}_j = \sum_{p,q} \frac{x_{ij}^p y_{ij}^q}{p!q!} \left(\frac{\partial^{p+q}\vec{S}_i}{\partial x^p \partial y^q}\right) \tag{2}$$

This expansion enables us to derive the local version of dipolar interaction when considering a tensor spin field composed of all spin derivatives: $(\vec{S}_i, \frac{\partial \vec{S}_i}{\partial x}, \ldots, \frac{\partial^{p+q}\vec{S}_i}{\partial x^p \partial y^q}, \ldots)$:

$$H_{dip} = \sum_i H_{dip,i} \tag{3a}$$

$$H_{dip,i} = \sum_{p,q} \frac{\vec{S}_i}{p!q!} * \frac{\partial^{p+q}\vec{S}_i}{\partial x^p \partial y^q} \sum_j{}' \frac{x_{ij}^p y_{ij}^q}{\left(x_{ij}^2 + y_{ij}^2\right)^{3/2}} - 3 \sum_{p,q,\alpha,\beta} \frac{S_{i,\alpha}}{p!q!} \frac{\partial^{p+q} S_{i,\beta}}{\partial x^p \partial y^q} \sum_j{}' \frac{r_{ij,\alpha} r_{ij,\beta} x_{ij}^p y_{ij}^q}{\left(x_{ij}^2 + y_{ij}^2\right)^{5/2}} \tag{3b}$$

Here ' means that summation excludes site i.

The spatial contributions of these expressions define local lattice sums $I_{i,p,q}$ and $L_{i,p,q,\alpha,\beta}$

$$I_{i,p,q} = \sum_j{}' \frac{x_{ij}^p y_{ij}^q}{\left(x_{ij}^2+y_{ij}^2\right)^{3/2}} \tag{4a}$$

$$L_{i,p,q,\alpha,\beta} = \sum_j{}' \frac{r_{ij,\alpha} r_{ij,\beta} x_{ij}^p y_{ij}^q}{\left(x_{ij}^2+y_{ij}^2\right)^{5/2}} \tag{4b}$$

In the case of an infinite 2D lattice, lattice sums $I_{i,p,q}$and $L_{i,p,q,\alpha,\beta}$ are site independent, but sums with large p and q diverge. Always in a formal infinite lattice, symmetry rules restrict the values of p, q, α, β for non-zero lattice sums. In the case of a finite sample which is a part of a lattice as in the case of a magnetic dot, lattice sums with large p and q are large but finite and symmetry rules are just approximately satisfied. The divergence of lattice sums for an infinite lattice means a non analytic behavior of the spin field. This non analyticity induces a largely observed complex magnetic domain arrangement in large samples [7].

The introduction of lattice sums gives the more compact writing of the local dipolar Hamiltonian:

$$H_{dip,i} = \sum_{p,q} \frac{\vec{S}_i}{p!q!} * \frac{\partial^{p+q}\vec{S}_i}{\partial x^p \partial y^q} I_{i,p,q} - 3 \sum_{p,q,\alpha,\beta} \frac{S_{i,\alpha}}{p!q!} \frac{\partial^{p+q} S_{i,\beta}}{\partial x^p \partial y^q} L_{i,p,q,\alpha,\beta} \tag{5}$$

In the case of magnetic dots this formula is very difficult to apply since lattice sums are site dependent. If approximations available for large samples are used, just a few lattice sums are non zero and these non zero lattice sums can be described from a very few parameters because of symmetry properties. Since exact numerical calculations for magnetic dots are already available from micromagnetic simulations [1, 2], Monte-Carlo calculations [3, 8, 9] or Langevin dynamics [10], it is interesting here to use these approximations which are valid for large samples in order to obtain here simple approximate expressions for magnetic dots.

Using a continuous treatment of lattice sums on an infinite lattice, simple relations are obtained:

$$I_{i,p,q} = K_{p+q} N_{p,q} \quad \text{and} \quad L_{i,p,q,\alpha,\beta} = K_{p+q} N_{p',q'} \tag{6}$$

In these relations K_{p+q} deals with the radial part while $N_{p,q}$ deals with the azimuthal contribution, and there are also simple relations between p', q' and p, q, due to the values of α and β, see Ref. [4] Eq. (16) for such relations for $p+q<9$.

Approximate relations (6) enable us to write the local dipolar Hamiltonian as the sum of a series relative to the order of spin field derivatives:

$$H_{dip,i} = \sum_{n=0} H_{dip,i,2n} \tag{7}$$

With for the first term:

$$H_{dip,i,0} = 2\pi S_i^2 K_0 - 3\pi K_0 \left(S_{i,x}^2 + S_{i,y}^2\right) = -\pi K_0 \left(S_{i,x}^2 + S_{i,y}^2 - 2S_{i,z}^2\right) \tag{8}$$

This term is due to the contribution of the demagnetizing field of an infinite sample, as involved in these approximations. Minimizing this term means all spins are in-plane. Practically this is the case for nearly all of spins since polar parts are quite restricted [1–3, 8–10]. Integrating by parts and neglecting the boundary contributions gives for the next contribution which applies on the spin gradient, where the local index i is omitted:

$$\frac{H_{dip,i,1}}{\pi K_2} = \frac{5}{8}\left[\left(\frac{\partial S_x}{\partial x}\right)^2 + \left(\frac{\partial S_y}{\partial y}\right)^2\right] - \frac{1}{8}\left[\left(\frac{\partial S_x}{\partial y}\right)^2 + \left(\frac{\partial S_y}{\partial x}\right)^2\right] - \frac{1}{2}\left[\left(\frac{\partial S_z}{\partial x}\right)^2 + \left(\frac{\partial S_z}{\partial y}\right)^2\right] + \frac{3}{2}\left(\frac{\partial S_x}{\partial x}\right)\left(\frac{\partial S_y}{\partial y}\right) \tag{9}$$

This quadratic dipolar contribution can be compared to Frank and Leslie Hamiltonians for nematic liquid crystals on liquid crystal director [11]. Using polar angles for spin direction gives

$$\begin{aligned} S_x &= \sin\psi\cos\theta \\ S_x &= \sin\psi\sin\theta \\ S_x &= \cos\psi \end{aligned}$$

Since spins are in plane at the exception of sharp polar places in real samples, the relation $\psi = \pi/2$ can be used.

So this quadratic part of the Hamiltonian in spin gradient reduces to

$$\frac{8H_{dip,i,1}}{\pi K_2} = \left(6\sin^2\theta - 1\right)\theta_x^2 - 6\sin 2\theta\theta_x\theta_y + \left(6\cos^2\theta - 1\right)\theta_y^2$$

Looking for a local arrangement around an arbitrary origin, it is useful to introduce polar coordinates (r, ϕ) for the sample plane, with

$$x = r\cos\phi$$
$$y = r\sin\phi$$

Now this part of the Hamiltonian reads:

$$\frac{8H_{dip,i,1}}{\pi K_2} = \frac{\theta_\phi^2}{r^2}\left(3\cos\left[2\left(\theta-\phi\right)\right]+2\right) + 6\frac{\theta_r\theta_\phi}{r}\sin\left[2\left(\theta-\phi\right)\right] + \theta_r^2\left(2-3\cos\left[2\left(\theta-\phi\right)\right]\right) \tag{10}$$

Looking for minimal solutions which do not depend on the radius, one obtains

$$\theta = \phi \pm \pi/2 + 2k\pi \tag{11}$$

These solutions are vortices of positive or negative chirality [4–6] located at this arbitrary origin. So the ground state is made of vortices. In large samples, there are many vortices, and this coexistence introduces other topological defects [4–6] such as antivortices or hyperbolic defects between vortices of same chirality and double circles between vortices of opposite chirality.

The next, quartic, step of the local dipolar Hamiltonian reads by means of integration by parts, when neglecting boundary terms:

$$\begin{aligned} 64\frac{H_2}{\pi K_4} \;=\; & -3\left(\frac{\partial^2 S_x}{\partial x^2}\right)^2 + \left(\frac{\partial^2 S_x}{\partial y^2}\right)^2 + \left(\frac{\partial^2 S_y}{\partial x^2}\right)^2 - 3\left(\frac{\partial^2 S_y}{\partial y^2}\right)^2 + 2\left(\frac{\partial^2 S_z}{\partial x^2}\right)^2 + 2\left(\frac{\partial^2 S_z}{\partial y^2}\right)^2 - 4\left(\frac{\partial^2 S_z}{\partial x\partial y}\right)^2 \\ & -6\left(\frac{\partial^2 S_x}{\partial x\partial y}\right)^2 - 6\left(\frac{\partial^2 S_y}{\partial x\partial y}\right)^2 - 4\frac{\partial^2 S_x}{\partial x\partial y}\frac{\partial^2 S_y}{\partial y^2} - 4\frac{\partial^2 S_y}{\partial x\partial y}\frac{\partial^2 S_x}{\partial y^2} - 4\frac{\partial^2 S_x}{\partial x\partial y}\frac{\partial^2 S_y}{\partial x^2} - 4\frac{\partial^2 S_y}{\partial x\partial y}\frac{\partial^2 S_x}{\partial x^2} \end{aligned} \tag{12}$$

Since the ground state magnetic structure of a magnetic dot is determined by the minimization of Eqs. (8) and (10), it is a mainly in-plane magnetic configuration with topological defects including quite restricted polar parts. So the quartic term (12) just introduces more complex topological defects as well as higher order contributions [4–6]. Most of its contribution consists in being a non linear part of the Hamiltonian.

3. NON LINEAR CONTRIBUTIONS AND CONSEQUENCES OF THEIR LOCALIZATION IN MAGNETIC DOTS

From Eq. (12), these non linear contributions are localized at the places where magnetization components vary, i.e., at domain walls and other defects. Since these terms include the square of gradients of magnetization components, non linear contributions are specifically localized at and close to polar vortices and to vortices more generally. For terms of higher order, i.e., with higher derivatives of the spin field, this localization is even stronger. Experimentally this localization as well as the specificity of involved terms can be used as a filtering device as already proposed for frequency doubling [12]. Vortex localization can be driven by different ways such as sample shaping or introduction of chemical point defects or coupling with a magnetic cantilever. This localization effect opens a large domain of new non linear features in magnetic nanodots and magnons.

Higher order terms involve higher order spin derivatives. So these non linear effects are also quite restricted to the same places: vortices and other topological defects.

As a matter of fact because of the out-of-equilibrium property of magnetic nanodots which is due to the nearly degeneracy of numerous configurations as in spin glasses, other non linear effects occur with energy dissipation for instance. This is the case of numerous slow gyrotropic motions [13] where a polar vortex writes a part of a spiral before being blocked at some nearly central position. This damped gyrotropic motion can be derived directly from Landau-Lifshitz equation of motion when accounting for resulting out-of-equilibrium magnetic moments in the sample, another non linear effect.

REFERENCES

1. Cowburn, R. P., et al., *Phys. Rev. Lett.*, Vol. 83, 1042, 1999.
2. Shinjo, T., et al., *Science*, Vol. 289, 930, 2000.
3. Litvinov, D. and S. Khizroev, *J. Appl. Phys,* Vol. 97, 071101, 2005.
4. Levy, J. C. S., *Phys. Rev. B*, Vol. 63, 104409, 2001.
5. Levy, J. C. S., *Acta Physica Polonica A*, Vol. 115, 999, 2009.
6. Levy, J. C. S., *Nanostructures and Their Magnetic Properties*, Vol. 117, Research Signpost, India, 2009.
7. Hubert, A. and R. Schaefer, *Magnetic Domains*, Springer, Berlin, 1998.
8. Vedmedenko, E. Y., A. Ghazali, and J. C. S. Levy, *Surf. Sci.*, Vol. 391, 402–404, 1998.
9. Vedmedenko, E. Y., A. Ghazali, and J. C. S. Levy, *Phys. Rev. B*, Vol. 59, 3329, 1999.
10. Depondt, P. and F. G. Mertens, *J. Phys.: Condens. Matter*, Vol. 21, 33605, 2009.
11. De Gennes, P. G. and J. Prost, *The Physics of Liquid Crystals*, Oxford University Press, Oxford, UK, 1995.
12. Hermsdoerfer, S. J., et al., *Appl. Phys. Lett.*, Vol. 94, 223510, 2009.
13. Zhu, X., et al., *Phys. Rev. B*, Vol. 71, 180408R, 2005.

Evidence of Ducting Mode Electromagnetic Wave Propagation in the Indoor Environment

A. Draganov, J. Weinfield, L. Haas, and M. Harlacher
Argon ST, Wholly Owned Subsidiary of the Boeing Company, USA

Abstract— This paper presents results from three experiments on RF signal propagation in a multi-story office building. In the first experiment, we measured and analyzed fading patterns of an RF signal in the ISM band. We show that experimental results are in good agreement with a model that assumes ducted wave propagation, in addition to random multipath. In the second experiment, we measure the time difference of arrival of a signal at two receiving antennas in the building. For half of the scenarios, results for time difference of arrival are consistent with the hypothesis of ducted wave propagation along building hallways, and not with the line of sight hypothesis. In the third experiment, we show that accumulated phase variations between a transmitter and a receiver as the receiver moved along a hallway are consistent with the hypothesis of the phase velocity being different from the speed of light as typical for waveguide modes.

1. INTRODUCTION

Wireless communication and radio-frequency (RF) navigation are converging to use similar signals and even sharing same devices. Both are adversely affected by multipath propagation of the signal, especially in the urban and indoor environment. While in the communications field the primary effect of multipath is the intersymbol interference and signal fading, navigation applications often require a discernible line of sight to determine the user position. The next great frontier in radio navigation is accurate indoor positioning, where the line of sight signal may not exist or is corrupted by small delay (fraction of the symbol) multipath.

Conventional RF navigation uses the Time of Arrival (TOA) of signals from multiple transmitters. For example, GPS has become a de facto standard for RF navigation in outdoor environments. However, use of GPS indoors is inhibited by its low signal strength and by severe multipath distortions [1]. That has spurred the use of other signals, such as those from Wi-Fi nodes [2], Ultra-Wideband (UWB) signals [3], or signals with specially designed waveforms [4]. Depending on the type and features of a particular signal, indoor positioning techniques exploit either TOA, signal strength, or their combination to estimate the receiver position. For example, UWB signals are uniquely suited to discriminate small delay multipath from the line of sight (LOS) and hence use time of arrival for positioning [3], though power limitations may hinder their detection for larger buildings. Wi-Fi signals from multiple stationary nodes can be received inside of the building with sufficient strength. Using these signals for positioning can be based on TOA, Received Signal Strength (e.g., see [5]) or on RF fingerprinting [6].

Thorough understanding of signal propagation delays in indoor environments is important for these emerging applications. Studies of RF propagation in indoor environments have been mostly concentrated on characterizing the delay spread, fading and signal strength [e.g., 7, 8]. In this paper, we investigate fading patterns, relative delays and phase variations of a signal in hallways of a multi-story office building. We show that some features are consistent with the model of ducted or waveguide propagation mode along a hallway, when the group delay is measurably lower than the speed of light. We present results of three experiments that support this propagation model. We start from deriving an equation for the autocorrelation matrix for signal power (Section 2), which will be also estimated in one of the experiments (Section 3). Then we proceed to describing two other experiments, one for Time Difference of Arrival (TDOA) measurements (Section 4) and another for accumulated phase variations as a function of the receiver position (Section 5).

2. AUTOCORRELATION MATRIX FOR SIGNAL POWER

We modify the classic Rician fading statistics by assuming that the RF signal in a hallway of a building comprises the following components:

1. Propagation along the hallway with some wavenumber k_0 (e.g., clockwise around hallways),
2. Propagation along the hallway in the opposite direction (e.g., counter-clockwise around hallways) with some wavenumber k_1,

3. Diffuse multipath

Wavenumbers k_0 and k_1 are not assumed to be necessarily equal to $\frac{\omega}{c}$, which is the wavenumber for the free-space propagation (ω = signal frequency and c = speed of light). We allow for values of k_0 and k_1 to be smaller, due to wave dispersion caused by ducting effects of the hallway propagation. Note that the Rician model assumes diffuse multipath and one major signal component that corresponds to the line of sight propagation.

Our model defines the fading statistics for the signal power. To make it more informative, we compute the mean and covariance of the signal power at two locations as a function of spatial separation between these two locations. For an array of N equidistant locations along the hallway, our computation yields an $N \times N$ matrix of power covariances. The final purpose of this derivation is to compare this matrix to one estimated by measuring signal strength at a large number of locations.

We start from the equation for the electrical field:

$$E = \sum_j E_j \exp\left(i\vec{k}_j \cdot \vec{x}\right) \tag{1}$$

where E_j are amplitudes of path components, $\vec{x}$ is an arbitrary position in space, and $\vec{k}_j$ are corresponding wave vectors. By convention, the two major paths are components $j = 0$ and $j = 1$; higher values of j correspond to weaker diffuse multipath components.

We use this equation at points $\vec{x}_A$, $\vec{x}_B$ to compute the covariance for power levels:

$$Q(A,B) = \overline{\left(|E_A|^2 - \overline{|E_A|^2}\right)\left(|E_B|^2 - \overline{|E_B|^2}\right)} \tag{2}$$

where the horizontal bar denotes mathematical expectation. We assume that wavevectors of diffuse multipath components are randomly distributed over angle and equal in magnitude, and that amplitudes of diffuse multipaths are independent of the direction of propagation. These assumptions yield a simplification in the expression for power covariance; the final result is as follows:

$$\begin{aligned} Q(A,B) \;=\; & 2\cdot|E_0|^2|E_1|^2\cos\left[\left(\vec{k}_0-\vec{k}_1\right)\cdot\Delta\vec{x}\right]\cdot J_0\left(\vec{k}\cdot\Delta\vec{x}\right) + 2\cdot|E_0|^2\sigma^2\cos\left(\vec{k}_0\cdot\Delta\vec{x}\right)\cdot J_0\left(\vec{k}\cdot\Delta\vec{x}\right) \\ & +2\cdot|E_1|^2\sigma^2\cos\left(\vec{k}_1\cdot\Delta\vec{x}\right)\cdot J_0\left(\vec{k}\cdot\Delta\vec{x}\right) + \sigma^4\cdot J_0^2\left(\vec{k}_1\cdot\Delta\vec{x}\right) \end{aligned} \tag{3}$$

This matrix can be computed for different separations between points A and B and compared with experimental estimates of power covariance.

3. AUTOCORRELATION MATRIX FOR SIGNAL POWER

We measured RF signal from a spread-spectrum, 1 Msps beacon in the ISM band (at 915 MHz) in the hallways of the tenth floor of a steel frame and concrete office building. The beacon was set up outside, approximately at the same elevation as the receiver. The receiver captured the signal while moving along the hallway on a cart. The speed of the receiver motion was approximately equal to 1.1 m/s. The signal captured by the receiver was correlated with the replica code waveform over 10 ms epochs to measure its amplitude and phase. Figure 1 shows typical signal fading as a function of position or time. Horizontal axis units are in 10 ms correlation epochs; thus the entire range of values corresponds to slightly more than 6 seconds in time or 6 meters in the distance. Note a quasiperiodic fading pattern, which is consistent with two major components in the signal that were propagating in opposite directions. From observations collected over a more than 100 m course, we estimate sample covariance matrices for 1-second segments. These matrices show that statistics for signal power changes along the course; one can also expect this from Figure 1, where the amplitude in the middle section of the plot appears to be varying slower than that on the right section. We fitted the estimated power covariance matrix to the model presented in the previous section by adjusting power levels and wavenumbers for the two major propagation components. Figure 2 shows values of matrix elements on the skew-symmetric diagonal as a function of the element number for both modeled and experimental results. The example in Figure 2 is representative, and the agreement between the model and the measurements is universally good, with few outliers.

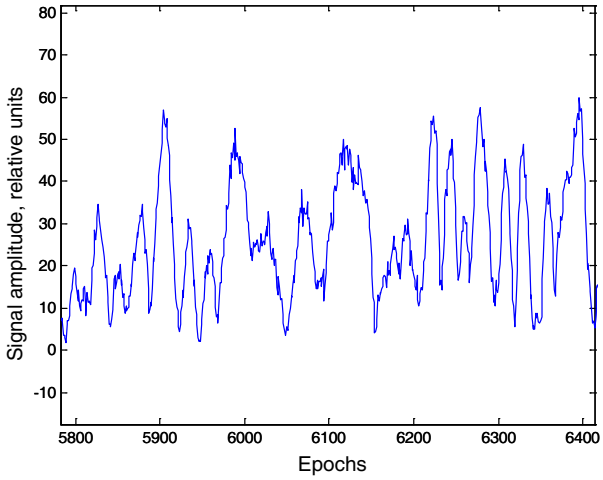

Figure 1: Fading pattern for signal in the hallway as a function of time/position.

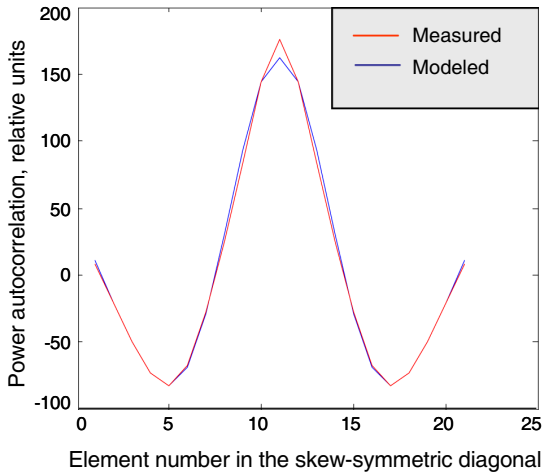

Figure 2: A representative example for signal power autocorrelation.

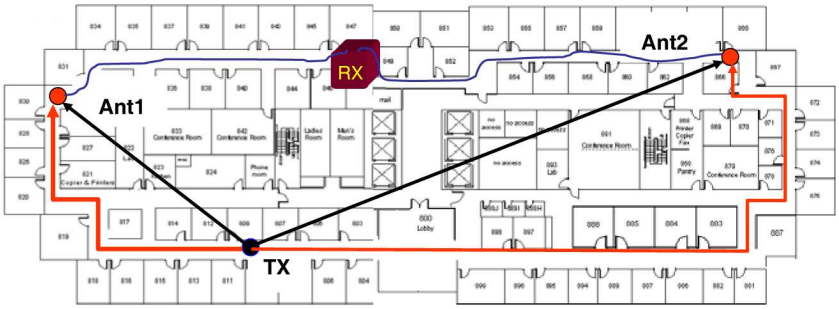

Figure 3: Direct and ducted propagation paths in the building.

4. PROPAGATION DELAY MEASUREMENTS

TDOA measurements are similar to TOA measurements; in navigation applications they yield information about the position of a receiver. TOA measurements rely on accurate time stamps at the transmitter (e.g., precise clocks onboard of GPS satellites). In a contrast, TDOA measurements do not require precise timing of the transmitted signal, but need a reference receiver at a known location. Typically, measurements are processed assuming the direct (line of sight) propagation.

If two receivers are synchronized and positions of the transmitter and receivers are accurately known, TDOA can be predicted from the geometrical distances between receivers and transmitters. In this case we can compare measured and predicted TDOA values to determine if the signal propagates through the line of sight. This was the goal of the experiment described in this section.

To accurately measure TDOA and to resolve small delay multipath, we used a relatively wide-band (20 MHz) spread spectrum signal in the ISM band (center frequency at 915 MHz). Two receive antennas were placed in different parts of the building and connected to a two channel receiver via coaxial cables of calibrated length. This ensured accurate synchronization of the received signals. A transmitter was placed on the same floor as the receivers. We measured TDOA for 6 different transmitter and receiver antenna placements. Figure 3 shows one such configuration on the floor plan of the building.

Received signals were correlated with the known replica of the modulation code. Due to the high bandwidth of the signal, we were able to resolve multiple arrivals of the signal at each antenna. Figure 4 shows correlations of the received signal with the replica as a function of replica delay for both antennas in the configuration which shown in Figure 3. TDOA in this test was measured to be 49 m, approximately the expected TDOA value for the ducted hallway paths. In other tests, the correlation function shows several major peaks with the leading peak not necessarily having the largest magnitude. TDOA was estimated between the first major peaks, even if they do not have the largest magnitude.

We then compared the measured TDOA values to predictions from two different models. In the first model, the earliest arrival is due to LOS propagation over a straight line through the building; such paths are shown in Figure 3 by black arrows. In the second model, we computed

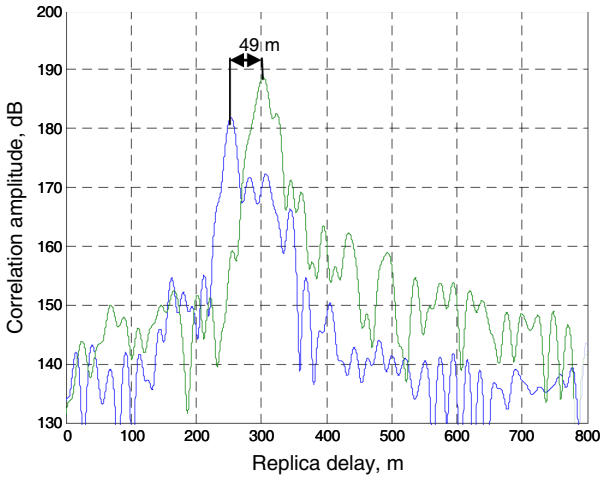

Figure 4: Correlations and relative delay between signals received at two antennas.

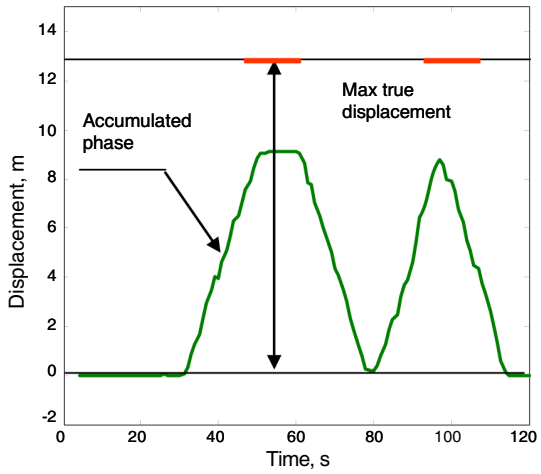

Figure 5: Accumulated phase variations compared to the true displacement of the receiver.

Table 1: Measured TDOA in comparison with the LOS and hallway propagation models.

Test No.	Measured TDOA (m)	LOS TDOA (m)	Hallway TDOA (m)
1	72	66	74.6
2	68	59	69.2
3	47	30.5	35.9
4	49	30	49
5	50	29	38.4
6	16	8	25.6

path lengths along hallways in the building that connect the transmitter and the receiver. Examples of such paths are shown in Figure 3 by red lines. Since we measure TDOA and not the absolute propagation delay, there is no guarantee that the direct path TDOA is shorter than hallway path TDOA. However, in practice that happened to be the case for all 6 setups.

Table 1 shows the measured TDOAs compared to the TDOA estimated from the LOS (model 1) and from hallway (model 2) distances. LOS distances do not provide a good estimate for measured TDOAs. Propagation distances computed along hallways provide a good approximation in 3 cases out of 6. These matching values are shaded in the table.

Results of this experiment are not conclusive, because not all measured values are in agreement with the models. Yet, they show better agreement with the hypothesis that RF signals propagate along building hallways rather than along the direct LOS.

For all model computations, we assumed propagation with the speed of light to compute TDOA. If we consider a ducted wave, its lower modes may propagate at the group velocity that is close to the speed of light, and higher modes can be slower. Thus, the correlation between the received signal and the replica may show several maxima (as they also would in the case of traditional multipath). Since measured TDOA values in Table 1 are for the first major maximum in the correlation, they are more likely to correspond to modes that propagate at the speed of light or to direct LOS propagation. In setups 3 and 5 measured TDOA values are greater than those predicted by both the LOS and the hallway propagation models. We can hypothesize that this may be due to a higher, slower hallway propagation mode, if the lower (faster) mode was not discernible in the received signal. However, there is not sufficient data to support this hypothesis at this time.

5. ACCUMULATED PHASE MEASUREMENTS

The final experiment described in this paper measured changes in the signal phase as the distance between the transmitter and the receiver varied. A receiver tracked RF signal in the ISM band (912.5 MHz) from a transmitter that was located in the same straight hallway. The receiver was rolled along the hallway on a cart, so that the distance to the transmitter varied. Local oscillators of the transmitter and the receiver were phase locked using a coaxial cable. The receiver used a

Phase Lock Loop (PLL) to track the phase of the received signal continuously. The signal had a spread spectrum with the 4.092 MHz chip rate. Figure 5 shows an example of variations in the accumulated phase, converted to meters as a function of time. It is compared to the changes in the distance. Multiple tests showed that the change in signal phase is consistently smaller than that predicted by the distance variations. Results from multiple experiments with the same setup were repeatable and suggest a scaling between the phase variations and the distance that is not consistent with the phase velocity being equal to the speed of light. Rather, they would correspond to the phase velocity that is greater than the speed of light, which may be explained if we assume a waveguide propagation mode between the transmitter and the receiver.

6. CONCLUSIONS

The propagation phenomenology of RF signals in the indoor environment is complex and includes a large number of paths that are subject to reflection, diffraction and scattering between the transmitter and the receiver. Yet, for many applications only some of these propagation paths matter, either because they channel the majority of the energy or because they reach the receiver earlier. In particular, for emerging indoor navigation applications it is important to know the timing and the direction of the first major arrival of the signal.

We present results of three experiments for RF wave propagation in an office building that suggest that at least in some cases RF energy tends to follow hallways in a ducted or waveguide mode. This may occur due to one of the following mechanisms. First, walls of the hallway can form a waveguide for the signal directly. Second, behind thin drywall walls there are vertical metal beams that create a periodic structure. The separation between the beams is approximately 0.6 m, which is on the order of the wavelength. Such periodic structure may create sufficient dispersion to slow down the electromagnetic wave that propagates along the hallway.

ACKNOWLEDGMENT

This work was partially supported by the Defense Advanced Research Projects Agency under the Robust Surface Navigation (RSN) program. The views, opinions, and/or findings contained in this article/presentation are those of the author/presenter and should not be interpreted as representing the official views or policies, either expressed or implied, of the Defense Advanced Research Projects Agency or the Department of Defense. The authors are also grateful to Michael Wenske for his help with the experiments and to Dr. Frank Gross for helpful discussions.

REFERENCES

1. Misra, P. and P. Enge, *Global Positioning System: Signals, Measurements, and Performance*, Ganga-Jamuna Press, Lincoln, 2006.
2. Krumm, J. and E. Horvitz, "Locadio: inferring motion and location from Wi-Fi signal strengths," *Proceedings of International Conference on Mobile and Ubiquitous Systems: Networking and Services, MobiQuitous 04*, Boston, USA, August 2004.
3. Fontana, R., L. Foster, B. Fair, and D. Wu, "Recent advances in ultra wideband radar and ranging systems," *IEEE International Conference on Ultra-Wideband, ICUWB*, Singapore, September 2007.
4. Progri, I., W. Michalson, J. Wang, and M. Bromberg, "Indoor geolocation using FCDMA pseudolites: Signal structure and performance analysis," *Navigation: Journal of The Institute of Navigation*, Vol. 54, No. 3, Fall 2007.
5. Hatami, A., K. Pahlavan, M. Heidari, and F. Akgul, "On RSS and TOA based indoor geolocation — A comparative performance evaluation," *WCNC — Wireless Communications and Networking Conference*, Las Vegas, USA, April 2006.
6. Swangmuang, N. and P. Krishnamurthy, "Location fingerprint analyses toward efficient indoor positioning," *Sixth Annual IEEE International Conference on Pervasive Computing and Communications*, Hong Kong, March 2008.
7. Woodward, G., I. Oppermann, and J. Talvitie, "Outdoor-indoor temporal & spatial wideband channel model for ISM bands," *VTC — IEEE Vehicular Technology Conference*, Amsterdam, Vol. 1, 136–140, September 1999.
8. Salous, S. and V. Hinostroza, "By-dynamic indoor measurements with high resolution channel sounder," *The 5th International Symposium on Wireless Personal Multimedia Communications*, Vol. 1, 262–266, Honolulu, USA, October 2002.

Some Examples of Uncorrelated Antenna Radiation Patterns for MIMO Applications

A. Alayon Glazunov[1] **and J. Zhang**[2]

[1]Electromagnetic Engineering Lab, KTH — Royal Institute of Technology, Sweden
[2]Centre for Wireless Network Design, University of Bedfordshire, UK

Abstract— In this paper, we provide some examples of an approach resulting in uncorrelated antenna radiation patterns at both ends of a MIMO (Multiple-Input Multiple-Output) wireless link in a given propagation channel. The patterns of antennas exciting dipole or dipole and quadrupole TE and TM modes are analyzed for two generic MIMO channel models based on the Kronecker correlation model with Laplacian angle-of-arrival (AoA) and angle-of-departure (AoD) distributions. The presented results are of a fundamental nature and essential to achieve the promise of MIMO systems.

1. INTRODUCTION

The radiation gain pattern is one of the most important figures of merit of an antenna. Indeed, together with the properties of the propagation channel, it determines the signal-to-noise ratio (SNR) of a wireless link and the correlation between antenna elements. The SNR and the correlation have both a great impact on the spectral efficiency of MIMO links over multipath wireless channels. Hence, an accurate account for the interactions between antennas and channels is essential to a successful implementation of MIMO technologies for 4G and beyond wireless systems. Although this topic has been extensively researched, a unified approach for the characterization of antenna-channel interactions has been introduced only recently. The proposed method develops a formalism to jointly characterize antennas and wireless propagation channels based on the antenna scattering matrix and the spherical vector wave (svw) expansion of the electromagnetic fields [2–4].

2. UNCORRELATED MIMO ANTENNAS IN KRONECKER CHANNELS

It can be shown that the MIMO channel transfer function is expressed as [1]

$$\mathbf{H} = \mathbf{RMT}, \tag{1}$$

where $\mathbf{T} \in \mathbb{C}^{M_t \times N_t}$ is the matrix containing the coefficients of the transmit antenna and $\mathbf{R} \in \mathbb{C}^{N_r \times M_r}$ is the matrix containing the receive antenna coefficients, M_t and N_t are the number of svw modes and the number of ports at the transmit antenna, respectively. M_r and N_r are the number of svw modes and the number of ports at the receive antenna, respectively. The mode-to-mode MIMO channel matrix, i.e., $\mathbf{M} \in \mathbb{C}^{M_r \times M_t}$ is a random matrix operator that maps the svw modes at the transmit antennas to the receive antennas, i.e., $\mathbf{M}$ describes the properties of the wireless channel in terms of the multimode expansion coefficients of the electromagnetic field.

In order to maximize the performance of MIMO systems it is often desirable to obtain uncorrelated channels, which is equivalent to a diagonal *full-correlation channel matrix* $\mathcal{R}_h = \langle \mathbf{h}\mathbf{h}^\dagger \rangle$. $\mathbf{h} = vec(\mathbf{H}) = (\mathbf{T}' \otimes \mathbf{R})\mathbf{m}$ and $\mathbf{m} = vec(\mathbf{M})$ are the vectorized forms (i.e., obtained by stacking the columns upon each other) of the $\mathbf{H}$-matrix and $\mathbf{M}$-matrix, respectively. The symbols $(\cdot)'$ and $(\cdot)^\dagger$ denote the matrix transpose and the hermitian matrix transpose operations, respectively, and $\otimes$ is the Kronecker matrix product symbol. Further assume the Kronecker channel model for the multimode channel, i.e.,

$$\mathcal{R}_m = \mathcal{R}'_{\mathbf{M}_t} \otimes \mathcal{R}_{\mathbf{M}_r}, \tag{2}$$

where $\mathcal{R}_m = \langle \mathbf{m}\mathbf{m}^\dagger \rangle$ is the *full-correlation channel matrix* of the multimode channel, $\mathcal{R}_{\mathbf{M}_r} = \langle \mathbf{M}\mathbf{M}^\dagger \rangle$ and $\mathcal{R}_{\mathbf{M}_t} = \langle \mathbf{M}^\dagger\mathbf{M} \rangle$, are the multimode channel correlation matrices at the receiver and the transmitter, respectively. It can then be shown that the transmit and receive antennas coefficients that diagonalize $\mathcal{R}_h = \langle \mathbf{h}\mathbf{h}^\dagger \rangle$ are given by

$$\mathbf{R} = \mathbf{U}^\dagger_{\mathbf{M}_r} \text{ and } \mathbf{T} = \mathbf{U}_{\mathbf{M}_t}, \tag{3}$$

where $\mathbf{U}_{\mathbf{M}_r}$ and $\mathbf{U}_{\mathbf{M}_t}$ are unitary matrices satisfying the eigenvalue decomposition

$$\mathcal{R}_{\mathbf{M}_r} = \mathbf{U}_{\mathbf{M}_r}\Sigma_{\mathbf{M}_r}\mathbf{U}^\dagger_{\mathbf{M}_r} \text{ and } \mathcal{R}_{\mathbf{M}_t} = \mathbf{U}_{\mathbf{M}_t}\Sigma_{\mathbf{M}_t}\mathbf{U}^\dagger_{\mathbf{M}_t}. \tag{4}$$

3. NUMERICAL EXAMPLES

We use a simplified channel model for the AoA (angle-of-arrival) and the AoD (angle-of-departure) for each of the two orthogonal polarizations. The two-dimensional Laplacian distribution in spherical coordinates is assumed, i.e.,

$$p_{\theta,\,\phi x}(\theta,\,\phi) = p_{\theta x}(\theta)p_{\phi x}(\phi) = Ae^{-(\sqrt{2}|\theta-\mu\theta x|/\sigma\theta x+\sqrt{2}|\phi-\mu\phi x|/\sigma\phi x)}\sin\theta, \tag{5}$$

where the elevation angle $\theta \in [0, \pi]$, azimuth angle $\phi \in [0, 2\pi)$ and x stands for either of $\hat{\theta}-$ or $\hat{\phi}-$ polarization, and the shape is controlled by the distribution parameters $\{\mu_{\theta x}, \sigma_{\theta x}, \mu_{\phi x}, \sigma_{\phi x}\}$, where the σ are a measure of angle spread and the μ denote the average AoA/AoD. The polarimetric properties of the channel are characterized by the cross-polarization ratio (XPR or χ defined as the ratio of the power of the vertically polarized waves to the power of horizontally polarized waves. Table 1. presents the parameters of two channels: Channel A, which describes a channel with uniform AoA and AoD distributions (large angle spread) and balanced polarization and Channel B, which has a uniform AoA distribution but a more selective AoD distribution (small angle spread) and has a stronger response for the vertically polarized component.

From now on we specialize results presented in Section 2 to a 2×2 MIMO antenna system with elements exciting dipole (i.e., $l = 1$) or dipole and quadrupole (i.e., $l = 1$ and $l = 2$) TE ($\tau = 1$) and TM modes ($\tau = 2$). For the sake of compactness we introduce a multi-index notation $\iota = 2(l^2 + l - 1 + m) + \tau$ to denote different multimodes at the transmitter; we use κ to denote the corresponding multi-index at the receiver. The azimuthal and radial dependencies are given by the m and l index, respectively. Fig. 1 illustrates the absolute value of the multimode ($l = 1$ only) correlation matrices at the transmitter and the receiver for Channel A in plots (a) and (b) and for Channel B in plots (c) and (d), respectively. As we can see from Figs. 1(a) and (b) a uniform spatial distribution results in *uncorrelated* field modes. Moreover, a balanced polarization gives modes with similar power. On the contrary, in Channel B shown see Figs. 1(c) and (d) the field modes become more *correlated* due to the low angle spread at the transmitter. In addition, since the channel favors the vertically polarized field component over the horizontally polarized field component (since $\chi > 1$), the power of the TM mode with multi-index $\iota = 4$ at the transmitter ($\kappa = 4$ at the receiver), i.e., $\tau = 2$, $l = 1$, $m = 0$ is higher compared with the other dipole modes.

Figure 2 shows the absolute value of transmit and receive antenna coefficients that diagonalize

Table 1: Parameters of the distributions (5), where we have further assumed that $\sigma = \sigma_{\theta x} = \sigma_{\phi x}$ at both the receive and the transmit antennas as well as $\mu_{\theta x} = \mu_\theta$ and $\mu_{\phi x} = \mu_\phi$.

	Channel A		Channel B	
	Tx	Rx	Tx	Rx
σ [rad]	10	10	0.1	10
μ_θ [rad]	$\pi/2$	$\pi/2$	$\pi/2$	$\pi/2$
μ_ϕ [rad]	0	0	0	0
χ [dB]	0		4	

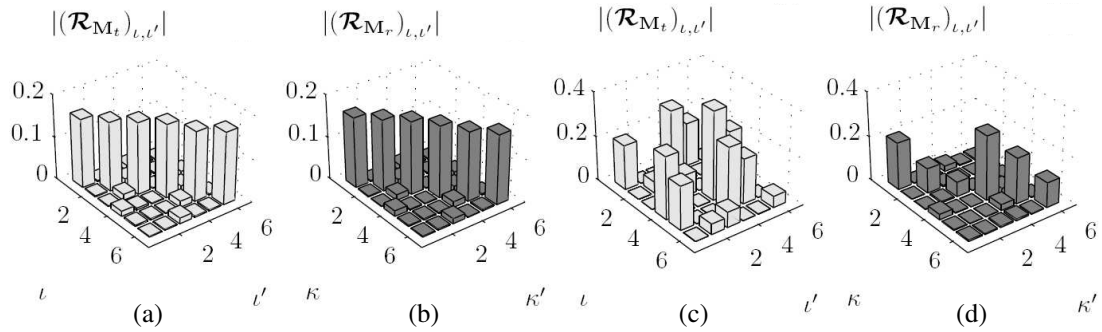

Figure 1: Absolute value of the multimode correlation matrices for Channel A (a) at the transmitter and (b) at the receiver, respectively. The corresponding values for Channel B are shown in (c) and (d), respectively.

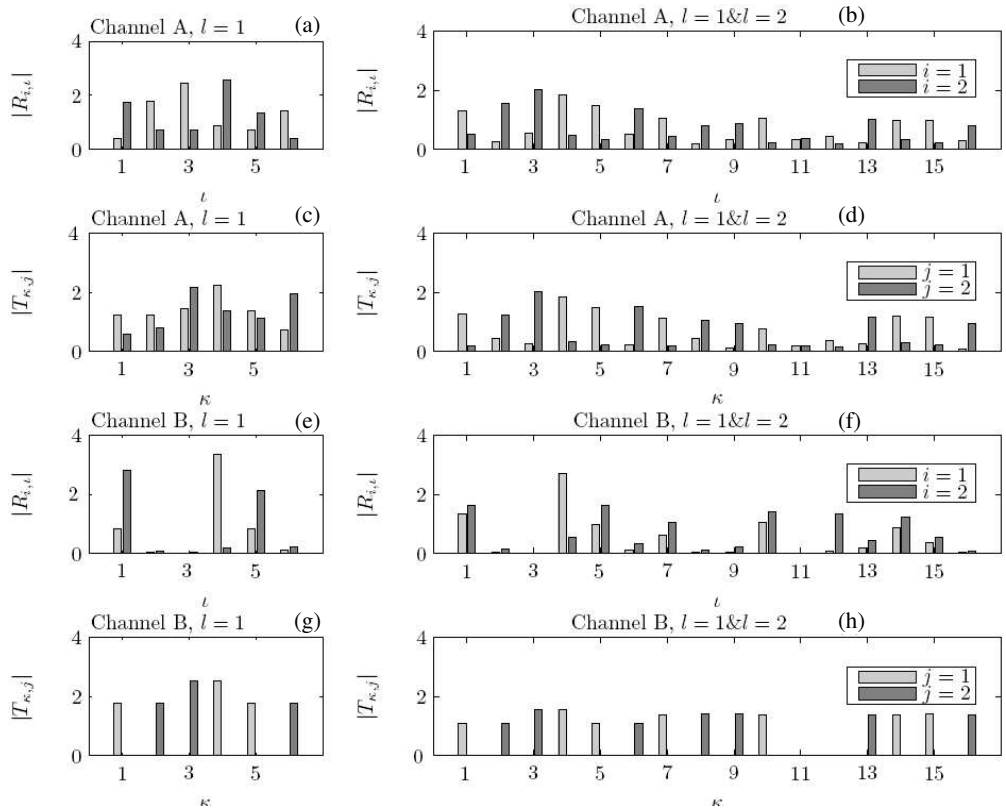

Figure 2: Absolute value of the transmit **T** and receive **R** antenna coefficients in Channels A and B for antennas exciting dipole modes only or dipole and quadrupole modes.

the 2×2 MIMO full-correlation matrix $\mathcal{R}_h$. according to (3) under assumption (2) with channel parameters given in Table 1. Four different cases are shown:

(i) dipole modes in Channel A are shown in Figs. 2(a) and (c),
(ii) dipole modes in Channel B are shown in Figs. 2(e) and (g),
(iii) dipole and quadrupole modes in Channel A are shown in Figs. 2(b) and (d) and
(iv) dipole and quadrupole modes in Channel B are shown in Figs. 2(f) and (h).

A closer inspection of Fig. 2 shows that the antenna elements are orthogonal indeed, e.g., in Fig. 2(a) the dipole modes excited by the receive antennas in Channel A in antenna $i = 1$ form an orthogonal vector to the dipole modes excited in antenna $i = 2$, i.e., $\sum_\iota R_{1,\iota} R^*_{2,\iota} = 0$, where $()^*$ denotes complex conjugate.

The orthogonality between antenna elements can be further illustrated by the partial radiation patterns of the corresponding antennas which are shown in Fig. 3. For the sake of brevity we show results for Channel B only. In Fig. 3, we use the following notation for the 3D radiation patterns: $G^{a'}_{bc}(\theta, \phi)$ and $G^{a''}_{bc}(\theta, \phi)$ denote antennas exciting dipole modes or dipole and quadrupole modes, respectively. The arguments are omitted in the figure for clarity. The superscript $a = r, t$ is used to denote Rx and Tx antennas, respectively. In turn, the subscript $b = \theta, \phi$ denotes the $\hat{\theta}-$ and the $\hat{\phi}-$ component, respectively; if this subscript is missing then the sum of the patterns is depicted representing the total radiation pattern. Finally, the subscript $c = 1, 2$ is used to differentiate between the antenna ports. It is worthwhile to note that patterns plotted in Figs. 3(a)–(f) correspond to modes shown in Fig. 2(e), patterns in Figs. 3(g)–(l) correspond to modes shown in Fig. 2(g), patterns in Figs. 3(m)–(r) correspond to modes shown in Fig. 2(f) and patterns in Figs. 3(s)–(x) correspond to modes shown in Fig. 2(h). As we can see, the orthogonal patterns correspond in many cases to antennas with orthogonal polarizations or orthogonal lobes, which obviously gives uncorrelated channels.

By comparing Figs. 3(a)–(f) with Figs. 3(g)–(l) we see that the orthogonal patterns have larger directivity at the transmit antenna side as compared to the also orthogonal receive antenna patterns since Channel B produces small angle spread at the transmitter side and large angle spread at the

receiver side from (see Table 1.). In addition, we can say that we have polarization diversity for the transmit antennas, while receive antennas combine polarization and pattern diversity. Furthermore, as we increase the multipole order to include both dipole and quadrupole modes, we see that at the receive antenna side the two ports have orthogonal lobes (see Figs. 3(m)–(r)) while at the transmit antenna side we see that orthogonal patterns are obtained by polarization diversity with larger directivity (see Figs. 3(s)–(x)).

We can then clearly see that our approach results in MIMO channel with diagonal full-correlation matrix as shown in Fig. 4. The power in each independent MIMO link will depend upon the propagation channel properties at both the Tx and the Rx. The more uniform in space and polarization balanced channel the more equal the power of each independent link (see Figs. 4(a)–(b)). However, as the channel becomes more selective in space and polarization the opposite effect

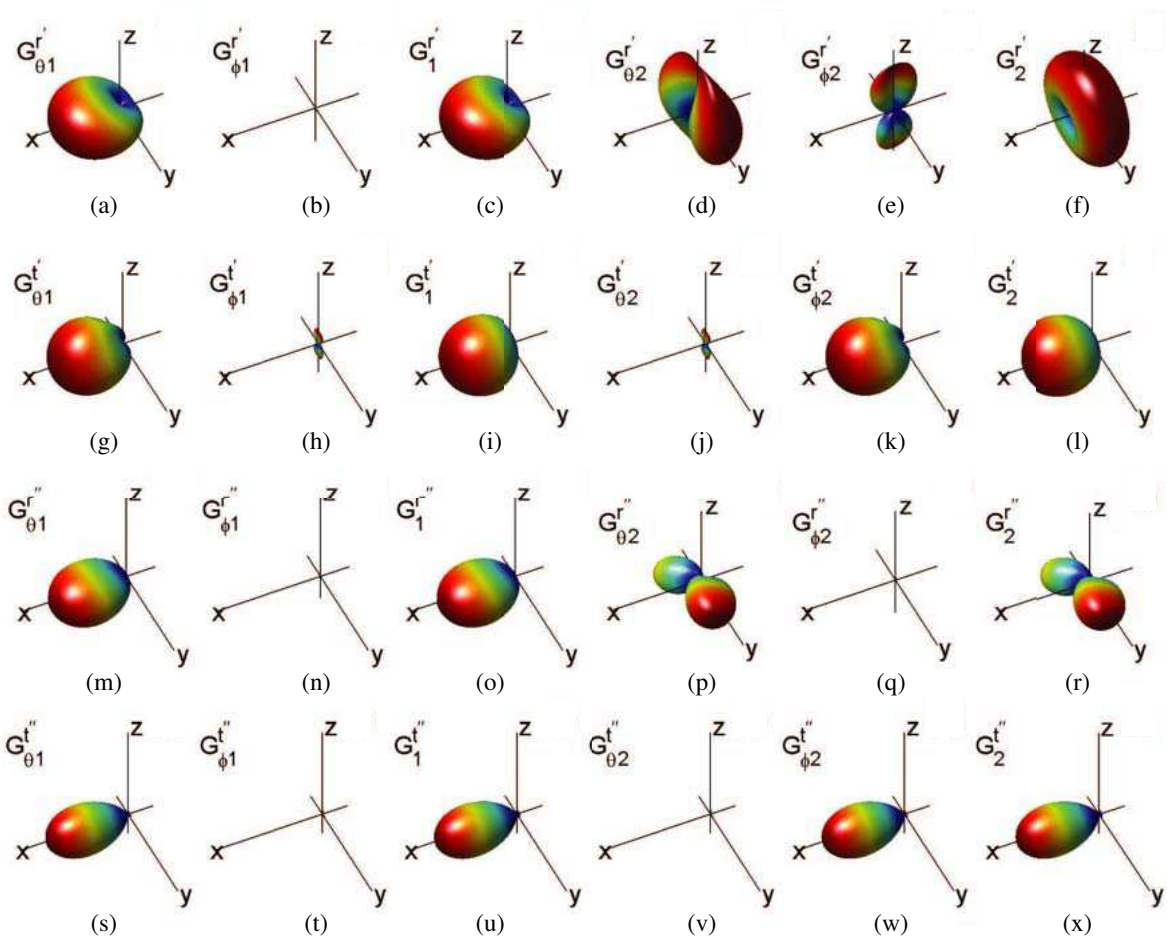

Figure 3: Orthogonal radiation patterns obtained for antennas exciting dipole modes (a)–(l) and dipole and quadrupole modes (m)–(x) in Channel B.

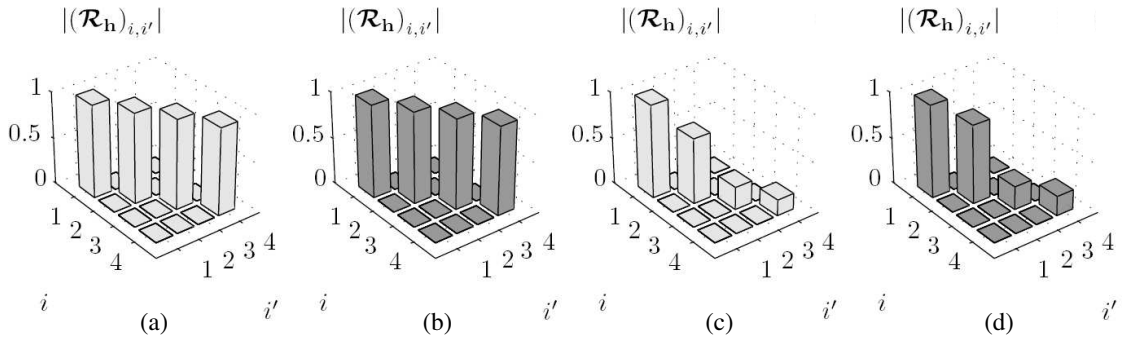

Figure 4: Absolute value of the MIMO full-correlation matrix $\mathcal{R}_h$ with orthogonal antennas for the four different cases considered, plots (a), (b), (c) and (d) show cases (i), (iii), (ii) and (iv), respectively.

becomes apparent (see Figs. 4(c)–(d)).

4. CONCLUSION

We have presented a method to produce orthogonal radiation patterns for MIMO antenna systems based on the spherical vector wave multimode expansion of the MIMO channel. We show that the transmit and receive antenna coefficients are the eigenvectors of the multimode correlation matrices at the transmit and receive antenna, respectively. The physical interpretation of the results is that orthogonal radiation patterns are naturally obtained as combination of orthogonal radiation patterns, orthogonal polarizations and space diversity, which are essential to achieve the promise of MIMO systems.

ACKNOWLEDGMENT

This work has been partly supported by the Marie Curie EU FP6 "GAWIND" project and the Marie Curie EU FP7 IAPP "IAPP@RANPLAN" project.

REFERENCES

1. Alayon Glazunov, A., "On the antenna-channel interactions: A spherical vector wave expansion approach," Doctoral Thesis, ISSN 1654-790X, No. 16, Electrical and Information Technology, March 2009.
2. Alayon Glazunov, A., M. Gustafsson, and A. F. Molisch, "On the physical limitations of the interaction of a spherical aperture and a random field," *IEEE Transactions on Antennas and Propagation*, Vol. 59, No. 1, January 2011.
3. Alayon Glazunov, A., M. Gustafsson, A. F. Molisch, F. Tufvesson, and G. Kristensson, "Spherical vector wave expansion of gaussian electromagnetic fields for antenna-channel interaction analysis," *IEEE Transactions on Antennas and Propagation*, Vol. 57, No. 7, 2055–2067, July 2009.
4. Alayon Glazunov, A., M. Gustafsson, A. F. Molisch, and F. Tufvesson, "Physical modelling of multiple-input multiple-output antennas and channels by means of the spherical vector wave expansion," *IET Microwaves, Antennas & Propagation*, Vol. 4, No. 6, 778–791, June 2010.

Clustering Impact on the Statistics of the Multipole Expansion Coefficients of a Wireless Channel

A. Alayon Glazunov[1] **and J. Zhang**[2]

[1]Electromagnetic Engineering Lab, KTH Royal Institute of Technology, Sweden
[2]Centre for Wireless Network Design, University of Bedfordshire, UK

Abstract— It has been widely known that experimental results show that multipath components seem to arrive at the receiver in concentrated groups. These groups of multipath components, or clusters, are usually a result of scattering from large physical structures. Their impact on the capacity of Multiple-Input Multiple-Output (MIMO) systems has been widely studied. However, their impact on the spherical vector waves (svw) expansion of the propagation channel has not yet been addressed in the literature. As we have recently shown, a svw expansion provides a compact and straightforward representation of both antennas and channels. This can potentially facilitate designing antennas tailored to take advantage of the spatial and polarimetric characteristics of the propagation environment, which is essential to the deployment of efficient wireless networks. In this paper, we therefore study the impact of clustering on the first and second order statistics of the multimode expansion coefficients. We adopt the simulation approach to exemplify our results and provide numerical examples.

1. INTRODUCTION

In order to offer better services, 4G and beyond wireless systems are designed to employ MIMO technologies where multiple antennas are deployed at both the transmit and receive sides. The performance of such technologies heavily depend upon the prevailing propagation conditions as well as the properties of the antennas. Therefore, their properties or rather the properties of the interaction between them require a comprehensive understanding for accurate modeling and design of antennas. In line with this we have devised a formalism to jointly characterize antennas and wireless propagation channels based on the antenna scattering matrix and the spherical vector wave (svw) expansion of the electromagnetic fields [1–3].

The clustering nature of the wireless multipath channel and its impact on the capacity of MIMO systems has been widely studied, see e.g., [5, 6]. In this contribution we address the impact of clustering in the angular domain on the svw expansion coefficients of the propagation channel. In our study we address the first and second order statistics of the svw modes under the Kronecker channel assumption and provide numerical simulation results.

2. GENERIC CHANNEL MODEL WITH 2 CLUSTERS

The statistical properties of the MIMO channel are readily characterized by the distributions of the angle-of-arrival (AoA) and the angle-of-departure (AoD) of the multipath components as well as their amplitudes, i.e., waves with arbitrary polarization departing from the transmit antenna and arriving at the receive antenna, respectively. The propagation channel can be modeled by a Gaussian vector field consisting of an unpolarized stochastic component with non-isotropic power angular spectra (PAS) [2]. Hence, each multimode coefficient in the svw expansion is a Gaussian variate and as a consequence the envelope of each multimode coefficient in the spherical vector wave expansion is a Rayleigh variate. For the sake of simplicity, we further consider the widely used Kronecker channel model which assumes that the AoA and AoD are statistically independent. We restrict our study to channels with up to two clusters. In this case the joint probability density function (joint pdf, which is basically the joint PAS normalized to unity) for the AoA and AoD has the following form

$$\begin{aligned} p_{\alpha\beta}(\theta_{\rm r},\phi_{\rm r},\theta_{\rm t},\phi_{\rm t}) \;=\; & c_1 p^{(1)}_{\theta_{\rm r}\alpha\beta}(\theta_{\rm r}) p^{(1)}_{\phi_{\rm r}\alpha\beta}(\phi_{\rm r}) p^{(1)}_{\theta_{\rm t}\alpha\beta}(\theta_{\rm t}) p^{(1)}_{\phi_{\rm t}\alpha\beta}(\phi_{\rm t}) \\ & + c_2 p^{(2)}_{\theta_{\rm r}\alpha\beta}(\theta_{\rm r}) p^{(2)}_{\phi_{\rm r}\alpha\beta}(\phi_{\rm r}) p^{(2)}_{\theta_{\rm t}\alpha\beta}(\theta_{\rm t}) p^{(2)}_{\phi_{\rm t}\alpha\beta}(\phi_{\rm t}), \end{aligned} \tag{1}$$

where the contributions from the two different clusters are denoted by sub- and super-indices 1 and 2, respectively; $\alpha = \{\theta, \phi\}$ and $\beta = \{\theta, \phi\}$ stands for $\hat{\boldsymbol{\theta}}$ or $\hat{\boldsymbol{\phi}}$ polarizations, c_1 and c_2 are weighting

factors such that $c_1 + c_2 = 1$. We further assume that the pdf of each cluster have the Laplacian distribution shape in spherical coordinates. For the AoA we then have

$$p_{\theta_{\mathrm{r}}\alpha\beta}(\theta) = A_\theta \mathrm{e}^{-\frac{\sqrt{2}|\theta-\mu_\theta|}{\sigma_\theta}} \sin\theta, \quad \theta \in [0,\pi] \tag{2}$$

$$p_{\phi_{\mathrm{r}}\alpha\beta}(\phi) = A_\phi \mathrm{e}^{-\frac{\sqrt{2}|\phi-\mu_\phi|}{\sigma_\phi}}, \quad \phi \in [-\pi,\pi), \tag{3}$$

where A_θ and A_ϕ are constants and the shape is controlled by the parameters μ_θ, σ_θ, μ_ϕ and σ_ϕ, where the σ are a measure of angle spread and the μ denote the average AoA. We assume a similar pdf for the AoD. The polarimetric properties of the channel are characterized by the cross-polarization ratio (XPR or χ) defined as the ratio of the power of the vertically polarized waves to the power of horizontally polarized waves. Here we assume that the powers of the cross-polarized components satisfy the identity $P_{\theta\phi} = P_{\phi\theta} = 0$ and therefore the XPR is completely determined by $\chi = \frac{P_{\theta\theta}}{P_{\phi\phi}}$ [3].

Table 1 shows the parameters of the four considered channels: Channel A, B, C and D. We have assumed balanced polarizations for all four channels, i.e., $P_{\theta\theta} = P_{\phi\phi}$. Hence, the response to vertically and horizontally polarized waves is similar in all cases. Channel A has only one cluster characterized by a large angle spread in both elevation and azimuth and therefore emulates a 3D uniform channel. Channels B and C have two clusters with different parameters of the AoA/AoD statistics, i.e., a combination of large and small angle spread clusters as illustrated in Fig. 1 for Channel C. Channel D has also two clusters, both with small angle spreads. The weighting factors $c_1 = 0.7$ and $c_2 = 0.3$ indicate that the likelihood of a contribution from *Cluster* 1 to the total number of multipaths is 70%, while for *Cluster* 2 it is 30%.

Table 1: Parameters of the distributions (1), (2) and (3).

	Channel A		Channel B		Channel C		Channel D	
	Tx	Rx	Tx	Rx	Tx	Rx	Tx	Rx
Cluster 1								
c_1	1.0		0.7		0.7		0.7	
σ_ϕ, [rad]	10	10	10	10	0.1	10	0.1	0.1
μ_ϕ, [rad]	0	0	0	0	0	0	$-\pi/4$	$\pi/6$
σ_θ, [rad]	10	10	0.1	10	0.1	10	0.1	0.1
μ_θ, [rad]	$\pi/2$	$\pi/2$	$\pi/2$	$\pi/2$	$\pi/2$	$\pi/2$	$\pi/2$	$\pi/2$
Cluster 2								
c_2	0		0.3		0.3		0.3	
σ_ϕ, [rad]			0.1	0.1	0.1	0.1	0.1	0.1
μ_ϕ, [rad]			0	0	$\pi/4$	$-\pi/4$	$\pi/6$	$-\pi/4$
σ_θ, [rad]			0.1	10	0.1	10	0.1	0.1
μ_θ, [rad]			$\pi/2$	$\pi/2$	$\pi/2$	$\pi/2$	$\pi/2$	$\pi/2$
χ, [dB]	0		0		0		0	

The relationship between the MIMO channel transfer function in terms of the svw expansion of the antennas, the channel and the AoA and AoD pdf is studied in [3]. There, we introduced the matrix $\mathbf{M} \in \mathbb{C}^{M_{\mathrm{r}} \times M_{\mathrm{t}}}$, which is a random matrix operator that maps the svw modes at the transmit antennas to the receive antennas. M_{t} and M_{r} are the number of relevant svw modes at the transmit and receive antenna, respectively. $\mathbf{M}$ describes the properties of the wireless channel in terms of the multimode expansion coefficients of the electromagnetic field and is the subject of our study. The focus of our work is to study the impact of clustering of the AoA and AoD on the statistics of $\mathbf{M}$ or equivalently its vectorized form $\mathbf{m} = \mathrm{vec}(\mathbf{M})$ obtained by stacking its columns one underneath the other. The second order statistics are characterized by the *full-correlation channel matrix* of the multimode channel

$$\boldsymbol{\mathcal{R}}_m = \langle \mathbf{m}\mathbf{m}^\dagger \rangle, \tag{4}$$

where $\langle\rangle$ denotes averaging over the random realizations of $\mathbf{m}$ and $(.)^\dagger$ denotes the hermitian matrix transpose operation.

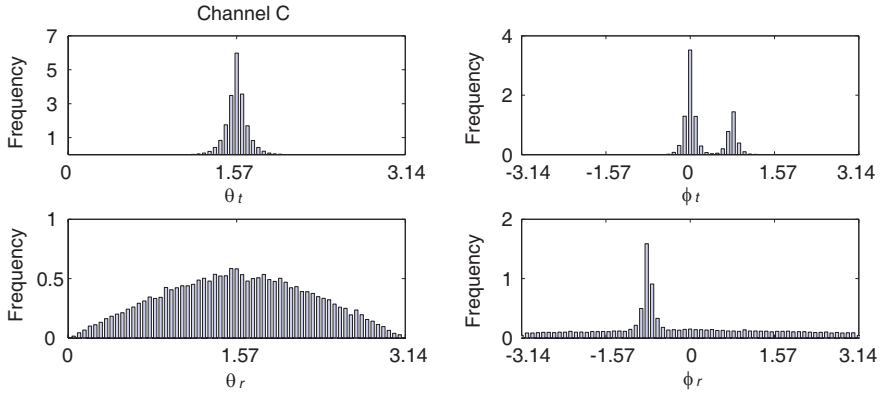

Figure 1: Pdf of the AoA and AoD corresponding to Channel C according to parameters in Table 1.

3. RESULTS AND ANALYSIS

Each svw mode can be characterized by three indices: τ, which denotes polarization, and m and l which give the azimuthal and radial dependencies, respectively. We now specialize our analysis to a MIMO propagation channel exciting dipole ($l = 1$) TE ($\tau = 1$) and TM ($\tau = 2$) modes, i.e., the six lowest svw modes. For the sake of compactness we introduce a multi-index notation $\iota = 2(l^2+l-1+m)+\tau$ to denote different multimodes at the transmit side. We use κ to denote the corresponding multi-index at the receive side. Hence an element of the multimode channel matrix is denoted as $M_{\iota,\kappa}$.

Figure 1 shows the average of the absolute value of each element of $\mathbf{M}$. As we can see, elements $|M_{3,3}| = |M_{4,4}| > |M_{\iota,\kappa}|$ for all other combinations of ι and κ, which is a result of a balanced XPR, i.e., $\chi = 0\,\mathrm{dB}$. The physical interpretation is, as expected, that the co-polarized dipole interactions (TM-TM and TE-TE interactions with $l = 1$ and $m = 0$) are the strongest in this type of channels. Moreover, the power into those modes increases as the angle spread of the clusters decreases.

Figure 2 shows the corresponding absolute value of the full-correlation matrix of the multimode channels defined above. Channel A shows a distinct diagonal structure of the correlation matrix since the PAS is spatially non-selective and has balanced polarizations. However, the powers of all modes are not equal since we have also assumed that $P_{\theta\phi} = P_{\phi\theta} = 0$. In particular, we have that $|M_{3,4}| = |M_{4,3}| = 0$; thus, $(\boldsymbol{\mathcal{R}}_m)_{(3,4)(\iota',\kappa')} = (\boldsymbol{\mathcal{R}}_m)_{(4,3)(\iota',\kappa')} = (\boldsymbol{\mathcal{R}}_m)_{(\iota,\kappa)(3,4)} = (\boldsymbol{\mathcal{R}}_m)_{(\iota,\kappa)(4,3)} = 0$ for all ι and κ, which also applies for all the other considered channels. In Fig. 2, this is shown by the orthogonal straight lines. The subindices (ι,κ) and (ι',κ') should be understood as the ones corresponding to element $(\boldsymbol{\mathcal{R}}_m)_{\iota+6(\kappa-1),\iota'+6(\kappa'-1)}$. As we go further to Channel B, C and D, we see that correlation between the modes increases due to more selectivity in the angular domain.

The full-correlation channel matrix, $\boldsymbol{\mathcal{R}}_m$, of the multimode channel can be treated in a similar way as the full-correlation matrix of the MIMO channel. For example, the eigenvalues $\boldsymbol{\mathcal{R}}_m$ denote the average powers of the independently fading matrix-valued eigenmodes of the multimode channel. Then, the offered degree of diversity can be quantified by the diversity measure (DM) defined as [4]

$$\Psi(\boldsymbol{\mathcal{R}}_m) = \frac{\left(\sum_{i=1}^{M_r M_t} \lambda_i\right)^2}{\sum_{i=1}^{M_r M_t} \lambda_i^2} \tag{5}$$

where λ_i are the eigenvalues of $\boldsymbol{\mathcal{R}}_m$. The larger the DM the greater the potential of diversity gain as illustrated in Fig. 4. We can see here that a channel with a flatter eigenvalue spectrum of $\boldsymbol{\mathcal{R}}_m$, e.g., Channel A has a larger DM than Channel D, which has a much faster decay in the eigenvalue spectrum. Here we see that for the considered channels the angle spread of each particular cluster plays a major role in the correlation characteristics of the multimode channel. Extrapolating, we may say that as the number of clusters increases the channel characteristics will tend to the characteristics of an isotropic or 3D uniform channel.

Figure 5 shows the cumulative distribution functions (cdf) of the envelopes of the 36 elements of matrix $\mathbf{M}$ for the four considered channels. By visual inspection we see that the cdfs seem to follow the Rayleigh distribution. This is a direct result of the channel model assumptions and the conservation of Gaussianity under affine transformations. Hence, the first order statistics of each svw is completely defined by its squared average shown in Fig. 2.

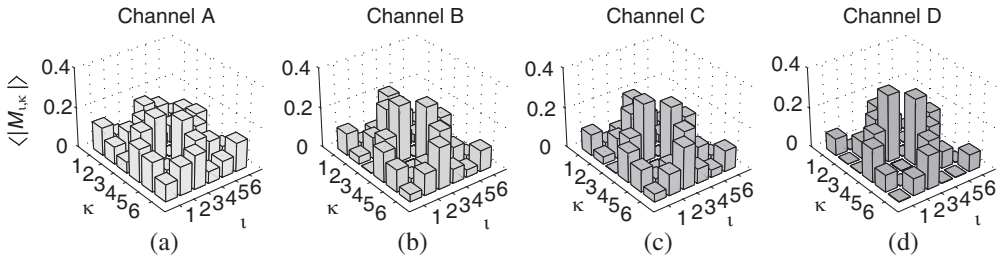

Figure 2: Aaverage of the absolute value of each element of $\mathbf{M}$ for the channels described in Table 1.

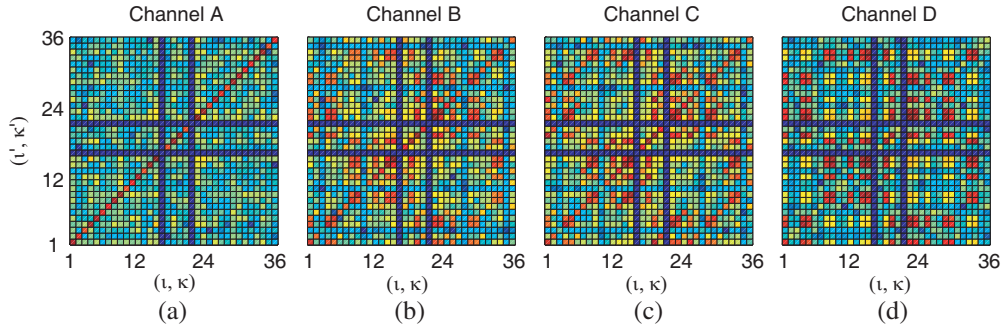

Figure 3: Absolute value of the full-correlation matrix $(\boldsymbol{\mathcal{R}}_m)_{(\iota,\kappa)(\iota'\kappa')}$ corresponding to the multimode channels described in Table 1. TE and TM dipole modes are considered

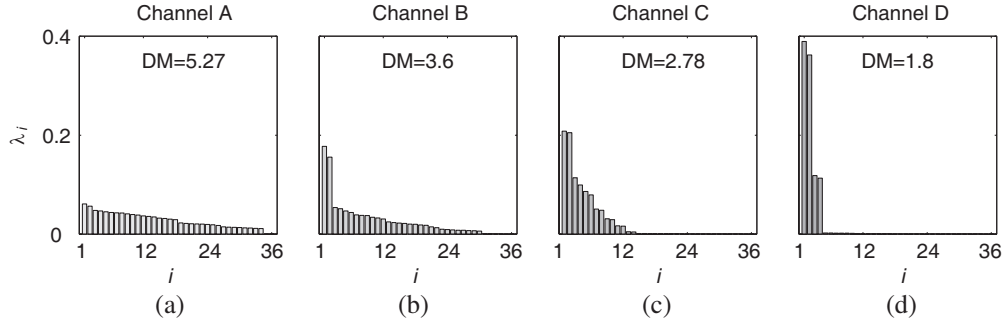

Figure 4: Eigenvalue spectrum of the full-correlation matrix $\boldsymbol{\mathcal{R}}_m$ corresponding to the multimode channels described in Table 1. The corresponding diversity measure is also given for each channel.

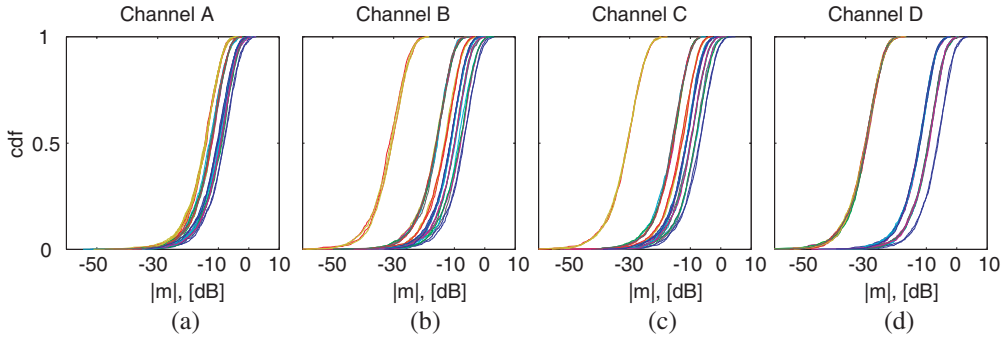

Figure 5: Cumulative distribution functions (cdf) of the envelopes of the 36 elements of matrix $\mathbf{M}$ for the multimode channels described in Table 1.

4. CONCLUSION

We have shown that the clustering of multipath components in Kronecker channels has a major impact on the first and second order statistics of the spherical vector waves (svw) expansion of the propagation channel mainly through the angle spread of each individual cluster. While the shape of

the distribution of the modes doesn't change, i.e., remains Rayleigh distributed, the average power of each mode changes as a function of the angle spread of the clusters. The correlation statistics and therefore the potential of a diversity gain highly depends upon the angle spread of each cluster. The spherical vector wave modes of the channel can be exploited in the same way as we exploit different antenna elements in MIMO systems. Hence, instead of tailoring antenna designs to the angular domain of the channel we could focus our efforts on the spherical vector wave multimode domain.

ACKNOWLEDGMENT

This work has been partly supported by the Marie Curie EU FP6 "GAWIND" project and the Marie Curie EU FP7 IAPP "IAPP@RANPLAN" project.

REFERENCES

1. Alayon Glazunov, A., M. Gustafsson, and A. F. Molisch, "On the physical limitations of the interaction of a spherical aperture and a random field," *IEEE Transactions on Antennas and Propagation*, Vol. 59, No. 1, January 2011.
2. Alayon Glazunov, A., M. Gustafsson, A. F. Molisch, F. Tufvesson, and G. Kristensson, "Spherical vector wave expansion of gaussian electromagnetic fields for antenna-channel interaction analysis," *IEEE Transactions on Antennas and Propagation*, Vol. 57, No. 7, 2055–2067, July 2009.
3. Alayon Glazunov, A., M. Gustafsson, A. F. Molisch, and F. Tufvesson, "Physical modelling of multiple-input multiple-output antennas and channels by means of the spherical vector wave expansion," *IET Microwaves, Antennas & Propagation*, Vol. 4, No. 6, 778–791, June 2010.
4. Ivrlac, M. T. and J. A. Nossek, "Quantifying diversity and correlation in Rayleigh fading MIMO communication systems," *Proceedings of the 3rd IEEE International Symposium on Signal Processing and Information Technology, 2003, ISSPIT 2003*, 158–161, 2003.
5. Li, K.-H., M. A. Ingram, and A. Van Nguyen, "Impact of clustering in statistical indoor propagation models on link capacity," *IEEE Transactions on Communications*, Vol. 50, No. 4, 521–523, April 2002.
6. Spencer, Q. H., B. D. Jeffs, M. A. Jensen, and A. L. Swindlehurst, "Modeling the statistical time and angle of arrival characteristics of an indoor multipath channel," *IEEE Journal on Selected Areas in Communications*, Vol. 18, No. 3, 347–360, March 2000.

Space Diversity Evaluation in Millimeter Band Wireless Communication Systems

Mehran Atamanesh and Forouhar Farzaneh
School of Electrical Engineering, Sharif University of Technology, Iran

Abstract— A simulation tool, based on Ray Tracing method, has been developed and validated for millimeter-wave band. This tool helps for predicting the signal level as well as the delay characteristics of a propagation channel. Since the resultant of the received replicas of the transmitted signal at receiver point can experience a deep fade and consequently the quality degradation, a proper diversity method can effectively alleviate this drawback. Using this simulation tool and extracting the received wave characteristics in a street scenario, an analytical expression for predicting the space diversity gain for the Selection Combining technique and Maximal-Ratio Combining technique has been proposed.

1. INTRODUCTION

In recent years, an ever-increasing growth of the demand for the new broadband communications services such as video conferencing, multi-media and high data-rate transmission has been observed. All these services need a higher data rate transmission than the conventional voice service and hence, need higher bandwidth [1]. Because of congestion in the frequency bands below 2 GHz, the attention of radio systems designers has tended to the higher frequency bands especially the unlicensed frequencies around 60 GHz [2–4]. Besides, in a typical wireless environment, the received signal is subjected to the fading phenomena and consequently quality degradation. One of the most effective methods to combat these phenomena is using diversity reception techniques [5].

In this paper, a software tool for predicting signal level in millimeter wave bands has been implemented which uses ray tracing method. In Section 2, the validation of this tool with the measurements will be presented. The space diversity will be studied in Section 3 with a proposed analytical expression and finally Section 4 draws the conclusion.

2. COMPUTATIONAL RESULTS AND VALIDATION

A good agreement between the simulated results with the ray tracing method and the measurements in an urban environment has been already shown [6, 7]. In ray tracing based on image method [8], the ray path will be determined when the position of the transmitter, receiver and objects causing propagation phenomenon are known. The objects have commonly flat surfaces (walls, ground). This method is useful for not too complicated environment, i.e., the propagation area with a relatively small number of reflecting surfaces. In this method, the first step is to find the virtual image of the transmitter relative to the surface, then by connecting the receiver and virtual image of the transmitter, it can be determined if the line intersects the object or not. If the answer is 'yes', the whole trajectory can be considered as a path from the transmitter, to the receiver. This procedure which takes into account the virtual image and determines the point of reflection on the surfaces is valid for multiple reflections of order N.

A program using MATLAB® has been written for predicting the signal level using image ray tracing method. For validation of this program we have chosen the measurement data of [9] at 62.4 GHz. Fig. 1 shows the environment of measurements. A vertically polarized 10 dBi standard horn antenna was used as the transmitter antenna. The E- and H-plane antenna beamwidth were 69° and 55°, respectively. It was set at a height of 3.1 m above ground. The received antenna was also mounted at a height of 2.8 m above the ground. It was also a vertically polarized omnidirectional antenna with a 3 dB elevation beamwidth of 6.5° and a gain of 6 dBi.

Measurements were made in two paths: LOS path along the street and equally spaced from the walls and the other path which includes LOS and NLOS parts. Simulation was made considering a permittivity and a conductivity of 6.81 and 0.95 S/m for the walls and 10 and 0.005 S/m for the ground, respectively. Fig. 2 shows the measured and simulated relative power of the LOS path. In the simulation, maximum number of reflections was set to two. Propagation through diffracted rays has a significant contribution to the received signal in the UHF-band microcellular wireless networks, but the power of the diffracted rays decays rapidly with the increasing of the electromagnetic wave frequency. Therefore, because of strong attenuation of edge diffraction in

millimeter wave, no diffracted ray was included in calculation of the relative received power. The walls were considered to be smooth. By comparing the measurement data with the simulation result, a good agreement can be concluded.

Figure 3 shows the measurement data and also simulated result made by [9] and also simulation result of our software of LOS and NLOS path. In this simulation, the maximum number of reflec-

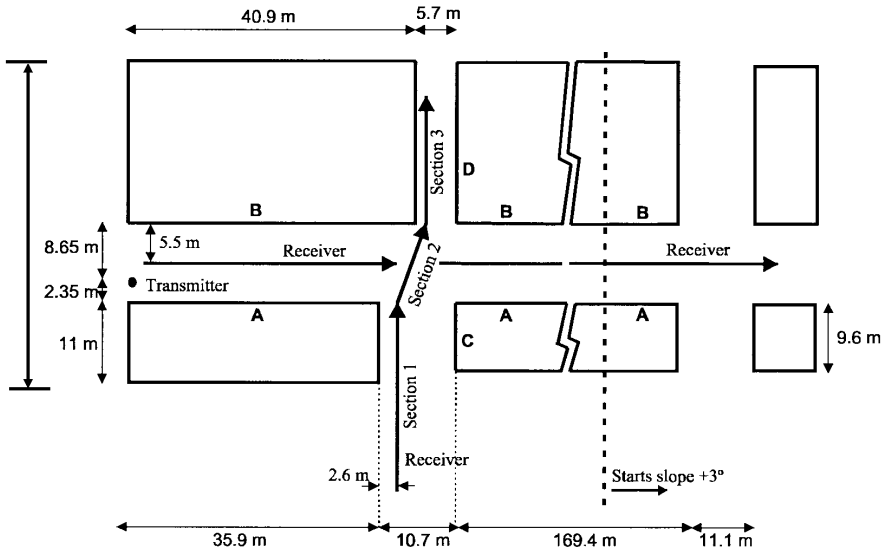

Figure 1: Measurement environment of [9].

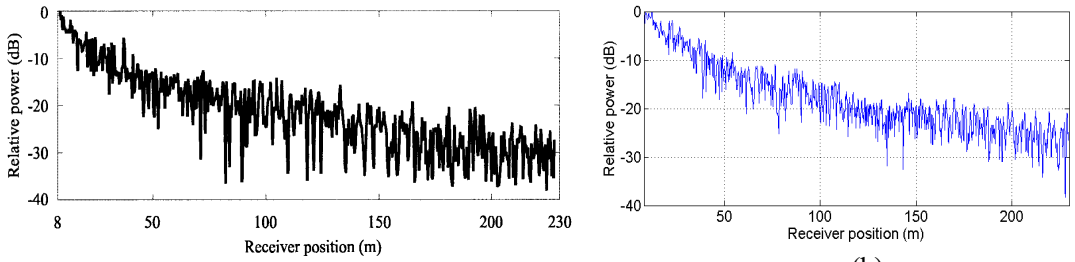

Figure 2: Relative power (dB) for LOS path. (a) Measured [9]. (b) Simulated.

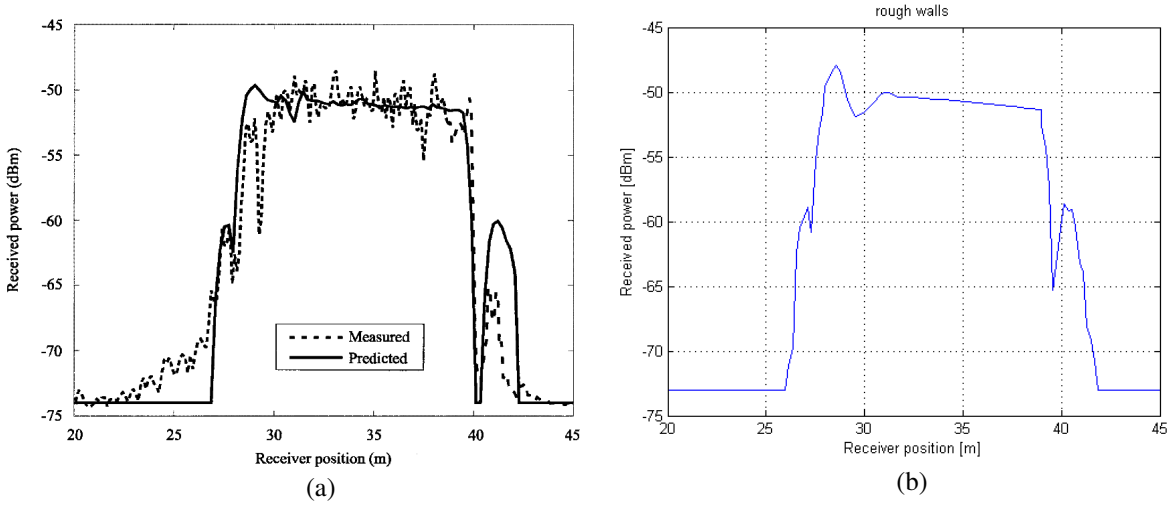

Figure 3: Received power (dBm) for LOS and NOLS path, (a) measurement and simulation in [9], (b) our simulation.

tions was set to two and no diffracted ray was included. Roughness standard deviation of 6.2 mm was taken into account for the walls. Assuming a Gaussian distributed surface roughness with standard deviation σ_h [m], the scattered electric field is computed using the following simplified formulation [10]:

$$R_s = R \cdot e^{-(g/2)} \tag{1}$$

where, R is the Fresnel reflection coefficient and g is a measure of the roughness of the surface which is calculated using:

$$g = \left(\frac{4\pi\sigma_h \cos\theta}{\lambda} \right)^2 \tag{2}$$

where, λ is the wavelength in meters and θ is the incident angle.

Again, by comparing the measurements with the simulation, a good agreement can be concluded from the above mentioned figure. There are also a little discrepancies which could arise from the difference between the angular separation of the rays or the differences between the antenna patterns in our simulation and those of [9].

3. DIVERSITY GAIN EVALUATION IN A STREET

For further simulation, we have chosen a street scenario, with the street width of 6 meters. The buildings' walls and the ground were assumed to have equal relative permittivity of 6 and equal conductivity of 0.1 S/m. Transmitter and receiver locations are shown in Fig. 4. The transmitter and receiver antennas are omni-directional and vertically polarized.

The electric filed was calculated using image method each 2 meters in a window of $40\lambda \times 40\lambda$ and with a step of $\lambda/5$ within the window. For space diversity implementation, we can either use a selection combiner or a maximal-ratio combiner. The combiner's output voltage can be calculated by (3) [11].

$$v_c = \begin{cases} \max(v_1(t), v_2(t)) & \text{for selection} \\ \sqrt{v_1^2(t) + v_2^2(t)} & \text{for maximal-ratio} \end{cases} \tag{3}$$

Diversity gains for each window were computed for various antenna separation and direction in the receiver. Fig. 5 shows the alignment of receiving antennas with respect to the transmitter.

After computing the diversity gain in each window, the gain values were averaged over the entire windows. Fig. 6 shows these values for different combining techniques.

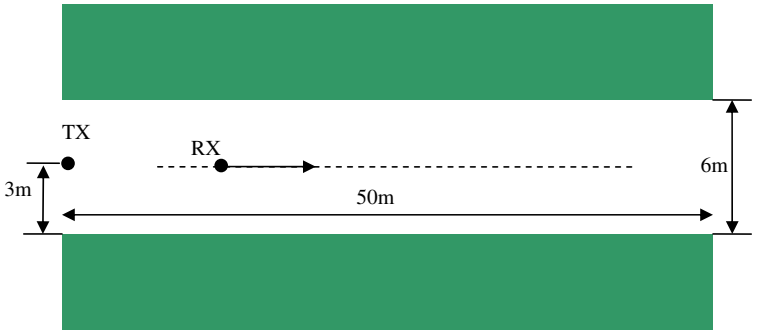

Figure 4: The simulation scenario.

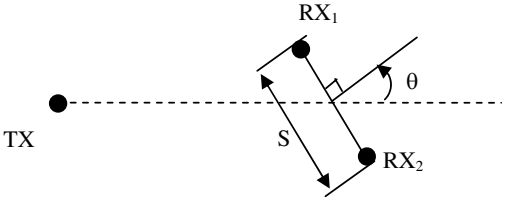

Figure 5: Receiving antennas alignment with respect to the transmitter.

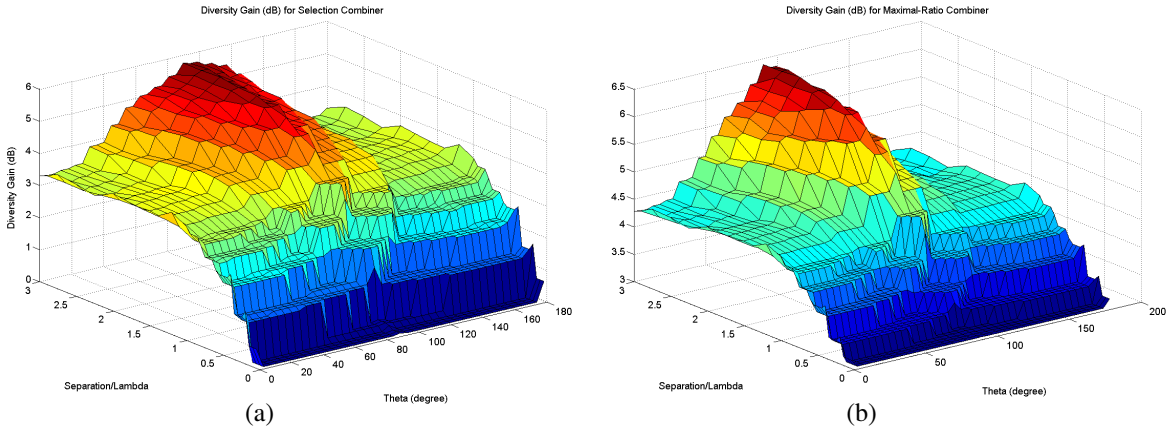

Figure 6: Diversity gain versus antenna separation and direction. (a) Selection combiner. (b) Maximal-ratio combiner.

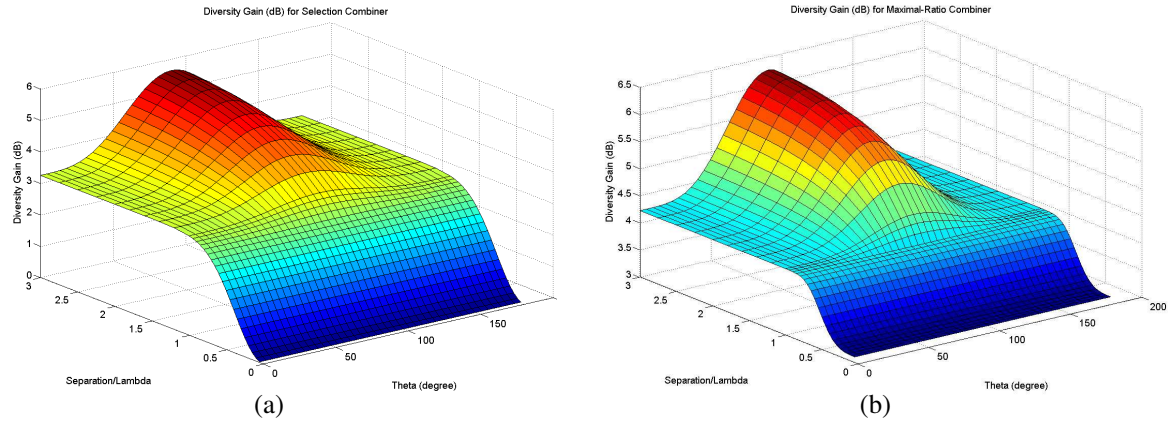

Figure 7: The fitted curves of diversity gain. (a) Selection combiner. (b) Maximal-ratio combiner.

Table 1: The parameters of (4) optimized using genetic algorithm.

Method	p_1	p_2	p_3	p_4	α	β	γ	η	K
SC	3.2399	3.2439	3.6071	2.0560	2.4695	3.5056	0.5373	1.7581	3.5794
MRC	4.2186	1.1180	8.7350	3.9031	2.1102	8.8265	1.6691	0.9564	4.2639

Now we try to find an analytical expression for describing the diversity gain. As it can be seen in Fig. 6, diversity gain increases with the ratio of S/λ, but it saturates for the larger values, therefore it can be approximated with an exponential function. On the other hand, in θ-direction, the diversity gain is periodic; we have assumed that the variation of diversity gain is proportional to $\sin^{\kappa}(\theta)$. Therefore we have chosen the following function for diversity gain:

$$G_{div} = p_1 - p_2 e^{-\alpha(S/\lambda)^{\beta}} + \left(p_3 - p_4 e^{-\gamma(S/\lambda)^{\eta}}\right) \sin^{\kappa}(\theta) \tag{4}$$

The above equation was optimized using genetic algorithm and the coefficients which minimize the deviation of (4) from the ray tracing. Table 1 shows the optimized parameter values.

Figure 7 also shows the fitted curves of diversity gain using (4).

As it can be seen in Fig. 7, the resulting curves are in well with the simulation results.

4. CONCLUSION

In this paper, we have presented the implementation a software tool for prediction of signal level in millimeter wave frequencies using ray tracing method. The results of the software were compared with the measurement data and a good agreement between measurement and simulation was

concluded. Using this software we obtained the diversity gain versus antenna separation and alignment. An analytical function was proposed for predicting the diversity gains in terms of distance and alignment of antennas for different combining techniques. The coefficients of this function have been optimized using genetic algorithm. The fitted function matches well with the simulation results.

REFERENCES

1. Prasad, R. and M. Ruggieri, *Technology Trends in Wireless Communications*, Artech House, Boston, London, 2003.
2. FCC, *Code of Federal Regulation, Title 47 Telecommunication*, Chapter 1, Part 15.255, October 2004.
3. ERC Recommendation 12-09, "Radio frequency channel arrangement for fixed service systems operating in the band 57.0–59.0 GHz which do not require frequency planning," The Hague 1998, revised Stockholm, October 2004.
4. ECC Recommendation (05)02, "Use of the 64–66 GHz frequency band for fixed services," June 2005.
5. Parson, J. D., *The Mobile Radio Propagation Channel*, 2nd Edition, John Wiley & Sons Ltd., 1992.
6. Erceg, V., A. J. Rustako, and R. S. Roman, "Diffraction around corners and its effects on the microcell coverage area in urban and suburban environments at 900 MHz, 2 GHz, and 6 GHz," *IEEE Transactions on Vehicular Technology*, Vol. 43, 762–766, August 1994.
7. Schaubach, K. R., N. J. Davis, and T. S. Rappaport, "A ray tracing method for predicting path loss and delay spread in microcellular environments," *42nd IEEE Vehicular Technology Conf.*, Vol. 2, 932–935, Denver, CO, May 1992.
8. Catedra, M. F. and J. P. Arriaga, *Cell Planning for Wireless Communications*, Artech House Publishers, Boston, London, 1999.
9. Hammoudeh, A. M., M. G. ı. S'anchez, and E. Grindrod, "Experimental analysis of propagation at 62 GHz in suburban mobile radio microcells," *IEEE Transactions on Vehicular Technology*, Vol. 48, 576–588, March 1999.
10. Beckmann, P. and A. Spizzichino, *The Scattering of Electromagnetic Waves from Rough Surfaces*, Artech House, Norwood, MA, 1987.
11. Turkmani, A. M. D., A. A. Arowojolu, P. A. Jefford, and C. J. Kellett, "An experimental evaluation of the performance of two-branch space and polarization diversity schemes at 1800 MHz," *IEEE Transactions on Vehicular Technology*, Vol. 44, No. 2, May 1995.

Angle of Arrival and Doppler Spectrum in the Presence of Generalized Two-dimensional Anisotropic Scattering

Petros Karadimas and Jie Zhang
Centre for Wireless Network Design (CWIND), Department of Computer Science and Technology
University of Bedfordshire, LU13JU, Luton, UK

Abstract— In this paper, we present a generalized theoretical model for the angle of arrival (AOA) in wireless channels when the scattering is two-dimensional (2-D) anisotropic. This model can constitute a platform for creating new angular distributions for the propagating multipath power and as such, a new distribution accounting for multi-modal arrival will be presented. The latter will represent the case that multipath power arrives into four angular sectors being parametrically defined with respect to the direction of the receiver motion. From the AOA, the power spectral density (PSD) of the received complex signal is analytically derived. Further generalization with multi-modal arrival into an arbitrary number of angular sectors can be treated similarly.

1. INTRODUCTION

In wireless channels, two dimensional (2-D) scattering occurs when the travelling distances between the transmitter, the surrounding scatterers and the receiver are long enough such that the propagation can be characterized as that from the horizon [1]. We consider the arrival of multipath power, but, as the wireless channel is reciprocal, the same analysis can be valid for the departure of multipath power. In the classical paper of Clarke [2], we can see the simplest 2-D scattering scenario with a uniform distribution for the azimuth angle of arrival (AOA) (i.e., 2-D isotropic scattering). 2-D anisotropic scattering is more realistic and is caused when a part of power is blocked by the channel obstacles (shadowing effect) and/or no multipath power arrives from certain directions due to lack of scattering objects in those directions and/or directional receiving antennas are employed. In such case, several distributions have been considered for the azimuth AOA, where the most commonly used distributions in the uplink case (i.e., mobile transmitter and static receiver) are the raised cosine [3], the restricted uniform [4], the Gaussian [5] and the Laplacian [6]. In the downlink case (i.e., static transmitter and mobile receiver) the most common distributions are the Laplacian [7] and von Mises [8].

From the directional statistics of the propagating multipath power, we can end up to the temporal autocorrelation function (ACF) and power spectral density (PSD) of the received complex signal. The time selectivity of wireless channels is explicitly related to these metrics (ACF and PSD) [9], from which we can further derive the level crossing rate (LCR) and average fades duration (AFD) (i.e., the second order statistics) [10, Ch. (6)]. Thus, the first step is to establish theoretical flexible models in order to characterize the directional statistics and maximize the benefits from future measurement campaigns. Then, the second step is the collection of real world data drawn from such measurement campaigns and the appropriate parameter tuning of available theoretical models. In this paper, we deal with the first step, i.e., the establishment of a new theoretical modeland we are focused on multi-modal propagation contrary to unimodal, which was considered in the majority of published research. A parameterized version with multi-modal arrival of multipath power into four distinct angular sectors is then studied and we proceed on the analytical derivation of the power spectral density (PSD) in a mobile wireless channel. In 2-D scattering environments, the PSD was analytically calculated for the case of uniform [2] and von Mises distribution [8] and an omni-directional receiving antenna. We can see analytical PSDs for 2-D isotropic scattering and directional receiving antennas in [11–13]. Asymmetrical and discontinuous PSDs, which can be arisen by 2-D anisotropic scattering, were presented in [10, Ch. (6)].

The remaining of this paper is organized as follows. Section 2 gives the theoretical model for the arrival of multipath power when the scattering is 2-D anisotropic and is confined into an arbitrary number of angular sectors. Accordingly, a generic form for the AOA distribution is presented. Section 3 presents a parameterized case study with multi-modal arrival into four angular sectors (one sector per each azimuth quadrant). In this case, the PSD of the received complex signal in the mobile wireless channel is analytically derived. Finally, Section 4 concludes this paper with a synopsis of the main results and advantages of the proposed theoretical model.

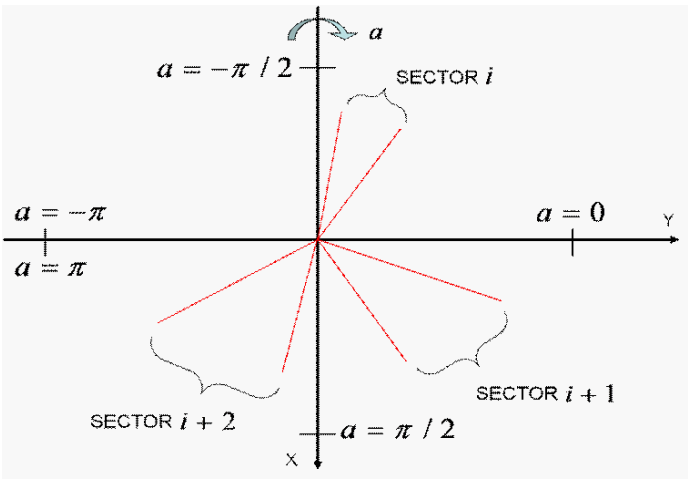

Figure 1: Azimuth AOA and discrete sectors of arrival.

2. THEORETICAL MODELING

We assume that multipath power propagates in the XY plane and the azimuth AOA a counts from the value $a = -\pi$ in the negative Y axis returning to the same point in the clockwise direction. An elemental probability dP_i is related to the arrival of multipath power into an elemental azimuth angle da within the 2-D azimuth sector i ($i = 1, 2, \ldots, I$, see Fig. 1) as

$$dP_i = S_i(a)da/a_T \tag{1}$$

where $S_i(a)$ are positive valued functions defined in the angular range of each sector i, which parameterize the arrival of multipath power in each sector i. Moreover, $a_T = \sum_i a_i$ is the total azimuth angle in which multipath power arrives and $a_i = \int_i da = \int_{A_{\min i}}^{A_{\max i}} da = A_{\max i} - A_{\min i}$ is the angular range for each sector i. With such a formulation, any arbitrary 2-D anisotropic scattering scenario can be modeled as the parametric percentage of contribution to the total received power of all sectors. The total azimuth angle will be

$$a_T = \sum_i (A_{\max i} - A_{\min i}) \tag{2}$$

where $A_{\min i}$ and $A_{\max i}$ are the minimum and maximum azimuth angles for each sector i, respectively ($-\pi \le A_{\min i} \le A_{\max i} \le \pi$). Moreover, the elemental probability dP_i will also arise from the AOA distribution denoted by $p_i(a)$in each sector i. Thus,

$$dP_i = p_i(a)da. \tag{3}$$

From (1) and (3), with the aid of (2), the distribution $p_i(a)$ will be

$$p_i(a) = \frac{S_i(a)}{\sum_i (A_{\max i} - A_{\min i})}. \tag{4}$$

Thus, from (4), the total distribution $p(a)$ will be

$$p(a) = p_i(a) \;\forall\; a \;\in\; \textit{angular range of sector } i. \tag{5}$$

The restricting condition for $S_i(a)$ arises with the aid of (4) and (5) as

$$\sum_i \int_i S_i(a)da = \sum_i (A_{\max i} - A_{\min i}). \tag{6}$$

3. A PARAMETERIZED CASE STUDY

We study the mobile wireless channel in the downlink case and without losing generality, we consider a standard direction for the receiver's motion and then we can parametrically define the arrival of multipath power with respect to that direction and plane. Thus, we consider that the receiver moves on the XY plane towards the positive Y axis. We assume that multipath power arrives into four distinct sectors confined to each one of the four azimuth quadrants. The four quadrants (Q1–Q4) in the azimuth XY plane are defined for values of as Q1: $0 \leq a \leq \pi/2$, Q2: $\pi/2 \leq a \leq \pi$, Q3: $-\pi/2 \leq a \leq 0$, and Q4: $-\pi \leq a \leq -\pi/2$. In the azimuth plane, the marginal angles $a_{\min i}$ and $a_{\max i}$, $(i = 1, 2, 3, 4)$, restrict the arrival of multipath power in each sector (S1–S4) as follows S1: $a_{\min 1} \leq a \leq a_{\max 1}$, S2: $\pi - a_{\max 2} \leq a \leq \pi - a_{\min 2}$, S3: $-a_{\max 3} \leq a \leq -a_{\min 3}$ and S4: $-\pi + a_{\min 4} \leq a \leq -\pi + a_{\max 4}$, where $0 \leq a_{\min i} \leq a_{\max i} \leq \pi/2$, $(i = 1, 2, 3, 4)$. The usefulness of such definitions for the sectors will be demonstrated during the calculation of the PSD. In Fig. 2, we can see the geometry for this specific case study with all the previously defined parameters.

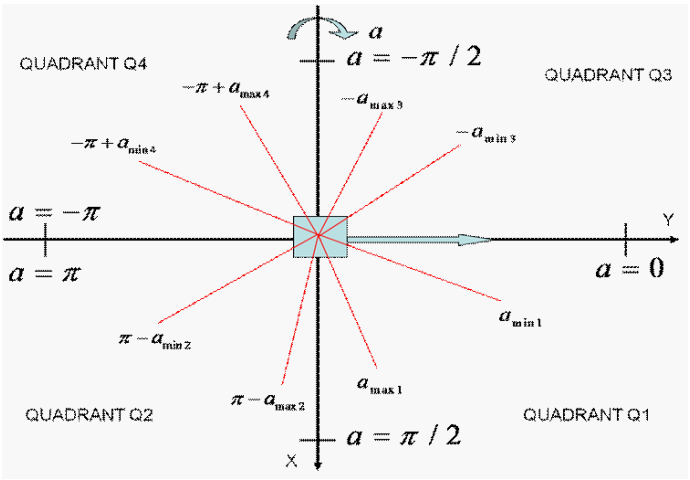

Figure 2: Geometry and sectors of arrival for the parameterized case study.

We consider positive valued constants for the contribution of each sector (i.e., no dependence from of a). For this case, the azimuth AOA distribution will be given with the aid of (4) and (5) as

$$p(a) = \begin{cases} S_1 \Big/ \sum_{i=1}^{4} (a_{\max i} - a_{\min i}), & a_{\min 1} \leq a \leq a_{\max 1} \\ S_2 \Big/ \sum_{i=1}^{4} (a_{\max i} - a_{\min i}), & \pi - a_{\max 2} \leq a \leq \pi - a_{\min 2} \\ S_3 \Big/ \sum_{i=1}^{4} (a_{\max i} - a_{\min i}), & -a_{\max 3} \leq a \leq -a_{\min 3} \\ S_4 \Big/ \sum_{i=1}^{4} (a_{\max i} - a_{\min i}), & -\pi + a_{\min 4} \leq a \leq -\pi + a_{\max 4} \\ 0, & otherwise \end{cases} \tag{7}$$

where S_i, $(i = 1, 2, 3, 4)$, are positive valued constants accounting for the contribution of each sector. The PSD $R(f)$ can be derived with the aid of [11, Eq. (5)] as

$$R(f) = R_1(f) + R_2(f) + R_3(f) + R_4(f) \tag{8}$$

where

$$R_1(f) = \begin{cases} \frac{S_1}{\sum_{i=1}^{4} (a_{\max i} - a_{\min i})} \cdot \frac{1}{\sqrt{f_{\max}^2 - f^2}}, & f_{\max} \cos a_{\max 1} \leq f \leq f_{\max} \cos a_{\min 1} \\ 0, & otherwise \end{cases} \tag{9}$$

$$R_2(f) = R_1(f)/_{f \to -f, a_{\min 1} \to a_{\min 2}, a_{\max 1} \to a_{\max 2}, S_1 \to S_2} \tag{10}$$

$$R_3(f) = R_1(f)/_{a_{\min 1} \to a_{\min 3}, a_{\max 1} \to a_{\max 3}, S_1 \to S_3} \tag{11}$$

$$R_4(f) = R_2(f)/_{a_{\min 2} \to a_{\min 4}, a_{\max 2} \to a_{\max 4}, S_2 \to S_4}. \tag{12}$$

with $f = f_{\max} \cos a$ the Doppler frequency shift. In (10)–(12), the notation after the slash implies substitution of the parameters at the left side of the arrows with the respective at the right side, arising from the definitions of the sectors of arrival with the aid of $a_{\min i}$ and $a_{\max i}$, $(i = 1, 2, 3, 4)$. The PSD is depicted graphically in Fig. 3 for a parameter set defined as $a_{\max 1} = a_{\max 3} = \pi/2.5$, $a_{\max 2} = a_{\max 4} = \pi/2.2$, $a_{\min 1} = \pi/6$, $a_{\min 2} = \pi/9$, $a_{\min 3} = \pi/3$, $a_{\min 4} = \pi/3.5$, $S_1 = 1.271$, $S_2 = 0.508$, $S_3 = 2.542$, $S_4 = 1.017$ and $f_{\max} = 91$ Hz. We see that the PSD becomes discontinuous and unsymmetrical, with these properties being strongly dependent on the parameters of the AOA distribution.

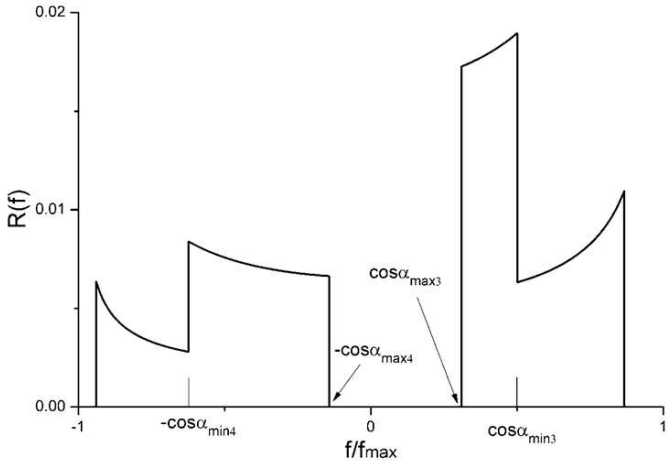

Figure 3: PSD of the received complex envelope.

4. CONCLUSIONS

A generalized theoretical model accounting for 2-D anisotropic scattering was studied and it was shown that it can be easily parameterized. With such formulation any 2-D anisotropic scattering scenario can be mapped onto the generalized model. Due to its high flexibility and easy parameterization, it can constitute a promising theoretical tool for applying it to future measurement campaigns and maximizing the benefits from them.

REFERENCES

1. Durgin, G. D. and T. S. Rappaport, "Theory of multipath shape factors for small-scale fading wireless channels," *IEEE Trans. Ant. and Propag.*, Vol. 48, No. 5, 682–693, May 2000.
2. Clarke, R. H., "A statistical theory of mobile-radio reception," *Bell Syst. Tech. J.*, Vol. 47, 957–1000, Jul./Aug. 1968.
3. Lee, W. C. Y., "Effects on correlation between two mobile radio base-station antennas," *IEEE Trans. Commun.*, Vol. 21, No. 11, 1214–1224, Nov. 1973.
4. J. Salz and J. H. Winters, "Effect of fading correlation on adaptive arrays in digital mobile radio," *IEEE Trans. Veh. Technol.*, Vol. 43, No. 4, 1049–1057, Nov. 1994.
5. Adachi, F., M. T. Feney, A. G. Williamson, and J. D. Parsons, "Cross-correlation between the envelopes of 900 MHz signals received at a mobile radio base station site," *IEE Proc.*, Vol. 133, No. 6, 506–512, Oct. 1986.
6. Pedersen, K. I., P. E. Morgensen, and B. H. Fleury, "Power azimuth spectrum in outdoor environments," *Electr. Letters*, Vol. 33, No. 18, 1583–1584, Aug. 1997.
7. Spencer, Q. H., B. D. Jeffs, M. A. Jensen, and A. L. Swindlehurst, "Modeling the statistical time and angle of arrival characteristics of an indoor multipath channel," *IEEE Journal Selec. Areas Commun.*, Vol. 18, No. 3, 347–360, Mar. 2000.
8. Abdi, A., J. A. Barger, and M. Kaveh, "A parametric model for the distribution of the angle of arrival and the associated correlation function and power spectrum at the mobile station," *IEEE Trans. Veh. Technol.*, Vol. 51, No. 3, 425–434, May 2002.
9. Bello, P. A., "Characterization of randomly time-variant linear channels," *IEEE Trans. Commun. Syst.*, Vol. 11, 360–393, Dec. 1963.
10. Patzold, M., "Mobile fading channels," *Chichester*, Wiley, U.K., 2002.

11. Gans, M. J., "A power-spectral theory of propagation in the mobile-radio environment," *IEEE Trans. Veh. Technol.*, Vol. 21, No. 1, 27–38, Feb. 1972.
12. Xu, C. Q., C. L. Law and S. Yoshida, "On the doppler power spectrum at the mobile unit employing a directional antenna," *IEEE Commun. Letters*, Vol. 5, No. 1, 13–15, Jan. 2001.
13. Ng, W. T. and V. K. Dubey, "Comments 'On the doppler power spectrum at the mobile unit employing a directional antenna'," *IEEE Commun. Letters*, Vol. 6, No. 11, 472–474, Nov. 2002.

A New Approach for Measurements of Signal Level Contents in a Real Wireless System in the City of Curitiba, Brazil

H. Tertuliano Filho[1], **G. D. Patriota**[1], **C. Alves**[1], **J. Carvalho**[1], **W. H. Fiorese**[1], **R. Schumacher**[1], **C. A. Dartora**[1], **and J. R. Descardeci**[2]

[1]Department of Electrical Engineering, Federal University of Parana, Curitiba 81531-990, PR, Brazil
[2]Center of Engineerings, Federal University of Tocantins, Palmas 77020-210, TO, Brazil

Abstract— This paper describes a study of the mobile radio signal's attenuation due the environment in the central and urban building-up area of Curitiba's downtown, a Brazilian city in the South of the country with more than two million inhabitants. The original results presented in this work are real life data collected from a major mobile operator in the city and it includes shapes of buildings in the region under study. The propagation model used for mobile radio channels was a free and adjustable model without diffraction. The morphology, the topography, the real images of the downtown and all technical parameters of the used radio-base channel are presented, explained and justified in this study. Only Omni-directional antennas were used and frequency hope was also considered. The analysis of the simulated results obtained using the PRORAD* software with practical data-base, proven that the proposed technique that uses one free propagation model enables the detection of the interference points in a system and uses this technique to avoid critical points; enables to cover a wide range of frequencies and technologies and provides average value of adjacent and co-channel interference over this single propagation model used appears to be viable in the 4G technology; giving appropriate solutions and offering advantages over existing usual techniques.

1. INTRODUCTION

The evolution of the telecommunications can be observed through the several generations that have succeeded in mobile communications. In only 20 years, the mobile communications have developed of a quite vague concept for an important market of 500 million users, or the equivalent approximately to 55% of the world plant of fix telephony. Until the moment, there are in use in Brazil two generations of mobile communications commercially denominated 2G and 3G. The Fourth Generation of Mobile Communications (4G), which is succeeding the 3G, it, is still a subject for the scientific community and the telecommunications market [1, 2]. Actually, the 4G is in final phase of studies and specification with the participation of equipments development companies and systems as Alcatel, Ericsson Telephone, Nokia Siemens Networks, network operators (NTT DoCoMo, for example), normative institutions, in this case, ITU Working Group 8F, and research and development centers all around the world, mainly in the European continent, in Japan and in the United States. An important directing outstanding for the development of 4G is the accomplishment a global network covering, looking for the integration of the several systems of existent telecommunications (3G, W-LAN, Bluetooth, PSTN, etc.) [3]. Thus, the intention is to create a great global network of mobile communications, independent of the system or technological generation in analysis. In this context, the satellites network is pointed as central piece for the constitution of the 4G network, providing the integration among the systems and enlarging the reach of the network for an area of global covering [4]. In this context, this research study presents an original proposal for a conception of a wireless prediction technique system in order to customize the effects of morphology and topography and also minimize the noise and interference parameters that degrade the capability of a real wireless system using a free propagation model with few adjustments. It's due, in view to measure the ideal level of the signal and compare with the collected drive-test real signal. The main goal it will be to select a free specified statistic propagation model but not the usual Cost 239, Lee-Picknard Optimized, Okumura-Hata or Modified Micro cells and use this free model to observe the behavior of the channel ERBCTRF01A, over co-channel and adjacent interference (this selected propagation model certainly it can be used in the 4G). For that, the downtown city of Curitiba in the south of Brazil with more than two million inhabitants will be used. The wireless specified system will be constituted of twelve base transceiver station BTS. It is important to observe that the master radio-base station will be located in the downtown of the city (Lat: 25 ° 27' 4.63" South and Long: 49 ° 14' 1.87" West) and the propagation predictions will be made both by the Brazilian software CelPlanWireless Global Technologies [5] and also with

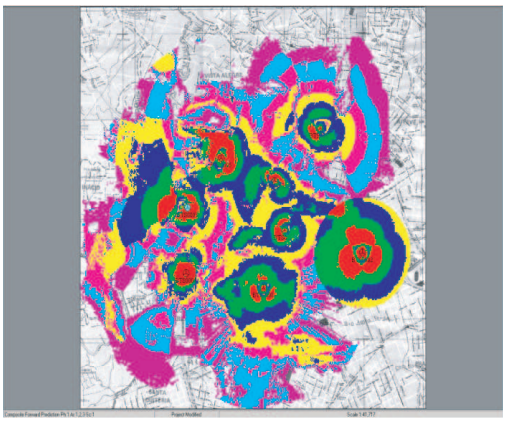

Figure 1: Summarized idea of the proposed simulation model prediction in Curitiba downtown using the CelPlanWireless Global Technologies, TEMS and PRORAD.

one American prediction software TEMS from Marconi. All obtained predictions results will be treated by the software PRORAD in view to use the statistic free model under development in Lab Telecom at UFPR. The morphology and the topography aspects of the city of Curitiba are very important and will be taken into consideration. Indeed, the building-up environment will be described in both software in terms of statistical parameters, such as the average row spacing and the building-up height distribution, as a basis for making propagation predictions for this free used model [6, 7]. In each simulation this specific propagation model used by PRORAD will be considered and the relevant aspects of interference will be inferred. After the simulation of this considered model, it will be possible to observe the best behavior of the considered channel, compare it with the real life data drive test and make adjustments. The central idea of this research study can be summarized and observed in the Figure 1. In order to certify the veracity of the obtained results it was been used to make predictions real database drive test for the downtown area including shapes of buildings in the region under study, omni-directional antennas and frequency hope. Than the comparative analysis of the simulated results obtained using PRORAD software with practical data-base, proven that the proposed technique that use one free propagation model give adequate solution and offers advantages over existing usual techniques like for instance:

1. Possibility to detect more precisely points of interference in a system and use this technique to avoid critical points, because in greatest cities, a physical free space to put antennas is not so easy to find out.
2. Possibility to cover a wide range of frequencies and technologies (FDMA, GSM, CDMA ONE ...).
3. Provide an average value of adjacent and co-channel interference over this single prediction mode used.

2. SIMULATIONS

The procedure for the accomplishment of the simulations was based on real life data collected by mine of one drive-test that has been supplied by a major local operator of cellular telephony, whereby through a simulation software (PRORAD) and a signal prediction it has obtained, with the integration of the data of drive-test, a level of signal considered for such tool. The software PRORAD developed at Lab Telecom at UFPR in version 1.0 was initially configured with the significant data of the relief, the morphology and the topography, beyond images of the city of Curitiba where drive-test was become fulfilled. At Figure 2 below, in (a) it can see the image of the route which the data was collected in the downtown of Curitiba in the urban area and also in the dense urban area. The colors in the figure represent the level of received signal in each point. In (b) it can see the topography for the same region.

The Table 1 shows the realized adjustments in BTS CTRF01A.

The antennas used in the simulations are from KATHREIN Mobilcom Brazil model 742212; the diagrams of irradiation for each TILT were supplied by the proper manufacturer. Figure 3 shows the diagram of irradiation of the horizontal opening, vertical opening and the diagram in 3D

(a) (b)

Figure 2: (a) Urban density of the region where it was made the drive-test. (b) Topography of the region where it was made the drive-test.

Table 1: Basic configurations of the radio transceiver station.

Forward Link	
Amplifier Output Power (W):	65.00
Transmission Loss (dB):	5.7
Cable Loss (dB/100 m):	2.43
Cable Length (m):	46
Connection Loss (dB):	0.5
Number of Connections:	4
Base Antenna Gain (dBd):	15.6
Minimum Access Level (dBm):	−100

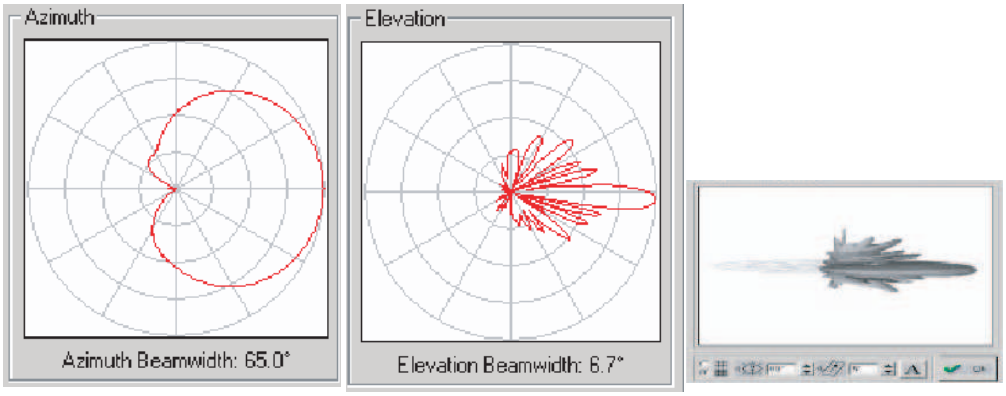

Figure 3: 2D and 3 D irradiation diagram of the antenna 742212.

respectively. It is important to say that for each electric TILT we have a new diagram of irradiation, in the case of the Figure 3 electric TILT has a value of 2 °.

For the visualization of the height, tilt, azimuth and geographic coordinates of the ERB our software PRORAD with Google Maps API integrations was used [8].

3. RESULTS

The PRORAD software after the adjusts in the main prediction parameters obtain the values of the average deviation, the standard deviation and also the radiated power for each type of considered morphology for the total amount of samples, the frequency, the channel, the azimuth and the power that it was considered. Figure 4 shows the graphic with these attenuation results due the environment with regard to the increase of the frequency.

The green line (level −25.42) shows the average level of the signal and the red line shows the linearization. It was used the same procedure to obtain the values of the average deviation, the standard deviation and radiated power only for at least 250 samples inside of the irradiation cone

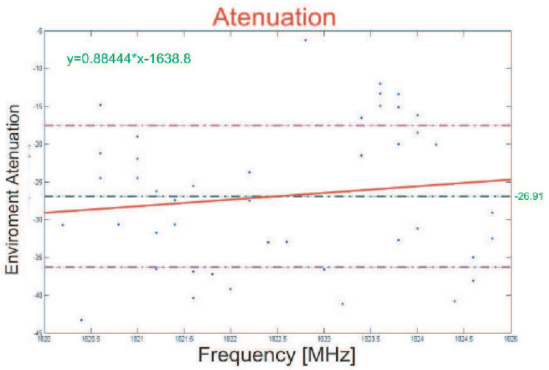

Figure 4: Attenuation due the environment for the specified frequency.

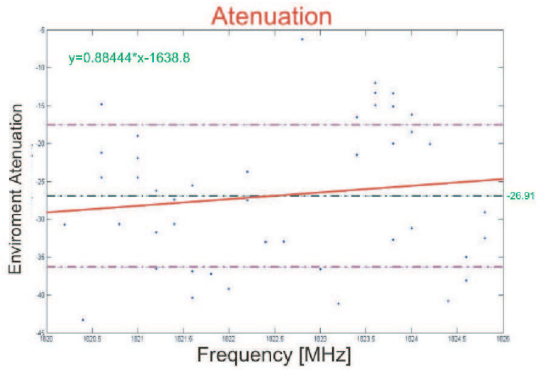

Figure 5: Attenuation due the environment using up 250 samples in the irradiation cone of the antenna.

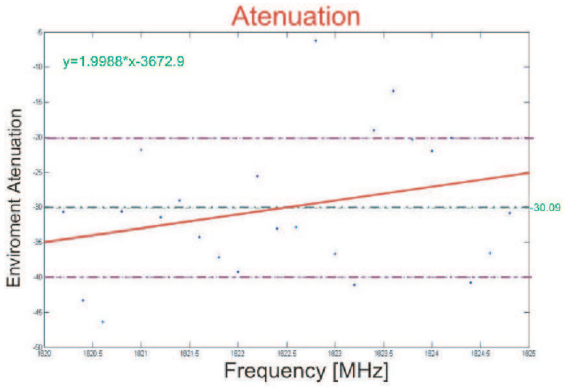

Figure 6: Attenuation due the environment for each frequency using samples above of 250 points.

up of the antenna. Figure 5 shows a graphic with these results inside the irradiation cone of the antenna.

The green line (level −26.91) shows the average level of the signal and the red line shows the linearization. Finally, the average attenuation of the environment calculated for each channel taken into consideration the frequency signal for each channel. Figure 6 is the graphic that shows the linearization and also the average value of the attenuation of the environment for each frequency using samples above 250 points where the green line shows the average level of the signal and the red line shows the linearization [6].

4. CONCLUSION

This paper presented the utilization of PRORAD software which uses a free and reconfigurable propagation model with free maps data-base to measure the attenuation of the radio-base channel due the environment in function of one specified level of frequency 1800 MHz. The downtown of the Curitiba city was used for obtain practical results. The intents were to obtain a prediction without adjustments in view to measure the ideal level of the signal in one specified channel and conclude comparing with the collected drive-test real signal. The environment attenuation effect was obtained for each channel and linearized in view to obtain the medium value of the attenuation in function of the desired frequency. The conclusion based in the obtained results of simulation is that the attenuation and frequency for one specified channel is better controlled when it uses statistic model of propagation. The simplicity of the software and the consistency of presented results shows some new aspects that it will be very useful in the system conception in the next 4G generation of mobile system as seen on [1].

ACKNOWLEDGMENT

The authors are grateful to Celplan Technologies, Campinas, Brazil for the permission to use the software under their responsibility to produce these important results, their scientific, support and technical cooperation and also to TIM — Telecom Italia Mobile for the furnished drive-test real-life data and all Telecommunication Laboratory staff for their help and aid.

REFERENCES

1. Yamao, Y., et al., "Radio access network design concept for the fourth generation mobile communication system," *IEEE Vehicular Technology Conference*, Vol. 3, 2285–2298, Tokio, Japan, 2000.
2. Varshney, U. and R. Jain, "Issues in emerging 4G wireless networks," *Computer Magazine — Communications*, June 2001.
3. Evans, B. G. and K. Baughan, "Visions of 4G," *Eletronics & Communication Engineering Journal*, December 2000.
4. Sun, J. Z., J. Sauvola, and D. Howie, "Features in future: 4G visions from a technical perspective," *IEEE Global Telecommunications Conference,* Vol. 6, 3533–3537, 2001.
5. "CelPlan," *CelPlan Technologies,* CelPlan, 2001, Web. 2, Apr. 2010, http://www.celplan.com/home.htm.
6. Andersen, J. B., T. S. Rappaport, and S. Youshida, "Propagation measurement and models for wireless communications channels," *IEEE Communications,* Vol. 33, No. 1, 42–49, 1995.
7. Sarkar, T. K., J. Zhong, K. Kyungjung, A. Medouri, and M. Salazar-Palma, "A survey of various propagation models for mobile communication," *IEEE Antennas and Propagation Magazine*, Vol. 45, No. 3, 51–82, June 2003.
8. "Google maps API family," Google Maps, Google, 2010, Web. 15, June 2010, http://code.google.com/intl/en/apis/maps/index.html.

Design of Lightning Systems with Usage Sensitivity Analysis for Improvement of Numerical Model

T. Kriz
Department of Theoretical and Experimental Electrical Engineering
Brno University of Technology, Kolejni 2906/4, Brno 612 00, Czech Republic

Abstract— The paper presents usage of the R-FEM method in the CFX environment. There is describes usage of the sensitivity analysis for improvement of numerical model and change dimensions of numerical model according to radiation pattern and required light distribution. The R-FEM method was used for modeling of special light sources and to compute lighting of surfaces from these sources with very good results. Basic description of the R-FEM method is described below. For modeling of the light sources in the CFX environment was used combination of the Finite Volume Method and the radiation method which are included with the CFX (The Discrete Transfer Model and The Monte Carlo Model). Numerical results are presented by model of head-lamp. Sensitivity analysis was used to change dimensions of numerical model according to lighting distribution.

1. INTRODUCTION

Various software tools for lighting systems design are available presently. These tools are focused to specific part of lighting systems problematic unfortunately. These programs are suitable for lamps calculation for interiors calculation or exterior calculation solely. Different numerical methods are used for the calculations in these programs.

There are used these methods for numerical modeling of lighting systems: Ray-Tracing, Radiosity, Flow method, Point method and Elementary transformation method. Ray-Tracing and Radiosity methods are most widely used methods in lighting systems. We can get realistic projection with this method. This methods are often used for project the 3D scenes and lighting calculation. It enables modeling of indirect lighting, shadows and color transition, by this we can manage realistic projection of the scene. Elementary transformation method is used for lighting calculation from lamp shield or calculation of light source with shield based on requirement on surface light. Flow and Point methods are intended to lighting calculation of room interior based on initial conditions (number of light sources and their shapes). The Point method is the simplified Flow method. There are used point light sources in Point method.

The disadvantage of the described methods is limited usability for close area in lighting system computation or their high computational time-consuming for good results resolution.

We are trying to find numerical method which enables the solving of the light from all areas of lighting systems. One possibility is usage of sophisticated numerical method together with finite volume method, for example the ANSYS CFX program. The ANSYS CFX program uses standard program tools such as modeling, discretization into a net of elements, solvers, evaluation, and interpretation of the results. The basic idea of problem is in the transformation of thermal field quantities into optical quantities. This can be done using the general rules described in [4]. In the following text the basics of modeling the primitive light problem are described.

2. THE R-FEM METHOD

The R-FEM method is a new way in the modeling of lighting systems. It utilizes the similarity between physical models. This paragraph demonstrates the usage of analogy between different physical models for the modeling of light problems. The R-FEM method is able to solve tasks that fulfill the condition $\lambda_S \ll \max(D) \wedge \lambda_S < 10 \cdot \max(D)$, where λ_S is the source of light wavelength and D is one of the geometrical dimensions of the modeling task. It can be used for models with more complicated physical structures than the methods mentioned up to now. An example of a more complicated physical problem, which we can solve by the R-FEM method, is the modeling of light intensity distribution in interior or exterior spaces with non-homogeneous environment, where the light has passed through some impure air (e.g., filled with smoke, fog, mist, vapour, dust, etc.) [3, 4].

3. THE USE OF THE R-FEM METHOD IN ANSYS CFX ENVIRONMENT

ANSYS CFX environment can be exploited for lighting system computation when we use analogy between thermal field quantities and optical quantities [3]. There are three basic principles for heat propagation by conduction, convection or radiation. Main principle of heat propagation for lighting system computation is heat transfer by radiation. There are four methods for calculation of heat propagation by radiation (Rosseland Model, P1 Model, Discrete Transfer Model and Monte Carlo Model) in ANSYS CFX, but only Discrete Transfer method and Monte Carlo method can be used for calculation of lighting systems with mirror surfaces.

3.1. Monte Carlo Model Principle

Monte Carlo model principle is based on interaction between photons and environment. The photons are emitted from a source through the model until their mass decreases to minimum. When the photons drop on surface they are reflected or absorbed. The photons sources are chosen by the emitted energy. In gas environment the part of photon energy is absorbed. Each volume element affects the absorption and scattering. Heat transfer is described by Equation (1). This method allows calculation of heat transfer independently of spectrum or performs calculation in the range of chosen frequencies. It is described in [6].

3.2. Discrete Transfer Model Principle

This method is based on tracing of the beam of rays which are emitted from the surface. The beam of rays is discretized on the particular volume elements. The beam of rays is tracked in the whole path during the passing by the domain. This Discrete Transfer model uses the same advance as the Monte Carlo model. It is described in [6].

$$\frac{dI_v\left(\mathbf{r},\mathbf{s}\right)}{ds} = \left[-\left(K_{av}+K_{sv}\right) I_v\left(\mathbf{r},\mathbf{s}\right) + K_{av} I_b\left(\nu,T\right) + \frac{K_{sv}}{4\pi} \int\limits_{4\pi} dI_v\left(\mathbf{r},\mathbf{s}'\right) \Phi\left(\mathbf{s}\cdot\mathbf{s}'\right) d\Omega' + S, \right] \quad (1)$$

where v is frequency, r is position vector, s is direction vector, s is path length, K_a is absorption coefficient, Ks is scattering coefficient, I_b is Blackbody emission intensity, I_v is Spectral radiation intensity which depends on position (r) and direction (s), T = local absolute temperature, Ω is solid angle, Φ is in-scattering phase function and S = radiation intensity source term [6].

The described methods we can use for the numerical modeling of lighting systems. The radiation approach can be used for modeling of heat transfer between surfaces only with or without reflecting the environment properties. It is possible to simulate various impurities in air (e.g., filled with smoke, fog, mist, vapour, dust, etc.). ANSYS CFX environment is useful to create the numerical model independent on radiation spectrum or numerical model for specific spectrum. With numerical model which depends on frequency we can obtain the results for various colors.

4. SENSITIVITY ANALYSIS AND RESULTS

The utilization of sensitivity analysis and numerical results from ANSYS CFX environment is described in this part. Sensitivity analysis was used for improvement of head-lamp numerical model. Head-lamp is in Fig. 1(a). To obtain the geometric model a 3D scanner has been used. Geometry from 3D scanner is shown the right part of Fig. 1. This geometrical model has been used to create the numerical model in ANSYS CFX environment. The numerical model consists of 329 856 nodes and 425 818 elements. The numerical model of reflector had used the Monte Carlo method. The emissivity of parabolic surfaces has been set to value 0.1 (without scattering) in the model. The numerical results represents the lighting level on area in 1 m distance from head-lamp. If the 3D scanner was used to obtain the geometrical model the position of light bulb was scanned with an error. To improve the geometrical model obtained by means of 3D scanner the sensitivity analysis has been used. Six numerical modes for sensitivity analysis has been. These simulations were created for each position of fibre (fibre was shift from original position about 1 mm in all directions ($\pm x$, $\pm y$, $\pm z$)). The influence of fibre shift was tested by sensitivity analysis. In this paper were used Two ways to obtain resulting Equations (2) and (3) has been used. Equation (2) uses the least square method with respect to position of fibre parameter $S(x, y, z)$. Numerical results were compared with measured values (right values) Fig. 2(a). Differences between node values were multiplied by weight matrix. Weight matrix is in Fig. 2(b). Weight matrix was used for forcing of desired lighting. Results calculated by Equation (2) are in Table 1 column NC. If

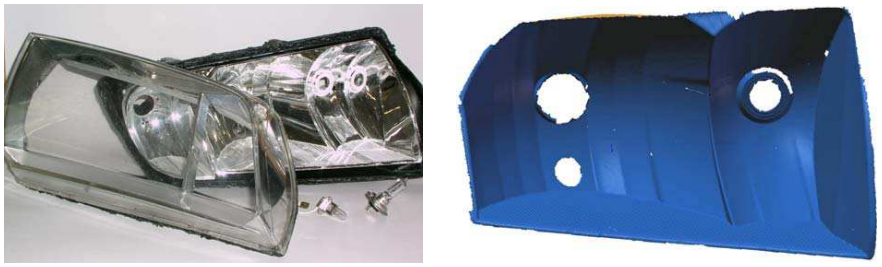

(a) (b)

Figure 1: (a) Model dimensions, (b) mesh.

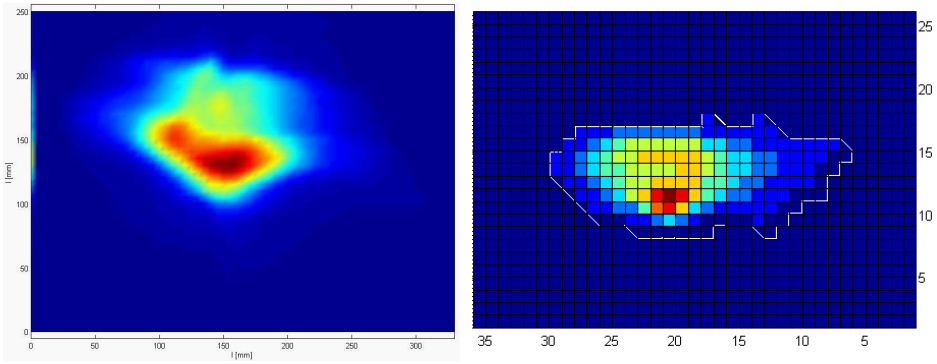

Figure 2: Measured results and weight matrix.

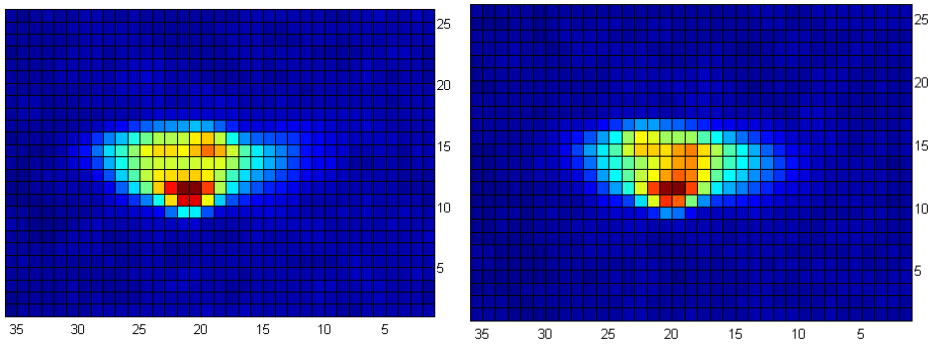

Figure 3: Numerical results for left and right shift.

the differences in node values are small it is better to use Equation (3). Results calculated by Equation (2) are in Table 1 column E.

We can use results from sensitivity analysis to calculate (in order to correct the results) the fiber position and to obtain desired lighting on observed surface. To correction calculation Equation (4) has been used.

$$F_{nc} = \sum \frac{\left(\frac{1}{mn} \sqrt{\sum_{j=1}^{n} \sum_{i=1}^{m} \left(\left(\mathbf{RR}_{i,j} - \mathbf{RS}_{i,j} \right) \mathbf{W} \right)^2} \right)}{\mathbf{S}\left(x, y, z\right)} \tag{2}$$

$$F_e = \sum \frac{\ln \sum_{j=1}^{n} \sum_{i=1}^{m} e^{(\mathrm{RR}_{i,j} - \mathbf{RS}_{i,j})\mathbf{W}}}{\mathbf{S}(x, y, z)} \tag{3}$$

where $\mathbf{RR}_{ij}$ is matrix of measured values, $\mathbf{RS}_{ij}$ is matrix of result from fibre shift and $\mathbf{S}(x, y, z)$ is vector of fibre shift.

$$C = \left(F_{S1} - F_{S2}\right) \mathbf{S}\left(x, y, z\right) \tag{4}$$

where C is calculated correction, F_{S1} and F_{S2} are results from sensitivity analysis and $\mathbf{S}(x, y, z)$ is shift vector.

Table 1: Sensitivity analysis results.

Shift	NC	E
Bottom	0.710022	0.670056143
Top	0.689317	0.571137901
Left	0.339652	0.381221151
Right	0.363001	0.359792912
Front	0.978571	0.93671214
Back	1	1

5. CONCLUSION

In this paper the utilization of sensitivity analysis for improvement of numerical model to obtain desired lighting in ANSYS CFX environment has been used. Two ways of sensitivity analysis has been presented. Equation (2) gives good results for sizeable nodes value. Equation (3) gives good results when differences between nodes values are very small.

ACKNOWLEDGMENT

The research described in the paper was financially supported by the research program MSM 0021630513 and project of the BUT Grant Agency FEKT-S-10-13.

REFERENCES

1. Kroutilova, E., M. Bernard, and P. Fiala, "Illumination of interiors by the hollow light guides," *14th International Conference Light*, Bratislava, 2003, ISBN 80-233-0488-7.
2. Kroutilova, E. and P. Fiala, "Light guide modeling," *Energy Forum*, 338–341, Technical University, Sofia, Bulgaria, 2004, ISBN 80-986-1619-1.
3. Kroutilova, E. "Automated system of calculation of reflecting surface of light sources," Ph.D. thesis, VUT v Brne, FEKT, Brno, srpen, 2004.
4. Fiala, P., E. Kroutilova, and T. Kriz, "Numerical modelling of the special light source with novel R-FEM method," *PIERS Proceedings*, 822–826, Cambridge, USA, July 2–6, 2008
5. Tsang, K.-F., W.-S. Chan, D. Jing, K. Kang, S.-Y. Yuen, and W.-X. Zhang, "Radiosity method: A new propagation model for microcellular communication," *Antennas and Propagation Society International Symposium*, Vol. 4, 2228–2231, June 21–26, 1998.
6. Ansys User's Manual, Svanson Analysys System, Inc., Huston, USA, registered ISO, 2008.
7. 9001 : 2000.
8. Kroutilova, E., "Zpusob navrhu odraznych ploch reflexnich zarizeni pomoci analogie teplotnho poleradiace a vlnove rovnice a zarizeni v podobe svetelne soustavy urcene pro numerickou optimalizaci pozadovanych svetelnych parametru odraznych ploch," Patent No. PV 2008-65, Leden, Czech Republic, 2008.

Artifact Removal Algorithms for Microwave Imaging of the Breast

Martin O'Halloran, **Martin Glavin**, **and Edward Jones**
Electrical and Electronic Engineering, National University of Ireland, Galway, Ireland

Abstract— One of the most important components of any Confocal Microwave Imaging (CMI) system for breast cancer detection is the early-stage artifact removal algorithm. The early-stage artifact is composed of the incident pulse combined with the reflection from the skin-breast interface and residual antenna reverberation, and must be removed from the received signal at each antenna before further processing can take place. If the early-stage artifacts are not removed, they could potentially mask energy reflected from shallow tumors located close to the surface of the skin, and also hinder the identification of tumors located deeper within the breast. Many existing artifact removal algorithms are based on variants of the assumption that the artifact in a particular channel can be estimated and effectively removed by creating a reference waveform. This reference waveform is typically based on the average of the artifact in all channels. The artifact in a particular channel is then removed by subtracting this reference waveform from the recorded signal. More sophisticated algorithms estimate the artifact in each channel as a filtered combination of all the artifacts, and have been shown to be more robust to normal variations in skin thickness. However, increased underlying dielectric heterogeneity, as highlighted by Lazebnik et al., could result in greater variation in the early-stage artifact, making the artifact removal process much more difficult. In this paper, several existing artifact removal are examined in this context of increased dielectric heterogeneity, and based on these results, suggestions for future work are presented.

1. INTRODUCTION

More than 40,000 women die annually in the United States from breast cancer, making it the leading cause of death in American women. One of the most promising alternate breast imaging modalities is microwave imaging. The physical basis for microwave imaging is the dielectric contrast between the constituent tissues of the breast and cancerous tissue at microwave frequencies. The Confocal Microwave Imaging (CMI) approach involves illuminating the breast with a UWB pulse, recording the backscattered signals and then using these signals to identify and locate significant dielectric scatterers within the breast. Regions of high energy within the resultant image may suggest the presence of tumours. However, recent studies have found the breast to be dielectrically heterogeneous. Significantly, Lazebnik et al. [1] found a very significant dielectric contrast between normal adipose and fibroglandular tissue within the breast. Comparison studies have examined the performance of several UWB beamforming algorithms in the dielectrically heterogeneous breast. However, no previous study has compared the performance of early-stage artifact removal algorithms. The early-stage artifact is composed of the input signal, the reflection from the skin-fat interface and any antenna reverberation. This artifact is typically several orders of magnitude greater than than the reflections from any tumours present within the breast. If the artifact is not removed effectively, it could easily mask tumours present within the breast. In this paper several existing artifact removal algorithms are described and compared, before suggestions for future development are presented.

2. ARTIFACT REMOVAL ALGORITHMS

Three artifact removal algorithms are considered: the Averaging method, the Rotating Antenna method and the Filtering method. In this paper, N antennas surround the breast (in a cylindrical array), and the sampled monostatic waveform at antenna i is denoted by $b_i(n)$.

2.1. Averaging Method

The Averaging method requires the generation of a *reference waveform*, w, which is representative of the artifact present in each channel. The reference waveform is created by simply calculating the average of the waveform across all received channels:

$$w(n) = \frac{1}{N}\sum_{i=1}^{N} b_i(n) \tag{1}$$

The ith signal following artifact removal, $S_i(n)$, is the calculated as $S_i(n) = b_i(n) - w(n)$.

2.2. Rotating Antenna Method

The Rotating antenna method is used to extract the breast response from the measured signals, which include the early-stage artifact [2]. Two sets of measured signal are collected: one with the antennas at one location and another after the antenna array has been rotated around the breast. Expressing the rotated signals as $r_i(n)$, the artifact removed signal from the ith antenna is calculated as $S_i(n) = b_i(n) - r_i(n)$.

2.3. Filtering Method

In order to compensate for intra-channel artifact variation, a filter-based artifact removal algorithm was developed by Bond et al. [3]. This algorithm involves estimating the artifact in each channel as a filtered combination of the artifacts in all the other channels, with the goal of removing the early-stage artifact while also being robust to normal variations in skin thickness and breast heterogeneity. The algorithm operates as follows: In order to estimate the early-artifact at a particular sample, n, a vector containing $2J+1$ samples, centred on the nth sample, from each of the other channels is created: $\mathbf{b}_N[n] = [\mathbf{b}_1^T[n-J], \ldots, \mathbf{b}_{i-1}^T[n], \mathbf{b}_{i+1}^T[n] \ldots, \mathbf{b}_N^T[n+J]]^T$. The artifact removal filters are designed to minimise the mean-squared error over the part of the signal containing the early stage artifact and therefore the filter weights are defined as:

$$\mathbf{q} = \min_{q} \sum_{n=n_0}^{n_0+m-1} \left| b_i[n] - \mathbf{q}^T \mathbf{b_N}[\mathbf{n}] \right|^2 \tag{2}$$

where $n = n_0$ and $n = n_0+m-1$ defined the start index and end index which contain the early-stage artifact. The artifact is then removed from the ith channel as $x_i[n] = b_i[n] - \mathbf{q^T b}_N[n]$.

3. TESTING AND RESULTS

A 2D Finite Difference Time Domain (FDTD) breast model was developed, based on an MRI-derived breast phantom, taken from the UWCEM breast phantom repository at the University of Wisconsin, Madison [4]. The antenna array consists of a number of elements modelled as electric-cu'rrent sources, equally spaced around the circumference of the breast, and placed on the skin. The antenna array is backed by a synthetic material matching the dielectric properties of skin. A 7.5 mm diameter tumor is positioned within the breast at location (80 mm, 100 mm). The FDTD model is shown in Figure 3. The input signal is a 150-ps differentiated Gaussian pulse. Each artifact removal algorithm is applied to the recorded signals and a simple delay and sum beamformer is used to create an image of the breast. In order to evaluate the performance of each artifact removal algorithm, the Signal to Mean Ratio (SMR) is calculated for each image. The SMR is defined as the ratio of the peak tumour response to the average response in the breast image. The resultant images created following the application of each artifact removal algorithm is shown in Figure 2, and the corresponding SMR values are shown in Table 1.

The filter-based artifact removal is shown to significantly outperform both the averaging and rotating antenna based methods. Bond's method appears to be more robust to local variations in skin thickness and underlying heterogeneity. The averaging method performers poorly due to the

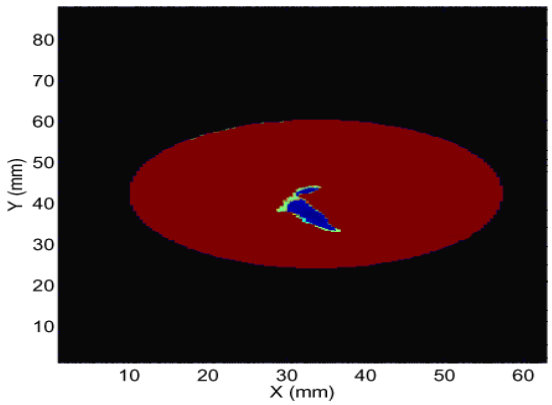

Figure 1: FDTD breast model.

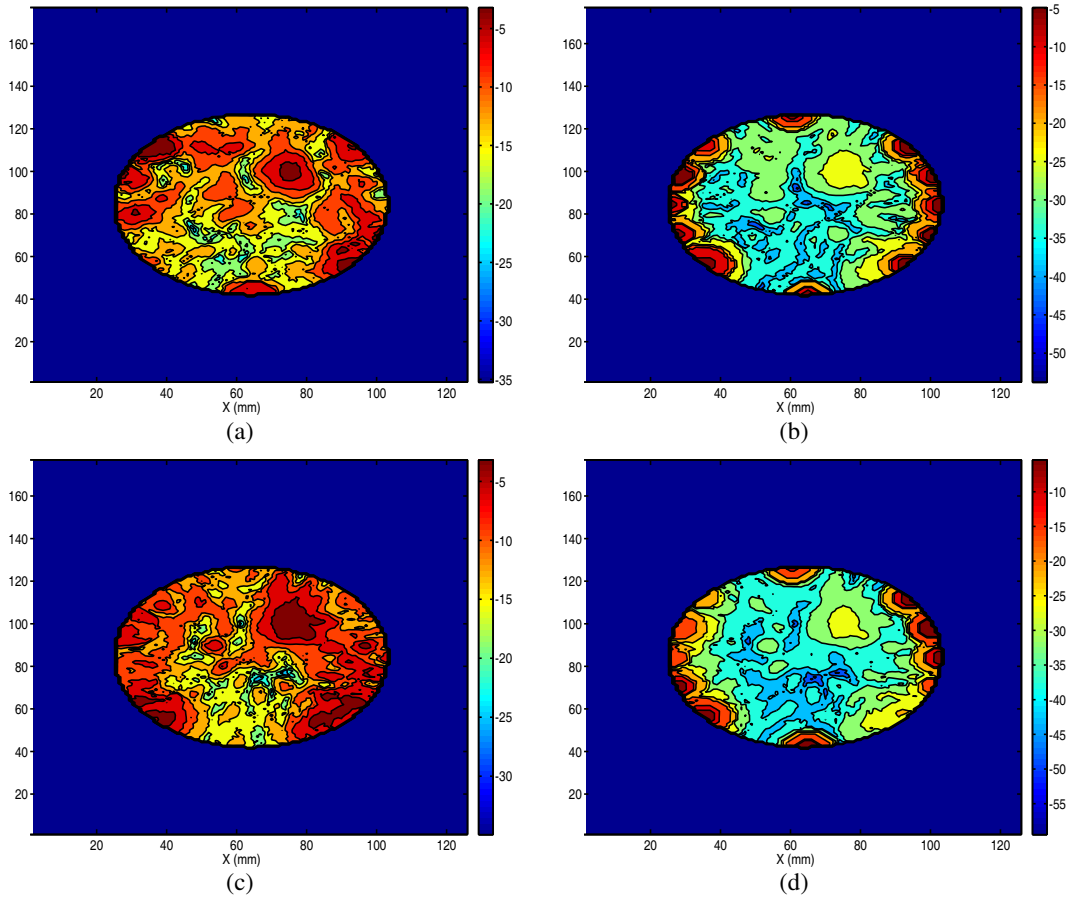

Figure 2: Image created following (a) ideal, (b) averaging, (c) filtering, and (d) rotating antennas artifact removal algorithms.

Table 1: SMR for each image created using four artifact removal methods.

Algorithm	Ideal	Averaging	Filtering	Rotating Antenna
SMR (dB)	29.17	16.45	28.67	21.18

fact that it fails to account for such variation. Similarly, the rotating antenna method results in a comparatively poor image. This may be due to the difficultly in selecting the optimum angle of rotation. A small rotation angles means that the algorithm is robust to local variations in the skin thickness, but it also means that tumour response in the original signal and rotated are more "time-aligned", and therefore the tumour response is more likely to be reduced following the artifact removal process. Future work should examine the performance of these filter-based methods using realistic breast phantoms or ideally clinical data. The extension of these algorithms to account for multistatic Radar signals should also be considered.

REFERENCES

1. Lazebnik, M., L. McCartney, D. Popovic, C. B. Watkins, M. J. Lindstrom, J. Harter, S. Sewall, A. Magliocco, J. H. Booske, M. Okoniewski, and S. C. Hagness, "A large-scale study of the ultrawideband microwave dielectric properties of normal breast tissue obtained from reduction surgeries," *Phys. Med. Biol.*, Vol. 52, 2637–2656, 2007.
2. Klemm, M., I. J. Craddock, J. Leendertz, A. W. Preece, and R. Benjamin, "Breast cancer detection using symmetrical antenna array," *The Second European Conference on Antennas and Propagation, EuCAP*, 1–5, 2007.
3. Bond, E. J., X. Li, S. C. Hagness, and B. D. V. Veen, "Microwave imaging via space-time beamforming for early detection of breast cancer," *IEEE Trans. Antennas and Propagat.*, No. 8, 1690–1705, August 2003.
4. UWCEM, (Last accessed: June 2010) Uwcem numerical breast phantoms repository, [Online], Available: http://uwcem.ece.wisc.edu/home.htm.

Influence of Weak Electromagnetic Fields on Cerebrovascular System of the Person

Yu. Ya. Varakin[1], **V. G. Ionova**[1], **G. V. Gornostaeva**[1], **E. A. Sazanova**[2, 3], **and N. P. Sergeenko**[2]

[1]Scientific Center of Neurology RAMS, Moscow, Russia
[2]Pushkov Institute of Terrestrial Magnetism, Ionosphere and Radio Wave Propagation RAS
Troitsk, Moscow Region, Russia
[3]Clinical Hospital of Russian Academy of Sciences, Troitsk, Moscow Region, Russia

Abstract— In this work, the statistical analysis of influence of heliogeomagnetic factors on frequency of occurrence of strokes according to the register of a stroke of the population of Moscow is presented to the various periods of geophysical activity.

It is shown, that during geomagnetic disturbances it is noted more than double, statistically authentic increase in number of strokes and death rate. These effects can be caused occurrence under the influence of physical processes during geomagnetic indignations of instability in a trombotsitarno-vascular link of a hemostasis. Physical mechanisms during disturbances under which direct influence changes in blood cells are discussed.

1. INTRODUCTION

For the last decades many new facts were accumulate which indicate on influence of disturbances of natural electromagnetic field, developing due to processes on the Sun and in the Earth magnetosphere on cerebro-vascular system of the person [1]. The modern concept of heterogeneity of the ischemic stroke, proving variety of the reasons and mechanisms of development sharp focal ischemic damage of a brain, has given an additional impulse for finding out of risk factors of development cerebro-vascular frustration and for search of ways of possible decrease in their negative effects. In this connection, various exogenic influences on a current cerebrovascular pathologies and development of the stroke is represented actual. The purpose of the present work is scientific and practical interest the analysis of features of strokes and death rate from it in the conditions of various heliogeomagnetic activity.

2. MATERIAL AND METHODS

The analysis was spent according to the register of strokes of Scientific center of neurology of the Russian Academy of Medical Science (1255 cases, among which were 590 men and 665 women), spent among the Moscow population during various heliogeomagnetic activity. The supervision period included 730 days (2 years for 365 days). 334 days corresponded quiet geomagnetic background, 112 days were before development of the main phase of the geomagnetic storm, 284 days corresponded to the active periods of geomagnetic storms. Cases of strokes and death rates from it for the patients with an atherosclerosis and an arterial hypertension for different age groups were analyzed.

For an estimate of a geomagnetic situation was used a K-coefficient of IZMIRAN observatory (Moscow, Russia), and also hourly Dst, and AE coefficients. The K-coefficient represents the numerical performance of a degree of disturbance, expressed in numbers, where to each number corresponds to amplitude of a geomagnetic field (in nTl) for a three-hour. Dst-the coefficient characterizes occurrence and development large-scale planetary geomagnetic storm. On the Earth also there are shorttime perturbations-substorms. Their beginning and the intensity describes AE-coefficient. In the Moscow region they are shown as well as world storms, but last usually 5–7 hours.

Statistical processing was spent by a method of variation statistics, with use of the correlation analysis. Estimations were carried out by Student criterion, reliable considered differences at $p < 0.05$.

3. RESULTS OF EXAMINATION

The number of the strokes during the various periods heliogeophysic conditions depending on age group is resulted in Table 1. It can be seen, that the greatest number of strokes were register during the magnetic storm in spite of the age of the patient.

In Tables 2 and 3 frequencies of strokes and death rate from it in various heliogeophysic conditions are resulted. From tables follows, that during the periods of the increased geomagnetic activity frequency of cases increase almost twice.

Let's notice, that all investigated samples were representative and estimations of the received results significant ($p < 0.0001$). Presence of an arterial hypertension at patients with an atherosclerosis leads to development of strokes and death rate from them above during the strengthening periods heliogeomagnetic activity is more often.

On Fig. 1 generalised on all groups of patients of the histogram of distributions of frequency of a stroke and death rate from it are resulted. The increase in these indicators already during disturbance preparation in circumterraneous space is visible. The further growth of characteristics during the periods of development of the disturbance is obvious.

Thus the carried out analysis of data of the Moscow register of a stroke has revealed in all considered groups of patients authentic increase in number of strokes and death rate from them in days of a magnetic storm and 2 days prior to its development.

Table 1: Distribution of the patients number who have had a stroke during the various periods of heliogeophysical activity on age according to the register.

Heliogeophysic activity	under 39 years old	40–59 years old	60–79 years old	80 years old and more
Quietly	3	97	170	72
2 days before magnetic storm	2	51	129	45
Magnetic storm	11	185	352	138
All	16	333	651	255

Table 2: Frequency of cases of the patients who have had a stroke with various diseases.

Heliogeophysic activity	atherosclerosis	atherosclerosis and an mild arterial hypertension	atherosclerosis and an moderate arterial hypertension
Quietlyt	0.20	0.47	0.30
2 days before magnetic storm	0.30	0.90	0.80
Magnetic storm	0.50	1.01	0.90

Table 3: Frequency of cases of a stroke with fatal outcome at patients with various diseases.

Heliogeophysic activity	atherosclerosis	atherosclerosis and an mild arterial hypertension	atherosclerosis and an moderate arterial hypertension
Quietlyt	0.08	0.15	0.14
2 days before magnetic storm	0.13	0.40	0.37
Magnetic storm	0.19	0.35	0.39

4. DISCUSSION

In works [2–4], it is shown, that electromagnetic disturbances in near Earth space influence on functional condition of system of a hemostasis and rheological properties of blood. Infringements in rheological properties of blood make essential impact on macro- and microcirculation. Also participation catecholamins in regulation of cellular functions is shown, including separate haemorheological

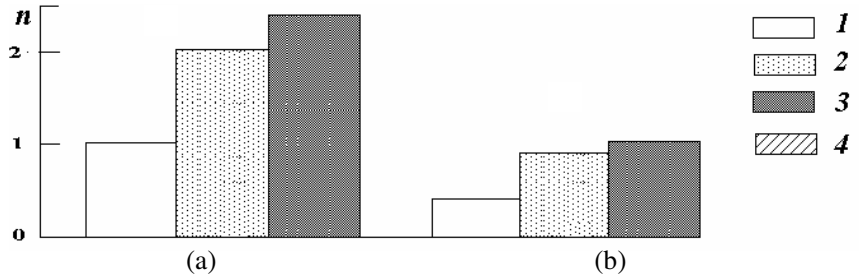

Figure 1: Analysis of (a) number of strokes and (b) death rates from it according to the register of strokes in quiet heliogeophysical conditions (1), before (2) and during (3) storms.

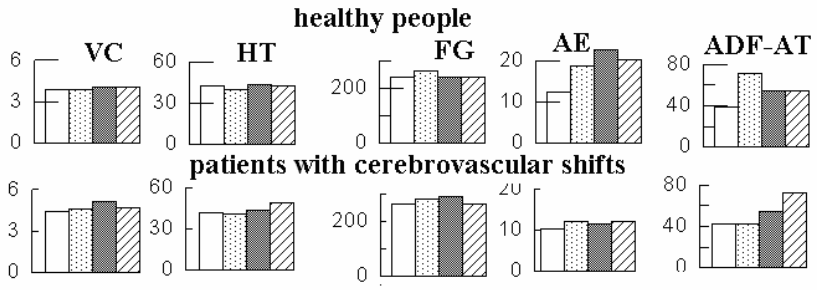

Figure 2: Dynamics rheological characteristics of healthy and patient in quiet conditions, before, during time and after a storm. VC — viscosity of an integral blood, HT — hematocrit, FG — concentration of Fibrinogenum, AE — ability of erythrocytes to aggregation, ADF-AT an adenosinediphosphatase acid induced platelet aggregation.

characteristics of erythrocytes, and platelet-vascular interactions. Stress hormones-catecholamins is directly or indirectly influence on lipase, phospholipases activity, intensity lipid peroxidation. These biochemical processes can be realised in increase of aggregative activity of blood cells, blood plates, causing activation of enzymes of system of a hemostasis and an angiospasm of microcirculation. The specified effects at sick of an atherosclerosis and a hypertension can lead to strokes.

Practically healthy and the patient organisms differently react to solar and geomagnetic storms. Conditions during disturbances are much heavier even for a healthy organism: for its normal functioning in the disturbance conditions protection of cellular membranes and many other things is required. The organism makes active the reserve mechanisms of adaptation to new conditions. The sick organism sometimes does not cope with this problem of adaptation as its reserve possibilities are exhausted. Therefore the condition of a sick organism during storms is characterised by oppression cellular and antibody responcse, level decrease endogenic antioxidants, increase atherogenic fractions in blood. On Fig. 2 dynamics of rheological characteristics healthy people and patients with cerebrovascular disease in quiet days, for two days before a geomagnetic storm, during indignations and in a current of three days after a storm (the same designations, as on Fig. 1) are presented.

It is visible, that the most of considered characteristics starts to change already before the beginning of a magnetic storm. This fact is important by working out of methods of medicamentous preventive maintenance and correction haemorheological shifts at the population in the conditions of disturbances. Also it is visible, that at healthy people parameters come nearer to norm, than at patients faster.

Haemorheological shifts and changes of neurotransmitter concentrations in a blood, associated with increased heliogeophysigal activity, allow to suggest, that under the circumstances a human organism is exposed a number of physical factors. These factors are associated with magnetospheres activity caused by action solar corpuscular streams. As these changes of parameters of a blood begin to occur prior to the beginning of magnetic storm and before any changes of an amplitude of a geomagnetic field, it may be safely suggested that one of the basic physical mechanisms at initial stages of perturbations can be a stochastic resonance. The exterior oscillations can synchronize or desynchronize rhythms of humoral systems of a human organism. It appears that the development of the resonant phenomena probably may lead a stress reaction with activation sympathoadrenal

system, that can result in increased aggregation of cell elements of a blood and increased of intensity of processes hemocoagulation.

From all spectrum of an electromagnetic field on a surface of the Earth, the biologically effective factor is in that frequency rang, where a level of a field is greatest, and the differences of its intensity from quiet conditions to disturbances are great enough. To such requirements satisfies a range of superlow frequencies, in which low-frequency "transparency window" of an ionosphere is situated. The electromagnetic waves with such frequencies freely reach the Earth, and the intensity of this low-frequency radiation increases 10–100-fold during disturbances [5].

In a low-frequency range, beside for micropulsations generated by processes in a magnetosphere of the Earth, and Shuman resonances, in a region of the Earth — the ionosphere is formed the resonator for Alfven waves. The resonancet structure of a spectrum of an atmospheric noise phon is regularly apparent feature of background electromagnetic noise within the frequency range 0.1–10 Htz. The Alfen's ionospheric resonancet structure of a spectrum is the fundamental characteristic of an electromagnetic field in a region of the Earth — ionosphere. The parameters of resonancet structure are controlled by a structure and degree of disturbance of an ionosphere in a point of observation.

In period after of a beginning geomagnetic storm and increase variations of amplitude of a geomagnetic field it appears to be a direct action of a geomagnetic field. Now it is reliably established, that inside of alive organisms it can be present nano crystals of ferromagnetic minerals, in particularly Fe3O4 [6]. It is defined, that they have a biogenic origin, i.e., are formed as a result of a crystallization directly in cell medium. The biogenic magnetite is found out in a brain and in the other human organs, also in birds, insects and bacteria. The presence of a magnetite in alive organisms is one of the possible reasons of their sensitivity to feeble magnetic fields and variations of a geomagnetic field.

The blood, due to erythrocytes, also can be considered as magnetic medium. The haemoglobin of erythrocytes is included atoms of iron having a non-zero magnet. moment Therefore medium containing such particles, is capable to show properties proper which are common to magnetics. In the disturbances conditions of an electromagnetic field with frequencies from several hertz up to several kilohertz increases, so the spontaneous magnetization of particles can lead to occurrence groups with oriented particle packing due to a parallel alignment of their magnet moments. Moving in a vasculature, this group represents soliton object or S-object. The vector of a magnetic flux of S-object is defined by product of a vector of a magnetic induction on a cross-sectional area of the channel, on which it moves.

5. CONCLUSION

Our investigation shows that the frequency of strokes can be connected with physical processes during disturbances of the geomagnetic field of the Earth. Results of the carried out research allow to assume, that one of leading mechanisms of influence the heliogeophysigal disturbances, capable to influence haemocirculation of the healthy person are as direct influences, and mediated (in particular, through catecholamins) their effects on rheological properties of blood. It is obvious, that ambiguity of reaction of difficult nonlinear systems what the human organism is, on weak external influences of heliogeophysigal character depends not only on properties of the influencing factor, but also from a condition of the organisms. At integrity internal part of a vascular channel at healthy people of change rheological properties of blood and activation of a trombotsitarno-vascular hemostasis connected with disturbances have reversible, adaptable character.

REFERENCES

1. Komarov, F. I., T. K. Breus, S. I. Rapoport, V. N. Oraevskii, Y. L. Gurfinkel, F. Halberg, G. Cornelissen, and S. I. Chibisov, "Medicobiological effects of solar activity," *Vestn. Ross. Akad. Med. Nauk*, No. 11, 37–49, 1994.
2. Ionova, V. G., E. A. Sazanova, N. P. Sergeenko, G. V. Gornostaeva, and K. D. Kanonidi, "Response of the human organism to heliogeophysical disturbances," *Biophysics*, Vol. 48, No. 2, 361–365, 2003.
3. Varakin, Y. Y., V. G. Ionova, E. A. Sazanova, and N. P. Sergeenko, "The Wavelet analysis at heliobiological connection," *Biophysics*, Vol. 49, No. 4, 684–687, 2004.
4. Varakin, Y. Y., G. V. Gornostaeva, V. G. Ionova, E. A. Sazanova, and N. P. Sergeenko, "Effects of Influence of heliogeomagnetic disturbances on the haemorheological characteristics of the people," *PIERS Proceedings*, 1583–1586, Xian, China, March 22–26, 2010.

5. Akasofu, S.-I. and S. Chapman, *Solar-terrestrial Physics: An Account of the Wave and Particle Radiations from the Quiet and the Active Sun, and of the Consequent Terrestrial Phenomena*, Oxford, Clarendon, 1972; Translated under the title Solnechno-zemnaya fizika, 509, Moscow, Mir, 1975.
6. Bingi, V. N., D. S. Chernavsky, and A. B. Rubin, "The factor of temperature and magnetic hum in conditions of a stochastic resonance of magnetosoms," *Biophysics*, Vol. 51, No. 2, 274–277, 2006.

Interpolation of 3D Magnetic Resonance Data

J. Mikulka[1], **E. Gescheidtova**[1], **and K. Bartusek**[2]

[1]Department of Theoretical and Experimental Electrical Engineering, Brno University of Technology
Kolejni 2906/4, 612 00 Brno, Czech Republic
[2]Institute of Scientific Instruments, Academy of Sciences of the Czech Republic
Kralovopolska 147, 612 64 Brno, Czech Republic

Abstract— This article deals with three-dimensional reconstruction methods of nuclear magnetic resonance images. The testing images were observed by tomography with basic magnetic field of 4.7 T at the Institute of Scientific Instruments (Academy of Sciences of the Czech Republic). The 20 slices of the test phantom were acquired. Two methods were found with the aim of getting utmost information about the shape of the testing phantom. One possible way is to increase the count of the sensed slices, but it implies decreasing of the signal to noise ratio. The second approach is finding the compromise between the effective count of slices and the following interpolation of other slices between the sensed ones. The both approaches were compared. Only 10 slices were used to compute the in-between others. It is better to use this approach because the computed slices can be compared with the real slices obtained by MR tomography. The results are described in the article. The images were interpolated in order to improve the following three-dimensional model creation.

1. INTRODUCTION

The advantages of the nuclear magnetic resonance (NMR) were described in many publications. It is approach to acquisition of spatial data of soft tissues. The main advantage is absolutely the fact of unproved negative effects of the electromagnetic radiation to human organism subject to prescribed hygienic regulations. Against to other tomography approaches the magnetic resonance images are with the higher resolution and quality. The observed images of sensed object can be used for three-dimensional model creation after the application of suitable preprocessing methods. The reconstructed object can be useful for example to the better diagnosis in medical sciences, for quantitative or qualitative description of tissues, tumors etc. The requirement is to have utmost slices for the three-dimensional model of sensed tissue. The signal-to-noise ratio (SNR) decreases with the increasing number of slices [1]. We have to specify compromises between the number of observed slices and satisfying SNR in images individually. However, if we actually need more slices for the 3D model creation, we can calculate the other images between observed ones. Two basic approaches are described for images interpolation of MR spatial data in this paper. The first method is based on ordinary averaging of neighboring pixels intensities with the same position in the frequency domain. We can get the images describing the real scene by Fourier transformation of each slices in the k-space, which we observed by tomography. We can get $(2n-1)$ images from original n images. This algorithm is repeatable. By the second approach we process directly the data in k-space. A vector of complex numbers is created by data observing with the same positions in the k-space. Then the frequency domain of this vector is obtained by Fourier transform [2, 3]. The frequency domain is extended by zero values for higher frequency parts. This extended spectrum is transformed back to the time domain by the inverse Fourier transformation. The length of the obtained vector depends on number of zeros included to frequency spectrum of the original vector. The flask with water was inserted to work space of tomography with the magnetic field 4.7 T (200 MHz for ^{1}H nuclei) for the testing. This article follows the previous research in this area, which was described in [4].

2. ASSEMBLY OF EXPERIMENT

The images obtained by MR tomography in the time domain (k-space) are then transformed by Fourier transform to the frequency domain. These images in the frequency domain represent the real scenes. The first method interpolates the three-dimensional data in the transformed frequency domain. The second method shows the possibility of data processing and interpolating the three-dimensional data in the original time domain — k-space. The example of experiment assembly is shown in Figure 1. In this case only one flask filled by water was used. In Figure 2 the procedure of scanned spatio-temporal slices processing and the transformation of the slices to the frequency domain is shown.

Figure 1: The example of phantom for testing process of proposed interpolation methods of spatial MR data.

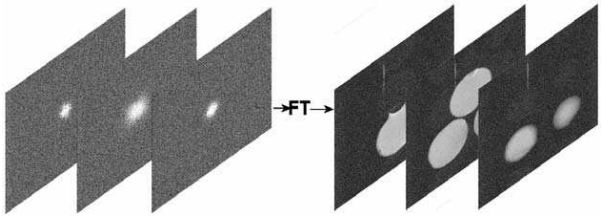

Figure 2: The procedure of obtaining the images by MR tomography. Three selected slices in the k-space on the left, three selected slices of phantom in the frequency domain on the right.

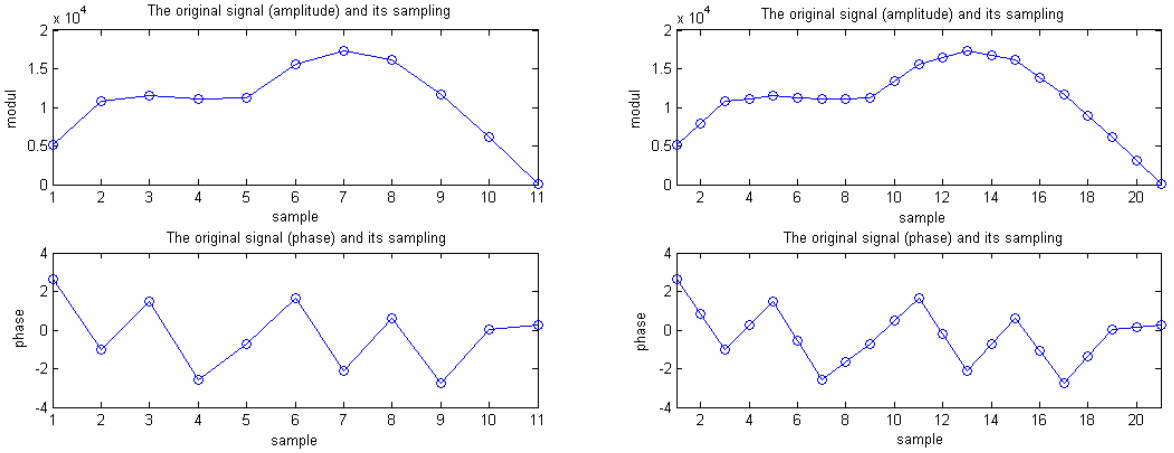

Figure 3: Interpolation of pixel intensity in the image between original slices by averaging. The pixel intensities vector (module, phase) is on the left, the pixel intensities resampled vector (module, phase) is on the right.

3. AVERAGING

The ordinary averaging method is used for nearby pixel intensities in the frequency domain for comparison of the proposed method of signal interpolation in the k-space, which are generated between two existing images obtained by MR tomography. The intensity of a new pixel is then given by the equation:

$$I_{new}(x,\, y) = \frac{I_{new-1}(x,\, y) + I_{new-1}(x,\, y)}{2}. \tag{1}$$

4. INTERPOLATION IN K-SPACE

This approach is a little bit complicated but it gives better results. The basic principle is to extend the spectrum of the obtained signal in the k-space, which arises by values of the nearby pixel intensities with the same positions. In Figure 4 we can see the original complex signal generated by nearby pixel intensities. The same resampled signal transformed to frequency domain with including the zero values for higher frequencies and transformed back to the k-space is shown on the right. It is clear that by this approach the signal was supplemented by new samples, witch interpolates the k-space in the space where no slices were obtained by the tomography. This interpolated k-space is then transformed by FT to frequency domain with $(2n-1)$ images.

5. EXPERIMENTAL RESULTS

The both methods (averaging in the frequency domain, extending the spectrum of k-space by zero values) were tested on 21 original slices of proposed phantom obtained by MR tomography at the Institute of Scientific Instruments of the ASCR in Brno. The algorithms were implemented in the Matlab software [3]. The set of 11 original slices was interpolated to 21 slices. The set of 10 new images were computed between the 11 original odd slices and compared with the original even ones. Several slices from the middle of the measured object are shown in Figure 5. Calculated slices

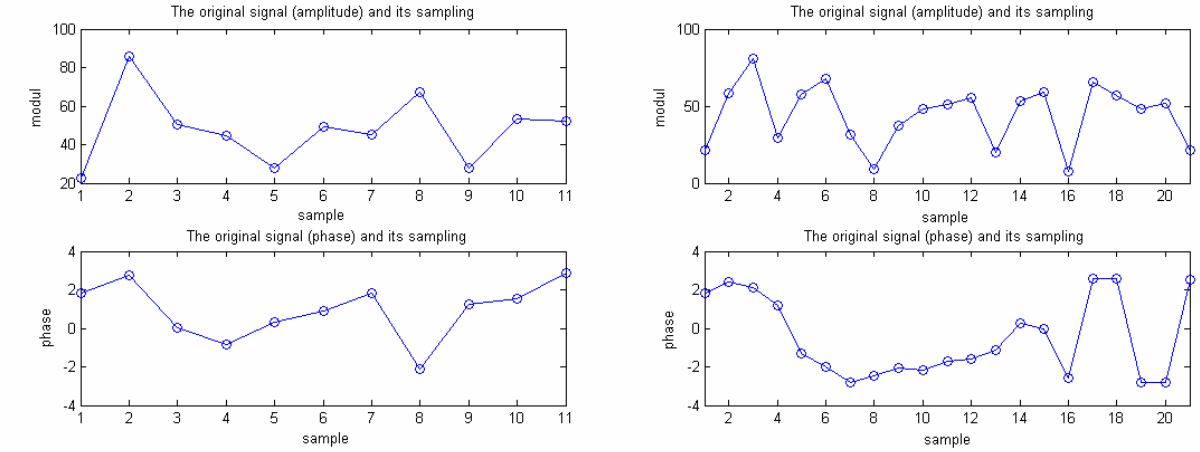

Figure 4: Interpolation of images between obtained slices by the spectrum adjustment in k-space. The original vector of k-space values (module, phase) is on the left, the resampled vector (module, phase) is on the right.

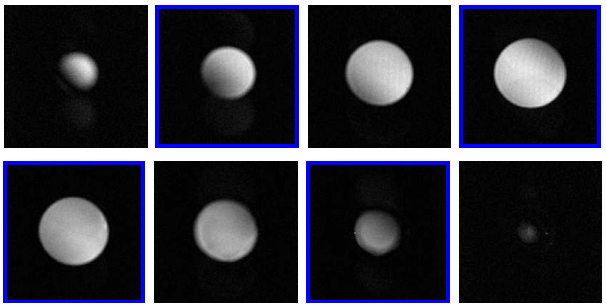

Figure 5: Several original slices in the middle of the measured object. Blue color signs images to be calculated.

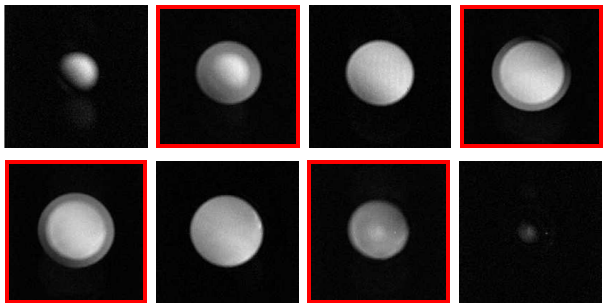

Figure 6: Calculation of images by averaging. Red color signs calculated images.

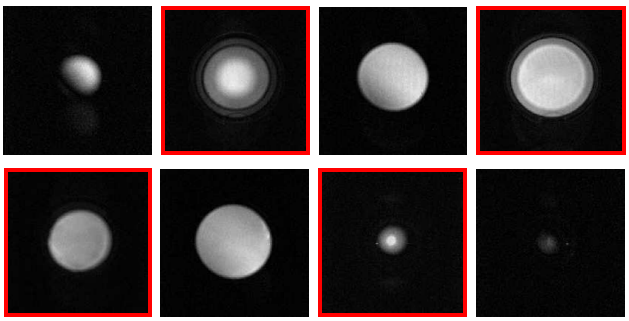

Figure 7: Calculation of images by extending the spectrum of signals in the k-space. Red color signs calculated images.

with use of the method of averaging in the frequency domain are shown in Figure 6. Calculated slices with use of the method of the spectrum extending in k-space are shown in Figure 7. All the calculated slices are red marked.

6. CONCLUSIONS

We can compare results obtained by both tested methods. The first one — the averaging method of the neighbor pixel intensities with the same position in the frequency domain gives the good results. The intensity of a new pixel in the interpolated image always reflects the values of obtained pixel intensities. There is a problem, after the segmentation of this image, the size of the segmented object will be always the same as in the neighbor image. But there is no other error brought into the image. It is clear that this method doesn't give any new spatial information, only the average

number of hydrogen nucleus in the area of interpolation we can get. By the second method — interpolation in k-space — an error due to resampling of the signal by extending its spectrum by zero values is brought. This signal is devaluated by harmonic spatial signal. There are spatial artifacts in more images. The processed images will be segmented, whereas the suitable level of intensity for the segmentation will be found. The resultant contours will be used for accurate three-dimensional model creation and it will be made the comparison of the both methods.

ACKNOWLEDGMENT

This work was supported within the framework of the research plan MSM 0021630513 and projects ME10123 and GACR 102/11/0318.

REFERENCES

1. Gescheidtova, E. and K. Bartusek, "Kriteria pro vyber vlnek pri zpracovani MR obrazu," *Elektrorevue* [online — (http://www.elektrorevue.cz)], Czech, 2009.
2. Vich, R. and Z. Smekal, *Cislicove Filtry*, Academia Praha, Czech, 2000.
3. Gonzales, R., et al., *Digital Image Processing Using Matlab*, Prentice Hall, 2009.
4. Mikulka, J. and K. Bartusek, "3D reconstruction in magnetic resonance imaging," *PIERS Online*, Vol. 6, No. 7, 617–620, 2010.

Homogeneous Phantom Model vs. Visible Human Dataset: Impact on MRI-induced Heating of Metal Implants

Eugenio Mattei, **Giovanni Calcagnini**, **Federica Censi**, **Michele Triventi**, **and Pietro Bartolini**
Department of Technology and Health, Italian National Institute of Health, Roma, Italy

Abstract— Numerical simulations were performed to evaluate the Specific Absorption Rate (SAR) induced at the tip of a pacemaker lead by the radiofrequency field used in MRI procedures (SEMCAD X, Speag). A realistic 34-tissue human model (Visible Human Dataset — VHD, ITIS Foundation) was used and both right and left pectoral implant locations were reproduced. The local SAR pattern computed for the VHD was then compared to the one of a homogeneous human-shaped phantom, a wide used numerical phantom, since it reproduces the in-vitro experimental set-up adopted for MRI safety studies. The local SAR at the pacemaker lead tip was −11.3% for the right implant and +0.3% for the left one in the homogeneous phantom, compared to the complete VHD. Other simplifications of the HVD, in terms of anatomical structures modeling, were also studied. In particular a homogeneous phantom with inside just the air cavities (lungs, trachea, upper airways, stomach and intestine lumens) and a homogenous phantom with inside the heart, the blood and the blood vessels. These partial simplifications of the complete VHD gave less accurate results than the fully homogeneous phantom. In particular, when air cavities are modeled inside the human trunk phantom, a significant overestimation of the local SAR induced at the lead tip was observed (+60.2% for the right implant and +136.0% for the left one, compared the complete VHD).

1. INTRODUCTION

Today, Magnetic Resonance Imaging (MRI) is strongly contraindicated for people with metal implants, such as a pacemaker or an implantable cardioverter/defibrillator. However, given the rapid expansion of technology in the fields of both MRI and device arrhythmia management, there is increasing interest in the issue of implantable device safety in the MRI environment. Considering the impressive progress in the use of diamagnetic material, the most important safety problem associated with MRI and medical implantable devices is the potential tissue heating induced by the radiofrequency (RF) fields. A large body of excellent work has been published in the past few years dealing with MRI induced heating of various kind of metallic implants [1–3]. The majority of these works have used in vitro phantoms to characterize interaction with the RF fields and highlight the technical difficulty of the experimental assessment of the compatibility of implantable devices with MRI units. In this field, computational techniques represent a favorable choice for the evaluation of implantable devices with the MRI environment. As the finite difference time domain (FDTD) method has been widely used for RF heating characterization, it is an excellent candidate to render an accurate estimate of the specific absorption rate (SAR) — and therefore heating — due to implantable devices during MRI experiments.

The representation of the anatomical structure of the human body as sets of minute elements (voxels) suitable to be imported into the FDTD environment has been obtained from MRI scans, X-ray computed tomography, or anatomical colored images of the Visible Human Project (VHP). These data are today largely available at a high resolution, so that almost all the various human tissues can be accounted for (Visible Human Dataset — VHD). However, the computational effort required by a modeling study of MRI fields with realistic human structures implanted with a metal device, such as a pacemaker or an ICD, is still very high and simplifications are often needed. In addition, in-vitro experimental set-ups use homogeneous phantoms, making comparison with VHD numerical models difficult.

In this work, we compared the RF-induced heating at a PM lead tip assessed using a complete VHD model with that one obtained with a homogeneous phantom, the latter being a wide used numerical phantom, since it reproduces the in-vitro experimental set-up adopted for MRI safety studies. In addition, we investigated how a partial simplification of the VHD affects the estimation of locally induced heating.

2. METHODS AND MATERIALS

MRI RF coil was modeled using a commercial FDTD (Finite Difference Time Domain) solver (SEMCAD X, version 11.0, SPEAG, Zurich). The model consists of a 16-rung low-pass birdcage coil,

whose structure was derived from a laboratory birdcage coil we have used in experimental studies [1] to reproduce an equivalent worst-case RF field generated during MRI procedures (Figure 1(a)). The coil is 60 cm high, with an inner radius of 30 cm. Two voltage sources were applied at one of the two external rings of the coil, with a 90° shift both in space and time. Inside the coil, a circularly polarized magnetic field was thus generated. The birdcage was loaded with a model of the human trunk made up of 34 different tissues with a resolution of 2 mm. Preliminary simulations were performed in order to set the amplitude of the voltage sources to obtain an averaged whole body SAR of 1 W/kg inside the VHD, not implanted with any metal object.

Finally, two typical PM implants were reproduced inside the human trunk model: in one, the PM chassis is located in the left pectoral region, few millimeters under the skin, and the lead is inserted into the left subclavian vein, through the left brachoencefalic vein, the superior cava vein, the right atrium, up to the right ventricle, where the tip was placed in contact with the heart wall. The other configuration reproduces a right-pectoral implant: the lead reaches the right atrium through the right subclavian vein, the right brachoencefalic vein, and the superior cava vein. The path from the right atrium to the right ventricle is the same for the two configurations (Figure 1(b)). A unipolar lead is modeled as an inner metal wire (radius = 1 mm), an external insulation sheath (radius = 2 mm), and an exposed bare tip of 1 mm.

The SAR distribution was computed for 4 phantoms:

- PHANTOM 1 — VHD: 34-tissues modeled VHD (complete VHD, provide by ITIS Foundation);
- PHANTOM 2 — HOM: a fully homogeneous phantom, with dielectric properties assumed uniform as the weighted mean value among body tissues;
- PHANTOM 3 — AIR: internal air cavities (mouth cavity, larynx, windpipe, lungs, stomach, intestine) in a homogeneous medium;
- PHANTOM 4 — HEART: blood, vessels, heart, all modeled with the dielectric properties of the blood, in a homogeneous medium;

The dielectric properties of the human VHD were derived from an open-source database available on internet [4], at the frequency of 64 MHz. For the homogeneous phantom, the dielectric properties were chosen as the weighted mean value of the human tissues at 64 MHz, resulting in a permittivity of 79 and a conductivity of 0.59 S/m.

The graded mesh used to run the FDTD algorithm was the same for all the phantoms, so to keep constant the spatial resolution of the resulting SAR patterns. The PM was placed in the same location in all the phantoms. Both the right and left pectoral implants were simulated. Phantom 1 was used as reference SAR pattern.

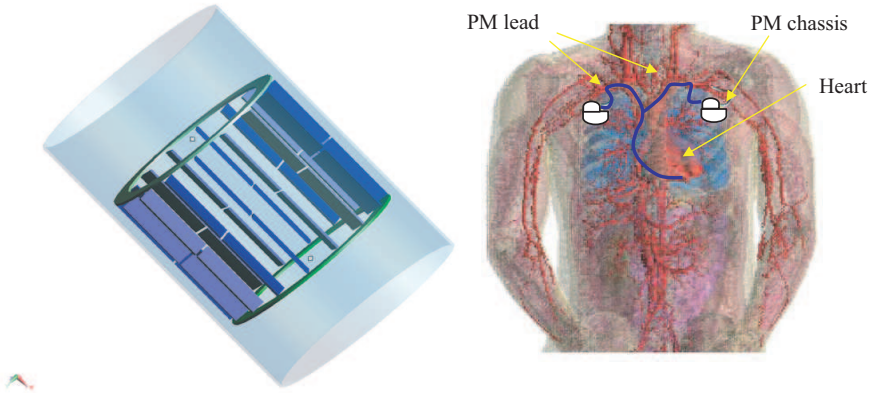

Figure 1: (a) Birdcage coil FDTD model; (b) PM implant configurations inside the HVD. Blood vessels and heart are highlighted.

Inside each phantom, a right and left pacemaker implant was reproduced, and the local SAR induced by the birdcage coil at the lead tip was estimated in both cases. An averaging mass of 1 mg was chosen for local SAR estimation. A volume of 1 mg represents a good trade-off between

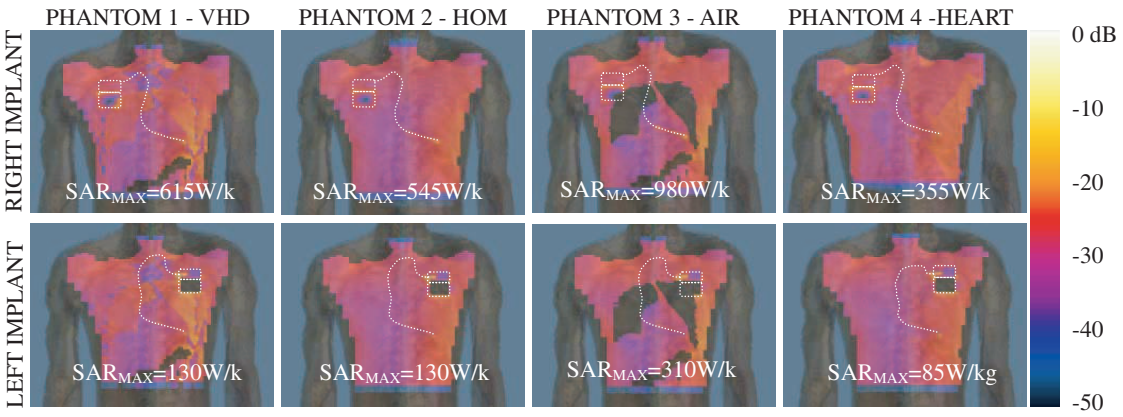

Figure 2: Local SAR patterns computed for phantoms 1–4 (refer to text) on a transversal plane through the pacemaker lead tip. Color-maps are expressed in dB, normalized to 1000 W/kg. The dotted white lines indicate the implant location and the lead path.

a volume big enough to reveal the increase in locally induced SAR, but not too small to be just a spurious "hot spot", unreliable for the evaluation of potential tissue damage due to RF exposure [6]. We also computed the whole-body averaged SAR induced by the RF field inside each phantom, with no implant inside. Thus, besides the effects on local SAR distribution of the different trunk models, we evaluated the impact on the overall exposure in terms of whole-body mean SAR as well.

3. RESULTS

The local SAR induced at the lead tip inside the complete VHD markedly differs if the pacemaker is implanted in the right or in the left pectoral region. The local SAR distribution (averaged over 1 mg mass) reached a maximum value at the lead tip of 615 W/kg for the right implant and 130 W/kg for the left one. Without any implant, the average whole-body SAR for the VHD was 1 W/kg. The other phantoms have been compared with these results. The average whole-body SAR computed for the four simplifications of the VHD did not substantially differ from the complete VHD: 1.1 W/kg — Phantom 2; 1.2 W/kg (Phantom 3); 0.9 W/kg (Phantom 4). On the other hand, the different models of human tissues play a major role in the estimation of the local SAR at the implant lead tip. The induced SAR in the fully homogeneous phantom (phantom 2) is pretty similar to the complete VHD -11.3% for the right implant and $+0.3\%$ for the left one), whereas the gap becomes much larger for other human-trunk models. In terms of percentage under/overestimation with respect to the complete HVD, the local SAR is $+136.0\%/+60.2\%$ (left/right implant) for phantom 3, and $-35.6\%/-42.2\%$ (left/right implant) for phantom 4. The overall local SAR patterns computed for phantoms 1–4 (averaged over 1 mg mass) are reported in Figure 2. Color-scale maps are given for a transversal plane through the implant lead tip and the maximum local SAR value are also reported.

4. DISCUSSION

Simulations on the complete VHD show that the local SAR reached at the pacemaker lead tip markedly differs between the two implant locations typically adopted in clinical practice: the right and left pectoral region. In the former, the induced SAR is over 4-time higher than in the latter. This result is consistent with other studies already published in the literature [1]. The different lengths and paths of the lead, as well as the path of the electrical currents induced by the birdcage coil may determine a different coupling between the metallic parts of the implant and the RF field, thus explaining such differences. We also studied the impact of a simplification of the complete VHD model by comparing different types of phantoms. Our first finding was that local SAR induced in the fully homogeneous phantom (made of a single domain with constant dielectric properties), is pretty close to the one computed for the complete VHD, for both implant locations. In the other types of phantom, which are somewhat half-way between the complete VHD and the fully homogeneous phantom, we found relevant differences. In particular, the modeling of the blood vessels and the heart inside the homogeneous phantom results in an underestimation of the local SAR at the lead tip. We can speculate that the higher conductivity of the blood compared to the homogeneous tissue is the cause of such an underestimation. On the other hand, an high overestimation was observed when air cavities are modeled inside the homogeneous phantom. Empty cavities in the

central portion create high E-field areas all along the cavities borders where PM leads are usually located. Thus, the induced currents on the lead will be much higher than in the other phantom types. Several papers corroborate this hypothesis, showing that the distance between the lead path and the phantom edges plays a major role in determining the amount of induced heating at the lead tip [1, 3].

5. CONCLUSIONS

We showed that a homogeneous phantom with constant dielectric properties represents a reliable simplification of the anatomical structure of human body tissues, in the evaluation of the RF induced local heating on metallic implants. Partial simplifications of the complete VHD give less accurate results.

REFERENCES

1. Mattei, E., M. Triventi, G. Calcagnini, F. Censi, W. Kainz, G. Mendoza, H. I. Bassen, and P. Bartolini, "Complexity of MRI induced heating on metallic leads: experimental measurements of 374 configurations," *Biomed Eng. Online*, Vol. 7, 11, Mar. 3, 2008.
2. Gimbel, J. R., "Magnetic resonance imaging of implantable cardiac rhythm devices at 3.0 tesla," *Pacing Clin. Electrophysiol.*, Vol. 31, No. 7, 795–801, Jul. 2008.
3. Lastname, F. M. and F. M. Lastname, "Title of the journal paper," *Journal Title Abbreviation*, Vol. 34, No. 10, 1064–1076, 1986.
4. Nordbeck, P., I. Weiss, P. Ehses, O. Ritter, M. Warmuth, F. Fidler, V. Herold, P. M. Jakob, M. E. Ladd, H. H. Quick, and W. R. Bauer, "Measuring RF-induced currents inside implants: Impact of device configuration on MRI safety of cardiac pacemaker leads," *Magn. Reson Med.*, Vol. 61, No. 3, 570-8, Mar. 2009.
5. Lastname, F. M., *Book Title*, Wiley-Interscience, New York, 1986.
6. "An internet resource for the calculation of the dielectric properties of body tissues in the frequency range 10 Hz–300 GHz," Institute for Applied Physics, Italian National Research Council, Nello Carrara, Florence, Italy, Last acces November 2010, http://niremf.ifac.cnr.it/tissprop/.
7. Mattei, E., M. Triventi, G. Calcagnini, F. Censi, and P. Bartolini, "Radiofrequency dosimetry in subjects implanted with metallic structures undergoing MRI: A numerical study," *Am. J. Biomed. Sci.*, Vol. 1, No. 4, 373–384, 2009.

Design and Fabrication of Planar Magnetoinductive Resonator Arrays for MRI System Field Shaping

P. Drexler, **D. Nespor**, **P. Fiala**, **R. Kubasek**, **and K. Bartusek**
Department of Theoretical and Experimental Electrical Engineering
Brno University of Technology, Kolejni 2906/4, 612 00 Brno, Czech Republic

Abstract— For the experiments with MR system sensitivity increasing by means of periodical metamaterial structures a magnetoinductive resonator array has to be designed. Proposed design guidelines for precise new array assembly are described and the results of new arrays measurement are presented. For the array's resonant frequency measurement the dip meter method is described. For resonant frequency measurement of single loop a return loss method is presented. As a suitable alternative a new coaxial shunt measurement method is proposed. The results of the new arrays measurement by means of coaxial shunt method are presented also.

1. INTRODUCTION

A possibility of manipulation of magnetic field distribution in magnetic resonance (MR) systems has been shown in recent works [1]. Some approaches consider this phenomenon as a subwavelength imaging which can be observed with metamaterial slabs [2]. The main goal of manipulation of magnetic field distribution in MR systems is to increase the received MR signal which is a response to radiofrequency sample excitation. A suitable shaped resonant device is placed in the MR system cavity close to the examined specimen. Coil radiated RF magnetic field pulse in the cavity excites the specimen nuclei in order to obtain the nuclei response. The resonant device affects the field distribution close to the specimen in order to increase the excitation field and response field in the area of the specimen. Published papers have shown a significant signal level increasing and the image quality improvement in medical type of magnetic resonance imaging (MRI) system [3]. The resonant device is configured as a coupled arrays of planar capacitance loaded ring resonators.

For the application in the experimental MRI system, we need to design a coupled resonator arrays with considerably smaller dimension, which is restricted by the tomograph cavity. Further, the operational frequency of the MR tomograph is $f \sim 200\,\mathrm{MHz}$, which is higher in compare to the medical type tomograph. In previous work [4], the theoretical approach to resonator arrays design has been presented. There has been presented some issues of the resonators fabrication and component selections. Early results have shown the need to careful resonators assembly. The suggested points of the design have been taken into the account in the next resonator arrays fabrication. The improved resonator arrays fabrication approach will be presented in the paper. There will bee showed the measured resonant characteristics of the arrays.

2. MEASUREMENT METHODS FOR RING RESONATORS

The previous work has dealt with the basic concept of magnetoinductive (MI) resonator array. In view of the intended application, the MI array can be considered as a magnetic field shaping lens. Each of the resonators in the array is characteristic by its resonant frequency which has to be equal to the others. The total frequency characteristic of the array consists of the superposition of partial resonant curves of each resonator, which are mutually coupled.

Measurement of resonant frequency of magnetoinductive (MI) resonator array has been described in [4]. The measurement method has utilized a grid dip oscillator with external coil to couple the RF energy to the array. This method has been used for measurement of the total frequency characteristic. The output frequency of the grid dip oscillator has been varied from 180 MHz up to 220 MHz. At the peak of resonant frequency of the whole array a remarkable drop of the oscillator's anode current has been observed as the resonator array drained the energy from the excitation LC circuit. The frequency of the maximal drop has been taken by means of spectral analyzer equipped with the wire loop at the input. An frequency counter may be used also. The schematic of the measurement setup is shown in Figure 1.

However, this method doesn't provide information on the particular resonators tuning accuracy. For the measurement of the single resonator resonant curve a method utilizing a small coil, directional coupler, frequency generator and spectrum analyzer has been proposed, see Figure 2 (left part). For the experiments the analyzer with built-in tracking generator and directional coupler has

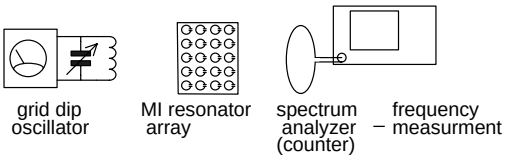

Figure 1: Setup for measurement of total resonant curve of the MI resonator array.

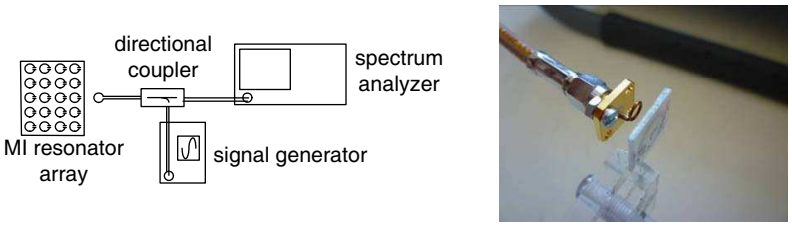

Figure 2: Setup for resonant curve of (a) single resonator measurement and (b) the loop probe detail.

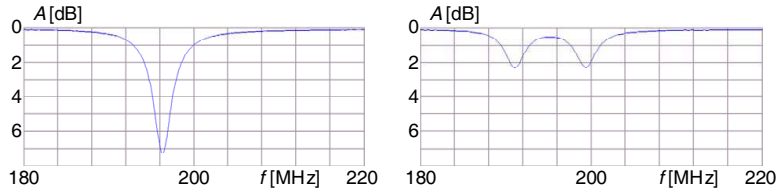

Figure 3: Loop probe return loss measurement in (a) proximity of single resonator and (b) two coupled resonators.

been used and the return loss of the small loop probe has been measured for single resonator. The detail of the loop probe is shown in Figure 2 (right part). At the resonant frequency the energy is drained by the resonator and the return loss drops. The frequency of the dip can be read utilizing analyzer's marker.

In the right part of Figure 2, a measurement of a single resonator with the loop probe is shown. The example of loop probe return loss is shown in the left part of Figure 3 as a remarkable drop with dip level above 7 dB. In the same configuration, a measurement of two coupled resonator (which are parallel) may be performed which is shown in the right of the Figure 3. The resonant curve has two dips around the original center resonant frequency. The dip level is decreased since the absorbed energy split in two branches.

3. THE RESULTS OF SINGLE RESONATORS MEASUREMENT

In [4], a design and fabrication of early experimental coupled MI resonator arrays has been described. Each array consists of 25 ring resonators (detail in Figure 4(a)). The inductance of the proposed resonator layout was calculated and the load capacity has been assembled as a combination of three capacitors in order to get the desired resonant frequency. Hence, it hasn't been bargain for a precise resonant frequency obtainment. It was sufficient for experimental development. The results of the total resonant curve of the arrays were presented in [4]. The discrepancy to the expected frequencies of resonant branches has been found out. One of the reasons is that the utilized dip meter measurement method (Figure 1) transformed an indispensable inductance of the dip meter's coil in to the array. This probably caused the disagreement to the expected results. Hence, this method has been brand as unsuitable because of the large probe inductance. The second reason was the inaccurate resonators mutual tuning. To find out the partial resonant frequencies of the resonators a measurement according to the loop probe return loss method has been performed. The resulting map of resonant frequencies of the resonators is shown in Figure 4(b). The considerable differences in resonant frequencies are evident.

The differences are caused by non-sufficiently accuracy of assembled capacitor and their combinations. Another source of the variance is un-reproducible soldering process of parallel capacitor combination (which is obvious in Figure 4(a)). The conclusion is that by the next MI array fabrication only one capacitor per ring has to be used to minimize the soldering-caused variance. The

197,88	193,49	195,37	196,16	195,69
196,00	193,00	199,16	197,26	194,58
199,14	196,47	194,90	197,10	197,57
195,69	194,12	196,17	196,95	196,94
194,43	196,16	198,52	193,80	193,49

(b)

198,04	198,67	197,73	196,63	198,20
198,51	200,24	197,26	196,78	197,41
198,51	199,45	198,04	198,35	198,04
197,26	198,98	198,82	198,35	197,73
197,24	198,67	197,41	197,73	198,35

(d)

200,22	199,78	199,75	200,43	198,98
199,16	199,45	199,29	198,98	198,51
199,77	198,55	200,22	198,20	200,08
199,45	199,92	199,16	199,16	199,16
201,65	201,02	201,80	200,24	199,92

(e)

(a) (c)

Figure 4: (a) Early MI array detail and (b) its map of resonant frequencies in MHz, (c) new MI array detail and (d) map of resonant frequencies for array with narrow strip in MHz and (e) for array with a broad strip in MHz.

capacitor with 1% accuracy has to be used also. The desired resonant frequency should be set by the ring dimension modification using the modified Wheeler formula or current sheet approximation formula [4]. Instead of the conventional soldering the reflow soldering using mask and soldering flux should be considered in order to preserve the assembly accuracy.

Considering the guidelines for precise resonators assembly a new MI resonator arrays has been fabricated (Figure 4(c)). The array has been assembled with 100 pF chip capacitors with 1% accuracy. One of the arrays has broader strip in compare to the second. The second array had a larger diameter. The dimensions of both have been calculated to obtain the same resonant frequency. The map of the resonant frequencies of the new array with narrow strip and larger diameter is shown in Figure 4(d). The map of the resonant frequencies of the new array with broad strip and smaller diameter is shown in Figure 4(e). The differences in resonant frequencies have been reduced. The resonant frequencies of the array with a broader strip were a slightly higher. This was probably caused by inaccuracy of the calculation relations [4]. The calculated inductance of the ring is 255.1 nH. The next step was to find out the total resonant curve of the MI array.

4. NEW METHOD FOR TOTAL RESONANT CURVE MEASUREMENT

The issue of suitable measurement method selection for total resonant curve of the array appears. The dip meter measurement method which has been described above is questionable. Due to its limited sensitivity the coil probe has to be placed close to the array which causes a large mutual inductance. The mutual inductance to the sensing coil may be decreased in case of measurement in MR system. It is possible to place the coil probe in larger distance thanks to much higher excitation field and very sensitive MR receiver channel. However, this method doesn't provide information about the resonant frequencies, only about their mutual differences.

A new method for total resonant curve of the MI array has been proposed. The method utilizes modified coaxial shunt which is equipped with feed-in and feed-out transmission lines — coaxial cables. To keep the simple design and fabrication the coaxial shunt has been designed as cubical configuration of N-female connectors, center conductor and side walls. However, the lengthwise dimension of 5 cm is considerably smaller in compare to the length of the wave with frequency 200 MHz on the line (0.99 m on coaxial cable with 0.66 velocity factor). Therefore, we can consider a quasistatic case and the impedance mismatch can be neglected. By the shunt design an issue of the necessity of all of the side walls occurred. The field distribution simulation outputs in the 4-walls shunt and the 1-wall shunt cross-sections are shown in Figures 5(a)–(d). The wall in Figures 5(c)–(d) is at the bottom. The simulation results indicate that the 1-wall shunt should be sufficient for the total resonant curves examination. The 3-walls shunt should be considered also because of reduced loss and easy array inserting. It should be noted that the most of the magnetic flux in the shunt is concentrated round the inner conductor. Therefore, the resonators which are situated closer to the inner conductor will have the major influence on the total resonance curve shape.

The 1-wall shunt is shown in Figure 6(a). In Figure 6(b), is a insertion loss of the 1-wall shunt in range of 180 MHz–220 MHz. The loss achieves a low value around 1 dB. The 3-walls shunt is shown in Figure 6(c). In Figure 6(d) is the insertion loss of the 3-walls shunt in the same range. The loss is under the level of 1 dB. When we cover the open aperture oft the 3-walls shunt we obtain a 4-walls shunt. The insertion loss measurement didn't show a significant effect of the cover to the insertion loss.

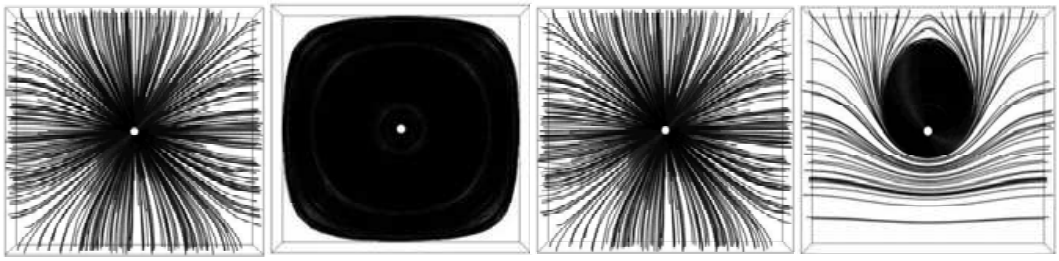

(a) (b) (c) (d)

Figure 5: Field lines for 4-walls shunt: (a) electric, (b) magnetic, for 1-wall shunt: (c) electric, (d) magnetic.

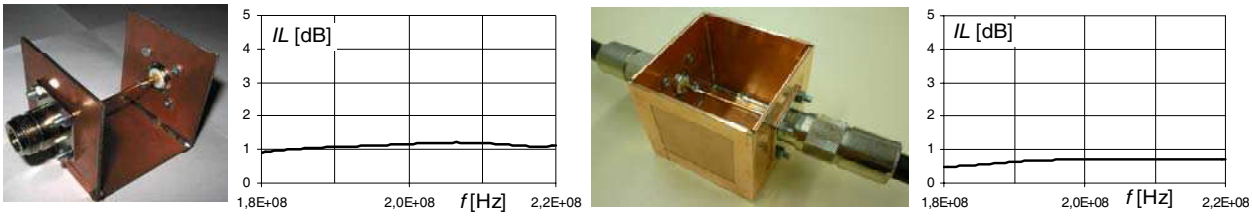

(a) (b) (c) (d)

Figure 6: (a) 1-wall shunt and (b) its insertion loss. (c) 3-walls shunt and (d) its insertion loss.

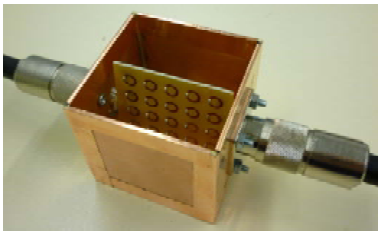

Figure 7: Position of resonator array in the 3-walls shunt.

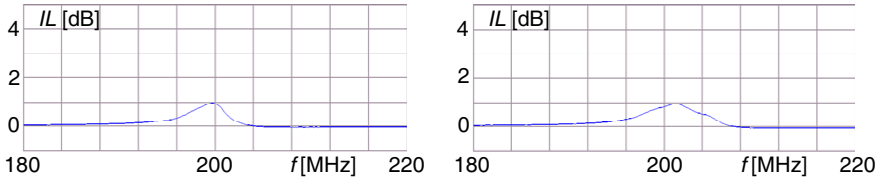

(a) (b)

Figure 8: Insertion loss measurement of array (a) with narrow strip and (b) with broad strip.

5. RESULTS OF NEW MI RESONATOR ARRAYS MEASUREMENT

A 3-walls shunt was used for the total resonant curve measurement. The resonator arrays have been placed in vertical position next to inner conductor as shown in Figure 7. The measurement has been performed for the array with a narrow strip and for the array with a broad strip. The results of the insertion loss measurement are shown in Figure 8. The maximum insertion loss of the array with a narrow strip is 0.9 dB at resonant frequency 199.77 MHz. The maximum insertion loss of the array with a broad strip is 0.9 dB at resonant frequency 201.188 MHz.

6. CONCLUSION

The ongoing work on the MI resonator array design and fabrication and the examination of arrays properties are described in this contribution. There were presented methods for capacitance loaded ring resonant frequency measurement. The method utilizing dip meter and frequency counter is simple, but requires a manual tuning of excitation frequency which results in inaccurate resonance determination. The method of loop probe return loss measurement utilizes a small coil and requires directional coupler and tracking generator. It is desirable to use a spectrum analyzer with built-in return loss measurement. This method is suitable for measurement of individual resonators in the array. For the total resonance curve measurement an alternative method utilizing coaxial shunt

has been proposed. Is has been shown that the simply box-shaped construction of the shunt can be used. Respecting the guidelines for precise array assembly a new samples have been prepared. The resonant frequency value variance has been reduced. The early results of the MI arrays resonant frequency measurement by means of coaxial shunt have been presented.

ACKNOWLEDGMENT

The work described in the paper was financially supported by the research project GA102/09/0314, research plan MSM 0021630513 and project of the BUT Grant Agency FEKT-S-10-13.

REFERENCES

1. Wiltshire, M. C. K., J. V. Hajnal, J. B. Pendry, D. J. Edwards, and C. J. Stevens, "Metamaterial endoscope for magnetic field transfer: Near field imaging with magnetic wires," *Optic Express*, Vol. 11, No. 7, 2003.
2. Wiltshire, M. C. K., J. B. Pendry, and J. V. Hajnal, "Sub-wavelength imaging at radio frequency," *Journal of Physics: Condensed Matter*, Vol. 18, No. 22, 2006.
3. Freire, M. J., R. Marques, L. Jelinek, and V. Delgado, "Potential applications of a $\mu = -1$ metamaterial superlens for magnetic resonance imaging," *Procedding of 3rd International Congress on Advanced Electromagnetic Materials in Microwaves and Optics*, 138–140, London, UK, 2009.
4. Bartusek, K., P. Drexler, P. Fiala, R. Kadlec, and R. Kubasek, "Magnetoinductive lens for experimental mid-field MR tomograph," *PIERS Online*, Vol. 6, No. 7, 621–624, 2010.

Measurement of Concentration and Mobility Spectrum of Air Ions in the Natural Environment

Z. Roubal[1], **K. Bartušek**[2], **Z. Szabó**[1], **and P. Drexler**[1]

[1]Department of Theoretical and Experimental Electrical Engineering, Brno University of Technology
Kolejní 2906/4, Brno 612 00, Czech Republic
[2]Institute of Scientific Instruments, Academy of Sciences of the Czech Republic
Kralovopolska 147, Brno 612 64, Czech Republic

Abstract— It was confirmed that the concentration of light air ions has a positive influence on human health. For an objective appraisal of the influence of synthetic sources of negative air ions, a comparison with the natural environment is necessary. The concentration of air ions and their mobility spectrum can be determined by the help of an aspiration condenser. Based on measurements using the condenser, the spectrum mobility can be calculated from the measured saturation characteristics. In the report, different options suggesting the most advantageous approach to the approximation of saturation characteristics are discussed from the point of view of minimal numeric error. The saturation characteristic approximations are made in Matlab. Using this method, the comparison of air ion spectra in different types of environment will be done. These types include a natural forest on the one hand and the production of a synthetic source of negative air ions on the other.

1. INTRODUCTION

In industrial zones, where the environment air is often polluted with dust and smog, the concentration of air ions can be regulated or measured only with difficulty. Any thus impaired area shows an inherent deficiency of negative ions and, conversely, an abundance of positive ions complementing the nano and microscopic dust particles. Significantly, the described aspects have a markedly negative effect on the overal degree of fatigue and professional performance of a human being [1, 2]. The impact of environment on a human organism has been analyzed in studies [1, 2]. In the DTEEE laboratories, the methodology supporting the measurement of air ions concentration and mobility spectrum utilizes an aspiration condenser [3], this method is dependent upon a suitable approximation of saturation characteristics. The presented article describes the method of determining the air ions mobility spectrum on the basis of the aspiration condenser saturation characteristics. Further, the proposed analysis will be complemented with the experimental measurement data.

2. ASPIRATION CONDENSER, MOBILITY SPECTRUM, SATURATION CHARACTERISTICS

An aspiration condenser (Gerdien tube, AC) is instrumental towards the measurement of air ions concentration assuming that the volume of tested air has not been limited or the ions are continuously generated. In the time domain, it is possible to measure by means of an AC only ions of one polarity; then, following a certain interval, ions of the other polarity can be measured. Ionized air is sucked into the AC by a ventilator. There is a homogeneous electric field set between the inner and the outer electrode. If an electric ion shows a negative electric charge and the collecting inner electrode has a positive electric potential, the ion is progressively attracted to the inner electrode. Provided that the ion impinges upon the electrode, it will induce an electric current that is measured by the help of a sensitive electrometric picoampermeter [4]. The velocity of the ions motion in the electric field can be described by mobility k [$\mathrm{m^2{\cdot}V^{-1}s^{-1}}$].

It is possible to determine boundary mobility k_m for every AC configuration.

All ions showing an index of mobility greater than k_m will impinge upon the inner electrode; however, only a proportionate part will impinge in ions whose mobility is smaller than k_m. Based on the aspiration condenser parameters, the air flow volume rate is defined as

$$M = \left(r_2^2 - r_1^2\right) - \pi \cdot v_x, \tag{1}$$

where M, r_2, r_1, v_x, ... are the air flow volume rate, the outer electrode radius, the inner electrode radius, and the air flow velocity, respectively.

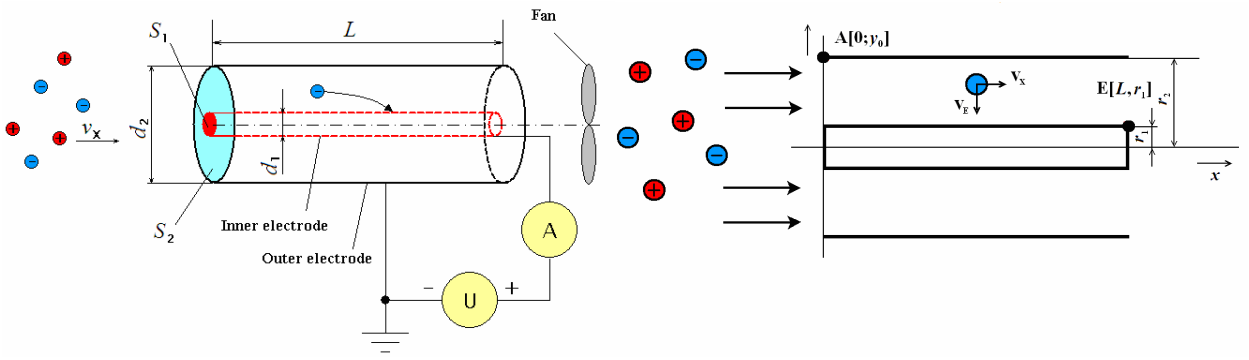

Figure 1: The basic principle of an aspiration condenser.

The main parameter applied for the definition of air ions mobility consists in boundary mobility k_m,

$$k_m = \frac{\varepsilon_0 \cdot \varepsilon_r \cdot M}{C_{AK} \cdot U_{AK}}, \tag{2}$$

where ε_0, ε_r, C_{AK}, U_{AK}, ... are the vacuum permittivity, the relative permittivity, the AC capacity, and the AC polarization voltage, respectively. Then, for current I measured by the electrometric picoampermeter, we can define

$$I_{k<k_m} = \frac{k}{k_m} \cdot n \cdot q \cdot M, \quad I_{k \geq k_m} = n \cdot q \cdot M, \tag{3}$$

where n, q ... are the volume concentration of ions and the elementary charge, respectively.

2.1. Concentration of the Volume Density of Ions

The condition of equivalence between an ion charge and an electron elementary charge is satisfied only in light ions, which implies that the condition is not valid in heavy ions that contain several charges of the described type. Then, the relevant situation is referred to as relative number of ions per volume unit. The starting point for the determination of an ion mobility consists in the quantity of charge q and volume concentration of electric charge.

$$n_{+-}(k_1, k_2) = \frac{\rho_{+-}(k_1, k_2)}{q}. \tag{4}$$

Now, net electric current in the circuit can be written in the form of

$$I = M \cdot \frac{1}{k_m} \int_0^{k_m} k \cdot \rho(k)\, dk + M \cdot \int_{k_m}^{\infty} k \cdot \rho(k)\, dk. \tag{5}$$

2.2. Mobility Spectrum

The saturation characteristic (saturation curve, SC) of an aspiration condenser is the dependence of the measured electric current passing through the AC upon polarization voltage U_{AK} (Fig. 2). The authors of report [3] have derived, using relation (5), the number of ions whose mobility is greater than k_m according to the following relation

$$\int_{k_m}^{\infty} n(k)\, dk = Z - U\frac{dZ}{dU}. \tag{6}$$

where the auxiliary variable Z is given by relation (7) and indicates the measured number of ions for the given saturation voltage

$$Z = \frac{I}{q \cdot M}. \tag{7}$$

The characteristic from (7) is graphically represented in Fig. 3. In order to determine the number of ions in the mobility interval, we need to perform the first-order derivative for two voltages between the AC electrodes and find the point of intersection with the y-axis, Fig. 3.

The resulting relation for the determination of the number of ions upon the given mobility interval for $k_{m1} < k_{m2}$ is provided by Equation (8).

$$n\left(k_{m1}, k_{m2}\right) = \int_{k_{m1}}^{\infty} n\left(k\right)\ dk - \int_{k_{m2}}^{\infty} n\left(k\right)\ dk. \tag{8}$$

The saturation characteristic shows a tendency to rise (rising pattern). Owing to edge effects on the AC, the characteristic is not ideal. The AC behaves as if it were provided with a higher number of collecting electrodes, and the measuring electrode appears to be the second item in line. The resulting curve resembles the characteristic of a two-electrode spectrometer with an AC [5].

3. SATURATION CHARACTERISTIC APPROXIMATION. MOBILITY SPECTRUM

The concentration of ions (8) is sensitive to noises in the measured signal. With respect to the accuracy requirement related to the expression of saturation characteristic, it is necessary to obtain no less than 200 values of measured current to express the point of characteristic including indeterminates of the A, B type. The tension on the electrode of polarization voltage U_{AK} is selected dynamically, namely in such a manner that, with small step values of stress increment, we proceed in maxima of the second-order derivatives of the SC (as exemplified in Fig. 3). The approximation can be performed using a polynomial or, rather more advantageously, a cubic spline. Fig. 5 shows a comparison of both approximations. Using relation (4), we obtained ion concentrations in the mobility interval between 2.3×10^4 and 6.7×10^4 [$\mathrm{m^2 \cdot V^{-1} \cdot s^{-1}}$].

The approximation by an SC polynomial is represented in Fig. 6; however, this approximation does not constitute a convenient alternative owing to its tendency to generate oscillation around the assumed value.

In the spline approximation, the process was tested of the deletion of errors resulting from A-type indeterminates. The final spectrum compared with the spline approximation is shown in Fig. 9.

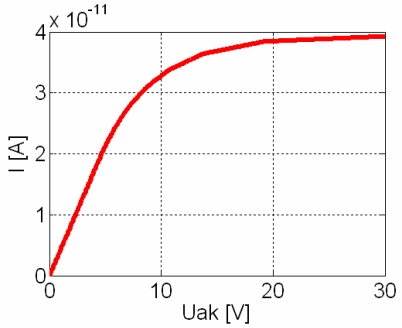

Figure 2: Saturation characteristic.

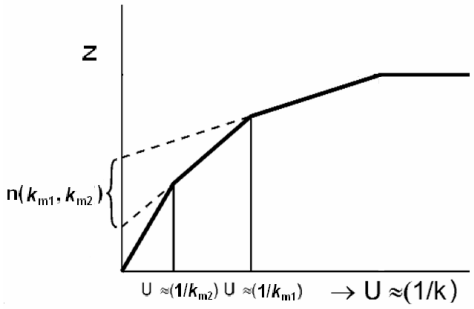

Figure 3: An illustration of the spectrum determination after conversion to Z.

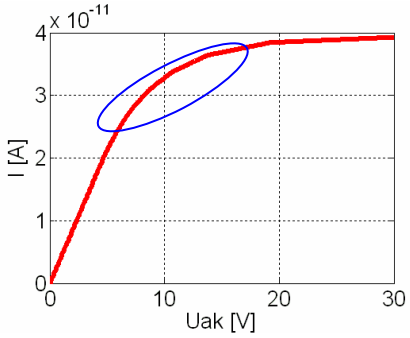

Figure 4: Critical area of measurement for the determination of air ions mobility spectrum.

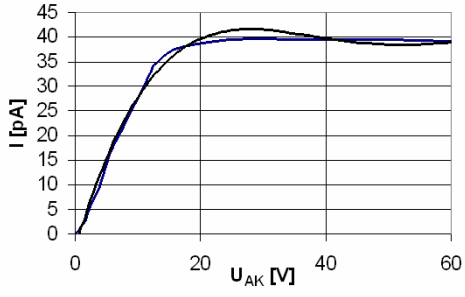

Figure 5: Polynomial (black curve) and spline (blue curve) interpolation.

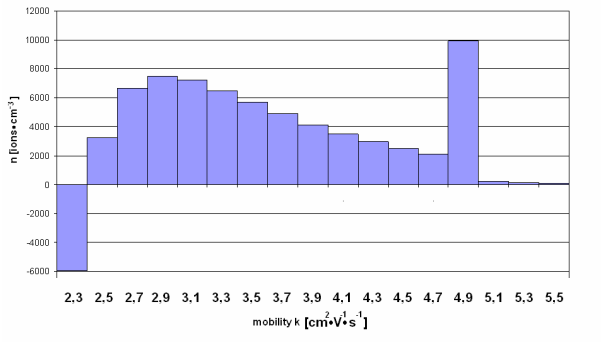

Figure 6: Spectrum for polynomial interpolation.

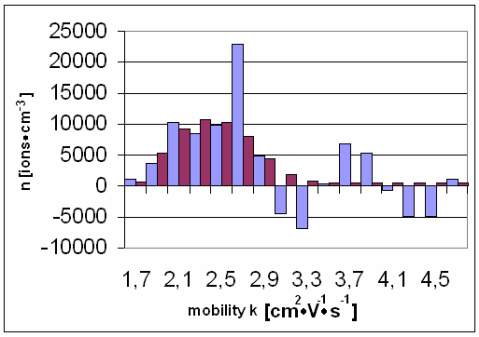

Figure 7: Spectrum for spline interpolation (blue) and averaging (violet).

4. AIR IONS CONCENTRATION SPECTRUM: MEASUREMENT EXPERIMENTS

The experiments were performed through the use of two aspiration condensers; we measured the concentration of both positive and negative ions. One (the first) of the two ACs applied was an automatized version utilized in [5], while the other one had been developed by the Institute of Scientific Instruments at the Academy of Sciences of the CR, Brno (Fig. 8). The source of ions was a BIV-06 commercial ion generator; Fig. 9 shows the relevant air ions mobility spectrum as measured by the AC at the DTEE (blue) and the AC at the ISI, AS CR Brno (red).

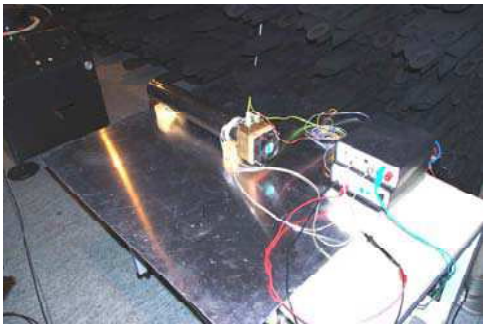

Figure 8: The ISI aspiration condenser measurement system.

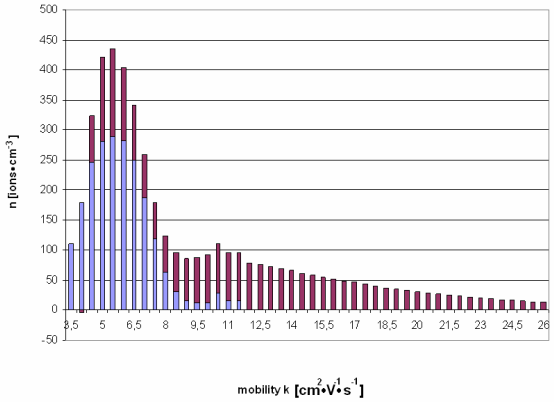

Figure 9: Comparison of the obtained mobility spectrum in both ACs.

5. THE MEASUREMENT OF AIR IONS CONCENTRATION SPECTRUM IN A CONIFEROUS FOREST: THE NATURAL ENVIRONMENT

Figure 10: The measuring system configuration in the Palackého vrch (Palacký Hill) forest.

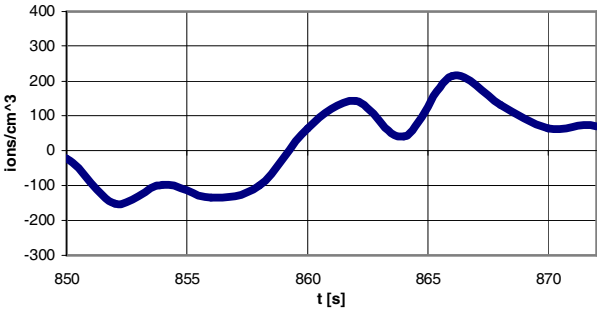

Figure 11: Time dependence of the number of ions: the forest.

6. CONCLUSION

The report contains a discussion related to the evaluation of saturation characteristics. The final stages of the experiment included both laboratory and open-space comparison of two aspiration condensers (ACs); within this process, the first-produced AC was tested using the other, calibrated one. The results of both theoretical and experimental qualities testing are comparable; significantly, critical spots and features of the ACs have been identified and described.

ACKNOWLEDGMENT

The work described in the paper was financially supported by the research project GA102/09/0314, research plan MSM 0021630513, and project of the BUT Grant Agency FEKT-S-10-13.

REFERENCES

1. Tikhonov, V. P., A. A. Temnov, V. A. Kushnir, T. V. Sirota, E. G. Litvinova, M. V. Zakharchenko, and M. N. Kondrashova, "Complex therapeutical effect of ionized air: Stimulation of the immune system and decrease in excessive serotonin. H_2O_2 as a link between the two counterparts," *IEEE Trans. Plasma Scien.*, Vol. 32, No. 4, 1661–1667, 2004.
2. Kondrashova, M. N., E. V. Grigigorreko, A. N. Tikhonov, T. V. Sirota, A. V. Temnov, I. G. Stavrovskaya, N. I. Kosyakova, N. V. Lange, and V. P. Tikonov, "The primary physicochemical mechanism for the beneficia biological/medical effects of negative air ions," *IEEE Trans. Plasma Scien.*, Vol. 28, No. 1, 230–237, 2000.
3. Vojtek T., T. Skoupil, P. Fiala, and K. Bartusek, "Accuracy of air ion field measurement," *PIERS Proceedings*, 412–415, Cambridge, USA, March 26–29, 2006,
4. Vojtek, T., T. Skoupil, P. Fiala, and K. Bartusek, "Accuracy of air ion field measurement," *PIERS Online*, Vol. 2, No. 4, 412–415, 2006.
5. Bartusek, K., "Merní spektrálních charakteristik iontových polí," *Elektrorevue*, [online], 2001, http://www.elektro-revue.cz/clanky/01038/index.html.
6. Roubal, Z. and M. Steinbauer, "Design of electrometric amplifier for aspiration condenser measurement," *PIERS Proceedings*, 1430–1434, Xi'an, China, March 22–26, 2010.

Cryogenic Technique for Cancer Destroying Optimalization

J. Hrozek and J. Mikulka
Department of Theoretical and Experimental Electrical Engineering, Brno University of Technology
Kolejni 2906/4, Brno 612 00, Czech Republic

Abstract— This paper deals with heat distribution in human tissues. The Bioheat equation is used for modeling of heat transfer in tissues. Software application Cryomodel is described in this paper. The Cryomodel is realized in Matlab software for simulation of cryosurgery operation. Simulation is realized in 3D space of tissue. The Cryomodel contains many adjustable parameters like: Temperature and diameter of cryoprobe and properties of tissue. The Cryomodel considers four layers of tissue and one centre of cancer. Layers of epidermis, dermis, subcutaneous fat and muscle for example. Optimization of tumor destroying is the main aim of this study. The Optimization is based on increasing of thermal conduction in tumor. This software application should be a good planning tool for doctors in practice.

1. INTRODUCTION

In medical applications of heat stimulations of tissue (hyperthermia and hypothermia) attributes of biological material for heat conduction and its effect on microcell system is used. Biological destroying effects on cell nucleus or cellulosa during the hyperthermia and gradient hypothermia are known. Injury of healthy cells is problem of applied hypothermia in radial direction from critical volume to cryoprobe [1, 2].

This paper deals with possibility of basic matter application into cell space. See Fig. 1. First way is application of basic matter into healthy cells in space B. Second way is application of basic matter into cancer cells in space A to shorten of cryoprobe application and minimizing of injury of the surrounding healthy tissue.

The Bioheat equation which is used in this paper was formulated by Henry Pennes in 1948. This fundamental equation is used without serious changes till now. The Bioheat equation is extended equation of heat transfer. All types of heat transfer diffusion equations are partial differential equation (PDE) of parabolic type. The Bioheat equation is:

$$\rho C \frac{\partial T}{\partial t} = \nabla \left(k \nabla T \right) + \rho_b w_b C_b \left(T_b - T \right) + \rho q_{met} \tag{1}$$

where ρ is density of tissue [kg/m^3], C is specific heat capacity [J/(kg·K)], T is temperature [K], t is time [s], k is thermal conductivity [W/(m·K)], b is blood, wb is blood perfusion [l/(s·kg)] and $qmet$ is metabolic heat generation rate [W/kg]. It is necessary to rewrite the Bioheat equation into formula (4) for computer processing. This equation is expressed by explicit method using a forward difference at time p and a second-order central difference see Equation (2) and (3).

$$\frac{T_j^{p+1} - T_j^p}{\Delta t} = \alpha \left[\frac{T_{j+1}^p - 2T_j^p + T_{j-1}^p}{(\Delta x)^2} \right]; \quad \alpha = \frac{k}{\rho C} \tag{2}$$

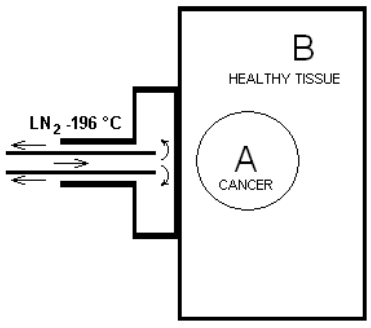

Figure 1: Scheme of cryosurgery.

where p is time level, i, j and k are calculated grid points, Δt is time [s], α is thermal diffusivity [m^2/s], Δx is edge of voxel [m].

$$T_{i,j,k}^{p+1} = \frac{\Delta t}{\rho C_{i,j,k} + \rho_b w_b C_b \Delta t} \cdot \frac{k}{(\Delta x)^2} \cdot \left(T_{i+1,j,k}^{p} + T_{i-1,j,k}^{p} + T_{i,j+1,k}^{p} + T_{i,j-1,k}^{p} + T_{i,j,k+1}^{p} + T_{i,j,k-1}^{p} - 6T_{i,j,k}^{p} \right) + T_{i,j,k}^{p} \cdot \frac{\rho C_{i,j,k}}{\rho C_{i,j,k} + \rho_b w_b C_b \Delta t} + \frac{\Delta t \left(\rho_b w_b C_b T_b + \rho q_{met} \right)}{\rho C_{i,j,k} + \rho_b w_b C_b \Delta t} \tag{3}$$

2. RUNNING APPLICATION

The Cryomodel application is able to solve a distribution of low temperatures in different human tissues. The temperature distribution is realized only for 3D space. Minimal dimension of edge of 3D space is limited by diameter of cryoprobe. This application counts with frozen and unfrozen regions also. It means that properties of tissues are depended on state (frozen/ unfrozen). This threshold is between -1°C and -8°C. The lower boundary is used in this study. Practical consequences of used frozen/ unfrozen condition are following: Frozen regions have higher thermal conduction and lower specific heat capacity than unfrozen regions therefore cooling rate and depth of penetration of low temperature are better for frozen state regions. This finding is fundamental. The Cryomodel consist three main sections. See Fig. 2.

"Control panel" section contains controls of simulation like Run, Save, Load and others. Check box "Set threshold" enables to see the region of killed cells (temperature below -13°C) only. User can select slice position (x means, that x = position of slider and y, z are from 1 to x dimension, z dimension). Button "Show C. R." shows cooling rates in defined depths 1, 2, to, 9 mm. Condition of cooling rate about 200°K·min^{-1} is necessary for good freezing process during the cryosurgery. "Show D.O.C" displays temperature dependence on depth.

In "Parameters of simulation" section is possible setup temperature and diameter of cryoprobe, dimensions of 3D matrix, layers and globe of tumor, time step, edge of voxel, threshold and time of during the simulation. The Cryomodel considers four layers of tissue and globe which represent a tumor. Setup of layer 4 is used for whole 3D matrix if the popup menu "Layer" is set on "4".

The "Properties of tissues" section consist density, thermal conductivity, specific heat, blood perfusion and metabolic heat generation. For each of four layers is possible select type of layers from popup menu and determine stability of simulation.

3. OPTIMIZATION

The main goal optimization of tumor destroying is based on increasing of thermal conductivity and decreasing of specific heat in tumor. In this case is higher drain of heat from tumor and time of

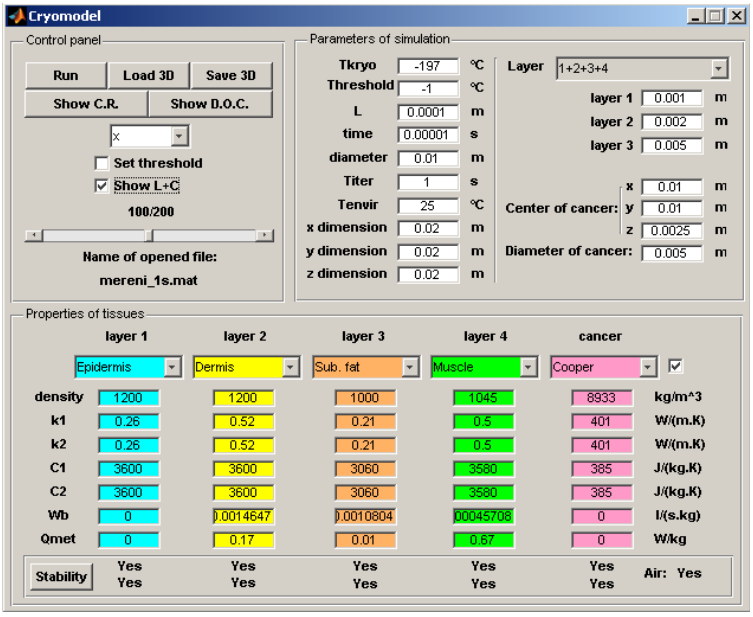

Figure 2: The running application.

cryoprobe application is shorter also. Healthy tissues are then less injured. Only the theoretical hypothesis is described in this paper. The globe of tumor is filled with thermal properties of optimized tumor. Surrounding space is filled with thermal properties of human tissue in four layers, epidermis, dermis, subcutaneous fat and muscle in this case. Average thermal conductivity of human tissue is about $0.5\,\mathrm{W{\cdot}m^{-1}{\cdot}K^{-1}}$ and average specific heat is about $3600\,\mathrm{J{\cdot}kg^{-1}{\cdot}K^{-1}}$. Results of simulation with optimized tumor are shown bellow on Fig. 3.

We can see that area inside of globe of tumor is frozen much more then healthy tissue in the same depth. Right side of Fig. 3 displays only region with temperature bellow −13°C. White lines display layers of tissue model and white circle displays globe of tumor. The same results are evident from Fig. 4.

On left side of Fig. 4 are displayed temperatures dependences of time in defined depth 1, 2, to, 9 mm. The cooling rate (gradient) $200\,\mathrm{K{\cdot}min^{-1}}$ is displayed like dotted line and temperature bellow -13 °C is displayed like dashed line. The cooling rate $200\,\mathrm{K{\cdot}min^{-1}}$ and temperature bellow −13°C simultaneously are the main conditions of total cells killing.

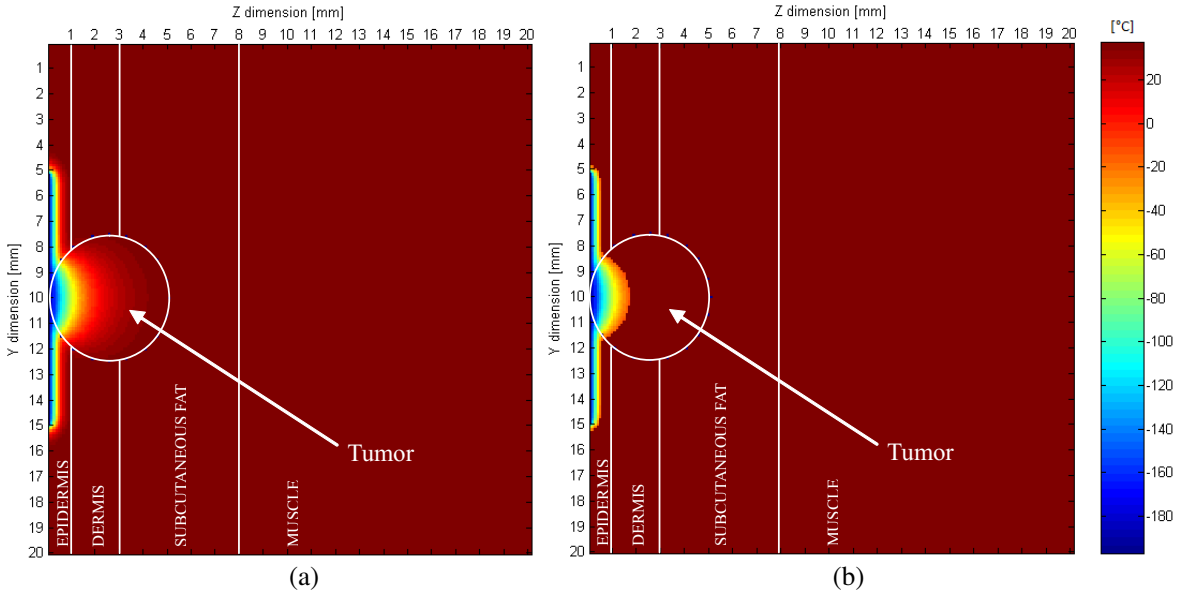

Figure 3: (a) Results of simulation after 1 s. (b) Displayed only region bellow −13°C.

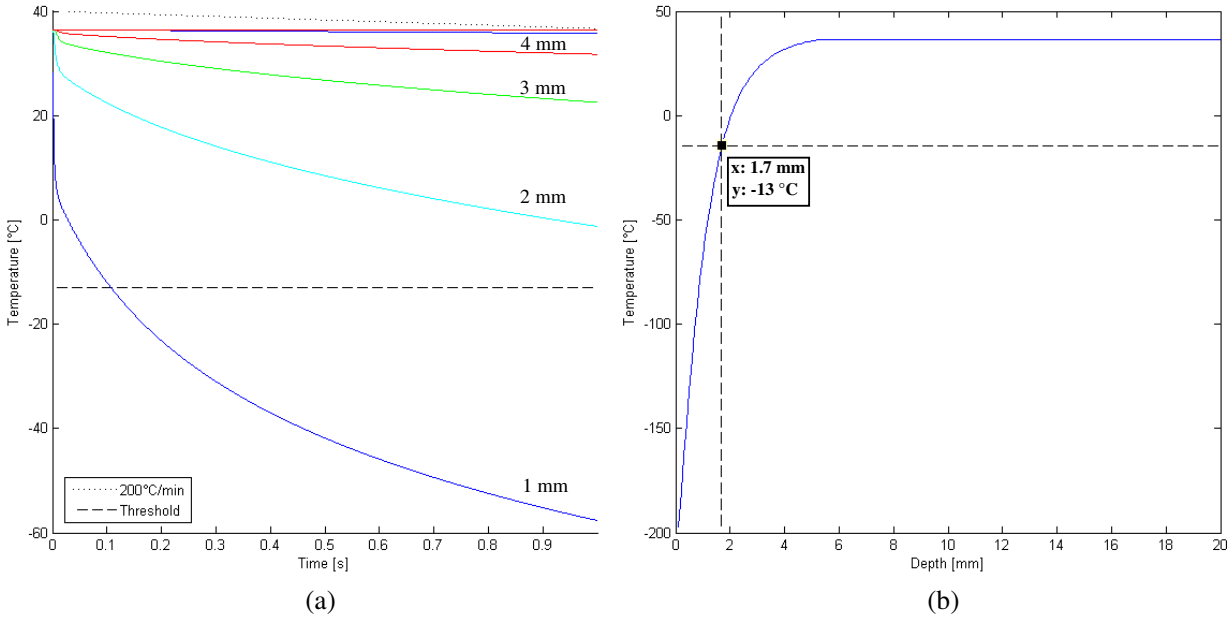

Figure 4: (a) Cooling rates for defined depths. (b) Depth of cooling after 0.01 s.

On right side of Fig. 3, we can see temperature dependence of depth in axes of cryoprobe. Temperature bellow −13°C is displayed like dashed line and depth with temperatures bellow −13°C is 1.7 mm.

4. CONCLUSIONS

This model study is based on finite difference method and numerical solution of Bioheat equation by Mr. Pennes (1948). The Cryomodel application has been tested for some properties of human tissue and has been compared with result from real experiment with potato. Only the model situation is describe in this paper. For confirrmation of theoretical hypothesis the parameters of optimmized globe of tumor has been used. Next research will be focused on real experiments. The aim is to find a procedure of real tumor and wart destroying optimization.

ACKNOWLEDGMENT

The research described in the paper was financially supported by FRVS (a fund of university development) by research plan No. MSM 0021630513 ELCOM, No. MSM 0021630516 and project of the BUT Grant Agency FEKT-S-10-13.

REFERENCES

1. Cho, Y., *Bioengineering Heat Transfer: Advances in Heat Transfer*, 443s, Academis Press Limited, London, 1992, ISBN 0-12-020022-8.
2. Zhmakin, A. I., *Fundamentals of Cryobiology: Physical Phenomena and Mathematical Models*, 280s, Berlin, Springer, 2009, ISBN 978-3-540-88784-3.
3. Akay, M., *Biomedical Engineering*, Vols. 1 and 5, John Wiley and Sons, Hoboken, 2006, ISBN-13: 978-0-471-24967-2.
4. Polanka, M., "Technical experiment based inverse tasks in mechanics [s.1.]," 141s, doctoral thesis, FSI VUT, 2006.
5. Schmid, G., et al., "Bestimmung der expositionsverteilung von HF feldern im menschlichen Köper, unter Berüksichtigung kleiner strukturen und thermophysiologisch relevanter parameter," *Bundesamtes fur Stratenschutz 38201*, 129, ARC-IT-0174, Salzgitter, Deutschland, 2008.

Image Reconstruction by EIT with Usage NMR

T. Kriz, J. Dedkova, and K. Bartusek
Department of Theoretical and Experimental Electrical Engineering, Brno University of Technology
Kolejni 2906/4, Brno 612 00, Czech Republic

Abstract— Paper presents the new proposal of a conductivity reconstruction inside an investigated sample. The principle of the recovering conductivity distribution is based on using measured values of magnetic field which produced the current injecting into the testing sample. The magnetic field can be measured near the testing sample in different direction. Based on simulation results the possibility of using different components of magnetic field as well as the influence of the position measured points is discussed.

1. INTRODUCTION

Standard EIT use a set of voltage measurements is acquired from the boundaries of an investigated volume, whilst this is subjected to a sequence of low-frequency current patterns. Reconstruction of interior conductivity σ in EIT is minimizing the suitable objective function. To minimize the objective function $\Psi(\sigma)$ we often use a deterministic approach based on the Least Squares method. To solve the inverse EIT problem is use the standard Tikhonov regularization method Another way to reconstruction of interior conductivity σ is use MREIT described in [1–3]. The basic principle of NMR is interaction between nucleus of atom place in static magnetic field $\mathbf{B}_0$ and hf magnetic field $\mathbf{B}_1$ which have frequency near nuclear spin frequency. Nucleus of atom radian frequency is direct proportional to static magnetic field $\mathbf{B}_0$

$$\omega = \gamma \mathbf{B}_0$$

Here ω is Larmor's frequency, γ is the gyro magnetic ration of spins and $\mathbf{B}_0$ is static magnetic field.

The 2D numerical model is used for a conductivity reconstruction in this paper. The current source is appended to the sample for measurement by NMR. Current that flows in conductive sample creates magnetic field that is measured by NMR. Magnetic field can be measured at each parts of sample by NMR. Because usage of NMR is problematic and expensive there was built measuring place for magnetic field measurement. Results from NMR and measured results were compared. Measured magnetic field can by convert to current density and used for reconstruction of interior conductivity.

2. BASIC THEORY

The EIT problem is recovering the conductivity distribution satisfying continuity equation

$$\mathrm{div}\mathbf{J} = 0. \tag{1}$$

The current density $\mathbf{J}$ in a linear medium with the interior conductivity σ can be obtain from electric field $\mathbf{E}$ or corresponding potential distribution Φ

$$\mathbf{J} = \sigma \cdot \mathbf{E} = -\sigma \cdot \mathrm{grad}\,\Phi \tag{2}$$

Further, we suppose the electric field in very thin layer of electrical conductive medium which can be described by the surface current density $\mathbf{K}$. The magnetic flux density $\mathbf{B}$ corresponding to $\mathbf{K}$, can be obtained according to the Biot-Savart Law

$$\bar{B} = \frac{\mu_0}{4\pi} \int_S \frac{\bar{K} \times \bar{R}}{R^3}\, dS \tag{3}$$

For further numerical simulations we divided the sample into *NE* triangle elements with centers $[x_t, y_t, z_t]$. We suppose that the current density $\mathbf{K}$ is constant on each element. The magnetic field in general point given by coordinates $[x_i, y_i, z_i]$ we can calculate using superposition principle

$$\vec{B}_i \approx \frac{\mu_0}{4\pi} \sum_{j=1}^{NE} \frac{\bar{K}_j \times \bar{R}_{ij}}{R_{ij}^3} \Delta S_j \tag{4}$$

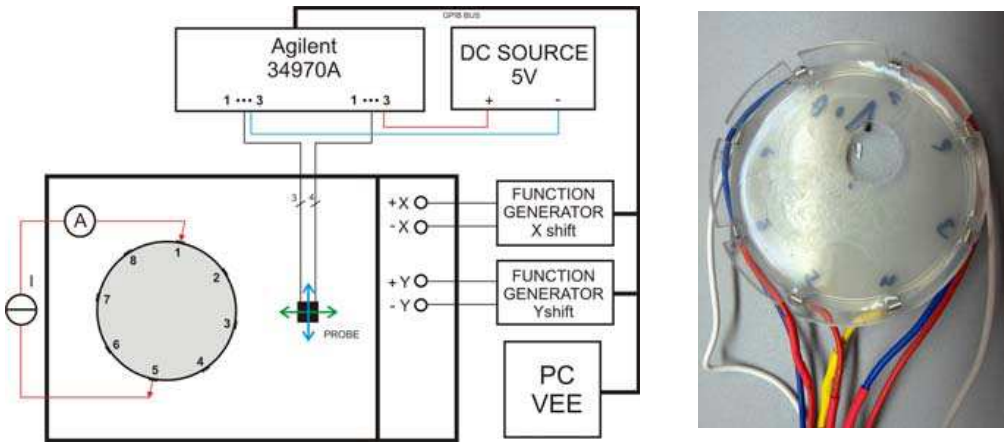

Figure 1: Arrangement for magnetic field measurement outside sample.

The vector $\mathbf{R}$ represents the distance between centre of actual element $[x_t, y_t, z_t]$ and point $[x_i, y_i, z_i]$. If we know certain components of magnetic field we can obtain the current density distribution see [5]. If we would like to obtain the NE values of K_x and K_y components of surface current density $\mathbf{K}$, we have to known for example the same number of B_x and B_y components of magnetic field

$$B_{ix} = \frac{\mu_0}{4\pi} \sum_{j=1}^{NE} R_{ijz} \frac{\Delta S_j}{R_{ij}^3} K_{jy}, \quad B_{iy} = -\frac{\mu_0}{4\pi} \sum_{j=1}^{NE} R_{ijz} \frac{\Delta S_j}{R_{ij}^3} K_{jx}, \quad i = 1, \ldots, NE$$

The matrix notation for these $2 \cdot NE$ algebraic equations is

$$\begin{bmatrix} B_{koefx} & 0 \\ 0 & B_{koefy} \end{bmatrix} \begin{bmatrix} K_x \\ K_y \end{bmatrix} = \begin{bmatrix} B_x \\ B_y \end{bmatrix} \quad \Leftrightarrow \quad \mathbf{B}_{koef}\mathbf{K} = \mathbf{B} \tag{5}$$

From system (5) we can obtain very easy wanted current density distribution

$$\mathbf{K} = \mathbf{B}_{koef}^{-1}\mathbf{B} \tag{6}$$

In the following part is shown an example of the magnetic field distribution and the corresponding surface current density distribution and the influence of the nonhomogeneity inside tested sample. From the difference of current density $\mathbf{K}$ in the sample without nonhomogeneity and with nonhomogeneity we can obtain the conductivity distribution with help the condition on the boundary between two media with different conductivities [5].

3. EXPERIMENT AND NUMERICAL SIMULATION RESULTS

Measuring workplace was built for measuring magnetic field outside a specimen. Arrangement of workspace is shown in Fig. 3 (left). For automatic measuring control was used HP VEE program. Magnetic field was measured by three probes. Each probe was used for a measurement of one component of magnetic field. Probes were placed on XY-writer. The position of probes at x direction and at y direction of probes was controlled by offset from function generator. Measuring points were loaded from a text file. AGILENT 34970A with multiplex card was used for measuring of probes output. The specimen is in Fig. 3 (right). The specimen consists from eight electrodes and as conductive medium was used agar. There are 8 electrodes for different excitation of a specimen. There were used agar with two values of conductivity ($\sigma = 0.2\,\mathrm{S/m}$ for homogenous region and $\sigma = 0.8\,\mathrm{S/m}$ for nonhomogenity).

The testing sample for numerical simulations is given by thin circle plate with diameter 0.055 m from agar again with conductivity $\sigma = 0.2\,\mathrm{S/m}$. The mesh of linear triangle for numerical simulations has $NE = 78$ elements. The B_x, B_y and B_z components of magnetic field on the plane in distances $z_v = 0.001\,\mathrm{m}$, $0.002\,\mathrm{m}$ and $0.004\,\mathrm{m}$ of the testing sample with nonhomogeneity is displayed in the Figs. 2, 3 and 4 (on the left B_x, in the middle B_y and on the right B_z, respectively). The nonhomogeneity in the sample is given by two subregions with conductivity $\sigma_{un} = 0.8\,\mathrm{S/m}$.

In Figs. 2, 3 and 4 we can see the magnetic field components in points $[x_t, y_t, z_v]$ which are placed in three different distances z_v.

The current density on the *NE* elements was recalculated with help (5) and (6), In the Fig. 5 are shown the differences between current density in the sample with and without nonhomogeneity. This vector is not dependent on the distance z_v where we measure magnetic field. It is evident than the difference current density vector positively identifies the nonhomogeneity locations.

The magnetic field outside the sample together with magnetic field inside the sample is shown in Fig. 6. We used also the B_x, B_y components of field outside sample to conductivity distribution reconstruction and we find that the reconstruction results are independent on the place of measuring probe.

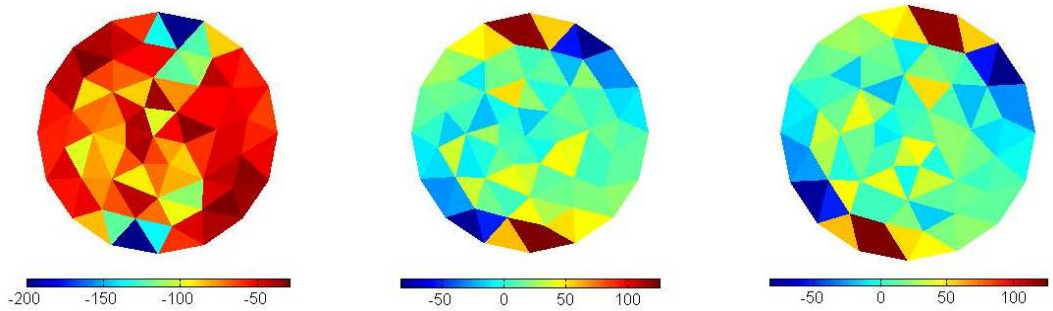

Figure 2: Magnetic field components in μT, $z_v = 0.001$ m.

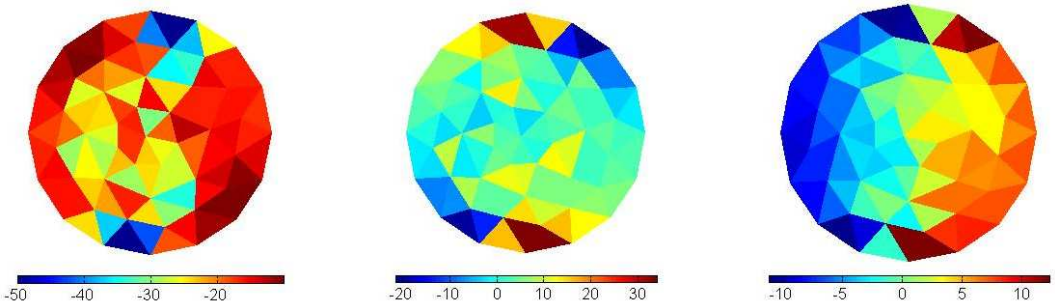

Figure 3: Magnetic field components in μT, $z_v = 0.002$ m.

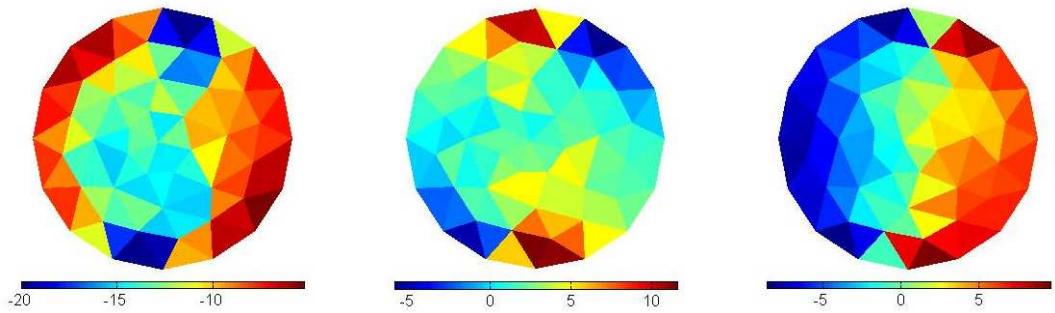

Figure 4: Magnetic field components in μT, $z_v = 0.004$ m.

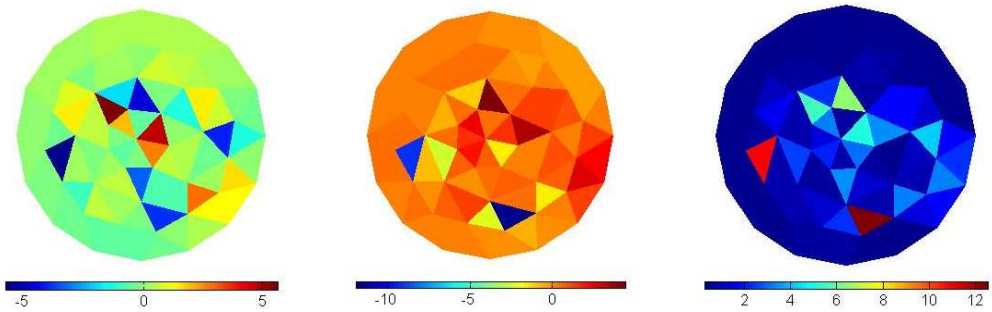

Figure 5: Components K_x, K_y and magnitude K of the current density difference vector in sample.

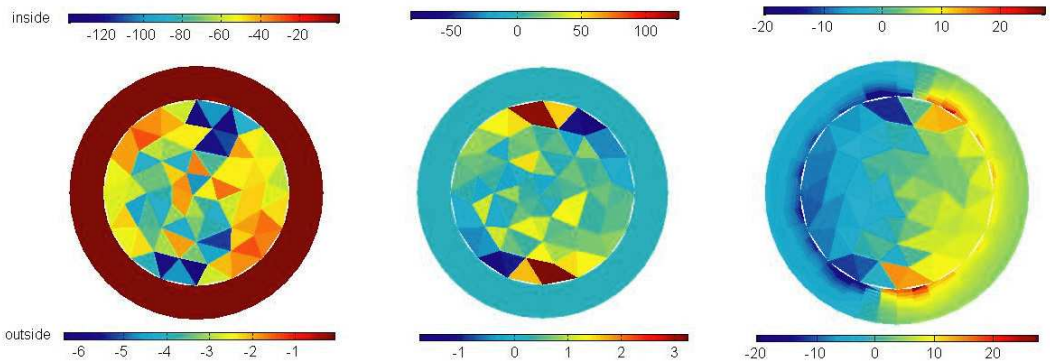

Figure 6: Magnetic field components inside and outside the sample $z_v = 0.001\,\mathrm{m}$.

4. CONCLUSIONS

In the paper is discussed the new feasible way to image conductivity reconstruction. Instead the NMR was used the simpler method to obtain the components of magnetic field near the sample with injected current. It was shown, that this way is very efficient technique to reliable detection of conductivity location with nonhomogeneties or same conductivity changes in measure sample. In comparison with NMR is this proposed solution cheaper and simplier.

ACKNOWLEDGMENT

The research described in the paper was financially supported by the research program MSM 0021630513 and project of the BUT Grant Agency FEKT-S-10-13.

REFERENCES

1. Vladingerbroek, M. T. and J. A. Den Boer, *Magnetic resonance imaging*, Springer-Verlag, Heidelberg, Germany, 1999, ISBN 3-540-64877-1.
2. Borsic, A., *Regularization Methods for Imaging from Electrical Measurement*, Ph.D. Thesis, Oxford Brookes University, 2002.
3. Zhang, X., D. Yan, S. Zhu, and B. He, "Noninvasive imaging of head-brain conductivity profiles," *IEEE Engineering in Medicine and Biology Magazine*, Vol. 27, No. 5, 78–83, 2008.
4. Seo, J. K., O. Kwon, and E. J. Woo, "Magnetic resonance electrical impedance tomography (MREIT): conductivity and current density imaging," *Journal of Physics: Conference Series*, Vol. 12, 140–155, 2005.
5. Ostanina, K., J. Dedkova, and T. Kriz, "Utilization of boundary conditions in MR image reconstruction," *PIERS Proceedings*, Marrakesh, Morocco, March 20–23, 2011

Utilization of Boundary Conditions in MR Image Reconstruction

K. Ostanina, J. Dedkova, and T. Kriz
Department of Theoretical and Experimental Electrical Engineering, Brno University of Technology
Kolejni 2906/4, Brno 612 00, Czech Republic

Abstract— This article discusses two-dimensional reconstruction of the internal conductivity distribution for a human head tissues imaging and for the determination of corresponding brain tissue changes with the help of the Magnetic Resonance Electrical Impedance Tomography (MREIT) method. MREIT is a bio-imaging modality providing cross-sectional conductivity images with a high spatial resolution from measurements of internal magnetic flux density produced by externally injected currents. The new algorithm for the image conductivity reconstruction, which uses the internal current vector information with respect to corresponding boundary conditions, was developed. This algorithm was applied to the several computer simulations to demonstrate the feasibility. Obtained conductivity reconstruction results are presented and the reached experience is discussed. The future research direction is also proposed.

1. INTRODUCTION

Recently the question of using MREIT for recovering the interior object conductivity σ when the current is applied on its boundary is very often discussed. The injecting currents produce the magnetic field, which has been used together with measured voltage-current data for recovering the conductivity distribution. While the EIT suffers from the ill-posed nature of the corresponding inverse problem, the MREIT has been presented as a conductivity imaging modality providing images with better spatial resolution and accuracy. Basic principles of MREIT and its application are described for example in [1–4]. Here described techniques utilize internal information on the induced magnetic field in addition to the boundary current-voltage measurements to produce three-dimensional images of internal current density and conductivity distributions. In this paper, a new way to obtain these distributions without knowledge of current-voltage data on the boundary of the proposed testing object is presented. It is shown that the proposed technique is convenient to identify the location of regions with different conductivity values.

2. BASIC THEORY AND PRINCIPLE OF IMAGE RECONSTRUCTION NOVEL

The current density $\mathbf{J}$ in a linear medium with the interior conductivity σ can be obtained from electric field $\mathbf{E}$ or corresponding potential distribution Φ

$$\mathbf{J} = \sigma \cdot \mathbf{E} = -\sigma \cdot \mathrm{grad}\Phi. \tag{1}$$

The EIT problem is a recovering of the conductivity distribution satisfying a continuity equation $\mathrm{div}\mathbf{J} = 0$. To describe the numerical model we use linear approximation of potential on elements (2)

$$\Phi \approx \sum_{i=1}^{NE} \Phi_i \cdot N_i. \tag{2}$$

We describe the field in very shallow layer of electrical conductive medium by the surface current density $\mathbf{K}$. The corresponding constant approximation of this parameter on elements (Fig. 1(a)) is given by (2)

$$\mathbf{K}^{(e)} = -\sigma^{(e)}\mathrm{grad}\Phi^{(e)} \approx -\sigma^{(e)} \sum_{j=1}^{3} \Phi_j^{(e)} \mathrm{grad} N_j^{(e)}. \tag{3}$$

Due to (3) the components K_x and K_y in element (Fig. 1(b)) can be described by

$$K_x^{(e)} = \sigma^{(e)} \left[(y_3 - y_2)\, \Phi_1^{(e)} + (y_1 - y_3)\, \Phi_3^{(e)} + (y_2 - y_1)\, \Phi_3^{(e)} \right], \tag{4}$$

$$K_y^{(e)} = \sigma^{(e)} \left[(x_2 - x_3)\, \Phi_1^{(e)} + (x_3 - x_1)\, \Phi_2^{(e)} + (x_1 - x_2)\, \Phi_3^{(e)} \right]. \tag{5}$$

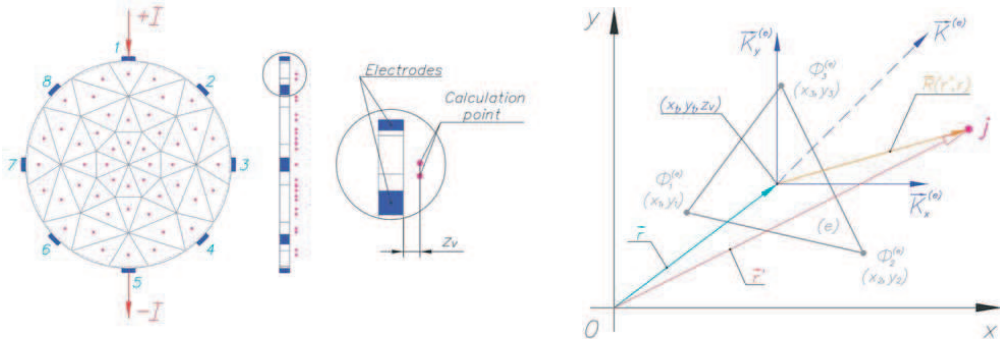

(a) (b)

Figure 1: (a) Arrangement for a testing experiment and (b) for a numerical model.

The magnetic flux density **B**, due to surface current density **K**, can be obtained according to the Biot-Savart Law

$$\mathbf{B}\left(r'\right) = \frac{\mu_0}{4\pi} \int\limits_S \frac{\mathbf{K}\left(r\right) \times \mathbf{R}\left(r', r\right)}{R^3\left(r', r\right)} dS, \tag{6}$$

$$\mathbf{B}_i \approx \frac{\mu_0}{4\pi} \sum_{j=1}^{NE} \frac{\mathbf{K}_j \times \mathbf{R}_{ij}}{R_{ij}^3} \Delta S_j \approx \sum_{j=1}^{NE} \mathbf{B}_{ij}, \tag{7}$$

where

$$\mathbf{B}_{ij} = \frac{\mu_0}{4\pi} \left[K_{jy} R_{ijz} \mathbf{u}_x - K_{jx} R_{ijz} \mathbf{u}_y + \left(K_{jx} R_{ijy} - K_{jy} R_{ijx}\right) \mathbf{u}_z\right] \cdot \frac{\Delta S_j}{R_{ij}^3}. \tag{8}$$

The explanation of all variables on right hand side of (8) is shown in Fig. 1(b). If we know some components of magnetic field **B,** we can obtain the surface current density distribution **K** and then the conductivity distribution σ in the specimen. If we would like to obtain the NE values of K_x and K_y components of surface current density **K**, we had to know for example the double number $2 \cdot NE$ of B_z component of magnetic field

$$B_{iz} = \frac{\mu_0}{4\pi} \sum_{j=1}^{NE} \left(\frac{R_{ijy} \Delta S_j}{R_{ij}^3} K_{jx} - \frac{R_{ijx} \Delta S_j}{R_{ij}^3} K_{jy} \right), \quad i = 1, \ldots, 2 \cdot NE. \tag{9}$$

The matrix notation of these $2 \cdot NE$ algebraic equations is

$$\begin{bmatrix} B_{\mathrm{koef}zx} & B_{\mathrm{koef}zy} \\ B_{\mathrm{koef}zx} & B_{\mathrm{koef}zy} \end{bmatrix} \cdot \begin{bmatrix} K_x \\ K_y \end{bmatrix} = \begin{bmatrix} B_z \\ B_z \end{bmatrix} \Leftrightarrow \quad \mathbf{B}_{\mathrm{koef}} \cdot \mathbf{K} = \mathbf{B}. \tag{10}$$

From (10) we can obtain very easily wanted current density distribution

$$\mathbf{K} = \mathbf{B}_{\mathrm{koef}}^{-1} \cdot \mathbf{B}. \tag{11}$$

In the following part some examples of the magnetic field distribution, the corresponding surface current density distribution and the influence of the nonhomogeneity in tested specimen to **K** distribution are shown. From the difference of current density **K** in the specimen without nonhomogeneity and with nonhomogeneity we can obtain the conductivity distribution using suitable filters based on the condition on the boundary between two media with different conductivities

$$\frac{K_{t1}}{\sigma_1} = \frac{K_{t2}}{\sigma_2} \quad \Rightarrow \quad \sigma_{2\mathrm{unknown}} = \frac{K_{t2}}{K_{t1}} \sigma_{1\mathrm{known}}. \tag{12}$$

Further, we use instead of the measured values of magnetic field the results obtained by numerical simulations for different arrangements of nonhomogeneity. More details about feasible arrangement and suitable measurement method are described in [5].

3. NUMERICAL EXPERIMENTS

The testing specimen is thin circle plate with diameter 0.055 m from Agar with conductivity $\sigma = 0.2\,\mathrm{S/m}$. In our computer simulations, we injected a current with amplitude 4–5 mA because 5 mA is considered to be the upper safe limit for human beings (International Electrical Code (IEC) Criteria 1973). The mesh of linear triangle for numerical simulation has $NE = 48$ elements. The B_x, B_y and B_z components of magnetic field on the surface at distance $z_v = 0.002\,\mathrm{m}$ of the testing specimen with nonhomogeneity is displayed in the Fig. 2. The conductivity of nonhomogeneity was $\sigma_{un} = 0.8\,\mathrm{S/m}$.

From (10) and (11) the current density on the elements NE was recalculated, the corresponding current density K is shown in Fig. 3. In the Fig. 4 the differences between current density in the specimen with and without nonhomogeneity are shown. In the Fig. 5 the ratio of those current densities is shown.

It is evident, that the most significant information about influence of nonhomogeneity on the specimen we can obtain from the difference field (Fig. 4). Other examples of influences of different case of nonhomogeneity on testing specimen are shown in Fig. 6.

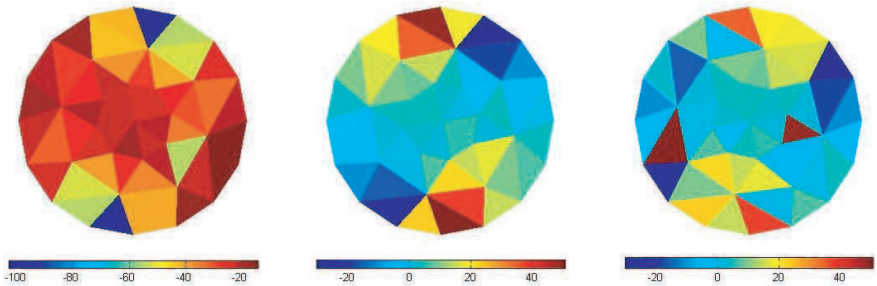

(a) (b) (c)

Figure 2: Magnetic field (a) B_x, (b) B_y and (c) B_z components in μT ($NE = 48$).

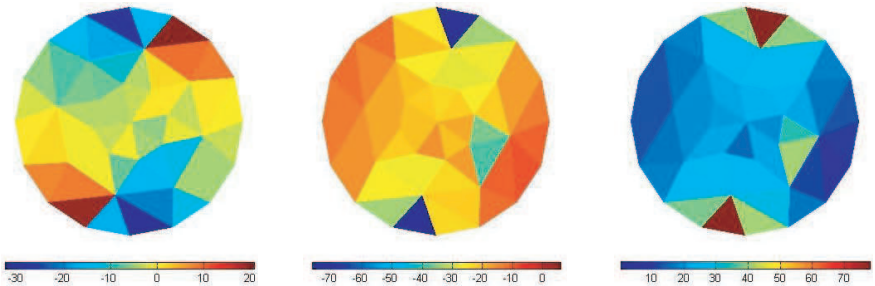

(a) (b) (c)

Figure 3: Components (a) K_x, (b) K_y and magnitude (c) K of the current density vector distribution in the specimen with a nonhomogeneity ($NE = 48$).

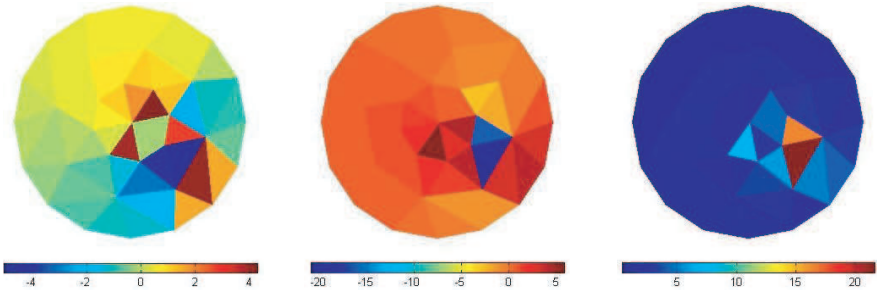

(a) (b) (c)

Figure 4: Components (a) K_x, (b) K_y and magnitude (c) K of the current density difference vector ($NE = 48$).

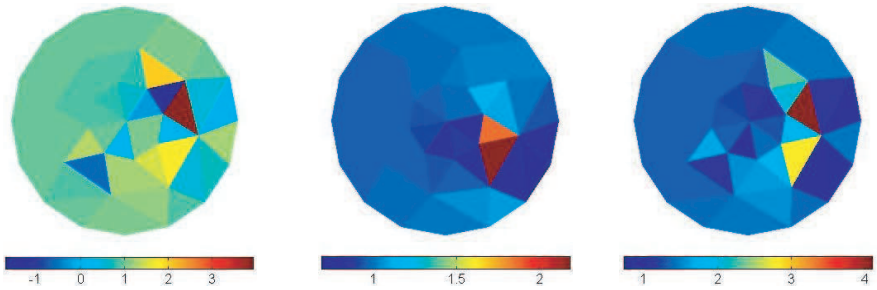

(a) (b) (c)

Figure 5: Components (a) K_x, (b) K_y and magnitude (c) K of the current density ratio vector in the specimen with and without nonhomogeneity ($NE = 48$).

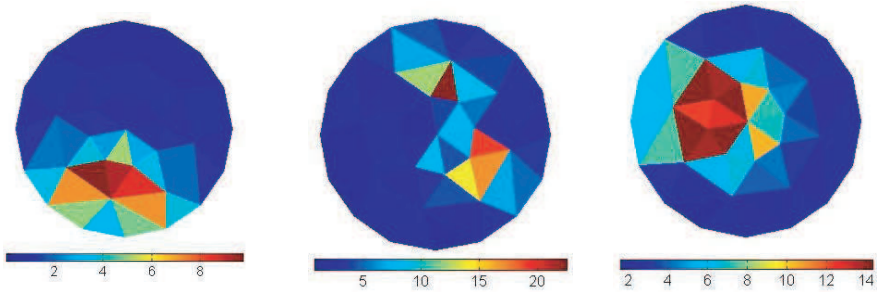

(a) (b) (c)

Figure 6: Magnitude K of current density difference vector for three different type of nonhomogeneity ($NE = 48$).

Using information given by current density difference and Equation (12) the location of a region with nonhomogeneity was identified very reliable. The unknown conductivity σ_{un} was obtained with relative error less than 15%.

4. CONCLUSIONS

The proposed new way of an image reconstruction enables to obtain demanded results very easily and quickly comparing with recently used methods for image reconstruction. But it demands the feasible measure device for reliable measurement of magnetic field components in range of μT. The possibilities of more general using of proposed method will be an object of our future research.

ACKNOWLEDGMENT

The research described in the paper was financially supported by the research program MSM 0021630513 and project of the BUT Grant Agency FEKT-S-10-13.

REFERENCES

1. Kwon, O., J.-Y. Lee, and J.-R. Yoon, "Equipotential line method for magnetic resonance electrical impedance tomography," *Inverse Problems*, Vol. 18, 1–12, 2002.
2. Zhang, X., D. Yan, S. Zhu, and B. He, "Noninvasive imaging of head-brain conductivity profiles," *IEEE Engineering in Medicine and Biology Magazine*, Vol. 27, No. 5, 78–83, 2008.
3. Jeon, K., C.-O. Lee, E. J. Woo, H. J. Kim, and J. K. Seo, "MREIT conductivity imaging based on the local harmonic B_z algorithm: Animal experiments," *IOP Publishing*, 2010.
4. Seo, J. K., O. Kwon, and E. J. Woo, "Magnetic resonance electrical impedance measurement tomography (MREIT): Conductivity and current density imaging," *Journal of Physics: Conference Series*, Vol. 12, 140–155, 2005.
5. Kriz, T., J. Dedkova, and K. Bartusek, "Image reconstruction by EIT with usage NMR," *PIERS Proceedings*, Marrakesh, March 2011.

The Vagarious Dispersive Behavior in a Magnetically Uniaxial Metamaterial around the Plasma Frequency

Dexin Ye[1], **Shan Qiao**[2], **Jiangtao Huangfu**[1], **and Lixin Ran**[1]

[1]Department of Information and Electronic Engineering, Zhejiang University, Hangzhou 310027, China
[2]Zhejiang University City College, Hangzhou 310015, China

Abstract— We investigate the dispersive behavior around the plasma frequency in a magnetically uniaxial metamaterial. We show by theoretical analysis, numerical calculation and simulation that when material loss is considered and the EM wave is oblique incidence, the negative refraction of energy and the negative group velocity of electromagnetic wave will be observed with little losses. Since the proposed magnetically uniaxial metamaterial can be constructed in the GHz frequency easily, the abnormal refraction and group velocity will be experimentally validated in the future.

1. INTRODUCTION

The wave propagation in a dispersive medium always captures the attentions of the researchers [1]. And the dispersion relationship is the most important physical quantities characterizing the propagation mode which describes the electromagnetic (EM) characteristics of a medium at different frequencies. Based on the dispersion, we can analyze the propagation mode, the phase velocity, the group velocity and the reflection and refraction between two different materials. For most inartificial material, the group velocity are positive and are always lower than c, c is the speed of light in free space, and the index of refraction is positive between two different medium. Whereas, in 1968, the existence of "electromagnetics of substances with simultaneously negative values of ε and μ" was postulated theoretically [2], and a description of some of the properties related to these medium was presented, such as negative index of refraction, negative phase velocity v_g [3, 4] and negative group velocity v_g, backward phase, reversed Doppler effect, etc.. The group velocity v_g also can be superluminal or negative ($\partial\omega/\partial k$ is negative) in the regime of anomalous dispersion [5–9], it has been thoroughly discussed [10] that the negative group velocity is not at all in conflict with relativity. Few instances of negative refraction are identified, which can all be measured experimentally.

In this letter, we introduce a new method to realize the negative group velocity and negative refraction of energy in the normal dispersive medium at different frequency. Theoretical analysis from the k-surface of the proposed normal dispersive uniaxial medium reveals that the group velocity can be negative with negative refraction of energy if the loss of the medium is taken into account. Since the proposed medium can be constructed in the GHz frequency, our result would be verified in the near future.

2. THEORETICAL ANALYSIS

We begin with a magnetically uniaxial effective medium with a scalar permittivity $\varepsilon_r = 1$ and a permeability tensor defined in an (x, y, z) Cartesian coordinates of

$$\bar{\bar{\mu}} = \mathrm{diag}(\mu_{rx}, \mu_{ry}, \mu_{rz})\mu_0 \tag{1}$$

Assume $\mu_{rx} = \mu_{ry} = 1$ and μ_{rz} follows the frequency dependence of Drude model, i.e., $\mu_{rz} = 1 - \omega_p^2/[\omega(\omega + i\gamma_e)]$. Here ω_p is the plasma frequency and γ_e is the damping frequency that characterizes the loss. For an incident wave with the electrical field polarized along the y direction and a wave vector $\bar{k} = \hat{x}k_x + \hat{z}k_z$, the dispersion relation is

$$k_x^2/\mu_{rz} + k_z^2 = \varepsilon_r k_0^2 = \varepsilon_r(\omega/c)^2 \tag{2}$$

We consider a TE incident wave with the electrical field polarize along the y-axis, propagating from the air to the uniaxial medium, as shown in Fig. 1.

According to the phase-matching condition $k_{1x} = k_{2x}(\bar{k}_1 = \hat{x}k_{1x} + \hat{z}k_{1z}$, $\bar{k}_2 = \hat{x}k_{2x} + \hat{z}k_{2z})$, for a given k_{1x} which is a real number and determined by the incident wave, we can get two solutions

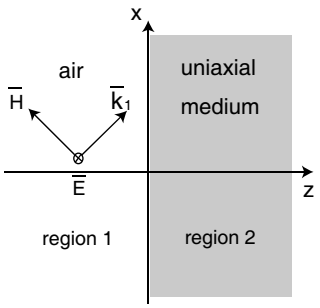

Figure 1: The sketch map of TE wave incidence on a plane boundary separating air and uniaxial medium.

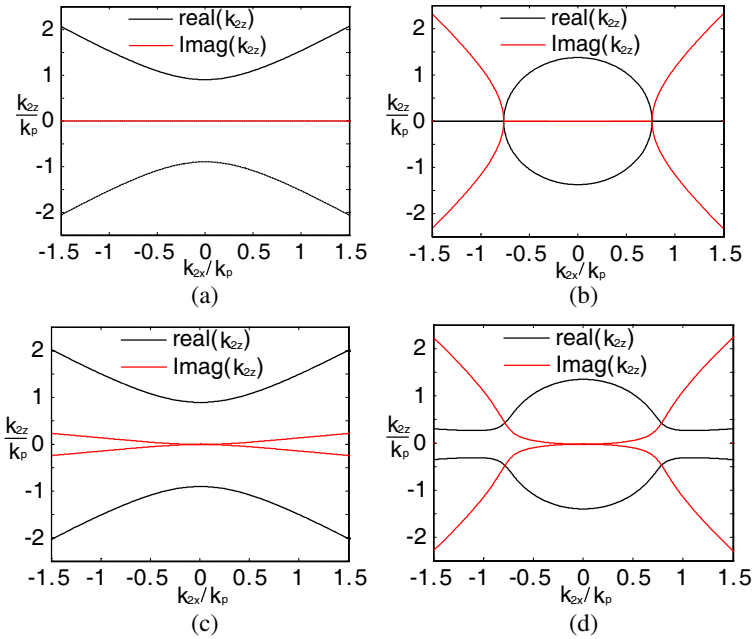

Figure 2: The k-surface of the dispersion relation of uniaxial medium(normalized by $k_p = \omega_p\sqrt{\varepsilon_0\mu_0}$) with different parameters, and (a) $\gamma_e = 0$, $\omega = 0.9\omega_p$, (b) $\gamma_e = 0$, $\omega = 1.1\omega_p$, (c) $\gamma_e = 0.05\omega_p$, $\omega = 0.9\omega_p$, (d) $\gamma_e = 0.05\omega_p$, $\omega = 1.1\omega_p$, where $k_{2x} = k_{1x}$ is a real number and determined by the incident wave in the air.

for k_{2z} which are opposite. For lossy case, the k_{2z} are complex value, so the real and the imaginary part should be plotted respectively in the figure of the k-surface [11].

As the operating frequency or the damping frequency changes, the k-surface will be different. In Fig. 3, we give the real and imaginary part of the k-surface with different frequency with a little loss ($\gamma_e = 0.02\omega_p$). There would be two complex roots for k_{2z}, and we choose the one with a positive imaginary part to satisfy the energy conservation law as shown in Fig. 3. The corresponding real part of k_{2z} given in Fig. 3(a) shows that the $real(k_{2z})$ (with little loss) decreases when the operating frequency increases while $k_{2x} \geq 0.04k_0$. Fig. 3 (b) shows that the $real(k_{2z})$ (with large loss) decreases when the operating frequency increases while $k_{2x} \geq 0.3k_0$. That is to say, a negative group velocity will be observed around the plasma frequency, and the phenomenon would be observed more easily and clearly below the plasma frequency because of the smaller imaginary part of k_{2z} and more vertical incidence. Fig. 3(c) shows the k_{2z} as a function of the frequency when the $\gamma_e = 0.02\omega_p$, we can find the $\partial\omega/\partial k_{2z}$ is negative around the plasma frequency which means that the negative group velocity appears. On the other hand, for anisotropic medium, where an index of refraction cannot be uniquely defined, the refraction has to be obtained from the dispersion relations and the fact that the direction of the Poynting vector coincides with $\nabla\bar{k}\omega$ which denotes the group velocity, so we can get the Poynting vector (the same direction with group velocity) according to the dispersion relation.

Figure 3(d) shows the illustration of the incidence waves and transmitted waves between the air and uniaxial medium. The black circle represents the free-space dispersion relation in the (kx, kz)

plane which supports an incident wave shown by the thin black arrow. The black hyperbola represents the dispersion relation of the medium. When a transmitted wave is supported, its wave-vector (the same direction with phase velocity) and power direction (the same direction with group velocity) are shown by a thin red arrow and a thick red arrow, respectively.

3. SIMULATION RESULT

Finally, the aforementioned theoretic result is validated by the numerical simulations based on the Finite Element Method (FEM) as Fig. 4 showed. Fig. 4(a) shows the snapshot of the electric field distributions of a gauss beam which is a little oblique incidence on a slab of uniaxial medium. We can find the wave vector (the same direction with phase velocity) in uniaxial medium coincides with the theoretic result as the Fig. 3(d) showed. And Fig. 4(b) shows the snapshot of the group velocity distributions in the uniaxial medium which denotes that the group velocity is reversed to the direction of propagation of EM wave.

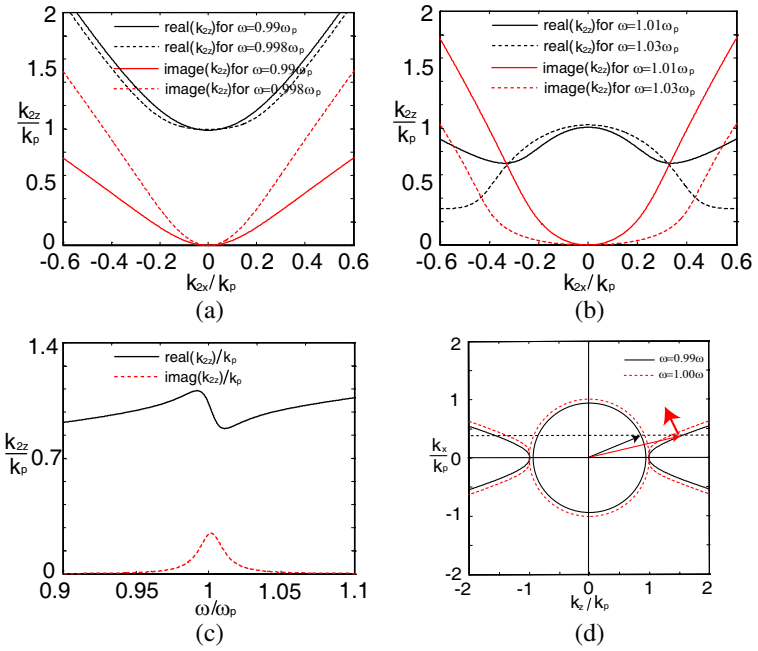

Figure 3: (a), (b) The k-surface with different operating frequency with $\gamma_e = 0.02\omega_p$. (c) The real and imaginary parts of k_{2z} as a function of the frequency with $k_{2x} = 0.1k_p$. (d) Illustration of the incidence waves and transmitted waves between the air and uniaxial medium.

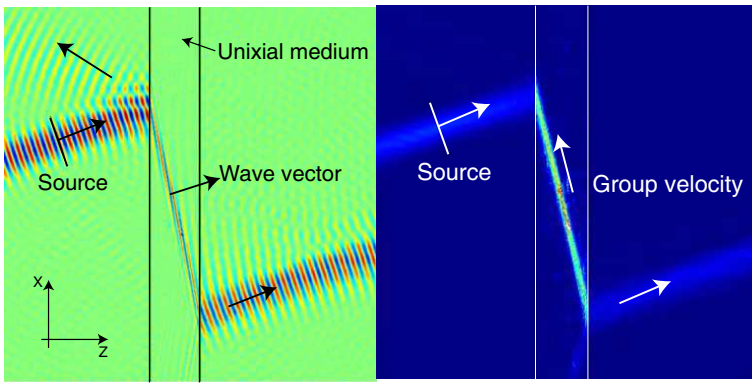

Figure 4: (a) Snapshot of the electric field distributions of a gauss beam oblique incidence on the uniaxial medium. (b) Snapshot of the group velocity distributions of a gauss beam incidence on the uniaxial medium.

4. CONCLUSIONS

In short, we investigated the k-surface of a uniaxial medium whose permeability along the optical axis obeys the Drude mode. When material loss is taken into account, we plot the real part and imaginary part of k-surface respectively. According to the theoretical calculation and simulation, we find the vagarious dispersive behavior in the uniaxial medium, a negative group velocity and a negative refraction index of energy are observed, which show that the loss of the media plays an important role in characterizing the medium. Since the proposed medium can be constructed in the GHz frequency such as metamaterial slabs of SRR based on magnetic resonance [12], our result may be verified in experiment in the near future.

ACKNOWLEDGMENT

This work is sponsored by the ZJNSF (No. Y1080715), 863 Project (No. 2009AA01Z227), in part by NSFC (No. 61071063, 60701007), NCET-07-0750 and the National Key Laboratory Foundation (No. 9140C5304020901).

REFERENCES

1. Brillouin, L., *Wave Propagation and Group Velocity Academic*, New York, 1960.
2. Veselago, V., "The electrodynamics of substances with simultaneously negative values of ε and μ," *Sov. Phys. Uspekhi*, Vol. 10, 509–514, 1968.
3. Ye, D. X., S. Qiao, J. T. Huangfu, and L. X. Ran, "Experimental characterization of the dispersive behavior in a uniaxial metamaterial around plasma frequency," *Optics Express*, Vol. 18, 22631–22636, 2010.
4. Shelby, R., D. Smith, and S. Schultz, "Experimental veri£cation of a negative index of refraction," *Science*, Vol. 292, 77–79, 2001.
5. Chiao, R. Y. and A. M. Steinberg, "Tunneling times and superlunminality," *Progress in Optics*, Vol. 37, 345–405, 1997.
6. Teinberg, A. M., P. G. Kwiat, and R. Y. Chiao, "Measurement of the single-photon tunneling time," *Phys. Rev. Lett.*, Vol. 71, 708–711, 1993.
7. Mojahedi, M., E. Schamiloglu, K. Agi, and K. J. Malloy, "Frequency domain detection of superluminal group velocities in a distributed bragg reflector," *IEEE Journal of Quantum Electronics*, Vol. 36, 418–424, 2000.
8. Mojahedi, M., E. Schamiloglu, F. Hegeler, and K. J. Malloy, "Time-domain detection of superluminal group velocity for single microwave pulses," *Phys. Rev. E*, Vol. 62, 5758–5766, 2000.
9. Mojahedi, M., K. J. Malloy, G. V. Eleftheriades, J. Woodley, and R. Y. Chiao, "Abnormal wave propagation in passive medium," *IEEE Journal of Selected Topics in Quantum Electronics*, Vol. 9, 30–39, 2003.
10. Garrett, C. G. B. and D. E. McCumber, "Propagation of a gaussian light pulse through an anomalous dispersion medium," *Phys. Rev. A*, Vol. 1, 305, 1970.
11. Qiao, S., G. A. Zheng, W. Ren, and L. X. Ran, "Possible abnormal group velocity in the normal dispersive anisotropic media," *Journal of Electromagnetic Waves and Applications*, Vol. 22, No. 10, 1309–1317, 2008.
12. Ziolkowski, R. W., "Propagation in and scattering from a matched metamaterial having a zero index of refraction," *Phys. Rev. E*, Vol. 70, 046608, 2004.

A Novel Preconditioner Based on CSL Operator for Solving the Helmholtz Equations

Yue Hui Li[1,2], **Zai-Ping Nie**[1], **Xiang Qian Zhang**[1], **and Xiang Yang Sun**[1]

[1]School of Electronic Engineering, UESTC, Chengdu, Sichuan 610054, China
[2]School of Mathematics and Computer Engineering, Xihua University, Chengdu 610039, China

Abstract— A novel preconditioner followed by the conjugate orthogonal conjugate gradient (COCG) iterative method is proposed for solving the large complex symmetric and highly indefinite systems of linear equations, which resulting from the Helmholtz equation discretized by edge-based finite element method (FEM). The proposed preconditioner is based on the complex shifted Laplace (CSL) operator and the modified AINV algorithm (MAINV), which derived from the basic AINV process with pivots compensation to avoid the breakdowns. Numerical tests on 3D waveguide discontinuity problem demonstrate the effectiveness of the proposed preconditioner, by comparison with other conventional preconditioners.

1. INTRODUCTION

The application of finite-element method (FEM) [1] to three-dimensional (3D) electromagnetic (EM) problems often yields a large sparse complex symmetric linear system of equations. Krylov subspace iterative methods are applicalbe to solve this large linear system [2]. In this paper, we employ the Conjugate Orthogonal Conjugate Gradient (COCG) algorithm [3], which is specially designed for symmetric complex and indefinite system. The FEM coefficient matrix usually has bad spectrum property, to get high efficiency, it's necessary to use some effective preconditioning techniques. In this paper, we propose a robust CSL-MAINV preconditioner for solving the large linear systems from EM problems.

2. THEORY

We consider solving edge FEM discretization the following Helmholtz boundary value problem $\nabla\times(\mu_r^{-1}\nabla\times\vec{E}(r))-k_0^2\varepsilon_r\vec{E}(r)=-jk_0Z_0\vec{J}(r)$, with boundary condition given by $\hat{n}\times\vec{E}=0$. Where $\vec{E}$ is electric field, $\vec{J}(r)$ is electric current source, k_0 and Z_0 are wave number and wave impedance in the free space, ε_r and μ_r are the relative permittivity and permeability respectively. Which result in a large sparse linear system: $(\mathbf{B}-\mathbf{Y})\mathbf{x}=\mathbf{b}$. Where $\mathbf{B}$ relates to the FEM discretization of $\nabla\times(\mu_r^{-1}\nabla\times\vec{E}(r))$, and $\mathbf{Y}$, the $k_0^2\varepsilon_r\vec{E}(r)$. We can rewrite it into the following form for convenience: $\mathbf{Ax}=\mathbf{b}$. with $\mathbf{A}\in\mathrm{C}^{n\times n}$, $\mathbf{b},\mathbf{x}\in\mathrm{C}^n$. For realistic values of the electromagnetic wave number k_0, the coefficient matrix $\mathbf{A}$ is usually complex symmetric (non-Hermitian), and highly indefinite, which makes the equation hard to solve. In order to attain efficiency, an appropriate preconditioning matrix $\mathbf{M}$ should be incorporated.

2.1. CSL Operator

Most of the conventional preconditioners are constructed based on $\mathbf{A}$. However, it is highly indefinite since $\mathbf{B}$ is a positive semidenifite matrix and $\mathbf{Y}$, a positive denifite ones. Inspired by the idea of preconditioning based on shifted Laplace operator [5], we can construct the preconditioning matrix based on the remedy case: $\hat{\mathbf{A}}=\mathbf{B}+(\kappa_1+i\kappa_2)\mathbf{Y},\kappa_1,\kappa_2\in\mathrm{R}$. By tuning parameters κ_1 and κ_2, matrix $\hat{\mathbf{A}}$ can be more definite. As a reasonable approximate of $\mathbf{A}$, $\hat{\mathbf{A}}$ is much better conditioned than the original one, and the inverse computation based on it is expected to be more robust. In this paper, the approximate inverse of $\hat{\mathbf{A}}$ can be computed by the following MAINV process.

2.2. MAINV Algorithm

The AINV algorithm, based on incomplete biconjugation (A-orthogonalization) of the unit basis vectors, builds a factorized sparse approximate inverse $\mathbf{M}$ of the form (since $\hat{\mathbf{A}}$ is symmetric) $\mathbf{M}=\mathbf{ZD}^{-1}\mathbf{Z}^T\approx\hat{\mathbf{A}}^{-1}$, where $\mathbf{Z}$ is a unit upper triangular matrix and $\mathbf{D}$ is diagonal. The basic AINV algorithm for symmetric case [4] can be written as follows.

Algorithm 1.

1 : Let $\mathbf{z}_i^{(0)} = \mathbf{e}_i \quad (1 \le i \le n)$
2 : for $i = 1, 2, \ldots, n-1$ do
3 : for $j = i, i+1, \ldots, n$ do
4 : $p_j^{(i-1)} := \hat{\mathbf{a}}_i^T \mathbf{z}_j^{(i-1)}$
5 : end do
6 : for $j = i+1, \ldots, n$ do
7 : $\mathbf{z}_j^{(i)} := \mathbf{z}_j^{(i-1)} - \left(p_j^{(i-1)}/p_i^{(i-1)}\right) \mathbf{z}_i^{(i-1)}$
8 : end do
9 : end do
10 : $p_n^{(i-1)} := \hat{\mathbf{a}}_n^T \mathbf{z}_n^{(i-1)}$
11 : let $\mathbf{z}_i := \mathbf{z}_i^{(i-1)}$ and $p_i := p_i^{(i-1)}$, for $1 \le i \le n$. return $\mathbf{Z} = [\mathbf{z}_1, \mathbf{z}_2, \ldots, \mathbf{z}_n]$ and $\mathbf{D} = \mathrm{diag}(p_1, p_2, \ldots, p_n)$.

where $\hat{\mathbf{a}}_i^T$ denote the ith row of $\hat{\mathbf{A}}$ and $\mathbf{e}_i$, the ith unit basis vector. The pivots p_i's are computed at step 4. Breakdown can occur when there is a zero pivot p_i, since step 7 cannot be carried out. In order to get a useful preconditioner, it's necessary to modify the basic algorithm. In the exact $\mathbf{A}$-orthogonalization process. However, because of dropping and the resulting loss of $\mathbf{A}$-orthogonality in the $\mathbf{z}$-vectors, one can have $\hat{\mathbf{a}}_i^T \mathbf{z}_i \ll \mathbf{z}_i^T \hat{\mathbf{A}} \mathbf{z}_i$. Therefore, whenever an pivot is small enough to satisfy the compensation criterion: $|\mathrm{Re}(p_i^{(i-1)})| < \sigma \|\mathrm{Re}(\hat{\mathbf{a}}_i^T)\|$, $\sigma \in \mathrm{R}$, the compensation should be executed, that is, to switch formula $p_i = \hat{\mathbf{a}}_i^T \mathbf{z}_i$ to the quadratic form: $p_i = \mathbf{z}_i^T \hat{\mathbf{A}} \mathbf{z}_i$. Consequently, the CSL-MAINV process leads to a high quality preconditioner $\mathbf{M}$.

3. NUMERIC EXPERIMENTS

To illustrate the performance of the proposed method, a 3-D discontinuity in the waveguide partially filled with three-dielectrics problem [6] is analyzed. The use of edge FEM result in a large sparse matrix equation with 23,651 unknowns. The CSL-MAINV algorithm is applied to COCG method to solve the large sparse and highly indefinite linear system. Besides, several conventional preconditioners, such as MAINV, AINV, IC, SSOR are also used for comparision. The iteration process of all avobe methods is terminated when the residual error $r = \|\mathbf{b} - \mathbf{A}\mathbf{x}\|/\|\mathbf{b}\|$ (in 10 dB) is reduced by -70 dB. Table 1 shows the iteration number and CPU time (in seconds) for each of the above methods. It can be observed that a considerable improvement in the computational cost is achieved over standard COCG and other conventional preconditioning methods.

Table 1: Iteration number and CPU time for several preconditioned, and unpreconditioned COCG methods.

preconditioner	CSL-MAINV	AINV	IC	SSOR	none
Iteration number	46	73	82	4692	28152
CUP time (s)	96	668	703	295	1093

4. CONCLUSIONS

In this paper, the CSL-MAINV preconditioner is applied to COCG method for solving the large, sparse, symmetric and highly indefinite FEM equations. Numerical results show that the proposed preconditioner can greatly reduce both the iteration number and the CPU time when compared with the conventional preconditioners. Therefore, the CSL-MAINV preconditioner is especially effective when edge FEM is applied to solve EM problems.

REFERENCES

1. Jin, J. M., *Finite Element Method in Electromagnetics*, 1, J. Wiley & Sons, New York, 1993.
2. Saad, Y., *Iterative Methods for Sparse Linear System*, 1, PWS Pub. Co., Boston, 1996.
3. Van der Vorst, H. A. and J. B. M. Melissen, *IEEE Trans. Magn.*, Vol. 26, 706–708, 1990.
4. Benzi, M., M. Tuma, and J. K. Cullum, *SIAM J. Sci. Comput.*, Vol. 22, 1318–1332, 2001.
5. Erlangga, Y. A., C. Vuik, and C. W. Oosterlee, *Appl. Numer. Math.*, Vol. 50, 409–425, 2004.

6. Lee, Y. H., Z. P. Nie, and X. Y. Sun, "Relaxed incomplete Cholesky factorization preconditioned symmetric LBCG algorithm for solving electromagnetic problems," *Journal of Electromagnetic Waves and Applications*, Vol. 23, No. 16, 2237–2249, 2009.

The Characteristics of 116 Ore Belt in the Shihu Gold Deposit of Western Hebei — Based on the EH-4, China

Liu Yang, **Songling Chen**, **Tagen Dai**, **and Haiyang Zou**
School of Geosciences and Environmental Engineering, Central South University
Changsha, Hunan 410083, China

Abstract— This paper studies the ore controlling law and metallogenic law of depth and margin of 116 ore belt in Shihu Gold Deposit based on the methods combining geological and geophysics, and submit a new prospecting targets, providing the basis for further geological exploration. It also provides guidance both theoretical and practical by studying the 116 ore belt in Shihu gold deposit geological features, geochemistry, genesis and metallogenic regularity, to the edge of Shihu gold prospecting prediction of deep, but also the production tried to explore the resource crisis mines how quickly and effectively search for known blind ore bodies of deep vein edge. EH4 is widely used in solid minerals, especially in finding concealed ore deposit. In this paper, the author adopted EH-4 method to make a synthetic study on 116 ore belt in Shihu gold deposit of western Hebei. The result showed that the geophysical method was quite useful in the exploration of concealed ore deposit.

1. INTRODUCTION

Shihu gold deposit is under the administrative divisions of Chenzhuang town Lingshou Country Hebei Province. And it is located 66 km to the west-north of Lingshou Country. The mining geographic coordinates are: Longitude $114°03'15'' \sim 114°04'21''$ and Latitude $38°39'04'' \sim 38°40'19''$. The mining area is 4.1 km^2.

Mining Ore formation is gneiss of Tuanpokou Formation of Archean Fuping Group, lithology is mainly a set of biotite plagioclase gneiss, plagioclase amphibolites, amphibole-plagioclase gneiss, with fibrolite K-feldspar leucoleptite and marble, that composed of senior metamorphic rocks. Most researchers believe that Tuanpokou group is the formation of gold ore source region layer, their views are consistent.

Mine is located in the NW wing of chenzhuang syncline, the overall structural outline for the east of the anticline pitching, structure and near-SN-, NW and EW to the fracture (fracture) structure. Structure acting mainly folds, fracture. Major fold structure withTulingdonggou anticline, Shihu syncline, Yankou reverse anticline syncline and Xionggou syncline. The former two larger scales, laid the structure of the main frame of mine. Major faults, nearly SN-, NW to, NE direction and NNW. Nearly SN-trending faults within the mining area is very developed, often in a certain direction for the change, generally expressed as the swinging to the NNE or NNW. Nearly SN-trending faults are mostly direct and guide mine ore, ore-hosting structure, at Shihu gold deposits are mainly 24, 28, 101, 102, 115, and 116, such as fault belt.

Mining Magmatic rocks are several varieties Yanshanian intrusion the Mapeng rock and granodiorite porphyry, quartz diorite porphyry rock, etc. dyke. Rock mining area is located in the northwest, north along the NNE Beiye-Mapeng-Yangjiazhuang deep faults and intrusion, space was rock strains-like, with the Fuping Group strata penetrated into contact, contact with extraversion.

With the gold mineralization is closely related to the mine wall rock alteration the type of very extensive, mainly solidification, pyrite, silicate, sericite rock-oriented, K-feldspar-oriented, green mud Petrochemical and local carbonate, kaolin-based and so on.

In general, the conductivity of gold-bearing quartz veins showed high resistance response. In this area of quartz vein-type gold deposits there were virtually fracture zones within the fracture zones due to strong water-rich, it showed low resistance response, and therefore show low resistance response to fracture broken belt. This choice of EH-4 to predict an extension of the deep veins trend 116 ore belt.

2. FIELD WORK METHOD AND TECHNOLOGY OF EH-4 SYSTEM

① Choice of operating frequency: The gneiss, with resistivity more than 1000 Ω·m, was the main bedrock in this project area. In order to meet the design requirement, we chose 10 Hz, the lowest operating frequency while detecting. Three frequency groups like the second, the third and the fourth were in our choice, ranging from 10 Hz to 99 kHz.

② Arrangement of observation points: The geophysical section line of survey area in Shihu gold deposit was located by our study team. We adopted GPS position and fix distance with measuring wire.

③ Systematic inspection: The parallel test was carried out the day before we began. It was required that the two magnetic bar parallel on the ground, $2 \sim 3$ m apart. The two electric dipole were arranged parallel, and be vertical to the bar. We observed the time series signal of electric field and magnetic field channels to make sure if it works properly.

3. DATA PROCESSING METHOD

The time series collected in field were pretreated firstly, and then changed to FFT. The imaginary and real component, and the phase data were obtained though it. The one-dimensional BOSTICK inversion was performed to transform from frequency to depth. Based on one-dimensional inversion, the two-dimensional electromagnetic was imaged fast and automatically by the two-dimensional imaging software used abroad.

The data obtained by inversion was done Kringing griddling in the XZ plane. Meeting the actual situation of electrical anisotropy, X-axis and Y-axis were to taken anisotropy method to search radius.

4. WORKLOAD COMPLETED AND QUALITY ASSEMENT

Only 5 representative profiles were arranged this time because of high investigation cost. They were Line 062, Line 056, Line 050, Line 053 and Line 057 respectively. The workload completed was list in Table 1 in details.

Table 1: The workload table of survey in 116 ore belt of Shihu Gold Deposit.

Survey-Line Number	Points Number	Dot Pitch (m)	Polar Distance (m)	Profile Length (m)
Line 062 Section	**26**	**20**	**20**	**500**
Line 056 Section	**26**	**20**	**20**	**500**
Line 050 Section	**26**	**20**	**20**	**500**
Line 053 Section	**26**	**20**	**20**	**500**
Line 057 Section	**26**	**20**	**20**	**500**
Total observation points		**78**		

The profile layout obeyed the following three principles. Firstly, it can basically reflect deep extension in the production midcourse of 116 ore belt. Secondly, it can reflect the extension of the all section of the ore belt roughly. Thirdly, it was favorable for verifying with pitting and drilling in near future. Base on these principles, the Line 062, Line 056, Line 050, Line 053 and Line 057 were layout.

5. ANOMALY INTERPRETATION OF 116 ORE BELT

5.1. Anomaly Interpretation of Line 062

Located at the northern tip of the surveyed area, the resistivity distribution of it showed the features of two-story structure. The first layer, low resistivity, was well distributed in the whole survey line, with 200–250 meter thickness. It can be inferred that it was formed by weathering surface dust from Quaternary sediments or rock. The second layer, high resistivity, was located below an elevation of 550 meters. It can be inferred that it were metamorphic rocks and the rocks is more complete. It appeared low resistivity body on the point of 300 meter elevation on the west of survey line. This body showed the feature of contour-intensive on the east side, from which it can be inferred that it caused by tectonic activity.

The survey line passed through two structures. F1 is at the point of 0 meter of the line, and tend to N-E, with angle of greater than 60 degrees. The cut is from 250-meter depth to 580-meter elevation. F2 is at the point of 120 meters of the line, almost paralleled development to F1. The cut depth is relatively shallow, about 600-meter elevation, and may be extended down to the of 500-meter elevation.

5.2. Anomaly Interpretation of Line 056

Two-story structure was also found here and the thickness of the low resistivity in the first layer was greater, nearly 400-meter thickness. The rocks of high resistance in the second layer were more complete, with obvious trend of development to the deep of the eastern survey line. There existed low resistivity body at the point of 0-meter elevation in the western survey line. The nature of survey line is unknown due to the limited length, and may be connected with tectonic activities. F1 was located at the point of 0-meter of the survey line, cutting to 400-meter elevation, while the F2 was at the 100-meter, cutting deep to about 300-meter elevation. There was a relatively high resistance body on the west of 400-650 meter elevation, with the resistance rate of 4000 Ohm. And it may due to the breaking of quartz veins.

5.3. Anomaly Interpretation of Line 050

The low resistivity body on surface was significantly thinner, about 100 thicknesses, and was evenly distributed throughout the survey line. F1 was in the 40-meter of the line, tend to the North -East, cutting to 450-meter elevation, and may be extended down to 300-meter elevation on the west of the line which belonged to low resistivity zone. That is to say, there was a development trend deep to west. F2 was in the 180-meter of the line, with tend to the North East, cutting to 500-meter elevation or deeper low resistance area. Although it showed the feature of high resistivity body in the deep near 100-meter, it was influenced by the F1 and F2 with different degrees.

5.4. Anomaly Interpretation of Line 053

It showed a three-layer structure, that is, low-high-low development. There was a low resistivity layer, 100-meter thickness, uniformly development along the survey lines, on the surface. The second layer was high resistivity, with elevation of 300-650 meter. Although it showed high resistance (5000–6000 ohm), its rock was not complete due to the impact of rock structure, showing different breaking situation. The elevation below 200 meters in the third layer was low resistivity, with the resistivity lower than 1000 ohm, and the reasons were still unknown. F1 was located from 40 meters of survey line cutting to 500 meter elevation. F2 was at 180 meters of the line and the cut depth was only to the 600-meter elevation.

5.5. Anomaly Interpretation of Line 057

It showed low resistance on the west of survey line while high resistance on the east. According to the morphological changes of contour, it can be divided into three structures. F1 was at 120 meters of the survey line, dip steep, nearly vertical, large cutting depth, cutting to the elevation of 100 meters. F1 was the dividing line for the high resistance and the low resistance zone. F2 was at 240 meters of the line, with cutting depth only to the elevation of 550 meters. F3 was located at 40 meters of the line; tend to northwest, angle of greater than 75 degrees, with cutting depth to 200 meters or deeper level.

6. CONCLUSION

In general, of the No. 116 ore belt, the low resistivity layer in the northern part was thick (measuring lines 062, line 056), while thinner in the Southern. The rock of high resistivity in the deep part was relatively complete in the northern, and was influenced by the structure in the south. F1 was almost paralleled development to F2. The cutting depth of F2 gradually became shallow from north to south, while the cutting depth of F1 except Line 057 was more similar. According to the resistivity change and the structural position, it can be inferred that these zones may be beneficial for ore forming such as the low resistance area (300-meter elevation) on the west of Line 062 of and relative high resistance (550-meter elevation), the low resistivity zone(0-meter elevation) on the west of Line 056 and relatively high resistance (elevation of 400–650 meters), the low resistivity zone (elevation of 300 meters on the west of Line 050 and the elevation of 150 meters on the east), the relative low resistivity zone(near elevation of 400 meters of Line 053), and the relative high resistance(the elevation of 150 meters of Line 057).

ACKNOWLEDGMENT

This paper is supported by National Science Foundation Project of Hunan Province (07JJ6071).

REFERENCES

1. Zhang, Y. X., S. L. Chen, and S. L. Peng, "Study on the gold ore structural controlling over TS ore-field, Lingshou, Hebei Province," *Geotectonical et Metallogenia*, Vol. 20, No. 1, 71–80, 1996.
2. Chen, G. D., "China metallogenic geotectonic map," Central South University of Technology Press, Changsha, 1999.
3. Yang, D. F. and G. S. Li, "Study on the ore-forming conditions and genesis of Tuling and Shihu gold deposit in the Taihang mountain region," *Journal of Changchun University of Earth Science*, Vol. 21, No. 1, 47–53, 1991.
4. Xi, C. Z., T. G. Dai, and W. Liu, "Geological-geochemical characteristics of the Shihu gold deposit in western Hebei Province," *ACTA Geoscientica Sinica*, Vol. 29, No. 4, 451–458, Aug. 2008.
5. Xi, C. Z., T. G. Dai, W. Liu, and H. J. Zhang, "Petrogeochemical characteristics of the intrusive bodies of Mapeng granitoids in western Hebei," *ACTA Petrologica et Mineralogica*, Vol. 27, No. 2, 113–120, Mar. 2008.

Application of EH4 in the II Forecast Area of Yushiwa Iron Mine of Hanxing Area, China

Gaofeng Du, **Tagen Dai**, **and Liu Yang**
School of Geosciences and Environmental Engineering, Central South University
Changsha, Hunan 410083, China

Abstract— Yushiwa iron mine is under the administrative divisions of Xixu town of She city in Hebei Province. The authors have reached the conclusion that the iron ore bearing horizon is the middle of Ordovician limestone, magmatic rocks in this area is for acid diorite, along with invasive structural vulnerability. EH4 is widely used in solid minerals, especially in finding concealed ore deposit. In this paper, the author adopted EH-4 method to make a synthetic study on the II forecast area of Yushiwa iron deposit in Hanxing area. The result showed that the geophysical method was quite useful in the exploration of concealed ore deposit.

1. INTRODUCTION

Yushiwa deposit area is situated in the north western end of Wuan depression, and the west of Taihang Taiwan's military security arch beam concave. Produced in the southwest subduction end of mine complex body of diorite, regional structure mainly are the two north-northeast trending faults (mine fracture, fracture from the well) and the North West, including the NNE trending faults control the Yanshanian rock depression west of Wuan output and distribution of iron ore. Jianshancun unit of Rock mass is exposed in the north of the mining, as in the Ordovician rock strata. Mine many times before and after the experience of a large number of pit mine production inspection and disclosure, indicating a single stratum in the Mainland layer, simple structure.

1.1. Stratum

Surface of mining within the mining right has been widely covered by the Quaternary, only partially exposed in the Ordovician limestone, and the distribution of erosion in the mountain valley in the Tertiary gravel surface can be seen. Layers summarized as follows:

1.1.1. Middle Ordovician

Middle Ordovician strata are the main exposed strata of mining area, from the Jianshan are exposed southeast to southwest, from the project to expose the surface erosion and mountains, rock mass from the south extension of the Jianshan are underlying in the Middle Ordovician strata. As the rock mass in the south to the Jianshan pitching by east of Huilancun to west of Jianshan, the formation tend to change gradually from SE to SW, dip angle $17^\circ \sim 32^\circ$, usually 22°. Investigation revealed that the layer consists of pure limestone, porphyritic spent limestone, dolomite limestone, argillaceous limestone and brecciated limestones.

1.1.2. Tertiary

Tertiary is widely distributed in central and southern mining area, from south to north thickening, survey shows by the thickness of a few meters to 180 meters thick, the general thickness of 40 meters to 100 meters, gravel, pebbles formed by different size, cement to clay, which sometimes can be seen from 1 to 5 m layer of red-brown loam, gravel, sandstone and quartz are dominated by feldspar and quartz sandstone, rounded degree is better sorting poor, large and small diameter by a few centimeters to a meter change. The overlying layer of gravel over the top of Ordovician limestone, showing unconformity.

1.2. Sturcture

The main structural system is the monoclinic structure of Mine Rock Southwest side part of Jianshan Southwest and Southeast presented the overlying limestone, the structure common control with the diorite contact zone distribution and changes in iron ore output and thereby control the location of occurrence, form and attitude.

Less of fault development in mining areas, in the mining area 200 meters north east, with east-west fault-Huilancun fault, and which western extension of the fault is unknown. According to mine observed, with 170 level in the lower plate to open up the new lane, as well as 150 level of Southeast entrance of Fujing, a large number of breccia development, coupled with the contact zone of the South East to extend the depth of steep drop Yunjialing ore body, delayed introduction of

the fault may cut the main ore body south west east, causing some of the main ore body ore south east of broken cover. According to speculation in the mining area east of the northern section of north-south along the Huoyaoku in the valley, suggesting that there is a fault.

1.3. Magmatic Rock

Yanshanian magmatic rocks are mainly of late-basic intrusive rocks, the Jianshan unit of volume of Kuangshancun .the rock north is Cejing, south to Yunjialing, Huaihegou, west of Shangjiaosi, east to the Guoerzhuang, exposed area of 35 km^2. Invasive Liangjiashan group, Majiagou, Taiyuan. Rock alteration and strong, there epidotization, chloritization, albitization so there is skarn rock, tremolite.

Only a strong bleaching of surface mining altered diorite from the mine in the mining area North West from north to south was inserted into the banded limestone, until the North to help the subsidence area, the high point of disappearing into the limestone outcrops south no help. Dioritic rocks in the main more insidious and contact discharge, according to survey revealed diorite rock in the mining area for the slow ramp-like shape to the south plunging, some lots ups and downs, the formation of uneven surface, the height difference up to 40 or so meters.

Jianshan Rock outcrop edge widespread skarn and carbonate flowers, rocks the body can also be found through the carbonate veins. In the contact zone near the impact due to alteration, diorite zoning phenomenon obviously, from the contact zone inward, distribution of skarn diorite, flash digenetic alteration, diorite.

2. DEPOSIT GEOLOGICAL CHARACTERS

2.1. Tipical Orebody Characters

The main ore mineral is Fe1 ore, ore body buried in the deepest and largest of its length 1990 m, maximum width of 510 meters, the general level of projection width of 300 $\sim$ 450 meters; maximum thickness of 62.4 m, the general thickness of 15 $\sim$ 20 meters. Ore reserves of 26,481,700 tons, accounting for the total ore reserves of 92.9; ore 40 $\sim$ 330 meters depth, occurrence of elevation of 89 $\sim$ 358 m, ore bodies NW$\sim$SE direction, inclination SW, steeply dipping, generally more than $10^\circ \sim 25^\circ$.

Ore body in the vertical pitching from NW to SE, so ore was from north to south, pitching angle of 5° around the general, form stable, local wavy or distorted, lens, like the overall look is layered. Ore body cross section display: $16''$ to 14 lines ore body thickness of 20 to 30 meters, the atmosphere was soothing wavy, slightly curved. In the $15'$ line CKF47 hole in the roof top of the limestone in the middle of the main ore body 6 to 7 layer lens small seam: $13' \sim 7$, a broad line of ore was slow saddle to AA' as the axis, the middle and upper lung thick and thin ends under the extension. Ore bodies are more regular and stable. Limestone in the region are also visible above the existence of small ore lenses; B2$\sim$B7 line ore bodies are more complex occurrences, changed greatly. Ore body east of occurrence as intrusive rock complex, multi-layer lens intrusi limestone rock, the ore body the appropriate changes, when combined hours, sub-multi-up, intermingled diorite and limestone skarn. Ore body is north west from the B3 line along the contact zone was pinch reproduction, ore bodies in the plane is divided into eastern and western parts of the eastern ore body is still Fe1-1, the western ore body Fe1-2, east west north ore body extended to B-3 after the pinch, the western ore body north west line extended to the B-5, was upside down saddle, the shape, attitude and stability.

Other ore bodies are small ore reserves of small, scattered in the upper part of Fe1. Region located NNE tectonic Mesozoic magmatic belt in the mine field tectonic magmatic activity within the region is very strong.

2.2. Ore Characters

2.2.1. Types of Ore

Apart from a small amount of oxide ore minerals, a number of mainly primary ore, oxide ore deposit, mainly in the upper oxidized zone, the ore oxidation strongly, as limonite. Original magnetite deposits mainly in the lower part of the deep oxidation to teach the basic without light or oxidation. By ore mining structure can be divided into a honeycomb structure of magnetite ore — hematite ore, bulk and powdered red limonite, magnetite-like infection stone, lump magnetite, banded skarn-like magnetite stone.

By ore minerals can be divided into magnetite with pyrite, carbonate rock, carbonate minerals magnetite, containing magnetite, pyrite diopside rock, chlorite magnetite rock, rock containing

pyrite and magnetite, serpentine Magnetite, pyrite and magnetite, limonite, magnetite rock ore and iron ore and other types of false red.

2.2.2. Mineral Composition

Relatively simple ore mineral composition, the main metal minerals to magnetite, followed by pyrite, chalcopyrite, plate magnets, etc., also were observed and a small amount of goethite chalcopyrite, bornite, chlorite, pyrrhonist, etc.

Magnetite: General for Taxing of semi-crystalline, mainly in the fine particle size between 0.05 to 1.2 mm in the majority in between from 0.3 to 0.5 mm. Microscope, the carbonate minerals are diopside ring with all the pyrite structure and is accountable to the formation of carbonate and other remnants of the structure and skeletal crystal structure. Iron black, semi-metallic luster. Content of 30% $\sim$ 90%, generally 60% to 80%, half from the form he shaped grains mainly octahedral and cube-shaped crystal form from the second, and occasionally tabular grain, diameter of 001 $\sim$ 5 mm, usually 0.1 $\sim$ 2 mm. At least two generations of magnetite formation to the first generation mainly smaller particle size, the second generation of coarse particle size, often output in the first generation of magnetite crystal holes or cracks, sometimes showed vein cutting across the first generation of magnetite.

Hematite illusion: the oxidation of the magnetite, a weak magnetic Aphanitic block or powder, steel gray, red brown or black iron, semi-metallic luster.

Pyrite: a half since Ta-shaped to form the main structure, since the form of small crystal structure, the other particle size from 0.1 to 1.2 millimeters between the individual large 2–3 mm, the majority of 0.6 mm. Pyrite in the ore occurrence in three states: one was his form of crystal-like spread infection ore, into a small package in the magnetite in the body, diameter of 0.01 $\sim$ 0.05 mm, or a similar text with the formation of magnetite like structure, with the formation of magnetite at the same time or earlier in magnetite; two were on their own, semi-euhedral granular structure, were disseminated in the ore or mass production, diameter 0.1 $\sim$ 0.5 mm, often among grain embedded with magnetite grains and chalcopyrite, bornite and other minerals, the most current development; 3 in the ore, and calcite, quartz vein was output, its diameter greater than 1 mm, and sometimes to 3 mm, this often hematite pyrite, limonite account retains its pseudomorphic. Some pyrite crystals and crushed with a skeletal structure.

Pyrrhonist: There are two kinds of occurrences, one produced in the massive skarn-type copper and zinc ore, with chalcopyrite symbiosis, a number of semi-self-shaped — it is shaped particle, the monomer size greater than 0.1 mm. The other vein lets disseminated produced in the quartz diorite, diorite, and particle size 0.06–0.2 mm.

Chalcopyrite: It can be divided into three types of outputs, one is the inclusion of fine, bulk distribution of stars in the pyrite, which was milk droplet structure, particle size 0.005 $\sim$ 0.05 mm, who reached a large 0.2 mm. The other is disseminated vein lets or irregular aggregates, distributed in the magnetite and pyrite grains, and they account for ablation, particle size 0.1 $\sim$ 0.2 mm, individual up to 0.6 mm. There is also a symbiotic with calcite, oxidation see chlorite, bornite side of the secondary response, and sometimes blue along with the joint account to be copper.

Major rock-forming minerals in the mineral diopside, chlorite, followed by tremolite, phlogopite, calcite, serpentine and minor quartz, epidote and sericite. Microscopy observation also shows that a small amount of brown muscovite and epidote, chalcedony, talc, apatite, magnesium silicate rock.

2.2.3. Ore Structure

Ore structure is form a half since — Ta-shaped, the main grain-like, less self-shaped crystal, the other still account for the residual, skeletal crystal, sieve-like, fake crystal, crushed, solid solution separation structure. Since the form of a half block from the more common form of structure or lump ore, more rigid, high taste; Ta-shaped crystal structure prevalent in the infection-like or banded ore; account of the residual structure of sparse infection was more common in the common ore generally low taste.

Ore with sparse to dense structure of the main infection-like, lump for the times, occasionally banded, spotted hybrid form, brecciated, honeycomb, powder and so on. Ore-like distribution infection more common, as the main ore body ore types; group minerals are distributed in north of the 7 line for more than 220 level, mostly for open-hearth furnace bonanza; other kinds of structural types of minerals only in some places, see the local that small amounts.

3. II FORECAST GEOPHYSICAL RESULT

II forecast area is laid three survey lines of Yushiwa in the total survey area, each line measuring 300 meters long, 200 meters from the line. The three lines only carried out high-frequency magneto telluric sounding.

Geophysical results show that in the surveyed area, 0 lines exist obvious low resistance high magnetic anomaly zone, named WT2, width 300 m, depth 490–580 m, forming a more favorable inference. Depth in the other section (400 m $\sim$ 1500 m) was not found significant low resistivity anomaly.

0 line EH-4 inversion results can be seen, the resistivity of 50–150 ohm m of upper stratum, presumed to be Tertiary gravel layer, thickness is about 100–240 meters, mixed with high resistance of local gravel layer body may be inferred. Ordovician limestone; intermediate formation resistivity range 180–700 ohms. m, presumed to reflect the Ordovician limestone, the thickness of about 270 m–370 m, the limestone of the conductive body inferred for the fracture zone, may be water; lower abdomen formation resistivity is relatively high, at 200–1000 ohms. m range of changes, presumed to reflect the diorite. Depth of 490–580 m in the range of a low resistance layer, the resistance rate of 10–30 ohms. M varies within a range of about 40–80 meters in thickness, we concluded that the low resistivity layer with the mineralization sites, denoted as WT2.

2 lines from the EH-4 inversion results can be seen in the overlying formation resistivity 10–150 ohms. M, presumed to be Tertiary gravel layer thickness of about 110–205 meters; intermediate formation resistivity range 200–700 ohms. m, presumed to reflect the Ordovician limestone, the thickness of about 120 m–180 m; lower formation resistivity is relatively high, at 300–2000 ohms. m range of changes, presumed to reflect the diorite.

4 lines from the EH-4 inversion results can be seen, the resistivity of 40–300 ohm stratum. M, presumed to be Tertiary gravel layer thickness of about 110–200 meters; intermediate formation resistivity range of 160–650 ohms. m, presumed to reflect the Ordovician limestone, the thickness of about 100 m–180 m; lower abdomen formation resistivity is relatively high, at 300–4000 ohms. m range of changes, presumed to reflect the diorite.

0 to 4 lines on the EH-4 inversion of data along with low resistivity anomaly (WT2) central depths of 550 meters a biopsy, the resistivity contour drawing, and the combination of EH-4 inversion transect comprehensive analysis of the low resistance measured in the vertical line exception WT2 direction is not continuous, only the 0 line section has shown, we concluded that the exception for the ore-forming conditions are better the lot, may be connected Yunjialing mine. The remaining depth was not found significant low resistivity anomaly.

ACKNOWLEDGMENT

This paper is supported by Handan-Xingtai Mine Authority and Central South University.

REFERENCES

1. "Taihang Mountain areas Hanxing type iron ore prospecting," Institute of Geological Sciences of North China, Hebei Geological Institute, 1–154, 1976 (law and internal data).
2. Shen, L. S., "A discussion about the concealed iron resource potential on the east side of Beijing-Guangzhou railway within Handan-Xingtai area," *Mineral Resources and Geology*, Vol. 22, No. 4, 314–318, 2008.
3. Zheng, J. M., "Southern Hebei Handan area of skarn iron ore fluid and ore-forming mechanism," Ph.D. Thesis, China University of Geosciences, Beijing, China, 2007.
4. Shen, B. F., A. M. Zhai, Z.H. Li, et al., "The chemical composition and its geological of contact metasomatic magnetite iron deposits in Southern Hebei," Vol. 25, No. 1, 10–18, 1982.
5. The South Final Report of Yuquanling iron ore reserves, Han-Xing Mine Authority, 2001.

Validity of Image Theorems under Spherical Geometry

Shaolin Liao[1], **Sasan Bakhtiari**[1], **and Henry Soekmadji**[2]

[1]Argonne National Laboratory, USA
[2]Hamilton Sundstrand, USA

Abstract— This paper deals with different image theorems, i.e., Loves equivalence principle, the induction equivalence principle and the physical optics equivalence principle, in the spherical geometry. The deviation of image theorem approximation is quantified by comparing the modal expansion coefficients between the electromagnetic field obtained from the image approximation and the exact electromagnetic field for the spherical geometry. Two different methods, i.e., the vector potential method through the spherical addition theorem and the dyadic Greens function method, are used to do the analysis. Applications of the spherical imaging theorems include metal mirror design and other electrically-large object scattering.

1. INTRODUCTION

Different image theorems have been widely used for electromagnetic modeling of mirrors and lens antenna [1, 2]. In [2], Rong and Perkins applied the image theorems to mirror system design for high-power gyrotrons. The author also theoretically evaluate the validity of the image theorems in the cylindrical geometry [1]. In this article, following similar procedures in [1], a closed-form formula for the discrepancy parameter, which is defined as the ratio of the spherical modal coefficient for image theorem to that of the exact field, has been derived for the spherical geometry.

2. IMAGE THEOREMS IN THE SPHERICAL GEOMETRY

Figure 1 shows the spherical geometry for image theorem analysis.

2.1. The Vector Potential Method

2.1.1. The Spherical Modal Expansion

In spherical coordinates, the electrical vector potential $\mathbf{F}(\mathbf{r})$ for $\mathbf{M}_s(\mathbf{r}')$ is given as [3, 4],

$$\mathbf{F}(\mathbf{r}) = \epsilon_0 \iint_{S'} dS'\ \mathbf{M}_s(\mathbf{r}')g(\mathbf{r}-\mathbf{r}') = \frac{-jk\epsilon_0}{4\pi} \iint_{S'} dS'\mathbf{M}_s(\mathbf{r}')h_0^{(2)}\left(k[r-r']\right) \tag{1}$$

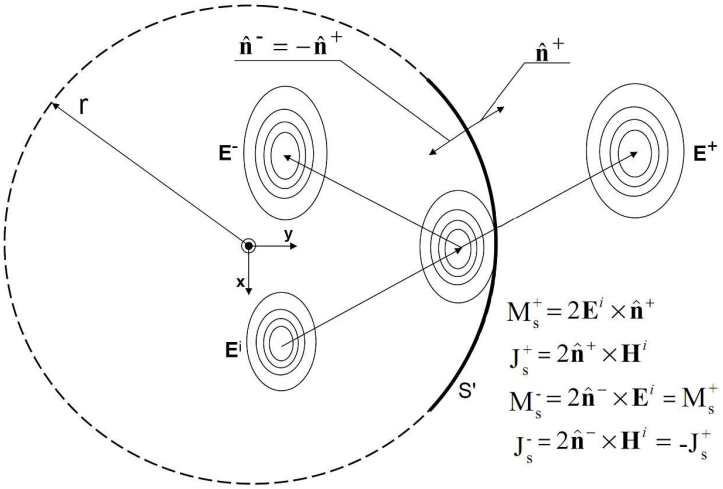

Figure 1: Image theorem in the spherical geometry: the incident field $\mathbf{E}^i$ propagates onto spherical surface S', then it may forward-propagate to $\mathbf{E}^+$ or it could be back-scattered to $\mathbf{E}^-$, depending on whether surface S' as a fictitious surface where the equivalence theorem applies on a PEC surface. $\hat{\mathbf{n}}^+$ and $\hat{\mathbf{n}}^-$ are the outward and inward surface normals on spherical surface S' respectively. $\mathbf{M}_s$ and $\mathbf{J}_s$ are equivalent surface currents for Love's equivalence theorem. $\mathbf{M}_s^+$ is the image approximation of Love's theorem and $\mathbf{M}_s^-$ is the image approximation for the induction theorem.

where, $h_0^{(2)}$ is spherical Hankel function of the second kind of order 0. According to the spherical addition theorem [3, 4],

$$h_0^{(2)}\left(k[r-r']\right) = \sum_{n=0}^{\infty}(2n+1)j_n(kr')h_n^{(2)}(kr) \times \sum_{m=0}^{n}(2-\delta_m^0)\frac{(n-m)!}{(n+m)!}P_n^m(\theta')P_n^m(\theta)\cos m(\phi-\phi') \quad (2)$$

where, j_n is the spherical bessel function of the first kind of integral order n; P_n^m is the associated Legendre polynomial and δ_m^0 is the Kronecker delta function ($\delta_m^0 = 1$ for m=0 and $\delta_m^0 = 0$ for m$\neq$ 0). Substituting (2) into (1), the modal expansion of $\mathbf{F}(r)$ is obtained as,

$$\begin{aligned}
\mathbf{F}(\mathbf{r}) &= \sum_{n=0}^{\infty}\sum_{m=0}^{n}\mathbf{f}_{\text{TE}}^{\mathbf{M}_s}(n,m)h_n^{(2)}(kr)P_n^m(\theta)\begin{matrix}\cos m\phi\\ \sin m\phi\end{matrix}\\
\mathbf{f}_{n,\text{ TE}}^{m,\mathbf{M}_s} &= \chi\iint_{S'}dS'\mathbf{M}_s(\mathbf{r}')j_n(kr')P_n^m(\theta')\begin{matrix}\cos m\phi'\\ \sin m\phi'\end{matrix}\\
\chi &= (2-\delta_m^0)\frac{-jk\epsilon_0}{4\pi}\frac{(2n+1)(n-m)!}{(n+m)!}.
\end{aligned} \quad (3)$$

The near field to far field transform of (3) in the spherical coordinate is given as [5],

$$\mathbf{F}(\mathbf{r})\Big|_{r\to\infty} = \frac{je^{-jkr}}{kr}\sum_{n=0}^{\infty}\sum_{m=0}^{n}j^n\mathbf{f}_{\text{TE}}^{\mathbf{M}_s}(n,m)P_n^m(\theta)\begin{matrix}\cos m\phi\\ \sin m\phi\end{matrix} \quad (4)$$

The duality relation can be used to obtain the magnetic vector potential $\mathbf{A}(\mathbf{r})$ for the $\mathbf{J}_s$ approximation as follows,

$$\begin{aligned}
\mathbf{A}(\mathbf{r}) &= \sum_{n=0}^{\infty}\sum_{m=0}^{n}\mathbf{g}_{\text{TE}}^{\mathbf{M}_s}(n,m)h_n^{(2)}(kr)P_n^m(\theta)\begin{matrix}\cos m\phi\\ \sin m\phi\end{matrix}\\
\mathbf{g}_{n,\text{ TE}}^{m,\mathbf{M}_s} &= \chi'\iint_{S'}dS'\ \mathbf{J}_s(\mathbf{r}')j_n(kr')P_n^m(\theta')\begin{matrix}\cos m\phi'\\ \sin m\phi'\end{matrix}\\
\chi' &= (2-\delta_m^0)\frac{-jk\mu_0}{4\pi}\frac{(2n+1)(n-m)!}{(n+m)!}.
\end{aligned} \quad (5)$$

2.1.2. The Back-scattered and forward-propagating Waves

Similar to the cylindrical geometry, we can separate (3) into back-scattered and forward-propagating waves as,

$$\begin{aligned}
j_n(kr') &= \frac{1}{2}\left\{h_n^{(1)}(kr') + h_n^{(2)}(kr')\right\} \quad (6)\\
\mathbf{f}_{n,\text{ TE}}^{m,\mathbf{M}_s\pm} &= \frac{\chi}{2}\iint_{S'}dS'\ \mathbf{M}_s(\mathbf{r}')h_n^{(1),(2)}(kr')P_n^m(\theta')\begin{matrix}\cos m\phi'\\ \sin m\phi'\end{matrix}
\end{aligned}$$

Since the spherical harmonics is a complete basis set, we can always express the initial incident electric field $\mathbf{E}(\mathbf{r}')$ on the initial spherical surface S' with radius of r_0 (in Figure 1) as follows,

$$\begin{aligned}
\mathbf{E}(\mathbf{r_0}) &= \sum_{n=0}^{\infty}\sum_{m=0}^{n}a_{n,o}^{m,e}\mathbf{M}_{n,o}^{m,e+}(\mathbf{r_0}) + b_{n,o}^{m,e}\mathbf{N}_{n,o}^{m,e+}(\mathbf{r_0})\\
\psi_{n,o}^{m,e+}(\mathbf{r_0}) &= h_m^{(2)}(kr_0)P_n^m(\cos\theta')\begin{matrix}\cos(m\phi')\\ \sin(m\phi')\end{matrix}\\
\mathbf{L}_{n,o}^{m,e+}(\mathbf{r_0}) &= \nabla\psi_{n,o}^{m,e+}(\mathbf{r_0})\\
\mathbf{M}_{n,o}^{m,e+}(\mathbf{r_0}) &= \nabla\times\left\{\mathbf{a}_r r\psi_{n,o}^{m,e+}(\mathbf{r_0})\right\}\\
\mathbf{N}_{n,o}^{m,e+}(\mathbf{r_0}) &= \frac{1}{k}\nabla\times\mathbf{M}_{n,o}^{m,e+}(\mathbf{r_0}).
\end{aligned} \quad (7)$$

From (3) and noting that $\mathbf{M}_s^+(\mathbf{r_0}) = 2\mathbf{E}(\mathbf{r_0}) \times \mathbf{a}_r$, on spherical surface S' in Figure 1,

$$\tilde{\mathbf{E}}(r_0) = -\frac{1}{\epsilon_0} \sum_{n=0}^{\infty} \sum_{m=0}^{n} \left\{ \mathbf{L}_{n,o}^{m,e+}(\mathbf{r}) \times \mathbf{f}_{n,\,\mathrm{TE}}^{m,\mathbf{M}_s} \right\} \tag{8}$$

$$\mathbf{L}_{n,o}^{m,e+}(\mathbf{r_0}) \;=\; \nabla \psi_{n,o}^{m,e+}(\mathbf{r_0})$$

The approximate field $\tilde{\mathbf{E}}(\mathbf{r}_0)$ on the initial spherical surface S' is obtained from (3) through image theorem approximation,

$$\tilde{\mathbf{E}}(\mathbf{r}_0) = \sum_{n=0}^{\infty} \sum_{m=0}^{n} \tilde{a}_{n,o}^{m,e} \mathbf{M}_{n,o}^{m,e}(\mathbf{r}_0) + \tilde{b}_{n,o}^{m,e} \mathbf{N}_{n,o}^{m,e+}(\mathbf{r}_0) \tag{9}$$

Now the deviation of the spherical coefficients $\tilde{a}_{n,o}^{m,e}, \tilde{b}_{n,o}^{m,e}$ in Eq. (9) from their exact values $a_{n,o}^{m,e}, b_{n,o}^{m,e}$ in Eq. (7) is defined as the discrepancy parameters ζ,

$$\begin{aligned} \zeta_{\mathrm{TE}}^{\mathbf{M}_s} &= \frac{\tilde{a}_{n,o}^{m,e}}{a_{n,o}^{m,e}} = -j2kr_0 h_n^{(2)}(kr_0) \frac{\partial [krj_n(kr)]}{\partial kr}\bigg|_{r=r_0} \\ \zeta_{\mathrm{TM}}^{\mathbf{M}_s} &= \frac{\tilde{b}_{n,o}^{m,e}}{b_{n,o}^{m,e}} = j2kr_0 j_n(kr_0) \frac{\partial [krh_n^{(2)}(kr)]}{\partial kr}\bigg|_{r=r_0} \end{aligned}$$

and,

$$\begin{aligned} \zeta_{\mathrm{TE}}^{\mathbf{M}_s,\pm} &= -j2kr_0 h_n^{(2)}(kr_0) \frac{\partial [krh_n^{(1),(2)}(kr)]}{\partial kr}\bigg|_{r=r_0} \\ \zeta_{\mathrm{TM}}^{\mathbf{M}_s,\pm} &= j2kr_0 h_n^{(1),(2)}(kr_0) \frac{\partial [krh_n^{(2)}(kr)]}{\partial kr}\bigg|_{r=r_0}. \end{aligned} \tag{10}$$

Similar expressions exist for $\mathbf{J}_s$ image approximation,

$$\begin{aligned} \zeta_{\mathrm{TE}}^{\mathbf{J}_s} &= \zeta_{\mathrm{TM}}^{\mathbf{M}_s}, \quad \zeta_{\mathrm{TM}}^{\mathbf{J}_s} = \zeta_{\mathrm{TE}}^{\mathbf{M}_s} \\ \zeta_{\mathrm{TE}}^{\mathbf{M}_s,\pm} &= \zeta_{\mathrm{TM}}^{\mathbf{J}_s,\pm} = [\zeta_{\mathrm{TE}}^{\mathbf{J}_s,\pm}]^* = [\zeta_{\mathrm{TM}}^{\mathbf{M}_s,\pm}]^*. \end{aligned} \tag{11}$$

2.1.3. The Dyadic Green's Function Method

The magnetic dyadic Green's function in the spherical coordinate is,

$$\begin{aligned} \bar{\mathbf{G}}_m(\mathbf{r}, \mathbf{r}') \;=\; & -\frac{\mathbf{a}_r \mathbf{a}_r}{k^2} \delta(\mathbf{r} - \mathbf{r}') - \sum_{n=-\infty}^{\infty} \frac{j\pi}{2kn(n+1)} \\ & \times \sum_{m=0}^{n} \frac{1}{Q_{nm}} \left\{ \mathbf{M}_{n,o}^{m,e}(\mathbf{r}') \mathbf{M}_{n,o}^{m,e+}(\mathbf{r}) + \mathbf{N}_{n,o}^{m,e}(\mathbf{r}') \mathbf{N}_{n,o}^{m,e+}(\mathbf{r}) \right\} \end{aligned}$$

and,

$$Q_{nm} = \frac{2\pi^2 (n+m)!}{(2 - \delta_m^0)(2n+1)(n-m)!} \tag{12}$$

where $\mathbf{M}_{n,o}^{m,e}$ ($\mathbf{N}_{n,o}^{m,e}$) is obtained by replacing $h_n^{(2)}$ with j_n in $\mathbf{M}_{n,o}^{m,e+}$ ($\mathbf{N}_{n,o}^{m,e+}$). The approximate field $\tilde{\mathbf{E}}(\mathbf{r})$ for $\mathbf{M}_s^+(\mathbf{r}')$ is given as,

$$\tilde{\mathbf{E}}(\mathbf{r}) = -\nabla \times \iint_{S'} dS' \; \mathbf{M}_s^+(\mathbf{r}') \cdot \bar{\mathbf{G}}_m(\mathbf{r}, \mathbf{r}') \tag{13}$$

Substituting (12) into (13) and using the orthogonal properties of spherical modal functions, the approximate field $\tilde{\mathbf{E}}(r_0)$ on initial spherical surface S' is obtained as,

$$\tilde{\mathbf{E}}(r_0) = \sum_{n=-\infty}^{\infty} \sum_{m=0}^{n} \frac{j\pi}{n(n+1)Q_{nm}} \begin{matrix} c_{n,o}^{m,e} \mathbf{M}_{n,o}^{m,e+}(\mathbf{r}) \\ d_{n,o}^{m,e} \mathbf{N}_{n,o}^{m,e+}(\mathbf{r}) \end{matrix} \times \iint_{S'} dS' \begin{matrix} [\mathbf{N}_{n,o}^{m,e}(\mathbf{r}')]^* \times \mathbf{M}_{n,o}^{m,e+}(\mathbf{r}') \\ [\mathbf{M}_{n,o}^{m,e}(\mathbf{r}')]^* \times \mathbf{N}_{n,o}^{m,e+}(\mathbf{r}') \end{matrix} \cdot \mathbf{a}_{r'}. \tag{14}$$

The evaluation of (14) also leads to (9) and (10).

2.1.4. The Analytical Formula for Image Theorems in the Spherical Geometry

Similar to the cylindrical geometry, $\zeta_{\mathrm{TE,TM}}^{\mathbf{M}_s,\mathbf{J}_s+}$ in (10) and (11) can be considered as theoretical formulas for evaluation of the image theorems for narrow-band fields in the spherical geometry. The large argument asymptotic behaviors of $\zeta_{\mathrm{TE,TM}}^{\mathbf{M}_s,\mathbf{J}_s+}$ for $r_0 \to \infty$ can be obtained by noting that,

$$h_n^{(2)}(kr_0) = [h_n^{(1)}(kr_0)]^* \sim \frac{1}{kr_0} j^{(n+1)} e^{-jkr_0},\ kr_0 \to \infty$$

$$\zeta_{\mathrm{TE,TM}}^{\mathbf{M}_s,\mathbf{J}_s+}\big|_{\,r_0\to\infty} = 1. \tag{15}$$

3. RESULTS AND DISCUSSION

Table 1 summarizes the properties of $\zeta_{\mathrm{TE,TM}}^{\mathbf{M}_s,\mathbf{J}_s\pm}$, for the back-scattered and forward-propagating waves respectively. For $r_0 \to \infty$, $\zeta_{\mathrm{TE,TM}}^{\mathbf{M}_s,\mathbf{J}_s} = \zeta_{\mathrm{TE,TM}}^{\mathbf{M}_s,\mathbf{J}_s+} + \zeta_{\mathrm{TE,TM}}^{\mathbf{M}_s,\mathbf{J}_s-}$ shows fast oscillations, which can be seen from Table 1. Mathematically, the oscillations only appear as modal expansion coefficients and disappear after the implementation of the double sums in (9). Physically, the oscillations are due to back-scattered fields, which approach 0 for $r_0 \to \infty$. For example, consider $\zeta_{\mathrm{TE}}^{\mathbf{M}_s-}$ in (10),

$$\tilde{\mathbf{E}}^-(r_0,\phi) = \sum_{n=0}^{\infty}\sum_{m=0}^{n} \left\{\zeta_{\mathrm{TE}}^{\mathbf{M}_s-}\ c_{n,o}^{m,e}\mathbf{M}_{n,o}^{m,e+}(\mathbf{r}_0) + \zeta_{\mathrm{TE}}^{\mathbf{M}_s-}\ b_{n,o}^{m,e}\mathbf{N}_{n,o}^{m,e+}(\mathbf{r}_0)\right\} \tag{16}$$

Changing the variable $\phi' = \phi - \pi$ and letting $r_0 \to \infty$, from Table 1, (16) reduces to,

$$\tilde{\mathbf{E}}^-(r_0,\phi')\Big|_{\,r_0\to\infty} = \sum_{n=0}^{\infty}\sum_{m=0}^{n} e^{-j2kr_0}\left\{c_{n,o}^{m,e}\mathbf{M}_{n,o}^{m,e+}(\mathbf{r}_0) - b_{n,o}^{m,e}\mathbf{N}_{n,o}^{m,e+}(\mathbf{r}_0)\right\}. \tag{17}$$

Now, the back-scattered field $\tilde{\mathbf{E}}^-(r_0,\phi')\big|_{\,r_0\to\infty} \to 0$ due to the fast variation phase term e^{-j2kr_0}, which means that the oscillation in $\zeta_{\mathrm{TE}}^{\mathbf{M}_s-}$ doesn't appear in the actual field evaluation for $r_0 \to \infty$.

Based on the above discussion, $\zeta_{\mathrm{TE,TM}}^{\mathbf{M}_s,\mathbf{J}_s\pm}$ is the theoretical formula of interest to evaluate the validity of image theorems.

It is also helpful to plot the corresponding threshold radius r_{th} with respect to n, for both $20\log_{10}(|\zeta_{\mathrm{TE}}^{\mathbf{M}_s+}| - 1)$ and $20\log_{10}\{\Im[\zeta_{\mathrm{TE}}^{\mathbf{M}_s+}]\}$, with different accuracies ranging from −60 dB to −30 dB (in 3 dB increment), as in Fig. 2. It can be seen from Fig. 2 that, in order to achieve an accuracy of −30 dB for $|\zeta_{\mathrm{TE}}^{\mathbf{M}_s+}|$ (with respect to 1), $r_{\mathrm{th}} \sim 8\lambda$ and $r_{\mathrm{th}} \sim 16\lambda$ for $n = 50$ and $n = 100$ respectively. However, for the imaginary part $\Im[\zeta_{\mathrm{TE}}^{\mathbf{M}_s+}]$, $r_{\mathrm{th}} \sim 9.5\lambda$ and $r_{\mathrm{th}} \sim 18\lambda$ are required for $n = 50$ and $n = 100$ respectively, which again implies that the imaginary part $\zeta_{\mathrm{TE}}^{\mathbf{M}_s+}$ dominates the accuracy of image theorems.

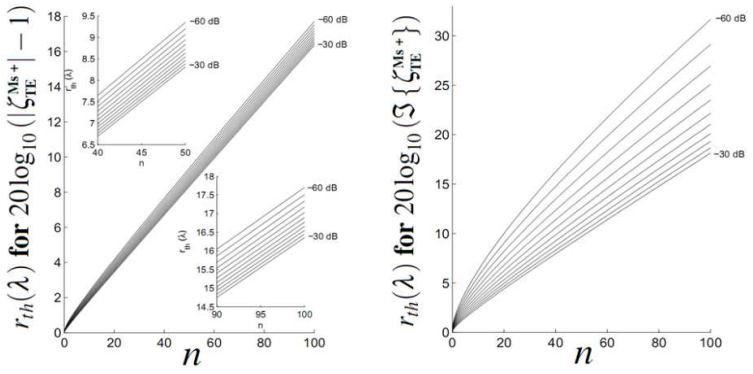

Figure 2: The spherical geometry-threshold radii rth vs. $n = 0$ to 100, for different accuracies, from −60 dB to −30 dB (in 10 dB increment, from bottom to top): (a) the magnitudes $20\log_{10}(|\zeta_{\mathrm{TE}}^{\mathbf{M}_s+}| - 1)$, and (b) the imaginary parts $20\log_{10}[\Im(\zeta_{\mathrm{TE}}^{\mathbf{M}_s+})]$. The inset plots in (a) are used to make the display clearer. Similar to the cylindrical geometry, imaginary parts $\zeta_{\mathrm{TE}}^{\mathbf{M}_s+}$ require larger threshold radii rth for the same accuracy.

Table 1: Summary of $\zeta^{+,-}_{\text{TE, TM}}(\mathbf{m}_s, \mathbf{j}_s)$ for the spherical geometry.

TE/TM modes and $\mathbf{M}_s/\mathbf{J}_s$	The relations	$\zeta^{+,-}_{\text{TE, TM}}(\mathbf{M}_s, \mathbf{J}_s)$	$r_0 \to \infty$
TE & $\mathbf{M}_s$ / TM & $\mathbf{J}_s$			
Sphere: back-scattered wave	$\zeta^{-}_{\text{TE}}(\mathbf{M}_s) = \zeta^{-}_{\text{TM}}(\mathbf{J}_s)$	$-jkr_0 h_n^{(2)}(kr_0) \frac{\partial[krh_n^{(2)}(kr)]}{\partial kr}\Big\vert_{r=r_0}$	$(-1)^n e^{-j2kr_0}$
Sphere: forward-propagating wave	$\zeta^{+}_{\text{TE}}(\mathbf{M}_s) = \zeta^{+}_{\text{TM}}(\mathbf{J}_s)$	$-jkr_0 h_n^{(2)}(kr_0) \frac{\partial[krh_n^{(1)}(kr)]}{\partial kr}\Big\vert_{r=r_0}$	1
TM & $\mathbf{M}_s$ / TE & $\mathbf{J}_s$			
Sphere: back-scattered wave	$\zeta^{-}_{\text{TM}}(\mathbf{M}_s) = \zeta^{-}_{\text{TE}}(\mathbf{J}_s)$	$jkr_0 h_n^{(2)}(kr_0) \frac{\partial[krh_n^{(2)}(kr)]}{\partial kr}\Big\vert_{r=r_0}$	$-(-1)^n e^{-j2kr_0}$
Sphere: forward-propagating wave	$\zeta^{+}_{\text{TM}}(\mathbf{M}_s) = \zeta^{+}_{\text{TE}}(\mathbf{J}_s)$	$[\zeta^{+}_{\text{TE}}(\mathbf{M}_s)]^*/[\zeta^{+}_{\text{TM}}(\mathbf{J}_s)]^*$	1

4. CONCLUSION

For spherical geometry, the theoretical formulas for evaluation of the image theorems (both $\mathbf{M}_s$ and $\mathbf{J}_s$ approximations) have been derived through two equivalent methods — the vector potential method and the dyadic Green's function method, for both TE and TM modes. The ratio of the spherical modal coefficient of the image theorem to that of the exact field is used as the criterion to determine the validity of the image theorem.

REFERENCES

1. Liao, S. and R. J. Vernon, "On the image approximation for electromagnetic wave propagation and pec scattering in cylindrical harmonics," *Progress In Electromagnetics Research*, Vol. 66, 65–88, 2006.
2. Perkins, M. P. and R. J. Vernon, "Iterative design of a cylinder-based beam-shaping mirror pair for use in a gyrotron internal quasi-optical mode converter," *29th Int. Conf. on Infrared and Millimeter Waves*, Karlsruhe, Germany, Sep. 27–Oct. 1, 2004.
3. Harrington, R. F., *Time-harmonic Electromagnetic Fields*, McGraw-Hill, Inc., 1961.
4. Stratton, J. A., *Electromagnetic Theory*, McGraw-Hill, Inc., 1941.
5. Abramowitz, M. and I. A. Stegun, *Handbook of Mathematical Functions*, Dover, New York, 1965.
6. Yaghjian, A. D., "An overview of near-field antenna measurements," *IEEE Trans. on Antennas and Propagat.*, Vol. 34, No. 1, 30–45, 1986.

A Novel and Simple Analytical Method for Analysis of AMC and EBG Properties of Lossless Artificial Impedance Surfaces

Mohsen Fallah, **Farrokh H. Kashani**, **and S. H. Mohseni Armaki**
Iran University of Science and Technology (IUST), Tehran, Iran

Abstract— In this paper, a novel and simple analytical method for analysis of AMC and EBG properties of a typical lossless artificial impedance surface (AIS) is investigated. The main contribution of the paper is to demonstrate that AMC and EBG behaviorsof an artificial impedance surface can be characterized analytically with using reflection coefficient for both TE and TM polarized oblique incidence plane waves. It is shown that the AMC properties (when the reflection phase varies in between +90 and −90 degrees) of an impedance surface can be obtained from reflection phase and EBG properties (stop bands for TE and TM surface wave modes) from poles of reflection coefficient. We have derived closed analytical formulas for the impedance surface and reflection coefficient for TE and TM waves for two conventional impedance surfaces such as: grounded dielectric slab and grounded dielectric slab with embedded metallic vias (wired media). The analytical results are verified with numerical simulations.

1. INTRODUCTION

Artificial impedance surfaces have been extensively investigated and proposed as ground planes for many active and passive planar microwave circuits and antennas during the last decade. Nearly all of the articles about high impedance surfaces (HISs) [1], Frequency selective surfaces (FSSs) [2], electromagnetic bandgap (EBG or PBG) structures [3], reactive impedance surfaces (RISs) [4], Artificial magnetic conductors (AMCs) [5] and etc., are examples of artificial impedance surfaces.

In this paper, it is presented that the electromagnetic properties of AISs such as AMC and EBG can be achieved analytically from reflection coefficient for TE and TM polarized oblique incidence plane waves. When incident plane wave is a propagating wave, AMC characteristics can be achieved from the phase of reflection coefficients of TE and TM modes. On the other hand, when incident plane wave is an evanescent wave (exponentially decaying from the surface), poles of reflection coefficient for TE and TM waves represents the surface wave modes. Indeed, dispersion characteristics of the surface wave modes are obtained by equating the denominator of reflection coefficient to zero [6]. As a result, analytical formulas for reflection coefficients of TE and TM modes are necessary and sufficient to AMC and EBG characterization of impedance surface.

To validate our analytical model, accurate analytical formulas for two conventional AISs (grounded dielectric slab and grounded dielectric slab with embedded metallic vias) are extracted and compared with numerical results.

2. ANALYTICAL FORMULATIONS AND VALIDATIONS

Before studying our analytical method, let's concentrate on electromagnetic properties of grounded uniaxial material slabs. Our impedance surfaces that are under study are subset of these structures. In Fig. 1, an illustrative picture of a grounded uniaxial material slab is shown. The properties of the material slab are described by the effective transverse and normal permittivity (ε_t and ε_n) and permeability (μ_t and μ_n), respectively. The surface impedance of this structure for both

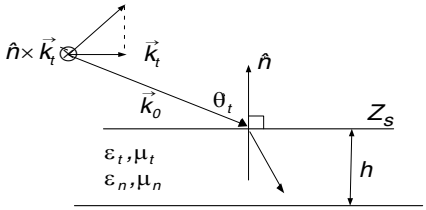

Figure 1: An illustrative picture of the grounded uniaxial material slab.

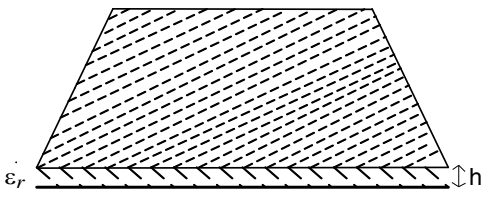

Figure 2: A grounded dielectric slab as an impedance surface.

polarizations given by [5]:

$$Z_S^{TM} = j\frac{\beta_{TM}}{\omega\varepsilon_t}\tan(\beta_{TM}h) \tag{1}$$

$$Z_S^{TE} = j\frac{\omega\mu_t}{\beta_{TE}}\tan(\beta_{TE}h) \tag{2}$$

where the normal components of the wave vectors in the uniaxial slabs are [5]:

$$\beta_{TM}^2 = \omega^2\varepsilon_t\mu_t - k_t^2\frac{\varepsilon_t}{\varepsilon_n} \tag{3}$$

$$\beta_{TE}^2 = \omega^2\varepsilon_t\mu_t - k_t^2\frac{\mu_t}{\mu_n} \tag{4}$$

and k_t is the transverse wave number. Let us next study several conventional impedance surfaces.

2.1. Grounded Dielectric Slab

Figure 2 is shown a grounded dielectric slab. In this special case, we have $\varepsilon_n = \varepsilon_t = \varepsilon_\circ\varepsilon_r$, and $\mu_n = \mu_t = \mu_\circ$. From (1)–(4), we have:

$$Z_S^{TM} = j\omega\mu_\circ\frac{\tan(\beta_{TM}h)}{\beta_{TM}}\left(1-\frac{\sin^2\theta}{\varepsilon_r}\right) \tag{5}$$

$$Z_S^{TE} = j\omega\mu_\circ\frac{\tan(\beta_{TE}h)}{\beta_{TE}}\left(1-\frac{\sin^2\theta}{\varepsilon_r}\right) \tag{6}$$

and

$$\beta_{TM}^2 = \beta_{TE}^2 = \beta = k^2\left(1-\frac{\sin^2\theta}{\varepsilon_r}\right) \tag{7}$$

where $k = \omega\sqrt{\varepsilon_t\mu_t}$, is wave number in host medium and θ is incidence angle. Based on (5)–(7), the angular dependency of the impedance surfaces in the TM and TE-polarized reduced with increasing ε_r.

For calculating reflection coefficient of this structure, we should use [7]:

$$\Gamma_s^{TM} = \frac{Z_s^{TM} - Z_0^{TM}}{Z_s^{TM} + Z_0^{TM}} = \frac{j\eta_s^{TM} - \eta_0\cos\theta}{j\eta_s^{TM} + \eta_0\cos\theta} \tag{8}$$

$$\Gamma_s^{TE} = \frac{Z_s^{TE} - Z_0^{TE}}{Z_s^{TE} + Z_0^{TE}} = \frac{j\eta_s^{TE} - \eta_0/\cos\theta}{j\eta_s^{TE} + \eta_0/\cos\theta} \tag{9}$$

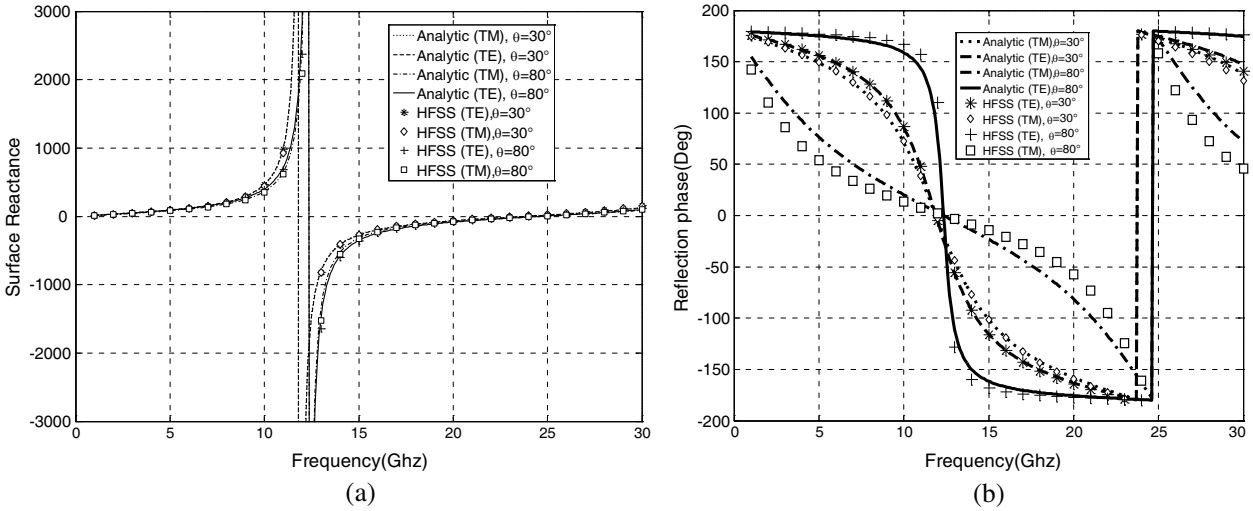

Figure 3: (a) The reflection phase and, (b) surface reactance for TE and TM polarized incident waves for a grounded dielectric slab for two different angle of incidence. The parameters of the surface are: $h = 2\,\text{mm}$ and $\varepsilon_r = 10.2$.

Phase diagram of these two above reflection coefficients (for propagation incident waves) gives AMC bandwidths and poles of them (for evanescent incident waves (where θ is imaginary)) gives natural modes (or equivalently surface waves modes). For validation of above equations, analytical and simulated results for reflection phase and surface reactance of a grounded dielectric slab is shown in Fig. 3. Analytical results show good agreement with HFSS numerical simulations.

2.2. Wired Grounded Dielectric Slab

The wired grounded dielectric slab is illustrated in Fig. 4. In this case, we have $\varepsilon_t = \varepsilon_\circ \varepsilon_r,\ \mu_n = \mu_t = \mu_\circ$. It is known that the wire medium suffers from spatial dispersion (SD) even at very low frequencies [7]. We have assumed that the structure has extreme anisotropy and so we can neglect the spatial dispersion [6] and use local model of wired medium. Therefore the relative effective permittivity of the wire medium along the metallic vias (normal direction) can be given as [6]

$$\varepsilon_n = \varepsilon_\circ \varepsilon_r \left(1 - \left(\frac{k_p}{k}\right)^2\right) \tag{10}$$

where $k = k_\circ \sqrt{\varepsilon_r}$ and is the wave number in the host medium, and k_p is plasma wave number and for square lattices is [6]

$$(k_p a)^2 = \frac{2\pi}{\ln\left(\frac{a}{2\pi r_\circ}\right) + 0.5275} \tag{11}$$

where a is the period of the vias and $r_\circ$ is the radius of the vias (see Fig. 4).

According to (1)–(4), surface impedance of wired medium for long wavelength for TM and TE polarized plane waves are

$$Z_S^{TM} = j\omega\mu_\circ \frac{\tan(\beta_{TM} h)}{\beta_{TM}} \left(1 - \frac{\sin^2\theta}{\varepsilon_n}\right) \tag{12a}$$

$$\beta_{TM}^2 = k^2 \left(1 - \frac{\sin^2\theta}{\varepsilon_n}\right) \tag{12b}$$

and

$$Z_S^{TE} = j\omega\mu_\circ \frac{\tan(\beta_{TE} h)}{\beta_{TE}} \tag{13a}$$

$$\beta_{TM}^2 = k^2 \left(1 - \frac{\sin^2\theta}{\varepsilon_r}\right) \tag{13b}$$

Above equation indicate that impedance surface in TE case is the same of grounded dielectric slab without vias. For TE modes, the electric field is perpendicular to the thin metallic wires. In this case, the electric field does not excite the wires, and the surface impedance for TE mode is the same as metal-backed dielectric slab without vias. Fig. 5 is shown reflection phase and surface reactance of a wired dielectric slab at incidence angle of 30 degree. As shown in this figure, HFSS numerical simulations verify the analytical results.

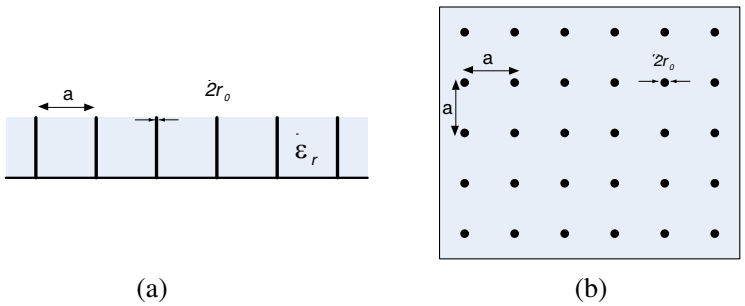

(a) (b)

Figure 4: Illustration of the wired dielectric slab, (a) from the side, (b) from above.

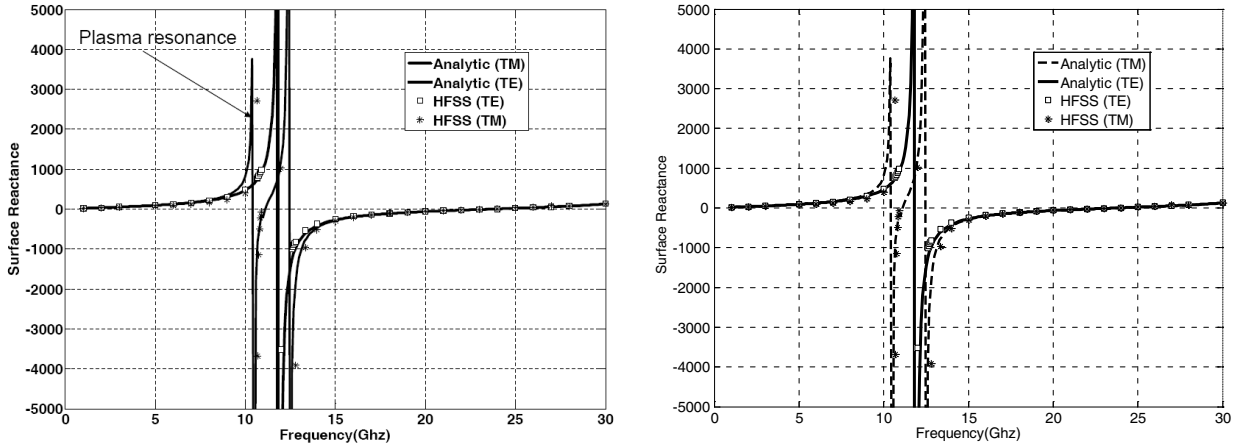

Figure 5: (a) The reflection phase and, (b) surface reactance for TE and TM polarized incident waves for a wired grounded dielectric slab for angle of incidence 30 degree. The parameters of the surface are: $h = 2\,\text{mm}$ and $\varepsilon_r = 10.2$, $a = 0.2\,\text{mm}$, $r_0 = 0.05\,\text{mm}$.

3. CONCLUSION

In this paper, a novel analytical method for analysis of lossless artificial impedance surfaces is investigated. In our presented method impedance surface is excited with two TE and TM test signals and reflection coefficient of this structure is calculated. The AMC properties of impedance surface can be obtained from reflection phase and EBG properties from poles of reflection coefficient. We have derived closed analytical formulas for the reflection coefficient for TE and TM polarized oblique incidence plane waves for two conventional impedance surfaces and verified with numerical simulations.

REFERENCES

1. Sievenpiper, D., L. Zhang, R. J. Broas, and N. G. Alexopolous, "High-impedance electromagnetic surfaces with a forbidden frequency band," *IEEE Trans. on MTT*, Vol. 49, No. 11, 1999.
2. Monoricho, A., G. Manara, and L. Lanuzza, "Synthesis of artificial magnetic conductors by using multilayerd FSS," *IEEE Antenna and Wireless Prop. Letters*, Vol. 1, No. 11, 2002.
3. Yang, F. and Y. Rahmat Samii, " Microstrip antennas integrated with EBG structures: A low mutual coupling design for array applications," *IEEE Trans. AP*, Vol. 51, No. 10, 2003.
4. Mosallaei, H. and K. Sarabandi, "Antenna miniaturization and bandwidth enhancement using a reactive impedance substrate," *IEEE Trans. AP*, Vol. 52, No. 9, 2004.
5. Luukkonen, O., C. R. Simovski, and S. A. Tretyakov, "Grounded uniaxial material slabs as magnetic conductors," *Progress In Electromagnetics Research B*, Vol. 15, 267–283, 2009.
6. Silveirinha, M. G., C. A. Fernandes, and J. R. Costa, "Electromagnetic characterization of textured surfaces formed by metallic pins," *IEEE Trans. AP*, Vol. 56, No. 2, 2008.
7. Luukkonen, O., M. G. Silveirinha, and A. B. Yakovlev, "Effects of spatial dispersion on reflection from mushroom-type artificial impedance surfaces," *IEEE Trans. MTT*, Vol. 57, No. 11, 2009.

Full Wave Analysis of Finite Uniform Metallic Grid FSS under Oblique Incidence Using Scale Changing Technique

Euloge B. Tchikaya[1, 2], **Farooq A. Tahir**[1, 2], **and Hervé Aubert**[1, 2]

[1]CNRS, LAAS, 7 avenue du colonel Roche, F-31077 Toulouse, France
[2]UPS, INSA, INP, ISAE, LAAS, Université de Toulouse, F-31077 Toulouse, France

Abstract— This paper presents an overview on *Scale Changing Technique* (SCT) global electromagnetic simulations used in the case of finite size Grid FSS consisting of rectangular perforations on a metallic screen. The grid structure, illuminated by an oblique incident plane wave, is analyzed using *Scale Changing Technique* which is based on the partition of the grid-plane into planar sub-domains defined at various scale-levels. Electromagnetic interaction between subsequent scales is modeled by mutually independent *Scale Changing Networks* and finally the complete structure can simply be represented by a cascade of these scale-changing networks. Simulation results of radiation diagram are shown in order to demonstrate the validity of the approach.

1. INTRODUCTION

Metallic frequency selective surfaces (FSSs) have been used extensively to fabricate a variety of micro and millimeter wave filters [1]. They consist of periodic structures in two dimensions that can provide frequency filtering to incoming electromagnetic waves as a function of the frequency and/or the angle of incidence [2]. A common FSS example is the mesh screen on the door of a microwave oven. By scaling the feature size of the periodic array of metallic elements that make up the FSS in accordance with the target operating frequency, these structures can also be designed for use at higher frequencies [3].

Although FSSs have long been studied, they have experienced tremendous growth in the last ten years with new applications emerging [3] (e.g., frequency filters or diplexers in high performance reflector antenna systems, advanced radome designs, and smart surfaces for stealth applications).

These screens have found wide use in various applications such as screening a radar transmitter/receiver from hostile emissions, to providing a reflective surface for beam focusing in reflector antenna system. They are designed to reflect or transmit electromagnetic waves with frequency discrimination.

These electromagnetic structures, involving both in large structures (in terms of wavelength) and fine details the system or structure are complex, and the number of scale levels in the system is high making the complexity higher [4].

In order to simulate such complex multi-scale structures, an efficient electromagnetic approach, named *Scale Changing Technique* (SCT) [5], is applied here for the global electromagnetic simulation of FSS consisting of uniform rectangular apertures or waveguides perforating a perfectly conductive and thick metallic plate. The SCT, a powerful tool for electromagnetic simulation of FSS, is based on the partition of discontinuity planes in multiple planar sub-domains of various scale levels. The electromagnetic coupling between scales is modeled by a *Scale Changing Network* (SCN) [6]. This method allows the global simulation of a finite-size thick metallic grid, taking into account the exact interactions between elements, while addressing the problem of excessive computation time and memory.

2. ELECTROMAGNETIC SIMULATION OF FREQUENCY SELECTIVE SURFACES

2.1. Scale Changing Technique

The SCT is an efficient monolithic (unique) formulation for the electromagnetic modeling of complex (multi-scale) structures, i.e., structures that exhibit multiple metallic patterns whose sizes cover a large range of scales [5]. As shown in Figure 1, we can easily see that a high scale ratio exists between the highest and the smallest dimensions. The starting point of the proposed approach consists of the coarse partitioning of this (complex) discontinuity plane into large-scale (called scale level $s_{\max}$) sub-domains of arbitrary shape; in each sub-domain a second partitioning is then performed by introducing smaller subdomains at scale level $s_{\max} - 1$; again, in each sub-domain introduced at scale level $s_{\max} - 1$ a third partitioning is performed by introducing smaller sub-domains at scale

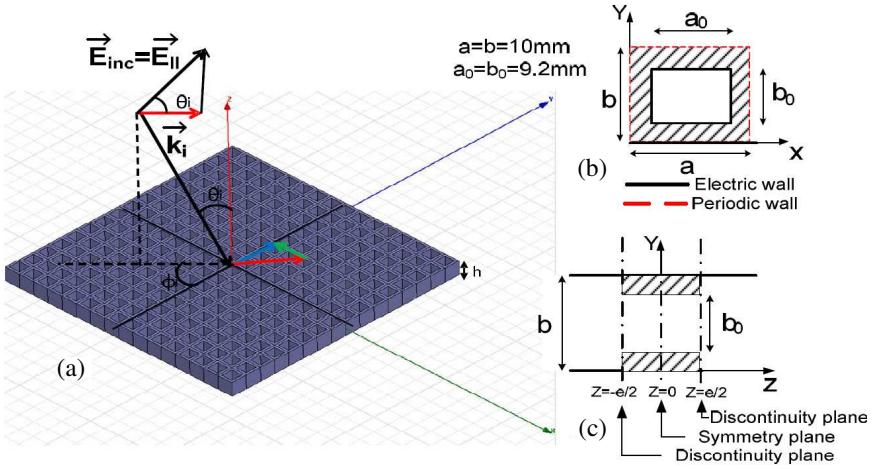

Figure 1: (a) Topology of the FSS consisting of uniform rectangular waveguides perforating a thick metallic plate; (b) Cross section of one cell with its artificial boundary conditions; (c) Side view of the cell. All cells in the grid have the same thickness h.

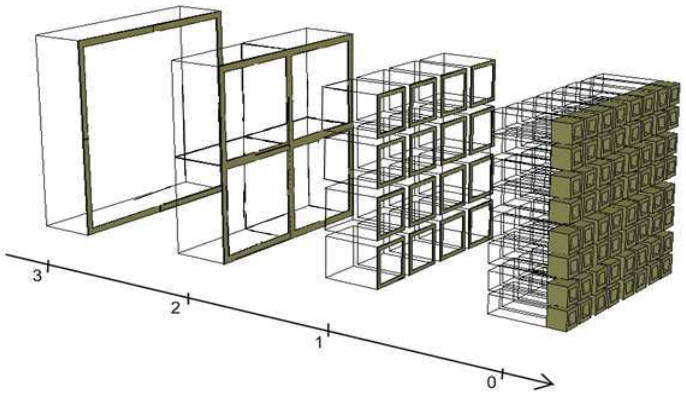

Figure 2: An example of partitioning of finite size (8×8) and thick metallic grid.

level $s_{\max} - 2$; and so on. Such hierarchical domain-decomposition, which allows to focus rapidly on increasing detail in the discontinuity plane, is stopped when the finest partitioning (scale level $s = 0$) is reached. An illustration of the partitioning of a metallic grid of 64 cells is sketched in Figure 2; four different scale levels exist when cells are grouped by four. Boundary conditions (perfect electric or perfect magnetic boundary conditions) are artificially introduced at the contour of all the subdomains generated by the partitioning process, taking into account the physics of the problem. The next step consists of computing the electromagnetic coupling between two successive scale levels via *Scale Changing Network* (SCN) [6].

The cascade of SCNs allows crossing the scale from the lowest scale ($s = 0$) to the highest one ($s = s_{\max}$). What is so special in this technique is that it is based on the connection of scale-dependent equivalent networks. The changing of dimensions at a given scale requires only the recalculation of the concerning equivalent network. This technique allows a substantial reduction in computational time and memory compared with classical numerical techniques, especially when the complexity (i.e., the number of scale levels) of the structure is high.

2.2. Simulated Array Antennas

The topology of the proposed FSS is shown in Figure 1(a). It consists of a metallic grid of thickness $h = 5\,\text{mm}$, with 10 mm inter-elements spacing. The dimensions of the apertures are uniform as illustrated. As a first step to demonstrate the potential of the method, we consider the radiation diagram of a finite size (256 cells) uniform FSS illuminated by an oblique and linearly polarized incident plane wave (E_0 denotes the incident electric field and k the free-space wave number). To obtain the radiation pattern, the density of the equivalent current on the structure surface is

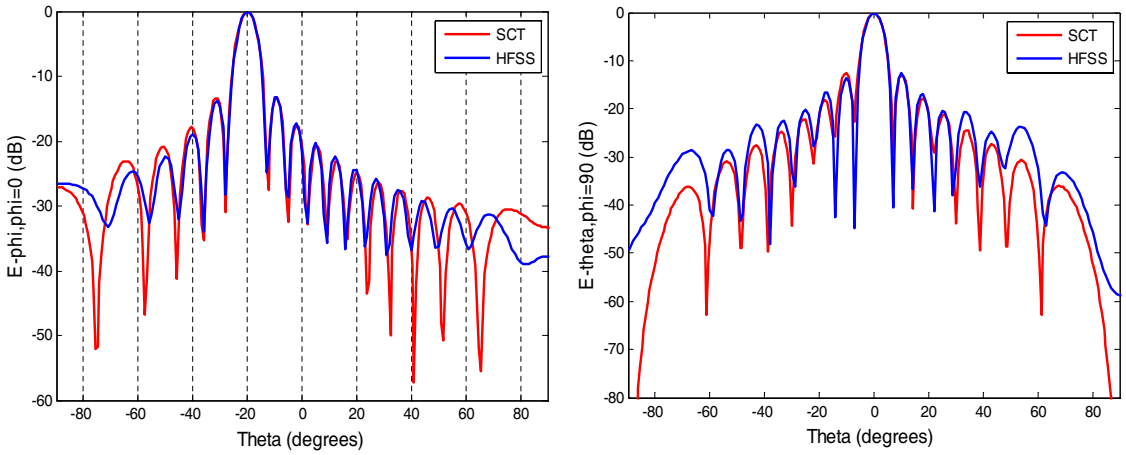

Figure 3: The simulated radiation patterns for uniform finite size and thick metallic grid in (a) E-plane and (b) H-plane @ 20 GHz ($\theta = 20°$, $\varphi = 0$).

calculated by the equation:

$$I_{eq} = [[Z_{freespace}] + [Z_s]^{-1}][V_{inc}] \tag{1}$$

with $Z_{freespace}$, the impedance in freespace, calculated with green functions, and the calculation of Z_s, the surface impedance, is done separately [5]. V_{inc} is the projection of the excitation on modal basis surrounding the grid. Note that once $Z_{freespace}$ and V_{inc} are calculated and saved, they can be reused for the calculation of the radiation pattern of another uniform grid as opposed to standard electromagnetic solvers which require the calculation to be completely redone whenever there is modification of an element cell of a grid.

3. RESULTS

To validate the approach, radiation patterns of the structure in Figure 1 are shown in this section. Figure 3 shows the radiation patterns in the case of 16 × 16-element uniform thick metallic grid shown simulated at a single point of frequency in the case of an oblique plane wave incidence. Ansoft HFSS [7] (version 12.0) was used for FEM implementation with 0.02 stopping criterion for the adaptive convergence solution. An excellent agreement between the HFSS and SCT results can be observed.

4. CONCLUSION

The *Scale Changing Technique* has been successfully applied to the electromagnetic modeling of a metallic grid of uniform thickness and uniform aperture cells. Very good agreement has been observed between computational results from SCT and FEM implemented in Ansoft HFSS under an oblique incidence plane wave excitation. Very good performances in terms of accuracy and computation time have been obtained.

The main advantage of the proposed approach based on SCT is that any modification in geometry of the structure at one scale-level only requires the calculation of two SCNs and not the recalculation of the complete structure, which means significant computational time saving in parametric analysis or optimization processes. Moreover, this technique has showed its compatibility to distributed Grid Computing with remarkable computation time reductions in two different applications: parallel and parametric [8].

ACKNOWLEDGMENT

Part of this work has been supported by Thales Alenia Space, Toulouse and the French Space Agency (CNES).

REFERENCES

1. Munk, B. A., *Frequency Selective Surfaces: Theory and Design*, Wiley, New York, 2000.

2. Pous, R. and D. M. Pozar, "A frequency-selective surface using aperture-coupled microstrip patches," *IEEE Transactions on Antennas and Propagation*, Vol. 39(1), No. 12, 1763–1769, 1991.
3. Monni, S., G. Gerini, and A. Neto, "Efficient design of a frequency selective surface for a multi functional radar: Theory and measurements," *Proc. Eur. Microwave Conf.*, Amsterdam, The Netherlands, Oct. 2004.
4. Koleck, T., H. Diez, and J. C. Bolomey, "Technique for analyzing finite frequency selective surfaces," *IEEE International Conference on Antennas and Propagation, Digest*, April, 14–17 1997.
5. Aubert, H., "The concept of scale-changing network in the global electromagnetic simulation of complex structures," *Progress In Electromagnetics Research B*, Vol. 16, 127–154, 2009.
6. Voyer, D., H. Aubert, and J. David, "Scale changing technique for the electromagnetic modeling of planar self-similar structures," *IEEE Transactions on Antennas and Propagation*, Vol. 54, No. 10, 2783–2789, Oct. 2006.
7. Ansoft HFSS Homepage, Copyright Ansys, 2010, http://www.ansoft.com/products/hf/hfss/.
8. Khalil, F., C. J. Barrios-Hernandez, A. Rashid, H. Aubert, Y. Denneulin, F. Coccetti, and R. Plana, "Parallelization of the scale changing technique in grid computing environment for the electromagnetic simulation of multi-scale structures," *International Journal of Numerical Modeling: Electronic Networks, Devices and Fields*, John Wiley & Sons, April 8, 2010, doi: 10.1002/jnm.760.

Rapid Idea of Located Defects on Grounding Systems

Moussa Lefouili[1], **Kamel Kerroum**[2],
Khalil El Khamlichi Drissi[2], **and Vesna Arnautovski-Tosera**[2, 3]

[1]LAMEL Laboratory, University of Jijel, B.P. 98 Ouled Aissa, Jijel 18000, Algeria
[2]LASMEA Laboratory, Blaise Pascal University, 24 Avenue des Landais, Aubière 63177, France
[3]Electrical Engineering and IT, University Ss. Cyril and Methodius, Skopje, Macedonia

Abstract— This study gives an original way to have a rapid idea of the position of the located defects on grounding systems. For determining electromagnetic fields' radiation, we use an easy method, based on: analytical formula; transmission line theory; and modified images theory, instead of complex method of Summerfield's integrals. The cartography of the electromagnetic fields radiated at the interface soil-air, by energized grounding systems (electrode or grid), can be used to detect and localize a defect on this systems. This model is aimed to help in electromagnetic compatibility (EMC) and lightning protection studies.

1. INTRODUCTION

The principal task of such grounding systems is to ensure the safety of personnel and prevent damage of installations and equipment. Defect on grounding systems may cause operation error, malfunction and destruction of components in electric and electronic systems connected to the grounding systems. As a consequence, electromagnetic compatibility (EMC) studies require the knowledge of the grounding systems performance. For modeling the transient behavior of grounding system, the most rigorous methods is electromagnetic field approach, because it solves full Maxwell's equations with minimum approximations.

This method can be implemented either by Method of moment (MoM) [1, 2] or by Finite Element Method (FEM) [3, 4]. However, their methods are more complicated to understand, because they are not directly solving the Maxwell's equations and they are too complex to be implemented [5]. Further, when the grounding structure is large, the computation time is very large. Another disadvantage of electromagnetic field approach is that, because of its frequency domain solution procedure, it cannot be easily modified to include non-linearity.

The injection of a transient current on the wire grid radiates electromagnetic fields at the surface. For modeling transient behavior grounding systems, instead of using complex method, we prefer an approach that summarizes each of three methods [6, 7]: analytical formula, based on electrical dipole theory for determining radiated magnetic field in infinite conductive medium, modified images theory for taking into account the interface in the half space, and transmission line approach for determining the longitudinal and leakage currents.

2. EXACT EXPRESSIONS OF ELECTROMAGNETIC FIELD IN A CONDUCTING MEDIUM

Consider an electric dipole of length (dl) immersed in a conducting medium (Figure 1) characterized by constitutive constants: conductivity (σ), permeability (μ), and permittivity (ε), and excited by an impulse current.

When the dipole is located in the origin of a Cartesian coordinate system (Figure 1) and oriented in the Z direction, the vector potential in the frequency domain is as follows:

$$\vec{A}(r,s) = \mu \frac{Idl}{4\pi r} e^{-\gamma r} \vec{K} \tag{1}$$

$$\text{with} \qquad \gamma = \sqrt{j\omega\mu(\sigma + j\omega\varepsilon)} \tag{2}$$

where: r = distance between the observation and source points.

From the tables of Laplace transforms [8], we take the inverse transformer of $e^{-\gamma r}$ and the vector potential in time domain.

2.1. Magnetic Field

By using:

$$\vec{H}(r,t) = \frac{1}{\mu} rot \vec{A}(r,t) \tag{3}$$

We take the magnetic field components in the time domain.

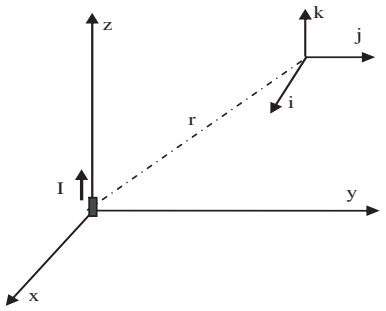

Figure 1: Electric dipole in conducting medium.

2.2. Electric Field

Using Maxwell equations, we take the electric field components in the frequency domain.

$$rot\vec{H} = \vec{J} + \frac{\partial}{\partial t}\vec{D} = \sigma\vec{E} + j\omega\varepsilon\vec{E} \Rightarrow \vec{E} = \frac{rot\vec{H}}{\sigma + j\omega\varepsilon} \tag{4}$$

Using the development taken in [9] and [6] by applying the convolution theorem of the Laplace transform, the electric field in the time domain can be obtained as.

3. MODIFIED IMAGES THEORY

In the semi-infinite medium, the interface is taken into account using modified images theory. This method was developed by Takashima et al. [10] the authors for calculating complex field in conducting media, shows that there exist dual relationships between a complex field due to an alternating current source in a conducting medium and an electrostatic field due to a charge in a dielectric medium. The dual relationships can be used to calculate complex fields in more complicated configurations. For buried grid (current source in soil), two cases can be considered for the position of the observation point.

3.1. Current Source and Observation Point in Soil

The electromagnetic field can be evaluated as a sum of the field of the current source and its image I' as follows:

$$I' = \frac{\underline{\varepsilon_1} - \varepsilon_0}{\underline{\varepsilon_1} + \varepsilon_0} I \tag{5}$$

$$\text{with} \qquad \underline{\varepsilon_1} = \varepsilon_1 + \frac{\sigma_1}{j\omega} \tag{6}$$

3.2. Current Source in Soil and Observation Point in Air

The electromagnetic field can be evaluated as the field due to the modified current source (I''):

$$I'' = \frac{2\varepsilon_0}{\underline{\varepsilon_1} + \varepsilon_0} I \tag{7}$$

4. LONGITUDINAL AND LEAKAGE CURRENT

For the transient analysis of Grounding systems (single conductor or grid), we use the transmission lines approach based on FDTD method. Lines equations in potential and current in temporal domain for one dimension are given by:

$$\begin{cases} \frac{\partial U}{\partial \chi} = -RI - L\frac{\partial I}{\partial t} \\ \frac{\partial I}{\partial \chi} = -GU - C\frac{\partial U}{\partial t} \end{cases} \chi = x \text{ or } y \tag{8}$$

R, L, C and G are the per unit length parameters of the buried conductors [11].

To determine the longitudinal and leakage currents in the electrode, we propose the direct resolution of the lines equations in the time domain by the finite differences time domain method (FDTD).

For buried grid to determine the longitudinal and leakage currents, we propose the direct resolution of the propagation equation [12] in the time domain by the finite differences time domain method (FDTD), while taking into account the conditions in extremities.

This propagation equation is obtained by combination of two equations in system (7) and it is given by:

$$\frac{\partial^2 U}{\partial x^2} + \frac{\partial^2 U}{\partial y^2} - 2(RC + LG)\frac{\partial U}{\partial t} - 2RGU - 2LC\frac{\partial^2 U}{\partial t^2} = 0 \tag{9}$$

The partial derivations in Equation (9) can be approximated by finite differences at point of coordinates (i, j, n), and by writing this equation on all points of the buried grid we can generate the following linear matrix equations:

$$[A][U] = [B] \tag{10}$$

The resolution of this system gives the node voltage on the buried grid. This resolution requires the knowledge of suitable conditions in extremities of the grid. The authors [12] proof that the voltage at the injection point and at the extremities (on borders of the grid) must be fixed. Once the transient voltages responses have been computed, the currents in different branches of grounding grid are obtained by numerical integration of the following current line Equation (8).

5. APPLICATION

In the following applications, the soil is assumed to be homogenous with a resistivity ρ, relative permittivity ε_r and a relative permeability μ. We use the typical double exponential lightning current impulse given by:

$$I(t) = I_0(e^{-\alpha t} - e^{-\beta t}) \tag{11}$$

5.1. Localization of Defect on Buried Conductor by Electric Field

We propose to characterize and localize a opening on buried horizontally electrode by comparison the electromagnetic fields variations along a profile at the soil interface, with and without fault (discontinuity). Two cases, single and double injection are considered in this work Figure 4.

For this analysis we consider the application (Figure 2) which consists of one electrode with 15 meters length, 1.4 cm diameter, buried at 1 meter depth in homogenous earth and presenting a defect (discontinuity) in any point along its length.

The defect is located by a comparison of the electromagnetic fields variations along a profile at the soil surface parallel and centered on the conductor with and without discontinuity.

In the simple injection, the electric field profiles, radiated by intact and opened electrode successively in its centre, at 4/6 and 5/6 of his length, are displayed in Figure 4.

The electric field of the intact electrode is characterized by the apparition of two lobes on both sides of the injection point; a third lobe appears to its second extremity. It brings us to conclude that the current leakage concentrates near the two end-points, provide a sink and a source. We clearly note the difference between the electric field profiles by the apparition of a lobe near the new endpoints when the conductor is broken.

It is evident from Figure 4, that electric field rise can be used to detect and locate openings in a buried conductor.

Figure 5 draws the modulus of the x-component of the total electric field along the 20 meter profile, radiated by intact and broken conductor at middle and at 3/4, in double injection case.

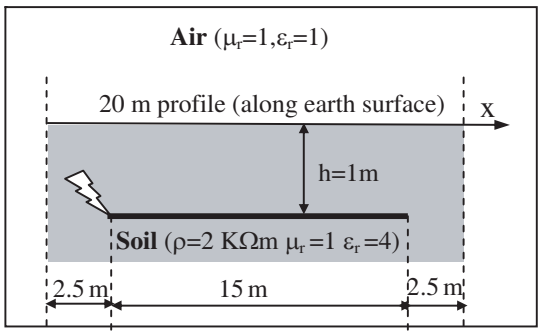

Figure 2: Buried conductor.

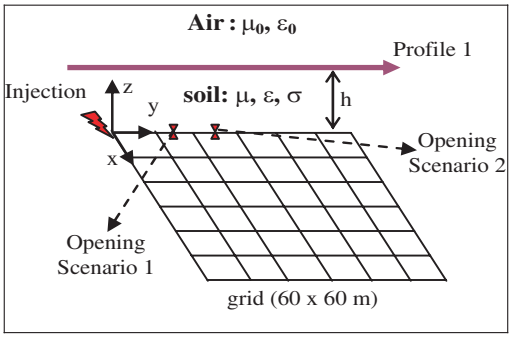

Figure 3: Buried grid.

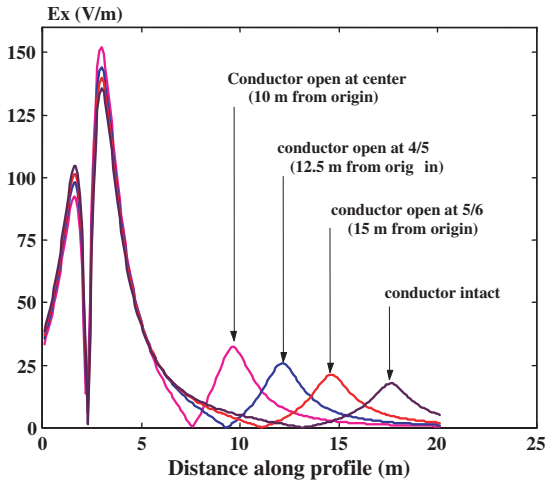

Figure 4: Electric field component Ex radiated by electrode with an without fault (simple injection).

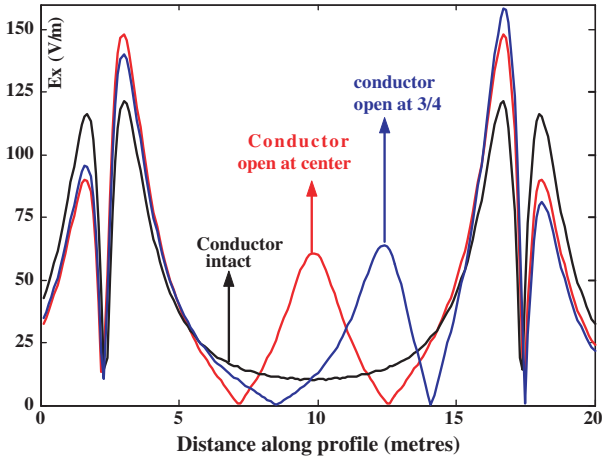

Figure 5: Electric field component Ex radiated by Electrode with an without fault (double injection).

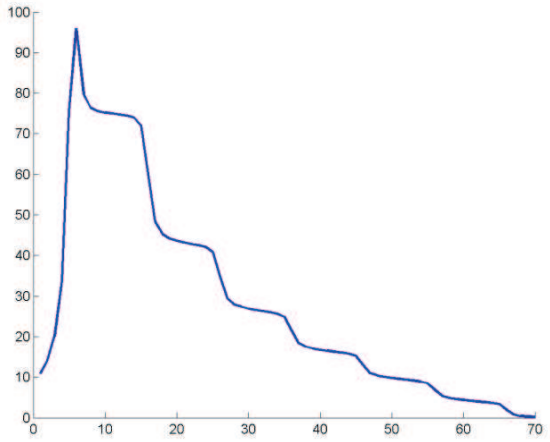

Figure 6: Magnetic field along profile 1 ($t = 20\,\mu S$) radiated by intact grid energized at corner.

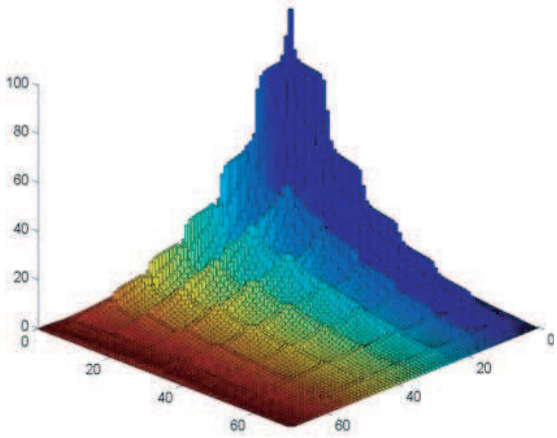

Figure 7: Magnetic field 3D ($t = 20\,\mu S$) radiated by intact grid energized at corner.

We also note that the displacement of the defect (discontinuity) drags the displacement of the third lobe by the end-points leakage effect. It is evident from Figures 4 and 5, that electric field rise can be used to detect and locate openings in a buried conductor.

5.2. Localization of Defect on Buried Grid by Magnetic Field

For analysis we take the same example treated by [1] , a 60 m by 60 m square ground grid with 10 m by 10 m meshes, made of copper conductors with 1.4 cm diameter, and buried at a depth of 0.5 m under the earth's surface. (Figure 2). The lightning stroke is fed at the corner point of the grid (Figure 2). As shows in Figure 2 the opening is make between 10 and 20 m (as scenario 1) and between 40 and 50 m (as scenario 2).

Figures 6 and 7 show respectively the magnetic fields to remote ground along 70 m profile at the soil surface and the spatial distribution form of the magnetic fields to remote ground at the soil surface (70 m × 70 m) parallel to and centred on the grid, as depicted in Figure 2, for corner point injection, when the grid is intact.

Figures 8 and 9 show respectively the magnetic fields to remote ground along 70 m profile at the soil surface and the spatial distribution form of the magnetic fields to remote ground at the soil surface (70 m × 70 m) parallel to and centred on the grid, as depicted in Figure 2, for corner point injection, when the grid is damaged as scenario 1.

Figures 10 and 11 show respectively the magnetic fields to remote ground along 70 m profile at the soil surface and the spatial distribution form of the magnetic fields to remote ground at the soil surface (70 m × 70 m) parallel to and centred on the grid, as depicted in Figure 2, for corner point injection, when the grid is damaged as scenario 2. We note that the displacement of the defect

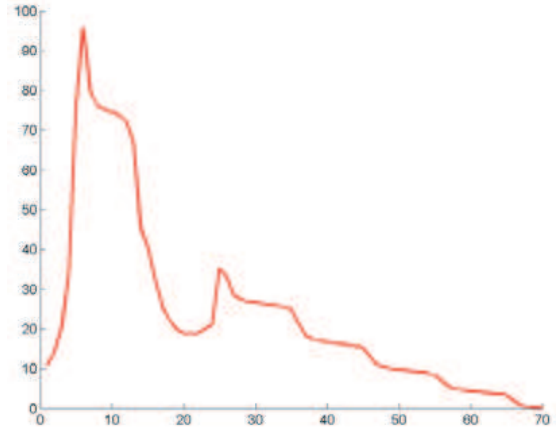

Figure 8: Magnetic field along profile ($t = 20\,\mu S$) radiated by damaged grid energized at corner (scenario 1).

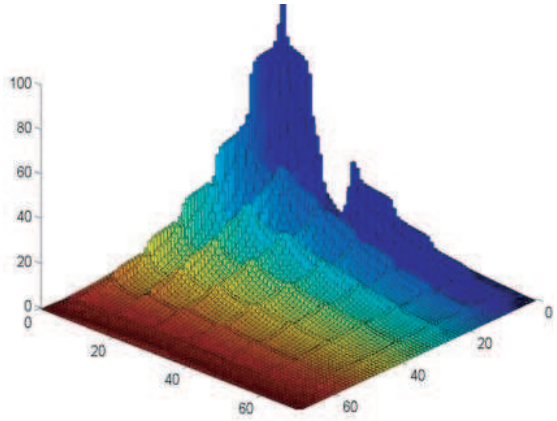

Figure 9: Magnetic field 3D ($t = 20\,\mu S$) radiated by damaged grid energized at corner (scenario 1).

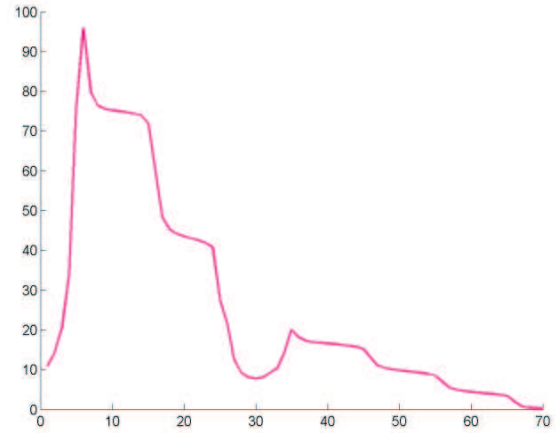

Figure 10: Magnetic field along profile ($t = 20\,\mu S$) radiated by damaged grid energized at corner (scenario 2).

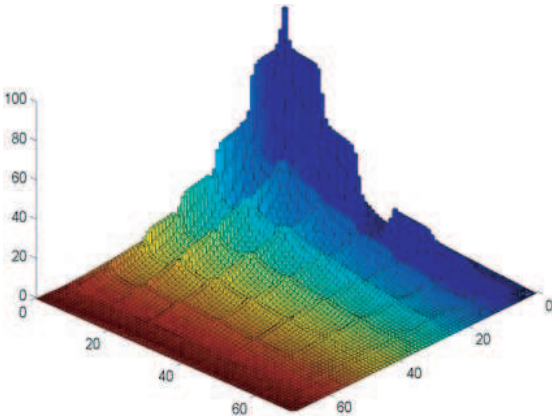

Figure 11: Magnetic field 3D ($t = 20\,\mu S$) radiated by damaged grid energized at corner (scenario 2).

(discontinuity) drags the displacement of the lobe on electric field and magnitude drops down on magnetic field. It is evident from this results that electromagnetic fields rise can be used to detect and locate openings on grounding systems energized by a transient current.

6. CONCLUSION

The cartography of the electromagnetic fields radiated at the surface of ground by buried grounding systems can be used to detect and localize a defect on this systems when they are energized by a transient current. This paper gives an original way to have rapid idea of the position of located defects.

This model is aimed to help in EMC and lightning protection studies, because it can calculate the temporal and spatial distribution of the electromagnetic fields around grounding systems, the transient impedance, the transient voltage, longitudinal and leakage current.

REFERENCES

1. Grcev, L. and F. Dawalibi, "Electromagnetic model for transients in grounding systems," *IEEE Trans. on Power Delivery*, Vol. 5, 1773–1781, 1990.
2. Grcev, L. D., "Computer analysis of transient voltages in large grounding systems," *IEEE Trans. on Power Delivery*, Vol. 11, No. 2, 815–823 April 1996.
3. Nekhoul, B., C. Guerin, P. Labie, G. Menier, R. Feuillet, and X. Brunotte, "A finite element method for calculating the electromagnetic fields generated by substation grounding systems," *IEEE Trans. on Magnetic*, Vol. 11, No. 3, 2150–2153, May 1995.

4. Nekhoul, B., F. Labie, F. Xzgainski, and G. Menier, "Calculating the impedance of a grounding systems," *IEEE Trans. on Magnetic*, Vol. 32, 1509–1512, 1996.
5. Liu, Y., N. Theethay, and R. Thottappillil, "An engineering model for transient analysis of grounding systems under lightning strikes: Non uniform transmission-line approach," *IEEE Trans. on Power Delivery*, Vol. 20, No. 2, 722–730, April 2003.
6. Lefouili, M., B. Nekhoul, B. Harrat, K. Kerroum, and K. El Khamlichi Drissi, "Transient EM fields generated by buried conductor," *International Review of Electrical Engineering (IREE) — Praise Worthy Prise*, Vol. 1, No. 1, 130–136, Marsh, April 2006.
7. Lefouili, M., B. Nekhoul, B. Harrat, K. Kerroum, and K. El Khamlichi Drissi, "Detection et localisation par rayonnement électromagnétique d'un défaut sur une électrode enterrée," *Revue Internationale de Génie Electrique (RIGE)*, Vol. 9, No. 2–3, 333–353, 2006.
8. Abramowitz, M. and I. A. Stegun, *Handbook of Mathematical Functions with Formulas, Graphs, and Mathematical Tables*, National Bureau of Standards, Dover, New York, 1964.
9. Song, J. and K.-M. Chen, "Propagation of EM pulses excited by an electric dipole in a conducting medium," *IEEE Trans. on Antenna Propagation*, Vol. 41, No. 10, 1414–1420, October 1993.
10. Takashima, T. N. and R. Ishibashi, "High frequency characteristics of impedance to grounding field distribution of ground electrodes," *IEEE Trans. Power Apparatus and Systems*, Vol. 100, No. 4, 1893–1899, 1981.
11. Sunde, E. D., *Earth Conducting Effects in Transmission Systems*, Dover Publications, inc., New York, N.Y., 1968.
12. Harrat, B., B. Nekhoul, M. Lefouili, K. Kerroum, and K. El Khamlichi Drissi, "Transient analysis of grounding systems associated to substation structures under lighting strokes," *JCOMS, Journal of Communications Software and Systems*, Vol. 3, No. 1, 59–64, March 2007.
13. Dawalibi, F., "Electromagnetic field generated by overhead short conductors part 1 — Single-conductor," *IEEE Trans. on Power Delivery*, Vol. 1, No. 4, 105–111, 1986.

Model to Predict Losses in the Permanent Magnets for Dynamic Applications

Z. Belli, **I. Boutana**, **and M. R. Mekideche**
Laboratoire d'études et de modélisation en électrotechnique (LAMEL)
Université de Jijel, Algérie

Abstract— In this paper, we present a model to estimate losses in permanent magnets system such as permanent magnets synchronous machine. This estimation allows us to prevent the demagnetization temperature due to an overheating of the magnet and then to design this kind of systems with good accuracy.

1. INTRODUCTION

Rare earth permanent magnets play a more and more important role as much as in our day-to-day life (hard disk drive positioning system, electric motors in domestic applications) as in industrial applications (high power motors or alternators). During the use of these systems, the magnets are subjected to electromagnetic, thermal and mechanical constraints. So, a strong increase of the temperature can lead to a partial or total demagnetization of the magnet, which can be reversible or irreversible depending on the temperature magnitude variation. Consequently, temperature evolution inside the material during regular working has to be controlled. Heating of magnets arise from the exterior of the magnets and from the interior of the magnets due to internal losses. In fact, by considering Faraday's law, when a conductive material is subjected to a time variable magnetic field, it leads to the generation of macroscopic eddy currents which induce losses in the material. For example, these losses can be very significant in a permanent magnet synchronous machine working at high speed. To design such machines, it is required to estimate accurately the losses in order to avoid demagnetization due to an overheating.

In several previous works such as [1] and [2], is proved that, in the context of electrical engineering modelling, rare earth permanent magnets can be modelled by a simple model when they experience a magnetic field up to the middle rang frequency. This model consists in describing a permanent magnet by its magnetic permeability and electrical conductivity. Based on the validity of this assumption, in this paper we extend the model to estimate losses in synchronous permanent magnet machines.

2. DESCRIPTION OF THE PROBLEM

To evaluate internal losses arising in permanent magnet materials due to internal or external sources, we use the approach which consider the permanent magnet as a conductive media verifying Ohm's law. The validity of the assumption is proved throughout combination experimental measurement of the impedance and computed one using 2D Finite Element electromagnetic field computation, both applied to a simple axisymmerical system composed of a coil surrounding a PVC tube. Inside this one permanent magnet samples are placed (replaced by a conductive material in the mathematical model) [1].

In this work, we extend the existing mathematical model to compute losses in permanent magnet inside the electrical systems such as permanent magnets synchronous machines. The study is based on the assumption considering that the permanent magnets subjected to an alternating magnetic field have the same behaviour as a homogeneous medium with constant magnetic permeability μ and electrical conductivity σ.

The corresponding mathematical model is based on the Maxwell's equations. For linear behaviour law of the material and in magnetodynamic harmonic regimen, the field equation is given in terms of magnetic potential vector as fellows:

$$rot\left(\frac{1}{\mu}rotA\right) + j\omega\sigma A = J \tag{1}$$

where A is the magnetic potential vector and J is the current density.

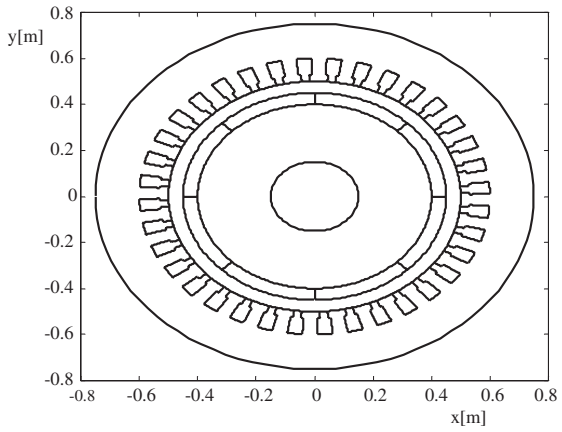

Figure 1: Studied permanent magnets synchronous machine.

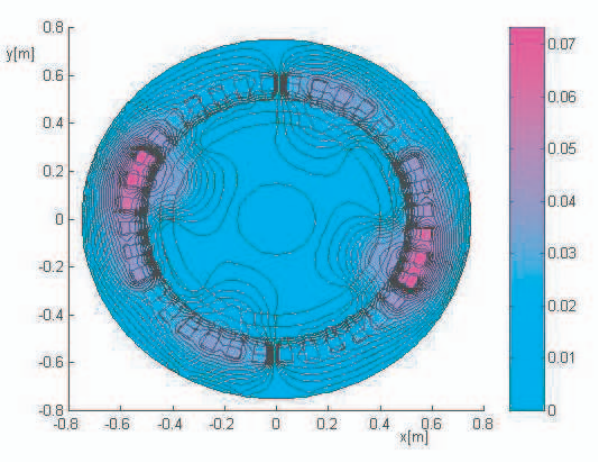

Figure 2: Magnetic potential lines in the machine.

To solve the above equation, we applied 2D Finite Elements model. This one allows us to compute the magnetic field in each node of the system. The resistance of the permanent magnets can be computed by:

$$R = \frac{\omega B}{J_{ind}} \tag{2}$$

where: J_{ind} is the eddy current density in permanent magnets.

The losses densities in permanent magnets are given by:

$$P = RJ_{ind}^2 \tag{3}$$

3. APPLICATION AND RESULTS

Among devices including permanent magnets we find synchronous permanent magnets machine. The studied machine is with 36 slots. The permanent magnets are placed on the polar pieces and they are characterized by: remnant flux density $B_r = 0.825$ [T] and electrical conductivity $\sigma = 0.66610^6$ $[\Omega\text{m}]^{-1}$ (BREMAG10).

Wide and high of the magnets are respectively: 120 and 50 [mm].

The current densities in the slots are: $J_a = 3\,[\text{A/mm}^2]$; $J_b = -1.5\,[\text{A/mm}^2]$; $J_c = -1.5\,[\text{A/mm}^2]$. Figure 1 shows the geometry of the considered machine.

The magnetic field in the machine is computed using 2D linear Finite Elements model in magnetodynamic regimen.

The lines of the magnetic potential vector obtained by Finite element field analysis in the case where the magnets are considered as conductive bulks are shown on the Figure 2.

For a frequency range of 1000 [Hz], the obtained resistance and density power losses for permanent magnets are respectively:

$$R = 3.7922 \cdot 10^{-4}\,[\Omega]$$
$$P = 6.115 \cdot 10^{11}\,[\text{W/m}^2]$$

4. CONCLUSIONS

In this paper, we have presented a model to predict losses that appear in permanent magnet systems such as synchronous permanent magnet machine. These losses must be controlled in order to prevent an overheating of the material. The presented work can be coupled to a thermal study in order to estimate the heating temperature.

REFERENCES

1. Benabou, A. "Permanent magnet modeling for dynamic applications," *Journal of Magnetism and Magnetic Material*, Vol. 320, 830–335, 2008.

2. Polinder, H. and M. J. Hoeijmakers, "Eddy current loses in the permanent magnets of a PM machine," *Proceedings of the Eighth International Conference on Electrical Machines and Drives,* 138–142, London, 1997.
3. Lipo, T. A., *Introduction to AC Machine Design*, Wisconsin Power Electronics Research Center University of Wisconsin, USA, 2004.

Analytical Model of TeraHertz Frequency Voltage Noise in Schottky-barrier Diodes and Heterostructure Barrier Varactors

F. Z. Mahi[1], **L. Varani**[2], **P. Shiktorov**[3], **E. Starikov**[3], **and V. Gruzhinskis**[3]

[1]Physics of Semiconductor Devices Laboratory (LPDS), University of Bechar, Algeria
[2]Institute of Electronics of the South (IES, CNRS UMR 5214), University of Montpellier II, France
[3]Semiconductor Physics Institute, Vilnius, Lithuania

Abstract— In this paper we propose an analytical model for the calculation of the spectral densities of current and voltage fluctuations in Heterostructure-barrier varactors and Schottky barrier diodes. The interpretation of different resonances appearing in the spectrum in terms of HBV or SBD structures is useful to optimize the order of the harmonics generated in the terahertz frequency region.

1. INTRODUCTION

Schottky barrier diodes (SBD) and heterostructure barrier varactors (HBV) are among the most interesting multiplier devices employed to generate terahertz radiation [1]. The SBD and HBV are elements characterized by nonlinear current-voltage and/or capacitance-voltage characteristics [1]. In particular, the HBV diodes present a symmetric capacity-voltage (C-V) and antisymmetric current-voltage (I-V) characteristics [2], which lead to produce only odd harmonics compared to the SBD.

The evaluation of the voltage noise spectrum demands an estimation of the intrinsic current noise which may influence the extraction of the high-order harmonics generated by the pumped SBD or HBV structures. In the first step calculation, the noise spectrum of current fluctuations flowing through the SBD and/or HBV is evaluated under a constant voltage condition (Thevenin current-noise generator). For the second step of voltage noise calculation, we consider the SBD and HBV operating in series with a parallel output resonant circuit when a high-frequency large-signal voltage is applied to the whole system.

In this contribution we propose an analytical model for the high-frequency noise spectrum in nanometric GaAs Schottky barrier diodes as well as heterostructure barrier varactors. The resonances discussion as a function of device structure enable the optimization of the harmonics generated in the terahertz frequency region.

2. ANALYTICAL MODEL

To extract the high order harmonics generated in the SBD and HBV structures we calculate the voltage noise spectrum. For this reason, the analytical calculation will be realized in two steps which are the current noise and voltage noise calculations.

In the first step, we consider the n^+n-barrier-nn^+ HBV structure shown in Figure 1. Here l_i is the length of the i-regions, N_i is the dopings of the i-region and l_d the length of the depletion region (see, e.g., [2]). According to the symmetry of the HBV structure $l_1 = l_3 = l_+$, $l_2 = l_4 = l_-$ and $L = 2l_+ + 2l_- + l_d$ is the total length of the HBV [2].

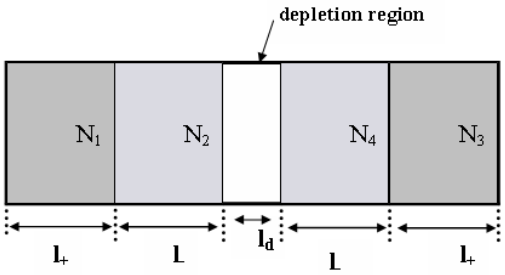

Figure 1: Schematic view of the n^+n-barrier-nn^+ HBV with: l_+ the length of the n^+ regions, l_- the length of n regions and l_d the length of the depletion region.

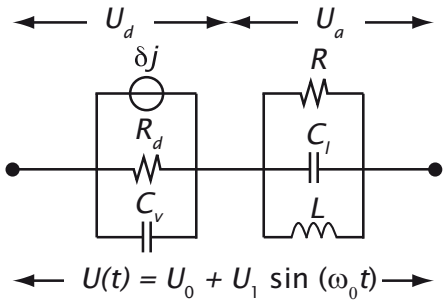

Figure 2: Equivalent scheme of a frequency multiplier consisting of a HBV connected in series with a parallel RLC-resonant circuit.

By following Ref. [2] the spectral density in the HBV structure can be represented as:

$$S_{ii}(\omega) = \left(\omega \frac{eA}{L}\right)^2 \sum_{j=1}^{4} \left| \sum_{i=1}^{4} N_i l_i b_{i,j} \right|^2 S_{ff}^j \tag{1}$$

where S_{ff}^j is the spectral density normalized to the total number of free carriers in the i-th regions, b_{ij} the elements of the inverse matrix expressed by the elements: $a_{11} = a_{33} = -\omega^2 + i\omega\nu_+ + \omega_+^2(1 - r_+)$, $a_{12} = a_{14} = a_{24} = a_{32} = a_{34} = a_{42} = -r_-\omega_-^2$, $a_{13} = a_{21} = a_{23} = a_{31} = a_{41} = a_{43} = -r_+\omega_+^2$, $a_{22} = a_{44} = -\omega^2 + i\omega\nu_- + \omega_-^2(1 - r_-)$, $r_i = \frac{l_i}{L}$ are the relative lengths and $\omega_i^2 = (e^2/\epsilon\epsilon_0 m)N_i$ is the plasma frequency of the i-regions. The spectral density of the whole SBD is calculated using Equation (1) with $i, j = 4$ regions ($\sum_{i=1}^{4}$) to $i, j = 2$ regions ($\sum_{i=1}^{2}$) [2].

In the second step we shall consider the HBV embedded into a particular parallel resonant circuit characterized by the inductance L and by the capacitance C_l, while the power losses and output from the resonator are described by the noiseless resistance R [3]. The corresponding equivalent scheme is presented in Figure 2. It is supposed that a microwave voltage $U(t) = U_0 + U_1 \sin(\omega_0 t)$ is applied to the whole circuit.

The HBV is characterized by the resistance $R_d(U_d)$ and by the varactor capacitance $C_v(U_d)$ which depend on the voltage drop U_d between the HBV terminals. The intrinsic noise of the HBV is described by the current fluctuations δj with spectral density $S_{ii}(\omega)$ [4]. The current flowing through the SBD depends on δj by the approximation [3]:

$$j_d(U_d) = R_d U_d + C_v(U_d)\frac{d}{dt}U_d + \delta j \tag{2}$$

In accordance with Refs. [4, 5] the equations describing the fluctuations of the voltage drop between the HBV terminals, δU_d, are obtained by linearization of the circuit equations of the equivalent scheme presented in Figure 2 and using Equation (2). The voltage drop fluctuations under the condition that the HBV varactor capacitance C_v^0 is constant are given by [5]:

$$\delta U_d(\omega) = -Z(\omega)\left[\delta j(\omega) + i\omega C_v^0 \sum_{n\neq 0}^{\pm\infty} \gamma_n \delta U_d(\omega - \omega_n)\right] \tag{3}$$

where γ_n is the odd harmonic contribution (for the HBV) of the varactor capacity [3]:

$$\gamma_n = \frac{1}{T_0 C_v^0}\int_0^{T_0} C_v[U_d(t)]\exp(-i\omega_n t)dt \tag{4}$$

and $Z(\omega)$ is the linear impedance of the HBV + circuit given by :

$$Z(\omega) = \frac{i\omega}{(C_l + C_v^0)\left(\omega_{res}^2 - \omega^2 + i\omega\nu_{RC}\right)} \tag{5}$$

Here $\omega_{res}^2 = 1/(C_l + C_v^0)L$ is the resonance frequency of the whole system (that is HBV + circuit), $\nu_{RC} = (R + R_d^0)/(C_l + C_v^0)RR_d^0$ is the inverse RC-relaxation time of the whole system and R_d^0 is

the constant component of the HBV resistance which can be obtained from the static $I(V)$ relation in full analogy with C_v^0.

The spectral density of voltage fluctuations is calculated by the multiplication $\delta U_d \delta U_d^*$ where δU_d^* is the conjugate voltage fluctuation. The zero-order approximation corresponding to γ_n=0 in Equation (3) is obtained by the usual relation between the voltage and current fluctuations [4, 5]:

$$S^0_{U_d U_d}(\omega) = |Z(\omega)|^2 \, S_{ii}(\omega) \tag{6}$$

where $S_{ii}(\omega)$ is the spectral density of current fluctuations. The first order approximation of the spectral density of voltage fluctuations $S^1_{U_d U_d}(\omega)$ is given by [3]:

$$S^1_{U_d U_d}(\omega) = |Z(\omega)|^2 \left[S_{ii}(\omega) + (\omega C_v^0)^2 \sum_{n \neq 0}^{\mp\infty} |\gamma_n|^2 \, S^0_{U_d U_d}(\omega - \omega_n) \right] \tag{7}$$

In the case of SBD voltage noise spectrum we change the harmonics n from odd for the HBV to $n = 1, 2, 3, 4, \ldots$ in Equation (7).

3. RESULTS AND DISCUSSION

The intrinsic current noise obtained for a GaAs n^+n-barrier$-nn^+$ HBV and n^+n-metal SBD is illustrated in Figure 3. The results represented by a dashed line in Figure 3 is obtained by the present analytical model and they are compared with the results of the SBD structure taken from Ref. [1].

For the two curves in Figure 3, the spectral density exhibits an initial growth proportional to ω^2 followed by two resonant peaks in the low and high frequency regions corresponding respectively to the carriers reflected by the barrier and to the hybrid plasma resonance frequency. In the case of the HBV structure the resonance peaks appear at higher frequencies compared to the SBD structure.

Figure 4 illustrates the HBV spectral density of $i = 6$ regions compared to $i = 4$ regions in Figure 3 (i.e., we apply the analytical model for $i = 6$).

The presence of a n^+, n^-, n^{--} regions leads to the appearance of an additional peak associated with the appearence of extra n^-n^{--} homojunction.

Figure 5 reports the comparison between the zero order approximation of voltage fluctuations in the HBV and SBD structures. The calculations use the parameters C_v^0 and R_d^0 obtained from the static $I-V$ and $C-V$ relations: C_v^0=5.9×10^{-3} Fm^{-2}, $R_d^0 = 10^{-6}\,\Omega$m^2 in the SBD and C_v^0=2×10^{-3} Fm^{-2}, R_d^0=3.7×10$^{-5}\,\Omega$m^2 in the HBV. The resonance noise appears around the frequencies $\omega_{res} = 0.6$ GHz and $\omega_{res} = 1$ THz in the SBD and in the HBV structures, respectively. We remark that the frequency position of the resonant noise increases in the HBV compared to the SBD structure.

Figure 6 presents the comparison of the spectral densities of voltage fluctuations between the SBD and the HBV calculated at the first order S^1 according to Equation (8). The first order

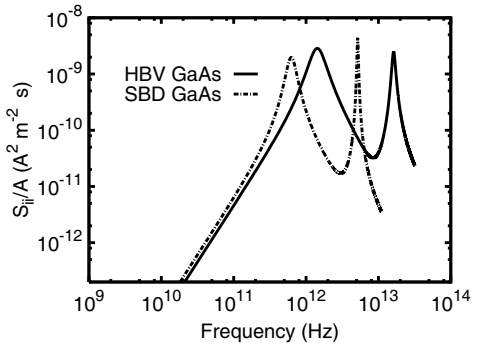

Figure 3: Spectral density of current fluctuations per unit surface in a GaAs n^+n-metal SBD and n^+n-barrier-nn^+ HBV. With: $l_1 = l_3 = 0.1\,\mu$m, $l_2 = l_4 = 0.1\,\mu$m, $N_1 = N_3 = 5 \times 10^{17}\,$cm^{-3} and $N_2 = N_4 = 5 \times 10^{18}\,$cm^{-3}.

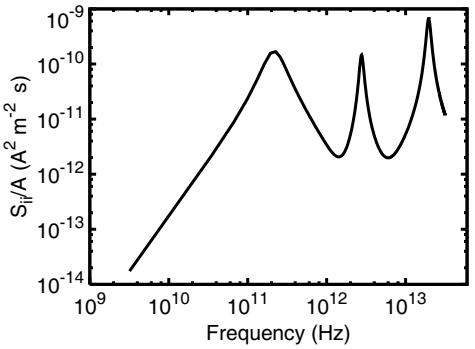

Figure 4: Spectral density of current fluctuations per unit surface in a HBV structure with $i = 6$ regions $n^+n^-n^{--}$-barrier-$n^{--}n^-n^+$ with: $l_1 = l_4 = 0.3\,\mu$m, $l_2 = l_5 = 0.5\,\mu$m, $l_3 = l_6 = 0.3\,\mu$m, $N_3 = N_6 = 10^{16}\,$cm^{-3}, $N_2 = N_5 = 10^{17}\,$cm^{-3}, $N_1 = N_4 = 5 \times 10^{18}\,$cm^{-3} and $l_d = 23\,$nm.

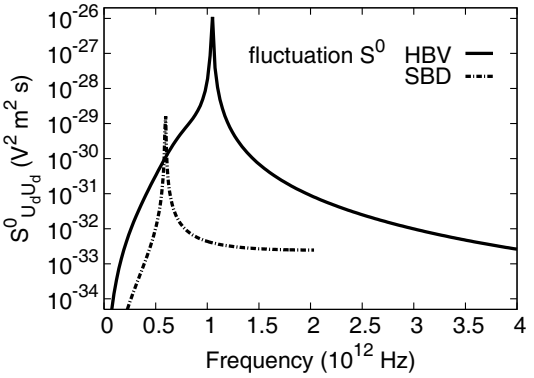

Figure 5: Voltage spectral density of zero-order approximation in a GaAs n^+n-metal SBD and n^+n-barrier-nn^+ HBV. With: $R = 10^{-8}\,\Omega\mathrm{m}^2$, $C_l = 1.1 \times 10^{-3}\,\mathrm{Fm}^{-2}$, $L = 10^{-23}\,\mathrm{Hm}^2$, $\nu_0 = 200\,\mathrm{GHz}$, $U_0 = 0.6\,\mathrm{V}$ and $U_1 = 0.2\,\mathrm{V}$.

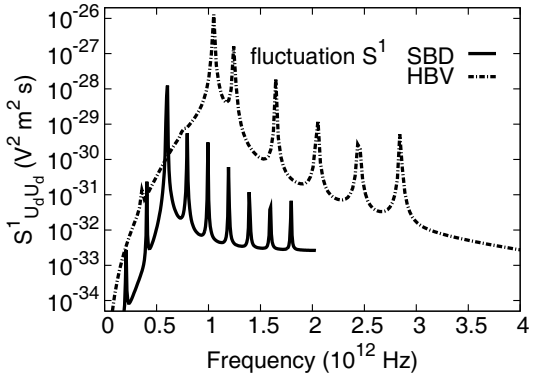

Figure 6: First-order iteration of spectral voltage fluctuations in a n^+n-barrier-nn^+ HBV and n^+n-metal SBD. With: $R = 10^{-8}\,\Omega\mathrm{m}^2$, $U_0 = 0.6\,\mathrm{V}$ and $U_1 = 0.2\,\mathrm{V}$.

iteration of the voltage noise exhibits a series of resonance peaks at frequencies $\omega = \omega_{res} + n\omega_0$ (here the circuit is tuned to the third order of harmonics $\omega_{res} = 3\omega_0$ and $n = 1, 2, 3, \ldots$ for the SBD while n is an odd integer for the HBV). For the HBV the resonance peaks appear in the terahertz region from 1 to 3 THz compared to the SBD where the peaks appear from 0.5 to 1.5 THz. Therefore the resonance frequency position increases significantly.

4. CONCLUSION

We have proposed an analytical model for the current and voltage noise in HBV and SBD structures which describes the high-frequency part of the electronic noise spectrum.

The model proposed for the HBV can calculate the intrinsic noise of i regions of any structure and the results can be useful to calculate the voltage noise of a frequency multiplier consisting of a SBD or a HBV embedded into an external resonant circuit for the extraction of the high-order harmonics. The resonance peaks appear in the voltage noise spectrum due to the periodic variation of the diodes capacitance with the frequency of the pumping signal and its harmonics. The resonances generated by the HBV structure appear in the $1 \rightarrow 3\,\mathrm{THz}$ region compared to the SBD where the resonances appear in the $0.5 \rightarrow 1\,\mathrm{THz}$.

ACKNOWLEDGMENT

This work is partly supported by the Algerian ministry of higher education and research through contract n. D03820070006.

REFERENCES

1. Shiktorov, P., E. Starikov, V. Gruzinskis, L. Reggiani, L. Varani, and J. C. Vaissiere, "Analytical model of high-frequency noise spectrum in Schottky-barrier diodes," *IEEE Electron Dev. Letters*, Vol. 26, No. 1, 2–4, 2005.
2. Mahi, F. Z., A. Helmaoui, L. Varani, P. Shiktorov, E. Starikov, and V. Gruzinskis, "Analytical model for the TeraHertz current noise in nanometric Schottky-barrier diodes and heterostructure barrier varactors," *Journal of Physics*, Conference Series 193, 2009.
3. Shiktorov, P., E. Starikov, V. Gruzinskis, L. Varani, J. C Vaissiere, L. Reggiani, S. Pérez, and T. Gonzàlez, "Theoretical investigation of large-signal noise in nanometric schottky-barrier diodes operating in external resonant circuits," *Acta Pysica Polonica A*, No. 107, 396–399, 2005.
4. Shiktorov, P., E. Starikov, V. Gruzinskis, S. Pérez, T. Gonzàlez, L. Reggiani, L. Varani, and J. C. Vaissière, "Theoretical ivestigation of schottky-brrier diode noise performance in external resonant circuits," *Semicond. Sci. Technol.*, Vol. 21, 550–557, 2006.
5. Pérez, S., T. Gonzàlez, P. Shiktorov, E. Starikov, V. Gruzinskis, L. Reggiani, L. Varani, and J. C. Vaissière, "Noise in Schottky-Barrier diodes: from static to large-signal operating," *Proceedings of SPIE*, No. 5470, 322–335, 2004.

Application of EH4 in the Zhayaoku Area of Fushan Iron Mine of Hebei, China

Gaofeng Du, **Tagen Dai**, **and Liu Yang**
School of Geosciences and Environmental Engineering, Central South University
Changsha, Hunan 410083, China

Abstract— Fushan iron mine is under the administrative divisions of Xixu town of She city in Hebei Province. The authors have reached the conclusion that the iron ore bearing horizon is the middle of Ordovician limestone, magmatic rocks in this area is for acid diorite, along with invasive structural vulnerability. EH4 is widely used in solid minerals, especially in finding concealed ore deposit. In this paper, the author adopted EH4 method to make a synthetic study on the Zhayaoku area of Fushan iron deposit in Hebei. The result showed that the geophysical method was quite useful in the exploration of concealed ore deposit.

Fushan iron deposit is under the administrative divisions of Xixu town of She city in Hebei Province. Adjacent to the Xixu village, 20 kilometers southwest from the She County, 80 km west of Handan City. Mine a long road through the east of Handan, southeast has long rail line through the convenient transportation.

Mining area of about 0.9643 square kilometers, mining geographical coordinates: latitude: $36°43'21'' \sim 36°40'47''$; longitude: $113°45'25'' \sim 113°47'14''$.

1. INTRODUCTION

Fushan in Shanxi Sino-Korean platform uplift potential above the Taihang Wu-an beam concave west. Mining area near the main structure with NNE Kelaoyao fault, the Mujing fault and the NE-SW Shexian fault. Fushan intrusive magmatic activity shall grams of the old kiln faults along the fault intersection with Shexian intrusion made of acid rock is saturated calc-alkaline rocks, rock outcrops were an average diameter of about 10 kilometers, slightly long things short irregular oval. Rock to the Lower Paleozoic Cambrian and Ordovician strata. The joints often capture many sizes limestone xenoliths, the contact zone with the development of a magmatic skarn and ore enrichment.

Fushan Iron mine is situated in the central of Fushan Mountain; the ground is very simple, mainly lower Paleozoic Cambrian and Ordovician strata, and the Quaternary strata which distributed in the mountain valley.

Mineralization of geological structures can be divided into two categories; this is before and after mineralization: mineralization by magmatic intrusion before the construction of the main formation; ore after construction was a product of the Himalayan period. And succeeded to the regional tectonic features, also north of the North East and the main east-west.

Since the Iron was founded, the scholars at home and abroad, many experts conducted Fushan rock system. Fushan intrusion is recognized as the Mesozoic, that is the product of magmatic activity, its shape was an exposed area of about 58 square kilometers of rock complex strains.

2. PHYSICAL PARAMETER

The geophysical work mainly on Fushan specimens of rocks and minerals mining physical parameters measured. Geological and geophysical personnel mine in the full cooperation of technical staff in the break near the mining area of explosives library collection specimens of rocks and minerals, including rock and mineral types are mainly limestone, diorite, and marble.

Rock and mineral specimens after 24 hours of soaking, independently developed by Central South University, SQ-3C-type dual-frequency electric meter to measure, then for each of the resistivity of rocks and minerals and Vice-frequency measurement results were analyzed.

Limestone resistivity maximum 7000 Ω·m, the minimum is 30 Ω·m, average 1000 Ω·m, and mainly concentrated in the $500 \sim 1000$ Ω·m; increase the maximum frequency of 6.7%, the minimum is 0.2%, average 3.14% and 1.5%, mainly to 5%;

Diorite resistivity maximum 3800 Ω·m, minimum value of 60 Ω·m, an average of 700 Ω·m, and are mainly concentrated in the $200 \sim 900$ Ω·m; increase the maximum frequency of 10%, minimum 0.5% average of 3.5%, and mainly concentrated in 2% to 4%;

Marble resistivity maximum 3900 Ω·m, the minimum is 130 Ω·m, an average of 662 Ω·m, and mainly concentrated in the 300 ∼ 700 Ω·m; increase the maximum frequency of 9%, the minimum is 1.5%, the average value of 4%, and mainly concentrated in 3% to 5%.

3. GEOPHYSICAL METHODS

Fushan Mine collected more than 150 pieces of rock and mineral analysis of properties of known specimens, the area of diorite, limestone (marble), skarn, magnetite exist between these types of rock electrical and magnetic difference. Magnetite has a resistivity minimum and the maximum magnetic characteristics, combined with the wild, according to the characteristics of operational, So EH4 conductivity imaging system selected as the work of this major work of geophysical methods.

EH4 are part of the controlled source and a combination of natural source magnetotelluric sounding system. Deep structure of natural background field through the source imaging (MT), its source of information for the 10–100 kHz. Shallow structure is through a new type of portable low-power transmitter 1–100 kHz artificial electromagnetic signals to compensate the shortage of natural signals to obtain high-resolution imaging.

EH4 conductivity imaging system has been successfully applied to domestic and Mineral, Coal, Water industry, prospecting, looking for water work. The new geophysical methods, to achieve a natural and artificial sources of collection and processing of the signal source, with detection depth (up to 1500 m), equipment, light, fast, low cost, high accuracy and so on, in geological exploration in to good effect.

4. ZHAYAOKU AREA

Fushan iron mine in the survey area, laid a total of seven lines, as measured line number from south to north, respectively −1, 0, 1, 2, 4, 6 and 8, respectively, measured length of 900 meters, 1300 meters, 1260 meters, 700 meters, 700 meters, 700 meters, 700 meters away from the survey line of 100 meters and 200 meters, measuring 20 m pixel pitch.

On the −1 line, 0 line, 1 line, 2 lines, 4 lines, 6 lines and 8 lines of high-frequency magnetotelluric sounding data inversion to explain, analyze them one by one below.

From −1 line EH-4 inversion results can be seen, divided into three strata, overlying formation resistivity of 10 to 1000 Ohm·m, presumed to be weathered diorite, weathered fracture is more developed, may contain a small amount of fracture water, the layer thickness of about 10 m∼420 m; intermediate formation resistivity range from 20 to 6000 Ohm·m, presumed to limestone, the thickness of about 680 m∼1300 m, and exposed at the surface. Limestone formations in a low resistivity anomaly body, the resistance rate of 10 ∼ 200 Ohm·m, abnormal width of 200 m, extending down the length of about 600 m, more favorable conditions for the forming section of the site, recorded as geophysical anomaly WT2. Stake 100 ∼ 200 m in between resistivity contour of the horizontal gradient in large inferred by a fault, denoted F3, Southwest tendency to dip about 85 degrees. Resistivity of the underlying strata of 300 to 2000 Ohm·meter range of changes, presumed to diorite.

0 line EH-4 inversion results can be seen, divided into three strata, overlying formation resistivity of 150 to 1000 Ohm·m, presumed to be weathered diorite, weathered fracture is more developed, may contain a small amount of The fracture water, the layer thickness of about 10 m∼400 m; intermediate formation resistivity range from 200 to 10,000 Ohm·m, presumed to limestone, the thickness of about 350 m∼1000 m, and exposed at the surface. In the limestone formation there are two low resistivity anomaly body, the forming section conditions were more favorable location, denoted geophysical anomaly WT2 and WT3. WT2 abnormal electrical resistivity is about 200 Ohm·m, abnormal extension along the survey line is about 500 m, the thickness of about 150 m. WT3 abnormal resistivity range from 100 to 200 Ohm·m, abnormal extension along the survey line is about 300 m, extending down to about 500 m. Abnormal WT2 and WT3 relatively large. Stake −50 ∼ 0 m in between resistivity contour changes in the large horizontal gradient is inferred by a fault, denoted F3, Southwest tendency to dip about 85 degrees. Stake 450 ∼ 500 m in between resistivity contour changes in the large horizontal gradient is inferred by a fault, denoted F4, South East tendency, the inclination is about 85 degrees. Underlying formation resistivity of 400 to 2000 Ohm·meter range change, presumed to diorite.

From a line of EH-4 inversion results can be seen, divided into three strata, overlying formation resistivity from 100 to 1,600 Ohm·m, presumed to be weathered diorite, weathered fracture is more developed, may contain a small amount of The fracture water, the layer thickness of about 10 m∼660 m; intermediate formation resistivity range of 300∼12,000 Ohm·m, presumed to limestone, the thickness of about 500 m∼1100 m, and exposed at the surface. Limestone formations in

a low resistivity anomaly body, resistivity about 300 Ohm·m, abnormal width of 100 m, extending down the length of about 400 m, more favorable conditions for the forming section of the site, recorded as geophysical anomaly WT3. Stake $-10 \sim 140$ m in between resistivity contour changes in the large horizontal gradient is inferred by a fault, denoted F3, Southwest tendency, the inclination is about 80 degrees. Stake $550 \sim 750$ m in between resistivity contour changes in the large horizontal gradient is inferred by a fault, denoted F4, South East tendency, the inclination is about 80 degrees. Resistivity of the underlying strata in the 1000 to 5000 Ohm·meter range of changes, presumed to diorite.

From the 2 lines of EH-4 inversion results can be seen in the underground medium divided into three layers overlying formation resistivity range from 200 to 5000 Ohm·m, presumed to diorite, weathering fissures, the layer thickness about 230 m∼500 m; intermediate formation resistivity range from 5000 to 15000 Ohm·m, presumed to limestone, the thickness of about 220 m; changes in the underlying strata resistivity range of $5000 \sim 8500$ Ohm·m, presumed to diorite. The low resistance sections no significant geophysical anomaly.

From the 4 lines of EH-4 inversion results can be seen in the underground medium divided into three layers overlying formation resistivity range from 100 to 3,000 Ohm·m, presumed to diorite, weathering fissures, the layer thickness about 180 m∼210 m; intermediate formation resistivity range from 3000 to 20000 Ohm·m, presumed to limestone, the thickness of about $550 \text{ m} \sim 620$ m; changes in the underlying strata resistivity range of 5000 to 12,000 Ohm·m, presumed to diorite. The low resistance sections no significant geophysical anomaly.

From the 6 lines of EH-4 inversion results can be seen in the underground medium divided into three layers overlying formation resistivity range of 500 to 5,000 Ohm·m, presumed to diorite, weathering fissures, the layer thickness about 260 m∼400 m; intermediate formation resistivity range from 5000 to 15000 Ohm·m, presumed to limestone, the thickness of about $350 \text{ m} \sim 580$ m; changes in the underlying strata resistivity range of 15000 to 40000 Ohm·m, presumed to diorite. The low resistance sections no significant geophysical anomaly.

From the 8 lines of EH-4 inversion results can be seen in the underground medium divided into three layers overlying formation resistivity range of 300 to 2000 Ohm·m, presumed to diorite, weathering fissures, the layer thickness about 260 m∼700 m; intermediate formation resistivity range from 2000 to 5000 Ohm·m, presumed to limestone, the thickness of about $160 \text{ m} \sim 600$ m; changes in the underlying strata resistivity range of 5000 to 12000 Ohm·m, presumed to diorite. Stake 450∼600 m in between resistivity contour changes in the large horizontal gradient is inferred by a fault, denoted by F2, North East tendency, the inclination is about 80 degrees. The low resistance sections no significant geophysical anomaly.

1 line, 0 line and the -1 line in the dot between -60 to 40 with a low resistivity anomaly, and from the surface down to a certain degree of extension of a line and the 0 line in the dot between 550 to 650 with a low resistance anomaly zone, extending from the surface down to a greater extent.

5. CONCLUSIONS

Explosive detective on Fushan District -1 8 line EH-4 inversion of data along the depth of 700 m a biopsy, a comprehensive analysis:

Line by Line No. $-1 \sim 1$ line between Stake between $-300 \sim 200$ m, there exists a continuous low resistance anomaly WT2, roof and floor depth of about $200 \sim 850$ m, the exception is not closed south direction. No. 0 line in the test line to 1 line between Stake between $480 \sim 720$ m, there is a continuous low resistance anomaly WT3, roof and floor depth of about $200 \sim 700$ m. Explosive detective area WT2 and WT3 abnormal conditions more favorable for the forming low resistivity anomaly.

ACKNOWLEDGMENT

This paper is supported by National Science Foundation Project of Hunan Province (07JJ6071).

REFERENCES

1. Geological Science Institute, China Academy of Hebei Taihang mountain area and geological, "Han xing type metallogenic regularities and iron Ore prospecting direction," *Internal Material*, 1–154, 1976.
2. Shen, L. S., "Hanxing area jingguang railway concealed rich iron ore resources potential of shallow," *Journal of Mineral and Geology*, Vol. 22, No. 4, 314–318, 2008.

3. Zheng, J. M., G. Q. Xie, M. H. Chen, et al., "Rock emplacement mechanism for skarns deposits in the area Han restricted — Xing skarn type for iron ore deposit geology," Vol. 26, No. 4, 481–486, 2007.
4. Liu, C. J., "Hebei iron bed xing hydrogeological conditions of recognition," *Journal of Metallurgy, Mining, Design and Construction*, Vol. 2, 1–6, 1994.
5. Shen, B. F., A. M. Zhai, Z. H. Li, et al., "The contact metasometic origin type iron bed in the chemical composition of magnetite characteristic and the geological significance of South of Hebei," Vol. 25, No. 1, 10–18, 1982.

Terahertz Current and Voltage Noise in Nanometric Schottky-barrier Diodes

A. H. Mahi[1], **F. Z. Mahi**[1], **and L. Varani**[2]

[1]Physics of Semiconductor Devices Laboratory (LPDS), University of Bechar, Algeria
[2]Institute of Electronics of the South (IES, CNRS UMR 5214), University of Montpellier, France

Abstract— In this paper we present an analytical model for the calculation of the spectral densities of current and voltage fluctuations in nanometric Schottky barrier diodes. The discussion of resonances appearing in the current spectrum in terms of applied voltage useful to optimize the order of harmonics generated by Schottky barrier diodes.

1. INTRODUCTION

The Schottky barrier diodes are widely used in terahertz systems as frequency multipliers. The physical property at the basis of the frequency multiplication is a strongly nonlinear current-voltage and/or capacitance-voltage characteristics, which is typical, for instance, of nonmetric GaAs Schottky-barrier diodes.

A critical parameter assessing its electrical performances under high-frequency large-signal operation is the intrinsic noise, which constitutes also an important limit for the extraction of the high-order harmonics. The intrinsic noise is described by the spectral density of current fluctuations, which has been recently investigated using an analytical method [1]. To extract the high-order harmonics generated by the SBD, we consider the Schottky multiplier operating in series with a parallel output resonant circuit when a high-frequency large-signal voltage is applied [2]. In this contribution we present two approaches of calculations for the noise description in SBD multipliers. One approach allowed us to determine the current spectral density and provides a discussion of the resonances appearing in the spectrum on the applied voltage drop. The second one allowed us to calculate the voltage noise which gives the order of harmonics generated.

2. ANALYTICAL MODEL

2.1. The Spectral Density of Current Fluctuations

We apply the theory to an n^+n-metal GaAs SBD at room temperature under a constant voltage applied between its terminals. The diode structure, reported schematically in Figure 1.

Under constant voltage conditions, the instantaneous response to any local perturbation originated by a scattering event of a free carrier results in the appearance inside the whole SBD of a homogeneous component of the electric field fluctuation ΔE [2]. At the initial stage this leads to a synchronous motion of all the free carriers in the SBD volume and, thus, to the formation of an uncompensated charge in regions internal to the borders between n^+, n and depletion regions. This extra charge initiates corrections of the initial field perturbation that are different in the n^+ and n regions, so that the further evolution of the collective shifts in the n^+ and n regions, δx_+ and δx_- respectively, become different and the $\delta E(x)$ fluctuation can be written as:

$$\delta E_i = \frac{e}{\varepsilon_0 \varepsilon_r} \begin{cases} -(1-r_+)N_+\delta x_+ + r_-N_-\delta x_-, & i=+ \\ r_+N_+\delta x_+ - (1-r_-)N_-\delta x_-, & i=- \end{cases} \tag{1}$$

where $r_i = \frac{l_i}{L}$ is the relative length of the i-region ($i = \pm$). To describe the dynamics of fluctuations of free carriers in the n^+ and neutral n regions, we take the advantage of the Langevin approach formulated by the following system of equations [3]:

$$\frac{d^2}{dt^2}\delta x_\pm + v_\pm \frac{d}{dt}\delta x_\pm = \frac{e}{m}\delta E_i + f_\pm \tag{2}$$

where $v_\pm$ is the momentum relaxation rate and $f_\pm$ the Langevin force describing the source of thermal fluctuations in the i-region. The previous system of Equations (1) and (2) can gives the evolutions δx_+ and δx_-. By taking into account that the Langevin forces $f_\pm$ in the n^+ and n regions

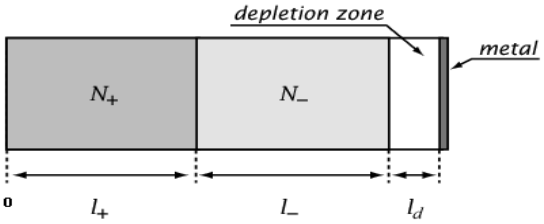

Figure 1: Schematic view of the n^+n-metal SBD. With l_+, l_- represent the length of the n^+ and n regions and l_d the length of the depletion region.

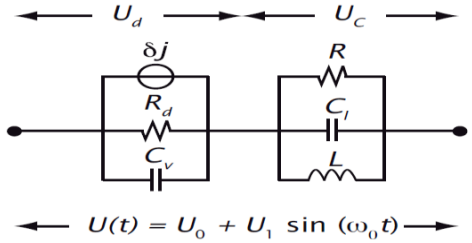

Figure 2: Equivalent scheme of a SBD connected in series with a parallel RLC-resonant circuit.

are uncorrelated, one obtains the spectral density of the thermal fluctuations of the SBD current as [4]

$$S_{JJ} = \frac{4kTAe^2}{mL^2}\left[v_+N_+l_+\left|\frac{\omega(a_{22}-a_{12})}{a_{22}a_{11}-a_{12}a_{21}}\right|^2 + v_-N_-l_-\left|\frac{\omega(a_{11}-a_{21})}{a_{22}a_{11}-a_{12}a_{21}}\right|^2\right] \tag{3}$$

The detailed expressions of the elements are: $a_{11} = {\omega_+}^2 - \omega^2 + i\omega v_+ + a_{21}$, $a_{21} = -r_+{\omega_+}^2$, $a_{12} = -r_-{\omega_-}^2$, $a_{22} = {\omega_-}^2 - \omega^2 + i\omega v_- + a_{12}$ and $\omega\pm = e^2N_i/\varepsilon_0\varepsilon_r m$ is the plasma frequency of free carriers in the i-region.

2.2. The Spectral Density of Voltage Fluctuation

For the calculation of voltage spectral density we consider the SBD embedded into a particular parallel resonant circuit characterized by the inductance L, the capacitance C_l and the resistance R. The corresponding equivalent scheme is presented in Figure 2. It is supposed that a microwave voltage $U(t) = U_0 + U_1\sin(2\pi v_0 t)$ applied to the whole circuit. The SBD is characterized by the resistance $R_d(U_d)$ and by varactor capacity $C_v(U_d)$. The current flowing through the SBD given by the approximation:

$$J_d(U_d) = J_d^s(U_d) + \delta J_d + C_v\frac{dU_d}{dt} \tag{4}$$

where $J_d^s(U_d)$ is the statistic $I(V)$ relation, δJ_d is current fluctuations source given by the Equation (3). By using the equations of circuit and the Equation (4) the voltage fluctuation given by [5]:

$$\delta U(\omega) = -Z(\omega)\left[\delta J_d(\omega) + i\omega C_v^0\sum_{n=0}^{\pm\infty}\gamma_n\delta U_d(\omega-\omega_n)\right] \tag{5}$$

where: $C_v^0 = \frac{1}{T_0}\int_0^{T_0} C_v dt$, $\gamma_n = \frac{1}{T_0C_v^0}\int_0^{T_0} C_v\exp(i\omega_n t)dt$ and $\omega_n = n\omega_0$. The constant T_0 and C_v^0 are expected the period of signal and varactor capacitance constant.

The impedance of system is given by

$$Z(\omega) = \frac{i\omega}{(C_l + C_v^0)\left[\frac{1}{(C_l+C_v^0)L} - \omega^2 + i\omega\frac{1}{(C_l+C_v^0)\frac{RR_d}{R+R_d}}\right]} \tag{6}$$

The fluctuation voltage given after the first iteration of Equation (7) by [4]:

$$S^1_{U_dU_d} = |Z(\omega)|^2\left[S^d_{jj}(\omega) + (\omega C_v^0)^2\sum_{n=0}^{\pm\infty}|\gamma_n|^2|Z(\omega-\omega_n)|^2S^d_{jj}(\omega-\omega_n)\right] \tag{7}$$

3. RESULTS AND DISCUSSION

The possible scenarios of modifications of the spectrum of current fluctuations are illustrated in Figure 3. For the case of a homogeneous structure and $l_d = 0$, the spectral density of current fluctuations exhibits the usual Lorentzian behavior (curve 1). The homojunction (see curve 2) leads to the appearance of a resonance peak associated to the plasma oscillations [3].

The presence of a depletion region but in the absence of any homojunction (see curve 3) leads to the appearance of an additional peak associated with carriers reflected by Schottky barrier [4].

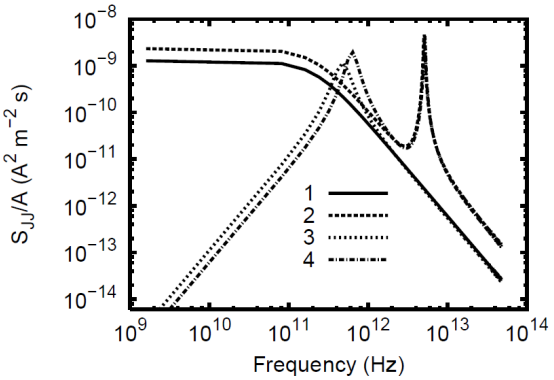

Figure 3: Spectrum of current fluctuations in a GaAs n^+n-metal. With: $l+ = l- = 0.1\,\mu m$ and $N_- = 5\times10^{16}\,cm^{-3}$. Curve 1: $l_d = 0$ and $N_+ = N_-$. Curve 2: $l_d = 0$ with $N_+ = 10N_-$. Curve 3: $N_+ = N_-$ and $l_d = 0.01\,\mu m$ and curve 4 corresponds to $l_d = 0.01\,\mu m$ with $N_+ = 10N_-$.

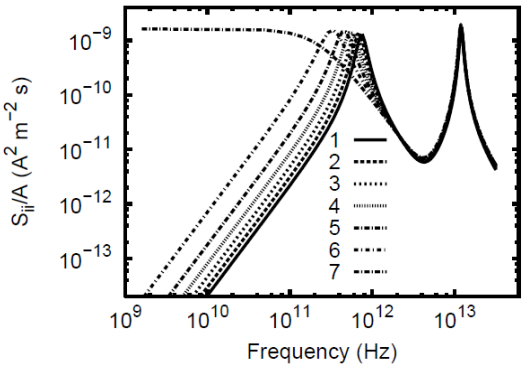

Figure 4: Spectral density of current fluctuations in a GaAs n^+-n-metal Schottky barrier diodes for different values of applied voltage. Curve 1: $U = 0.7\,V$. Curve 2: $U = 0.75\,V$. Curve 3: $U = 0.8\,V$. Curve 4: $U = 0.85\,V$. Curve 5: $U = 0.9\,V$. Curve 6: $U = 0.95\,V$ and curve7: $U = 1\,V$.

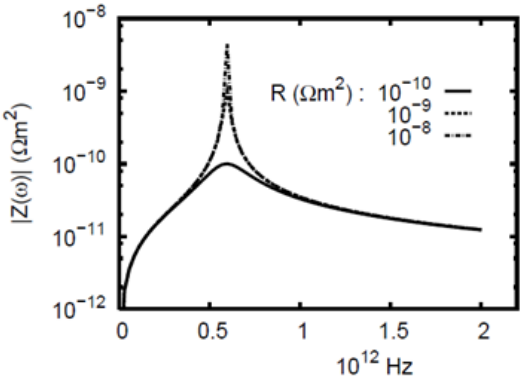

Figure 5: Impedance of system: SBD+ circuit resonant for different values of load resistance R. With $f_0 = 200\,GHz$, $T = 300\,K^0$, $U_0 = 0.6\,V$ and $U_1 = 0.2\,V$.

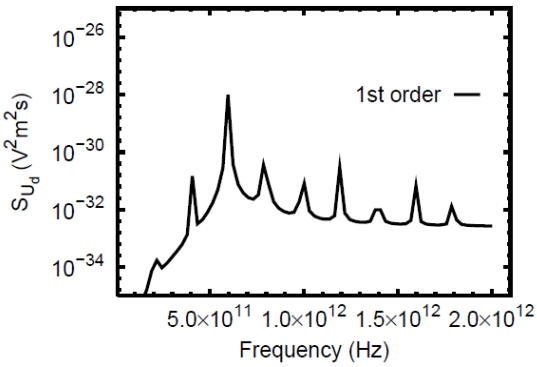

Figure 6: First iteration of the spectral density of voltage with $R = 10^{-8}\,\Omega\,m^2$, $T = 300\,K$, $U_0 = 0.6\,V$ and $U_1 = 0.2\,V$.

In the case of a complete structure (curve 4), the presence of two resonant peaks in the low and high frequency regions corresponding respectively to the carriers reflected by the Schottky barrier and to the hybrid plasma resonance frequency.

Figure 4 presents the spectra of current fluctuation flowing through the SBD for different fixed values of the voltage U. We observe a red-shift of the low frequency resonance peak by increasing of the applied voltage. In Figure 4, we can separate three areas; the low frequency $f < 0.1\,THz$ where the shot noise takes place, the second at $0.1 < f < 10\,THz$ corresponding to the resonance of carries reflected by Schottky barrier and the region at $f > 10\,THz$ related to the plasma resonance. Only in the second region exhibits a significant variation of spectrum with U we can introduce the capacitance multiplication effect witch determined by the depletion region $l_d(U_d)$.

Figure 5 presents the impedance of the whole system. We observe the appearance of the impedance peaks around the resonance frequency 600 GHz. The impedance peak increase when the load resistance increases. We extract the load resistance value $R = 10^{-8}\,\Omega\,m^2$ which can over the calculation of voltage noise.

Figure 6 presents the spectral density of voltage fluctuations calculated in the first order. We remark that the first order iteration gives merely a qualitative description of the origin of the resonance noise peaks at the frequencies $\omega = \omega_{res} + n\omega_0$. The peaks indicate the order harmonics generated by varactor capacitance of Schottky barrier diodes.

4. CONCLUSIONS

We have presented an analytical calculation of the spectral densities of current and voltage fluctuations in Schottky-barrier diodes. The model allows us to describe precisely the high-frequency part of the noise spectrum up to the THz region and to determine partial contributions originated by the carriers of n^+ and n regions. The discussion of the results can be useful for optimizing the order of harmonics generated by SBD.

REFERENCES

1. Shiktorov, P., E. Starikov, V. Gruzinskis, L. Reggiani, L. Varani, and J. C. Vaissière, "Analytical model of high-frequency noise spectrum in Schottky-barrier diodes," *IEEE Electron Device Letters*, Vol. 26, No. 1, 2–4, January 2005.
2. Shiktorov, P., E. Starikov, V. Gruzinskis, S. Pérez, T. Gonzalez, L. Reggiani, L. Varani, and J. C Vaissière, "Monte Carlo simulation of Schottky diodes operating under terahertz cyclostationary conditions," *IEEE Electron Device Letters*, Vol. 25, No. 1, 1–3, January 2004.
3. Bulashenko, O. M., P. Gaubert, L. Varani, J. C. Vaissière, and J. P. Nougier, "Impedance field and noise of sub micrometer n^+nn^+ diodes analytical approach," *Journal of Applied Physics*, Vol. 88, No. 8, 4709–4716, October 15, 2000.
4. Mahi, F. Z., A. Helmaoui, L. Varani, P. Shiktorov, E. Starikov, and V. Gruzhinskis, "Calculation of the intrinsic spectral density of current fluctuations in nanometric Schottky-barrier diodes at terahertz frequencies," *Physica B*, Vol. 403, 3766–3768, October 2008.
5. Gonzalez, T., D. Pardo, L. Reggiani, and L. Varani, *J. Appl. Phys.*, Vol. 82, 2349, 1997.

A Set of New SDA Basis Functions with Strongly Decaying Properties

F. Z. Siabah, M. Bouchaour, M. T. Benhabiles, and M. L. Riabi
Laboratory of Electromagnetism and Telecommunications, University Mentouri
Route Ain-El-Bey, Constantine 25000, Algeria

Abstract— Four smooth pulses with strongly decaying spectra are investigated as piecewise basis functions suitable for the SDA analysis of microstrip lines with open sidewalls, such that the integral tail slow convergence problem is canceled. These pulses are inedited and they fulfill all of the SDA theoretical requirements. Besides the computational enhancement of the method, the proposed functions yield a continuous current density profile which restitutes with a maximum of accuracy the physical reality.

1. INTRODUCTION

The global accuracy of the Spectral Domain Approach tightly depends on the evaluation of the impedance matrix inner products involved in the Galerkin procedure. One reason for inaccuracy and computation burden arises from improper integrals with slow convergence rate and oscillating tails, as the spectral variable tends to infinity. This drawback is particularly embarrassing in open side structures.

State-of-the-art SDA basis functions for the current density modeling in microstrip lines are mostly full-domain orthogonal polynomials or special functions. The latter show drastic limitations in matter of spectrum decay, due to the sharp edge conditions. The wavelets have been vaunted for the space multi-resolution analysis capabilities, but sharing the same spectral properties with the full-domain polynomials, the sole advantage they introduced since their wide use in the Galerkin method was the matrix sparseness. Any promising alternative regarding the spectrum decay can only be expected from piecewise functions, as the rooftop pulse, which shows an asymptotic behavior in α^{-2}, and which is referred in the present work as the most decaying spectrum among state-of-the-art basis functions.

The most widely adopted solution to tackle the tail drawback with classic basis functions consists in decomposing the integral in two parts, an asymptotic part which is evaluated by a closed form analytical expression, and a relatively fast decaying part which is computed numerically. References [1–4] show different variants to process this solution.

We propose an approach that definitely cancels the integral tail problem by the introduction of piecewise basis functions with strongly decaying spectra, such that a very low bound for the numerically computed integral gives a highly accurate evaluation, and the asymptotic part is practically inexistent.

2. THEORETICAL BACKGROUND AND SUBJECT SPECIFICATION

The leading idea behind the basis functions investigated in the present work follows the observation that the decaying spectrum properties of a finite width pulse are closely tied to the smoothness the pulse tends to its zero value. This property is quantitatively expressed by the pulse continuity, and the order of continuous derivatives it can have.

It is theoretically established that if p is the lowest discontinuous derivative order of the pulse, its spectrum decays asymptotically as α^{-p-1}.

More than to prospect for such a pulse, the true challenge was to provide one which fulfills at the same time all of the SDA requirements for the basis functions, which are

1 – To form a complete basis for the Hilbert space expansion of the strip current density
2 – To restore a good approximation of the actual current density with a low number of expansion terms
3 – To fit the current density boundary conditions
4 – To yield a positive definite impedance matrix

The result of our investigation is four smooth pulses which are: the Raised Cosine pulse, a nearly Gaussian pulse $G(x)$, a trigonometric pulse built on an exponential stump $T(x)$, and a quadratic

pulse composed of three parabolic chips $Q(x)$. The analytic expression of these pulses and their Fourier transform, if available, are given in Table 1.

The Raised Cosine is widely known in signal processing [5], but it has not been used as SDA basis function in the literature. The three other pulses are original and validated as SDA basis functions in the present work.

The pulses shapes are visualized in Figure 1. Their corresponding Fourier transforms in logarithmic scale real magnitude as a function of the wave number normalized to the half of the pulse width, are given in Figure 2.

It is rather meaningful for the global SDA process to see the effect of these basis functions on the decay of the impedance matrix components. Figure 3. shows the variation of the inner products integrands $J_z Z_{zz} J_z$, as a function of the wave number normalized to the half of the pulse width. These plots are produced without loss of generality with the matrix terms of the first index for the current density expansion, J_{z0}. The rooftop is shown as the most decaying state-of-the-art basis function; all the plots represent real magnitudes in logarithmic scale.

Table 1: The basis functions and their fourier transforms.

Ref.	Analytic expression	Fourier Transform
Raised Cosine	$f(x) = \begin{cases} \cos^2\left(\frac{\pi x}{\Delta}\right) & \text{if} \quad \lvert x\rvert \le \frac{\Delta}{2} \\ 0 \quad \text{if} \quad \lvert x\rvert > \frac{\Delta}{2} \end{cases}$	$\tilde{f}(\alpha) = \frac{\pi^2 \sin\left(\frac{\pi\Lambda\alpha}{2}\right)\cos\left(\frac{\pi\Lambda\alpha}{2}\right)}{\left(\frac{\pi\Lambda\alpha}{2}\right)(\pi^2-(\pi\Lambda\alpha)^2)}$
G-Pulse	$G(x) = \begin{cases} \exp\left(\frac{2.079x^{\acute{e}}}{x^{\acute{e}} - \left(\frac{\Delta}{2}\right)^{\acute{e}}}\right) & \text{if} \quad \lvert x\rvert < \frac{\Delta}{2} \\ 0 \quad \text{if} \quad \lvert x\rvert \ge \frac{\Delta}{2} \end{cases}$	Numerically Computed
T-Pulse	$T(x) = \begin{cases} \frac{\int_{-\frac{\Delta}{2}}^{x} \exp\left(\frac{(4t+\Delta)^{\acute{e}}}{(4t+\Delta)^{\acute{e}} - \Delta^{\acute{e}}}\right) dt}{\int_{-\frac{\Delta}{2}}^{0} \exp\left(\frac{(4t+\Delta)^{\acute{e}}}{(4t+\Delta)^{\acute{e}} - \Delta^{\acute{e}}}\right) dt} & \text{if} \quad -\frac{\Delta}{2} \le x \le 0 \\ T(-x) \quad \text{if} \quad 0 \le x \le \frac{\Delta}{2} \\ 0 \quad \text{if} \quad \lvert x\rvert > \frac{\Delta}{2} \end{cases}$	Numerically Computed
Q-Pulse	$Q(x) = \begin{cases} 2\left(\frac{2x}{\Delta}+1\right)^2 & \text{if} \quad -\frac{\Delta}{2} \le x \le -\frac{\Delta}{4} \\ 1-2\left(\frac{2x}{\Delta}\right)^2 & \text{if} \quad -\frac{\Delta}{4} \le x \le \frac{\Delta}{4} \\ 2\left(\frac{2x}{\Delta}-1\right)^2 & \text{if} \quad \frac{\Delta}{4} \le x \le \frac{\Delta}{2} \\ 0 \quad \text{if} \quad \lvert x\rvert > \frac{\Delta}{2} \end{cases}$	$\tilde{Q}(\alpha) = \frac{\sin\left(\pi\alpha\frac{\Delta}{2}\right)\sin^2\left(\frac{\pi\alpha\Delta}{4}\right)}{\left(\pi\alpha\frac{\Delta}{2}\right)^3}$

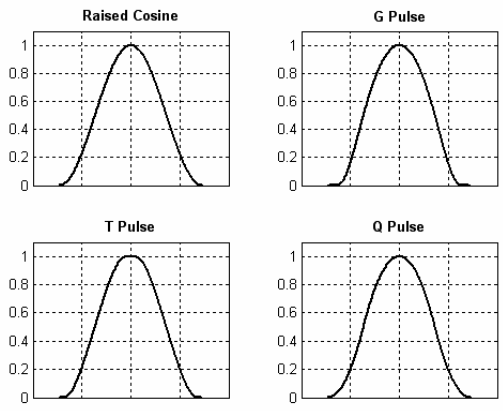

Figure 1.

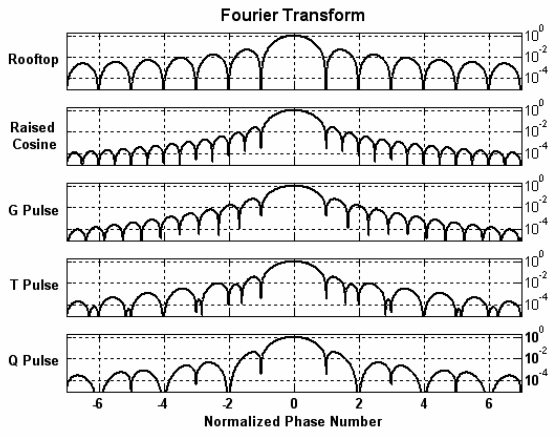

Figure 2.

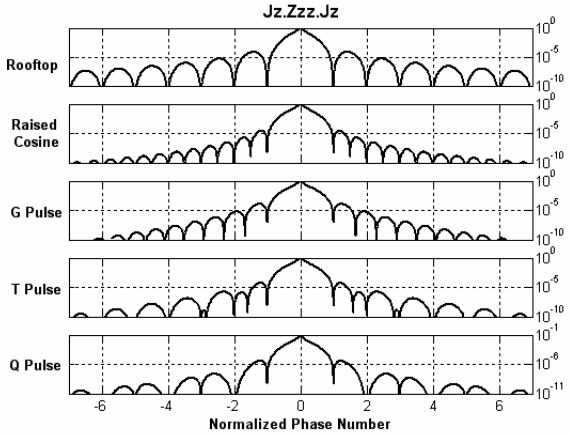

Figure 3.

Table 2: Comparative computed data.

Basis Functions	Number of Cells	Computed ε_{eff}	Integration Bound $(\alpha^2+\beta^2)^{1/2}$
Ref [6-TABLE II]	99	8.8097	$466.95k_o$
Raised Cosine	31	8.8071	$270.75k_o$
G(x)	31	8.8086	$264.66k_o$
T(x)	31	8.8093	$257.02k_o$
Q(x)	31	8.8108	$356.27k_o$

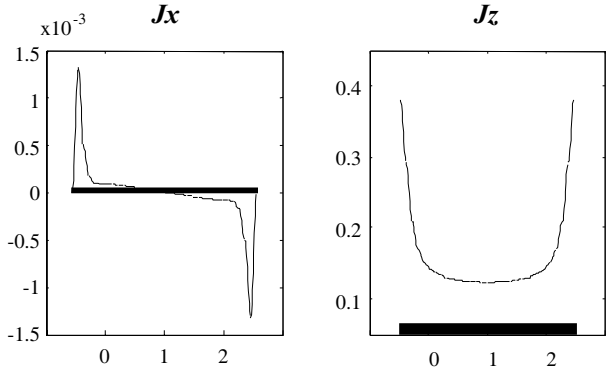

Figure 4.

3. QUANTITATIVE VALIDATION

Computational validation is held by reference to the canonical data from [6] for a confirmed effective permittivity ε_{eff} value. The basis functions introduced in the present work verify a secure threshold of integrals convergence for $(\alpha^2+\beta^2)^{1/2}$ below $360k_o$, whereas this bound is located above $460k_o$ for the rooftop pulse, keeping all other parameters identical. The numerical results of the computation are presented in Table 2.

3.1. Continuity of the Current Density Profiles

Besides the decaying spectrum, another substantial advantage to be pointed out about these pulses is the continuity of the restored space domain profiles of the strip current density.

Basically, one computational source of inaccuracy with piecewise basis functions is the first order discontinuity of the restituted current density at the cell transitions, which is commonly called the stairs aspect. Due to the smoothness and completeness of the basis functions introduced in the present wok, the cell transition discontinuity is drastically reduced, as it can be observed in Figure 4. The plots represent the computed transverse and longitudinal strip current densities as taken at the output of the pure SDA process with no further curve fitting nor any kind of post-processing treatment. These profiles are set-up with the Raised Cosine pulses as basis functions, and there is no difference concerning this side of the study between the four pulses introduced in the present

paper. We believe that the profiles given in Figure 4 reconstitute with a maximum of accuracy the actual physical current density in the open microstrip line. The edge effects are rendered with a tangible pertinence, without computational expenses. Observe also the scale disproportion between the transverse and the longitudinal current densities, which is averagely of two magnitude orders.

4. CONCLUSIONS

The numerical features of four new piecewise basis functions are exhaustively investigated with regard to various aspects of the SDA applied to the microstrip line. Besides the advantages induced by the spectrum decay, the computed current profiles give a realistic restitution of the physical current density on the strip.

REFERENCES

1. Park, S. O. and C. A. Balanis, "Analytical technique to evaluate the asymptotic part of the impedance matrix of Sommerfeld-type integrals," *IEEE Trans. on Antennas and Propagation*, Vol. 45, No. 5, 798–805, 1997.
2. Demuynck, F. J., G. A. E. Vandenbosch, and A. R. Van de Capelle, "The expansion wave concept — Part I: Efficient calculation of spatial Green's functions in a stratified dielectric medium," *IEEE Trans. on Antennas and Propagation*, Vol. 46, No. 3, 397–406, 1998.
3. Amari, S., R. Vahldieck, and J. Bornemann, "Using selective asymptotics to accelerate dispersion analysis of microstrip lines," *IEEE Trans. on Microwave Theory and Techniques*, Vol. 46, No. 7, 1024–1027, 1998.
4. Ooi, B. L., P. S. Kooi, and M. S. Leong, "Application of Sonie-Schafheitlin formula and sampling theorem in spectral domain method," *IEEE Trans. on Microwave Theory and Techniques*, Vol. 49, No. 1, 210–213, 2001.
5. Harris, F. J. "On the use of windows for harmonic analysis with the discrete Fourier transform," *Proc. IEEE*, Vol. 66, No. 1, 51–83, 1978.
6. Coen, G., N. Faché, and D. De Zutter, "Comparison between two sets of basis functions for the current modeling in the Galerkin spectral domain solution for microstrips," *IEEE Trans. on Microwave Theory and Techniques*, Vol. 42, No. 3, 505–513, 1994.

Novel FDTD Method with Low Numerical Dispersion and Anisotropy

Xiang-Qian Zhang, **Zai-Ping Nie**, **Ming-Yao Xia**, **Shi-Wen Qu**, **and Yue-Hui Li**
School of Electronic Engineering, University of Electronic Science and Technology of China, China

Abstract— The numerical dispersion and numerical anisotropy of the standard finite difference time domain (FDTD), six points lattice FDTD and high order FDTD (2, 4) are studied and compared. A new FDTD method with low numerical dispersion and anisotropy are developed. The method of confirming the weighting factor and the optimal factor in this method are given. The numerical dispersion and anisotropy of the proposed method are studied. The amended method of the numerical dispersion of the proposed method and the amended factor are given. The numerical experiment shows that the numerical dispersion and anisotropy of the proposed method are greatly reduced and the accuracy of the FDTD method is improved greatly by using the proposed scheme.

1. INTRODUCTION

The standard finite-difference time-domain (FDTD) method [1] (Yee scheme) has been widely used to solve Maxwell's equation in numerous electromagnetic applications [2], However, the anisotropic numerical dispersion inherent in the Yee FDTD method prohibits its application to electrically large problems. Many researchers have proposed various FDTD schemes to reduce the dispersion error over the past decades. The research trend for the low-dispersion FDTD schemes can be mostly categorized into two groups. The first approach is to use a high-order approximation for time and/or space derivation such as Fang's (2, 4) method [3]. The second approach approximations the spatial derivative in second-order accuracy using more spatial sampling points (larger computational stencil), and includes such methods as Forgy's scheme [4], non-stand (NS) FDTD scheme [5] and ID-FDTD scheme [6].

The ID-FDTD scheme uses more spatial sampling points on the Yee grid than the Yee scheme to approximation the spatial derivative in Maxwell's equation [6]. The finial spatial difference equation known as ID-finite difference (FD) equation, is a linear combination of the traditional central difference equation and a new difference equation based on the extra sampling points. The weighting factor for the linear combination is analytically determined based on the dispersion relation, which can generate a negligible anisotropy of the dispersion, however, the numerical phase velocity is slower than the exact one in a dielectric or conducting medium.

In this paper, a new FDTD scheme based on six points FD is proposed and the dispersion relation of the six points FDTD scheme, standard FDTD scheme and higher order FDTD (2, 4) scheme are well compared. Additionally, a new ID-FDTD scheme is proposed based on a linear combination of the traditional central difference equation and a new difference equation based on the six sampling points.

2. THE COMPARISON OF THE THREE FDTD SCHEMES

The classical FDTD method, as proposed By Yee [1], is second-order accurate in both space and time (FDTD (2, 2)). The general numerical dispersion relation of the Yee algorithm for the TM_z model was derived as

$$\left[\frac{1}{c\Delta t}\sin\left(\frac{\omega\Delta t}{2}\right)\right]^2 = \left[\frac{1}{\Delta x}\sin\left(\frac{\tilde{k}_x\Delta x}{2}\right)\right]^2 + \left[\frac{1}{\Delta y}\sin\left(\frac{\tilde{k}_y\Delta y}{2}\right)\right]^2 + \left[\frac{1}{\Delta z}\sin\left(\frac{\tilde{k}_z\Delta z}{2}\right)\right]^2 \quad (1)$$

More accurate approximations to derivatives are provided by high order finite difference schemes. Here a second order in time and fourth order in space scheme (FDTD (2, 4)) is described. In this scheme, the positions of the electric and magnetic field components remain the same as those of the FDTD (2, 2) scheme. The FDTD (2, 4) stencil uses central finite differences, forth-order accurate in space and second-order-accurate in time:

$$\frac{\partial F^n(i,j,k)}{\partial x} = \frac{9}{8}\frac{F^n(i+1/2,j,k) - F^n(i-1/2,j,k)}{\Delta x} - \frac{1}{24}\frac{F^n(i+3/2,j,k) - F^n(i-3/2,j,k)}{\Delta x} + o(\Delta x^4) \quad (2)$$

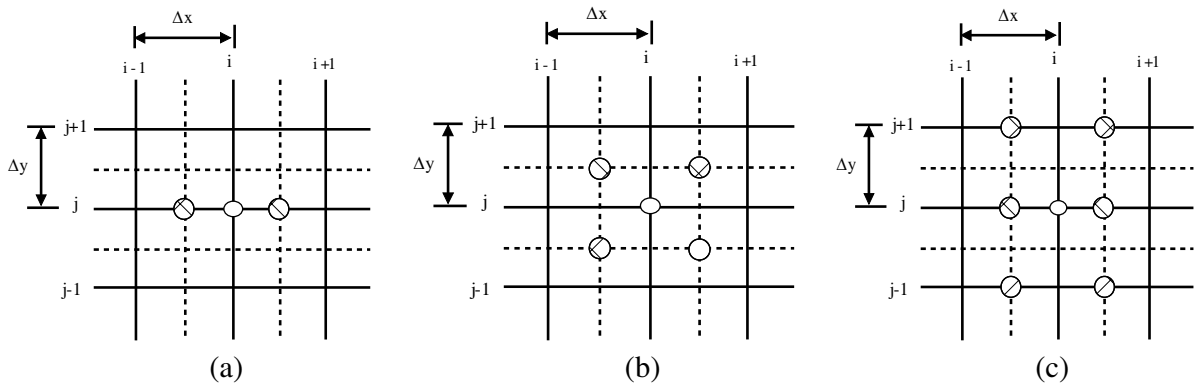

Figure 1: Graphical depiction of three FD approximation to $\partial/\partial x$ in 2-D.

The dispersion equation for FDTD (2, 4) was derived by Fang [3] as

$$\left[\frac{1}{c\Delta t}\sin\left(\frac{\omega\Delta t}{2}\right)\right]^2 = \left(\frac{1}{\Delta x}\right)^2\left[\frac{9}{8}\sin\left(\frac{\tilde{k}_x\Delta x}{2}\right)-\frac{1}{24}\sin\left(\frac{3\tilde{k}_x\Delta x}{2}\right)\right]^2 + \left(\frac{1}{\Delta y}\right)^2\left[\frac{9}{8}\sin\left(\frac{\tilde{k}_y\Delta y}{2}\right)-\frac{1}{24}\sin\left(\frac{3\tilde{k}_y\Delta y}{2}\right)\right]^2 + \left(\frac{1}{\Delta z}\right)^2\left[\frac{9}{8}\sin\left(\frac{\tilde{k}_z\Delta z}{2}\right)-\frac{1}{24}\sin\left(\frac{3\tilde{k}_z\Delta z}{2}\right)\right]^2 \quad (3)$$

The standard FDTD method approximates the spatial derivative using the second order central finite-difference (FD) scheme, as given in (4), As mentioned earlier, the formulation samples fields at two 1-D lines, the x- and y-axes, as seen in Fig. 1, which may cause anisotropic dispersion. To sample fields in an isotropic manner in a 2-D space, another FD scheme of the same order of accuracy can be used, as given by (5). The new sampling points for (5) are show in Fig. (1)b. for the approximation of $\partial/\partial x$. Since the standard FDTD does not calculate fields at the new points, the fields should be estimated using the fields in the adjacent grids [6]. Fig. 1(c) shows the possible fields to estimate the fields at the new sampling points in Fig. 1(b). Three or two fields can be used for the estimation at each point in Fig. 1(b). If a linear interpolation is adopted for the estimation, a new FD scheme is obtained, as in (6).

$$\frac{\partial f}{\partial x}\Big|_{i,j} \cong \frac{\tilde{d}_x^2 f_{i,j}}{\Delta x} = \frac{f_{i+1/2,j}-f_{i-1/2,j}}{\Delta x} \quad (4)$$

$$\frac{\partial f}{\partial x}\Big|_{i,j} \cong \frac{\tilde{d}_x^4 f_{i,j}}{2\Delta x} = \frac{\tilde{d}_x^2 f_{i,j+1/2}+\tilde{d}_x^2 f_{i,j-1/2}}{2\Delta x} \quad (5)$$

$$\frac{\partial f}{\partial x}\Big|_{i,j} \cong \frac{\tilde{d}_x^6 f_{i,j}}{2\Delta x} = \frac{\tilde{d}_x^2 f_{i,j+1}+2\tilde{d}_x^2 f_{i,j}+\tilde{d}_x^2 f_{i,j-1}}{4\Delta x} \quad (6)$$

where Δx and Δy are defined in Fig. 1(a). In (4)–(6), the superscripts indicate the number of sampling points.

The dispersion equation for the six points difference scheme is

$$\left[\frac{1}{c\Delta t}\sin\left(\frac{\omega\Delta t}{2}\right)\right]^2 = \frac{1}{\Delta x^2}\left[1-\sin\left(\frac{\tilde{k}_y\Delta y}{2}\right)\right]^2\sin^2\left(\frac{\tilde{k}_x\Delta x}{2}\right) + \frac{1}{\Delta y^2}\left[1-\sin\left(\frac{\tilde{k}_x\Delta x}{2}\right)\right]^2\sin^2\left(\frac{\tilde{k}_y\Delta y}{2}\right) \quad (7)$$

The numerical dispersion and numerical anisotropy of FDTD (2, 2), FDTD (2, 4) and six points difference scheme are presented and compared in Fig. 2. Here, grid-sampling densities $N_\lambda = 10$ and $S = 0.7$ for the three schemes.

The numerical dispersion of the six points FD scheme turn out to be a little more anisotropic than that of the Yee scheme. However, the angular dependency is opposite that of the Yee algorithm; that is, at $\varphi = 0°$ and 90°, the phase velocity reaches its maximum value and becomes minimal at $\varphi = 45°$, which is still anisotropic, as expected.

3. THE NEW FDTD METHOD

By approximating the spatial derivative with a weighted sum of $\tilde{d}_u^2$ and $\tilde{d}_u^6$, a new FD scheme can be obtained.

$$\tilde{d}_u f_u = (1-\alpha)\tilde{d}_u^2 f_u + \alpha \tilde{d}_u^6 f_u \quad 0 \le \alpha \le 1 \tag{8}$$

where u is x or y, and α is a weighting factor which must be determined. To reduce the computational complexity of the proposed difference scheme, (8), the scheme can be modified as

$$\tilde{d}_u f_u = (1-\frac{\alpha}{2})\tilde{d}_u^2 f_u + \frac{\alpha}{4}\left(\tilde{d}_u^2 f_{u+1} + \tilde{d}_u^2 f_{u-1}\right) \quad 0 \le \alpha \le 1 \tag{9}$$

Following [2], The numerical dispersion relation of the new FDTD method can be derived for nonconductive media ($\sigma = 0$) as

$$\begin{aligned}\left[\frac{1}{c\Delta t}\sin\left(\frac{\omega\Delta t}{2}\right)\right]^2 &= \frac{1}{\Delta x^2}\left[1-\alpha\sin\left(\frac{\tilde{k}_y\Delta y}{2}\right)\right]^2\sin^2\left(\frac{\tilde{k}_x\Delta x}{2}\right) \\ &\quad + \frac{1}{\Delta y^2}\left[1-\alpha\sin\left(\frac{\tilde{k}_x\Delta x}{2}\right)\right]^2\sin^2\left(\frac{\tilde{k}_y\Delta y}{2}\right)\end{aligned} \tag{10}$$

where c is the free space light velocity, $\tilde{k}_x = \tilde{k}\cos\varphi$, $\tilde{k}_y = \tilde{k}\sin\varphi$, $\tilde{k}$ is a numerical wavenumber, and φ is the azimuth angle.

If a square grid is assumed, and after some algebraic manipulations, (10) can be rewritten as

$$\frac{1}{\Delta^2}C_+C_\times\left(\alpha - \frac{2}{C_+}\right)^2 - \frac{1}{\Delta^2}\left(\frac{4C_\times}{C_+} - C_+\right) - \frac{1}{(c\Delta t)^2}\sin^2\left(\frac{\omega\Delta t}{2}\right) = 0 \tag{11}$$

where $\Delta x = \Delta y = \Delta$, and $C_+ = \sin^2(\frac{\tilde{k}_x\Delta}{2}) + \sin^2(\frac{\tilde{k}_y\Delta}{2})$, $C_\times = \sin^2(\frac{\tilde{k}_x\Delta}{2})\sin^2(\frac{\tilde{k}_y\Delta}{2})$.

Since (11) is a quadratic equation about α, the exact solutions of (11) can be given analytically as

$$\alpha = \frac{2}{C_+}\left[1 - \sqrt{1 - \frac{\Delta^2 C_+}{4C_\times}\left(\frac{1}{\Delta^2}C_+ - \frac{1}{(c\Delta t)^2}\sin^2\left(\frac{\omega\Delta t}{2}\right)\right)}\right] \tag{12}$$

In (12), $\tilde{k}$ can be analytically calculated at $\varphi = 0°$ as

$$\tilde{k} = \frac{2}{\Delta}\sin^{-1}\left[\frac{\Delta}{c\Delta t}\sin\left(\frac{\omega\Delta t}{2}\right)\right] \tag{13}$$

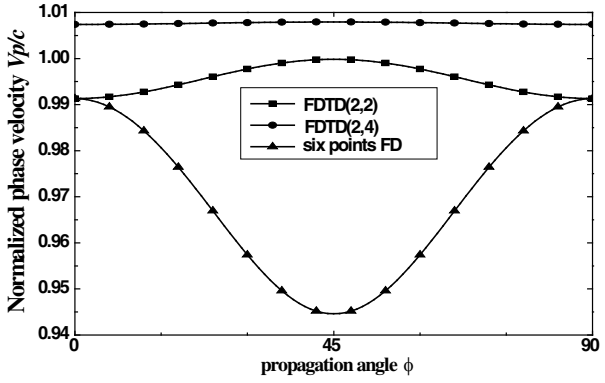

Figure 2: Plots of the numerical dispersions as a function of the propagation angle, $N_\lambda = 10$ is assumed and comparison with FDTD (2, 2) and FDTD (2, 4)' schemes.

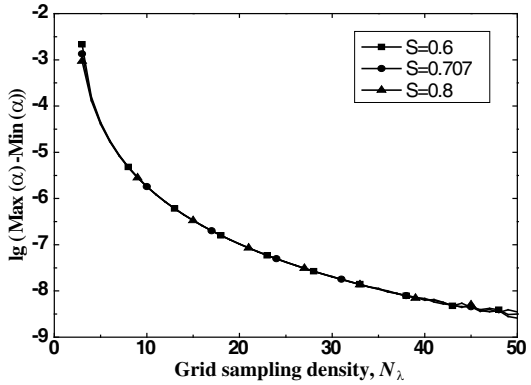

Figure 3: Plot of the variation of α as a function of a grid sampling density, $N_\lambda = \lambda/\Delta$, and Courant number ($S$).

Equation (13) can give zero dispersion over all azimuth angles, but α is a function of the azimuth angles φ, grid size, and time step. To determine an optimal constant α first, the variation of α as a function of the azimuth angles for a fixed grid size is investigated. Fig. 3 shows the difference between the maximum and minimum ofαalong the azimuth angles versus the grid size and Courant number, $S = c\Delta t/\Delta$. As seen in this figure, for a grid smaller than $\lambda/10$, the difference is below 10^{-6} for any time step, and thus α can be considered as a constant over the azimuth angles. Therefore, an optimal α can be simply estimated as the mean value of α over the azimuth angles.

Figure 4 shows the estimated optimal α as a function of grid size and time step, which shows that α remains almost constant for a wide range of grid sizes and is insensitive to the choice of the Courant number. Therefore, α can be assumed to be constant (≈ 0.167) over a wide range of frequencies.

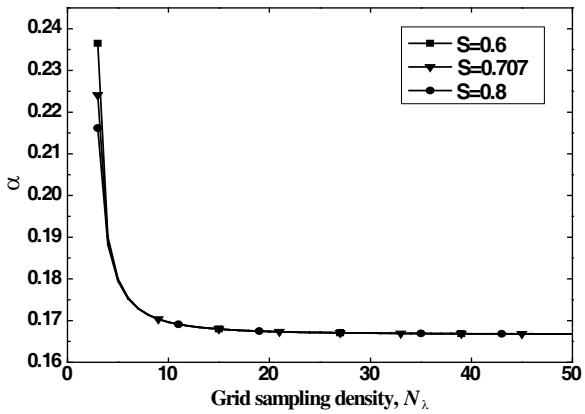

Figure 4: Optimal α versus the sampling density for Courant number, $S = 0.6$, 0.707 and 0.8.

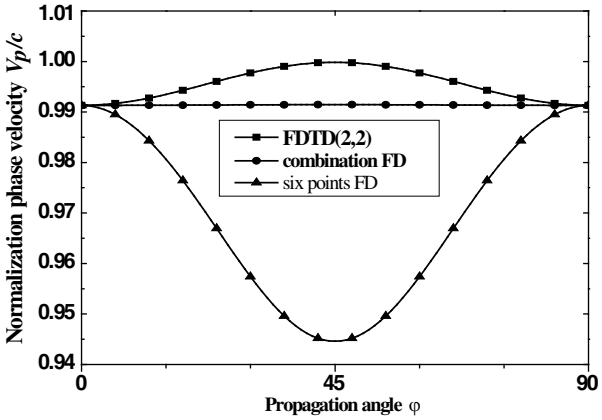

Figure 5: Plot of the numerical dispersions as a function of the propagation angle, $N_\lambda = 10$ is assumed and comparison with FDTD (2, 2) and six points FD' schemes.

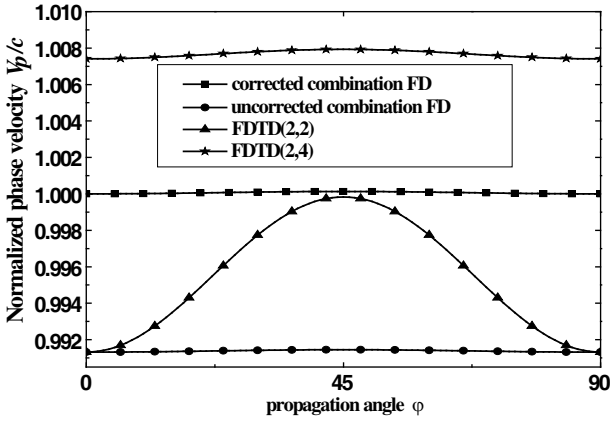

Figure 6: Plot of the numerical dispersions as a function of the propagation angle, $N_\lambda = 10$ is assumed and comparison with FDTD (2, 2), FDTD (2, 4), and uncorrected combination FD' schemes.

Table 1: Comparation of the numerical dispersion and numerical anisotropy of the three finite difference schemes.

	$\left(\frac{V_p}{C}-1\right)\Big\vert_{0^\circ}$	$\left(\frac{V_p}{C}-1\right)\Big\vert_{45^\circ}$	abs	$\frac{abs}{abs\vert_{combination}}$
The corrected FDTD scheme	0	1.3×10^{-4}	1.3×10^{-4}	1
FDTD (2, 2)	8.6×10^{-3}	1.68×10^{-4}	8.5×10^{-3}	66
FDTD (2, 4)	7.41×10^{-3}	7.93×10^{-3}	5.2×10^{-4}	4

Using the optimal $\alpha \approx 0.167$, an isotropic numerical phase velocity can be achieved and the numerical dispersion and numerical anisotropy of the combination six points FD, FDTD (2, 2) and the six points FD schemes are compared in Fig. 5. but the numerical phase velocity of the proposed method is slower than the exact one. However, by simply scaling ε and/or μ, the numerical phase velocity can be easily adjusted to be close to the exact value over all azimuth angles. The scaling factor was chosen to make the fastest phase velocity the exact one ($\varphi = 0^\circ$), which is mathematically expressed as $k_{exact}/\tilde{k}' = 1$. Here, k_{exact} is the exact wave number, $\tilde{k}'$ is (13) but replacing c with c/sc, and making sc the scaling factor. The above equation can be solved analytically, and the closed form of sc is given by [6]

$$sc = \frac{\sin(k_{exact}\Delta/2)}{\sin(\omega\Delta t/2)/S}, \quad \varepsilon' = sc \times \varepsilon, \quad \mu' = sc \times \mu \tag{14}$$

The numerical dispersion and numerical anisotropy of the four finite difference (FD) are compared in Fig. 6. Fig. 6 shows that the numerical dispersion and numerical anisotropy of the corrected FDTD with six points difference is the smaller than that of the uncorrected scheme, and the numerical dispersion and numerical anisotropy of the corrected FDTD with the six points difference is the smallest in the four FD schemes.

In order to compare the numerical dispersion and numerical anisotropy of the three FD schemes quantitatively, the Table 1 is given as follows. Where the *abs* stands for the $abs((V_p/C-1)|_{45^\circ} - (V_p/C-1)|_{0^\circ})$. The numerical anisotropy of the corrected FDTD scheme is the same as 1/66 of that of the FDTD (2, 2) scheme and 1/4 of that of the FDTD (2, 2) scheme. The maximum numerical dispersion of the corrected FDTD scheme is the same as 1/67 of that of the FDTD (2, 2) scheme and 1/61 of that of the FDTD (2, 2) scheme.

4. CONCLUSION

In this paper, a nearly no dispersion FDTD scheme, which uses the standard Yee grid, was proposed. The proposed method replaces the convention central FD scheme with a new FD formulation which samples fields in a spatially isotropic manner. It was shown that the proposed algorithm has a nearly isotropic dispersion and exact phase velocity, whose isotropic property is superior to that of the existing methods such as the FDTD (2, 2) and FDTD (2, 4) scheme.

REFERENCES

1. Yee, K. S., "Numerical solution of initial boundary value problems involving Maxwell equations in isotropic media [J]," *IEEE Transactions on Antennas and Propagation*, Vol. 14, No. 3, 302–307, 1966.
2. Taflove, A. and S. C. Hagness, *Computational Electrodynamic: The Finite-Difference Time-Domain Method [M]*, Artech House, Boston, 2000.
3. Fang, J., "Time domain finite difference computation for Maxwell's equations," Ph.D. dissertation, Univ. California, Berkeley, CA, 1989.
4. Forgy, E. and W. Chew, "A time-domain method with isotropic dispersion and increased stability on an overlapped lattice," *IEEE Transactions on Antennas and Propagation*, Vol. 50, No. 7, 983–996, 2002.
5. Cole, J., "A high accuracy FDTD algorithm to solve microwave propagation and scattering problems on a coarse grid," *IEEE Transactions on Antennas and Propagation*, Vol. 43, No. 9, Part 1, 2053–2058, 1995.
6. Koh, I., H. Kim, J. Lee, et al., "Novel explict 2-d FDTD scheme with isotropic dispersion and enhangced stability," *IEEE Transactions on Antennas and Propagation*, Vol. 54, No. 11, Part 2, 3505–3510, 2006.

The Equivalent Rest-mass of Photon

Antonio Puccini
Department of Neurophysiology, Order of Malta, Naples, Italy

Abstract— The photon (P), one of the elementary particles of the *Standard Model*, is considered massless. The Universal Gravitation Law states that the gravity force (GF) takes place only between bodies having a mass. Einstein's prediction, based on the Theory of General Relativity, provides that the light is conditioned by the action of the GF. However observations showed that the P *feels* GF. Lord Eddington, with his famous observation in 1919, confirmed completely what Einstein had said. During a sun eclipse, indeed, it was possible to observe that the light coming from far away stars, when passing next to the sun rather than propagate in straight line, followed a trajectory bended towards the sun.

We know that two massless Ps, meeting, *materialise* in a couple of quark-antiquark, or even in a couple muon-antimuon which, summed up, have a mass of 400 electrons.

The energetic value (E) of the P is represented by the *Planck's constant* (h) — equal to $6.625 \cdot 10^{-27}$ [erg $\cdot$ sec] — times its frequency (f): $E = hf$.

The value of f is not defined, but extremely variable, according to the EM spectrum. Thus we should indicate f with 10^n [1/s], where n can start from 0, that is one cycle per second (we cannot exclude it), to a very high frequency γP. Thus it is possible to represent the E of a P in this way: $E = h \cdot 10^n$ [1/s].

If we apply the Principle of Equivalence Mass-Energy ($E = mc^2$) to the P, our calculations show that the P has a minimum *equivalent rest-mass* (*Zero Point Mass*) equal to 10^{-48} [g].

1. INTRODUCTION

The P is the *light quantum*, the electromagnetic radiation (*EMR*) *quantum*, which energetic value is represented by the *Planck's constant* (h) — equal to $6.625 \cdot 10^{-27}$ [erg$\cdot$ sec] — times the number of oscillations the P makes in a second, that is times its frequency (f):

$$E = hf. \tag{1}$$

As we learn from the electromagnetic spectrum the number of oscillations (10^n) of a *EMR quantum* can be considerably different. It starts from 10^{27} c.s., or more, of a highly energetic γP, to an *extremely low frequency* P, which may have few oscillations per second, or just one cycle per second (we cannot exclude it). Thus the value of f in Eq. (1) is not defined, but extremely variable, according to the EM band we consider. Thus we should indicate f with 10^n [1/s], where n can start from 0, that is one oscillation per second (since $10^0 = 1$), to 27 [c/s] of a very high frequency γP, or even a bit further. Thus it is possible to represent the energy of a P as follows:

$$E = h \cdot 10^n \text{ [1/s]}, \tag{2}$$

where n, of course, gives the number of oscillation per second. What cannot be accepted is $f = 0$, since the P is always emitted by the EM source along with an oscillating propagation motion, besides $f = 0$ would cancel the energy of the P itself, as we infer from (1). Moreover it is the Quantum Mechanics (QM) itself, through Heisenberg Uncertainty Principle (HUP), to avoid a P with $f = 0$, since a P which does not oscillate is a motionless P, in this case we would know simultaneously 2 *complementary parameters* of the same particle: its position and *momentum*.

2. DISCUSSION

Along with the Eq. (1), Feynman said: "the energy of a P is Planck's constant times the frequency. That is true, but since the frequency of light can be anything, there is no law saying that energy has to be a certain definite amount. Unlike Dennis' blocks, there can be any amount of energy, at least as presently understood. So we do not understand this energy as counting something at the moment, but just as a mathematical quantity, which is an abstract and rather peculiar circumstance" [1]. However if we consider the minimum oscillation as a point of reference (hypothetically possible) which a P can make in a second, that is one oscillation, $f = 10^0$ [1/s], we have:

$$E = h \cdot 10^0 \text{ [1/s]} = h \cdot 1 \text{ [1/s]}. \tag{3}$$

In this way the (3) can represent the possible Minimum Energy State of a P. At this concern Chandrasekhar said: "a fundamental consequence of the quantum nature of the matter is that the lowest possible energy for a system cannot be zero, it must have a value $\neq 10$, it is called *Zero Point Energy*" [2]. It is clear that the Eq. (3) gives a limit case, the minimum value hypothetically possible. Besides Einstein Principle of Equivalence Mass-Energy, represented by Eq. (4):

$$E = mc^2, \tag{4}$$

refers first of all to values *at rest* of the particle considered. This is how Einstein himself defined this Principle: "it represents the connection between *inertial mass* and energy" [3]. Thus, according to this Law, if we wish to study the *inertial mass* of a particle, it seems important to consider first the *inertial energy* of the particle itself, which should correspond, be *equivalent*, just to its possible, hypothetical *value of minimum energy* which, in the case of P, is represented by the Eq. (3). Thus, if we substitute the values of (3) with those of Eq. (4), we have:

$$m = E/c^2 = h(10^0\,[1/\mathrm{s}])/c^2 = (6.6252 \cdot 10^{-27}\,[\mathrm{erg}\cdot\mathrm{s}]) \cdot (1\,[1/\mathrm{s}])/(2.9979 \cdot 10^{10}\,[\mathrm{cm/s}]). \tag{5}$$

If we write the (5) according to the *cgs* system we have:

$$m = (6.6252 \cdot 10^{-27})/(2.9979)^2 \cdot 10^{20}\,[\mathrm{erg}]/[\mathrm{cm/s}]^2. \tag{6}$$

Since the *erg* value is expressed in $[\mathrm{g}\cdot\mathrm{cm/s^2}\cdot\mathrm{cm}]$, that is in $[\mathrm{g}\cdot\mathrm{cm^2/s^2}]$, we have:

$$\begin{aligned} m &= 6.6252/(2.9979)^2 \cdot 10^{(-27-20)} \left[\mathrm{g}\cdot\mathrm{cm^2/s^2}\right] / \left[\mathrm{cm^2/s^2}\right] \\ &= 6.6252/8.9874 \cdot 10^{-47} \left[\mathrm{g}\cdot\mathrm{cm^2/s^2}\right] \cdot \left[\mathrm{s^2/cm^2}\right]. \end{aligned} \tag{7}$$

Then we have:

$$m = 0.7372 \cdot 10^{-47}[\mathrm{g}], \tag{8}$$

and:

$$m = 7.372 \cdot 10^{-48}[\mathrm{g}]. \tag{9}$$

This is the hypothetical minimum *inertial mass* (*rest mass*) of the P, the smallest possible, since we considered the minimum possible oscillation for the P, that is one oscillation per second! It is an extremely low value, yet $\neq 0$. We may call it: *Zero Point Equivalent-Mass* of the P.

3. CONCLUSIONS

In order to simplify the calculations we considered the smallest *inertial energy* of the P. Eq. (9) takes into account the minimum possible frequency for the P, that is $n = 0$, as we have from Eq. (2). However, it is clear that it is not possible to know with accuracy what the P *minimum energy state* can be: this *undetermination* goes within the QM. That is the minimum value of n in Eq. (2) *cannot be determined with accuracy*, moreover it can change in different circumstances. Thus we can write the P *inertial-mass* formula as follows:

$$m = 7.372 \cdot 10^{-48}[\mathrm{g}\cdot\mathrm{s}] \cdot 10^n\,[1/\mathrm{s}] = 7.372 \cdot 10^{-48+n}\,[\mathrm{g}]. \tag{10}$$

Thus, in case the P at the *inertial state* oscillates, about 100 times per second, $10^2\,[1/\mathrm{s}]$, we have that (10) is as follows:

$$m = 7.372 \cdot 10^{-48+2} = 7.372 \cdot 10^{-46}[\mathrm{g}]. \tag{11}$$

If n was 3, we would have $m = 7.372 \cdot 10^{-45}\,[\mathrm{g}]$. However the *inertial mass* of the P does not change significantly.

What do we get from these calculations? The P is not so evanescent, ethereal, it carries an equivalent mass equal to its energy divided c^2 [5, 6]. This should not amaze us. The Universal Gravitation Law states that the gravity force (GF) takes place only between bodies having a mass. Einstein's prediction, based on the Theory of General Relativity, provides that also the light is conditioned by the action of the GF. In fact observations show that the P *feels* the GF, as confirmed firstly by Lord Eddington in 1919 during a sun eclipse. Besides we know that two massless Ps, meeting, *materialise* in a couple of quark-antiquark, or even in a couple muon-antimuon which, summed up, have a mass of 400 electrons. If we apply the Principle of Equivalence Mass-Energy ($E = mc^2$) to the P, we learn that the P may have a minimum *equivalent rest-mass* equal to $10^{-48}\,[\mathrm{g}]$, considering the possibility of one oscillation per second of the examined P.

As we know Feynman stated: "energy and mass differ only by a factor c^2" [1]. Besides: "along with $E = mc^2$, each mass can be expressed in terms of an *equivalent-energy*" [7]. Thus, the opposite may be true too: each energy can be expressed in terms of a *equivalent-mass*.

REFERENCES

1. Feynman, R. P., *The Feynman Lectures on Physics*, Vol. 1, 4–10, 1989; Zanichelli ed., Vol. 1, 17–7, Bologna, 2001.
2. Chandrasekhar, B. S., *Why Things Are the Way They Are*, Cambridge University Press, 1989; il Saggiatore ed., 304, Milano, 2004.
3. Galison, P., *It Must Be Beautiful: Great Equations of Modern Science*, Graham Farmelo ed., 2002; il Saggiatore ed., 119, Milano, 2005.
4. Kane, G., *The Particle Garden*, Gordon Kane ed., 1995; TEA ed., 172, Milano, 2002.
5. Puccini, A., "About the zero mass of photom," *Progress In Electromagnetics Research*, Vol. 55, 117–146, 2005.
6. Puccini, A., "Light weights," *Progress In Electromagnetics Research B*, Vol. 8, 161–177, 2008.
7. *Nuclear Physics*, Vol. 31, National Academics Press, The National Academy of Science, USA, 1986.

A Mechanical Effect Induced by Electromagnetic Radiation May Explain the Wave Function Collapse of a Quantum Object

Antonio Puccini
Department of Neurophysiology, Order of Malta, Naples, Italy

Abstract— When we try to observe a quantum object ($|\psi\rangle$) during its unitary evolving phase (U phase), the Wave Function Collapse of the measured quantum object (QO) set up. The latter undergoes a jump of the quantum state: $|\langle\psi|\phi\rangle|^2$. We have that before the measurement the QO is *delocalised* and behaves almost as a wave. In fact in the experiment of the two holes (if we do not make any measurement) the QO leaves on the screen an interference figure, typical of waves. In the same experiment, if we try to see where the QO passes, we have that it is *localized* and leaves on the screen only point like marks, as a corpuscle.

The experiment shows clearly that as we light the QO, the light modifies its behaviour, going from an undulating-like behaviour to a corpuscular-like one. What makes the differences in the observed QO? What induces the Wave Function Collapse, that is the reduction of the state vector in the QO? We need to remember that the *momentum* (p) of any particle, including the photon (P), is given by the well known formula $p = h/\lambda$, where h is Planck's constant and λ (along with de Broglie's intuitions) corresponds to wave length of the considered particle. Thus a single visible P of a mean wave length has *a momentum* of $p = h/5 \cdot 10^{14}$ [c/s].

Our calculations show that this P has: $p = 1.1623 \cdot 10^{-22}$ [g· cm/s], that is one hundred times bigger than the mass of a proton. We think that it is this huge impact force, carried out by the P, to induce the Wave Function Collapse of the QO hit by the electromagnetic radiation.

1. INTRODUCTION

Quantum Mechanics (QM) gives particles, that is quantum objects (QO), a their own wave function (WF), indicated with $\Psi(x)$, or simply Ψ. It describes both their wave and particle character. These characters, however, are not well outlined. The WF square modulus of a QO, indicated by $\|\Psi\|$, or $|\Psi|^2$, is a measurement of the probability (and only the probability) that the QO is, in a specific moment, in a certain position in the space. QOs do not have defined properties until we observe them, until we make a measurement (M). We can just presume approximately their structure and behaviour, but we have no certitude. In other words, even doing our best we can never have information about the structure of the QO during its linear evolution phase (or U phase). Indeed, as we learn from QM, the observation, the M, modifies the physical system (in the microscopic world) we are examining: not only does it deviate immediately the trajectory of the observed QO but, what is even more interesting, very likely it generates also a deep change in its physical states. It is not known what is the intimate mechanism that, with the M, induces the (temporary) transformation of the QO, that is the transformation of its quantum state, known as quantum jump, represented by the QM formalism:

$$\langle\Psi|\phi\rangle|^2 \tag{1}$$

which describes the probability that a QO, its WF, represented by $\langle\Psi|$, under the effect of a M jumps in one of the possible selfstates, indicated by $|\phi\rangle$. What happens is that with the M, quantum states collapse, that is quantum superimpositions which characterize the WF of the QO observed. The M generates the WF collapse (WFC) of the examined QO. Before the M the QO is potentially detectable in one of the points of its wave volume, each point corresponding to a probability amplitude. During this evolution phase of the QO, probably the quantum superimpositions are distributed, spread, throughout the available space. This physical condition of the QO lasts until it is disturbed, observed. Whereas with the M we have the collapse of the superimpositions of the different quantum states characterizing the QO: they may converge in a circumscribed, localised, space. Thus, the M of the position of a QO generates the so called reduction of quantum superimpositions which characterize it, also known as Amplitude Reduction, or Reduction of the state vector (R Process).

2. DISCUSSION

We learn from the Double Hole Experiment (DHE) that a single QO, not observed, goes surprisingly through both holes at the same time (in fact both photomultipliers go on), each connected to one hole [1], and the QO creates on the back screen an interference figure, typical of waves. We learn from the DHE that when we try to see the QO, it passes through only one of the two holes (never both at the same time: only one photomultiplier goes on, randomly [1]), and it does not create interferences on the screen: it gets there as a corpuscle, a particle (not a wave any more). The M induces immediately the WFC of the observed QO. The M makes the state of the particle jump in a localized state. Thus the QO is now localized in a determined point. The QO goes from the evolution phase U to the R phase. The linear evolution phase U was brilliantly described by Schrodinger through the mathematical formalism of the QM ($i\hbar d\psi/dt = H\psi$). On the contrary, for the WFC "both the fundamental equations of the QM, and Schrodinger equation are mute" [2], they cannot interpret it. Let's try to understand what happens during the R process, what induces the R process and the WFC. What is sure is that in order to make a M of a particle we need to light it. Whether we use the visible light or we use a X ray microscope we are still talking about electromagnetic radiation (EMR), Ps in short.

How is it possible to explain that then? How can a massless particle induce such a disarrangement in the physical structure of the particle it interacts with? Thus, as we can infer from the DHE, also a single P, of course massless, can generate the implosion of a massive, real particle. It is normal to think that it is the energy of the P to induce it. However this explanation does not persuade us completely. How can a massless particle induce, likely, such a volume reduction (in the observed QO), to make its quantum superimpositions converge and collapse in a circumscribed point which were previously delocalized throughout the available space? Among the several hypothesis to interpreter the WFC and the M's Paradox, we share the latter to which, among others, complies Penrose: "the WFC is a real event, objective, not hypothetical. The space where the WFC occurs must be a real space too and represented by Hilber space" [3]. How is it possible to explain in the DHE that the impact on the screen leaves completely different imprints? Both if we watch it and if we don't. Maybe the WFC does not occur always there. If it happened always there we should not have different figures on the screen. We may say that it is the M to modify things. However if we better look at it we realize that the change induced by the M occurs before the screen. That is the M changes the way the QO passes through the hole: we learn it from the DHE. Indeed, if the QO is observed, it will pass only through one hole, randomly [1], whereas if it is not observed it will always pass through both holes simultaneously [1]. Hence we can infer that the main change the M induces in the DHE occurs in the behaviour variations of the QO when passing through the holes. The traces the QO left on the screen are just the consequence of the way it passed through the holes.

Thus, in the case of DHE, the effect of the M on the QO occurs before it passes through the holes: it is here we have to find the solution to the M's Problem. We learn from the DHE that every time we light a QO we change significantly its behaviour, the way it goes through the holes. Hence we get three important data from the DHE: 1) the M of a QO is determined by the impact, the interaction, between the QO and the EMR; 2) this interaction occurs before the QO passes through the holes; 3) what remains on the screen is just a direct consequence of the two data. It is not little. Thus a new character enters in the enigma of the M's Paradox and the search for the intimate mechanism laying behind the WFC: the light, the EMR.

It seems that with the M, that is the light action, the QO takes off its undulating suit and wears on a corpuscular one (in fact ones struck by the light our QO will not leave interference figures on the screen any more, but only localized point like marks, typical of a corpuscular behaviour). Thus, experimental data confirm that the interaction with the light can induce a complete transformation of the behaviour, and presumably of the physical structure of the QO undergoing a M. Again we wonder: how can the simple energy of a massless particle (i.e., a normal P) make such a change?

As we learn from Planck and Einstein [4, 5], the P is the light quantum, the EMR quantum, which energetic value is represented by the energy of Planck's constant (h): $6.625 \cdot 10^{-27}$ [erg·sec], times the number of oscillations the P makes in a second, that is times its frequency (f):

$$E = hf \tag{2}$$

As we learn from Weinberg "a normal luminous wave has a high number of Ps which travel together. Each of them carry a very well defined energy and a momentum" [6]. We see than, as all elementary

particles, also the P has a its own momentum (p) represented in the formula:

$$p = h/\lambda \tag{3}$$

where λ is the wave length of the considered radiant particle. The mean wave length of a P in the optical band corresponds to 500 nanometres or $5 \cdot 10^{-5}$ [cm] and its p is:

$$p = 6.625 \cdot 10^{-27}\,[\mathrm{erg} \cdot \mathrm{s}]/5 \cdot 10^{-5}\,[\mathrm{cm}] \tag{4}$$

Since $1\,\mathrm{erg} = \mathrm{g} \cdot \mathrm{cm}^2/\mathrm{s}^2$, we can write the Equation (4) in another way:

$$p = 6.625 \cdot 10^{-27}\,[\mathrm{g} \cdot \mathrm{cm}^2/\mathrm{s}]/5 \cdot 10^{-5}\,[\mathrm{cm}] \tag{5}$$

We can develop the Equation (5):

$$p = 1.325 \cdot 10^{-22}\,[\mathrm{g} \cdot \mathrm{cm}/\mathrm{s}] \tag{6}$$

3. CONCLUSIONS

What do we get from these calculations? The P is not so evanescent. If we consider that an electron weighs $9 \cdot 10^{-28}$ grams, then P which hit it will make a Force even bigger. This should not amaze us. As we know "when the P weighs upon a surface which absorbs it completely, the P transfers an impulse equal to its momentum (referred to the area unit, this force is a pressure)" [7]. Maybe now we can try to understand why a P, apparently immaterial, can induce the WFC of the struck QO in the M process. It is a typically mechanical effect, we think, carried out by the momentum of the P (it can be compared to a dynamic-mass, carried by the P in motion, which effects are not detectable till the P interacts), to make collapse, implode, the WF of the particle we wish to examine. In order to detect it, it is necessary to see it, to use the EMR. Nor should we be surprised by the mechanical-effect generated by the P: we will list several mechanical actions carried out by the EMR, as the photoelectric effect, the Compton effect, the Raman effect, or the chlorophyllian photosynthesis [8]. All of them take place when EMR beam of a certain frequency reaches the metal-target, hitting the electrons and pushing them away. It is clear that it is a mechanical action to push away the electrons [9]. This action is represented by a push-effect undergone by the electron when it is struck by a P. It is said that it is caused by the energy of the P, however it seems an approximate explanation. In our opinion it seems much more likely that it is the momentum of the P to be transferred to the struck electron, exerting on it a force, a pressure (the radioactive pressure), enough to push it away.

REFERENCES

1. Feynman, R. P., *The Feymann Lectures on Physics*, California Institute of Technology, 1965; Zanichelli ed., Vol. 3, No. 1, 7–10, 2001 (Bo).
2. Miller, A. I., *It Must Be Beautiful*, Great Equations of Moderne Science, by Graham Farmelo, 2002; Il Saggiatore ed., 116–117, Milano, 2005.
3. Penrose, R., *The Road to Realaty*, Roger Penrose, 2004; RCS ed., 517, 518, 786, Milano, 2005.
4. Planck, M., *Verhandlungen der Deutschen Physikalischen Geseehaff*, Vol. 2, 237–245, 1900.
5. Einstein, A., *Annalen der Physik*, Vol. 17, 132–148, 1905.
6. Weinberg, S., *The First Three Minutes*, A Modern View of the Origin of the Universe, 1977 by Steven Weinberg; Mondadori ed., 65–66, Milano, 2001.
7. Frova, A., *La Fisica Sotto Il Naso*, RCS ed., Vol. 131, 346, Milano, 2005.
8. Puccini, A., "About the zero mass of photon," *Progress In Electromagnetics Research*, Vol. 55, 117–146, 2005.
9. Fermi, E., *Atomi, Nuclei, Particelle*, Boringhieri ed. (To), Vol. 24, 2009.

Quantum Mechanics Suggests that Photons with Different Energy Do Not Travel at the Same Speed

Antonio Puccini
Department of Neurophysiology, Order of Malta, Naples, Italy

Abstract— Heisenberg's Uncertainty Principle states that time (Δ_T) and energy (Δ_E) are two parameters *canonically conjugated* and each other correlated by the well known Heisenberg's equation: $\Delta_E \cdot \Delta_T \geq h/2\pi$, where h is the Planck's constant. Hence we know that the members on the left are inversely proportional, thus as one of them increases the other will have to decrease proportionally. Besides if we consider photons (Ps) with different energy, those having a bigger energy will travel in a shorter time, and vice versa. As we know the P also carries a *momentum* (p), divided by the wavelength (λ): $p = h/\lambda$. Therefore, p is not constant for the electromagnetic waves, but is inversely proportional to λ.

Let us calculate the p of the P travelling with a radio wave, where λ is equal to 1 cm:

$$p = 6.625 \cdot 10^{-27}\,[\mathrm{erg} \cdot \mathrm{s}]/1\,[\mathrm{cm}].$$

Since $1\,\mathrm{erg} = \mathrm{g} \cdot \mathrm{cm/s^2} \cdot \mathrm{cm}$, we can write:

$$\begin{aligned} p &= 6.625 \cdot 10^{-27}\,[\mathrm{g} \cdot \mathrm{cm^2/s}]/1\,[\mathrm{cm}], \\ p &= 6.625 \cdot 10^{-22}\,[\mathrm{g} \cdot \mathrm{cm/s}]. \end{aligned}$$

The mean P's p of the visible light will be:

$$\begin{aligned} p &= 6.625 \cdot 10^{-27}\,[\mathrm{erg} \cdot \mathrm{s}]/5 \cdot 10^{-5}\,[\mathrm{cm}], \\ p &= 1.325 \cdot 10^{-27}\,[\mathrm{g} \cdot \mathrm{cm^2/s}]/10^{-5}\,[\mathrm{cm}], \\ \text{we have:}\quad p &= 1.325 \cdot 10^{-22}\,[\mathrm{g} \cdot \mathrm{cm/s}]. \end{aligned}$$

whereas, let us calculate the p of a P travelling with a γ ray, with $\lambda = 10^{-12}$ [cm]:

$$p = 6.625 \cdot 10^{-27}\,[\mathrm{erg} \cdot \mathrm{s}]/10^{-12}\,[\mathrm{cm}] = 6.625 \cdot 10^{-15}\,[\mathrm{g} \cdot \mathrm{cm/s}].$$

That is, the p of a γP is ten millions bigger than the p of a mean P of visible light, and 1000 billiards bigger of the p of a radio P!

We should consider that the p is a *motion* magnitude, thus the bigger a P's p the bigger the *motion*: that is the P's *motion* is not the same for all Ps, it is inversely proportional to the λ of the considered band, along with the well known equation: $p = mv$, hence we know that the velocity (v) of a particle, in a given direction, is directly proportional to its p.

1. INTRODUCTION

As we know electromagnetic waves (EMWs) are characterised by the ratio:

$$\lambda = \frac{v}{f}, \tag{1}$$

where λ is the wavelength, v is the speed of the wave itself, and f is the frequency. It is easy to notice that λ and f are inversely proportional. The third parameter in the Eq. (1), that is v is considered just the same as the speed of light in vacuum (c) and is valid for all the EMWs: 299792.458 ($\pm$0.4) km/sec, or $2.9979 \cdot 10^{10}$ cm/sec [1]. We should add to the three parameters mentioned (v, λ, f), essential to trace the identity of each EMW, a fourth one, equally essential: the *energy* (E), that is the E carried by the wave itself. E is strictly related to the EMW frequency (f). In our case we have (2):

$$E = fh. \tag{2}$$

It is known as Planck-Einstein's equation, where h is the Planck's constant: $6.625 \cdot 10^{-27}$ [erg $\cdot$ sec]. All EMWs carry a certain quantity of E, however this E can have a huge difference between one wave and another, in strict relation with the huge frequency variability with which EMWs propagate.

2. DISCUSSION

As enunciated by the Quantum Mechanics "a photon (P) is like a particle: it carries an E and a *momentum* (p). The E of a P is a certain constant times the f of the P: $E = hf$. Such a P also carries a p, and the p of a P is h divided by the wavelength (λ)" [2] (3):

$$p = h/\lambda. \tag{3}$$

Therefore, the p is inversely proportional to λ. Along with Eq. (3), we calculate the p of the mean P of the visible light:

$$p = h/\lambda = 6.625 \cdot 10^{-27}\ [\text{erg}\ \cdot \text{s}]\,/5 \cdot 10^{-5}\,[\text{cm}]. \tag{4}$$

Since 1 erg $= \text{g} \cdot \text{cm/s}^2 \cdot \text{cm}$, we can write:

$$p = 1.325 \cdot 10^{-27}\ \left[\text{g} \cdot \text{cm}^2/\text{s}\right]\,/10^{-5}\,[\text{cm}], \tag{5}$$

and we have:

$$p = 1.325 \cdot 10^{-22}\,[\text{g} \cdot \text{cm/s}]. \tag{6}$$

Let us consider instead the p of a P travelling with a radio wave, where λ is equal to 1 cm:

$$p = 6.625 \cdot 10^{-27}\,[\text{erg} \cdot \text{s}]/1\,[\text{cm}]. \tag{7}$$

In this case, we notice that the p corresponds to Planck's constant:

$$p = 6.625 \cdot 10^{-27}\,[\text{g} \cdot \text{cm/s}]. \tag{8}$$

We can notice that the value of the p of a P travelling with a radio wave of low frequency is 5 orders of power lower than the p of a visible P.

Let us calculate the p of a P travelling with a γ ray, with $\lambda = 10^{-12}$ [cm]:

$$p = 6.625 \cdot 10^{-27}\,[\text{erg} \cdot \text{s}]/10^{-12}\,[\text{cm}] = 6.625 \cdot 10^{-15}\,[\text{g} \cdot \text{cm/s}]. \tag{9}$$

That is the p of a γP is 10 million times bigger than the p of a mean P of the visible light, and 1000 billions times bigger than the p of a P radio! In this respect, we need to keep in mind that the p is a *motion* magnitude, thus the bigger the p of a P, the bigger the *motion*. As a consequence a bigger p indicates a higher speed of the P itself, as we can infer from the well known Eq. (10):

$$p = mv. \tag{10}$$

As a consequence the bigger the energetic charge discharged by the EM source, the bigger the propulsive push given to the Ps released. Thus the P may travel with a frequency, p and speed (v), directly proportional to the energy freed by the EM source. It may be surprising but the Eq. (10) is valid for the P too, although it is considered massless. It is well known that the P has a its own p: "as all other particles the P has a its own p ($p = mv$), though it is massless" [3]. From Eq. (10), we can infer that in a particle, p and v are directly proportional. If we better look we learn that the propagation speed of the particle depends on its p: that is, taking its value from Eq. (3), it is p to determine the v of a particle. Hence, particles with a bigger p will have a bigger v too, that is they will travel with a bigger speed. This is true for Ps too. This is confirmed by calculations showed. It is indisputable that the p of a γP is slightly bigger than the p of a visible P or a radio P. Thus, along with Eq. (10), also the propagation speed (v) of a γP will be bigger than that of Ps of the optical band or radio bands.

To support these results, we can quote three examples from experiments described in literature or from astrophysical observations which, we think, have not been considered in their complete significance:

1) Feynman says: "It is important to clarify that in the partial reflection from two glass surfaces the variation circle between 0 and 16% repeats more rapidly with the blue light than with the red one. In fact, as we can notice in the figure, the rotation speed of the hand of the imaginary chronometer changes with the colour of the light" [4]: see Fig. 1. "If we look at the figure, we notice that the blue light, in the same unity of time, has formed 5 waves, whereas the red light formed only 3: that is the blue light covers a longer distance than the red light, in the same time. That is the blue light (which is more frequent than the red light) travels with a higher speed of the red light

(which is less frequent). Well, we can repeat the experiments thousand times, they will always give the same result. The example presented is quite easy, it cannot conceal any mistake" [4]. Feynman, one of the most experts of the light's secrets, continues: "the reflection cycles repeat with different intervals because the hand of the imaginary chronometer has to go more quickly when it follows a blue P, than when it follows a red P. In fact, the rotation speed of the hand is the only difference between a red P and a blue one, or a P of any other colour, including X rays and radio waves" [4]. It comes out then, that the blue colour travels with a higher speed than the red one, in the same time. That is a P with a higher f (the blue photon) travels with a higher speed than another P with a f just a bit lower (the red one). Let's analyse now how Ps reflect, that is how they behave in a diffraction reticule. "This particular reticule is made to measure for the red light, it would not work with the blue light because the hand of the imaginary chronometer has to go more quickly when it follows a blue P than when it follows a red P" [4]. We had already under our eyes that the blue light, more frequent and more energetic, travelled more quickly than a P with a lower f and E, such as the red P. We quote: "nature has made several types of diffraction reticules, under the shape of crystals. A salt crystal reflects, only for some angles, X rays, which are light for which the hand of the imaginary chronometer rotates with very high speed, even ten thousand times higher than the visible light. There is a probability amplitude also for propagation speeds higher or lower than the visible light. We have seen that the light does not propagate only on a straight line, now we find that it does not always travel with the speed of light! It could be surprising that to the propagation of a P with different speeds from the conventional one, correspond probability amplitudes which are not null" [4].

2) At the beginning of last century "Lenard had discovered that when the light hit certain metals it caused the emission of electrons from their surface, just as the light had the power to push out the electrons from the atoms. When physicists started to make experiments on this phenomenon (photoelectric effect) they realized, with great surprise, that if they raised the light intensity, the energy of the emitted electrons did not increase; what influenced them instead, were the different colours of the wavelength of the light used: for instance, the blue light gave the electrons a bigger speed than the yellow light. A blue weak light caused the emission of fewer electrons than an intense yellow light, however the few electrons pushed out by the blue light had a bigger speed than any electron pushed out by the yellow light. A red light of any intensity did not cause at all the emission of electrons in certain metals. None of these phenomena could be explained by the old theories of light. Why ever the blue light was able to do something which the red light was not able to do? Einstein found the answer: an electron had to be hit by a *quantum* of E higher than a minimum value in order to absorb enough E to abandon the surface of the metal" [5]. That is, higher than the E which keeps the electron linked to the atom: *threshold value* or *shearing value*. This is illustrated in Einstein's Equation (11):

$$E_{kin} = h \cdot f - E_{link}, \tag{11}$$

where E_{kin} is the kinetic energy acquired by the hit electron, that is the speed it goes away; $h \cdot f$ is the energy of the incident P; E_{link} gives the *binding energy* of the electron, that is the necessary E to free it from the metal (it is also called *extraction work*).

To be more precise, we need to state that it is just the p of the P which needs to have the necessary *power* to remove the electron from the hit metal.

We have seen the big differences that there are between the p of a γP and the p of a visible P or a radio P. It is this difference that explains why the Compton Effect is not elicited by radio Ps, or visible Ps, or UV Ps. It is necessary the *collision power* generated by the p of a XP to generate the Compton Effect. This is indisputable.

Let's analyze now why, differently from blue Ps, red Ps (with the exception of caesium and rubidium, where the binding energy of the electron is very weak) are able to remove the electron from the metal. We learn from Asimov "a violet light *quantum* has double E of a *quantum* of red light" [5]. We have a confirmation if we calculate the value of the *momenta* of respective Ps. Let's consider a P travelling with red light, $\lambda = 780$ nanometres, that is $7.8 \cdot 10^{-5}$ [cm].

Let us calculate its p:

$$p = h/\lambda = 6.625 \cdot 10^{-27}\,[\text{erg} \cdot \text{s}]/7.8 \cdot 10^{-5}\,[\text{cm}], \tag{12}$$

$$p = 6.625 \cdot 10^{-27}\,[\text{g} \cdot \text{cm}^2/\text{s}]/7.8 \cdot 10^{-5}\,[\text{cm}], \tag{13}$$

$$p = 0.8493 \cdot 10^{-22}\,[\text{g} \cdot \text{cm/s}] = 8.493 \cdot 10^{-23}\,[\text{g} \cdot \text{cm/s}]. \tag{14}$$

This is the p of a red P. Let us calculate now the p of a P of the violet band, close to blue, with $\lambda = 390$ nanometres, that is $3.9 \cdot 10^{-5}$ [cm]:

$$p = 6.625 \cdot 10^{-27} \text{ [erg } \cdot \text{s]}/3.9 \cdot 10^{-5} \text{ [cm]} = 6.625 \cdot 10^{-27} \text{ [g} \cdot \text{cm}^2/\text{s]}/3.9 \cdot 10^{-5} \text{ [cm]}. \quad (15)$$

We have :

$$p = 1.6987 \cdot 10^{-22} \text{ [g} \cdot \text{cm/s]}. \quad (16)$$

We notice that the p, that is the impulse, the *power* with which the violet P hits the electron is exactly double of the power with which the p of the red P impacts on the electron. This is why, differently from blue or violet Ps, the red P is not able to remove the electron from the target metal. It is useful to state that the removal of the electron from a metal, by a *sufficiently energetic* P, consists in a *mechanical* phenomenon imputable to the collision undergone by the electron, that is the mechanical impact, the *power* with which the P hits the electron: this power is ascribable to the impulse, that is the value of the p of the incident P. This value doesn't have to be lower than the binding energy of the hit electron. We already knew that from Einstein [6]. Why do electrons hit by a blue light move away from the metal with a bigger speed compared to those hit by red light? We learn from Asimov: "Anyway, the higher the energy of the quantum, the higher also the speed of the electron removed from the metal" [5]. However, we think it is still not sufficiently precise and satisfying to ascribe only to the P' E (thus to its f) the physical explanation of the phenomenon. We infer from the formula:

$$f_{\min} = w/h, \quad (17)$$

where w is the *extraction work* of the electron from the metal, equal to its E_{link}, $f_{\min}$ is the minimum frequency the P has to have to be able to remove the electron. According to which physical modalities the only E of the P can give a bigger or lower speed to the hit electron? Perhaps it is better to say: the e*nergy* of the p is the impulse emitted by the P enough to remove the hit electron from the metal. The bigger the value of p (a sit is possible to infer from our calculations), the bigger the speed with which the electron is removed.

Therefore, the fact that electrons hit by light with different λ (and thus different p) move away with different speed means that different Ps too propagate with different motion values, since the impulse carried by the P, through its p, is passed almost entirely to the electron [7, 8].

What is lost is only the quantity of E and motion equal to the value of w in Eq. (17). It is thus possible to explain Lenard'observations.

3) As we know the *Cherenkov light* (CL) which, as we know, is produced by the collision of γPs with the molecule of the terrestrial atmosphere, removing the electrons with a speed bigger than the solar light's one in the high atmosphere. Also the CL, emitted by these electrons, travels with a higher speed than the common visible light in the atmosphere [9, 10]. The reason of these different velocities has not yet been studied in depth: we deduce, according to the showed calculations, that the peculiar phenomenon of the CL depends on the different f and p of the Ps. Since we are talking about an EM radiation induced by γPs, the CL can represent a concrete proof, real, that γPs too travel with a speed bigger than the visible light, since only γPs accelerate the electrons to a speed bigger than the solar light in the atmosphere. This is supported by our calculations — see Eq. (9) — which show how the p of a γP is 10^7 times bigger of the p of a common visible P.

3. CONCLUSION

We have a confirmation from the Quantum Mechanics, with Heisemberg Ucertainty Principle (HUP), concerning energy (Δ_E) and time (Δ_t) [11]. Heisemberg's ratio is expressed as follows:

$$\Delta_E \cdot \Delta_t \geq h/2\pi. \quad (18)$$

Thus, in order to keep constant or more or less unchanged this ratio, we have that as one of the two terms of the multiplication changes — expressed by the left-hand side of the Eq. (18) — the other will automatically have to compensate the other term [12]. If we apply the HUP to the EM radiation, we have that if Δ_E increases respect to the E carried by the visible Ps, as it happens with a X or a γP for instance, as a consequence the Δ_t value will have to decrease correspondently. So the travelling time of this P will have to be shorter than the travelling time of a visible P, in the same unity of time and space. That is the speed of a XP or a γP is higher than the speed of a visible P. In the same way those Ps carrying a lower E (and a lower p) than the optic Ps, should travel with a speed proportionally lower. This should happen with infrared Ps, microwaves and radio Ps.

REFERENCES

1. Sawyer, K., *National Geographyc Italia*, Vol. 4, 13, 1999.
2. Feynman, R. P., *The Feynman Lectures on Physics*, Californian Institute of Technology, 1965; Zanichelli Ed., Vol. 1, 11–17, Bologna, Italy, 2001.
3. Lesch, H., *Physik fur die Westentasche*, Verlag P., Munchen, 2003; Ponte alle Grazie Ed., Vol. 39, Milano, 2007.
4. Feynman, R. P., *QED: The Strange Theory of Light and Matter*, Richard P. Feynman, 1985; Adelphi Ed., 51–52, Milano, 1989.
5. Asimov, I., *Asimov's New Guide to Science*, 1984; Mondadori Ed., 417–418, Milano, 2004.
6. Einstein, A., *Annalen der Physik*, Vol. 17, 143, 1905.
7. Fermi, E., *Atomi Nuclei Particelle*, Boringhieri Ed. (To), Vol. 24, 2009.
8. Puccini, A., "About the zero mass of photon," *Progress In Electromagnetics Research*, Vol. 55, 117–146, 2005.
9. Cherenkov, V. A., *Doklady Akademy Mauk SSSR*, Vol. 2, 451, 1934.
10. Feynman, R. P. *The Feynman Lectures on Physics*, California Institute of Technology, 1965; Zanichelli Ed., Vol. 1, No. 51, 2–3, Bologna, Italy, 2001.
11. Heisemberg, W., *Zeitschrift fur Physik*, Vol. 43, 184–185, 1927.
12. Puccini, A., "Uncertainty principle and electromagnetic waves," *Journal of Electromagnetic Waves and Applications*, Vol. 19, No. 7, 885–890, 2005.

Low Frequency Surface Plasmon Polaritons on a Periodically Structured Metal Strip with High Confinement of Fields

Jin Jei Wu[1], **Her-Lih Chiueh**[3], **Tzong-Jer Yang**[1], **Di Chi Tsai**[1], **Hung Erh Lin**[2], **Bear Hu**[1], **Ricardo Wu**[1], **Daniel Wang**[1], **Hung Jung Chang**[1], **Chun Cheng Li**[1], **and Ing-Jar Hsieh**[1]

[1]Department of Electrical Engineering, Chung Hua University, Hsinchu 30012, Taiwan, R.O.C.
[2]College of Engineering, Chung Hua University, Hsinchu 30012, Taiwan, R.O.C.
[3]Department of Electronic Engineering, Lunghwa University of Science and Technology
Kueishan, Tayouan 333, Taiwan, R.O.C.

Abstract— One novel conception is proposed in this paper to reduce the crosstalk between transmission lines. We developed a new kind of microstrip line on which the spoof surface plasmon polaritons (SPPs) can propagate in the microwave regime. The microstrip line structure is designed by introducing periodical subwavelength hairpin structure on the lateral edge of conventional microstrip lines. The dispersion relation and bandwidth in the microwave regime are calculated and analyzed by numerical methods. Besides, such periodically structured microstrip lines are fabricated and experimentally verified to support spoof SPPs in the frequency range between 200 MHz and 8 GHz. To take a comparison with the quasi-TEM modes on conventional microstrip lines, the spoof SPPs can be highly localized on the surface of the structured microstrip lines, so the crosstalk between the conventional and the structured microstrip lines is very weak. For instance, the crosstalk between one conventional microstrip line and one structured microstrip line whose period constant is 1 mm are between −15.81 dB and −33.99 dB when the distance between the two microstrip lines is the same as the width of the microstrip line, which is much lower than the crosstalk between two conventional microstrip lines. Therefore this new kind of periodically structured microstrip line will be potential application in the high density microwave circuits or high speed systems.

1. INTRODUCTION

The restrain of the crosstalk between microstrip lines has always been a hot topic in the high speed and high density microwave circuits. The crosstalk becomes a serious problem especially when the microstrip lines are very close to each other. The origin of the crosstalk between microstrip lines has attracted intensive attention these years. For example, FDTD method and circuit approach have been used to analyze the crosstalk between the microstrip lines with finite length [1]. On the other hand, the issue on how to reduce the crosstalk between microstrip lines is highly intensive to study. For instance, wedge shapes are introduced into the microstrip line to reduce the crosstalk [2].

Surface plasmon polaritons (SPPs) on the metal surface are the electromagnetic (EM) excitation that propagates along the metal-dielectric interface, and their fields are evanescent both in the metal and the dielectric. SPPs provide a new solution to solve this issue, which highly localize the EM fields on the metal surface, and therefore are widely studied recently years [3]. So it is natural to expect the SPPs will be of great value for designing circuits with low crosstalk if they were introduced into the microwave regime. However, metals resemble perfect electric conductor (PEC) in the microwave regime, so EM fields are highly delocalized on smooth metal surfaces. Accordingly it is impossible to directly apply SPPs to microwave transmission lines. Recently a novel conception of low frequency SPPs has been proposed [4, 5]. By periodically corrugated subwavelength holes on the metal surface, the penetration of the EM fields into the metal increases. The EM modes on such periodically structured metal surface are referred to as spoof SPPs, whose existing frequencies are controlled by the geometric parameters of the structure. This conception has been theoretically [6] and experimentally [7] verified correctly in the microwave regime.

A novel microstrip line structure whose lateral edge is periodically corrugated with subwavelength hairpin grooves is proposed in this paper. Such hairpin-structured microstrip line support spoof SPPs in the microwave regime, which helps to improve the confinement of the EM fields on the microstrip line. So such structured microstrip line can be used to design microwave circuits with low crosstalk, and a directional coupler composed of a conventional and a hairpin-structured microstrip line. We find that such coupler has much lower crosstalk in comparison with the coupler composed by two conventional microstrip lines. Therefore the hairpin-structured microstrip line can be used in high density microwave circuits.

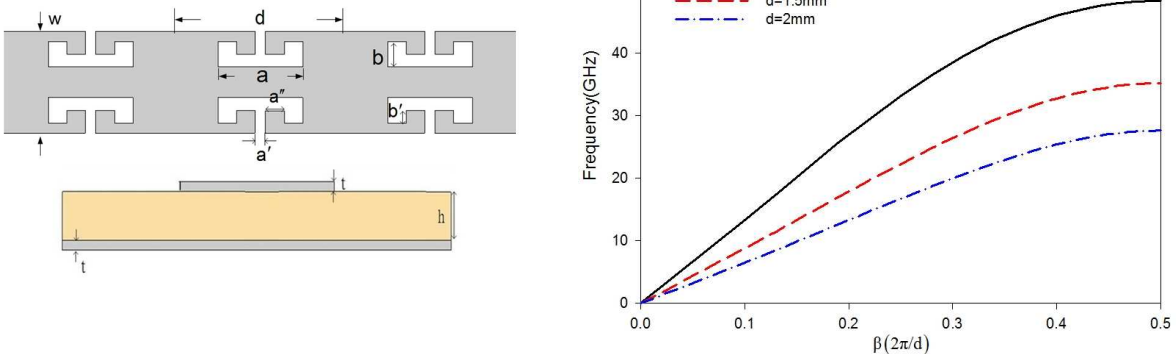

(a) (b)

Figure 1: (a) Hairpin type periodically corrugated metal strip line structure. (b) Dispersion curves for corrugated metal strip lines with three different periods of 1.0 mm, 1.5 mm and 2.0 mm.

2. NUMERICAL ANALYSIS

Consider the structured microstrip line shown in Fig. 1, which is formed by periodically corrugated subwavelength hairpin grooves on the lateral edge of a conventional microstrip line. The width of the microstrip line is $w = 1.2\,\text{mm}$, and the period constant d of the groove array is in a subwavelength scale. The length of the square opening of the hairpin groove is $a' = 0.1w$, the groove depth is $b = 0.25w$. Besides, we have $b' = b/2$, and the normalized groove width is $\bar{a} = a/d = 0.5$ The thickness of the microstrip line and the substrate are $t = 0.0175\,\text{mm}$ and $h = 0.508\,\text{mm}$, respectively. The permittivity of the dielectric in the substrate is $\varepsilon_r = 3.37$. It should be noted that the conventional microstrip line without subwavelength groove array has a characteristic impedance of $50\,\Omega$. We are interested in the propagating properties of the spoof SPPs on the hairpin-structured microstrip line. Fig. 1(b) shows the dispersion relations of the spoof SPPs modes (also called SPP bands) on the structured microstrip lines with different period constant d. The propagation constants (β) of spoof SPPs are restrained within the first Brillouin zone, i.e., $|\beta| \leq \pi/d$ indicating that the actual frequency range of the SPP bands changes with the periodic constant. The asymptotic frequency (f_s) of spoof SPPs, which is evaluated at the edge of the first Brillouin zone ($\beta = \pi/d$), is $f_s \approx 48.4\,\text{GHz}$ for $d = 1.0\,\text{mm}$, $f_s \approx 35.2\,\text{GHz}$ for $d = 1.5\,\text{mm}$ and $f_s \approx 27.6\,\text{GHz}$ for $d = 2.0\,\text{mm}$, respectively, as shown in Fig. 1(b). For these different period constants, the asymptotic frequencies are all in the microwave regime, which provides solutions for the EM fields to be highly localized on the surface of the microstrip line at microwave frequencies.

3. RESULTS AND MEASUREMENT

In order to verify that the hairpin-structured microstrip line can restrain the crosstalk between lines, we designed and analyzed the microstrip line coupler shown in Fig. 2(a) in our experiments. The propagating properties of the hairpin-structured microstrip line are analyzed by measuring the S-parameters using a R&S ZVB8 VNA whose operating frequency range is between 300 kHz and 8 GHz. The microwave signal is injected from Port 1, and the S-parameters are measured on all of the four ports. The coupling efficiency are related with S_{41}, i.e., the crosstalk. The geometric parameters of the hairpin-structured microstrip line are the same as in the numerical analysis, and the same dielectric is used here as in the simulation. The measured S-parameters are depicted in Fig. 2(b), and the S_{21} and S_{41} curves measured on a coupler composed of two conventional microstrip lines are shown in black lines for comparison. The blue dot-dashed lines are the S-parameters when the hairpin-structured microstrip line in the coupler has a periodic constant of $d = 2\,\text{mm}$. At 8 GHz, S_{21} and S_{41} are $-1.53\,\text{dB}$ and $-17.42\,\text{dB}$, respectively. As the frequency increases, the S_{41} curve of the structured coupler deviates from that of the conventional coupler more and more, indicating restrain of the crosstalk. If we decrease the periodic constant to $d = 1\,\text{mm}$, S_{21} and S_{41} are $-1.49\,\text{dB}$ and $-33.99\,\text{dB}$, respectively, at 8 GHz, which indicates that smaller period constant helps to further restrain the crosstalk. So such hairpin-structured microstrip line and the conventional microstrip line can be used alternatively in the high density microwave circuits or high speed systems.

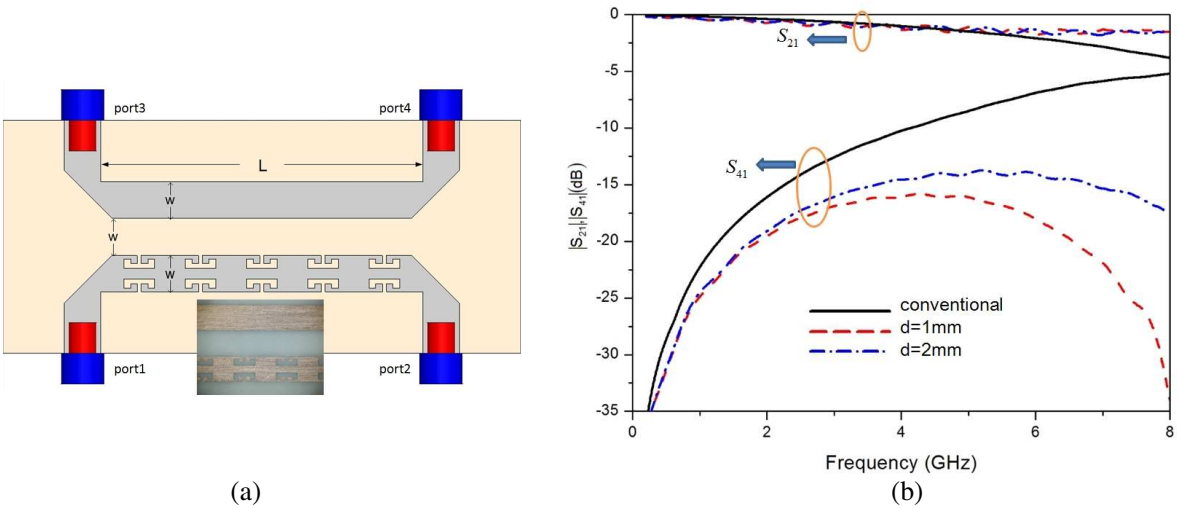

Figure 2: (a) Experimentally measured structure: haipin type periodically corrugated couple metal strip line, (b) experimentally measured data of S parameters with the structure parameters: $w = 1.2\,\text{mm}$, $L = 10\,\text{cm}$, $b = 0.25w$ and $a' = 0.1w$ and $a'' = (a - a')/2$, $b' = b/2$.

4. CONCLUSION

A new microstrip line with subwavelength hairpin grooves on its edge is proposed. The properties of such microstrip lines have been numerically and experimentally analyzed in the microwave regime. The confinement of the EM fields on the structured microstrip line does really exist and is determined by the periodic constant of the hairpin groove array. So such hairpin-structured microstrip line can be used in high density microwave circuits or high speed systems.

ACKNOWLEDGMENT

We would like to acknowledge the National Science Council of ROC for the financial support through the grant number NSC 98-2221-E-216-001.

REFERENCES

1. Xiao, F., W. Liu, and Y. Kami, "Analysis of crosstalk between finite-length microstrip lines: FDTD approach and circuit-concept modeling," *IEEE Transactions on Electromagnetic Compatibility*, Vol. 43, No. 4, 573–578, 2001.
2. Mallahzadeh, A. R., A. Ghasemi, S. Akhlaghi, B. Rahmati, and R. Bayderkhani, "Crosstalk reduction using step shaped transmission line," *Progress In Electromagnetics Research C*, Vol. 12, 139–148, 2010.
3. Raether, H., *Surface Plasmons*, Springer-Verlag, Berlin, 1988.
4. Pendry, J. B., L. Martin-Moreno, and F. J. Garcia-Vidal, "Mimicking surface plasmons with structured surfaces," *Science*, Vol. 305, 847–848, 2004.
5. Jiang, T., L. Shen, X. Zhang, and L.-X. Ran, "High-order modes of spoof surface plasmon polaritons on periodically corrugated metal surface," *Progress In Electromagnetics Research M*, Vol. 8, 91–102, 2009.
6. Wu, J. J., T. J. Yang, and L. F. Shen, "Subwavelength microwave guiding by a periodically corrugated metal wire," *Journal of Electromagnetic Waves and Applications*, Vol. 23, No. 11, 11–19, 2009.
7. Hibbins, P., B. R. Evans, and J. R. Sambles, "Experimental verification of designer surface plasmons," *Science*, Vol. 308, 670–672, 2005.

Selective and Collaborative Optimization Methods for Plasmonics: A Comparison

S. Kessentini[1], D. Barchiesi[1], T. Grosges[1], and M. Lamy de la Chapelle[2]

[1]Project Group for Automatic Mesh Generation and Advanced Methods
Gamma3 Project (UTT-INRIA), University of Technology of Troyes, France
[2]CSPBAT CNRS-FRE3043, UFR SMBH, University of Paris 13, France

Abstract— In this paper, we optimize the size parameters of hollow nanospheres and nanoshells used in cancer photothermal therapy and we focus on two practical therapy cases: the visible range for shallow cancer and the near infrared for deep cancer. For this, we consider analytical models: the Mie theory for coated spheres. The investigated optimization methods are the Evolutionary Method (EM) and the Particle Swarm Optimization (PSO) which are based on competitiveness and collaborative algorithms, respectively. A comparative study is achieved by checking the efficiency of the optimization methods, to improve the nanoparticles efficiency.

1. INTRODUCTION

The biomedical application of plasmonic resonances of metal nanostructures, taking advantage of the acute interaction, between light and metallic objects, remains an open domain even if some recent experimental studies have been already devoted to applications. For instance, the first successes of cancer treatment using nanoparticle-based photothermal therapy (PTT) are encouraging for more investigation in this field to ensure strong and tunable surface plasmon resonance (SPR) for efficient heat conversion. Nevertheless, at our knowledge, up to now, no optimization method has been developed to improve the efficiency of these plasmonic structures, through the mastering of the nanoparticles shape and size.

The nanoshells and the hollow nanospheres are among the most commonly used nanoparticles for PTT. The nanoshells are made of a silica core coated with a thin gold shell while the hollow nanospheres look like a gold bubble. For PTT applications, the illumination of the nanostructure induces an elevation of temperature which is used to burn the cancer cells. The absorption band of these particles can be tuned by adjusting the thickness of the gold shell and the inner radius and thus would enable both strong scattering and absorption efficiency [1]. Therefore, they can be used as contrast agents with dual functions for imaging as well as therapy. In this study, the target is to maximize the electromagnetic absorption of either the nanoshell, or of the hollow nanosphere, computed using the Mie theory (coated sphere) [2], responsible for heating process in PTT. For this, two optimization methods are investigated.

The meta-heuristics used in this study are the Evolutionary Method (EM) which is based on competitiveness and the Particle Swarm Optimization (PSO) which is based on a collaborative search algorithm. Some modifications of these conventional methods were proposed [3, 4] to get faster convergence in the optimization of planar biosensor. The optimization of nanoparticles differs from the one of planar biosensor in terms of the mathematical properties of the model (different topology) — even if the best parameters should correspond in both cases to a plasmon resonance — and the target of the optimization (the maximum of absorbed intensity in the metal instead of the maximum of the reflected intensity). It should be mentioned that a problem of optimization in plasmonics is based on a complex model of interaction between light and matter, depending on many material and geometrical parameters, and therefore requires always the use of rapid optimization method. This paper is organized as follows: the second section presents the PTT using gold nanoshell, hollow nanosphere and other nanoparticles. In the third section, the optimization methods used in this study are briefly described. In the fourth section, simulation results in some commonly used experimental conditions are presented and discussed before concluding.

2. PHOTOTHERMAL THERAPY USING GOLD NANOPARTICLES

The basic concept of nanoparticle-based PTT is the combination of: gold nanoparticles (Au NPs) — which are biocompatible, nontoxic and easily conjugated to antibodies — and suitable light source to allow a safe delivery of heat to a tumor volume. The predominating benefit of such treatment is that it is both safe and efficient [5] as the healthy tissues are almost prevented from the heat

damage, which is inevitable in other thermal treatments (microwave and RF ablation, magnetic thermal ablation, focused ultrasound therapy, etc.). Broadly two optical windows exist in tissue. The main one lies between 600 and 1300 nanometers (nm) and a second from 1600 to 1850 nm [6]. Most biological tissues have a relatively low light absorption coefficient in the visible (VIS) and near infrared (NIR) regions (600–1300 nm) known as the tissue optical window or therapeutic window. Over this window, organic molecules have limited absorption [5], whereas Au NPs absorb light millions of times stronger than the organic molecules. Almost all the absorbed light is converted to heat via nonradiative processes [7]. Therefore, cancer cells embedded with Au NPs receive sufficient heat to induce their necrosis via thermal effect with minimal damage to the surroundings. PTT in the visible region is suitable for shallow cancer (e.g., skin cancer) whereas for in vivo therapy of tumors under skin and deeply seated within tissue, NIR light is required because of its deep penetration due to minimal absorption and scattering-limited attenuation of the hemoglobin and water molecules in tissues in this spectral region. Therefore, in this paper, we are interested in the optimization of gold nanoparticles both in the VIS and NIR regions.

Among the Au NPs used in PTT: nanoshells, nanospheres, nanorods and hollow nanospheres. In 2003, Hirsch et al. [8] firstly demonstrated the NIR PTT both in vitro and in vivo using gold nanoshells. Nanospheres are shown to be of interest only for shallow cancer in the visible range [7]. While, in many experimental studies nanorods are shown to be more efficient than nanoshells and therefore require lower laser intensity for photothermal therapy [7]. Nevertheless, these studies consider only some samples of nanoshells (not optimized). For instance, some experiments [9] show that gold nanorods have optical cross-sections comparable to nanoshells, however, at much smaller effective size. Similarly, nanorods were found to exhibit higher absorption efficiency than nanoshells with the same volume of metal [10]. However, theoretical results show that much improved absorption efficiency could be obtained with nanoshells [11]. Regarding hollow nanospheres, no similar comparison was reported but the advantages of having spherical shape were demonstrated. In fact, most of Au NPs have sizes that are too large or shapes that are too complex for biomedical applications. The right size and shape are needed for effective delivery to locations of interest for detection, imaging, or PTT. In addition, the spectral bandwidth of the surface plasmon absorption should ideally be narrow for a better match with the laser wavelength. The breakdown of the symmetry of nanostructures produces different modes and thus broad spectrum absorption. Therefore, in the ideal case, nanostructures with narrow but tunable absorption band, small size, and spherical shape are preferred [12, 13]. Hollow nanospheres guarantees such tunable resonance of plasmon absorption at different wavelength ranging from VIS to NIR as they were synthesized with great precision and controlled dimensions [1].

In what follows, the purpose is to find the best parameters set (r and e) to maximize the absorbed density of electromagnetic power, through a more efficient method than the basic double loop on these parameters.

3. OPTIMIZATION USING EVOLUTIONARY METHOD AND PARTICLE SWARM OPTIMIZATION

In this section, brief overviews of the methods used to optimize the structure (inner radius r and shell thickness e of nanoshells or hollow nanospheres) for getting a maximal absorption $M(t)$ in the shell, are given. For the above mentioned reasons, in this study, the target is to maximize the electromagnetic absorption of objects with spherical symmetry enabling PTT in VIS and NIR, i.e., hollow nanosphere and nanoshell. Actually, under continuous illumination by a laser at wavelength λ_0, the absorbed density of power is a function the inner radius r and the thickness of gold e: $M(r,e) = \pi c \Im(\varepsilon)|\mathbf{E}|^2/\lambda_0$, with c the speed of light in vacuum, $\Im(\varepsilon)$ the imaginary part of the permittivity of the absorbing medium (gold), $\mathbf{E}$ the electric field in this medium which is produced by the illumination, and λ_0 the illumination wavelength. In thermal problems, $M(r,e)$ is the source term of the heat equation. The electric field absorbed in the investigated nanoparticle (dielectric spheres with Au coating or hollow gold shells) is computed using Mie theory [2, 11]. The purpose of the optimization is to find as quickly as possible the best parameters (r,e) to reach the target $\max(M(r,e))$. Therefore, the fitness function of the optimization is $M(r,e)$.

3.1. ANUHEM

Evolutionary Methods were first introduced by Schwefel in 1995 [14] and also, among all, applied to the resolution of inverse problem [15]. The evolutionary method investigated in this study is a modified evolutionary method: the Adaptive Non Uniform Hyper Ellistist Evolutionary Method

(ANUHEM) [4]. The evolutionary scheme consists basically of four steps: initialization, recombination, mutation and selection. A first population of parameters $x(1) = (r_i, e_i)$, $(i = 1 \dots \mu)$, with μ "parents", is randomly generated and $M(x(1)) = M(1)$ is evaluated and then begins the evolutionary loop on generation (or step) t:

1. *Recombination* (or crossover): randomly extracted elements of the initial population are combined together to lead to a secondary population of λ elements. The quality of each element (inverse value of the fitness function in case of minimization problem) is used to weight each element, leading to a barycentric approach.
2. *Mutation*: these elements are randomly mutated through a non-uniform law and evaluated $(M(x(t)) = M(r_j, e_j) = M(t)$ with $(j = 1 \dots \lambda)$ is computed). The Non-Uniform law is $NU(T, b, t) = 1 - U(0,1)^{(1-t/T)^{b(t)}}$, where $U(0,1)$ is the Uniform Law in $[0,1]$, t is the generation (iteration step), T is the maximum of allowed generations for the process, $b(t)$ is the adaptive term determining the degree of non-uniformity of the fitness function and given by the ratio of the standard deviation of the population to the standard deviation (std) of the fitness function, and this, for each element of $x(t)$: $b(1) = 1$ and $b(t+1) = std(M(t))/std(x(t))$.
3. *Selection*: the μ best elements are selected (the μ bests of $\max_j(M(t))$). This step is highly *selective*.
4. The initial population becomes the selected one.

ANUHEM uses the non-uniform mutation that increases the search capability of the algorithm, and weighted recombination that enables faster convergence toward the best set of parameters, compared to other evolutionary scheme [4].

3.2. PSO and Adaptive PSO (APSO)

Particle swarm optimization (PSO) was first introduced by Kennedy and Eberhart in 1995 [16] and imitates the swarm behavior to search the best solution. The PSO is basically a *cooperative* method where the vector of parameters $x(t)$ at step t is considered as a particle. The searched parameters are therefore considered as particles of a swarm which communicate good positions to each other and adjust their own position and velocity $V(t)$ based on these best positions as following:

$$V(t+1) = \omega(t)V(t) + U_1 c_1(t)(p(t) - x(t)) + U_2 c_2(t)(g(t) - x(t)) \quad (1)$$

$$x(t+1) = x(t) + V(t+1) \quad (2)$$

where $U_i\,(i = 1, 2)$ are independent random uniform variables between 0 and 1, $p(t)$ is the particle best position at step t, $g(t)$ is the global best over previous generations, $\omega(t)$ is the inertial weight and $c_i(t)$ $(i = 1, 2)$ are the acceleration coefficients. Equation (1) is used to calculate the particle new velocity using its previous velocity and the distances between its current position and its own best found position, i.e., its own best experience $p(t)$ and the swarm global best $g(t)$. Then the particle moves toward a new position following Equation (2). Similarly to ANUHEM, the particles keep moving in this method until the stop criteria are met (similar stop criteria will be adopted in section 4). The success of PSO strongly depends on values taken by c_1 and c_2. Zhan et al. outlined the necessity of updating these parameters following the evolutionary state determined using the mean distance between all the particles and the best one [17]. The method is fully described in [17] and cannot be summarized here. APSO was efficiently applied to a set of test functions and an improvement of the convergence speed of this method was proposed in a previous study [18] by decreasing the impact of the particles getting out of the domain of the physically acceptable parameters.

4. RESULTS AND DISCUSSION

Firstly, the endogenous parameters related to the model, and the exogenous ones related to optimization methods are fixed. The hollow particles can be made in sizes ranging from 10–12 nm in radius (outer radius) and 3 nm in shell thickness with a precision of 0.6 nm [1]. For this we can consider hollow gold nanospheres and nanoshells having an inner radius within the range 5–50 nm and a metal thickness 2–30 nm which is an ideal range for biological applications that require small particles to be incorporated into living cells. Two different wavelengthes are considered $\lambda_0 = 633$ nm in the VIS range and $\lambda_0 = 800$ nm in the NIR range; which correspond to the treatment of shallow cancer (the case studied is skin dermis with refractive index 1.55 [6]) and deep cancer (the case studied is subcutaneous fat with refractive index 1.44 [6]), respectively. The exogenous parameters

Table 1: Optimization of hollow gold nanosphere and silica-gold nanoshell absorption through the size control (inner radius: r and shell thickness: e) to maximize the absorption. The target is $M = \max(|E|^2)$ in the metal.

		$\lambda_0 = 633\,\text{nm}$		$\lambda_0 = 800\,\text{nm}$	
		hollow nanosphere	nanoshell	hollow nanosphere	nanoshell
Best solution	e,r (nm)	$r = 7$, $e = 3$	$r = 5.5$, $e = 3$	$r = 25.5$, $e = 3$	$r = 21$, $e = 3$
	M	$M = 103$	$M = 82.5$	$M = 149$	$M = 139$
Standard PSO	Success (%)	86.7%	79.7%	89.7%	84.6%
	Evaluations	285	320	278	325
APSO	Success (%)	98.8%	100%	100%	100%
	Evaluations	217	307	158	220
ANUHEM	Success (%)	100%	100%	100%	100%
	Evaluations	106	120	259	183

used for ANUHEM are the size of the initial and secondary populations $\mu = 5$, $\lambda = 25$ (typically $5 \leq \frac{\lambda}{\mu} \leq 7$ is the most efficient as discussed in [4, 14]) and $T = 40$ [3]. For PSO and APSO, the population size is set to 20. $c_1 = 0.738$ and $c_2 = 1.51$ and ω is linearly decreased for PSO whereas the parameters are updated following the evolutionary state as mentioned in [17] for APSO. The same stop criteria are defined for all optimization schemes: the loops are interrupted if the distance between all particles/seeds ($x(t)$), at iteration t, is lower than 1 nm, or if the number of evaluations of the fitness function M exceeds 1000. Let us underline that if an approximation of the best solution is computed through a systematic double loop on r and e, 4592 evaluations are required with a discretization of 0.5 nm.

A classical test of efficiency of the optimization methods consists in repeating several realizations of the optimizations, and the success rate is defined by the percentage of realizations that succeed to find the best solution. Thousand realizations are done for both algorithms: the success percentage and the mean number of evaluations needed to converge are reported in Table 1, as well as the best parameters (r and e) that guarantee the maximal absorption.

Results show that the standard PSO fails to avoid local optima: about 15% of failure for the different cases (particles are trapped in local optima). Therefore, improved PSO like APSO (almost 100% of successful trials) should be used for further SPR optimization schemes. Comparing APSO to ANUHEM, we find that APSO is faster for the optimization of hollow nanosphere for treatment of deep cancer ($\lambda_0 = 800\,\text{nm}$) and that ANUHEM is more interesting in the other cases. Consequently, both strategies of optimization could be retained for plasmonics more complex problems. Both methods enable rapid convergence to the global optimal solution and thus their efficiency is confirmed. The maximum local field absorption is obtained at a wavelength of 800 nm for an inner radius of 25.5 and 21 nm for hollow nanosphere and silica-gold nanoshell, respectively (same shell thickness of 3 nm). This result is consistent with the optimization of the absorption cross section [11]. Similar results are obtained in the VIS which show that optimized hollow nanospheres are slightly larger in size. However, they exhibit more absorbtion and then would be more recommended mainly as forming a uniform shell on the silica core is very difficult for small clusters [7, 12].

5. CONCLUSION

The absorption of gold nanoshell and hollow nanosphere in two practical cases (shallow cancer and deep cancer) by means of the Mie theory has been optimized. The optimized results enables a comparison between silica-gold nanoshell and hollow nanosphere, and show that hollow nanosphere are slightly larger in size but exhibits more absorbtion. The radius of hollow nanosphere is greater than this of the nanoshell for both VIS and NIR wavelengthes ranges, but it has better efficiency in NIR. The thickness of the shell is always 3 nm, despite the change of the inner material in the two configurations. Concerning the optimization methods, the selective ANUHEM and cooperative APSO have comparable performances and succeed to avoid local optima (unlike the standard PSO). For further applications (other wavelengths and/or tissues and other SPR schemes), these two optimization methods could be used to optimize more complex plasmonic structures, the number of required evaluations to reach convergence being at least one order of magnitude less than that

required by systematic search.

ACKNOWLEDGMENT

This work was supported by the "Conseil Régional de Champagne Ardenne", the "Conseil Général de l'Aube" and the *Nanoantenna* European Project (FP7 Health-F5-2009-241818).

REFERENCES

1. Adam, M. S., T. Y. Olson, C. E. Talley, and J. Z. Zhang, "Synthesis, characterization, and tunable optical properties of hollow gold nanospheres," *J. Phys. Chem. B*, Vol. 110, 19935–19944, 2006.
2. Bohren, C. F. and D. R. Huffman, *Absorption and Scattering of Light by Small Particles*, New York, Wiley-Interscience, 1998.
3. Kessentini, S., D. Barchiesi, T. Grosges, L. Giraud-Moreau, and M. Lamy de la Chapelle, "Adaptive non-uniform particle swarm optimization: Application to plasmonic design," *International Journal of Applied Metaheuristic Computing, Special Issue on: Metaheuristics and Their Applications to Industrial Engineering*, to appear 2010.
4. Barchiesi, D., "Adaptive non-uniform, hyper-ellitist evolutionary method for the optimization of plasmonic biosensors," *Proceedings of International Conference on Computers and Industrial Ingineering (CIE39)*, Vol. 1, No. 3, 542–547, 2009.
5. Liu, C., C. Chris Mi, and B. Q. Li, "Energy absorption of gold nanoshells in hyperthermia therapy," *IEEE Transactions on Nanobioscience*, Vol. 7, No. 3, 206–214, 2008.
6. Duck, F. A., *Physical Properties of Tissue A Comprehensive Reference Book*, Academic Press, London, San Diego, 1990.
7. Huang, X. and M. A. El-Sayed, "Gold nanoparticles optical properties and implementations in cancer diagnosis and photothermal therapy," *Journal of Advanced Research*, Vol. 1, No. 1, 13–28, 2010.
8. Hirsch, L. R., et al., "Nanoshell-mediated near-infrared thermal therapy of tumors under magnetic resonance guidance," *Proc. Natl. Acad. Sci.*, Vol. 100, No. 23, 13549–13554, USA, Nov. 2003.
9. Prashant, K. J., K. S. Lee, I. H. El-Sayed, and M. A. El-Sayed, "Calculated absorption and scattering properties of gold nanoparticles of different size, shape and composition: Application in biological imaging and biomedicine," *J. Phys. Chem. B*, Vol. 110, No. 14, 7238–7248, 2006.
10. Harris, N., M. J. Ford, P. Mulvaney, and M. B. Cortie, "Tunable infrared absorption by metal nanoparticles: The case of gold rods and shells," *Gold Bulletin*, Vol. 41, No. 1, 2008.
11. Grosges, T., D. Barchiesi, T. Toury, and G. Grehan, "Design of nanostructures for imaging and biomedical applications by plasmonic optimization," *Opt. Lett.*, Vol. 33, No. 23, 2812–2814, 2008.
12. Zhang, J. Z., "Biomedical application of shape-controlled plasmonic nanostructure: A case study of hollow gold nanospheres for photothermal ablation therapy of cancer," *J. Phys. Chem.*, Vol. 1, 686–695, 2010.
13. Adam, M. S. and J. Z. Zhang, "Novel optical properties and emerging applications of metal nanostructures," *J. Physical Chemistry C*, Vol. 112, 10323–10337, 2008.
14. Schwefel, H., *Evolution and Optimum Seeking*, John Wiley & Sons Inc., New York, 1995.
15. Macias, D., A. Vial, and D. Barchiesi, "Application of evolution strategies for the solution of an inverse problem in near-field optics," *J. Opt. Soc. Am. A*, Vol. 21, No. 8, 1465–1471, 2004.
16. Kennedy, J. and R. Eberhart, "Particle swarm optimization," *Proc. IEEE International Conference on Neural Networks*, Vol. 4, 1942–1948, Path, Australia, 1995.
17. Zhan, Z.-H., J. Zhang, Y. Li, and H. S.-H. Chung, "Adaptive particle swarm optimization," *IEEE Transactions on Systems, Man, and Cybernetics — Part B: Cybernetics*, Vol. 39, No. 6, 1362–1381, 2009.
18. Kessentini, S. and D. Barchiesi, "A new Strategy to improve particle swarm optimization exploration ability," *Proc. Second Global World Congress on Intelligent Systems*, Wuhan, China, Dec. 2010.

Electromagnetic Heat-induced in Meso-structures: Computation of Temperature in Metallic Dimers

D. Barchiesi[1], **T. Grosges**[1], **E. Kremer**[2], **and M. Lamy de la Chapelle**[3]

[1]Project Group for Automatic Mesh Generation and Advanced Methods
Gamma3 Project (UTT-INRIA), University of Technology of Troyes, France
[2]XLIM, Department of OSA, CNRS-UMR 6172, University of Limoges, France
[3]CSPBAT CNRS-FRE3043, UFR SMBH, University of Paris 13, France

Abstract— The illumination of a dimer metallic nanostructure is known to produce an intense source of light, with nanometric size. This confinement of light in the gap between the two material structures can induce an increase of the absorption of the electromagnetic energy in the nanaoantenna itself, and therefore its warm-up. The multiphysics problem associated to this photo-thermal effect is modeled through a Finite Element Method (FEM). This contribution consists in computing both the electromagnetic field and the temperature, and discussing the influence of the gap, in the case of a bow-tie nanoantenna. The applications could be the development of nanodevices with thermal properties.

1. INTRODUCTION

The concept of micro-thermic was recently introduced in nanotechnology [1, 2]. The topics of interest were essentially the thermal radiations of Atomic Force Microscope (AFM) and the thermal gradient distribution [3, 4]. Nevertheless, only a few experimental data on the thermal properties of nano-materials are available [5, 6] but a large new field of investigation is open, experimentally and theoretically, on the thermal effects at the micro and nanoscale [7, 8]. The fluorescence lifetime of molecules in the vicinity of metallic nanostructures is known to depends on materials and separation [9, 10] but also on temperature. Therefore, a temperature mapping near nanostructures has been recently proposed, by measuring fluorescence anisotropy [6]. Despite this lack, it is straightforward that laser induced effects can lead to non negligible thermal effects on near-field optics probes. Therefore, it becomes necessary to develop theoretical and numerical models in photo-thermics [11, 12] in order to predict the elevation of temperatures in such structures.

Among the family of nanosensors and nanodevices, the nanoantennas that are of great interest in various engineering domains (optics, photonics, biology...), the bow-tie nanoantenas support multiple resonances and have promising spectral properties [13, 14]. In such dimer nanoantennas, a strong field enhancement appears in the gap, depending on material and geometry of the two top-to-tail gold triangles [13, 15] which can lead to act as thermal nanometric source [16].

In this paper, we investigate the influence of the gap which is a critical parameter of nanoantennas, on the photo-induced heating, through FEM solving of the electromagnetic and thermic partial differential equations, in a $(2D)$ geometry. The paper is organized as follows. Section 2 is devoted to describe the method used to compute the coupled partial differential equations (PDE), including optical and thermal contributions. In Section 3, a discussion on the physical parameters, and numerical results are given. The application to bow-tie nanoantenna are presented and discussed, before concluding.

2. MODEL AND FEM FORMULATION

FEM has proved to be an efficient method for the computation of electromagnetic field around nanostructures [8]. The main advantages of the FEM are first its ability to treat any type of geometry and material inhomogeneity (with complex permittivity) [8], second the control of the accuracy of computation to evaluate accuracy of solutions, by using a non regular mesh of the domain of computation. The FEM is also known to be efficient in the resolution of multiphysics problems as well as non linear ones.

The PDE system is formed of the Helmholtz' for non-magnetic material with harmonic time dependence, and the Poisson's equations (the stationary heat equation, coupled by a source term

in the second one [12]:

$$\left[\nabla\cdot\left(\frac{1}{\epsilon_r(y,z)}\nabla\right)+\frac{\omega^2}{c^2}\right]H_x(y,z)\;=\;0 \tag{1}$$

$$\left[\nabla\cdot(\lambda(y,z)\nabla)\right]T(y,z)+\frac{\omega\epsilon_0\Im(\epsilon_r(y,z))}{2}\left|\mathbf{E}(y,z)(\epsilon_r)\right|^2\;=\;0, \tag{2}$$

where $\nabla=(\partial_x,\partial_y,\partial_z)$ is the differential vector operator, in cartesian coordinates, $\cdot$ is the scalar product, c is the speed of light in vacuum, ω the angular frequency of the monochromatic wave, $\lambda(y,z)$, the thermal conductivity, $\epsilon_r(y,z)$ the relative permittivity of media, and ϵ_0, the permittivity of vacuum. The shape of the gold bow-tie nanoantenna is defined in the (y,z) plane, as the electric field $\mathbf{E}(y,z)$ which is deduced from the magnetic field $H(y,z)$ along x direction, through the Maxwell-Ampere's equation.

The boundary conditions result from the integration of the PDE and therefore from the flux continuity [17]:

$$\mathbf{n}_{12}\cdot\left[\left(\frac{1}{\epsilon_2}\nabla H_2\right)-\left(\frac{1}{\epsilon_1}\nabla H_1\right)\right]=0\quad\text{ and }\quad\mathbf{n}_{12}\cdot[(\lambda_2\nabla T_2)-(\lambda_1\nabla T_1)]=0 \tag{3}$$

where $\mathbf{n}_{12}$ is the normal to the boundary vector, ϵ_k, $k=1,2$, are the complex permittivity and λ_i, the thermal conductivity of the nanoantenna and surrounding medium respectively. The electromagnetic boundary condition (Eq. (3)) in 2D geometries, is formally equivalent to the continuity of the tangential component of the electric field. The boundary conditions on the fictitious external boundary of the domain of computation (vacuum), corresponding to the free propagation of the diffracted field H_2-H_i [17] and to the incoming illumination H_i, are defined by:

$$\mathbf{n}_{12}\cdot[(\nabla H_2)]=\jmath\left[\mathbf{k}\cdot\mathbf{n}\right]\vec{H}_i+\jmath\frac{\omega}{c}(H_2-H_i)\quad\text{ and }\quad\mathbf{n}_{12}\cdot[(\lambda_2\nabla T_2)]=0, \tag{4}$$

where H_i is the illuminating monochromatic, lying along x, magnetic field: $H_i=H_i^0\exp(j\omega t-\jmath\mathbf{k}\cdot\mathbf{r})$, with $\mathbf{k}=(0,\omega/c,0)$, the wave vector, and j the square root of -1. The solution of this FEM formulation, including a improved remeshing procedure, has been checked and compared with rigorous Mie theory [18–20]. To evaluate the temperature, the power P of the laser and the numerical aperture NA of the objective lens used to focus the beam of power on the nanoantenna must be used to calculate the amplitude of the incoming magnetic field: $H_i^0=\omega\frac{NA}{1.22}\sqrt{\frac{2P\pi\epsilon_0}{c}}$.

3. PHYSICAL PARAMETERS AND NUMERICAL RESULTS

In the photo-thermal problem, two parameters are involved: the relative permittivity $\epsilon_r(y,z)$ and the thermal conductivity $\lambda(y,z)$. The relative permittivity appears in both Equations (1) and (2) and is consequently a critical parameter for the heating computation. Nevertheless, unlike models of phase change [8], we can suppose that there are no variations of material properties or of geometry of the nanoantenna. Actually, the temperature elevation is supposed to be small enough to be able to neglect dilations [6, 11]. The corresponding correction of the optical properties of such nanostructures has been rarely introduced, for the following reasons that are directly related to the typical size L of the nanostructures:

- No quantum effects are observed at this scale in metallic structures. As to it, the thermal De Broglie wavelength of a conduction electron in the gold nanostructure being Λ, the quantum effect can be neglected if the mean-free path of electrons is greater than $\Lambda=4\,\text{nm}$.
- the thermal dilation of nanostructures is neglected and therefore, neither variation of density nor change in optics properties has been took into account [21].
- Indeed, the size of each triangle of the bow-tie is almost one order of magnitude greater than the nanometric critical size for bulk permittivity validity of gold spherical nanoparticles [22]. If the size of the nanostructure is smaller than the bulk mean-free path of electron in gold ($l_e\approx 42\,\text{nm}$), the effective mean-free path of electron is reduced typically to the size of the nanostructure [23]. Moreover, the mean-free path of photon in a gold sphere of radius 45 nm, for $\lambda_0=600\,\text{nm}$, through Mie theory has been found to be smaller than the bulk value: 11 nm [24]. Nevertheless, the non negligible decrease of the imaginary part of the

permittivity of nanostructures has been observed for silver nanowires by fitting models with experiments [25]. In that paper, the imaginary part of the effective permittivity of silver has been shown to be the bulk one divided by three.

Therefore, even if in the investigated case of nanoantenna, the size L of the nanoantenna verifies $L > l_e > \Lambda$, a correction of the imaginary part of the permittivity is proposed to take into account the balance between diffusive and ballistic electrons in the nanostructures. The correction of the imaginary part of the permittivity $\Im(\epsilon_r)$, which is proportional to the electric conductivity of material, is deduced from the model described in [26]. The ratio of the imaginary part of the permittivity of the nanomaterial (ϵ_r) to the bulk one (ϵ_b) is known for nanowires [26]: $\Im(\epsilon_r) = C\Im(\epsilon_b) = \left[1 + \frac{3}{16}(1-p)l_e\frac{3L}{S}\right]^{-1}\Im(\epsilon_b)$, where p is the fraction of electrons scattered elastically at the surface of material, $l_e = 42\,\text{nm}$ the electron mean-free path in bulk gold, $3L$ the perimeter of the triangular cross-section and $S = L^2\sqrt{3}/4$ the cross-sectional area.

The evaluation of C for bow-tie shape remains open and therefore, we evaluate its variation for p in the interval $[0;1]$, including the geometry of each nanostructure of the bow-tie antenna: $C \in [0.71;1]$. Usually the parameter p is estimated to get the best fit with experimental data. In the following, $C = 0.83$ is used, corresponding to an equal contribution of diffuse and specular reflections of electron at surface, $p = 0.5$, and therefore, $\epsilon_r = -9.5 + j$ for gold at $\lambda_0 = 632.8\,\text{nm}$ (instead of $\epsilon_r = -9.5 + 1.22j$ for bulk material). This correction induces the decrease of the source term of the heat equation (Eq. (2)). The imaginary part of the permittivity of gold appears in Eqs. (1)–(2)) as a pure factor and therefore, the temperature variation in gold is proportional to it.

The choice of the edges $L = 2r\sqrt{\frac{\pi}{\sqrt{3}}} = 134\,\text{nm}$ of the equilateral triangular shapes of the bow-tie nanoantenna is governed to maintain the equivalent surface of matter equal to its of a cylindrical particle with radius $r = 50\,\text{nm}$ used in the above correction of constants [26]. This typical size is three times greater than the bulk mean-free path of electrons in gold ($l_e = 42\,\text{nm}$). Therefore the condition $L > l_e > \Lambda$ is satisfied. The other numerical parameters of the photo-thermal problem are following in the SI system: $\omega = 2.9767.10^{15}\,\text{rad}\cdot\text{s}^{-1}$ (i.e., the wavelength in vacuum is $\lambda_0 = 632.8\,\text{nm}$), $\epsilon_1 = (-9.5 + j)$, $\epsilon_2 = 1$, $P = 30\,\text{mW}$, $NA = 0.6$, $\lambda_1 = 118\,\text{W}\cdot\text{m}^{-1}\cdot\text{K}^{-1}$, $\lambda_2 = 0.026\,\text{W}\cdot\text{m}^{-1}\cdot\text{K}^{-1}$. The radius of the domain of computation is $1\,\mu\text{m}$. To avoid sharp tip effects in computations, we use quadratic polynomial of interpolation in the FEM formulation and spline rounding of the triangles vertices with 5 nm radius of curvature (Fig. 1(a)).

Figure 1(a) illustrate the refinement of the mesh where the electric field gradient is maximum. The length of the edges of the cells of the mesh is smaller than 0.2 nm, to describe accurately the skin effect in the vicinity of the interface between gold and air. With FEM, the accuracy is the maximum of the difference of the norms of unknowns ($|\mathbf{E}|$ and T respectively), between nodes and interpolation values along edges of each cell. This accuracy also called error, is lower than $-30\,\text{dB}$ (Fig. 1(b)) and therefore, the maximum of the variations of the computed solutions are lower than 10^{-3} between adjacent nodes. Moreover the insets in each figure show the acuteness of each unknown of the photothermal problem, related to the small mesh size shown in Fig. 1(a). Fig. 1(d) is the source term of the Poisson's equation, that can be compared to those in [12] for example. This source term exhibits a strong variation in gold. Its maximum is in the vicinity of the gap. Despite its shape, a first inspection of Fig. 1(e) shows an uniform heating of the whole structure as in Ref. [12]. The temperature elevation is more than 200 K, under the hypothesis that all the laser power (30 µm) is concentred in a zone of diameter 1.3 µm, without loss of energy. An extrapolation of the curves in Fig. 3 of Ref. [11] with light flux of $2.3\cdot10^6\,\text{W}\cdot\text{cm}^{-2}$, for nanospheres gives an elevation of temperature greater than 200 K, which is consistent with our results. Similarly, the PDE Equations (1) and (2), exhibit a difference of temperature, proportional to the incoming power. The obtained temperature elevation in gold is one order of magnitude greater than this in a single structure [6], but are consistent with the measurement of temperature in the gap of a rods dimer [12]. Actually, the temperature is directly related to the confinement of the intensity depends on the radius of curvature of the triangles vertices, on the

Instead of insulating boundaries, we also use effusive external boundaries, to enable a loss of thermal energy through the fictive external boundary but we do not observe induced variations of the elevation of temperature in gold. Thus, we are encouraged to conduct a study of the temperature variation depending on the gap. Fig. 1(f) shows the dependance of the intensity of the electric field, of the heat source and of the temperature variation, as functions of the gap. The homogenization of temperature in the whole nanostructure is responsible of the quasi-linear decrease of temperature

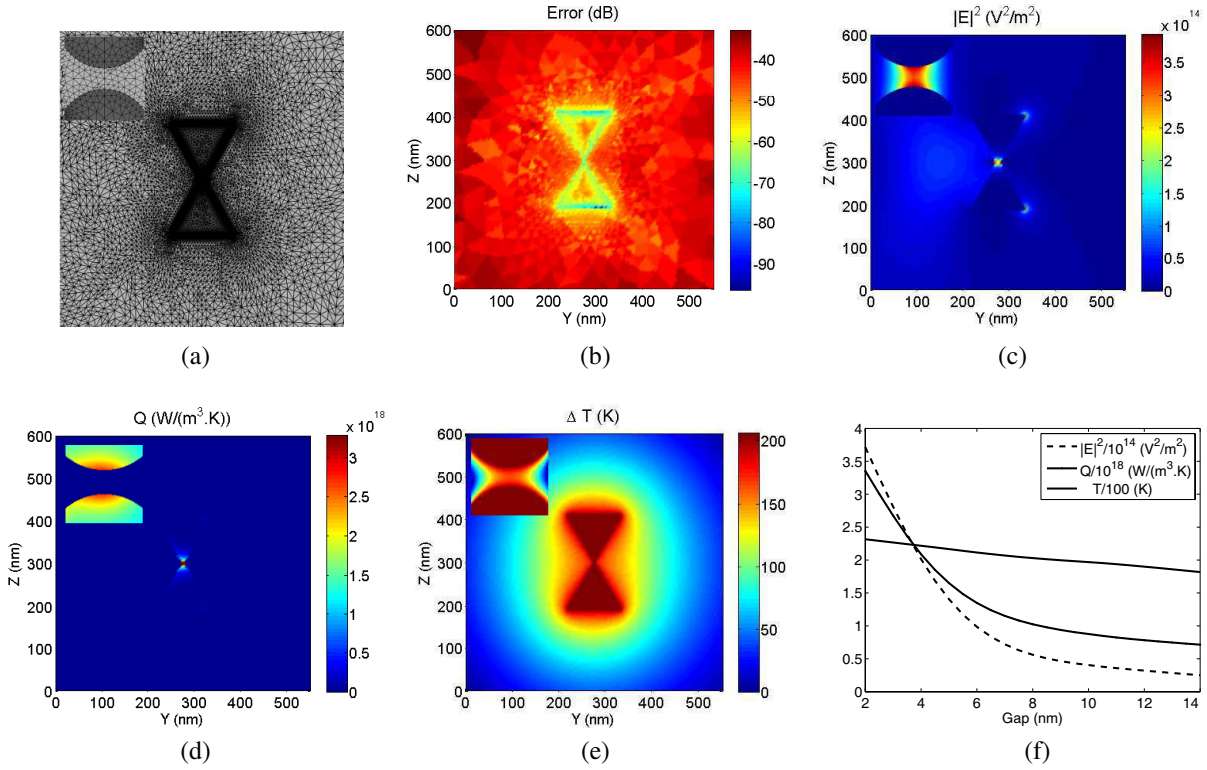

Figure 1: (a) Example of mesh. The distance between nodes can be much smaller than 0.1 nm to reach convergence [18]. The mesh is refined on the boundary of nanoantenna and in the gap, where the gradient of the electric field is maximum. (b) Global error evaluated on the mesh. (c) Intensity of the electric field for a gap of 2 nm. (d) Density of power absorbed in the gold nanostructure (source term of Eq. (2)). (e) Temperature elevation. (f) Variations as a function of the gap width for the maximum of electric field intensity, the maximum of the source term of the heat equation (in gold) and the elevation of temperature.

elevation, whereas the intensity and the source terms exhibits much stronger variations. gap and on the incoming power.

4. CONCLUSION

FEM has been applied to the computation of temperature elevation in bow-tie nanoantenna illuminated by a continuous laser. The photo-thermal heating strongly depends on the gap between the two dimers. From a theoretical discussion on the validity of the physical parameters used in the model as well as the careful bench of the numerical method, we deduce temperature elevations close to those reported in recent papers. Let us underline that the temperature variation depends on both imaginary part of the permittivity, and also on the thermal conductivity. This fact prohibits any attempt to recover equivalent thermal conductivity, directly from the temperature measurement of the nanostructures. This problem opens up an interesting thought about the resolution of the photothermal inverse problem. Regarding models, we plan to investigate two tracks of interest: the resolution of the problem with photothermal parameters obeying the laws of nonlinear behavior on the one hand, and secondly the transition in 3D.

ACKNOWLEDGMENT

This work was supported by the "Conseil Régional de Champagne Ardenne", the "Conseil Général de l'Aube" and the *Nanoantenna* European Project (FP7 Health-F5-2009-241818).

REFERENCES

1. Ambrosioa, A., M. Allegrini, G. Latini and F. Cacialli, "Thermal processes in metal-coated fiber probes for near-field experiments," *Applied Physics Letters,* Vol. 86, 203109, 2005.
2. Kittel, A., W. Mller-Hirsch, J. Parisi, S.-A. Biehs, D. Reddig, and M. Holthaus, "Near-field heat transfer in a scanning thermal microscope," *Physical Review Letters,* Vol. 95, 224301, 2005.

3. Erickson, E. S. and R. C. Dunna, "Sample heating in near-field scanning optical microscopy," *Applied Physics Letters,* Vol. 87, 201102, 2005.
4. De Wilde, Y., F. Formanek, R. Carminati, B. Gralak, P.-A. Lemoine, K. Joulain, J.-P. Mulet, Y. Chen, and J.-J. Greffet, "Thermal radiation scanning tunnelling microscopy," *Nature*, Vol. 444, 740–743, 2006.
5. Gucciardia, P. G., S. Paranè, A. Ambrosio, M. Allegrini, A. D. Downes, G. Latini, O. Fenwick, and F. Cacialli, "Observation of tip-to-sample heat transfer in near-field optical microscopy using metal-coated fiber probes," *Applied Physics Letters,* Vol. 86, 203109, 2005.
6. Baffou, C., M. P. Kreuzer, F. Kulzer, and R. Quidant, "Temperature mapping near plasmonic nansotructures using fluorescence polarization anistropy," *Optics Express,* Vol. 17, 3291–3298, 2009.
7. La Rosa, A. H., B. I. Yakobson, and H. D. Hallena, "Origins and effects of thermal processes on near-field optical probes," *Applied Physics Letters,* Vol. 67, 2597–2599, 1995.
8. Grosges, T., S. Petit, D. Barchiesi, and S. Hudlet, "Numerical modeling of the subwavelength phase-change recording using an apertureless scanning near-field optical microscope," *Optics Express*, Vol. 12, 5987–5995, 2004.
9. Pagnot, T., D. Barchiesi, and D. van Labeke, "Use of a scanning near-field optical microscope architecture to study fluorescence and energy transfer near a metal," *Optics Letters*, Vol. 22, 120–122, 1997.
10. Parent, G., D. van Labeke, and D. Barchiesi, "Fluorescence lifetime of a molecule near a corrugated interface: Application to near-field microscopy," *Journal of the Optical Society of America A,* Vol. 16, 896–908, 1999.
11. Govorov, A. O. and H. H. Richardson, "Generating heat with metal nanoparticles," *Nano Today*, Vol. 2, 30–38, 2007.
12. Baffou, G., C. Girard, and R. Quidant, "Mapping heat origin in plasmonic structures," *Physical Review Letters*, Vol. 104, 136805, 2010.
13. Fischer, H. and O. J. F. Martin, "Engineering the optical response of plasmonic nanoantennas," *Optics Express*, Vol. 16, 9144–9154, 2008.
14. Huang, J.-S., J. Kern, P. Geisler, P. Weinmann, M. Kamp, A. Forchel, P. Biagioni, and B. Hecht, "Mode imaging and selection in strongly coupled nanoantennas," *Nano Letters,* Vol. 10, 2105–2110, 2010.
15. Yang, L., C. Du, and X. Luo, "Numerical study of optical properties of single silver nanobow-tie with anisotropic topology," *Applied Physics B*, Vol. 92, 53–59, 2008.
16. Baffou, G., R. Quidant, and C. Girard, "Thermoplasmonics modeling: A Green's function approach," *Phys. Rev. B*, No. 82, 165424, 2010.
17. Jin, J., *The finite Element Method in Electromagnetics,* John Wiley and Sons, 1993.
18. Grosges, T., A. Vial, and D. Barchiesi, "Models of near-field spectroscopic studies: Comparison between finite-element and finite-difference methods," *Optics Express,* Vol. 13, 8483–8497, 2005.
19. Borouchaki, H., T. Grosges, and D. Barchiesi, "Improved 3D adaptive remeshing scheme applied in high electromagnetic field gradient computation," *Finite Element Analysis and Design*, Vol. 46, 84–95, 2010.
20. Grosges, T., H. Borouchaki, and D. Barchiesi, "New adaptive mesh development for accurate near-field enhancement computation," *Journal of Microscopy*, Vol. 229, 293–301, 2008.
21. Rashidi-Huyeh, M. and B. Palpant, "Counterintuitive thermo-optical response of metal-dielectric nanocomposite materials as a result of local electromagnetic field enhancement," *Physical Review B,* Vol. 74, 075405, 2006.
22. Scaffardi, L. B. and J. O. Tocho, "Size dependence of refractive index of gold nanoparticles," *Nanotechnology,* Vol. 17, 1309–1315, 2006.
23. Moroz, A., "Electron mean free path in a spherical shell geometry," *Journal of Physical Chemistry C,* Vol. 112, 10641–10652, 2008.
24. Zhang, D. Z., G. Zheng, Z. Li, and J. Yang, "Mean free path of photon in gold supsension," *Optics Communications,* Vol. 105, 33–35, 1994.
25. Laroche, T., A. Vial, and M. Roussey, "Crystalline structure's influence on the near-field optical properties of single plasmonic nanowires," *Applied Physics Letters*, Vol. 91, 123101–123104, 2007.
26. Sondheimer, E. H., "The mean free path of electrons in metals," *Advances in Physics*, Vol. 50, 499–537, 2001.

Generation of Encryption Keys from Plasmonics

M. François[1], **T. Grosges**[1], **D. Barchiesi**[1], **and R. Erra**[2]

[1]Project Group for Automatic Mesh Generation and Advanced Methods, Gamma3 Project (UTT-INRIA)
STMR CNRS UMR 6279, University of Technology of Troyes, France
[2]Network & Information Security, Ecole Supérieure d'Informatique, Electronique, Automatique (ESIEA)
France

Abstract— The development of new generators of encryption secret-keys with a high level of security is a challenging topic of research. Here we show how the use of plasmonic response of a nanoobject under light illumination can produce a complex electromagnetic signal satisfying statistical requirements of randomness and which can be used as a secret-key in an encryption scheme.

1. INTRODUCTION

The plasmonics has opened the experimental and theoretical ways of the design of efficient systems, for various applications (sensors, imaging and burning biomedicine applications, security ...) [1–3]. For cryptographic applications, the main question would be: How to generate secret keys for data encryption, with a high level of security? The challenge is to produce a random signal from physical origin, that do not have the drawbacks of the pseudo-random generators. This idea has impassioned the researchers for few decades and since then, much of techniques were developed [4, 5]. We recently proposed the use of the measurement of near-field signal diffracted by nanoobjects, to ensure the secure and enduring data storage [3].

In this paper, we propose a new method of pseudorandom key generation, from the computation of electromagnetic field produced through a plasmonic device. Indeed, not only do these models provide complex field patterns, but also they have the advantage of being very sensitive to many parameters, since they describe a resonance. The results of calculations remaining deterministic, we propose a numerical method to further ensure the quality of key products and avoiding conventional hacking attacks, the underlying purpose being to be able to destroy and to regenerate the key libitum, for the secure enduring data storage.

We show that the use of nano-objects permits to produce a complex optical map, which can have all necessary cryptographic qualities, verifying the maximum level of the Shannon's entropy [6] and is compliant with the classical tests on randomness binary sequences [7] permitting to be used as a secret key for encryption. The high level of security of this key generator is related to the number of freedom degrees used to generate the secret key and the physical complexity of the plasmonic structures. These degrees of freedom can be shared into two families of parameters, of completely different origin. The first one ($\mathcal{K}_S$) is related to the physical parameters required to model the nanostructure (materials, shapes, sizes ...). From the constructed 3D spatial map, a second set of parameters ($\mathcal{M}_S$) is assigned to a numerical process consisting in an adaptive remeshing process ensuring a quality target of a maximum Shannon's entropy as well as a cryptographic statistical robustness of the pseudorandom character of the key.

2. FROM ELECTROMAGNETIC MODEL TO SECRET KEY

The computation of the interaction between light and 3D nanostructures, is usually obtained from the resolution of the vectorial Helmholtz's equations for the electric and the magnetic field vectors $\mathbf{E}$ and $\mathbf{H}$, with ϵ_r and μ_r, the relative permittivities and permeabilities of involved materials, respectively:

$$\nabla \times \left(\frac{1}{\mu_r} \nabla \times \mathbf{E} \right) - k_0^2 \epsilon_r \mathbf{E} = \mathbf{0} \quad \text{and} \quad \nabla \times \left(\frac{1}{\epsilon_r} \nabla \times \mathbf{H} \right) - k_0^2 \mu_r \mathbf{H} = \mathbf{0} \tag{1}$$

The resolution of such a system of partial differential equations is achieved numerically in a 3D spatial domain Ω and the intensities $I_E(x,y,z) = |\mathbf{E}(x,y,z)|^2$ and $I_H(x,y,z) = |\mathbf{H}(x,y,z)|^2$ in the 3D space are computed. In this first validation approach, we use the Mie's theory of diffraction of light by an homogeneous and non magnetic spherical particle ($\mu_r = 1$), illuminated by a monochromatic plane wave.

The results are complex maps of fields with interferences patterns and localized strong field enhancements, especially if a plasmon resonance occurs. In this case, the sensitivity of the numerical results to the various involved parameters of computation is increased [8]. It is the reason why, the exact reproducibility of this map is very difficult without any knowledge of the model and computational parameters used. The complexity of the model parameters can be grouped as a key set $\mathcal{K}_S$ containing:

1. Optical parameters: the wavelength of the light source $\lambda = 2\pi/k_0 \in \mathbb{R}$ and the choice of material permitivitties $\epsilon_p(\lambda) \in \mathbb{C}$ and $\epsilon_m \in \mathbb{C}$ for the surrounding medium;
2. Geometrical parameter: the radius of the nano-sphere $r_p \in \mathbb{R}$.

In theory the physical parameters used seem to take an infinity of values ($\mathbb{R}$, $\mathbb{N}$ or $\mathbb{C}$). It should be noted that the intervals of variation of these values are not necessarily limited for compliance with realistic existing material parameters. Of course, the deterministic maps $I_E(x, y, z)$ and $I_H(x, y, z)$ necessitate a specific numerical processing to transform them into an efficient secret key $\Psi(n)$ which satisfies the criteria of maximum Shannon's entropy [6] and cryptographic basic properties (see Figs. 1(a)–(d)).

A two-steps numerical process is then achieved on the intensity maps in order to satisfy both criterion of maximum entropy and randomness statistical characteristics. The first step to satisfy the criterion of maximum entropy in the random key, consists in an homogenization of occurrence of intensities through the redistribution of intensity level by a 3D adaptive meshing process [9] with an a posteriori error estimator based on the maximum entropy as explained in Ref. [3]. This adaptive scheme of remeshing of the domain (x, y, z), uses selected frequencies of each intensity levels occurrence, as target. Second order polynomials are used to interpolate the intensity levels, to generate additional points in the tomography map (or equally to suppress the nodes corresponding to too numerous intensity levels) and to translate the intensity levels I_E and I_H of the maps $I_E(x, y, z)$ and $I_H(x, y, z)$ as a 256-levels representation to match the conventional storage of digital

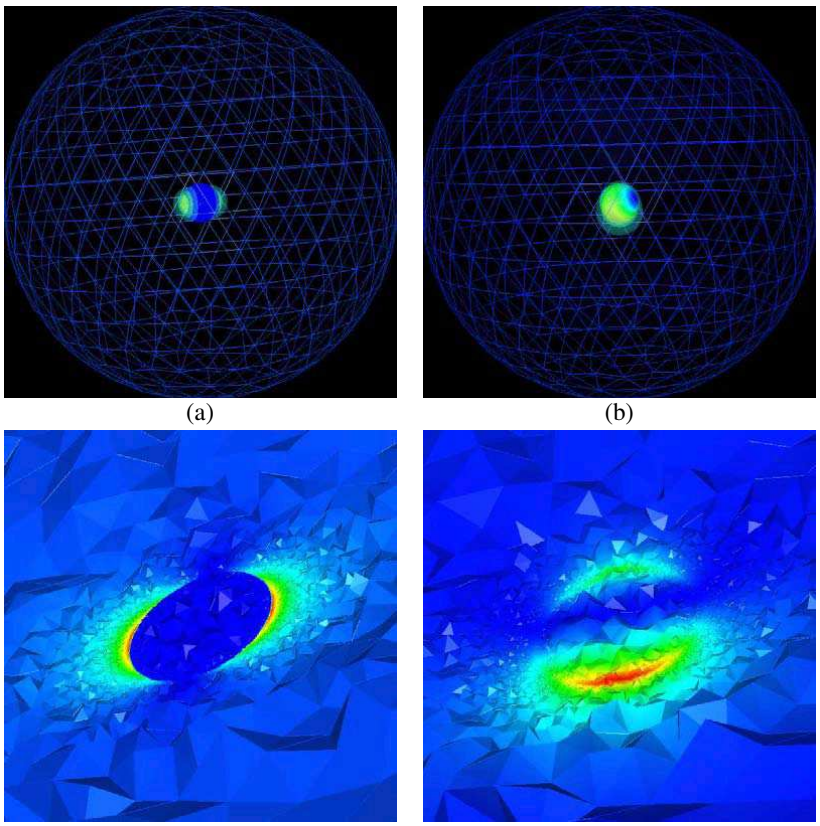

Figure 1: Visualization of (a) the electric field intensity $I_E(x, y, z)$ around the nanostructure and (b) the magnetic field intensity. Spatial cut in the computational domain, along the (O, x, y) axis (the plane of polarization), of (c) the electric field intensity and (d) the magnetic field intensity.

files as bytes. Each point of the the domain (x, y, z) is labeled by an integer (n) (the node number) and the map $I_E(x, y, z)$ (resp. $I_H(x, y, z)$) is therefore transformed to a map $I_E(n)$ (resp. $I_H(n)$) satisfying the equal occurrence of each intensity level. Consequently, an uniform law of probability governs the frequencies associated to the intensities.

Second, a xor operator is applied by matching $I_E(n)$ and $I_H(n)$ in order to produce a new map $\Psi(n)$ ensuring the statistical characteristics of randomness as well as cryptographic primitive characteristics against complexity. This map is given by:

$$\Psi(n) = \alpha_1 I_E(n) \oplus \alpha_2 I_H(n), \quad \text{with} \quad \alpha_1, \alpha_2 \in \mathbb{R} \times \mathbb{R}. \tag{2}$$

The produced numerical encryption key $\Psi(n)$ is therefore deduced from the plasmonic electromagnetic computations and reaches the level of security needed for cryptographic applications (see Fig. 2(c)). This last part of the key consists in a set of numerical parameters $\mathcal{M}_S$ associated to the remeshing process and are summary by:

1. The adaptive remeshing process parameters $h_{\min}$, $h_{\max}$, $\delta_\phi \in \mathbb{R} \times \mathbb{R} \times \mathbb{R}$, the minimum and maximum distance between nodes after remeshing and the maximum tolerance between the levels of signal at two adjacent nodes, respectively. The number of nodes $N \in \mathbb{N}$ of the initial computation and their spatial coordinates $\{(x_i, y_i, z_i),\ 1 \leq i \leq N\} \in \mathbb{R}^{3N}$.
2. Combinatory parameters through the xor operator: α_1 and $\alpha_2 \in \mathbb{R} \times \mathbb{R}$.

Therefore, the numerical complexity of the model, its sensitivity to parameter, in the plasmon resonance case and the numerical parameters used for meshing and homogenization are parts of the global set of parameters $\mathcal{M} = \mathcal{K}_S \cup \mathcal{M}_S$. The exact reproducibility of the secret key $\Psi(n)$ is almost impossible if the exacts parameters used are unknown. Indeed, in the vicinity of the plasmon resonance, an error on one of the used parameters can lead to variations in the produced image map (in term of the exact value of the pixels in the formed image). Therefore, even if the attacker decides to test all possibilities (brute-force attack), the process will fail (in a limited finished time).

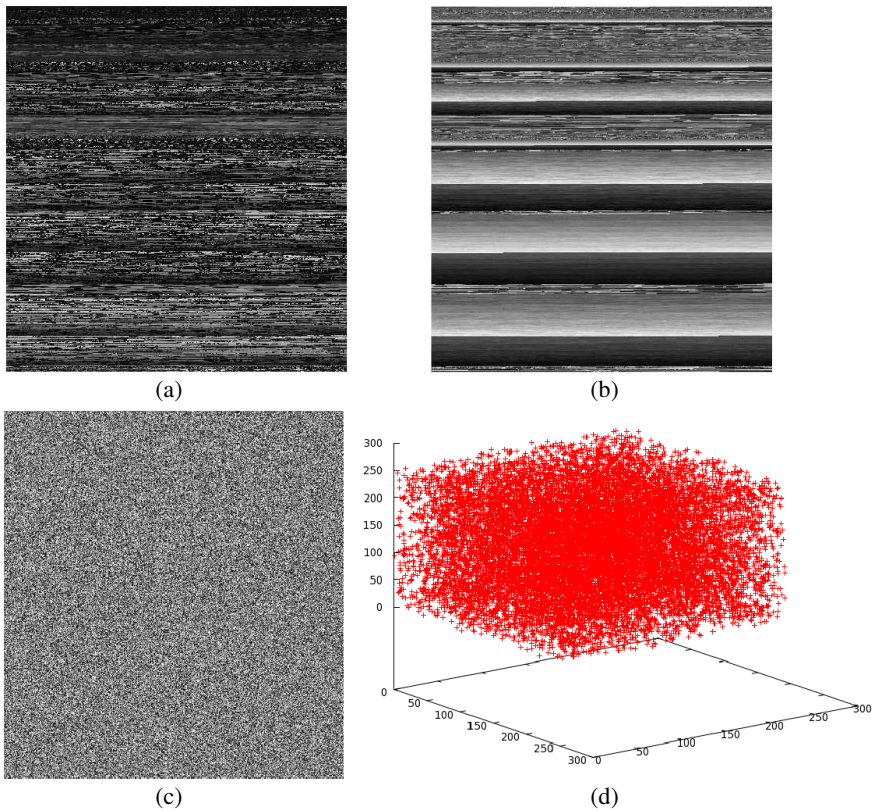

Figure 2: The 2D corresponding images, in gray levels, of the maps (a) I_E, (b) I_H before processing and (c) $\alpha_1 I_E(n) \oplus \alpha_2 I_H(n)$ after homogenization and application of xor operator. (d) Projection of the intensities, grouped per block of three, on the 3D space. The total size of each image is 243.200 pixels (475×512), each pixel being expanded on 8 bytes (256 levels).

Table 1: Results of NIST tests, Shannon's entropy, rank of the matrix and bits distribution of the images. The size of each image is 243.200 pixels (475×512).

Images	NIST Tests	Shannon's Entropy	Rank	% of '0' in the binary sequence	% of '1' in the binary sequence
Image of Fig. 2(a)	Failure	6.686822 bits/level	Full	62.51	37.49
Image of Fig. 2(b)	Failure	7.753889 bits/level	Full	52.64	47.36
Image of Fig. 2(c)	Success	7.999197 bits/level	Full	50.01	49.99

Indeed, the limit of brute-force attack on a key depends on the entropy of the key and is currently limited at 128 bits of entropy. In the present case, the generated key exceed largely 128 bits of entropy and overpass the lower limit.

3. RESULTS AND DISCUSSION

Here, we present an example of the construction of the secret-key $\Psi(n)$. As indicated above, the Mie's theory enables to compute the electromagnetic fields at $\lambda_0 = 550\,\text{nm}$, with a gold sphere of radius $r = 10\,\text{nm}$, a relative permittivity $\epsilon_r = -5.947 + j2.090$ and a computational domain Ω of radius $R = 500\,\text{nm}$.

The randomness of the key and its cryptographic robustness must be evaluated through statistical tests provided by NIST, which consists in a statistical package of fifteen tests developed to quantify and to evaluate the randomness of (arbitrarily long) binary sequences produced by either hardware or software based cryptographic random or pseudorandom number generators [7]. The cryptographic robustness of the 3D maps I_E (resp. I_H) and $\Psi(n)$ is checked, as they can be viewed as vectors of values in the order of nodes numbering (or 2D maps for overview in Figs. 2(a), (b)). We can remark that the images of Figs. 2(a), (b) lets appear low structures but are not random enough, as attests its corresponding NIST tests (see Table 1), to ensure a cryptographic quality. The images of Figs. 2(a), (b) have a low entropy. This mainly comes from the fact that there are many missing levels of intensities. We also remark the non regularity in the occurrence of the various value (62.51% of 0 against 37.49% of 1 for the image of Fig. 2(a)). The images of Fig. 2(c), (d), obtained after renumbering of nodes, homogenization of occurrences and xor operator seem let appear randomness characteristics. The derived secret-key $\Psi(n)$, obtained after a xor operation between $I_E(n)$ and $I_H(n)$, presents the characteristics of randomness (see Fig. 2(c)) and pass all the NIST tests successfully. We can also remark that its 3D projection, as elements vector taken three by three, filled all the space as a random sequence (see Fig. 2(d)). The key $\Psi(n)$ can be now viewed as a random octal sequence, cryptographically stronger, and can be used with more security in many cryptographic schemes.

4. CONCLUSION

We have introduced a new method to generate random key from plasmonic device. The entire process used to produce key has successfully passed all the standard statistical tests of randomness. Of course, to validate definitively the scheme, a specific characterization of the complexity of the model should be carefully conducted, to evaluate the number of significant digits of each parameter, which are involved in the first step of the process. Also, this aspect of validation has to take into account the parameters in $\mathcal{M}_S$. More complex models with much more physical parameters should be also used in the process of key generation.

REFERENCES

1. Barchiesi, D., D. Macías, L. Belmar-Letellier, D. van Labeke, M. Lamy de la Chapelle, T. Toury, E. Kremer, L. Moreau, and T. Grosges, "Plasmonics: Influence of the intermediate (or stick) layer on the efficiency of sensors," *Appl. Phys. B — Lasers Opt.*, Vol. 93, No. 1, 177–191, 2008.
2. Grosges, T., D. Barchiesi, T. Toury, and G. Gréhan, "Design of nanostructures for imaging and biomedical applications by plasmonic optimization," *Opt. Lett.*, Vol. 33, No. 23, 2812–2814, 2008.
3. Grosges, T. and D. Barchiesi, "Toward nano-world based secure encryption for enduring data storage," *Opt. Lett.*, Vol. 34, No. 14, 2421–2423, 2010.
4. Refregier, R. and B. Javidi, "Optical image encryption based on input plane and Fourier plane random encoding," *Opt. Lett.*, Vol. 20, No. 7, 767–769, 1995.

5. Corndorf, E., C. Liang, G. S. Kanter, P. Kumar, and H. P. Yuen, "Quantum-noise randomized data-encryption for WDM fiber-optic networks," *Comput. Commun. Rev.*, Vol. 34, No. 5, 21–30, 2004.
6. Shannon, C. E., "A mathematical theory of communication," *Bell Syst. Techn. J.*, Vol. 27, 379–423, 623–656, 1948.
7. Rukhin A., J. Soto, J. Nechvatal, M. Smid, E. Barker, S. Leigh, M. Levenson, M. Vangel, D. Banks, A. Heckert, J. Dray, and S. Vo, *A Statistical Test Suite for Random and Pseudorandom Number Generators for Cryptographic Applications*, National Institute of Standards and Technology Special Publication, 800-22rev1, April 2010.
8. Barchiesi, D., E. Kremer, V.-P. Mai, and T. Grosges, "A Poincaré's approach for plasmonics: the plasmon localization," *J. Microscopy*, Vol. 229, No. 3, 525–532, 2008.
9. Borouchaki, H., T. Grosges, and D. Barchiesi, "Improved 3D adaptive remeshing scheme applied in high electromagnetic field gradient computation," *Finite Elem. Anal. Des.*, Vol. 46, No. 1–2, 84–95, 2010.

Design and Fabrication of a Modular Eddy Current Micro Sensor

T. Griesbach, **M. C. Wurz**, **and L. Rissing**
Institute for Micro Production Technology, Center for Production Technology
Leibniz Universitaet Hannover, Garbsen, Germany

Abstract— In order to provide a contactless measurement technique for the detection of surface damages, a modular design of an eddy current micro sensor was developed and fabricated in thin-film technology. The sensor is intended to be applied for the detection of cracks in ferrous and non-ferrous metals. The sensor consists of two parts, a single-turn excitation coil and an anisotropic magneto-resistance (AMR) sensor. The AMR sensor detects the change of the magnetic field induced in the sample by the excitation coil. The sensor is capable of detecting defects which are smaller than 50 µm.

1. INTRODUCTION

Modern production technology requires the acquisition of manifold process data. First of all, having basic information on the production process ensures a certain reliability during the fabrication. Second, the acquired process data are used to verify the quality of a product at the end of the production. A novel approach is proposed within the Collaborative Research Center 653 which is funded by the DFG (German Research Foundation). In order to come up with "genetically intelligent" (gentelligent) machine tools or components, various sensors were developed to gather process data not only during the production, but also later on during the entire life cycle [1]. So far, a family of modular magnetic micro sensors covering both, force and strain measurements were developed [2]. In order to provide a contactless measurement technique to examine products during the production process, a modular design of an eddy current micro sensor was developed and fabricated in thin-film technology.

The eddy current technique (ECT) is one of the most important non-destructive testing method and a common tool for the inspection of defects and material properties. Actually, ECT is applied in a wide application area. For example, it is used for the evaluation of nuclear equipment, aircraft, and engine parts [3]. This paper describes the design and the measurement principle of a new eddy current micro sensor. In contrast to existing systems, the eddy current sensor is fabricated completely applying Micro Electro-mechanical System (MEMS) technology. As a result, the small dimensions of such a micro sensor enable the accumulation of information in areas which are not accessible so far.

2. SENSOR CONCEPT

The modular eddy current sensor consists of two parts, a single-turn excitation coil and an anisotropic magneto-resistance (AMR) sensor. Fig. 1 depicts the detection principle of the eddy current sensor. The excitation coil is fed with an alternating current, which generates a magnetic field around this coil. According to Faraday's Induction Law, eddy currents are induced in an electrically conducting probe and create an electromagnetic field by themselves. This field counteracts with the field of the excitation coil. The sensing axis of the AMR sensor is in plane with the surface of the probe and detects the total magnetic field generated by the excitation coil and the eddy currents induced in a defect-free specimen (Fig. 1(a)). In the case of a defect, the output signal from the sensor changes caused by the disturbance of the eddy-current flow path (Fig. 1(b)).

3. MODELLING AND SIMULATION

To achieve an optimal sensor design, Finite Elements Method (FEM) analyses were carried out using the simulation software ANSYS^{TM}. The geometry of the eddy current sensor components was derived from the results of the simulation. The single-turn excitation coil has a footprint of 560 µm × 770 µm. The width of the lead is 70 µm and its height amounts to 5 µm. For the AMR sensor geometry, a meander was chosen. The total length of the meander amounts to 855 µm. The width of the leads is 20 µm, and the insulation distance between the leads amounts to 5 µm. The requirement the excitation coil has to fulfill is to induce eddy currents in an electrically conducting probe. The simulations were carried out by modelling the excitation coil as a circle ring, which is arranged in a distance of 5 µm above the probe material. As sample material, Cu was chosen. A

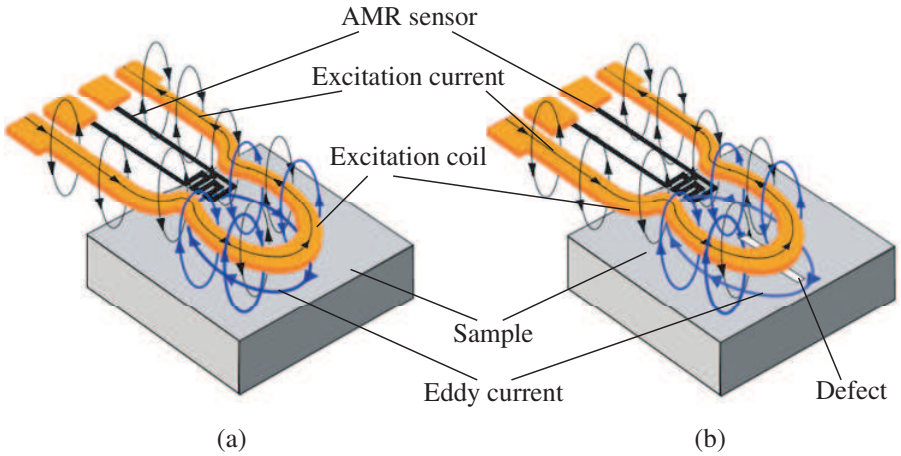

Figure 1: Principle of the detection by an eddy current sensor: (a) defect-free surface; (b) with a defect in the surface of the probe.

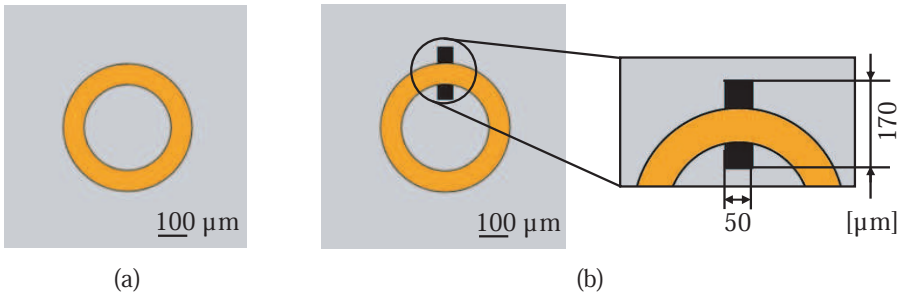

Figure 2: Simulation model: (a) without a defect in the surface; (b) with a defect in the surface of the probe.

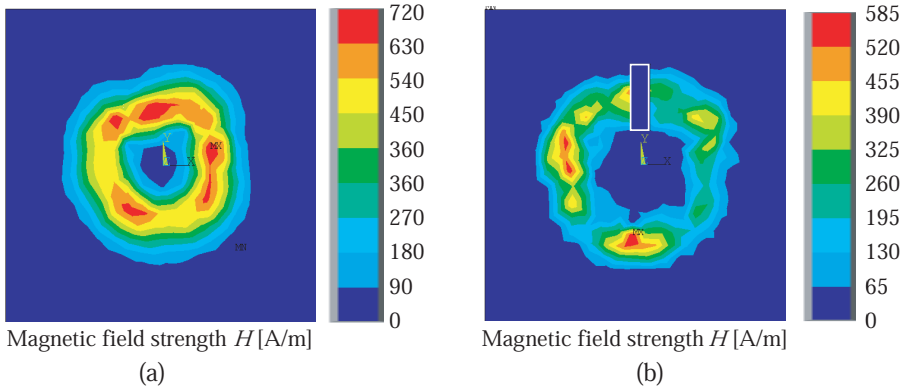

Figure 3: Simulated magnetic field strength of the excitation coil: (a) without a defect in the surface; (b) with a defect in the surface of the probe.

crack with a footprint of 50 µm × 170 µm served as a surface defect in the simulations. The behavior of the system was investigated in a frequency range from 500 kHz up to 5 MHz. The simulation model of the investigated system is shown in Fig. 2.

In Fig. 3, the distribution of the magnetic field caused by the eddy currents induced in the probe is shown. In the presence of a defect, the magnetic field decreases caused by the disturbance of the eddy-current flow path (Fig. 3(b)). The highest magnetic field generated by the eddy currents was found for a defect-free specimen and amounts to 720 A/m (Fig. 3(a)). For the investigated system a magnetic field of 585 A/m was calculated in the presence of a defect. The simulation was conducted at a frequency of 500 kHz. The applied excitation current was 0.3 A.

4. FABRICATION PROCESS

The micro eddy current sensor was fabricated on a Si wafer with a thermal oxide layer on top and consists of two parts, a single-turn excitation coil and an AMR sensor. For the fabrication of micro

molds, used as a mask for the electrodeposition of the sensor elements, UV depth photolithography was applied. Fig. 4 shows the fabrication sequence for the modular eddy current sensor.

As a first step, a Cr adhesion layer was sputter deposited, followed by an Au layer serving as a conductive seed layer for the following electroplating process of the alignment marks and the IMPT logo. To pattern the micro molds for electroplating, a positive photoresist was used. Then, the Ni alignment marks were electroplated (Fig. 4(a)). Subsequently, the photoresist was stripped. In the next step, the micro molds for the contact pads and the excitation coil were created. For depositing both, the micro molds were filled up with electroplated Cu (Fig. 4(b)). A removal of the seed layer was required to inhibit short circuits (Fig. 4(c)). It was executed by Ion Beam Etching (IBE). For the fabrication of the meander structure and the electrical connections of the AMR sensor, micro molds were patterned again using a positive photoresist. Afterwards, a 25 nm thick NiFe81/19 layer was deposited for the meander structure, followed by a Cu layer for the electrical connections. Both layers were fabricated by sputter deposition (Fig. 4(d)). Fig. 5 depicts micrographs of the photoresist mask for the sputter deposition of the meander structure (Fig. 5(a)) and the finished eddy current sensor, respectively (Fig. 5(b)).

5. EXPERIMENTAL RESULTS

To characterize the fabricated eddy current sensors, electrical resistance measurements were conducted. The aim of these investigations was the characterization of the AMR sensor and the dependence of the magnetic field created by the sensor on the electrical resistance R. The results were compared to the simulated magnetic field of the eddy currents in the surface of the probe material.

The resistance measurements were conducted by changing the magnetic field angle α and conducting successive measurements of the Ohmic resistance with an ohmmeter. The measurements were conducted for a magnetic field strength of 600 A/m and 800 A/m, respectively. Fig. 6 depicts the variation of the electrical resistance of a completed AMR sensor as a function of the angle of the applied magnetic field. The electrical resistance of the AMR sensor shows a dependence on the applied external magnetic field. By increasing the magnetic field from 600 A/m to 800 A/m, the electrical resistance of the AMR sensor decreases from 653.2 Ω to 651.4 Ω. In comparison to the simulated magnetic field variation of the eddy currents, the presence of a defect will change the electrical resistance of the AMR sensor 1.8 Ω at the maximum.

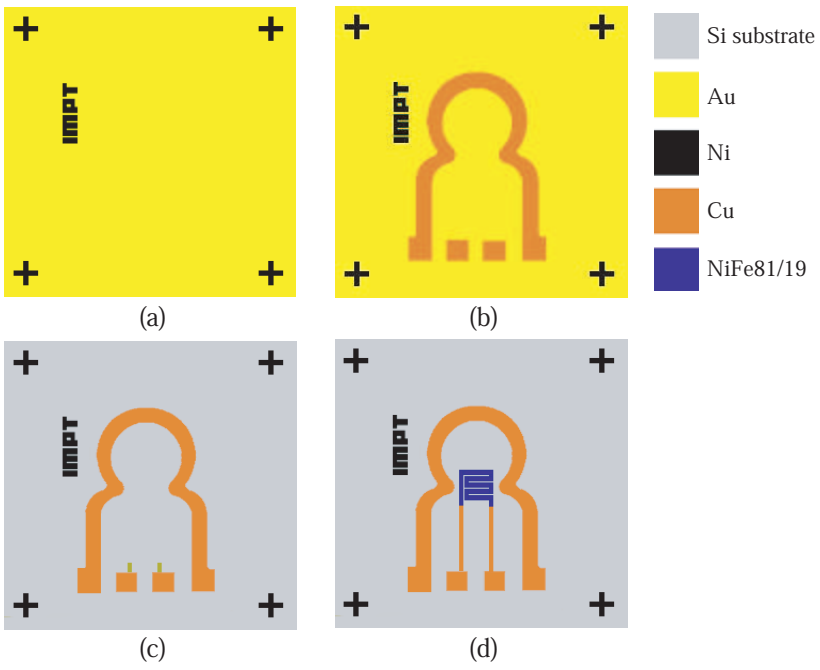

Figure 4: Fabrication sequence of the modular eddy current sensor.

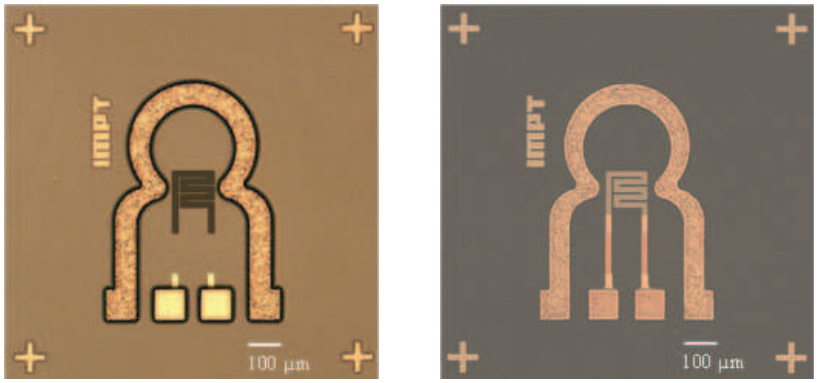

(a) (b)

Figure 5: Micrographs of the modular eddy current sensor: (a) photoresist mask of the meander structure; (b) completed micro sensor system.

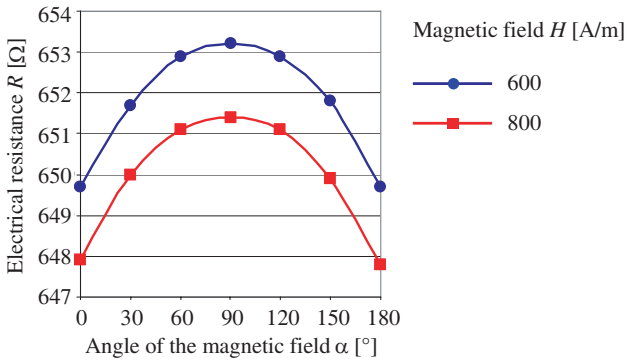

Figure 6: Resistance variation of a fabricated AMR sensor as a function of the angle of the magnetic field and the applied magnetic field strength.

6. CONCLUSION AND OUTLOOK

A modular design of an eddy current sensor was successfully developed and fabricated in thin-film technology. The sensor can be applied for the detection of defects in electrically conducting samples which are smaller than 50 µm. Simulations show that the output signal from the AMR sensor obviously changes dependant on the disturbance of the eddy current flow path. Experimental investigations proved the feasibility of the sensor principle. The micro sensors are ultimately intended to be integrated into gentelligent machine tools or components to gather process data during the entire life cycle.

ACKNOWLEDGMENT

This research is sponsored in part by the German Research Foundation (DFG) within the Collaborative Research Center (SFB) 653 “Gentelligent Components in their lifecycle”.

REFERENCES

1. Denkena, B., K. Hasenfuß, C. Liedtke, *Genetik und Intelligenz in der Produktionstechnik, ZWF Zeitschrift Fuer Wirtschaftlichen Fabrikbetrieb*, Spur, G. Editors, Vol. 100, No. 10, 569–572, 2005.
2. Hansen, S., L. Rissing, and H. H. Gatzen, “A concept for a toolbox of components for modular magnetic microsensors,” *Symposium on Magnetic Materials, Processes and Devices, 210th Meet. of The Electrochemical Society 2006*, ECS Transactions, Vol. 3, No. 25, 235–246, Cancun, Mexico, 2006.
3. Yamada, S., K. Chomsuwan, T. Hagino, M. Iwahara, and H. Tian, “Metallic bead detection by using eddy-current probe with SV-GMR Sensor,” *Papers of Technical Meeting on Magnetics, IEE Japan*, Vol. MAG-04, No. 144–156, 19–22, 2004.

Wireless Electronic Structural Surveillance Sensors Using Inductively Coupled Sacrificial Transducers

P. Pasupathy[1], **A. Abu Yousef**[2], **D. P. Neikirk**[1], **and S. L. Wood**[2]

[1]Department of Electrical and Computer Engineering
The University of Texas at Austin, USA
[2]Department of Civil Architectural and Environmental Engineering
The University of Texas at Austin, USA

Abstract— In order to monitor the corrosion of the steel reinforcement in concrete we developed our low cost, wireless, battery free, Electronic Structural Surveillance (ESS) corrosion sensors. The ESS sensors use an unpowered embedded resonant L-C tag read by an external reader using an inductively coupled impedance measurement. Our previous embedded sensors use a steel wire which corrodes when the conditions in the concrete promote corrosion. Such a sacrificial transducer in its native environment is the most direct method of monitoring corrosion. In the previous generation design, this transducer was connected directly to the sensor, hence breaching the hermetic seal protecting the sensor circuit. A new transduction scheme will be discussed which incorporates a fully exposed sacrificial transducer element that is inductively coupled to the sensor resonant circuitry, hence providing a non-contact interaction. The strength of the interaction of the fully exposed, sacrificial transduction layer is set by flux screening and mutual inductance effects. This design also allows the transducer to make use of a variety of materials and morphologies.

1. INTRODUCTION

The steel reinforcement in concrete structures is subject to corrosion. Detection of this corrosion is an important area in Structual Haelth Monitoring (SHM). It continues to be a challenging problem since, monitoring large structures with long lifetime without frequently breaching the concrete cover requires economical, energy efficient and nondestructive techniques. Our efforts to address this problem resulted in the development of our low-cost, wireless, battery-free Elctronic Structural Surveilance (ESS) sensors [1, 2]. The ESS platform uses inductive coupling between an embedded sensor and an external reader. A schematic view of the passive wireless sensor and the reader is shown in Figure 1(a) and its equivalent circuit model is shown in Figure 1(b). The sensor is constructed using a tag, which is resonant sensing (RLC) circuit. The tag us connected to a transducer which changes one or more of tha tag's circuit components (e.g., R/C) altering

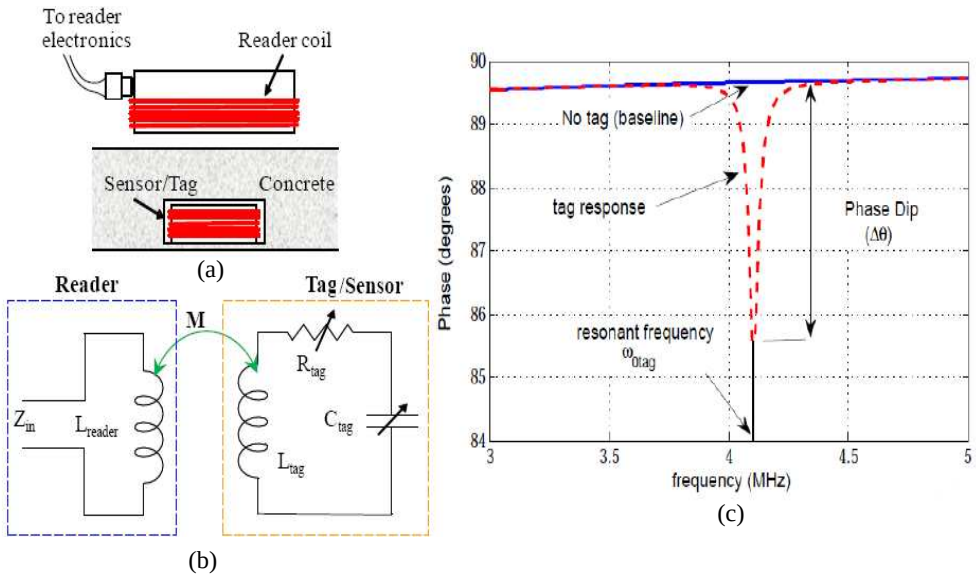

Figure 1: (a) Electronic Structural Surveillance (ESS) platform and (b) its equivalent circuit. (c) Phase (θ) response of the impedance (Z_{in}).

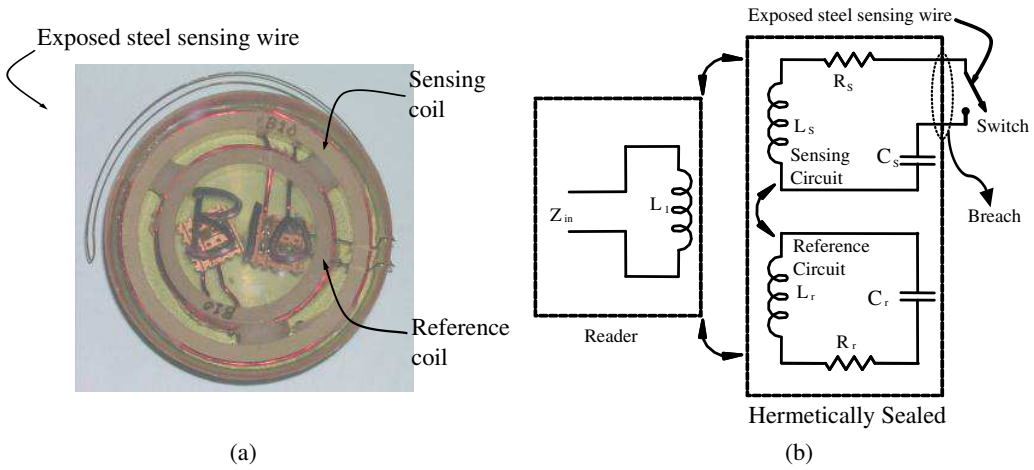

Figure 2: (a) ESS corrosion sensor with a hermetically sealed tags and an exposed DC connected transducer. (b) Equivalent circuit as coupled to a reader coil.

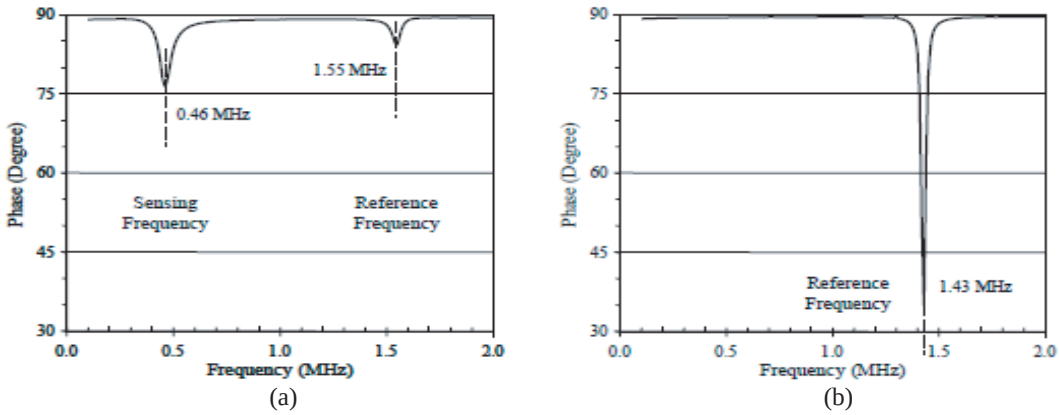

Figure 3: Phase response of the threshold corrosion sensor in its (a) uncorroded and (b) corroded states.

its resonance characteristics. The phase of the impedance response measured at the input of the reader coil is shown in Figure 1(c). When the tag is present, it produces a dip in this baseline phase response at the resonant frequency of the tag (ω_{otag}). The response can be characterized by the phase dip ($\Delta\theta$), the center frequency (ω_o) and the width ($\Delta\omega$) of the resonance. Corrosion is the best monitored in the material and the surrounding where it occurs. Our embedded sensors use a steel wire which corrodes when exposed to the concrete. This sacrificial transducer was used as a resistive transducer altering the resonance response of the tag. This resistive transducer was DC connected to the sensor which breaches the hermrtic seal protectin the sensor circuit. We briefly discuss the performance of these corrosion sensors and the problems encounteded duo to such a DC connection which are addressed by the inductively coupled transduction scheme.

2. BACKGROUND AND MOTIVATION

In our prior work [2, 3] we developed ESS sensors to monitor the initiation of corrosion of the steel reinforcement embedded in concrete. The sensors were designed using two passive resonant RLC circuits (tags). The two tags have slightly separated resonance frequencies. One tag was used to provide a reference resonance and the other was connected to a transducer and served as the sensing tag. A steel wire was used as the sacrificial corroding transducer and the sensor was hermetically sealed in epoxy except for the steel wire. Figure 2(a) shows a picture of the hermetically sealed sensor with concentric sensing and reference coils, and the exposed steel wire. An equivalent circuit of the sensor along with the coupled reader coil is shown in Figure 2(b). The exposed steel wire functions as a resistive transducer. Figure 3 shows the phase response of the sensor in its uncorroded (a) and corroded (b) state. The sensing tag was designed to have a lower resonance frequency than the reference. As it corrodes, its resistance increases damping the resonance response of the sensing tag until only the higher resonance frequency of the reference tag remains. Long term exposure

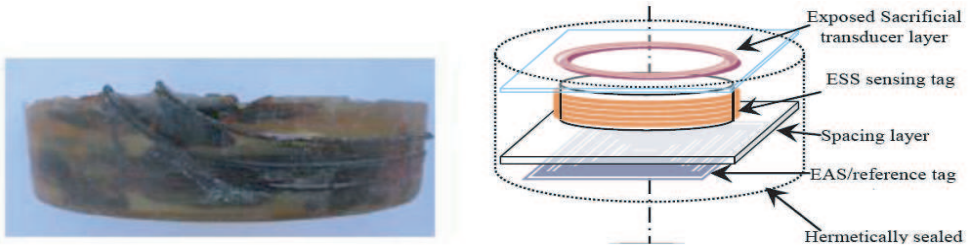

(a) (b)

Figure 4: (a) Corrosion inside the epoxy housing in the DC connected sacrificial transducer. (b) Sensor design using inductively coupled sacrificial transducer avoids breaching the hermetic seal.

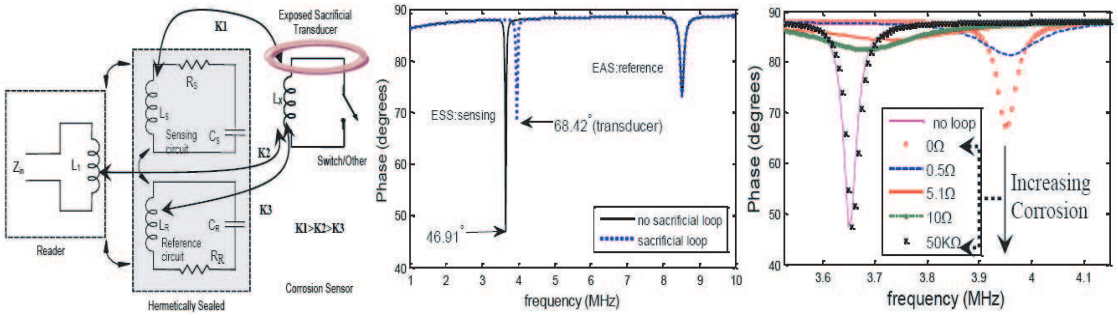

(a) (b) (c)

Figure 5: (a) Equivalent circuit of the sensor using an inductively coupled transduction scheme. (b) Phase response shows that the transducer affects the sensing tag's response. (c) Corrosion emulated by increasing the resistance of the transducer loop shows that the response reverts to the "no loop" state when corroded.

tests have verified the effectiveness of this design as a threshold corrosion sensor [5]. During the long term exposure tests, in all sensors that were subjected to moisture variations, the epoxy housing suffered degradation due to penetration of corrosion (Figure 4). While this did not adversely affect the sensor response, it can potentially limit the life time of the sensors. It is apparent from Figure 2 that the steel wire resistive transducer requires a DC connection to the sensing coil. This DC connection requires breaching the epoxy housing. This compromises the hermetic seal providing an ingress point for corrosion and could lead to corrosion of the reference/sensor coil. In addition, the connection between the sacrificial steel wire and the copper wire used to wind the sensing coil is an electrochemically sensitive bimetallic junction. To reduce the probability of corrosion compromising the sensor coils, this weak point must be eliminated. This is achieved by using an inductively coupling between the transducer and the sensing coil.

3. INDUCTIVELY COUPLED SACRIFICIAL TRANSDUCER

To overcome the infiltration of the epoxy housing by corrosion in the previous generation design using a DC connected sacrificial transducer, a new transduction scheme was proposed [4]. In this configuration (Figure 4(b)), the corroding element is inductively coupled to the sensing tag but is physically isolated from it. Thus the sensor and the reference tags are in hermetically sealed package. While the transducer can interact using either inductive or capacitive coupling, our current work focuses on inductively coupled transducers. This coupled interaction with the sensing tag avoids breaching the hermetic seal protecting the sensing and reference tag (resonators) from their harsh surroundings. At the same time, since the sacrificial transducer is fully exposed to this environment, its ability to directly monitor of corrosion remains unaffected. The design in Figure 4(b) consists of an ESS tag which is a five turn (22AWG) cylindrical short solenoid with a diameter of 2 inches and is resonant at $f_o = 3.6\,\text{MHz}$. The commercially available Electronic Article Surveillance (EAS) or anti-theft tag as the reference tag with a resonance frequency $f_o = 8.2\,\text{MHz}$. A single turn (loop) of wire functions as the simplest inductively coupled transducer. An equivalent circuit and the phase response of such a sensor is shown in Figure 5. The dielectric spacer in Figure 4(b) ensures that the transduction layer is closely coupled to the sensing tag and weakly coupled to both the reference tag and the reader i.e., $K_1 > K_2 > K_3$. Further, the transducer loop is chosen such that its diameter is equal (matched) to that of the sensing coil. A single turn (18AWG) coil with a diameter of 4 inches is used as the reader coil. The impedance response is acquired using an HP 4194 Impedance

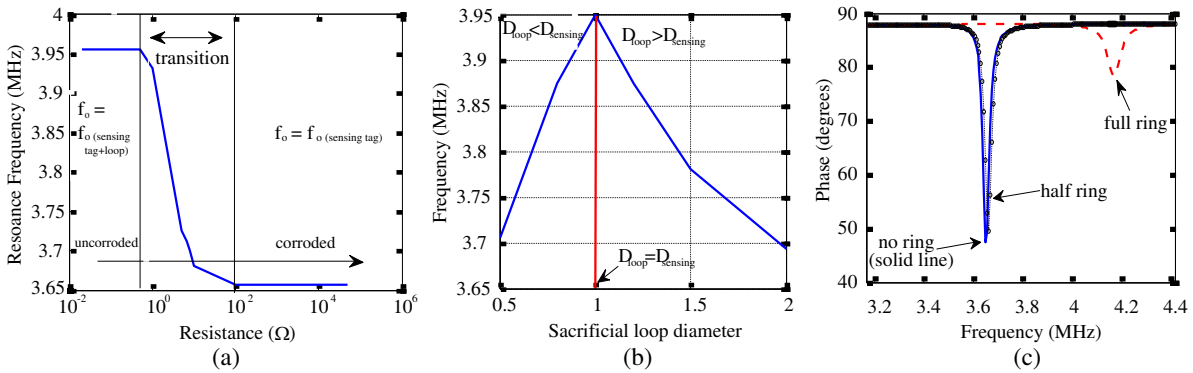

Figure 6: Effect of increased (a) loop resistance or corrosion and (b) loop diameter on the combined resonance frequency of the sensing tag and transducer. (c) Phase response of a ring shaped transducer.

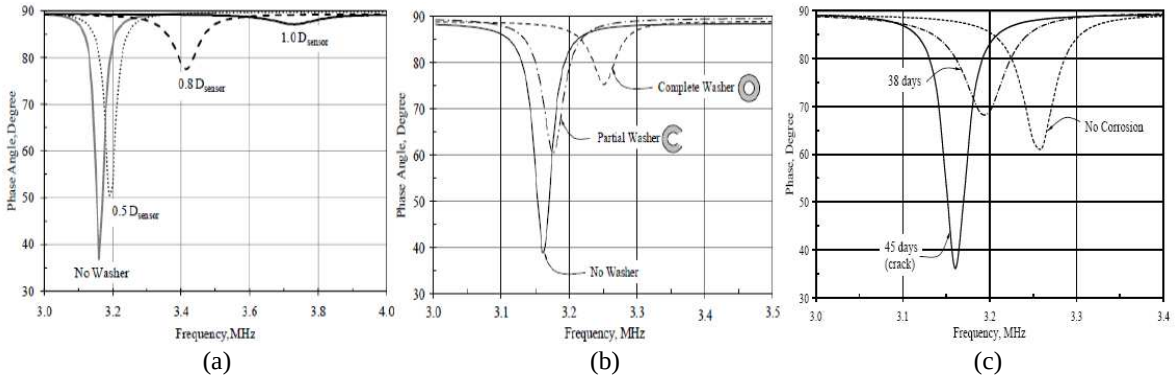

Figure 7: (a) and (b) Results of parametric tests performed on the inductively coupled steel washer as the transducer. (c) Results of salt water corrosion test performed on the steel washer.

analyzer. All measurements were performed at a fixed distance ensuring that the reader and sensor were coaxial In the phase response in Figure 5(b),the presence of a sacrificial "matched loop" produces a $\sim 20^0$ drop in phase dip and shifts the sensing tags resonance frequency from 3.6 to 3.9 MHz. A corrosion test was emulated by adding resistances to this matched loop (Figure 5(c)). As resistance (corrosion) increases it damps the loop response. When fully corroded, the transducer loop becomes an open circuit and the combined resonance reverts to its no loop state. Since we can "recover" the sensing tag's response, the reference tag appears to be redundant. Thus, the design is simplified by eliminating the reference tag and using just the sensing tag and the transducer. The change in the combined resonance frequency (f_o) of the tag and inductively coupled transducer in response to increasing corrosion (Figure 6(a)) shows a clear transition region between the corroded and uncorroded state. In this region the sensor can be potentially used as an analog corrosion sensor. Figure 6(b) indicates that the largest dynamic range in f_o i.e., shift from no loop response of the sensing tag is obtained when the loop diameter equals sensing coil diameter. A matched ring shaped coupled transducer was made out of Aluminum foil. The phase response (Figure 6(c)) indicates that it might be better suited to threshold sensor applications.

The parametric tests above were replicated while using a thin (1–2 mils) steel washer (ring) as the inductively coupled sacrificial transducer. The washer was chosen due to ease of fabrication, larger sensing area and unlike coils, washers have no solder joints. Initial tests with washers of various diameters attest that even for washers, the shift in resonant frequency (f_o) or dynamic range is maximum when the outer diameter of the washer is equal to the sensing coil (Figure 7(a)). Care should be taken that the washer is not too large or else it will entirely shield the sensing coil's response. We expect that as the washer corrodes, its area will reduce. When testing with washers with decreasing effective shielding areas (Figure 7(b)) we observe the phase response shifts back to the no washer state. We observe no damping effects in this response since there is no resistive loading of the transducer. However, when performing salt water exposure tests on the steel washer, the phase response (Figure 7(c)) exhibits damping similar to the resistance loaded loop transducers. The uniform corrosion that occurs when exposed to salt water changes the cross sectional area of

the washer thus increasing its resistance. Further parametric studies in salt water and concrete for washers and coils currently underway will inform the development of these sensors.

4. CONCLUSIONS

Our new sensor design aimed at corrosion monitoring, uses an inductively coupled sacrificial transducer. The transducer is fully exposed to its environment and is inductively coupled to the sensing tag (resonator). The environment affects the material properties of the transducer resulting in resistive loading and/or shifted resonance of the sensing tag via mutual inductance and frequency flux screening effects. We have made an initial study of the transducer shapes, size and materials. Using the optimum transduction layer morphology and material will extend its use to a range of environmental sensing applications.

ACKNOWLEDGMENT

The sponsors of this work include the National Institutes of Standards and Technology - Technology Innovation Program (NIST-TIP) and the National Science Foundation (NSF) grant number CMMI-0825486. Any opinions, findings, and conclusions or recommendations expressed in this publication are solely those of the author(s).

REFERENCES

1. Novak, L. J., K. M. Grizzle, S. L. Wood, and D. P. Neikirk, "Decelopment of state sensors for civil engineering structures," *Proceedings of SPIE's*, Vol. 5057, 358–363, San Diego, USA, March 2003.
2. Simonen, J. T., M. M. Andringa, K. M. Grizzle, S. L. Wood, and D. P. Neikirk, "Wireless sensors for monitoring corrosion in reinforce concrete members," *Proceedings of SPIE's*, Vol. 5391, 2004.
3. Andringa, M. M., D. P. Neikirk, N. P. Dickerson, and S. L. Wood, "Unpowered wireless corrosion sensor for steel reinforced concrete," *4th IEEEInternational Conference on Sensors,* 155–158, Irvine, Ca, November 2002.
4. Pasupathy, P., S. Munukutla, D. P. Neikirk, and S. L. Wood, "Versatile wireless sacrificial transducers for electronic structural surveillance sensors," *IEEE Sensors 2009*, Christchurch, New Zealand, October 2009.
5. Yousef, A. A., P. Pasupathy, S. L. Wood, and D. P. Neikirk, "Passive sensors for detecting corrosion in concrete bridge decks," *7th International Bridge Engineering Conference*, San Antonio, Texas, December 2010.

A Meta Model for Damage Prognosis of Concrete Structure

Othman Sidek, S. A. Quadri, and Shahid Kabir
Collaborative Microelectronic Design Excellence Centre (CEDEC)
Universiti Sains Malaysia, Engineering Campus, Malaysia

Abstract— Deterioration of concrete structures is a big problem; premature or unexpected failures of these structures are often catastrophic. Damage prognosis has become a new research focus that tries to use damage diagnosis knowledge to inform the responsible authorities on the expected remaining service life of the structure. The purpose of prognosis is to extract damage features from input–output or output-only data and model damage evolution to predict the remaining life of the structure. In this paper, we are presenting a reduced order model (Meta model) prototype for damage prognosis of concrete structure, which captures the relationship between inputs and outputs without providing a detailed description of the physics and geometry.

1. INTRODUCTION

Due to the increasingly high demands for safety and low cost maintenance, the use of a real-time structural health management (SHM) system for building structures is becoming more and more attractive. The degradation of concrete structures is always accompanied by many factors if these are detected at an early stage before significant degradation occurs, life of the structure can be extended by the performance of relatively low cost but timely maintenance measures. The integrity of a structural dynamic system is assessed using SHM/NDE by first diagnosing damage within the system and then second developing a prognosis for the system given the diagnosis and any information regarding the future operating environment. The problem particularly encountered for concrete structures is the sensitivity of NDE techniques to many characteristics of the material itself (heterogeneity) and of its environment. Thus reliable information is often difficult to extract. Many complementary techniques are essential to be combined for a better estimation of indicators and so to improve diagnosis and prognosis in Concrete structures [1]. The state-of-the-art in SHM/NDE gives operators information about damage but rarely produces accurate prognoses because diagnostic features are measurable and are often largely independent of the kind of system being monitored, whereas prognostics depend significantly on the system's operating environment under investigation and the material/structural constitutive behavior.

A prototype, meta model for damage prognosis is presented, developed by capturing relationship between Input and output features and thus applying analytical tools like polynomials, exponential decays and neural networks the redundant detailed description of physics and geometry can be eliminated. Design of experiments (DoE) [2] techniques will be applied to reduced variables to get judicious subset of finite elements. The functional Meta model can explore the relationships between input and output put entities thus reliable predictions can be done on collected data.

2. STRUCTURAL DAMAGE FACTORS

Structural damage occurs due to structural overloading or due to environmental conditions or infrastructure decay or combined effects. Concrete can undergo physical deterioration (cracking, frost, fire, etc.), chemical deterioration (sulphate attack, acid attack, sea water attack, alkali-aggregate reaction, leaching, etc.) and reinforcement corrosion [3, 4]. Corrosion of reinforcement bars in concrete is recognized as a major problem in the maintenance of the structural integrity of structures.

The concrete pH is usually in the range 12–13.5 and provides chemical protection to the rebars due to steel passivation. However, as the structure ages, severe corrosion problems may occur. The most important causes of corrosion initiation of reinforcing steel are the presence of chloride ions and carbon dioxide on the steel surface. Chloride ion causes local destruction of the passive film leading to localized corrosion. Carbon dioxide, on the other hand, reacts with the hydrated cement matrix, leading to a pH decrease and subsequent loss of steel passivity and to corrosion initiation. The corrosion of reinforcing steel in concrete is a major problem for civil engineers and surveyors as they maintain an ageing infrastructure. Potentially corrosion rehabilitation is a very large market for those who develop the expertise to deal with the problem. It is also a major headache for those who are responsible for dealing with structures suffering from corrosion [5–7]. Corrosion monitoring

in concrete is difficult because it involves many variables. The temperature and the concentration of dissolved species, such as chlorides, dramatically affect the type of corrosion and its rate. The controlling parameters generally fluctuate with time, requiring frequent, real-time measurements.

The freeze/thaw effect is one of the damage mechanisms that accounts significantly for the deterioration of concrete. It occurs when the concrete structure is saturated with water and subjected to repeated freezing and thawing cycles, an occurrence which is common in a cold climate environment [8] Fatigue failure plays an important role in concrete engineering by influencing failure mechanisms and accelerating structural degradation [9].

Extensive research on structural health monitoring, damage diagnosis and damage pattern recognition has been developed over the last two decades. Recently, damage prognosis has become a new research focus that tries to use damage diagnosis knowledge to inform the responsible authorities on the expected remaining service life of the structure such that efficient maintenance operations can be scheduled.

3. DAMAGE PROGNOSIS AND VARIOUS MODELS

Prognosis is usually defined as "the ability to perform a reliable and sufficiently accurate prediction of the remaining useful life of equipment in service" [10]. Consequently, the primary function of the prognostic is to project the current health state of equipment into the future by taking into account estimates of future usage profiles. This definition implies a degree of uncertainty because prognosis involves a projection into the future and the future cannot be predicted with certainty. Therefore, the result of the prognosis process can be summarized as follows: "If the forecast situation of a "degraded" system is considered as "safe" or "satisfactory" to perform the system goals, no action needs to be planned. The system will evolve to another acceptable degraded state and it can drift under control. Several maintenance alternatives must be investigated through the prognosis process if the forecast situation is not acceptable. In the latter case, it means that the current situation identified by the monitoring process will be used to assess new forecast situations resulting in the "virtual" deployment of each alternative (combining simultaneously the degradation and the restoration of the system). Then, the results of the different assessments will be used by the aided-decision-making module to select, by comparison, the most efficient maintenance policy. The execution of the prognosis process is therefore related to its integration with the monitoring and decision-making processes. From an engineering point of view, the deployment of the prognosis process can come from three types of approaches as classified by Byington et al. [11].

1) Experience-based prognostics: use statistical reliability to predict probability of failure at any point in time.
2) Evolutionary/statistical trending prognostics: multivariable analysis of system response and error patterns compared to known fault patterns.
3) Model-based prognostics: fully developed functional and physics-of-failure models to predict degradation rates at given loads and conditions.

In model based approach, assessment techniques can generally be classified as either physics-based or data-based, though practically speaking, a combination of the two will usually be employed. The physic-based assessments are especially useful for predicting system response to new loading conditions and/or new system configurations (damage states). However, physics-based assessment techniques are typically computationally intensive. Data-based assessment techniques, on the other hand, rely on previous measurements from the system to assess the current damage state, typically by means of some sort of pattern recognition method, such as neural networks. However, although data-based assessment techniques may be able to indicate a change in the presence of new loading conditions or system configurations, they will perform poorly when trying to classify the nature of the change. Thus, it is not uncommon to use the results from a physics-based model to train a data-based assessment technique to recognize damage cases for which no experimental data exists. Typically the balance between Physics-based models and data-based techniques will depend on the amount of relevant data available and the level of confidence in the physics-based models. Once the current damage state has been assessed, the prognosis problem can begin to be addressed by determining the goal for the prognosis.

4. META DATA MODEL

There are many damage prognosis models developed in the history, most on basis of desired particular application [12]. Here the purpose of prognosis is to extract damage features from input–output

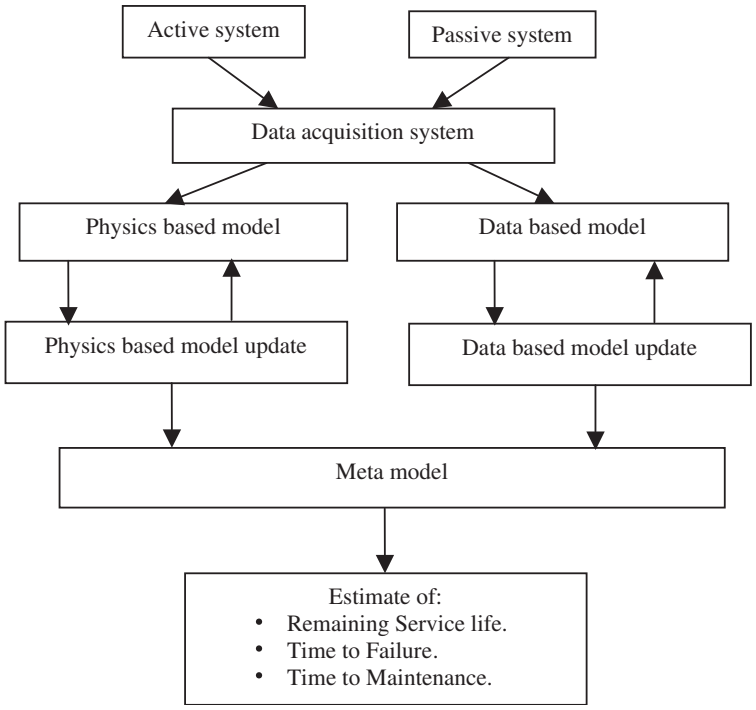

Figure 1: Meta data model for damage prognosis of concrete structure.

or output-only data and model damage evolution to predict the remaining life of the concrete structure. The prototype of Meta data model for damage prognosis of concrete structure is given in Figure 1.

Structural health monitoring techniques require the use of built-in sensors in a network to monitor external conditions and structural integrity. In general, there are two types of sensor-based diagnostic and monitoring systems: *active sensing* (e.g., [13, 14]) and *passive sensing* (e.g., [15, 16]). In our model both type of sensors are used to collect the data from the concrete structure. Data from the Active system and passive system is fed to data acquisition system. The physics based model and data based model are shown with update mechanism.

The high-fidelity, multi-scale physics models can provide unprecedented predictive capability for damage initiation and evolution, but these models are not suitable for on-board, near-real-time DP assessments. To address this issue, we are developing reduced order models referred to as metamodels that are based on outputs from the large-scale physics-based models. Metamodels capture the relationship between inputs and outputs without providing a detailed description of the physics and geometry. Examples include polynomials, exponential decays, and neural networks. Metamodels can run on microprocessors and therefore can be directly integrated with the sensing system. The process of developing the metamodels requires the ability to validate the physics-based models and the ability to quantify and propagate uncertainty through these models. Validation refers to the adequacy of a model to describe a particular physical phenomenon, and requires a comparison of the predictions with data collected during a series of physical experiments. Metamodels must be trained to identify their unknown parameters. Their quality must also be evaluated independently from the training step. Because analyzing a detailed finite element model at every combination of input variables is computationally prohibitive, training is generally based on a subset of carefully selected runs. Design of experiments (DoE) [2] techniques will be used to explore large design spaces and to select a judicious subset of finite element analyses.

5. CONCLUSION

Structural damage diagnosis continues to be an important area for basic research and development, damage prognosis has emerged as the next critical challenge in structural health monitoring (SHM) and non-destructive evaluation (NDE). The current work is focused on the development of a prototype prognosis model which explores remaining useful lifetime of concrete structure. The reduced order model referred as Meta model is able to capture the relationship between input and

output damage features from large scale physics based and data based models without providing a detailed description of physics and geometry, thus reducing redundancy. The future work is to make able proposed Meta data prognostic model for monitoring real time health condition of a concrete structure as well as provide an estimate of the residual strength and remaining useful lifetime to optimize the maintenance activity and provide safety.

REFERENCES

1. Marie-aude, P., G. Vincent, B. Denys, and M. Joseph, "Possibilistic NDT data fusion for evaluating concrete structures," *Proceeding of 7th International Symposium on Nondestructive Testing in Civil Engineering, NDTCE'09*, Nantes France, July 2009.
2. Wu, C. F. J. and M. Hamada, *Experiments: Planning, Analysis, and Parameter Design Optimization*, 1st Edition, John Wiley and Sons, Canada, 2000.
3. Mehta, P. K. and P. J. M. Monteiro, *Concrete: Microstructure Properties and Materials*, McGraw-Hill, New York, 2006.
4. Gani, M., *Cement and Concrete*, Chapman & Hall, London, 1997.
5. Broomfield, J. P., *Corrosion of Steel in Concrete: Understanding, Investigation and Repair*, 2nd Edition, Taylor & Francis, 2006.
6. Bentur, A., S. Diamond, and N. S. Berke, *Steel Corrosion in Concrete: Fundamentals and Civil Engineering Practice*, 1st Edition, Taylor & Francis, 1997.
7. Pedeferri, P., B. Polder, L. Bertolini, and B. Elsener, *Corrosion of Steel in Concrete: Prevention, Diagnosis, Repair*, 1st Edition, Wiley-VCH, Weinheim, 2004.
8. Neville, A. M., *Properties of Concrete*, 4th Edition, Addison Wesley Longman Limited, 1997.
9. Petryna, Y. S., D. Pfanner, F. Stangenberg, and W. B. Kratzig, "Reliability of reinforced concrete structures under fatigue," *Journal of Reliability Engineering and System Safety*, Vol. 77, 253–261, 2002.
10. Lebold, M. and M. Thurston, "Open standards for condition-based maintenance and prognostic systems," *Proceedings of the Fifth Annual Maintenance and Reliability Conference, MARCON*, Gatlinburg, USA, 2001.
11. Byington, C., M. Watson, M. Roemer, and T. Galie, "Prognostic enhancements to gas turbine diagnostic systems," *Proceedings of the IEEE aerospace Conference*, Big Sky, USA, 2001.
12. Farrar, C. R., H. Sohn, F. M. Hemez, M. C. Anderson, M. T. Bement, P. J. Cornwell, S. D. Doebling, N. Lieven, A. N. Robertson, and J. F. Schultze, "Damage prognosis: Current status and future needs," Los Alamos National Laboratory Report, LA-14051-MS, 2003.
13. Chang, F.-K. and S. Beard, "Active damage detection in filament wound composite tubes using built-in sensors and actuators," *Journal of Intelligent Material, Systems and Structures*, Vol. 8, 891–897, 1997.
14. Chang, F.-K. and J. B. Ihn, "Detection and monitoring of hidden fatigue crack growth using a built-in piezoelectric sensor/actuator network: Part II," *Smart Materials and Structures*, Vol. 13, No. 03, 621–630, 2004.
15. Chang, F.-K. and R. E. Seydel, "Impact identification of stiffened composite panels: Part I: System developments," *Smart Materials Structures*, Vol. 10, 354–369, 2001.
16. Park, J., "Impact identification in structures using a sensor network: The system identification approach," Ph.D. Thesis, Department of Aeronautics and Astronautics, Stanford University, 2005.

Multi Agent System for Agile Wireless Sensor Network to Monitor Structures

Othman Sidek, S. A. Quadri, and Shahid Kabir
Collaborative Microelectronic Design Excellence Centre (CEDEC)
Universiti Sains Malaysia, Engineering Campus, Malaysia

Abstract— The rapid and enormous construction of structures calls for rigorous SHM programme during construction, operation and maintenance. Thus much of the structures success or failure depends upon efficient SHM programs. The basic technology underlying SHM to detect cracks and failures is incorporated by Wireless Sensor Network technology. Thus the agility of WSN is a prominent factor for successful SHM programme. Unpredictable external events such as earth quake or high impact are an inevitable fact of life. For such an event WSN should be active and efficient enough to perform the assigned task without failure. The NMAOS (Never miss an opportunity scheme) a prototype based on Multi agent technology is proposed in this paper to provide agility to Wireless Sensor Network.

1. INTRODUCTION

The majority of SHM related research completed to date has focused exclusively on surface structures such as bridges and buildings and seems to have attained some level of maturity [1–5]. On-structure long-term monitoring systems have been implemented on bridges in Europe [6–9], the United States [10, 11], Canada [12, 13], Japan [14, 15], Korea [16, 17], China [18–20] and other countries [21, 23]. Successful SHM program relies on efficient and active Wireless Sensor Network performance.

Agility is defined as the capability of a WSN in timely capturing the event response of the monitored structure, processing the measured data and extracting the relevant features, and interpreting the results. The importance of WSN agility in the context of earthquake monitoring of bridges is described by Liang Cheng and S. N. Pakzad [24]. K. Wardhana and F. Hadipriono of Ohio State University [26] looked at 503 U.S. bridges that had failed between 1989 and 2000. The failed bridges included everything from spans designed to carry pedestrians over roadways to floating pontoon bridges across lakes. "Failure" was defined as anything from collapse to damage so serious the bridge had to be closed. Overall, they found that 53% of the failures came during floods, when raging waters undermine bridge footings or batter the structures with debris. The great floods of 1993 were particularly hard on bridges across the Midwest. Earthquakes brought down another 3% of the bridges. A collision with a car or a boat was the second leading cause of bridge failure, bringing down about 12%. Fourteen bridges were felled by a collision with a car or truck, while ships and barges toppled 10. Three bridges failed after collisions with trains. "Overloading" took third place in the survey. Roughly 10% of the bridges failed after too many people or cars crowded on to the span. The study notes that 107 people were injured after a walkway collapsed at an auto racetrack in North Carolina. Deterioration and design flaws, potential factors in the collapse of the Interstate 35 West Bridge in Minnesot were responsible for about 9% of the failures. Twenty bridges, for instance, failed due to corroded steel or related deterioration. In most of the collapses if we observe carefully the collapse was sudden with in fraction of seconds. From various sources it is a fact that the incidence of collapse is unpredictable and mostly happens suddenly causing disaster.

Here our point of interest is when we rely on SHM technology to monitor bridges, there should be maximum reliability, such that there should not be any human life losses due to passive state of monitoring system. For Such reliability we are proposing a model based on Multi agent technology for Agile Wireless sensor network.

2. PREVIOUS WORK

Over the past few years Multi-agent technology has come to be perceived as crucial technology not only for effectively exploiting the increasing availability of diverse, heterogeneous and distributed online information sources, but also as a framework for building large, complex and robust distributed information processing systems which exploit the efficiencies of organized behavior. Given the

general benefits of multi-agents, researchers have explored the possibility for WSN applications [27–29].

A design method for MAS based SHM system has been presented by the Yuan, Lai, & Zhao [30]. They presented a new parallel distributed SHM technology based on a smart WSN and multi-agent system for large scale engineering structures. Using this technology, the health monitoring system becomes a distributing parallel system instead of a serial system. Jian Wu and Shenfang Yuan [31] presented a multi-agent design method and system evaluation for WSN based SHM to validate the efficiency of the multi-agent technology. Through the cooperation of six different agents for SHM applications, the distributed wireless sensor network can automatically allocate SHM tasks, self-organize the sensor network and aggregate different sensor information.

The basic Idea of MAS technology proposed in our prototype is not different from the earlier models except that the aspect of WSN agility has been given prime importance such that the SHM programme should not miss a single opportunity resulting failure or non capture of data at the time of any unpredicted calamity.

3. PROTOTYPE

3.1. NMAOS

NMAOS (Never miss an opportunity scheme) is a prototype based on Multi agent technology for Agile Wireless sensor network. A multi-agent system (MAS) is a system composed of multiple interacting intelligent agents. To apply multi-agent technology to a distributed SHM system, each component or subsystem in the structural health monitoring system should be changed to an agent. According to the subsystem's functions, six kinds of agent are defined as follows for the purpose of attaining agile WSN for SHM system. The basic Idea of pulse-based media access control (PB-MAC) from [24] has been utilized as the theme of Model. The experience gained in Golden Gate Bridge (GGB) shows that existing non preemptive MAC without priority support has failed to capture earthquake signals in practice, and using a reset message flooding based on the existing MAC protocols will take a long time to propagate through a large WSN due to hidden terminals [32], which may also lead to the loss of the opportunity of capturing earthquake signals by the WSNs. PB-MAC is an out-of-band MAC in which the control channel only carries pulses and the data channel only carries packets, such as trigger-message, time-sync and data packets. A regular pulse consists of an active part of a coded length in a single-tone wave and a random pause part in two sub-parts, i.e., a contention window of a fixed size and a residual pause of a random length, where the contention window is cut into equal size contention sub-windows. A node transmits regular pulses in the control channel when it is transmitting a packet in the data channel. The active part of a pulse signals a busy data channel, while the pause part is mainly for collision detection. Any transmitting node hearing a pulse aborts its transmission. The length L of the active part of the pulse indicates the priority level P of the data packet in transmission; a longer active part indicates a higher level of priority for the data packet [33, 34]. The MAS prototype model for agile WSN is given in Figure 1.

3.2. Comparison Logic

When a node detects a pulse in the control channel, it measures the length of the pulse's active part. If the active length is a valid coding length for priority level information, the information L is decoded. Thus every receiver of the pulse has the knowledge of the priority level of the packet in transmission L_r. When a packet source S_i detects a busy control channel but finds that the priority levels L_i of its packet is higher than the priority level L_r of the packet in transmission, the source S_i starts a random back off timer as soon as the pulse in the control channel pauses. A packet source with a lower priority packet will defer and check the control channel status later. A higher level of priority acquires a smaller sub-window and thus a shorter delay. The source with the shortest back off delay (i.e., of the highest level of priority such as the trigger message's priority level) acquires the medium before other sources do, and this source becomes the winner source S_v in this round of contention. Thus S_o can detect the pulse of S_v and releases both channels. In the PB-MAC design, a relay scheme of pulses by the intended packet receiver is also designed to suppress hidden terminals [33, 34].

3.3. Triggering Agent

The successful dissemination of trigger messages in WSNs can make a difference between capturing a bridge's response to an event (earthquake/high impact) and missing the opportunity to do so. To achieve this goal to enable a WSN to capture the critical information, trigger message dissemination

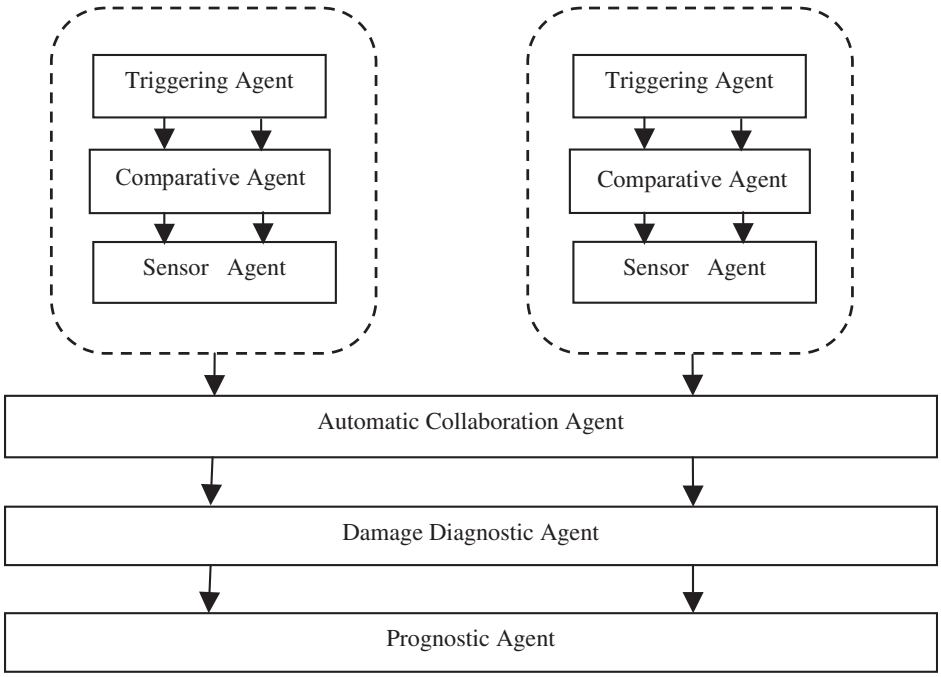

Figure 1: The multi-agent architecture for Agile WSN.

needs timely and lossless medium access in WSNs. A trigger message from a nearby observation site can be timely propagated across a WSN to preempt current tasks such as energy-saving sleeping and scheduled data transmissions so that the sensor network can be forced into a record ready state before the earthquake waves reach the monitored bridge. A self learning intelligent based software system which predicts the maximum peak load on the structure (bridge) for example at some particular time may trigger more priority messages to active monitoring system.

3.4. Comparative Agent

The comparative Logic is embedded in the comparative Agent, which accomplish the task of preempting current tasks such energy-saving sleeping and scheduled data Transmissions and allow trigger pulse to activate the whole system to monitor the structure at any disastrous event.

3.5. Sensor Agent

The Sensor agent is responsible for sensing parameters, such as stress, stain, displacement, acoustic, pressure, and temperature. Sensing agents can be implemented by smart sensors with an on-board microprocessor. There are sub agents in the sensor agent to accomplish many tasks such as data processing and disseminating.

3.6. Automatic Collaborating Agent

It is implemented by software in the power full desktop workstation that has wireless links to the sensor nodes and communicates with the cluster heads to a cluster-star framework which can completely support low-power, multi-point, and heterogeneous operations with a distributed synchronization mechanism. It takes care of clustering, fusing and communication of data exchange between different agent entities.

3.7. Damage Diagnostic Agent

It comprises of real time automated reasoning and decision making integrated software system. Several models and techniques [35–37] are available which can be used for exact and accurate assessment of cracks and disorders in the infrastructures constituting the damage as whole. A model's principal purpose is to predict, from first principles, the measurement system's response to specific anomalies in a given material or structure, (e.g., cracks, voids, distributed damage, corrosion, deviations in material properties from specification, and others). Thus, a measurement model includes the configuration of the probe and component being inspected, as well as a description of the generation, propagation and reception of the interrogating energy. Numerical results based on a reliable model are very helpful in the design and optimization of efficient testing configurations. Model is

also indispensable in the interpretation of experimental data and the recognition of characteristic signal features. A measurement model is a virtual requirement for the development of an inverse technique based on quantitative data. A measurement model whose accuracy has been tested by comparison with experimental data provides a practical way of generating a training set for a neural network or a knowledge base for an expert system.

3.8. Prognostic Agent

The task of the prognostic agent is to evaluate the remaining life-time of the structure at a given state of damage and future loading. These future load spectra can be either damage tolerance or safe-life philosophy. The results of damage diagnostic agent provide information on the current state of the structure for prognostics. Material-level modeling of constitutive properties, supported by experimental results, provides the input for damage growth law. A damage growth law together with a multi scale structural model forms the input to a module on probabilistic prognosis, which in turn provides information on damage evolution and remaining life. Depending on its magnitude, the resulting statement of failure probability may either result in a recommendation for repair or replacement of a structural component, or, when the probability is low, for an additional cycle in the diagnostics/prognostics loop of the structural health management system. Accordingly, the strategy of the integrated system comprises that after damage diagnosis by the active damage agent the current health status of the structure is submitted to the prognostic agent to achieve certain prognostic information. Prognostic models [38–41] are widely available for predicting damage growth and estimating residual strength and remaining useful lifetime (RUL) of structures made of metals or composites. In order to yield accurate predictions of damage growth and residual strength, one key issue is to create a proper link between the diagnostic outputs and prognostic inputs.

4. CONCLUSION

Agility of WSN is an important factor contributing to reliable and successful SHM program. A prototype NMAOS (Never miss an opportunity scheme) based on Multi agent technology is proposed in this paper. The model uses PB-MAC based technique of triggering a message of high priority to preempt the current passive state of WSN and make it active for sensing and capturing data at the time of any unpredicted event of high impact on structure. Our future step is to verify and validate the cognitive Multiagent based prototype in real time situation to develop an agile Wireless Network System to monitor structures.

REFERENCES

1. Pandey, A. K. and M. Biswas, "Damage detection in structures using changes in flexibility," *Journal of Sound and Vibration*, Vol. 169, 3–17, 1994.
2. Farrar, C. R. and D. A. Jauregui, "Comparative study of damage identification algorithms applied to a bridge: I. Experiment," *Smart Materials and Structures*, Vol. 7, 704–719, 1998.
3. Aktan, A. E., F. N. Catbas, K. A. Grimmelsman, and C. J. Tsikos, "Issues in infrastructure health monitoring for management," *Journal of Engineering Mechanics, ASCE*, Vol. 126, 711–724, 2000.
4. Brownjohn, J. M. W., P. Moyo, P. Omenzetter, and Y. Lu, "Assessment of highway bridge upgrading by dynamic testing and finite-element model updating," *Journal of Bridge Engineering, ASCE*, Vol. 8, 499–506, 2003.
5. Moyo, P., "Structural performance monitoring and health assessment of highway bridges," Ph.D. thesis, Nanyang Technological University, Singapore, 2002
6. Andersen, E. Y. and L. Pedersen, "Structural monitoring of the great belt east bridge," *Proceeding of the Third Symposium on Stait Crossing*, Edited by J. Krokebogr, Vol. 94, 189–195, Balkema, 1994.
7. Myrvoll, F., K. A. Aarnes, R. M. Larssen, and K. Gjerding-Smith, "Full scale measurements for design verification of bridges," *Proceedings of the 18th International Modal Analytical Conference Society for Experimental Mechanics*, 827–835, Bethel, CT, 2000.
8. Brownjohn, J. M. W., "Lessons from monitoring the performance of highway bridges," *Proceedings of the International Workshop on Advanced Sensors, SHM and Smart Structures*, 2003.
9. Casciati, F., "An overview of SHM expertise within the European Union," *Structural Health Monitoring and Intelligent Infrastructure*, 31–37, Balkema, 2003.

10. Pines, D. J. and A. E. Aktan, "Status of structural health monitoring of long span bridges in the United States," *Progress in Structural Engineering and Materials*, Vol. 4, No. 4, 372–380, 2002.
11. Wang, M. L., "State-of-the-art applications in health monitoring," *Workshop on Basics of SHM and Optical Sensing Technologies in Civil Engineering*, 113–142, Taiwan National Central University, 2004.
12. Cheung, M. S. and N. Naumoski, "The first smart long-span bridge in Canada — Health monitoring of the confederation bridge," *Proceedings of the 1st International Workshop on SHM of Innovative Civil Engineering Structures*, 31–44, Winnipeg, Canada, 2002.
13. Mufti, A. A., "SHM of innovative Canadian civil engineering structures," *SHM*, Vol. 1, 89–103, 2002.
14. Wu, Z. S., *Structural Health Monitoring and Intelligent Infrastructure*, 153–157, Balkema, 2003.
15. Fujino, Y. and M. Abe, "SHM — Current status and future," *Proceedings of the 2nd European Workshop on SHM*, 3–10, Lancaster, PA, 2004.
16. Wu, Z. S. and M. Abe, *SHM and Intelligent Infrastructure*, 99–111, Balkema, 2003.
17. Yun, C. B., J. J. Lee, S. K. Kim, and J. W. Kim, "Recent R &D activities on SHM for civil infra-structures in Korea," *KSCE Journal of Civil Engineering*, Vol. 7, 637–51, 2003.
18. Xiang, H. F., "Health monitoring status of long-span bridges in China," *Proceedings of the Workshop on Research and Monitoring of Long Span Bridge*, 240–231, 2000.
19. Zingoni, A., *Progress in Structural Engineering, Mechanics and Computation*, 599–608, Balkema/Taylor and Francis, London, 2004.
20. Wong, K. Y., "Instrumentation and health monitoring of cable-supported bridges," *Structural Control and Health Monitoring*, Vol. 11, 91–124, 2004.
21. Chang, F. K., *SHM: Current Status and Perspectives*, 410–417, Technomic Press, Lancaster, 1997.
22. Chase, S. B. and A. E. Aktan, *Health Monitoring and Management of Civil Infrastructure Systems*, 113–121, The International Society for Optical Engineering, Bellingham, 2001.
23. National Highways Authority of India, Instrumentation (SHM) for Yamuna Bridge at Allahabad/Naini, tender document, 2002, available at http://www.nhai.org/nit.htm.
24. Cheng, L. and S. N. Pakzad, "Agility of WSN for earthquake monitoring of bridges," *Proceeding of the 6th International Conference on Networked Sensing Systems*, 1–4, Pittsburgh, USA, 2009.
25. Pakzad, S. N., G. L. Fenves, S. Kim, and D. E. Culler, "Design and implementation of scalable WSN for structural monitoring," *Journal of Infrastructure Engineering, ASCE*, Vol. 14, 89–101, 2008.
26. Wardhana, K. and F. C. Hadipriono, "Discussion of study of recent building failures in the US," *Journal of Performance of Constructed Facilities*, Vol. 19, No. 2, 182–192, 2005.
27. Helvik, B. E. and O. Wittner, "Using the cross-entropy method to guide/govern mobile agent's path finding in networks," *Proceedings of 3rd International Workshop on Mobile Agents for Telecommunication Applications*, 255–268, 2001.
28. Kumar, S., D. Shepherd, and F. Zhao, "Collaborative signal and information processing in micro-sensor networks," *IEEE Signal Processing Magazine*, Vol. 19, 13–14, 2002.
29. Qi, H., S. S. Iyengar, and K. Chakrabarty, "Multi-resolution data integration using mobile agents in distributed sensor networks," *IEEE Trans Systems, Man, and Cybernetics, Part C: Applications and Review*, Vol. 31, 383–391, 2001.
30. Yuan, S. F., X. S. Lai, and X. Zhao, "Distributed SHM system based on smart wireless sensor and multi-agent technology," *Smart Materials and Structures*, Vol. 15, 1–8, 2006.
31. Wu, J., S. Yuan, S. Ji, G. Zhou, Y. Wang, and Z. Wang, "Multi-agent system design and evaluation for collaborative wsn in large SHM," *Expert Systems with Applications*, Vol. 37, 2028–2036, 2010.
32. Wang, Q., Y. Zhu, and L. Cheng, "Reprogramming wireless sensor networks: Challenges and approaches," *IEEE Network*, Vol. 20, No. 3, 48–55, May/June 2006.
33. Peng, J. and L. Cheng, "A distributed MAC scheme for emergency message dissemination in vehicular ad hoc networks," *IEEE Transactions on Vehicular Technology, Special Issue on Vehicular Communications Networks*, Vol. 56, No. 6, 3300–3308, 2007.

34. Peng, J. and L. Cheng, "A MAC protocol for disseminating loss and delay sensitive messages in wireless packet networks," Tech Report LU-CSE-06-012, Department of CSE, Lehigh University, 2006.
35. Chang, F.-K. and R. E. Seydel, "Impact identification of stiffened composite panels, Part I: System developments," *Smart Materials and Structures*, 2001.
36. Park, J., "Impact identification in structures using a sensor network: The system identification approach," Ph.D. Dissertation, Department of Aeronautics and Astronautics, Stanford University, 2005.
37. Mueller, I., C. Larrosa, S. Roy, and F.-K. Chang, "An integrated diagnostic and prognostic SHM technology for Structural Health Management," Stanford University, 2000.
38. Hashin, Z., "Failure criteria for unidirectional fiber composites," *Appl. Mech.*, Vol. 47, 329–334, 1980.
39. Chang, F.-K and X. L. Qing, *Recent Advances in Structural Joints and Repairs for Composite Materials*, Edited by L. Tong and C. Soutis, 101–140, Kluwer Academic Publisher, 1997.
40. Shahid, I. and F.-K. Chang, "Progressive failure analysis of laminated composites subjected to in-plane and shear loads," Department of Aeronautics and Astronautics, Stanford University, 1993.
41. Choi, H., "Damage in graphite/epoxy laminated composites due to low-velocity impact," Ph.D. Dissertation, Department of Aeronautics and Astronautics, Stanford University, 1990.

Optical Image Analysis Based Concrete Damage Detection

Akram Salem[1], **Shahid Kabir**[2], **and Atif Musbah**[1]

[1]School of Civil Engineering, Engineering Campus, Universiti Sains Malaysia (USM), Malaysia
[2]Sustainable Materials and Infrastructure (SMI) Cluster
Collaborative μ-electronic Design Excellence Centre (CEDEC)
Engineering Campus, Universiti Sains Malaysia (USM), Malaysia

Abstract— The deteriorating condition of concrete infrastructure and the prohibitive costs required for upgrading them require the development of innovative and effective decision support tools. Such tools will enable predictions about the condition and future performance of concrete structures and the allocation of limited funds for optimized maintenance that yields improved reliability and minimum life cycle costs. Furthermore, improved control on the variability between predicted and actual repair quantities would tend to reduce the long-term unit price of repair work, as contractors adapt to less instances of work shortfalls. There is a growing need for precise and reliable methods that use non-destructive testing (NDT) techniques to assess the deterioration in concrete structures and the extent of associated damage. Current use and development of monitoring methods and imaging techniques employing NDT is limited due to the unavailability of enough experimental data and field applications. This research aims to enhance image processing methods for application to imagery of concrete blocks that were exposed outdoors to the elements, and concrete slabs that were kept in the laboratory in controlled environments, in order to extract quantitative deterioration information from the concrete images obtained using various NDT imaging methods. Evaluations are done on the efficiency of the various types of NDT imaging methods of colour and greyscale imagery, in detecting different types of concrete deterioration and correlation between damage quantities obtained from processing of the concrete imagery and test measurements recorded for the laboratory specimens is established.

1. INTRODUCTION

The deteriorating condition of concrete infrastructure and the prohibitive costs required for upgrading them require the development of innovative and effective decision support tools. Such tools will enable predictions about the condition and future performance of concrete structures and the allocation of limited funds for optimized maintenance that yields improved reliability and minimum life cycle costs. Furthermore, improved control on the variability between predicted and actual repair quantities would tend to reduce the long-term unit price of repair work as contractors adapt to less instances of work shortfalls. There is a growing need for precise and reliable methods that use non-destructive testing (NDT) techniques to assess the deterioration in concrete structures and the extent of associated damage.

Current use and development of monitoring methods and imaging techniques employing NDT is limited due to the unavailability of enough experimental data and field applications. The lack of this type of research is largely due to the fact that traditionally civil engineering has shown little interest in these techniques mainly because of insufficient knowledge of the available methods, as well as technical limitations and their related high costs. Over the years, though, many technological obstacles, such as computer efficiency, infrared camera resolution, equipment transportability, as well as the price of equipment, have been greatly reduced. The development of NDT imaging methods is very promising because it also provides a better understanding of the physio-chemical phenomena that interact within the concrete.

Certain imaging methods have proven to be very efficient in collecting concrete data. However; acquiring data is only the first step in assessing and evaluating concrete deterioration. This data has to be processed and interpreted in order to present the information in a more meaningful and useful format. If efficient and accurate imaging techniques can be developed, this approach can be a highly potential source of reliable information concerning the actual condition of concrete, which can be used to predict the safety and serviceability of concrete structures. The use of image processing methods on NDT imagery for the extraction of concrete deterioration information can be compared with visual inspection approaches that were traditionally employed to evaluate the condition of a concrete structure in service. Contrary to visual inspections, which, in most cases, remain qualitative, the proposed methods employ classification techniques, which present

the greater advantage of providing quantitative information due to their capacity to analyze images, pixel by pixel, based on their numerical properties. Also, acquiring most of the types of NDT imagery employed in this research is not relatively costly, time consuming, or a disruption to traffic, thus allowing for more frequent monitoring, which is another important factor in effective bridge maintenance [1]. As a result, the information obtained from the approaches described in this study can be used to supplement visual inspections. The quantitative nature of this data and its regular collection can promote the establishment of deterioration criteria through the determination of correlation between deterioration factors and damage within concrete. Furthermore, these techniques present the potential to be incorporated into an automated monitoring system for concrete infrastructure. Up to now, automated recognition of deterioration modes in concrete from monitoring data has been the object of very few research projects. In this context, this study constitutes an important contribution to a better understanding of automated image analysis, and how such tools can be used to assist inspectors in the assessment of the condition of concrete structures in order to provide more reliable concrete monitoring and decision making. The objective of the current study is focused on the quantifying surface cracks in concrete structures by using optical imaging technique and analysis of other concrete deterioration problems like erosion, spalling, pop outs and corrosion in concrete structures by using Optical imaging technique.

2. RESEARCH METHODOLOGY

Optical images present image data of the surface as it directly measures the absorption and scattering properties of the structure under investigation. High-resolution digital cameras are employed to capture the live images, which are instantly transferred to a computer to conduct digital image processing. By applying a wide range of algorithms, together with a sophisticated computer software system, image segmentation, feature classification, image interpretation, and pattern recognition can be implemented efficiently, automatically or semi-automatically with certain interactive manipulations by the operator. Optical imaging and digital image processing play an important role in Non-Destructive Testing. There are a number of advantages over other commonly used algorithms are typically required for long term health monitoring and for damage detection after a catastrophic event. Among the many methods for long term health monitoring are the methods that estimate changes in structural frequencies, mode shape curvatures or strain mode shape changes, matrix update methods which measure changes in mass, stiffness and damping matrices, and hybrid matrix update methods [2]. Provide extensive discussion on the advantages and disadvantages of these methods. For extreme event damage monitoring, as mentioned previously, nonlinear methods is required. Although methods have been developed for nonlinear components, treatment of nonlinear systems has been considered only to a limited extent [3, 4]. Non-destructive testing methods include the rebound method, ultrasonic method, ray techniques such as ultrasound and electromagnetic methods. For example, optical imaging can acquire information (i.e., images) of a component without direct contact. It is also an area scanning method, capable of instantaneous recording of a two-dimensional image of an object. Once the live images are taken, appropriate image processing reveals potential damages within the structure under investigation. NDT techniques can also be used to monitor the integrity of the structure throughout its design life. For this projects which is damage analysis of structures built with concrete, NDT techniques did not alter the concrete or impair the function of the structure. Analytical methods for structural dynamic property identification are typically divided into time domain and frequency domain techniques. System identification methods are further divided into linear and nonlinear methods. The goal of these techniques is to evaluate the dynamic structural characteristics, such as stiffness, damping, structural period, and mode shapes, and monitor changes in their values or signatures as extreme dynamic loads are applied to the structure. Changes in modal parameters alone, such as natural frequencies and eigen-mode shapes have shown not to be robust estimators of structural damage (Loh, 1995). Data collection was carried out at the selected sites using the equipments (digital photo camera7.2-megapixel, ultra-compact camera). The equipment is actually very good for applications in concrete; it is very useful in NDT imaging to assist in the evaluation of concrete structures. Story drifts, large rotations, and shear force, and strain distributions can be benchmarked to establish performance criteria and show promise as reliable indicators of structural damage. Earthquakes, hurricanes and tornadoes impose random and extreme loads on structures, thus the response of the structure is also random and usually nonlinear. Six optical images were collected from different structure parts of the Seri-Empagan mosque which have different degree and kinds of damages such as; cracks, popouts, erosion, spalling and corrosion. Accordingly, the

nonlinear behavior of the structural components needs to be considered in these algorithms. Also, different damage method and the core test method. In this study minimum distance supervised classification is used to cluster pixels in the data set into classes corresponding to user defined training classes. Minimum distance classifies image data on a database file using a set of 256 possible class signature segments as specified by signature parameter. Each segment specified in signature, for example, stores signature data pertaining to a particular class. Only the mean vector in each class signature segment is used. Other data, such as standard deviations and covariance matrices, are ignored (though the maximum likelihood classifier uses this). The result of the classification is a theme map directed to a specified database image channel. A theme map encodes each class with a unique gray level. The gray-level value used to encode a class is specified when the class signature is created. If the theme map is later transferred to the display, then a pseudo-cooler table should be loaded so that each class is represented by a different color. This was done to generate or prepare images that were ready for quantified measurement routines during the result preparation stage. This stage covers a wide range of possible image enhancement operations, including removal of artifacts, shading corrections, contrast/brightness optimizing, filtering, thresholding/segmenting, feature identification, feature reconstruction, arithmetic and logical image operations and final images generation. This often means that a 'binary' image is produced which has a bit depth of only two, i.e., it consists of areas/features of either black or white. Colour images can also be prepared for measurement, but their sensitivity to colour variation is very high given that true-colour images (24 bit or more) can cover a possible digital spectrum of several millions of colours. The significance of this is that segmentation either at this stage or during measurement stages can include pixels not related to a region of interest (ROI) or exclude pixels of an ROI, as such, great care was exercised when designing the routines to achieve this.

3. RESULTS AND DISCUSSION

Optical Images of parts of concrete structures in the mosque which were damaged were taken with the use of digital camera. After application of the texture analysis, and other optical imaging techniques to the image sample, the resulting processed images were employed as input images in the analysis software in order to perform the classifications. Classification is a method by which labels are attached to pixels according to their spectral characteristics by a computer, which is trained beforehand to recognize pixels with similar spectral properties. The images were classified and analyzed by using an image classification and analysis software called ENVI v4.0. The width and length of the cracks are then determined and calculated accordingly.

Figure 1 presents the classifications of the different input images resulting from the image processing technique. The following tables provides the number of pixels in each class, the percentage of pixels in each class in relation to the whole input image sample, the individual classification accuracies for each class:

Image data must be interpreted with care. It should always be noted that statistically, the small area analyzed using the camera is almost certainly not representative of the employed to quantify the amount of damage found for a particular input image. Consequently, the percentage of pixels in the damage class is used as an indication of the total amount of damage in the image sample as established by the input image. At the completion of a classification process, it is necessary to assess the accuracy of the results obtained. This provides a degree of confidence relating to the

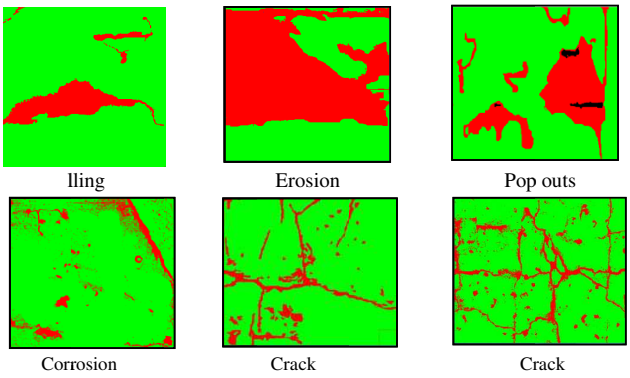

Figure 1: Classified images.

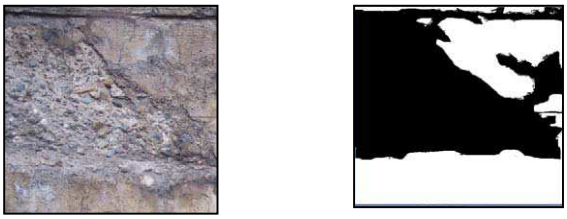

Figure 2: Images of erosion damage.

Table 1: Class statistics summary report.

Erosion	No Damage
20.1624%	79.8376%

results and serves to indicate whether or not the analysis objectives have been achieved. Accuracy is determined empirically, by selecting a sample of pixels from the classified image and checking their labels against classes determined from verification data (ground truth data). From these checks, the percentage of pixels from each class in the image labelled correctly by the classifier can beestimated, along with the proportions of pixels from each class erroneously labelled into every other class. In order to better represent the damage class and to further analyse surface damage, the classified images were converted into binary images. This process simplifies the image by assigning the pixels that represent the damage in the concrete a value of 1 (black) and the background pixels a value of 0 (white). Manual or automated methods are then used to count or sum the pixels to calculate total wide-crack length, as well as average wide-crack width. Figure 2 shows the grayscale image and the binary image of the erosion damaged concrete, the image was classified and analyzed by using ENVI v4.0. Table 1 shows the class statistics summary which indicates the number of pixels classified into each object class, and the percentage of the image occupied by each class. Table 2 shows the accuracy of the classification of the image, while Tables 3 and 4 shows the ground truth in pixels and in percentage respectively.

4. CONCLUSION

The results of this research confirm the major hypo Research of this thesis, that statistical texture analysis is quite an efficient method for the discrimination of different types of deterioration, such as cracks, spalling, corrosion, pop-outs, erosion, and corrosion stains, from optical concrete imagery. Quantification of the amount of surface deterioration present in the image samples was effectively performed using class statistics summaries from the classifications. Further damage quantities were obtained for the imagery after conversion of the thematic maps into binary images, such as total crack length and average crack width, by using pixel summations. Lastly, the image processing method used in this research for analysing deterioration in concrete was quite effective and efficient in providing good results. The results of; crack, spalling, pop outs, corrosion and erosion can be classified easily by using static method through optical image. More so, it is also cost- and time-effective quantitative evaluations of concrete damage and the approach allow assessments to be carried out more often, and can be used to supplement visual inspections. The future work recommended is to investigate other imagery techniques like colour or thermographic imagery techniques in order to comparison between the results of the three methods, and also more concrete damages can be studied.

REFERENCES

1. Abudayyeh, O., M. Al Bataineh, and I. Abdel-Qader, "An imaging data model for concrete bridge inspection," *Advances in Engineering Software*, Vol. 35, 474–480, 2004.
2. Doebling, et al., 1996.
3. Carino, N., "Non-destructive test methods to evaluate concrete structures," *Proceedings of the 6th CANMET/ACI International Conference on Durability of Concrete*, Thessaloniki, Greece, 2003.
4. Büyüköztürk, O., "Imaging of concrete structures," *NDT & E International*, Vol. 31, No. 4, 233–243, 1998.

Sensors-based Noise Removal Method from Pile Integrity Test (PIT) for Concrete Marine Piles

S. Mohsen[1], **S. Asaei**[2], **Shahid Kabir**[1], **and Atif Musbah**[1]

[1]School of Civil Engineering, University Sains of Malaysia (USM), Engineering Campus
P. Pinang, Malaysia
[2]Collaborative Micro Electronic Design Excellence Centre (CEDEC)
Universiti Sains, Engineering Campus, Nibong Tebal, Penang, Malaysia

Abstract— Marine piling is the most commonly used method for offshore construction. Cast-in-situ piles are the most helpful columns substantially used in marine structures. Considering the aggressive condition of the marine environment within the vicinity of piles, these columns are susceptible to corrosion. The piles must be tested to address their deficiencies, and the pile integrity test (PIT) method is widely used. This method is based on waves made by some special hammers that beat the piles, and the response waves are recorded. However in this case, the noise produced by marine waves must be taken into account. This paper describes the method adopted for measuring marine pile noise, which is designed based on wave force and the beating period of marine waves. In this method, a system of sensors is simultaneously deployed at the front side of piles through wave vectors. This system allows the measurement of the beating intensity sequence of wave collisions with piles, which may interrupt the response waves recorded by the PIT system. This enables the prompt determination of the effects of any wave collision. Relevant formulas are used to measure force and time, and to generate the most accurate graphs.

1. INTRODUCTION

Anyone with experience in reinforced concrete construction has encountered columns that, upon dismantling of the forms, exhibit air voids and honeycombing. Although these columns may have been cast with good-quality concrete, in properly assembled forms and with careful vibration, they still exhibit defects. Cast-in-situ piles are also columns, but instead of forms made of wood or metal, we have a hole in the ground. This hole may pass through layers of dumped fill, loose sand, organic matter, and ground water, which may be fast flowing or corrosive. Obviously, these conditions are not conducive to high-quality end products. In most sites, we still manage to get excellent piles. However, this is only a tribute to a dedicated team that makes the feat possible: a geotechnical engineer, structural engineer, quantity surveyor, contractor, site supervisor, and quality control laboratory personnel. This is obviously a chain, the strength of which is determined by the weakest link. One of the most helpful methods in determining the deficiency of piles is through the pile integrity test (PIT) method. This is a dynamic method using sonic waves and pertinent response. The sonic test is a powerful quality-control tool, but we must never forget that it is not omnipotent. The sonic method is based on the use of stress waves; hence, it can only identify pile attributes that influence wave propagation.

In this process, noise is often an unintended by-product of offshore activities, and increasing levels of man-made sounds in the ocean (whether deliberately generated or not) lead to concerns over marine noise pollution and its effect on marine life [9]. Noise is the enemy of all physical measurements, and its magnitude in relation to the measured signal is of utmost importance. In sonic tests, there are numerous sources of noise as follows [5]:

- Surface (Rayleigh) waves created by hammer blows are reflected from the boundaries, causing high-frequency noise.
- Often, a short piece of casing is used at the top of a pile during concreting and is later pulled out, resulting in a sharp decrease in the cross section at the bottom of the casing. This decrease creates regularly repetitive reflections, which (except for the first one) appear as medium-frequency noise.
- Trimming of the pile tops usually leaves a rough surface. A concrete protrusion may break and create random noise when hit with a hammer.
- High-frequency noise may also be produced by careless hammer blows, which may hit reinforcement bars.

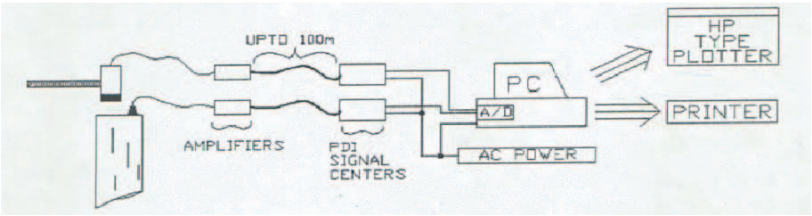

Figure 1: PIT system.

- The top of a pile may produce pure noise (usually of a wavy form) when it is not trimmed enough, or not at all.
- Underwater and ambient acoustic noise in the ocean [10]
- Piling noise [11]
- Road and traffic noise [13]
- Acoustic sounds of marine animals, such as mammals [12, 15]
- Sea waves that frequently beat against piles.

These noise sources may lead to severe misinterpretations by inexperienced individuals. Faulty piles may be declared sound, and vice versa. Needless to say, a noisy signal is practically worthless because it masks important features that could otherwise be detected. The force of sea waves relates to wave height. The waves run into or splash against pile bodies, creating noise. Figure 1 shows the manner of execution by the PIT system, which depends on beating the top of piles using special hammers. It means that every simultaneous beating may be recorded by this system, leading to errors in system estimation. These sources of noise may pose as genuine responses to PIT hammers, which beat the top of piles. It therefore follows that the proposed model eliminates the noise from the output graph of the PIT system. By measuring the force of the wave corresponding to beating time, we generate a separate noise graph due to sea waves. Finally, by subtracting the PIT system record graph from the noise recording, a pure graph of hammer response is obtained. Many attempts, such as spatial variations in radiated acoustic fields, have been made to assess noise from various sources. Hydrophones have been deployed from vessels to traverse fields along a radial transect from the location of focal piles [1, 3, 4]. However, there is no study that focuses on wave collision with pile bodies, which creates noise and may lead to system miscalculations. In this study, wave force measurement is considered. This has also been a concern of many investigations on the mutual interplay between piles or cylinders and sea waves [19] and on other aspects [16, 20].

2. METHODOLOGY

To obtain the amplitude of wave force in the PIT test, special buoys must be installed within the vicinity of the pile to record the height of waves beating against the pile body during the PIT test. The deployed recording systems may consist of broadband arrays operated from an operator near the pile location. This combination enables the simultaneous recording of the entire piling sequence from fixed locations using the PIT system to assess changes in the source of noise over time and to record them simultaneously using the height measuring system. Figure 2 shows a schematic illustration of typical system deployment in measuring height of waves. Generally, buoy systems must be deployed at the nearest space to the pile body. The application of the wave height measurement buoy, such as the one nearest to the pile, eliminates the time delay during the recording of the wave height. To estimate the force of waves beating against the pile body, arithmetic correlation is proposed in the literature to identify the force due to sea waves. To draw the two-dimensional time-collision force, two components time and force are required. Proposed relations determine the force and net force location. They are used to determine the sea wave response, which is recorded by the PIT sensor. The important parameters that describe waves are their length and height, and the water depth over which they are propagating. All other parameters, such as wave-induced water velocities and accelerations, can be determined theoretically from these quantities. In Figure 2, a two-dimensional schematic diagram of a wave propagating in the x direction is shown. The length of the wave (L) is the horizontal distance between two successive wave crests, or the high points on a wave, or alternatively the distance between two wave troughs (Figure 2). The wave length is later shown to be related to water depth (h) and wave period (T),

which is the time required for two successive crests or troughs to pass a particular point. The wave has to move a distance L in time T; hence, the speed of the wave, called celerity (C) is defined as $C = L/T$. While the wave form travels C, the water comprising the wave does not translate in the direction of the wave. The coordinate axis used to describe wave motion is located at the still water line, $z = 0$. The bottom of the water body is at $z = -h$ [4]. The step estimation of wave force is as follows.

L_0 determination:

$$L_0 = \frac{9.81T^2}{2\pi} \tag{1}$$

In this equation, T is the wave period as described earlier.

The method of iteration determines factor L (wave length) according to the following formula:

$$\frac{L}{L_0} = \tanh\left(\frac{2\pi h}{L}\right) \tag{2}$$

where h is the water depth within the vicinity of the pile body (see Figures 2 and 3).

After obtaining factor L from Equations (1) and (2), factor k is obtained:

$$k = \frac{2\pi}{L} \tag{3}$$

To determine the Reynolds factor, there is a need to calculate the horizontal celerity of wave particles directly related to the height of the sea wave:

$$u = -\frac{\partial\phi}{\partial x} = \frac{H}{2}\sigma\frac{\cosh k(h+z)}{\sinh kh}\cos(kx - \sigma t) \tag{4}$$

where h is water height and H is wave height.

The horizontal and vertical velocity components as a function of position are 90" out of phase; the extreme values of the horizontal velocity appear at the phase positions $(kx - \sigma t) = 0, \pi \ldots$. (under the crest and trough positions), whereas the extreme vertical velocities appear at $\pi/2$, $3\pi/2 \ldots$ (water surface displacement is zero). Determination of the Reynolds number is identified the C_m and C_d factors. In general, C_d and possibly C_m variable as the Reynolds number surely does. Therefore, we cannot integrate equations of force determination that appear directly. If we take constant values of C_d and C_m and use the linear wave theory and consider only the local acceleration term, the integration can be carried out up to the mean free surface to give an approximation of the total force to consider. In practice, CD is generally in the order of unity and depends on piling roughness in addition to Reynolds number.

$$R_e = \frac{UD}{\upsilon} \tag{5}$$

where U is wave particle velocity obtained during the previous stage (Equation (4)), D is the cylindrical pile section diameter, and υ is kinematic viscosity, which is conventionally postulated

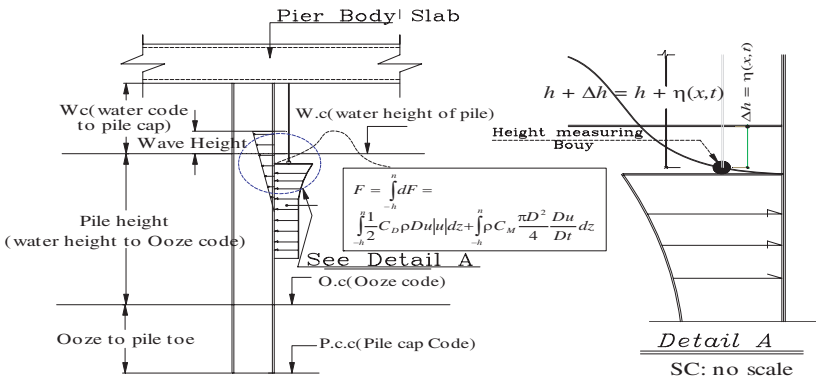

Figure 2: Force applied on the pile body due to sea wave (relevant to wave height).

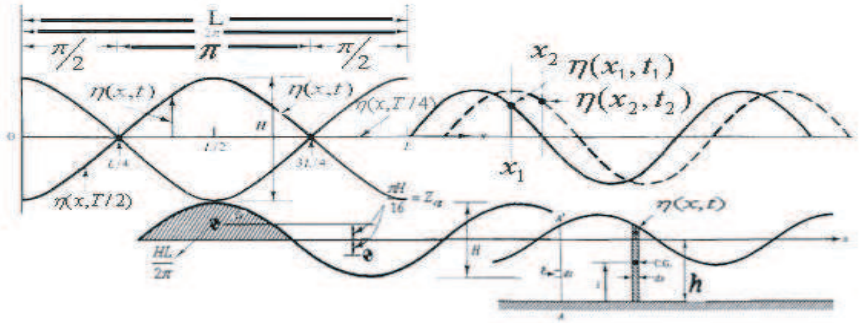

Figure 3: Water surface displacement associated with a standing water wave and ∂t variable interval depends on wave height and location.

for sea water as $1 \times 10^{-5}\,\mathrm{Ft}^2/\mathrm{sec}$

$$\begin{cases} R_e\langle 1\times 10^5 \Rightarrow C_d \cong 1.2 \\ 1\times 10^5\langle R_e\langle 4\times 10^5 \Rightarrow 0.7\langle C_d\langle 1.2 \\ R_e\rangle 4\times 10^5 \Rightarrow 0.6\langle C_d\langle 0.7 \end{cases} \quad \begin{cases} R_e\langle 2.5\times 10^5 \Rightarrow C_m = 2.0 \\ 2.5\times 10^5\langle R_e\langle 5\times 10^5 \Rightarrow C_m = 2.5 - \frac{R_e}{5\times 10^5} \\ R_e\rangle 5\times 10^5 \Rightarrow C_m\langle 1.5 \end{cases} \tag{6}$$

The specification of coefficient n, which is the relation of C_g (group velocity of the wave) and C (wave velocity), is as follows:

$$C_g = nC \Rightarrow n = \frac{C_g}{C} = \frac{1}{2}\left(1 + \frac{2kh}{\sinh 2kh}\right) \tag{7}$$

Calculation of total force of wave:

To determine the total force on a vertical pile, the force per unit elevation must be integrated over the immersed length of the pile. The force consists of the sum of two forces: drag and inertia.

$$\begin{aligned} F &= \int_{-h}^{\eta} dF = \int dF_d + \int dF_I = \int_{-h}^{\eta} \frac{1}{2} C_d \rho D u\,|u|\,dz + \int_{-h}^{\eta} \rho C_m \frac{\pi D^2}{4}\frac{Du}{Dt}dz \\ &\Rightarrow \frac{C_d}{8}\rho g D H^2 n\cos^2(\sigma t) + C_m \rho g \frac{\pi D^2}{8} H \tanh kd \sin(-\sigma t) \end{aligned} \tag{8}$$

Calculation of the location of net force by calculating the bending moment

$$\begin{aligned} \mathrm{M} &= \int_{-h}^{\eta}\left(\frac{C_d}{2}\rho D u^2 + C_m \rho \frac{\pi D^2}{4}\frac{\partial u}{\partial t}\right)(d+h)dz = \frac{C_d}{8}\rho g D H^2(\sigma t)d\left[\frac{1}{2} + \frac{1}{2n}\left(\frac{1}{2} + \frac{1-\cosh 2kh}{2kh\sinh 2kh}\right)\right] \\ &+ \frac{C_m}{8}\rho g \pi D^2 H d \tanh kd \sin(-\partial t)\left(1 + \frac{1-\cosh kh}{kh\sinh kd}\right) \end{aligned} \tag{9}$$

Determination of force place from the pile basement

$$d = \frac{M}{F} \tag{10}$$

It should be noted that according to Figure 3, the coefficient of ∂t depends on the location of the wave related to time. Furthermore, in the force determination formula, the maximum force obtained at the mode, drag and inertia forces, become equal.

$$F_d = F_I$$

To draw the noise graph, we consider the graph of the wave blowing force corresponding to time. In the last stage, we subtract the PIT system recording from the noise graph. At this stage, a pure graph without sea wave noise is generated. To seek a pure graph, we subtract the PIT result from the recorded noise, and use simple software, such as Excel or MATHlab.

3. CONCLUSIONS

This paper proposes a methodology developed for measuring marine piling noise, which is designed to record the noise response produced by waves that frequently beat against pile bodies. In this method, recording wave noise by calculating the force of the collision between waves and pile bodies is adopted. By calculating the wave force while the PIT system operator is beating against a pile head using special hammers, noise amplitude corresponding to time is recorded simultaneously. Finally, the obtained graphs are subtracted against each other to collect the most pure response graph of the PIT system. This may be performed using simple software, such as Excel or MATHlab. Pure graphs provide operators information with the least instrumental error.

REFERENCES

1. De Jong, C. A. F. and M. A. Ainslie, "Underwater radiated noise due to the piling for the Q7 offshore windfarm park," *J. Acoust. Soc. Am.*, Vol. 123, 2987, Full paper reproduced in *Proceedings of the 9th European Conference on Underwater Acoustics (ECUA2008)*, M. Zakaria, Ed., Société Française d'Acoustique, 2008.
2. Lepper, P. A and S. P. Robinson, "Monitoring the temporal and spatial characteristics of the noise radiated from marine piling (A)," *J. Acoust. Soc. Am.*, Vol. 123, No. 5, 2987, 2008.
3. Matuschek, R. and K. Betke, Measurements of construction noise during pile driving of offshore research platforms and wind farms, *Proc. NAG/DAGA Int. Conference on Acoustics*, 2009.
4. Dean, R. G. and R. A. Dalrymple, *Water Wave Mechanics for Engineers and Scientists*, University of Florida, University of Delaware, Reprinted the book on 2000.
5. Amir, J. M., "Pile integrity testing (PIT)," April 2009.
6. Robinson, S. P., P. A. Lepper, P. D. Theobald, J. Ablitt, G. Hayman, G. A. Beamiss, and S. Dible, "A methodology for the measurement of radiated noise from marine piling," 2009.
7. Amoser, S., L. E. Wysocki, and F. Ladich, "Noise emission during the first powerboat race in an Alpine lake and potential impact on fish communities," *Journal of the Acoustical Society of America*, Vol. 116, 3789–3797, 2004.
8. Kastelein, R. A., P. Bunskoek, M. Hagedoorn, W. W. L. Au, and D. de Haan, "Audiogram of a harbor porpoise (Phocoena phocoena) measured with narrow-band frequency-modulated signals," *Journal of the Acoustical Society of America*, Vol. 112, 334–344, 2002.
9. Madsen, P. T., M. Wahlberg, J. Tougaard, K. Lucke, and P. Tyack, "Wind turbine underwater noise and marine mammals: Implications of current knowledge and data needs," *Marine Ecology Progress Series*, Vol. 309, 279–295, 2006.
10. McDonald, M. A., J. A. Hildebrand, and S. M. Wiggins, "Increases in deep ocean ambient noise in the northeast Pacific west of San Nicolas Island, California," *Journal of the Acoustical Society of America*, Vol. 120, 711–718, 2006.
11. Nedwell, J. R., R. Workman, and S. J. Parvin, "The assessment of likely levels of piling noise at Greater Gabbard and its comparison with background noise, including piling noise measurements made at Kentish Flats," Subacoustech Report, 633R0115, Southampton, 2005.
12. Nowacek, D. P., L. H. Thorne, D. W. Johnston, and P. L. Tyack, "Responses of cetaceans to anthropogenic noise," *Mammal Review*, Vol. 37, 81–115, 2007.
13. Öhrström, E., A. Skånberg, H. Svensson, and A. Gidlöf-Gunnarsson, "Effects of road traffic noise and the benefit of access to quietness," *Journal of Sound and Vibration*, Vol. 295, 40–59, 2006.
14. Richardson, W. J., C. R. Greene Jr., C. I. Malme, and D. H. Thomson, *Marine Mammals and Noise*, Academic Press, San Diego, 1995.
15. Southall, B. L., A. E. Bowles, W. T. Ellison, J. J. Finneran, R. L. Gentry, C. R. Greene Jr., D. Kastak, D. R. Ketten, J. H. Miller, P. E. Nachtigall, W. J. Richardson, J. A. Thomas, and P. L. Tyack, "Marine mammal noise exposure criteria: Initial scientific recommendation," *Aquatic Mammals*, Vol. 33, 411–521, 2007.
16. Duclos, G., C. Josset, A. H. Clément, L. Gentaz, and C. Colmard, "Hydrodynamic efficiency of a new design of half-submerged breakwater compared to a rectangular caisson," *ASCE Journal of Waterway, Port, Coastal and Ocean Engineering*, Vol. 130, No 3, 127–133, 2004.
17. Linton, C. M. and D. V. Evans, "The interaction of waves with arrays of vertical circular cylinders," *J. Fluid Mech.*, Vol. 215, 549–569, 1990.

18. Spring, B. H. and P. L. Monkmeyer, "Interaction of plane waves with vertical cylinders," *Proceeding 14th International Conference on Coastal Engineering,* Chapter 107, 1828–1845, 1974.
19. Berggren, L. and M. Johansson, "Hydrodynamic coefficients of a wave energy device consisting of a buoy and a submerged plate," *Applied Ocean Research*, 1992.
20. Wu, B. J., Y. H. Zheng, Y. G. You, X. Y. Sun, and Y. Chen, "On diffraction and radiation problem for a cylinder over a caisson in water of finite depth," *International Journal of Engineering Science*, Vol. 42, 1193–1213, 2004.

Sub-surface Concrete Structure Damage Quantification Using TIR and Visual Inspection

Atif Musbah[1], **Shahid Kabir**[2], **and Akram Salem**[1]

[1]School of Civil Engineering, Engineering Campus, Universiti Sains Malaysia (USM), Malaysia
[2]Sustainable Materials and Infrastructure (SMI) Cluster
Collaborative μ-electronic Design Excellence Centre (CEDEC), Engineering Campus
Universiti Sains Malaysia (USM), Malaysia

Abstract— Infrared (IR) thermography has become a common technique for non-destructive inspections in various engineering fields. The IR thermography technique identifies and measures near surface defects by detecting the temperature gradient on the surface of a target object (e.g., a concrete wall). This study concerns the evaluation of the efficiency of the different types of NDT imaging methods of thermographic, colour, and greyscale imagery, in detecting various types of concrete damage. Data from the NDT imaging techniques are used to quantify near-surface structural damage by using image processing techniques, and validation of damage quantities is done with data from visual inspection. In terms of imagery, the thermographic classifications produced higher accuracies than the greyscale classifications. This is partly due to the fact that thermographic images contain less variability within the concrete imagery, and at the same time increase the visibility of cracks that may be otherwise imperceptible. The results show good correlation between damage quantities obtained through the image processing techniques applied to the IR thermography and optical imaging and the results obtained through visual inspection using the Feeler gauge and crack detection microscope.

1. INTRODUCTION

In the last decade, non-destructive testing (NDT) has become prevalent in studying the condition of existing infrastructures caused by rapid deterioration [1–3]. Early detection of building deficiencies (e.g., surface cracks, subsurface defects) allows early repairs and makes possible large savings on maintenance costs. The application of thermography for NDT (TNDT) in concrete structures has been growing rapidly in the industry. It is simple operation and global testing nature makes it an ideal method for building/civil engineering applications [4].

2. DATA DESCRIPTION

The imagery data were obtained, from the field, thermographic and optical images were taken for all the field samples. An optical camera was employed to acquire the greyscale images from the field, and the thermographic images were obtained through the use of the infrared camera of FLIR Systems. The crack width is measured by visual inspection using feeler gauge and also analyzed in the ENVI 4.0 software.

3. PROCESSING METHODS

In order to perform the damage analysis, the two types of imagery, thermographic and greyscale, of the different concrete field samples were processed using statistic method (supervised classification) and the maximum likelihood technique. These techniques can be applied through a variety of image processing software; in this study, the Environment for Visualizing Images (ENVI0.4) image processing system by Research Systems Inc, were employed.

Median filters are a group of filters based on ranking pixel grey-values. They smooth an image while preserving edges larger than the kernel size by replacing each centre pixel with the median value found within the neighborhood of the filter.

Classification is a method by which labels are attached to pixels according to their spectral characteristics by a computer, which is trained beforehand to recognize pixels with similar spectral properties. Typically, this process involves the analysis of digital image data and the application of statistically based decision rules for determining the object class of each pixel in an image; the pixels are then classified into their respective classes [5]. Classification of the concrete imagery by using ENVI 0.4 software is one step in the methodology for this study.

Maximum likelihood classification assumes that the statistics for each class in each band are normally distributed and calculates the probability that a given pixel belongs to a specific class.

Unless probability of threshold is selected, all pixels are classified. Each pixel is assigned to the class that has the highest probability [5].

The classified images were converted into binary images. This process simplifies the image by assigning the pixels that represent the damage in the concrete a value of 1 (black) and the background pixels a value of 0 (white). Manual or automated methods are then used to count or sum the pixels to calculate total wide-crack length, as well as average wide-crack width.

3.1. Visual Inspection

Visual inspection is one of the most versatile and powerful of the NDT methods, and it is typically one of the first steps in the evaluation of a concrete structure [6].

In this study, Feeler gauge has been used to measure the crack and this instrument is used to measure the dimensions of width of the crack in concrete on surfaces. Crack detection microscope also is used in this study, which is used to measure the crack in concrete and rocks.

4. RESULTS OF THE CLASSIFICATION

The results of the classification can be presented in two forms: a table that provides the classification statistics of the number of pixels in the whole image that belongs to each class, or a classified image. The results of the optical images were presented first and then the thermographig images are followed, then a comparison between them is made, after that the results are validated by using visual inspection methods (feeler gauge and crack detection microscope).

4.1. Optical Image-1 (Field Sample)

The image of dimensions 650×534 pixels was taken from field sample, the image consist of different degrees of the crack damage, hair line crack and heavy crack as shown in Figure 1(a) and also presented the classified image in Figure 1(b) then binary image as shown in Figure 1(c). The result of Classification Statistics that presented the number of pixels in the whole image that belongs to each class is shown in Table 1.

Table 1. Classification statistics.

Heavy crack	Hairline crack	No crack	Number of the pixels
2.5906%	9.8614%	87.5480%	347.100

(a) Input data (b) Output data (c) Binary image

Figure 1. Optical image (field sample).

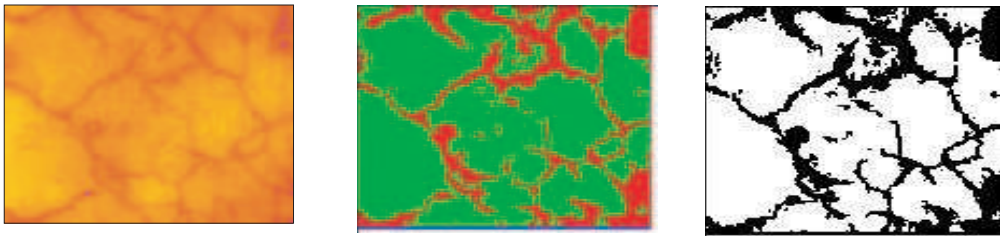

(a) Input data (b) Output data (c) Binary

Figure 2. Thermographic image (field).

4.2. Thermographic Image (Field Sample)

Damage analysis was carried out on TIR images of the field samples of dimensions 178 × 165 pixels in order to determine the contribution of such imagery to the analysis of crack damage. The analysis conducted for concrete of the field sample is presented below. The original greyscale image is presented Figure 2(a) the classified image in Figure 2(b), then binary image is presented in Figure 2(c). Results of the classifications done for the TIR images of the field samples are presented in Table 2, which shows the Classification Statistics.

4.3. Damage Analysis of Field Samples Using Optical and TIR Images

In this part thermographic image of dimensions 320 × 240 pixels and optical image samples of dimensions 2580 × 1932 pixels are compared in order to investigate the difference between the two methods of inspection, the comparison was made images taken from the same location and both of them have cracks. Figure 3(a) shows the input optical and thermographic images and Figures 3(b) and (c) show the classified optical image and thermographic images shown in Figure 3(d). The black line seen around the image is a wire that was used as a reference to set the layout of the image, Figures 3(e) and (f) show the binary image of optical and thermographic.

Results of the classifications done for the optical and TIR images of the field samples are presented in Table 3, which Classification Statistics of optical image shown in Table 3(a) and Classification Statistics of TIR images shown in Tables 3(b).

Figure 4 shows the different of the damage statistics of field samples by using optical image and TIR image. The output of thermgraphic classification given higher accuracies than the output of the grayscale classification, and also the size of the crack in the thermgraphic image is bigger than the grayscale image and that due to the thermgraphic image contains less variability within the concrete imagery, as well as increase the visibility of the crack.

Table 2. Classification statistics.

Crack	No Crack	Number of the pixels
26.7075%	73.2925%	29.370

Table 3. Classification statistics of grayscale and TIR.

	Crack	No Crack	Border	Number of the pixels
(a)	5.5381%	92.1472%	2.3146%	4.984.560
(b)	26.7995%	68.669%	4.5313%	4.5313%

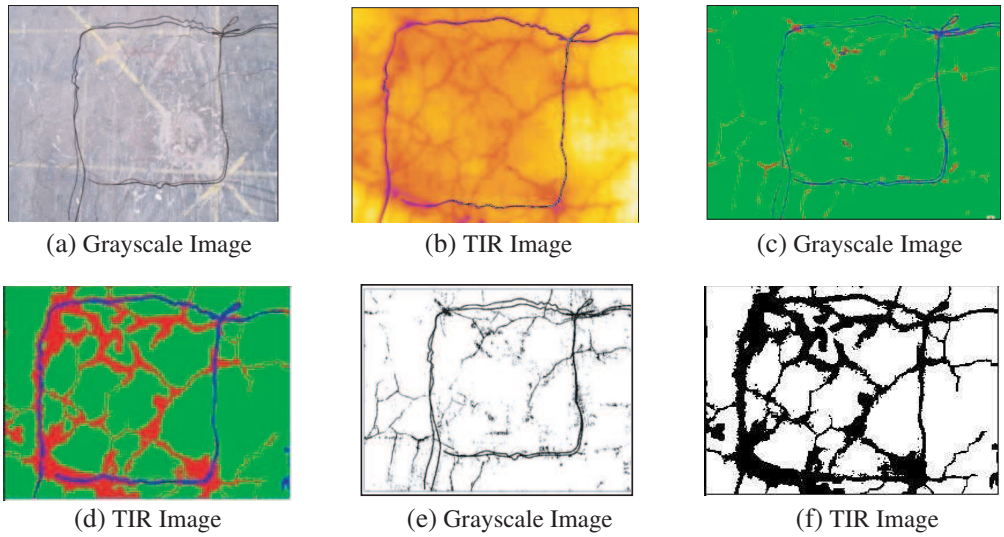

(a) Grayscale Image (b) TIR Image (c) Grayscale Image

(d) TIR Image (e) Grayscale Image (f) TIR Image

Figure 3.

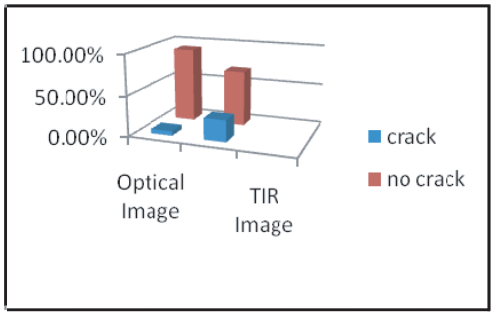

Figure 4. Comparison of damage statistics for the two different types of field samples.

Table 4. Average crack width and total crack length.

Dimensions	**Optical image number (1)**	**Optical image number (2)**	**The optical image number (3)**
Average crack width	0.6 mm	0.20 mm	1.04 mm
Total Length	38.09 mm	23.66 mm	15.34 mm

Table 5. Comparison of results between visual inspection and image processing.

Max-Min width	Field		
	Visual inspection		Image processing (mm)
	Feeler gauge (mm)	Crack detection Microscope (mm)	
Max.	1.3	1.2	1.3
Min.	0.25	0.2	0.26

4.4. Crack Quantification

In order to quantify the total length of cracks from the imagery of the laboratory specimens, the number of pixels along the length of each branch of the cracks was summed and the total multiplied by the pixel resolution of 0.26 mm. In order to quantify the total length of cracks from the images, the number of pixels along the length of each branch of the cracks was summed and the total multiplied by the pixel resolution of 0.26 mm. For the optical image number (1) that was taken from the field, the total length was found to be 23.66 mm, and for the optical image in Figure 3(a) the total length was 15.34 mm. The average crack width was determined by measuring the width at several points along the cracks. Figure 4 shows binary image for measurement of crack width which is an example of this analysis applied on the classification of the field sample; which shows the crack damage with examples of crack segments. And provides examples of crack width measurements for the specimen; each square represents one pixel at a resolution of 0.26 mm. As a result, the average width of cracks in the image number (1), 0.20 mm. Table 5 shows the comparison of the results obtained from the visual inspection by feeler gauge and that was obtained by using the image processing technique as well as microscope crack detection instrument.

From Table 5 shows the difference between the results obtained by using different methods is not much, in the field samples, the maximum crack width by using visual inspection (Feeler gauge) was found to be 1.3 mm, and by using crack detection microscope was found to be 1.2 mm, and by using image processing techniques it was found to be 1.3 mm, and that shows the image processing techniques can be used to detect the cracks in the concrete and used to supplement visual inspection.

5. CONCLUSION

Several objectives have been achieved in this study. Basically, surface crack, subsurface crack defects in concrete structures are shown to be detected successfully by using optical image and thermography.

In terms of imagery, the thermographic classifications produced higher accuracies than the greyscale classifications. This is partly due to the fact that thermographic images contain less variability within the concrete imagery, and at the same time increase the visibility of cracks that may be otherwise imperceptible.

6. RECOMMENDATIONS

The quantitative analysis resulting from these approaches can also be used for the development of an automated system for crack assessment to determine the different levels of cracks from concrete imagery. An automated system would facilitate the analysis and classification of a large volume of image data. Surface crack detection by TIR can be applied for surface crack monitoring on bridge structures. Beam samples with static stress which causes surface cracks can be monitored by TIR.

REFERENCES

1. Büyüköztürk, O., "Imaging of concrete structures," *NDT&E International*, Vol. 31, No. 4, 233–243, 1998.
2. Khan, M. S., G. A. Washer, and S. B. Chase, *Evaluation of Dual Band Infrared Thermography System for Bridge Deck Delamination Surveys*, SPIE, 1998.
3. Washer, G. A., "Developments for the non-destructive evaluation of highway bridges in the USA," *NDT&E International*, Vol. 31, No. 4, 245–249, 1998.
4. Starnes, M. A., N. J. Carino, and E. A. Kausel, "Preliminary thermography studies for quality control of concrete structures strengthened with FRP composites," *Journal of Materials in Civil Engineering, ASCE*, 266–273, 2003.
5. Richards, J. A. and X. Jia, *Remote Sensing Digital Image Analysis: An Introduction*, 3rd Edition, Springer-Verlag, New York, 1999.
6. Perenchio, W. F., "The condition survey," *Concrete International*, Vol. 11, No. 1, 59–62, 1989.

Infrared Thermography for Assessing and Monitoring Electrical Components within Concrete Structures

Mohd Shawal Jadin[1], **Soib Taib**[1], **and Shahid Kabir**[2]

[1]School of Electrical and Electronic Engineering, Universiti Sains Malaysia
Nibong Tebal 14300, P. Pinang, Malaysia
[2]Collaborative Micro-electronic Design Excellence Centre (CEDEC)
Universiti Sains Malaysia, Nibong Tebal 14300, P. Pinang, Malaysia

Abstract— The paper presents the application of infrared thermography (IRT) for assessing and monitoring electrical components within concrete structures. It is well known that the integrity of a power system is of paramount importance when it supplies electricity throughout a facility, especially during peak time. Overloading, load imbalance, corrosion and loose connection of electrical components can produce a thermal anomaly or hot spot. The abnormality of the components will occur when its internal temperature reached beyond its limits. Consequently, the overheating of the electrical component within the concrete structure can potentially result in unplanned power outages, possible injury and fire hazard. In addition, the efficiency of an electrical system becomes low prior to failure, thus energy is spent generating heat in the structure, causing unnecessary loses. Therefore, early prevention is required to avoid future faults and increase the reliability of the electrical components. Conventionally, for a large building and wide area of power distribution systems, the inspection of electrical power components within the structure requires extra manpower to conduct the test and take a lot of time as well as cost. Furthermore, only certified and experienced personnel can justify the severity of the problematic components. This is due to the complex analysis and various factors should be considered during the inspection especially when the cables are deep into the structure. Therefore, this research proposed a new method of an intelligent monitoring system for electrical components by diagnosing its thermal profiles. The system uses infrared thermographic camera or thermal imager in order to capture the thermal behavior of electrical components in the concrete structure. The main feature of the proposed system is to automatically identify the thermal anomaly in electrical components and classify its level of severity if the anomaly is detected. A new method of inspection is introduced by implementing the combination of an advanced image processing technique and artificial intelligence system. Finally, the system will give a complete analysis report, including the most suitable action to be taken for the problem that was detected.

1. INTRODUCTION

In 1800, William Hershel has discovered infrared radiation and it was the first experiment that showed there were forms of light not visible to the human eye [1, 2]. The infrared wavelength spectrum is ranged from about 1 mm down to 750 nm. All objects emit energy proportional to its surface temperature. As infrared energy functions outside the dynamic range of the human eye, special equipment is required to transform the infrared energy to another signal, which can be seen by human eye. For this purpose, infrared imagers were developed to see and measure this heat. Nowadays, various types of IRT imager with more advanced and sophisticated features have been developed [3]. The basic concepts of IRT imager or well known as thermographic camera is that it can captures the image of the thermal pattern and measures the emissive power of a surface in an area at various temperature ranges. The digital image of IRT is called as thermograms. Each pixel of a thermogram has the specific temperature value, and the image's contrast is derived from the differences in surface temperature.

Temperature and the resulting thermal behavior of electrical components are the most critical factors in the reliability of any operation or facility [4]. The abnormality of the components will occur when its internal temperature reached beyond its limits. Electrical components such as buried electrical cable and wiring within a concrete wall and structure can produce overheating whilst under load. This will result a high surface temperature over a buried electrical supply and can, of course, indicate a potential of fire risk [5]. In addition, the efficiency of an electrical supply becomes low prior to failure, thus energy is spent generating heat, causing unnecessary loses.

IRT camera can detect the abnormality of power components without interrupting the power system operation. However, most of the inspection can only be done by well-qualified and experienced personnel. Otherwise, the inspection will result a wrong interpretation. Commonly,

the thermographic inspection of electrical components will take a lot of time and high inspection cost [6]. Therefore, applying an automatic analyzing system can overcome this situation. The thermal abnormality of electrical components can be detected with quickly and accurately even the expert or experienced personnel are not present. This paper proposed an automatic IRT diagnosis system for monitoring the reliability of electrical power components.

2. TYPICAL FAULTS IN ELECTRICAL COMPONENTS

All electrical devices are usually rated for power, which indicates the amount of energy that the devices can conduct without being damaged. If the device is operated at a power above its specifications, the excess power can reduce the device's life cycle and efficiency. Basically, faults in electrical power system can be classified into few categories, i.e., poor connection, short circuit, overloading, load imbalance and improper component installation [3, 7–11]. In most cases, the major cause of overheating in utility components is the change in resistance due to loose connection [12]. The loose connection causes electricity to use smaller area of the defective connection than required for proper current flow and therefore, increases the resistance and temperature of the connection. Any problem, which accompanies a change in resistance of the equipment, causes it to consume more power than the intended load.

According to a thermographic survey conducted during the period of 1999–2005 [13], it was found that 48% of the problems were found in conductor connection accessories and bolted connections. This is mainly resulted from the loose connection, corrosion, rust and non-adequate use of inhibitory grease. On the other hand, 45% of the thermal anomalies appear in disconnectors contacts. Most of the anomalies are due to deformations, deficient pressure of contact, incorrect alignment of arms and dirtiness. Only 7% of the problems were found in electrical equipments.

Another major cause of overheating in electrical components within the structure is overloading. Through IRT camera, the sign of overloading can be seen clearly even if the cable was located deep into the concrete where the red region which has high temperature value covered all parts of the components or cables. Fig. 1 shows an example of overheating due to overloading in an electrical cable within a concrete wall. By utilizing IRT technology, the thermal image will clearly indicates the problematic area. The suspected area can be easily indentified and interpreted. Nevertheless, in some cases, the interpretation of thermographic image cannot be done directly except for an experienced and qualified thermographers. There are some thermographic characteristic should be understood.

3. SYSTEM DEVELOPMENT

Conventional inspection of electrical power components requires a large amount of workers as well as time and cost. In this exercise only certified and experienced personnel can justify the level of severity of the suspected components. This is due to the complex analysis and various factors should be considered during the inspection. Therefore, this research proposed a new method of intelligent monitoring system for electrical power equipments by diagnosing its thermal profiles.

3.1. System Configuration

The main feature of the proposed system is to automatically detect the thermal hot spots and potential fault location within the concrete structure. The development of monitoring system is to analyze the running state of electrical components using the combination of artificial intelligence and advanced image-processing technique. The general block diagram of the proposed system is shown in Fig. 2.

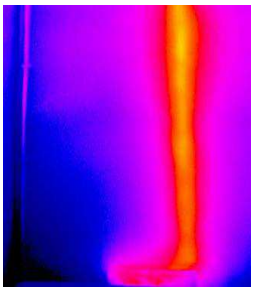

Figure 1: IRT image of cable fault in concrete wall.

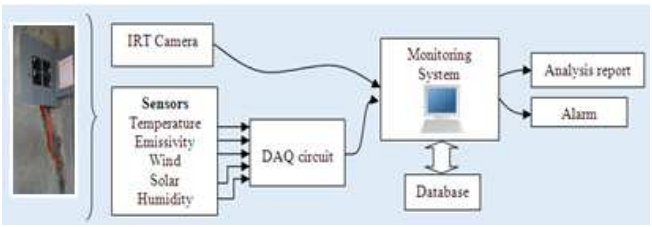

Figure 2: General block diagram.

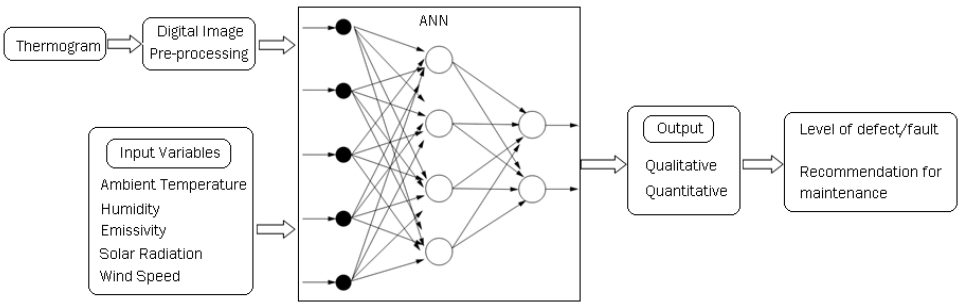

Figure 3: General structure of the analyzing process.

The image of the electrical components within the concrete structure is captured and then sends to the monitoring system for further analysis. It is a very challenging task in recognizing the electrical equipments from the complex background in order to judge whether troubles has happened or potential troubles would happen and finding position of suspected equipments. Therefore, an image processing technique must be applied to filtering and enhancing the captured image. The overall process of the system includes several steps: images' preprocessing, feature extraction, type recognition, state analysis and classification. After capturing the IRT images, the computer must preprocess the images in order to improve images quality, including images' smoothing, eliminating noise, filtering, enhancing edges, etc. the next step is finding the interest region by segmenting the images. The segmentation process will highlight the hot spot in the suspected component. The image features then become the inputs of neural network that has been trained.

3.2. Faults Classification

Analysis of thermal signatures and the relation to various operating parameters must be accomplished. The task of determining fault modes is essentially a pattern recognition problem that is an ideal application for a neural network. For this reasons, multilayer perceptron (MLP) neural network (NN) will be implemented to achieve this. The general structure of the analyzing process is shown in the Fig. 3. The difficulty of the research is to get the accurate reading of the actual temperature of the electrical power equipments. This is due to various factors that will affect the measurements. The factors can be classified into two categories, i.e., internal factors and externals factors. Internal factors are related to the target components such as the component's emissivity and thermal gradient. External factor is about the environmental factors such as wind speed, precipitation, solar radiation and ambient temperature. Prior to analysis, all the related data must be collected as the input variables. Therefore, a set of sensors for data acquisition is required.

The output will be justified according to qualitative and quantitative analysis. By combining these two methods, it is expected to increase the accuracy of inspection. The level of severity of the suspected electrical equipments in the concrete structure can be classified according to standards [14] as shown in Table 1. The recommended action should be taken according to the level of priority. The final process of the inspection is preparing the analysis report. Analysis report will contain all the required information for the future analysis and maintenance. This will include the location, date, specific problem, corrective action, infrared image and visible light image. Additional specific information related to equipment's temperature vs. acceptance criteria, ambient temperature conditions, equipment's load (for electrical equipment), and type of IRT camera are useful for subsequent data analysis and future inspection.

Table 1: Classification of thermal profile of electrical components.

Priority	ΔT (°C)-similar components	ΔT (°C) over ambient	Recommended Action
4	1–3	1–10	Minor problem
3	4–15	11–20	Repair as time permits
2	- - -	21–40	Serious problem
1	> 15	> 40	Critical, Repair immediately

4. CONCLUSION

It is clearly shown that early prevention is required to avoid future faults and increase the reliability of the electrical power components within concrete structure. Since the electricity demand has increased day by day, IRT inspection should be done regularly especially in building where most of the electrical cable or components are within the concrete structure. By implementing an automatic diagnosis system, it can provide faster and more accurate IRT analysis for hazard protection. The classification procedure is a useful tool and plays an important role in predictive and preventive maintenance program.

ACKNOWLEDGMENT

This research was supported by Fundamental Research Grant Scheme (FRGS), Universiti Sains Malaysia and Universiti Malaysia Pahang.

REFERENCES

1. Lizak, F. and M. Kolcun, "Improving reliability and decreasing losses of electrical system with infrared thermography," *Acta Electrotechnica et Informatica*, Vol. 8, No. 1, 60–63, 2008.
2. Chou, Y. and L. Yao, "Automatic diagnostic system of electrical equipment using infrared thermography," *Proceedings of International Conference of Soft Computing and Pattern Recognition*, 155–160, 2009.
3. Braunovic, M., N. K. Myshkin, and V. V. Konchits, *Electrical Contacts Fundamentals, Applications and Technology*, CRC Press, 2007.
4. Chuck, H., *Handbook of Nondestructive Evaluation*, 1st Edition, McGraw-Hill Professional, 2001.
5. Epperly, R., G. Heberlein, and L. Ead, "A tool for reliability and safety: Predict and prevent equipment failures with thermography," *Proceedings of Petroleum and Chemical Industry Conference*, 59–68, 1997.
6. Cao, Y., X.-M. Gu, and Q. Jin, "Infrared technology in the fault diagnosis of substation equipment," *Proceedings of International Conference on Electricity Distribution*, China, 2008.
7. Balaras, C. A. and A. A. Argiriou, "Infrared thermography for building diagnostics," *Energy and Buildings*, Vol. 34, 171–183, 2002.
8. Dos Santos, L., E. C. Bortoni, L. E. Souza, G. S. Bastos, and M. A. C. Craveiro, "Infrared thermography applied for outdoor power substations," *Proceedings of SPIE*, 69390R-69390R-11, 2008.
9. Hou, N., "The infrared thermography diagnostic technique of high-voltage electrical equipments with internal faults," *Proceedings of International Conference on Power System Technology*, 110–115, Beijing, China, 1998.
10. Kregg, M. A., "Benefits of using infrared thermography in utility substations," *Proceedings of SPIE*, 249–257, 2004.
11. Azmat, Z. and D. Turner, "Infrared thermography and its role in rural utility environment," *Proceedings of Rural Electric Power Conference*, B2/1–B2/4, 2005.
12. Martínez, J. and R. Lagioia, "Experience performing infrared thermography in the maintenance of a distribution utility," *Proceedings of International Conference on Electricity Distribution*, Vienna, 2007.
13. Titman, D. J., "Applications of thermography in non-destructive testing of structures," *NDT & E International*, Vol. 34, No. 2, 149–154, 2001.
14. "Standard for infrared inspection of electrical systems & rotating equipment," Infraspection Institute, 2008.

Detection and Quantification of Corrosion Damage Using Ground Penetrating Radar (GPR)

Shahid Kabir[1] **and Ahmad Zaki**[2]

[1]Sustainable Materials and Infrastructure (SMI) Cluster
Collaborative μ-electronic Design Excellence Centre (CEDEC), Engineering Campus
Universiti Sains Malaysia (USM), Malaysia
[2]School of Civil Engineering, Engineering Campus, Universiti Sains Malaysia (USM), Malaysia

Abstract— This research aims to detect the damage due to corrosion of reinforcing steel in concrete structures using ground penetrating radar (GPR) and conventional method, half-cell potential (HCP). A method to accelerate corrosion of steel rebar in concrete samples to different degrees is applied, the method consists of introducing a direct current (DC) power supply and 5% sodium chloride (NaCl) solution as an electrolyte to the rebar to induce significant corrosion within a short period of time. The 2 GHz GPR is used to detect the corrosion in the reinforced concrete slabs after 28 days of standard moist preservation. The results are compared with those obtained using the HCP method. Both of the GPR and the HCP show good performance in determining the degree of corrosion.

1. INTRODUCTION

Corrosion is a worldwide problem facing the concrete structures [1]. Many reports have highlighted that concrete structures are damaged by corrosion all over the world [2–5]. Major cause of damages are inadequate planning, wrong estimation, and bad workmanship. The damages need to be repaired and maintained [6, 7]. The structures need to be repaired after a short service life [8]. The repair and maintenance of concrete structures are nearly as important as new constructions. Consequently, visual inspection of whole structure is regular inspection to asses the condition of corrosion in concrete structures. However, if there are no conclusions can be obtained by visual inspection, a reliable inspection method is needed before the functionality of a structure is seriously damaged [8–11].

Non-destructive testing (NDT) is objective corrosion inspection method. The NDT method should be done without damaging the concrete. The NDT methods can be applied to both new and old structures. For new structures, the principal applications are likely to be quality control of materials or construction. In the old structures, the NDT methods are expected to provide the needed feedback in monitoring for detection and identification of the deterioration [12]. Half-cell potencial, one of NDT methods were used widely to test the rebar corrosion. This paper presents applicability of GPR that allows the detection of rebar corrosion in concrete. The GPR results are compared with half-cell potential results in order to provide a more in-depth evaluation of corrosion of concrete structures and to increase the accuracy and reliability of deterioration assessment for monitoring and safety analysis.

2. REVIEW

2.1. Half-cell Potential (HCP)

The HCP is the mostly useful method for assessing corrosion of the rebars. Basically, the HCP measurements are simple, inexpensive and virtually NDT to provide a condition of the corrosion activity and identify risk of corrosion zones. These measurements can be used to estimate the corrosion risk of steels even if there are no signs of corrosion on the concrete surface, which is a significant advantage for inspecting existing concrete structures. The HCP could localize the chloride-induced corrosion of the rebars and improve the quality of condition assessment [13]. The HCP provides information to calculate the probability of corrosion degree and in some cases information on the possible presence of damage if this corrosion is in advanced stage [8, 10]. Interpretation of HCP test results is carried out as per the ASTM C876 guidelines [15] The ASTM C876 states that the probability of corrosion is less than 10% if the potential is greater than -200 mV, whereas potential values lower than -350 mV indicate a high probability of corrosion ($> 90\%$) However, this test does not allow the detection of delamination in a direct manner.

2.2. Ground Penetrating Radar (GPR)

The GPR is an electromagnetic investigation method. It is also known as surface penetrating radar or electromagnetic reflection method. Mostly it is used in reflection mode where a signal is emitted via an antenna into the structure under investigation. Reflected energy caused by changes in material properties is recorded and analysed [7]. The GPR is a potential method for periodic inspection and maintenance of concrete structures [9, 16, 17]. GPR has become a valuable tool for the NDT of concrete structures for technological advancements over the past decade [9]. In detail, GPR technology is employed for: localization and estimation of reinforcing bars, localization and the dimensions of voids, localization of cracking, localization and dimensions of voids, localization of honeycombey or cracking, corrosion detection, and estimation of bar size [18–21]. GPR is capable for direct and early detection of corrosion. However, most of corrosion detection are accomplished in laboratory and need advances study related to corrosion and the GPR universally [22].

3. METHODS

In sample preparations, rebars are immersed in a solution of 5% sodium chloride (NaCl). The rebars is exposed to the solution using DC power supply with some duration of rebar exposure (0, 1, 3, and 7 days). 0 day for no corrosion rebar, 1 day for corrosion, 3 days for middle corrosion and 7 days for high corrosion. The corrosing rebars is defined as the anode while a rebar facing the corrosing rebars is defined as the cathode. The current of 10 V (Volt) and 1 A (Ampere) are applied in the corrosion process. Furthermore, the corroded rebars are induced to concrete mixture. The concrete slab dimension are $l = 1$ m, $w = 1$ m, and $h = 0.3$ m. The concrete grade is C30. Portland cement, uncrushed sand, crushed limestone with a maximum aggregate size of 20 mm are used to prepare the concrete mixture. The y-type reinforced bars (rebars) with 20 mm diameter is selected.

The 2 GHz of GPR manufactured by IDS (Ingegneria Dei Sistemi S.p.A) Italy and the digital half-cell manufactured by SCRIBE, were employed to detect the corrosion in reinforced concrete slabs after 28-days of standars moist curing. The GPR results could be proposed in a-scan, b-scan, c-scan, and 3D image. In this paper, authors used 3D image as the GPR data for corrosion detection. In the other hand, the HCP is adjusted at 10 mV. Desired grid on the 1 m^2 surface of concrete slab is marked out. The grid size is 10×10 cm. The four rebars are placed in b, d, f, and h to represent no corrosion, low corrosion, middle corrosion, and high corrosion, respectively. Eight points is taken for each rebar for HCP test. The point is taken from point 1 until the end of rebar on concrete structure in point 8. The grid of b_1–b_8 for no corrosion rebar, d_1–d_8 for low corrosion rebar, f_1–f_8 for middle corrosion rebar, and h_1–h_8 for high corrosion rebar.

4. RESULTS

B-scan is the raw data from scanning that already been filtered. Figure 1 shows the b-scans at different location of scanning but in same direction of tranverse. Figures 1(a) and (c) are the location of rebar at the end and beginning. There is no corroded rebar in that figure. Figure 1(b) is the location of corroded rebar in three rebar with different degree of corrosion, but the wave shows same characteristic for the all four rebar with Figures 1(a) and (c).

The view of corroded rebar also can be seen in Figure 2. C-scan at depth 0.10 m can view the clearly rebar but the image is not clear to view the different degree of corrosion. The 3D image of GPR data showed that the corrosion can be detected for high corrosion. However, the GPR could not visualized for low and middle corrosion because the image is not clear, as shown in Figure 3. The unclearness image of rebar in low and middle corrosion was caused by human error in sample

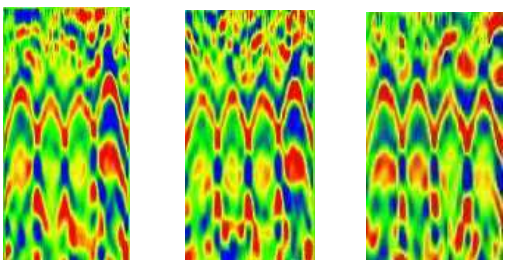

Figure 1: B-scans data, (a) at the end of rebar, (b) at corroded rebar, (c) at beginning of rebar.

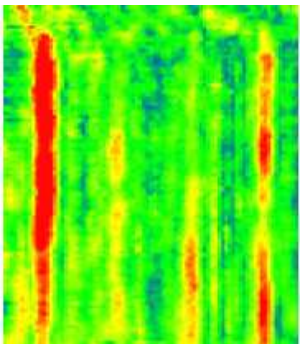

Figure 2: C-scan data.

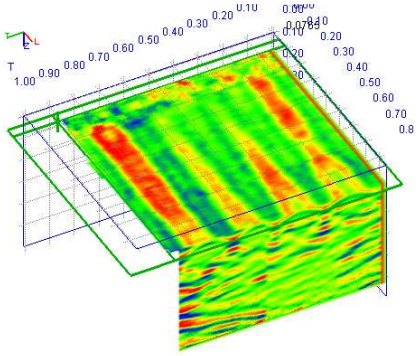

Figure 3: The 3D image of GPR.

Table 1: Digital half-cell grid.

1											
2											
3			**−155**		**−162**		**−178**		**−201**		
4			**−152**		**−152**		**−185**		**−205**		
5			**−150**		**−153**		**−182**		**−201**		
6			**−151**		**−158**		**−184**		**−202**		
7			**−150**		**−157**		**−185**		**−205**		
8			**−157**		**−166**		**−187**		**−203**		
9			**−155**		**−173**		**−187**		**−205**		
10			**−155**		**−173**		**−184**		**−206**		
	A	B	C	D	E	F	G	H	I	J	K

preparation. The error is especially in use of the vibrator stick to compact the rebars. Therefore, the end of rebar is not same high with the beginning of rebar.

Table 1 below shows the grid and the potential reading on pre-determined grid. Test area is $1\,\mathrm{m}^2$ and the grid size is 10 cm, horizontally and vertically. As presented in Section 3, number of points taken is 8 for each rebar. For rebar exposure times 0, 1, and 3 days the percentage chance of corrosion activity is 5%. And for 7 days exposure time, the value for percentage chance of corrosion activity is 50%.

5. CONCLUSION

This paper shows the detection corrosion of GPR and half-cell potential. The 3D image of GPR data showed that the corrosion can be detected for high corrosion. There is different pattern on corroded rebar and the diameter of corroded rebar less than uncorroded rebar. The GPR give results that are compared with half-cell potential. The half-cell potential give results that 7 days of exposure time of rebar (high corrosion) have 50% probability in value and 5% chance of corrosion activity for no corrosion, low corrosion and middle corrosion. Therefore, the GPR have applicability to detection corrosion of corroded rebar in advance stage base on the image. The authors of this paper believe that image proceesing techniques should be used to get best classification and interpretation the GPR images of corrosion.

REFERENCES

1. Badawi, M. and K. Soudki, "Control of corrosion-induced damage in reinforced concrete beams using carbon fiber-reinforced polymer laminates," *Journal of Composites for Construction*, Vol. 9, No. 2, 195–201, 2005.
2. Ahmad, S., "Reinforcement corrosion in concrete structures, its monitoring and service life prediction-a review," *Cement and Concrete Composites*, Vol. 25, Nos. 4–5, 459–471, 2003.
3. Yingshu, Y., J. Yongsheng, and P. S. Surendra, "Comparison of two accelerated corrosion techniques for concrete structures," *ACI Structural Journal*, Vol. 104, No. 3, 344, 2007.

4. Capozucca, R., "Damage to reinforced concrete due to reinforcement corrosion," *Construction and Building Materials*, Vol. 9, No. 5, 295–303, 1995.
5. Cleland, D. J., K. M. Yeoh, and A. E. Long, "Corrosion of reinforcement in concrete repair," *Construction and Building Materials*, Vol. 11, No. 4, 233–238, 1997.
6. Nagi, M., "Corrosion evaluation of reinforced concrete bridges," *ASCE*, 16–16, 2005.
7. Hugenschmidt, J. and R. Mastrangelo, "GPR inspection of concrete bridges," *Cement and Concrete Composites*, Vol. 28, No. 4, 384–392, 2006.
8. Elsener, B., C. Andrade, J. Gulikers, R. Polder, and M. Raupach, "Hall-cell potential measurements — Potential mapping on reinforced concrete structures," *Materials and Structures*, Vol. 36, No. 7, 11, 2003.
9. Wiggenhauser, H. and H. W. Reinhardt, "NDT in civil engineering: experience and results of the for 384 research group," *AIP Conference Proceedings*, Vol. 1211, 47–54, 2010.
10. Rhazi, J., O. Dous, and S. Laurens, "A new application of the GPR technique to reinforced concrete bridge decks," *Proceedings of 4th Middle East NDT Conference and Exhibition*, Kingdom of Bahrain, December 2007.
11. Arndt, R. and F. Jalinoos, "NDE for corrosion detection in reinforced concrete structures — A benchmark approach," *Proceedings of Non-destructive Testing in Civil Engineering*, Nantes, France, June 30–July 3, 2009.
12. Bu yu ko ztu rk, O, "Imaging of concrete structures," *NDT and E International*, Vol. 31, No. 4, 233–243, 1998.
13. Elsener, B., "Half-cell potential mapping to assess repair work on RC structures," *Construction and Building Materials*, Vol. 15, Nos. 2–3, 133–139, 2001.
14. ASTM C876-09, "Standard test method for half-cell potentials of uncoated reinforcing steel in concrete," 1991.
15. Clemena, G. G., *Short Pulse Radar Methods*, CRC Press, 1991.
16. Laurens, S., J. P. Balayssac, J. Rhazi, G. Klysz, and G. Arliguie, "Non-destructive evaluation of concrete moisture by GPR: Experimental study and direct modeling," *Materials and Structures/Materiaux et Constructions*, Vol. 38, No. 283, 827–832, 2005.
17. Maierhofer, C. and S. Leipold, "Radar investigation of masonry structures," *NDT and E International*, Vol. 34, No. 2, 139–147, 2001.
18. Barrile, V. and R. Pucinotti, "Application of radar technology to reinforced concrete structures: A case study," *NDT and E International*, Vol. 38, No. 7, 596–604, 2005.
19. Maierhofer, C., "Nondestructive evaluation of concrete infrastructure with ground penetrating radar," *Journal of Materials in Civil Engineering*, Vol. 15, No. 3, 287–297, 2003.
20. Bungey, J. H., "Sub-surface radar testing of concrete: A review," *Construction and Building Materials*, Vol. 18, No. 1, 1–8, 2004.
21. He, X. Q., Z. Q. Zhu, Q. Y. Liu, and G. Y. Lu, "Review of GPR rebar detection," *PIERS Proceedings*, 804–813, Beijing, China, March, 23–27, 2009.
22. Kim, W., "Ground penetrating radar application for non-destructive testing: Bridge deck inspection and dowel bar detection," Ph.D. Thesis, University of Missouri-Rolla, 2003.

Radar-based Quantification of Corrosion Damage in Concrete Structures

Ahmad Zaki[1] **and Shahid Kabir**[2]

[1]School of Civil Engineering, Engineering Campus, Universiti Sains Malaysia, Malaysia
[2]Sustainable Materials and Infrastructure (SMI) Cluster
Collaborative μ-Electronic Design Excellence Centre (CEDEC), Engineering Campus
Universiti Sains Malaysia, Malaysia

Abstract— The ground penetrating radar (GPR) methods has been found to be useful in evaluating the corrosion damage in the concrete structures. However, the GPR image is very difficult to be interpreted because it requires processing technique. This paper studies the GPR to detect the corrosion of concrete structure using image processing technique. The reinforced of concrete slabs are corroded as results of impressed current method to accelerated the corrosion. The GPR are used for detection the corrosion damage in the concrete slabs. The GPR data showed that the corrosion can be detected, however need to analyzed and interpretation by using image processing and discriminant analysis. Image processing technique is applied for quantification of corrosion data while discriminant analysis is applied to classify the data.

1. INTRODUCTION

Many reports had highlighted the seriousness of the corroded infrastructure problem all over the world. The cost to rehabilitate existing deteriorated infrastructure worldwide reached billion of dollars [1]. An urgent need for the advances of effective inspection method had been denoted out to detect corrosion of the concrete structures. Non-destructive testing (NDT), an objective corrosion inspection method could lead to cost savings of billions of dollars worldwide by the detection of corroded reinforcement in concrete at an early stage, before the functionality of a structure is seriously damaged [2]. The NDT of ground penetrating radar (GPR) method had been found to be useful in evaluating existing reinforced concrete structures for continued use or reparation [3–5].

The GPR was becoming more and more popular as a concrete inspection method. The GPR was significant technology for locating embedded targets in concrete structures. The NDT method of GPR had allowed a reliable and efficient inspection of the structural integrity of reinforced concrete [6]. However, the results of GPR image was very difficult to interpret. It may require the skills of an experienced operator and the use of lengthy manual post-processing and subjective expertise to produce a reliable end result [6–8]. Recent years, many automatic techniques had been developed for interpreting the GPR data. Study done by [9] had developed system based on a neural network classifier. Image processing techniques are employed to provide a high resolution image and good interpretation of data image of the GPR. The systems consist of a pattern recognition stage with additional pre-processing technique and feature-extraction stage to obtain input fed into neural network.

In addition, Al-Nuaimy et al. [10] had developed guidelines and recommendations for GPR data acquisition and interpretation. Image processing techniques were employed to provide a high resolution image, an accurate depth and location information, and to facilitate straightforward data interpretation. However, the success had so far been limited to straightforward cases such as buried object location [9, 11]. Therefore, in this paper, authors investigate the corrosion in reinforced concrete structures by proposing the use of image processing techniques to extract features differentiating corrosion and no corrosion of reinforced concrete structures from the GPR data and to obtain the best interpretation for corrosion detection. In addition, for the further process the use of discriminant analysis for decision of the data whether corrosion or no corrosion is applied.

2. SAMPLE PREPARATION AND DATA ACQUISITION

In this paper, the reinforced concrete slabs with dimension $l = 1\,\mathrm{m}$, $w = 1\,\mathrm{m}$, and $h = 0.3\,\mathrm{m}$ was prepared. The concrete grade is C30. Portland cement, uncrushed sand, crushed limestone with a maximum aggregate size of 20 mm were used to prepare the concrete mixes. A water-cement (W/C) ratio of 0.5 were kept in-variant in all concrete mixes. The y-type reinforced bars (rebars) with length approximately 1 m were selected with diameter 20 mm. The rebars was immersed in a

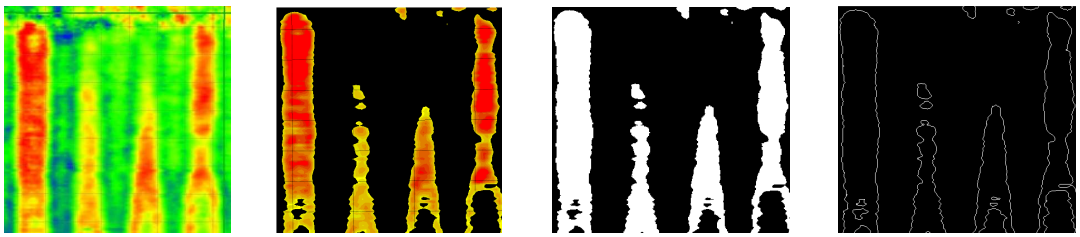

(a) GPR data (b) K-means clustering (c) binary image (d) boundary image

Figure 1: Image processing data.

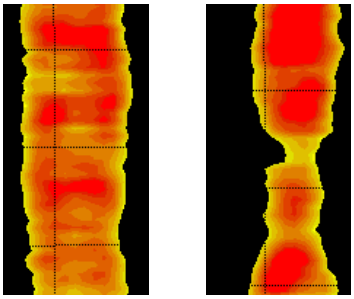

(a) (b)

Figure 2: Segmented images, (a) no corrosion segment, (b) corrosion segment.

solution of 5% NaCl (0 day for no corrosion, 1 day for low corrosion, 3 days for middle corrosion, and 7 days for high corrosion) using direct current (DC) power supply. The direction of current was adjusted so that the corroding rebars was served as the anode, while rebar facing the corroding rebars was served as the cathode. The current of 10 V (volt) and 1 A (ampere) were applied in the corrosion process. In the last process, the corroded rebars are induced to concrete mixes. The 2 GHz of GPR manufactured by IDS (Ingegneria Dei Sistemi S.p.A) Italy, was used to detect the corrosion in reinforced concrete slabs after 28-days of standars moist curing. The result could be proposed in a-scan, b-scan, c-scan, and 3D image. In this paper authors used 3D image as the GPR data for corrosion detection.

3. IMAGE PROCESSING TECHNIQUES

Imaging of concrete structures had presented many challenges due to the fact that concrete was a non-homogeneous material [12]. In this paper, authors used k-means clustering and edge detection image processing techniques to detect and to investigate corrosion and non corrosion image from GPR data of concrete structures.

3.1. *K*-means Clustering

K-means clustering technique divided a digital image into multiple segments. The image segmentation results could be used to derive region-wide color and texture features, which in turn, together with the segment location, boundary shape, and region size, can be used to extract semantic information [13]. To simplify the representation of an image into something that was more meaningful and easier to analyze was the direction of this technique. For example, we needed object in one color in colourfull image, so the segmentation would present image with one color only separately. Each of the pixels in a region were similar with respect to some color characteristics [14]. In this work, as preprocessing image of color based segmentation using k-means clustering was applied using matlab 7. The data given by GPR was clustered by the k-means method, which aims to partition the points into k groups of color images.

3.2. Binary and Boundary Image

For analysis, the used cluster image were converted to binary image using matlab 7 toolbox for calculation of area of object, i.e., corossion and no corossion or sum of white pixels in corossion and no corossion images. In addition for further analysis this work also applied perimeter toolbox in matlab 7 for calculation boundary pixel analysis. The original image of GPR data, k-means clustering image, binary image, and boundary image gained using matlab 7 simulation were shown

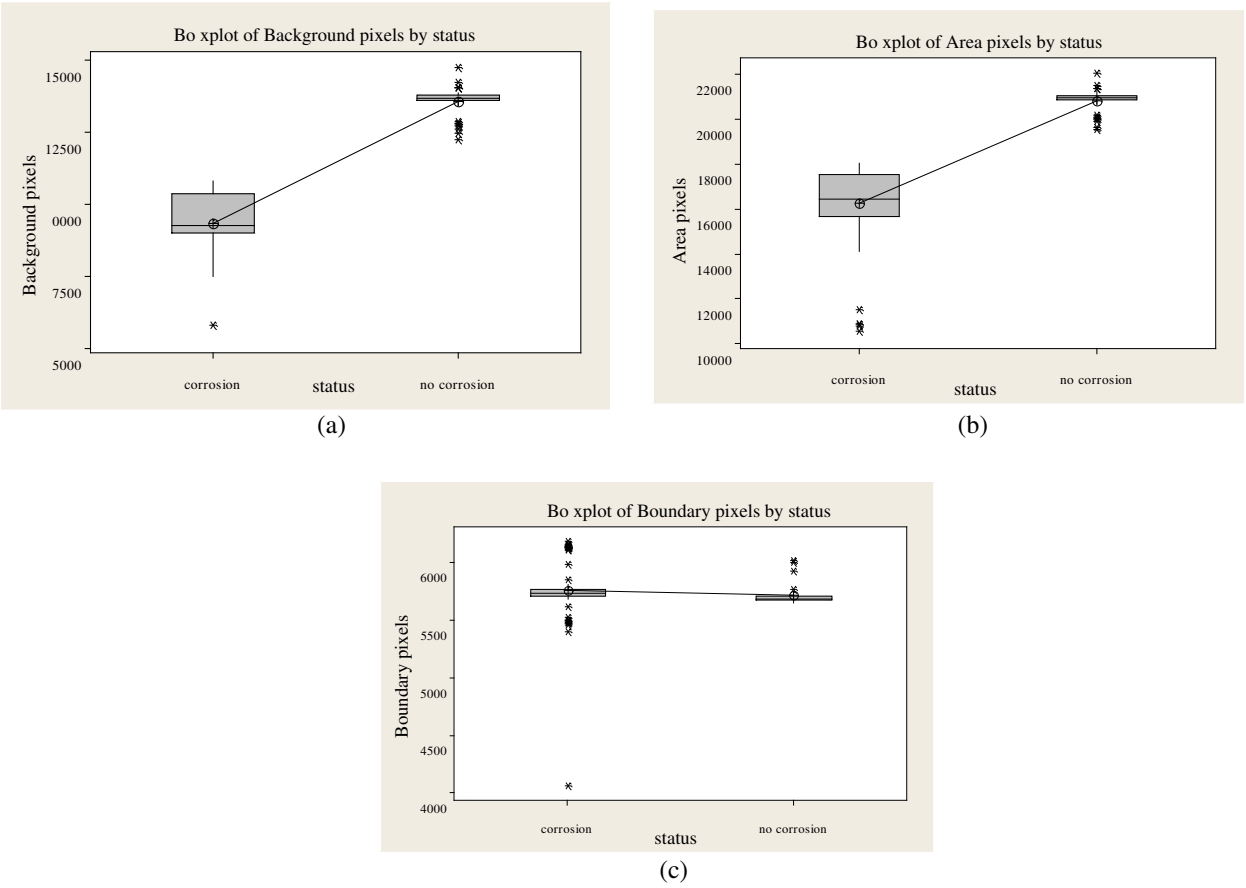

Figure 3: The capability of three features for differentiating corrosion and no corrosion.

Table 1: Classification for three features.

Features	Corrosion	No corrosion	P
Background	9307 ± 956	13545 ± 527	0.00
Area	16252 ± 1515	20818 ± 531	0.00
Boundary	$5757,9 \pm 241,4$	$5713,5 \pm 87,7$	0.29

*P value < 0.05 for capable features

in Figure 1.

4. DISCRIMINANT ANALYSIS

In this work, discriminant analysis (DA) was used to determine the important of image features for GPR data classification. The DA was a very popular supervised learning technique. DA was fast, easy to implement and readily available in statistical packages. In this paper, we used minitab version 14.12 statistical software for classification process. The first process was to show the applicability of the used features using one-way anova statistical operation. If the features had P value < 0.05, so the feature was compatible features. According to [15], DA was a classification method that can predict group membership of a newly sample observation. Three features, i.e., sum of background pixels, area of object, and boundary pixels as input into DA were obtained from processed images which segmented images were taken no corrosion and corrosion separately with size 100×200 pixels as shown in Figure 2.

5. RESULTS AND DISCUSSIONS

Total 143 data images was divided to corrosion 108 and no corrosion 35. Table 1 was tabulated for proving the capability of the three features.

In addition, the capability of three features for differentiating corrosion and no corrosion was shown clearly in Table 1. The background and area were capable to differentiate corrosion and no

Table 2: Classification using linear discriminant analysis.

Put into Group	corrosion	no corrosion
corrosion	108	0
no corrosion	0	35
Total N	108	35
N correct	108	35
Accuracy		100%

corrosion significantly proved with P value 0.00. The capable features was then processed using DA to show the accuracy of classification. Linear discriminant analysis was used for process. The result for linear DA was shown in Table 2.

Based on Table 2 the classification of corrosion and no corrosion was proved excellent result 100%. According to the result, we analyzed that these data were not complicated data due to high accuracy performance of DA classification. Most probably, these results were influenced by effective image processing technique for segmentation the object of interest and other object in images.

6. CONCLUSION

This paper presented the observation of GPR data with two conditions of concrete structures. Image processing techniques were used to process the image data to obtain features to classify the image into two classes using linear discriminant analysis. The accuracy results presented in Table 2 had proven image processing to be effective for detecting the corrosion and no corrosion in concrete structures using GPR data. The use of discriminant analysis for classification our data had been proved excellent due to not complicated data. The authors of this paper believe that the used techniques could be used to classify the other damage images.

REFERENCES

1. Almusallam, A. A., "Effect of degree of corrosion on the properties of reinforcing steel bars," *Construction and Building Materials*, Vol. 15, No. 8, 361–368, 2001.
2. Arndt, R. and F. Jalinoos, "NDE for corrosion detection in reinforced concrete structures — A benchmark approach," *Proceedings of Non-destructive Testing in Civil Engineering*, Nantes, France, 2009.
3. Barnes, C. L., J. F. Trottier, and D. Forgeron, "Improved concrete bridge deck evaluation using GPR by accounting for signal depth-amplitude effects," *NDT and E International*, Vol. 41, No. 6, 427–433, 2008.
4. Laurens, S., J. P. Balayssac, J. Rhazi, G. Klysz, and G. Arliguie, "Non-destructive evaluation of concrete moisture by GPR: Experimental study and direct modeling," *Materials and Structures/Materiaux et Constructions*, Vol. 38, No. 283, 827–832, 2005.
5. Kim, W., "Ground penetrating radar application for non-destructive testing: Bridge deck inspection and dowel bar detection," Ph.D. Thesis, University of Missouri-Rolla, United States, Missouri, 2003.
6. Chang, C. W., C. H. Lin, and H. S. Lien, "Measurement radius of reinforcing steel bar in concrete using digital image GPR," *Construction and Building Materials*, Vol. 23, No. 2, 1057–1063, 2009.
7. Maierhofer, C. and S. Leipold, "Radar investigation of masonry structures," *NDT and E International*, Vol. 34, No. 2, 139–147, 2001.
8. Maierhofer, C., "Nondestructive evaluation of concrete infrastructure with ground penetrating radar," *Journal of Materials in Civil Engineering*, Vol. 15, No. 3, 287–297, 2003.
9. Al-Nuaimy, W., Y. Huang, M. Nakhkash, M. T. C. Fang, F. T. Nguyen, and A. Eriksen, "Automatic detection of buried utilities and solid objects with GPR using neural networks and pattern recognition," *Journal of Applied Geophysics*, Vol. 43, Nos. 2–4, 157–165, 2000.
10. Al-Nuaimy, W., S. Shihab, and A. Eriksen, "Data fusion for accurate characterisation of buried cylindrical objects using GPR," *Proceedings of Tenth Internutional Conference on Ground Penetrating Radar,* 359–362, Delft, Netherland, 2004.
11. He, X. Q., Z. Q. Zhu, Q. Y. Liu, and G. Y. Lu, "Review of GPR rebar detection," *PIERS Proceedings*, 804–813, Beijing, China, March 23–27, 2009.

12. Buyukozturk, O., "Imaging of concrete structures," *NDT and E International*, Vol. 31, No. 4, 233–243, 1998.
13. Junqing, C., T. N. Pappas, A. Mojsilovic, and B. Rogowitz, "Adaptive image segmentation based on color and texture," *Proceedings of International Conference on Image Processing*, 777–780, 2002.
14. Likas, A., N. Vlassis, and J. J. Verbeek, "The global k-means clustering algorithm," *Pattern Recognition*, Vol. 36, No. 2, 451–461, 2003.
15. Sueyoshi, T., "DEA-discriminant analysis: Methodological comparison among eight discriminant analysis approaches," *European Journal of Operational Research*, Vol. 169, No. 1, 247–272, 2006.

Determining the Effect of Faraday-rotation and Optimum Rotation Angle in Different Types of Magneto-optical PBG Structures

Othman Sidek, Muhammad Hassan Bin Afzal, and Shahid Kabir
Collaborative Micro-Electronic Design Excellence Centre (CEDEC)
Universiti Sains Malaysia, Malaysia

Abstract— The MO-PBG structures have been used in industrial arena with wide popularity and greater authority. Basically, the unique characteristics such as trapping light and transmitting the signal without allowing them to reflect back has made this structural concept widely acceptable and user friendly. Although, these properties can be significantly improved by introduced defect on the lattice structure. In recent studies and findings, it has been revealed that, periodic multi-layered Magneto-Optical (MO) structure consisted of magneto-optical and dielectric layers including defects can boost the Faraday rotation of polarized light when weigh against bulk magneto-optical material. The defining characteristics of a MO-PBG structure are the periodicity of dielectric materials along with one or more axis. In case of MO-PBG structures, when the light is transmitted pass through the magnetized substance and reflected from Magneto-Optical substance known as Faraday Effect. Two very essential effects are required special attention while designing the Magneto-Optical PBG structure such as oblique incidence of the incoming signal and the beam size. To achieve a better transmission it is needed to attain the ideal 45° of Faraday rotation and the ideal beam size. Usually there are two types of problems occurred while designing these types of MO-PBG structures. Firstly the overall transmission is being reduced for 45° of Faraday rotation. Three to four defects can be introduced in these structures to improve the overall transmission quality. Now the second problem arises as the thickness of these structures increases notably and goes over 40 μm. Because of these two effects, the overall performance of MO-PBG structures decreased significantly. But by using certain amount of defects and a well constructed structure could help to overcome these problems and achieve the 45° of Faraday rotation and much improved transmission properties. A front-end programme was designed to evaluate the different properties and performances of MO-PBG structures under different circumstances. It also notifies the users about different layers of MO-PBG structures and their properties such as variation in rotation degree, in transmittance and also in thickness. The present paper deals with different types of MO-PBG structures and properties, the Faraday rotation effect, bulk thickness and probable solution to overcome these problems. The output results attained such as the best possible rotation degree for each MO-PBG structure and thickness are consistent with reference data.

1. INTRODUCTION

The Magneto-optic is a comprehensive study of character of light while it's propagating all the way through the magneto-optic material. Magneto-optical effects are an aftermath of differential interaction of left and right circularly polarized radiation carrying net angular momentums. Just because both of the left and right polarized radiation plays an important role in case of magneto-optical effect, that is why if we observe closely their behaviours, we can have a clear understanding about the polarization method behind this magneto-optical method. MO-PBG structures are an innovative type of materials displaying remarkable and attractive properties in the interaction with light. Research works and studies in magneto-optical effects gained a wider interest in early 70's. During that time, lots of research papers have been published regarding magneto-optical concept. All of these papers, on the subject of a tenth discussed about infrared spectra (two-magnon absorption, magnon-phonon absorption, etc.), then almost four in ten papers were described and discussed the phenomena in the visible spectrum (exciton absorption, exciton-magnon absorption and so on), and about one-tenth of those research papers were concerned about ion-pair spectra and optical scattering. The residual four-tenths of these papers discussed and focused attention on magneto-optics in the constricted look, including the Faraday Effect, Kerr effect, Cotton-Mouton effect and magnetic circular dichroism [1]. Along with the time, the extensive uses of magneto-optical structures and concept in various applications, made a clear, positive and useful impact on modern science.

2. MAGNETO-OPTICAL PHOTONIC BANDGAP (MO-PBG) STRUCTURE

Equations, Photonic bandgap structures are the frequency bands represents in the form of periodic structures, which is incident light robustly being reflected. There are different types of periodic structures such as film stack, fibre brag grating and photonic crystals [2]. These MO-PBG structures can be divided into three categories according to spatial constructions 1-D, 2-D, and 3-D structure. The figure below will help to understand the construction and working ways of different structures.

Here the different colours present the materials with different constants. The defining characteristics of a MO-PBG structure are the periodicity of dielectric materials along with one or more axis [3]. Though, these different types of photonic bandgap structure inside the main system, actually dominate the nature and characteristics of them. Also they produce a large amount of Faraday Effect and Kerr effect as well with a very small thickness. Because these effects, the performance of MO-PBG structures has been decreased significantly. But by using certain amount of defects and a well constructed structure could help to overcome these problems and achieve the 45° of Faraday rotation. Both of Faraday Effect and Kerr Effect occur in different situation. When the light is transmitted pass through the magnetized media and reflected from magneto optical material known as Faraday Effect. Conversely, when the light is reflecting back from that magneto optical material is known as Kerr effect. A diagram below will help to understand this concept [4].

3. FARADAY ROTATION EFFECT ON MO-PBG STRUCTURE

In 1845, Michael Faraday discovered the first physical phenomenon linking light and magnetism. He was able to rotate the polarization of light when he induced a magnetic field in the same direction as the path of the light. This effect, known as the Faraday Rotation or Faraday Effect, only occurs when light passes through transparent dielectrics. A Faraday rotation occurs, when the light is passing through some materials and these materials are uncovered to a parallel magnetic field. Basically, A Faraday Rotation effect is an observable fact that helps to rotate the polarization of the light [5]. Prominent English Physicist and Chemist Michael Faraday first discovered the experimental evidence of connecting light and magnetism. Later he also discovered that, if a magnetic field is induced in the same route as the path of the light, then the polarization of the light can be rotated. This effect is also known as Faraday Rotation. This Faraday Rotation Effect has been illustrated in the diagram below [6, 7].

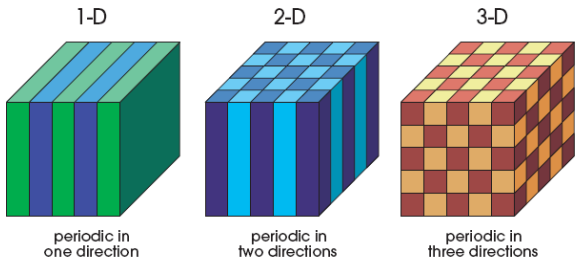

Figure 1: A very normal example of 1-D, 2-D and 3-D MO-PBG structures.

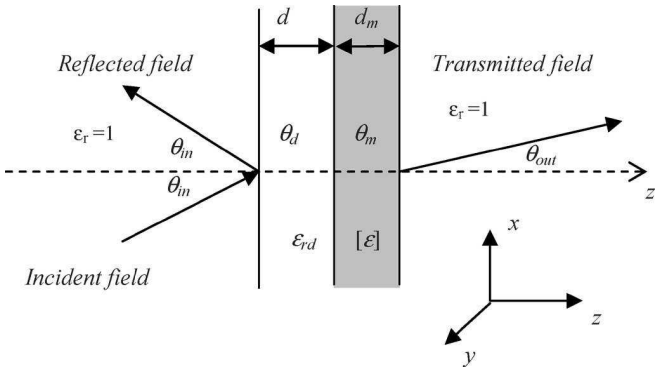

Figure 2: Schematic of the incident, reflected, and transmitted fields from a dielectric stack containing one dielectric layer of thickness d and one MO layer of thickness dm.

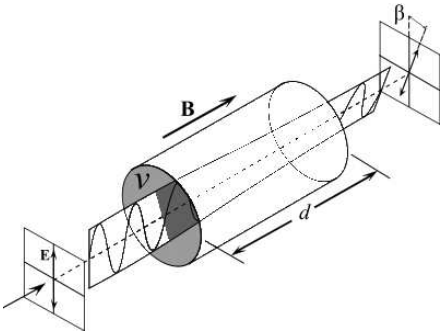

Figure 3: Faraday effect or Faraday rotation.

Here, the relation between the angle of rotation of the polarization and the magnetic field in a diamagnetic material is: $\beta = vBd$, where,

β represents the angle of rotation (in radians);

B represents the magnetic flux density in the direction of propagation (in teslas);

d represents the length of the path (in meters) where light and magnetic field interact.

4. A FRONT-END PROGRAM TO OVERCOME SETBACKS

A front-end visual C++ program was designed to evaluate the different properties and performances of MO-PBG structures under different circumstances. It also notifies the users about different layers of MO-PBG structures and their properties such as variation in rotation degree, in transmittance and also in thickness. The front-end program has been designed to help a general user to have an in-depth understanding about various types of MO-PBG structure, their distinctive features, and characteristics. A user can easily evaluate and make a decision about a structure type in different circumstances. It also notifies the user about maximum possible Faraday rotation degree without gaining a bulky thickness. It also suggests the user about the most economical MO-PBG structure with better performance.

5. RESULT & DISCUSSION

It was required to modify the program and generate different values for different structures. Later it is required to compare the output results with the provided literature materials such as Sakaguchi and Sugimoto [8]. On the source of provided values and characteristics of different structures in this paper, the experimental work has been carried out through the whole study. The resultant properties of different structures keep up a correspondence with the result provided in the literature. The significant characteristics have been observed during the experimental period such as, as the repetition number (n) increases, the degree of rotation is also increases. Regarding the output characteristics of different structures and their layer formation, some of them share same values such as GM as well as G2, MG as well as M2, GMMG as well as MGGM and G2M2 as well as M2G2. But three stack layers possess different characteristics than other structures and thus contain unique characteristics than others. Degree of Rotation largely depends on number of layers of structures. When the thickness is less, it produces large degree of rotation, but the transmittance decreases significantly. It has been found that, multiple stacks of the basic structures pick up transmittance without any decline in the rotation. A rotation of close to 45 degree which is essential for isolators is achievable at a transmittance of around 0.8 (the optical loss is less than 1 dB). Specifically, it is promising to obtain a multilayer Faraday rotator applicable to isolators by optimizing the periodic structures. Now, let's consider three stacking layer types of MO-PBG structures. For single layer structure we will take GM, for double stack layer GMMG and for triple stacking layer we will consider GMMG3.

Now from Figure 4, if we consider about single stack layer GM properties, it achieves the rotation degree of 43.7, though the transmittance decreases significantly due to the thickness of structure. In double stack layer, the thickness is now much improved than before, and the transmittance also increases. But the main problem here is the rotation degree is 28.3, which is much small to achieve the goal. In case of three stack layer, here the thickness is significantly increases due to the apparent fact of three layers. That's why the transmittance also increases as 0.990. But the rotation degree is still 36.6 which no close enough to the 45 degree compare to single stack layer. So, this three

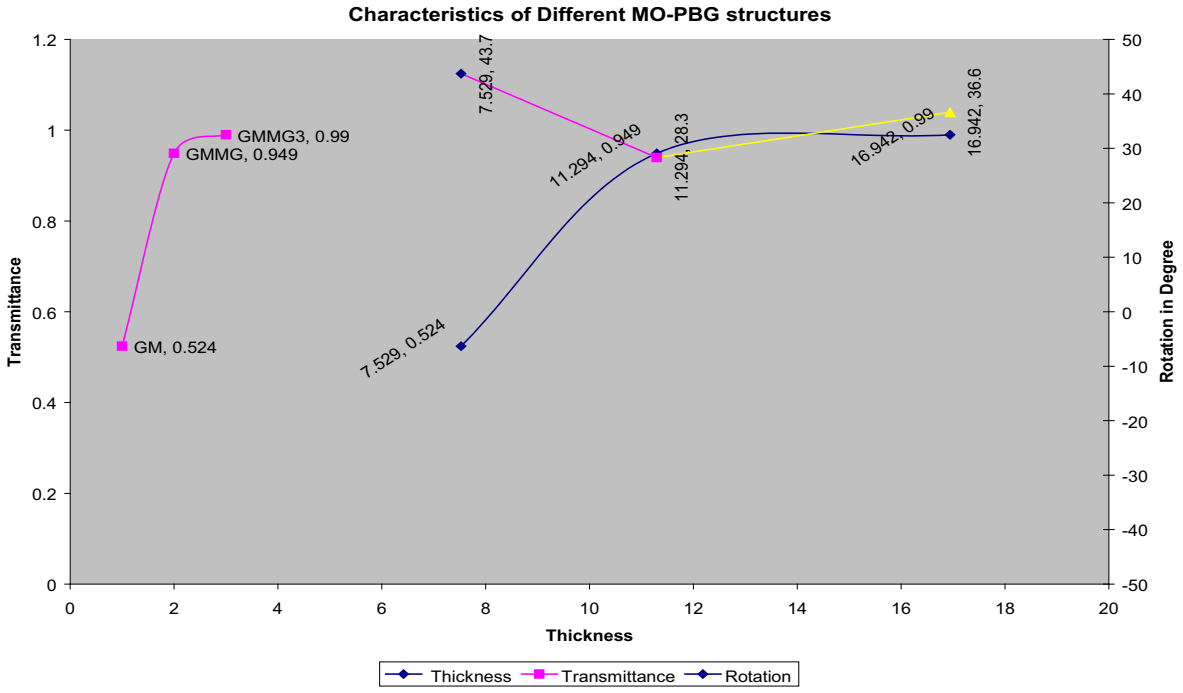

Figure 4: A statistical assessment of different MO-PBG layers.

stack layer GMMG3 exhibits the smallest rate of decrease in transmittance against the increase in rotation, although the rotation remains at 36.6 degree at which the transmittance is 0.990. This will achieve the main goal that is transmittance of more 0.8 in fact it is close to 1 [8].

6. CONCLUSION

This program will allow the users to put values and then they will see the output and also the required layers stacking in MO-PBG structures, which will help them to realize and design the most effective MO-PBG structure with maximum transmittance and a rotation close to 45 degree. The aim of this project is to facilitate one to grasp about the very significance of MO-PBG structures in modern era science and technology with a wide opportunity. Several industrial applications being run with the concept of MO-PBG structures, and if these structures used with the best possible outcome by rise above those setbacks, then it is an enormous contentment regarding the objective of this paper.

REFERENCES

1. Tshusima, K., "Magneto-optics: It's past and present," *IEEE Translation Journal on Magnetic in Japan*, Vol. 1, No. 8, 1985.
2. Levy, M., H. C. Yang, M. J. Steel, and J. Fujita, "Flat-top response in one-dimensional magnetic photonic bandgap structures with Faraday rotation enhancement," *Journal of Lightwave Technology*, Vol. 19, No. 12, 1964–1969, 2001.
3. Joannopoulos, J. D., R. D. Meade, and J. N. Winn, "Photonic crystals: Molding the flow of light," Princeton University Press, New Jersey, 2008, Web-Link: http://ab-initio.mit.edu/book/photonic-crystals-book.pdf.
4. Vukovic, A., P. Sewell, and T. M. Benson, "Analysis of 3-D diffraction effects and oblique incidence in magneto-optic photonic bandgap structures," *Journal of Lightwave Technology*, Vol. 24, No. 7, 1964–1969, 2006.
5. Padmaraju, K., "Faraday rotation," Department of Physics and Astronomy, University of Rochester, Rochester, New York, 2008.
6. http://en.wikipedia.org/wiki/Faraday_effect.
7. http://www.uop.ca/uop-research/magnetooptic-materials-and-integrated-optical-isolators.
8. Sakaguchi, S. and N. Sugimoto, "Multi-layer films composed of periodic magneto-optical and dielectric layers for use as Faraday rotators," *Optics Communication*, Vol. 162, No. 1–3, 64–70, 1999.

Underwater Communication Systems: A Review

Mohd Ansor Bin Yusof[1] **and Shahid Kabir**[2]

[1]School of Electrical and Electronic Engineering
Universiti Sains Malaysia, Engineering Campus, Nibong Tebal, P. Pinang, Malaysia
[2]Sustainable Materials and Infrastructure (SMI) Cluster
Collaborative μ-electronic Design Excellence Centre (CEDEC)
Engineering Campus, Universiti Sains Malaysia (USM), Malaysia

Abstract— There is a high demand for underwater communication systems due to the increase in current human underwater activities. Underwater communication systems employ either sonar or electromagnetic waves as a means of transferring signals. These waves are different physically and electrically, and thus the systems that employ them also differ in their design architecture, wave propagation and devices used for emission and reception. As a result, the two systems have varying advantages and limitations. This paper presents an in-depth review of underwater communication based on sonar and electromagnetic waves, a comparison of the two systems and a discussion of the environmental impacts of using these waves for underwater communication. In the tradeoff between preserving the underwater environment and the need for underwater communication, it appears that underwater electromagnetic wave communication has the most potential to be the environmentally-friendly system of the future.

1. INTRODUCTION

Demands for inter-medium communication systems are increasing due to ongoing expansion of trans-medium human activities [1]. Communication crossing air-water boundaries in particular, is attracting interest, as underwater communication itself continues to grow steadily [2]. There are only two types of waves that could be used to establish underwater communication systems, sonar waves and electromagnetic waves; in some cases both of these waves are used together. These two waves are different in nature; sonar waves are caused by a physical vibration of particles and electromagnetic waves are caused by interference in an electromagnetic field. Due to their physical nature, sonar waves perform very well when they are used in an underwater environment itself but impractical for underwater communication involving the air-water interface. However, it is possible to employ electromagnetic waves for underwater communication, as well as for the trans-boundary air-water and the underwater itself. Although all underwater communication systems are the same in terms of circuitry, they are different in terms of the device employed for emitting or transmitting and receiving these waves. A transducer called a hydrophone is used to emit and receive sonar waves, and electromagnetic waves are transmitted and received using antenna [3]. In term of system architectures, underwater sonar communication has two modes of architecture, the passive mode and active mode. Similarly underwater electromagnetic communication also has two categories; the buoyant system and the direct linkage system.

2. UNDERWATER SONAR COMMUNICATION SYSTEM

For several years, sonar waves were used in various underwater communications activities and such underwater communication is commonly known as sonar communication. The general layout of a sonar communication system is shown in Figure 1. In this figure, the system consists of two sets of transducers connected to processing circuitry [4]. The processing circuitry is kept in a water proof body, but the transducers are kept into water environment. Commonly this underwater transducer is called hydrophone. The first set of hydrophone is the emitter hydrophone (T_{dx}) that changes an electrical signal into sonar waves, which enable propagation in almost half hemispherical direction into water. The second hydrophone is the receptor hydrophone (R_{dx}), which receives in-coming sonar waves and changes them back into electrical signals. The performance of hydrophone depends on the underwater vibration sensitivity and it is either a pressure sensor or a capacitive sensor. The emitter hydrophone (T_{dx}) and receptor hydrophone (R_{dx}) may have the same or different vibration sensitivity depending on particular application. The processing circuitry in a sonar communication system is cascaded electronic circuits such as an amplifier, comparator, signal generator and many other processing circuits. The main purpose of the circuitry is to process the differences (in time or in phase) between emitted and received sonar waves, and then to make decisions based on these

differences. From Figure 1 itself sonar communications can be divided into two types: passive sonar and active sonar communication [5]. The passive sonar communication system is only able to receive sonar waves traveling in the water environment. On the other hand, the active sonar communication system emits into and as well as receive sonar waves in the underwater.

2.1. Active Sonar Communication System

A basic block diagram of an active sonar communication system is presented in Figure 2. In this figure, a complete active sonar communication system has two separate sub-systems and each sub-system is fixed with two sets of hydrophones: the T_{dx} hydrophone and the R_{dx} hydrophone. The electronic signal processing conducted in each sub-system was as explained in the previous section. But in such active sonar communication system the sonar wave itself is relayed among these underwater hydrophones. The sonar wave emitted by a T_{dx} hydrophone of one sub-system is received by the R_{dx} hydrophone of other subsystem. This same flow of sonar wave is performed on the opposite way. However these two pairs of hydrophone are not allowed to receive any sonar wave emitted form its own sub-system T_{dx} hydrophone. This condition implies such active sonar communication system has two different frequencies of sonar wave. Such described an active sonar communication system with its block diagram in Figure 2 is called the full duplex active sonar communication system because the sonar wave is relayed just among those two pairs of hydrophone. The full duplex active sonar communication system as shown in Figure 2 can be simplified into an active sonar communication system which has only one sub-system with a pair of hydrophone as shown in Figure 3. Specifically such active sonar communication system is called the half duplex active sonar communication system. This half duplex active sonar communication system receives its own emitted sonar wave after reflection from a dummy target. Therefore such active sonar communication system operates with only a single frequency. Once again the electronic signal processing involves in this system is as same as explained before. Both active sonar systems use the audible frequency range (50 Hz $\sim$ 20 kHz), but in certain applications, it is as high as 50 kHz [6].

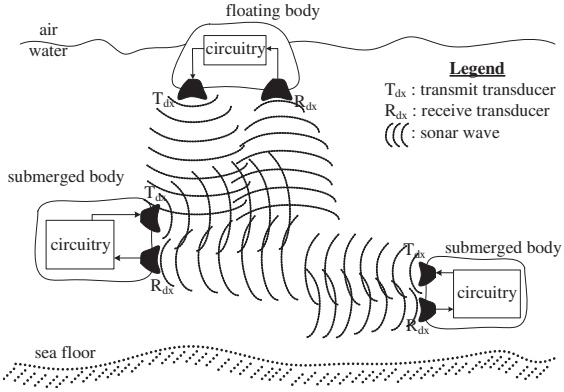

Figure 1: General layout of sonar communication system.

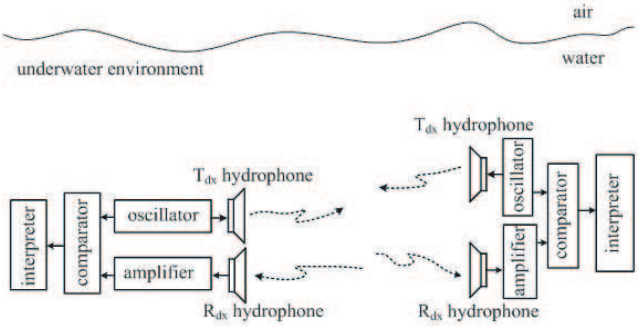

Figure 2: Block diagram of full duplex active sonar communication system.

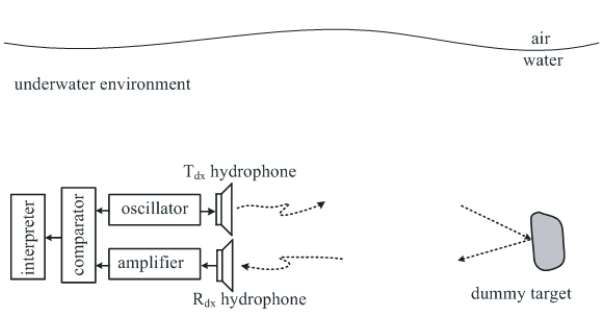

Figure 3: Block diagram of half duplex active sonar communication system.

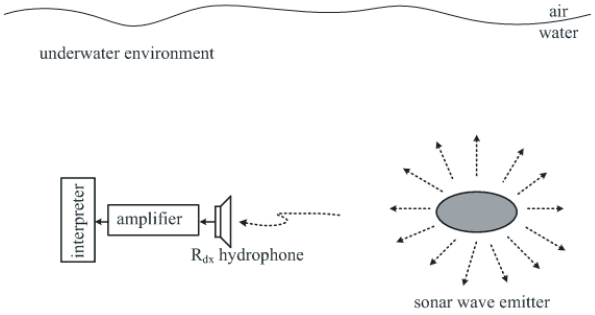

Figure 4: Layout of passive (simplex) sonar communication system.

2.2. Passive Sonar Communication System

The passive sonar communication system has just one set of R_{dx} hydrophones [6] and its general layout is as shown in Figure 4. The passive sonar communication system only detect any sonar waves emitted by underwater entities, such as moving submarines, crowds of fish or even the rotating of a vessel's propeller. The detected sonar wave is converted into equivalent electrical signals and is processed as explained before. In communication terminology, the passive sonar communication system is referred to as a simplex communication system because it only receives any emitted underwater sonar wave. The passive system usually uses the audible frequency range (50 Hz $\sim$ 20 kHz) and may even use a higher range if needed.

3. UNDERWATER ELECTROMAGNETIC COMMUNICATION SYSTEM

Underwater communication is not restricted only to communication within an underwater environment itself but it may also include communication paths that cross the air-water boundary [7]. For such trans-air-to-water underwater communication, electromagnetic waves are the best choice, since these waves are not adversely affected by the air-water boundary, which could be either air-seawater or air-fresh water interfaces. Therefore the underwater electromagnetic communication system could be classified according to its system design architecture, merely, the buoyant electromagnetic communication system and the direct linkage electromagnetic communication system.

3.1. Bouyant Communication System

Figure 5 shows the general architecture of a buoyant communication system with the complete system has three main circuits: an underwater transceiver, an interface circuit and an in-air transceiver. The underwater transceiver is connected through a very long cable to the interface circuitry encapsulated in the floating buoy. Electrical signals flow between the underwater transceiver in the submerged body to the interface circuitry in the floating buoy through the long wire cable. The buoy is employed not only for keeping the interface circuitry water-proof, but it also acts as a floating agent for holding and to erect the in-air antenna [7]. On the in-air side, the in-air antenna converts the electrical signal received from the interface circuit into electromagnetic waves. Then the transmitted electromagnetic wave is received by another in-air antenna attached to another part of an in-air transceiver. On the way back, an electrical signal generated by the in-air transceiver is converted into electromagnetic waves and then sent to the buoy's antenna and back to the underwater transceiver through the same long wire cable. Obviously in both to-and-fro paths, the propagation of electromagnetic waves is simply relayed between a pair of in-air antenna without the need to cross the physical boundary of air-to-water. Therefore, the buoyant communication system is not a truly underwater system. Such communication is just like other common and well known air-to-air electromagnetic communication. In terms of frequency, the buoyant underwater electromagnetic communication system may use any allocated frequency range, usually in MHz, and may be as high as GHz.

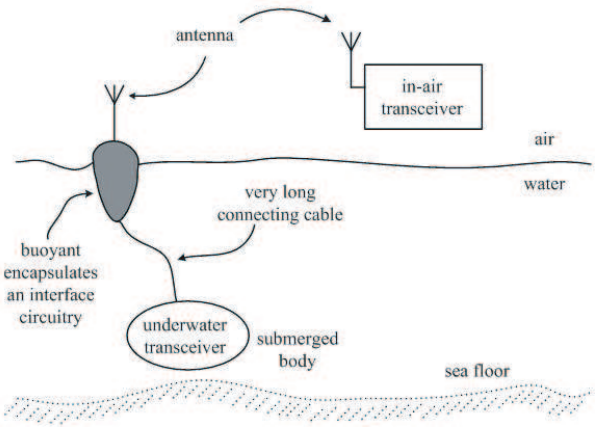

Figure 5: System architecture for a buoyant communication system.

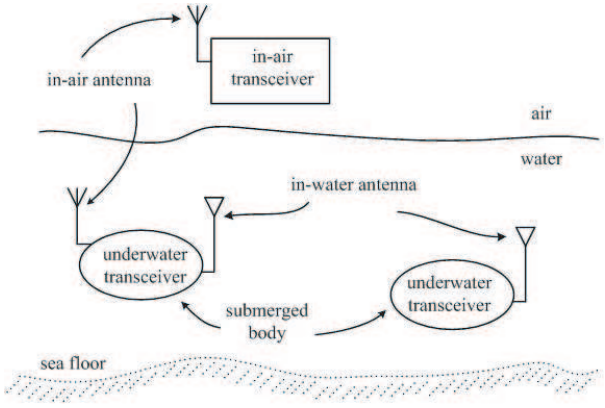

Figure 6: The direct underwater communication system.

3.2. Direct Underwater Communication System

In the direct underwater communication system, the propagation of electromagnetic waves is relayed between a pair of antenna in which both antennas can be in different mediums; one set of antenna can be submerged in water and the other set can be in the air. Another possible arrangement is both set of antenna are submerged in the underwater [8]. Figure 6 shows the concept of direct underwater communication systems, which demonstrate the use of both pairs of antenna. There is an in-water antenna attached to the underwater transceiver with its complement in-water antenna is attached to another underwater transceiver. This pair of in-water antenna is purposely for transmitting and receiving electromagnetic waves propagating within the underwater environment itself. The other antenna arrangement is an-air antenna attached to the underwater transceiver with its pair is an in-air antenna connected to the in-air transceiver. Therefore in the later arrangement, the propagation of electromagnetic waves passes to-and-fro directly over the physical boundaries of air-water. In terms of frequency, both sets of antennas operate at different frequency ranges. For over several years before, the frequency ranges of electromagnetic waves used for underwater communication systems have been either LF (below 100 kHz), VLF (below 20 kHz), or even ELF (below 10 kHz) [9]. Consequently, the constructed antennas in this direct underwater communication system commonly are in the form of very long wire cables, which can be as long as 300m. Due to current demand such very low frequency is no longer practical and therefore higher frequency ranges in MHz is required.

4. SONAR AND ELECTROMAGNETIC UNDERWATER COMMUNICATIONS: DISTINCTIONS AND LIMITATIONS

Sonar waves and electromagnetic waves are totally different in their physical appearance and they have their own unique characteristics that distinguish them. Due to these differences; both of them have their own advantages and limitations in their employment in underwater communication. Regarding path propagation, sonar waves can only propagate through any medium in which physical vibration can be performed with its propagation speed varies according to the physical characteristics of the propagation medium. There is no doubt that sonar waves are a good means for the underwater communication itself but for communication that involves crossing the air-water boundary, sonar waves are not practical. Its amplitude is seriously attenuated over the crossing boundaries of the air-water. On the other hand, electromagnetic waves, which are simply an interference of the electromagnetic fields that surround everything, can propagate through any physical substance; even into free space with its speed of propagation remains almost constant in any medium of propagation.

The passive system can only pick up sonar waves, whereas the active system can not only pick up these waves but can also emit them. These modes show a practical application within underwater itself. Conversely, the electromagnetic underwater communication system design using electromagnetic waves is quite effective, whether using the buoyant mode or direct linkage mode design architecture. In the buoyant system architecture, electromagnetic waves propagate just between the in-air antennas. However, in the direct linkage design architecture, the waves propagate across the air-water boundaries. Commonly sonar communication systems employ sonar wave with audible frequency range (50 Hz $\sim$ 20 kHz) but it may goes to MHz in particular application. Conversely, electromagnetic underwater communication systems employ an electromagnetic wave with frequency as low as ELF to GHz. The buoyant communication system may use MHz to GHz frequency but the direct underwater communication systems normally use ELF and LF frequencies. The deeper under water the lower the frequency is used, maybe even as low as 5 Hz.

Concerning about environmental issues, the passive sonar communication system and both modes of electromagnetic underwater communication system do no imposes any disturbances to underwater species because these systems do not emit any harmful waves into underwater environment. Similarly the active sonar communication system is also not endangering to underwater inhabitants if it emit non-disturbance, low power and over limited period sonar wave into the underwater. The active sonar communication system will disturb and destroy the underwater life if it emits ELF and very powerful sonar wave, in some case as high as 240 dB, into the underwater.

5. CONCLUSIONS

Construction of underwater communication systems may use either sonar wave or electromagnetic wave. The passive sonar communication system simply picks up any sonar waves propagating in the underwater but the active sonar communication system receives as well as emits sonar wave in the underwater. Both passive and active mode use a hydrophone as the device for emitting

or receiving sonar waves in the underwater itself. These sonar communication modes are not practical for air-water trans-boundary communication due to the greatly amplitude attenuation as they cross the air-water interface. Alternatively electromagnetic wave communication systems are practical for cross-boundary air-water underwater communication with almost without any limitation of speed and amplitude attenuation. These systems employ just a pair of antenna for both transmit and receiving any electromagnetic wave. Generally, underwater electromagnetic communication systems are divided into two types of architecture: the buoyant system and the direct linkage system. In the buoyant system, the waves travel just between a pair of antenna in the air but in the direct linkage system, the electromagnetic waves relies between a set of in-air antenna and underwater antenna over directly crossing the air-water boundary, or they simply travel between a pair of antenna that are entirely in the underwater. Concerning the environmental effects the passive and electromagnetic underwater communication systems have been used for decades without any apparent harmful side effects to the underwater environment or inhabitants. For the active underwater sonar systems, however, there are two conditions; the low power active sonar communication system is considered relatively safe for the underwater environment. The only harmful system that endangers to the underwater environment and species is the high-power low-frequency active sonar communication system.

REFERENCES

1. Headrick, R., "Growth of underwater communication techonogy in the U.S. Navy," *IEEE Communication Magazine*, 80–82, Jan. 2009.
2. Nagothu, K., M. Joordens, and M. Jamshidi, "Communications for underwater robotics research platforms," *2nd Annual IEEE Conference on Signals, Circuits and Systems*, 1–6, Montreal, Canada, 2008.
3. Prasad, S. E., R. Blacow, J. Frank, and D. Waechter, "Deployable sonar systems for underwater communications," Apr. 2009, http://www.sensortech.ca/site/content/2002-03.pdf.
4. Sattar, J., G. Dudek, O. Chiu, I. Rekleitis, P. Gigu'ere, A. Mills, N. Plamondon, C. Prahacs, Y. Girdhar, M. Nahon, and J.-P. Lobos, "Enabling autonomous capabilities in underwater robotics," *IEEE/RSJ International Conference on Intelligent Robots and Systems*, 3628–3634, Nice, France, Sep. 2008.
5. Hung, V. M. and U. J. Na, "Remote control system of a 6 DOF underwater robot," *International Conference on Control, Automation and Systems 2008*, 2575–2580, Seoul, Korea, 2008.
6. Shaw, A., A. I. Al-Shamma'a, S. R. Wylie, and D. Toal, "Experimental investigation of electromagnetic wave propagation in seawater," *Proceeding of the 36th European Microwave Conference*, 572–575, Sep. 2006.
7. River, D. F. and R. Bansal, "Towed antennas for US submarine communications: A historical perspective," *IEEE Antennas and Propagation Magazine*, Vol. 46, No. 1, 23–36, Feb. 2004.
8. Beeman, J. W., C. Grant, and P. V. Haner, "Comparison of three underwater antennas for use in radiotelemetry," *North America Journal of Fisheries Management*, 275–281, 2004.
9. Hovem, J. M., S. Yan, X. Bao, and H. Dong, "Modeling underwater communication links," *Second International Conference on Sensor Technologies and Applications (SENSORCOMM '08)*, 679–686, 2008.

Novel Techniques for UWB Microwave Imaging of Objects with Canonical Shape

Gianluigi Tiberi[1], **Navid Ghavami**[2], **David J. Edwards**[2], **and Agostino Monorchio**[1]

[1]Department of Information Engineering, University of Pisa, Via G. Caruso 16, Pisa I-56122, Italy
[2]Department of Engineering Science, University of Oxford, Parks Road, Oxford, UK

Abstract— This paper describes the development of a new algorithm for use in a recently established technique for medical imaging based on ultrawideband (UWB) microwave signals rather than ionizing radiations such as x-rays. The method is based on Huygens principle (HP), which removes the need to solve inverse problems and, consequently, the need for matrix generation/inversion. In addition to its simplicity, it is shown that HP enables the detection of the extent to which different tissues, or differing conditions of tissues, can be discriminated and render contrast in the final image. Validation of the technique through measurement on cylinder with inclusions is presented.

1. INTRODUCTION

There is a considerable interest in the development of imaging methods for medical applications. Addressing an imaging problem involves estimating the distribution of the field within a volume V based upon observations of the field on the surface of V, and this involves estimating the distribution of dielectric properties within the target volume. Current medical imaging technologies are able to produce well defined tomographic reconstructions of living tissues using a range of approaches. Most common are ultrasound scanners, x-ray based Computed Tomography (CT) and the RF technique of Nuclear Magnetic Resonance Imaging (known as MRI). Each one of these techniques has its own drawbacks. Concerning breast cancer detection, the limitations of conventional x-ray mammograms are well-recognized: for example, this technique, even in high resolution images, with relatively low radiation doses, misses approximately 15% of all cancers whilst 75% of the identified breast lesions are in fact benign [1]. Consequently, microwave imaging is one promising nonionizing and noninvasive alternative screening technology.

Microwave imaging has attracted growing attention in the last decade, especially for its applicability to breast cancer detection (motivated by the significant contrast in the dielectric properties at microwave frequencies of normal and malignant tissues). Current research in microwave breast imaging can be divided mainly into microwave tomography and ultrawideband (UWB) radar techniques. In tomographic image reconstruction, a nonlinear inverse scattering problem is solved to recover an image of the dielectric properties in the breast [2]. In contrast to tomography, the UWB radar approach solves a simpler computational problem by seeking only to identify the significant scatterers [3]. In order to reconstruct the image, beamforming techniques of varying complexity are required. Thus, further research and novel approaches need to be exploited to open new horizons in microwave imaging. In this context, the aim of this paper is to develop a novel, fast and accurate UWB microwave imaging method. In particular, a method based on the principles of physical optics is introduced. The method deals with Huygens Principle (HP): using HP to forward propagate the waves removes the need to solve inverse problems and, consequently, no matrix generation/inversion is required. Together with its simplicity, the methodology permits the capturing of the extent to which different tissues, or differing conditions of tissues, can be discriminated, and hence render contrast in the final image. Moreover, UWB allows all the information in the frequency domain to be utilized by combining the information from the individual frequencies to construct a consistent image. In the following sections, validation of the technique through measurements on cylinder with inclusion has been performed and results are presented, illustrating the capability of the method to identify the presence and location of significant scatterers. Potential applications would be breast cancer detection, internal organ imaging, and whole body imaging.

2. THE HUYGENS PRINCIPLE BASED PROCEDURE

Consider a cylinder in free space, having a radius a_0 illuminated by a transmitting line source tx_m located at $(\rho_{m\text{-}source}, \phi_{m\text{-}source})$ and operating at a frequency f. We assume that the dielectric properties of the cylinder, i.e., the dielectric constant ε_{r1} and the conductivity σ_1, are known. The

cylinder is envisaged to contain an inclusion (Fig. 1(a)), here assumed to be cylindrically-shaped and with a higher dielectric constant than ε_{r1}. The problem consists of identifying the presence and location of the inclusion by using only the field measured outside the cylinder. Suppose the field at the points $\mathrm{rx}_{np} \equiv (\rho_{np}, \phi_{np})$, displaced along the surface, is known:

$$E^{known}_{\mathrm{tx}_m}\Big|_{\mathrm{rx}_{np}} = E^{known}_{np,\mathrm{tx}_m} \text{ with } np = 1, \ldots, N_{PT} \tag{1}$$

Re-stating Huygens Principle (HP), we note: "Each locus of a wave excites the local matter which reradiates a secondary wavelets, and all wavelets superpose to a new, resulting wave (the envelope of those wavelets), and so on" [4]. Therefore we consider what happens if we apply HP using $E^{known}_{np,\mathrm{tx}_m}$ as locus of a wave. With the aim in mind of exploiting such a strategy, we calculate the field inside the cylinder as superposition of the fields radiated by the N_{PT} observation points of Eq. (1):

$$E^{rcstr}_{HP}(\rho, \phi; \mathrm{tx}_m; f) = \sum_{np=1}^{N_{PT}} E^{known}_{np,\mathrm{tx}_m} G(k_1 \left|\rho_{np} - \rho\right|) \tag{2}$$

where k_1 represents the wave number for the media constituting the cylinder. In (2), the string *rcstr* is used to indicate the "reconstructed" internal field, while the string HP indicates that an HP based procedure will be employed. The reconstructed field will depend on the illuminating source and the frequency.

In Eq. (2), for purpose of generality, the Green's function G is used to forward propagate the field; however, when dealing with 2D problems, Bessel functions can be used. It has to be emphasised that HP does not give the correct internal field, even when dealing with homogeneous problems. This derives from the essence of HP, which is formulated for far field phenomena, i.e., it refers to a propagating wave front. In this case, we are not interested in evaluating the internal field, but we want to see if HP can capture the contrast and locate an inclusion within a volume. The capability of capturing the contrast is due to the difference in properties between the two media, which is not taken into account by Equation (2). It follows that the reconstructed field will exhibit a mismatch in the region of transition of the two media. This mismatch opens the way for a new strategy for detection and localization. Considering the problem in more detail, suppose the external cylinder is illuminated using a range of different frequencies and from different illuminating points; all the reconstructed fields will exhibit the mismatch, which will be always located in the region of transition of the two media.

Thus, by summing incoherently all the solutions, i.e., the reconstructed fields, the inclusion will be detected and localized. Mathematically speaking, assuming we use M transmitting sources tx_m with $m = 1, 2, \ldots, M$, and N_F frequencies f_i, it follows that the intensity of the final image I can

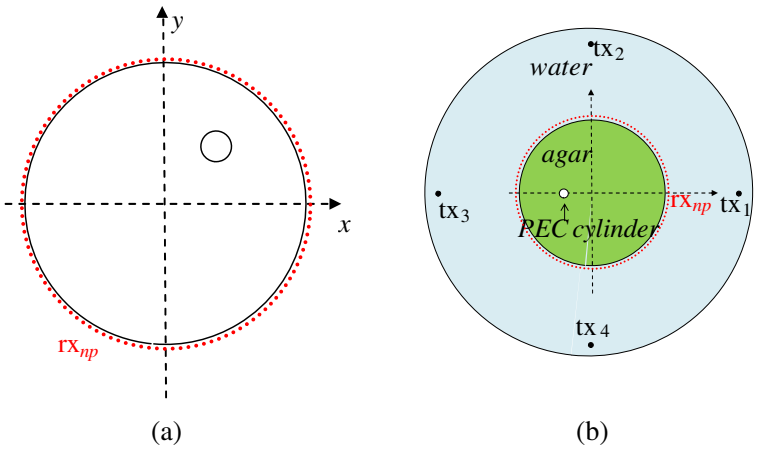

Figure 1: (a) pictorial view of the problem, with the red and black dots representing the receiving and transmitting positions, respectively; (b) pictorial view of the Agar Agar cylinder used for validation through measurements.

be obtained through the following equation:

$$I(\rho,\phi) = \sum_{m=1}^{M}\sum_{i=1}^{N_F} \left| E_{HP}^{rcstr}(\rho,\phi;\mathrm{tx}_m;f_i)\right|^2 \tag{3}$$

The resolution is expected to achieve the optical resolution limit of $\lambda_{1,f\max}/4$ where $\lambda_{1,f\max}$ represents the wavelength in the cylinder calculated at the highest frequency; this gives a rule of thumb for determining the highest frequency to be used. Many imaging algorithms present the drawback that an image of the transmitter appears in the calculated fields, and it can indeed mask the image in the area of interest. To remove the image of the transmitter, we apply the HP to:

$$E_{HP}^{rcstr}(\rho,\phi;\mathrm{tx}_m;f) = \sum_{np=1}^{N_{PT}} \left(E_{np,\mathrm{tx}_m}^{known} - avg_M\left\{E_{np,\mathrm{tx}_m}^{known}\right\}\right) G(k_1\left|\rho_{np}-\rho\right|) \tag{4}$$

where $avg_M\{E_{np,\mathrm{tx}_m}^{known}\}$ represents the average of signals obtained illuminating the object using M different transmitter positions. This in effect smears out the transmitter image.

Finally it is important to point out that the use of the Green's function implies a singularity for $|\rho_{np}-\rho| = 0$; this singularity can be cancelled by performing a multiplication between the same Green's function and $|\rho_{np}-\rho|$. Moreover, when dealing with a medium with high losses, Eq. (2) can be used substituting k_1 with $\mathrm{Real}\{k_1\}$ so as to compensate field attenuation (which could mask the target feature).

The proposed HP based procedure differs considerably from Kirchhoff migration methods [5], whose algorithms usually perform time reversal and back-propagation to find the phase, i.e., time, traces. Conversely, here we are not interested in finding the phase traces: in fact, we use HP with the aim of reconstructing the field. In the reconstruction process, a mismatch appears when going from a media to another, and the capability of capture the mismatch boundaries represent the key feature of the proposed method allowing detection. This difference between the proposed HP based procedure and Kirchhoff migration methods is further supported by the observation that here the position of the transmitter is not required in any step of the image reconstruction algorithm.

3. VALIDATION THROUGH MEASUREMENTS: AGAR-AGAR CYLINDER

The capability of the HP procedure to detect and locate an inclusion has been verified through measurements. In this context, the proposed HP based procedure has been applied to a human tissue like example. To achieve this purpose, a cylindrical container (plastic glass) with radius of 4.2 cm was filled with agar-agar gel approximating a high-water-content human tissue; a small PEC cylinder (1 mm radius) representing a tumor has been positioned inside the agar-agar gel, at the distance of 1 cm from the centre. Moreover, the thin layer of glass can be viewed as representing the skin layer covering the tissue simulant.

The agar-agar was dissolved in hot water at approximately 95°C and then cooled to room temperature to form a semitransparent jell. The dielectric constant and the conductivity are functions of the concentration of the agar-agar [6]; for this experiment we used a concentration of approximately 8% of agar-agar in water, leading to $\varepsilon_{r1} = 70, \sigma_1 = 1\,\mathrm{S/m}$ at 1 GHz. By comparing these values with those given in [7], it can be noted that the dielectric constant and the conductivity of agar-agar are similar to the actual dielectric properties of human tissues. It is worthwhile to point out that the loss-tangent of the agar-agar is even greater than that encountered in some human tissue imaging problems; thus, it follows that the example here presented can be considered representative of lossy media imaging problems.

To couple the microwave energy into the agar-agar cylinder more efficiently, both transmitting and receiving antennas are immersed in a matching medium. Here, for simplicity, water has been used as matching medium. Explicitly, the agar-agar cylinder was positioned inside a container having 20 cm radius and filled with water (see Fig. 1(b)). Frequency-domain ultrawideband (UWB) measurements were performed, using a vector network analyzer (VNA) arrangement to obtain the transfer function. Discone antennas, vertically polarized and omni-directional in the azimuth plane were used, after calibration. Importantly the consideration of the transfer function S_{21} leads to an appropriate selection of the band to be used. In fact, due to the high conductivity of water, very high losses are expected for high frequencies. It was observed that the S_{21} amplitude for the longest path falls below the noise level for $f > 1.6$ GHz; this measurement only used the nominal output

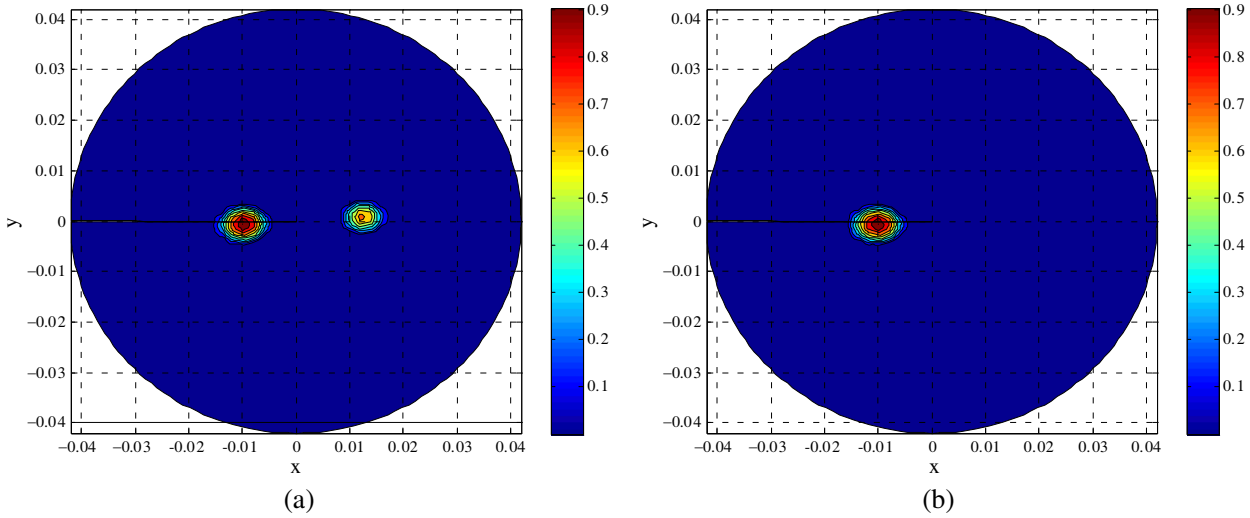

Figure 2: The Agar Agar results: (a) normalized intensity obtained through Eq. (3) when using 90° phi-spaced transmitting antennas and the band 1–1.6 GHz; (b) normalized intensity obtained through Eq. (3) when breaking the symmetry of the illuminating sources (x- and y-axes are in meters).

power level of the VNA (2 mW) and thus, only the band 1–1.6 GHz was used, recording the transfer function at 1601 discrete frequencies (frequency sampling $\Delta f = 0.375$ MHz). Obviously, the upper frequency limit can be increased if a matching liquid with lower losses is used, or if a proper amplifier is introduced in the measurement system (subject to clinical power level considerations). For each set of measurements, the location of the transmitting antenna was fixed at approximately 15 cm away from the center of the cylinder, while the receiver antenna was positioned close to the external surface of the agar-agar cylinder and mounted on a computer-controlled rotating stage with 3 degrees of angular resolution. Thus, the field $E^{known}_{np,\mathrm{tx}_m}$ at $N_{PT} = 120$ equally *phi*-spaced points lying on the external surface is measured; the number of points leads to a spatial sampling of approximately $0.1\lambda_{1,f\,\max}$, where $\lambda_{1,f\,\max}$ represents the wavelength in the agar-agar cylinder calculated at the highest frequency (1.6 GHz). A total number of $M = 4$ sets of data was recorded (with $m = 1, 2, \ldots, 4$), changing the position of the transmitting antenna along *phi* with a step of 90 degrees (see Fig. 1(b)); next, the average of the 4 set is computed, i.e., $avg_M \left\{ E^{known}_{np,\mathrm{tx}_m} \right\}$, and HP is applied as illustrated in Eq. (4). Fig. 2(a) shows the normalized intensity obtained through Eq. (3). A peak can be clearly detected in the region of the inclusion: thus, both detection and localization are achieved. As can be seen, another spot having approximately the same intensity, can be detected in the figure; this corresponds to the "mirror image" of the object with respect to the y-axis and is due to the ambiguity introduced by the symmetry in the position of the illuminating sources used in the measurements. This artifact can be removed by increasing the number of illuminating sources or, alternatively, by breaking the symmetry of the illuminating sources themselves. In this context, in order to remove the ghost image, the same experiment was repeated using only $M = 3$ illuminating sources with a transmitting step of approximately 120 degrees. The resulting image is shown in Fig. 2(b): it can be seen that the false image has successfully been removed. From the figures, it can be stated that the resolution, i.e., the dimension of the region whose normalized intensity is above 0.5, is approximately 5 mm; this value is in agreement with the optical resolution limit of $\lambda_{1,f\,\max}/4$ where $\lambda_{1,f\,\max}$ represents the wavelength in the cylinder calculated at the highest frequency, i.e., 1.6 GHz. In general, it will be realized that a measurement regime can be adopted which avoids any ambiguities (non-unique solutions) by breaking any symmetry in the transmitter and receiver positions. Moreover, it can be shown that the minimum number of $M = 3$ illuminating sources is required to smears out the transmitter image (see Eq. (4)).

4. CONCLUSION

A novel microwave imaging procedure based on the principle of physical optics has been introduced. In particular, the method uses the Huygens Principle (HP). Using HP to forward propagate the wave removes the need to solve any inverse problem; thus, no matrix generation/inversion is re-

quired. Together with its simplicity, another benefit of HP is its capability of capturing the contrast (dielectric variation). The method allows all the information in the frequency domain to be utilized by combining the information from the individual frequencies to construct a consistent image with a resolution of approximately one quarter of the shortest wavelength in the dielectric medium. The power levels used are well within safety limits, while the bands satisfy the UWB rule of being at least 25% of the center frequencies.

ACKNOWLEDGMENT

This research was supported by a Marie Curie Intra European Fellowship within the 7th European Community Framework Programme and supported by UK Engineering and Physical Sciences Research Council.

REFERENCES

1. Patlak, M., S. J. Nass, I. C. Henderson, and J. C. Lashof, *Mamography and Beyond: Developing Technologies for the Early Detection of Breast Cancer*, Intitute of Medicine, National Academy Press, Washington, DC, 2000.
2. Meaney, P. M. and K. D. Paulsen, "Nonactive antenna compensation for fixed-array microwave imaging: Part II — Imaging results," *IEEE Trans. Med. Imag.*, Vol. 18, No. 6, 508–518, Jun. 1999.
3. Bond, E. J., X. Li, S. C. Hagness, and B. D. van Veen, "Microwave imaging via space-time beamforming for early detection of breast cancer," *IEEE Trans Antennas and Propagation*, Vol. 51, No. 8, 1690–1705, 2003.
4. Enders, P., "Huygens' principle as universal model of propagation," *Lat. Am. J. Phys. Educ.*, Vol. 3, No. 1, Jan. 2009.
5. Zhuge, X., T. G. Savelyev, A. G. Yarovoy, L. P. Ligthart, and B. Levitas, "Comparison of different migration techniques for UWB short-range imaging," *European Radar Conference, EuRAD 2009*, 184–187, 2009.
6. Iizuka, K., "An agar-agar chamber for study of electromagnetic waves in an inhomogeneous medium," *IEEE Transactions on Antennas and Propagation*, Vol. 19, No. 3, 365–377, 1971.
7. Gabriel, C., S. Gabriely, and E. Corthout, "The dielectric properties of various tissues," *Phys. Med. Biol.*, Vol. 41, 2231–2249, 1996.

High Resolution Optical Profilometry Using Diffractive Tomographic Microscopy

S. Arhab, **G. Soriano**, **K. Belkebir**, **A. Sentenac**, **and H. Giovannini**
Institut Fresnel (CNRS UMR 6133), Aix-Marseille Université
Campus de St Jérôme, Marseille 13013, France

Abstract— In this paper, we numerically demonstrate that an iterative inverse method based on a rigourous wave scattering model can be used to retrieve the profile of a rough metallic interface from the complex scattering amplitude in far-field. Transversal resolution is subwavelength, and below the classical resolution limit when the profile is sufficiently rough for multiple interactions to occur. Large profiles, with tens of wavelength, can thus be investigated.

1. INTRODUCTION

Far-field optical profilometry is a non contact surface metrology technique that is used to determine the topography of surfaces at a sub micrometer scale. It has important applications in the industrial domain (for exemple for controlling fabrication processes or characterizing optical components) and many systems are commercially available. Interferometric techniques, confocal scanning [1] or chromatic arrangements can give nanometric vertical resolutions provided the surface slopes are small enough so that, locally, the incident beam is considered to be reflected by a horizontal plane at a given height. Hence, the lateral resolution of such techniques is generally greater then the incident wavelength (typically more than one micron). Now, with the improvements of nanofabrication especially in the micro-electronic domain, there is a strong need for optical instruments able to retrieve the roughness of surfaces with typical transverse dimension about 100 nm.

Recently, it was shown that tomographic diffractive microscopy could be a powerful technique for determining the reflectance of rough surfaces with high resolution [2–4]. This approach consists in recording many holograms of the sample under various incident angles. The reflectance of the surface is retrieved by Fourier transforming the set of holograms. Using Fraunhofer approximation, it is possible to estimate the height of the profile from the reflectance with nanometer accuracy. This simple numerical reconstruction procedure relies on two restrictive hypothesis, paraxial approximation and single scattering regime. Now, these hypothesis cannot be assumed when high transverse resolution is sought. Indeed, the paraxial approximation does not hold when high numerical aperture objectives are used and surfaces presenting small transverse dimensions often support multiple scattering.

In this letter, we investigate, with synthetic data, the performances of tomographic diffractive microscopy for profilometry applications, especially when the reconstruction algorithm is based on a rigorous modeling of the light-surface interaction. We show, with several simulated experiments, that the transverse resolution and axial accuracy is much better than that obtained with the classical fourier transform treatment. Contrary to the non-linear inversion approaches already proposed for tomographic diffractive microscopy [3], this algorithm is adapted to profile reconstruction and can deal with large samples (about one hundred of wavelengths).

In a tomographic diffractive microscopy experiment, the surface is illuminated successively by a collimated laser beam under different angles of incidence. For each illumination, the complex amplitude of the far-field diffracted by the surface (namely the hologram in Fourier space) is measured along various directions of observation thanks to an interferometry [2, 3, 5].

2. SURFACE SCATTERING

For simplicity, we consider two-dimensional scattering from a rough surface illuminated by time-harmonic electromagnetic beams at pulsation $\omega = kc$. In a Cartesian coordinates system (x, y, z) the invariance direction is the y-axis and the surface is described by the profile $\Gamma : z = \eta(x)$, with a normal unit vector $\hat{\mathbf{n}}$ directed toward the air $z > \eta(x)$.

With a $\exp(-i\omega t)$ time dependence assumed and in the TE case, $\psi^{\text{inc}}(\mathbf{r}, \theta_0)$ is the y-component of the complex incident electric field at point $\mathbf{r} = (x, z)$ of the incident beam centered on the illumination angle θ_0. ψ^{inc} writes as the sum of downward propagating plane waves

$$\psi^{\text{inc}}(\mathbf{r}, \theta_0) = \frac{g}{2\sqrt{\pi}} \int_{|k_x|<k} \exp(ik_x x - i\sqrt{k^2 - k_x^2}z) \exp\left[-(k_x - k\sin\theta_0)^2 g^2/4\right] \mathrm{d}k_x, \qquad (1)$$

where g is the tapering parameter [6] that sets the footprint size of the beam on the profile.

The total field $\psi = \psi^{\text{inc}} + \psi^{\text{sca}}$ is the sum of the incident and scattered field, and satisfies boundary conditions on Γ that depends on the polarization and the nature of the scattering medium $z < \eta(x)$. In the TE case and for a 1D perfectly conducting surface, the Dirichlet boundary condition applies:

$$(\mathbf{r} \in \Gamma \Leftrightarrow z = \eta(x)) \Rightarrow \psi(\mathbf{r}, \theta_0) = 0. \tag{2}$$

In far-field along the direction of the wavevector $\mathbf{k} = k\frac{\mathbf{r}}{r} = (k\cos\theta, k\sin\theta)$, the scattered field writes in the air as a cylindrical wave

$$\psi^{\text{sca}}(\mathbf{r}, \theta_0) \sim \frac{(1+i)e^{ikr}}{4\sqrt{\pi kr}} s(\theta, \theta_0) \tag{3}$$

which complex amplitude is proportionnal to the so-called scattering amplitude $s(\theta, \theta_0)$, that depends on both the illumination angle θ_0 and the detection angle θ. Note that the optical intensity is classically defined as $I = |s|^2$.

The direct surface scattering problem corresponds to the calculus of $s(\theta, \theta_0)$ for a given profile $z = \eta(x)$, while the inverse surface profiling is then stated as determining the surface $\eta(x)$ from the knowledge of the complex — modulus and phase — scattering amplitude $s(\theta, \theta_0)$.

3. THE FRAUNHOFER APPROXIMATION

When single scattering is assumed, like in the Kirchhoff-tangent plane approximation [7], the scattering amplitude simply writes

$$s(\theta, \theta_0) = N(\theta, \theta_0) \int e^{-(x/g)^2 - iQ_z\eta(x)} e^{-iQ_x x} \mathrm{d}x \tag{4}$$

$$N(\theta, \theta_0) = rk^2 \frac{1 + \cos\theta\cos\theta_0 - \sin\theta\sin\theta_0}{Q_z} \tag{5}$$

with $Q_x = k(\sin\theta - \sin\theta_0)$ and $Q_z = k(\cos\theta + \cos\theta_0)$. The geometrical coefficient $N(\theta, \theta_0)$ is independent of the roughness η, and $r = -1$ is the Fresnel coefficient for the TE reflexion by a perfectly conducting plane.

If a supplementary paraxial approximation $Q_z = 2k = 4\pi/\lambda$ is done, the integral in (4) turns to the Fourier transform of function $f(x) = e^{-(x/g)^2 - 2ik\eta(x)}$. The Fraunhofer estimate of the roughness is thus obtained by reagencing the data to build $\tilde{f}(Q_x) = \frac{s(\theta,\theta_0)}{N(\theta,\theta_0)}$, then to compute the original $f(x)$ and to retrieve the height function $\eta(x) = \frac{\lambda}{4\pi} \arg f(x)$.

This simple inversion technique is used in most holographic or phase microscopy experiments [4]. The transverse resolution is then easily estimated from the spatial frequency span of $\tilde{f}$ that is accessible with the given illumination and detection angles. Note that in [8], single scattering inversions of two-dimensional surfaces are performed without any paraxial approximation, but with similar results. Here, the major approximation is single scattering.

4. DIRECT SCATTERING

If neither single scattering nor paraxial scattering are assumed, the link between the profile and the scattered field is functional and nonlinear.

Following the boundary integral formalism [9] that enforces the Maxwell's equations, and with the Dirichlet boundary condition $\psi(\mathbf{r} \in \Gamma, \theta_0) = 0$, the scattering amplitude

$$s(\theta, \theta_0) = -\int_{\mathbf{r}\in\Gamma} \partial_n\psi(\mathbf{r}, \theta_0) \exp(-i\mathbf{k}\cdot\mathbf{r}) \mathrm{d}\mathbf{r}, \;\; \mathbf{k} = (k\sin\theta, k\cos\theta) \tag{6}$$

is related to $\partial_n\psi$ the normal derivative of the electrical field. This normal derivate is itself the solution of the boundary integral equation

$$\int_{\mathbf{r}'\in\Gamma} G(\mathbf{r}, \mathbf{r}') \partial_n\psi(\mathbf{r}', \theta_0) \mathrm{d}\mathbf{r}' = -\psi^{\text{inc}}(\mathbf{r} \in \Gamma, \theta_0), \tag{7}$$

with kernel $G(\mathbf{r}, \mathbf{r}') = -i\mathrm{H}_0^+(k|\mathbf{r} - \mathbf{r}'|)/4$ the 2D free space Green function (H_0^+ being the Hankel function of zero order and of the first kind) and right hand side ψ^{inc} the incident field on Γ.

Solving Equation (7) and then computing s through formula (6) can be mathematically represented by the direct or forward scattering nonlinear operator $\mathbf{F}$:

$$\mathbf{F} : \eta \to s = \mathbf{F}\eta \tag{8}$$

5. INVERSE SCATTERING

As $\mathbf{F}$ cannot be directly inversed, the inversion problem is generally recasted as an optimization problem. In this section the authors describe the Newton-Kantorovitch (NK) method [10] to solve the nonlinear functional equation $s = \mathbf{F}\eta$. The NK method iteratively builds up the solution of this equation by successively solving the forward problem and a local linear inverse problem.

Now on, η is the real profile that is to be retrieved from s, and at each iteration step, an estimate η_{n+1} of the surface profile function is given by

$$\eta_{n+1} = \eta_n + f, \tag{9}$$

where η_n is the previous estimate and f is an update correction function. We aim here at minimizing the difference between far-field measures $\mathbf{F}\eta$ and calculus $\mathbf{F}\eta_{n+1}$. For this, we consider $\mathbf{D}$ the Fréchet derivative of nonlinear operator $\mathbf{F}$ at height η_n that is defined by

$$\mathbf{D}f = \left.\frac{\partial}{\partial t}\mathbf{F}(\eta_n + tf)\right|_{t=0} = \lim_{t\to 0}\frac{\mathbf{F}(\eta_n + tf) - \mathbf{F}\eta_n}{t} \tag{10}$$

and that turns to be a linear operator. At this iterate,

$$\mathbf{D}f = \mathbf{F}\eta - \mathbf{F}\eta_n \tag{11}$$

is the local linear inverse problem that we solve to determine f. Unfortunately, Equation (11) is ill-posed and needs regularization. The authors use a zeroth-order standard Tikhonov regularization [11]

$$\left[\mathbf{D}^\dagger\mathbf{D} + \mu^2\mathbf{I}\right] f = \mathbf{D}^\dagger(\mathbf{F}\eta - \mathbf{F}\eta_n) \tag{12}$$

where μ is the regularization parameter, $\mathbf{I}$ is the identity, and $\mathbf{D}^\dagger$ is the adjoint of linear operator $\mathbf{D}$.

6. OPTICAL SURFACES PROFILOMETRY

In the following, the wavelength is set to $\lambda = 633\,\text{nm}$, with both incidences and scattering angles regularly sampled between $-45°$ and $+45°$ with a $1°$ step. The numerical aperture is thus $NA = 0.71$ and the single scattering analysis states [12] that the minimum distance between two resolved points is $\lambda/(4\,NA) = 223\,\text{nm}$.

We consider two rough surfaces that are realizations of Gaussian processes with Gaussian autocorrelation functions. They share the same height root mean square of 60 nm, with correlation lengths of $\ell = 500\,\text{nm}$ and $\ell = 100\,\text{nm}$. Each profile is 60 µm-long, with a beam parameter $g = 15\,\mu\text{m}$. To compute the data, the profile is regularly sampled with $N = 4096$ points, while for inversion, the estimated profile only counts $N = 2048$ points. All scattered fields are computed thanks to the rigorous direct model (Section 4) where the integral equation Equation (7) is cast into a linear system with a full matrix of order N, according to the now classical procedure detailed in [13]. $\mathbf{F}\eta$ and $\mathbf{F}\eta_n$ are composed of M^2 complex values, with $M = 91$. In its discretized form, $\mathbf{D}$ is a M^2 by N rectangular matrix.

For the smooth surface with correlation length $\ell = 500$ nm larger than the Fraunhofer resolution $\lambda/(4\,NA) = 223$ nm, both the NK and linear inversion methods provide a good reconstruction of the profile Figs. 1(a) and 1(b). The axial accuracy of the reconstruction given by the NK algorithm is spectacular (within the nanometer). For the rougher surface, $\ell = 100\,\text{nm}$, the reconstruction given by the NK algorithm is still accurate while that obtained under the Fraunhofer approximation clearly misses the high frequencies of the actual profile, Figs. 1(c) and 1(d). This exemple stresses the importance of a rigorous modeling of the light-surface interaction when surfaces with subwavelength transverse features are to be studied. Note that the edges of the profile are poorly reconstructed by the Fraunhofer method, as it can be seen on Fig. 1(b). This is a numerical artifact due to our implementation of the Fraunhofer method.

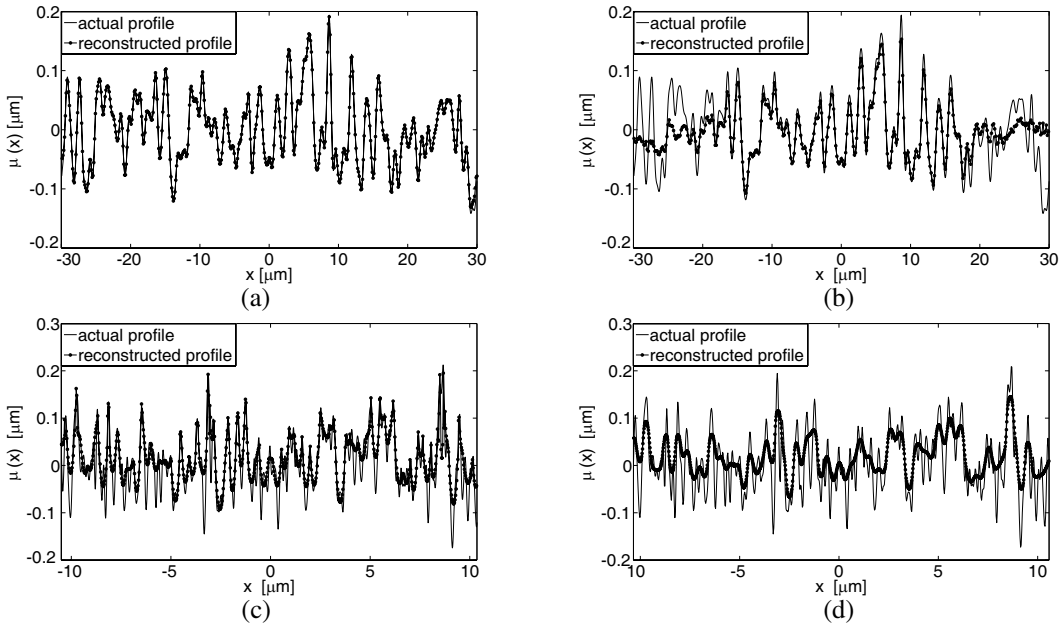

Figure 1: Reconstruction of 60 μm long rough surfaces with Gaussian correlation with rms height of 60 nm different values of the correlation length ℓ. (a)–(b) $\ell = 500$ nm while (c)–(d) $\ell = 100$ nm. (a)–(c) Reconstructed profiles using NK and (b)–(d) are reconstucted profiles using the Fraunhofer approximation. (c)–(d) Only the 20 μm central part is reported.

7. CONCLUSION

In conclusion, we believe that tomographic diffractive microscopy combined with a rigorous model of the light-surface interaction is an interesting tool for profilometry applications. The occurence of multiple scattering, which usually plagues most optical imaging instruments, could even be an advantage.

REFERENCES

1. Brakenhoff, C. J., P. Blom, and P. Barends, "Confocal scanning light microscopy with high aperture immersion lenses," *J. Microsc.*, Vol. 117, 219–232, 1979.
2. Alexandrov, S. A., T. R. Hillman, T. Gutzler, and D. D. Sampson, "Synthetic aperture fourier holographic optical microscopy," *Phys. Rev. Lett.*, Vol. 97, Art. No. 168102, 2006; *Erratum*, Vol. 98, No. 9, Mar. 2, 2007.
3. Maire, G., F. Drsek, J. Girard, H. Giovannini, A. Talneau, D. Konan, K. Belkebir, P. C. Chaumet, and A. Sentenac, "Experimental demonstration of quantitative imaging beyond abbe's limit with optical diffraction tomography," *Phys. Rev. Lett.*, Vol. 102, 213905–4, 2009.
4. Haeberlé, O., K. Belkebir, H. Giovannini, and A. Sentenac, "Tomographic diffractive microscopy: Basics, techniques and perspectives," *J. of Mod. Optics*, Vol. 57, 686–699, 2010.
5. Lauer, V., "New approach to optical diffraction tomography yielding a vector equation of diffraction tomography and a novel tomographic microscope," *J. Microsc.*, Vol. 205, 165–176, February 2002.
6. Thorsos, E. I., "The validity of the Kirchhoff approximation for rough surface scattering using a Gaussian roughness spectrum," *J. Acoust. Soc. Am*, Vol. 83, No. 1, 78–92, 1988.
7. Beckmann, P. and A. Spizzichino, *The Scattering of Electromagnetic Waves from Rough Surfaces*, International Series of Monographs on Electromagnetic Waves, Pergamon Press, 1963.
8. Wombell, R. J. and J. A. DeSanto, "Reconstruction of rough-surface profiles with the Kirchhoff approximation," *Journal of the Optical Society of America A*, Vol. 8, No. 12, 1892–1897, 1991.
9. Colton, D. and R. Kress, *Integral Equations in Scattering Theory*, Wiley-Interscience, New York, 1983.
10. Roger, A., "Newton-Kantorovitch algorithm applied to an electromagnetic inverse problem," *IEEE Transactions on Antennas and Propagation*, Vol. 29, No. 2, 232–238, 1981.

11. Tikhonov, A. N. and V. A. Arsenin, *Solutions of Ill-posed Problems*, J. Wiley & Sons, Inc., 1977.
12. Haeberlé, O., A. Sentenac, and H. Giovannini, "An introduction to diffractive tomographic microscopy," *Modern Research and Educational Topics in Microscopy*, Vol. 2, A. M. Vilas and J. D. Alvarez (Eds.), 2007.
13. Tsang, L., J. A. Kong, K. H. Ding, and C. O. Ao, *Scattering of Electromagnetic Waves: Numerical Simulations*, Wiley Series in Remote Sensing, Wiley-Interscience, 2001.

Experimental Study on Imaging Algorithm with Simple UWB Radar for a Target with Translation and Rotation

T. Sakamoto and T. Sato
Graduate School of Informatics, Kyoto University, Yoshida-Honmachi, Sakyo-ku, Kyoto 606-8501, Japan

Abstract— Developing a reliable surveillance system is important to resolve the social concern of terrorist activities. Radar systems can offer additional functions to conventional camera-based surveillance systems. Most conventional radar imaging algorithms employ a large-scale antenna array to obtain a high-resolution image, which makes the practical use of radar imaging technology prohibitively expensive. A simplified radar system with only three antennas has been proposed to estimate the translatory motion of a target. However, this method assumes that the target only undergoes translation and no rotation, which is unrealistic. This paper proposes a new method to estimate the translation and rotation of a target even though the target shape is unknown. The proposed method employs five antennas to optimize an assumed elliptical model using the data recorded by the radar system. The proposed method is applied to experimental data to demonstrate its effectiveness in a realistic environment.

1. INTRODUCTION

There is a great demand for the development of a cost-effective and reliable surveillance system to prevent criminal and terrorist activities. Conventional systems are mostly based on optical cameras because of their low-cost and high-resolution imaging capabilities. Another approach is the use of a radar system, which can obtain certain target characteristics that conventional systems cannot. This technology has attracted considerable attention, especially after the standardization of ultra wide-band (UWB) signals in the United States, because it enables high-resolution ranging of the order of a few centimeters.

A number of UWB radar imaging methods and systems have been proposed that are better than conventional camera-based systems in terms of accuracy and resolution [1–3]. However, conventional radar imaging methods are not sufficiently cost-effective for many applications because most such systems employ a large-scale antenna array, making the entire system considerably more expensive than conventional camera-based systems and hence unsuitable for practical use.

Matsuki et al. proposed a UWB radar imaging method employing only three antennas to estimate the translatory motion of a target [4]. This method assumes that the shape of a local target a circular and optimizes this three kinds of ranging data corresponding to line three degrees of freedom of a circle (the two coordinates of the center position and the radius). However, this method cannot estimate the rotation of the target and thus is difficult to apply to actual data.

This paper presents a UWB radar system that uses five antennas for the simultaneous estimation of the target's shape, translation, and rotation. The performance of the proposed method is evaluated experimentally.

2. SYSTEM MODEL

A two-dimensional model is assumed for simplicity, and our objective is to estimate a two-dimensional target shape under this assumption. A five-element linear antenna array is installed, and each antenna element is placed along a straight line at fixed intervals of $\Delta x = 0.2\,\mathrm{m}$, as shown in Fig. 1. The straight line could correspond to a wall or the ceiling of a hallway; the problem could be the imaging of the cross section of a human walking along the hallway.

Each of the antennas is connected to a pulse generator and a receiver via an RF switch. In addition, each antenna is operated as a mono static radar system with modulation to avoid interference among antennas. Any modulation can be employed as long as the base functions are orthogonal to each other so that they realize a multiple access system. Pulses are transmitted from each antenna at time intervals of Δt, and the resultant echoes are received at the same antenna.

The target is assumed to have an unknown boundary $(X_0(\xi), Y_0(\xi))$, where $0 \leq \xi \leq 2\pi$ is a parameter. This expression of the target shape $(X_0(\xi), Y_0(\xi))$ needs to satisfy the following conditions:

$$\int_0^{2\pi} X_0(\xi)d\xi = 0, \quad \int_0^{2\pi} Y_0(\xi)d\xi = 0. \tag{1}$$

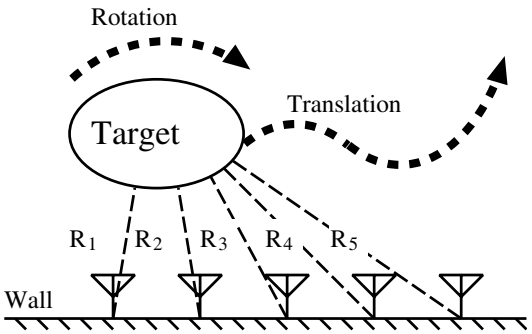

Figure 1: Assumed system model.

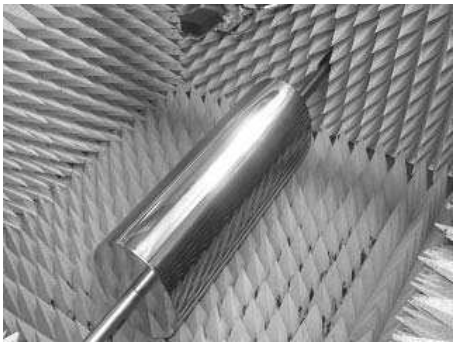

Figure 2: Experimental setup for UWB radar imaging.

These conditions imply that the centroid of the boundary is at the origin of the assumed coordinates. Under these conditions, we can define rotation independently of the shape of the target. The target undergoes translation $(X_T(t), Y_T(t))$ and rotation $\phi(t)$ with time t. The target boundary $(X(\xi,t), Y(\xi,t))$ at time t is expressed as

$$\begin{bmatrix} X(\xi,t) \\ (Y(\xi,t) \end{bmatrix} = R\left(\phi(t)\right) \begin{bmatrix} X_0(\xi) \\ Y_0(\xi) \end{bmatrix} + \begin{bmatrix} X_T(t) \\ Y_T(t) \end{bmatrix}, \tag{2}$$

where $R(\phi)$ denotes the rotation matrix

$$R(\theta) = \begin{pmatrix} \cos\theta & -\sin\theta \\ \sin\theta & \cos\theta \end{pmatrix}. \tag{3}$$

The distance between each antenna and the scattering center of the target is measured as $R_i(t)$ $(i = 1, 2, \ldots, 5)$ using the i-th antenna at each time step $t = n\Delta t$. The purpose of this paper is to develop a method to estimate the translation $(X_T(t), Y_T(t))$, rotation $\phi(t)$, and the target shape $(X_0(\xi), Y_0(\xi))$ using the ranging data $R_i(t)$ $(i = 1, 2, \ldots, 5)$.

3. PROPOSED METHOD

A previous work [4] proposed a method based on fitting using a circular model for estimating the target translation and shape. Because a circle has three degrees of freedom, three antennas were used in their study. However, this method cannot estimate target rotation because a circle is symmetric. We propose a new method that uses an elliptical model instead of a circular one to estimate both the rotation and the translation and thus obtain a target image.

The proposed method estimates the local target shape for each time step $t = t_n$ using an elliptical model with five parameters a, b, x_0, y_0, and θ. The ellipse is expressed as

$$\left(\frac{\cos^2\theta}{a^2} + \frac{\sin^2\theta}{b^2}\right)(x-x_0)^2 + \left(\frac{\sin^2\theta}{a^2} + \frac{\cos^2\theta}{b^2}\right)(y-y_0)^2 + \sin 2\theta \left(\frac{1}{a^2} - \frac{1}{b^2}\right)(x-x_0)(y-y_0) = 1, \tag{4}$$

where a and b are the long and short axes of the ellipse, respectively; (x_0, y_0) is the center of the ellipse; and θ is the rotation angle. The distance between the i-th antenna and the corresponding scattering center $c_i(a, b, x_0, y_0, \theta)$ is defined as $r_i(a, b, x_0, y_0, \theta)$. The variables c_i and r_i are calculated using the i-th antenna position x_i. The scattering center $c_i(a, b, x_0, y_0, \theta)$ is equivalent to the point on the ellipse closest to the antenna x_i because there is no point closer to the antenna than the foot of perpendicular on a convex curve.

We define a cost function

$$F_n(a, b, x_0, y_0, \theta) = \sum_{i1}^{N_a} \left| r_i(a, b, x_0, y_0, \theta) - R_i(t_n) \right|^2, \tag{5}$$

where N_a is the number of antennas. By minimizing this cost function, we determine the most likely parameter set of an ellipse.

Note that the parameters a, b, x_0, y_0, and θ should be treated differently because they denote different serial parameters: whereas a and b indicate the target shape, the other parameters indicate the target motion. Using these characteristics, we introduce a smoothing process for a and b; we independently estimate the other parameters x_0, y_0, and θ, which are updated at each time step, without smoothing.

The proposed optimization procedure for a and b is expressed as

$$(\hat{a}, \hat{b}) = \arg\min_{(a,b)} \sum_{n0}^{N_{obs}} \min_{(x_0,y_0,\theta)} F_n(a, b, x_0, y_0, \theta), \tag{6}$$

where N_{obs} is the total number of time steps for which the observed data are analyzed using the proposed method. The parameters (a, b) are estimated using a linear search algorithm. For each (a, b), the remaining parameters (x_0, y_0, θ) are optimized using the Levenberg-Marquardt algorithm.

To conduct the optimization, it is necessary to calculate the scattering center points $c_{n,i}$, $i = 1, 2, \ldots, 5$ for each time step $t = t_n$. To find the scattering centers, the optimized elliptical parameters $(x_{0n}, y_{0n}, a_n, b_n, \theta_n)$ and each antenna position x_i are used. The scattering center point $c_{n,i}$ is estimated as the foot of the perpendicular line drawn through the i-th antenna position. This process can be computed analytically.

The model assumes the fixed parameters a and b throughout the entire data set; however, this does not necessarily mean that the target is modeled as an ellipse because the estimated motion is compensated for in order to obtain the final image, as explained later. In this process, each set of only five points of the final image are simultaneously on the same ellipse.

In this way, the optimization is stabilized because the number of degrees of freedom is reduced from five to three i.e., (x_0, y_0, θ). Although a linear search is relatively time consuming, the procedure does not take long because there are only two parameters to be optimized in this case.

4. PERFORMANCE EVALUATION OF THE PROPOSED METHOD USING EXPERIMENTAL DATA

We apply the proposed method to experimental data recorded with the UWB experimental system shown in Fig. 2. In this system, an elliptical cylinder in an anechoic chamber is secured with thin bars on both sides. This cylinder is connected to a rotation actuator that can be electronically operated. In this system, the antennas are scanned instead of the target itself because the received signals are exactly the same as those in the system model assumed in this paper. Note that this system is set up to simulate two-dimensional imaging data. Therefore, the antennas at the top of the figure are scanned in the direction perpendicular to the target cylinder.

The transmitting and receiving antennas are placed close to each other and scanned simultaneously. These UWB antennas have a bandwidth of 2.0 GHz and a center frequency of 3.0 GHz. The bandwidth corresponds to a resolution of 7.5 cm. The antennas are ceramic patch antennas with a beam width wide enough to cover the target; this setup does not significantly differ from the system model assumed for the computer simulation. A wide-band impulse with a width of 80 ps is generated by a signal generator and input to one of the antennas, whereas the signal received by the other antenna is amplified and A/D converted using a sampling oscilloscope. The digitized data are analyzed using the proposed imaging method.

The target has an elliptical section with a long axis of $a = 0.15$ m and a short axis of $b = 0.10$ m. The assumed motion is $X_T = X_0 + v_x t$, $Y_T = Y_{T0}$, and the assumed rotation is $\phi(t) = \phi_0 + \omega_\phi$, where $X_0 = -0.1$ m, $v_x = 1.0$ m/s, $Y_{T0} = 0.435$ m, $\phi_0 = -1.24$ rad, and $\omega_\phi = 3.5$ rad/s. The five antennas are spaced at intervals of 10 cm.

Figure 3 shows the signals received by the third antenna (central antenna) under the conditions assumed above. Here, the signals are received every 5 ms and the waveforms appear smooth because they are output via a matched filter. We first extract the peak points of each waveform to calculate $R_k(t)$ and then apply the two-step optimization method with the fixed shape parameters. The estimated values of a and b are 15.6 cm and 9.9 cm, respectively. These values are then used to estimate other parameters.

Figure 4 shows the rotation angle estimated using the proposed optimization method with the fixed shape parameters. The figure shows that the proposed method works well even for the experimental data although it has an error of 5.6° at $t = 0.16$ s and 13.8° at the final time step, $t = 0.24$ s. The solid lines in Fig. 5 show the actual target shapes moving to the right while rotating counter-clockwise. Here, triangles on the x-axis show the five antenna positions. The estimated

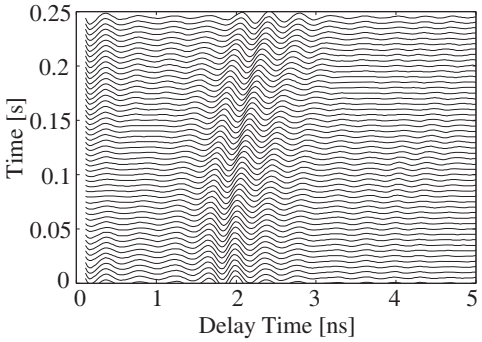

Figure 3: Signal measured with the center antenna of the experimental system.

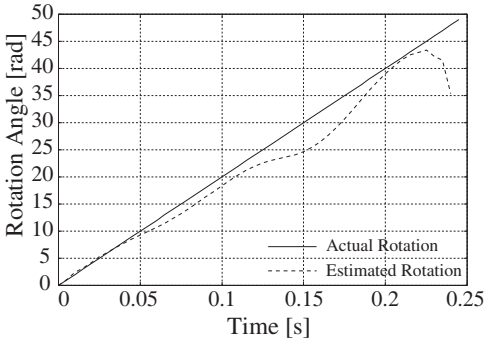

Figure 4: Actual and estimated rotation angles for experimental data.

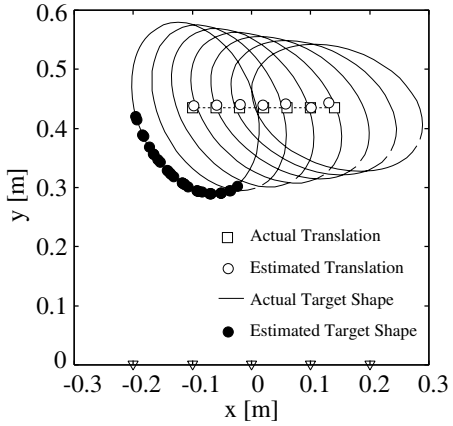

Figure 5: Target shape estimated from experimental data using the proposed method.

target shape is shown in Fig. 5 with black dots along with the estimated translation (x_0, y_0); it is observed that the proposed method accurately estimates the target shape from the experimental data.

5. CONCLUSION

In this paper, we proposed a new imaging method for UWB radar using five antennas. The method uses the motion of a target, which comprises both translation and rotation, to obtain a target image by compensating for the estimated motion. The two-step optimization method with fixed parameters was applied to experimental data recorded by a UWB radar experimental system to demonstrate the practicality of the proposed method. The results demonstrate that the proposed method is able to estimate a target shape even if the translation, rotation, and shape of a target are unknown.

REFERENCES

1. Yarovoy, A. G., T. G. Savelyev, P. J. Aubry, P. E. Lys, and L. P. Ligthart, "UWB array-based sensor for near-field imaging," *IEEE Transactions on Microwave Theory and Techniques,* Vol. 55, No. 6, Part 2, 1288–1295, June 2007.
2. Jofre, L., A. Broquetas, J. Romeu, S. Blanch, A. P. Toda, X. Fabregas, and A. Cardama, "UWB tomographic radar imaging of penetrable and impenetrable objects," *Proceedings of the IEEE*, Vol. 97, No. 2, 451–464, 2009.
3. Huang, Q., L. Qu, B. Wu, and G. Fang, "UWB through-wall imaging based on compressive sensing," *IEEE Transactions on Geoscience and Remote Sensing*, Vol. 48, No. 3, March 2010.
4. Matsuki, Y., T. Sakamoto, and T. Sato, "Study of a method for 2-D imaging of simple-shaped targets with arbitrary motion using UWB radar with a small number of antennas," *Proceeding of the 20th International Conference on Applied Electromagnetics and Communications*, September 2010.

Miniaturized Printed Yagi Antenna for 2.45 GHz RFID Readers

G. Bulla[1, 2], M. T. Le[1], A. A. A. de Salles[2], and T. P. Vuong[1]

[1]Institut de Microélectronique Electromagnétisme et Photonique
Laboratoire d'Hyperfréquences et de Caractérisation, Grenoble Institute of Technology (GINP), France
[2]Electrical Engineering Department, Federal University of Rio Grande do Sul (UFRGS), France

Abstract— In this paper, a miniaturized printed Yagi antenna with bent arms is proposed for radio frequency identification (RFID) readers operating at the frequency of 2.45 GHz. The proposed antenna design, analysis and characterization has been performed using CST electromagnetic simulation software. The antenna was fabricated with ROGERS4003 substrate. Reflection coefficient and directivity results were simulated and measured.

1. INTRODUCTION

The idea of Radio Frequency Identification (RFID) of objects and remote control of devices was first introduced in 1948 by H. Stockman [1]. In recent years, RFID has been widely used in service industries as an automatic identification tool [2]. A basic RFID system comprises a radio-scanner unit, called reader, and a set of remote transponders, denoted as tags, which include an antenna and a microchip transmitter with internal read/write memory. Several frequency bands have been standardized for this technology, low frequency (LF, 125–134 kHz), high frequency (HF, 13.56 MHz), ultra-high frequency (UHF, 860–960 MHz) and microwave (2.4 GHz and 5.8 GHz). The systems using the UHF band and 2.45 GHz band are believed suitable for long-distance communication utilizing a passive type RFID [3, 4]. However, because the UHF band overlaps with the frequency of a cellular phone, the UHF band is not preferable. Therefore, the 2.45 GHz band is preferred [3]. Several papers have been published on designing RFID antennas [5–7]. In [5], a miniaturized printed dipole antenna with the V-shaped ground is proposed for RFID readers operating at the frequency of 2.45 GHz. A compact folded printed dipole antenna for UHF RFID reader is presented in [6]. In [7] the GA is used to design a UHF RFID bow-tie tag antenna. In [8] a hybrid approach involving Bacterial Swarm Optimization (BSO) and Nelder-Mead (NM) algorithm is used to design a bow-tie antenna for 2.45 GHz Radio Frequency Identification (RFID) readers.

Printed Yagi antennas are attractive alternatives to conventional wire Yagi antennas since they can be manufactured using printed circuit techniques and are thus readily amenable to large scale integration with microstrip technology. In this paper, a new microstrip-fed printed Yagi antenna working at 2.45 GHz for RFID reader application is presented. By bending the arms of the Yagi antenna a new miniaturized antenna is designed.

2. ANTENNA DESIGN

The initial configuration is a printed Yagi antenna have an arm with length L and a distance D from the ground plane, one radiator with length Lr is also present. ROGERS4003 substrate with height 0.8 mm was used. The two arms of the Yagi antenna are printed on opposite sides of the substrate to maintain the correct phasing between the arms. This is similar to the approach taken in [9]. In order to maximize end-fire radiation, the printed dipole is designed so that it is approximately a quarter wavelength ($D = \lambda/4$) from the ground plane. The length L was chosen in order to obtain the antenna resonance at 2.45 GHz and Ld was chosen in order to maximize the directivity. The final length L is 25 mm. The miniaturization is achieved by bending both arms of the Yagi antenna at a position Lm. The final geometry has $Lm = 15.5$ mm. The total size of the arm is the same as the initial design. The total width of the miniaturized Yagi antenna is about 30% smaller than the initial design. The configurations for both antennas are shown in Figure 1. An array with 2 miniaturized antennas elements was also designed and analyzed.

3. RESULTS

The miniaturized antenna was prototyped. Simulated and measured reflection coefficient results are shown in Figure 2. Good agreement between simulated and measured results is observed. The relative bandwidth is about 14% for both antennas (miniaturized and non-miniaturized antenna). The central frequency of the initial antenna is close to 2.45 GHz. A small increase in the central frequency is observed when the dipole arms are bent.

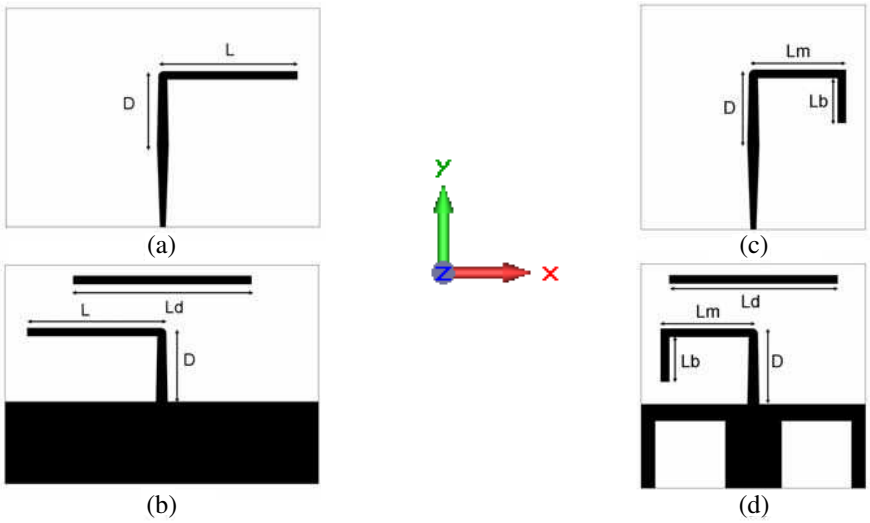

Figure 1: Initial antenna geometry. (a) top face, (b) bottom face, and miniaturized antenna geometry, (c) top face, (d) bottom face.

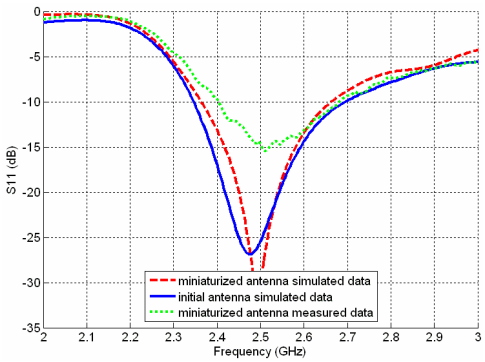

Figure 2: Reflection coefficient results.

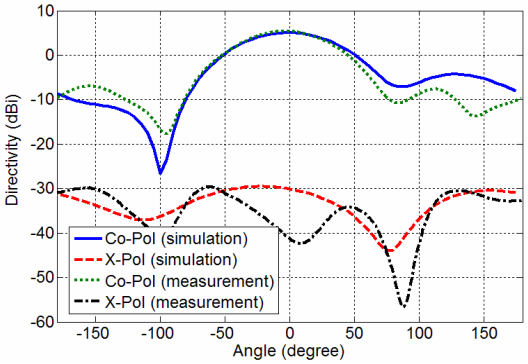

Figure 3: Simulated and measured results for the miniaturized yagi antenna directivity at xy plane.

The initial antenna shows 6.41 dBi directivity, 70.4° for the angular width at the xy plane, and 133° for the angular width at the zx plane. The miniaturized antenna shows 4.9 dBi directivity, 80° for the angular width at the xy plane, and 165° for the angular width at the zx plane. The directivity for the xy plane is show in Figure 3. The array of antennas with 2 miniaturized elements shows 7.4 dBi directivity, 43° for the angular width at the xy plane, and 161° for the angular width at the zx plane.

4. CONCLUSION

In this paper, a miniaturized printed Yagi antenna with bent arms was proposed for radio frequency identification (RFID) readers operating at the frequency of 2.45 GHz. The proposed antenna design, analysis and characterization has been performed using CST electromagnetic simulation software. The antenna was fabricated with ROGERS4003 substrate.

The miniaturized antenna has 30% smaller width in regard to the original antenna width. Although miniaturized, the antenna has good radiation characteristics. The initial antenna had directivity of 6.4 dBi while the miniaturized antenna had directivity of 4.9 dBi.

REFERENCES

1. Stockman, H., "Communication by means of reflected power," *Proc. IRE*, 1196–1204, Oct. 1948.
2. Finkenzeller, K., *RFID Handbook: Radio-frequency Identification Fundamentals and Applications*, 2nd Edition, Wiley, 2004.

3. Jin, A., S. Takahashi, and K. Shimamura, "A basic study on communication capability of 2.45 GHz band RFID tag and communication quality with a reader," *Proceedings of Int. Conference on Next Era Information Networking, NEINE*, 330–335, Kochi-city, Japan, Sep. 26–27, 2004.
4. Hung, W. S. and W. Ismail, "RFID transponder using bow tie antenna for wireless application," *Proceedings of International RF and Microwave Conference Proceedings*, Putrajaya, Malaysia, Sep. 12–14, 2006.
5. Fan, Z., S. Qiao, H. F. Jiang Tao, and L. X. Ran, "A miniaturized printed dipole antenna with V-shaped ground for 2.45 GHz RFID readers," *Progress In Electromagnetics Research*, Vol. 71, 149–158, 2007.
6. Li, X., L. Yang, S.-X. Gong, Y.-J. Yang, and J.-F. Liu, "A compact folded printed dipole antenna for UHF RFID reader," *Progress In Electromagnetics Research Letters*, Vol. 6, 47–54, 2009.
7. Delichattsios, S. A., "GA optimization for RFID broadband antenna applications," http://fab.cba.mit.edu/classes/MIT/862.0 6/students/alki/GA_pdf.pdf.
8. Mahmoud, K. R., "Design optimization of a bow-tie antenna for 2.45 GHz RFID readers using a hybrid BSO-NM algorithm," *Progress In Electromagnetics Research*, Vol. 100, 105–117, 2010.
9. Tefiku, F. and C. A. Grimes, "Design of broad-band and dual and antennas comprised of series-fed printed-strip dipole pairs," *IEEE Trans. Antennas and Propagat.*, Vol. 48, No. 6, Jun. 2000.

A Matrix-vector-potential Analysis of the Bi-elliptical Toroidal Helical Antenna

S. A. Adekola[1,2], **A. Ike Mowete**[1], **and H. A. Muhammed**[1]

[1]Department of Electrical and Electronics Engineering, Faculty of Engineering
University of Lagos, Lagos, Nigeria
[2]Department of Electrical and Electronics Engineering, Niger Delta University
Wilberforce Island, Yenegoa, Nigeria

Abstract— This paper develops exact expressions for the radiation field integrals of a single-wound bi-elliptical toroidal helical antenna, based on the vector magnetic potential approach. Using the conventional thin-wire approximation in which current flow is constrained along the wire's axis, a vector-potential integral is developed for the problem in terms of the unknown current distribution and physical attributes of the wire antenna, with the integrals' integrands expressed in matrix format. Entries into these integrand matrices lend themselves into certain physical interpretations, which facilitate a number of conclusions concerning the physics of the problem. For example, it becomes readily discernible that the antenna's radiation field admits description as a sum of two expressions; one deriving from the main loop, and the other associated with the poloidal loops of the antenna. These same conclusions were arrived at from the results of the empirical investigations reported in the open literature by Wanamassa et al. [1], and Corum [2].

Analytical results obtained in the paper also clearly indicate that the radiation fields may also be attributed to contributions associated with electric and magnetic currents excited in the antenna's main loop and poloidal loops, respectively. It is shown in the paper that the field expressions developed by the analytical approach reported, also serve as corresponding expressions for certain other configurations of the toroidal antenna as special cases.

1. INTRODUCTION

The Toroidal helical antenna belongs to a relatively new class of antennas, which is attracting increasing investigative attention from the scientific community [3–7]. Representative research efforts are typified by the presentations in the foregoing references, and they have provided considerable insights into the radiation mechanisms that may be associated with toroidal antennas. Miron [4], for example, described an analytical for the theoretical study of the radiating properties of the Contra-Wound Toroidal Helical Antenna (CWTHA), and using the Numerical Electromagnetic Code (NEC) obtained results that indicated that the air-cored CWTHA is a poor radiator, characterized by high values of reactance close to odd-numbered resonances. Hansen and Ridgeley [3, 5], derived exact vector potential expressions for the antenna and obtained computational results that described the CWTHA as a poor radiator of dipole fields, in addition to having small values of directivity, gain, and bandwidth. Another significant contribution was made by Le-Wei and his associates [6], who using analysis involving the simplifying assumption of a constant current distribution for the helix wire, were able to derive closed-form solutions for the vector potential integrals (and associated far-zone fields) earlier formulated by Hansen and Ridgeley [3, 5]. Because the main focus of the analyses referred to above has been on the arguably very important problem of deriving closed-form expressions for vector magnetic potential of CWTHA antenna configuration, this same simplifying assumption of uniform (or constant) current distribution was utilized in all cases.

In this paper, we also present a derivation of integral expressions for the vector potential and associated radiation fields, but in this case for the more general bi-elliptical (torus cross-section and torus former are both of the elliptical geometry) toroidal helical antenna. The formulation has the novelty of presenting the integrands of the integral expressions in matrix format, making it possible to give certain useful conclusions about the physics of the problem. It is suggested by the analytical results, for example, that the antenna's radiation field derive from equivalent electric and magnetic currents excited by the antenna's main loop and poloidal loop, respectively.

Because the only unknown quantity in the integral expressions is the current distribution on the presumably thin-wire antenna, and since the derivations have their basis in the geometry of the problem, the integrations are particularly suited to a solution informed by the circuit-geometric moment-method approach. Indeed, we have since obtained useful computational results from a

moment-method implementation of the analytical results presented in this paper, and the results indicate that with this formulation, it is possible to carry out simulations that will characterize the electromagnetic response parameters of the antenna, including impedance characteristics.

2. ANALYSIS

The bi-elliptical toroidal helical antenna of interest to this presentation is depicted in Fig. 1 as having an elliptical main loop of dimensions represented by b and ρ for the major and minor axes, respectively. The poloidal loop, shown oriented perpendicular to the XY-plane is also of the elliptical geometry having dimension symbolized by p and q for its major and minor axes.

For the thin-wire antenna, vector magnetic potential is given by

$$\mathbf{A}(\mathbf{r}) = \frac{\mu}{4\pi} \int\limits_{antenna} I(r') \frac{e^{-jkR}}{4\pi R} dr' \hat{\mathbf{a}}_r \tag{1}$$

with the conventional notations. From the geometry of Fig. 1, it is readily deduced that that the general source point is specified by the expression

$$\mathbf{r}' = \hat{\mathbf{a}}_x \left[b\beta(\phi') + d\delta(\phi') \cos N\varphi'\right] \cos\varphi' + \hat{\mathbf{a}}_y \left[b\beta(\phi') + d\delta(\phi') \cos N\varphi'\right] \sin\varphi' + \hat{\mathbf{a}}_z d\delta(\phi') \sin N\varphi' \tag{2}$$

in which N represents the number of turns, and where

$$\beta(\varphi') = \sqrt{\frac{1-e^2}{1-e^2\cos^2\varphi'}} \tag{2a}$$

and

$$\delta(\varphi') = \sqrt{\frac{1-\xi^2}{1-\xi^2\cos^2 N\varphi'}} \tag{2b}$$

where e and ξ are the eccentricities of the major and the poloidal loops, respectively, and are given by $e = \sqrt{b^2 - p^2}$ and $\varepsilon = \sqrt{d^2 - q^2}$. For simplicity, henceforth $\beta(\phi')$ and $\delta(\phi')$ will be referred to as β' and δ', respectively.

When use is now made of the fact that according to (2),

$$d\mathbf{r}' = \left\{\hat{\mathbf{a}}_x \left(-X'\sin\varphi' + Z'\cos\varphi'\right) + \hat{\mathbf{a}}_y \left(X'\cos\varphi' + Z'\sin\varphi'\right) + \hat{\mathbf{a}}_z Z'\right\} d\varphi', \tag{3}$$

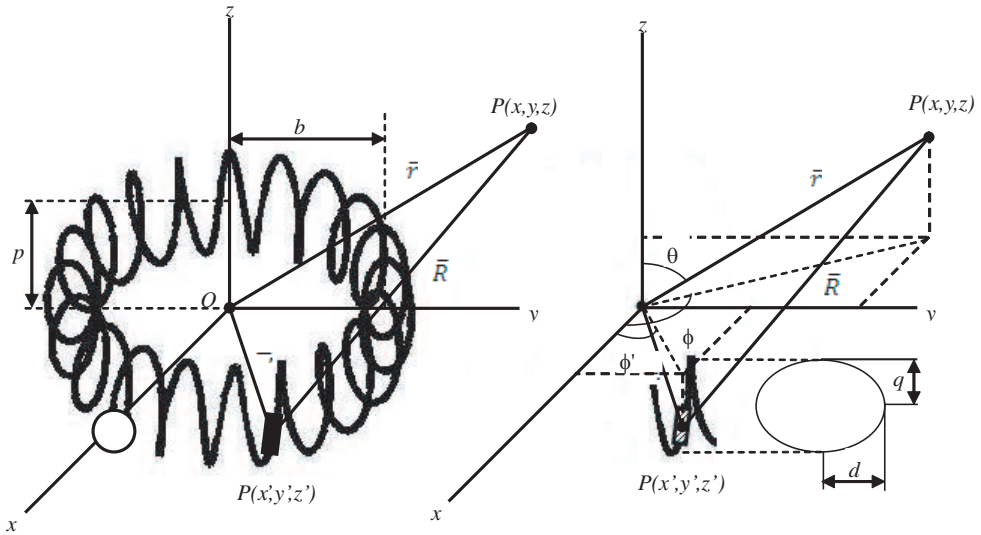

Figure 1: Problem geometry for the bi-elliptical toroidal helical antenna.

we find that the Cartesian components of the vector potential emerge as

$$A_x = \frac{-\mu}{4\pi}\int_0^{2\pi} I\left(\varphi'\right)\left(X'\sin\varphi' - Z'\cos\varphi'\right)\frac{\exp\left(-jkR\right)}{R}d\phi' \tag{3a}$$

$$A_y = \frac{\mu}{4\pi}\int_0^{2\pi} I\left(\varphi'\right)\left(X'\sin\varphi' + Z'\cos\varphi'\right)\frac{\exp\left(-jkR\right)}{R}d\phi' \tag{3b}$$

$$A_z = \frac{\mu}{4\pi}\int_0^{2\pi} I\left(\varphi'\right)Z'_1\frac{\exp\left(-jkR\right)}{R}d\phi' \tag{3c}$$

In 3(a) to 3(c), use has been made of the expressions

$$X' = b\beta' + d\delta'\cos N\varphi', \tag{4a}$$

$$\text{with}\quad Z' = b\beta' P' + d\delta'\left(NQ'\cos N\varphi' - N\sin N\varphi'\right), \tag{4b}$$

$$\text{and}\quad Z'_1 = d\delta'\left(NQ'\cos N\varphi' + N\sin N\varphi'\right), \tag{4c}$$

provided that it is understood that

$$P' = -\frac{1}{2}\frac{e^2\sin 2\varphi'}{1-e^2\cos^2\varphi'} \tag{5a}$$

$$\text{and that}\quad Q' = -\frac{1}{2}\frac{\xi^2\sin 2N\varphi'}{1-\xi^2\cos^2 N\varphi'} \tag{5b}$$

If we carry out a Cartesian-to-spherical coordinate transformation on each of (3a) to (3c), we obtain the corresponding spherical coordinates equivalents of the three expressions as

$$A_r = \frac{\mu}{4\pi}\int_0^{2\pi} I\left(\varphi'\right)\left\{b\beta'\begin{bmatrix}0\\P'\\1\end{bmatrix}^T + d\delta'\begin{bmatrix}NQ'\\N\\1\end{bmatrix}^T\begin{bmatrix}\sin N\varphi' & \cos N\varphi' & 0\\ \cos N\varphi' & -\sin N\varphi' & 0\\ 0 & 0 & \cos N\varphi'\end{bmatrix}\right.$$
$$\left.\begin{bmatrix}\cos\vartheta & 0 & 0\\ 0 & \sin\vartheta & 0\\ 0 & 0 & \sin\vartheta\end{bmatrix}\begin{bmatrix}1\\ \cos\left(\varphi-\varphi'\right)\\ \sin\left(\varphi-\varphi'\right)\end{bmatrix}\right\}\frac{\exp\left(-jkR\right)}{R}d\varphi', \tag{6a}$$

$$A_\vartheta = \frac{\mu}{4\pi}\int_0^{2\pi} I\left(\varphi'\right)\left\{b\beta'\begin{bmatrix}0\\P'\\1\end{bmatrix}^T - d\delta'\begin{bmatrix}NQ'\\N\\1\end{bmatrix}^T\begin{bmatrix}\sin N\varphi' & \cos N\varphi' & 0\\ \cos N\varphi' & -\sin N\varphi' & 0\\ 0 & 0 & -\cos N\varphi'\end{bmatrix}\right.$$
$$\left.\begin{bmatrix}\sin\vartheta & 0 & 0\\ 0 & \cos\vartheta & 0\\ 0 & 0 & \cos\vartheta\end{bmatrix}\begin{bmatrix}1\\ \cos\left(\varphi-\varphi'\right)\\ \sin\left(\varphi-\varphi'\right)\end{bmatrix}\right\}\frac{\exp\left(-jkR\right)}{R}d\varphi', \tag{6b}$$

$$A_\varphi = \frac{\mu}{4\pi}\int_0^{2\pi} I\left(\varphi'\right)\left\{b\beta'\begin{bmatrix}1\\-P'\end{bmatrix}^T + d\delta'\begin{bmatrix}1 & -NQ'\\ o & N\end{bmatrix}\begin{bmatrix}\cos N\varphi'\\ \sin N\varphi'\end{bmatrix}\begin{bmatrix}\cos\left(\varphi-\varphi'\right)\\ \sin\left(\varphi-\varphi'\right)\end{bmatrix}\right\}\frac{\exp\left(-jkR\right)}{R}d\varphi' \tag{6c}$$

following the substitution, as applicable, of (4a), (4b), and (4c), into (3a), (3b), and (3c).

In order to carry out the integration specified by Eq. (6), it is necessary to express the separation of the field and source points; and to that end it is readily established that

$$R \triangleq \left|\mathbf{r}-\mathbf{r}'\right| = \left(\begin{bmatrix}d\delta'\\ b\beta'\\ r\end{bmatrix}^T\begin{bmatrix}d\delta' & b\beta'\\ b\beta' & d\delta'\\ r & 0\end{bmatrix}\begin{bmatrix}1\\ \cos N\varphi'\end{bmatrix}\right.$$
$$\left. -2r\left(\begin{bmatrix}0\\ b\beta'\end{bmatrix}^T + d\delta'\begin{bmatrix}\sin N\varphi'\\ \cos N\varphi'\end{bmatrix}\right)\left(\begin{bmatrix}\cos\vartheta & 0\\ 0 & \sin\vartheta\end{bmatrix}\begin{bmatrix}1\\ \cos\left(\varphi-\varphi'\right)\end{bmatrix}\right)\right)^{1/2} \tag{7}$$

And with the vector potentials so completely defined, the associated radiation fields are readily determined from the well-known expression

$$\mathbf{E} = -j\omega\mathbf{A}, \tag{8}$$

for the time-harmonic variation implicitly utilized in the foregoing derivations.

3. DISCUSSION OF ANALYTICAL RESULTS

One important development in this presentation is that the radiation fields due to the bi-elliptical toroidal antenna can be expressed in terms of radiation integrals, whose integrands emerge in compact planar matrix formats. We find from (6), (7), and (8), for example, that the φ-component of the radiation field admits description as

$$E_\varphi = -\frac{j\omega\mu}{4\pi}\int_0^{2\pi} I(\varphi')\left[\begin{array}{l}\left[b\beta'\begin{bmatrix}1\\-P'\end{bmatrix}^T + d\delta'\begin{bmatrix}\cos N\varphi'\\ \sin N\varphi'\end{bmatrix}^T\begin{bmatrix}1 & -NQ'\\ 0 & N\end{bmatrix}\right]\begin{bmatrix}\cos(\varphi-\varphi')\\ \sin(\varphi-\varphi')\end{bmatrix} \\ \times\dfrac{\exp\left(-jk\sqrt{\begin{bmatrix}d\delta'\\ b\beta'\\ r\end{bmatrix}^T\begin{bmatrix}d\delta' & b\beta'\\ b\beta' & d\delta'\\ r & 0\end{bmatrix}\begin{bmatrix}1\\ \cos N\varphi'\end{bmatrix} -2r\left[\begin{bmatrix}0\\ b\beta'\end{bmatrix}^T + d\delta'\begin{bmatrix}\sin N\varphi'\\ \cos N\varphi'\end{bmatrix}^T\right]\begin{bmatrix}\cos\theta & 0\\ 0 & \sin\theta\end{bmatrix}\begin{bmatrix}1\\ \cos(\varphi-\varphi')\end{bmatrix}}\right)}{\sqrt{\begin{bmatrix}d\delta'\\ b\beta'\\ r\end{bmatrix}^T\begin{bmatrix}d\delta' & b\beta'\\ b\beta' & d\delta'\\ r & 0\end{bmatrix}\begin{bmatrix}1\\ \cos N\varphi'\end{bmatrix} -2r\left[\begin{bmatrix}0\\ b\beta'\end{bmatrix}^T + d\delta'\begin{bmatrix}\sin N\varphi'\\ \cos N\varphi'\end{bmatrix}^T\right]\begin{bmatrix}\cos\theta & 0\\ 0 & \sin\theta\end{bmatrix}\begin{bmatrix}1\\ \cos(\varphi-\varphi')\end{bmatrix}}}\,d\varphi'\end{array}\right] \tag{9}$$

In this manner, it becomes possible to identify and describe the electromagnetic interactions between the structural members of the antenna. Terms involving the parameters b, β', and P', for instance, are clearly associated with the main loop, whereas those involving d, δ', Q', and N derive from the poloidal loops. Accordingly, we may conclude that radiation fields arise from the interactions of two different fields in the manner described elsewhere in the open literature [1–3].

It is also worth remarking that the results obtained in this paper represent a general case of certain geometrical shapes that derive from choice of values for b, d, N, e, and ξ; if for example, we set $a, b \geq 0$ $(a, b \neq 0)$, then $N \leq 0$ gives the left handed toroidal helical antenna, whilst $N \geq 0$ yields the right-handed toroidal helical antenna. Finally, we further remark that these analytical results have been implemented in a moment-method based computation of numerical results, in which piecewise-linear functions were utilized as basis functions in the procedure for determining an approximation for the unknown current distribution appearing in (9); the outcomes of that computational effort are the subject of a forthcoming paper.

4. CONCLUDING REMARKS

We have in this presentation, described a vector magnetic potential analysis of the bi-elliptical toroidal helical antenna. Expressions derived for the vector potentials and associated radiation fields emerged in terms of integrals, whose integrands were represented in compact planar matrix formats, to facilitate an insight into the physics of the antenna's radiation mechanism. In particular, it becomes possible, with the analytical results, to examine those contributions to the antenna performance metrics, which may be separately ascribed to the main and poloidal loops. The expressions are based on the geometrical shape of the antenna, thus making them particularly suitable for implementation in a moment-method environment, where excellent numerical approximations to the current distribution can be easily determined.

We shall, in a forthcoming paper, present computational results obtained from a moment-method (with piece-wise or triangular basis functions) implementation of the analytical results.

REFERENCES

1. Wanamassa, M. A., K. I. Elberon, and W. A. S. Fair Haven, "Helical coil coupled to a live tree to provide a radiating antenna," U. S. Patent Number 3646562, February 29, 1972.

2. Corum, J. F., "Toroidal antenna," U. S. Patent Number 4622558, November 11, 1986.
3. Hansen, R. C. and R. Ridgley, "Modes of the contrawound toroidal helix antenna," *Microwave and Optical Technology Letters*, Vol. 23, No. 6, December 20, 1999.
4. Miron, D. B., "A study of the CTHA based on analytical models," *IEEE Trans. Antennas Propagat.*, Vol. 49, 1130–1137, August 2001.
5. Hansen, R. C. and R. D. Ridgley, "Fields of the controwound toroidal helix antenna," *IEEE Trans. Antennas Propagat.*, Vol. 49, 1138–1141, August 2001.
6. Li, L.-W., P.-N. Jiao, X.-W. Shi, and J. A. Kong, "Closed-form solution to electromagnetic fields in far zone radiated by toroidal antennas," *IEEE Trans. Antennas Propagat.*, Vol. 52, 2381–2390, September 2004.
7. Pertl, F. A., J. E. Smith, and R. S. Nutter, Jr., "An analysis of the CTHA's resonance currents and the resulting radiation shapes," *IEEE Trans. Antennas Propagat.*, Vol. 53, 377–385, September 2004.
8. Lu, Y. and Y. Rahmat-Samii, "Toroidal helical antennas-analysis and optimization," *IEEE Antennas and Propagation Society Symposium*, Vol. 3, 1310–1313, July 2000.

Design of an Antenna with Reconfigurable Band Rejection for UWB Cognitive Radio

M. Al-Husseini[1], Y. Tawk[2], C. G. Christodoulou[2], K. Y. Kabalan[1], and A. El-Hajj[1]

[1]ECE Department, American University of Beirut, Beirut 1107 2020, Lebanon
[2]ECE Department, University of New Mexico, Albuquerque, NM 87131, USA

Abstract— Ultra-wideband cognitive radio (UWB-CR) features the use of UWB transmission as the enabling technology for cognitive radio, in both the underlay and overlay spectrum sharing approaches. In this paper, we propose an antenna that is suitable for underlay and overlay UWB cognitive radio. The antenna can be operated as ultrawideband, for underlay CR and for sensing in the overlay CR, and is reconfigurable in terms of the ability to selectively have a band stop in the WiMAX and WLAN bands, to prevent interference to primary users operating in these bands, when used in the overlay CR mode.

1. INTRODUCTION

Increasing demand on radio spectrum has resulted from the emerging of feature-rich and high-data-rate wireless applications. The scarcity of the spectrum and the inefficiency in its usage, as caused by the current radio spectrum regulations, necessitate the development of new dynamic spectrum allocation policies to better exploit the existing spectrum.

The current spectrum allocation regulations assign specific bands to particular services, and grant licensed band access to licensed users only. Cognitive Radio (CR) [1] is expected to revolutionize the way spectrum is allocated. In a CR network following the hierarchical access model [2], the intelligent radio part allows unlicensed users (secondary users) to access spectrum bands licensed to primary users, while avoiding interference with them. In this model, two approaches to spectrum sharing between primary and secondary users have been considered: spectrum underlay and spectrum overlay. In the underlay approach, secondary users should operate below the noise floor of primary users, and thus severe constraints are imposed on their transmission power (should be less than $-42\,\mathrm{dBm/MHz}$). One way to achieve this is to spread the transmitted signals of secondary users over an ultra-wide frequency band, leading to a short-range high data rate with extremely low transmission power. The spectrum overlay (also termed opportunistic spectrum access or OSA) approach imposes restrictions on when and where secondary users may transmit rather on their transmission power. In this approach, secondary users avoid higher priority users through the use of spectrum sensing and adaptive allocation. They identify and exploit the spectrum holes defined in space, time, and frequency. The underlay and overlay approaches in the hierarchical model are illustrated in Fig. 1. They can be employed simultaneously for further spectrum efficiency improvement.

Ultrawideband (UWB) communication, on the other hand, is commonly achieved using the impulse radio based UWB technology (IR-UWB), or the Orthogonal Frequency Division Multiplexing based UWB (UWB-OFDM). IR-UWB is carried out by transmitting extremely short pulses, whereas in OFDM-based UWB, orthogonal subcarriers are employed to modulate the transmitted data. As per FCC regulations, UWB systems are allowed to operate in the 3.1–10.6 GHz band without a license requirement, but under very strict transmission power limits. This property of UWB, in addition to its other advantages, makes it very suitable as the enabling technology for underlay Cognitive Radio [3].

Though usually associated with the underlay mode, UWB can also be used in the overlay Cognitive Radio mode (also called opportunistic spectrum access or OSA). In the overlay mode, the transmitted power can be increased to a level that is comparable to the power of licensed systems (an advantage would be long-distance communication as compared to short- and medium-range communication in the underlay case), but this requires the UWB transmitter to avoid spectrum bands that are used by other systems. This can be achieved in UWB-OFDM by turning off the subcarriers in the bands used by primary services, and in IR-UWB by using adaptive UWB pulses characterized by the ability to form, in their spectral masks, notches in the bands used by existing narrow-band wireless services operated in the 3.1–10.6 GHz UWB range [4].

In the overlay UWB scenario, the antenna at the front-end of the Cognitive Radio device should be capable of operating over the whole UWB range, for sensing and determining the bands that

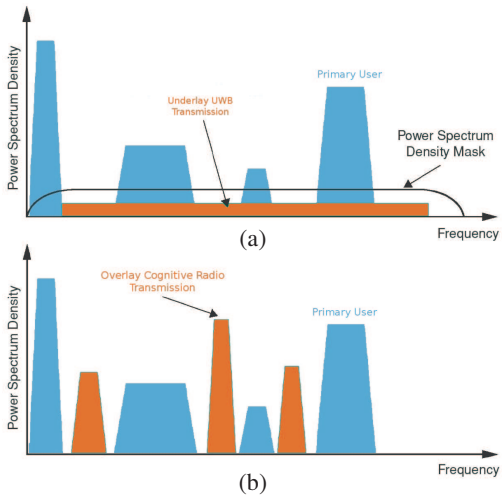

Figure 1: (a) Underlay and (b) overlay spectrum sharing approaches.

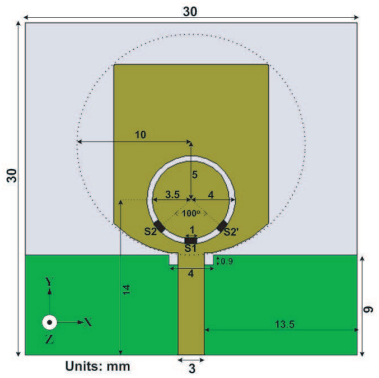

Figure 2: Antenna configuration.

are being used by primary users, but should also be able to induce band notches in its frequency response to prevent interference to these users. For underlay UWB cognitive radio, the antenna should be ultrawideband, with no band notches needed. In this paper, we propose an antenna that is suitable for both underlay and overlay UWB cognitive radio. It can be operated as ultrawideband, and is reconfigurable in terms of the ability to selectively have band stops in the WiMAX (3.5 GHz) and WLAN (5.2 GHz) bands.

2. ANTENNA CONFIGURATION

Depicted in Fig. 1, the antenna is a monopole printed on a 1.3-mm-thick Rogers RO3006 substrate with $\varepsilon_r = 6.15$, and features a partial rectangular ground plane with a small slit below the microstrip feed line, for matching purposes. The patch is rectangular in shape, but the corners of the rectangle around the feed line are rounded to create a matching section. The dimensions of the different parts are optimized for an impedance bandwidth covering the whole UWB range.

To obtain a reconfigurable band notch, a ring slot is etched on the patch, and three electronic switches, S_1, S_2 and S_2', are mounted across it, as shown in Fig. 1. When any of the switches is ON, the slot will behave as a complementary split-ring resonator (CSRR). CSRRs and their dual-counterparts, the split-ring resonators [5], are employed in [6] in the design of UWB antennas with fixed notched bands. When all three switches are OFF, the antenna has a UWB response, which is required for underlay operation and for sensing in the overlay scenario. When only S_1 is ON, the antenna has a band rejection in a frequency range used by WiMAX. When S_2 and S_2' are ON, a notch appears in the WLAN 5.2 GHz band. The dimensions of the ring slot and the locations of the switches are well selected to have the notches in these two frequency ranges of interest. To target other bands, the slot dimensions and the positioning of the switches could be changed.

3. RESULTS AND DISCUSSION

The antenna was designed and simulated using Ansoft HFSS. A prototype was fabricated, and the return loss was measured for the three switching cases: Case 1 where all three switches are OFF, Case 2 where only switch S_1 is ON, and Case 3 where S_2 and S_2' are ON (S_1 being OFF).

The computed and measured return loss plots of the antenna, for the three switching states, are shown in Figs. 3 and 4, respectively. Good analogy is shown between the simulated and measured results. For Case 1, a UWB response is obtained, which is needed for underlay CR operation and for sensing in the overlay UWB scenario. In this case, no current is allowed inside the part of the patch surrounded by the slot. Case 2 results in a band notch centered at 3.6 GHz. This notch helps prevent interference to a primary user operating in the WiMAX band. In Case 3, on the other hand, the notch occurs at 5.2 GHz, thus avoiding interference with a primary user communicating in the WLAN 5.2 GHz band. The notches are strong, with values better than −2 dB.

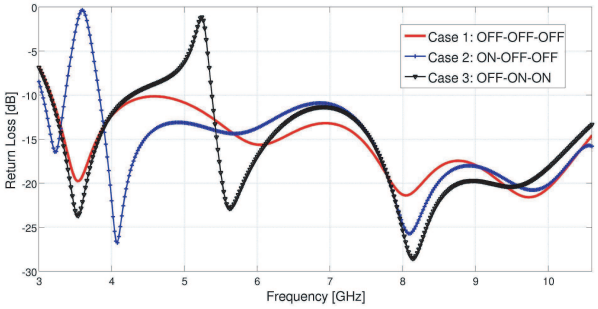

Figure 3: Simulated return loss.

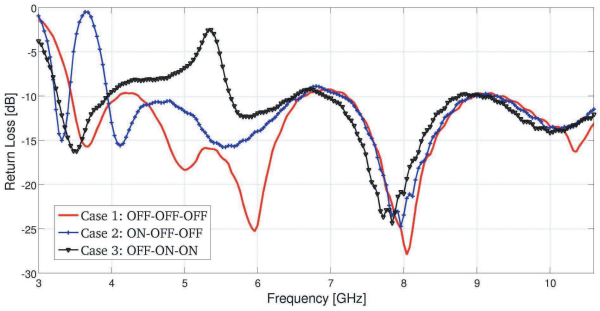

Figure 4: Measured return loss.

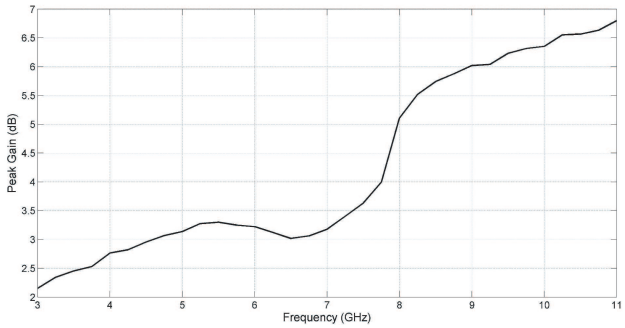

Figure 5: Peak gain for Case 1.

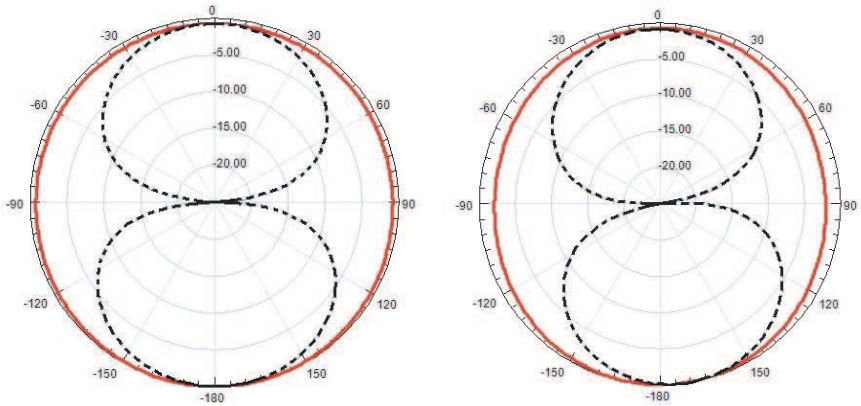

(a) 3.6 GHz (b) 5.2 GHz

Figure 6: Radiation patterns for Case 1 in the H-plane (solid line) and E-plane (dotted line).

In its band(s) of operation, the antenna has omnidirectional patterns and good gain values. The computed peak gain for Case 1 is plotted in Fig. 5. At 3.6 GHz, the peak gain for Case 1 is about 2.5 dB. At 5.2 GHz, the gain is 3.2 dB. This shows that when the notches are removed, the antenna retrieves good gain values in the previously notched bands. The normalized radiation patterns for Case 1, at 3.6 and 5.2 GHz, are shown in Fig. 6. The omnidirectionality of the patterns is clear. However, in the high portion of the UWB range, the patterns become less omnidirectional, and this justifies the higher-than-expected peak gain values when the frequency is very large.

Cases 2 and 3 have comparable gain and pattern characteristics, except in the notched bands where the gain drops to negative values due to severe reflections at the antenna's port.

4. CONCLUSION

In this paper, we proposed the design of an antenna for use in UWB-CR applications. The presented antenna has a UWB response, and can have a reconfigurable band notch caused by a ring slot etched in the patch, and controlled by electronic switches mounted across the slot. The antenna can be operated with UWB-CR systems in both the underlay and overlay modes.

REFERENCES

1. Mitola, J. and G. Q. Maguire, "Cognitive radio: Making software radios more personal," *IEEE Pers. Commun.*, Vol. 6, No. 4, 13–18, Aug. 1999.
2. Chen, K.-C. and R. Prasad, *Cognitive Radio Networks*, John Wiley & Sons, West Sussex, United Kingdom, 2009.
3. Arslan, H. and M. Sahin, "UWB-based cognitive radio networks," *Cognitive Wireless Communication Networks*, E. Hossain and V. Bhargava, Ed., Springer, US, 2007.
4. Zhang, H., X. Zhou, and T. Chen, "Ultra-wideband cognitive radio for dynamic spectrum accessing networks," *Cognitive Radio Networks*, Y. Xiao and F. Hu, Ed., CRC Press, Boca Raton, Florida, 2009.
5. Pendry, J. B., A. J. Holden, D. J. Robbins, and W. J. Stewart, "Magnetism from conductors and enhanced nonlinear phenomena," *IEEE Trans. Microw. Theory Tech.*, Vol. 47, No. 11, 2075–2084, 1999.
6. Zhang, Y., et al., "Planar ultrawideband antennas with multiple notched bands based on etched slots on the patch and/or split ring resonators on the feed line," *IEEE Trans. Antennas Propagat.*, Vol. 56, No. 9, 3063–3068, Sep. 2008.

Overview of Reconfigurable and Compact Antennas Using a Magneto-dielectric Material

L. Huitema[1], **M. Hajj**[1], **T. Monédière**[1], **D. Souriou**[2], **A. Chevalier**[2], **J.-L. Mattei**[2], **and P. Queffelec**[2]

[1]Xlim Laboratory, 123 av. Albert Thomas, Limoges 87060, France
[2]Labsticc Laboratory, UMR CNRS 3192, 6 av. Le Gorgeu 29238, Brest cedex 3, France

Abstract— This paper presents two novel designs based on the design of a 3D compact inverted F antenna which is dedicated to low frequencies handheld applications. Good performances, compactness and low frequencies are obtained thanks to a magneto-dielectric material. Indeed, using a magneto-dielectric material in comparison to use a pure dielectric material allows obtaining a wideband compact antenna. A complete study will show the advantage of using a magneto-dielectric material. Since reconfigurable radiation patterns allow improving the quality and reliability of wireless links, for both designs, two antennas are used to release this feature over its matched band.

1. INTRODUCTION

An overview of the challenges to design reconfigurable and compact antennas is presented in this paper. Two novel designs dedicated to low frequencies handheld applications are explained. Since reconfigurable radiation patterns allow improving the quality and reliability of wireless links, the first design exhibits a wideband compact antenna with pattern diversity. This pattern diversity is obtained thanks to two orthogonally co-located antennas. The second one explains a tunable frequency antenna thanks to a varactor component. Both designs are based on the design of a 3D compact Inverted F Antenna (IFA) and are suitable for mobile devices. Good performances, compactness and low frequencies are obtained thanks to a magneto-dielectric material elaborated with nanoferrites particles. The study presented in this paper is developed in the framework of a project called NAOMI supported by the French Research Agency. In a first section, only the design of one radiating element will be studied, followed by a comprehensive study on the contribution of using a magneto-dielectric material. Later, the study will focus on the design of the two global structures and present both simulations and measurements.

2. CONTRIBUTION OF USING A MAGNETO-DIELECTRIC MATERIAL IN ANTENNAS

The antenna structure presented in this section is based on the IFA [1, 2] design as shown in Fig. 1. Its structure is similar to a quarter wavelength monopole, where the top section has been bent to be parallel to the ground plane. This horizontal section involves a capacitive effect and then influences the input impedance. This effect could be compensated by adding a shorting line, that is to say a ground return. So, this shorting line allows adjusting the return loss because it involves a parallel resonance allowing to set the input impedance without adding any matching circuit. Moreover, in order to decrease the global antenna dimensions, the monopole has been folded on itself on one hand and loaded by a magneto-dielectric material on the other hand. The antenna is studied on a 230 mm × 130 mm ground plane, defined by the project specifications to correspond to a standard DVB-H handheld receiver. Multiple feeding mechanisms are possible, in this case, the radiating element is fed by a 50 Ω coplanar waveguide printed on a FR4 substrate ($\varepsilon_r = 4.9$).

The magneto-dielectric material used is a Ni-Zn ferrite ceramic with nanosized grains, with a composition of $Ni_{0.5}Zn_{0.3}Co_{0.2}Fe_2O_4$. Ferrite nanoparticles were prepared by a co-precipitation method, and then submitted to appropriate thermal treatments and shaping by uniaxial pressing. The electromagnetic characteristics (complex permittivity and complex permeability) of the obtained material are shown Fig. 2. More detailed on the material elaboration are available in [3, 4]. Its dimensions are 15 mm × 10 mm × 4 mm. The next subsection will show the performances of this antenna and the relevance of using a magneto-dielectric material.

In order to show the contribution of the magneto-dielectric material, the best way is to compare its real input impedance and its return loss with its equivalent in a dielectric material case. Let us notice that the matching band is due to the quarter wavelength resonance of the monopole loaded

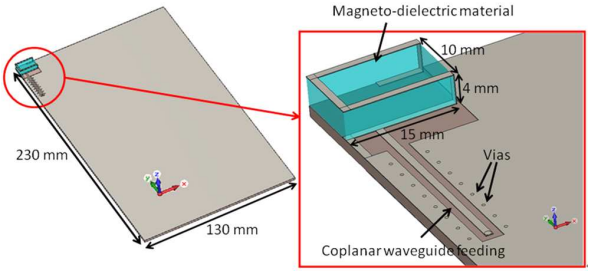

Figure 1: Design of the proposed antenna.

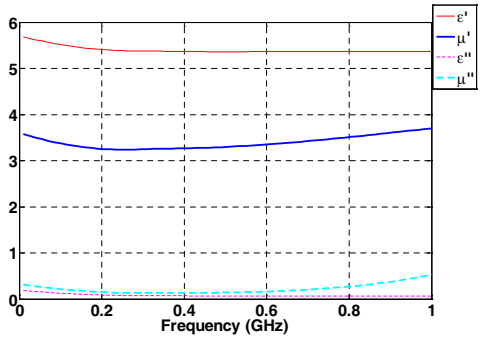

Figure 2: Electromagnetic characteristics of the magneto-dielectric material.

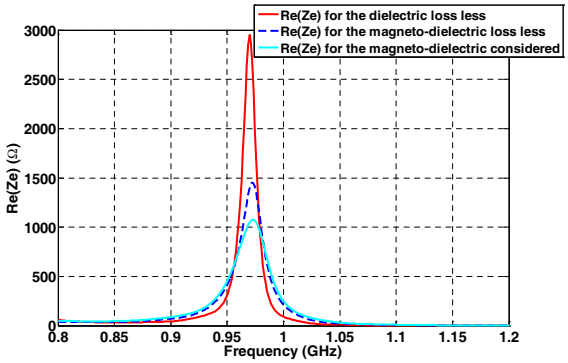

(a)

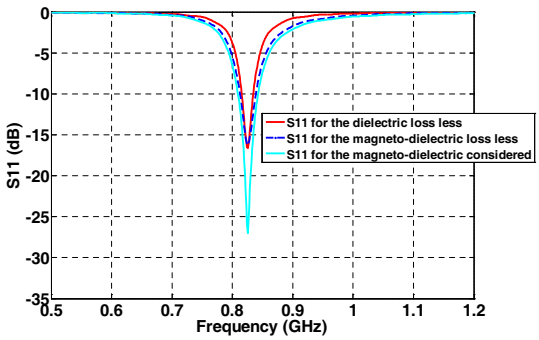

(b)

Figure 3: (a) Real part of the input impedances for the loss less dielectric, the loss less magneto-dielectric and the considered magneto-dielectric. (b) Return losses of the input impedance for the dielectric loss less, the magneto-dielectric loss less and the magneto-dielectric considered.

Table 1: Compared simulated results for the three materials.

	Dielectric loss less	Magneto-dielectric loss less	Magneto-dielectric considered
Resonance frequency	970 MHz	972 MHz	972 MHz
Impedance bandwidth ($S_{11} < -6\,\mathrm{dB}$)	4.12%	5.93%	7.14%
Total efficiency	83%	83%	68%
Maximum realized gain	2.8 dB	2.8 dB	1.95 dB

by the material. So its resonance is a $\lambda_g/4$ one with $\lambda_g = \lambda_0/\sqrt{\varepsilon' \cdot \mu'}$. Thus, the comparison will be done for a same product $\varepsilon' \cdot \mu'$. Moreover, losses affect the input impedance and the return loss, thus the Figs. 3(a) and (b) show respectively the real input impedance and the return loss when magneto-dielectric $(\varepsilon'_{\mathrm{magneto}}, \mu'_{\mathrm{magneto}})$ is considered, as well the one when a loss less magneto-dielectric and a loss less dielectric are used, like $\varepsilon'_{\mathrm{dielectric}} = \varepsilon'_{\mathrm{magneto}} \cdot \mu'_{\mathrm{magneto}}$. Real input impedances clearly show that the radiation Q factor is lower for the magneto-dielectric material than for the dielectric material. So the antenna matching is easier for a magneto-dielectric material.

This is underlined by the Fig. 3 and the Table 1, which sums up the impedance bandwidth for the three cases. Moreover, the Table 1 specifies the total efficiency and the realized gain at the matching frequency. Remind that the total efficiency and the realized gain take into account all kind of losses in the antenna and even the cables and connectors losses.

So, this study clearly shows the contribution of using a magneto-dielectric material. To satisfy the DVB-H application, the realized gain must be higher than $-6\,\mathrm{dB}$ at 790 MHz and higher than $-4.5\,\mathrm{dB}$ at 862 MHz. Considering that and the obtained realized gain in the case of the magneto-dielectric considered in this letter, it is possible to integrate a second radiating element around the

first one. For that, a parametric study has been done in order to determine how to integrate the second element. It is the subject of the next section.

3. OVERVIEW OF THE TWO DESIGNS

3.1. First Design

The antenna structure presented in this subsection is based on the antenna studied in the previous section. In order to obtain pattern diversity, two of the previous radiating elements are orthogonally integrated. They are both fed by a coplanar waveguide. The antenna is studied on a 230 mm × 130 mm ground plane, defined by the project specifications to correspond to a standard DVB-H handheld receiver. The allocated area dimensions for this antenna composed of two radiating element are $\lambda_0/22 \times \lambda_0/12$ at 800 MHz.

They are both fed by a coplanar waveguide. The global structure is presented in Fig. 4. This antenna has a 17.5% bandwidth as shown in Fig. 5 with a realized gain higher than the one required by the DVB-H application as shown in Fig. 6(a). Let us notice that there is a very good agreement between all measurements and simulations. Performances of wireless communication systems can be greatly improved by using antenna diversity techniques. The parameter presented to evaluate diversity performances is the effective diversity gain (EDG) [5]. The efinition of the diversity gain and the way to measure it in a mode-stirred reverberation chamber is presented in [5]. The cumulative probability density (CDF) is calculated from the signal to noise ratio (SNR) measurements. The CDF curves are plotted in the Fig. 6(b) at 830 MHz. In abscissa, the threshold SNR is normalized by the SNR of the reference antenna. Let us notice that the reference antenna is a half wave length dipole antenna, that is to say a 19 cm length dipole. It is obvious that the diversity techniques enhance the reception quality while the effective diversity gain at 1% probability level is higher than 0 dB. This one is around 5 dB at 830 MHz. Thus, the antenna system presented in this letter is more compact than a classical dipole and the application of diversity techniques allows to enhance the quality and the reliability of the wireless link.

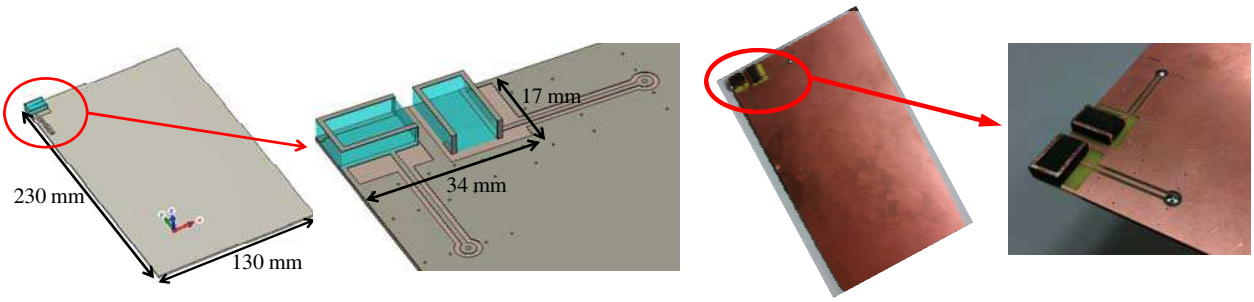

Figure 4: Design of the first proposed antenna.

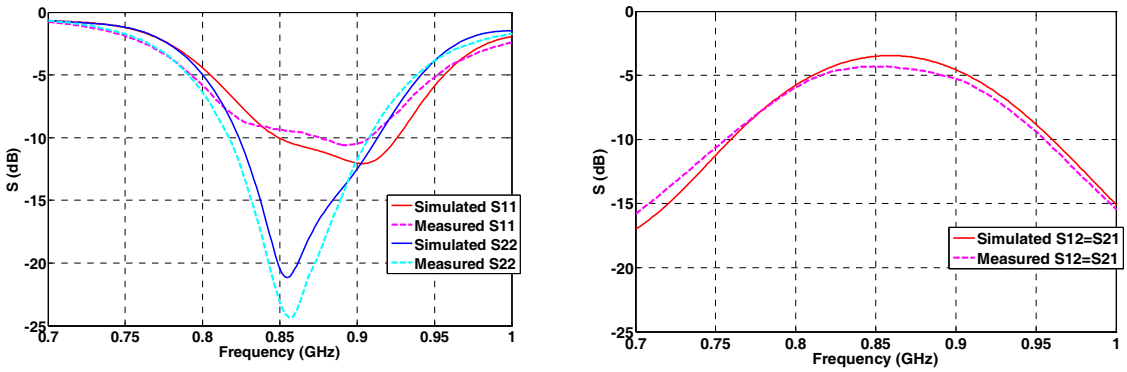

Figure 5: S parameters and realized gain of the proposed antenna.

3.2. Second Design

The value added by this new design, based on the first one, is to integrate a varactor component allowing the frequency tunability of the antenna on the entire DVB-H band. The global structure,

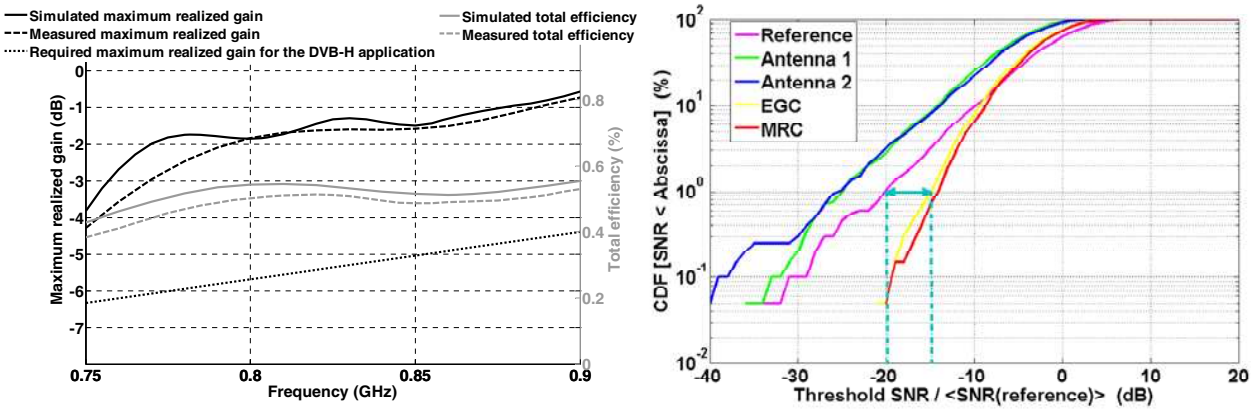

(a) (b)

Figure 6: (a) Measured and simulated realized gain and total efficiency. (b) Effective diversity gain at 830 MHz.

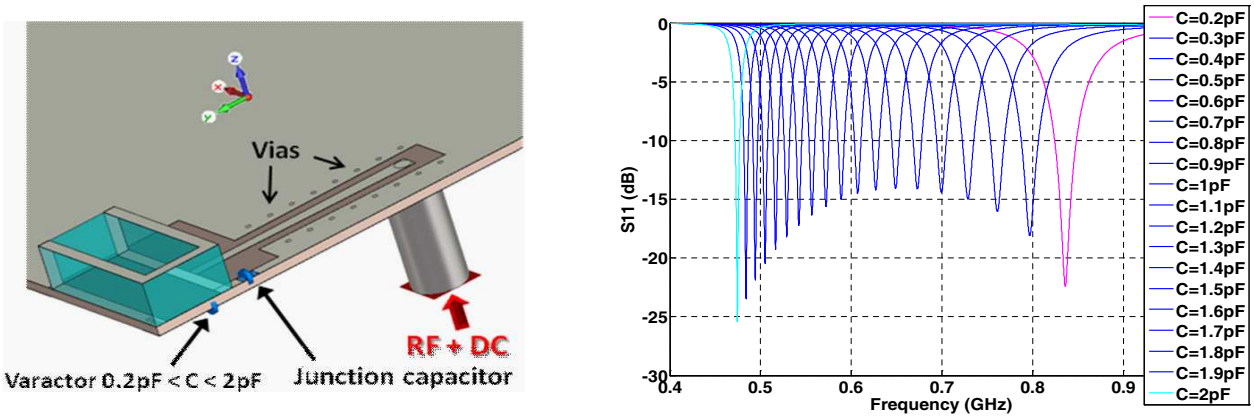

(a) (b)

Figure 7: (a) Design of the second proposed antenna. (b) Simulated S_{11} for each capacitor value.

owning two radiating element on both sides of the 230 mm × 130 mm ground plane, is presented Fig. 7(a). It also uses magneto-dielectric material. S_{11} parameters (for each reverse voltage of the varactor component) are shown Fig. 7(b). Thus, the DVB-H band going from 470 MHz to 862 MHz is covered and the allocated area dimensions for this antenna composed of two radiating element are $\lambda_0/47 \times \lambda_0/53$ at 470 MHz.

4. CONCLUSIONS

The contribution of using a magneto-dielectric material has been shown in a first time. Indeed, the comparison of simulation results has clearly confirmed that using a magneto-dielectric allows enhancing the bandwidth. Thanks to this material, two designs of antennas have been presented. The first one is matching on the nine channels of the DVB-H band with the realized gain higher than the one required for the DVB-H application. The allocated surface for antenna system is 34 mm × 17 mm, that is lower than $\lambda_0/11 \times \lambda_0/22$. Next, diversity techniques have been applied with the presentation of the effective diversity gain. These parameters underline the reconfiguration of the radiation pattern and the enhancement of the reception quality by integrating two radiating elements. The second design integrates a varactor component allowing the frequency tunability of the antenna on the entire DVB-H band. The allocated area dimensions are $\lambda_0/47 \times \lambda_0/53$ at 470 MHz. Thus, thanks to a magneto-dielectric material, two designs of very compact antennas have been done with good performances at very low frequencies.

REFERENCES

1. Ling, C.-W., C.-Y. Lee, C.-L. Tang, and S.-J. Chung, "Analysis and application of an on-package planar inverted-F antenna," *IEEE Transactions on Antennas and Propagation*, Vol. 55,

No. 6, 1774–1780, June 2007.

2. Ammann, M. J. and L. E. Doyle, "A loaded inverted-F antenna for mobile handset," *Microwave and Optical Technology Letters*, Vol. 28, 226–228, 2001.
3. Souriou, D., J.-L. Mattei, A. Chevalier, and P. Queffelec, "Influential parameters on electromagnetic properties of nickel-zinc ferrites for antenna miniaturization," *J. Appl. Phys.*, Vol. 107, 09A518, 2010.
4. Thakur, A., A. Chevalier, J.-L. Mattei, and P. Queffelec, "Low-loss spinel nanoferrite with matching permeability and permittivity in the ultrahigh frequency range," *J. Appl. Phys.*, Vol. 108, 014301, 2010.
5. Kildal, P. S., K. Rosengren, J. Byun, and J. Lee, "Definition of effective diversity gain and how measure it in a reverberation chamber," *Microwave and Optical Technology Letters*, Vol. 34, 56–59, 2002.

A Frequency Reconfigurable Microstrip Rectangular Patch Antenna Using Stubs

Lama Mokalled, **Mohammed Al-Husseini**, **Ali Ramadan**, **Karim Y. Kabalan**, **and Ali El-Hajj**
ECE Department, American University of Beirut, Beirut 1107 2020, Lebanon

Abstract— This paper presents a frequency reconfigurable microstrip antenna for operation in the ISM, WiMAX and U-NII bands. The antenna, which is printed on a 1.6-mm-thick FR4 epoxy substrate, originally resonates at 2.4 GHz (ISM band), where it has good omnidirectional patterns. To obtain resonances in the 3.5 and 5.5 GHz bands, two matching stubs have been connected to the feed line via two electronic switches. When the two switches are OFF, the antenna still resonates at 2.4 GHz. Activating one switch gives resonance at 3.5 GHz, and when the other switch is ON, the antenna is operable in the 5.5 GHz band. Three types of stubs are attempted: open, shorted, and balanced. The effect of each type on the antenna's radiation patterns is also discussed.

1. INTRODUCTION

In high-performance aircraft, spacecraft, satellite, and missile applications, where size, weight, cost, performance, ease of installation, and aerodynamic profile are constraints, low-profile antennas may be required [1]. Presently, there are many other government and commercial applications, such as mobile radio and wireless communications that have similar specifications. To meet these requirements, micro strip antennas can be used [2]. These antennas are low profile, conformable to planar and non planar surfaces, simple and inexpensive to manufacture using modern printed-circuit technology, mechanically robust when mounted on rigid surfaces, compatible with MMIC designs, and when the particular patch shape and mode are selected, they are very versatile in terms of resonant frequency, polarization, pattern, and impedance [3].

Reconfigurability in antenna systems is a desired feature that aims at designing frequency, polarization, and/or pattern tunable antennas [4]. These antennas have the advantage of being remotely tunable without re-building the platform on which the antenna structure is placed. In [5], a novel microstrip dual-band fed patch antenna with two parasitic invert L stubs for 2.4/5-GHz wireless applications is presented.

Frequency reconfigurability of an antenna can be attained by using electronic switches to either change the electrical length of the antenna, thus changing its operation frequency, or by changing its impedance as seen at its input port [6]. In this paper, frequency reconfigurability is accomplished using stubs that do the impedance matching. Three types of stubs are considered: open stubs, shorted stubs, and balanced stubs. For all three types, the design is done such that when the first switch (S_1) is ON and the second (S_2) is OFF, a 3.5 GHz resonance frequency is reached. On the other hand, when S_1 is OFF and S_2 is ON, a resonance at 5.5 GHz is obtained. The effect of each stub type on the antenna radiation characteristics is discussed.

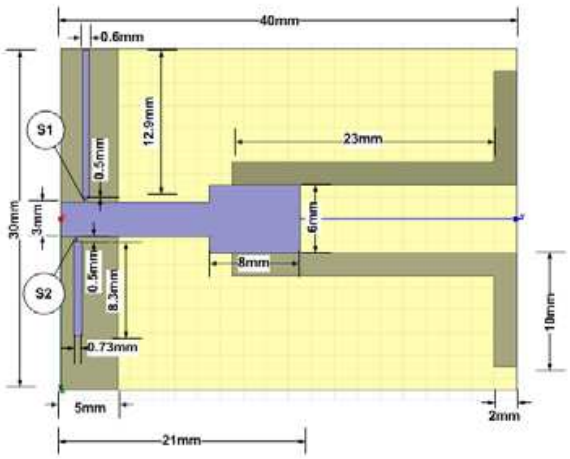

Figure 1: Open end.

2. ANTENNA CONFIGURATION

The antenna is based on a $30 \times 40 \times 1.6\,\text{mm}^3$ FR4 epoxy substrate, and a $6 \times 8\,\text{mm}^2$ rectangular patch fed by a microstrip line. The ground plane has a partial rectangular part, and two L-shaped strips placed symmetrically with respect to the patch for optimal radiation characteristics. The detailed configuration of the antenna is given in Figs. 1–3, for the open, shorted, and balanced stubs cases, respectively.

The open-stub case is the easiest to implement; however, the resulting radiation patterns are not fully omnidirectional at 3.5 GHz and 5.5 GHz. This is because the stubs radiate when S_1 or S_2 is ON. Increasing the characteristic impedance of the open stub lines does not entirely solve the problem. The use of shorted stubs leads to improved radiation omnidirectionality at 3.5 GHz.

Balanced stubs seem to provide better omnidirectional patterns in the 5.5 GHz band. In this case, switches $S_{1,1}$ and $S_{1,2}$ are used to connect to the two balanced stubs responsible for resonance at 5.5 GHz. Switch S_2 connect to the single matching that gives resonance at 3.5 GHz.

3. RESULTS

The designs have been simulated using Ansoft HFSS and ADS Momentum. For each matching stub type, the locations and lengths of the stubs have been found.

Figure 4 shows the computed return loss plots, for the three stub design types, with resonance at 2.4 GHz. This is the case when all switches are OFF. In Fig. 5, the return loss plots are given for the case with operation at 3.5 GHz.

The return loss, initially computed in HFSS, is also verified using ADS Momentum. Fig. 6 shows the return loss of the open-end stub case, at 2.4 GHz. In Fig. 7, the S_{11} plots for the short-end

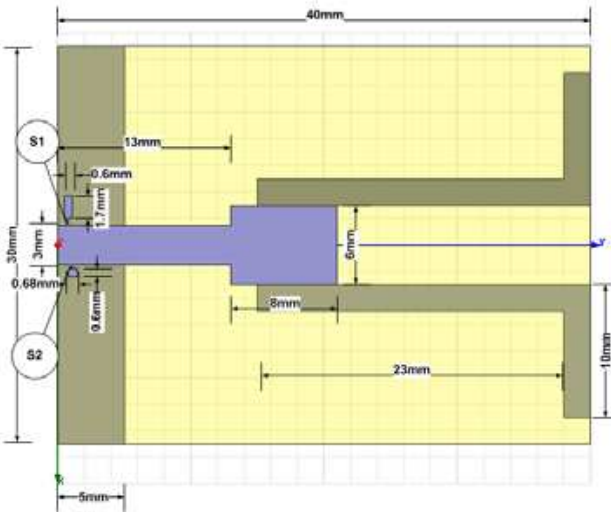

Figure 2: Short end.

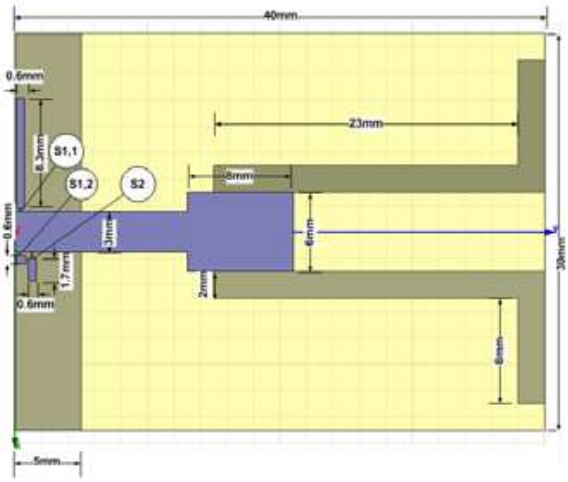

Figure 3: Balanced stub.

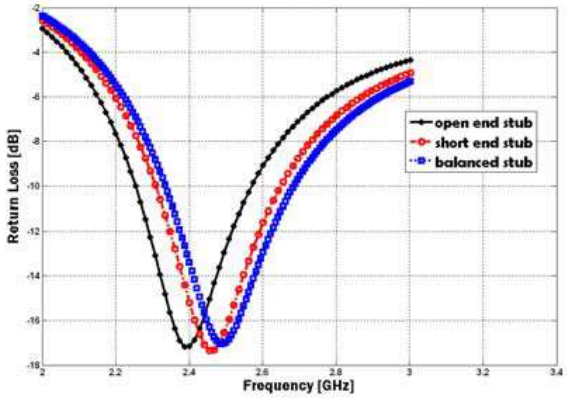

Figure 4: Return loss for the designs at 2.4 GHz.

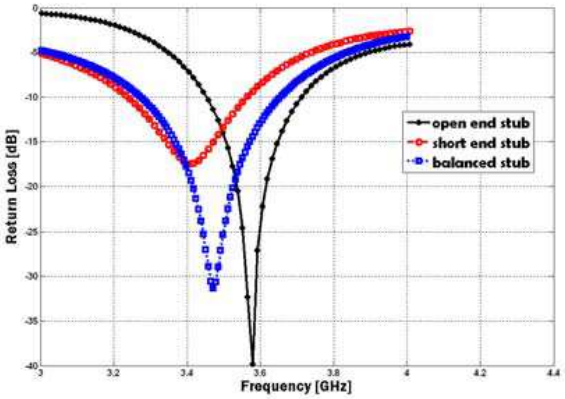

Figure 5: Return loss for the designs at 3.5 GHz.

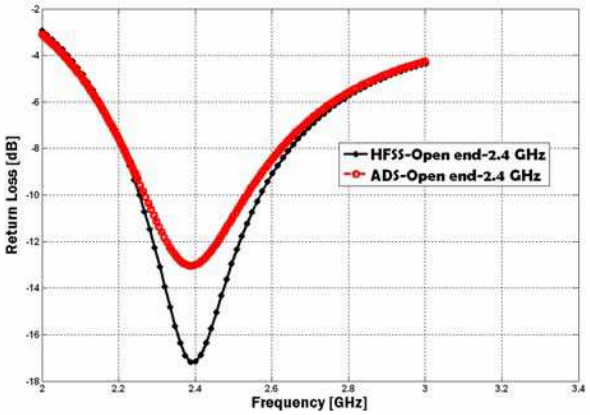

Figure 6: Return loss for the open end case at 2.4 GHz.

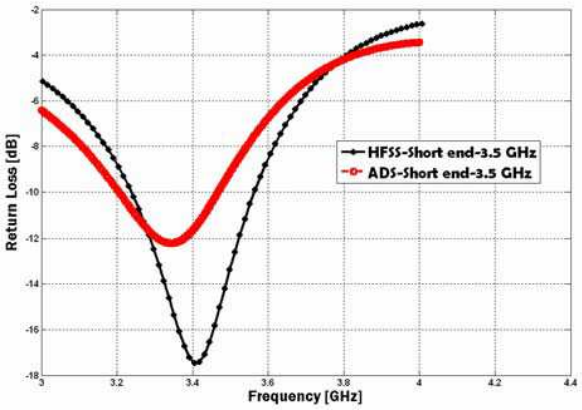

Figure 7: Return loss for the short end case at 3.5 GHz.

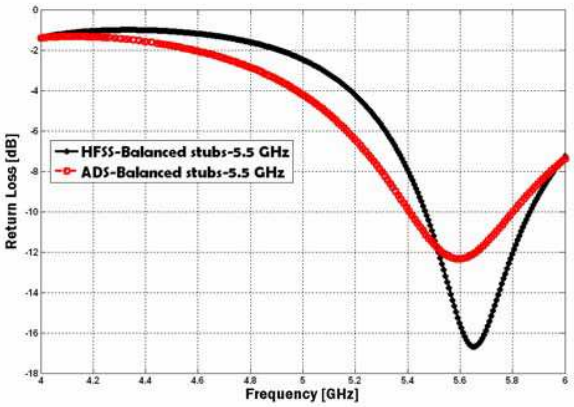

Figure 8: Return loss for the balanced stub case at 5.5 GHz.

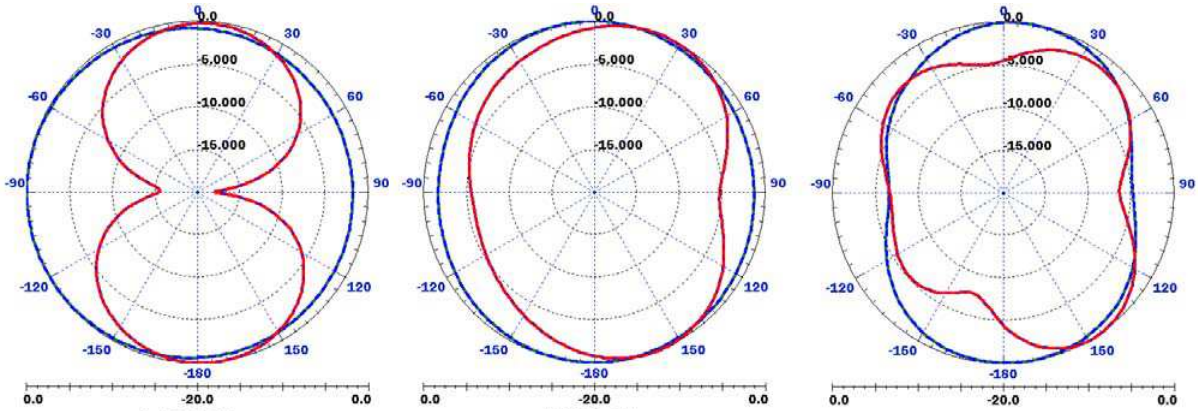

(a) 2.4 GHz (b) 3.5 GHz (c) 5.5 GHz

Figure 9: Radiation patterns for the open-end stubs case.

stub case are compared at 3.5 GHz, and in Fig. 8, those for the balanced stub case are contrasted at 5.5 GHz. Adequate similarity is witnessed between the two simulators' results, indicating the validity of the design procedure.

Figures 9–11 show the computed radiation patterns of the three stub types, in the H-plane (blue line) and the E-plane. While the printed monopole-type antenna in hand is expected to yield omnidirectional patterns, with equal radiation in the H-plane, the activation of the stubs, at 3.5 and 5.5 GHz, does affect the omnidirectionality of the patterns. The open-end stubs result in the least omnidirectional patterns. The use of short-end stubs improves the patterns at 3.5 GHz,

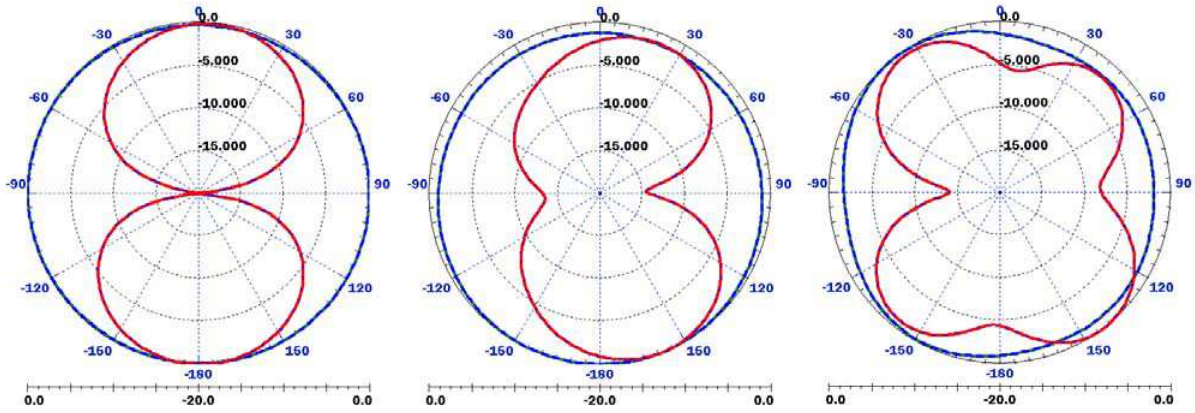

(a) 2.4 GHz (b) 3.5 GHz (c) 5.5 GHz

Figure 10: Radiation patterns for the short-end stubs case.

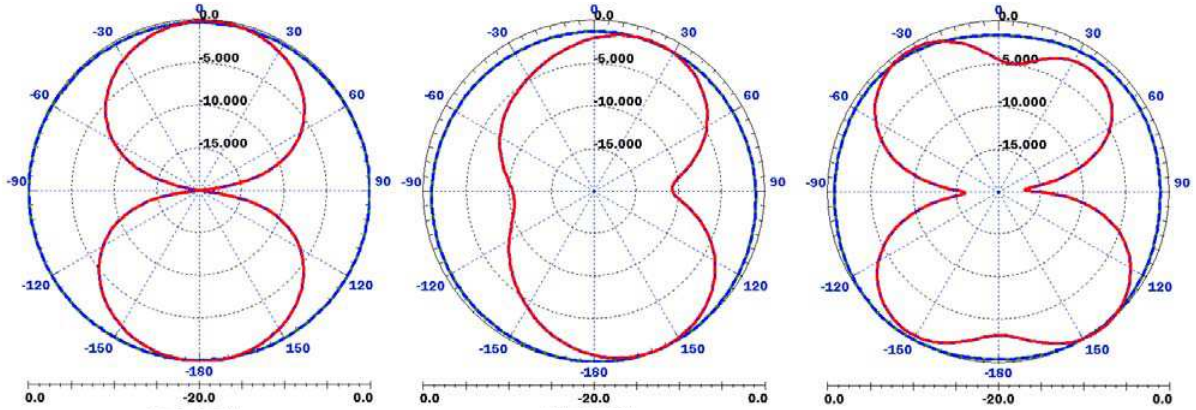

(a) 2.4 GHz (b) 3.5 GHz (c) 5.5 GHz

Figure 11: Radiation patterns for the balanced stubs case.

but not enough at 5.5 GHz. Due to their nature, shorted stubs are known to cause less radiation off their edges. Balanced stubs, on the other hand, have proven optimal in terms of the resulting 5.5 GHz radiation patterns. This is because they are best in keeping some symmetry in the flow of electric current.

4. CONCLUSION

This paper presented a frequency-reconfigurable microstrip-fed antenna that can be operated in the 2.4, 3.5 and 5.5 GHz bands. The antenna is based on a rectangular patch and a ground plane featuring a rectangular section and two symmetrical L-shaped strips. The antenna was designed for a center operation frequency of 2.4 GHz. Later, matching stubs were connected to the feed line via electronic switches. By turning ON and OFF the switches, the connected stub(s) lead(s) to impedance matching at 3.5 or 5.5 GHz. Open, shorted and balanced stubs were attempted. Amongst the three types, the balanced stubs, designed for the 5.5 GHz operation, resulted in the best omnidirectional patterns at this frequency. Compared to the open stub case, the shorted stubs provided better omnidirectional patterns at 3.5 GHz.

ACKNOWLEDGMENT

This work is partially supported by the American University of Beirut Research Board and by the Faculty of Engineering and Architecture of the university.

REFERENCES

1. Balanis, C. A., "Antenna theory: A review," *Proceedings of the IEEE*, Vol. 80, 7–23, 1992.
2. Park, S. Y., S. J. Oh, J. K. Park, and J. S. Kim, "Dual-band antenna for WLAN/UWB applications," *Microwave Conference, 2009, APMC 2009*, 2707–2710, Asia Pacific, 2009.

3. Bernhard, J. T., R. Wang, R. Clark, and P. Mayes, "Stacked reconfigurable antenna elements for space-based radar applications," *IEEE Antennas and Propagation Society International Symposium*, 158–161, Vol. 1, 2001.
4. Duffy, S., C. Bozler, S. Rabe, J. Knecht, L. Travis, P. Wyatt, C. Keast, and M. Gouker, "MEMS microswitches for reconfigurable microwave circuitry," *IEEE Microwave and Wireless Components Letters*, Vol. 11, 106–108, 2001.
5. Peng, L. and C. L. Ruan, *A Microstrip Fed Patch Antenna with Two Parasitic Invert L Stubs for Dual-band WLAN Applications*, Springer Science and Buisness Media, LLC, 2009.
6. Song, Z., Y. Liu, and W. Chen, "Reconfigurable multiple-band antenna using switches," *8th International Symposium on Antennas, Propagation and EM Theory, 2008, ISAPE 2008*, 316–319, 2008.

Modeling and Simulation of Temperature Distribution in Laser-tissue Interaction

A. Yasin Citkaya and S. Selim Seker
Department of Electrical & Electronics Engineering, Bogazici University
Istanbul 34342, Turkey

Abstract— In this paper, modeling and simulation of interaction between light sources and living biological tissue is studied. One of the most important results of physical interactions of light with biological tissue is thermal changes which is a consequence of absorption of light. The severity of the effects are dependent upon several factors, including exposure duration, wavelength of the beam, energy of the beam, the area and type of tissue exposed to the beam. The temperature response of tissue irradiation is governed by extensively used Pennes bio-heat equation in a 3-dimensional space. The Pennes equation is solved for a single layer model of the human skin to predict the temperature distribution using different laser light source radiation burns at as steady state. The numerical solutions are obtained by the Finite Element Method (FEM), in which the geometry studied is divided into a finite element mesh. This method gives better description of the geometry with smaller number of nodes. Less memory space and disk space with shorter run times make this method more advantageous to other numerical solution techniques. Temperature contours and penetration depths are plotted in three dimensional spaces. These results are compared with finite volume approach which exists in literature. In this work, it is demonstrated that by adjusting exposure duration, wavelength of the beam, energy of the beam, and the area and type of tissue, temperature effects on tissue can be altered.

1. INTRODUCTION

Laser light sources are used in many medical treatment applications to generate thermal effects in tissue. In these treatments, it is very important to control the temperature increase and distribution otherwise high temperatures could lead to thermal damages in the surrounding tissue. The temperature distribution mainly depends on exposure duration, wavelength of the beam, energy of the beam, the area and type of tissue exposed to the beam. One of the more commonly used mathematical models for describing the temperature distribution inside biological tissues is the Pennes bioheat equation [1]. Although various improved and alternative models exist in literature, due to its accuracy and its simplicity in numerical coding the Pennes bio heat equation is still widely in use.

With the advancement of computational technology, mathematical modeling of temperature distribution in human tissue is become prevalent. In order to adopt bioheat equation to investigate the temperature distribution, several mathematical models are being used. Although several analytical and numerical methods have been developed in literature, finite difference and finite element methods are commonly used ones.

In this paper, the developed human skin model is used to predict the temperature distribution during laser treatment. Finite element method is applied for modeling of numerical simulations to predict the temperature changes in human skin. The objective of this research is modeling the laser-tissue interaction to optimize the effective parameters in order to understand optimal laser dosage to prevent the damage. The severity of the damage depends on several factors, including exposure duration, wavelength of the beam, energy of the beam, and the area and type of tissue exposed to the beam.

Physical interaction of light with biological tissue is aimed to be modeled in recent research papers. The objective consists mainly of two concerns: the optical propagation of light, and its thermal distribution in biological tissue. Different approaches, such as seven flux model [2], Kubelka-Munk [3], and Monte Carlo method, has been developed for optical propagation; whereas thermal modeling part has a special attention given with the usage of most widely known approach: the bio-heat equation by Pennes. Pennes' extensively used bio-heat equation has better resemblance with the experimental results than the effective thermal conductivity [4]. Studies in literature also show that the control volume based finite difference procedure can also be an alternative for finite element method used for the solution of bio-heat transfer equation. Simulations of biological tissue with Pennes equation are quite good for microvessels; however in case of large vessels, more complex method is needed [5].

2. MATHEMATICAL MODELING

The mathematical model is based on the well Pennes' bioheat equation:

$$\delta_{ts}\rho C\frac{\delta T}{\delta t} + \nabla\cdot(-k\nabla T) = \rho_b C_b \omega_b (T_b - T) + Q_{met} + Q_{laser} \tag{1}$$

where ρ, C, k are, respectively, the density, the specific heat and the thermal conductivity of the tissue, Q_{met} the metabolic heat generation per unit volume, ω_b is the blood perfusion rate, C_b is the specific heat of blood, T_b the temperature of arterial blood, and T is the local tissue temperature.

The heat conduction term in the Pennes' bioheat equation considering blood perfusion and metabolic heat generation is based on the classical Fourier's law that implies an infinite thermal propagation speed [7]. The absorption of light in tissue causes a local elevation in temperature. Tissue heat transfer due to the deposited light is described by the bioheat transfer equation taking into account conduction, convection by blood and possible heat sources (Q). Convection between tissue surface and surrounding air, radiation and evaporation are processes that have to be modelled as appropriate boundary conditions.

$$q_{conv} = h_{amb}(T_s - T_{amb}) \tag{2}$$

where q_{conv} is the heat flux owing to convection and T_s is the temperature at the surface of the skin exposed to the environment. Assuming that the average temperature at the surface of the skin is 34°C, and using values of $h_{amb} = 10$ and $T_{amb} = 25$°C, q_{conv} is calculated to be $90\,\mathrm{Wm}^{-2}$ [8].

The laser energy radiated at each end of a fiber act as a spatial heat source defined by

$$Q_{laser} = aI_0 e^{-k_{dis}A} \tag{3}$$

In the above equation, the variable I_0 is the intensity of the laser. I_0 is calculated by assuming an area of tissue, and an output power of the laser. The variable k_{dis} is the dissipation constant, and describes the loss of energy over time in the tissue. The variable A is the normal distance between the end point of the fiber and points in the laser beam.

Without loss of generality, several assumptions can be made for simplicity such that the absorbtion coefficient of the skin for CO_2 radiation is nearly the same as water ($\mu_a = 792\,\mathrm{cm}^{-1}$) [9], and for Nd : YAP radiation is aproximately $\mu_a \cong 10\,\mathrm{cm}^{-1}$. Based on these assumptions, results reveal that 65% of incident radiation is absorbed within the first 0.015 mm layer for CO_2, and within the first 1 mm for Nd : YAP. However, striking results about the differences between CO_2 Nd : YAP effects were obtained for the irradiation of white skin. Despite of the usage of higher surface charge density for Nd : YAP, the induced basal skin temperature increase was approxiamety 0.1 of that obtained with CO_2.

3. FINITE ELEMENT METHOD SIMULATIONS

The numerical solution relies on the Finite Element Method (FEM), in which the geometry studied is divided into a finite element mesh with a computer software that makes it possible to numerically solve partial differential equations. Thus, instead of trying to solve a highly non-linear problem

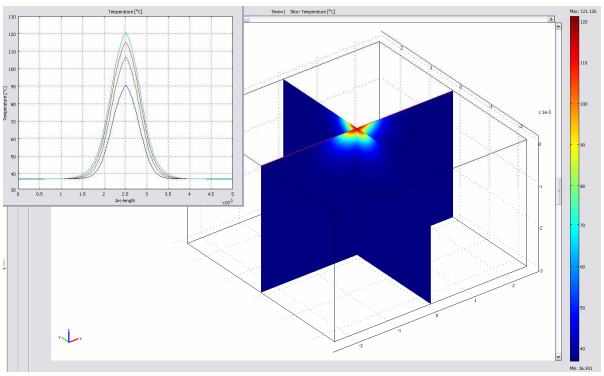

Figure 1: CO_2 laser source, longitudinal view.

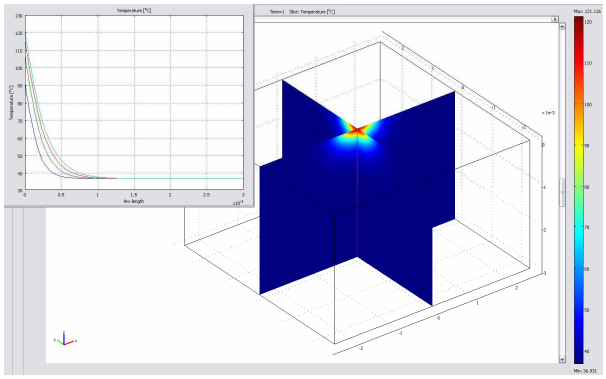

Figure 2: CO_2 laser source, cross sectional view.

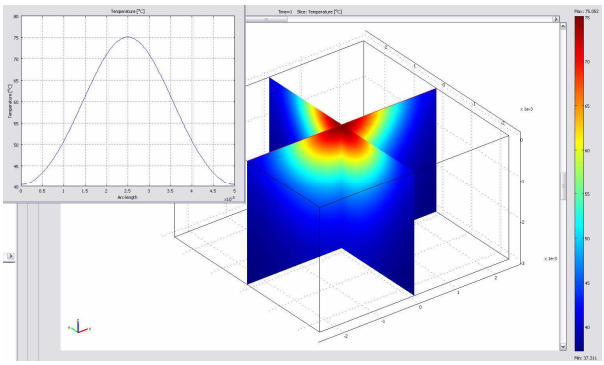

Figure 3: Nd : YAG laser source, longitudinal view.

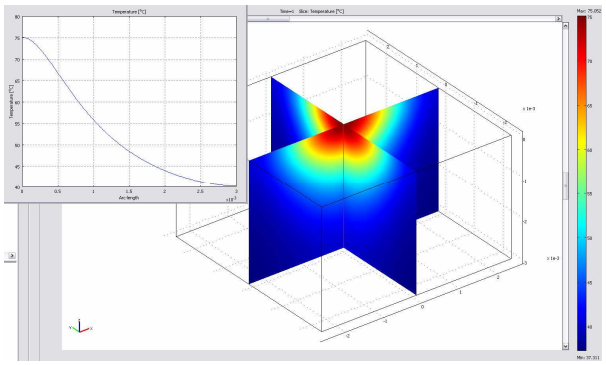

Figure 4: Nd : YAG laser source, cross sectional view.

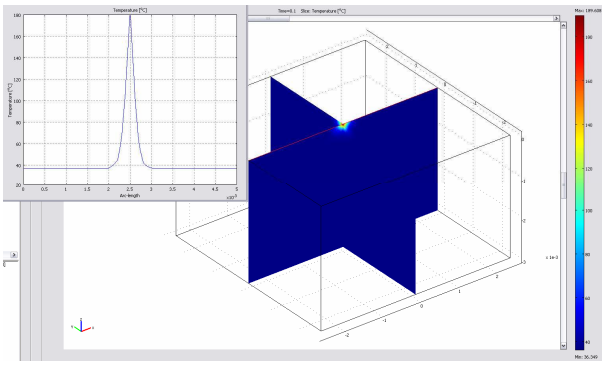

Figure 5: ArF excimer laser source, longitudinal view.

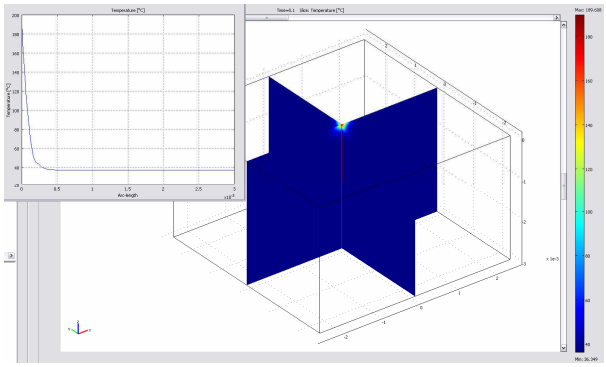

Figure 6: ArF excimer laser source, cross sectional view.

on the entire geometry, an approximate solution is sought in each element. If this element is considerably small the physical problem is assumed to vary linearly.

The computational model is simulated for a $5 * 5 * 3$ mm single layer tissue. The bottom surface of the tissue is assumed to be located within the body core. We applied several laser light sources including CO_2, Nd : YAG and ArF excimer laser. For the first simulation 10600 nm CO_2 laser in IR region used and absorbivity value of 79200 m^{-1} is used for skin. Additional simulation results are given for 1064 nm Nd : YAG laser in NIR region again for skin and 1000 m^{-1} absorbivity coefficient is used. Finally in UV region, 193 nm ArF excimer laser is used and absorbivity value of 255800 m^{-1} is accepted for human eye lens. Cross sectional and longitudinal views of simulations for the three types of laser source are given in the following figures.

4. CONCLUSIONS

In this paper, a single layer model of the human skin to predict the temperature distribution is developed and simulated for laser light. In order to describe the heat flux flow, Pennes bio-heat equation has been chosen as a basis, and the results are obtained numerically using the finite element method. These outcomes show off good agreement when compared with the solutions from literature obtained using established finite volume approaches.

The results obtained from the study reveal the important parameters, which significantly affect the thermal response of skin towards heat, as exposure duration and wavelength of the beam, as well as the area and type of the tissue.

Further improvements to the analysis carried out in this study can be established in future studies in such a way that multi layer modeling and simulation of the biological tissue will be a more realistic model to increase the reliability of the approach, for better understanding of the physiological response of the skin tissue.

The heating effect of several light sources on human skin tissue has not been reported yet; and the safety distance of lights have not yet been proposed. Though there are some efforts by International Commission on NonIonizing Radiation Protection (ICNIRP), the International Electrotechnical Commission (IEC) and American National Standards Institute (ANSI) to develop

regulation about light hazards concentrated not only on skin tissue, but also on eye injury due to radiated energy. Consequently, the thermal analysis carried out in the present work can be used for this goal as well.

ACKNOWLEDGMENT

This paper is supported by Boğaziçi University Foundation (BUVAK).

REFERENCES

1. Pennes, H. H., "Analysis of tissue and arterial blood temperatures in the resting human forearm," *Journal of Applied Physiology*, Vol. 1, 93–122, 1948.
2. Yoon, G., A. J. Welch, M. Motamedi, and M. C. J. Van Gemert, "Development and application of three-dimensional light distribution model for laser irradiated tissue," *IEEE Journal of Quantum Electronics*, Vol. 23, No. 10, 1721–1733, 1987.
3. Vo-Dinh, T., *Biomedical Photonics Handbook*, CRC Press, Boca Raton, 2003.
4. Kolios, M. C., A. E. Worthington, M. D. Sherar, and J. W. Hunt, "Experimental evaluation of two simple thermal models using transient temperature analysis," *Physics in Medicine and Biology*, Vol. 43, 3325–3340, 1998.
5. Verhey, J. F., Y. Mohammed, A. Ludwig, and K. Giese, "Implementation of a practical model for light and heat distribution using laser-induced thermo therapy near to a large vessel," *Physics in Medicine and Biology*, Vol. 48, 3595–3610, 2003.
6. Dua, R. and S. Chakraboty, "A novel modeling and simulation technique of photo-thermal interactions between lasers and living biological tissues undergoing multiple changes in phase," *Computers in Biology and Medicine*, Vol. 35, 447–462, 2005.
7. Zhou, J., Y. Zhang, and J. K. Chen, "An axisymmetric dual-phase-lag bioheat model for laser heating of living tissues," *International Journal of Thermal Sciences*, Vol. 48, 1477–1485, 2009.
8. Ng, E. Y. K., H. M. Tan, and E. H. Obi, "Prediction and parametric analysis of thermal profiles within heated human skin using the boundary element method," *Phil. Trans. R. Soc.*, 655–678, 2010.
9. Plaghki, L. and A. Mouraux, "How do we selectively activate skin nociceptors with a high power infrared laser? Physiology and biophysics of laser stimulation," *Neurophysiol Clin*, Vol. 33, No. 6, 269–277, 2003.

Using Bioheat Equation 3D WEB-spline Prediction of Ocular Surface Temperature

F. C. Kunter and S. S. Seker
Department of Electrical and Electronics Engineering, Bogazici University, Turkey

Abstract— A bioheat transfer model of the human eye is constructed using weighted extended b-splines as shape functions for the finite element method. This newly developed computational approach is employed to calculate the steady-state temperature distribution in a normal human eye. Three dimensional modeling is simulated using these new finite elements in conjunction with linear, quadratic and cubic b-splines. Our findings indicate that weighted extended b-spline solutions improve the computational methods for health care.

1. INTRODUCTION

Modeling of the heat distribution in the human eye has been popular for the last century with different kinds of techniques taking advantage of the advancements in computational technology. In earlier studies, the finite difference time domain method (FDTD) was used to solve Pennes bioheat equations numerically. One of the first eye models in the literature was developed by Taflove [1]. They used the FDTD to calculate the transient solutions of the temperature distribution in a microwave-irradiated human eye. AI-Badwaihy [2] also examined the thermal effects of microwave radiation on the human eye for the steady-state temperature distribution [3, 4] then developed a mathematical model based on the FDTD method to calculate the transient and steady-state temperature distributions in the normal unexposed human eye using the data he observed from the measurements on rabbit eyes.

Amara [5] and Scott [6] constructed a two dimensional (2D) FEM of the human eye to analyze the temperature profile during steady-state. Later Scott [7] used her model to compute the temperature rise in the eye when exposed to infrared radiation. The study of Scott [6, 7] was improved by Ng [8, 9], and Ooi [10] respectively. They presented a 2D and three dimensional (3D) finite element and 2D boundary element human eye models which were developed to simulate thermal steady-state conditions of the eye based on the properties and parameters reported in the open literature.

In the present paper, FEM with weighted extended b-splines (web-spline) are applied to analyze the steady-state temperature distribution in 3D models of the human eye with no external sources. B-splines as piecewise polynomial approximations are widely used in many applications. De Boor [11]'s contributions suggest the use of b-splines as finite elements basis functions. Despite the fact that boundary conditions and stability requirements prevent b-splines from being used on uniform grids, these difficulties can be overcome with the new method called web-spline. Hollig [12] constructed the web-spline method and used it with the FEM. Thus the combined advantages of standard finite elements and b-spline representations inspired many authors to work on this new subject [13–15]. The benefits of using web-splines in approximating the heat distribution in the eye are that no mesh generation is required and uniform grids are used instead of irregular partitions of domain, thus eliminating the difficult and time consuming preprocessing step. In fact, as reported in this paper, high accuracy can be obtained with relatively few parameters.

2. MATHEMATICAL MODEL OF THE HUMAN EYE

The 3D models of the human eye are developed in this section. Simplifying assumptions concerning the geometry and structure of the eye are made in order to validate our web-spline model of the human eye using the latest studies done with FEM. The eye is divided into six regions comprising the cornea, the aqueous humor, the lens, the iris, the vitreous humor, and the sclera. Each region is assumed to be homogeneous and isotropic. The thermal properties for each region are obtained based on [8] and the value for each is tabulated in Table 1. In addition, the coordinates of each region are modeled as in [8].

The governing differential equation for temperature distribution is the Pennes bioheat transfer equation:

$$\rho c \frac{\partial T}{\partial t} = \nabla(k \nabla T) + H \quad \text{in} \quad \Omega \,(\text{inside the eye}) \tag{1}$$

Table 1: Properties of the human eye for different domains [8].

Domains	Thermal Cond. (W $m^{-1}C^{-1}$)	Density (kgm^{-3})	Specific Heat Cap. ($Jkg^{-1}C^{-1}$)
Cornea	0.58	4178	1050
Aqueous humor	0.58	3997	996
Lens	0.40	3000	1050
Iris	1.0042	3180	1100
Vitreous humor	0.603	4178	1000
Sclera	1.0042	3180	1100

where Ω is the domain studied and Γ_1, Γ_2, Γ_3 are its boundaries. The boundary conditions are specified on the pupillary axis, the sclera and the cornea, given in (2), (3), and (4), respectively.

$$k\frac{\partial T}{\partial n} = 0 \quad \text{on} \quad \Gamma_1(\text{the pupillary axis}) \tag{2}$$

$$-k\frac{\partial T}{\partial n} = h_s(T - T_b) \quad \text{on} \quad \Gamma_2(\text{the sclera}) \tag{3}$$

$$-k\frac{\partial T}{\partial n} = E + h_c(T - T_{amb}) + \sigma\varepsilon(T^4 - T_{amb}^4) \quad \text{on} \quad \Gamma_3(\text{the anterior cornea surface}) \tag{4}$$

The parameters k, ρ, and c which refer to thermal conductivity, specific heat capacity, and density, respectively, are assumed constant within each region and with temperature variations. The coefficients h_s ($65\,\mathrm{Wm^{-2}C^{-1}}$) and h_c ($10\,\mathrm{Wm^{-2}C^{-1}}$) describe the thermal exchanges by convection on the eye surface, respectively, from sclera to body core and from cornea to the surroundings. The other terms describing the radiative heat transfer are represented by T, unknown temperature (°C); t, time (s); E, evaporation rate ($40\,\mathrm{Wm^{-2}}$); T_{amb}, ambient temperature ($25°C$); T_b, blood temperature (37°C); n, the unit vector outward normal (m); σ, Stefan constant ($5.67 \times 10^{-8}\,\mathrm{Wm^{-2}K^{-4}}$); ε, emissivity of corneal surface (0.975); H, heat source ($\mathrm{Wm^{-3}}$).

The initial temperature distribution ($t = 0$) is found by solving the steady-state heat transfer equation with no external heat sources as in,

$$\nabla(k\nabla T) = 0 \tag{5}$$

3. SIMULATION RESULTS

In this section, we investigate the steady-state temperature distribution in 3D unexposed human eye model, with the use of the web-spline method. Grid convergence analysis has been done. The simulations are performed using linear, quadratic and cubic b-splines with 0.125 grid width. In order to confirm the validity of our results, we compare them with those reported in [6, 8], and [9]. We adjust the thermal properties of the eye tissue constants and size of our model to those in [9].

The 3D model is constructed by revolving one half of the 2D model 360° around its horizontal pupilliary axis and is depicted in Figure 1. First, grid convergence analysis is illustrated in Figure 2 for cubic b-splines where the optimum grid width is calculated to be 0.125 (5203 grids) when the gradient of the graph approaches zero. Thus, it is assumed that any decreases in the grid width do not change the simulation results.

Overview of the 3D human eye model for two layers with the outer, the extended inner and the standard inner cubic web-splines for a grid width of 0.125 are shown in Figure 3. There are 2843 extended inner b-splines marked with blue circles, 1754 outer b-splines marked with white circles and 606 standard inner b-splines which appear in the middle layer of the sphere. If larger grid width had been used, all inner b-splines would be affected by the outer b-splines and become extended inner b-splines.

The numerical value of the temperature in the thermal pattern of the eye model is calculated to be 34.52°C for linear, 34.55°C for quadratic, and 34.62°C for cubic web-splines at the center of the corneal surface. Figure 4 plots the local temperature variation along the horizontal pupilliary axis for the FEM models developed by [6]'s 2D, [9]'s 3D models, and the current 3D cubic web-spline model. The temperature distribution of the 3D web-spline model is very similar to those in [6] and [9]. Slight differences in the compared results are mostly attributable to the differences in the modeling of the human eye.

Figure 1: The 3D human eye model.

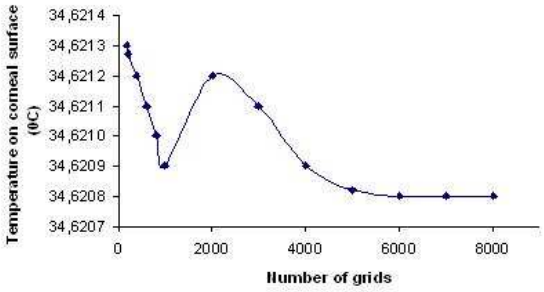

Figure 2: Grid convergence for the 3D web-spline model.

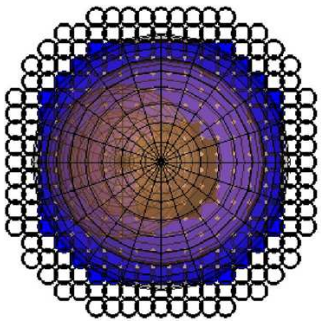

Figure 3: Grid representation for the 3D human eye model.

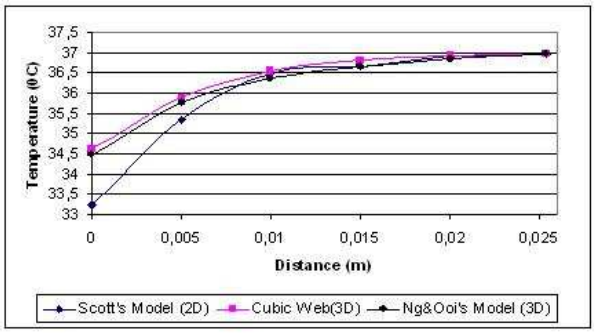

Figure 4: Comparison of the results for the 3D model using the methods in [6, 9] and the cubic web-spline method.

Table 2: Comparison between the results of FEM and the web-spline method on the corneal surface with the mean value of 34.65°C.

Author	Method used	Temp. Value (°C)	Absolute Diff. (°C)	Percentage Diff. (°C)
[6]	FEM	33.25	1.4	4.04
[8]	FEM	33.64	1.0	2.91
[9]	FEM	34.48	0.17	0.49
Kunter (3D)	Web-spline (linear)	34.52	0.13	0.38
Kunter (3D)	Web-spline (quadratic)	34.55	0.1	0.29
Kunter (3D)	Web-spline (cubic)	34.62	0.03	0.09

The simulation results are compared with the values reported by [8] in which they summarized the results of the corneal surface temperature obtained from the previous studies including the experimental and numerical studies with the mean value of 34.65°C.

Table 2 summarizes the comparisons between the FEM results on the corneal surface inside the human eye model and the web-spline model. When we compare the simulation results with the mean value of 34.65°C on the corneal surface, the current 3D model obtained a discrepancy of only 0.178% while the result of [8] produced a discrepancy of 0.455% and [9] produced a discrepancy of 0.33%. There are some deviations in the results. The reasons for these deviations are the different ambient temperature used (20°C versus 25°C) and the different approximations of material properties in the model. The choice of 25°C ambient temperature in the current model is based on a typical laboratory condition in Turkey. In [8], the iris and ciliary body were assumed to have properties similar to aqueous humor whereas the current model obtained different properties for iris and sclera.

The number of grids generated in the 3D web-spline model is 2904, 4272, and 5203 for linear, quadratic and cubic b-splines, respectively, whereas 54,796 elements had been used in [9]. The computation time is 1.2 s, 1.4 s, and 1.5 s for linear, quadratic and cubic b-splines,respectively.

Highly accurate results have been obtained with this new model at very low computation time, since it does not use mesh generation.

4. CONCLUSION

A FEM with web-splines, which models the heat transfer in the normal unexposed 2D and 3D representations of the human eye have been developed and employed to calculate the steady-state temperature distribution based on the properties and parameters reported in the literature. Error analysis indicates that our web-spline based method is successful in determining the temperature distribution in the eye. The errors decrease with increasing basis spline degrees. Besides diminishing the number of nodes, low computational time is also achieved by the web-spline method. The results indicate that FEM with web-spline method is observed to offer a much better performance than the standard FEM.

Grid width (h) optimization is done by decreasing h in dependence of the domain. It is observed that below 0.125 in 3D web-spline models, decreasing h does not affect the results substantially. Thus, for saving the computational power and memory, higher numbers of grids are not tested. With the grid convergence number estimates, it is shown that this method reaches higher precision in a shorter period of time with fewer nodes.

This new method bridges the gap between geometric modeling and numerical simulation. In this paper, we introduce and implement a minimal degree variant of the web-method for 2D and 3D boundary value problems. It is intended primarily for simulations where computational speed is of key importance and only moderate accuracy in simulation parameters is required (e.g., because of missing precision of the physical model, measurement errors, etc.). Pennes' bioheat transfer equation as a basic model problem already exhibits the essential features of the new method, in particular, the treatment of domains with complicated boundaries via a special integration technique.

ACKNOWLEDGMENT

This paper was supported by Bogazici University Foundation (BUVAK).

REFERENCES

1. Taflove, A. and M. Brodwin, "Computation of the electromagnetic fields and induced temperatures within a model of the microwave-irradiated human eye," *IEEE Trans. Microw. Theory Tech.*, Vol. 23, No. 11, 888–896, 1975.
2. AI-Badwaihy, K. A. and A. B. Youssef, *Biological Effects of Electromagnetic Waves*, C. C. Johnson and M. L. Shore, ed., Vol. 1, 61–78, HEW Publication, 1976.
3. Lagendijk, J. W., "A mathematical model to calculate temperature distributions in human and rabbit eyes during hyperthermic treatment," *Phys. Med. Biol.*, Vol. 27, No. 11, 1301–1311, 1982.
4. Hirata, A., S. Matsuyama, and T. Shiozawa, "Temperature rises in the human eye exposed to EM waves in the frequency range 0.6–6 GHz," *IEEE Trans. Electromagn. Compat.*, Vol. 42, No. 4, 386–393, 2000.
5. Amara, E. H., "Numerical investigations on thermal effects of laser ocular media interaction," *Int J. Heat Mass Trans.*, Vol. 38, 2479–2488, 1995.
6. Scott, J. A., "A finite element model of heat transport in the human eye," *Phys. Med. Biol.*, Vol. 33, No. 2, 227–241, 1988.
7. Scott, J. A., "The computation of temperature rises in the human eye induced by infrared radiation," *Phys. Med. Biol.*, Vol. 33, No. 2, 243–257, 1988.
8. Ng, E. Y. K. and E. H. Ooi, "FEM simulation of the eye structure with bioheat analysis," *Comput. Methods Programs Biomed.*, Vol. 82, No. 3, 268–276, 2006.
9. Ng, E. Y. K. and E. H. Ooi, "Ocular surface temperature: A 3D FEM prediction using bioheat equation," *Comput. Biol. Med.*, Vol. 37, 829–835, 2007.
10. Ooi, E. H., W. T. Ang, and E. Y. K. Ng, "Bioheat transfer in the human eye: A boundary element approach," *Eng. Anal. Bound. Elem.*, Vol. 31, 494–500, 2007.
11. De Boor, C., "On calculating with B-splines," *J. Approx. Theory*, Vol. 6, 50–62, 1972.
12. Hollig, K., *Finite Element Methods with B-splines*, Vol. 26, Frontiers in Applied Mathematics, Society for Industrial and Applied Mathematics (SIAM), Philadelphia, 2003.

13. Apaydn, G., S. Seker, and N. Ari, "Weighted extended B-splines for one dimensional electromagnetic problems," *Applied Mathematics and Computation*, Vol. 190, 1125–1135, 2007.
14. Apaydn, G., S. Seker, and N. Ari, "Application of web-spline method in electromagnetics," *International Journal of Electronic and Communication (AEU)*, Vol. 62, 163–173, 2008.
15. Kunter, F. C, G. Apaydin, N. Ari, and S. Seker, "Web-spline solution of axisymmetric cylindrical problems," *Asia Pacific Microwave Conference*, Hong Kong and Macau, December 2008.

On the Integration of Behavioral Component Descriptions in the Full-wave Transmission-line Modeling Method

I. Scott[1], **G. Kergonou**[1], **C. Christopoulos**[1], **F. Canavero**[2], **S. Greedy**[1], **Dave W. P. Thomas**[1], **and P. Sewell**[1]

[1]George Green Institute for Electromagnetics Research, University of Nottingham
University Park, Nottingham NG7 2RD, UK
[2]Dipartimento di Elettronica, Politecnico di Torino
Corso Duca degli Abruzzi, 24, Torino 10129, Italy

Abstract— The simulation of complex digital systems incorporating ICs, lumped components, and field phenomena is a necessary activity for many applications. Predicting the practical behavior of systems based upon just the schematical circuit diagrams (which indicate topology) fails to include the consequences of field effects (which require geometrical information), which given the ever increasing frequencies of modern digital systems, are of paramount importance. On the other hand, comprehensive simulation of IC packages using full-wave models is prohibitively computationally expensive and time consuming to complete. Embedding behavioral level descriptions of complex electronic components within a full-wave field solver circumvents these problems, and forms the subject of this paper. The Transmission-Line Modeling (TLM) method is used as the full-wave solver, and two behavioral models, "macro" and "IBIS", are embedded into the TLM to model the sources and loads presented by complex ICs. The two methods of representing the IC behavior are then illustrated and compared with a canonical test structure.

1. INTRODUCTION

Behavioral models seek to reproduce the input/output port nonlinear behavior of digital integrated circuits (ICs). For example, the IBIS (Input/Output Buffer Information Specification) standard [1, 2] describes a component by using a collection of voltage and current lookup tables. Macromodels on the other hand, rely on a local linear state-space parametric representation of the currents as a function of the voltages [3]. Both descriptions hide the IC internal structure and enable the insertion of active components as sub-structures within circuit simulators or full-wave solvers. The last option greatly increases the EM simulator capacity where the ideal diode is the only fully inserted nonlinear device. Also, a wider selection of systems can be efficiently modeled. This is both commercially and technologically essential for accurate prediction of electromagnetic compatibility and signal integrity of high-speed electronic applications.

The Transmission-Line Modeling (TLM) [4] method offers a suitable environment for incorporating active non-linear models. The method exploits the analogy between field propagation in space and voltage/current propagation in a transmission-line network. It has the advantage of calculating field components at the same time and at the same location, with guaranteed stability due to the underlying electrical circuit formulation [4]. Coupling IC behavioural models can be realised in two ways: either through an external link to a circuit simulator such as SPICE [5], or by direct embedding [6]. The first approach gives access to a wide range of models via the SPICE libraries. Unfortunately, the calculation speed is hindered due to the repeated need to invoke SPICE for every time-step of the EM solver. The second option removes the slow speed problem. It forms the subject of this paper which builds upon the previous macromodel research [7] to include an IBIS description of a component. Since the IBIS standard is widely used in industry, it offers a wide selection of devices that can be inserted without the need to use the SPICE libraries. The paper is organized as follows. Section 2 reviews the IBIS component description while Section 3 develops the new IBIS-TLM interface. Finally, Section 4 provides a comparison of the TLM-IBIS and TLM-macromodel hybridization before concluding with a discussion on the topics raised and further research suggestions.

2. REVIEW OF IBIS

The IBIS file of a component contains a collection of lookup tables of voltages (V) and currents (I), along with temperature ranges, package parameters (resistance, inductance, and capacitance), die capacitance, voltage ranges and pin configurations. The tables define the I-V relationship of the pullup/pulldown transistors' and clamping diodes of the generic buffer shown in 1. This

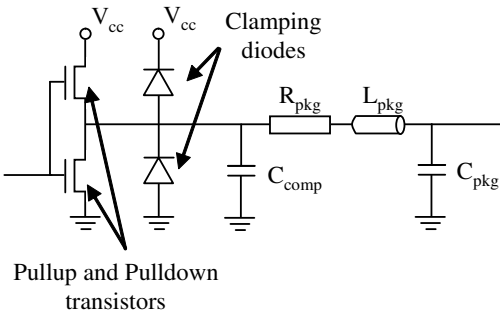

Figure 1: IBIS buffer representation. I-V tables are stored for each of the components (pulldown and pullup transistors and the clamping diodes).

representation enables the consideration of the input and output ports of a complex device while removing the need to model the internal device structure.

Depending on the input or output port, the I-V tables differ. For a receiver, only one or both of the clamping diodes are actually necessary. For a driver, the clamping diodes along with the transistors are considered. The inclusion of all or just some of the clamps/transistors is device dependant. Reference [2] contains the methodology behind the IBIS I-V tables and their usage. It also details how the current is determined as a function of the incident voltage. We will assume in the following that the IBIS current is calculated as in [2] and focus solely upon the interface of IBIS with TLM.

3. TLM-IBIS INTERFACE

TLM is based upon the analogy between the propagation of electromagnetic fields and voltage impulses traveling on discrete transmission-lines. In its simplest form the TLM method discretizes a homogenous space into cubes of side Δl, termed nodes. Voltage impulses scatter at each node according to network theory and subsequently propagate to the neighboring nodes. At any one time-step there are two quantities present upon each transmission-line connecting to each node, the reflected voltage V^r and the incident voltage V^i. Repetition of this scatter-propagate procedure provides an explicit and stable time stepping algorithm that mimics electromagnetic field behavior [4]. For our purposes, this description of TLM is adequate.

Figure 2(a) shows the new IBIS-TLM interface. It consists of a 1D TLM line, termed 'circuit TLM', linking the 3D TLM mesh to the IBIS model. The circuit TLM contains the IBIS package components through the R_{pkg} resistance and Z_{pkg} impedance, calculated from the inductance and capacitance package values. It also includes the IBIS die capacitance C_comp through the TLM link-node impedance Z_{C_comp}. The circuit TLM is connected to the TLM mesh at the boundary of a single cell. The cell is defined by the free space impedance Z_0, which entails a change in impedance at the connection. This is solved using the standard TLM formulation [4]. On the other side, the circuit TLM is interfaced to the IBIS component description. At that level the situation is complicated by the non-linear nature of the IBIS termination. Fig. 2(b) presents the Thevenin circuit at the interface. For the case of a driver, V_{Drv} is the IBIS source voltage, i is the current provided by the IBIS load, while V^r is the reflected voltage from the TLM node interfacing with the IBIS boundary. The subscript k denotes the TLM time-step.

For the driver, the non-linear equation at the interface between IBIS and TLM at time-step k is

$$2_kV^r - iZ_{C\_comp} - {}_kV_{Drv} - {}_kV = 0. \tag{1}$$

The conventional Newton-Raphson method is used to solve for the unknown quantities (i and V) using the IBIS lookup tables to define i given V [2]. Knowing V, the reflection of the IBIS termination at the TLM port can be calculated as

$${}_kV^i = {}_kV - {}_kV^r + {}_kV_{Drv}. \tag{2}$$

where the IBIS term (V_{Drv}) is now injected onto the TLM node. In this manner the IBIS termination is completely defined from the TLM perspective. Equations (1)–(2) are repeated for each time-step of the TLM simulation. In a similar fashion, the load interface is given by

$$2_kV^r - iZ_{C\_comp} - {}_kV_{TLM} = 0, \tag{3}$$

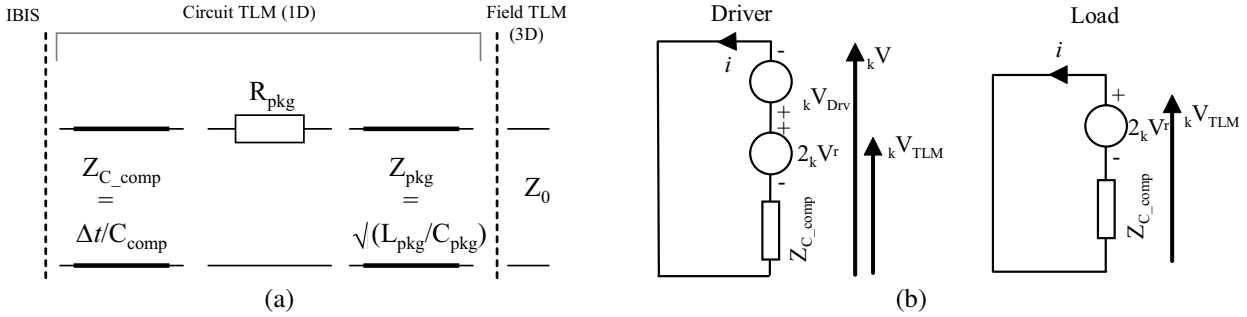

Figure 2: IBIS-TLM interface: (a) Circuit TLM. Δt is the temporal sampling of the TLM model. (b) Thevenin circuits for the IBIS driver and load interfaces.

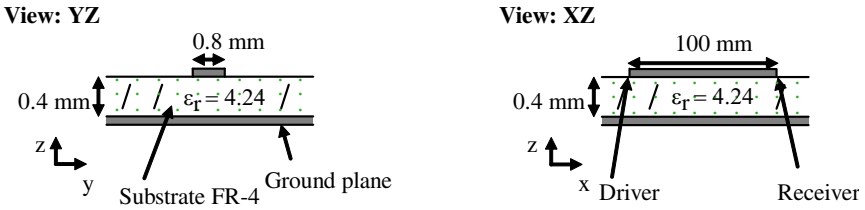

Figure 3: Test structure. 50 Ω microstrip track on FR4 substrate of height 0.4 mm and track width 0.8 mm. The driver inverter feeds the line at x, and the load inverter is placed at $x + 100$ mm.

where it is seen the IBIS voltage and TLM voltage are the same. The incident TLM voltage is ${}_kV^i = {}_kV_{TLM} - {}_kV^r$, since the IBIS source term is no longer present. Equations (1)–(3) allow the embedding of an IBIS description of a component as a boundary condition to a TLM node. The Newton-Raphson procedure typically converges within 5–10 iterations, so is of limited computational impact in comparison to the TLM simulation.

4. MACROMODEL AND IBIS COMPARISON

In this section we provide full-wave simulation results obtained with a simple microstrip test structure and the embedding of the macromodel and IBIS behavioral models. The macromodel-TLM hybridisation [7] is based on the Z-transform TLM formulation [8]. This TLM form enables a device insertion at the node center through a current source of the conductance of the component. The macromodels are generated from the $M\pi$ log (Macromodeling via Parametric Identification of LOgic Gates) software [3] using the HSPICE model supplied by the IC manufacturer. The models are established with a sampling time T_s different from the TLM time step Δt, they are thus resampled to Δt.

Figure 3 describes the test structure. It consists of a SN74AHC1GU04 single inverter IC [9] that drives a 50 Ω microstrip line loaded by a second SN74AHC1GU04 IC. The strip is 0.8 mm wide, 100 mm long, zero-thickness and perfectly conducting. The substrate is 0.4 mm thick with a relative permittivity $\varepsilon_r = 4.24$ and assumed lossless. For IBIS-TLM, the dielectric permittivity of the substrate is included through the use of stubs [4]. The configuration is surrounded by matched boundary conditions in the lateral and top faces and a perfect electric conductor at the substrate base.

The behavioural models are embedded in a single TLM cell: at the cell boundary for the IBIS-TLM and through a current source at the cell centre for the macromodel-TLM. The driver and receiver are located at the $x = 10.4$ mm and $x = 110.4$ mm nodes for the IBIS (macromodel) simulation. The macromodels are created under the power supply: $V_{CC} = 4.4$ V; $V_{ref} = 0$ V. It is noted that the macromodel has no internal link between receiver and driver for a single IC, so it is not possible to measure both at the same IC.

Figure 4 presents the results for both full-wave simulations with $V_{CC} = 4.4$ V, the spatial sampling $\Delta l = 0.4$ mm, the temporal step $\Delta t = 0.67$ ps, and for a 10 MHz signal.

The results indicate a close match between the two modelling methods for the rising edges at the driver and receiver, with a slight overshoot for the IBIS-TLM. The falling edges do not match as closely, but the same behaviour is observed. The differences can be explained by 1) the package

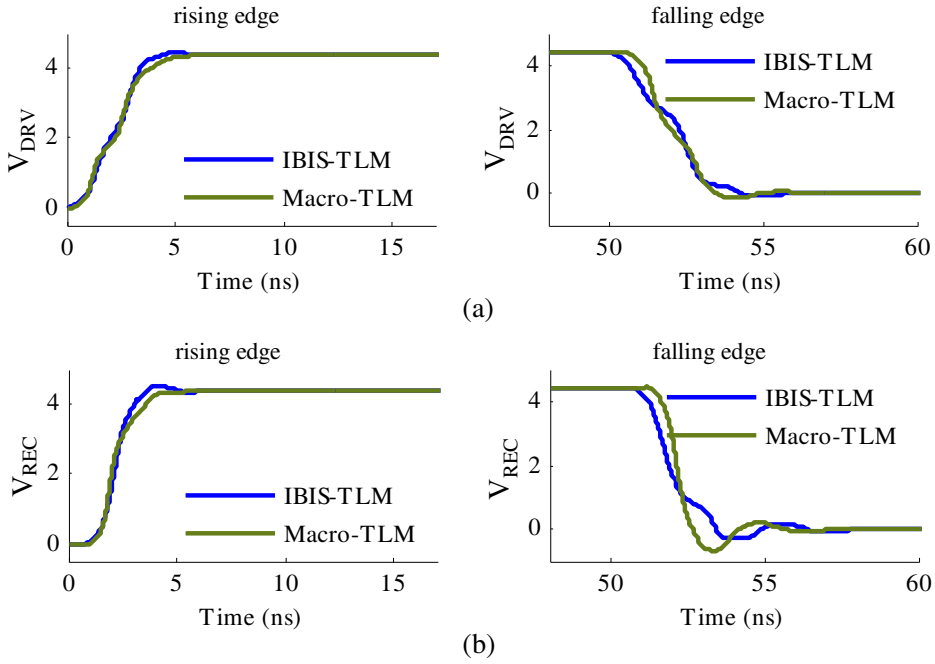

Figure 4: Rising and falling edges of the voltages for macro and IBIS models embedded into the TLM full-wave model of 3. $\Delta l = 0.4\,\text{mm}$, $\Delta t = 0.67\,\text{ps}$.

parameters and die capacitance (only for the IBIS model) that differ and 2) the process to generate the models. For example, to check the macromodel behaviour (before running the EM simulation), HSPICE simulations have been carried out. One with the transistor description of the IC; the other one with the driver and receiver macromodels. The results suggest a model limitation as the ripple presence on the falling edge of the driver does not appear with the transistor description model. In fact, the macromodels are generated under a long transmission-line hypothesis while we are dealing here with a short transmission-line (propagation delay about 0.67 ns).

5. CONCLUSION

The paper reported on the use of behavioral models within the full-wave field solver TLM. The formulation of the new IBIS component description when embedded into a TLM node was given. It was seen the behavioral component descriptions can be placed at a node centre or boundary, and that the choice between the two does not affect the results. IBIS component descriptions are widely available from IC manufacturers, and so, by successfully embedding an IBIS model into TLM, the paper has demonstrated the wide scope for using behavioral models inside field models. The inclusion of a complete IC port using only a single TLM node, minimizes the runtime of the numerical simulation, while allowing the modeling of complex components and devices. Future work will look at experimental validation of the results and the embedding of more complex structures, attempting to form a link between the input and output ports on a single IC using the IBIS model.

ACKNOWLEDGMENT

This work has been supported by the European grant MTKI -CT-2006-042707 and EPSRC EP/G00-9201/1.

REFERENCES

1. Leventhal, R. and L. Green, *Semiconductor Modeling: For Simulating Signal, Power, and Electromagnetic Integrity*, Springer, New York, NY, USA, 2006.
2. Mirmak, M., ed., *IBIS Modeling Cookbook, for IBIS Version 4.0*, The IBIS Open Forum, 2005.
3. Steviano, I. S., C. Siviero, F. Canavero, and I. Maio, "Behavioral modeling of digital devices via composite local-linear state-space relations," *IEEE Transactions on Instrumentation and Measurement*, Vol. 57, No. 8, 1757–1765, 2008.
4. Christopoulos, C., *The Transmission-Line Modeling Method: TLM*, Wiley-IEEE Press, 1995.

5. So, P. P. M. and W. J. R. Hoefer, "A TLM-SPICE interconnection framework for coupled field and circuit analysis in the time domain," *IEEE Transactions on Microwave Theory and Techniques*, Vol. 50, No. 12, 2728–2733, 2002.
6. Sobhy, M., E. Hosny, P. Russer, B. Isele, and C. Christopoulos, "Interfacing the transmission line method (TLM) and state-space (SS) techniques to analyse general non-linear structures," *Computation in Electromagnetics Conference*, 299–302, 1994.
7. Kergonou, G. and F. Canavero, "Hybridisation of non-linear behavioural models with the TLM full-field model," *EPEPS 2010*, 73–76, Austin, TX, USA, 2010.
8. Paul, J., C. Christopoulos, and D. W. P. Thomas, "Generalized material models in TLM — Part I: Materials with frequency-dependent properties," *IEEE Trans. on AP*, Vol. 47, No. 10, 1528–1534, October 1999.
9. http://www.ti.com/.

3D FEA of SMPM Accounting for Skew and End Windings

M. Hédi Gmiden and H. Trabelsi
Sfax Engineering School, University of Sfax, Tunisia

Abstract— This paper presents the use of the three dimensions finite element method for analyzing the surface mounted permanent magnet motor. The saturation of the motor is taken into account in determination of the flux distribution and the inductances. Skew and end windings are also taken into account. The results are presented and compared to demonstrate the effect of skew and end windings.

1. INTRODUCTION

Skew is applied to electrical machines in order to reduce undesirable effects such as cogging torques, higher-harmonic air-gap fields, torque ripple, vibrations, and noise [1]. In permanent magnet synchronous machines, generally, cogging torque is reduced by skewing the stator slots. The skewing of a cylindrical machine induces an electrical field in the azimuthally direction. The skewing destroys the typical translatory symmetry of a cylindrical machine. Different approaches for accounting skew have been reported. Commonly, multiple slices, each of them represented by a two-dimensional finite-element (FE) model, are connected in series in order to account for the skewing [2]. This approach mainly increases the computational cost of finite element machine simulations.

End winding inductance is generally treated as a small negligible component of the winding inductance in many motor applications [3]. However, the end winding inductance may actually be a significant percentage of the phase inductance, particularly for motors with low length/diameter ratio, small inherent phase inductances, or long-pitched windings. Some researchers have reported that the end winding inductance has a substantial influence in axial air-gap flux machines [4]. Hence, for such cases, the accurate calculation of the end winding inductance is necessary. Different methods for the calculation of end winding inductance have been reported [5, 6]. Of these, finite element analysis (FEA) has been directly applied to calculate inductance or used in conjunction with analytical methods. However, although the improved accuracy, FEA tends to be time-consuming, particularly when 3-dimensional analysis is used. Care should be taken when working with FEA modeling to ensure numerical accuracy. Therefore, an analytical technique is still attractive. Some researchers have reported on the derivation of fast analytical techniques [7], but the accuracy may be variable due to the simplifications made.

In the following, the three dimension finite element model of the study motor with the specific meshing are presented. Next, the key issue of the procedure: how to account skew and end winding of SMPM is discussed. Finally the obtained results are both presented and discussed achieving by a conclusion.

2. 3-D FE MACHINE MODELS

Three phase SMPM with stator slots (Figure 1) having no skewing and with different angle of skewing have been analyzed for two type of excitation, only permanent magnet (PM) excitation

Stator outer diameter	120 mm
Stator inner diameter	75 mm
rotor outer diameter	74 mm
rotor inner diameter	26 mm
Stator pole number	4
Stator slot number	24
Stack length	65 mm
Airgap length	0.5 mm
Slot area	65 mm^2

Table 1: Motor data.

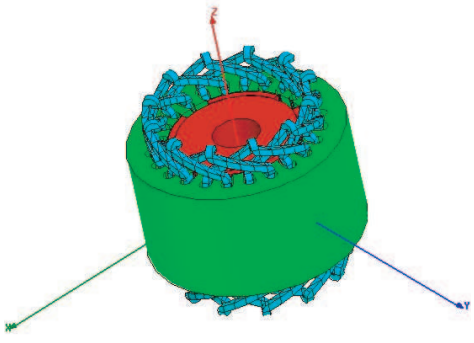

Figure 1: Three phase SMPM model.

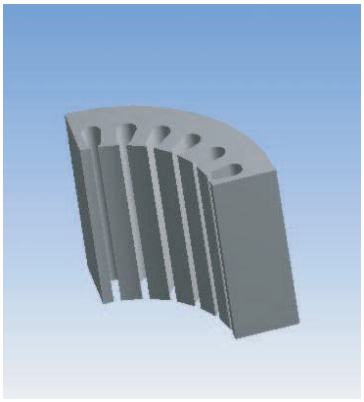

Figure 2: Stator slots having no skewing.

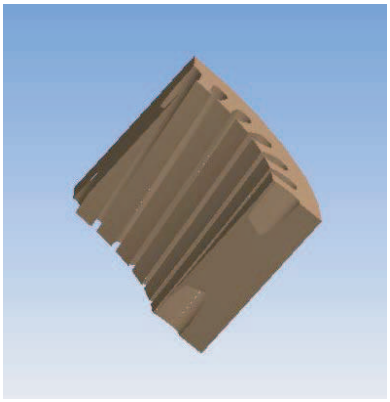

Figure 3: Stator slots with skew.

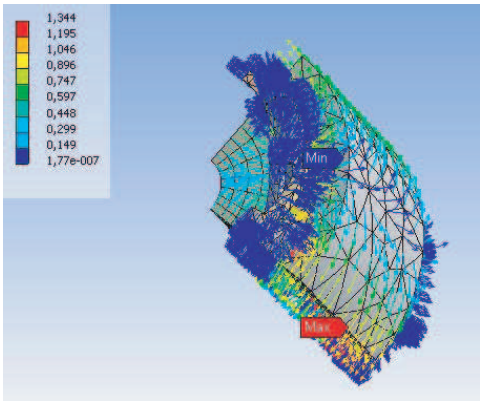

(a)

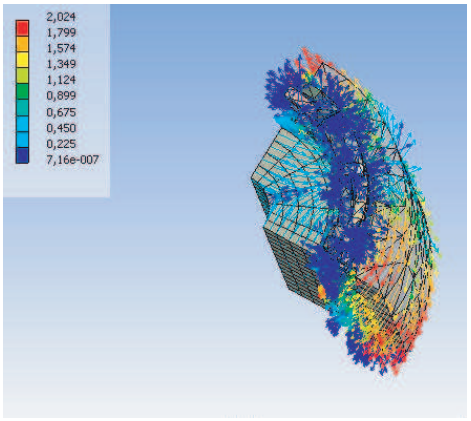

(b)

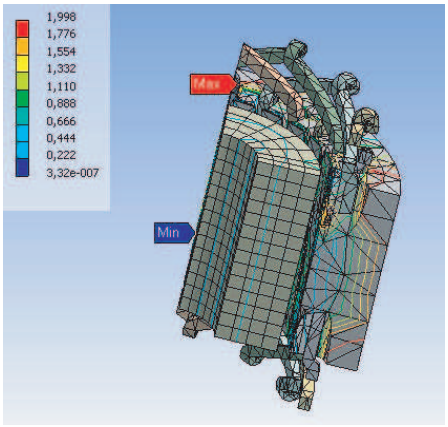

(c)

Figure 4: The flux distribution (a) by the magnet excitation, (b) by the stator current excitation and (c) by the magnet and the stator current.

and combined PM excitation current excitation for windings. Table 1 gives the details of the motor analyzed.

Figures 1 and 2 represent the stator slots having no skewing and with skew.

3. SIMULATION RESULTS

Figure 4(a) shows the flux distribution at different part of motor when only the magnet excitation is applied. Figure 4(b) represents the flux distribution at different region of motor when only the stator current excitation is applied. Figure 4(c) shows the flux distribution produced by the magnet and the stator current.

The value of inductance and the flux are illustrated in the Table 2. The Figure 5 shows the

Table 2: Inductance and flux.

Inductance (mH)	3.06
Flux (mwb)	9.3

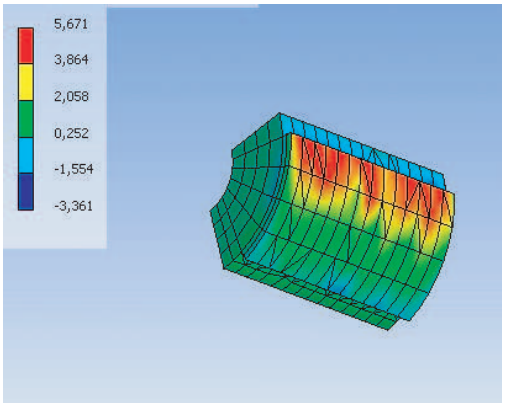

Figure 5: Torque at the rotor.

torque at the rotor.

4. CONCLUSIONS

In this paper, the effect skewed stator slots on the various performance parameter of a SMPM motor for only permanent magnet excitation and appropriate winding excitation pattern has been presented. It is observed that by skewing the cogging torque is reduced.

REFERENCES

1. Jaykumark, K., et al., "Three dimensional finite element analysis of doubly salient permanent magnet motor with skewed rotor teeth," *Finite Differences, Finite Elements, Finite Volumes, Boundary Elements (F-and-B'08)*, Malta, September 11–13, 2008.
2. De Gersem, H., K. Hameyer, and T. Weiland, "Skew interface conditions in 2-D finite-element machine models," *IEEE Transactions on Magnetics*, Vol. 39, No. 3, May 2003.
3. Tounzi, T., et al., "3-D approaches to determine the end winding inductances of a permanent-magnet linear synchronous motor," *IEEE Transactions on Magnetics*, Vol. 40, No. 2, March 2004.
4. Bumby, J. R.,et al., "Electromagnetic design of axial-flux permanent magnet machines," *IEE Proc.— Electr. Power Appl.*, Vol. 151, No. 2, 2004.
5. Chen, S., Z. Q. Zhu, and D. Howe, "Calculation of d- and q-axis inductances of PM brushless ac machines accounting for skew," *IEEE Transactions on Magnetics*, Vol. 41, No. 10, October 2005.
6. Geuzaine, C. and Remacle, J. F., "Gmsh: A 3-D finite element mesh generator with built-in pre- and post-processing facilities," *International Journal for Numerical Methods in Engineering*, Vol. 79, No. 11, 1309–1331, September 10, 2009.
7. Hsieh, M. F., et al., "Investigation on end winding inductance in motor stator windings," *IEEE Transactions on Magnetics*, Vol. 43, No. 6, June 2007.

Performance Improvement of Different Topologies of Claw Pole TFPM Based on a 3D FEA

Anis Njeh and Hafedh Trabelsi
CES, Sfax Engineering School, University of Sfax, BP 1173, 3038 Sfax, Tunisia

Abstract— The transverse flux permanent magnet machine (TFPM) is currently given an increasing attention, especially in electric and hybrid propulsion applications because of the highest output torque per unit volume ratio compared to the conventional electric machines. Although significant works have been carried out on the earlier topologies, much improvement of the TFPM performances is still required.

Tow topologies of claw pole TFPM are considered. The first one is the surface mounted magnets claw pole. The second one is the buried mounted magnet claw pole topology with flux concentrated design. Let us consider the same motor sizing, pole pair number and the same used materials features, the present work deals with, in a first step, a structure and flux path comparison between the tow topologies, then in a second step, a 3D Finite Element Analysis (FEA) based investigation of the output torque and the cogging torque of the proposed claw pole TFPM topologies for Performance improvement by increasing the output torque, doing so the influence of the cogging torque is analyzed.

1. INTRODUCTION

The transverse flux permanent magnet machines (TFPMs) are Introduced in the middle of the eighteenth's by *Weh* [1], TFPMs are presently considered as viable candidates for electric and hybrid propulsion applications. Such interest is mainly due to their high power density. Currently, many automotive manufacturers are involved in R&D projects focusing efficient and cost effective TFPM designs [2–6].

Claw pole TFPM combine the advantage of high specific torque and the ease manufacturing, It allows an easy assembly of any number of axially arranged phases.

Of particular interest is the three-phase TFPM, which takes advantage of using standard converters.

In a previous work [7, 8], a claw pole with 234 mm rotor diameter and 80 poles is studied for the choice of an optimized design illustrated in Figure 1, the rotor is made up of buried magnets alternated with soft magnetic composite (SMC) blocs.

A 50 pole concept of claw pole TFPM is constructed at university of Newcastle, the flux leakage is studied in [10], the rotor as illustrated in Figure 2 is made up of surface mounted magnets.

Guo with university of technology of Sydney [11] compared between tow types of 20 poles TFPMs with surface mounted magnets.

For instance, a comparison between the buried magnets claw pole topology and with surface magnets one is required considering the same dimensions and pole pair number and the same features of the used material.

Figure 1: Clawpole with buried.

Figure 2: Rotor with mounted magnets surface mounted magnets.

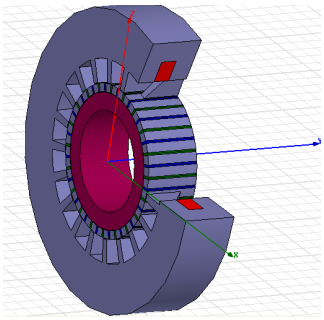

(a)

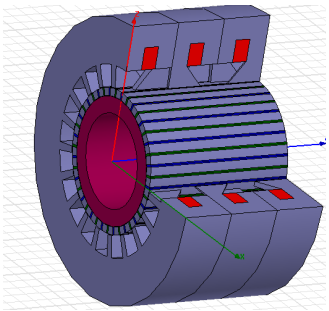

(b)

Figure 3: (a) Single phase with buried magnets topology. (b) Three phase machine with buried magnets.

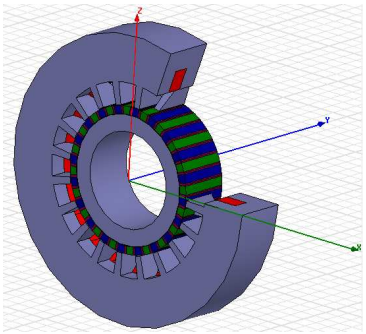

Figure 4: Single phase with surface magnets topology.

Although the claw pole with flux concentrating topology, exhibits at first glance a higher output torque, which reduces the magnet volume and machine cost, a comparative study and a FEA of the tow topologies is required to improve the TFPM performances, the paper develops this idea.

2. DESIGNED CLAW POLE TOPOLOGIES

2.1. Introduced Topologies

Figure 3(a) illustrate a single phase 40 pole concept of a claw pole TFPM The stator magnetic circuit is made up of SMC. It consists of a cylindrical set cut into two parts with claw pole teeth facing the rotor magnetic circuit. The stator electrical circuit is a simple ring winding which is inserted in a circumferential slot, in between the two parts of the stator SMC-made magnetic circuit. The rotor magnetic circuit is made up of buried magnets with tangential magnetization mounted with opposite magnetization in a flux concentrating arrangement alternated by SMC-made blocs which represent the rotor poles.

In order to obtain a smooth torque the solution is a three phase machine. After a previous study of the possible combination of the three phase arrangement [12], an aluminum barrier inserted in between stator phases is required for cogging torque reduction, so the simpler to manufacture is with the stator teeth of adjacent phases are shifted by 120°-electrical angle and the rotor poles are aligned as illustrated in Figure 3(b).

One other topology where the stator as previously described and the rotor magnetic circuit is made up of 40 surface magnets with radial magnetization, representing the rotor poles, the magnets are mounted with opposite magnetization and alternated by aluminum made blocs. A necessity of an inner SMC cylindrical part is required for the flux continuity as shown in Figure 4 for a single phase concept.

2.2. Used Materials

The designed topologies of the claw pole TFPM are made up of the following:

- SMC material: Somaloy 500 (0.6% LB1) [9] which is suitable for high-frequency operation and offers the feasibility of smooth 3D flux path.
- Magnet material: samarium-cobalt (Sm-Co) giving the possibility of working at high temperature and his high resistance to corrosion and oxidation which is crucial for automotive application.
- Non magnetic material: Aluminum.
- Winding material: Copper

3. FEA OF THE DESIGNED TOPOLOGIES

3.1. FEA Study Domain

For the sake of accurate results, the FEA is limited to a study domain which represents tow pole pitches of the total domain. The study domain presents 18°-mechanical angle.

Figure 5 illustrate the rotor study domain of the claw pole with surface mounted magnets and the magnetic flux distribution highlight the necessity of the use of the soft magnetic composite in the rotor magnetic circuit.

Figure 6 illustrate the flux distribution in the stator teeth and in the rotor study domain of the buried magnet topology.

3.2. Influence of the Magnet Opening Angle

Varying the magnet arc angle is a technique applied in most permanent magnet machine to improve the machine performance, this technique can be applied to increase the output torque produced by the interaction between stator and rotor poles. While varying the pole opening angle the flux linkage will be varied.

This technique consist of the study of the influence of the magnet opening angle on the output torque and in what follows, be applied for the surface and the buried magnet claw pole topologies to analyze the influence of this parameter on the machine performance and cost effectiveness directly linked to the rotor magnet opening angle.

While applying this technique for adjusting the magnet opening angle, the other dimensional parameters are kept constant.

3.3. FEA Results and Comparison

The magnet thickness of 5 mm kept constant, for the tow topologies, the same excitation current density of 6×10^6 A/m^2 and the pole pitch angle is 9°-mechanical angle corresponding to 180°-electrical angle, considering the rotor position of 4.5°-mechanical angle while varying only the magnet opening angle the obtained results are illustrated in Figure 7. The output torque of the buried topology is higher than the torque obtained with surface magnet one. Considering the opening angle of 90°-electrical angle one have up to three time greater torque, the torque is higher for the surface mounted magnet topology only for 180°-electrical angle where the pole opening angle is null of the buried magnet machine. For performance improvement of the surface mounted topology using this technique, the torque is proportional to the magnet opening angle and the highest value is of 4.8 Nm for a 180° magnet opening angle (a pole pitch).

From the point of view cost effectiveness the best choice is the buried magnet topology with 90° magnet opening angle because the highest torque is almost constant of 7 Nm while varying the magnet opening angle between 90° and 160°.

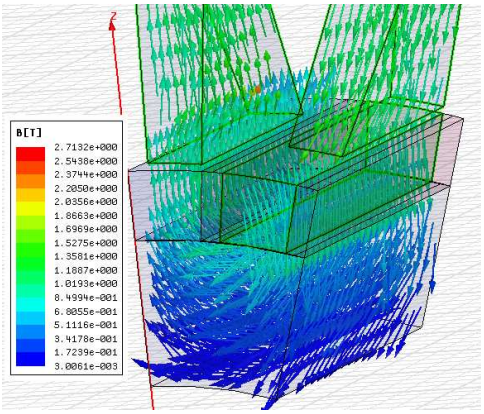

Figure 5: Study domain of the surface magnet topology.

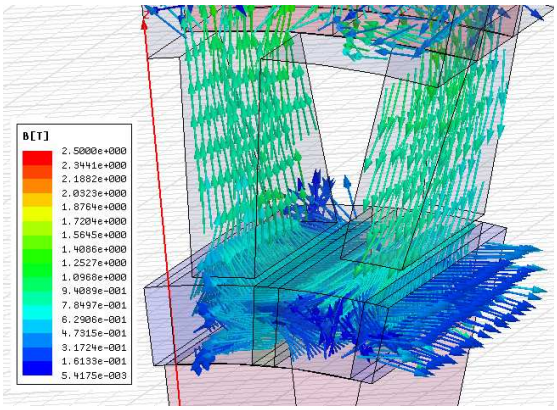

Figure 6: Study domain of the buried magnet topology.

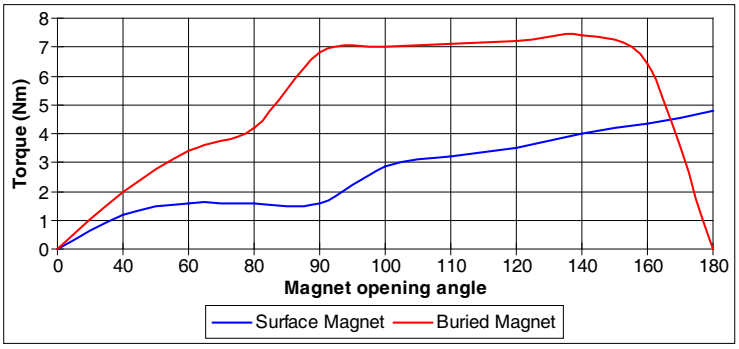

Figure 7: Magnet opening angle influence on the output torque.

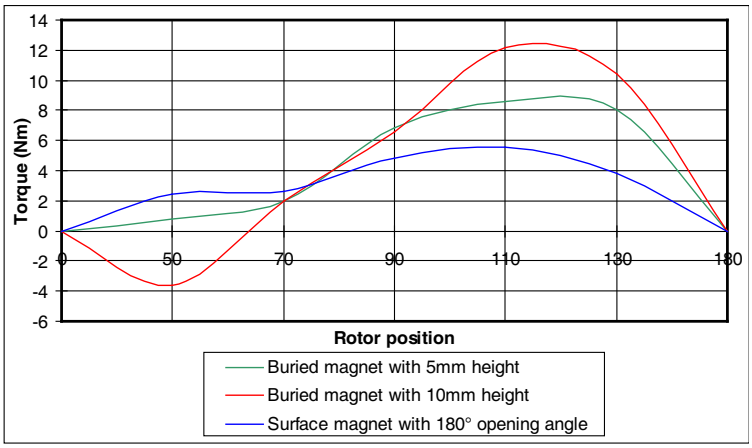

Figure 8: Torque-angle curves.

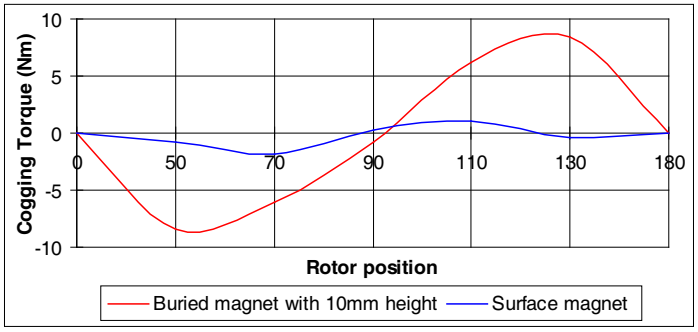

Figure 9: Cogging torque-angle curves.

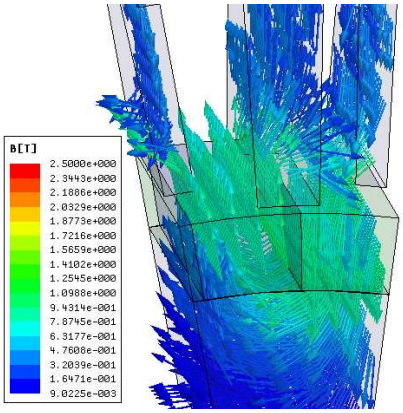

Figure 10: Flux shuntage phenomenon.

3.4. Torque-angle Curve

In what follow, we consider the torque-angle curves of the buried magnet topology with 5 mm and 10 mm height, the magnet opening angle is of 90°, the surface magnet topology with 180° opening angle is considered also. The obtained results are illustrated in Figure 8. The torque-angle curves present parabolic shapes with maximum torques located at $\theta m = 120°$ for the buried magnet topologies. Of particular interest is the increase of the output torque which attempt 12.2 Nm in the case of the buried magnet topology with 10 mm magnet height, compared to the 5 mm one. Such increase reaches about 3 Nm in the maximum output torque. The torque-angle curve of the surface magnet topology present a lower torque peak value of 5.5 Nm.

The negative part of the buried magnet torque-angle curve lead to the high value of the cogging torque which superimposed with the output torque.

3.5. Effect of the Cogging Torque

The claw pole TFPMs suffers from the high value of the cogging torque which decrease the machine performances, much previous work [12, 13] are focused upon the cogging torque reduction, especially in propulsion applications where a ripple-free torque represents a crucial requirement for passenger comfort. In a previous work a magnet opening angle up to 90° lead to high amplitude of the cogging torque [13], doing so and for the cogging torque effect analysis the considered topologies are the buried magnet topology with 90° opening angle, and the surface magnet topology with 180° opening. The obtained results are illustrated in Figure 9, as illustrated the cogging torque amplitude is highest in the case of the buried magnet topology, the week value of the cogging torque of the surface mounted topology lead to the flux shuntage phenomenon illustrated in Figure 10.

4. CONCLUSION

Tow topologies of the claw pole TFPM are distinguished, the structure and flux path are different. The magnet opening angle technique is applied in the case of the tow claw pole TFPM topologies.

Doing so, the magnet arc has an important effect on the machine torque production capability.

For performance improvement of the surface mounted topology, the highest torque is almost 5 Nm for a 180° magnet opening angle, with a week value of the cogging torque due to the flux shuntage phenomenon.

In spite of the buried magnet topology with a half magnets volume (90° magnet opening angle, 5 mm height) exhibits 7 Nm as a highest torque, and for almost the same magnets volume (90° magnet opening angle, 10 mm height) we obtain 12 Nm as highest torque, but the cogging torque amplitude reach important values which degrading the motor performance. This problem can be solved with a three phase machine as mentioned above.

REFERENCES

1. Weh, H. and H. May, "Achievable force densities for permanent magnet excited machines in new configurations," *Proc. Int. Conf. Electrical Machines*, 1107–1111, Munchen, Germany, 1986.
2. Huang, S., J. Luo, and T. A. Lipo, "Analysis and evaluation of the transverse flux circumferential current machine," *Proc. IEEE IAS Annual Meeting*, 241–247, New Orleans, USA, October 1997.
3. Weh, H., "The transverse flux (TF) machines in drive and generator application," *Proc. IEEE/KTH Stockholm Power Tech. Symposium*, Vol. Invited Speakers' Sessions, 75–80, Stockholm, Sweden, June 1995.
4. Mitcham, A. J. and T. W. Bolton, "The transverse flux motor: A new approach to naval propulsion," *Proc. Symposium on Motor Technology for Underwater Naval Sea Application*, 73–80, Rhode Island, USA, June 1997.
5. Blissenbach, R., G. Henneberger, U. Schafer, and W. Hackmann, "Development of a transverse flux traction motor in a direct drive system," *Proc. Inter. Conf. on Electrical Machines*, Vol. 3, 1457–1460, Espoo, Finland, 2000.
6. Kastinger, G., "Design of a novel transverse flux machine," *CD-ROM Inter. Conf. Electrical Machines*, Bruges, Belgium, August 2002.
7. Mansouri, A., A. Njeh, Z. Makni, H. Trabelsi, A. Masmoudi, and A. Antably, "On the torque production capability of a claw pole TFPM," *International Journal of Applied Electromagnetics and Mechanics*, Vol. 19, 391–394, 2004.
8. Masmoudi, A., A. Njeh, A. Mansouri, H. Trabelsi, and A. Elantably, "Optimizing the overlap between stator teeth of a claw pole TFPM," *IEEE Transactions on Magnetics*, Vol. 40, No. 3, 1573–1578, May 2004.
9. Somaloy 500, Hoganas, Product Guide, Sweden, 1997.
10. Ibala, A., A. Masmoudi, G. Atkinson, and A. G. Jack, "Investigation of the leakage fluxes of smc made magnetic circuit claw pole TFPMs," *Ecologic Vehicles and Renewable Energies Monaco*, March 26–29, 2009.
11. Guo, Y. G., J. G. Zhu, P. A. Watterson, and W. Wu, "Comparative study of 3D flux electrical machines with soft magnetic composite cores," *IEEE Industry Application Conference, 37th IAS Annual Meeting*, Vol. 2, 1147–1154, 2002.
12. Njeh, A., A. Masmoudi, and A. Elantably, "3D FEA based investigation of the cogging torque of a transverse flux permanent magnet machine," *IEEE Int. Electric Machines and Drives Conf.*, Wisconsin, 2003 [CDROM].
13. Masmoudi, A., A. Njeh, and A. Elantably, "On the analysis and reduction of the cogging torque of a claw pole transverse flux permanent magnet machine," *European Transactions on Electrical Power*, Vol. 15, No. 6, 513–526, 2005.

On the Iron Losses Computation of a Three Phase PWM Inverter-fed SMPM by Using VPM and Transient FEA

Ali Mansouri and Hafedh Trabelsi
Laboratory of Computer, Electronics & Smart Engineering Systems Design
Engineering School of Sfax, ENIS, Route de Soukra, Km 3.5-BP W, 3038, Tunisia

Abstract— This paper deals with the iron losses computation in a pulse-width-modulation (PWM) inverter fed surface mounted permanent magnet motor (SMPM). The used iron loss model has been developed in earlier works and validated for the evaluation of both no-load and sinusoidal load iron losses of the SMPM. This model requires the separation of the iron losses into hysteresis, classical eddy currents and excess losses components. The use of such model needs the knowledge of the magnetic field distributions and variations through the magnetic circuit. This has been obtained by using a 2D transient finite element analysis (FEA). In order to estimate accurately the hysteresis losses component the hysteresis phenomenon must be incorporated into FEA field equations. In this work, the inverse vector Preisach hysteresis model (VPM) is used for the modeling of the ferromagnetic materials, which is limited to the stator regions. This is due to the low hysteresis losses and time magnetic field variations in the rotor running at synchronous speed. Therefore, the computational method of the PWM fed-inverter SMPM iron losses consists of the VPM incorporated into transient FEA and coupled with iron loss analytical model. In a first step, the machine features, such as the air gap induction and the output torque are investigated. And in a second step, the iron losses are computed. A special attention is paid to the iron losses computation.

1. INTRODUCTION

Synchronous machines with permanent excitation fed by PWM inverters prove themselves to be sufficiently adaptable to the demands of the drive applications, owing to their control flexibility and their high output torque. Electric vehicle and hybrid propulsions, ship propulsion, and industrial robots are some applications which highly benefit from permanent magnet machine drives. Such a trend has led to the introduction of a new class of electric machines, termed "converter-fed machines". This has been made possible thanks to the emergence of power electronic converters which removed the need of a sinusoidal distribution of the stator winding in order to couple efficiently with the sinusoidal voltage supply, as the basis for machine design. However, in high-speed applications of PWM inverter-fed permanent magnet machines, the core losses in ferromagnetic parts of the electrical machine become a dominant component of the total machine losses. These core losses amount to 20–25% of the total losses [1]; this estimation is made up only for sinusoidal supplies. It has been shown in many works [2, 3] that under a PWM inverter or non sinusoidal supplies, the iron losses in electrical machines increase. Therefore, in order to design an optimized drive, it is imperative to evaluate accurately these losses and take them into consideration during the motor design process. In literature, several methods dealing with the iron losses modeling in magnetic materials under non-sinusoidal and PWM supplies have been proposed [4–6]. The major aim of the present paper is to compute the core losses in a 9.42 kW PWM fed surface mounted permanent magnet motor. This computation is made by coupling transient FEA fields with analytical developed models. An efficient way to accurately estimate these iron losses and more precisely the hysteresis ones, is to incorporate the hysteresis phenomenon into FEA magnetic fields equations. Many studies concerning the hysteresis modeling show that the Preisach model is very commonly used for hysteresis modeling in ferromagnetic materials [7, 8]. It has been found to sufficiently satisfy the requirements of accuracy and efficiency [9] Because of its capability of providing relatively accurate estimations, in addition to its generality and robustness [9].

2. ANALYSIS METHOD

In this paper, the transient FEA has been performed to calculate the magnetic field within the magnetic circuit of the studied permanent magnet machine. The modeling of the ferromagnetic parts of the machine was made up with two models: Due to the low hysteresis losses in the rotor running at synchronous speed, the rotor core has been modeled by means a single valued B-H function; and in contrast of the rotor core, the stator core has been modeled through the VPM by incorporating the hysteresis phenomenon into FEA fields.

In order to incorporate the VPM into FEA fields, formulated in terms of potential vector A, an interface is required; this interface is obtained through the iterative procedure: fixed point technique. In which the nonlinear relationship between B and H is written as follows [10]:

$$B = \nu_{FP} H + R_{FP} \tag{1}$$

R_{FP} is the fixed-point residual iteratively computed, and υ_{FP} is the fixed-point coefficient.

Coupling Eq. (1) to appropriate Maxwell equations, the magnetic problem is then formulated in terms of magnetic potential vector as illustrated in Eq. (2). The solution starts initially with an arbitrary value of R_{FP}, providing the magnetic potential vector A value, from which the magnetic induction B is calculated. By using B as the input of the VPM, the value of the magnetic intensity H is deduced. With B and H known, a new value of R_{FP} is calculated using formula (1). This value is again used; this procedure is repeated until the problem convergence is reached.

$$-\nabla \cdot (\nu_{FP}(\nabla A_z)) + \sigma \frac{\partial A}{\partial t} + (\nabla \times R_{FP})_z = J_z \tag{2}$$

Az is the z-component of A, σ is the conductivity and J_z is the z-component of the current density J.

3. IRON LOSSES MODELING

The local flux density patterns within a rotating electrical machine are quite complex. The flux density locus at one position can be alternating (1 dimensional) with or without harmonics, two dimensional or even 3 dimensional rotating with purely circular or elliptical patterns. The existence of elliptically distorted rotating field throughout the magnetic circuit makes the modeling of the iron losses a very difficult task.

According to [11], the conventional model of iron losses separates the iron losses into three terms being the static hysteresis losses P_h, the classical eddy current loss P_c and excess loss P_e: $P = P_h + P_c + P_e$

$$P_h = \frac{1}{T} \int_T \left[\left(\left| H_x \frac{dB_x}{dt} \right|^{\frac{2}{\beta}} + \left| H_y \frac{dB_y}{dt} \right|^{\frac{2}{\beta}} \right)^{\frac{2}{\beta}} \right] dt \tag{3}$$

$$P_c = k_c \int_T \left(\left(\frac{dB_x}{dt} \right)^2 + \left(\frac{dB_y}{dt} \right)^2 \right) dt \tag{4}$$

$$P_e = k_c \int_T \left[\left(\left(\frac{dB_x}{dt} \right)^2 + \left(\frac{dB_y}{dt} \right)^2 \right)^{\frac{3}{4}} \right] dt \tag{5}$$

where:

- B_x, B_y, H_x and H_y are respectively the orthogonal components of the flux density B and intensity H both in the stator yoke and teeth obtained by FEA.
- f the frequency, and β, k_h, k_c and k_e are respectively the Steinmetz, hysteresis, eddy current and excess constants depending on the material and determined from the sinusoidal iron losses.

The hysteresis losses, the eddy current losses and the excess losses can be obtained by discretizing the last three equations in the time domain when doing the stepped transient FEA [12].

4. ANALYSED PERMANENT MAGNET MOTOR

Figure 1 shows a fourth of the studied permanent magnet motor, a 3-phase, 4-pole, and 24-slots configuration. The stator is made of a laminated core and a three phase stator armature windings which are fed by a three-phase PWM inverter. The rotor has an iron core and thin permanent magnets mounted on the surface of this core. Alternating magnets of the opposite magnetization direction produce radially directed flux density across the air gap. This flux density then reacts with currents in windings placed in slots to produce torque.

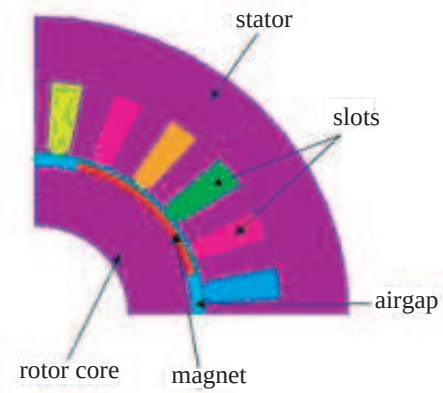

Figure 1: Fourth of the analysed SMPM.

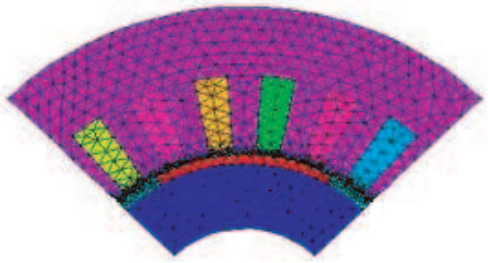

Figure 2: Meshed Fourth of the analysed SMPM.

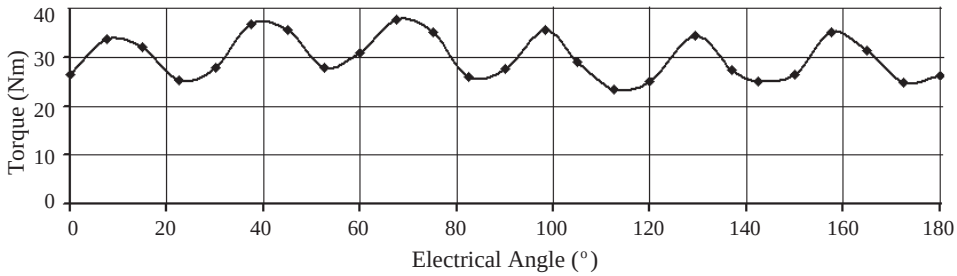

Figure 3: Torque of the analysed SMPM.

Table 1: Stator iron losses with PWM and sinusoidal supplies.

	PWM	**Sinusoidal**
Eddy current losses	47.6 W	42.3 W
Hysteresis losses	50.8 W	42.7 W
Excess losses	7.2 W	7.6 W
Total losses	105.6 W	92.6 W

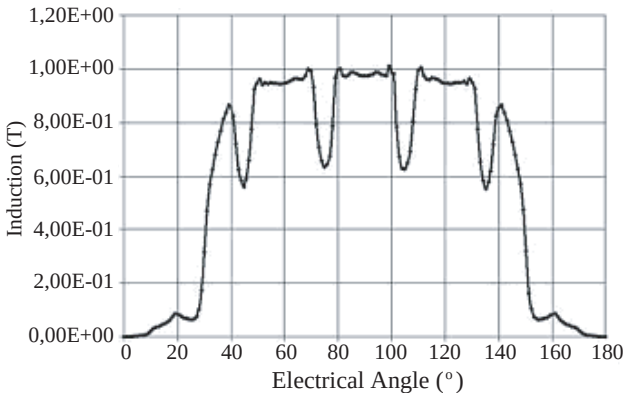

Figure 4: Airgap flux density.

5. SIMULATION RESULTS

In order to foresee the machine features, the studied 9.42 kW SMPM has been subject of a deep investigation by FEA. In particular of interest: the air gap flux density and the provided output torque.

In contrast of the sinusoidal supply transient analysis simulation, where the voltage at each time step is easily computed, in the PWM supply simulation, the voltage has to be defined at each time step.

Referring to Fig. 3, one can clearly notice the existence of ripple in the torque curve; this is due to the so called ripple torque of the machine. As far as the torque, the ripple marked in the airgap flux density waveform is due to the slotting effect.

The computed iron losses with transient finte element analysis of the studied SMPM drive are presented in Table 1, in particular a total losses of 105.74 W ($J_s = 1.910^6$ A/m^2) are obtained. By comparing these losses to those obtained with a pure sinusoidal supply (92.65 W), we can remark that the estimated iron losses under PWM supply are actually scaled from those obtained with sinusoidal supply. This increase is due on, one hand; to the fact that the PWM supply contains several harmonics porvinding the total iron losses, and on the other hand to the important increase of the eddy currents because of the largest dynamic excitation

6. CONCLUSIONS

The use of the permanent magnet machine in drive propulsion applications at variable speed requires its control which makes the PWM wave an inevitable way. However, under a PWM inverter or generally non sinusoidal supplies, the iron losses in electrical machines increase. In the present work, the iron loss modeling of a PWM fed SMPM has been presented and used in conjunction with time-stepped transient FEA to estimate iron losses. By comparing these losses to those obtained under a purely sinusoidal supply an increase in the iron losses in noticed this is because of the existence of harmonics in PWM supply.

The numerical modeling, based on the finite element method is a good approach to study the behavior of the machine. Nevertheless, an experimental validation of the numerical results remains indispensable for an accurate consideration of the iron losses in the magnetic circuit of the machine.

REFERENCES

1. Mohan, N., T. M. Undeland, and W. P. Robbins, *Power Electronics: Converters, Applications and Design*, 2nd Edition, John Wiley & Sons Inc., 1991.
2. Boglietti, A., P. Ferraris, M. Lazzari, and M. Pastorelli, "About the possibility of defining a standard method for iron loss measurements in soft magnetic materials with inverter supply," *IEEE Trans. Magn.*, Vol. 33, No. 5, December, September/October 1997
3. Boglietti, A., P. Ferraris, M. Lazzari, and M. Pastorelli, "Effects of different modulation index on the iron losses in soft magnetic materials supplied by PWM inverter," *IEEE Trans. Magn.*, Vol. 29, No. 6, 3234–3236, 1993.
4. Tsai, W. C., "Effect of inverter parameters on iron losses in a PWM inverter-fed induction motor," *Fourth International Conference on Innovative Computing, Information and Control (ICICIC),* 914–917, December 7–9, 2009.
5. Boglietti, A. and A. Cavagnino, "Iron loss prediction with PWM supply: An overview of proposed methods from an engineering application point of view," *Electric Power Systems Research*, Vol. 80, No. 9, 1121–1127, September 2010.
6. Boglietti, A., A. Cavagnino, D. M. Ionel, M. Popescu, D. A. Staton, and S. Vaschetto, "A General model to predict the iron losses in inverter fed induction motors," *IEEE Energy Conversion Congress and Exposition, ECCE,* 1067–1074, 2009.
7. Mayergoyz, I. D., "Mathematical models of hysteresis," *IEEE Transactions on Magnetics*, Vol. 22, No. 5, September 1986.
8. Mayergoyz, I. D. and G. Friedman, "Isotropic vector Preisach model of hysteresis," *J. Appl. Phys.*, Vol. 61, No. 8, April 15, 1987.
9. Mansouri, A. and H. Trabelsi, "Incorporation of vector Preisach hysteresis model in transient finite element analysis for a SMPM," *Int. Review of Electrical Engineering*, Vol. 2, No. 3, 448–454, 2007.
10. Mansouri, A., H. Trabelsi, and M. H. Gmiden, "Investigation of the iron losses in a SMPM by using vector preisach model and finite element analysis: Analysis of the effect of sizing parameters," *EVER'09*, Monte-Carlo, Monaco, France, March 26–29, 2009,
11. Lin, D., P. Zhou, W. N. Fu, Z. Badics, and Z. J. Cendes, "A dynamic core loss model for soft ferromagnetic and power ferrite materials in transient finite element analysis," *IEEE Transaction on Magnetics*, Vol. 40, No. 2, 1318–1321, March 2004.
12. Trabelsi, H., A. Mansouri, and M. H. Gmiden, "On the modeling of a SMPM and the iron losses calculation in transient FEA," *Trans. on Systems, Signals and Devices (TSSD) Issues on Power Electrical Systems*, Vol. 3, No. 1, 2008.

The Methods of Measuring Attenuation of Thin Absorbent Materials Used for Electromagnetic Shielding

L. Nowosielski, R. Przesmycki, M. Wnuk, and J. Rychlica
Faculty of Electronics, Military University of Technology
Gen. S. Kaliskiego 2 str., Warsaw 00-908, Poland

Abstract— The article concerns the problems connected with electromagnetic compatibility. Two methods of measuring attenuation of thin absorbent materials used for electromagnetic screens are described here. The measurements have been conducted in a coaxial measuring line, which provides a large broad band of realized measurements. The first method is based on measuring the signal level with a measuring receiver at the output of the coaxial measuring line. The second method is based on measuring parameters of S matrix with the use of a network analyzer, which allows to determine the amount of absorbed energy and reflected by a sample. Exemplary measurements of attenuation have been conducted for two samples in the frequency range from 200 MHz to 5200 MHz.

1. INTRODUCTION

Along with an increasing number of devices producing electromagnetic radiation there is a need of protecting devices and people against undesirable electromagnetic radiation. The problem of protection against undesirable radiation is particularly important in the issues of electromagnetic compatibility. One of the methods of protection against reactions of undesirable radiation is electromagnetic screens. Generally we can distinguish two ways of functioning of electromagnetic shields — through reflection of incident electromagnetic wave or absorption of electromagnetic energy. Taking into account the screening efficiency an ideal electromagnetic screen should be distinguished by a low reflection coefficient and a high value of absorption of incident radiation. Coefficients of reflection and absorption (transmission) depend on electric and magnetic properties of material and change in the function of frequency. In order to achieve desirable parameters of reflection and transmission, composites composed of materials with different properties are often used. However in this case the values of reflection and transmission coefficients may also depend on polarization and angle of incident radiation. Currently different methods of screening are used in the microwave range as well as in the low frequency range. For electromagnetic screening in the microwave range graphite materials are used, which are additionally shaped in the form of pyramids. On the other hand, large screening efficiencies in the low frequency range are obtained by using ferrite materials, which have extra magnetic properties. In most cases walls of non-reflection chambers are covered with two layers: One is built from ferrite plates and the other from graphite pyramids. However such screening methods are only convenient for use in non-reflection chambers since ferrite plates are very heavy and have a solid form, whereas graphite pyramids occupy large volume. At present electromagnetic screens are very applicable and must be characterized by particular electromagnetic parameters, depending on purpose. Effective electromagnetic screens ought to be characterized by the following properties:

— work in a determined frequency range or extremely at broadband,
— have a solid or plastic form,
— have a particular coefficient of reflection and absorption.

2. MICROWAVE MEASURING SET ON THE BASIS OF COAXIAL LINE

For conducting tests on attenuation of thin absorbent materials and screening cloths a microwave measuring set shown in Figure 1 has been worked out. With the use of the above mentioned set we can measure and determine values of combined coefficients of S matrix, which later can be used for calculation of attenuation and absorption coefficients of a particular screening material. The measuring set in the present configuration allows to measure in the frequency range from 45 MHz to about 6 GHz. Band limitations for this set are caused by the set structure on the basis of the coaxial line (measuring line), a possessed measuring device (network analyzer, signal generator, measuring receiver) and also potentials of implemented measuring software. If this band is exceeded, there occur difficulties in the process of calibration.

Figure 1: View of microwave measuring set on the basis of coaxial line.

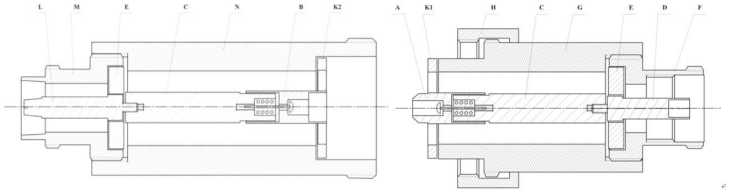

Figure 2: Structure of measuring line.

The measuring line for testing thin absorbent materials (foil used for screens) and screening cloths is made in the form of the coaxial measuring line which allows to measure selected cloths in the shape of a ring with diameter up to 30 mm. An assumption for designing the measuring line was obtaining the value of characteristic impedance — $Z_0 = 50\,\Omega$. By using dependences (1), the values of transverse dimensions of the measuring line were calculated as follows: outside diameter of the line — 24,1 mm, inside diameter of the line — 10,5 mm.

$$Z_0 = \frac{60}{\sqrt{\varepsilon_r \cdot \mu_r}} \cdot \ln \frac{a}{b} = 60 \cdot \ln \frac{12,05}{5,25} \cong 50, \tag{1}$$

where: $\varepsilon_r = 1$ & $\mu_r = 1$ — relative permittivity and magnetic permeability of dielectric filling the space between ducts.

The coaxial measuring line with specific dimensions given above was mainly made of brazen alloy and also of the phosphorus — bronze alloy, which provides good conductivity. The whole is made of two parts screwed together which allows for mounting of the tested material sample inside the line. The way of execution of the measuring line makes such mounting of the sample inside possible to provide a very good galvanic contact with the body and internal line pins. In Figure 2, the structure and longitudinal cross-section of the measuring line is presented The measuring line is a dismountable element. The body (elements G & N) is made of well-conducting brazen alloy and is screwed together with the use of element-H, which has a internal thread. The core of the whole element consists of the elements: A, B, C, D & L made of brazen alloys or the phosphorus — bronze alloys. In the place of the sample mounting the core is made of the phosphorus — bronze alloy (elements A & B) and has such a functionality that after placing the sample, the core presses down firmly an inside cut-out of the sample, providing in this way a good galvanic contact. It was guaranteed by making some special telescopic spring-loaded mechanisms. Samples placed in the measuring line must have specific dimensions adjusted to the size of brazen rings K1 & K2 between which the sample is placed. After careful placement of the sample between the rings, they get screwed together with small screws. After placing the sample, the rings are screwed together which provides a good galvanic contact of the sample with the whole body. On the left and right side of the element reductions are screwed into the line body (elem. F & M) with teflon plates (elem. E) and the core (elem. D & L). On both sides it gives a chance for transition to attached coaxial cables.

3. MEASUREMENTS OF THIN ABSORBENT MATERIALS WITH THE BASIC METHOD

The measurement of attenuation of thin absorbent materials was conducted with the use of a measuring position, which block diagram is presented in Figure 3. The measurements with the basic method was divided into two stages. The first stage is a standardization measurement during which the signal level is measured. Here the signal directly passes through the measuring line (without the placed tested material sample). The second stage is a principal measurement, in which the signal level is measured (but the signal passes through the measuring line with the placed tested material sample inside). Due to obtained results from both measuring stages it is possible to calculate attenuation of the tested material sample A with using the dependence:

$$A = E_1 - E_2, \tag{2}$$

where: E_1 — the signal level at the output of the measuring line without the placed material sample for a particular frequency, E_2 — the signal level at the output of the measuring line with the placed material sample inside the concentric line for a particular frequency.

The measuring methodology is based on measurement of the signal level at the output of the measuring line without the sample and with the sample placed in a microwave set for measuring attenuation. A test signal is generated by a microwave generator in a given frequency range. A received signal at the output of the measuring line is measured with a measuring receiver. The whole measuring process is controlled by specialized software, which graphic interface is shown in Figure 4. The designed program allows for automatic execution of basic preparatory activities, realizing measurements themselves and making correct diagrams presenting the obtained results. The application allows to introduce an initial and final frequency of the measuring range, defining the measuring step and the test signal level coming from the signal generator.

4. MEASURING OF THIN ABSORBENT MATERIALS WITH THE EXTENDED METHOD

The measurement of attenuation of thin absorbent materials with the extended method was conducted with the use network analyzer. The system measures modules and phases of S matrix coefficients. The measurements were divided into two stages. First of all calibration measurements are made with the use of three additional elements: dilation, closure, matched load. The view of the measuring set and network analyzer is shown in Figure 5. Calibration measurements help to eliminate systematic errors and are realized during each measurement. Calibration coefficients are determined as a result of the solution of system of equations on the basis of measurements with calibration elements and direct port connection of the network analyzer. Proper measurements come down to determining module and phases of 4 coefficients of coaxial line dispersion with the tested material sample located between two rings in the measuring line ($S_{[11]}$, $S_{[21]}$, $S_{[12]}$, $S_{[22]}$).

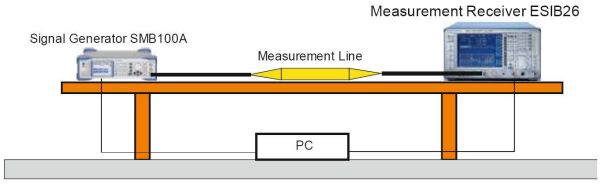

Figure 3: Block diagram of measuring position.

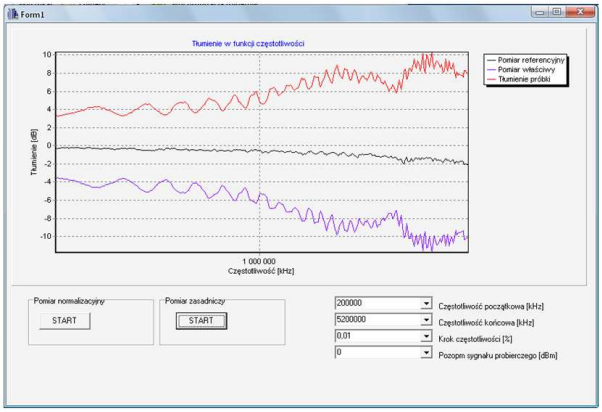

Figure 4: Graphic interface of the worked out application controlling the measuring process.

Figure 5: View of the whole measuring position.

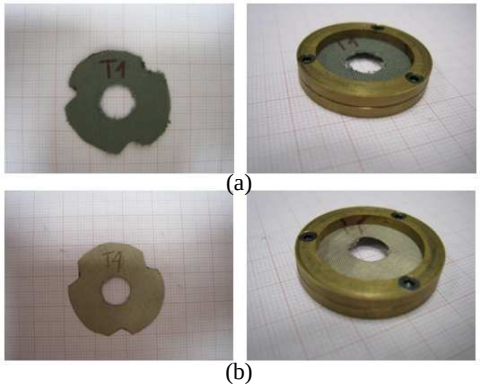

Figure 6: View of particular measuring samples. (a) Sample No. 1 — material cloth (T1). (b) Sample No. 2 — metalized cloth (T4).

In order to conduct the test with the extended method it is necessary to perform the following actions:

a) prepare the measuring set for testing and determine measuring parameters,
b) with the use of tips of calibration elements make the system calibration in order to eliminate systematic errors from the proper measurement,
c) prepare samples by cutting out the previously described suitable shape from a larger fragment of the material,
d) the cut-out sample place between the rings K1 & K2, and screw together with small screws in places where the sample should have appropriate cut-outs,
e) carefully place the ring inside the measuring line and press down the internal core to the inside cut-out of the sample,
f) screw two parts of the measuring line together and measure the parameters of S matrix, record the measuring results, which are input data for calculations of the sample attenuation (absorption and reflection).

5. THE MEASURING RESULTS

To present measuring abilities of the described methods, the measurements of attenuation of the material samples used for electromagnetic screens in the frequency range from 200 MHz to 5200 MHz were conducted. The research subjects were two samples of thin materials used for electromagnetic screens. The first sample was a material cloth, whereas the other was a metalized cloth. Views of particular samples are presented in Figure 6.

In Figure 7, the measured attenuation values of two samples in the frequency function determined with the use of the basic and extended method have been shown.

The measured values of S matrix elements with the use of the extended method $S_{[11]}$, $S_{[21]}$, $S_{[12]}$ & $S_{[22]}$, presented in the linear measure, with using analytic dependences (dependences from 3 to 5) allow to calculate the amount of energy absorbed and reflected by a given sample at particular frequencies:

$$A_0 = -10\log(1-|S_{11}|^2), \tag{3}$$

$$A_C = -10\log\frac{|S_{21}|^2}{1-|S_{11}|^2}, \tag{4}$$

$$A = -10\log(1-|S_{11}|^2) - 10\log\frac{|S_{21}|^2}{1-|S_{11}|^2}, \tag{5}$$

where: A_0 — reflection attenuation, A_C — absorption, $A = (A_0 + A_C)$ — total attenuation.

On the basis of the above mentioned dependences the calculations of the amount of energy absorbed and reflected by the examined samples were made. The results of calculations for particular frequencies from the measuring range are shown in Figure 8 and Figure 9. A confirmation of correctness of the dependence (5) is the fact that the numerical value of attenuation measured with the extended method is comparable with the values of the total attenuation coefficient A, on which additionally the measuring results with the basic method were placed in order to confirm correctness of two described methods.

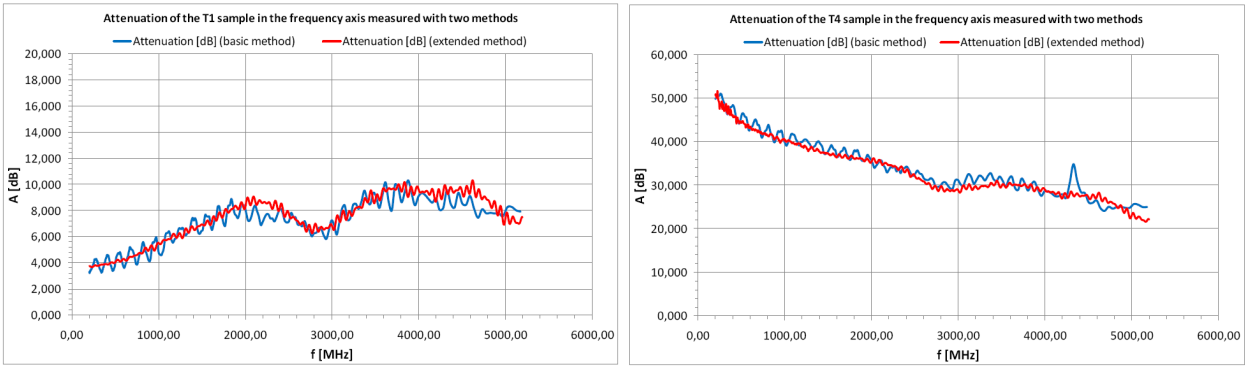

Figure 7: Diagrams of attenuation in the frequency function for two samples measured with two methods.

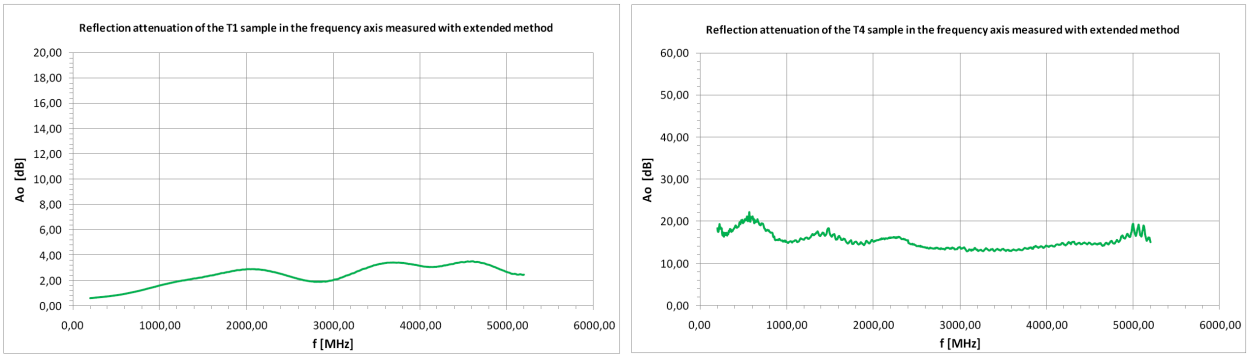

Figure 8: Diagrams of reflection attenuation in the frequency function for two samples calculated from the dependence (3).

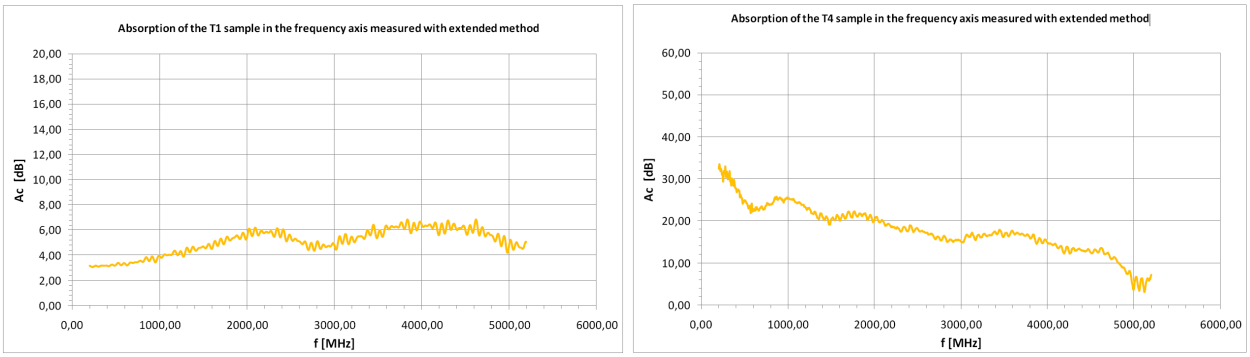

Figure 9: Diagrams of absorption in the frequency function for two samples calculated from the dependence (4).

6. CONCLUSIONS

In the work two methods of measuring attenuation of thin absorbent materials used for electromagnetic screens in a broad frequency range have been presented. The property measurements of the tested materials can be used for designing absorbers, which reflection & absorption properties may be modified — depending on their purpose. When using the suggested methods, one can determine values of attenuation and after further statistical analysis evaluate how much energy is absorbed and reflected by a given sample at particular frequencies.

The conducted attenuation tests for 2 kinds of materials in the frequency function have shown that both samples T1 and T4 are materials attenuating the energy of electromagnetic field in the whole range of tested frequencies, whereas total attenuation of the sample T1 is much lower than the sample marked T4. The sample T1 along with the increase of frequency reveals a higher and higher attenuation coefficient. After dividing total attenuation into reflection attenuation and absorption, in case of the sample T1 we can state that it has good properties absorbing the energy of electromagnetic field, since absorption is twice higher than reflection attenuation. Looking at the diagram of the sample T4 we can see that this material has much higher values of reflection attenuation (about 20 times higher) than the sample T1, which — with screening materials — is an unfavourable phenomenon because reflected waves return to electromagnetic environment and may introduce additional interference. In case of the sample T4 total attenuation along with the increase of frequency decreases from the level of about 50 dB to 30 dB for higher frequencies. It is necessary to notice that a component of reflection attenuation makes here about 50% of the total material attenuation. On the basis of measuring the selected screening materials we can state that the sample T1 has better desirable attenuation properties than the sample T4, since modern screening materials should reveal better absorbent properties and have a low value of reflection losses.

REFERENCES

1. Kubacki, R., L. Nowosielski, and R. Przesmycki, "Technique for the electric and magnetic parameter measurement of powdered materials," *Computotional Methods and Experimental Measurements XIV*, Vol. 48, 241–250, Wessex Institute of Technology, Anglia Str., 2009, ISSN 1743-355X.

Small Chambers Shielding Efficiency Measurements

Rafal Przesmycki, **Marian Wnuk**, **Leszek Nowosielski**, **and Kazimierz Piwowarczyk**
Faculty of Electronics, Military University of Technology
Gen. S. Kaliskiego 2 Str., Warsaw 00-908, Poland

Abstract— The article concerns the problems connected with electromagnetic compatibility. The methodology of shielding efficiency measurements of small chambers (e.g., casing of the personal computer (PC) and the 'racks') assigned for installing devices or electronic components in the frequency range from 80 MHz to 1000 MHz as well as the description of measuring position have been presented in it. The designed method of shielding efficiency measurement of small chambers comes down to making two measurements of the level of electromagnetic field strength for a particular probing frequency. The first measurement is performed as so-called reference measurement, whereas the second is principal measurement. The results of the research conducted in accordance with the designed measuring methodology concerning attenuation measurements contributed by the central processing unit casing from four sides of the object and their analysis from the perspective of using casing as a protection element against undesirable electromagnetic emission have been presented in the article.

1. INTRODUCTION

Worldwide valid standardization documents concerning the methodology of measuring attenuation of screening objects are applicable only in measuring shielding efficiency of chambers with inner dimensions not smaller than $1.5\,\mathrm{m} \times 1.5\,\mathrm{m} \times 1.5\,\mathrm{m}$. Because of that there occurred a need of working out a methodology of measuring screening cages (chambers) with smaller dimensions. The main obstacle in using methodologies presented in available standardization documents is a limited space inside the research object which does not allow for locating a standard receiving antenna inside the examined object due to limited sizes. Very efficient measuring antennas available on the market have dimensions which make them impossible to locate inside chambers with smaller dimensions than $1.5\,\mathrm{m} \times 1.5\,\mathrm{m} \times 1.5\,\mathrm{m}$. In order to find sensors, which due to their overall dimensions can be placed in small dimension spaces, an analysis of contemporary antenna devices and measuring instruments of electromagnetic field strength has been conducted.

The conclusions from the conducted analysis are as follows:

- The only devices which allow to measure electromagnetic field strength inside small spaces are electromagnetic field measuring probes. Sample field probes available on the market are shown in Figure 1.
- Electromagnetic field probes, due to lack of tuned bandwidth filters, allow to measure electromagnetic field strength in a very wide frequency band without necessity of their retuning.
- Due to broad-band character of work, field probes are characterized by small sensitivities like $0.05\,\mathrm{V/m}$ which significantly limits the dynamics range of measuring screening efficiency. In order to make measuring attenuation of chambers with large values possible it is necessary to use test signals with significant power levels which allow for their measurement after passing through screening structures of the research object.

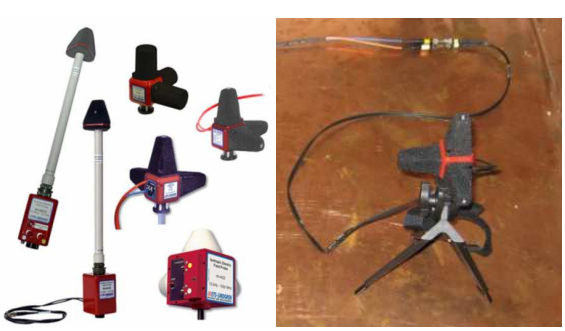

Field probes of the Lindgren company [1]

Field probe EMR-300 of the Wandel & Goltermann [2]

Figure 1: Sample probes for measuring electromagnetic field strength.

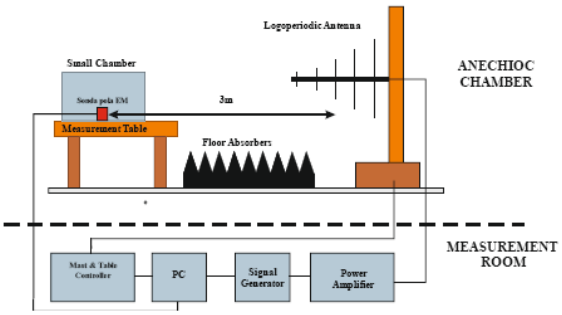

Figure 2: Block diagram of the position for measuring shielding efficiency of small chambers.

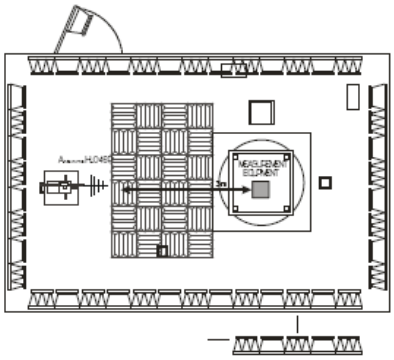

Figure 3: Arrangement diagram of the antenna HL046P towards the examined object in anechoic chamber.

2. THE RESEARCH METHOD PRINCIPLES

For measuring efficiency of screening chambers it is necessary to arrange the measuring position in configuration as it is shown in Figure 2. Whereas in Figure 3 an arrangement of the examined object and test antenna in the anechoic chamber is presented. The HL046P antenna is used as a transmitting antenna in the frequency range from 80 MHz to 1000 MHz. Particular attention should be paid to RF cable connections in the whole slotted line. If some changes in the position configuration were made before the measurements then it is necessary to conduct an inspection of all connections in the RF line before its activation.

A significant element during arranging the measuring position is connecting the electromagnetic field probe placed inside the examined chamber to the computer operating the measuring process. This connection is made with the use of light pipe. For that reason the examined chamber should be equipped with a light pipe adapter. The designed method of shielding efficiency measurement of small chambers comes down to making two measurements of the level of electromagnetic field strength for a particular probing frequency. The first measurement is performed as so called standardization measurement. With determined value of the signal level generated by the probing signal transmitter the level of electromagnetic field strength is measured in the place of installation of field probe which functions as a measuring instrument of electromagnetic field strength. During standardization measurement the transmitting antenna of the probing signal transmitter and the field probe are located opposite each other (without the examined chamber) within the distance equal to the required distance, due to construction reasons of the examined chamber when the field probe is situated inside the examined chamber. The measurements can be made on discrete frequencies or in a set band with determined step. Measured values of electromagnetic field strength corresponding with particular measuring frequencies should be remembered. After performing standardization measurement it is necessary to conduct principal measurement during which the transmitting antenna of the probing signal transmitter is placed outside the examined screening chamber whereas the field probe is located inside the examined screening chamber. With determined value of the signal level generated by the probing signal transmitter the level of electromagnetic field strength is measured in the place of installation of the field probe. Measurements should be performed in the same way as during standardization measurement on discrete frequencies or in the set band with determined step. Measured values of electromagnetic field strength corresponding with particular measuring frequencies should be remembered. After subtracting the recorded levels of electromagnetic field strengths corresponding with particular frequencies of the probing signal during standardization and basic measurements we will obtain the difference in levels of received signals in dB, which makes the value of attenuation contributed by the examined chamber. In such a way we can get characteristics of screening efficiency in the frequency function.

3. MEASURING POSITION

In order to measure the value of attenuation contributed by the casing of the examined chamber a measuring set is required which includes the measuring signal transmitter and the measuring instrument of electromagnetic field strength. Particular parts of the measuring set include also software which activated on operating computer makes the measuring process automation possible.

(a)

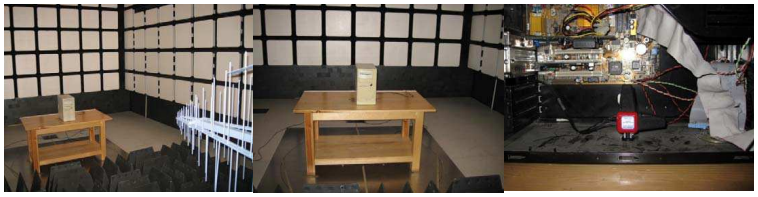

(b)

Figure 4: The measuring position for measuring attenuation contributed by screening casings. (a) The measuring position prepared for conducting standardization measurement of PC casing. (b) The measuring position prepared for conducting principal measurement of PC casing.

The photos of sample configuration of the measuring position are presented in Figures 4(a) and 4(b).

Block diagram of the position for measuring shielding efficiency of small chambers is shown in Figure 2. The position includes the measuring signal transmitter and the measuring instrument of electromagnetic field strength as well as specialized operating software.

3.1. Measuring Signal Transmitter

The measuring signal transmitter includes: signal generator, power amplifier, operating computer and transmitting antenna. The signal generator is the source of the measuring signal working in the frequency range covering the required range for measuring shielding efficiency. For strengthening the measuring signal generated by the signal generator the power amplifier is used which works in the required frequency range. Maximal signal level at the power amplifier output is dependent on the attenuation contributed by walls of the screening chamber casing. The strengthened measuring signal is provided at the input of the transmitting antenna. The transmitting antenna should cover the frequency range required during this kind of measurements. The process of the measuring frequency selection and the RF measuring signal level is steered by software installed on the operating computer. For that purpose the discussed research procedure uses: SMB100A signal generator by working in the 9 kHz–6 GHz band and having necessary parameters, RF amplifier of BLWA0810-160/100D, working in the 80 MHz–1000 MHz band, NRP power meter along with measuring probes (used to control electromagnetic field strength), test antenna (transmitting) working in the frequency range from 80 MHz to 1000 MHz. In the discussed measuring position the log-periodic antenna HL046P is used.

3.2. Electric Field Probe

The electromagnetic field strength meter includes the computer operating the measuring process and the electromagnetic field probe. In the set of transmitter and receiver one computer operating the measuring process is used. The field probe is used for measuring electromagnetic field strength. Through the remote control interface the software installed on the operating computer reads off the level of electromagnetic field strength in the place of the field probe installation. After performing standardization and basic measurements and on the basis of the recorded levels of electromagnetic field strength the software installed on the operating computer calculates the attenuation contributed by the examined chamber casing in the frequency function. The mentioned research procedure uses the HI-6005 electric field probe produced by the ETS LINDGREN company.

3.3. Application Steering the Measuring Process

The whole process of measuring shielding efficiency is managed by the EMC32 software installed on the PC operating computer. The above mentioned software manages the process of standardization and basic measurements. The final effect of both measuring cycles are two files with levels of electromagnetic field strength in the frequency function adequately outside the examined chamber as well as inside it. Calculation of the difference of levels of field strengths, based on the above mentioned files and conducted with the use of MS Excel software, gives the value of attenuation

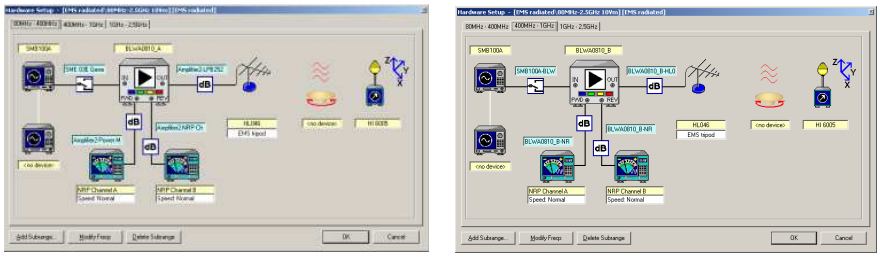

The 80-400 MHz frequency range. The 400MHz-1000 MHz frequency range.

Figure 5: Graphic interface of the EMC32 application for equipment configuration of the measuring position for two measuring ranges.

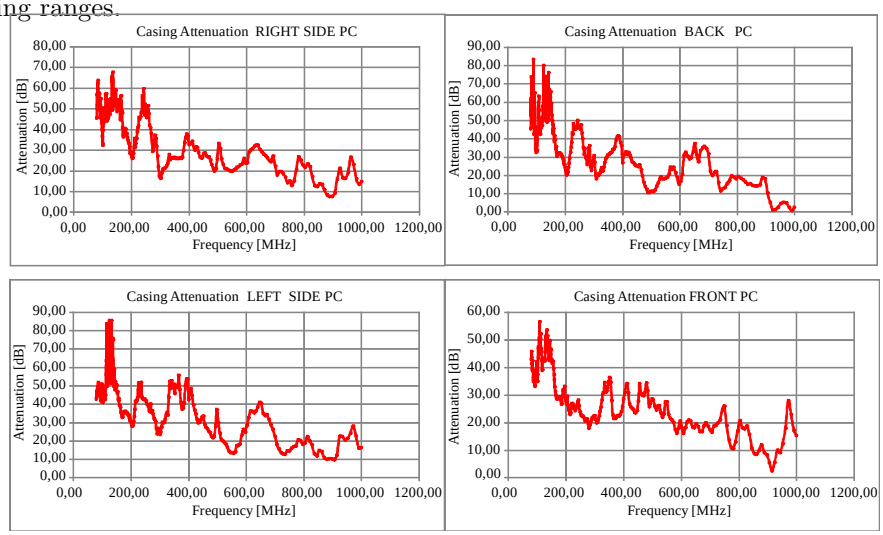

Figure 6: The measured attenuation contributed by the PC casing from 4 sides of the research object for vertical polarization of the test antenna.

contributed by the examined chambers. Configuration of the EMC32 software for measuring chamber attenuation takes place with the use of the GUI interface shown in Figure 5. Configuration of the operating software is divided into two frequency ranges due to operated frequency ranges by particular devices which are parts of the probing signal transmitter.

In order to conduct the research by the designed method with the use of electromagnetic field probe it is necessary to perform the following activities. Turn on supply of measuring devices and leave them to obtain proper stability. Place the field probe within the distance of 3 m in direction of maximum radiation of the test antenna, in accordance with guidelines. Turn on the generator and set its output level in such a way to make the field strength level measured with the use of the field probe amount to 0.1 of maximal value of the signal generated during the research. Generate electromagnetic field on the initial frequency of 80 MHz. Gradually increase the level of electromagnetic field strength until obtaining the maximal value possible to generate by the used measuring equipment. Retune the generator in the frequency range covered by the designed procedure with maintaining the signal level equal to the established value of the EM field strength for both polarizations of the test antenna. Place the field probe inside the examined chamber and then place the chamber in such a place to make a distance of the probe within 3 m in direction of maximal radiation of the test antenna. Generate electromagnetic field on the initial frequency 80 MHz. Gradually increase the level of the EM field strength until achieving the maximum value possible to generate by the used measuring equipment. Retune the generator in the frequency range included in the designed procedure with maintenance of the signal level equal to the established value of the EM field strength. On the basis of the obtained measuring results from two stages of the research calculate attenuation of the examined chamber.

4. THE MEASURING RESULTS

To present measuring abilities of the described position the measurements of screening efficiency of the PC central processing unit in the frequency range from 80 MHz to 1000 MHz were made. During

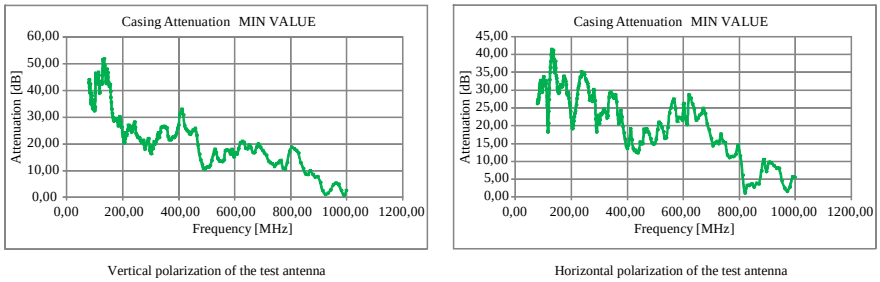

Figure 7: The measured result attenuation contributed by the PC casing.

the research the measurements of attenuation contributed by the PC casing were conducted from four sides of the research object for two polarizations of the test antenna. The results for vertical polarization are presented in Figure 6. As the result attenuation of the examined PC casing the minimum value from the measured attenuations contributed by the casing for particular sides of the examined object was accepted. The diagrams of the result attenuation for both polarizations of the test antenna are shown in Figure 7.

From the presented measuring results we can see that the smallest attenuation is contributed by the PC casing placed from behind the transmitting antenna of the test signal due to a large amount of technological crevices in this kind of constructions. Attenuation contributed by the examined PC casing decreases in the frequency function due to a large amount of small crevices of different casing sizes which for increasing test frequencies function as wave-guides, thus having influence on decrease of contributed attenuation.

The above presented and discussed measuring results of attenuation contributed by the PC casings aim at giving reader a picture of the way one can analyze the results of the PC casing measurements on the basis of the results of measurements conducted according to the methodologies described in this study.

5. CONCLUSIONS

This measuring position is designed for determining efficiency of screening small chambers (e.g., the PC central processing units and racks) assigned for installation of electronic devices or components in the frequency range from 80 MHz to 1000 MHz. The shielding efficiency measurements of small screening chambers should be carried out in some research environment allowing for attenuation of test signal used for probing the examined object to the permissible level by separate regulations valid in the area of conducted research. Because of significant levels of the test signal generated during the measurements the whole position should be placed inside the anechoic chamber with wall attenuation providing attenuation of the test signal with a value not disturbing other radio communication services in their work. Due to small sensitivities of the field probe like 0.05 V/m and equipment abilities of generating the EM field with high values the designed measuring method limits the dynamics range of the screening efficiency measurement. In order to make measuring attenuation of chambers with large values possible it is necessary to use test signals with significant power levels which enable their measurement after passing through screening structures of the research object and what is very expensive because of specialist equipment required for this kind of measurements.

REFERENCES

1. www.ets-lindgren.com.
2. www.atecorp.com.
3. Nowosielski, L., R. Przesmycki, M. Wnuk, and K. Piwowarczyk, "RF immunity testing of information technology equipment in the frequency bandwidth (80–1000) MHz," *Electrical Review 3/2010*, ISSN 0033–2097.

Procedure for Absorption Measurements of Absorbing Materials

K. Piwowarczyk, **M. Bugaj**, **L. Nowosielski**, **and R. Przesmycki**
Faculty of Electronics, Military University of Technology
2, Gen. S. Kaliskiego Str., Warsaw 00-908, Poland

Abstract— The aim of this work is to present the procedure for absorption measurements of absorbing materials. In presented procedure as the electromagnetic wave absorption measure was used the signal levels difference between probe signal level reflected from the reflector material not covered and covered by the absorbing material.

1. INTRODUCTION

The aim of this work is to present the procedure for absorption measurements of absorbing materials. In presented procedure as the electromagnetic wave absorption measure was used the signal levels difference between probe signal level reflected from the reflector material not covered and covered by the absorbing material. It is a measure of strength of the electromagnetic wave absorbed by a absorbing material for a given incident power. The presented measurement procedure requires two flat aluminium panels, where one is used as reflector material (reference) and the other is coated with absorbing material. The panel is fixed on a support, which is positioned in front of the receiving and transmitting antennas. With this method is necessary to make two separate measurements of the signal level reflected by the plate with and without absorbing material. In the paper the methodology, detailed description of laboratory stand and laboratory stand calibrating procedure were presented.

The absorption of broadband absorber constructed as flat and impregnated with a magnetic material was successfully evaluated using described method in the frequency range of (1–10) GHz. The measurements were carried out in the anechoic chamber located at Laboratory of Electromagnetic Compatibility, Faculty of Electronics, Military University of Technology in Poland. In this paper, the measurements results and discussion on the results are presented too. The description of measuring-samples displayed on the Table 1.

2. DESCRIPTION OF THE MEASURING-METHOD

The method of measurement to determine the level of absorption material is based on measuring the absorption of the tested materials with respect to the aluminum plate without marked absorption material (sample No. 0). Block diagram of the test bench shown in Figure 1.

Measurement of absorption characteristics of the material was divided into three stages.

The first step was to find the distance in a distant area of antennas, for which we receive a minimum received signal reflected from the chamber walls and a wheelchair, without the metal plate. Then a moving trolley was set in the distant zone corresponding to the dimensions of the antenna (transmitter/receiver) and all frequency testing. In this way was searched the lowest value signal for all measurement frequencies. This was to ensure the greatest dynamic range in relation to the level of the signal reflected from a metal plate mounted on a trolley. As a result of the tests fixed the distance between the antennas and a moving trolley equal to 2.52 m. This distance was constant at all measuring frequencies and all tested samples.

Table 1: The description of measuring-samples.

Sample No.	Amount Layer	Tickness [mm]
1	2	15
2	3	16
3	2	13
4	2	13
5	1	9
6	1	-
7	1	-

The second step was to put samples No. 0 on the trolley and the reference measuring. During the reference measurement was measured in the signal reflected from the board of reference. Sample No. 0 was not covered with absorbent material (Figure 3).

In the third stage was carried out measuring the level of the signal reflected from the plate bearing the absorbing material (Figure 4). In the developed method of measurement, as a measure of absorption of electromagnetic wave absorbing materials was adopted relative difference of measured levels in these two stages. The level of absorption of different materials, the absorption was determined for levels of signal reflected from a metal plate without any absorbent material. Figure 2 shows the setting of the measuring stand antennas.

During the measurements the signal was generated by the microwave generator through a horn transmitting antenna. The reflected signal from the surface covered with absorbent material was measured by the receiving horn antenna and microwave receiver. Measurements were performed in the anechoic chamber to minimize reflections (Figures 3 and 4). During the measurements used the following measuring equipment:

- H.F. source — generator HP 8362 Series, working with the HP 8530 microwave receiver,
- two horn antenna,
- frequency converter Agilent 8511,
- specialized microwave receiver HP 8530,
- bench with shift table.

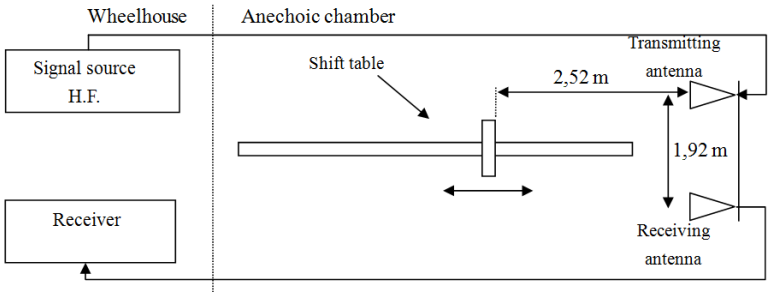

Figure 1: The block diagram of the position for measuring.

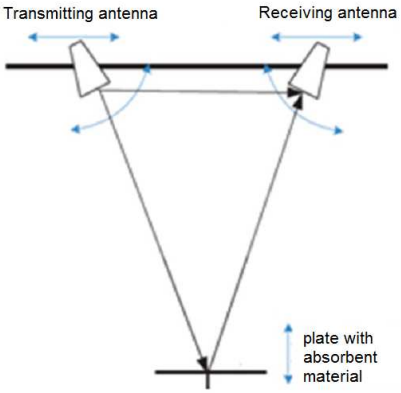

Figure 2: Arrangement diagram of measuring antennas in anechoic chamber.

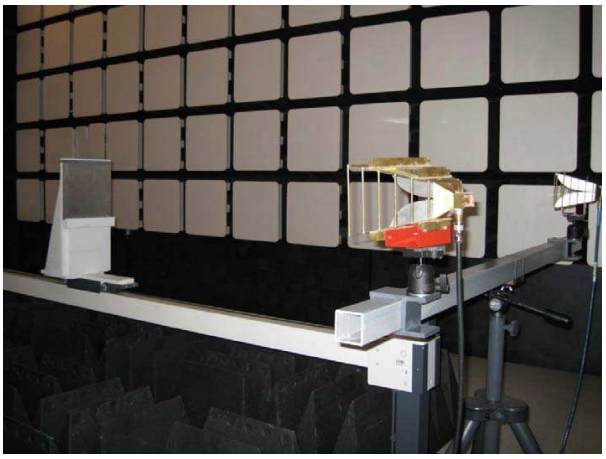

Figure 3: The measuring position prepared for conducting standardization measurement with metal plate.

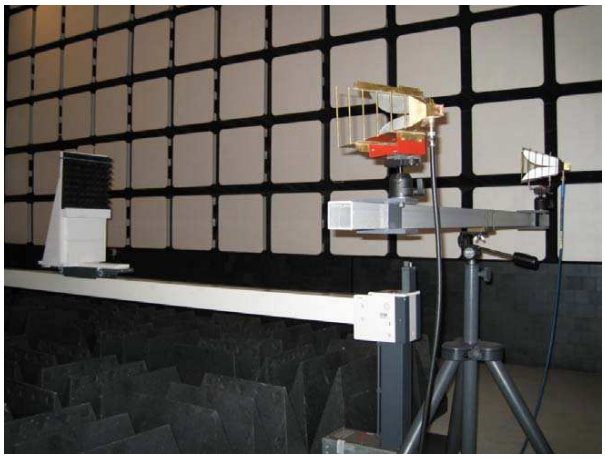

Figure 4: The measuring position prepared for conducting principal measurement with absorbing plate.

3. MEASUREMENT RESULTS

Table 2 shows the levels of reflected signals from the environment chamber, and subsequent sample measurements. Table 3 presents the results of absorption of various samples and the dynamic range of measurements. Absorption values of individual samples in function of frequency are shown in Figures from 5 to 11.

Table 2: Received signal levels for individual samples of material.

f [GHz]	Background level [dBm]	Sample No. 0 [dBm]	Sample No. 1 [dBm]	Sample No. 2 [dBm]	Sample No. 3 [dBm]	Sample No. 4 [dBm]	Sample No. 5 [dBm]	Sample No. 6 [dBm]	Sample No. 7 [dBm]
1	−64.0	−39.9	−42.9	−47.6	−46.0	−*	−45.7	−49.6	−49.0
2	−49.6	−37.8	−42.4	−46.8	−42.5	−*	−43.3	−53.2	−52.9
3	−45.7	−34.5	−36.8	−40.1	−37.4	−*	−37.6	−62.1	−59.3
4	−50.7	−39.1	−41.0	−45.0	−42.5	−*	−42.6	−71.9	−81.0
5	−55.8	−42.4	−46.2	−49.0	−47.0	−*	−47.7	−64.3	−67.4
6	−65.5	−43.0	−45.1	−47.8	−45.7	−45.0	−46.8	−75.0	−70.0
7	−63.7	−50.6	−49.2	−54.4	−49.5	−48.6	−48.6	−58.7	−58.1
8	−63.2	−51.0	−51.4	−59.0	−52.1	−50.5	−51.2	−63.7	−63.1
9	−59.5	51.4	−51.9	−55.9	−52.9	−51.2	−54.3	−80.9	−75.8
10	−69.5	61.5	−61.6	−64.9	−62.5	−60.9	−63.1	−75.2	−75.1

**Due to plate bending measurements have not been conducted*

Table 3: The level of absorption signal for individual samples of material and dynamic range measurements.

f [GHz]	Sample No. 0 [dBm]	Sample No. 1 [dBm]	Sample No. 2 [dBm]	Sample No. 3 [dBm]	Sample No. 4 [dBm]	Sample No. 5 [dBm]	Sample No. 6 [dBm]	Sample No. 7 [dBm]	Dynamic range measurements [dBm]
1	3	7.7	6.1	−*	5.8	9.7	9.1	24.1	3
2	4.6	9	4.7	−*	5.5	15.4	15.1	11.5	4.6
3	2.3	5.6	2.9	−*	3.1	27.6	24.8	11.2	2.3
4	1.9	5.9	3.4	−*	3.5	32.8	41.9	11.6	1.9
5	3.8	6.6	4.6	−*	5.3	21.9	25	13.4	3.8
6	2.1	4.8	2.7	−*	3.8	32	27	22.5	2.1
7	−1.4	3.8	−1.1	−*	−2	8.1	7.5	13.1	−1.4
8	0.4	8	1.1	−*	0.2	12.7	12.1	12.2	0.4
9	0.5	4.5	1.5	−*	2.9	29.5	24.4	8.1	0.5
10	0.1	3.4	1	−*	1.6	13.7	13.6	8	0.1

**Due to plate bending measurements have not been conducted*

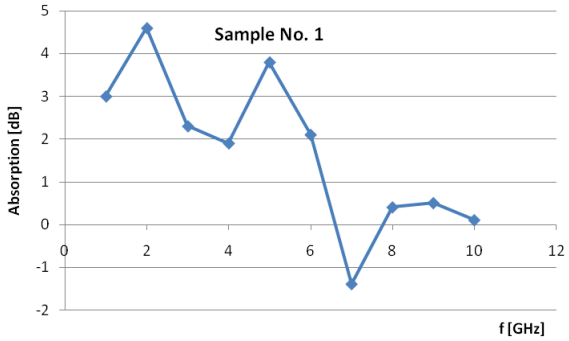

Figure 5: Absorption of the No. 1 sample in the frequency axis.

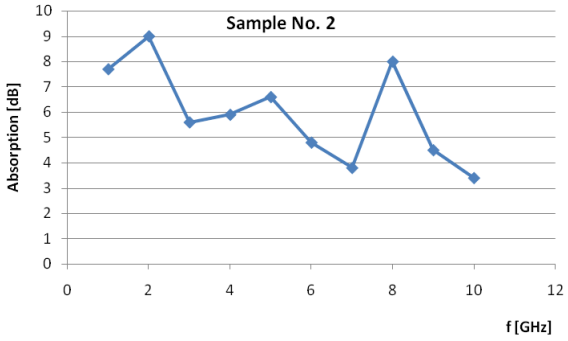

Figure 6: Absorption of the No. 2 sample in the frequency axis.

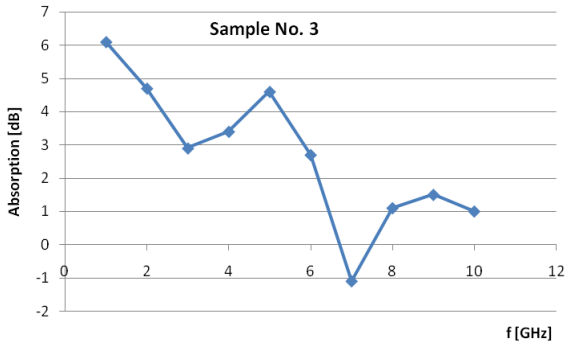

Figure 7: Absorption of the No. 3 sample in the frequency axis.

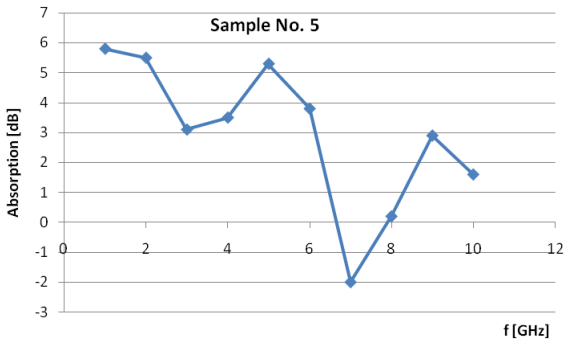

Figure 8: Absorption of the No. 5 sample in the frequency axis.

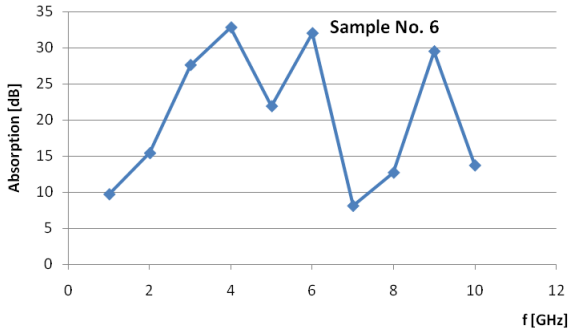

Figure 9: Absorption of the No. 6 sample in the frequency axis.

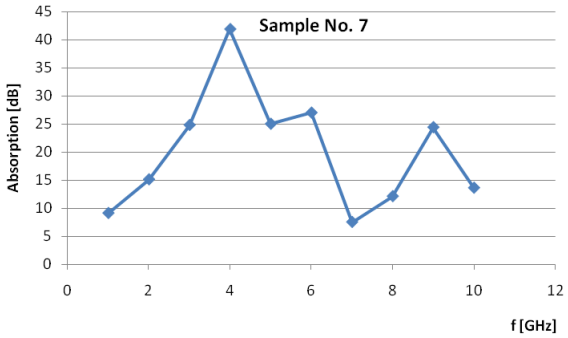

Figure 10: Absorption of the No. 7 sample in the frequency axis.

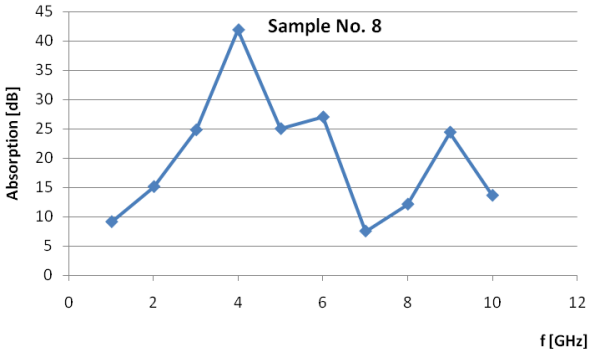

Figure 11: Absorption of the No. 8 sample in the frequency axis.

4. CONCLUSIONS

Analyzing the results of Table 3, it can be concluded that the best absorption for the flat samples were obtained for sample No. 2. The best results have given the absorption of the sample Nos. 6 and 7 These samples were made of absorbent materials in the shape of cones. Differences in absorption of various samples in the frequency function, results from the fact that materials have different characteristics absorption for different testing frequency.

Used the test stand has a significant drawback. It applies a small dynamic range of measurement set out in column 9 in Table 3. The dynamic range was defined as the difference between the level of the reflected signal from the metal plate and the level of the signal reflected from the environment (background level). An important factor influencing the dynamic range is the crosstalk between the transmitting antenna and receiving (insufficient insulation of the transmitting antenna and a receiver). When analyzing the absorption of individual samples shown in Table 3 and Figures 5 to 11, should take into account the dynamic range shown in Table 3. In cases where the measured values of absorption exceeds the dynamic range of the result should be regarded as debatable.

Negative values are result from values of uncertainty measurement the absorption in the test stand. The value absorption should be positive.

REFERENCES

1. Kubacki, R., *Microwave Antennas — Technology and Environment*, Publishing Houses of Communication & Telecommunication, Warsaw, 2008.
2. Orliński, B., "Research procedure PB-01 — Measurement of characteristics of antenna radiation," Laboratory of Electromagnetic Compatibility WEL WAT, Warsaw, 2005.
3. Mirabel, C. R., M. M. Inacio, and F. Roselena, "Radar cross section measurement (8–12 GHz) of magnetic and dielectric microwave absorbing thin sheets," *Revista de Fisica Aplicada e Instrumentacao*, Vol. 15, No. 1, 2002.

Multilayer Microstrip Antenna on Flat Base in the X Band (8.5 GHz–12 GHz)

M. Wnuk, R. Przesmycki, L. Nowosielski, and M. Bugaj
Faculty of Electronics, Military University of Technology
Gen. S. Kaliskiego 2 Str., Warsaw 00-908, Poland

Abstract— This report concerns problems connected with aerial techniques. A structure of microstrip antennas on dielectric base operating in the X band (8.5 GHz–12 GHz) has been described here. The mentioned antennas have been made as multilayer microstrip antennas slotted-supplied on flat base. In this article, there have been discussed antennas in form of antenna with a single radiator and array consisting of four radiators linearly-located and supplied in phase. In the article there has also been presented the measurement methodology of antenna parameters such as: antenna pattern, standing wave-ratio and antenna gain. For made models of antennas there have been conducted measurements of antenna electrical parameters in non-reflection chamber and placed in the article the results of the conducted measurements of the above mentioned antennas & comparison of them.

1. INTRODUCTION

Microstrip structures in aerial technique occurred relatively late. However recently there has been noticed an unusual development of constructing these antennas and enormous interest in their abilities as far as modern technology is concerned. Nowadays microstrip antennas are widely used in all radio-communication fields. It is due to simplicity of their construction, making facility and relatively low production costs. An important advantage of these antennas is their shape, small dimensions, little weight and esthetics of appearance. Microstrip antennas also provide high repeatability of parameters and big resistance to weather conditions.

2. MULTILAYER ANTENNAS SLOTTED — SUPPLIED

Microstrip antenna consists of metallic strap called radiator, printed on thin grounded dielectric base (screen). Lately more often there have been used multilayer structures which allow to obtain bigger and bigger operating band of antenna. One of crucial problems of microstrip antennas is their stimulation. In the simplest cases a single radiant element can be supplied by coaxial line, microstrip line or electromagnetic coupling. A more interesting and practical way of supplying multilayer antennas is slotted supply as shown in Figure 1.

The slotted-supplied antenna can be characterized in the following way: Due to lack of mechanical connections this antenna is of high reliability, very difficult in production, isolation of active arrays from radiant elements is possible, it is possible to adjust matching by selecting slot width, narrow operation band for single-layer antennas (1–5%), level of undesirable radiation −29 dB, (but below mass plane). For structures of multilayer slotted-supplied antennas the above mentioned parameters can be improved to a large extent. A sample antenna made in multilayer technology can be constructed in the following way. Radiant element is a rectangular patch etched on the upper side of the upper layer of laminate and stimulated by the slot cut in the screen covering the upper side of the lower layer of laminate. The slot can be supplied by asymmetrical strap line or concentric line.

This kind of antennas have the following features: Parameters of laminate for antenna and supplying line can be selected optimally, it is possible to obtain a very low level of undesirable radiation, necessity of precise assembly of packet occurs, difficult theoretical analysis, the biggest band width and opportunities to adjust impedance. We can state that for both classical and multilayer antennas presence of dielectric causes decrease of dimensions of radiant element in comparison with the variant without dielectric. One of the crucial disadvantages of classical strip antennas is their relatively small watt-hour efficiency. To a large extent it results from losses in dielectric. However in multilayer antennas radiated electromagnetic wave is significantly 'formed' not in dielectric but in free space. Therefore we can expect minor losses.

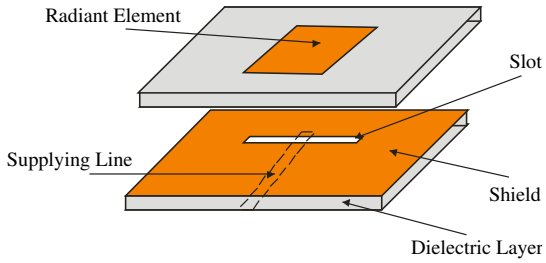

Figure 1: Microstrip antenna slotted-supplied.

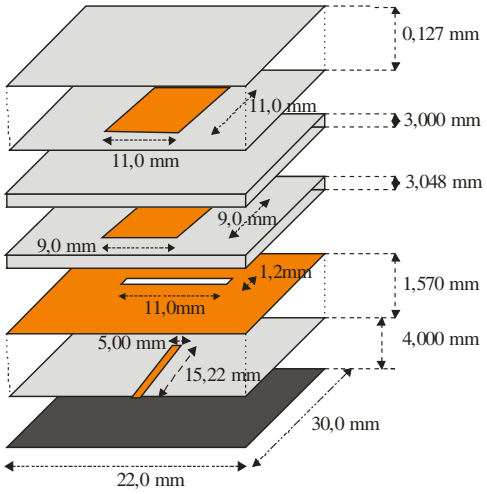

Figure 2: Structure of radiant element.

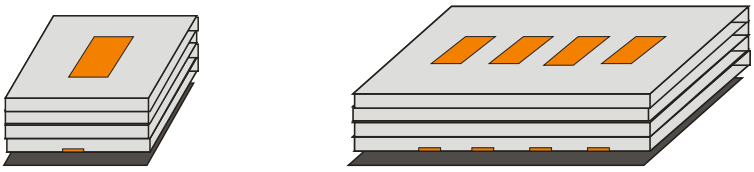

Figure 3: Construction of microstrip antennas. (a) Single element antenna 1×1, (b) four element antenna 4×1.

3. STRUCTURE OF RADIANT ELEMENT

Radiant element of the mentioned antennas consists of four, situated in parallel, one above the other, laminate plates and metal plate which is the shield of antenna. The structure of single radiant element has been shown in Figure 2. In the structure of antenna there have been used dielectrics of various electrical and geometrical parameters (different thickness). The first layer is dielectric which is 1.57 mm thick and has permittivity equal to 2.2. In this layer supplying line has been placed from the bottom and screen with designed supplying slot from the top. The second layer is dielectric which is 3.048 mm thick and has permittivity of 2.94. This layer contains only radiant element situated at the top of dielectric. The third layer is polimethacrylamidal foam — 3.0 mm thick and with permittivity of 1.07. The last layer is dielectric — 0.127 mm thick and with permittivity equal to 2.2, on which there is placed the second radiant patch occurring in parallel and in axis with relation to the first radiant patch in the second layer.

4. CONSTRUCTION OF ANTENNA

In the article there have been discussed two microstrip antennas, different in the number of active elements (radiators). The antennas were designed on the basis of the structure of active element presented above, setting up their operation at frequency 10 GHz. The first antenna has the single radiant element (Figure 3(a)), the second one consists of array of 4 active elements linearly placed, supplied in parallel and in phase (Figure 3(b)).

5. RESULTS OF MEASUREMENTS

In the article there has been briefly described the methodology of measurements, designed in the Laboratory of Electromagnetic Compatibility, Faculty of Electronics, Military University of Technology, and concerning antenna parameters. These are measurement methods determining such parameters as: standing wave ratio (SWR), input impedance, antenna pattern and antenna gain.

5.1. Measurement of Standing Wave Ratio and Input Impedance of Microstrip Antennas

Measurement of VSWR and input impedance requires conducting calibration of measuring position. Calibration allows to minimize systematic errors which could appear during measurements.

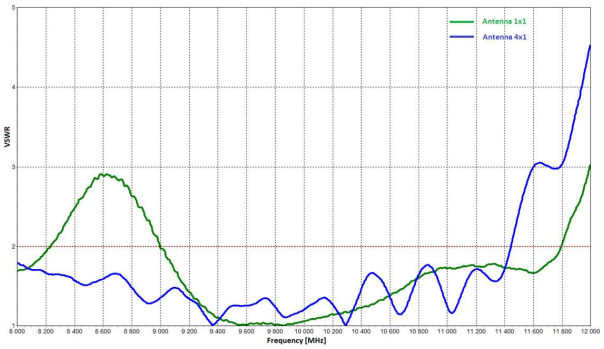

Figure 4: The VSWR course of tested antennas in the frequency function.

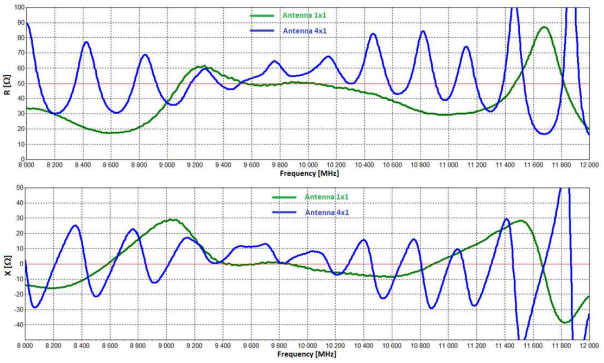

Figure 5: The input impedance course ($Z = R+jX$) of tested antennas in the frequency function.

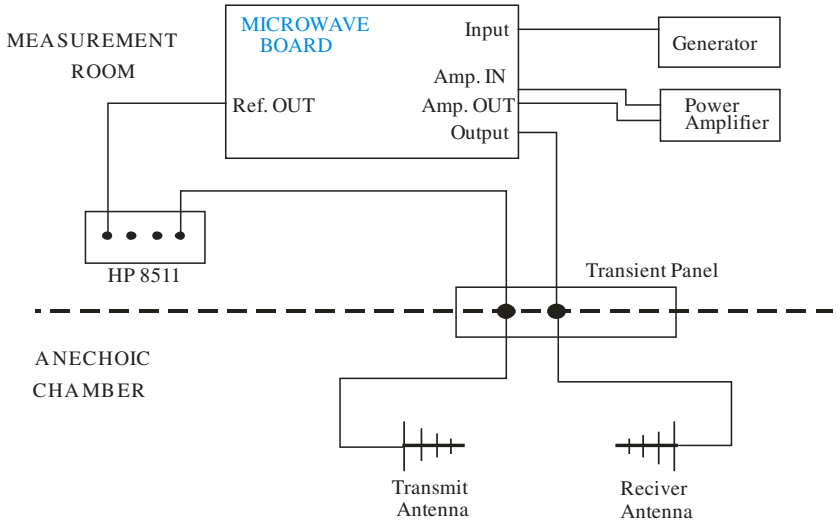

Figure 6: Block diagram of measuring position for antenna patterns measurements.

Because for VSWR measurements and input impedance for various types of antennas there can be used different kinds of ducts, it is calibration that will provide elimination of influence of their parameters on the measurement result. After performing calibration of measuring position and verification of correctness of the performed calibration, to slotted line in the place of matched load it is necessary to connect the tested antenna. Connection should be made in such a way that measuring cable is connected directly to antenna input or by using minimum essential number of adapters necessary for change of connection standard. Due to frequency band in which designed microstrip antennas operate, the measurements have been conducted in the range from 8 GHz to 12 GHz. The measurement results of VSWR and input impedance of the discussed microstrip antennas in the function of frequency are presented below. Accordingly in Figure 4 & Figure 5, there has been shown the VSWR course and the input impedance course (real and imaginary part) in the frequency function for the mentioned microstrip antennas.

5.2. Measurement of Microstrip Antennas Patterns

For measuring antenna patterns it is necessary to draw up measuring position in the configuration shown in Figure 6.

Measuring of antenna patterns is performed in the below mentioned way. For initial position of rotary head desired power in the generator output is set and the first measuring frequency. Measurement of the power level of reference signal is conducted as well as test signal received by the tested antenna. After finishing measurement there comes retuning of the signal source and measuring both signals for next declared frequency. These measurements are carried out in turn until the last assigned frequency. According to the assigned step, rotary head performs rotation of the tested antenna to the next angular position and stops. Finishing measurements takes place after measuring power levels for the whole full rotation angle of the tested antenna.

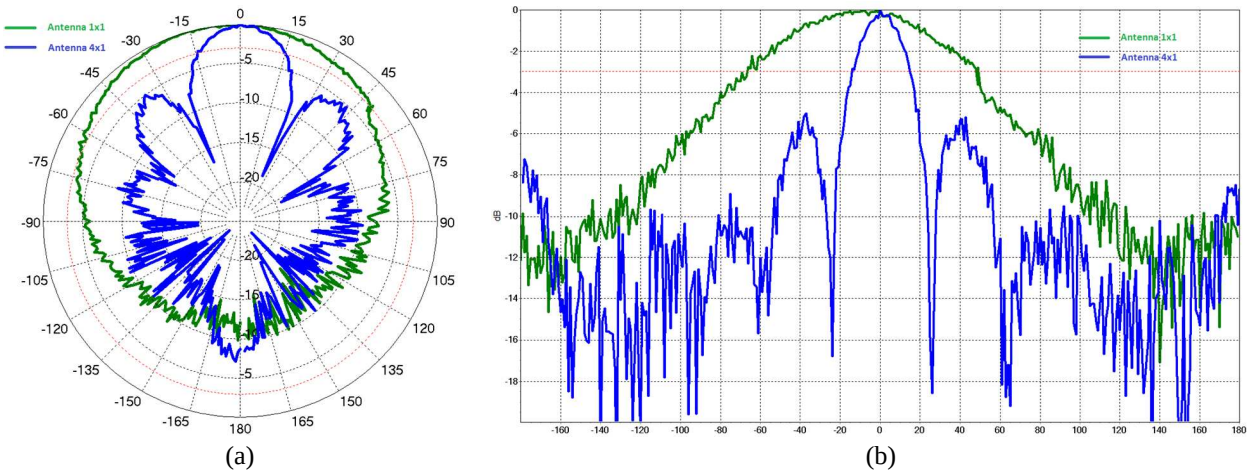

Figure 7: Normalized antenna patterns of microstrip antennas for the 10 GHz frequency in plane of vector E. (a) Polar coordinates, (b) rectangular coordinates.

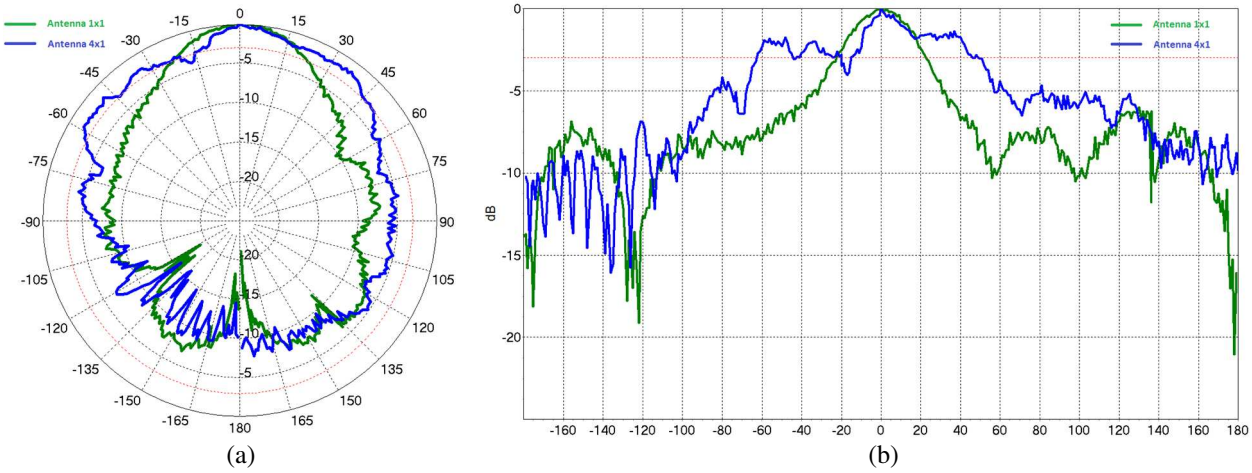

Figure 8: Normalized antenna patterns of microstrip antennas for the 10 GHz frequency in plane of vector H. (a) Polar coordinates, (b) rectangular coordinates.

On the basis of VSWR results and input impedance of the discussed microstrip antennas, the measurements of antenna characteristics have been made in the range of frequency of operating band of antennas, taking into account edges of frequency interval of operating band of antenna and mind-band frequency. The measurement results of the discussed microstrip antennas in the angle function for selected frequencies of the whole operating band are practically identical. Because of that, below there are presented normalized characteristics of the discussed microstrip antennas for the selected frequency 10 GHz in polar and rectangular coordinates in plane of vector E (Figure 7(a) & Figure 7(b)) and vector H (Figure 8(a) & Figure 8(b)).

5.3. Measuring Microstrip Antennas Gain

For measuring antenna gain it is necessary to draw up measuring position in the configuration presented in Figure 6. While measuring antenna gain with the comparative method it is necessary to have detailed information on the course of gain of ancillary antenna. This antenna is used as a model antenna, to which power gain of the tested antenna will be determined. The second ancillary antenna is used as a transmitting antenna and should provide only radiation of electromagnetic wave of desired frequency, in relatively narrow angular sector. Comparative method consists in performing measurements of the signal received by model antenna and tested antenna, and on this basis determining relative gain difference of both antennas. Having information about relative gain difference of both antennas it is possible to assign the gain value of the tested antenna from the relation presented below:

$$G_B[\text{dBi}] = G_W[\text{dBi}] + P_B[\text{dBm}] - P_W[\text{dBm}], \tag{1}$$

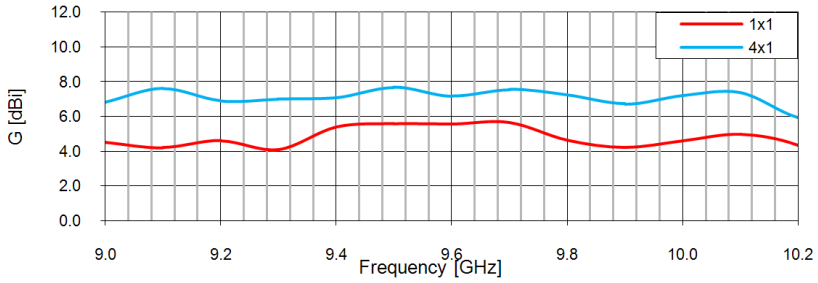

Figure 9: Gain of the tested antennas in the frequency function $G[\text{dBi}] = f(f[\text{GHz}])$.

where: $G_B[\text{dBi}]$ — assigned gain of the tested antenna for specific frequency referring to isotropic antenna; $G_W[\text{dBi}]$ — read out from calibration chart model antenna gain for particular frequency with reference to isotropic antenna; $P_B[\text{dBm}]$ — measured power level of the signal received by the tested antenna for specified frequency; $P_W[\text{dBm}]$ — measured power level of the signal received by model antenna for specified frequency.

Due to the range of frequency in which designed microstrip antennas work and measuring possibilities, measurements of antenna gain have been made for selected frequencies in the range from 9 GHz to 10.2 GHz. The results of power gain measurements of the discussed microstrip antennas are shown in Figure 9.

6. CONCLUSIONS

After analyzing the measurement results of the discussed microstrip antennas we can state that presented antennas are characterized by good mechanical and electrical parameters. Depending on needs, particular antennas can be used in various fields. The form of radiation characteristics is in accordance with theoretical assumptions. In plane of vector E usable width of the main lobe narrows down along with increase of number of active elements in aerial array, improving the value of antenna gain as well. However in plane of vector H we do not increase the number of active elements, so characteristics for both antennas are similar. Some asymmetry of characteristics in both planes can result from asymmetry of antenna construction and inaccuracy of setting phase centre of antenna during performed measurements. Operating band of designed antennas is located in range of X band (8 GHz–12.5 GHz). For antenna with single radiant element operating band is located in the frequency range from 9 GHz to 11.6 GHz, while for antenna with four radiant elements operating band is within frequency ranging from 8.9 GHz to 11.4 GHz. Using the equation presented below:

$$\Delta f = \frac{f_{\max} - f_{\min}}{f_{\text{center}}} * 100\% = 2 * \frac{f_{\max} - f_{\min}}{f_{\max} + f_{\min}} * 100\%, \tag{2}$$

where: $f_{\max}$ — maximum frequency of antenna operating bandwidth, $f_{\min}$ — minimal frequency of antenna operating bandwidth, f_{center} — center frequency of antenna operating bandwidth, it is possible to calculate the antenna relative bandwidth which equals according 25.2% (for 1×1 antenna) and 24.6% (for 4×1 antenna) thus confirming the assumption that multilayer structures allow for designing antennas of relatively wide operating band what has been rather difficult so far.

REFERENCES

1. Kubacki, R., *Microwave Antennas — Technology and Environment*, Publishing Houses of Communication & Telecommunication, Warsaw, 2008.
2. Orlinski, B., "Research procedure PB-01 — Measurement of characteristics of antenna radiation," Laboratory of Electromagnetic Compatibility WEL WAT, Warsaw, 2005.
3. Orlinski, B., "Research procedure PB-02 — Measurement of coefficient of standing wave and input impedance of antennas," Laboratory of Electromagnetic Compatibility WEL WAT, Warsaw, 2005.
4. Przesmycki, R., "Research procedure PB-05 — Measurement of antenna power gain," Laboratory of Electromagnetic Compatibility WEL WAT, Warsaw, 2007.

Active Microstrip Antennas Operating in X Band

Marek Bugaj, **Rafal Przesmycki**, **Leszek Nowosielski**, **and Kazimierz Piwowarczyk**
Faculty of Electronics, Military University of Technology, Gen. S. Kaliskiego 2 Str., Warsaw 00-908, Poland

Abstract— The paper describes problems related to antenna technology. The paper shows the construction of active microstrip antennas on a dielectric substrate operating in X band (8.5 GHz–12 GHz). The article presents two active antennas have been designed as a multilayer structure of microstrip antennas performed on two different shapes of the substrate. The microstrip patch is feed by microstrip line trough slot in the common ground plane. The first of these antennas is the four elements array on flat substrate consisting of four dielectric layers. The second antenna is the four elements array located on the conformal substrate consists of two dielectric layers. For so performed antenna models were made measurements in the anechoic chamber of typical electrical parameters, such as standing wave ratio, input impedance, radiation pattern, gain. The article also analyzes the results of computer simulations and measurements, thereby demonstrating the advantages and disadvantages of microstrip antennas placed on different surfaces.

1. INTRODUCTION

The microstrip antennas have been one of the most innovative fields of antenna techniques for the last fifteen years. In high-performance spacecraft, aircraft, missile and satellite applications, where size, weight, cost, performance, ease of installation, and aerodynamic profile are constraints, low profile antennas may be required. Presently, there are many other government and commercial applications, such as mobile radio and wireless communications that have similar specifications. To meet these requirements, microstrip antennas can be used. These antennas are low-profile, conformable to planar and non-planar surfaces, simple and inexpensive to manufacture using modern printed circuit technology, mechanically robust when mounted on rigid surfaces, compatible with MMIC designs, and when particular patch shape and mode are selected they are very versatile in terms of resonant frequency, polarization, pattern, and impedance. In addition, by adding loads between the patch and the ground plane, such as pins and varactor diodes, adaptive elements with variable resonant frequency, impedance, polarization, and pattern can be adjusted [1]. Radiating patch may be square, rectangular, circular, elliptical, triangular, and any other configuration. In this work, rectangular microstrip antennas are the under consideration (Figure 1).

The methods of analysis and projection of microstrip antennas have developed simultaneously with the development of aerials [3]. Nowadays several methods of analyzing the antennas on dielectric surface are used, however, the most commonly used ones are the full wave model based on Green's function and the method of moments where analysis relies on solution of integral equation, concerning electric field, with regard to unknown currents flowing through elements of the antenna and its feeding system [2].

2. ANTENNA ARRAYS

The aggregate at least two antennas is called an antenna array. Accordingly most often uses half-wave antennas or microstrip antennas. Typically, antennas are usually spaced half a wavelength

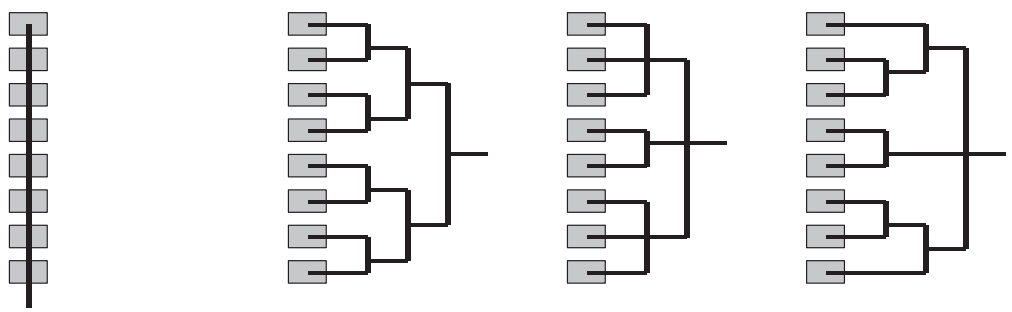

Figure 1: Methods of the power supplies of microstrip lineal parley: (a) In series. (b) Parallels.

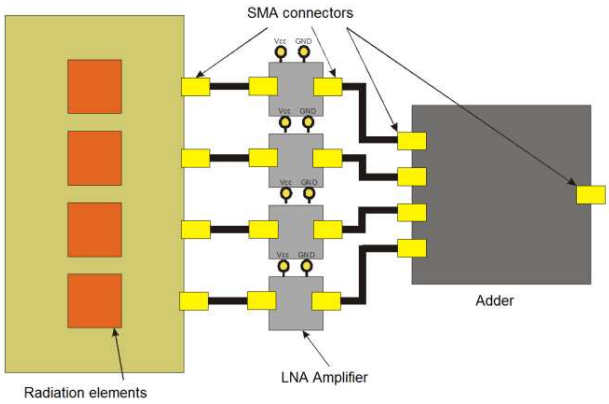

Figure 2: Constructions of the antenna array.

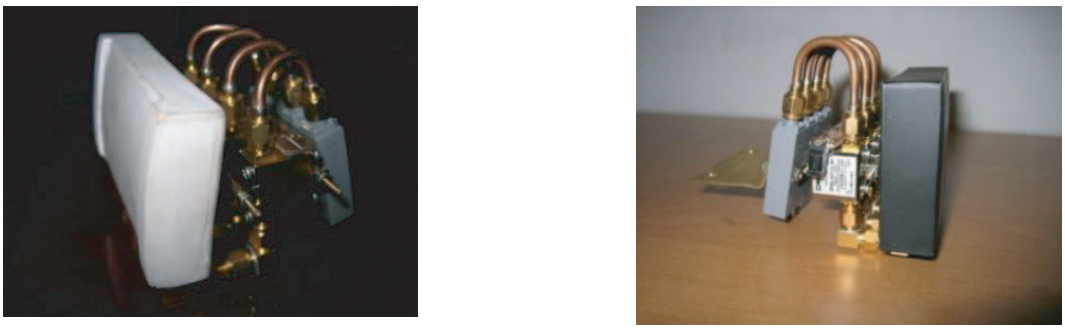

(a) (b)

Figure 3: View of model active antenna: (a) Conformal. (b) Planar.

apart. This allows us to obtain the desired radiation characteristics of such antenna system. Antenna arrays can be feed in series or in parallel, or a combination of the power of parallel and serial.

When the array antenna is fed in series then supply lines are connected to the radiating elements as shown in Figure 1(a). If the array is fed in parallel (Figure 1(b)), the input signal is separated into individual patches (radiators). Such methods fed of antenna elements give the possibility to form amplitude and phase of individual radiating elements, which leads to changes in the shape of the radiation pattern.

If a single antenna (radiator) does not provide the desired energy gain, or if the presence of interference requires the elimination of incoming signals from a particular direction, we can combine several antennas (radiators) in a single antennas array.

3. CONSTRUCTION OF THE ANTENNA ARRAY

In the paper there have been discussed two microstrip active antennas, different in number of layers. The microstrip planar active antenna consists of four layers with two radiators. Radiators are microstrip patches. The microstrip patch is feed by microstrip line trough slot in the common ground plane. Coupling of the slot to the dominant mode of the patch and the microstrip line occurs because the slot interrupts the longitudinal current flow in them. The microstrip conformal active antenna consists of two layers with one radiator. In structural of antennas there have been used dielectrics of various electrical and geometrical (thickness) parameters.

Microstrip active antenna array consist of radiator, printed on thin grounded dielectric base, LNA amplifier and adder. For the construction of antennas used for the following items: Power Divider/Combiner (Adder) MCLI4-8, MMIC Amplifier 6884–700. To connect the array elements were used: Semi-Rigid Coax Cable 0.141" — EZ141/M17. Schematic construction of the antenna array is shown in Figure 2. Planar active antenna and conformal active antenna uses the same model of the adder and the amplifier.

Figure 3 shows the models of active antennas: conformal and planar. Antenna is shown along with components and antennas ready models.

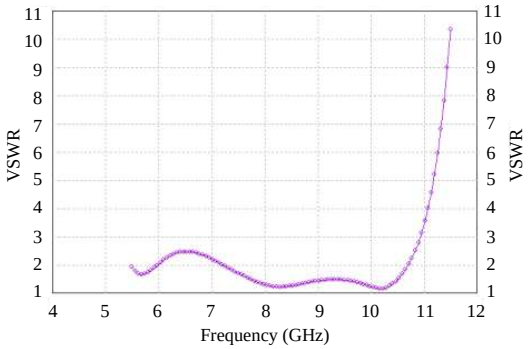

Figure 4: The VSWR course of planar active antennas in the frequency function.

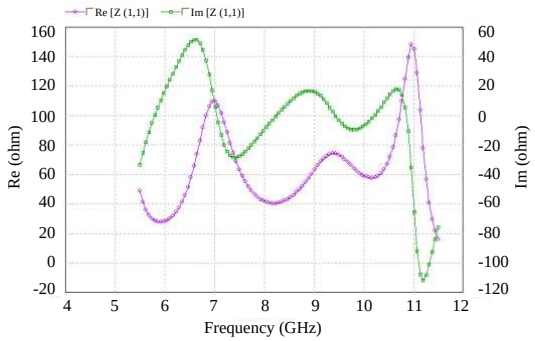

Figure 5: The input impedance course of planar active antennas.

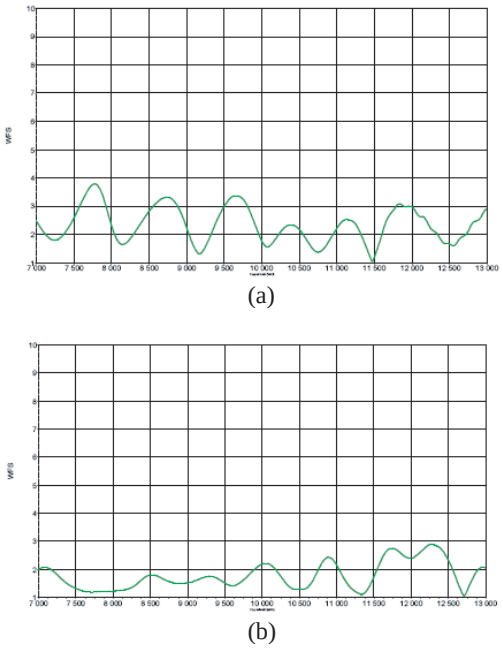

Figure 6: The VSWR course of tested antennas in the frequency function: (a) Conformal active antenna. (b) Planar active antenna.

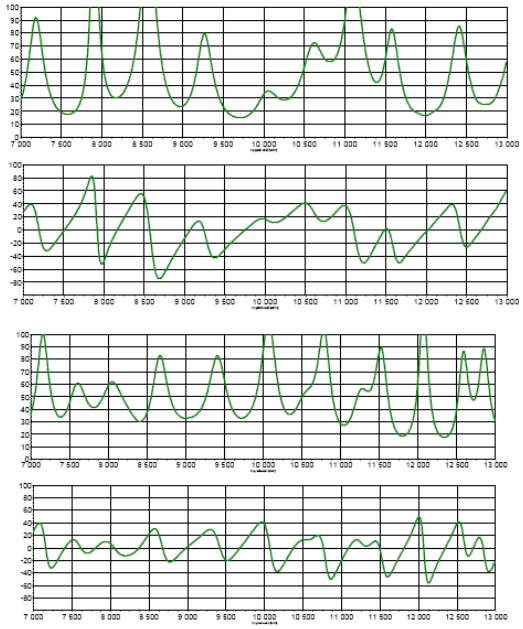

Figure 7: The input impedance course of tested antennas in the frequency function: (a) Conformal active antenna. (b) Planar active antenna.

The construction of antenna was covered with special foam with the permeability near unity. The foam acts as a protective element antennas.

4. THE RESULTS OF COMPUTER SIMULATIONS

In the process simulation of antennas have been determined the following parameters: VSWR, gain, radiation patterns and input impedance. In Figures 4 and 5 are shown VSWR and input impedance for an antenna built on a flat surface.

The antenna operates in the band from 7.2 to 10.7 GHz. For this range the value of VSWR < 2, input resistance varies in the range from 41 [Ω] to 65 [Ω] and the reactance in the range of -28 [Ω] to 18 [Ω].

5. THE MEASUREMENT RESULTS

In order to investigate the antenna were measured the following parameters: VSWR, gain, radiation patterns and input impedance. The measurement of VSWR and input impedance (real and imaginary part) of the discussed microstrip active antennas in frequency domain are presented in Figures 6 and 7.

Measurments of antenna gain have benn made for selected frequencies in the range from 8 GHz to 12 GHz. The result of the power gain measurments of the discussed microstrip active antennas

are shown in Figure 8.

On Figure 9 shows the radiation characteristics of antennas in two planes. The shape of the radiation characteristics is consistent with theoretical assumptions. In the plane E vector useful width of the main beam narrows with increasing the active elements in array antenna also improves the value of energy gain. Using the antenna gain amplifier provides power at 14 [dBi] for conformal antennas, and 17 [dBi] for a flat antenna.

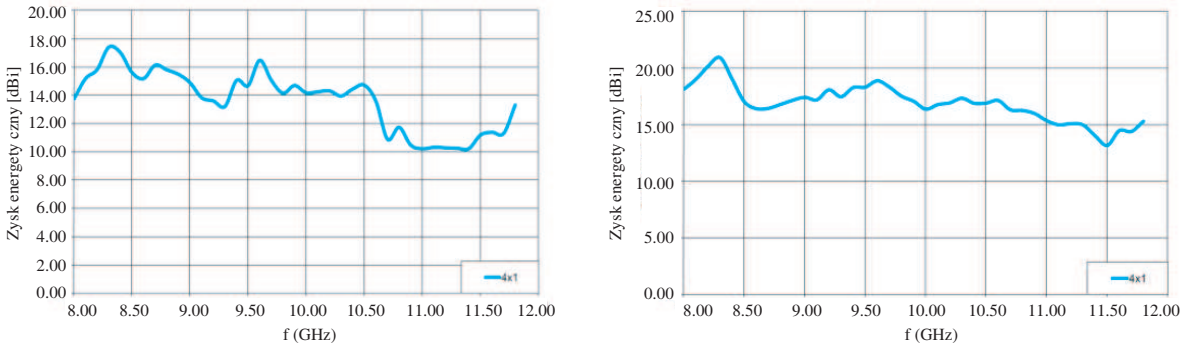

Figure 8: Gain of the tested active antennas in frequency function: (a) Conformal active antennas. (b) Planar active antennas.

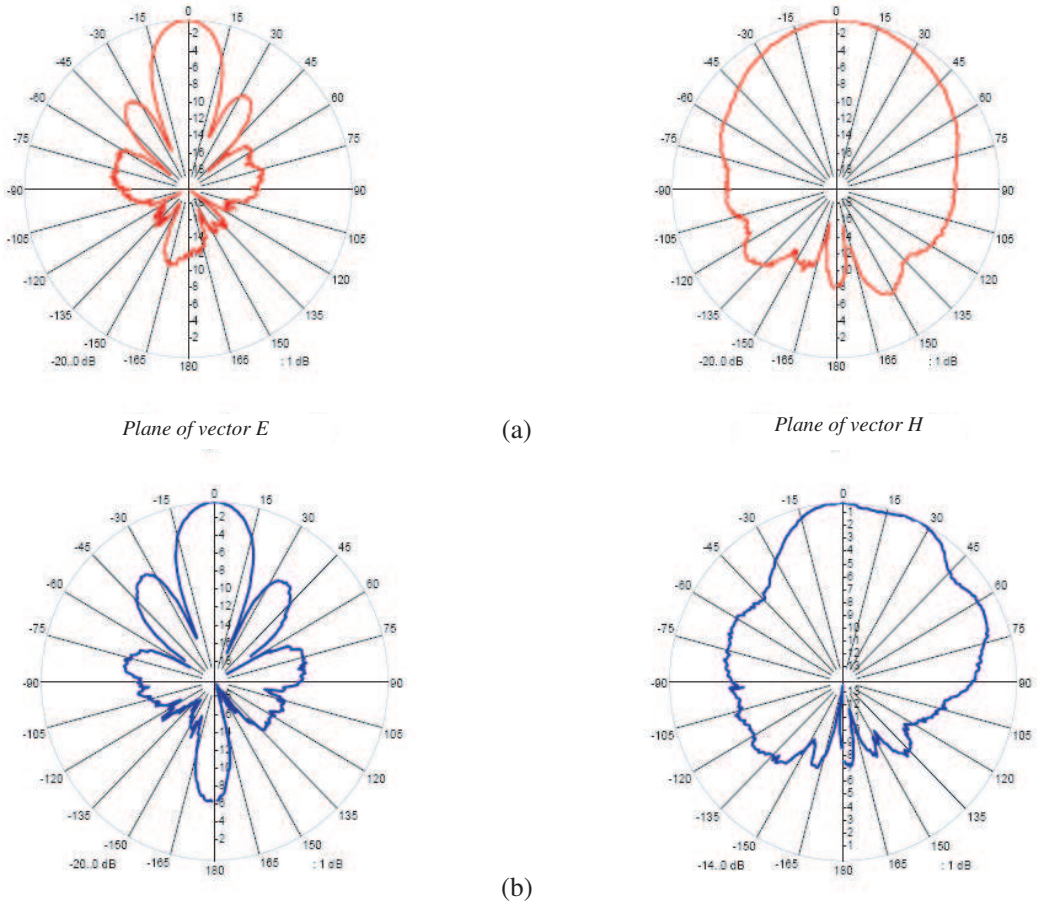

Figure 9: Normalized antenna patterns for 10.4 GHZ for: (a) Conformal active antenna. (b) Planar active antenna.

6. CONCLUSION

The results of the study are satisfactory. The analysis of the antenna was done by the usage of IE3D — Zeland Software (method of moments — MoM) and CST Microwave Studio. The method has been applied to the microstrip-fed slot antenna and to the aperture coupled antenna with a good result when compared with measured data. The coupling aperture when used judiciously can give rise to a considerable increase in bandwidth. Measurements confirmed the calculations. The bandwidth of aerial is the result of way feed as well as the utilization to build the many-layers substrates and selection they parameters. The result for the physical model confirms the correctness of the analysis and calculations obtained using the calculation method based on the method of moments. Operating band of designed active antennas is located in X band.

REFERENCES

1. Turker, N., F. Gunes, and T. Yildirim, "Artificial neural design of microstrip antennas," *Turk. J. Elec. Engin.*, Vol. 14, No. 3, 445–453, TUBITAK, 2006.
2. Pozar, D. M. "A reciepprocity mothod of analisis for printed slot and slot-coupled antennas," *IEEE Trans. Antennas Propaga.*, Vol. 34, No. 12, 1439–1446, Dec. 1986.
3. Bugaj, M. and M. Wnuk, "Optimization parameters of dielectric in aperture-coupled stacked patch antenna on bandwidth," *MIKON-2010: International Conference on Microwave, Radar and Wireless Communications*, 2010.

Efficient Method of 3G Signal Detection

Paweł Skokowski and Jerzy Łopatka
Faculty of Electronics, Military University of Technology, Gen. S. Kaliskiego 2 Str., Warsaw 00-908, Poland

Abstract— This paper concerns the problems of efficient methods enabling detection of the 3G signals. Worked out procedures enable detection of the 3G signal in uplink and downlink transmission using spectrum and autocorrelation function analysis. Proposed method is realized using software application, which means that additional devices are not required. The practical application of worked out detection methods are proposed too. Efficiency tests of proposed detection method are also introduced in the work. Authors decided to accept the probability of detection (Pd) as the basic merit of the proposed method efficiency.

1. INTRODUCTION

There is a lot of standards used for the wireless transmission using different techniques of modulation and exploit channels with various bandwidths. Systems are expected to be faster, safer, interferences resistant and should effectively use available frequency band. Some of them use the shareable sets of frequency channels that require an effective recognition of the working system. Monitoring of their work and whole electromagnetic situation is important in government reconnaissance systems and in cognitive radios. Narrowband emissions, with large SNR can be easily detected, using simple level detectors. More sophisticated is detection of wideband DSSS signals, hidden below the background noise level. Universal Mobile Telecommunications System (UMTS) uplink signal, transmitted with relatively low level by mobile terminal additional spreaded and scrambled before transmission is one of the most interesting cases.

2. PROBLEMS

For analysis of DSSS signals specialized devices like spectrum analyzers or dedicated software can be used [2–5]. They enable monitoring of UMTS Uu interface and require cooperation with system operator. The measurement device must be logged into the system and as a system's element, the device knows all information about signal processing in physical layer like: scrambling code, spreading factor etc.. Currently available solutions are mainly devoted to analysis only the IuB interface what means they are able to analyse only the communication protocol. Analysis using non-cooperative (means that analysis is performed without logging into the system and knowledge about transmitted signal parameters what is very difficult) systems are limited. It seems that the most important thing is to detect radio transmission especially in case of electromagnetic warfare, signal detection (for example to prevent RC-IED) and recognition to prevent terrorist attacks, crimes etc..

3. 3G SIGNAL DETECTIONS

Proposed method is realized using software application, which means that additional devices like UMTS receiver are not required (except broadband receiver). As a broadband receiver USRP2 (Universal Software Radio Peripheral version 2) was used with daughterboard WBX. Technical parameters of this hardware are as follows [10]:

- 50 MHz to 2.2 GHz coverage
- Transmit Specs:
  - 50–100 mW (17–20 dBm) from 50 MHz to 1.2 GHz
  - 30–70 mW (15–18 dBm) from 1.2 GHz to 2.2 GHz
  - 25+ dB Output power control range under software control
- Receive Specs:
  - Noise figure of 5–7 dB
  - IIP3 of 5–10 dBm
  - IIP2 of 40–55 dBm
  - At every frequency there is a gain setting which gives a noise figure of less than 8 dB while simultaneously giving an IIP3 of better than 0 dBm and an IIP2 of better than 40 dBm.

As one can see, radio parameters especially for receiving part have poor performance. Authors decided to use this hardware because this is low cost Commercial Off The Shelf (COTS) equipment and additionally this is Software Defined Radio (SDR) platform, what means it can be used for many others purposes.

The analysis is based on the data in complex IQ form, representing recorded real uplink UMTS signal. To conduct the analysis assumed is that studied signal is a signal in the digital form, with the predetermined length of record and known sample frequency. Tests are conducted in the "off-line" mode.

Detection of the signal in radio channel (for appropriate UMTS frequency band) is possible by determining its spectrum or spectrogram. Unfortunately this method require signals with large SNR, so it can be used for detection of UMTS downlink signals, that have bigger power. After detection of the downlink signal, frequency 190 MHz lower (FDD duplex difference) should be checked to find the presence of uplink signal.

On Fig. 2, it can be seen that it is possible to detect signal in uplink. In case when broadband receiving signal has lower power or is hidden below noise level (Fig. 6), detection using spectrum analysis is impossible using simple level detectors or even using DAM (Delay And Multiply) detectors. It means that classic detectors are not efficient in detection for spreaded signals.

Detection can be investigated also using correlation analysis. If in the radio channel no transmission exists, the autocorrelation function of noise looks like presented on Fig. 3. Similar results we can achieve for UMTS signal hidden below noise level. However, Fig. 4 shows that for longer analysis time of UMTS uplink signal, the autocorrelation shape is completely different and some

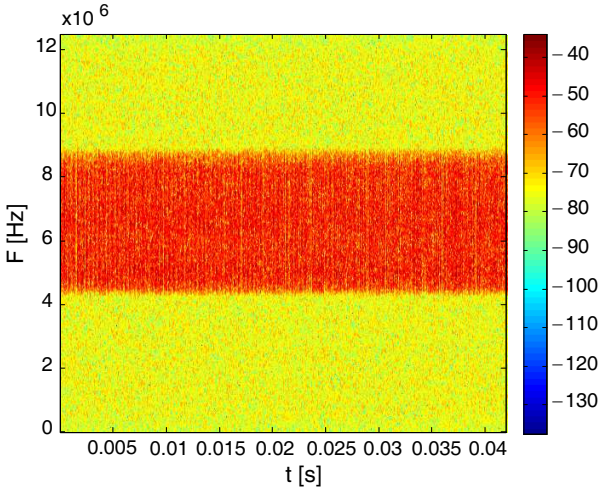

Figure 1: UMTS downlink signal spectrogram.

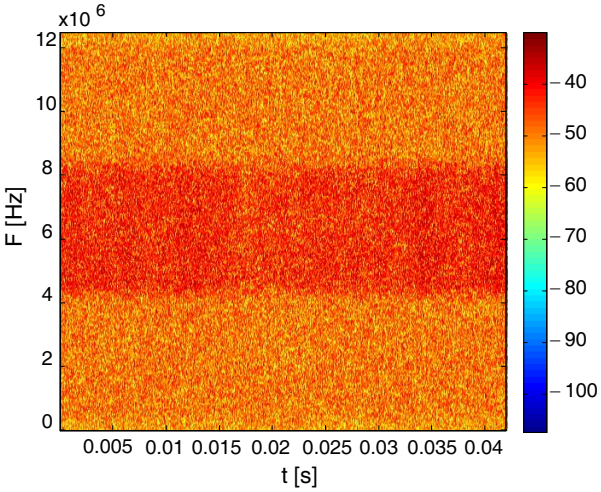

Figure 2: UMTS uplink signal spectrogram.

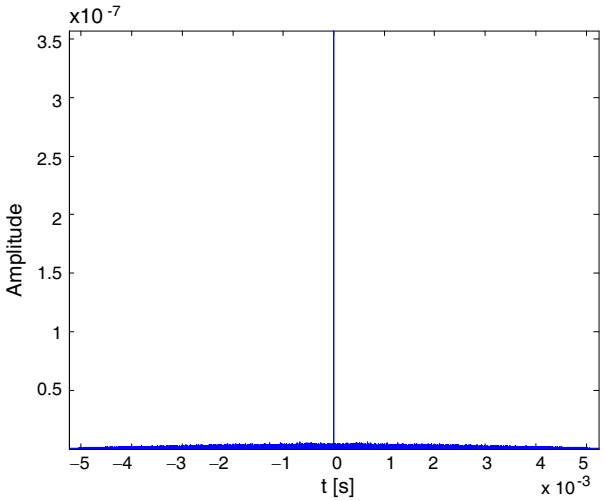

Figure 3: Autocorrelation function of analyzed 3G uplink signal.

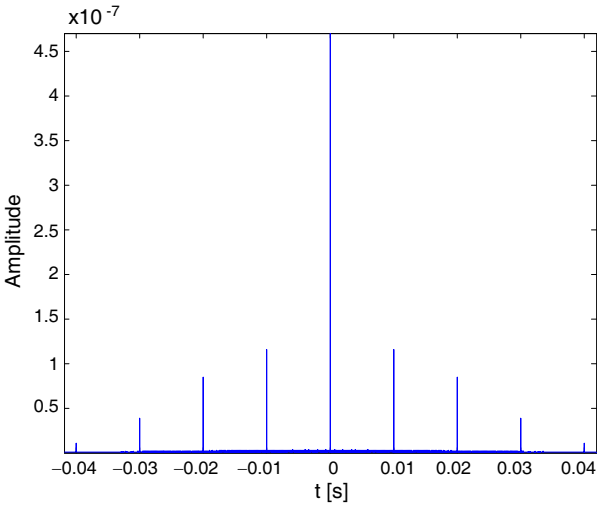

Figure 4: Autocorrelation function of analyzed 3G uplink signal, longer time of analysis.

periodicity related to transmitted data structure can be detected. Estimated period time equals 10 ms which is the same as frame duration for UMTS signal [7–9]. This property was used for signal detection.

In general, the correlation function requires normalization to produce an accurate estimate. The autocorrelation biased estimator is computed by equation:

$$R_{xx} = \frac{1}{N} \sum_{n=0}^{N-1-|k|} x(n)x^*(n-k) \tag{1}$$

Detection algorithm is very simple. If for 10 ms in autocorrelation function, is a local maximum 15 dB bigger than autocorrelation function for noise only, detector decides about occurrence of transmission. To improve elaborated detector efficiency for signals with lower SNR method of autocorrelation (R) summation for data with time offset equals two frame duration was made:

$$R_{sum} = abs\left[\sum_{i=1}^{N} \mathrm{Re}(R_i) + \mathrm{Im}(R_i)\right] \tag{2}$$

This operation, for $N = 16$ improves UMTS detector's ability by 3 dB. On Fig. 5, result for this operation is presented. Increasing number of summation from 16 to 32 improves detector's

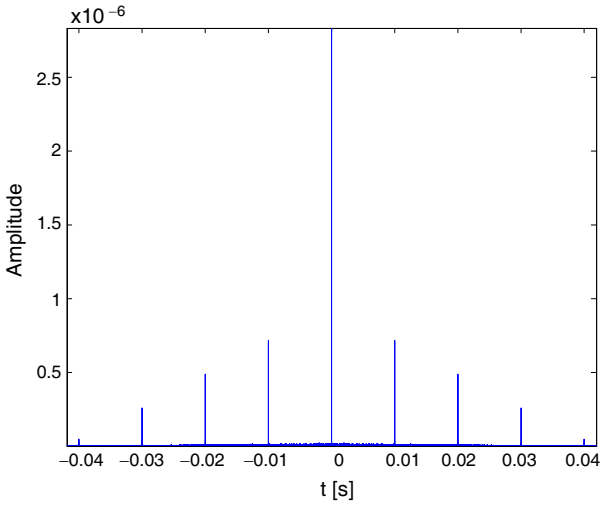

Figure 5: Sum of autocorrelation functions of analyzed 3G uplink signal.

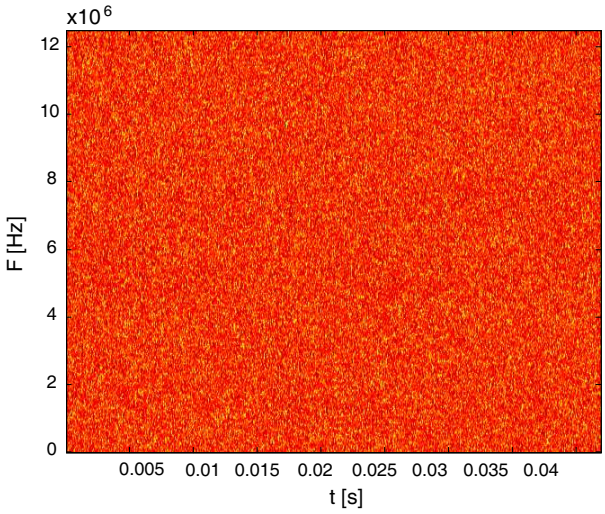

Figure 6: UMTS uplink signal spectrogram for SNR = −15 dB.

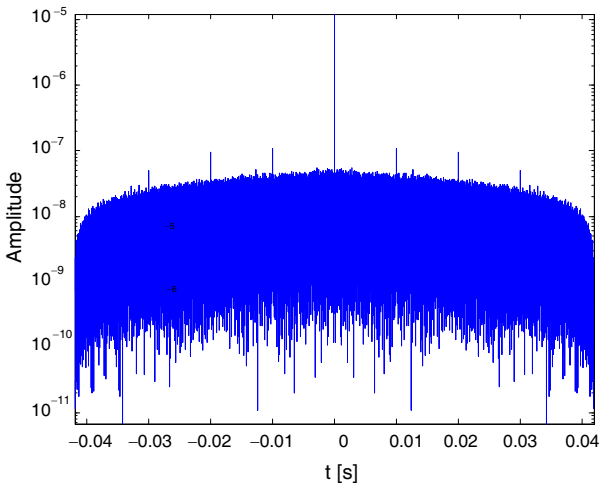

Figure 7: Autocorrelation function of analyzed uplink signal for SNR = −15 dB.

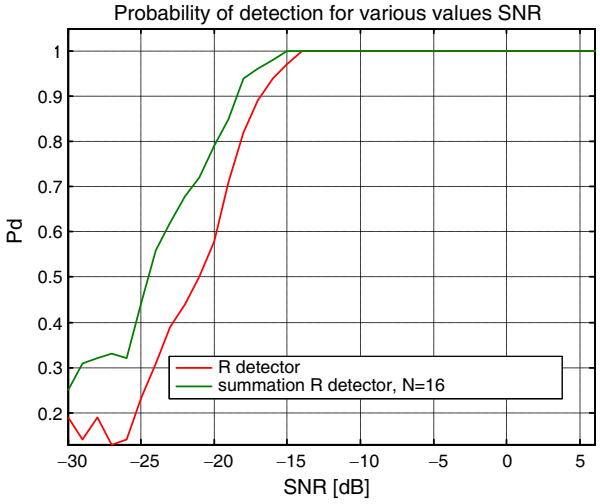

Figure 8: Probability of detection for various SNR values for elaborated detectors.

efficiency, but the computation process is much longer.

4. DETECTOR EFFICIENCY

To verify robustness of the elaborated detection method against noise, a complex white Gaussian noise was added to the recorded signal. For various values of SNR number of tests were carried out to detect signal. As a merit of methods quality, a probability of detection (Pd) was used. Performed tests for SNR from -30 dB to 6 dB showed that correct signal detection is possible for UMTS uplink signals with SNR ≥ -20 dB. Results for probability of detection for various values of signal to noise ratio are shown on Fig. 8.

5. CONCLUSION

Worked out procedures enable detection of the 3G signal in uplink and downlink transmission using spectrum and autocorrelation function analysis method. For classic level detectors signal can be detected only if power of receiving signal is bigger than noise level. Elaborated method using autocorrelation detectors is efficient for signals SNR ≥ -20 dB.

The elaborated method of detection can be used for "off-line" monitoring of UMTS signals. Proposed methods can be also used to design device working in a real time, enabling the detection of UMTS signals in the on-line mode for government reconnaissance, to prevent RC-IED attacks or as a signal sensing part of monitoring manager in cognitive radios.

REFERENCES

1. Skokowski, P. and J. Lopatka, "Technical analysis of the wireless local area network signals," *Proceedings of the 1st International Conference on Signal Processing and Telecommunication Systems ICSPCS'2007*, 649–659, Gold Coast, Australia, 2007.
2. "Testing and troubleshooting digital RF communications receiver designs," Application Note 1314, Agilent Technologies.
3. Castro, J. P., *The UMTS Network and Radio Access Technology*, John Wiley & Sons Ltd., West Sussex, England, 2001.
4. Agilent Signal Studio for HSDPA over W-CDMA, Technical Information, Agilent.
5. MS2781A Spectrum Analysis and Vector Signal Analysis with Bandwidths to 50 MHz, Technical Information, Anritsu.
6. Licitra, G., D. Palazzuoli, A. S. Ricci, and A. M. Silvi, "UMTS signal measurements with digital spectrum analysers," *Radiat Prot Dosimetry*, Vol. 111, No. 4, 397–401, Regional Agency for Environmental Protection of Tuscany, Italy, 2004.
7. 3GPP TS 25.213 Spreading and Modulation (FDD), Version 4.1.0, June 2001.
8. 3GPP TS 25.214 Physical Layer Procedures (FDD), Version 4.4.0, March 2003.
9. 3GPP TS 25.215 Physical Layer Measurements, Version 5.4, March 2003.

MIMO Implementation with Alamouti Coding Using USRP2

Anna Kaszuba, Radoslaw Checinski, and Jerzy Lopatka
Faculty of Electronics, Military University of Technology, Warsaw 00-908, Poland

Abstract— In this paper authors present a novel implementation of 2 × 2 MIMO system with Orthogonal Frequency-Division Multiplexing (OFDM) modulation using GNU Radio with USRP2. GNU Radio is a library designed for signal processing, which allows users to create streams of thesignal processing by combining ready components. In addition with software defined radio it offers testing of theoretical models under real-world conditions. Model of transmitter was created by using algorithm and methods which are implemented in GNU Radio SISO OFDM modulator. Authors extended them by Alamouti SFBC coder, because it is very effective and also simple in implementation. The Alamouti SFBC is a rate-1 code. It takes two time-slots to transmit two symbols. The receiver decoding is provided by determining channel estimation matrix and maximum-likelihood detector. Experimental results of MIMO link performance are also presented.

1. INTRODUCTION

Fast evolution of mobile communication faces growing users' demands for throughput, quality of service and coverage. Basic fault of indoor mobile systems is their low throughput. The most promising data transmission technology, which is able to fulfill these requirements, is Multiple Input Multiple Output (MIMO). Currently this technology is a common subject of research. There is increasing number of standardization documents and recommendations describing MIMO implementation in specific system solutions [3–5]. MIMO in comparison with SISO allows to increase radio channel capacity and the quality of service, exploiting the spatial diversity and overcoming the effects of multipath fading.

GNU Radio is an open-source software development toolkit for building any kind of real-time signal processing applications [6]. It includes a core runtime library for signal processing and examples of signal processing blocks. GNU Radio programs are written using Python and C++ programming languages (signal processing blocks are written in C++ and put together in Python flow-graphs). Users can modify existing or create new signal processing blocks [10]. GNU Radio also provides a graphical, similar to the Matlab Simulink, user interface called GNU Radio Companion. It enables user to create signal flow graphs and automatic generates flow-graph Python source code. Many open-source project is using GNU Radio (openBTS, IEEE802.11 OFDM frame encoder) [8, 9].

Application written in GNU Radio can be implemented on software defined radios (SDR). SDR technology in connection with GNU Radio enables realization any kind of radio emission without integration into hardware. Example of SDR module is Universal Software Radio Peripheral 2 (USRP2). This universal platform converts radio signals to digital samples and sends them to host computer, where signal processing take place. Various plug-on daughterboards allow the USRP2 to be used on different radio frequency bands.

This paper focuses on the implementation of MIMO system with Alamouti coding in GNU Radio and USRP2. Sections 2 and 3 present hardware and software configuration of MIMO test bed. Section 4 contains experimental results of MIMO link performance. Conclusion and future work are described in Section 5.

2. HARDWARE CONFIGURATION OF MIMO TESTBED

The MIMO test bed, described in this section bases on Universal Software Defined Peripheral v2, which is commonly used for various radio systems demonstrations. Figure 1 presents setup of the transmitter and receiver part. System design is identical for receiver and transmitter. It is build from 2 USRP2s, GPS Disciplined Clock and computer with Open Source Software (Linux, GNU Radio, UHD). This software is used to control hardware and also it is responsible for signal processing.

Computer used in research was equipped with: Intel Core i7 with four core processor running at 1.6–2.8 GHz and 4GB DDR3 RAM working at 1333 MHz. Communication between computer and USRP2 was provided by 1 Gigabit cable which offers wideband signal transmission and two network interfaces. First interface was the standard network controller installed on computer main board, the second one was Gigabit Ethernet ExpressCard adapter. Additionally each USRP2s was

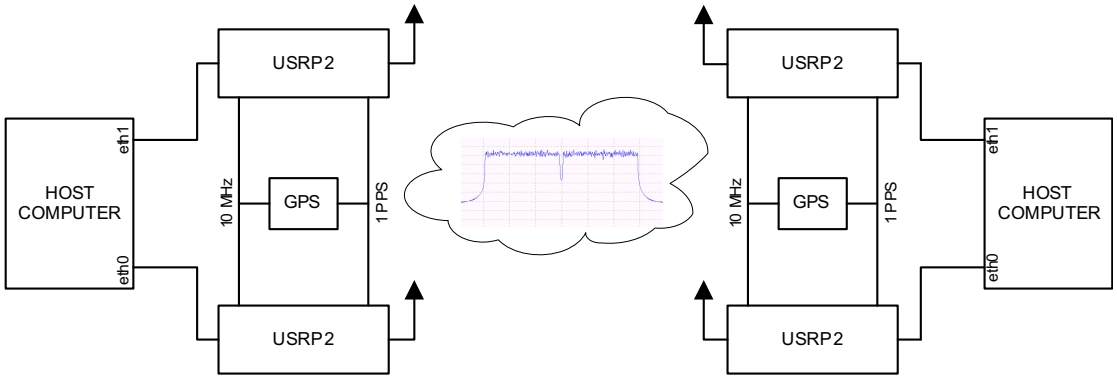

Figure 1: MIMO test bed setup.

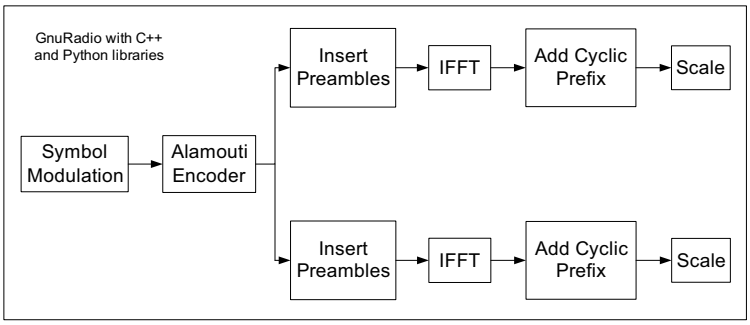

Figure 2: Structure of MIMO OFDM modulator.

equipped with WBX daughterboard. These type of RF frond-end are capable of working with frequency from 50 MHz to 2.2 GHz with maximum bandwidth of 25 MHz. The USRP2s provide transmission through single antenna, therefore each data stream required separate USRP2s unit. Consequently the main issue was providing synchronization between two units at transmitter section, and independently receiver section. There were also a problem with frequency synchronization between transmitter and receiver. As a solution were proposed two GPS signals (10 MHz, 1PPS), connected via SMA connector. Frequency synchronization was provided by locking of USRP2 internal oscillator to external 10 MHz clock. One pulse per second signal provides the same time reference to all USRP2. It calibrates time stamp of samples.

3. SOFTWARE IMPLEMENTATION

In development process only open-source software was used (GNU Radio version 3.3.1 and UHD). The UHD is the universal hardware driver for Ettus Research LLC products (including USRP2) [7]. It is used by host computer to communicate with the USRP2 over UDP/IP protocol. Data streams in UHD API are time stamped to the precision of a clock tick.

Operating system installed on test bed PC was the Ubuntu 10.04 LTE (lucid) 64bit distribution with Linux 2.6.32-26-generic kernel.

3.1. Transmitter

Transmitter part designed in GNU Radio Companion consists three main blocks: File Source, MIMO OFDM Modulator and Multi USRP Sink. File Source is a block which main task is reading data form a file and streaming it to other blocks. MIMO OFDM Modulator block wasn't included in GNU Radio Companion, therefore it was developed in purpose of MIMO test bed. It's structure is presented in Figure 2. The MIMO modulator structure is based on SISO modulator structure implemented in GNU Radio [2]. It contains mapper's block dividing input stream into various number of carriers, which number depends of number of occupied tones. Each of occupied tones is modulated using chosen modulation scheme (BPSK, QPSK, QAM, etc.). It is worth to put the emphasis on the fact that four center subcarriers have a zero value, and are not used in data transmission.

Alamouti encoder realizes Space Frequency Block Codes. This method is very simple to implement. If we have $s1$ and $s2$ as a two consecutive subcarriers, in the first symbol the following

subcarrier will be $s1$ and $-s2*$ and in the second one: $s2$ and $s1*$ [1]. After every 44 OFDM symbols two preamble symbols are added. One of them is a known sequence of bits in transmitter and receiver and second one is filled with zero value. Sequence of symbol transmitted in the first path differs from those in second path. It allows to calculate channel estimation matrix in receiver. Following blocks make inverse Fast Fourier Transform, add Cyclic Prefix, scaling samples amplitude, and sending data to USRP2 (Multi USRP Sink).

3.2. Receiver

Receiver part is designed using three blocks: Multi USRP2 Source, MIMO OFDM demodulator and File Sink. First block reads data that comes from two USRP2s and stream them to demodulator. Structure of MIMO OFDM demodulator (Figure 3) is very similar to SISO demodulator, already implemented in GNU Radio [2].

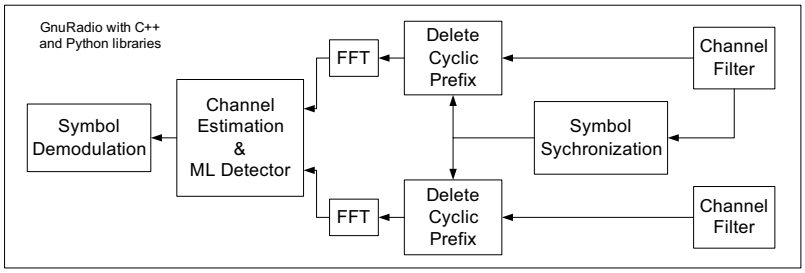

Figure 3: Structure of MIMO OFDM demodulator.

The second receiver path is added, algorithm of channel estimation calculation is upgraded and maximum likelihood detector is implemented. As the inputs there are two channel filters. The next block is a maximum likelihood OFDM synchronizer. Consecutive blocks delete cyclic prefix and execute Fast Fourier Transform. Data from two path are acquired in following block, which calculates a channel estimation for four paths and performs incoming signal detection. In proposed solution Maximum Likelihood Detector was used, which algorithm can be written as:

$$s_{ml} = \arg\min \|x - H \cdot s_i\|^2 \tag{1}$$

whereas x are received data, H is a channel estimation matrix. Decision is taken on the basis of the maximum likelihood vector s_i of data which might be transmitted and then demapping process take place. Demodulated data are saved to a file in the File Sink block.

4. EXPERIMENT RESULTS

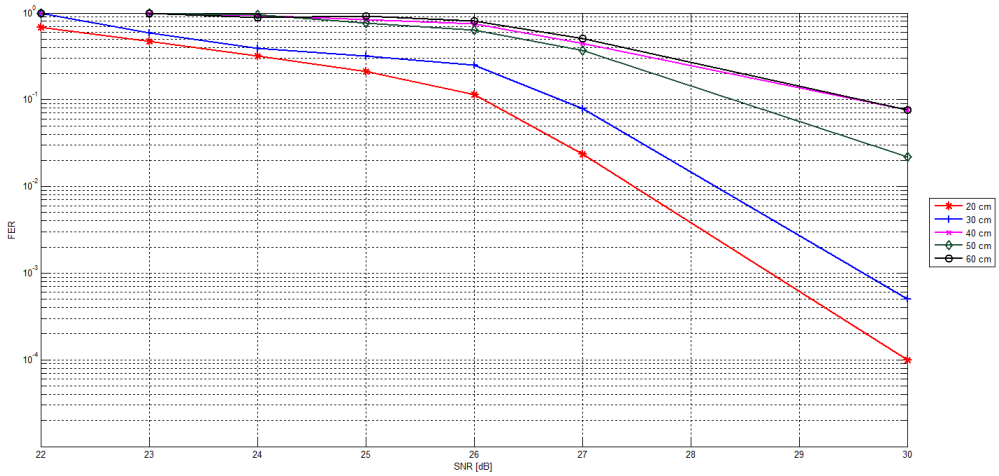

Figure 4: Frame error rate (FER) versus SNR. FFT length = 256, occupied tones = 192, sample rate = 3.125 MS/s, bit rate = 3.5 Mbit/s, bandwidth = 2.32 MHz.

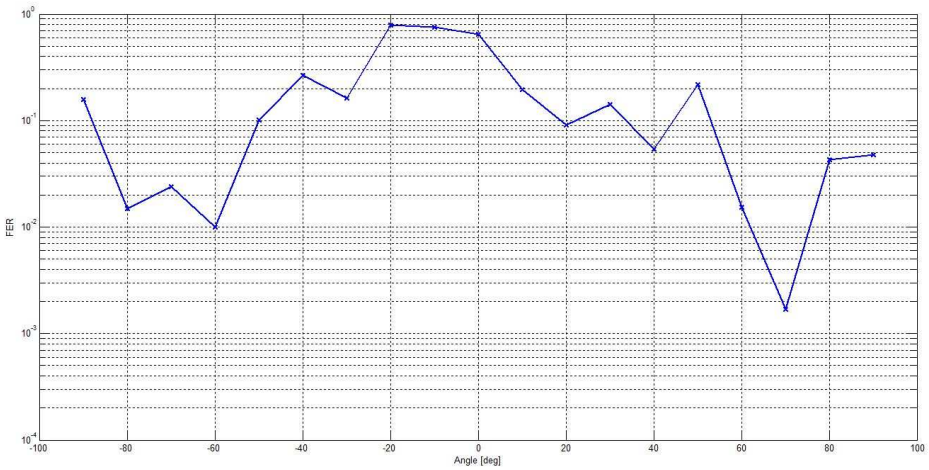

Figure 5: Frame error rate (FER) versus antennas' angle. FFT length = 256, occupied tones = 192, sample rate = 3.125 MS/s, bit rate = 3.5 Mbit/s, bandwidth = 2.32 MHz.

5. CONCLUSION AND FUTURE WORK

The results show that USRP2 modules enable real-time implementation of MIMO link, with relatively high throughput. Such a platform is a low cost solution and elaborated waveform is flexible and easy to modify, because of fully software implementation.

Authors are planning to expand existing implementation of synchronization using pilot symbols. Additionally they want to compare various method of detection with maximum likelihood detection.

REFERENCES

1. Alamouti, S. M., "A simple transmit diversity technique for wireless communications," *IEEE Journal on Select Areas in Communications*, Vol. 16, No. 8, 1451–1458, 1998.
2. Rondeau, T. W., M. Ettus, and R. W. McGwier, "Open source transparency for OFDM experimentation," *Proceedings of the SDR '08 Technical Conference and Product Exposition*, Washington, October 2008.
3. Ryu, H.-G., "System design and analysis of MIMO SFBC CI-OFDM system against the nonlinear distortion and narrowband interference," *IEEE Transactions on Consumer Electronics*, Vol. 54, No. 2, 368–378, 2008.
4. Gesbert, D., M. Shafi, D.-S. Shiu, P. J. Smith, and A. Naguib, "From theory to practice: An overview of MIMO space-time coded wireless systems," *IEEE Journal on Select Areas in Communications*, Vol. 21, No. 3, 281–302, 2003.
5. Oestges, C. and B. Clerckx, *MIMO Wireless Communications: From Real-world Propagation to Space-time Code Design*, Academic Press, 2007.
6. GNU Radio, http://gnuradio.org/.
7. UHD, http://code.ettus.com/redmine/ettus/projects/uhd/.
8. OpenBTS, http://openbts.sourceforge.net/.
9. IEEE802.11a/g/p OFDM Frame Encoder, https://www.cgran.org/wiki/ftw80211ofdmtx.
10. Blossom E., *How to Write a Signal Processing Block*, 2006.

Optoelectronic Phase Noise System Designed for X-band Sources Measurements in Metrology Applications

A. Hmima[1], **N. Cholley**[1, 2], **E. Pavlyuchenko**[1], **M. Zarubin**[1], **Y. K. Chembo**[1], **and P. Salzenstein**[1, 2]

[1]Franche-Comté Électronique Mécanique Thermique Optique Sciences et Technologies (FEMTO-ST)
Centre National de la Recherche Scientifique (CNRS), UMR 6174
ENSMM, 26 Chemin de l'Épitaphe, 25030 Besançon, France
[2]LNE-LTFB, Laboratoire Temps Fréquence de Besançon Associated to Laboratoire National de Métrologie et d'Essais (LNE), Besançon, France

Abstract— The performance advances in communication systems as well as Radar system, precision navigation, space application and time and frequency metrology require more stable frequency and low phase noise system. In this paper we present a configuration of phase noise measurement system operating in X-band using a photonic delay line as a frequency discriminator. This system doesn't need any excellent frequency reference and works for any frequency between 8.2 and 12.4 GHz. Using cross correlation on 500 averages, noise floor of the instrument is respectively −150 and −170 dBc/Hz at 10^1 and 10^4 Hz from the 10 GHz carrier (−90 and −170 dBc/Hz including 2 km delay lines). This instrument was developed in the context of association with the national french metrology institute (laboratoire national de métrologie et d'essais, LNE). This calibration system is to be integrated in measurements means of the accredited laboratory to improve the Calibration Metrology Capabilities (CMC) of the LNE.

1. INTRODUCTION

Radio frequency [1, 2] or microwaves oscillators or optoelectronic oscillators with fiber delay line [3, 4] and their further development with optical resonators [5–8], and cryogenic sapphire oscillators [9] can all present interesting performances with ultra-stable signals in short term domain characterized by a low phase noise. A convenient method is to lock the oscillator to be measured on a reference standard [10–12]. However it is only possible to determine the phase noise for oscillators compared to another one with the same frequency if noise is expected to be better than a synthesizer. That's why there is a need to develop methods based on the use of two delay lines and cross correlation to be able to characterize an oscillator without referring to another one with the same delivered frequency. In this short paper is presented the development made on an instrument dedicated to such measurement for metrology applications.

2. BASIC CONCEPTS

A quasi-perfect RF-microwave sinusoidal signal can be written as:

$$v(t) = V_0[1 + \alpha(t)]\cos(2\pi\nu_0 t + \varphi(t)) \tag{1}$$

where V_0 is the amplitude, ν_0 is the frequency, $\alpha(t)$ is the fractional amplitude fluctuation, and $\varphi(t)$ is the phase fluctuation. Equation (1) defines $\alpha(t)$ and $\varphi(t)$ in low noise conditions: $|\alpha(t)| \ll 1$ and $|\varphi(t)| \ll 1$.

Short-term instabilities of signal are usually characterized in terms of the single sideband noise spectral density PSD $S(f)$. S is typically expressed in units of decibels below the carrier per hertz (dBc/Hz) and is defined as:

$$\mathscr{L}(f) = \frac{\text{one-sidebande noise power in 1 Hz bandw}}{\text{carrier power}} = \frac{1}{2}S_\varphi(f) \tag{2}$$

This definition includes the effect of both amplitude and phase fluctuations. However, the amplitude and phase noise have to be known separately because they act differently in the circuit. For example, the effect of amplitude noise can be reduced by amplitude limiting mechanism and mainly suppressed by using a saturated amplifier. Phase noise of microwave oscillators can usually be characterized by heterodyne measurement. Whereas, for such a system, we need a reference oscillator operating exactly at the frequency of the device under test (DUT) with lower phase

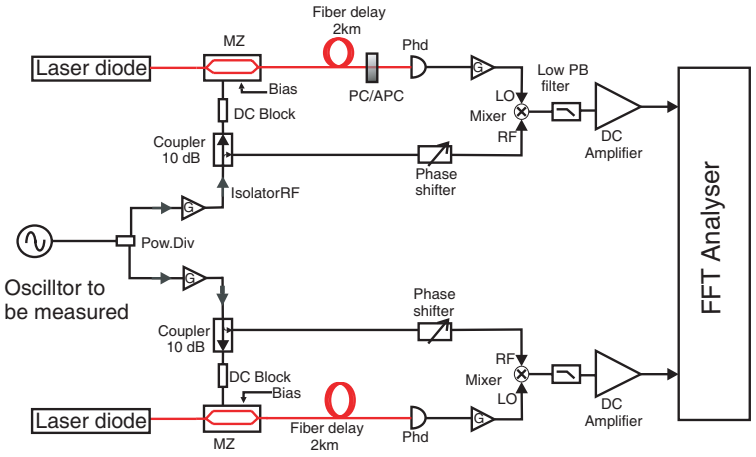

Figure 1: Phase noise bench.

noise. Any reference is required for homodyne measurement with delay line discriminator [12–14]. At microwave frequencies electrical delay is not suitable because of its high losses. However photonic delay line offers high delay and low attenuation equal to 0.2 dB/km at $\lambda = 1.55\,\mu$m.

Optoelectronic phase noise measurement system [12–14] is shematized on Fig. 1. It consists on two equal and fully independent channels. The phase noise of the oscillator is determined by comparing phase of the transmitted signal to a delayed replica through optical delay using a mixer. It converts the phase fluctuations into voltage fluctuations. An Elecrooptic modulator allows modulation of the optical carrier at microwave frequency. The lenght of the short branch where microwave signal is propagating is negligible compared to the optical delay line. Mixers are used as phase detectors with both saturate inputs in order to reduce the amplitude noise contribution. The low pass filters are used to eliminate high frequency contribution of the mixer output signal. DC amplifiers are low flicker noise.

The oscillator frequency fluctuation is converted to phase frequency fluctuation through the delay line. If the mixer voltage gain coefficient is $K\varphi$ (volts/radian), then mixer output rms voltage can be expressed as [13]:

$$V_{\text{out}}^2(f) = K_\varphi^2 |H_\varphi(jf)|^2 S_\varphi(f) \tag{3}$$

where $|H_\varphi(jf)|^2 = 4\sin^2(\pi f\tau)$ is the transfer function of optical delay line, and f is the offset frequency from the microwave carrier. The Equation (3) shows that the sensitivity of the bench depends directly on K_φ^2 and $|H_\varphi(jf)|$. The first is related to the mixer and the second essentially depends on the delay τ. The maximum measurement bandwidth is practically set to $0.95/\tau$ [13], so the choice of an appropriate delay is so important. Several measurements [13] shows that $\tau = 10\,\mu$s give good agrement between bandwidth and sensitivity.

In practice, an FFT analyzer is needed to measure the spectral density of noise amplitude $V_{\text{out}}^2(f)/B$, where B is the bandwidth used to calculate $V_{\text{out}}(f)$. The phase noise of the DUT is finally defined by Equation (4) and taking into count the gain of DC amplifier G_{dc} as:

$$\mathscr{L}(f) = \frac{S_\varphi(f)}{s} = \frac{V_{\text{out}}^2(f)}{2K_\varphi^2|H_\varphi(jf)|^2}\frac{1}{G_{\text{dc}}^2}\frac{1}{B} \tag{4}$$

3. RESULTS, INTERPRETATION AND EVALUATION OF THE UNCERTAINTY

The measured phase noise includes the DUT noise and the instrument background. The crosscorrelation method allows to decrease the cross spectrum terms of uncommon phase noise as $\sqrt{1/m}$, where m is the average number. Thereby uncorrelated noise is removed [12, 13] and sensitivity of measure is improved.

To validate the measure of our phase noise bench, we need to compare datasheet of the commercial frequency synthesizer **Anritsu** 69000B with the phase noise we measure using our bench. The Fig. 2(a) shows the result of this measure. We can see that our bandwidth is limited to 100 kHz ($\tau = 10\,\mu$s) and the measured phase noise corresponds to the datasheet.

Figure 3 represents the background phase noise of the bench after performing 500 averaged with cross-correlation method, when removing the 2 km optical delay line. In this case, phase noise of

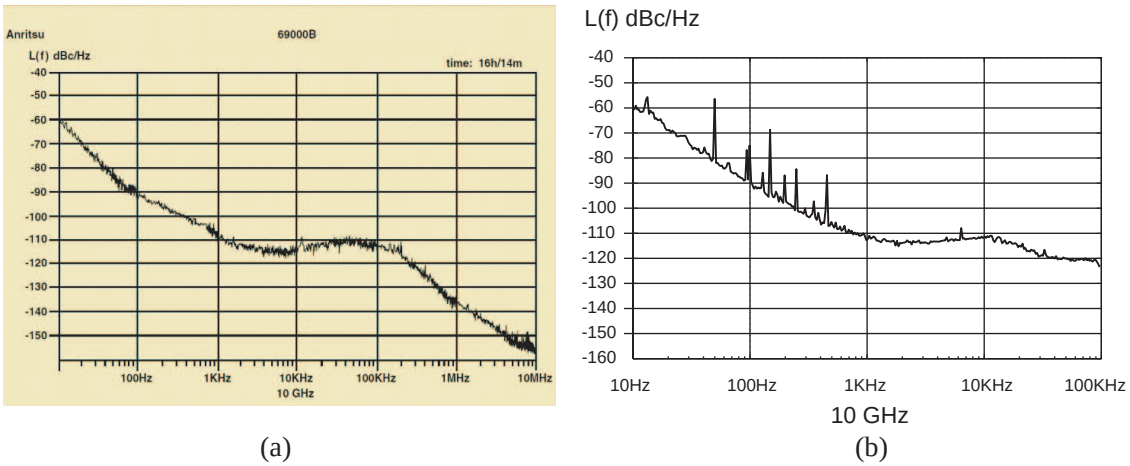

Figure 2: Phase noise measurement: (a) Datasheet of 10 GHz phase noise of commercial Anritsu 69000B series synthesizer, (b) phase noise of the commercial synthesizer measured with our bench with $K_\varphi = 425\,\mathrm{mV/rad}$ and $G_{\mathrm{dc}} = 40\,\mathrm{dB}$.

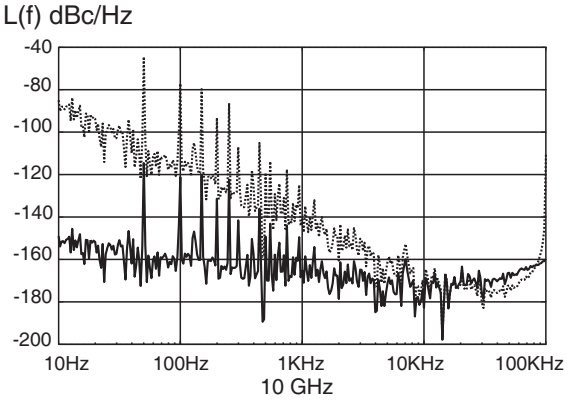

Figure 3: Phase noise floor of the bench measured with Anritsu synthesizer (500 averages).

the 10 GHz synthesizer is rejected. The solide curve shows noise floor (without optical transfer function) respectively better than −150 and −170 dBc/Hz at 101 and 104 Hz from the 10 GHz carrier. Dotted curve is the noise floor when optical fiber is introduced.

There are two categories of uncertainties terms [14]: the first category is called "type A", statistic contribution such as reproducibility, repeatability, special consideration about Fast Fourier Transform analysis, and the experimental standard deviation. Second family of uncertainties contributions is "type B" and due to various components and temperature control, but also to the asymmetry of the instrument. Experience with or general knowledge of the behavior and properties of relevant materials and instruments, manufacturer's specifications, data provided in calibration and other certificates, uncertainties assigned to reference data taken from handbooks. By the way, uncertainty on $\mathscr{L}(f)$ strongly depends on propagation of uncertainties through the transfer function as deduced from Equation (4). Global uncertainty is strongly related to repeatability of the measurements. Elementary term of uncertainty for repeatability is ±1.63 dB. Other elementary terms still have lower contributions. Its leads to a global uncertainty of ±1.67 dB [15].

4. CONCLUSION

Performances and first consideration about estimation of the uncertainty was a bit detailed in this paper to show the main advantage of the instrument developed for metrology applications. With high performance better than −150 dBc/Hz at 10 Hz from the 10 GHz carrier, integration in the mean of the accredited laboratory is expected and the new field of capabilities in terms of calibration of single source in X-band will be soon achieved in order to extend the CMC of the LNE.

ACKNOWLEDGMENT

This work was partly supported by the Laboratoire National de M'etrologie et d'Essais (LNE) under contract number LNE/DRST 10 7 002.

REFERENCES

1. Salzenstein, P., A. Kuna, L. Sojdr, and J. Chauvin, "Significant step in ultra high stability quartz crystal oscillators," *Electronics Letters*, Vol. 46, No. 21, 1433–1434, 2010.
2. Salzenstein, P., A. Kuna, L. Sojdr, F. Sthal, N. Cholley, and F. Lefebvre, "Frequency stability measurements of ultra-stable BVA resonators and oscillators," *Electronics Letters*, Vol. 46, No. 10, 686–688, 2010.
3. Yao, X. S. and L. Maleki, "High frequency optical subcarrier generator," *Electronics Letters*, Vol. 30, No. 18, 1525–1526, 1994.
4. Ilchenko, V. S., X. S. Yao, and L. Maleki, "High-Q microsphere cavity for laser stabilization and optoelectronic microwave oscillator," *Proceedings of SPIE*, 3611, San Jose, US, January 1999.
5. Volyanskiy, K., P. Salzenstein, H. Tavernier, M. Pogurmirskiy, Y. K. Chembo, and L. Larger, "Compact optoelectronic microwave oscillators using ultra-high Q whispering gallery mode disk-resonators and phase modulation," *Optics Express*, Vol. 18, No. 21, 22358–22363, 2010.
6. Tavernier, H., P. Salzenstein, K. Volyanskiy, Y. K. Chembo, and L. Larger, "Magnesium fluoride whispering gallery mode disk-resonators for microwave photonics applications," *IEEE Photonics Technology Letters*, Vol. 22, No. 22, 1629–1631, 2010.
7. Salzenstein, P., H. Tavernier, K. Volyanskiy, N. N. T. Kim, L. Larger, and E. Rubiola, "Optical mini-disk resonator integrated into a compact optoelectronic oscillator," *Acta Physica Polonica A*, Vol. 116, No. 4, 661–663, 2009.
8. Schliesser, A. and T. J. Kippenberg, "Cavity optomechanics with whispering-gallery mode optical micro-resonators," *Acta Avances in Atomic, Molecular and Optical Physica*, Vol. 58, 207–323, 2010.
9. Benmessai, K., P. Y. Bourgeois, M. E. Tobar, N. Bazin, Y. Kersale, and V. Giordano, "Amplification process in a high-Q cryogenic whispering gallery mode sapphire Fe3+ maser," *Measurement Science and Technology*, Vol. 21, No. 2, 025902, 2010.
10. Walls, F. L., "Suppressed carrier based PM and AM noise measurement techniques," *Proceedings IEEE International Frequency Control Symposium and Exposition*, 485–492, Orlando, US, May 1997.
11. http://cp.literature.agilent.com/litweb/pdf/5951-6743.pdf.
12. Salzenstein, P., J. Cussey, X. Jouvenceau, H. Tavernier, L. Larger, E. Rubiola, and G. Sauvage, "Realization of a phase noise measurement bench using cross correlation and double optical delay line," *Acta Physica Polonica A*, Vol. 112, No. 5, 1107–1111, 2007.
13. Volyanskiy, K., J. Cussey, H. Tavernier, P. Salzenstein, G. Sauvage, L. Larger, and E. Rubiola, "Applications of the optical fiber to the generation and to the measurement of low-phase-noise microwave signals," *Journal of the Optical Society of America B*, Vol. 25, No. 12, 2140–2150, 2008.
14. Working Group 1 of the Joint Committee for Guides in Metrology, "Evaluation of measurement data — Guide to the expression of uncertainty in measurement," September 2008, http://www.bipm.org/utils/common/documents/jcgm/JCGM 100 2008 E.pdf.
15. Pavlyuchenko, E., "Uncertainty budget on optoelectronic phase noise measurement bench," Internal Report, Contract LNE/DRST 10 7 002, 7, February 2011.

Application of EH4 in the I Forecast Area in Yushiwa Iron Deposit of Hanxing Area, China

Zhaohui Ke, **Songling Chen**, **Tagen Dai**, **and Gaofeng Du**
School of Geosciences and Environmental Engineering, Central South University
Changsha, Hunan 410083, China

Abstract— Yushiwa area in north western of the Wuan depression depression,and west of the Taihang concave arch, China. The authors have reached the conclusion that the iron ore bearing horizon is middle Ordovician, the magmatic rock mass is Late in the Yanshan-mafic intrusions. EH4 is widely used in solid minerals, especially in finding concealed ore deposit. In this paper, the author adopted EH4 method to make a synthetic study on I forecast area in Yushiwa iron Deposit of Hanxing area. The result showed that the geophysical method was quite useful in the exploration of concealed ore deposit.

1. INTRODUCTION

Yushiwa deposit area is situated in the north western end of Wuan depression, and the west of Taihang Taiwan's military security arch beam concave. Produced in the southwest subduction end of mine complex body of diorite, regional structure mainly are the two north-northeast trending faults (mine fracture, fracture from the well) and the North West, including the NNE trending faults control the Yanshanian rock depression west of Wuan output and distribution of iron ore. Jianshancun unit of Rock mass is exposed in the north of the mining, as in the Ordovician rock strata. Mine many times before and after the experience of a large number of pit mine production inspection and disclosure, indicating a single stratum in the Mainland layer, simple structure.

1.1. Stratum

Surface of mining within the mining right has been widely covered by the Quaternary, only partially exposed in the Ordovician limestone, and the distribution of erosion in the mountain valley in the Tertiary gravel surface can be seen. Layers summarized as follows:

1.1.1. Middle Ordovician

Middle Ordovician strata are the main exposed strata of mining area, from the Jianshan are exposed southeast to southwest, from the project to expose the surface erosion and mountains, rock mass from the south extension of the Jianshan are underlying in the Middle Ordovician strata. As the rock mass in the south to the Jianshan pitching by east of Huilancun to west of Jianshan, the formation tend to change gradually from SE to SW, dip angle $17^\circ \sim 32^\circ$, usually 22°. Investigation revealed that the layer consists of pure limestone, porphyritic spent limestone, dolomite limestone, argillaceous limestone and brecciated limestones.

1.1.2. Tertiary

Tertiary is widely distributed in central and southern mining area, from south to north thickening, survey shows by the thickness of a few meters to 180 meters thick, the general thickness of 40 meters to 100 meters, gravel, pebbles formed by different size, cement to clay, which sometimes can be seen from 1 to 5 m layer of red-brown loam, gravel, sandstone and quartz are dominated by feldspar and quartz sandstone, rounded degree is better sorting poor, large and small diameter by a few centimeters to a meter change. The overlying layer of gravel over the top of Ordovician limestone, showing unconformity.

1.2. Sturcture

The main structural system is the monoclinic structure of Mine Rock Southwest side part of Jianshan Southwest and Southeast presented the overlying limestone, the structure common control with the diorite contact zone distribution and changes in iron ore output and thereby control the location of occurrence, form and attitude.

Less of fault development in mining areas, in the mining area 200 meters north east, with east-west fault — Huilancun fault, and which western extension of the fault is unknown. According to mine observed, with 170 level in the lower plate to open up the new lane, as well as 150 level of Southeast entrance of Fujing, a large number of breccia development, coupled with the contact zone of the South East to extend the depth of steep drop Yunjialing ore body, delayed introduction of

the fault may cut the main ore body south west east, causing some of the main ore body ore south east of broken cover. According to speculation in the mining area east of the northern section of north-south along the Huoyaoku in the valley, suggesting that there is a fault.

1.3. Magmatic Rock

Yanshanian magmatic rocks are mainly of late-basic intrusive rocks, the Jianshan unit of volume of Kuangshancun. the rock north is Cejing, south to Yunjialing, Huaihegou, west of Shangjiaosi, east to the Guoerzhuang, exposed area of 35 km^2. Invasive Liangjiashan group, Majiagou, Taiyuan. Rock alteration and strong, there epidotization, chloritization, albitization so there is skarn rock, tremolite.

Only a strong bleaching of surface mining altered diorite from the mine in the mining area North West from north to south was inserted into the banded limestone, until the North to help the subsidence area, the high point of disappearing into the limestone outcrops south no help. Dioritic rocks in the main more insidious and contact discharge, according to survey revealed diorite rock in the mining area for the slow ramp-like shape to the south plunging, some lots ups and downs, the formation of uneven surface, the height difference up to 40 or so meters.

Jianshan Rock outcrop edge widespread skarn and carbonate flowers, rocks the body can also be found through the carbonate veins. In the contact zone near the impact due to alteration, diorite zoning phenomenon obviously, from the contact zone inward, distribution of skarn diorite, flash digenetic alteration, diorite.

2. GEOPHYSIC CHARACTER

Based on the mining of ore-forming geological conditions and specific geological physical properties, has arranged the following geophysical methods to extract deep geological information of physical properties, to probe measuring area of deep favorable metallogenic conditions of an extension of the trend, with the geological means delineate Houxu exploration target area.

(1) High-frequency magnetotelluric sounding (EH-4) Geophysical Exploration Study — Exploration and the tendency of the rock towards the extension as well as contact with the mineralization is closely related to the situation with the distribution.

(2) Measurement of magnetic scanning of geophysical prospecting — measuring the magnetic anomaly detection, combined high-frequency magnetotelluric sounding (EH-4) work circle.

3. I FORECAST AREA

I forecast area have 21 survey lines laid in Yushiwa, in addition to 12 line is 500 meters length, the remaining measured length of 400 meters, 50 meters from the line. $0 \sim 20$ lines for high-precision magnetic survey, carried out at 0, 4, 8, 12, 16, 20 line frequency magnetotelluric sounding. Geophysical results showed that 12 lines of the surveyed area, there is ~ 20 lines of high magic obvious abnormalities with low resistance, the bandwidth is about $120 \sim 200$ m, depth 180–400 m, towards the north west, named WT1 also the rest of the deep survey area (400 m $\sim$ 1500 m) no significant low resistivity anomaly, and the inference of deep engagement with what are diorite.

Magnetic data processing results in a black coil set for the magnetic anomalies of regional areas with relatively high (greater than 350 nt), the width is about 120 meters, abnormal body toward the direction and have the same mining, inference in the main vein has been adopted and the west side of Limestone diorite rock in the contact zone, there may be a small layer of magnetite ore body development, but does not rule out contacts with the surrounding rock itself has magnetic anomalies caused by non-magnetic ore.

From 0 line of EH-4 inversion results can be seen, the resistivity of 10–120 ohm $\cdot$ m in upper stratum, presumed to be Tertiary gravel layer, and it thickness is about 80 m–110 m; intermediate formation resistivity range 180–400 ohms $\cdot$ m, presumed to reflect the Ordovician limestone, the thickness of about 50 m–235 m; lower formation resistivity is relatively high, at 500–10000 ohms $\cdot$ m range of changes, presumed to diorite reflected. Stake 280 points in the vicinity of the resistivity in the horizontal contour gradient greater inferred by a fault, denoted by F1.

4 lines from the EH-4 inversion results can be seen, the resistivity of 10–170 ohm $\cdot$ m in upper stratum. Presumed to be Tertiary gravel layer, and it thickness is about 105 m–120 m; intermediate formation resistivity range 400–1000 ohms $\cdot$ m, presumed to reflect the Ordovician limestone, the thickness of about 100 m–210 m; lower abdomen relatively high resistivity of formation, in the 1000–10000 ohms $\cdot$ m range of changes, presumed to diorite reflected. Stake 200 points in the vicinity of the resistivity in the horizontal contour gradient greater inferred by a fault, denoted by F1.

8 lines from the EH-4 inversion results can be seen in the overlying formation resistivity 10–200 ohms · m, presumed to be Tertiary gravel layer, and it thickness is about 80 m–100 m; intermediate formation resistivity range 500–800 ohms · m, presumed to reflect the Ordovician limestone, the thickness of about 50 m–330 m; lower abdomen relatively high resistivity of formation, in the 1000–10000 ohms·m range of changes, presumed to diorite reflected. Stake 110 points in the vicinity of the resistivity in the horizontal contour gradient greater inferred by a fault, denoted by F1.

12 lines from the EH-4 inversion results can be seen in the overlying formation resistivity 10–200 ohms · m, presumed to be Tertiary gravel layer, and it thickness is about 95 m–110 m; intermediate formation resistivity range 350–900 ohms · m, presumed to reflect the Ordovician limestone, the thickness of about 230 m–300 m; lower abdomen formation resistivity is relatively high, at 900–10000 ohms·m range of changes, presumed to diorite reflected. Depth of 180–380 m in the range of a low resistance layer, which is divided into two low resistance Stake 0–320 m layer, there is limestone, resistivity range of about 160–240 ohms · M, and thickness of about 20–30 m; Stake 320–500 meters into a relatively thick low resistivity layer 150 meters thick, the resistance rate of 50–120 ohms · m range of changes, we concluded that the low resistivity layer with the mineralization Lot, denoted by WT1.

16 lines from the EH-4 inversion results can be seen in the overlying formation resistivity 10–210 ohms·m, presumed to be Tertiary gravel layer, and it thickness of about 65–80 meters; intermediate formation resistivity range of 100–500 ohms·m, presumed to reflect the Ordovician limestone, the thickness of about 50–215 meters; lower abdomen formation resistivity is relatively high, at 800–10000 ohms · m range of changes, presumed to reflect the diorite. Within 100–300 meters in depth with a low resistance layer, the resistivity of 50–200 ohms · M, varies within a range of about 20–100 meters in thickness, we concluded that the low resistivity layer with the mineralization sites, denoted by WT1.

20 lines from the EH-4 inversion results can be seen in the overlying formation resistivity 50–200 ohms·m, presumed to be Tertiary gravel layer, and it thickness of about 80–100 m; intermediate formation resistivity range of 150–300 ohms · m, presumed to reflect the Ordovician limestone, the thickness of about 200 m–320 m; lower abdomen relatively high formation resistivity, resistivity at 150–1000 ohms·m range of changes, presumed to diorite reflected. Depth of 300–380 m in the range of a low resistance layer resistivity of 10–50 ohms · M varies within a range of about 60–70 meters in thickness, we concluded that the low resistivity layer with the mineralization sites, denoted by WT1.

4. CONCLUSION

$0 \sim 20$ lines of EH-4 inversion of data along with low resistivity anomaly (WT1) center slice depth of 200–360 m range, the resistivity contour drawing: 0 lines, 4 line and 8-line addition to the shallow gravel layer showed low resistance characteristics, the in limestone and diorite near the contact surface with no obvious low resistivity anomaly, no clear signs of mineralization. And 12 lines, 16 lines and 20 lines except the shallow gravel layer was low resistance characteristics, the in limestone and diorite near the contact resistance was low resistivity shows the depth range of 180–400 meters, forming condition of relative favorable inference has been taken in the surrounding rock in the west of the main veins, which may contain magnetite vein lets, but does not rule out contacts with the surrounding rock itself has a relatively low resistivity and high magnetic characteristics. In the deep (400–1500 m): 6 line low resistivity anomalies were found in distinct zones in the depth range inferred no magnetite occurrence.

ACKNOWLEDGMENT

This paper is supported by Handan-Xingtai Mine Authority and Central South University.

REFERENCES

1. Institute of Geological Sciences of North China, Hebei Geological Institute, "Taihang Mountain areas Hanxing type iron ore prospecting," 1–154, Law and (Internal Data), 1976.
2. Shen, L. S., "A discussion about the concealed iron resource potential on the east side of Beijing-Guangzhou railway within Handan-Xingtai area," *Mineral Resources and Geology*, Vol. 22, No. 4, 314–318, 2008.
3. Zheng, J. M., "Southern Hebei Handan area of skarn iron ore fluid and ore-forming mechanism," Ph.D. Thesis, China University of Geosciences, Beijing, 2007.

4. Shen, B. F., A. M. Zhai, Z. H. Li, et al., "The chemical composition and its geological of contact metasomatic magnetite iron deposits in southern Hebei," Vol. 25, No. 1, 10–18, 1982.
5. Han-Xing Mine Authority, "The south final report of Yuquanling iron ore reserves," 2001.

Determination of Thermal Model Parameters for Stator Slot Using Numerical Methods

L. Idoughi, **X. Mininger**, **L. Bernard**, **and F. Bouillault**
LGEP, CNRS UMR 8507, Supélec, Université Paris-Sud, UPMC Paris 6
Plateau de Moulon, 11 Rue Joliot Curie, F 91192 Gif sur Yvette Cedex, France

Abstract— The aim of the method detailed in this paper is to get the equivalent thermal model parameters for stator with complex slot geometries. The method is based on the discretization of the geometry using a Finite Integration Technique to calculate equivalent thermal parameters with a good accuracy.

1. INTRODUCTION

In the thermal modeling of electrical machines, one of the main problems concerns their winding where the temperature often rises to its maximum value. Temperature rise in stator windings decreases insulation system performances, can reduce life time of the motors and may even lead to the motor failure [1, 2]. Appropriate models for the windings are necessary to find the hot spot of the machine [3]. They can then be integrated in the overall thermal modeling of the machine to be more accurate. The usual approach is the application of lumped parameter which is used for a very long time [1, 2, 4, 5]. The demerit of this method concerns the determination of the model parameters with a good accuracy when complex geometries are considered [4, 6]. The objective of the present study is then to describe an accurate thermal model parameters with low calculation cost for stators with complex slot geometries, allowing the estimation of maximum and mean temperatures in the winding. The method proposed here is based on the discretization of the geometry using a Finite Integration Technique (FIT) in order to obtain a first order equivalent thermal model for the transient analysis of one desired temperature in the slot.

2. WINDING MODELING

The homogenization of the winding is first necessary to obtain thermal modeling of the stator slot that is a complex heterogeneous structure requiring careful modeling. The objective is then to replace the conductors and the resin by one homogenous material that reproduces a similar thermal behaviour. Several techniques can be used to determine the effective thermal conductivity λ_e of the composite material; its value can be obtained from experimentation, from average calculation using numerical tools considering random geometries or from an analytical approach [7]. Here Milton's estimation has been considered in order to obtain the equivalent thermal conductivity. It can be used for any composite made of two isotropic randomly distributed phases. Microstructural informations are included in Milton's homogenization such as the shape of inclusions that is considered

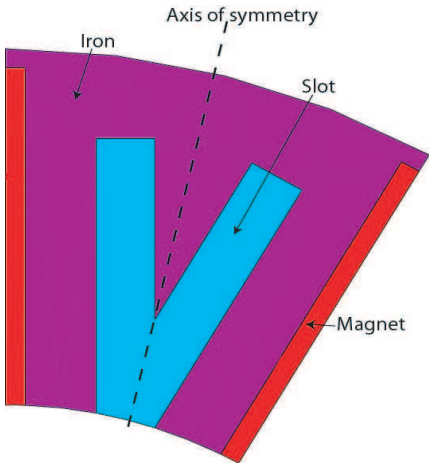

Figure 1: Stator slot of flux-switching machine.

cylindrical [8]. Considering a composite made of circular copper conductors and a resin matrix with thermal conductivity 401 and 0.25 W/m/K respectively, the application of this estimation gives an effective conductivity of the winding of 0.8469 W/m/K for a 50% filling rate. The study does not consider insulated conductors because of the enamel thermal property that is similar to the one of resin.

3. EQUIVALENT THERMAL MODEL OF THE SLOT

The aim of this part is to determine one thermal model for each node of the slot (Figure 1). Here two cases with hypothesis are considered: uniform or piecewise uniform temperature on the boundary of the slot.

3.1. Isothermal Slot Border

In this first case, the slot/iron interface is considered isothermal to be isothermal with temperature T_f. Splitting the temperature vector into two parts, the unknown temperatures T_i can be expressed as functions of temperature T_f:

Thermal equations:

$$\begin{cases} \mathrm{div}(\vec{\varphi}) + p = \rho C_p \dfrac{\partial T}{\partial t} \\ \vec{\varphi} = -\lambda \cdot \vec{grad}(T) \end{cases}$$

FIT

Matrix equations:

Thermal resistances

$$\begin{cases} -\tilde{S}\hat{\varphi} + P = C \cdot \dfrac{dT}{dt} \\ \hat{\varphi} = M_\lambda \hat{h} = M_\lambda \hat{S}^T T \end{cases} \Leftrightarrow \begin{pmatrix} T_1 \\ \vdots \\ T_n \end{pmatrix} + (\tau_{RC}) \frac{d}{dt} \begin{pmatrix} T_1 \\ \vdots \\ T_n \end{pmatrix} = \begin{pmatrix} R_1 \\ \vdots \\ R_n \end{pmatrix} P_0 + \begin{pmatrix} 1 \\ \vdots \\ 1 \end{pmatrix} T_f$$

where R_i represents immediately the equivalent thermal resistances between the considered point i in the slot and the slot/iron boundary. (τ_{RC}) is a full matrix deduced from the inversion of the submatrix of $\tilde{S}M_\lambda\tilde{S}^t$ corresponding to the unknowns T_i multiplied by the corresponding thermal capacity matrix. A first order model could be deduced by choosing the highest eigen value $\tau_{\max}$ as time constant of the first order system, then the thermal capacities are deduced: $\tau_{\max} = R_i C_i$.

The Figure 2(a) shows the equivalent thermal model obtained with the first assumption.

Note that for symmetry reasons, the thermal study is focused only on one half of the geometry.

3.2. Non-isothermal Slot Border

In this second case, the slot/iron interface is non-isothermal but we can suppose that several parts of the border are isothermal at different temperatures (Figure 2(b)). Here for this example, three parts are isothermal at T_{f1}, T_{f2} and T_{f3}. As seen in the first case, the unknowns temperature T_i

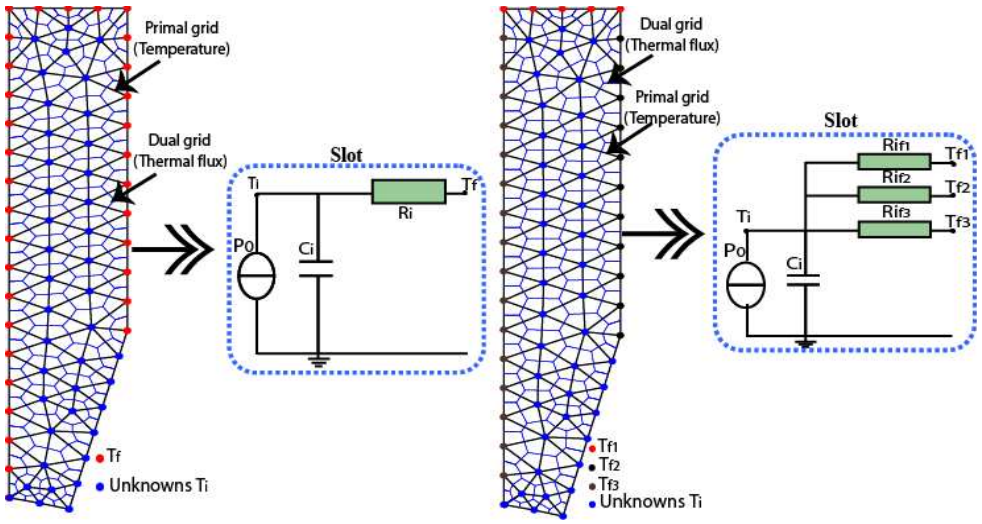

(a) Isothermal slot border (b) Non-isothermal slot border

Figure 2: Equivalent thermal models of half of the slot.

can be expressed as functions of different temperatures T_{f1}, T_{f2} and T_{f3}:

$$\begin{pmatrix} T_1 \\ \vdots \\ T_n \end{pmatrix} + (\tau_{RC}) \frac{dT}{dt} \begin{pmatrix} T_1 \\ \vdots \\ T_n \end{pmatrix} = - \begin{pmatrix} x_1 \\ \vdots \\ x_n \end{pmatrix} \cdot T_{f1} - \begin{pmatrix} y_1 \\ \vdots \\ y_n \end{pmatrix} \cdot T_{f2} - \begin{pmatrix} z_1 \\ \vdots \\ z_n \end{pmatrix} \cdot T_{f3} + \begin{pmatrix} R_1 \\ \vdots \\ R_n \end{pmatrix} \cdot P_0$$

The thermal resistances of the Figure 2(b) are calculated as following:

$$R_{if1} = \frac{R_i}{x_i}, \quad R_{if2} = \frac{R_i}{y_i} \quad \text{and } R_{if3} = \frac{R_i}{z_i}.$$

4. SIMULATION RESULTS

A stator slot of flux-switching machine is considered to validate the proposed equivalent thermal model. Figure 3 presents the simulation results obtained for the hot spot, including the comparison with the finite element method (FEM) implemented in the ANSYS software.

Using a FEM model taking into account the presence of the iron as a reference, the results obtained with the equivalent model in the static and transient analyses present a good accuracy in the case of the non-isothermal border. The isothermal-border hypothesis, giving the smallest thermal model, seems here to be inadequate, leading to a too low hot spot temperature.

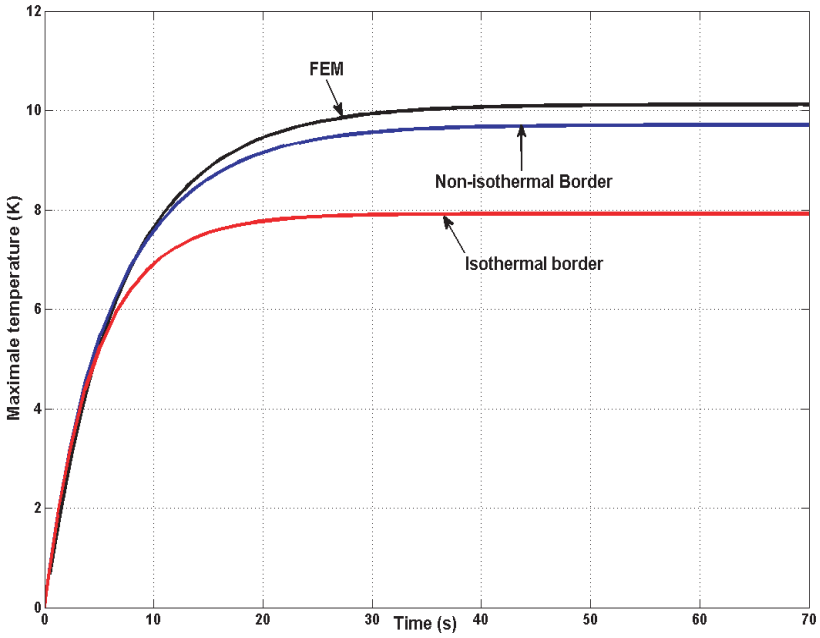

Figure 3: Simulations results.

5. CONCLUSION

A new methodology using a mesh-based numerical method (FIT) in order to obtain the model parameters has been presented with aim of evaluating quickly one particular temperature in the slot (hot spot). For more complex geometries, non-isothermal slot border should be taken into account in the equivalent thermal model in order to calculate the parameters of the model with a good accuracy.

REFERENCES

1. Gnacinski, P., "Windings temperature and loss of life of an induction machine under voltage unbalance combined with over-or undervoltages," *IEEE Trans. on Energy Conversion*, Vol. 23, No. 2, June 2008.

2. Fouladgar, J. and E. Chauveau, "The influence of the harmonics on the temperature of electrical machines," *IEEE Trans. on Magnetics*, Vol. 41, No. 5, May 2005.
3. Faiz, J., B. Ganji, C. E. Castensen, K. A. Kasper, and R. W. De Doncker, "Temperature rise analysis of switched reluctance motors due to electromagnetic losses," *IEEE Trans. on Magnetics*, Vol. 45, No. 7, July 2009.
4. Nerg, J., M. Rilla, and J. Pyrhönen, "Thermal analysis of radial-flux electrical machines with a high power density," *IEEE Trans. on Industrial Electronics*, Vol. 55, No. 10, October 2008.
5. Harris, A. M. E. C., T. M. Jahns, and K. M. Rahman, "Thermal analysis of multibarrier interior PM synchronous machine using lumped parameter model," *IEEE Trans. on Energy Conversion*, Vol. 19, No. 2, June 2004.
6. Okoro, O. I., "Steady and transient states thermal analysis of 7.5 KW squirrel-cage induction machine at rated-load operation," *IEEE Trans. on Energy Conversion*, Vol. 20, No. 4, December 2005.
7. Trigeol, J.-F., Y. Bertin, and P. Lagonotte, "Thermal modeling of an induction machine through the association of two numerical approaches," *IEEE Trans. on Energy Conversion*, Vol. 21, No. 2, June 2006.
8. Milton, W., "Bounds on the transport and optical properties of a two component composite material," *J. Appl. Phys.*, Vol. 52, 5294–5304, 1981.

The Physical Regularization of Incorrect Electrodynamic Problems

V. A. Neganov and D. P. Tabakov
Povolzhskiy State University of Telecommunications and Informatics, Samara, Russia

Abstract— In modern computer-aided design (CAD) in the solution of the boundary electrodynamic problems are used direct and indirect mathematical methods. The first part include such methods as the finite elements method and the method of Finite Difference Time Domen (FDTD).

Indirect methods are based on receiving of analytic solution of auxiliary problem that is about a structure's excitation with elementary current source that is called Green's function. If this function can be defined analytically, then the solution's efficiency cardinally increases and the dimension decreases, because calculations are performed only on radiating surface.

A significant advantage of indirect mathematical methods to direct is the fact, that they allow to eliminate various kinds of improperty in antennas' computing [1]: The gap between the surface density of electric current on the antenna and the magnetic field, the emergence of unstable solutions, etc.

Despite the fact that the Green's function can be determined analytically only for a limited number of structures, indirect methods can solve a wide range of electrodynamic problems. The report focuses on a variety of integral equations (IE), obtained for some types of spiral antennas. Both the correct and incorrect physical models are considered. Incorrect model based on the use of thin wire approximation and leads to Fredholm's IE of first kind (it includes Hallen's and Pocklington's IE), which have a known problem — The possible instability of the solution. Correct models lead to IE containing hypersingularities, logarithmic and. These IE have a stable solution, but requires a lot of computing time. Earlier, singular IE were successful used by authors to analyze a tubular electric oscillator [2], loop antenna [3], linear and curved microstrip antennas.

1. INTRODUCTION

In antennas theory the problem is incorrect if the basic principles of the electrodynamics are violated. Firstly, the cause of it can be in non-self-consistent of physical models of problems [4]. For example — non-self-consistent physical model of thin electrical oscillator (Figure 1(a)) and Hertz dipole. The incorrectness follows from the fine stranded approach that doesn't allow to bind the surface current density η_z with magnetic field on an antenna: $\eta_z = H_\varphi$.

Secondly, the incorrectness of these problems can be caused of an incorrect mathematical model of the structure. Incorrect mathematical operations on correct physical model lead also to an absence of a binding between integral presentation of electromagnetic fields and surface electrical and magnetic current densities: $\vec{\eta}^e = [\vec{H}, \vec{n}_0]$ $\vec{\eta}^m = [\vec{n}_0, \vec{E}]$ on the basic surface S ($\vec{n}_0$ — external normal vector to surface S).

Thirdly, incorrect problems are due to a using of non-self-consist mathematical models of integral presentations of the electromagnetic field (EMF) near from basic surface S, for that singular integral equations are written for correct definition of surface electrical and magnetic current densities.

In this article two models of classical radiated structure of thin electrical oscillator are treated. A comparative mathematical modeling has been carried out.

2. POCKLINGTON AND HALLEN INTEGRAL EQUATIONS

Integral equations (IEs) of Pocklington and Hallen are usually used for a calculation of radiating current's distribution and input impedance of oscillating antennas. It can be written on symmetrical

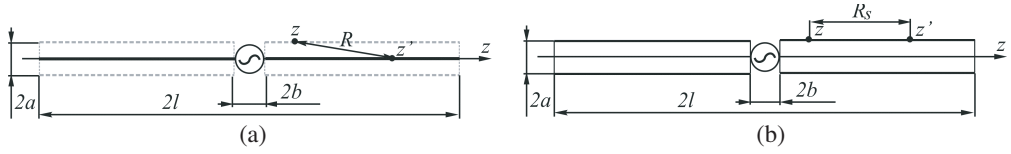

Figure 1: Physical models of symmetrical electrical oscillator: (a) fine stranded model, (b) tubular model.

oscillator in relation to full current $I(z)$ [5]:

$$\int_{-l}^{l} I(z')G(z,z')dz' = C\cos kz - i\frac{2\pi U}{W_c}\sin k|z|. \tag{1}$$

Here $G(z,z') = e^{-ikR(z,z')}/R(z,z')$ — the kernel of IE, $R(z,z') = \sqrt{a^2+(z-z')^2}$ — a distance between the point of source $q\{\rho'=0,z'\}$ on axis of the oscillator and the point of view $p\{\rho=a,z\}$ on perfectly comducting cylindrical surface. W_c — enviroment characteristic impedance, a- cylinder's radius, C — unknown constant, $k=2\pi/\lambda$ — wave number.

Physical model that correspond to Hallen IE is shown on Figure 1(a): In fact, the gap between the current on a string $\rho=0$ and the field on the perfectly conducting cylindrical surface $\rho=a$ was made artificially.

Besides, the infinitly thin string of current hasn't any surface, and the gap, where the external EMF with volltage of U is placed, has infinitly small width $2b\to 0$. Such approaches like this in some cases can lead to instability and to physical inadequacy of a solution [4]. Never the less, the main dignity of (1) is a simple expression for IE's kernel.

It should be noted that for this model it is possible to write more general Pocklington's IE, but physically incorrect as well [5]:

$$\int_{-l}^{l} I(z')\left(k^2+\frac{\partial^2}{\partial z^2}\right)G(z,z')dz' = \frac{4\pi}{iW_c}E(z), \tag{2}$$

Here $E(z)$ — the electromagnetic field's intensity of EMF's generator. It equals to zero everywere except within the gap: $E_l^{cm}(z) = \frac{1}{2b}\begin{cases} 1, z\in[-b;b] \\ 0, z\notin[-b;b] \end{cases}$.

3. INCORRECT INTEGRAL PRESENTATIONS OF THE ELECTROMAGNETIC FIELD

Let's consider the electromagnetic field that is created by incorrect model of antenna. In cylindrical coordinate system it has only three components: E_ρ, E_z and H_φ:

$$\begin{aligned}
E_\rho(\rho,z) &= \frac{W_c}{4\pi i}\int_{-l}^{l} I(z')\frac{\partial^2}{\partial\rho\partial z}\frac{e^{-ik\sqrt{\rho^2+(z-z')^2}}}{k\sqrt{\rho^2+(z-z')^2}}dz', \\
E_z(\rho,z) &= \frac{W_c}{4\pi i}\int_{-l}^{l} I(z')\left(k^2+\frac{\partial^2}{\partial z^2}\right)\frac{e^{-ik\sqrt{\rho^2+(z-z')^2}}}{k\sqrt{\rho^2+(z-z')^2}}dz', \\
H_\varphi(\rho,z) &= -\frac{k}{4\pi}\int_{-l}^{l} I(z')\frac{\partial}{\partial\rho}\frac{e^{-ik\sqrt{\rho^2+(z-z')^2}}}{k\sqrt{\rho^2+(z-z')^2}}dz'.
\end{aligned} \tag{3}$$

Evidently, integrals divergent with $\rho=0$. It means it isn't possible to go back from the string of a current to the field $\{E_\rho,E_z,H_\varphi\}$, but it is possible with $\rho=a$. So, fine stranded approach is one of causes of the field's gap in the near zone of radiation.

4. PHYSICAL REGULARIZATION OF ELECTRODYNAMIC PROBLEMS

A method of the physical regularization (MPR) assumes a taking into account all of physical aspects of solved problem. The first and the most easily implemented step of MPR is a taking into account the EMF gap with finit size. Thus we obtain the following equation:

$$\int_{-l}^{l} I(z')G(z,z')dz' = C\cos kz - i\frac{2\pi U}{kbW_c}\psi(z), \tag{4}$$

here

$$\psi(z) = \begin{cases} 1 - \cos(kb)\cos(kz), & z \in [-b, b], \\ \sin kb \sin k|z|, & z \notin [-b, b]. \end{cases}$$

But is can be called a not full regularization, because it reduced only to correct current exitation. This IE is equivalent to Pocklington's IE (2) written for a gap with finit size.

This approach is considered in [5], but, unfortunately without numerical results. Comparative results of the IE's calculations are showed in Figure 2. The calculations were performed using a stitching method of N discrete points [6]. One can see that this method allows to increase radius a of soleved oscillator with a saving of result's stability. Never the less the solution are incorrectness because a using of incorrect model.

The second and the most effective step of MPR is a using of tubular model of an oscillator (Figure 1(b)). In this case surfaces of the observation and currents are combined. It corresponds to a passing from Pocklington's and Hallen's IE to singular integral equation (SIE). For the electric oscillator you can obtain the SIE with logarithmic singularity and hypersingularity related to full current $I(z')$, $(z \in [-l; l])$:

$$\int_{-l}^{l} I(z')R(z,z')dz' + \int_{-l}^{l} I(z')\ln|z-z'|dz' + \int_{-l}^{l} \frac{I(z')}{(z-z')^2}dz' = \sigma E^{cm}(z), \tag{5}$$

where $R(z, z')$ is a regular kernel of the SIE, σ is a constant.

Also for a tubular model you can obtain the SIE with a Cauchy's singularity related a derivative of the current $J(z) = \partial I(z)/\partial z$. It was done in [4]:

$$\int_{-l}^{l} J(z')R(z,z')dz' + \int_{-l}^{l} \frac{J(z')}{z-z'}dz' = \sigma E^{cm}(z). \tag{6}$$

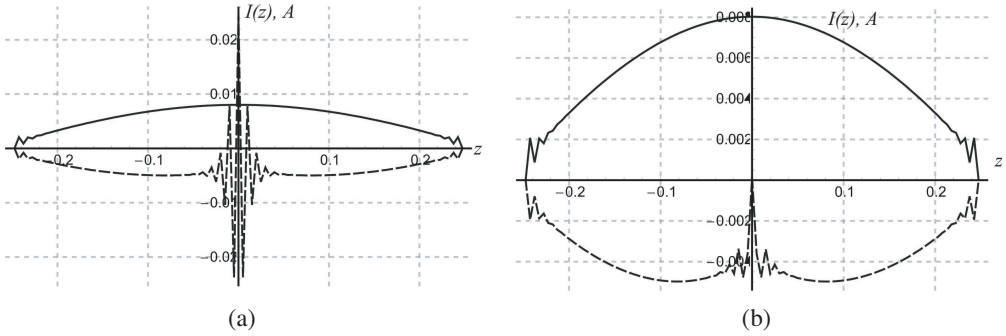

(a) (b)

Figure 2: The calculation's results of Hallen IE for a halp-wave oscillator: (a) with infinitly small gap, (b) with a gap of 0.01λ. Solid lines — Re$I(z)$. Dashed lines — Im$I(z)$. $\lambda = 1$ M, $a = \lambda/100$, $N = 101$.

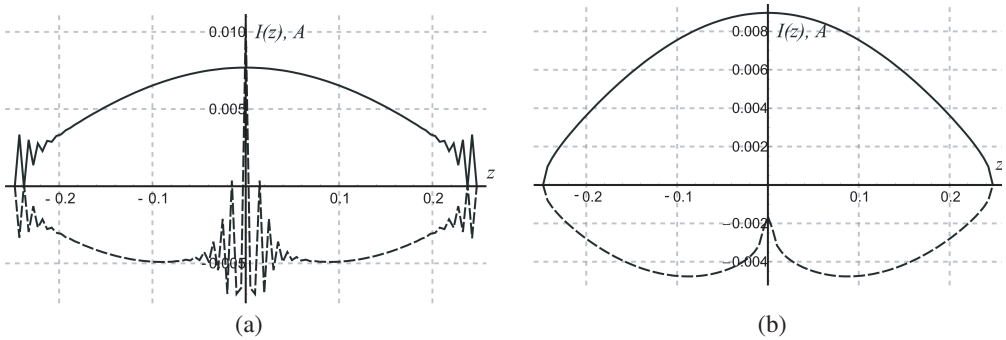

(a) (b)

Figure 3: Calculation of (a) Hallen IE and (b) SIE for half-wave oscillator. Solid lines —Re$I(z)$. Dashed lines — Im$I(z)$. $\lambda = 1$ M, $a = \lambda/75$, $N = 101$, $2b = 0.01\lambda$.

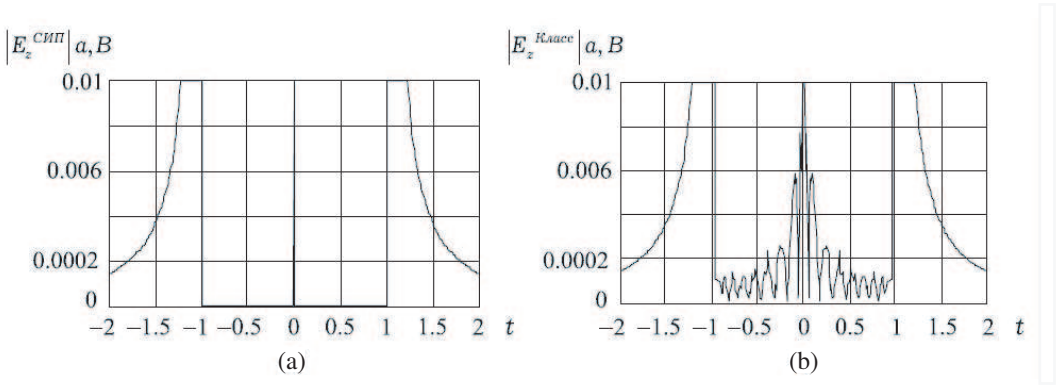

Figure 4: The component (a) E_z on the oscillator's surface (SIR) and (b) E_z with incorrect kernel. $t = z/l$, $2l = 0.5\lambda$.

Here $R(z, z')$ is a regular kernel of the SIE, σ is a constant. SIE (6) was obtained by one of authers of the tubular model that is shown in Figure 1(b).

The tubular model is physically correct and there aren't any problems with stability due to a solving of the obtained SIE. Its disadvantage is in the relatively complicated kernel.

Comparative results of obtained SIE and Hallen's IE with finit gap are shown in Figure 3. Also a calculation was perforemed using the method of a stitching in descrete points.

And finally, the third step of the physical regularization is a taking into account a finit conductivity of a metall. For a thin-walled model of the oscillator this SIE was obtained:

$$\nu I(z) + \int_{-l}^{l} I(z')G(z, z')dz' = C\cos kz - i\frac{2\pi U}{kbW_c}\psi(z),$$

where ν — some constant. A thickness is equal or less then a skin-layer of correspondent frequency. Calculation has shown that the solution almost doesn't depend on a metall conductivity.

5. SINGULAR INTEGRAL REPRESENTATIONS OF THE ELECTROMAGNETIC FIELD

In [7] for a tubular model singular integral representations of the electromagnetic field are written: (SIR EMP [4]):

$$\begin{aligned} E_i(\rho, z) &= \int_{-l}^{l} J(z')[G_i(\rho, z - z') + S_i(\rho, z - z')]dz',\ i \equiv \rho, z; \\ H_\varphi(\rho, z) &= \int_{-l}^{l} I(z')[G_\varphi(\rho, z - z') + S_\varphi(\rho, z - z')]dz', \end{aligned} \tag{7}$$

where G are regular kernels, S are singular kernels ($S(\rho \to a, z \to z') \to \infty$). It should be noted that in (7) with $\rho = a, z \in [-l; l]$ the boundary conditions are fullfilled with analitical occuracy:

$$H_\varphi(a, z) = \eta_z^e(z); \quad E_\rho(a, z) = -\frac{1}{i\omega\varepsilon_a}\frac{\partial\eta_z^e(z)}{\partial z}; \quad E_z(a, z) = -E_z(a, z),$$

and a SIR of an EMP for E_z passes to SIE (6). And it isn't observated in (3) эТОГО. Finally, in Figure 4 are shown numerical results of comparative calculations of the electric field on a tubular oscillator's surface using two kernels: incorrect (that follows from fine stranded approach) and a kernel with Cauchy singularity of the tubular model. In calculation was used a current from SIE (6).

One can see that the boundary condition doesn't fullfill with incorrect kernel.

6. CONCLUSION

In this article basic princips of the method of a physical regularization were outlined. A using of the MPR gives correct mathematical models of antennas.

On example of the easiest rediation structure the advantages of the MPR were shown. One can see that in this case SIEs have stable and physically adequate solutions. It was shown that physical model of fine stranded oscillator makes solutions of oscillator tasks incorrect (and with not only Hadamard incorrectness) — mathematical models as Pocklington and Hallen IE that is a cause of a gap between the volume current density and the electromagnetic field's intensity. It is way this model can't be used for calculation of the antenna's near-field. Instead this one tubular model was offered. It leads to mathmatical model in the form of the SIE that with SIP allows to correctly analyze the antenna's electromagnetic near-field. In far-field zone there aren't incorrect problems and the regularization isn't neseccery.

REFERENCES

1. Neganov, V. A., *Physical Regularization of Some Incorrect Problems of the Electrodynamic*, 432, Sains Press, Moscow, 2008.
2. Neganov, V. A., E. I. Nefyodov, and G. P. Yarovoy, "Electrodynamic methids of design of microwave devices and antennas," *Radio I Svyaz*, 415, Moscow, 2002.
3. Neganov, V. A. and D. P. Tabakov, "An applying of singular integral equations to electrodynamic analysis of flat ring antenna," *A Physic of Wave Processes and Radiotechnical Systems*, 4–6, 2008.
4. Neganov, V. A., *Physical Regularization of Ill-posed Problems of the Electrodynamics*, 432, Sains-Press, Moscow, 2008.
5. Neganov, V. A., E. A. Pavlov, and G. P. Yarovoy, "Radiation and diffraction of electromagnetic waves," *Radio and Communications*, 264, 2004.
6. *Computational Methods in Electromagnetics*, Mitra, R., Editor, M. Mir, 1977.
7. Neganov, V. A., D. P. Tabakov, and G. P. Yarovoy, "Modern theory and practice of antennas," *M.: Radio*, Neganova, V. A., Editor, Sec. 716, 2009.
8. Neganov, V. A., E. I. Nefedov, and G. P. Yarovoy, "Electrodynamic methods of designing microwave devices and antennas," *Radio and Communications*, Neganova, V. A., Editor, Sec. 415, 2002.
9. Tikhonov, A. N. and V. Y. Arsenin, *Methods for Solving Ill-posed Problems*, 288, Nauka, Moscow, 1979.

Novel Concept of ENG Metamaterial in Rectangular Microstrip Patch Antenna (Partially Loaded Case) for Dual Band Application

Mahdy Rahman Chowdhury Mahdy, **Md. Rashedul Alam Zuboraj**,
Abdullah Al Noman Ovi, **and Md. Abdul Matin**
Department of Electrical and Electronic Engineering
Bangladesh University of Engineering and Technology, Dhaka, Bangladesh

Abstract— Prior to this work, radiation pattern of conventional TM_{020} mode of very large rectangular patch antenna was modified using MNG metamaterial. But the idea of using ENG metamaterial to modify any mode is different and a novel concept. Using this novel idea design of dual band rectangular patch antenna partially loaded with ENG metamaterial has been introduced here. Interface resonance has been used successfully to excite modified $TM_{0\delta0}$ mode for dual band application. In case of using ENG metamaterial (partially loading case), 'Zero radiation problem' appears in sub-wavelength rectangular patch antennas. But in this paper, potential application of ENG metamaterial (mode modification) for conventional rectangular patch antennas has been shown with the help of proposed novel idea. This metamaterial based partially loaded rectangular patch antenna is not only a good resonator, but also a good radiator. But obviously the most interesting fact is that our idea creates the new way to use ENG (or MNG) metamaterial to load partially the rectangular microstrip antenna for $TM_{0\delta0}$ $(1 < \delta < 2)$ mode modification.

1. INTRODUCTION

Miniaturized dual frequency patch antennas provide an alternative to large bandwidth planner antennas. A unique radiating structure is desirable to accomplish these operations. Metamaterial based patch antennas may be only the good solutions to meet all these requirements. Alu et al. [1] has proposed design method to obtain sub-wavelength rectangular patch antennas using DPS-ENG bi-layer. But it has been shown that such rectangular patches give broadside null radiation pattern [1, 2]. This has been referred as 'zero radiation problem' [3]. Before and even after the work of Alu et al., several works have been proposed in case of partially loaded rectangular microstrip patch antenna, but they were without considering the radiation efficiency of such cavities [2, 4, 5]. It has been predicted that: these rectangular antennas partially loaded with metamaterial can only be good resonators but may not be good radiators [6]. Later, Jiang Xiong et al. [7] showed that using MNG metamaterials, modification of conventional TM_{020} mode radiation pattern is possible for very large patch antennas.

In [8], we have proposed an algorithm for radiation pattern modification using metamaterial (for any patch size). Applying that algorithm, a novel design of small rectangular microstrip patch antenna partially loaded with ENG metamaterial for dual band applications will be shown here. We will use unconventional $TM_{0\delta0}$ modes $(1 < \partial < 2)$ for dual band applications.

2. NOVEL DESIGN USING ENG METAMATERIAL

Here, we are going to introduce the novel concept of ENG metamaterial to excite unconventional $TM_{0\delta0}$ mode $(1 < \partial < 2)$. Using this interface resonance mode, it has been possible to design our proposed dual band rectangular microstrip patch antenna. Such $TM_{0\delta0}$ interface resonant mode gives satisfactory radiation pattern due to the proper use of our algorithm [8].

We will introduce modified $TM_{0\delta0}$ interface resonance mode (f_r has been chosen 3.33 GHz, higher than conventional TM_{010} mode at 2.22 GHz and lower than conventional TM_{020} mode) and will get a good broadside radiation pattern. Here $k_1\eta L$ will be chosen greater than 180° and less than 225° for getting 'interface resonance' using ENG metamaterial to get interface resonance at 3.33 GHz. Then applying our algorithm [8] we get:

Using the optimized parameters and Lorentz model, we will get the desired broadside radiation patterns (Figures 5 and 6). Actually, SNG or DNG metamaterials are inherently dispersive and lossy [1]. So, without using dispersive lossy model (i.e., Lorentz model), the simulated results

cannot give proper realistic results. Here we have used Lorentz model for ENG (Figure 2) [9–11]:

$$\epsilon(\omega) = \epsilon_\infty + \frac{(\epsilon_s - \epsilon_\infty)\omega_0^2}{\omega_0^2 - \omega^2 + j\omega\delta} \tag{1}$$

where $\epsilon_s = 1.7564$, $\epsilon_\infty = 1$, $\omega_0 = 1.63362818 \times 10^{10}$ rad/s, $\delta = 50$ MHz.

The radiation pattern found by simulation tells that at broadside it gets maximum radiation for dual bands (Figures 4 to 6). The directivity of the antenna at broadside is 7.9 dBi (Figure 6) for unconventional $TM_{0\delta 0}$ mode at 3.292 GHz. So, the novel idea is properly justified with mathematical

Chosen resonant frequency, f_r	ϵ_2 (at f_r)	η	$\frac{E_{z_2}}{E_{z_1}}$ (at boundaries)
$f_r = 3.33$ GHz	-0.1813	0.6687	-0.9233

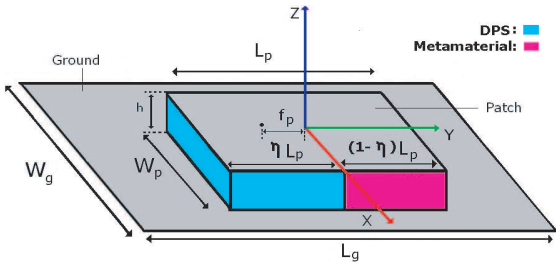

Figure 1: Geometry of a rectangular microstrip patch antenna partially loaded with metamaterial (ENG). f_p = feed position from DPS and metamaterials interface. η = filling ratio of the antenna. f_r = chosen resonant frequency. Detailed information and constitutive parameters are: $L_g = 60$ mm, $W_g = 60$ mm, $\epsilon_{1r} = 3$, $\mu_{1r} = 1$, $L_p = 40$ mm, $W_p = 30$ mm, $f_p = 10.748$ mm, $h = 1$ mm, $\eta = 0.6687$, $\mu_{2r} = 1$ and ϵ_{2r} (at f_r) $= -0.1813$ in case of ENG loading.

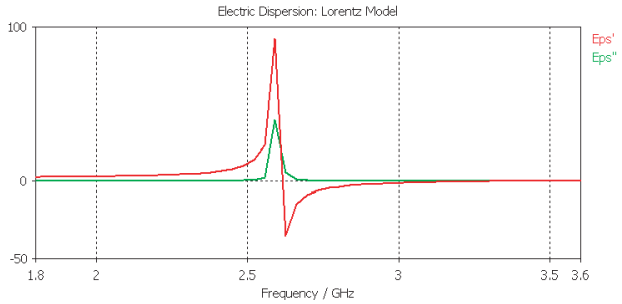

Figure 2: Lorentz dispersive model for proposed antenna.

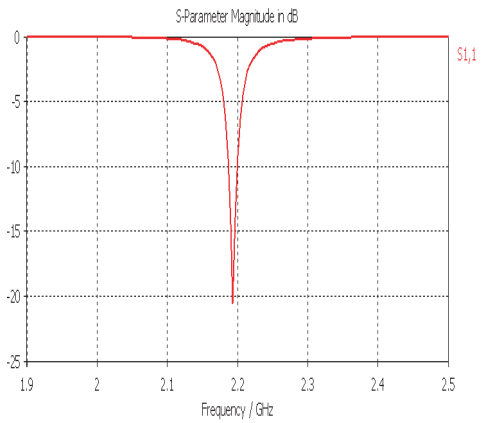

Figure 3: S-parameter performance of conventional 40 mm × 30 mm patch antenna using DPS only.

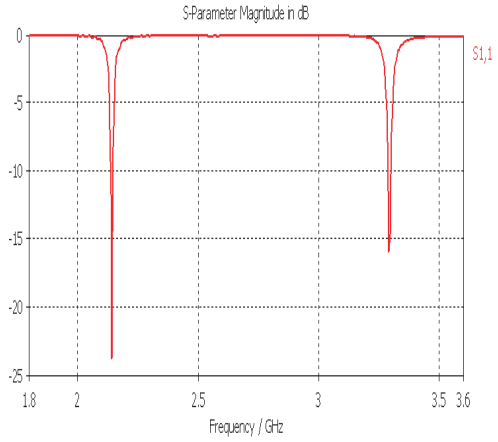

Figure 4: S-parameter performance of proposed 40 mm × 30 mm dual band antenna loaded with ENG.

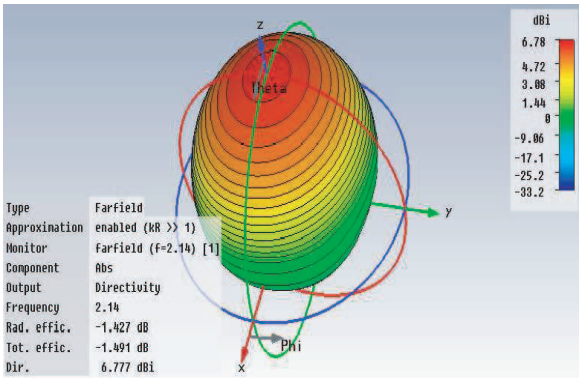

Figure 5: Conventional TM_{010} mode 3-D radiation pattern (at 2.14 GHz).

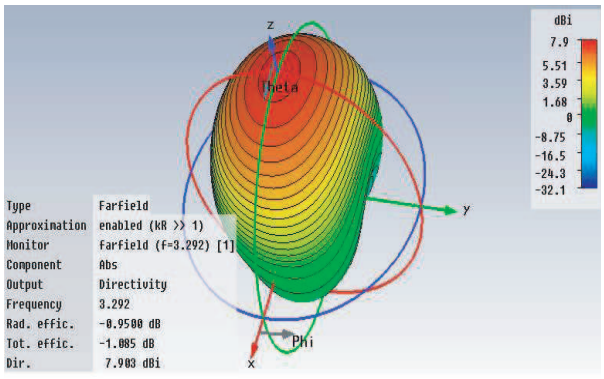

Figure 6: Unconventional $TM_{0\delta0}$ mode 3-D radiation pattern (at 3.292 GHz).

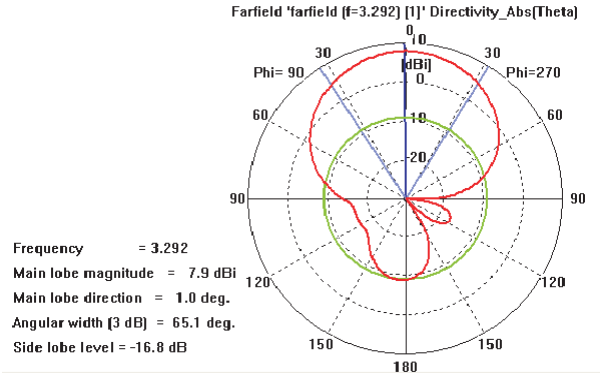

Figure 7: Unconventional $TM_{0\delta0}$ mode radiation pattern (polar plot) at principal E-plane.

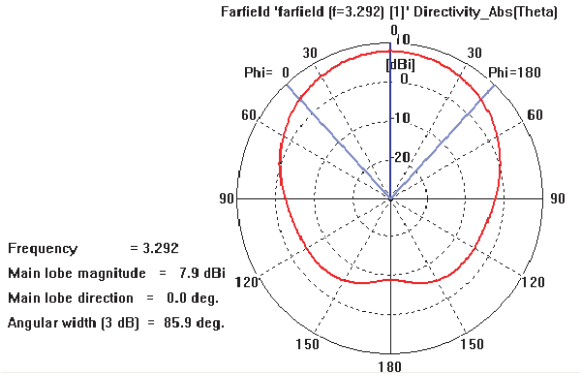

Figure 8: Unconventional $TM_{0\delta0}$ mode radiation pattern (polar plot) at principal H-plane.

calculation, code based simulation and 'CST Microwave Studio' [9] based realistic simulation.

3. CONCLUSION

However, TM_{020} mode modification using ENG metamaterial is impossible [12]. But ENG metamaterial can be used for very small patches to very large patches for frequency ratio range: 1.3 to 1.6 [12]. Besides, MNG metamaterial can not be used for dual band application in such small patches for its nature of deteriorating the radiation pattern of conventional TM_{010} mode [12]. Thus, ENG metamaterial can be used significantly for such dual band designs for low to medium frequency ratio applications. Moreover, using this kind of 'interface resonance' ($TM_{0\delta0}$ mode $(1 < \partial < 2)$) such frequency ratio control without cutting any slot or using any shorting pins is quite satisfactory. This is because such degrees of freedom for choosing resonant modes, high directivity for both bands (above 6 dBi) and very low level of cross polarization can not be found in case of dual band antennas by any other means. Therefore, the proposed designs will be attractive for wireless applications in multi path environment. They are also well suited to compact and low cost active circuit applications at microwave frequencies.

REFERENCES

1. Alù, A., F. Bilotti, N. Engheta, and L. Vegni, "Subwavelength, compact, resonant patch antennas loaded with metamaterials," *IEEE Transactions on Antennas and Propagation*, Vol. 55, No. 1, January 2007.
2. Zheng, K. S., W. Y. Tam, and D. B. Ge, "Impedance matching of rectangular microstrip antennas partially loaded with DNG metamaterials," *38th European Microwave Conference, EuMC 2008*, October 2008.
3. Zheng, K. S., W. Y. Tam, and D. B. Ge, "Broadside subwavelength microstrip antennas partially loaded with metamaterials," *2008 International Workshop on Metamaterials*, 39–42, November 2008.

4. Xu, W., L. W. Li, H. Y. Yao, T. S. Yeo, and Q. Wu, "Left-handed material effects on waves modes and resonant frequencies: Filled waveguide structures and substrate-loaded patch antennas," *Journal of Electromagnetic Waves and Applications*, Vol. 19, No. 15, 2033–2047, 2005.
5. Yang, R., Y. Xie, D. Li, J. Zhang, and J. Jiang, "Bandwidth enhancement of microstrip antennas with metamaterial bilayered substrate," *Journal of Electromagnetic Waves and Applications*, Vol. 21, No. 15, 2321–2330, 2007.
6. Capolino, F., *Handbook of Artificial Materials: Applications of Metamaterials*, Vol. 2, 18.1–18.14, Taylor and Francis, CRC Press, October 2009.
7. Xiong, J., H. Li, Y. Jin, and S. He, "Modified TM_{020} mode of a rectangular patch antenna partially loaded with metamaterial for dual-band applications," *IEEE Antennas and Wireless Propagation Letters*, Vol. 8, 2009.
8. Mahdy, M. R. C., M. R. A. Zuboraj, A. A. N. Ovi, and M. A. Matin, "A novel design algorithm' and practical realization of rectangular patch antenna loaded with SNG metamaterial," *Progress In Electromagnetics Research M*, Vol. 17, 13–27, 2011.
9. CST Microwave Studio 2009, CST of America, Available: http://www.cst.com.
10. Feise, M. W., J. B. Schneider, and P. J. Bevelacqua, "Finite-difference and pseudo spectral time-domain methods applied to backward-wave metamaterials," *IEEE Transactions on Antennas And Propagation*, Vol. 52, No. 11, November 2004.
11. Shelby, R. A., D. R. Smith, and S. Schultz, "Experimental verification ofa negative index of refraction," *Science*, Vol. 292, No. 1, 77–79, April 2001.
12. Mahdy, M. R. C., M. R. A. Zuboraj, A. A. N. Ovi, and M. A. Matin, "Novel design of triple band rectangular patch antenna loaded with metamaterial," *Progress In Electromagnetics Research Letters*, Vol. 21, 99–107, 2011

Input Impedance Calculation for Coax-fed Rectangular Microstrip Antenna with and without Airgaps Using Various Algorithms

K. Chemachema and A. Benghalia
Department of Electronics, University of Constantine, Algeria

Abstract— Abstract-Multilayered-perceptron-based neural models for calculating the input impedance of coax-fed rectangular microstrip antenna with and without airgaps are presented eight learning algorithms: LM Trainlm — Levenberg-Marquardt, BFG trainbfg — quasi-Newton backpropagation, RP trainrp — Resilient Backpropagation, SCG trainscg — Scaled Conjugate Gradient, CGF traincgf — Fletcher-Powell Conjugate Gradient, OSS trainoss — One-Step Secant, GDX traingdx — Variable Learning Rate Backpropagation, GDM Traingdm — Gradient descent with momentum are used to train the multilayered perceptrons. The input impedance results obtained by the neural models are in very good agreement with the results of Aboud. The LM algorithm converges rapidly after some point, but only after the other algorithms has already converged.

1. INTRODUCTION

Neural network techniques are being applied to different branches of microwave engineering for optimisation. Microstrip antennas have been extensively investigated experimentally, analytically, and numerically for decades, many numerical methods have been serving the engineers and research in the analysis and design of these conformal antennas for many years [1, 2].

The antenna can be fed either by fabricating a strip line to the patch or by means of a coaxial arrangement. One can visualise the flow of electromagnetic energy in the following way. Waves are guided along the coaxial line to the feed point. The energy then spreads out into the region under the patch, some of which crosses the boundary of the patch and radiates into the half space above the patch. It is obvious that the airgap idea is a general one in the sense that it can be applied to patches of arbitrary shape. It can also be applied to dual-frequency stacked antennas as well as arrays of identical elements. The method is particularly attractive for arrays, as the resonant frequencies of all of the elements, and therefore of the array, can be tuned by a single adjustment of H_A (Figure 1) [5].

2. INPUT IMPEDANCE OF A RECTANGULAR MICROSTRIP ANTENNA WITH AIRGAP

In this method, the region between the patch and the ground plane is considered as a cavity bounded by electric walls on the top and the bottom and by a magnetic wall (to simulate the open-circuit condition) on the sides.

Figure 1 shows the geometrical configuration of a rectangular microstrip antenna with an airgap. Here, we model the rectangular microstrip antenna by an equivalent single-layer structure of total height $H = H_D + H_A$ and an equivalent permittivity of [5]. The resonant frequency of a particular mode is determined by the permittivity of the substrate, the shape and size of the patch, and, to some extent, by the thickness of the substrate [7].

$$f_R = \frac{V_0}{2\sqrt{\varepsilon_{dyn}}}\sqrt{\left[\left(\frac{m}{W_{eff}}\right)^2 + \left(\frac{n}{L_{eff}}\right)^2\right]} \tag{1}$$

V_0 is the velocity of light, ε_{dyn} is the dynamic permittivity which is calculated by the Modified Wolff Model (MWM) [4], W_{eff} and L_{eff} are given by [7].

$$\varepsilon_{re} = \frac{\varepsilon_r \cdot (H_D + H_A)}{(H_D + H_A \cdot \varepsilon_r)} \tag{2}$$

The input impedance is then obtained as:

$$Z(f) = \frac{R}{1 + Q_T^2\left[\frac{f}{f_R} - \frac{f_R}{f}\right]^2} + j\left[X_L - \frac{RQ_T\left[\frac{f}{f_R} - \frac{f_R}{f}\right]}{1 + Q_T^2\left[\frac{f}{f_R} - \frac{f_R}{f}\right]^2}\right] \tag{3}$$

R, Q_T, X_L are given by [3].

3. APPLYING THE NEUROCOMPUTING TECHNIQUE

The analysis side of the problem, the similar terminology to the synthesis mechanism is used, but the input impedance of the antenna is obtained from the output for a chosen $\tan\delta$, patch dimensions, the diameter of the probe D_0 and located feed X_0 at the input side (Figure 2).

The data base, made up 240 examples (W, L, D_0, X_0, $\tan\delta$, (R_{in}/Z_0) and (X_{in}/Z_0)), is conceived starting from the results of the model of Aboud. This data base is subdivided there after between a whole of training and another of test. The base of training is made up of 100 examples, the base of test as for it is made of 20 elements which are reserved for the final measurement of the performance.

First of all, it can be used in the narrow range: $2.95\,\text{cm} \leq W \leq 5.7\,\text{cm}$, $1.95\,\text{cm} \leq L \leq 3.8\,\text{cm}$, $0.002 \leq \tan\delta \leq 0.003$, $0.065\,\text{cm} \leq D_0 \leq 0.127\,\text{cm}$ and $0\,\text{cm} \leq X_0 \leq 0.635\,\text{cm}$.

The neural models based on MLPs have been used to compute the input impedance of rectangular antenna. MLPs can be trained by many different learning algorithms [6]. In this paper, MLPs are trained with the use of LM, OSS, BFG, RP, SCG, GDX, GDM, CGF algorithms.

The number of neurons in the hidden layers and training epochs for neural models for rectangular microstrip antenna without and with airgaps proposed in this paper are given in Table 1. In Table 1, 24×13 means that the numbers of neurons were 24 and 13 for the first and second hidden layers, respectively. The input layers of the MLPs have a tangent hyperbolic function, the output layer has linear function and the hidden layers have a sigmoid function and tangent hyperbolic function. Initial weights of the neural models were set up randomly.

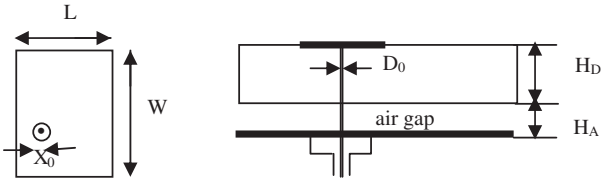

Figure 1: Geometry of a rectangular microstrip antenna with an airgap.

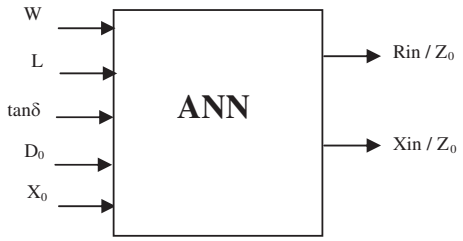

Figure 2: Neural network structure.

Table 1: The number of neurons in the hidden layers and training epochs for neural models for rectangular microstrip antenna with and without airgap.

Learning algorithms	Without airgap $H_A = 0\,\text{mm}$			With airgap $H_A = 0.5\,\text{mm}$		
	The number of neurons in the hidden layers	The number of training epochs	SSE	The number of neurons in the hidden layers	The number of training epochs	SSE
LM	24×13	13	0.073	10×25	13	0.026
OSS	22×6	131	0.097	14×36	166	0.098
BFG	31×19	36	0.098	33×16	35	0.088
RP	21×15	76	0.099	22×8	63	0.087
SCG	12×11	64	0.099	3×28	114	0.099
GDX	29×7	1102	0.099	11×37	1132	0.099
GDM	27×9	5101	0.099	40×38	1094	0.099
CGF	20×13	284	0.098	31×5	162	0.098

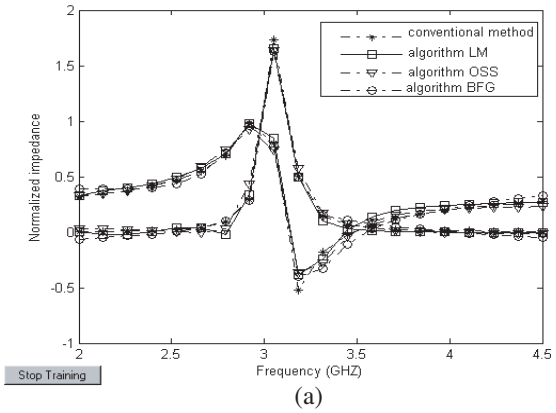

(a)

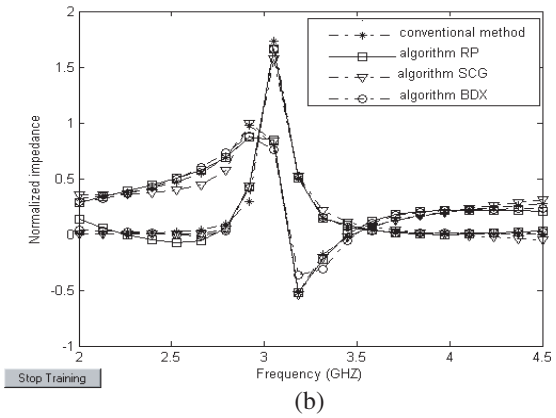

(b)

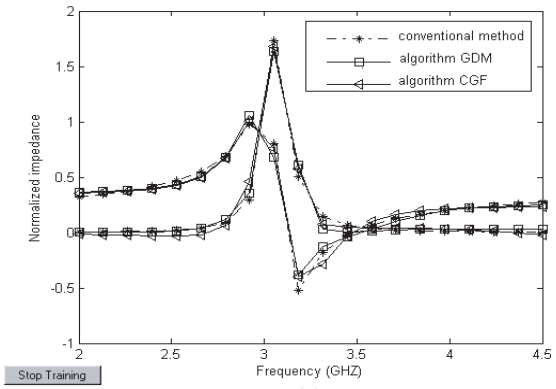

(c)

Figure 3: Normalized resistance and reactance of the optimized rectangular microstrip antenna without airgap for $L = 3.05\,\text{cm}$; $W = 4.55\,\text{cm}$; $\varepsilon_r = 2.33$; $\tan\delta = 0.002$; $D_0 = 0.127\,\text{cm}$; $X_0 = 0.54\,\text{cm}$: (a) Algorithms LM, OSS, BFG. (b) Algorithms RP, SCG, GDX. (c) Algorithms GDM, CGF.

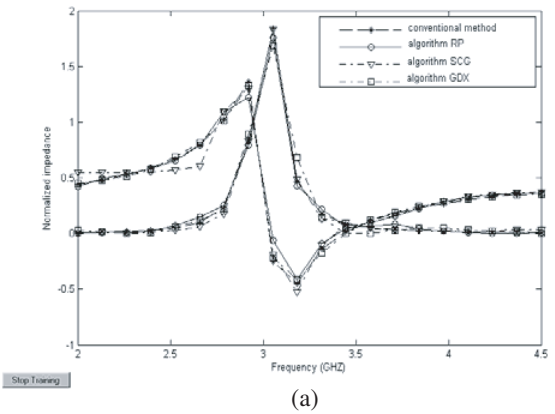

(a)

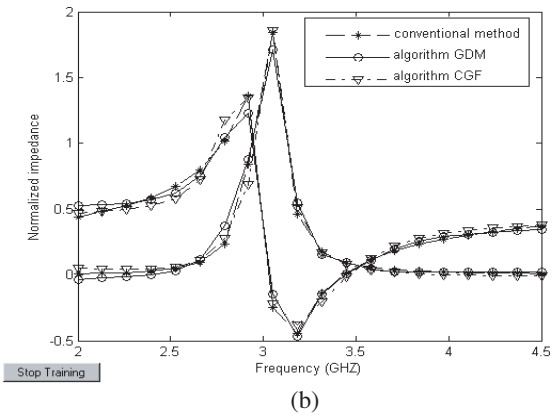

(b)

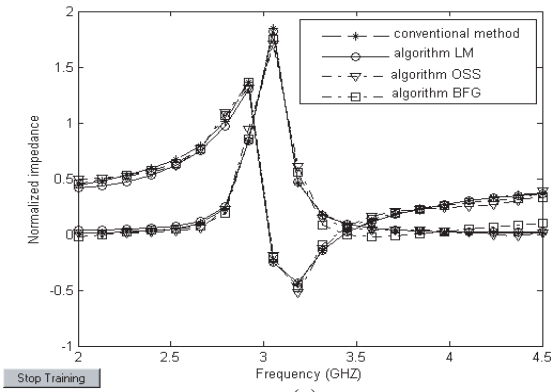

(c)

Figure 4: Normalized resistance and reactance of the optimized rectangular microstrip antenna witht airgap for $L = 3.05\,\text{cm}$; $W = 4.55\,\text{cm}$; $\varepsilon_r = 2.33$; $\tan\delta = 0.002$; $D_0 = 0.127\,\text{cm}$; $X_0 = 0.54\,\text{cm}$: (a) Algorithms RP, SCG, GDX. (b) Algorithms GDM, CGF. (c) Algorithms LM, OSS, BFG.

4. RESULTS AND DISCUSSIONS

When the performances of neural models presented in this paper and in [6] are compared with each other, the best result is obtained from the MLP network trained by the LM algorithm, as shown in Table 1.

For comparison, the results obtained via conventional methods [3], the neural models are given in Figure 3 and Figure 4. Figure 3 represents the normalized input impedance of rectangular microstrip patch antenna without airgap calculated by the neural models [6] trained by eight algorithms. It can be observed that the impedance from the neural net matches fairly well with the true value. The impedance of the resulting antenna with airgap from the ANN is plotted against

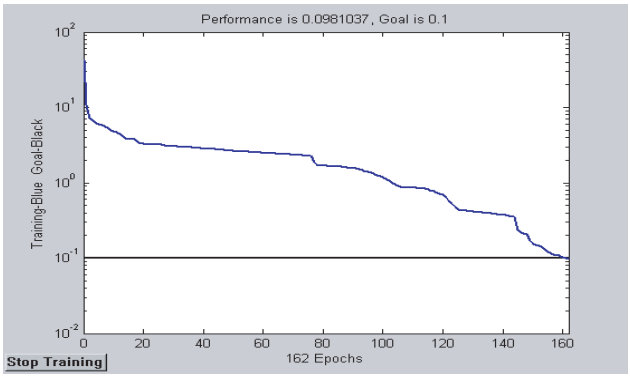

Figure 5: Training graph results for synthesis of rectangular microstrip antenna with airgap.

the exact impedance calculated by for the same optimized geometry (Figure 4). It shows that they are in good agreement.

Figure 5 shows the neural network training graph results obtained from the MLP network trained by the CGF algorithm, for the synthesis for input impedance of rectangular microstrip patch antenna with airgap ($H_A = 0.5\,\text{mm}$). It is apparent from this figure, training performs in 162 epochs. We pass the full set of input samples through the neural network to compute the least squared error function we will use in the back propagation of the errors step. Each such pass is called an epoch. From this figure it is clear that error minimizes from 0.098 to nearly 10^{-1}.

5. CONCLUSIONS

ANNs are trained by eight learning algorithms to obtain better performance and faster convergence with a simpler structure. The best result is obtained from the MLPs trained by the LM algorithm.

For engineering applications, this simple model is very useful. By using the MATLAB neural network toolbox, a single-layered neural network with a linear transfer function can easily be realized and its weights, which are stored in a matrix, can be set to the adequate values.

REFERENCES

1. Vegni, L. and A. Toscano, "Analysis of microstrip antennas using neural networks," *IEEE Transactions on Magnetics*, Vol. 33, No. 10, 1414–1419, 1979.
2. Carver, K. R. and J. W. Mink, "Microstrip antenna technology," *IEEE Transactions on Antennas and Propagation*, Vol. 29, 2–24, 1981.
3. Aboud, F., J. P. Damiano, and A. Papiernik, "Accurate model for the input impedance of coax-fed rectangular microstrip antenna with and without airgaps," *6th International Conference on Antennas and Propagation (ICAP 89)*, 102–106, Coventry, England, April 1989.
4. Verma, A. K. and Z. Rostamy, "Resonant frequency of uncovered and covered rectangular microstrip patch using modified wolff model," *IEEE Transactions on Theory and Techniques*, Vol. 41, No. 1, 109–116, 1993.
5. Dahrele, J. S. and K. F. Lee, "Theory and experiment on microstrip antennas with airgaps," *Proc. IEE*, Vol. 132, No. 7, 455–460, 1985.
6. Maren, A., C. Harston, and R. Pap, *Handbook of Neural Computing Applications*, Academic Press, London, 1990.
7. Garg, R. and S. A. Long, "Resonant frequency of electrically thick rectangular microstrip antenna," *Electron Lett.*, Vol. 23, No. 5, 1149–1159, 1987.

Helically Corrugated Feed Antenna with Far out Sidelobes Reduction

S. H. Mohseni Armaki[1], **F. Hojat Kashani**[2], **J. Rashed-Mohassel**[1], **and M. Fallah**[1]

[1]Iran University of Science and Technology (IUST), Tehran, Iran
[2]University of Tehran, Tehran, Iran

Abstract— This paper presents experimental studies of a helically corrugated circular waveguide (HCCW) antenna feed. The experimental results agree with the simulated results and demonstrate a moderate influence on suppression far out sidelobes of open ended HCCW.

1. INTRODUCTION

The helically corrugated waveguide (HCCW) in its many applications has attracted considerable interest as device for the propagation of electromagnetic energy [1–4]. In usual way open ended circular cylindrical waveguide (CCW) was being used as feed antenna. In an open ended CCW, there is spillover of radiated power through far-out side lobes, and this become more predominant in the E-plane. The reason for this is that fields diffracted by the open end of waveguide induced conduction currents on the outer wall of the waveguide, which in turn radiate and contribute to increases spillover. With a view to reducing spillover a suggestion was presented by Narasimhan [5]. Another way is using helically corrugation in inner surface of CWW as shown in Fig. 1.

2. DESIGN AND FABRICATION

The HCCW has a small pitch $p = 4\,\text{mm}$, radius $a = 18\,\text{mm}$, shallow slot depth $s = 3.5\,\text{mm}$ and narrow slot width $w = 2\,\text{mm}$ as shown in Fig. 1. The important matter in this structure is group velocity or $\partial\omega/\partial\beta$. In a dispersive medium the group velocity on any wave propagating through it is dependent on the frequency of the wave. By using HFSS software, we simulated $\omega - \beta$ diagram

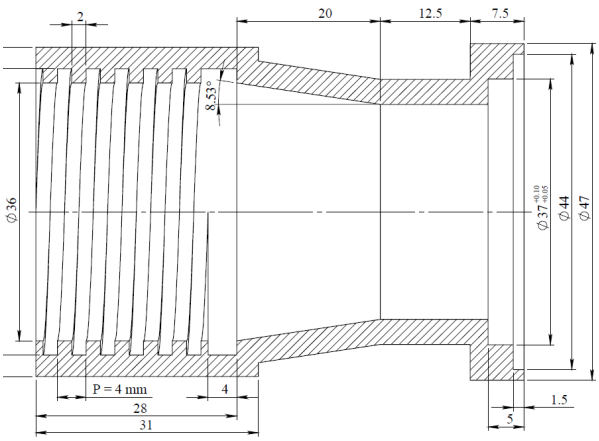

Figure 1: Dimensions of HCCW. All dimensions in mm.

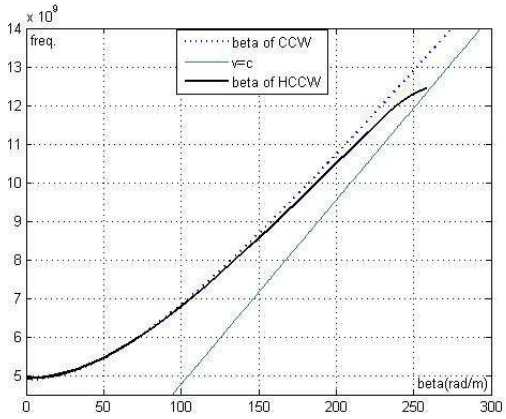

Figure 2: Propagation characteristics of TE_{11} mode in HCCW & CCW.

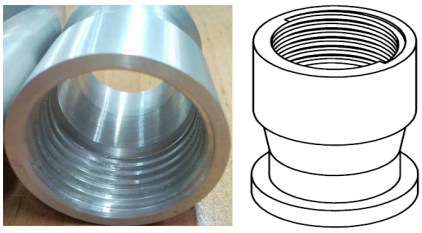

Figure 3: Photo of fabricated HCCW.

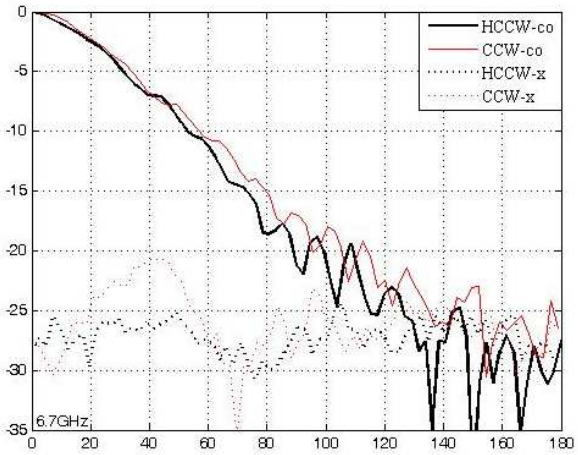

Figure 4: Measured co polar E-plane & cross polar Patterns for CCW & HCCW at 6.7 GHz.

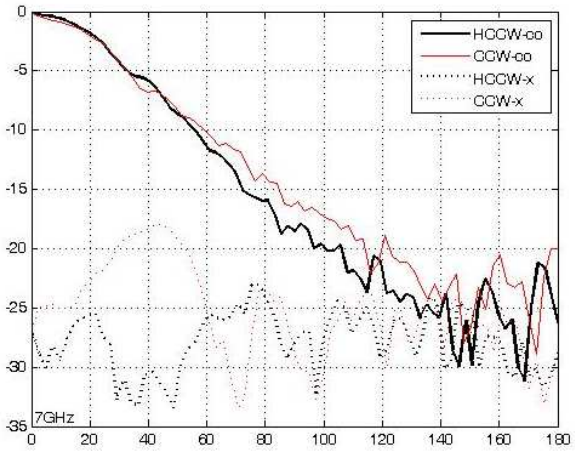

Figure 5: Measured co polar E-plane & cross polar Patterns for CCW & HCCW at 7 GHz.

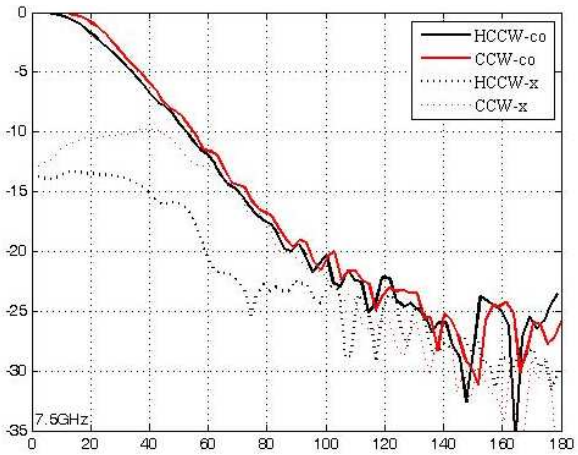

Figure 6: Measured co polar E-plane & cross polar Patterns for CCW & HCCW at 7.5 GHz.

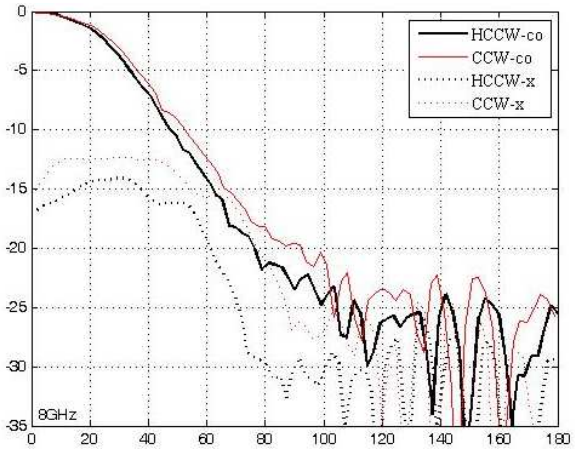

Figure 7: Measured co polar E-plane & cross polar Patterns for CCW & HCCW at 8 GHz.

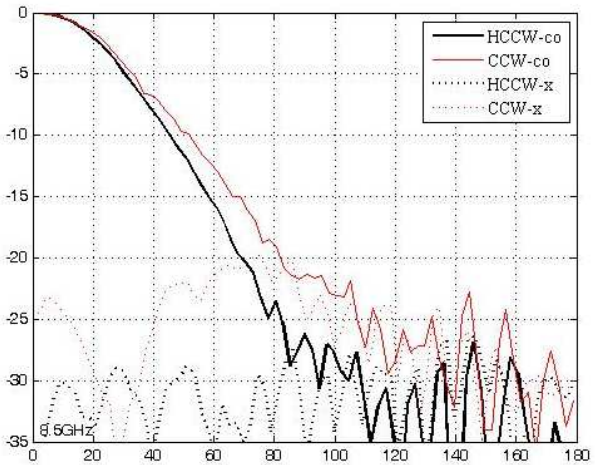

Figure 8: Measured co polar E-plane & cross polar Patterns for CCW & HCCW at 8.5 GHz.

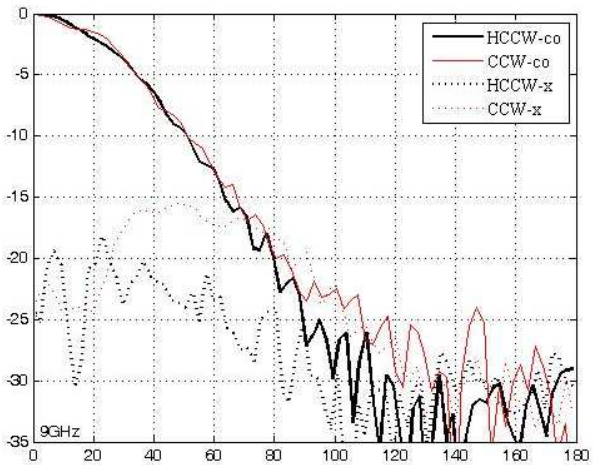

Figure 9: Measured co polar E-plane & cross polar Patterns for CCW & HCCW at 9 GHz.

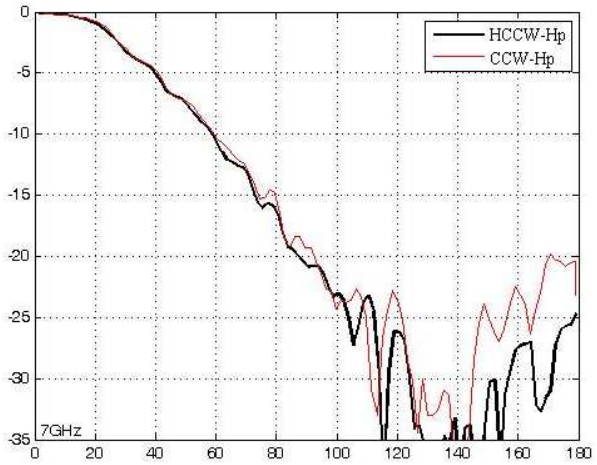

Figure 10: Measured co polar H-plane Patterns for CCW & HCCW at 7 GHz.

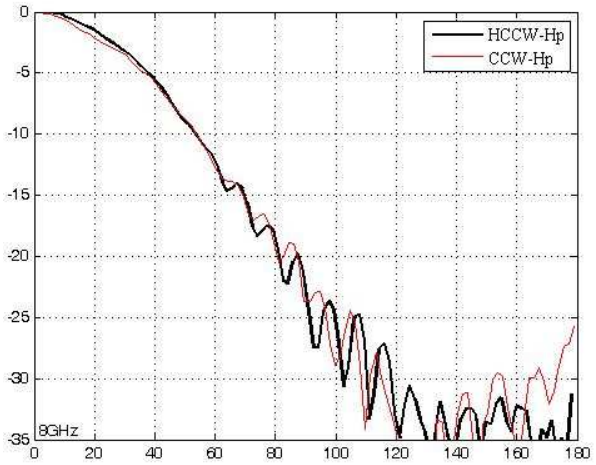

Figure 11: Measured co polar H-plane Patterns for CCW & HCCW at 8 GHz.

of this HCCW as shown in Fig. 2. Inspection of Fig. 2 reveals that for that particular combination of a, s, p and w, the $\omega - \beta$ curve of HCCW virtually coincides with that of TE_{11} mode of CCW. Fig. 3 shows the photo of fabricated HCCW.

3. MEASUREMENTS AND DISCUSSION

Measurements were made for different frequencies for the E-plane, the H-plane and the cross polarization ($\varphi = 45°$) on HCCW and CCW. Only the E-planes and two H-plane results are presented. The H-plane patterns were approximately the same for two antennas. The results are shown in Figs. 4–11.

4. CONCLUSION

In this paper, we have presented the experimental study on reduction far out spillover radiation pattern of feed antennas. Measurements reveal that helically corrugations do help reduction of far out sidelobes and cross polarization levels. Moreover, only with helically corrugation it is possible to realize reduction in far out sidelobes over a broad band (about 28 percent) without any significant deterioration of the other radiation characteristics.

REFERENCES

1. Foulds, K. W. H., et al., "Propagation of an electromagnetic wave through a helical waveguide," *IEE Proc.*, Vol. 11, No. 11, 1789–1798, Nov. 1964.
2. Tang, C. C. H., "On the wave propagation and mode conversion in a helically corrugated multimode circular waveguide," *IEEE Trans. on Microwave Theory and Techniques*, Vol. 14, No. 6, 275–284, Jun. 1966.
3. Ghosh, S. and G. P. Srivastava, "Corrugated waveguide with helically continues corrugation," *IEEE Trans. on Antenna and Propagat.*, Vol. 27, No. 4, 564–567, Jul. 1979.
4. Wei, Y., et al., "Experimental demonstration of the effect of groove shape on the wave properties of the helical groove waveguide," *IEEE Microwave and Wireless Components Letter*, Vol. 13, No. 11, 484–486, Nov. 2003.
5. Narasimhan, M. S. and K. R. Govind, "Radiation characteristics of a corrugated circular cylindrical waveguide horn exited in the TE_{11} mode," *IEEE Trans. on Antenna and Propagat.*, Vol. 36, No. 8, 1147–1152, Aug. 1988.

Design and Development of Monopulse Dual Mode Corrugated Horn

S. H. Mohseni Armaki[1], **F. Hojat Kashani**[1], **J. Rashed-Mohassel**[2], **and M. Fallah**[1]

[1]Iran University of Science and Technology (IUST), Iran
[2]University of Tehran, Iran

Abstract— This paper describes the design and test of a small flare angle conical corrugated feed horn antenna which can generate sum and difference patterns suitable for monopulse tracking in remote sensing earth stations. The prototyped horn designed here operates in the frequency range 7–9 GHz for sum mode and 7.5–9 GHz for difference mode. The gain of sum pattern is 22 dB with at least 32 dB cross-polarization. The measured results validate that the feed antenna operation is satisfactory for 20% bandwidth.

1. INTRODUCTION

Momopulse refers to the ability to obtain complete angle error information on a single pulse. The aim of monopulse antenna is to generate the signals required for azimuth and elevation plane error channels. This feature may be achieved by either multiple antennas or multimode propagation feed antenna. The last technique is found to be better in terms of size, complexity and accuracy.

Corrugated feed horns provide better performance and lower cross polarization levels than a smooth walled horn. The monopulse antenna with corrugated feed is a reliable and accurate automatic remote sensing satellite tracking system. It utilizes the higher order modes HE_{21} or TE_{21} to perform is tracking task. For the circular polarization, it was sufficient to process the signal of a single mode only. Now in the modern earth stations use of HE_{21} or $TE_{21}$is enough for tracking in either linear or circular polarized cases [1].

In this paper, a simple wideband circularly polarized TE_{21}-mode tracking corrugated horn is exhibited for application in remote sensing earth stations. It utilizes TE_{11} mode to produce sum pattern and TE_{21} mode to provide the difference pattern. The horn operates in 7-9GHz for sum mode and 7.5–9 GHz for difference mode. The design of the feed is done based on Granet et al. report [6] and Clarricoats book [7] and it is simulated using HFSS code [8]. The final measurements have shown satisfactory results with symmetrical E & H plane sum & difference radiation patterns, good impedance matching with $Rl < -18$ dB over a bandwidth of 2 GHz, low cross polar levels and good deep null.

2. FEED STRUCTURE

The schematic drawing of tracking corrugated horn is shown in Fig. 1. It consists of input mode converter and a conventional corrugated horn.

Input waveguide is exited by TE_{11} mode, and a mode converter is required to convert TE_{11} & TE_{21} modes to HE_{11} & HE_{21} modes respectively. Any mismatch between the modes in the circular waveguide and the modes in the throat section of the corrugated horn will give rise to mode conversion to higher order modes. There are three types of mode converters. In this paper, we have used variable-depth-slot mode converter. Because of the excitation of unwanted mode and reduction in efficiency, the mode converter is an important element.

A small flare conical corrugated horn structure is designed and analyzed using HFSS code. The targets of the design are: to reduce cross-polarization level for desired frequency bandwidth, to ensure transmission of HE_{11} & HE_{21} modes only, and keep the aperture efficiency high for sum & difference patterns.

3. MODE CONVERTER

To ensure good propagation conditions for HE_{11} & HE_{21} modes, the radius at the input to the mode converter should be chosen such that $k_l a_m \geq 3.054$ where k_L is free space wave number corresponding to lowest frequency, $f_L = 7.5$ GHz. Here, we choose $a_m = 21$ mm.

Figure 2 can be used to choose the depth of the first slot. When $f_H = 9$ GHz, the first slot admittance S_1 should be infinite. From the intersection point of straight line $k_H a_m = 3.95$, we get the longitudinal coordinate of that point $r_1/r_0 = 0.53(w/p = 0.78)$ that is $s_1 = 18.3$ mm. The other parameters according to [6] are as follows: number of mode converter slots, $N_{Mc} = 5$, slot pitch, $p = 7$ mm, $s_2 = 16.5$ mm, $s_3 = 14.8$ mm, $s_4 = 13$ mm, and $s_5 = 11$ mm.

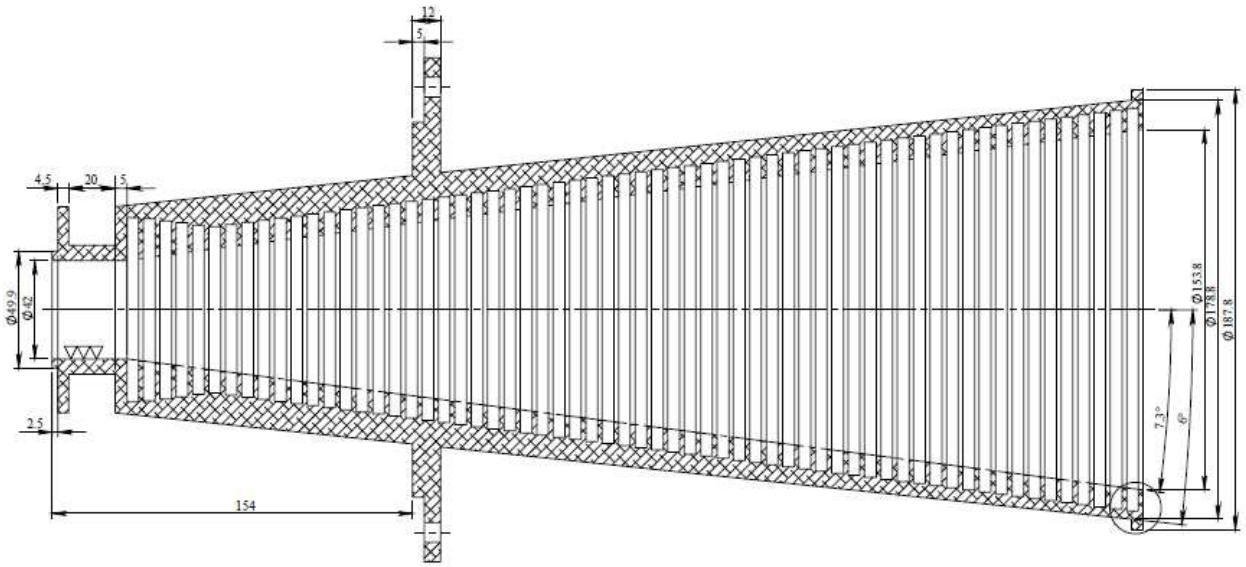

Figure 1: Schematic drawing of a circular corrugated horn.

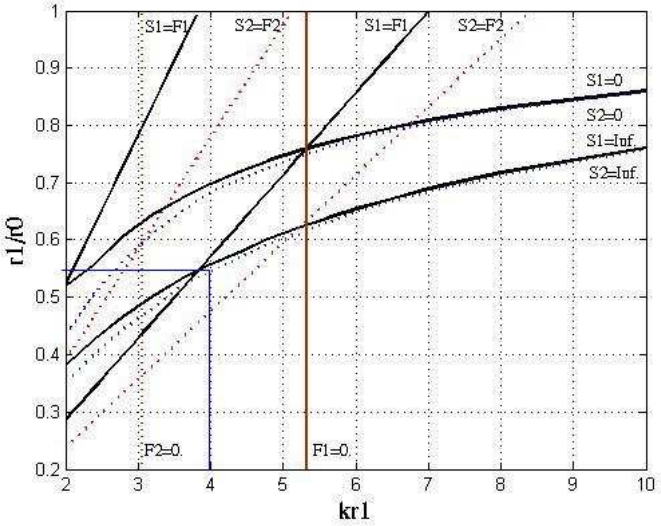

Figure 2: Parametric dependence curves of special points on characteristics $m = 1$ and $m = 2$ modes.

Simulation of the converter can be done by approximating the mode converter as a series of constant diameter corrugated waveguides. The results from field matching studies supports that a prefect match will be obtained when the guide wavelengths in the two waveguides have the same value [7]. Sharp changes in guide wavelength along the mode converter are indicative of a change in impedance and can cause higher order modes to be exited.

Curves of Fig. 3 and Fig. 4 show the normalized guide wavelength against normalized slot depth for various normalized inner radii for HE_{11} & HE_{21} modes respectively [7]. These curves are related for the fields with a slot width of $0.1\lambda$and ridge width of 0.05λ. Matching trajectory for corrugated mode converter obtained by plotting the inner radius and slot depth for each corrugation. For an assessment of good matching, the trajectory at the upper, center, and lower frequencies for HE_{11} & HE_{21} modes must be placed on the guide wavelength curves.

4. CORRUGATED HORN

Three dimensional structure of corrugated horn is chosen based on theoretical calculations [6]. The semi angle θ_0 and radius of aperture a_0 is determined by the required beamwidth and the operating frequency. We choose $a_0 = 160\,\text{mm}$ and $\theta_0 = 7°$. 57 slots are used in this horn. Slots are resonant

at balanced frequency of $f_c = 8.2\,\text{GHz}$. The slot parameters are: $p = 7\,\text{mm}$, $w = 5\,\text{mm}$ and $s = 9.3\,\text{mm}$.

5. MEASUREMENTS

The tacking corrugated horn is realized and simulated for the frequency range 7–9 GHz. The horn geometry is shown in Fig. 1. Analysis is carried out using HFSS code. The measured return loss is shown in Fig. 5. It is observed that the return loss in the sum mode is better than 18 dB.

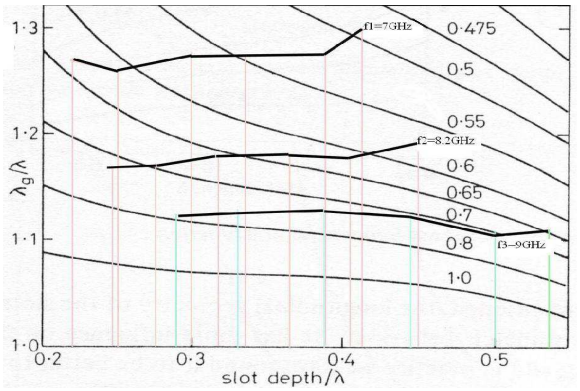

Figure 3: Trajectories of three frequencies for HE_{11} mode.

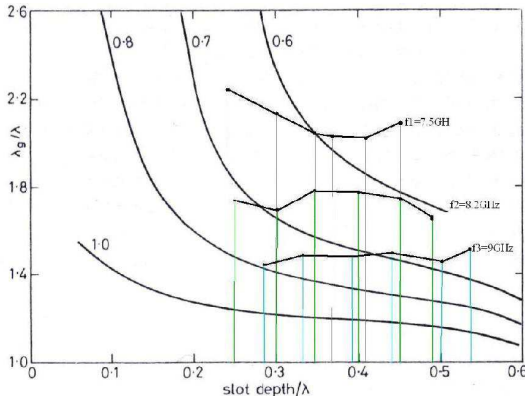

Figure 4: Trajectories of three frequencies for HE_{21} mode.

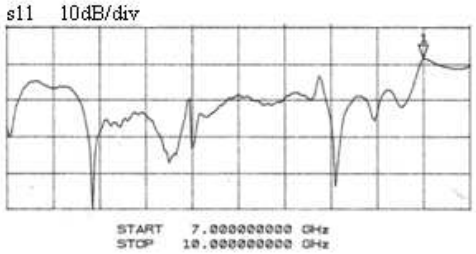

Figure 5: Measured return loss.

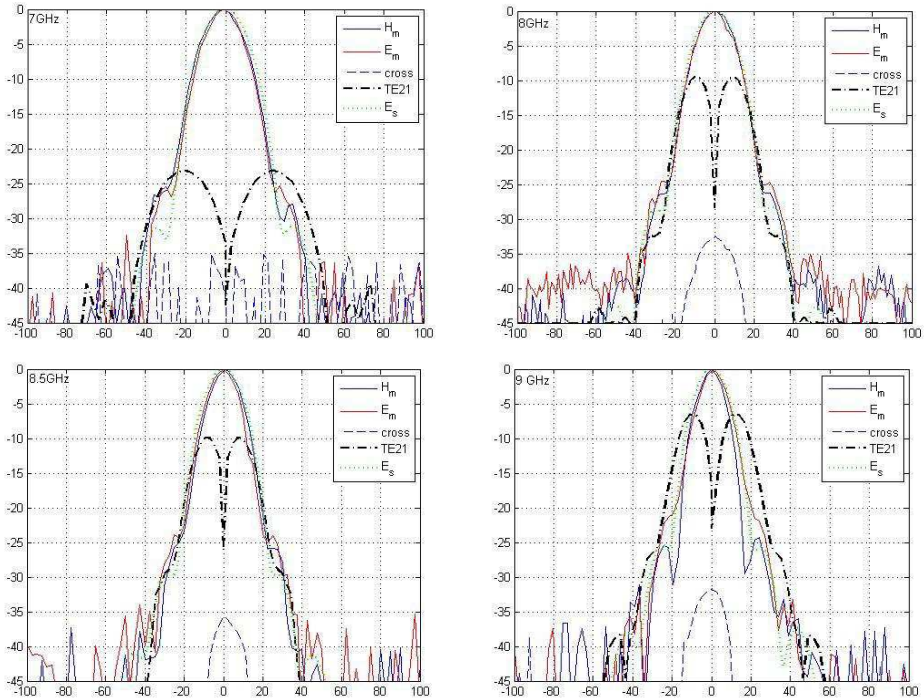

Figure 6: Simulated and measured E & H plane sum and difference radiation pattern; m: measured, s: simulated.

The measured and simulated sum and difference patterns at 7, 8, 8.5 and 9 GHz frequencies are given in Fig. 6. It is observed that the sum copolar pattern demonstrate a high degree of symmetry. The cross-polarization peak levels at mentioned frequencies are below −32 dB.

6. CONCLUSION

This paper presents the design and simulation of simple monopulse tracking circularly feed horn for remote sensing earth stations. The feed design and simulation given here, has been validated experimentally. Good agreement between simulation and experimental data is observed.

REFERENCES

1. Sakr, L., "The higher order modes in the feeds of the satellite monopulser tracking antenna," *IEEE Melecon*, 453–457, May 7–9, Cairo, 2002.
2. Watson, B. K., N. D. Dang, and S. Gohsh, "A mode extraction network for RF sensing in satellite reflector antenna," *Int. Conf. on Ant. & Prop. IEE Conf. Publ.*, 323–327, April 1981.
3. Vu, T. B., "Corrugated horn as high-performance monopulse feed," *Int. J. Electronics*, Vol. 34, No. 4, 433–444, April 1973.
4. Lenzing, E. H. and H. F. Lenzing, "Characteristics of the TE_{21} mode in circular apertures as used for satellite tracking," *IEEE Trans. on Aerospace and Electronic Systems*, Vol. 37, No. 3, 1113–1117, July 2001.
5. Du, B., E. K. N. Yung, K. Z. Yang, and W. J. Zhang, "Wide-band linearly or circularly polarized monopulse tracking corrugated horn," *IEEE Trans. on Antenna and Propagat.*, Vol. 50, No. 2, 192–197, February 2002.
6. Granet, C. and G. L. James, "Design of corrugated horns: A primer," *IEEE Antennas and Propagation Magazine*, Vol. 47, No. 2, 76–83, April 2005.
7. Clarricoats, P. J. B. and A. D. Olver, "Corrugated horns for microwave antennas," *IEE Electromagnetic Wave Series*, 18, London, 1984.
8. HFSS, "High frequency structure simulator," v 11, Finite Element Package, Ansoft Corp., 2008

Novel Application of MNG Metamaterial in Rectangular Microstrip Patch Antenna (Partially Loaded Case) for Dual Band Application

Mahdy Rahman Chowdhury Mahdy, **Md. Rashedul Alam Zuboraj**,
Abdullah Al Noman Ovi, **and Md. Abdul Matin**
Department of Electrical and Electronic Engineering
Bangladesh University of Engineering and Technology, Dhaka, Bangladesh

Abstract— Prior to our current work, impossibility of sub-wavelength rectangular MSA has been demonstrated. However, in this paper it has been possible to get unconventional low value of fundamental resonance ($TM_{0\delta0}$ mode $(0 < \delta < 1)$) with quite satisfactory radiation using MNG metamaterial partially in rectangular patch antenna. As a result, not only more than 50% size reduction but also dual band performance has been achieved by our proposed rectangular patch antennas. In case of such rectangular patch antenna, arbitrary low value of resonance along with arbitrary small length of the antenna is impossible. But yet low value of fundamental resonance ($TM_{0\delta0}$ mode $(0 < \delta < 1)$) using interface resonance has been reported here. Moreover, we have shown that MNG metamaterial can not be loaded in small or medium sized rectangular MSA to modify any modes higher than fundamental TM_{010} mode. In such cases surprisingly conventional TM_{010} mode radiation pattern deteriorates. All the ideas regarding this metamaterial based rectangular microstrip patch antenna have been verified with analytical calculations, our proposed algorithm based simulated results and 'CST MICROWAVE STUDIO' based realistic simulations.

1. INTRODUCTION

Miniaturized dual frequency patch antennas provide an alternative to large bandwidth planner antennas. A unique radiating structure is desirable to accomplish these operations. Metamaterial based patch antennas may be only the good solutions to meet all these requirements. Alu et al. [1] has proposed design method to obtain sub-wavelength rectangular patch antennas using DPS-ENG bi-layer. But it has been shown that such rectangular patches give broadside null radiation pattern [1, 2]. This has been referred as 'zero radiation problem' [3]. Before and even after the work of Alu et al., several works have been proposed in case of partially loaded rectangular microstrip patch antenna, but they were without considering the radiation efficiency of such cavities [2, 4, 5]. It has been predicted that: These rectangular antennas partially loaded with metamaterial can only be good resonators but may not be good radiators [6]. Later, Jiang Xiong et al. [7] showed that using MNG metamaterials, modification of conventional TM_{020} mode radiation pattern is possible for very large patch antennas.

In [8], we have proposed an algorithm for radiation pattern modification using metamaterial (for any patch size). Applying that algorithm, a novel design of small rectangular microstrip patch antenna partially loaded with MNG metamaterial for dual band applications will be shown here. We will use unconventional $TM_{0\delta0}$ modes $(0 < \partial < 1)$ for dual band applications. Moreover we will show the impossibility of dual band application of small or medium size rectangular MSA loaded with MNG metamaterial.

2. NOVEL DESIGN OF DUAL BAND MSA USING MNG METAMATERIAL FOR POSSIBLE LOWER FREQUENCY APPLICATION: POSSIBLE AND IMPOSSIBLE PHENOMENON

Prior to our work, applying ENG metamaterial, sub-wavelength resonance at 0.48 GHz has been found in rectangular microstrip antenna using 50 mm × 40 mm patch [1]. But it had broadside null at that frequency. Now we will use that design but using MNG metamaterial to modify the radiation pattern. We will get better radiation at broadside using same antenna but with different constitutive parameters. Here, using our algorithm (with a conventional size); an unconventional plasmonic $TM_{0\delta0}$ mode $(0 < \delta < 1)$ will be produced for resonance at possible low frequency. All our analytical results have been verified using 'MATLAB' based codes and 'CST MICROWAVE STUDIO' based realistic simulated results. To introduce modified unconventional $TM_{0\delta0}$ mode $(0 < \delta < 1)$ with 50 mm × 40 mm patch (Using MNG metamaterial), at first fr has been chosen 1.47 GHz (lower than TM_{010} mode at 1.57 GHz, using DPS only). But 'interface resonance' has

been found at 1.224 GHz (Figure 3). This valuable 'shifting phenomenon' has also been found with $TM_{0\delta 0}$ modes ($0 < \delta < 1$) in different sized patches for application in other bands. This valuable shifting may not be avoidable for this specific mode. Later, this mode at 1.224 GHz will show a good broadside radiation pattern. Here $k_1\eta L$ will be chosen greater than 135° and less than 180° for getting this 'interface resonance' with MNG metamaterial. Then applying our algorithm [8] we get:

Chosen resonant frequency, fr	μ_2 (at fr)	η	$\frac{E_{z_2}}{E_{z_1}}$
1.5 GHz	−0.1091	0.8176	−0.78

Using these optimized parameters, Lorentz model, we get the desired broadside radiation patterns (Figure 4 and Figure 5). Actually, SNG or DNG metamaterials are inherently dispersive and lossy. So, without using dispersive lossy model (i.e., Lorentz model), the simulated results cannot give proper realistic results. Here we have used Lorentz model for MNG:

$$\mu(\omega) = \mu_\infty + \frac{(\mu_s - \mu_\infty)\omega_0^2}{\omega_0^2 - \omega^2 + j\omega\delta}$$

where, $\mu_\infty = 1.0$, $\mu_s = 1.488$, $\omega_0 = 7853981634$ rad/s, $\delta = 50$ MHz.

The radiation pattern found by simulation tells that at broadside it gets maximum radiation. The directivity of the antenna at broadside is 5.571 dBi for unconventional plasmonic mode (Fig-

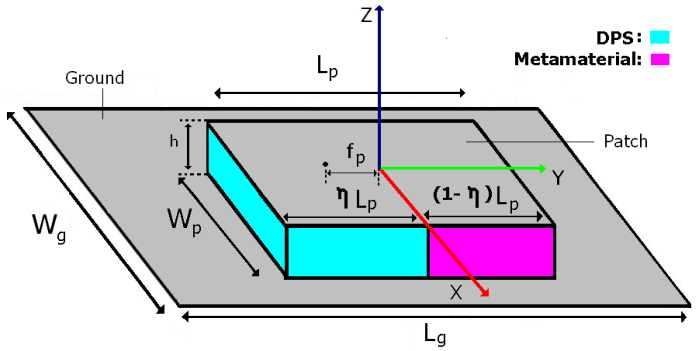

Figure 1: Geometry of a rectangular microstrip patch antenna partially loaded with metamaterial (ENG). fp = feed position from DPS and metamaterials interface. η = filling ratio of the antenna. fr = chosen resonant frequency. Detailed information and constitutive parameters are: Case-1: $Lg = 75$ mm, $Wg = 75$ mm, $\in_{1r}= 3.8$, $\mu_{1r} = 1$. $Lp = 50$ mm, $Wp = 40$ mm, $fp = 21.4356$ mm, $h = 5$ mm, $\eta = 0.8176$, μ_{2r}(at fr) $= -0.1091$ and $\in_{2r}= 5.1$ in case of MNG loading. (First design) Case-2: $Lg = 80$ mm, $Wg = 70$ mm, $\in_{1r}= 3$, $\mu_{1r} = 1$. $Lp = 40$ mm, $Wp = 30$ mm, $fp = 10.788$ mm, $h = 1.7$ mm, $\eta = 0.5197$, μ_{2r}(at fr) $= -0.1089$ and $\in_{2r}= 1$ in case of MNG loading. (Second design).

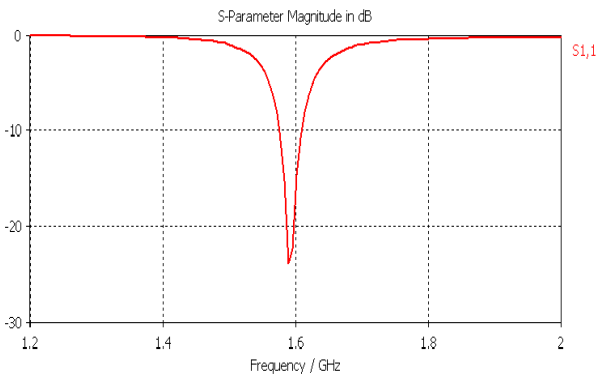

Figure 2: S-parameter performance of conventional 50 mm × 40 mm patch antenna using DPS only.

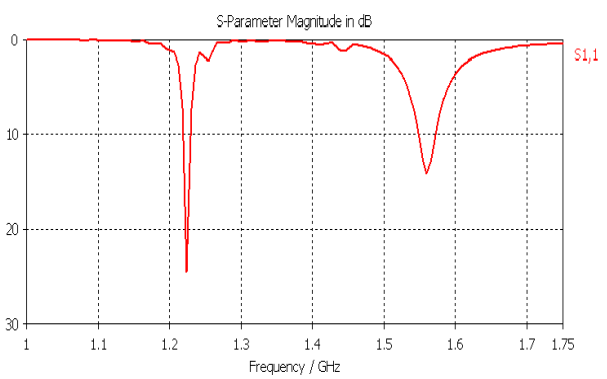

Figure 3: S-parameter performance of proposed 50 mm × 40 mm dual band antenna loaded with MNG.

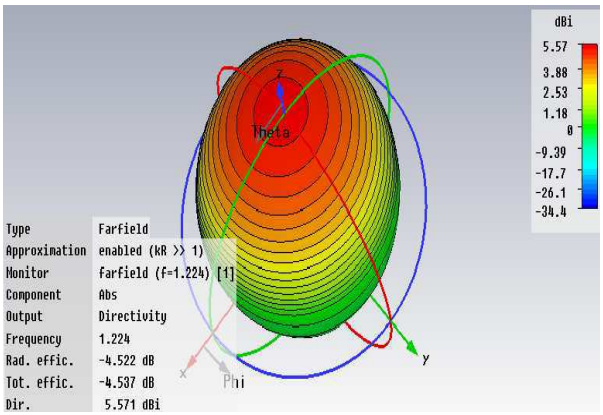

Figure 4: Unconventional $TM_{0\delta0}$ mode 3-D radiation pattern (at 1.224 GHz) (satisfactory radiation).

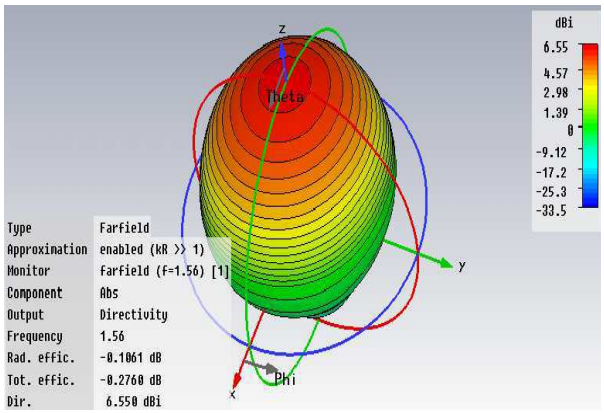

Figure 5: Conventional TM_{010} mode 3-D radiation pattern (at 1.56 GHz).

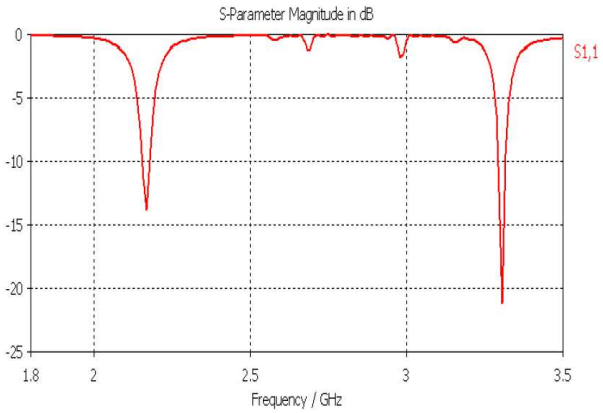

Figure 6: S-parameter performance of proposed 40 mm × 30 mm dual band antenna loaded with MNG.

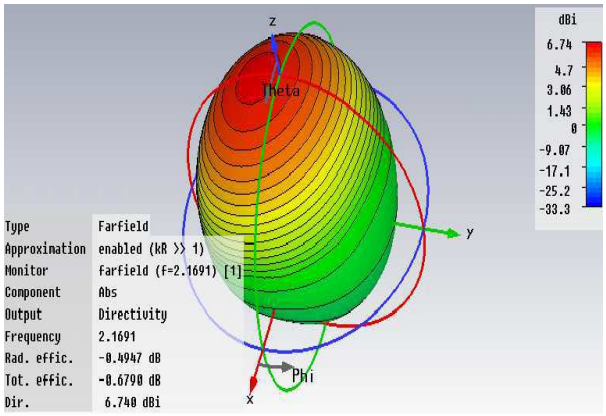

Figure 7: Conventional TM_{010} mode 3-D radiation pattern (at 2.1691).

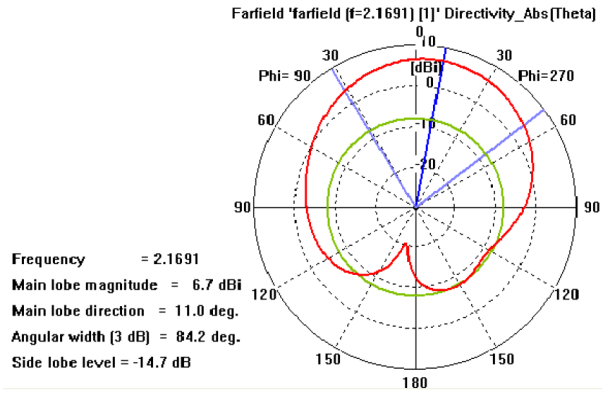

Figure 8: Conventional TM_{010} mode radiation pattern (polar plot) at principal E-plane (unsatisfactory radiation).

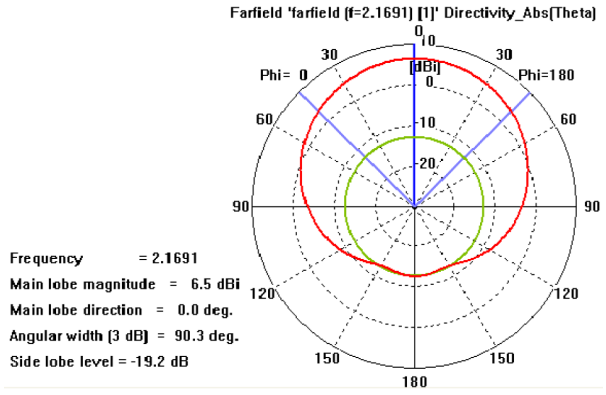

Figure 9: Conventional TM_{010} mode radiation pattern (polar plot) at principal H-plane.

ure 4). So, the idea proposed here is properly justified withmathematical calculation, code based simulation and 'CST Microwave Studio' based realistic simulation.

If we wanted to get resonance with conventional rectangular microstrip patch antenna at 1.224 GHz, we have to use $\in_1 = 3.8$, $\mu_1 = 1$, $L = 62.3$ mm, $W = 62.3$ mm. So, the % size reduction-

$$SR = \frac{(62.3) \times (62.3) - (50 \times 40)}{(62.3) \times (62.3)} \times 100\% = 48.4707\% \quad (1)$$

Hence such MNG metamaterial based rectangular microstrip patch antennas can be used for miniaturized novel designs along with dual band applications.

Following the same procedure like above and using our algorithm [8], here we will show that any mode higher than fundamental TM_{010} mode be modified but dual band performance is dissatisfactory of small and medium patch antennas using MNG metamaterial. This is because, surprisingly, MNG loading deteriorates the fundamental TM_{010} mode. The principal E-plane radiation pattern of TM_{010} mode is mainly affected for this MNG loading. Consider a 30 mm × 40 mm patch. The necessary parameters are given in Figure 1. [Lorentz model parameters are: [$\mu_\infty = 1.0$, $\mu_s = 2.0259$, $\omega_0 = 16336281800$ rad/s, $\delta = 50$ MHz].

3. CONCLUSION

In case of rectangular patch antenna, arbitrary low value of resonance along with arbitrary small length of the antenna is impossible (sub-wavelength antenna). But using unconventional $TM_{0\delta0}$ mode ($0 < \delta < 1$) in such rectangular MSA (partially loaded with MNG) low frequency with almost or more than 50% size reduction is possible. Moreover, any mode higher than conventional TM_{010} mode cannot be modified using MNG metamaterial. Only for very large patches this modification is possible. However, Use of such 'interface resonance' ($TM_{0\delta0}$ mode ($0 < \delta < 1$)) for size reduction without cutting any slot or using any shorting pins is quite satisfactory. This is because such small size, high directivity for both bands (above 6 dBi) and very low level of cross polarization can not be found in case of dual band antennas by any other means.

REFERENCES

1. Alù, A., F. Bilotti, N. Engheta, and L. Vegni, "Subwavelength, compact, resonant patch antennas loaded with metamaterials," *IEEE Transactions on Antennas and Propagation*, Vol. 55, No. 1, January 2007.
2. Zheng, K. S., W. Y. Tam, and D. B. Ge, "Impedance matching of rectangular microstrip antennas partially loaded with DNG metamaterials," *38th European Microwave Conference, EuMC*, October 2008.
3. Zheng, K. S., W. Y. Tam, and D. B. Ge, "Broadside subwavelength microstrip antennas partially loaded with metamaterials," *International Workshop on Metamaterials*, November 2008.
4. Xu, W., L.-W. Li, H.-Y. Yao, and T.-S. Yeo, "Left-handed material effects on waves modes and resonant frequencies: Filled waveguide structures and substrate-loaded patch antennas," *Journal of Electromagnetic Waves and Applications*, Vol. 19, No. 15, 2033–2047, 2005.
5. Yang, R., Y. Xie, D. Li, J. Zheng, and J. Jiang, "Bandwidth enhancement of microstrip antennas with metamaterial bilayered substrate," *Journal of Electromagnetic Waves and Applications*, Vol. 21, No. 15, 2321–2330, 2007.
6. Capolino, F., *Handbook of Artificial Materials: Applications of Metamaterials*, Vol. 2, 18.1–18.14, Taylor and Francis, CRC Press, October 2009.
7. Xiong, J., H. Li, Y. Jin, and S. He, "Modified TM_{020} mode of a rectangular patch antenna partially loaded with metamaterial for dual-band applications," *IEEE Antennas and Wireless Propagation Letters*, Vol. 8, 2009.
8. Mahdy, M. R. C., M. R. A. Zuboraj, A. A. N. Ovi, and M. A. Matin, "A novel design algorithm' and practical realization of rectangular patch antenna loaded with SNG metamaterial," *Progress In Electromagnetics Research M*, Vol. 17, 13–27, 2011.
9. CST Microwave Studio, CST of America [Online], 2009, Available: http://www.cst.com.

Novel Design of Dual Band Rectangular Microstrip Patch Antenna Partially Loaded with MNG Metamaterial for S-band Application

Mahdy Rahman Chowdhury, **Md. Rashedul Alam Zuboraj**,
Abdullah Al Noman Ovi, **and Md. Abdul Matin**
Department of Electrical and Electronic Engineering
Bangladesh University of Engineering and Technology, Dhaka, Bangladesh

Abstract— Miniaturized size and high directivity performance of an antenna are primary requirements for modern satellite based communication systems. Prior to our work, it has been shown that the size of rectangular microstrip patch antenna cannot be made arbitrarily small. But more than 50% size reduction of such an antenna has been possible using our proposed algorithm. In this paper, novel designs of such an antenna partially loaded with MNG metamaterial has been proposed for S-band applications. In case of first design, using interface resonance, $TM_{0\delta 0}$ mode $(0 < \delta < 1)$ has been excited at 2.47 GHz with only a 25 mm × 15 mm rectangular patch. At both bands (2.47 GHz and 3.01 GHz), this antenna shows quite satisfactory radiation performance (directivity above 5.5 dB at broadside for both bands). Again, more than 50% size reduction has been possible here with respect to conventional rectangular patch antenna. All our analytical results have been verified using 'MATLAB' based codes and 'CST MICROWAVE STUDIO' based realistic simulated results.

1. INTRODUCTION

Miniaturized dual frequency patch antennas provide an alternative to large bandwidth planner antennas. A unique radiating structure is desirable to accomplish these operations. Metamaterial based patch antennas may be only the good solutions to meet all these requirements. Alu et al. [1] has proposed design method to obtain sub-wavelength rectangular patch antennas using DPS-ENG bi-layer. But it has been shown that such rectangular patches give broadside null radiation pattern [1, 2]. This has been referred as 'zero radiation problem' [3]. Before and even after the work of Alu et al., several works have been proposed in case of partially loaded rectangular microstrip patch antenna, but they were without considering the radiation efficiency of such cavities [2, 4, 5]. It has been predicted that: these rectangular antennas partially loaded with metamaterial can only be good resonators but may not be good radiators [6]. Later, Jiang Xiong et al. [7] showed that using MNG metamaterials, modification of conventional TM_{020} mode radiation pattern is possible for very large patch antennas.

In [8], we have proposed an algorithm for radiation pattern modification using metamaterial (for any patch size). Applying that algorithm, a novel design of small rectangular microstrip patch antenna partially loaded with ENG metamaterial for dual band applications will be shown here. We will use unconventional $TM_{0\delta 0}$ modes $(1 < \partial < 2)$ for dual band applications.

2. NOVEL DESIGN OF RECTANGULAR MSA USING MNG METAMATERIAL FOR S-BAND

Prior to our work, applying MNG metamaterial, TM_{020} mode of conventional rectangular microstrip antenna has been modified using 72.8 mm × 50 mm patch. But here, using our 'General Idea' and 'Better Radiation Conditions' (with a conventional size), an unconventional $TM_{0\delta 0}$ mode $(0 < \delta < 1)$ will be produced for S-band application. All our analytical results have been verified using 'MATLAB' based codes and 'CST MICROWAVE STUDIO' [9] based realistic simulated results. Using our algorithm [8] here an efficient dual band antenna with more than 50% reduced size will be introduced. We will introduce an MNG based antenna for dual band application (more than 50% reduced size than conventional one) in S-band region using different plasmonic mode $(0 < \delta < 1)$. To introduce modified unconventional $TM_{0\delta 0}$ mode $(0 < \delta < 1)$ with 25 mm × 15 mm patch (Using MNG metamaterial), at first fr has been chosen 2.85 GHz (lower than TM_{010} mode at 3.02 GHz, using DPS only). But 'interface resonance' has been found at 2.47 GHz (Figure 4). This valuable 'shifting phenomenon' has also been found with $TM_{0\delta 0}$ modes $(0 < \delta < 1)$ in different sized patches for application in other bands. This valuable shifting may not be avoidable for this specific mode. Later, this mode at 2.47 GHZ will show a good broadside radiation pattern. Here $k_1\eta L$ will be chosen greater than 135° and less than 180° for getting this 'interface resonance' with MNG metamaterial. Then applying our algorithm [8] we get:

Chosen resonant frequency, f_r	μ_2 (at f_r)	η	$\frac{E_{z_2}}{E_{z_1}}$
2.85 GHz	−0.0561	0.8160	−0.8244

Using these optimized parameters, Lorentz model, we get the desired broadside radiation patterns (Figure 5 and Figure 6). Actually, SNG or DNG metamaterials are inherently dispersive and lossy [1]. So, without using dispersive lossy model (i.e., Lorentz model), the simulated results cannot give proper realistic results. Here we have used Lorentz model for MNG [7, 9]:

$$\mu(\omega) = \mu_\infty + \frac{(\mu_s - \mu_\infty)\omega_0^2}{\omega_0^2 - \omega^2 + j\omega\delta}$$

where, $\mu_s = 1.3164$, $\mu_\infty = 1$, $\omega_0 = 1.5707963270 \times 10^{10}$ rad/s, $\delta = 50$ MHz.

The radiation pattern found by simulation tells that at broadside it gets maximum radiation. The directivity of the antenna at broadside is 5.778 dBi for unconventional plasmonic mode (Figure 5). So, the idea proposed here is properly justified with mathematical calculation, code based simulation and 'CST Microwave Studio' based realistic simulation.

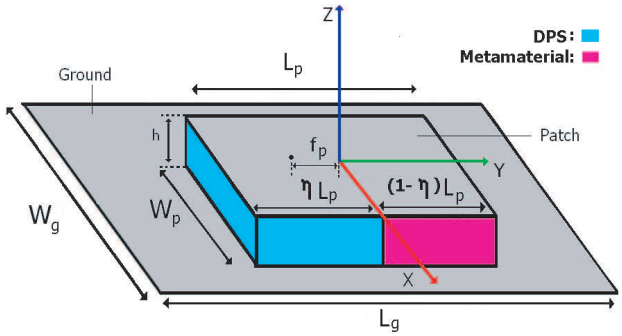

Figure 1: Geometry of a rectangular microstrip patch antenna partially loaded with metamaterial (MNG). f_p = feed position from DPS and metamaterials interface. η = filling ratio of the antenna. f_r = chosen resonant frequency. Detailed information and constitutive parameters are: $L_g = 40$ mm, $W_g = 40$ mm, $\varepsilon_{1r} = 4.4$, $\mu_{1r} = 1$. $L_p = 25$ mm, $W_p = 15$ mm, $f_p = 9.983$ mm, $h = 1.7$ mm, $\eta = 0.8160$, μ_{2r} (at f_r) $= -0.056$ and $\varepsilon_{2r} = 5.1$ in case of MNG loading.

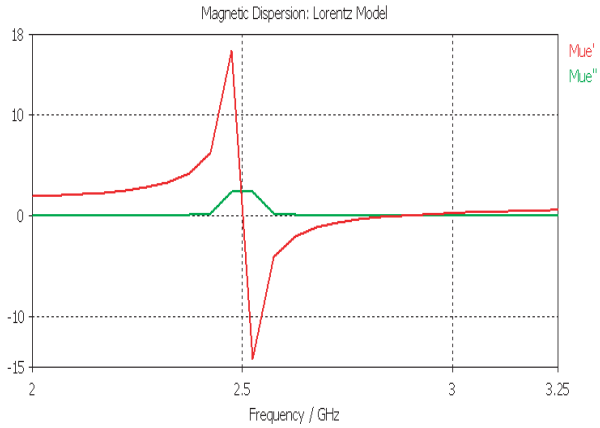

Figure 2: Lorentz dispersive model for proposed antenna.

If we wanted to get resonance with conventional rectangular microstrip patch antenna at 2.47 GHz, we have to use $\in = 4.4$, $\mu = 1$, $L = 29.5$, $W = 29.5$. So, the % size reduction —

$$SR = \frac{(29.5) \times (29.5) - (25 \times 15)}{(29.5) \times (29.5)} \times 100\% = 56.9089\%$$

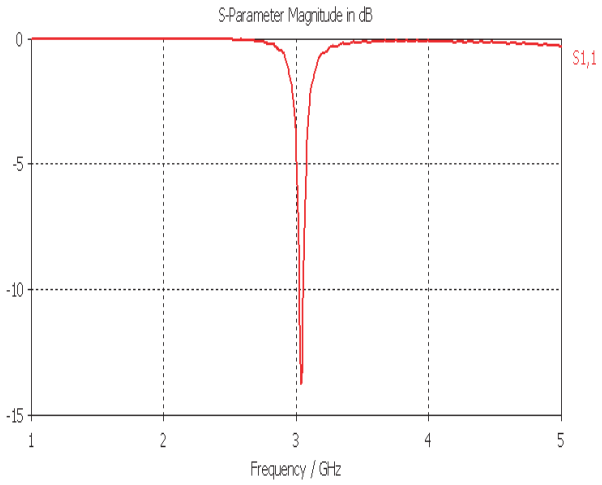

Figure 3: S-parameter performance of conventional 25 mm × 15 mm antenna using DPS only only (ϵ_1= 4.4, $\mu_1 = 1$).

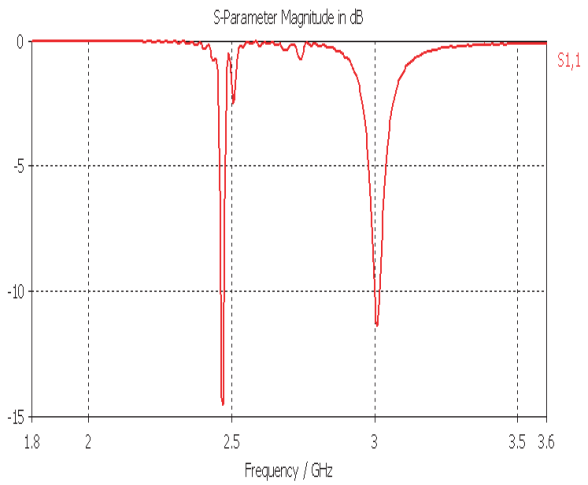

Figure 4: S-parameter performance of proposed 25 mm×15 mm dual band rectangular patch antenna (Figure 1) using DPS and metamaterial. TM_{010} at 3.01 GHz and $TM_{0\delta0}$ at 2.47 GHz.

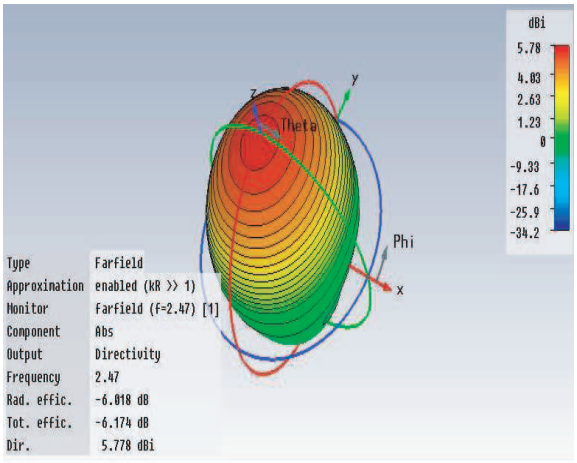

Figure 5: Unconventional $TM_{0\delta0}$ mode 3-D radiation pattern (at 2.47 GHz).

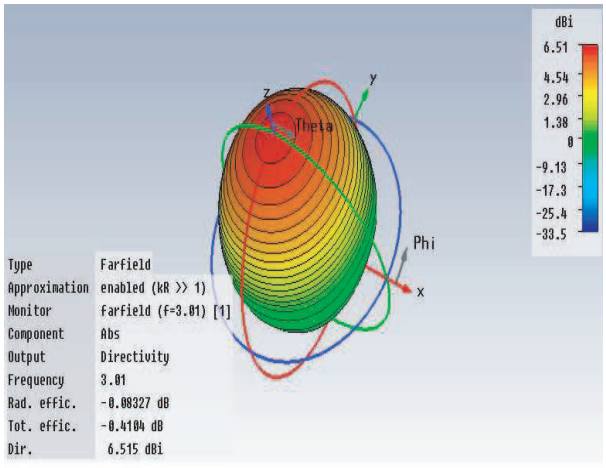

Figure 6: Conventional TM_{010} mode 3-D radiation pattern (at 3.01 GHz).

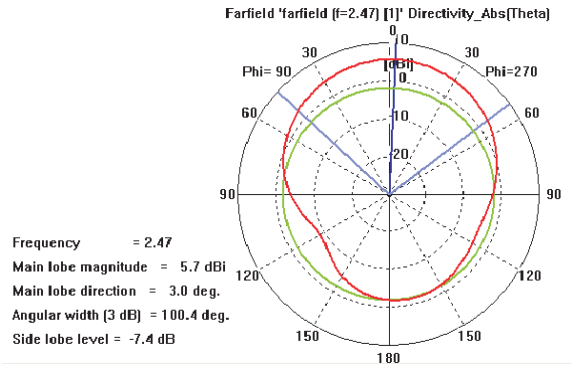

Figure 7: Unconventional $TM_{0\delta0}$ mode radiation pattern (polar plot) at principal E-plane.

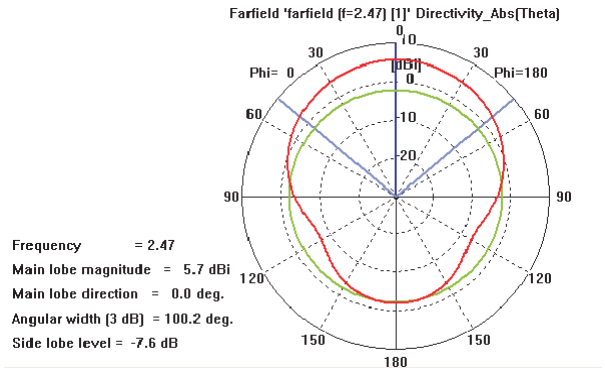

Figure 8: Unconventional $TM_{0\delta0}$ mode radiation pattern (polar plot) at principal H-plane.

Hence such MNG metamaterial based rectangular microstrip patch antennas can be used for miniaturized novel designs along with dual band applications.

3. CONCLUSION

In this contribution, ultimately we have found that only MNG metamaterial can be used potentially in rectangular MSA for size reduction with high directivities for both bands. In fact, in case of rectangular patch antenna, arbitrary low value of resonance along with arbitrary small length of the antenna is impossible(sub-wavelength antenna). But using unconventional $TM_{0\delta0}$ mode $(0 < \delta < 1)$ in such rectangular MSA (partially loaded with MNG) low frequency with almost or more than 50% size reduction is possible. Use of such 'interface resonance' ($TM_{0\delta0}$ mode $(0 < \delta < 1)$) for size reduction without cutting any slot or using any shorting pins is quite satisfactory. This is because such small size, high directivity for both bands (above 6 dBi) and very low level of cross polarization can not be found in case of dual band antennas by any other means. Therefore, the proposed antennas can be used efficiently in wireless communication systems, radio sensors, RFID tags, RADAR applications and so on.

REFERENCES

1. Alù, A., F. Bilotti, N. Engheta, and L. Vegni, "Subwavelength, compact, resonant patch antennas loaded with metamaterials," *IEEE Transactions on Antennas and Propagation*, Vol. 55, No. 1, 13–25, January 2007.
2. Zheng, K. S., W. Y. Tam, and D. B. Ge, "Impedance matching of rectangular microstrip antennas partially loaded with DNG metamaterials," *38th European Microwave Conference, 2008. EuMC 2008*, 678–681, October 2008.
3. Zheng, K. S., W. Y. Tam, and D. B. Ge, "Broadside subwavelength microstrip antennas partially loaded with metamaterials," *2008 International Workshop on Metamaterials*, 39–42, November 2008.
4. Xu, W., L.-W. Li, H.-Y. Yao, and T.-S. Yeo, "Left-handed material effects on waves modes and resonant frequencies: Filled waveguide structures and substrate-loaded patch antennas," *Journal of Electromagnetic Waves and Applications*, Vol. 19, No. 15, 2033–2047, 2005.
5. Yang, R., Y. Xie, D. Li, J. Zheng, and J. Jiang, "Bandwidth enhancement of microstrip antennas with metamaterial bilayered substrate," *Journal of Electromagnetic Waves and Applications*, Vol. 21, No. 15, 2321–2330, 2007.
6. Capolino, F., *Handbook of Artificial Materials: Applications of Metamaterials*, Vol. 2, 18.1–18.14, Taylor and Francis-CRC Press, October 2009.
7. Xiong, J., H. Li, Y. Jin, and S. He, "Modified TM_{020} mode of a rectangular patch antenna partially loaded with metamaterial for dual-band applications," *IEEE Antennas and Wireless Propagation Letters*, Vol. 8, 2009.
8. Chowdhury, M. R., M. R. A. Zuboraj, A. A. N. Ovi, and M. A. Matin, "Possible size miniaturization of a rectangular microstrip patch antenna partially loaded with metamaterial," *Progress In Electromagnetics Research Letters*, under review.
9. CST Microwave Studio 2009, CST of America, Available: http://www.cst.com.

New Formulation of the Method F.W.C.I.P. for the Modelling of a Planar Circuit Integrating a via-hole

Sameh Toumi, **Fethi Mejri**, **and Taoufik Aguili**
Laboratoire des Systèmes de Communication, École Nationale d'Ingénieurs de Tunis (ENIT), Tunisia

Abstract— In our work the structure microstrip is a planar circuit, single layer, consisting of a metallic conductor connected to ground through a via-hole deposited on the upper surface of a dielectric substrate and fed by a localised auxiliary source. The fundamental mode of propagation of such support is not spread TEM (transverse electromagnetic) because the transverse section is not homogeneous. However, since the amplitudes of the longitudinal components of electric and magnetic fields are sufficiently low to be neglected, therefore we speak of quasi-TEM mode. Then is possible to make the modeling of the structure as a transmission line of characteristic impedance Zc immersed in an equivalent homogeneous area characterized by a relative permittivity ε_{reff}. We are interested in this work for via-holes in planar technology that allow better use of both sides of a printed circuit substrate. To model the structure of such iterative method we must take into account the presence of the via-hole in the circuit. In this formulation the TE (transverse electric), TM (transverse magnetic) and TEM modes are used as the basis of numerical spectral domain in which the FFT (Fast Fourier Transform) is projected. Subsequently, the concept of fast wave is introduced to translate the boundary conditions and continuity of relation on different parts of the interface in terms of waves. The method consists in determining an effective relation to link the incident and the reflected waves in the different dielectric layers by expressing the reflexions in the modal domain and the boundary conditions and continuity, expressed in terms of waves in space domain. We use the iterative process to pass from an area to another by means of the FMT (Fast Modal Transform) thus making it possible to accelerate the iterative process and then the convergence of the method. This formulation keeps the advantages of the iterative method in particular the simplicity of implementation and speed of execution compared to other methods. The structure study gives us the convergence of the impedance input Ze and the same results obtained by the analytical formula.

1. INTRODUCTION

The technology microstrip remains one of the most successful and it until the millimeter-length wavelengths. It is widely asked by the industrialists, because contrary to the other technologies the libraries of electric models are very supplied and facilitate enormously the conception of the complex circuits.

With the intense evolution of new constituents and new technologies of manufacturing, as well as the extension of the use of devices in the domains of the microwaves, the industrialists and the researchers will be obliged to improve and to adapt their tools of simulations, what requires the development of new extraction technique of the parameters of these devices. All these incitements gave birth to several numeric methods to resolve the problems of electromagnetism [1, 2].

To make the study of the microwave planar structures integrating passive components (line micro strip , antenna planar, filter pass bandage) or located active (diodes and transistors), simple or multilayer, of some geometry or complex form, we chose the iterative method (F.W.C.I.P) [1, 3, 4]. This method uses Transformed by Fourier into mode FMT (Fast Modal Transform) who is based on Transformed by FFT (Fast Fourier Transform), to pass of the spatial domain in the spectral or modal domain.

The convergence and the speed of convergence of our iterative method (F.W.C.I.P) gives a robustness with regard to the other numeric methods used to resolve the problems of electromagnetism.

In this article we propose an electromagnetic modeling of a structure planar constituted by a metallic driver connected to the mass through a via-hole deposited on the superior face of a substrate dielectric and fed by a localized auxiliary source $S_0\{E_0, J_0\}$.

2. STRUCTURE OF STUDY

The structure of study is a circuit planar, simple layer, constituted by a thin dielectric substrate, on which is deposited a line micro strip of characteristic impedance Z_c, connected to the ground through a via-hole and the localized source of field $S_0\{E_0, J_0\}$.

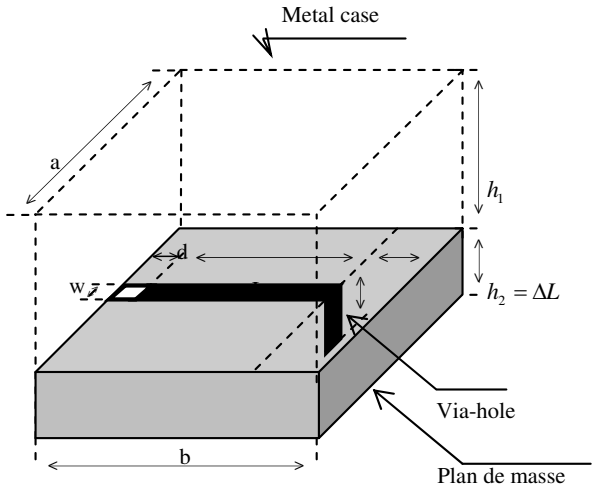

Figure 1: Line court-circuitee by a via-hole.

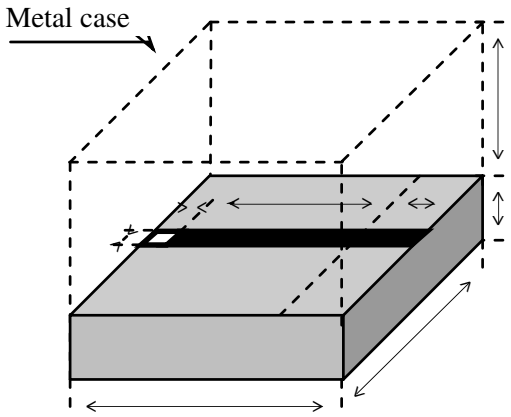

Figure 2: Presentation of a line micro strip short circuited.

This circuit is situated between two dielectric medium, of permittivity relative ε_{r1} and ε_{r2} supposed without losses and is placed in a metallic case (see Figure 1).

3. CALCULE ANALYTIQUE DU CHAMP VIA-HOLE

Let be the general formulae of the field via-hole:

$$\vec{E}^{I}_{via\_hole} = \sum_{n} a_n^{\alpha} \frac{1}{Y_{1n}^{\alpha} + Y_{2n}^{\alpha}} f_n(x) \frac{sh(P_n(y))}{sh(P_n L)}$$

with L is the length of the metal.

$$\vec{E}^{II}_{via\_hole} = \sum_{n} a_n^{\alpha} \frac{1}{Y_{1n}^{\alpha} + Y_{2n}^{\alpha}} f_n(x) \frac{sh(P_n(y-b))}{sh(P_n b)}$$

3.1. Calculation of a_n^{α}

In our application we chose a case with walls electric where the functions of modes are respectively expressed by the following relations (oz):

$$\begin{cases} f_{nz}^{TE}(x) = -\sqrt{\dfrac{2}{a}} \dfrac{n\frac{\pi}{a}}{\sqrt{\left(\frac{n\pi}{a}\right)^2 + \beta^2}} \sin\left(\dfrac{n\pi x}{a}\right) e^{-j\beta z} \end{cases}$$

$$\begin{cases} f_{nz}^{TM}(x) = -\sqrt{\dfrac{2}{a}} \dfrac{j\beta}{\sqrt{\left(\frac{n\pi}{a}\right)^2 + \beta^2}} \sin\left(\dfrac{n\pi x}{a}\right) e^{-j\beta z} \end{cases}$$

$P_n(\varepsilon_r)$: The constant of distribution is express in the spectral domain according to the geometrical sizes and various characteristic elements of the middle k consider.

$$\begin{aligned} P_n^2 &= \left(\frac{n\pi}{a}\right)^2 + \beta^2 - k_0^2 \varepsilon_r, \quad \text{avec} \quad k_0^2 = \omega^2 \mu_0 \varepsilon_0 \\ a_n^{\alpha} &= b_1 \langle f_n, \phi_1 \rangle^{\alpha} + b_2 \langle f_n, \phi_2 \rangle^{\alpha} \end{aligned}$$

We take $b_1 = 1$ and we have to find b_2.

We know that $\vec{E} = \hat{Z} J = \vec{0}$ on the metal, and $J = \sum_n a_n^{\alpha} f_n^{\alpha} = \sum_m b_m \phi_m = b_1 \phi_1 + b_2 \phi_2$.

We chose the trial functions as follows: $\phi_m = \cos\frac{m\pi(x-x_1)}{w}$; and we chose: $\phi_2 = \cos\frac{2\pi(x-x_1)}{w}$ et $\phi_4 = \cos\frac{4\pi(x-x_1)}{w}$, with $x_1 = \frac{a-w}{2}$.

On the metal we have $E = \hat{Z}J = 0 \Rightarrow \hat{Z}\sum_m b_m\phi_m = \sum_m \left\langle \phi_p \hat{Z}\phi_m \right\rangle b_m = 0.$

Now by definition we know:

$$b_2 = -\frac{\sum_n \langle \phi_1, f_n\rangle^\alpha z_n \langle f_n, \phi_1\rangle^\alpha}{\sum_n \langle \phi_1, f_n\rangle^\alpha z_n \langle f_n, \phi_2\rangle^\alpha} = -\frac{\sum_n \langle \phi_2, f_n\rangle^\alpha z_n \langle f_n, \phi_1\rangle^\alpha}{\sum_n \langle \phi_2, f_n\rangle^\alpha z_n \langle f_n, \phi_2\rangle^\alpha}$$

with: $\langle \phi_1, f_n\rangle^\alpha = \int_{\frac{a-w}{2}}^{\frac{a+w}{2}} \int_0^\infty \phi_1(x) f_n^\alpha(x) dxdz.$

Let us know b_2 we can calculate a_n^α:

$a_n^\alpha = b_1 \langle f_n, \phi_1\rangle^\alpha + b_2 \langle f_n, \phi_2\rangle^\alpha.$

$k_0 = \frac{\omega}{c}$: Number of wave in the space the vacuum.

$c = \frac{1}{\sqrt{\mu_0\varepsilon_0}}$: Celerity of the light $(3.10^8\,\mathrm{m/s})$.

a, b: are respectively dimensions along the axis (ox) and (oy).

α: Indicator of mode TE, TM.

k: Medium considered $k \in \{1, 2\}$.

ε_{r_k}: Relative permittivity of the medium k.

ε_0: Permittivity of the vacuum (F/m).

μ_0: Magnetic permeability of the vacuum (H/m).

ω: Angular pulsation equalizes with $2\pi f$ (rd/s).

$\beta = \frac{2\pi}{\lambda_g}$: Constant of propagation.

$Y_{1n}^\alpha, Y_{2n}^\alpha$ Admittance of mode brought back to the level of the interface Ω it depends on the thickness of dielectric "the H" of the medium considered. Its expression according to the modes TE or TM:

$$Y_{1n}^{TE}(\varepsilon_r) = \frac{P_n(\varepsilon_r)}{j\omega\mu_0} \text{ and } Y_{1n}^{TM}(\varepsilon_r) = \frac{j\omega\varepsilon_0\varepsilon}{P_n(\varepsilon_r)}$$

3.2. Calculation of β

Initially one has calculates with the iterative method (F.W.C.I.P) then one compared our results with the analytical formulas and software ADS. In the iterative method we considers:

$$Z_{incc} = jZ_c tg(\beta L)$$

and

$$Z_{inco} = -jZ_c \cot g(\beta L) \Rightarrow Z_c = \sqrt{Z_{incc}Z_{inco}}$$

Then we can calculate $\beta = \frac{1}{L} Arctg\left(-j\frac{Z_{incc}}{Z_c}\right)$.

Finally we can calculate the fields' via-hole $\vec{E}^I_{\text{via-hole}}$ and $\vec{E}^{II}_{\text{via-hole}}$ after that we make normalization as follows:

$$\langle \alpha E, \alpha E\rangle = \alpha^2 \int_0^a \int_0^b |E|^2 dxdy = 1.$$

4. IMPLEMENTATION OF VIA-HOLE FIELD IN THE ITERATIVE METHOD (F.W.C.I.P)

We were interested in this work in via-holes in planar technology who allow a better use of the two faces of the substrate of a printed circuit. To model of such structure the iterative method was reformulated to take into account the presence of this last in the circuit. In this formulation the modes TE, TM and TEM are used as bases numerical field spectral.

Iterative method [1–4] is based on two types of waves; incidental (A_k) and reflected (B_k) expressed respectively in the fields' space and modal by the relations (1) and (2). The passage of these waves from one field to another is ensured by the iterative process using the FMT, which is not other than the FFT balanced on each mode. The use of the FMT reduced the computing time and accelerates the convergence of the method but requires description in pixels of the interface. In any point of this interface a vector of wave associated with the electromagnetic field is defined $\left(\vec{E}, \vec{H}\right)$.

Operational equations which govern the iterative method:

$$\begin{cases} A_k^n = \hat{\Gamma}_\Omega B_k^n + A_k^0 & (1) : \text{Spacefield} \\ B_k^n = \hat{\Gamma}_k A_k^{n-1} & (2) : \text{Spectralfield} \end{cases}$$

where A_k^0 is the incidental wave initializing the iterative process; it is emitted by a source of excitation (level) on both sides of surface Ω. $\hat{\Gamma}_\Omega$ is the operator of diffraction giving the incidental waves starting from the waves reflected in the space field. It describes the boundary conditions and of continuity on the various constituent areas the plan Ω structure. One finds in this parameter the image of the circuit to be analyzed. $\hat{\Gamma}_k$ is the operator of modal reflection giving the waves reflected starting from the incidental waves in the modal field.

To see the influence of the field via-hole in the case we must write the new expression of the coefficient of reflection $\hat{\Gamma}_k$ as follows:

$$\hat{\Gamma}_k = \sum_{n>0,m>0} |f_{mn}^{\alpha}\rangle \frac{1 - Z_{0k} Y_{mn}^{\alpha,k}}{1 + Z_{0k} Y_{mn}^{\alpha,k}} \langle f_{mn}^{\alpha}| + |f_0^{\alpha}\rangle \Gamma_0 \langle f_{mn}^0|$$

with f_0^{α}: present the fundamental field via-hole $E_{\text{via-hole}}^{I,II}$ calculated previously.

Being $\Gamma_0 = \frac{Z_{TEM} - Z_0}{Z_{TEM} + Z_0}$, where $Z_{TEM} = Z_c\left(\frac{w}{L}\right)$, and $Z_0 = \frac{Z_{01} Z_{02}}{Z_{01} + Z_{02}}$.

Z_{0k}: Intrinsic impedance of the medium k, it is given by the following relation: $Z_{0k} = \frac{\eta}{\sqrt{\varepsilon_{r_k}}}$.

w: The thickness of metal.

Z_c: Characteristic impedance.

5. VALIDATION OF THE METHOD

The three-dimensional layouts of Figures 3 and 4 show well that the boundary conditions and of continuity of the current in all the circuit are correctly checked. According to Figure 3, we check well that the current is the maximum on the level of via-hole. Figure 4 shows that the current is minimal at the end of an open line.

6. PRESENTATION OF THE IMPEDANCE OF ZE ENTRY ACCORDING TO THE HEIGHT OF THE LOWER SUBSTRATE

In this paragraph one will present a comparison between the results of Ze according to the height of the lower substrate h_2 of an open line microphone-ribbon and another related to the mass through one via-hole, while keeping same dimensions.

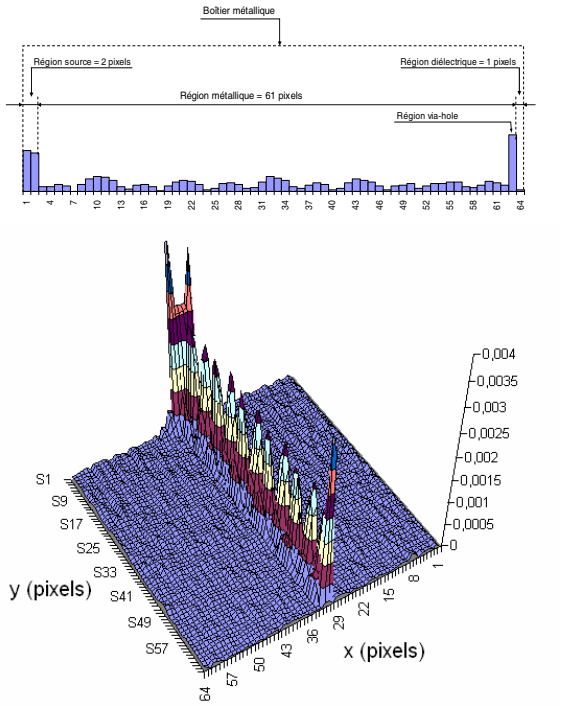

Figure 3: Distribution of the Jy current on the line with via-hole.

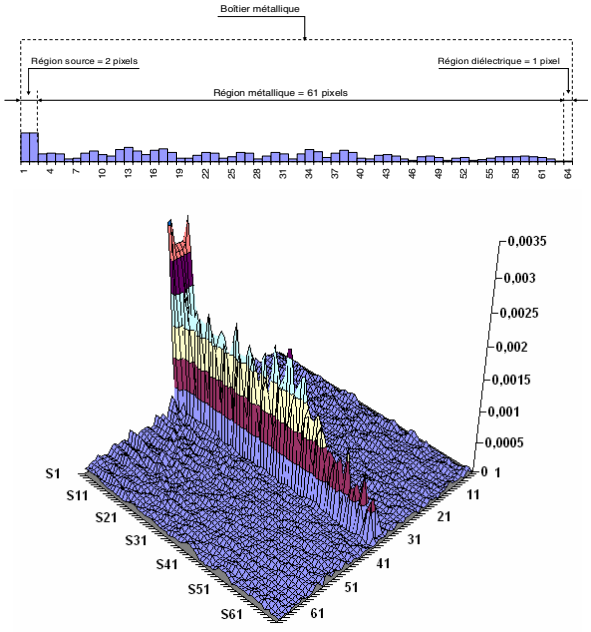

Figure 4: Distribution of the Jy current on the open line without via-hole.

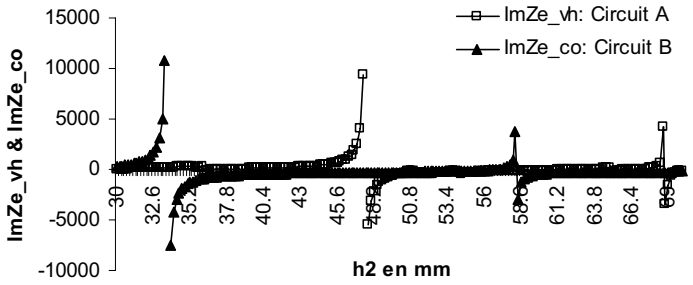

Figure 5: Presentation of Ze according to the height h_2 Circuit A: line shorted-circuit through a via-hole. Circuit B: open line.

7. CONCLUSION

The notice of the Figure 5 a dephasing between the two curves of circuit A and circuit B.

According to these results obtained we can notes that a line micro strip connected to the ground through a via-hole and the localized source of field $S_0\{E_0, J_0\}$ behaves like a line micro ribbon short circuited (Figure 2).

REFERENCES

1. Baudrand, H. and R. S. N'gongo, "Applications of wave concept iterative procedure," *Microwave Theory & Tech.*, Vol. 1, 187–197, 1999.
2. N'gongo, R. S. and H. Baudrand, "Modélisation des circuits actifs planaires de forme arbitraire par une méthode itérative," *JT'99, Journées sur les Télécommunications*, Gammarth, Tunis, Janvier 29–31, 1999.
3. N'gongo, R. S. and H. Baudrand, "A new approach for microstrip active antennas using modal F.F.T algorithm," *IEEE AP-S International Symposium Ind. USNC/URSI National Radio Science Meeting*, Orlando, USA, July 11–16, 1999.
4. N'Gongo, S. R., "Modelisation electromagnetique des circuits planaires. Application a l'influence du boitier," These de doctorat, I.N. Polytechnique de Toulouse, 1999.

Fine Synchronization with UWB TH-PAM Signals in Ad-Hoc Multi-user Environments

M. Hizem and R. Bouallegue
6'Tel Research Unit, Higher School of Communications of Tunis, Sup'Com, Tunisia

Abstract— To synchronize Ultra-Wideband (UWB) signals with pulse amplitude modulation (PAM) and time hopping (TH) spreading in ad-hoc multi-user environments, we propose in this paper to develop and test a novel fine synchronization algorithm in both data-aided (DA) and non-data-aided (NDA) modes. The proposed synchronization scheme is decomposed into two successive floors or steps. The first floor consists on a coarse synchronization which is based on timing with dirty templates (TDT) acquisition scheme. In the second floor, we consider a new fine algorithm which provides an ameliorated estimate of timing offset. Simulation results and comparisons are also presented to confirm our theoretical analysis and performance improvement (in terms of mean square error) compared to the original TDT algorithm in multi-user environments.

1. INTRODUCTION

Currently, the most important discussion subject in UWB ad-hoc impulse radios is how to obtain the best possible synchronization and more specifically an efficient timing offset estimation. The synchronization complexity is accentuated in UWB systems compared to others due to the fact that waveforms are impulse-like and have low amplitude. Furthermore, the difficulty of timing UWB signals is provoked by the dense multipath channel unknown at the synchronization step. These reasons explain why synchronization has taken so much importance in UWB literature (see e.g., [1–7]). An algorithm has grown substantially in recent years is timing with dirty templates (TDT) introduced in [8] and developed for UWB signals.

In this paper, we develop a novel fine synchronization algorithm for UWB TH-PAM signals. To ameliorate the synchronization performance, our contribution is to realize a fine synchronization floor and insert it after the coarse one (which is TDT). The principle is to make a fine search for the exact moment of pulse beginning (timing offset) by correlating two consecutive symbol-long segments of the received waveform in an interval that corresponds to the frames number included in one data symbol. Simulations and comparisons show that our synchronizer improves the corresponding system performance in terms of mean square error (MSE) compared to the original TDT.

The rest of this paper is organized as follows. Section 2 describes the UWB TH-PAM system in multi-user environments. Section 3 outlines first the TDT algorithm and upper bounds on the mean square error are derived in both non-data-aided (NDA) and data-aided (DA) modes. Then, we presented our novel fine synchronization. In Section 4, simulation results are carried out to corroborate our analysis. Conclusions are given in Section 5.

2. SYSTEM MODEL FOR MULTI-USER LINKS

The UWB time hopping impulse radio signal considered in this paper is a stream of narrow pulses, which are shifted in amplitude modulated (PAM). The same modulated pulse is repeated N_f times (frames number) over a T_s period (symbol time). During each duration frame T_f, a data-modulated ultra-short pulse $p(t)$, with duration $T_p \ll T_f$, is transmitted. The transmitted waveform from the uth user is:

$$v_u(t) = \sqrt{\varepsilon_u} \sum_{k=0}^{+\infty} s_u(k) p_{u,T}(t - kT_s) \tag{1}$$

where ε_u represents the energy per pulse, $s_u(k)$ are differentially encoded symbols and drawn equiprobably from finite alphabet. In our case, $s_u(k)$ symbolize the binary PAM information symbols and $p_{u,T}(t)$ indicates the transmitted symbol:

$$p_{u,T}(t) := \sum_{i=0}^{N_f-1} p(t - iT_f - c_u(i)T_c) \tag{2}$$

where T_c is the chip duration and $c_u(i)$ is the user-specific pseudo-random TH code during the ith frame.

The transmitted signal propagates through the multipath channel corresponding to each user. The UWB channel is modeled as tapped-delay line with L_u taps, where $\{\alpha_{u,l}\}_{l=0}^{L_u-1}$ and $\{\tau_{u,l}\}_{l=0}^{L_u-1}$ is amplitude and delay of the L multipath elements, respectively. The channel is assumed quasi-static and among $\{\tau_{u,l}\}_{l=0}^{L_u-1}$, τ_0 represents the propagation delay of the channel. Thus, the received waveform from all users is:

$$r(t) = \sum_{u=0}^{N_u-1} \sqrt{\varepsilon_u} \sum_{l=0}^{L_u-1} \alpha_{u,l} v_u(t - \tau_{u,l} - \tau_u) + \eta(t) \tag{3}$$

where N_u is the users number, τ_u is the propagation delay of the uth user's direct path and $\eta(t)$ is the zero-mean additive Gaussian noise (AGN). The global received symbol-long waveform is therefore given by:

$$p_{u,R}(t) := \sum_{l=0}^{L_u-1} \alpha_{u,l} p_{u,T}(t - \tau_{u,l}) \tag{4}$$

Assuming that the nonzero support of waveform $p_{u,R}(t)$ is upper bounded by the symbol time T_s, the received waveform in (3) can be rewritten as:

$$r(t) = \sum_{u=0}^{N_u-1} \sqrt{\varepsilon_u} \sum_{k=0}^{+\infty} s_u(k) p_{u,R}(t - kT_s - \tau_u) + \eta(t) \tag{5}$$

In the next step, we will develop a low-complexity fine synchronization algorithm using original TDT approach and system model described in this section, in order to find the desired timing offset. It will be evaluated in both non-data-aided (NDA) and data-aided (DA) modes.

3. FINE SYNCHRONIZATION ALGORITHM FOR MULTI-USER UWB TH-PAM IMPULSE RADIOS

As cited previously, our proposed synchronization scheme consists of two complementary floors. The first is based on coarse synchronization approach that is TDT developed in [8]. The second consists of a novel fine synchronization algorithm which more improves the timing offset found in the first floor. We will first outline the TDT approach for multi-user UWB TH-PAM impulse radios to better understand the whole synchronization scheme suggested in this paper.

3.1. Multi-user TDT for UWB TH-PAM Impulse Radios

The basic idea behind TDT is to find the maximum of square correlation between pairs of successive symbol-long segments. The description of our system model with first stage synchronization (TDT) is given in Fig. 1. First, we analyze $\tilde{\tau}_0$ representing the estimate offset of τ_0 with deriving upper bounds on their mean square error (MSE) in both NDA and DA modes.

For multi-user UWB TH-PAM systems, a correlation between the two adjacent symbol-long segments $r(t - kT_s)$ and $r(t - (k-1)T_s)$ is achieved. Let $x(k;\tau)$ the value of this correlation $\forall k \in [1, +\infty)$ and $\tau \in [0, +T_s)$,

$$x(k;\tau) = \sum_{u=0}^{N_u-1} \int_0^{T_s} r(t - kT_s) r(t - (k-1)T_s) dt \tag{6}$$

Applying the Cauchy-Schwartz inequality and substituting the expressions of $r(t - kT_s)$ and $r(t - (k-1)T_s)$ to (6), $x(k;\tau)$ becomes:

$$x(k;\tau) = \sum_{u=0}^{N_u-1} s_u(k-1)[s_u(k-2)\varepsilon_{u,A}(\tilde{\tau}_u) + s_u(k)\varepsilon_{u,B}(\tilde{\tau}_u)] + \xi(k;\tau) \tag{7}$$

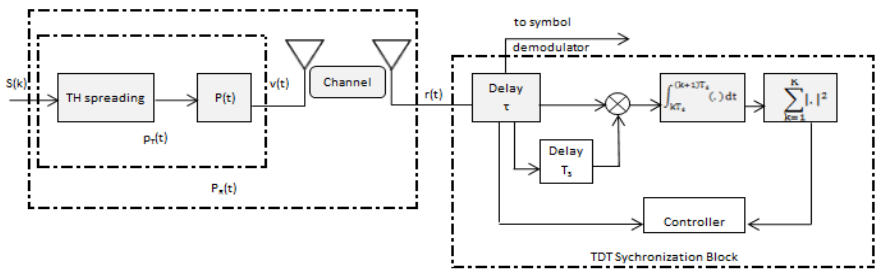

Figure 1: Description of our model with first stage synchronization.

where $\varepsilon_{u,A}(\tilde{\tau}_u) := \varepsilon_u \int_{T_s-\tilde{\tau}_u}^{T_s} p_{u,R}^2(t)dt$, $\varepsilon_{u,B}(\tilde{\tau}_u) := \varepsilon_u \int_0^{T_s-\tilde{\tau}_u} p_{u,R}^2(t)dt$, $\tilde{\tau}_u := [\tau_u - \tau]_{T_s}$ and $\zeta(k;\tau)$ corresponds to the superposition of three noise terms [8] and can be approximated as an additive white Gaussian noise (AWGN) with zero mean and $\sum_\xi$ power. As mentioned in [8], the noise-free part of the desired user's samples at the correlator output complies with

$$\chi_0(k;\tau) = \varepsilon_{0,A}(\tilde{\tau}_0) - \varepsilon_{0,B}(\tilde{\tau}_0) \tag{8}$$

Substituting the above equation into (7), we find:

$$x(k;\tau) = \chi_0(k;\,\tau) + \sum\nolimits_{u\neq 0} s_u(k-1)[s_u(k)\varepsilon_{u,B}(\tilde{\tau}_u) + s_u(k-2)\varepsilon_{u,A}(\tilde{\tau}_u)] + \xi(K;\,\tau) \tag{9}$$

where $s_u(k)$'s are zero-mean information symbols emitted by the $(u \neq 0)$th user. If we calculate the average (without squaring), we obtain $E\{x(k;\tau)\} = \varepsilon_{0,B}(\tilde{\tau}_0) - \varepsilon_{0,A}(\tilde{\tau}_0)$ since $E\{\chi_u(k;\tau)\} = 0$ [8]. In the practice, the mean square of $x^2(k;\tau)$ is estimated from the average of different values $x^2(k;\tau)$ for k ranging from 0 to $M-1$ obtained during an observation interval MT_s. In what follows, we summarize the TDT algorithm for multi-user UWB TH-PAM impulse radios in its NDA form and then in its DA form.

Non-Data-Aided Mode:

For the NDA synchronization mode, the timing algorithm is defined as follows:

$$\begin{aligned} \hat{\tau}_{u,\,\mathrm{nda}} &= \arg\max\nolimits_{\tau\in[0,\,T_s]} E\{x^2(k;\,\tau)\} \\ x_{\mathrm{nda}}(M;\,\tau_u) &= \frac{1}{M}\sum\nolimits_{m=0}^{M-1}\left(x(k;\,\tau)\right)^2 \end{aligned} \tag{10}$$

The estimator can be verified to be m.s.s consistent by deriving the mean and variance of $x_{\mathrm{nda}}(M;\tau_u)$. It has been demonstrated that the single-user TDT estimator is operational even in a multi-user environment [8].

Data-Aided Mode:

The samples number M necessary for trustworthy estimation can be clearly reduced if a DA approach is pursued. The delays can be considerably reduced with using training sequences with alternating sign between the symbols $s(m-2)$ and $s(m)$. This observation propose that the training sequences $\{s(k)\}$ for DA TDT mode follow the following alternation $[1, 1, -1, -1]$; i.e.,:

$$s(k) = (-1)^{\lfloor \frac{k}{2} \rfloor} \tag{11}$$

This pattern is particularly attractive, since it simplifies the proposed algorithm to become in the DA mode:

$$\begin{aligned} \hat{\tau}_{0,\,\mathrm{da}} &= \arg\max\nolimits_{\tau\in[0,\,T_s]}\{x_{\mathrm{da}}(M;\tau)\} \\ x_{\mathrm{da}}(M;\tau) &= \left(\int_0^{T_s} r(t+\tau)r(t+\tau+kT_s)dt\right)^2 \end{aligned} \tag{12}$$

with $E\{(-1)^{\lfloor \frac{k}{2} \rfloor} r(t+\tau+kT_s)\} = \sqrt{\varepsilon}[p_{0,R}(t+T_s-\tilde{\tau}_0) + (-1)^k p_{0,R}(t-\tilde{\tau}_0)]$ which signifies that the single-user TDT estimator can also be functional in a multi-user scenario.

3.2. Fine Synchronization Algorithm Proposed

In this part, we present the second floor or step of our synchronization approach in multi-user UWB TH-PAM systems. This second floor realizes a fine estimation of the frame beginning, after a coarse research in the first (TDT approach). The concept which is based this floor is really straightforward. The idea is to scan the interval $[\tau_1 - T_{\mathrm{corr}},\, \tau_1 + T_{\mathrm{corr}}]$ with a step noted δ by making integration between the received signal and its replica shifted by T_f on a window of width T_{corr}. τ_1 being the estimate delay removed after the first synchronization floor. We can write the integration window output for the nth step $n\delta$ as follows:

$$Z_n = \sum\nolimits_{k=0}^{K-1}\left|\int_{\tau_1+n\delta}^{\tau_1+n\delta+T_s} r(t-kT_s)r(t-(k+1)T_s)dt\right| \tag{13}$$

where $n = -N+1, \ldots, 0, \ldots, N-1$, $N = \lfloor T_{\mathrm{corr}}/\delta \rfloor$ and K is number of frames considered for improving the decision taken at the first floor. The value of n which maximizes Z_n provides the exact moment of pulse beginning that we note $\tau_2 = \tau_1 + n_{\mathrm{opt}}\delta$. Therefore, the fine synchronization is performed.

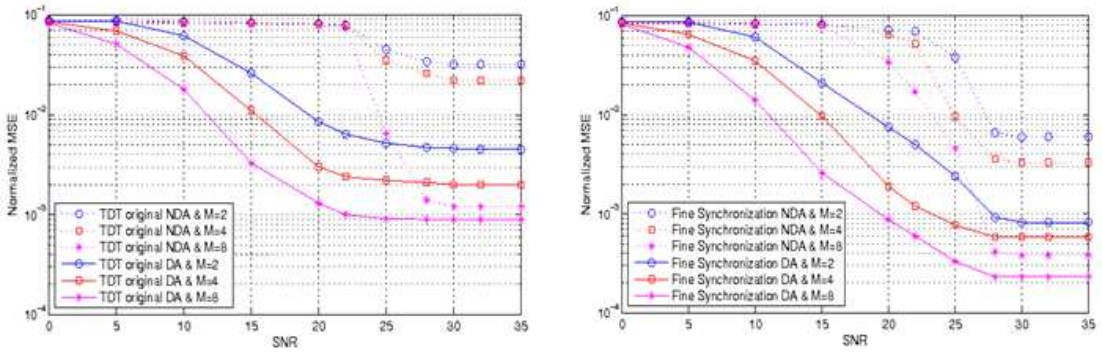

Figure 2: Normalized MSE of multi-user original TDT synchronizer and our multi-user fine synchronization.

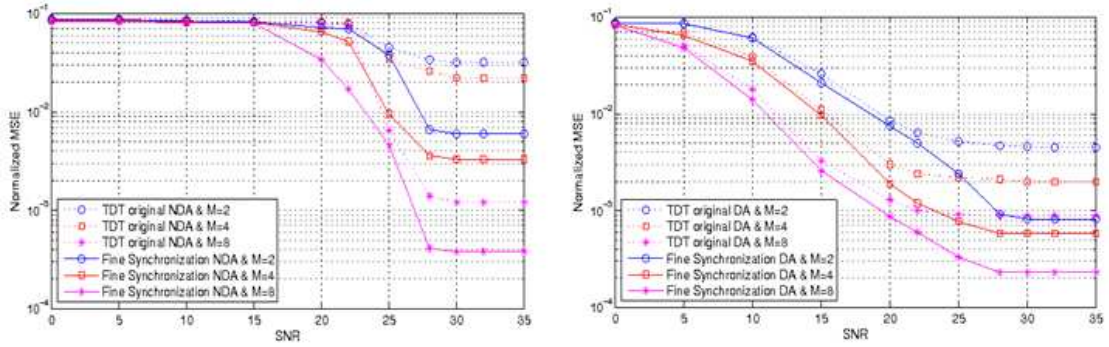

Figure 3: Performances comparison in NDA and DA modes with multi-user environments.

4. SIMULATION RESULTS

In this section, we will evaluate the performance of our proposed fine synchronization approach for UWB TH-PAM signals in ad-hoc multi-user environments. The UWB pulse is the second derivative of the Gaussian function with unit energy and duration $T_p \approx 0.8\,\text{ns}$. The sampling frequency chosen in the simulations is $f_c = 50\,\text{GHz}$. The width integration window value's T_{corr} is 4 ns. The performance is tested for various values of M.

In Fig. 2 on left, we first test the mean square error (MSE) corresponding to (10) and (12). From the simulation results, we note that increasing the duration of the observation interval M leads to improved performance for both NDA and DA modes. We also note that the use of training sequences (DA mode) leads to improved performance compared to the NDA mode. In Fig. 2 on right, we compare the new fine synchronization approach performances in both NDA and DA modes. In Fig. 3, we compare the performances of both original TDT and fine synchronization approach for different values of M. In comparison with the original TDT approach, we note that the new approach greatly outperforms the NDA mode and offers a slight improvement in DA mode. This performance improvement is enabled at the price of fine synchronization approach introduced in second floor which can further improve the timing offset found in first floor.

5. CONCLUSIONS

In this paper, we propose a novel fine synchronization scheme using TDT algorithm for UWB radio system in multi-user links. With the introduced fine synchronization algorithm, we can achieve a fine estimation of the frame beginning. The simulation results show that even without training symbols, our new synchronizer can enable a better performance than the original TDT in NDA mode and offers a slight improvement in DA mode.

REFERENCES

1. Homier, E. A. and R. A. Scholtz, "Rapid acquisition for ultra-wideband signals in the dense multipath channel," *Proceedings of Conference UWB System Technologies*, 105–110, Baltimore, MD, May 2002.
2. Tian, Z. and G. B. Giannakis, "Data-aided ML timing acquisition in ultra-wideband radios," *Proceedings of Conference UWB System Technologies*, 245–250, Reston, VA, November 2003.

3. Yang, L., Z. Tian, and G. B. Giannakis, "Non-data aided timing acquisition of ultra-wideband transmissions using cyclostationarity," *Proceedings of International Conference Acoustic, Speech, Signal Processing,* 121–124, China, April 2003.
4. Aedudodla, S., S. Vijayakumaran, and T. F. Wong, "Ultra-wideband signal acquisition with hybrid DS-TH spreading," *IEEE Transactions on Wireless Communications*, Vol. 5, No. 9, 2504–2515, 2006.
5. Dang, Q. H., A. Trindade, and A. J. Van der Veen, "Signal model and receiver algorithms for a transmit-reference ultra-wideband communication system," *IEEE Journal Select. Areas Commun.*, Vol. 24, No. 4, 773–779, 2006.
6. Luo, X. and G. B. Giannakis, "Low-complexity blind synchronization and demodulation for ultra-wideband multi-user ad hoc access," *IEEE Transactions on Wireless Communications*, Vol. 5, No. 7, 1930–1941, 2006.
7. Ying, Y., M. Ghogho, and A. Swami, "Code-assisted synchronization for UWB-IR systems: Algorithms and analysis," *IEEE Transactions on Signal Processing*, Vol. 56, No. 10, 5169–5180, 2008.
8. Yang, L. and G. B. Giannakis, "Timing UWB signals using dirty templates," *IEEE Transactions on Communications*, Vol. 53, No. 11, 1952–1963, 2005.

Performance Parameter of Hybrid Wireless-optical Broadband-access Network (WOBAN): A Study on the Physical Layer of Optical Backhaul and Wireless Front-end

Redhwan Q. Shaddad, Abu Bakar Mohammad, and Abdulaziz M. Al-Hetar

Photonic Technology Center, InfoComm Research Alliance
Universiti Teknologi Malaysia, Johor 81310, Malaysia

Abstract— The hybrid wireless-optical broadband-access network (WOBAN) is a promising broadband access network. It provides blanket coverage of broadband and flexible connection for wireless end-users. In this paper, the architecture of the WOBAN is proposed and designed based on both a wavelengths division multiplexing/time division multiplexing passive optical network (WDM/TDM PON) at the optical backhaul and wireless fidelity/worldwide interoperability for microwave access (WiFi/WiMAX) technologies at the wireless front-end. The power budget of the optical backhaul based on maximum split ratio of 1/32 for each wavelength channel and a fiber length of 23 km from the central office (CO) to the access point (AP) is analyzed with bit error rate (BER) of 10^{-9}. Most of the existing works, based on performance evaluation are concerned on network layer aspects. We report the performance analysis in terms of BER, eye diagram, error vector magnitude (EVM), and signal-to-noise ratio (SNR) of the WOBAN physical layer. It is demonstrated 2 Gb/s for downstream/upstream can be achieved at optical backhaul for each wavelength channel, at data rates of 54 Mb/s (WiFi) and 30 Mb/s (WiMAX) per AP along a 50 m and 5 km wireless links respectively.

1. INTRODUCTION

The main purpose of the communication networks generally is to provide access to information when we need it, where we need it, and in whatever format we need it in. Optical and wireless access networks have arised to provide these requirments for different applications, appropriate in access applications today. These access networks are two promising broadband access technologies for high-capacity access networks and provide different levels of bandwidth, which shows a good match in capacity scales [3–6].

Bandwidth demand in access networks continues to grow rapidly due to the increasing number of technology-smart users. A WOBAN is an optimal combination of an optical backhaul and a wireless front-end for an efficient access network [1, 5]. In this paper, the optical backhaul of the WOBAN is implemented by using a cost-effective WDM/TDM PON. WDM/TDM PON has been considered as a promising option due to its large throughput [7], and it provides great scalability because it can support different wavelengths over the same fiber infrastructure [1]. It supports data rate up to 2 Gb/s symmetrical operation. The wireless front-end is implemented by using WiFi or WiMAX technique [7]. WiFi technologies are widely exploited in commercial products due to their low cost, high data rate, and easy deployment in wireless local area networks (WLANs) [6, 7]. WiFi supports data rate up to 54 Mb/s along a 50 m wireless link. WiMAX provides point-to-multipoint wireless connections with a transmission rate of 70 Mb/s and can be used for longer distances [6]. So WiMAX is particularly suitable for wireless metropolitan-area networks (WMANs) [1]. Most of the existing works, based on performance evaluation are concerned on network layer aspects. We report the performance analysis in terms of BER, eye diagram, EVM, and SNR of the WOBAN physical layer.

2. PROPOSED ACCESS NETWORK ARCHITECTURE

The proposed WOBAN architecture is shown in Figure 1. At the backhaul of the network, optical line terminal (OLT) is built in the CO and connected by an optical fiber. Then, a remote node (RN) distributes the data to manifold optical network units (ONUs). In the front-end, a set of wireless routers forms a wireless mesh network (WMN). Mobile and stationery end users are connected to the network through these nodes, whose locations are fixed in the WMN. A selected set of these routers (gateways) are connected to the optical backhaul. Usually, each gateway is attached with one ONU [3]. As shown in Figure 1, the wireless mesh routers automatically establish and maintain the connectivity as indicated by the dashed line, and the gateway router has a connection to the

Internet via the optical backhaul. The upstream traffic from the end user is collected by the nearby mesh router. If the gateway router Gx is the destination gateway, the packets are relayed to this gateway router on one of the available paths, such as, the path P1 or P2.

The downstream optical signals are created by the OLT and propagated along the optical fiber to the integrated ONU/AP gateway. The ONU/AP gateway in the WOBAN converts the downstream optical signals received from the RN into downlink wireless signals that will be sent to the WMN. At the upstream direction, the uplink wireless signals are received by the ONU/AP and converted to the upstream optical signals that will be sent to the CO. The OptiSystem 8.0 and Advanced Design System (ADS) 2008 software tools are used to accomplish design and simulate the performance of the WOBAN.

3. SIMULATION DESIGN

WOBAN design comprises of multiple users connected to a CO represented by an OLT connected to multiple ONUs through 23 km of single mode fiber (SMF). The wavelength assignment and bandwidth allocation is done at the CO. Each ONU is integrated with an AP. The WOBAN is designed to operate at 2 Gb/s symmetrical for each wavelength at BER of 10^{-9}. The wireless access used is the WiFi or WiMAX technology with a data rate of 54 Mb/s or 30 Mb/s respectively.

The optical backhaul is accomplished by using WDM/TDM PON as shown in Figure 2. The OLT assigns $N = 4$ wavelengths to transmit the downstream which propagates along 23 km SMF with attenuation 0.2 dB/km. The downstream is demultiplexed according to their wavelengths by the arrayed-waveguide-grating (AWG) router. Then it splits at passive splitter/combiner (PS/C) to M optical signals. The upstream data is transmitted in the reverse way from each ONU to OLT. Figure 3 shows the allocated wavelengths of the downlink/uplink channels which are selected from conventional band (CB) with 200 GHz channel spacing for each link. Also the uplink channels are separated by 100 GHz downlink channels. This optical backhaul provides 2 Gb/s downstream/upstream for each wavelength channel. The wireless gateway AP is considered as the main part, which is integrated with ONU. The carrier frequency is set to 5.2 GHz and 2.35 GHz for each WiFi and WiMAX transceivers respectively. The orthogonal frequency division multiplexing (OFDM) technique is used in these transceivers. Each of the OFDM based IEEE 802.11a

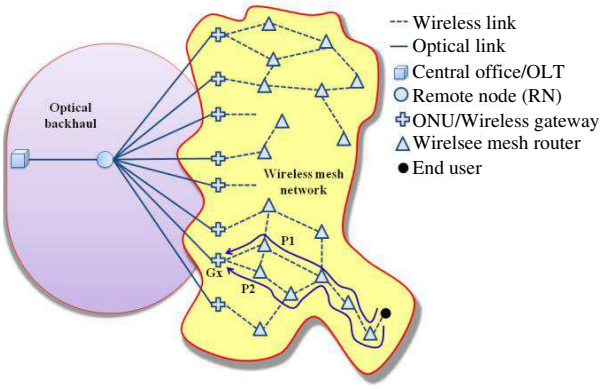

Figure 1: WOBAN architecture.

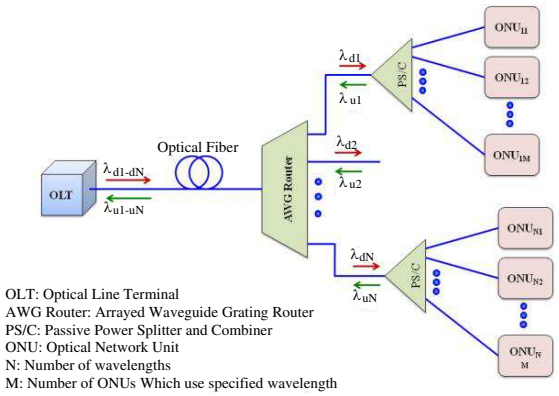

Figure 2: Optical backhaul design.

Table 1: General specifications of wireless front-ends.

	WiMAX	WiFi
Transmitter Power	−10 dBm	−16 dBm
Carrier frequency	2.35 GHz	5.2 GHz
Channel bandwidth	10 MHz	20 MHz
Data rate	30–70 Mb/s	54 Mb/s
Link Range	5 km	50 m
Radio technology	OFDM (256-Channels)	OFDM (64-Channels)
Modulation	BPSK, 64-QAM, 256-QAM	BPSK, 64-QAM

(WiFi) or IEEE 802.16a (WiMAX) transceiver in AP consists of two main parts: WLAN digital signal processing (DSP) subsystem and radio frequency (RF) modulator/demodulator. The general specifications of the wireless front-ends are summarized in Table 1.

4. SCALABILITY ANALYSIS

In this section, the scalability of the optical backhaul in term of the number of supported AP is analyzed. The number of ONU/APs is limited by the power budget of the link and available wavelengths. According to the general specifications of optical elements as listed in Table 2, the approximated number of ONU/APs can be calculated.

The power budget for the downlink/uplink can be stated as [2]:

$$P_T - 2 \times I_{AWG} - \alpha \times L - I_{SA} - 10\log(S) \geq R_{sen} \tag{1}$$

where P_T is the transmission power, R_{sen} is the receiver sensitivity, I_{AWG} is the insertion loss of AWG router, L is the fiber length, α is the fiber attenuation, I_{SA} is the loss of splicing and aging in the link, and S is the splitter ratio of the PS/C for each wavelength channel. According to Eq. (1), the maximal splitter ratio of the PS/C is then limited by:

$$10\log_{10}(S) \leq 15.4 \rightarrow S \leq 34 \tag{2}$$

Therefore the maximum number of supported APs is 32 for each wavelength up/downlink.

5. RESULTS AND DISCUSSION

BER performance is carried out at both ONU and OLT receivers for the downlink/uplink wavelengths using bi-directional transmissions. Figure 4 shows the BER performance in the downstream/u-

Table 2: General specifications of optical elements.

Symbol	Description	Value	Unit
P_T	Transmission power	0	dBm
R_{sen}	Receiver sensitivity	−30	dBm
I_{AWG}	Insertion loss: AWG	4	dB
N	Port size of AWG	4–16	none
α	Attenuation	0.2	dB/km
L	Fiber length	23	km
I_{SA}	Splicing and aging loss on the link	2	dB
S	Splitter ratio of PS/C	4–32	none

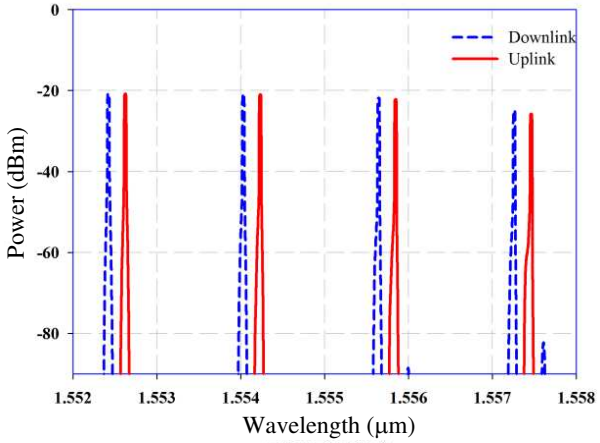

Figure 3: Allocated wavelengths of the down/uplinks channels for the optical backhaul.

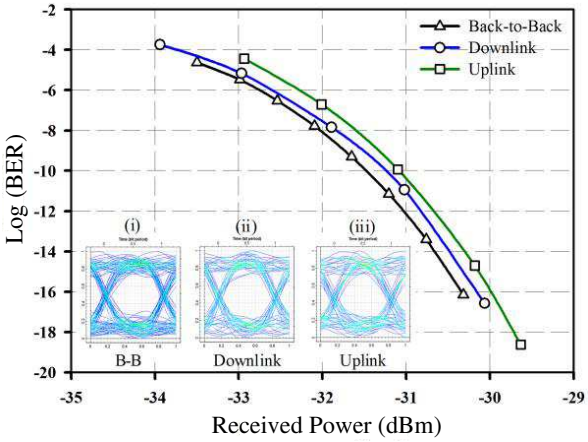

Figure 4: BER performance of the downlink/uplink in the optical backhaul.

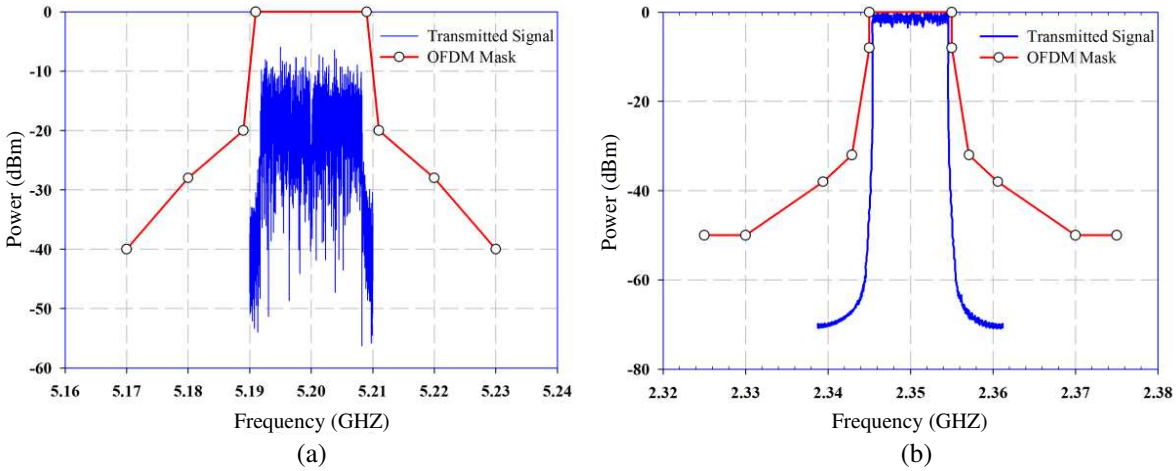

Figure 5: The spectrum of the transmitted RF power signal from (a) WiFi AP, (b) WiMAX AP.

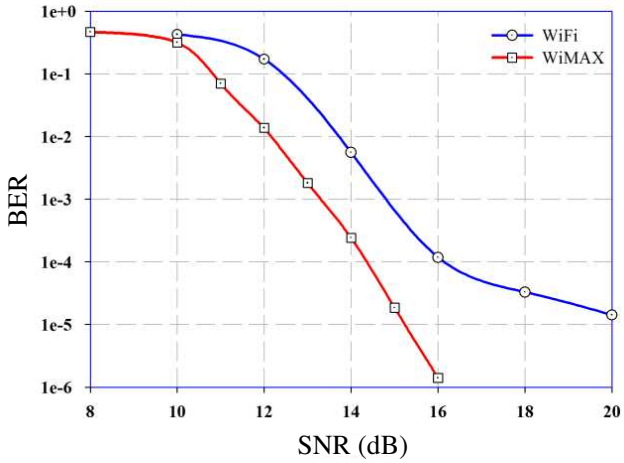

Figure 6: BER versus SNR at the wireless AP receiver.

pstream direction for the downlink/uplink channels versus the received optical power at receiver side of ONU and OLT respectively. The power penalty at a BER of 10^{-9} is only ≈ 0.4 dB after the transmission over a 23 km SMF. The eye diagrams at the back-to-back transmission, downlink transmission, and uplink transmission are also shown in Figure 4 as insets (i), (ii) and (iii), respectively. The eye diagrams of the received electrical signal at ONU and OLT show slight differences and good quality system for downlink and uplink respectively.

There are two types of APs, WiFi APs and WiMAX APs. In the AP transceiver, signaling bits are modulated in one OFDM symbol by using phase shift keying (PSK) technique. On the other hand, the data is modulated in many OFDM symbols by using 64 QAM technique with average transmitter power is 16 dBm and 10 dBm at use WiFi and WiMAX recepectively. Figures. 5(a) and (b) show the spectrums of the RF transmitted power signal in case WiFi AP and WiMAX AP respectively. The WiFi carrier frequency 5.2 GHz with bandwidth of 20 MHz is investigated. In addtion, the WiMAX carrier frequency 2.35 GHz with bandwidth of 10 MHz is investigated. Figures. 5(a) and (b) show the transmit spectrum mask for each used technique. Typically, the spectrum mask is defined by the reference level power which gives the maximal allowed out-of-band radiation power at a given frequency [9].

Figure 6 shows the BER versus signal to noise ratio SNR for the received signal at AP; since the effect of phase noise and frequency offset are considered at the simulation of AP. The better performance occurs when the SNR is greater than 18 dB and 15 dB in the WiFi and WiMAX AP receiver respectively; at a BER less than 10^{-5}. For 64 QAM modulated OFDM in the WiFi and WiMAX AP receiver, maximum EVM of -32 dB and -31 dB have been estimated respectively. This EVM performance allows perfect symbol detection at the receivers.

6. CONCLUSIONS

In this paper, architecture of WOBAN was proposed and designed as a suitable technique for future access networks. The scalability of the optical backhaul in term of the number of supported AP is analyzed. In conclusion, the proposed WOBAN achieved the data rate of 2 Gb/s for downstream/upstream over 23 km fiber length followed by 50 m and 5 km wireless link with a data rate of 54 Mb/s and 30 Mb/s respectively.

ACKNOWLEDGMENT

The authors would like to thank the Ministry of Science, Technology and Innovation (MOSTI), Malaysia for sponsoring this work under project vote number 73720.

REFERENCES

1. Sarkar, S., S. Dixit, and B. Mukherjee, "Hybrid wireless optical broadband access network (WOBAN): A review of relevant challenges," *J. Lightwave Technol.*, Vol. 25, 3329–3340, 2007.
2. Chen, T., H. Woesner, Y. Ye, and I. Chlamtac, "WiGEE: A hybrid optical/wireless gigabit WLAN," *Proceeding of IEEE Global Telecommunications Conference*, 321–326, 2007.
3. Shaw, W., S. Wong, N. Cheng, K. Balas, X. Zhu, M. Maier, and L. Kazovsky, "Hybrid architecture and integrated routing in a scalable optical-wireless access network," *J. Lightwave Technol.*, Vol. 25, 3443–3451, 2007.
4. Lim, C., A. Nirmalathas, M. Bakaul, P. Gamage, K. Lee, Y. Yang, D. Novak, and R. Waterhouse, "Fiber-wireless networks and subsystem technologies," *J. Lightwave Technol.*, Vol. 28, 390–405, 2010.
5. Reaz, V. R., S. Sarkar, D. Ghosal, and B. Mukherjee, "Hybrid wireless-optical broadband access network (WOBAN): Capacity enhancement for wireless access," *Proceeding IEEE Global Telecommunication Conference*, 2008.
6. Ghazisaidi, N., M. Maier, and C. Assi, "Fiber-wireless (FiWi) access networks: A survey," *IEEE Commun. Mag.*, Vol. 24, 160–167, 2009.
7. Guan, X., "Dual-band CMOS WLAN transceiver RF front-end design," Ph.D. dissertation, Illinois Institute of Technology, USA, 2007.
8. Pan, Z., C. Yu, and A. Willner, "Optical performance monitoring for the next generation optical communication networks," *Opt. Fiber Technol.*, Vol. 16, 20–45, 2010.
9. Schulze, H. and C. Lders, *Theory and Applications of OFDM and CDMA: Wideband Wireless Communications*, John Wiley and Sons, 2005.

Properties of Spread-F in High and Low Latitude Ionospheres

J. K. Shi[1], **W. Tao**[1], **G. J. Wang**[1], **G. Zherebotsov**[2], **O. Pirog**[2], **and A. Stepanov**[3]

[1]State Key Laboratory for Space Weather, CSSAR/CAS, Beijing, China
[2]Institute of Solar-Terrestrial Physics, RAS, Irkutsk, Russia
[3]Institute of Cosmophysical Research and Aeronomy, RAS, Yakutsk, Russia

Abstract— The ionospheric spread-F has many significant effects on radio waves that propagation through the Earth's atmosphere, such as refraction, reflection, absorption, time delay, phase change, amplitude change, Doppler shifts, and so on. In this paper, we used the data from DPS-4 Digisondes at low latitude station Hainan (19.4°N, 109.0°E), China, and high altitude stations Yakutsk (62°N, 129°E) and Zhigansk (66°N, 123°E), Russia to study the ionospheric Spread-F (SF) properties during geo-magnetic storm time. Some new results are obtained by data analysis. In Hainan and Yakutsk, SF was observed only in night time, but in Zhigansk it was also observed in day time. The SF seems more activity over Yakutsk. The SSF concerned with equatorial plasma bubble is only observed at low latitude station Hainan and the branch SF is only observed at high latitude stations Yakutsk and Zhigansk. For most cases start time of SF is later if the station latitude is lower. This implies that plasma instability caused ionospheric irregularity is propagation from high latitude to low latitude ionosphere.

1. INTRODUCTION

The spreading of ionogram trace from its usual form was related very early to existence of irregularity structure, termed as Spread F (SF) irregularities [1]. The characteristics and physical mechanism of SF have been important aspects in ionospheric studies. These irregularities are perturbations in the F region and have many significant effects on radio waves that propagation through the Earth's atmosphere, such as refraction, reflection, absorption, time delay, phase change, amplitude change, Doppler shifts, and so on. As we know, the radio communication with satellites, positioning/navigation, and spacecraft telemetry and control are now so sensitive to ionospheric variation which could seriously affect or disrupt the system performance due to the effects of ionosphere on radio signals. Therefore, the research on characteristics of SF has important significance for science, also for application research.

The morphology of SF in low latitude ionospheric region has been studied by many authors and some characteristics of SF have been obtained, such as its seasonal and longitudinal variations of occurrence, effects of solar activity, seasonal meridian winds and magnetic field declination, and so on [2–5]. The research on SF behaviors in the storm times in low latitude region also has been experienced for half century, and some results have been obtained [6–8].

The characters of the high-latitude SF are more complex as magnetic field-lines connect the high latitudes to the outer part of the magnetosphere: SF often occurs during day and night in the area near to magnetic pole during the winter; and its occurrence remains high in the night while it falls to $50 \sim 60$ percentage in the noon during the summer [9]. Solar activity also has important effects on the behavior of the high latitude SF [10].

However, so far, no report on comparison study of SF between the high and the low latitude ionospheres was found. In this paper, we used the data from DPS-4 digisondes located at low latitude and high latitude region to study the ionospheric Spread-F properties during the storm time. The results show that propagation of the plasma instability caused SF is from high latitude ionosphere to the low latitude.

2. DATA AND ANALYSIS METHOD

We use the ionograms derived from DPS-4 digisondes at Hainan, Yakutsk, and Zhigansk to determine SF which can be divided into four types based on their tracing characteristics. They are Frequency Spread-F (FSF), Range Spread-F (RSF), Mixed Spread-F (MSF) and Branch Spread-F (BSF) [11]. Also, according to the observation at Hainan station, from the RSF we draw a so called Strong range Spread-F (SSF) which is indicative of equatorial plasma bubble as an independent type of SF to do research. The SSF is identified by two criteria, i.e., it extends beyond the critical frequency of F2 layer and makes the foF2 couldn't be defined, and its duration is more than 1 hour [12–15].

In the present work, we analyzed the SF characteristics in three different latitude stations during the six magnetic storm times in 2006, and did a comparing study on the features of SF between the high and the low latitude stations. The period and the Dst index for the six storms are: (1) March 6 to 8, Dst = −40 nT; (2) April 4 to 6, Dst = −87 nT; (3) April 9 to 11, Dst = −80 nT; (4) April 14 to 16, Dst = −111 nT; (5) July 27 to 29, Dst = −47 nT; (6) August 19 to 21, Dst = −71 nT.

The ionopheric stations names and their coordinates are listed in the Table 1.

Table 1: The list of ionospheric stations.

Station	Geographic latitude	Geographic longitude	Dip-latitude
Zhigansk	66.3°	123.4° (8.2 h)	55.2°
Yakutsk	62.0°	129.6° (8.6 h)	50.9°
Hainan	19.5°	109.1° (7.3 h)	8.1°

3. ANALYSIS AND RESULTS

Some properties of SF observed at the three stations during the six storms have been studied. Fig. 1 shows the occurrence features of SF at the high and the low latitude stations during the storm time from March 6 to 8, 2006. In Fig. 1, abscissa denotes universal time (UT) from 00 : 00 on March 4 to 24 : 00 on March 10, y-axis denote Dst value as shown in blue curve. From top to bottom patterns in Fig. 1, different types of SF are presented in turn for Zhigansk, Yakutsk and Hainan stations. Different box stands for different type of SF, i.e., FSF, RSF, MSF and SSF (please see that indicated beside the figure), respectively. The left and right sidelines of the box correspond to the start and ending time of SF, width of the box represent the SF duration.

From Fig. 1, we can see that, at all the three stations, the SF was observed in an extended period including pre-storm and post-storm times from March 4 to 10. The SF mainly occurred in the night time at the three stations, and the occurrence rate of SF at the high latitude stations is higher than that at Hainan station. The SSF only occurred at Hainan station (from 21 : 30 LT to 22 : 30 LT on March 4).

During the storm time from March 6 to 8, the SF was found at the two high latitude stations (Zhigansk and Yakutsk). The SF mainly took place in the night time over the two stations, and was more active over Yakutsk station. However, it is worth noting that SF was detected not only in night time, but also in the afternoon (from 17 : 30 to 18 : 15 LT) on March 7, and in the morning (from 8 : 15 to 12 : 00 LT) on March 8. However, SF has not been found at the low latitude Hainan station during the storm time.

During the post-storm time, from March 9 to 10, the SF still mainly occurred in the night time over the two high latitude stations, while SF was not found at Hainan Station.

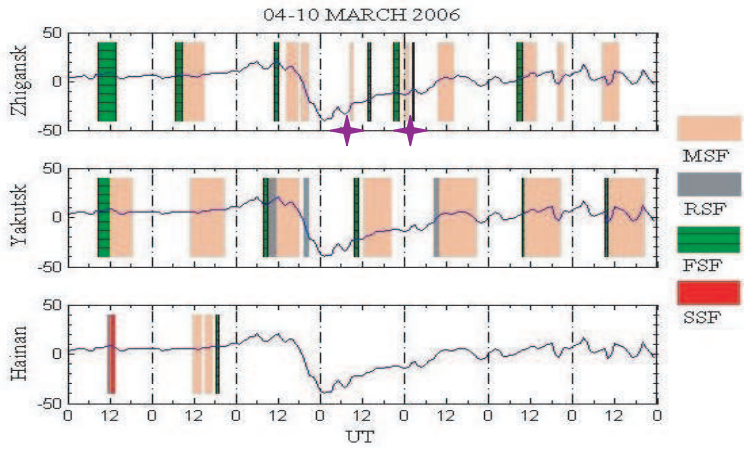

Figure 1: SF features observed at the three stations during the storm time on March 6–8, 2006.

In total, the SF mainly occurred at night over the high latitude stations, and the appearance of SF over Yakutsk was more active than that over Zhigansk and Hainan. From the view of start

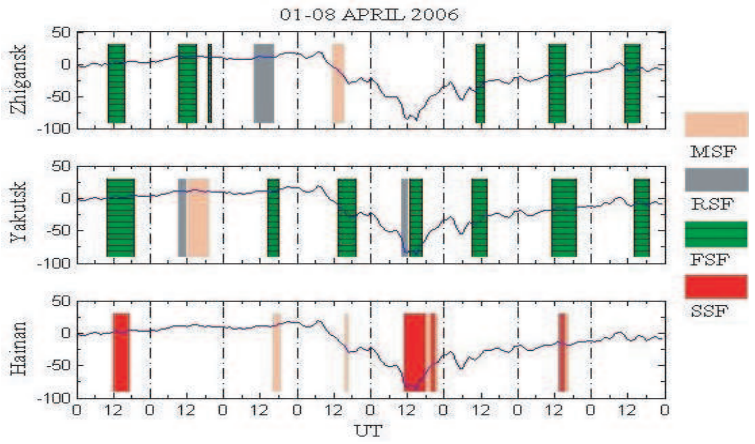

Figure 2: SF features observed at the three stations during the storm time on April 4–6, 2006.

time of SF observed at the three stations, we can say that the start time of SF will be later if the latitude of the station is lower.

Figure 2 shows the occurrence features of SF over the high and the low latitude stations during the storm time from April 4 to 6, 2006. The function of the Fig. 2 is similar to that of Fig. 1

From Fig. 2, we can see that SF in the ionosphere over the Yakutsk station was more active than that over the Zhigansk (with latitude higher than Yakutsk's) and Hainan (low latitude) stations. The SF also mainly occurred in the night time for all the three stations. Also, the start time of SF observed will be later if the latitude of the station is lower.

From Fig. 2, we can also see that SF was found in the ionosphere over Yakutsk and Hainan stations while it disappeared over Zhigansk station in night of April 5. In fact, at Zhigansk station, SF was found several days before and after April 5 of 2006 but echo signals of ionograms in the night of the April 5 were very weak and disappeared sometimes. Therefore, the reason for SF was not found over Zhigansk on the April 5 may be that the storm enhanced ionospheric absorption of radio wave over Zhigansk station, which results in no signal return and SF couldn't be found. Furthermore, SSF associated with equatorial plasma bubble was found over Hainan station around midnight of the April 5 and lasted about 6 hours. Again SSF shortly occurred over Hainan at midnight of April 7 of 2006 after the storm time.

We also analyzed SF in the other four storm times. The results were similar to those of the two storm times. It should be mentioned that, at the high latitude stations, there was no BSF observed during the six storms, but it can be observed in other time.

4. CONCLUSIONS

We used the data from DPS-4 digisondes located at high and low latitude regions to study ionospheric sprand-F properties during geomagnetic storm time. The stations are: Hainan station with dip-latitude of 8.1°N, Yakutsk station with dip-latitude of 50.9°N, and Zhigansk station with dip-latitude of 55.2°N. According to the observation at Hainan station, from the RSF we drawn a so called SSF which is indicative of equatorial plasma bubble as an independent type of SF to do research. Six storm times in 2006 were selected for this study. The main results are as follows.

(1) In the six storm times, in the ionosphere over the Zhigansk station, SF can be found in the afternoon and morning. But over the Yakutsk and the Hainan station, SF can only be found in the night time. SF over the Yakutsk station was more active than that over the Zhigansk station. Maybe it is because that absorption of radio wave is too strong in ionosphere over there.

(2) The SSF which concerned with the equatorial plasma bubble in the low latitude ionosphere is only found at the low latitude station Hainan, but not found at the high latitude stations Yakutsk and Zhigansk. The branch SF is never found at the low latitude station Hainan but it can be found at the high latitude stations Yakutsk and Zhigansk.

(3) The start time of SF will be later if the latitude of the station is lower. This implies that propagation of the plasma instability which caused the ionospheric irregularities is from the high latitude ionosphere to the low latitude.

In this paper, combining the observation and some theoretic theory, we also made some discussions on some properties of SF observed at the three stations. The properties of SF from the

high latitude region to the low latitude region and its physics mechanism still need to be further investigated, for example, for the BSF only occurred at the high latitude ionosphere and never occur at the low latitude ionosphere. Especially, for the propagation of the plasma instability caused ionospheric irregularities from the high latitude ionosphere to the low latitude, we need further observation and theoretical study to understand it.

ACKNOWLEDGMENT

This research work is supported by the Natural Science Foundation of China grants 40904039, 41074114, 40921063 and by the Project Supported by the Specialized Research Fund for State Key Laboratories.

REFERENCES

1. Booker, H. G., and H. W. Wells, "Scattering of radio waves by the F-region of the ionosphere," *Terr. Magn. Atmos. Electr.*, Vol. 43, No. 3, 249–256, 1938, doi:10.1029/TE043i003p00249.
2. Maruyama, T. and N. Matuura, "Longitudinal variability of annual changes in activity of equatorial spread F and plasma bubbles," *J. Geophys. Res.*, Vol. 89, No. A12, 10,903–10,912, 1984, doi:10.1029/JA089iA12p10903.
3. Aarons, J., "The longitudinal morphology of equatorial F layer irregularities relevant to their occurrence," *Space Sci. Rev.*, Vol. 63, 209, 1993.
4. Fejer, B. G., L. Scherliess, and E. R. de Paula, "Effects of the vertical plasma drift velocity on the generation and evolution of equatorial spread F," *J. Geophys. Res.*, Vol. 104, No. A9, 19,859–19,869, 1999, doi:10.1029/ 1999JA900271.
5. Huang, C., W. Burke, J. Machuzak, L. Gentile, and P. Sultan, "DMSP observations of equatorial plasma bubbles in the topside ionosphere near solar maximum," *J. Geophys. Res.*, Vol. 106, 8131, 2001.
6. Lyon, A., N. Skinner, and R. Wright, "The belt of equatorial spread-F," *J. Atmos. Terr. Phys.*, Vol. 19, 145, 1960.
7. Aarons, J., et al., "Seasonal and geomagnetic control of equatorial scintillations in two longitudinal sectors," *J. Atmos. Terr. Phys.*, Vol. 42, 861, 1980.
8. Rastogi, R., J. Mullen, and E. MacKenzie, "Effect of geomagnetic activity on equatorial radio VHF scintillations and spread F," *J. Geophys. Res.*, Vol. 86, 3661, 1981.
9. Xiong, N. L., C. C. Tang, and X. J. Li, *Introduction to Ionospheric Physics*, Wuhan, 1999.
10. Singleton, D. G., "The morphology of spread-F occurrence over half a sunspot cycle," *J. Geophys. Res.*, Vol. 73, No. 1, 295–308, 1968, doi:10.1029/JA073i001p00295.
11. Piggott, W. R. and K. Rawer, *URSI Handbook of Ionogram Interpretation and Reduction*, 2nd Edition, 4-21–4-22, 1978.
12. Argo, P. E. and M. C. Kelley, "Digital ionosonde observations during equatorial spread F," *J. Geophys. Res.*, Vol. 91, No. A5, 5539–5555, 1986, doi:10.1029/JA091iA05p05539.
13. Wang, G. J., J. K. Shi, et al., "Seasonal variation of spread-F observed in Hainan," *Advances in Space Research*, Vol. 41, No. 4, 639–644, 2008.
14. Wang, G. J., J. K. Shi, et al., "The statistical properties of spread F observed at Hainan station during the declining period of the 23rd solar cycle," *Annales Geophysicae*, Vol. 28, No. 6, 1263–1271, 2010.
15. Wang, G. J., J. K. Shi, et al., "Strong range spread-F characteristics observed in Hainan during intense storm," *Chin. J. Space Sci.*, Vol. 27, No. 5, 379–383, 2007.

Monitoring of Thermal Dome as an Iridescent Sphere above the Atmosphere

Shigehisa Nakamura
Kyoto University, Japan

Abstract— This work concerns to a thermal dome as an iridescent sphere appeared above the atmosphere. The author is a modeling for realize what is a possible process of iridescent sphere above the atmosphere in a physical scope. One of the iridescent spheres in the photographic illustration must be caused by a explosive thermal energy release. A simple formulation for the thermal dome may be effective for understanding the process of the thermal dome above the atmosphere. The author would introduce a key to see the physical process of this thermal dome formation.

1. INTRODUCTION

In this work, a process is noted by a model for a thermal dome as an iridescent sphere appeared above the atmosphere in a scope of fluid dynamics. By this time, the author has had monitored the thermal patterns on the ocean surface. His interest is also in the physical process of a thermal dome above the atmosphere. One of the keys must be obtained by introducing a dynamical model. In order to realize this process the author introduced some note in relation to a similar process ever seen on the earth surface.

2. DATA SOURCE

One example of the iridescent spheres appeared above the atmosphere off Scandinavia and northern China in 1988 [1]. The data is found in a form of photographic illustration. That is, Reed [1] introduced one of the typical illustrations of the iridescent spheres. This illustration was one example provided by Danny Stillman. In this work, simply the author would focus his interest to introducing a physical model of the thermal dome.

3. ATMOSPHERIC LAYER

The interested atmospheric layer in this work must be between tropopause and earth surface. This layer is called as troposphere. In the troposphere, atmospheric convection is taken to be constructed to be a conservative system. In the troposphere, vertical distribution of the atmospheric temperature can be described as

$$T(z) = \Gamma z + T_0 \tag{1}$$

where, $T(z)$ is an equivalent potential temperature at the height z above the earth surface, and $T_0 = T(z = 0)$. In the actual atmospheric layer, $\Gamma = 4°\mathrm{C}$ per 1000 m (for example, Kimura, [2]).

4. FORMULATION

In the scope of hydrodynamics, a model is introduced in a form of mathematical formulation. Generally, the model should be for three dimensional in process. Essentially, the equation of motion introduced is nonlinear, though a linealized approximation in the equation could be considered with a fairly good approximation. In this case, the equation for the potential temperature should be also introduced.

5. CONDITIONS

In the model, boundary conditions must be considered for T on the earth surface and the tropopause. Mean field of the winds is excluded so that the disturbances can be obtained an approximated solution solving the linealized equation. Nevertheless, a case of a thermal sphere above the atmosphere can be taken as free from the boundary conditions, if the thickness of the atmospheric layer is large enough comparing to the scale of the thermal dome in interest.

Several cases must be considered at solving the equation to see the process. That is,

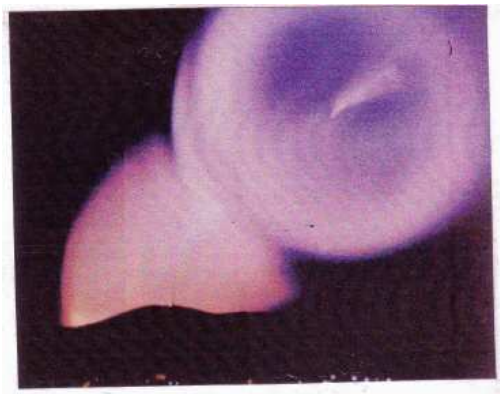

Figure 1: One example of the iridescent spheres above the atmosphere off Scandinavia. (by the courtesy of T. C. Reed and Danny Stillman)

(1) Fireworks using a gunpowder in a classic manner
   (a) Shoot up vertically in order to get the capsule up to the aimed altitude,
   (b) The trigger let the capsule to fire at no vertical motion where the capsule in height of the aimed altitude successfully.
(2) Environment control by using dynamite
   (a) Set up the position of the firing operation in the schedule,
   (b) Follow the land-cruisers, shovels, and scrapers,
   (c) Pass a roll over for flatten the ground surface or the related operations.
(3) Operate to fire or crush in the certain position in the atmospheric layer
   (a) Shoot up a capsule containing a gunpowder, or trinitrotoluene, or nuclear reactor,
   (b) Control to work the trigger for firing or for the purpose in plan.

to the details, it is recommended to refer to the other related guidelines.

6. DISCUSSIONS

For a convenience, the author here introduce some discussions about the illustration as shown in Figure 1 in order to realize the process of a thermal dome formation. Looking at the pattern of the dome, it can be seen that a point source moving in the atmospheric layer at the trigger for firing in operation. A line of light in the dome area seems to be suggesting the orbit of the capsule on a ballistic orbit. The author has,no data to the details so that it seems too hard to tell a certain deterministic notice. Nevertheless, the past examples of the explosive thermal energy release are taken to show us an essentially common process is found in the illustration. What is essential is axis of the acceleration.

Reed [1] noted that the thermal dome is expanded very rapidly, at around 3 km/s, with the centers remaining quite transparent. The author has no idea to give any comment for the speed of the dome expanding. Although, it is sure that this speed is about one third of the critical velocity on the ballistic orbit, and is also approximately one third of the speed of an existing satellite in the steady polar orbital motion.

As far as the author concerns, he thinks that it is hard to give any deterministic notice under this condition without any detail of the scientific data in need.

7. CONCLUSIONS

A model of a thermal dome above the atmosphere is introduced in order to what process was in the illustration including an ilidescent sphere. With consideration of the related factors and conditions, the author may take it as that the illustration is showing a thermal dome formed around the axis of the acceleration along the ballistic orbit.

REFERENCES

1. Reed, T. C., "The Chinese nuclear tests, 1964–1996," *Physics Today*, Vol. 61, No. 9, 47–53, the American Institute of Physics, September 2008.
2. Kimura, R., *Introduction to Geophysical Hydrodynamics*, 247, Tokyo-Do Publisher, Tokyo, 1983.

Monitoring of Thermal Dome in the Earth Surface Layer

Shigehisa Nakamura
Kyoto University, Japan

Abstract— In order to see specific pattern of the monitored thermal dome formed on the atmospheric layer on the earth, a model is introduced for helping to obtain the pattern of the thermal dome in a form of mathematical expression. The solution is constructed by the interesting factors at determining the shape of the thermal dome envelope. Some note is given to remark for various cases of actual pattern under impulsive and steady heat sources.

1. INTRODUCTION

In order to see specific pattern of the thermal dome found in the atmospheric layer on the earth. For a convenience, a formulation is introduced for a model of the interested thermal dome. Generally, problem is for a nonlinear process. Approximated formulation might give us a mathematical description in convenience. A solution for a linear equation of flow in the interested layer could be a suggestion for an actual thermal process. A numerical model must be convenient for obtaining a solution approximately though it is hard yet to identlfy any model is properly applicable to the actual processes of thermal dome formation. Several actual cases are introduced briefly with some notes.

2. MODEL OF THERMAL DOME

In order to describe a thermal dome in the atmospheric layer on the earth surface, it is used that a model is assumed to be constructed by a formulation of fluid dynamics of atmosphere in the troposphere defined as that between the tropopause and the earth surface. In the troposphere, vertical distribution of the atmospheric temperature can be described as follows,

$$T(z) = \Gamma_z + T_0, \tag{1}$$

where, $T(z)$ is an equivalent potential temperature at the height z above the earth surface, and $T_0 = T\,(z = 0)$. In the actual atmospheric layer, $\Gamma = 4$ degree C per 1000 m (for example, Kimura, [1]).

As for a case of heat island in an urban area, Kimura had given a brief note with his model for application to the case in the city area of Tokyo [2]. In his work, a thermal dome is a model for an urban area in a local small area on the earth with an assumption of a centered steady heat source in an interested thermal dome.

3. FORMULATION

In order to formulate a process in this work, now, a recti-linear coordinate system of $(0 - x, y, z)$ with the vertical axis (z) is introduced as the reference.

Assume a heat source located at the origin of the coordinate system, the thermal dome modeling in a stratified atmospheric layer on the earth surface can be formulated to make ease in a mathematical reduction at obtaining a solution. In this case, the expression form can be simplified as follows, i.e.,

$$[u(x, y, z; t), v(x, y, z; t), w(x, y, z; t), p(x, y, z; t)] = [u(r; t), v(r; t), w(r; t), p(r; t)]. \tag{2}$$

With what is noted above, the equation of motion for the interesting model can be written in a form as follows, for the velocity field of $U = u$ and the pressure field p,

$$(\partial U/\partial t) + U\nabla U = -(1/\rho)\nabla p + \nabla(v\nabla U), \tag{3}$$

where the desity field ρ in a layer of isotropic air particles with a dynamic viscosity constant $v(= \mu/\rho)$ in brief, though the exact expression of v in a general form must be a tensor.

As for the equation of potential temperature in the thermal field, it can be written as

$$(\partial T/\partial t) + U\nabla T = \nabla(\kappa\nabla T), \tag{4}$$

where the notation κ for diffusion coefficient (as an approximation of tensor).

4. TWO DIMENSIONAL STEADY PROCESS

As for a two dimensional process, the above Equations (2), (3) and (4) form a simultaneous equation system for the case of two dimensional problem on heat island or cool island [2]. In this work, a set of approximated Linear equations is considered for obtain an asymptotic solution in the atmospheric layer on the earth surface.

The boundary conditions are as follow for convenience, i.e.,

$$u = 0,\ w = 0,\quad \text{and}\quad T = T_0 \cos kx,\quad \text{for}\quad z = 0, \tag{5}$$

and

$$u \to 0,\ w \to 0,\quad \text{and}\quad T \to 0,\quad \text{for}\quad z \to \infty, \tag{6}$$

After rewriting introducing several parameters and applying the Cauchy-Rieman relation to introduce a stream function, the reduced form of the equation is obtained as follows,

$$(\partial^2 T/\partial x^2) + (E_0^2/Pr)(\partial^6 T/\partial z^6) = 0, \tag{7}$$

where, $E_0 = v^2/(\alpha g \Gamma L^4)$, and $Pr = v/\kappa$. When rewriting the above (6) after introducing that $(l/Ra) = (E_0^2/Pr)$ with a consideration of z/δ, then, an order estimation of the thermal dome formation in scale must be expected as that evaluated $\delta^6 = (l/Ra)$. In the equation of the above (7), time factor is implicit under the specific assumptions and conditions.

5. VERTICAL SECTION OF THERMAL DOME

The solution of the Equation (7) can be obtained with an assumption of $T = \theta(\eta)\cos kx$ for $\eta = z/\delta$. Now, the equation is rewritten as

$$(d^6\theta/d\eta^6) = k^2\theta \tag{8}$$

Substituting $\theta = \exp(\sigma\lambda\eta)$ with $\sigma^6 = k^2$, then, $\lambda^6 = 1$. So that, six eigen values of the Equation (8) are expected. The Equation (8) have six roots, nevertheless three roots in term of positive real part do not satisify the boundary condition for $z \to 0$. Then, the solution satisfying the necessary conditions for $z = 0$ can be written as

$$\theta = (1/2)\exp(-\sigma\eta) + (1/\sqrt{3})\exp(-\sigma\eta/2)\cos[(\sqrt{3}/2)\sigma\eta - (\pi/6)] \tag{9}$$

The author has now obtained a solution for the interested two dimensional problem in a vertical cross section with the vertical axis passing the origin in the coordinates. Obtained solution tells us that a form of the interested thermal dome is determined by the heat source pattern on the earth surface. An assumption makes it possible to describe the heat source pattern by a mathematical function.

6. IMPULSIVE THERMAL ENERGY RELEASE

In the actual case of an impulsive thermal energy release, it is hard to measure the related dynamical and physical factors in the interested area covering the thermal dome with a centered thermal source.

In a case of an impulsive thermal energy release, process of a thermal dome formation must surely be transitional. It must be not visible to see a thermal dome formation.

Adding to the above noted, an explosive thermal energy release must be a shock front in a form of a semi-sphere on the earth surface.

Growing stage of the thermal dome must be seen to find a transparent dome with a centered column of the upwelling flow with a circular shock front on the earth surface.

It can be seen in a photographic monitoring on board of an aircraft, for example. There might be many cases though the author would introduce some typical cases.

In Figure 1, a photographic monitoring (courtesy of USAF) is introduced in order to see a visible pattern of the typical one case of the explosive thermal energy releases [3]. This shows a column at the centered thermal source where an impulsive energy was released just 500 m above the ground surface. The circular ring of the white clouds shows the shock front on the ground surface around the thermal source. This thermal pattern could be understood by a simple two-dimensional model (for example, [1] and [2]). Nevertheless, it is necessary to find a numerical solution for a three-dimensional thermal process under several conditions.

In Figure 2, a photograph (courtesy of USAF) is introduced a thermal dome as a visible pattern for a case of the explosive thermal energy release just under the sea surface in the ocean. The

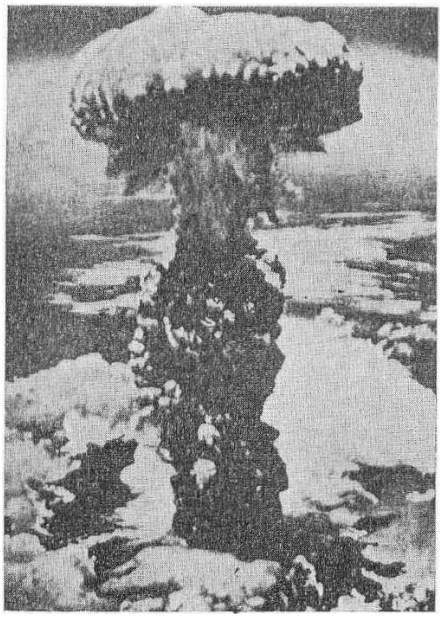

Figure 1: Thermal dome pattern at an explosive nuclear energy release on 9 Auguest 1945 at Nagasaki [3], (by the courtesy of USAF).

Figure 2: Thermal dome pattern at an explosive nuclear energy release on 1 March 1954 at Bikini Lagoon, in the western Pacific [4] (by the courtesy of USAF).

vertical column of the water mass is seen to form the thermal dome in the stratified atmospheric layer just above the centered thermal source. In the photograph, it can be seen a set of multiple thermal dome in a high air induced after the thermal impact at the thermal releasing center, on the sea surface, and on the sea floor of the Atoll [4]. A cloud ring can be seen in the photograph on the sea surface at distance as a signal to show where the shock front is propagating. A thermal front in a two-dimensional model might be completely different from the actual transitional thermal front even in the stratified atmospheric layer on the ocean.

This thermal pattern in Figure 2 is obtained as a picture for demonstrating a visible pattern. So that, it should be followed by a successive numerical modeling in order to detect three-dimensional thermal pattern which might be realized in the electromagnetic waves in the infrared band.

One of the other examples is an iridescent spheres appeared above the atmosphere [5]. Reed [5] noted that the thermal dome is expanded very rapidly, at around 3 km/s, with the center remaining quite transparent. The author has no idea to give any comment for the speed of the dome expanding without some additional data and information. Nevertheless, it is sure that this speed is about one third of the critical velocity on the ballistic orbit for the unidentified flying material. Adding to that, the speed of the above iridescent sphere is approximately one third of the speed of an existing satellite in the steady polar orbital motion. At this stage, it seems to be hard to give any deterministic notice under the author's stand point without any additional scientific data in need.

7. DISCUSSIONS

The author has introduced first a simple model for mathematical solution for a thermal dome in the atmospheric layer on the earth surface. This solution suggests a specific structure of the atmospheric convection at the core of the thermal dome in fact. The specific photographs are ever obtained by the optical camera (in the visible band) on board of an air craft. Some of these are the examples of an explosive nuclear energy release (for example, [3] and [4]). An illustration is given in the photographs in Figures 1 and 2. Each of the cases in the figures is a shot at an instance of the transitional process, though each of the photographs shows that the final stage of the energy release supports approximately the model of a thermal dome pattern. In the model, it is referred to consideration in an approximated formulation for a mathematical solution with an infinitely asymptotic solution. The solution is apparently independent of the time factor in this work under the assumptions and the given conditions. This solution could help us at realizing the pattern in a scope of physical process even though the mathematical model of the two dimensional ones should be taken as an approximated thermal dome pattern.

An application of the model introduced in this work might be well considered for the heat island developed in the urban area seems to be supporting the solution in this work [2] apparently. Adding to the above, a case of continuous volcanic explosions could be realized even though the volcanic processes are not so simple in fact.

A set of approximated linear equations are introduced for a key to the formulation or to a numerical modeling in a more advanced step after some example for an illustration in this work, the solution looks to be supported by the optical monitoring of the thermal dome in the atmospheric layer on the earth boldly. A nonlinear problem with a consideration of time variable must be raised for the next step in order to promote the related research works.

8. CONCLUSIONS

The author noted some specific pattern of the thermal dome first as a solution in an approximated linear problem in relation to a possible pattern of the thermal dome in the actual atmospheric layer on the earth surface. Some remarks are given for application of the thermal dome model. Exactly speaking, a three-dimensional model must be developed for the next step in order to have an advanced dynamical understanding of this work. It should be made to see what is the thermal structure inside the thermal dome. A more advanced research is expected for understanding the thermal dome formation process.

REFERENCES

1. Shono, S., *Introduction to Geophysical Hydrodynamics*, 247, Tokyo-Do Publisher, Tokyo, 1983.
2. Kimura, R., "Dynamics of steady convections over heat and cool islands," *Journal of Meteorological Society of Japan*, Vo1. 53, 440–457, 1975.
3. Araki, T. and H. Motojima, *The Effects of Explosive Nuclear Energy Releases at Hirosima and Nagasaki*, 504, Iwanami Publishers, Tokyo, 1979.
4. Kawasaki, S., Fukuryuumaru, No. 5 Mmorial, Tokyo East Park, Tokyo, 104, 2004.
5. Reed, T. C., "The Chinese nuclear tests 1964–1996," *Physics Tiday*, Vo1. 61, No. 9, 47–53, AIP (the American Institute of Physics), 2008.

Monitoring of Thermal Dome Shock Front Pattern on the Earth

Shigehisa Nakamura
Kyoto University, Japan

Abstract— This is a note about a case of thermal dome formed after an explosive energy release in the ocean surface layer on the Earth. A theoretical model is introduced for realizing the pattern of the thermal dome in a mathematical expression. The solution is constructed by the main factors related to the physical process of the dome formation. Some notices are given to see what about the actual pattern was monitored.

1. INTRODUCTION

In order to realize specific pattern of the thermal dome formed in the atmospheric layer on the ocean surface layer covering a coral lagoon on the Earth crust. For a convenience, a linear formulation is introduced under an assumption of no circular motion around a thermal source point. A solution is expressed by several physical factors which help us to see what specific thermal dome pattern is. Actually the process of the thermal dome must be a kind of non-linear one, nevertheless an approximated process could be obtained by solving a linear problem. Then, it could be given some remarks for the following works to an advanced research and applications.

2. SAMPLE CASE OF THERMAL DOME

In order to demonstrate a thermal dome in the atmospheric layer above the ocean surface layer which covering a coral lagoon on the Earth crust, a model is assumed to be constructed by a fluid dynamics of atmosphere in the troposphere between the tropopause and the Earth surface.

In the troposphere, vertical distribution of the atmospheric temperature can be described as

$$T(z) = \Gamma_z + T_0 \tag{1}$$

where, $T(z)$ is an equivalent potential temperature at the height above the sea surface, and $T_0 = T(z = O)$. In the actual atmospheric layer, it can be expressed as $\Gamma = 4°\mathrm{C}$ per 1000 m (for example, [1])

As for a case of heat island in an urban area, Kimura had written his brief note in his publication [2]. In this case, a local small area on the Earth surface is assumed as a heat source (positive for heating or negative for cooling) of the thermal dome formed on land. There has no land surface condition considered except the atmospheric condition.

As for the ocean surface layer, an assumption is as that the uniform thermal layer of the sea water about 200 m or less. Under the sea surface, a spread of coral lagoons is considered to cover the Earth crust.

A heat source is assumed to be a point source just under the ocean surface.

As for the mean field of winds above the sea surface, this field is excluded out of the resultant field of the winds in order to distinguish the variations of the wind field which is generated and affected by an energy release at the heat source located at the origin of a co-ordinates system. When the heat source is assumed to be located at a point, a convenient co-ordinates system must be in a semi-spherical field on the sea surface, and a cross section of the interested thermal dome might be expected as a semi-circular space above the sea surface.

3. FORMULATION

Now, assuming a semi-spherical co-ordinates system (r, θ, ϕ; t), each of the velocity components in the interested field can be expressed by gradient of r, θ, and ϕ, respectively. Considering the axis of r is taken to be vertical positive and the plane formed by the axes θ and ϕ fit on the ocean surface with the origin 0, then, the velocity field can be expressed as follow if the angular velocity is negligible for an assumption of only rotational motion but any motion across the circular shell of the semi-sphere. That is,

$$[u(r,\theta,\phi;t), v(r,\theta,\phi;t), w(r,\theta,\phi;t)] = [u(r,\theta;t), v(r,\theta;t), w(r,\theta;t)] \tag{2}$$

when zero velocity for the radial component of ϕ.

Then, equation of motion for the interested process is written as foflow for the cross section:

$$(\partial u/\partial t) + u(\partial u/\partial t) + v(1/r)(\partial u/\partial \theta) = -(1/\rho)(1/r)(\partial p/\partial r) + \alpha g T + \nabla(\nu \nabla u) \tag{3}$$

and,

$$(\partial v/\partial t) + u(\partial v/\partial r) + v(1/r)(\partial v/\partial \theta) = -(1/\rho)(-\partial p/\partial \theta) + \nabla(\nu \nabla v) \tag{4}$$

As for the equation of potential temperature in the atmospheric layer,

$$(\partial T/\partial t) + u(\partial T/\partial r) + v(1/r)(\partial T v/\partial \theta) + v\Gamma = \nabla(\kappa \nabla T) \tag{5}$$

When the thermal energy radiation is radiated at the point source located at the origin, the thermal disturbances out of the heat source is essentially propagate radial.

4. PATTERN OF THERMAL DOME

In a case of thermal dome produced by the enormous amount of thermal energy release as a result of a nuclear reaction process, it can be expected a radial propagation of the front formed by the thermal energy radiation quickly before any thermal convective motion is induced in the atmospheric zone. A spherical shock front might be formed even if any human body was on the paths of the thermal radiation.

When the energy was radiated after a nuclear reaction, the first radiation should be propagated in the speed of the electromagnetic waves (that is to say, instantaneously). Then, thermal energy must be followed to that after completing the energy exchange process between the radiation beams out of the source and the atomic or molecular particles on the paths of the radiations of the electromagnetic power out of the source. This might be called "Fire Ball". With the time elapse, the fire ball grew quickly in a short time. Inside of the fire ball, there might had been generated the complicated motions of the atmosphere trapped by the fire ball. The thermal energy in the fire ball might surely be diffused out across the surface of the fire ball.

The ocean water might be forced to be activated by the nuclear effect though the thermal effect to the ocean surface water was easily happened to generate an evaporated water mass pinnacle at the origin. The water vapor must have formed a dense cloudy column to make a mushroom shape shell just as the thermal front of the dome. The growth of the speed was so quick that there must surely be generated a spherical shock front because this speed is beyond the propagation speed of the electromagnetic waves induced by the nuclear reaction. One of the examples is shown in Figure 1. To the details, it must be seen in the other publications appeared already in the past [3].

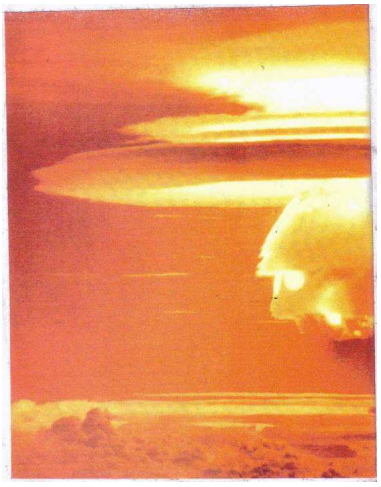

Figure 1: Thermal dome pattern at an explosive nuclear energy release on 1 March 1954 at Bikini Lagoon in the Northwestern Pacific (by the courtesy of USAF).

5. EXPLOSIVE THERMAL ENERGY RELEASE

In Figure 1, a case of the explosive thermal energy releases is introduced. There might be any cases of the other similar thermal processes.

The author would here give a note to several patterns of the energy release.

(1) One of the most primitive examples is to make a fire by burning of wood tips or of charcoal carbon tips.
(2) Fossil fuels are effective in the history of the human activity.
(3) Dynamite is one of the typical materials as an explosive thermal energy release must be effective in practical purpose for public works. The dynamite was used for battle in the past.
(4) Nuclear reaction has been utilized for the electric power supply for the public works and citizen services under a well-controlled power release system. Nevertheless, the nuclear reaction (atomic fissures and/or fusions) was used in the world war in order to assure that this was effective to make an explosive thermal energy release as was widely known.
(5) Primitive nuclear reaction can be make an effective explosive thermal energy release after a trigger strong radiation beam to activate the all of the constituents in the atmosphere, in the waters and on the land surface. The activated materials are changed to be another form of forced radioactive materials which consist in any form of ashes produced at the nuclear reaction by the explosive energy release.
(6) The activated ashes were transferred into the atmospheric layer after induced convective winds to diffuse out around the surrounding areas.
(7) As for the case introduced in Figure 1, the ocean water and coral pieces are activated to be

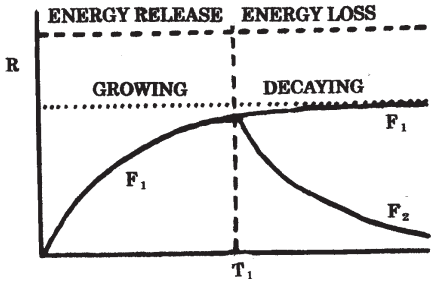

Figure 2: Schematic relation of thermal shock front in relation to energy release model.

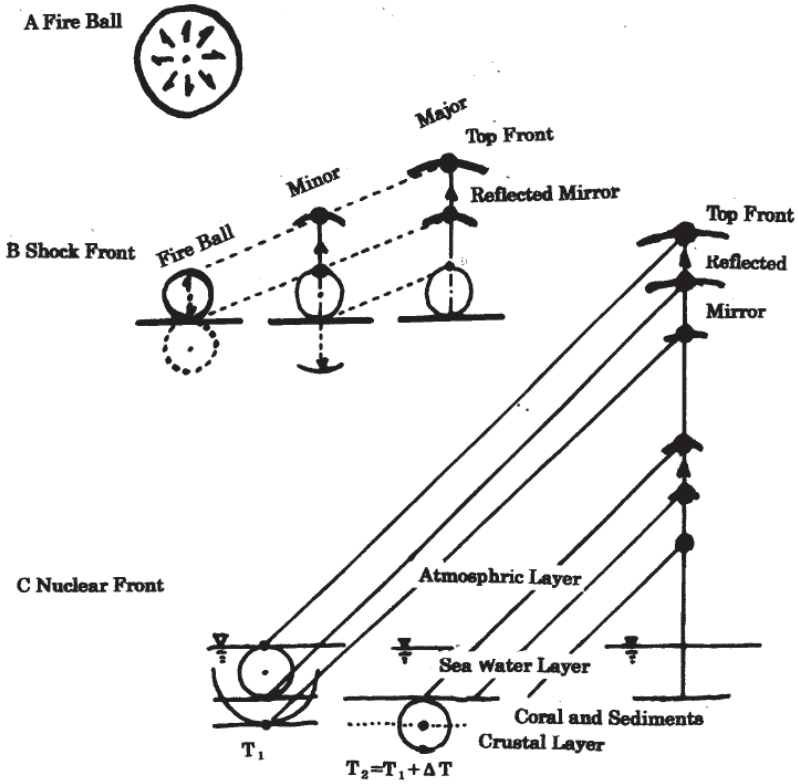

Figure 3: Evolution of thermal shock front pattern. A-Fire Ball, B-Shock front on the Earth surface, C-Shock front above the sea.

the contents of the strong radioactive isotopes. The accuracy of the trigger at each nuclear reactor must be caused to form a crown cap as a set of the main three sheets. The reflected radiations and shock front must be effective to form the minor set of the caps under the main caps set. The shock front in form of a fringe of the cloud on the land surface can be seen.

(8) The first step was the radioactive isotopes production in advance of the shock front in the atmospheric layer as a thermal dome.

(9) The explosive thermal energy release was the second step in the case of the nuclear reaction in the case of Figure 1.

To the details, it could be found what was seen at that time in the other publications.

6. CONCLUSIONS

The author has had a chance to see a process of a thermal dome after an energy release at a point source. Especially, the thermal energy is generated by a nuclear energy release might cause to form a shock wave as a front of the thermal dome in a form of a fire ball. The author could introduce in this work one of the examples out of the photographs of a thermal dome formed after a nuclear energy release on the ocean surface layer. This is a key to promote an advanced research successively.

REFERENCES

1. Kimura, R., *Introduction to Geophysical Hydrodynamics*, 247, Tokyo-Do Publishers, Tokyo, 1983.
2. Kimura, R., "Dynamics of steady convections over heat and cool islands," *Journal of Meteorological Society of Japan*, Vol. 53, 440–457, 1975.
3. Kawasaki, S., *Fukuryuumaru-5 Memorial*, 104, Tokyo East Park, Tokyo, 2004.